

Materials

FY 2023 Annual Progress Report

Vehicle Technologies Office

(This page intentionally left blank)

Disclaimer

This report was prepared as an account of work sponsored by an agency of the United States government. Neither the United States government, nor any agency thereof, nor any of their employees, makes any warranty, express or implied, or assumes any legal liability or responsibility for the accuracy, completeness, or usefulness of any information, apparatus, product, or process disclosed or represents that its use would not infringe privately owned rights. Reference herein to any specific commercial product, process, or service by trade name, trademark, manufacturer, or otherwise does not necessarily constitute or imply its endorsement, recommendation, or favoring by the United States government or any agency thereof. The views and opinions of authors expressed herein do not necessarily state or reflect those of the United States government or any agency thereof.

Acknowledgments

First and foremost, the Principal Investigators (PIs) from industry, academia, and the national laboratories who supplied the content of these reports are to be acknowledged and commended for their outstanding research. It is their work that moves our nation forward to improve and make transportation more affordable, as well as increase energy security.

Thank you to the project managers at the National Energy Technology Laboratory for continued support administering these projects.

We would also like to acknowledge Idaho National Laboratory and Energetics for their help in preparing and publishing this report.

Jerry L. Gibbs

Acting Team Lead for the Materials Technology
Program and Technology Development Manager for
the Powertrain Materials Core Program
Vehicle Technologies Office

Christopher Schooler

Technology Development Manager
Automotive Metals and Multi-Material Joining of
Lightweight Materials
Vehicle Technologies Office

H. Felix Wu, Ph. D

Technology Development Manager
Carbon Fiber and Polymer Composites for
Lightweight Materials
Vehicle Technologies Office

Acronyms and Abbreviations

Symbols

β	a phase in a metal alloy
Δ	change (in a specific value)
ε	strain
η	viscosity
η'	metallic phase
μ	micron (when referring to size)
μ	viscosity (when used in Darcy's law)
μm	micrometer
$\mu\Omega$	microohm
Θ	designation used for microscale intermetallic precipitates mostly located at the grain boundaries in the as-cast state of aluminum
Θ'	designation for nanoscale intermetallic precipitates present in the grain interiors of cast-aluminum alloy
ρ	density (when referring to concentration)
σ	stress (or strength, when referring to physical properties)
T_{IPST}	symbol for the in-plane shear-strength
1D	one-dimensional
2D	two-dimensional
2NN	second nearest neighbor
2T	two sheet stack-up
24EMI	a liquid high-temperature performance 2-ethyl-4-methyl imidazole for use in filament winding, electrical laminates, coatings and laminating adhesives
3D	three-dimensional
3DP	three-dimensional printing
3T	three sheet stack-up
3Cr-XHTS	three chromium eXtreme High-Temperature Strength
316L	the low-carbon version of 316 stainless-steel commonly used in chemical and petrochemical industry, in food processing, pharmaceutical equipment, medical devices, in potable water, wastewater treatment, in marine applications and architectural applications near the seashore or in urban areas
4140	a medium-carbon alloy steel that contains manganese, molybdenum, and chromium that offers high-fatigue strength, excellent toughness, and impressive resistance to impact and abrasion
4XT	4X Technologies
5xxx	series designation for aluminum alloyed with magnesium
6xxx	series designation for aluminum alloyed with magnesium and silicon
7xxx	series designation for aluminum alloyed with zirconium

A

a	absorption rate
Å	angstrom
A	area
A _{ivf}	interfacial void area fraction
A2	designation for a disordered phase of material
A12	a high-strength hard aluminum that can be strengthened by heat-treatment with moderate plasticity in annealed, quenched and tempered, and hot states that is good for resistance spot-welding
A206	aluminum alloy having a high percent of copper (5%) with excellent strength at high-temperatures and excellent machinability
A319	aluminum alloy having a composition of 6% silicon and 3.5% copper alloy with 1.0 iron maximum that has excellent casting and machining characteristics and very good corrosion resistance and weldability
A356	aluminum alloy with greater elongation, higher strength, and considerably higher ductility than Alloy 356 because of lower iron content that is typically used for airframe castings, machine parts, truck chassis parts, aircraft and missile components, and structural parts requiring high-strength
A380	the most commonly specified aluminum alloy that has the best combination of casting, mechanical, and thermal properties; exhibits excellent fluidity, pressure tightness, and resistance to hot-cracking; and is used for a wide variety of products including chassis for electronic equipment, engine brackets, gearbox cases, household furniture, power, and hand tools
A383	a common aluminum die-casting alloy with a higher level of silicon and lower copper with improved corrosion resistance, resistance to hot-cracking, fluidity, and strength at elevated temperatures compared to A380
AA	Aluminum Association (when used with a series e.g., AA1100 series)
AA1100	a pure aluminum alloy with excellent forming characteristics and machinability, especially when the alloy is machined in hard temper
AA1350	a high aluminum content (99.5%) alloy that is highly conductive with good formability used in electronics
AA4043	a wrought aluminum alloy with good corrosion resistance typically used as filler material for welding of aluminum parts containing high amounts of 4.5% and 6.0% silicon
AA4047	aluminum silicon brazing or filler alloy with good corrosion resistance
AA5052	aluminum alloy most suited to forming operations, with good workability and higher strength than that of either 1100 or 3003. Although not heat-treatable, it is stronger than most of the 5xxx series of aluminums
AA5356	an alloy in the wrought aluminum-magnesium family (5000 or 5xxx series) used primarily used as welding filler
AA6022	heat-treatable low copper precipitation-hardenable aluminum sheet alloy containing 0.8% to 1.5% silicon, 0.45% to 0.70% magnesium, and 0.25% zinc

AA6061	precipitation-hardening aluminum alloy containing 0.8% to 1.2% magnesium and 0.4% to 0.8% silicon as its major alloying elements
AA6082	a medium strength alloy with excellent corrosion resistance and the highest strength of the 6000 series alloys used as a structural alloy
AA6101	aluminum alloy with good mechanical strength and high-electrical conductivity
AA6111	wrought aluminum alloy that is heat-treatable and possesses high-strength and excellent stretch-forming characteristics containing 0.6% to 1.1% silicon, 0.5% to 1.0% magnesium, 0.1% to 0.45% manganese, 0.5% to 0.9% copper, and 0.15% zinc
AA6451	aluminum alloy that combined aspects of both AA6111 and AA6016A and is essentially a lower level of copper (<0.4 wt.%) version of AA6111 used for production from recycled process scrap
AA7055	aluminum alloy containing zinc, magnesium, chromium, and copper as hardeners, as well as small amounts of iron, silicon, manganese, and titanium with the highest total strength, good fracture toughness, and a strong ability for fatigue crack propagation with a microstructure that is resistant to intergranular fracture and corrosion
AA7075	aluminum alloy with strength comparable to many steels, good fatigue strength, and average machinability
AA7085	a high-strength and high hardenability forging aluminum alloy that has excellent fracture toughness
ABAQUS or Abaqus	software suite for finite element analysis and computer-aided engineering
ABB Robotics	a robotics and machine automation suppliers with a comprehensive and integrated portfolio covering robots and machine automation solutions
<i>ab-initio</i>	an adjective meaning “starting from or based on first-principles”
ABL	acrylonitrile-butadiene-lignin
ABS	acrylonitrile-butadiene-styrene
A/cm ²	amps per square centimeter
ACMZ	designation for aluminum alloys containing aluminum, copper, manganese, and zirconium
ACNM	designation for aluminum alloys containing aluminum, cesium, nickel and manganese
AF	as-fabricated
AFD	aminophenyl disulfide
AFM	atomic force microscopy
Ag	silver
AI	artificial intelligence
AISI 8620	a steel commonly used as a low-alloy material for carburizing, with excellent carburizing response and good hardenability that has lower cost, better machinability, and availability
Al	aluminum
Al ₂ Ca	aluminum-calcium

Al-Ce-Ni	aluminum alloy demonstrating high mechanical properties at room and elevated temperatures along with good casting properties
Al ₂ Cu	aluminum-copper (2:1)
Al ₁₃ Fe ₄	a complex intermetallic phase that precipitates from cast-Al-Si alloys and is the most aluminum-rich intermetallic phase in the Al-Fe system
Al ₂ O ₃	aluminum oxide
Al ₃ Ni	nickel aluminide
AlSi10Mg	traditional cast-aluminum alloy used in aerospace and automotive applications because of its lightweight, low thermal expansion, and good weldability and mechanical properties
Al ₃ Zr	zirconium aluminide
Alloy 380	one of the most commonly specified aluminum alloys with the best combination of casting, mechanical, and thermal properties that exhibits excellent fluidity, pressure tightness, and resistance to hot-cracking and used for a wide variety of products including chassis for electronic equipment, engine brackets, gearbox cases, household furniture, power, and hand tools
Alloy 52100	a high carbon steel that develops very high hardness after heat-treatment to provide wear resistance
AM	additive manufacturing, additive manufactured, or additively manufactured (when referring to processes)
AM60	a castable magnesium alloy with excellent ductility, superior energy absorbing properties, and good strength and castability
ANL	Argonne National Laboratory
AOP	annual operating plan
AP	atmospheric plasma
APO	atmospheric plasma-oxidation
APS	Advanced Photon Source
APT	atom probe tomography
AS	as-solutionized (when referring to metallurgy)
AS	advancing side (when referring to a friction-stir processed nugget)
ASCENDS	<u>A</u> dvanced data <u>SCiEN</u> ce toolkit for non- <u>D</u> ata <u>SC</u> ientists
ASTM	American Society for Testing and Materials
ASTM B117	American Society for Testing and Materials standard test method for a controlled corrosive environment that has been used to produce relative corrosion resistance information for specimens of metals and coated metals exposed in a given test chamber
ASTM D454	American Society for Testing and Materials standard test method that is used in to evaluate the pull-off strength of air barrier membranes to verify product performance and field installations under real conditions

ASTM D638	American Society for Testing and Materials standard test method to determine the tensile strength of both reinforced and non-reinforced plastics
ASTM D790	American Society for Testing and Materials standard test method to determine the flexural (bending) properties of reinforced and unreinforced plastics, high-modulus composites, and electrical insulation materials
ASTM D2344	American Society for Testing and Materials test standard designed to measure the short-beam strength of high-modulus fiber-reinforced polymer matrix composites
ASTM D3039	American Society for Testing and Materials standard test method for tensile strength of composite materials
ASTM D3518	American Society for Testing and Materials standard test method for in-plane shear of composite materials
ASTM D5470	American Society for Testing and Materials standard that measures the steady-state thermal impedance of electrical insulating materials used to enhance heat-transfer in electrical and electronic applications
ASTM D7136	American Society for Testing and Materials standard test method to measure the damage resistance of a laminated composite plate subjected to a drop-weight impact event using a hemispherical striker
ASTM D7896-19	American Society for Testing and Materials standard test method for thermal conductivity, thermal diffusivity, and volumetric heat capacity of engine coolants and related fluids by a transient hot-wire liquid thermal conductivity method
ASTM E2248	American Society for Testing and Materials standard test method for impact testing of miniaturized Charpy v-notch specimens
at.%	atomic percent
ATR-FTIR	attenuated total reflectance – Fourier-transform infrared
a.u.	atomic unit
AutoML	automatically trained machine learning (model)
AUTO-SMART	Acellent Technologies, Inc. product name for a sensor system that assists with vehicle self-sufficiency
AZ31B	most widely available magnesium grade alloy, high-strength-to-weight ratio with a composition of 2.5% to 3.5% aluminum and 0.7% to 1.3% zinc
AZ91D	a high-purity magnesium cast alloy that has excellent corrosion resistance, excellent castability, and good strength
B	
B	boron
B2	designation for FeSi-type ordered phase
bal	balance
BCC or bcc	body-centered cubic
BEV	battery electric vehicle
BF	bright-field

BiW or BIW	body-in-white
BJAM	binder-jet additive manufacturing
BM	base material
BMS	battery monitoring system
BSE	backscatter electron
B/U	bending/unbending
C	
°C	degrees Centigrade
°C/min	degrees Centigrade per minute
°C/s	degrees Centigrade per second
C	carbon
C _p	specific heat capacity
C _s	chip size
C10100	copper that is oxygen-free with high-thermal-conductivity used for electrical and electronic conductors, wave guides, cavity resonators, super conductor matrixes, vacuum tube and solid-state devices, and glass to metal seals
C11000	copper that has high-electrical and thermal conductivity, good corrosion resistance and solderability used for welding fixtures, anodes, bus bar in electrical power installations, ground straps, commutators and current carrying hardware.
ca.	circa (approximately)
Ca	calcium
CA	cellular automation or cellular automata
CAD	computer-aided design (or drawing)
CADWIND	software for filament-wound composite materials used to optimize the winding process, save material costs, and achieve shorter production times
CALPHAD	<u>CAL</u> culat <u>ion</u> of <u>PHA</u> se <u>D</u> iagrams
CAN	covalent adaptable network
CAN-CFRC	covalent adaptable network-based carbon fiber-reinforced composite
CB	carbon black
CCB	cross car beam
CCF	continuous carbon fiber
Ce	cerium
CeO ₂	cerium dioxide or cerium(IV) oxide
CET	columnar to equiaxed transition
CF	carbon fiber
CF-ABS	carbon fiber-reinforced acrylonitrile-butadiene-styrene

CFC	carbon fiber composite
Cfm	cubic feet per minute
CFRC	carbon fiber-reinforced composite
CFRP	carbon fiber-reinforced polymer
CFRPPA	carbon-fiber-reinforced polyphthalamide
CFRV	carbon fiber-reinforced vitrimer
CFTF	Carbon Fiber Technology Facility
CLC	closed-loop control
cm	centimeter
cm ²	square centimeter
cm ³	cubic centimeter
cm ³ /min	cubic centimeter per minute
CNG	compressed natural gas
CNT	carbon nanotube
cN/tex	centiNewton per grams per 1,000 meters of fabric (tex)
Co	cobalt
CO ₂	carbon dioxide
CO ₂ e	carbon dioxide equivalent
COF or CoF	coefficient of friction
COMSOL	a cross-platform finite element analysis, solver, and multiphysics simulation software that allows conventional physics-based user interfaces and coupled systems of partial differential equations
COVID-19	coronavirus disease of 2019
cP	centipoise
CP	commercially pure (or procured)
CPEC	close proximity electromagnetic carbonization
Cr	chromium
CRADA	Cooperative Research and Development Agreement
CS	cold-spray
.csv	comma separated values (file extension)
Cu	copper
CU	Clemson University
CU-ICAR	Clemson University International Center for Automotive Research
CuO	copper(II) oxide or cupric oxide
CUV	crossover utility vehicles

CV	coefficient of variation
CVD	chemical vapor deposition (or deposited)
D	
d	diameter
D	diffusion coefficient
Da	Dalton
DAQ	data acquisition
DAS	dendrite arm spacing
DAX	data analysis expression
dB	decibels
DCB	double cantilever beam
DFT	density functional theory
DIC	digital image correlation
DIN	Deutsches Institut für Normung
DIW	direct ink writing
DMA	dynamic mechanical analysis
DNN	deep neural network
DO ₃	designation for Fe ₃ Si-type ordered phase
DOE	U.S. Department of Energy
DP	dual-phase
DP590	dual-phase steel with low tensile strength (590 MPa) and low yield frequently used in automotive body-structure applications requiring high-energy absorption
DP780	dual-phase steel widely used in the manufacture of automobile reinforcing plates, wheels, chassis, bumpers, body frame because of its high-strength and high-formability
DP980	dual-phase steel with low and intermediate tensile strength and low yield ratio
DSC	differential scanning calorimetry
dtex	mass per unit length in grams per 10,000 meters
DuAlumin-3D	an aluminum alloy with a combination of tensile, creep, fatigue, and corrosion properties superior to all known cast, wrought and printable aluminum alloys
E	
E'	storage modulus
E _{corr}	corrosion potential
E _p	pitting potential
e-axle	electric axle

EBM	Eagle Bend Manufacturing
EBSD	electron backscatter diffraction
EC	electrical conductivity
EDM	electro-discharge machining
EDS	energy-dispersive spectroscopy
EERE	Office of Energy-Efficiency and Renewable Energy
e.g.	abbreviation meaning “for example”
EG	ethylene glycol
EIS	electrochemical impedance spectroscopy
EKKcapcast	software for simulating casting processes
EM	electromagnetic
e-motor	electric motor
EPA	Environmental Protection Agency
et al.	abbreviation for “et alia” meaning “and others”
etc.	abbreviation for “et cetera” meaning “and other things” or “and the rest”
EV(s)	electric vehicle(s) (when referring to types of vehicles)
<i>ex-situ</i>	off-site or out of place

F

FARS	Fatality Analysis Reporting System
FCA US LLC	Fiat Chrysler Automobiles U.S. Limited Liability Company
FCC or fcc	face-centered cubic
FDS	flow-drill screw
Fe	iron
FeCl ₃	iron chloride
Fe ₃ O ₄	iron (II,III) oxide
FEA	finite element analysis
FEM	finite element method (or model)
FIB	focused ion beam
FLIR	forward-looking infrared
FMVSS	Federal Motor Vehicle Safety Standard
FOA	Funding Opportunity Announcement
FRP	fiber-reinforced polymer
FSP	friction-stir processing
FSW	friction-stir welding

FTIR	Fourier-transform infrared spectroscopy
FV	front-view
FY	fiscal year
G	
g	gram(s)
G'	storage modulus
GAM	generalized additive model
GB	grain boundary (when referring to metallurgy)
GB	gigabyte (when referring to computation)
g/cc or g/cm ³	grams per cubic centimeter
gf	gram-force
GF	glass fiber
GFRP	glass fiber-reinforced polymer
GHG	greenhouse gas
GM	General Motors LLC
GNP	graphene nanoparticles
g/mol	grams/mole
GPa	gigapascals
GREET [®]	<u>G</u> reenhouse gases <u>R</u> egulated <u>E</u> missions and <u>E</u> nergy use in <u>T</u> echnologies
GSAS	General Structure Analysis System
gsm or g/m ²	grams per square meter
H	
h or hr	hour(s)
H	symbol for the magnetic field
H ₂	hydrogen
H11	chromium-based steel alloy from the “H” family of steels with outstanding impact toughness
H13	a 5% chromium ultra-high-strength tool steel alloy with higher content of molybdenum and vanadium
H19	super work hardening temper
HAADF	high-angle annular dark-field
HAZ	heat-affected zone
HCF	high-cycle fatigue
HD	heavy-duty
HDG	hot-dip galvanized (or hot-dip galvanizing)

HDPE	high-density polyethylene
HDT	heavy-duty truck
HEV	hybrid electric vehicle
HiVe	high-velocity (riveting)
(hkl)	Miller indices (100)
HPDC	high-pressure die-casting
HPPC	hybrid pulse power characterization
HP-RTM	high-pressure resin transfer molding
HRC	Hardness Rockwell – C scale
HT	high-temperature
HTC	high-temperature carbonization
Hv	Vickers hardness
Hz	hertz
I	
i.e.	abbreviation for “id est,” a Latin phrase meaning “that is”
I _G /I _D	Ratio of the intensities of the G band to the D band for Raman spectra
IACMI	Institute for Advanced Composites Manufacturing Innovation
IACS	International Annealed Copper Standard
ICE(V)	internal-combustion-engine (vehicle)
ICME	integrated computational materials engineering
ICP-OES	inductively coupled plasma - optical emission spectrometer
ID	identification (when followed by a number)
Igor Pro	a fully interactive software environment for experimenting with scientific, engineering data, and producing publication-quality graphs and graphics
IH	Induction-heating
IIHS	Insurance Institute for Highway Safety
IM6	carbon fiber with shear properties equivalent to those of standard AS type fibers for use in prepregging and filament winding
IM10	carbon fiber with high-tensile-strength, intermediate modulus, and good shear-strength for use in weaving, prepregging, filament winding, braiding, and pultrusion
ImageJ	a Java-based image processing and analysis software that allows users to process and analyze scientific images on various platforms
IMGenie	A series of hardware by Acellent Technologies, Inc. that supports “passive” data acquisition from a network of piezoelectric sensors mounted on or embedded within a structure providing a complete solution for impact detection, temperature mapping, and load/strain monitoring on all types of structures

in.	inch
in./min	inches per minute
in./s	inches per second
InSb	indium antimonide
<i>in-situ</i>	on-site or in place
IPF	inverse pole figure
I(q)	intensity as a function of the reciprocal space vector
IR	infrared
J	
.jpg	joint photographic group, a commonly used method of lossy compression for digital images
J	joule
J/g	joules per gram
J/kg*K	joules per kilogram degree Kelvin
JCP	Joining Core Program
JH	Jackson-Hunt
K	
<i>k</i>	thermal conductivity
K	degree Kelvin
K ₂ CO ₃	potassium carbonate
K ₂ TiF ₆	potassium fluortitanate
kA/cm ²	kiloamp per square centimeter
KBF ₄	potassium borofluoride
keV	kiloelectron volt
kg	kilogram
kg CO ₂ -e/kg	kilogram of carbon dioxide equivalent per kilogram (of material)
kgf or kgF	kilogram-force
kg/mm ²	kilogram per square millimeter
kHz	kilohertz
kJ	kilojoule
km	kilometer
kN	kilonewton
KSII	designation for a lap-shear test, cross-tension sample
Ksi, ksi, and kpsi	kilopound per square inch

kV	kilovolt
kWh/kg	kilowatt-hour per kilogram
kW	kilowatt
kW/m ²	kilowatt per square meter
L	
L	liter
L1 ₂	designation of a crystal lattice structure with all of the atoms located on the sites of a face-centered cubic lattice
lb.	pound(s)
LBNL	Lawrence Berkeley National Laboratory
LCA	life cycle analysis
LCCF	low-cost carbon fiber
LCEA	life cycle energy assessment
LCS	low-carbon steel
LD	light-duty
LFP	lithium-iron(Fe) phosphate
LGK	Lipton-Glicksman-Kurz
Li	lithium
LightMAT	Lightweight Materials Consortium
LiNO ₃	lithium nitrate
LLC	limited liability company
LLNL	Lawrence Livermore National Laboratory
LMCP	Lightweight Metals Core Program
LMJ	liquid-metal jetting
LPBF	laser powder bed fusion
LPPSC	low-pressure precision sand casting
LS-DYNA	advanced, general purpose, multiphysics simulation software package.
LSS	lap-shear strength
LTC	low-temperature carbonization
LTP	local thermomechanical processing
LW	lightweight
M	
m	mass (when referring to a body of matter)
m	meter (when referring to length)

m	dynamic viscosity of the fluid (when referring to the fluid)
m ²	square meter
M	magnification ratio (when referring to optics)
M	molecular weight (when referring to a material property)
M	molar (when referring to the amount of a substance)
M300	an age-hardenable martensitic tool steel with exceptional mechanical properties, specifically a high-tensile-strength and hardness; it is easily heat-treated, with superior mechanical properties being achieved after age-hardening
MA	Massachusetts
mAh/s	milliamp hours per second
MAP	microwave assisted plasma
MAS	microalloyed steel
MAT_58	a damage mechanics-based model provided by LS-DYNA
MAT8	a material property definition card used to define the properties for planar orthotropic elastic materials in two dimensions
MAT221	a material property definition card that defines an orthotropic material with optional simplified damage and optional failure for composites
MATLAB	<u>MAT</u> rix <u>LAB</u> oratory, a multi-paradigm numerical computing environment and programming language
MB	megabyte
MCVN	miniaturized Charpy v-notch
MCE	multi-cylinder engine
Mcyc	motorcycle
MD	molecular dynamics
MESC(s)	multifunctional energy-storage composite(s)
Mg	magnesium
MgCO ₃	magnesium carbonate
MgO	magnesium oxide
Mg ₂ Si	magnesium silicide
Mg(OH) ₂	magnesium hydroxide
MgZn ₂	dizinc magnesium
MHHDP	methylhexahydro dimethyl phthalic ester
MHHPA	methylhexahydrophthalic anhydride
MI	Michigan
MIC	maximal information coefficient
min	minute(s)

mJ	millijoule
MJ	megajoule
MJ·m ⁻³	megajoule per cubic meter
MJ/kg	megajoule per kilogram
ml or mL	milliliter
ML	machine learning
mm	millimeters
mm ²	square millimeters
mm ³	cubic millimeters
mm ³ /nm	cubic millimeters per nanometer
mm/min	millimeter per minute
mm/sec or mms ⁻¹	millimeter per second
MMC	metal-matrix composites
Mn	manganese
Mo	molybdenum (when referring to the element)
Mo	Mouromtseff Number (when referring to heat-transfer)
mol	mole (a standard scientific unit in chemistry)
MOOSE	multiphysics object-oriented simulation environment
MP159	a nickel-cobalt based multiphase alloy with properties that enables ultra-high-strength, toughness, good ductility and excellent corrosion resistance
MPa	megapascals
mph	miles per hour
MR	Molecular Rebar®
MRD	Molecular Rebar Design, LLC
m/s	meters per second
MS	melt-spinning
MSC	Materials Sciences, LLC
Msi or msi	million pounds per square inch
MSIA	multiscale image analysis
MS/m	megasiemens per meter
MSU	Michigan State University
M-TOW	multi-tow
MUST-FE	multi-spatial and time-resolution finite element
mV	millivolts
MW	molecular weight (when referring to chemicals)

MWCNT	multiwall carbon nanotube
mW/cm ²	megawatts per square centimeter
MX or MXene	carbides and nitrides of early transition metals (M) interleaved with a number of layers of carbon or nitrogen elements (X)
MY	model year
N	
N	nitrogen (when referring to a gas)
N	Newton (when referring to a force)
NaCl	sodium chloride
NaHCO ₃	sodium bicarbonate
NaOH	sodium hydroxide
Nb	niobium
NbC	niobium carbide
NBR	nitrile butadiene rubber
Nd	neodymium
Nd-YAG	neodymium-doped yttrium-aluminum-garnet
NDE	nondestructive evaluation
NETL	National Energy Technology Laboratory
Nf	number of cycles to failure
NFE	non-federal entity
NHSTA	National Highway Transportation Safety Administration
Ni	nickel
nm	nanometer(s)
nm ³	cubic nanometer
NMC	nickel-manganese-cobalt
NMC622	Ni _{0.6} Mn _{0.2} Co _{0.2} O ₂ (NMC622)
N/mm	Newtons per millimeter
nm/sec	nanometer per second
NMP	N-methylpyrrolidone
NMR	nuclear magnetic resonance
NMVC-R ²	<u>n</u> ano- and <u>m</u> icro-filler <u>r</u> einforced <u>v</u> itrimer <u>c</u> omposites made from <u>r</u> ecycled milled carbon fibers
NN	neural network
No.	number
NP	nanoparticle

NREL	National Renewable Energy Laboratory
ns	nanosecond
NVH	noise, vibration, and harshness
O	
O	monatomic oxygen
O ₂	diatomic oxygen
OCP	open circuit potential
OD	outer diameter
OEM	original equipment manufacturer
OM	optical microscopy
OMEGA	<u>O</u> ptimization <u>M</u> odel for reducing <u>E</u> missions of <u>G</u> reenhouse Gases from <u>A</u> utomobiles
OpenFOAM	Open-Source Field Operation and Manipulation
OPF	oxidized precursor fiber
OPP	out-of-plane printing
ORNL	Oak Ridge National Laboratory
OSU	The Ohio State University
P	
P (or p)	pressure
P	power
PA	polyamide
PA-66	polyamide 66 (or nylon 66)
PAG	polyalkylene glycol
PAH	polyaromatic hydrocarbon
PAN	polyacrylonitrile
.pbix	Power BI file extension
Pb	lead
PC	polycarbonate (when referring to a material)
PC	PrintCast or PrintCasting (when referring to an additive manufacturing process)
PCA	principal component analysis
PCC	Pearson Correlation Coefficient
PCE	polynomial chaos expansion
Pd	palladium
PDF	probability density function
PE	polyethylene

PECAN	polyester-based covalently adaptable network
PEEQ	the ABAQUS parameter name for the equivalent plastic strain
PEI	polyethyleneimine
PEO	plasma-electrolytic oxidation
PET	polyethylene terephthalate
PFIB	plasma focused ion beam
PFRP	polymer-fiber-reinforced polymer
PFZ	precipitate free zone
pH	potential hydrogen used to rank the relative basicity or acidity of substances to other substances, based on the amount of hydrogen ion activity in a substance
PI	principal investigator (when referring to the project)
PI	powder impregnation (when referring to the method)
PLA	polylactic acid
PLC	Public Limited Company (when referring to the company)
PLC	programmable logic controller (when referring to equipment)
PMCP	Powertrain Materials Core Program
PNNL	Pacific Northwest National Laboratory
Power BI	a common business intelligence data visualization and reporting platform by Microsoft
PP	polypropylene (when referring to polymers)
PPA	polyphthalamide
p-PDA	p-phenylenediamine
ppi	pores per square inch
ppm	parts per million
PPO	peak power output
PPS	pedestrian protection system
PPTA	polyparaphenylene terephthalamide
psi	pounds per square inch
Pt	platinum
PU	pickup (truck, when referring to vehicles)
PUE	power ultrasonic edge
PUSP	power ultrasonic-based surface processing
PUT	pickup truck
PVA	polyvinyl alcohol
PVC	polyvinyl chloride

PVDF	polyvinylidene difluoride
PVP	polyvinylpyrrolidone
PyCaret	a Python open-source machine learning library designed to make performing standard tasks in a machine learning project easy
PZT	lead zirconate titanate

Q

Q (with number)	quarter (when referring to a specific period within a year)
Q or q	heat flux (when referring to the amount of heat that flows per unit of time)
Q or q	scattering vector (when referring to an ultra-small-angle X-ray scattering vector)
Q or q	reciprocal space vector (when referring to reciprocal space)
QoI	quantity of interest

R

R	resistance (when referring to electrical resistance and conductance)
R	an environment for statistical computing and graphics (when referring to software)
R&D	research and development
R&DD	research, development, and deployment
R ²	coefficient of determination
R _a	surface roughness
rad/s	radian per second
RAPID	a photopolymer resin that changes its physical properties when introduced to light
RBF	rotating beam fatigue
RC	recycled content
rCF	recycled carbon fiber
R//CPE	resistance constant phase element
RE	rare-earth
ReaxFF	reactive force field
ReaxFF MD	reactive force field molecular dynamics
rFCP	rotated functional principal component
Rh	rhodium
RH	relative humidity
RL _{db}	return loss in decibels
rpm or RPM	revolution(s) per minute
RR	rolling resistance
RR350	an alloy that evolved from a World War II aircraft application by Rolls Royce

RS	retreating side
RSCF	rolling sliding contact fatigue
RSW	resistance spot weld (or welding)
r/t	radius-to-thickness ratio
RT	room temperature
RTM	resin transfer mold (or molding)
RVE	representative volume element
S	
s	seconds (when referring to time)
s	aspect ratio (when referring to fiber length/diameter)
S	longitudinal tensile strength
S ₁₁	symbol for the reflection coefficient
S/μm	siemens per micrometer
SAXS	small angle x-ray scattering
Sb	antimony
SBIR	Small Business Innovative Research
S-Bpin	borylated styrene-ethylene-butylene-styrene triblock copolymer
Sc	scandium
SCE	saturated calomel electrode
SCF	short carbon fiber
SDF	Sudamericana De Fibras
SE	secondary electron (when referring to microscopy)
SE	shielding effectiveness (when referring to electromagnetic interference)
SEBS	styrene-ethylene-butylene-styrene (technically, polystyrene-b-poly[ethylene-co-butylene]-b-polystyrene)
sec.	second
SECCM	scanning electrochemical cell microscopy
SEM	scanning electron microscope (or microscopy)
SF-TP or SFT	short-fiber-reinforced thermoplastic
ShAPE™	<u>s</u> hear- <u>a</u> ssisted <u>p</u> rocessing and <u>e</u> xtrusion
SHM	structural health monitoring (when referring to monitoring vehicle conditions)
SHM	simple harmonic motion (when referring to impact testing)
Si	silicon
SiC	silicon carbide
SiO ₂	silicon oxide

SLA	stereolithography
SLIC	sustainable lightweight intelligent composite
SMC	sheet molding compound
S-N	stress-number of cycles
Sn	tin
SNL	Sandia National Laboratories
SOC	state of charge
SOH	state of health
SPD	severe plastic deformation
Sp.Gr.	specific gravity
SPGE	sorbitol tetraglycidal ether
SPH	smooth-particle hydrodynamics
SPR	self-piercing rivet (or riveting)
Sr	strontium
SRNL	Savannah River National Laboratory
SRPC	self-reinforced polymer composite
SS	stainless-steel
STEM	scanning transmission electron microscope (or microscopy)
.stl	stereolithography, a standard data transmission file format
STQ	solution-treated and quenched
STTR	Small Business Technology Transfer Research
SuRF	Scale-up Research Facility
SUV	sport-utility-vehicle
SZ	shear zone
T	
t	time (when referring to time)
T	temperature (when referring to temperature)
T	tension (when referring to stress-strain relationships)
T	Tesla (when referring to the magnetization field)
T	transverse (when referring to direction)
T _c	cooling temperature
T _g	glass transition temperature
T _m	melting temperature
T5	temper designation for aluminum that is cooled from an elevated-temperature shaping process then artificially aged

T6	temper designation for aluminum that is heat-treated at a temperature between 325°F and 400°F to increase the strength
T7	temper designation for aluminum that is aged at 100–120°C for several hours and then at 160–180°C for 24 hours or more to provide maximum stability and good properties at elevated temperatures with intermediate mechanical properties and to maximize the thermal conductivity
TA	thickening agent
tan δ	loss factor
TC	thermal conductivity (when referring to the ability to conduct or transfer heat)
TC	thermocouple (when referring to a sensor)
TCI	terephthaloyl chloride
TCR	temperature coefficient of resistivity
TEA	techno-economic analysis
TEM	transmission electron microscope (or microscopy)
TESPD	bis-(triethoxysilylpropyl)-disulfide
TESPT	bis-(3-triethoxysilylpropyl)-tetrasulphane
TFP	tailored-fiber placement
T _g	glass transition temperature
TGA	thermogravimetric analysis
Thermo-Calc	software package for thermodynamic
THF	tetrahydrofuran
Ti	titanium
Ti ₃ AlC ₂	titanium alumina carbide
Ti-6Al-4V	a Grade 5 alloy consisting of a two-phase α + β titanium alloy with aluminum as the alpha stabilizer and vanadium as the beta stabilizer.
TiB ₂	titanium boride
TiO ₂	titanium dioxide or titania
Ti ₃ C ₂	titanium carbide
TIM	thermal-interface material (when referring to material property)
TIM	temperature inference model (when referring to heat-transfer modeling)
Tl	thallium
Tm	thulium
TMAZ	thermomechanically affected zone
TMD	transition metal dichalcogenide
TMF	thermomechanical fatigue
TMP	thermomechanical processing

TN	Tennessee
TPM	thermal-pseudo-mechanical
TPU	thermoplastic polyurethane
TRL	technology readiness level
TS	tensile strength
TV	top-view
TX	Texas
TYS	tensile yield strength

U

UAM	ultrasonic additive manufacturing
UCB	University of California–Berkeley
UCC	ultraconductive copper
UD	unidirectional
UD-CCM	University of Delaware Center for Composite Materials
UDRI	University of Dayton Research Institute
UHMWPE	ultra-high-molecular weight polyethylene
UHSS	ultra-high-strength steel
UJ	ultrasonic-based spot-joining
UMAT	<u>user-defined mechanical material</u> behavior - a user subroutine that can be used to define the mechanical constitutive behavior of a material.
UNT	University of North Texas
URJ	ultrasonic rivet joining
U.S.	United States
U.S. DRIVE	U.S. Driving Research and Innovation for Vehicle efficiency and Energy sustainability
USA	United States of America
USAMP	U.S. Automotive Materials Partnership
USAXS	ultra-small angle x-ray scattering
USC	University of Southern California
USGS	U.S. Geological Survey
USW	ultrasonic welding
UTS	ultimate tensile strength
UV	ultraviolet

V

v	velocity
---	----------

V	vanadium (when referring to the element)
V	volt or voltage (when referring to electricity)
V or v	volume (when referring to quantity) or wear volume (when referring to wear rate calculations)
V_f	volume fraction
V_h	horizontal speed
V_i	initial speed
V_s	speed of screw drill
V_{see}	saturated calomel electrode potential
V/g	volts per gram
Vac	vacancy
VAN	vector network analyzer
VAR	vacuum arc remelted
VARTM	vacuum-assisted resin transfer molding
VDA	Verband der Automobilindustrie
VEA	volumetric energy absorption
VFAW	vaporizing foil actuator welding
VIN	vehicle identification number
viz.	“videlicet;” a contraction of the Latin phrase “videre licet,” meaning “it is permitted to see” (synonym: namely).
VMT	vehicle miles traveled
vol. %	volume percent
Vortec L96	an engine produced by General Motors for use in its full-size heavy-duty pickup trucks, vans, and SUVs.
vs.	versus
VSP	viscous solution printing
VTO	Vehicle Technologies Office
W	
w	weight
W	watts (when referring to electrical energy)
W	tungsten (when referring to the chemical element)
WAIM	water-assisted injection-molding
WAXS	wide-angle x-ray scattering
WCM	wet compression molding
WJP	water jet peening

W/m-°C	watts per meter degree Centigrade
W/m-K	watts per meter-Kelvin
W/m ² -K	watts per square meter-Kelvin
WSU	Washington State University
w/v%	percent of weight to volume
wt% or wt.%	percent by weight

X

X35	a high-quality grade 35 structural carbon steel widely used in the construction and machine building industries
XCT	x-ray computed tomography
Xe	xenon
XGBoost	an optimized distributed gradient boosting library
XPS	x-ray photoelectron spectroscopy
XRD	x-ray diffraction
XRT	x-ray tomography

Y

Y	yttrium (when referring to the element)
Y	admittance (when referring to the admittance matrix)
YAG	yttrium-aluminum-garnet
Yb	ytterbium
YS	yield strength

Z

Zn	zinc
ZnFe ₂ O ₄	zinc ferrite
ZnO	zinc-oxide
Zn(OH) ₂	zinc hydroxide
Zr	zirconium

Executive Summary

The Materials Technology subprogram supports the mission of the Vehicle Technologies Office (VTO) to accelerate the deployment of clean energy technologies toward achieving net-zero emissions in the transportation sector. The Powertrain Materials Core Program (PMCP) research portfolio seeks to develop higher performance materials that can deliver the required electrical, thermal, and strength properties needed to improve efficiency of vehicle powertrains including power electronics. The Lightweight Materials research portfolio enables improvements in vehicle efficiency by providing properties that are equal to or better than traditional materials at a lower weight. Because it takes less energy to accelerate a lighter object, replacing cast-iron and traditional steel components with lightweight materials, such as advanced high-strength steels (AHSS), magnesium (Mg) alloys, aluminum (Al) alloys, and fiber-reinforced polymer composites can directly reduce a vehicle's energy consumption. By 2030, the Materials Technology research activities seek to demonstrate a 25% glider lightweighting which includes body, chassis, and interior at less than \$5 per kilogram (kg) cost savings compared to 2021 Mustang Mach E or a 2021 Chevrolet Suburban.

Powertrain Materials Core Program

In fiscal year (FY) 2023, the PMCP portfolio continued transitioning research from materials for improving internal combustion engines (ICE) to materials improvements for electric vehicle powertrain components. The work presented in this report represents the efforts in four main thrust areas: (1) Thrust 1- Lightweight Alloys for Electric Vehicle (EV) Propulsion; (2) Thrust 2 - Materials and Lubricants for Heavy Duty (HD) EVs and EV Propulsion; (3) Thrust 3 - Advanced Processing and Additive Manufacturing (AM) for EVs; and (4) Thrust 4 - Advanced Characterization and Computation. Efforts for two legacy ICE projects are also reported.

The environment for powertrain materials during operation is extremely harsh and include high-temperatures and corrosive conditions. Fundamental studies of fatigue, creep, and corrosion in advanced cost-effective lightweight alloys and the use of Al-nickel (Ni) alloys were conducted for improving electrical propulsion. Higher temperature Al alloys and composites were investigated for lightweight brake systems. High-performance soft magnetic materials were examined for electric motor laminates. Ferrous alloys for fatigue-resistant, lightweight geartrains and new lubricant strategies such as carbon nanotube coatings for superlubricity for advanced thermal management in HD EV systems were also studied. Fundamental development of non-equilibrium processing and design of sustainable Al feedstock for additively-manufactured alloys along with advanced ceramics and processing for wireless charging systems were advanced during FY 2023. Advanced characterization, including thermal, electrical, and magnetic properties, was conducted on research samples and computational analysis and life cycle analysis were provided as they apply to the use of EVs.

AM offers unprecedented possibilities to fabricate unique and complex near-net-shape components leading to significant savings by decreasing tooling and materials cost, accelerating prototype development, offering unique properties, and increasing system efficiency through advanced designs not achievable via conventional fabrication processes. In-depth understanding of the relationship between microstructure and processing parameters could result in unique microstructures and enhanced or geometrically tailored properties for a wide range of powertrain materials and components. Work in this area addresses the specific challenges and opportunities associated with AM for future LD and HD vehicles and electronic components. Key factors, such as cost, influence of feedstock characteristics, volatilization of species, cooling rates, non-equilibrium phases, materials properties, non-uniform geometry-dependent thermal history, and thermal cycling were assessed for existing and new materials via both modeling and experimental studies.

Lightweight Materials

In FY 2023, the Lightweight Materials technology area portfolio included research in the following three focus areas: (1) the Lightweight Metals Core Program (LMCP) for improving the properties and manufacturability of light metals, such as AHSS, Al-alloys, and Mg-alloys; (2) the Composites Core Program (CCP) for reducing the cost of carbon fibers (CFs) and polymer composites and developing Integrated Computational Materials Engineering (ICME) frameworks for manufacturing of polymer composites; and (3) the Joining Core Program (JCP) for developing novel joining methods to enable multimaterial systems. The LMCP was restructured into four thrust areas in FY 2023 and the CCP will be restructured to consist of four thrust areas in FY 2024.

Several lightweight metals projects addressed the challenges for the development of lightweight metals: Al sheet materials with locally modified properties; form-and-print and cast-and-print AM for localized property enhancement of high-strength Al sheet and Al castings; local thermomechanical processing to address challenges to implementing Al sheet; solid phase processing of Al castings; power ultrasonic surface processing (PUSP) of die-cast Al alloys; cast Mg alloy surface modifications to improve the corrosion performance by surface alloying; local thermomechanical property modification of Mg castings via solid solid-phase processing techniques; advanced characterization and modeling; residual stress characterization, prediction, and optimization; and material life cycle.

CF and polymer composites also have the potential to reduce component weight by more than 60%. One of the main barriers to widespread implementation is the high-cost of CF, which is due in large part to the cost of input material (precursor) and the CF conversion process. In addition to a successfully commercialized plasma-oxidation technology, several projects are addressing this challenge by developing higher throughput conversion of CF, thus further lowering manufacturing costs and increasing production rates. CCP projects are investigating various approaches to meet DOE's cost targets (no more than \$5 per pound material cost). One challenge to implementing polymer composites is related to the time required to manufacture components. Six projects are investigating new manufacturing methods including AM and tailored-fiber placement for lightweight and low-cost composite structures and 3D printed hybrid composite materials with sensing capabilities for advanced smart vehicles. Two projects are addressing polymer matrix composites via tailored vitrimer chemistry and functional composites with hierarchical structures. Additional projects are assessing opportunities to process CF by alternative low cost, high-throughput methods and use of ultra-lightweight, ductile, and large diameter CF for repairable, stamp-formed composites as well as developing alternate or recycled reinforcing fibers. In FY 2023, five Small Business Innovation Research (SBIR) were continued into Phase II. These projects addressed sustainable lightweight intelligent composites for next-generation vehicles, integrated self-sufficient multifunctional sensors for autonomous vehicles, conductive lightweight hybrid polymer composites from recycled CFs, design rules of rubber for lightweight fuel efficient tires, and green composites (vitrimer) for high performance, repairable, recyclable, and bio-sourced automotive components.

The most effective way to reduce the overall weight of a vehicle is to tailor the material selection to each component's needs. However, joining dissimilar materials to create a multimaterial structure is a significant challenge. In FY 2023, the JCP renewed its efforts by extending joining methods previously developed to additional material pairs, advancing solid-state joining toward industry readiness, investigating surface modifications to improve adhesion and corrosion resistance, and using artificial intelligence for weld quality control. The methods developed in the JCP include solid-state welding, ultrasonic welding, novel methods for mechanical fastening (high-rate riveting), and adhesives. Solid-state welding, including an impact welding process investigated by one project, allows for joining materials with vastly different melting temperatures, which is not possible with fusion welding. The portfolio also includes a project that models the effect of galvanic corrosion on a wide variety of joining methods and surface modifications of material combinations to predict the effect on joint strength and fatigue life. One project uses machine learning (ML) to predict the quality and failure of Al-to-steel joints.

(This page intentionally left blank)

Table of Contents

- Vehicle Technologies Office Overview 1
- Materials Technology Program Overview 3
- I Powertrain Materials 7**
 - I.1 Powertrain Materials Core Program (PMCP)..... 7
 - I.1.1 Thrust 1: Lightweight Alloys for Electric Vehicle Propulsion 7
 - I.1.1.1 Task 1A. Fundamental Studies of Al-Ni Alloys for Improved Electrical Propulsion (Oak Ridge National Laboratory)..... 7
 - I.1.1.2 Task 1B. Higher Temperature Aluminum Alloys and Composites for Lightweight Brake Systems (Oak Ridge National Laboratory)..... 14
 - I.1.1.3 Task 1C. Fundamentals of Fatigue and Creep in Advanced Lightweight Alloys: Cost-Effective Lightweight Alloys for Electric Vehicle Propulsion (Oak Ridge National Laboratory) 20
 - I.1.1.4 Task 1D. Fundamentals of Corrosion Behavior in Advanced Lightweight Alloys for Electric Vehicle Propulsion (Oak Ridge National Laboratory)..... 27
 - I.1.1.5 Task 1E. Lightweight Materials for Improved Electrical Properties (Oak Ridge National Laboratory) 34
 - I.1.1.6 Task 1G. Fundamentals of Thermal Properties in Lightweight Alloys for Electric Vehicle Propulsion (Oak Ridge National Laboratory) 40
 - I.1.1.7 Task 1H. Hybrid Dispersion-Strengthened Aluminum-Matrix Composites for Higher Efficiency Electric Vehicle Powertrains: Cost-Effective Lightweight Alloys for Electric Vehicle Propulsion (Pacific Northwest National Laboratory)..... 46
 - I.1.1.8 Task 1I. Design of Sustainable Lightweight Cast Alloys for Electric Vehicles (Oak Ridge National Laboratory) 53
 - I.1.2 Thrust 2: Materials and Lubricants for Heavy-Duty Electric Vehicles and Electric Vehicle Propulsion..... 59
 - I.1.2.1 Task 2A. High-Performance Soft-Magnetic Materials for Motor Laminates (Fe-Si) via Shear-Rolling (Oak Ridge National Laboratory)..... 59
 - I.1.2.2 Task 2B. Ferrous Alloys for Fatigue-Resistant, Lightweight Geartrains for Heavy-Duty Electric Vehicle Systems (Oak Ridge National Laboratory) 65
 - I.1.2.3 Task 2C. New Lubricant Strategies for Advanced Thermal Management of Heavy-Duty Electric Vehicles (Oak Ridge National Laboratory) 72
 - I.1.2.4 Task 2D. Carbon Nanotube Coatings for Superlubricity and Thermal Management of Heavy-Duty Electric Vehicles (Oak Ridge National Laboratory) 78
 - I.1.2.5 Task 2E. Solid-Phase Joining and Processing Methods Towards Efficient, Heavy-Duty Electric Vehicle Motors (Pacific Northwest National Laboratory) 84
 - I.1.3 Thrust 3: Advanced Processing and Additive Manufacturing for Electric Vehicles..... 95
 - I.1.3.1 Task 3A. Fundamental Development of Additive Manufactured Lightweight Alloys for Electric Vehicle Propulsion (Oak Ridge National Laboratory) 95
 - I.1.3.2 Task 3B. Fundamentals of Non-Equilibrium Processing for Additive Manufacturing Alloys (Oak Ridge National Laboratory)..... 102

I.1.3.3	Task 3C. Advanced Ceramics and Processing for Wireless Charging Systems (Ferrites) (Oak Ridge National Laboratory).....	108
I.1.3.4	Task 3D. Novel, Ultra-High Conductivity Materials (Copper Tape + Carbon Nanotubes) for Electric Vehicles (Oak Ridge National Laboratory).....	114
I.1.3.5	Task 3E. Print Casting of Lightweight Metal-Matrix Composites for Battery Enclosures with Impact Resistance and Thermal Management (Oak Ridge National Laboratory).....	121
I.1.3.6	Task 3F. Ultra-Conductor Development for Enhanced Electric Vehicle Performance (Pacific Northwest National Laboratory).....	127
I.1.3.7	Task 3G. Design of Sustainable Aluminum Alloy Feedstock for Additive Manufacturing (Oak Ridge National Laboratory).....	132
I.1.3.8	Task 3H. Fundamentals of Printable Higher Temperature Steels for Die-Cast Tooling and Inserts (Oak Ridge National Laboratory).....	138
I.1.4	Thrust 4: Advanced Characterization and Computation.....	144
I.1.4.1	Task 4A. Advanced Characterization Coordination of Multi-Lab Characterization (Task 4A1) (Oak Ridge National Laboratory).....	144
I.1.4.2	Task 4A. Advanced Characterization of PMCP Research Samples: Characterization of Thermal, Electrical, and Magnetic Properties (Task 4A3) (Oak Ridge National Laboratory).....	155
I.1.4.3	Task 4A. Advanced Characterization: Argonne Advanced Characterization (Task 4A4) (Argonne National Laboratory).....	163
I.1.4.4	Task 4A. Advanced Characterization: PNNL Advanced Characterization (Task 4A5) (Pacific Northwest National Laboratory).....	169
I.1.4.5	Task 4B. Advanced Computation: Advanced Computational Materials (Task 4B1) (Oak Ridge National Laboratory).....	177
I.1.4.6	Task 4B. Advanced Computation: Analysis of EVs for the International Energy Agency (Task 4B2) (Oak Ridge National Laboratory).....	184
I.1.4.7	Task 4B. Advanced Computation: Life Cycle Analysis (LCA) of EVs, GREET® (Task 4B4) (Argonne National Laboratory).....	189
I.2	Legacy Internal-Combustion-Engine (ICE) Powertrain Materials.....	195
I.2.1	Low-Mass and High-Efficiency Engine for Medium-Duty Truck Applications (General Motors).....	195
I.2.2	Lightweight and Highly Efficient Engines Through Al and Si Alloying of Martensitic Materials (Oak Ridge National Laboratory).....	208
II	Lightweight Materials.....	215
II.1	Lightweight Metals Core Program.....	215
II.1.1	Thrust 1. Selective Processing of Al Sheet Materials (Tasks 1A, 1B, and 1C) (Pacific Northwest National Laboratory and Oak Ridge National Laboratory).....	215
II.1.2	Thrust 2. Selective Processing of Aluminum Castings (Tasks 2A1, 2A2, 2B, and 2C) (Pacific Northwest National Laboratory and Oak Ridge National Laboratory).....	237
II.1.3	Thrust 3. Selective Processing of Magnesium Castings (Tasks 3A1, 3A2, and 3B) (Pacific Northwest National Laboratory and Oak Ridge National Laboratory).....	258
II.1.4	Thrust 4. Characterization, Modeling, and Life Cycle (Tasks 4A1, 4A2, 4A3, 4C1, and 4C2) (Pacific Northwest National Laboratory, Oak Ridge National Laboratory, and Argonne National Laboratory).....	281

II.2	Light Metals.....	312
II.2.1	Developments of a Novel Magnesium Alloy for Thixomolding® of Automotive Components – LightMAT (Oak Ridge National Laboratory).....	312
II.3	Carbon Fiber and Polymer Composites.....	318
II.3.1	Composites Core Program	318
II.3.1.1	High-Temperature Carbon Fiber Carbonization via Electromagnetic Power (Oak Ridge National Laboratory).....	318
II.3.1.2	Additive Manufacturing for Property Optimization for Automotive Applications (Oak Ridge National Laboratory).....	328
II.3.1.3	3D-Printed Hybrid Composite Materials with Sensing Capability for Advanced Vehicles (Oak Ridge National Laboratory).....	336
II.3.1.4	New Frontier in Polymer Matrix Composites via Tailored Vitrimer Chemistry (Oak Ridge National Laboratory).....	344
II.3.1.5	Adopting Heavy-Tow Carbon Fiber for Repairable, Stamp-Formed Composites (Oak Ridge National Laboratory)	351
II.3.1.6	Multimaterial Functional Composites with Hierarchical Structures (Oak Ridge National Laboratory)	359
II.3.1.7	Ultra-Lightweight, Ductile Carbon Fiber-Reinforced Composites (Oak Ridge National Laboratory).....	366
II.3.1.8	Low-Cost, High-Throughput Carbon Fiber with Large Diameter (Oak Ridge National Laboratory).....	372
II.3.1.9	Carbon Fiber Technology Facility (Oak Ridge National Laboratory).....	379
II.3.1.10	Ultra-Lightweight Thermoplastic Polymer/Polymer-Fiber Composites for Vehicles (Pacific Northwest National Laboratory and Oak Ridge National Laboratory).....	391
II.3.1.11	Efficient Synthesis of Kevlar and Other Fibers from Polyethylene Terephthalate (PET) Waste (Pacific Northwest National Laboratory).....	410
II.3.1.12	Additively Manufactured, Lightweight, Low-Cost Composite Vessels for Compressed Natural Gas Fuel Storage (Lawrence Livermore National Laboratory).....	418
II.3.1.13	Biobased, Inherently Recyclable Epoxy Resins to Enable Facile Carbon-Fiber Reinforced Composites Recycling (National Renewable Energy Laboratory)	424
II.3.1.14	Soft Smart Tools Using Additive Manufacturing (Savannah River National Laboratory)	431
II.3.1.15	Multifunctional Smart Structures for Smart Vehicles (Ford Motor Company).....	436
II.3.1.16	Development of Tailored-Fiber Placement, Multifunctional, High-Performance Composite Material Systems for High-Volume Manufacture of Structural Battery Enclosure (General Motors).....	448
II.3.2	Small Business Innovation Research (SBIR).....	464
II.3.2.1	Sustainable Lightweight Intelligent Composites (SLIC) for Next Generation Vehicles (Newport Sensors, Inc.).....	464
II.3.2.2	Integrated Self-Sufficient, Structurally Integrated Multifunctional Sensors for Autonomous Vehicles (Acellent Technologies, Inc.)	472
II.3.2.3	Conductive Lightweight Hybrid Polymer Composites from Recycled Carbon Fibers (RockyTech Ltd.).....	486
II.3.2.4	Changing the Design Rules of Rubber to Create Lighter Weight, More Fuel-Efficient Tires (Molecular Rebar Design, LLC).....	492

II.3.2.5	Green Composites for Future Vehicles, Vitrimer Matrix + Natural and Recycled Fiber Composite Materials for High Performance, Repairable, Recyclable, and Bio-Sourced Automotive Components (Mallinda, Inc.).....	499
II.4	Joining of Dissimilar Materials	507
II.4.1	Joining Core Program (JCP)	507
II.4.1.1	Machine Learning for Joint Quality Control (Pacific Northwest National Laboratory and Oak Ridge National Laboratory)	507
II.4.1.2	Extending High-Rate Riveting to New Material Pairs (Pacific Northwest National Laboratory).....	521
II.4.1.3	Solid-State Joining of Multimaterial Autobody Parts Toward Industry Readiness (Pacific Northwest National Laboratory and Oak Ridge National Laboratory)	536
II.4.1.4	Surface Modifications for Improved Joining and Corrosion Resistance (Pacific Northwest National Laboratory, Oak Ridge National Laboratory, and Argonne National Laboratory).....	551
II.4.1.5	Extending Ultrasonic Welding Techniques to New Material Pairs (Oak Ridge National Laboratory)	571
II.4.2	Multi-Materials Joining.....	577
II.4.2.1	Manufacturing Demonstration of a Large-scale, Multimaterial Passenger Vehicle Subsystem (Clemson University).....	577
III	Crosscutting Activities	593
III.1	Lightweight Materials Crosscutting	593
III.1.1	Updated Analysis of the Relationship Between Light-Duty Vehicle Mass, Footprint, and Societal Fatality Risk per Vehicle Mile of Travel (Lawrence Berkeley National Laboratory)	593

List of Figures

Figure I.1.1.1.1. SEM-SE micrographs of Al ₃ Ni microfiber in Al-6Ni alloys with the addition of Zr, Ti, V, and Fe by wt.% for (a) as-cast alloys and alloys heat-treated at (b) 350 °C and (c) 450 °C for 200 h. Source: ORNL.....	9
Figure I.1.1.1.2. 3D reconstruction of Al matrix by APT analysis: (a) Al-6Ni-0.4Zr, (b) Al-6Ni-0.3Ti, (c) Al-6Ni-0.3V, and (d) Al-6Ni-0.5Fe alloys heat-treated at 400 °C for 200 h. Source: ORNL.....	10
Figure I.1.1.1.3. APT analysis for Al/Al ₃ Ni interface after heat-treated at 400 °C for 200 h. (a) 3D construction showing Zr segregating at the Al/Al ₃ Ni interface, and (b) concentration profiles for Zr, Ti, V, and Fe. Source: ORNL.....	11
Figure I.1.1.1.4. Effect of various microalloying elements on the thermal conductivity of Al-Ni alloys heat treated at various temperatures for 200 h. Source: ORNL.....	11
Figure I.1.1.1.5. Effect of microalloying elements on the Al ₃ Ni microfiber morphology evolution across various heat-treatment temperatures: (a) average fiber length, (b) average fiber diameter, and (c) average aspect ratio. Source: ORNL.....	12
Figure I.1.1.1.6. The relationship between electrical conductivity and thermal conductivity is characterized for all alloys. Source: ORNL.....	12
Figure I.1.1.2.1. Strain-rate vs. applied stress during compression-creep experiments at 300 °C for a variety of ACMZ alloys. Source: ORNL.....	16
Figure I.1.1.2.2. A comparison of microhardness stability at RT due to 400 °C exposure for an AlCuMgAgSc alloy from (a) Xue et al. [2] and (b) the ORNL work reported here. The ORNL data is notably similar to the alloy without the Sc addition in the original work, which indicates a lack of thermal stability. Source: ORNL.....	17
Figure I.1.1.2.3. Brake performance testing results: (a) Images of the worn surfaces of the pads, pad height loss, and average friction coefficient; and (b) average cross-sectional worn surface profile of the rotors. Source: ORNL.....	18
Figure I.1.1.2.4. A number of lightweight alloys were tested with an improved brake pad material, namely Wilwood purple. None of the Al alloys had improved performance relative to cast-iron. 3D-printed DuAlumin-3D had improved brake performance compared to the cast Al-Cu alloys. Source: ORNL.....	18
Figure I.1.1.3.1. Minimum creep strain rate vs. applied stress during <i>in-situ</i> (tensile) and <i>ex-situ</i> (compression) creep tests at 300 °C. Source: ORNL.....	22
Figure I.1.1.3.2. Crystal plane (hkl) specific lattice strain evolution in (a, c) α-Al matrix and (b, d) θ' precipitates during 300 °C in situ creep tests in ACMZ and RR350 alloys. Source: ORNL.....	22
Figure I.1.1.3.3. TEM images of a 300 °C/68 MPa crept RR350 sample showing dislocation structure (a) near and (b) away from GBs. Arrows indicate dislocations. Source: ORNL.....	23
Figure I.1.1.3.4. Minimum creep strain rate vs. applied stress at 200 °C for Al-Ni Zr and commercial AA1350 conductor Al alloys. Source: ORNL.....	23
Figure I.1.1.3.5. (a) EBSD grain map of AF LMJ Al-Si-Mg alloy. SEM image of (b)AF and (c) T6 aged alloy. The build direction is vertical upwards. (d) Tensile stress-strain curves. Source: ORNL.....	24

Figure I.1.1.3.6. (a) Maximum stress vs. cycles to failure in HCF tests of T6-aged LMJ (vertical) and cast-Al-Si-Mg (or A356) alloys. (b) Fractograph of an LMJ Al-Si-Mg sample fractured at 75 MPa. Source: ORNL.....	25
Figure I.1.1.4.1. Schematic description of electrochemical cell—EIS and polarization conditions—and two circuit models for impedance-data fitting. R_1 is solution resistance, R_2 is charge-transfer resistance, and R_f is permeable-film resistance. CPE_0 and CPE_1 account for non-ideal capacitive behavior associated with R_2 and R_f , respectively. Source: ORNL.....	28
Figure I.1.1.4.2. (a) Typical Nyquist-impedance-spectra and (b) representative polarization curves of AM Al alloys with arrows designating pitting potential (E_p) values. Source: ORNL.....	29
Figure I.1.1.4.3. (a) R_2 or $R_f + R_2$ and (b) E_p as a function of E_{corr} . In (b), $E_p = E_{corr}$ line is presented as a guide to assess the difference between E_p and E_{corr} data. Source: ORNL.....	29
Figure I.1.1.4.4. Cross-sectional SEM image and EDS characterization maps (Al, Mg, Si, and O) of Al10SiMg after 168 h in 3.5 wt.% NaCl. Source: ORNL.....	30
Figure I.1.1.4.5. Cross-sectional SEM image and EDS characterization maps (Al, Ce, Mn, Ni, and O) of ACNM450 after 168 h in 3.5 wt.% NaCl. Source: ORNL.....	30
Figure I.1.1.4.6. Cross-sectional SEM image and EDS characterization maps (Al, Ce, Mn, Ni, Zr, and O) of ACNMZ after 168 h in 3.5 wt.% NaCl. Source: ORNL.....	31
Figure I.1.1.4.7. Cross-sectional SEM image and EDS characterization maps (Al, Ce, Mn, Ni, Zr, and O) of ACNMZ350 after 168 h in 3.5 wt.% NaCl. Source: ORNL.....	31
Figure I.1.1.4.8. Cross-sectional SEM image and EDS characterization maps (Al, Ce, Mn, Ni, Zr, and O) of ACNMZ450 after 168 h in 3.5 wt.% NaCl. Source: ORNL.....	31
Figure I.1.1.4.9. Cross-sectional SEM image and EDS characterization maps of deeper corrosion attacks in ACNMZ (left and center) and ACNM450 (right) after 168 h in 3.5 wt% NaCl. Source: ORNL.....	32
Figure I.1.1.5.1. Plots showing the effect of isothermal aging on the (a) hardness and (c) EC of the Al-Zr-Sn alloy at 400 °C (dashed lines) and 425 °C (solid lines). Plots showing the effect of isothermal aging on the (b) hardness and (d) EC of the Al-Sn (light blue triangles) and Al-Zr-Sn (red circles) at 200 °C. The measured EC values of the CP-Al feedstock material and high-purity (99.9999 wt%) Al are shown in (c) and (d). Source: ORNL.....	36
Figure I.1.1.5.2. Plots showing the effect of isochronal aging on (a) hardness and (b) EC for Al-0.34Zr wt.% (black diamonds), Al-0.09Sn wt.% (blue triangles), and Al-0.34Zr-0.09Sn wt.% (red circles). Source: ORNL.....	37
Figure I.1.1.5.3. APT reconstructions highlight the Sn precipitates with green 3 at.% Sn isoconcentration surfaces for the 200 °C isochronally aged (a) Al-Sn and (b) Al-Zr-Sn alloys. Zr atoms are shown in purple, and Sn atoms in green. A proximity histogram (c) showing the average Sn (green triangles) and Zr (purple circles) concentrations across the interface, at 0 nm between the matrix and the Sn precipitates for the Al-Zr-Sn alloy. The weighted-average Zr concentration in the Al matrix and the Sn precipitates for all Sn precipitates from three APT datasets is shown as a dashed-purple line in (c) for the Al-Zr-Sn alloy. Bright-field TEM images along the $\langle 110 \rangle$ zone axis of the Sn precipitates (indicated by arrows) showing Moiré fringes at (d) lower and (e) higher magnification. Source: ORNL.....	37

Figure I.1.1.5.4. (a) Sn-centered radial-distribution function (RDF) analysis showing a tendency of Zr atoms to cluster with Sn relative to the weighted-average bulk composition of Zr in the matrix. RDF function derived from APT analysis. (b) High-resolution annular dark-field image showing Al₃Zr precipitate nucleus next to an Sn particle. Source: ORNL..... 38

Figure I.1.1.6.1. A schematic of overall workflow to predict thermal properties (via surrogate EC) in lightweight alloys via the data analytics approach. Source: ORNL..... 41

Figure I.1.1.6.2. Correlation analysis between input features (i.e., cooling rate of step-mold, duration, and temperature of T5 heat-treatment, and thickness of samples) and EC and hardness of A380 alloy. Two different algorithms, linear and non-linear, were used: (a) PCC and (b) MIC. Source: ORNL..... 42

Figure I.1.1.6.3. Accuracy of trained random-forest ML models for (a) electrical conductivities and (b) hardness of A380 alloy with various T5 heat-treatment conditions. Source: ORNL..... 43

Figure I.1.1.6.4. SEM micrographs and XCT analysis of Aural 5 alloys from two different fabrication techniques: (a) and (c) HPDC sample provided by Ford; (b) and (d) 4 mm step-mold from ORNL. The color profile for (c) and (d) represents the volume of porosity. Source: ORNL..... 43

Figure I.1.1.6.5. Average volume percentages of A380 as a function of various T5 heat-treatment conditions. Source: ORNL..... 44

Figure I.1.1.6.6. Experimentally validated ML-identified T5 heat-treatment conditions of A380 alloy with improved EC and hardness. Source: ORNL..... 45

Figure I.1.1.7.1. (a) CoF evolution during the brake test. (b) Worn cast-iron rotor with the wear-track and profilometry results from the wear-track. (c) Worn Al composite rotor with the wear-track and profilometry results from the wear-track. (d) Average CoF and wear rates for the cast-iron and composite rotors. Source: PNNL..... 48

Figure I.1.1.7.2. (a) and (b) EBSD orientation maps of the A206-1 vol.% *in-situ* TiB₂ + 9 vol.% powder TiB₂ composite. (c) EBSD phase map of the composite. Source: PNNL..... 49

Figure I.1.1.7.3. SEM and EDS images of friction-consolidated AA 7075 composites with 0% (top) and 24 vol.% (bottom) of TiB₂. Source: PNNL..... 50

Figure I.1.1.7.4. (a) Engineering stress-strain curves and mechanical properties (inset table) of T6 heat-treated friction-consolidated samples with 0, 12, and 24 vol.% TiB₂. (b) DIC shows the strain distributions on the 24 vol.% sample during tensile tests, (c) average microhardness results for the samples in their as-processed and T6 conditions. Source: PNNL..... 51

Figure I.1.1.8.1. (a) BSE-SEM image and (b) BSE-SEM image with corresponding EDS elemental maps of as-cast-Al-4.3Mg-1.6Fe alloy. Source: ORNL..... 55

Figure I.1.1.8.2. (a) Lower- and (b) higher magnification BSE-SEM images of as-cast 1.6Si alloy. (c) EDS elemental maps corresponding to the SEM image in (b). Source: ORNL..... 55

Figure I.1.1.8.3. BSE-SEM image and corresponding EDS elemental maps of as-cast 1.6Si alloy showing primary Al₁₃Fe₄ phase, as indicated by arrows. Source: ORNL..... 56

Figure I.1.1.8.4. BSE-SEM images at (top) lower and (bottom) higher magnifications of as-cast (a) 0.2Si and (b) 1.0Si alloys. Source: ORNL..... 56

Figure I.1.1.8.5. (a) Tensile stress-strain curves of as-cast alloys and (b) summary of tensile properties. Cross-section BSE-SEM images at (top) lower and (bottom) higher magnifications of (c) 0Si and (d) 1.6Si fractured tensile samples. The yellow outline in (c) indicates an inhomogeneity in the as-cast alloy. Source: ORNL.	57
Figure I.1.2.1.1. FeSi phase diagram. Source: ORNL [2].	60
Figure I.1.2.1.2. (a) As-cast developmental Fe-(5-6.5) wt.% Si-X alloys. (b) Hot-rolled plate of one developmental alloy rolled to a thickness of ~2 mm. (c) Sheet rolled to a thickness of ~0.4 mm at RT from plate shown in (b). Source: ORNL.	61
Figure I.1.2.1.3. (a) Ring-sample fabricated from rolled Fe-(4-6.5)Si-X alloys. (b) Image of the Brockhaus MPG-200 electrical steel tester. (c) Core-loss values as a function of frequency at flux densities of 0.5 and 1.0T. Source: ORNL.	62
Figure I.1.2.1.4. Calculated thermodynamic phase diagram for the Si-rich portion of the FeSi phase diagram based on [10]. Source: ORNL.....	63
Figure I.1.2.2.1. Manufacturing route and activities for design and fabrication of developmental alloys and subsequent machining, testing, and evaluation of RSCF specimens. Source: ORNL.	67
Figure I.1.2.2.2. Carburizing simulations show C content as a function of distance from the surface and time for (a) 16MnCr5 and (b) 16MnCr5+5Al. Phase fractions predicted after 12 h of carburizing at 930°C in (c) 16MnCr5 and (d) 16MnCr5+5Al. Source: ORNL.	68
Figure I.1.2.2.3. (a) Hardness traverses for ORNL 16MnCr5 and ORNL 16MnCr5+5Al after carburizing for 12 h at 930°C, quenching, and tempering at 200°C for 1.5 h. (b) Core strength and (c) toughness for ORNL 16MnCr5 and ORNL 16MnCr5+5Al after carburizing process. Microstructure near carburized surface of (d) ORNL 16MnCr5 and (e) ORNL 16MnCr5+5Al. (f) Core microstructure of ORNL 16MnCr5+5Al. In (e) and (f), dark regions are martensite, and light regions are ferrite. Source: ORNL.	69
Figure I.1.2.2.4. SEM images of the wear surfaces of (a) PCS-52100 and (b) ORNL 52100 after wear-testing in accordance with the protocol in [3]. Source: ORNL.	70
Figure I.1.2.3.1. Organic modifications for improving the oil suspendability of CNTs (R - hydrocarbon chain). Source: ORNL.....	73
Figure I.1.2.3.2. ORNL's surface modifications for CNTs for stable suspension in both polar and non-polar fluids. Source: ORNL.	74
Figure I.1.2.3.3. Images of surface-modified CNTs show stable suspension in water and a polar oil (PAG). Source: ORNL.	74
Figure I.1.2.3.4. Surface-modified CNTs showing: (a) stable suspension without a dispersant such as PIBSI in a non-polar oil (Valvoline EV base oil) at RT, (b) stable suspension with PIBSI in Valvoline EV base oil at RT, (c) unstable suspension without PIBSI in Valvoline EV base oil at 100 °C, and (d) stable suspension with PIBSI in Valvoline EV base oil at 100 °C. Source: ORNL.....	75
Figure I.1.2.3.5. Surface modification effective in mitigating oil thickening upon the addition of CNTs. (a) Polar oil (PAG) and (b) non-polar oil (Valvoline EV d4 base). Source: ORNL.	75
Figure I.1.2.3.6. Distinct impact of various types of CNTs on the oil TC. Source: ORNL.	76
Figure I.1.2.4.1. CNT coating on Type 316 stainless disk (a and b) and stainless foil (c and d). Source: ORNL.	80

Figure I.1.2.4.2. A modified ASMT D5470-17 standard test to quantify the impact of the CNTs as thermal-interface materials. (a, b) Experimental setup, (c) schematic showing the compacted CNT coating at the thermal-interface, and (d) infrared image of the contact pair. Source: ORNL.	80
Figure I.1.2.4.3. Temperature profiles captured by the IR camera (a) with the CNT coating, (b) without the CNT coating, (c) using silicone paste, and (d) using silicone paste containing 1 wt% CNT particles. Source: ORNL.	81
Figure I.1.2.4.4. Preliminary results suggest improved cooling efficiency by the CNT coating when applied to a stainless-steel foil. (a) Bare SS foil (silver) and CNT-coated SS foil (black) wrapping thermocouples first heated by a hot plate and then cooled by the airflow inside a fume hood; SEM images showing the CNTs. (b) Temperature profiles suggesting increased heating and cooling rates by the CNT coating. Source: ORNL.	82
Figure I.1.2.5.1. Schematic of the (a) AlCu hybrid rotor, and (b) joining of Al to grooved Cu shorting bar. Source: PNNL.	85
Figure I.1.2.5.2. (a) Schematic drawing showing isometric view of a mock end-cap setup. (b) Al to Cu shorting bar mock end-cap setup, ready to be welded in a rotary FSW system at PNNL. (c) Top-view of end-cap rotor. (d) Bottom view of end-cap rotor. Source: PNNL.	86
Figure I.1.2.5.3. (a–f) End-cap rotor back view with red arrows showing cross-sections for optical imaging. Unetched transverse cross-sections are shown in (a) and (c), while etched longitudinal cross-sections are provided in (b) and (d). (e) Bottom view of end-cap rotor. (f) Magnified view of the image highlighted by the red box in (e). (g–h) X-ray computed tomography of top-view from linear welds showing (g) Cu-interlocking (red arrows) and (h) distribution of Cu particles (white arrow) following FSW. Source: PNNL.	87
Figure I.1.2.5.4. (a) Cross-sectional view of mock end-cap setup for a single-pass FSW to join the Al end-cap to a Cu shorting bar. (b) Crown surface showing a linear FSW joint using single-pass. (c) A series of 4× lines of transverse cross-section images showing defect-free joints. Source: PNNL.	88
Figure I.1.2.5.5. (a) Pullout load comparison for (b) linear welds at RT and HT with end-cap welds and die-cast Al-Cu. Source: PNNL.	88
Figure I.1.2.5.6. (a) Two full-sized rotors made using the process developed in this work. (b) Load vs. displacement value obtained after full-size rotor testing and estimated die-cast rotor strength for benchmarking. (c–f) Al-Cu hybrid rotors being pull-tested. Source: PNNL.	89
Figure I.1.2.5.7. (a) FSP of FeSi alloy. (b–e) FSP samples with 4–6% Si content. (f–g) Wire-extrusion samples with 4 and 5 wt.% Si. Source: PNNL.	90
Figure I.1.2.5.8. (a) Low-magnification BSE-SEM images of Fe-4.0%Si. (b) High-magnification BSE images of edge region. (c) Low-magnification IPF map of the corresponding region shown in (a). (d) High-magnification BSE images of core region. Source: PNNL.	90
Figure I.1.2.5.9. (a) Low-magnification image showing the basin-shaped nugget after FSP of Fe-5%Si steel. (b) Higher magnification IPF map showing grain size and distribution in nugget. (c) High-magnification EBSD image showing absence of any large precipitate in nugget. (d) Stress-strain curve of the friction-stir processed Fe-5%Si steel. Source: PNNL.	91

Figure I.1.2.5.10. (a) IPF map of the nugget region of the Fe-6.5%Si electrical steel, showing the fine grain microstructure and grain size distribution. (b) High-magnification BSE image of the same region. (c) Nanoindentation load vs. displacement curves. Source: PNNL.....	92
Figure I.1.2.5.11. (a) Hardness and (b) coercivity values of high-Si containing electrical steel produced by FSP, BJAM, and MS. Source: PNNL.....	93
Figure I.1.2.5.12. Results of hot and cold-rolling on Fe-4%Si, showing comparison of performance between as-received and FSP conditions. Source: PNNL.	93
Figure I.1.3.1.1. A summary of AF microstructure of Al-1Zr-0.09Sn alloy: SEM micrographs showing the typical microstructures at (a) low and (b and c) high magnifications; (d) elemental distribution maps of all elements (Al, Zr and Sn) together, and individual Zr and Sn; (e and f) IPF colored maps, aligned along build direction, showing the typical grain structure; and (g) a map, corresponding to (f), showing the distribution of low-angle (red and green lines) and high-angle (blue lines) grain boundaries. Source: ORNL.	97
Figure I.1.3.1.2. XRD spectra obtained from AF Al-1Zr-0.09Sn alloy. Source: ORNL.	97
Figure I.1.3.1.3. (a) A summary of AF microstructure of Al-2Ni-1Zr alloy: SEM micrographs showing the typical microstructures at (a) low and (b-c) high magnifications; (d-e) IPF colored maps, aligned along the BD, showing the typical grain structure; and (f) a grain boundary distribution map, corresponding to (e), showing the distribution of low-angle (red and green lines) and high-angle (blue lines) grain boundaries. Source: ORNL.	98
Figure I.1.3.1.4. (a) Tensile properties of AF Al-2Ni-1Zr and Al-1Zr-0.09Sn alloys at 20 and 200 °C and (b) evolution of the EC of Al-2Ni-1Zr and Al-1Zr-0.09Sn alloys as a function of isochronal aging heat treatments. Source: ORNL.	99
Figure I.1.3.1.5. Tensile properties of AF (a) Al-1Zr-0.09Sn and (b) Al-2Ni-1Zr alloys at 200 °C. (c) Evolution of the EC of Al-2Ni-1Zr and Al-1Zr-0.09Sn alloys as a function of isochronal aging heat-treatments compared to Al-0.34Zr-0.09Sn and Al1350. Source: ORNL.	100
Figure I.1.3.2.1. Flowchart on developing the CA framework on modeling the nucleation and growth of dendritic solidification, eutectic solidification, and their competition under different cooling conditions. Source: ORNL.....	103
Figure I.1.3.2.2. (a) Growth of Al-dendrite of Al-4 wt.% Cu in 5 K undercooled melt after 0.256 s. (b) Comparison of CA simulated velocity of dendrite tip at steady-state with the analytical LGK solution vs. liquid undercoolings. (c-d) Effect of cooling rate on grain size for Al-4 wt.% Cu alloy in the isothermal field under 100 K/s and 1,000 K/s. The magenta highlight shows difference in dendrite size for two cooling rates. Source: ORNL.....	104
Figure I.1.3.2.3. Validation of the eutectic model: (a) Lamella spacing vs. undercooling relationship as obtained from the JH Model. Growth of lamella at two different times (b-c) with initial spacing equal to that at the extremum point, (d-e) with initial spacing larger than that at the extremum point, and (f-g) initial spacing smaller than that at the extremum point. Source: ORNL.	105
Figure I.1.3.2.4. Microstructure of Al-25 wt.% Cu after solidification at 100 K/s, 1000 K/s, and 10,000 K/s (left to right). Source: ORNL.....	106
Figure I.1.3.3.1. Zeta potential as a function of pH for the $Ni_{x-1}Zn_xFe_2O_4$ powder samples. Note, the dotted lines merely guide the eye. Source: ORNL.	111

Figure I.1.3.4.1. (a) Comparison of resistivity as a function of temperature (275–375 K), and (b) current density for single and double CNT layer UCC architectures. Plots display significantly reduced resistivity and increased ampacity as compared to reference Cu substrates (see table insets). To demonstrate consistency and reproducibility, ampacity from two different pieces for each sample is shown. Source: ORNL.....	117
Figure I.1.3.4.2. (a) Cross-sectional STEM image of the FIB sample and (b, c) Z-contrast STEM images of the Cu/CNT/Cu/CNT/Cu double layer UCC sample on a 28 μm Cu substrate. Source: ORNL.....	118
Figure I.1.3.4.3. (a) Density of states in electronic states of pressurized semiconducting (11,0) CNTs showing a reduced band gap due to CNT-CNT interactions. (b,c,d) N, O, and Cu doping help to significantly increase the electron density near the Fermi level, transforming semiconducting CNTs into metallic CNTs. Source: ORNL.....	119
Figure I.1.3.5.1. Process for synthesizing interpenetrating phase composite materials using the PC technique. The reinforcing lattice is printed using a laser powder bed fusion process, filled with liquid-metal using pressure die-casting, and then post-processed to optimize the properties. Source: ORNL.....	122
Figure I.1.3.5.2. A portion of the ORNL-produced AM lattices using 316L stainless-steel. Source: ORNL.....	123
Figure I.1.3.5.3. Process of upscaling individual unit cell from 2.5 mm cube to a 10 \times 10 unit cell populated cell block. Source: ORNL.....	124
Figure I.1.3.5.4. Slab production process with 54 cell block repetitions. Source: ORNL.....	124
Figure I.1.3.5.5. Lattice tessellation reduction approach - over an order of magnitude reduction in surface geometry with no loss in physical build resolution. Source: ORNL.....	125
Figure I.1.3.5.6. The HPDC molds machined and ready for infiltration. Source: Falcon Lakeside Manufacturing.....	125
Figure I.1.3.6.1. EC of ShAPE™ AA1100-graphene composites with varying graphene content demonstrating lower TCR than AA1100 along the length of the wires showing <0.6% IACS variability. Source: PNNL.....	129
Figure I.1.3.6.2. Change in EC of commercially procured AA1100 wire from McMaster Carr, ShAPE™ AA1100 wire (ShAPE™ control), and ShAPE™ Al/graphene ultra-conductor wire with 0.1 wt.% graphene after cold drawing and annealing at (a) 250°C and (b) 400°C with respect to their as extruded or as-procured condition. Source: PNNL.....	130
Figure I.1.3.7.1. A summary of the AF microstructure of the Al-Si-Cu-Mg-Fe alloy: (a) IPF colored map showing the grain structure; SEM micrographs showing microstructures at (b) lower and (c) higher magnifications. Melt pool boundaries are outlined by dotted lines in (b) and (c). The BD is vertically upwards. The microstructures correspond to the alloy produced at 370 W and 1,600 mm/s scanning speed. Source: ORNL.....	134
Figure I.1.3.7.2. APT results for the Al-Si-Cu-Mg-Fe alloy in anAF state. The table in the inset lists the matrix composition, excluding the Si-particle observed at the left bottom edge of the tip. Source: ORNL.....	134

Figure I.1.3.7.3. (a) Tensile properties of the as-fabricated (AF) AlSiCuMgFe alloy processed with different processing parameters. (b) A comparison of tensile properties with other relevant AM Al-Si-Mg based alloys whose tensile data are reproduced from Refs. [3]–[6]. Source: ORNL.....	134
Figure I.1.3.7.4. A summary of the as-solutionized microstructures of the Al-Si-Cu-Mg-Fe alloy: (a) IPF colored map showing the grain structure; (b) and (c) SEM micrographs showing microstructures in melt pool interiors at (b) lower and (c) higher magnifications; (d) SEM micrograph showing microstructure near a melt pool boundary; and (e–g) EDS maps, corresponding to (d), showing elemental distributions of (e) Al, (f) Si, and (g) Fe. Source: ORNL.....	135
Figure I.1.3.7.5. Evolution of hardness as a function of aging time at 180 °C: (a) direct aging of the alloy after fabrication and (b) aging of the alloy after initially solutionizing at 530 °C for 1 h. AF stands for as-fabricated state, while AS refers to the solutionized and quenched state. Source: ORNL.	136
Figure I.1.3.8.1. (a) Low-magnification optical micrograph and (b) high-magnification SEM images of Alloy 2 after aging for 4 h at 650 °C. Source: ORNL.....	140
Figure I.1.3.8.2. Hardness of cast developmental die steels after STQ and then subsequent aging at 550 °C for 4 h. Source: ORNL.	140
Figure I.1.3.8.3. Top-view of the Alloy 7 sample after laser track passes. On the track designated “1,” a single laser pass was made. On track “2,” two laser passes were made back and forth. On track designated “3,” three laser passes were made. Source: ORNL.....	141
Figure I.1.3.8.4. (a) Hardness traverses as a function of distance from the laser remelted material of Alloy 7 after laser remelting and subsequent aging at 550°C for 4 h. EBSD IPF maps of the BCC phase/martensitic microstructure phase corresponding to a region of (b) laser remelted and aged material and (c) a region away from the laser remelted material in the HAZ after aging. Source: ORNL.	142
Figure I.1.3.8.5. Measured TC of Alloy 7 and H13. The TC of M300 is derived from [3]. Source: ORNL.	142
Figure I.1.4.1.1. Thrust 4 coordination of the multi-lab characterization. Researchers identify an EV material problem to be solved and propose work. Upon successful review and ranking, funds are awarded with advanced characterization (and computation) and analyses ensuing. Discussions and meetings occur often between researchers at the national laboratories through hybrid meetings and email. Results are converted into research products with the goal of their application within future EVs. Source: ORNL.	145
Figure I.1.4.1.2. Al-Sn blanks were prepared by wire electro-discharge machining (EDM) sheets that are sufficiently thin to mitigate the need for a post-EDM grinding as part of the metallographic preparation needed to achieve polished foils with ~150 micron thicknesses. Source: ORNL.	147
Figure I.1.4.1.3. APT maps of the Al matrix by for the (a) Al-6Ni-0.4Zr, (b) Al-6Ni-0.3Ti, (c) Al-6Ni-0.3V, and (d) Al-6Ni-0.5Fe alloys heat-treated at 400 °C for 200 h. The blue and purple dots are the Al and Zr atoms, respectively. 3 at.% Zr isoconcentration surfaces are displayed in (a) to highlight the Al ₃ Zr L1 ₂ precipitates in the matrix. Source: ORNL.....	148

Figure I.1.4.1.4. (a) A high-angle annular dark-field image of a typical Sn-rich nanoparticle in an Al-Zr-Sn alloy, with an associated nanocluster consistent with the Al ₃ Zr phase. (b) A similar nanoparticle and Al ₃ Zr nanocluster. A hypermap of the elements was obtained showing the overlap of the Zr and Sn maps in (c); separate maps in (d) and (e) clearly differentiate the locations of Zr (Area 1) and Sn (Area 2), respectively. (f) Energy-dispersive x-ray spectra from Areas 1–3 in (c) also confirm only Sn in the nanoparticle and only Zr in the nanocluster. Source: (a) ORNL, (b–f) Thermo Fisher Scientific [1].....	149
Figure I.1.4.1.5. Raman spectra from CNTs. Source: ORNL.	151
Figure I.1.4.1.6. Al-Sn blanks were prepared by wire EDM sheets that are sufficiently thin to mitigate the need for a post-EDM grinding as part of the metallographic preparation needed to achieve polished foils with ~150 μm thicknesses. Source: ORNL.	152
Figure I.1.4.1.7. (a) SAXS data measured during isothermal hold at the APS showing changes in the intensity at a small size (~3*10 ⁻¹ Å). (b) Single scan of a previously heat-treated sample measured at ORNL showing a good signal over the range of interest. Source: ORNL.....	152
Figure I.1.4.2.1. Selected results of Task 2C-23 on TC improvement: (a) non-polar Valvoline EV d4 base oil; and (b) polar PAG 4 cSt base oil. Source: ORNL.....	156
Figure I.1.4.2.2. Improved thermal impedance measurement system: (a) Location of the load cell and the infrared (IR) camera, (b) stainless-steel and Al bar between the heating and cooling stage, (c) a CNT-coated sample, and (d) its interface relationship. Source: ORNL.	157
Figure I.1.4.2.3. (a) Infrared image showing temperature gradient and interface resistance. Source: ORNL.	158
Figure I.1.4.2.4. Pure Al ingot with 4-step thickness and EC indicating the effect of cooling rate. Source: ORNL.	159
Figure I.1.4.2.5. Thermal diffusivity, thermal expansion, and specific heat of 3D-printed Al alloys for (a) T6 heat-treated and (b) AF conditions. Source: ORNL.....	160
Figure I.1.4.2.6. Sintering of three ferrites up to 1500 °C with the onset of shrinkage at 600 °C and 900 °C. Source: ORNL.	161
Figure I.1.4.2.7. Electrical resistivity and Seebeck coefficient of 4140 and X35 tool steels to 600 °C. Source: ORNL.....	161
Figure I.1.4.2.8. Total TC of X35 with electron and phonon contributions. Source: ORNL.	162
Figure I.1.4.3.1. The transmission geometry x-ray diffraction setup at beamline 1-ID-E in the APS, where the x-ray beam path is marked in white with solid line showing the incident beam and dashed lines showing transmitted/diffracted beams. Source: ANL.....	165
Figure I.1.4.3.2. Photograph and schematic drawings of synchrotron x-ray diffraction arrangements for the study of ShAPE™-processed Al specimens received from PNNL. Source: ANL.....	165
Figure I.1.4.3.3. 2D-transmission Debye-Scherrer patterns obtained for (a) drilling and (b) hammering / mortar + pestle routes. Source: ANL.	166

Figure I.1.4.3.4. Integrated and indexed 1D-patterns of the various sample conditions: (a) Fe-6Si slow-cooled for 30 min from 1100 °C, (b) Fe-6Si-2Cr slow-cooled for 30 min from 1100 °C, (c) Fe-6Si quenched from 1100 °C, and (d) Fe-6Si-2Cr quenched from 1100 °C. The peaks indexed using blue diamonds are signatures of BCC-Fe major phase. The peaks corresponding to the crystal structures of minor intermetallic phases, B2 and DO ₃ , are marked using black circles and red squares, respectively. Source: ANL.	167
Figure I.1.4.3.5. (a) Beam profile scan at center = 9.85, width ≈ 2.4 mm. (b) Micro-diffraction patterns measured two ShAPE™-processed Al specimens received from PNNL measured with a 10 keV beam. Source: ANL.....	168
Figure I.1.4.4.1. (a) TEM bright-field images and EDS maps of Al, C, O, and Sc. (b) STEM-HAADF and EDS maps of the Al-oxide layer found between the C graphene grain and the Al. (c) Electron energy loss spectroscopy plots of the different zones probed across the oxide layer. Source: PNNL.	171
Figure I.1.4.4.2. (a) 3D reconstruction of the Al-GNP specimen with (b) individual maps of different ionic species. (c) 3D atomic map of the Al-GNP with the iso-volume enclosing the region with a minimum of 0.5 at.% of C. (d) Concentration (atomic and ionic) plots of the region of interest found in (c). Source: PNNL.	172
Figure I.1.4.4.3. (a) SEM image of the fragmented Cu in the Al matrix. (b) EDS of the fragmented Cu and Al in the matrix reveals the mixing of Al and Cu. (c) SEM image of the Cu/Al interface showing different contrasts from regions rich in Al and Cu elements along with precipitates rich in Mg and Si, as shown in (d). (e–f) SEM and EDS of the hybrid joint of the Al/Cu interface coated with Ni. Source: PNNL.....	173
Figure I.1.4.4.4. (a-c) BSE images and EDS maps of the AA206- AA206- 10 vol.% TiB ₂ (1% <i>in-situ</i> + 9% powder). (d-f) IPF-z map on the composite at low and high-magnification showing the grain size variation of Al and TiB ₂ along with phase map evolution. (g-h) STEM and HAADF images of the composite showing different phases such as TiB ₂ , Al ₂ Cu, and TiWB ₂ within the Al matrix. Source: PNNL.	174
Figure I.1.4.4.5. EBSD IPF images of (a) Fe-5Si, (b) Fe-6Si and (c) Fe-6.5Si in the center of SZ. (d) Histogram plot of the average grain size. (e) XRD patterns in the center of SZ. Source: PNNL.	175
Figure I.1.4.4.6. (a) TEM dark-field image of the Fe-6.5Si alloy using the [111] superlattice reflection circled in the electron diffraction pattern. (b) High-resolution TEM image of the Fe-6.5Si alloy along the [110] zone axis, and (c) the corresponding inverse fast Fourier-transform image obtained by masking four <111> reflections in the fast Fourier-transform pattern. Source: PNNL... ..	176
Figure I.1.4.5.1. (a), (b), and (c) melting of bare Cu-NP on CNT-infused Cu substrate and graphene-infused Cu substrate; (d) melting temperature as a function of NP sizes; and (e) scaling of melting temperature. Source: ORNL.	179
Figure I.1.4.5.2. Calculated (red) and experimental (blue) Al resistivity as a function of temperature; insert: Al _{1-x} Zr _x calculated residual resistivity as a function of Zr concentration, x. Source: ORNL.	180
Figure I.1.4.5.3. (a) Two-dimensional growth of Al-dendrite of Al-4 wt.% Cu in a 5K undercooled melt after 0.256 seconds. (b) Comparison of CA simulated velocity of dendrite tip at steady-state with the analytical LGK solution at multiple liquid undercooling values. (c) Snapshots of three-dimensional growth of Al-dendrite simulated on OpenFOAM. Source: ORNL.	181

Figure I.1.4.5.4. Comparison of the predicted TC with the measured values. (a) The predicted trend agrees well with the measured values. (b) Elemental conductivity should be considered for correct prediction of Al-3Ni and Al-3Ni-0.45Zr. Source: ORNL..... 182

Figure I.1.4.6.1. DOE-ORNL virtual workshop speakers. Source: ORNL..... 186

Figure I.1.4.6.2. Four sets of samples were made available for the DOE-ORNL round-robin. Source: ORNL. 187

Figure I.1.4.7.1. Critical materials analysis workflow. Source: ANL..... 191

Figure I.1.4.7.2. U.S. critical materials demand of global supply for LD vehicles only, by material, for 0% and 100% electric vehicle adoption rates, as well as scenarios with 100% EVs with lightweighting or alternative LFP battery chemistry. Source: ANL. 192

Figure I.1.4.7.3. U.S. critical materials demand of global supply for LD vehicles and MD/HD vehicles, by material, for 0%, 50%, and 100% EV adoption rates. Source: ANL. 193

Figure II.3.1.1.1. Example of VNA cavity measurement. The band of operation of the generator covers only the central delimited by the vertical marker on this plot. This measurement shows a very high reflection, which is not desirable. Source: ORNL..... 322

Figure II.3.1.1.2. Example of return loss measurement evaluated with the generator at low-power over its full band of operation. The return loss value is lower than in Figure II.3.1.1.1, but still unacceptable. Source: ORNL. 322

Figure II.3.1.1.3. (a) Typical pattern of reflection measured across the full band of operation with the generator at low-power. The center of the band of operation is marked by an orange dot, in the middle of the “power set” line. The return loss value is greater than the minimal acceptable value of -10 dB. (b) An example of an inconsistent pattern of reflection. The value of the reflection is similar but shifted. The vertical line (purple) indicates the selected frequency of operation, which is different in both examples. Source: ORNL..... 322

Figure II.3.1.1.4. Measurement of the return loss with the generator using simplified transmission line. The best tuning-point can be as good as -22.5 dB (0.6% reflection). Source: ORNL. 323

Figure II.3.1.1.5. (a) Pattern of reflection measured across the full band of operation with the generator at low-power. The presence of three peaks can be seen, with the two best values observed at -16 dB and -29 dB (Note: on this instrument, the Y-axis is inverted). (b) Pattern of reflection ($S_{1,1}$) measured with the VNA across the same span of frequencies. Only one broad peak at -20 dB is measured. Both measurements are performed on the HTC reactor using a simplified transmission line. Source: ORNL. 324

Figure II.3.1.1.6. Carbonization in one step of four tows of 50,000 filaments of commodity-grade OPF using two EM powered furnaces setup inline. One process condition corresponds to one assigned color identification (COLOR ID). Source: ORNL. 324

Figure II.3.1.2.1. (a) A multimaterial bumper being printed on the 3DP 3D Platform™ printer using filament-based feedstock. (b) 3D-printed multimaterial bumper structure. Source: ORNL..... 329

Figure II.3.1.2.2. Supportless armrest structure design for OPP. Source: ORNL..... 330

Figure II.3.1.2.3. Robotic arm control for the OPP (wrapping) on the armrest design. Source: ORNL. 331

Figure II.3.1.2.4. OPP with inserted support blocks in the armrest design. Source: ORNL.	331
Figure II.3.1.2.5. Optimized supportless armrest structure.. Source: ORNL.....	332
Figure II.3.1.2.6. Workflow of the ML-based inverse design framework. Source: UCB.....	333
Figure II.3.1.2.7. Workflow of the integrated ML model. (a) The inverse model takes 16 mechanical properties as an input and predicts the design parameters of the lattice in a sequential manner. (b) The forward models evaluate the mechanical properties of the designed lattice. Source: UCB.	333
Figure II.3.1.2.8. Prediction accuracy of forward models for (a) a low rate and (b) a high-rate. Source: UCB.....	334
Figure II.3.1.2.9. (a) Training data and selected target property set mapped onto the design space for low- and high-loading rate tests, and (b) the refined design with the geometrical and material combination Source: UCB.....	335
Figure II.3.1.3.1. Schematic of the tasks for enhanced organic-inorganic interface between the CF and polymer matrix and real-time evaluation of material properties with embedded sensors. Source: ORNL.	338
Figure II.3.1.3.2. Mechanical test results showing the tensile properties of an unmodified vs. modified surface of CF with crown ether silanes, which improves adhesion properties and enhances wettability. A schematic representation of the surface modification scheme with the addition of dendrimeric amines is also shown. Source: ORNL.	339
Figure II.3.1.3.3. FEA simulations. (a) Schematic of the data-driven method based on FEA and ML experiments that characterize interfacial properties without pre-determined model forms for PVDF as a matrix and MXenes (MoS_2) as the filler showing elastic, piezoelectric, and dielectric (isotropic and anisotropic) properties. PVDF nanocomposites were fabricated by 3D-printing for process-property relationships. (b) The distribution of stress with similar composition via FEA simulation of a 3D-printed sandwich structure. (c) The electric potential output as a function of increasing MoS_2 orientation (angle). Source: ORNL.	340
Figure II.3.1.3.4. (a) A new co-extrusion assembly was designed to have both the fiber and the epoxy matrix under the same pressure environment. (a) 3D-printing of epoxy and continuous CF was initially achieved with the modified Hyrel attachment. Source: ORNL.....	341
Figure II.3.1.3.5. (a) Raman spectroscopy data together with (b) SEM imaging confirmed the distribution and effect of the MoS_2 on the PVDF matrix and morphology. (c) The protocol for preparation of the 3D-printable ink and (d-e) the rheological (storage and loss modulus) and shear-thinning viscosity properties of the ink comparing the 8% MoS_2 composition with pristine PVDF. The scheme for 3D-printing is shown on the right. Source: ORNL.....	342
Figure II.3.1.5.1. Fabricated composite tensile specimen (a) before and (b) after tensile testing. Source: ORNL.	353
Figure II.3.1.5.2. Stress vs. elongation plot summarizing the tensile performance of the five composite specimens. Source: ORNL.....	353
Figure II.3.1.5.3. About 30–40% improved ultimate elongation of the composites was demonstrated when the polymer matrix was immobilized on the fibers. Y-axis data shows the ratio of ultimate elongations in the composites to the neat matrix at different discontinuous CF volume fractions. Source: ORNL.	354

Figure II.3.1.5.4. SEMs of fracture surfaces of CF-reinforced thermoplastic composites show (a) a lack of fiber-matrix adhesion and (b) an appropriate fiber-matrix adhesion that minimizes early fiber pullout, leading to increased strength and ultimate elongation. Source: ORNL.....	354
Figure II.3.1.5.5. Time series of standardized interfacial characterization study. (a) An iPP pellet in a sample environment. (b) Conformal melt pool of the iPP prior to CF insertion. (c) CF insertion in the center of the melt pool. (d) Solidified polymer sample with opaque microstructure resulting from crystallite scatter ready for pullout testing. Source: ORNL.....	355
Figure II.3.1.5.6. Apparent interfacial shear-stress across a library of thermal envelopes for crystallization. A refinement of the preparation methods leads to consistent values for interfacial properties for the challenging iPP-CF system. Source: ORNL.....	356
Figure II.3.1.5.7. (a) FTIR and (b) x-ray data of different CF-PP composites. Source: ORNL.....	356
Figure II.3.1.5.8. Nucleation of PP crystals in the presence of CF. (a–c) The DSC data of the studied samples. The first, second, and third heating cycles were presented correspondingly. (d–e) The first and second cooling cycles, respectively. (f) The measured crystallinity of PP in the CF-PP composites by wt.%. Source: ORNL.....	357
Figure II.3.1.6.1. (a) A schematic of the electrospinning setup with the PAN dope pumped by a syringe pump and connected to a high-voltage power supply to deposit the nanofibers on a unidirectional CF fabric on a rotating grounded drum. (b)–(d) SEM images of the resulting nanofibers on the CF. Source: ORNL.....	360
Figure II.3.1.6.2. (a) A picture and SEM image of the ABS pellets and PAN nanofibers with a schematic of the melt-mixing process. (b) Two chemical structures showing the PAN cyclization process and PAN/ABS crosslinking. (c) Four schematics showing the different experiments that were run to validate PAN/ABS crosslinking. Source: ORNL.....	361
Figure II.3.1.6.3. (a) Rheology results for ABS and ABS/PAN composites heat-treated at various temperature. (b) Pictures of the composites before and after the solubility tests. (c) The tensile test results for the ABS compared to ABS/PAN samples made with PAN nanofiber versus PAN powder. (d) Solid-state NMR results showing peak-broadening after heat-treatment indicating crosslinking between ABS and PAN. Source: ORNL.....	362
Figure II.3.1.6.4. (a) A schematic showing how the composites were fabricated for the AFM studies. (b) OM image showing the cross-section of two CF plies with the area of interest for AFM studies highlighted with the dashed line box. (c) A schematic showing the cross-section of a CF composite and an AFM cantilever on top probing the cross-section of the composite. (d) A map of the slope of the force vs. displacement curve from the indentation tests. (e) A plot showing the force vs. displacement for the indentation tests. Source: ORNL.....	363
Figure II.3.1.6.5. Three maps with the slope of the force versus displacement curves from the AFM tests: (a) CF with no nanofibers in ABS, (b) nanofibers on the CF in ABS heated to 150 °C, and (c) nanofibers on the CF in ABS heated to 220 °C. Source: ORNL.....	363

Figure II.3.1.6.6. (a) A schematic showing the composite stacking sequence of +45 and -45°. (b) A schematic of the uniaxial tensile tests performed. (c) A bar plot showing the in-plane shear-strength of the tensile tests samples at different heat-treatment temperatures. (d) A photo of the fracture surface from the tensile tests. Four SEM images of the fiber surface at the fracture surface are shown for (e) the baseline sample with no nanofibers, (f) the sample with the nanofibers at 150 °C, (g) the sample with nanofibers at 220 °C, and (h) the sample with nanofibers at 250 °C. Source: ORNL.	364
Figure II.3.1.7.1. (a) Schematic of the large area high-resolution projection stereolithography system. (b) Large area high-resolution projection stereolithography 3D printing system with a large format printing vat the team developed. Source: ORNL.	367
Figure II.3.1.7.2. (a) 3D-printed large-size high-resolution Voronoi vase made of CFRP. The vase is designed to have gradient unit cell size and strut thickness varying from 50 μm to 2 mm. (b) 3D-printed hollowed car bumper. Each half (~55 cm) was printed separately and bonded together to make a full-size (110 cm) bumper. Source: ORNL.	368
Figure II.3.1.7.3. Cure depth as a function of energy density for CFRP resin with different fiber concentrations. As the resin has a greater amount of fibers, the curing depth decreases. Source: ORNL.	369
Figure II.3.1.7.4. Measured fiber length distribution histogram of two types of CFs. Source: ORNL.	369
Figure II.3.1.7.5. Cure depth as a function of energy density for CFRP resin with two different fiber lengths: 70 μm and 315 μm . Source: ORNL.	370
Figure II.3.1.7.6. Cure depth as a function of energy density for CFRP resin with different initiator concentrations. Source: ORNL.	370
Figure II.3.1.7.7. (a) Schematic of a typical bottom-up projection SLA system. (b) Measured viscosity of CFRP resin with different fiber concentrations (e.g., 0, 5, 10, 25 wt.%) in shear-rate domain. Source: ORNL.....	371
Figure II.3.1.8.1. Pronounced “dog-boned shape” of the dry-spun precursor. Source: ORNL.....	374
Figure II.3.1.8.2. Advanced plasma-oxidation system co-developed by 4XT and ORNL. Source: ORNL.	376
Figure II.3.1.8.3. Advanced surface treatment co-developed by 4XT and ORNL. Source: ORNL.	376
Figure II.3.1.8.4. Low (bottom) and high (top) temperature carbonization furnaces. Source: ORNL.	376
Figure II.3.1.8.5. Sizing application and dryer (foreground) integrated with surface treatment system (background). Source: ORNL.	377
Figure II.3.1.9.1. CF manufacturing process and cost analysis. Source: ORNL.	380
Figure II.3.1.9.2. Embodied energy for PAN and coal pitch precursor and CF manufacturing. Source: ORNL.	381
Figure II.3.1.9.3. Multiscale R&D approach. Source: ORNL.....	383
Figure II.3.1.9.4. Pitch material from different sources. Source: ORNL.....	385
Figure II.3.1.9.5. Reactor bed design. Source: ORNL.....	385
Figure II.3.1.9.6. Polymerization product of naphthalene precursor with FeCl_3 . Source: ORNL.....	386

Figure II.3.1.9.7. Carbon mesophase content at low-, medium-, and high-loadings. Source: ORNL.	386
Figure II.3.1.9.8. Reactor bed design. Source: ORNL.....	387
Figure II.3.1.9.9. Homogeneous solubility of metal catalyst in alcohols prior to contact with porous graphitic material. Source: ORNL.....	387
Figure II.3.1.9.10. (a) SEM showing the morphology of deposited surface catalyst. (b) EDS overlay suggesting a 13 at.% of Fe on the graphitic material. Source: ORNL.....	388
Figure II.3.1.9.11. (a) X-ray photoelectron wide-scan spectra quantifying the at.% of Fe at 7. (b) A high-resolution scan of the Fe 2p orbital bonding environment. Deconvolution of the high-resolution spectra will be performed to fully assign the Fe oxidation state and coordination state. Source: ORNL.....	388
Figure II.3.1.9.12. Binder pitch feedstock for next trials in pellet/flakes form to avoid issues associated with feed instability from caking events. Source: ORNL.....	389
Figure II.3.1.10.1. PFRP plate manufacturing process with controlled unidirectional fiber length from a woven PP fabric. The PFRP plate was used for injection-molding to fabricate samples for the evaluation of fiber lengths. Source: PNNL.....	393
Figure II.3.1.10.2. (a-b) PFRP plates with controlled unidirectional fiber length from a woven PP fabric. The PFRP plate was used for injection-molding to fabricate samples for the evaluation of fiber lengths for (c) three different injection-molding parameters. Source: PNNL.....	394
Figure II.3.1.10.3. (a–b) Filament winding of unidirectional UHMWPE fibers on HDPE films, (c) compression molding process of the composite, and (d) UHMWPE-fiber-reinforced HDPE composites. Source: PNNL.....	394
Figure II.3.1.10.4. (a) Longitudinal tensile strength and (b) modulus of unidirectional UHMWPE-polymer-fiber-reinforced HDPE composites ($V_f = 30\%$) as a function of processing temperature in compression molding. The results were plotted together with melting behaviors of UHMWPE fiber and HDPE matrix. Source: PNNL.....	395
Figure II.3.1.10.5. Displacement as a function of temperature for UHMWPE fiber at a constant load of 0.01 N obtained from dynamic mechanical analysis. Source: PNNL.....	395
Figure II.3.1.10.6. Normalized maximum principal strain field and fracture morphologies of UHMWPE-polymer-fiber-reinforced HDPE composites fabricated at the temperature of (a) 140 °C or (b) 160 °C. This figure corresponds to the results almost at the peak load of the composite under uniaxial tension. Source: PNNL.....	396
Figure II.3.1.10.7. Mechanical recycling of self-reinforced PP woven composites by injection-molding using chopped composite chips. Source: PNNL.....	397
Figure II.3.1.10.8. Process conditions for the mechanical recycling of self-reinforced PP woven composites by injection-molding using chopped composite chips. Source: PNNL.....	398
Figure II.3.1.10.9. Recycled PP composites via injection-molding with different sets of parameters: (a) $T = 170^\circ\text{C}$ and $C_s = 0.5 \text{ in.} \times 0.5 \text{ in.}$; (b) $T = 180^\circ\text{C}$ and $C_s = 0.5 \text{ in.} \times 0.5 \text{ in.}$; (c) $T = 170^\circ\text{C}$ and $C_s = 0.25 \text{ in.} \times 0.25 \text{ in.}$; and (d) $T = 180^\circ\text{C}$ and $C_s = 0.25 \text{ in.} \times 0.25 \text{ in.}$. Note: injection speed, screw speed, and the cooling process were all fixed. Details can be found in the report. Source PNNL.....	398

Figure II.3.1.10.10. (a) Longitudinal tensile strength and (b) elastic modulus of UHMWPE-fiber-reinforced HDPE composites as functions of processing temperature, processing pressure, and fiber volume fraction. Source: PNNL.....	399
Figure II.3.1.10.11. UHMWPE-fiber-reinforced HDPE composites with the same $V_f = 38\%$ and $P = 1.25$ MPa but different temperatures: (a) $T = 140^\circ\text{C}$ and (b) $T = 150^\circ\text{C}$. Source PNNL.	400
Figure II.3.1.10.12. (a) Summary of impact resistances of CFRP and PFRPs. (b) Through-thickness views of perforated CFRP and PFRPs using X-ray micro computed tomography scan. (c) Summary of the CFRP and PFRPs for low-energy, multiple impact performances. Source: PNNL.	401
Figure II.3.1.10.13. The overall hot process to fabricate SRPC laminate using PP fiber reinforcement and PP-compatible matrix. (a) PP fiber wound on a stainless-steel frame. (b) PP fiber sandwiched by two PP-compatible matrix sheets. (c) Scheme of the hot press process. (d) Waterjet-cutting. (e) Dumbbell-shaped tensile specimen of SRPC laminate. Source: ORNL.	402
Figure II.3.1.10.14. Mechanical properties of PP fiber, PP-compatible matrix, and SRPC laminate containing 30 wt.% PP fibers along with those of bulk PP as a reference. Source: ORNL.	402
Figure II.3.1.10.15. (a) Melt-fiber-spinning. (b) Fiber drawing a fiber bundle in a custom-mold. (c) Before and (d) after hot compaction. (e) Digital image of compaction process. Strap specimen (f) before and (g) after tensile testing. Source: ORNL.....	403
Figure II.3.1.10.16. The mechanical properties of PP fiber-reinforced PP composites fabricated at various compaction temperatures of 130°C , 140°C , 150°C , and 160°C . Source: ORNL.	404
Figure II.3.1.10.17. Recycling process for the polymer-polymer composite. (a) Melt-spun polymer-fiber. (b) Shortened polymer-fiber lengths after cutting. (c) Feeding the cut fiber into a micro-compounder. (d) Re-melted polymer material. (e) Shredded materials in a metal frame. (f) Hot compaction resulting in a plaque. (g) Waterjet-cutting of the plaque. (h) Final tensile bar. Source: ORNL.	405
Figure II.3.1.10.18. Stress-strain curves of recycled polymer-polymer composite. Source: ORNL. ..	406
Figure II.3.1.10.19. DSC thermogram showing melting behavior of highly oriented polyethylene fiber (black) and ethylene copolymer (red). Onset of melting occurred at approximately 140°C and 90°C for the polyethylene and ethylene copolymer, respectively. Source: ORNL.	406
Figure II.3.1.10.20. (a) The laboratory-scale winder setup used to produce uniaxial composites features a motor-driven carriage for fiber-tow placement and a rotating mandrel holder in which (b) a winding plate is secured. (c) This shows a schematic representation of the multilayer composites as constructed within this work. Alternating ethylene copolymer sheets and wound fiber layers are laid up prior to pressing. (d) Photograph displaying pressed composite material prior to the (e) laser cutting of tensile specimens. (f) subsequent attachment of GFRP thermoset tabs to the specimen grip regions prior to tensile testing. Source: ORNL.	407
Figure II.3.1.10.21. Results from the tensile tests of the composite samples. The samples displayed a UTS of 717 ± 87 MPa, a 19.7 ± 2.6 GPa modulus, and a > 500 MPa UTS at 5% elongation. Source: ORNL.....	408
Figure II.3.1.11.1. Direct depolymerization of PET waste and concerted repolymerization. Source: PNNL.	411

Figure II.3.1.11.2. (a) PET-derived PPTA fiber wound on a bobbin. (b) SEM of PET-derived fiber. Source: PNNL.	412
Figure II.3.1.11.3. (a) Fiber diameter decreased as draw ratio increased. (b) Mechanical test results for as-spun and heat-treated fibers. Source: PNNL.	412
Figure II.3.1.11.4. PNNL's and commercial (Kevlar 29) synthesis approach to PPTA. Source: PNNL.	413
Figure II.3.1.11.5. Block flow diagram of the proposed Kevlar fiber synthesis from waste-PET via hydrolysis. Source: PNNL.	414
Figure II.3.1.11.6. Chemical pathways used to generate PPTA precursors (Scheme 1a) terephthalate salt and (Scheme 1b) TPA from waste-PET. Source: PNNL.	414
Figure II.3.1.11.7. (a) Minimum selling price of TPA produced from waste-PET compared to an enzymatic approach [2]. (b) Comparison with petroleum-derived TPA. Source: PNNL.	415
Figure II.3.1.11.8. Minimum selling price of waste-PET derived aramid fiber. Source: PNNL.	415
Figure II.3.1.11.9. LCA Results of waste-PET derived TPA and aramid fiber. Source: PNNL.	416
Figure II.3.1.12.1. Schematic of an AM-CNG storage vessel concept. (a) External rigid structural layers of the vessel: load-bearing resin filaments (blue) filled with short and continuous CF (white). (b) Continuous filament material is applied to the midbody yielding maximum hoop strength. (c) Short-fiber extrusion used to fabricate complex end caps. Flexible and cross-linkable polymer compositions reinforced with nanoplatelets shown in (b) and (c) will be printed to serve as the inner layers of a vessel (yellow and blue layers represent the inner gas barrier and transition to structural layers, respectively). Source: LLNL.	419
Figure II.3.1.12.2. Project schedule. Source: LLNL.	420
Figure II.3.1.12.3. (a) Optimization informed CADWIND visualization for the midbody sections of the scaled-test vessel, forming toolpath instructions for the midbody print of the hybrid vessel. (b) "Printed" midbody structural section on a dummy mandrel form following the generated code (pre-top-coat addition). Source: LLNL.	421
Figure II.3.1.12.4. A representation of the 3D-printed coupon-scale structures fabricated for tensile testing. Source: LLNL.	422
Figure II.3.1.12.5. From left to right: mandrel form showing the complete liner zone, incorporating bosses; beginning of structural midbody print; near completion of midbody long-fiber print showing wrap around boss region; and application of the topcoat layers (incomplete). Source: LLNL.	423
Figure II.3.1.12.6. A complete gas bottle test article shown after thermal-cure and prior to mandrel and shaft removal. Source: LLNL.	423
Figure II.3.1.13.1. Project overview. Source: NREL.	425
Figure II.3.1.13.2. PECAN resin chemistry in which bioderived epoxies and anhydrides are combined to a crosslinked network and can be recycled with methanol. Source: NREL.	426

Figure II.3.1.13.3. (a) Methanolysis mechanism for the PECAN-CFRCs. (b) Dynamic mechanical analysis (DMA) temperature sweeps (single-cantilever, 1Hz) of the storage modulus and the tan delta are shown for three generations of chopped CFRP. (c) Virgin and (d) recovered fibers are shown for woven composite depolymerization experiments. DMA temperature sweeps are also shown across (e) the first, (f) the second, and (g) the third-generation for woven PECAN CFRPs. Source: NREL.....	427
Figure II.3.1.13.4. (a) Stress relaxation experiments were performed with differing loadings of 2-ethyl-4-methyl imidazole (24EMI) catalyst. (b) Repair of the PECAN resin is demonstrated with pictures of repaired PECAN coupon, broken coupon, and epoxy-amine control repair. (c) DMA thermograms of the control and test resins. (d) Thermoforming experiments were performed using a male/female mold and neat resin within a heated hydraulic press. (e) Using the same geometry, a thermoformed panel of PECAN-CFRC is shown with two differing elevations. (f) DMA iso-stress experiments (single-cantilever) at 35 °C (dotted) and 180 °C (solid) are shown for PECAN CFRP (black), neat resin (green), and test resin with 10 wt.% 24EMI. Stresses for each experiment were chosen as 1/1000 of the storage modulus of the material at 35 °C. Source: NREL.....	428
Figure II.3.1.13.5. Techno-economic analysis results for the circularity of the PECAN-CFRCs. (a) The MSP for the different scenarios studied here. (b) The sensitivity of the rCF MSP relative to the feedstock cost noting the base case and a scrap estimate price. Source: NREL.....	429
Figure II.3.1.14.1. Diagram of 3D printing equipment for CCF composites: Source: SRNL.....	433
Figure II.3.1.14.2. (a) Schematics of thermocouple printing process. (b–c) SEM images of inks printed using the protocol shown in (a) demonstrate a uniform MWCNT and CB dispersion on the substrate. (d) Thermal sensors printed on the 3D-printed thermoplastic part and Kapton. (e) Typical thermoelectric response of the thermal sensor shown in (d). (f) 3D-scan of the tool before and after 10,000 cycles showing no deformation. Source: SRNL and CU ICAR.....	434
Figure II.3.1.14.3. (a) LCEA scenarios and (b) LCEA results using SimaPro and Ecoinvent 3.0 database. Source: CU ICAR.	434
Figure II.3.1.15.1. Project task breakdown. Source: Ford.....	437
Figure II.3.1.15.2. Task list for component design work stream. Source: Ford.....	437
Figure II.3.1.15.3. Molding tool prior to shipment to MSU. Source: Ford.	438
Figure II.3.1.15.4. CCB molding tool prior to shipment to MSU. Source: Ford.	439
Figure II.3.1.15.5. CCB sample parts from tool commissioning trials in June 2023. Source: Ford..	439
Figure II.3.1.15.6. TGA graph of 40% reinforced PA66. Source: Ford.....	440
Figure II.3.1.15.7. Polymer composite specimens before and after the burn-off test (top), and weight fractions of each reinforcement fiber obtained after the analysis (bottom). (1) refers to early developmental batches that were used during the past studies, and (2) refers to the batch produced on production intent equipment. Source: Ford.....	440
Figure II.3.1.15.8. Parts produced during valve gate sequencing studies. Source: Ford.	441
Figure II.3.1.15.9. A comparison of water channel wall thickness with pack time. Source: Ford....	441
Figure II.3.1.15.10. A comparison of water channel wall thickness with pack time. Source: Ford...	442
Figure II.3.1.15.11. M-Tow preforms produced in support of CCB molding studies. Source: Ford...	442

Figure II.3.1.15.12. M-Tow checking fixtures developed to improve dimensional accuracy of preforms. Source: Ford.....	443
Figure II.3.1.15.13. Fully functional over-molded electronics module. Source: Ford.....	443
Figure II.3.1.15.14. Dimensional check using 3D scanning of a fully populated electronics module. Source: Ford.....	444
Figure II.3.1.15.15. (Top) Over-molded films and (bottom) over-molded fully populated films for development activities. Source: Ford.	444
Figure II.3.1.15.16. End-of-arm tooling for insertion of items to be over-molded plus removal of molded parts. Source: Ford.....	445
Figure II.3.1.15.17. CCB injection-molding tool with end-of-arm. Source: Ford.	445
Figure II.3.1.15.18. Location of removable inserts for running with or without M-Tow preforms. Source: Ford.	446
Figure II.3.1.15.19. Sample CCB parts produced in support of recycling studies. Source: Ford.	446
Figure II.3.1.15.20. Shredded materials produced from CCB components. Source: Ford.	447
Figure II.3.1.16.1. DIC results showing axial, transverse, and shear strain for the baseline and curved path specimens. Red indicates highest strain and pink indicates lowest strain. Source: Teijin.....	450
Figure II.3.1.16.2. NN predictions for GF composites and CF composites. Source: USC.	451
Figure II.3.1.16.3. Prior and updated PDF of the QoI. Source: USC.	452
Figure II.3.1.16.4. Prior and updated PDF of the first mean/scale random variables. Source: USC.	452
Figure II.3.1.16.5. (a) Impact test setup. (b) Impact sequence of the damage localization specimens consisting of two orthogonal 3-branch sensors. Source: Columbia University.....	453
Figure II.3.1.16.6. Full-scale thermal model of hybrid composite test sample with convective heat-transfer applied to the top surface. Source: Columbia University.....	455
Figure II.3.1.16.7. Hybrid composite test sample with embedded temperature sensors used for environmental chamber experiment to demonstrate thermal response at different composite layers. Source: Columbia University.....	455
Figure II.3.1.16.8. Experimental setups and results for the environmental chamber and heat lamp temperature response tests. Source: Columbia University.	456
Figure II.3.1.16.9. Finalized materials and process for the components of the composite battery enclosure. Source: GM.	457
Figure II.3.1.16.10. Parts consolidation advantages of composite material design compared to baseline metallic design. Source: GM.	457
Figure II.3.1.16.11. Design of composite mini-battery enclosure. Source: GM.....	458
Figure II.3.1.16.12. Virtual simulation of composite mini-battery enclosure (9.5 mm of intrusion). Source: GM.....	458
Figure II.3.1.16.13. Manufactured cover and tray components for the mini-battery enclosure. Source: GM.....	459

Figure II.3.1.16.14. Test fixture engineered for the battery enclosure. Source: GM.....	459
Figure II.3.1.16.15. Steel enclosure and composite mini enclosure under sled test. Source: GM...	459
Figure II.3.1.16.16. Deformed shape of the steel and composite mini enclosure at the instant of maximum intrusion. Source: GM.....	460
Figure II.3.1.16.17. Comparison of results between the crash experiments and simulations (steel enclosure) for (a) the pole force and (b) the cover displacement. Source: GM.....	460
Figure II.3.1.16.18. Comparison of experimental and numerical results (mini-battery enclosure) for (a) the pole force and (b) the cover displacement. Source: GM.....	461
Figure II.3.1.16.19. Comparison of pole intrusion between (a) the composite mini enclosure and (b) the steel enclosure. Source: GM.	461
Figure II.3.1.16.20. Resin filling of the mold at various injection times. Source: ESI Group.....	462
Figure II.3.1.16.21. SHM circuitry for the tray component. Source: Columbia University.....	462
Figure II.3.2.1.1. (a) SLIC composite design and (b) cross-sectional view showing sandwich structure. Source: Newport Sensors, Inc.....	465
Figure II.3.2.1.2. SLIC specimens for tensile, bending, and impact tests. Source: Newport Sensors, Inc.	466
Figure II.3.2.1.3. Block diagram of SLIC dual-sensing system. Source: Newport Sensors, Inc.	466
Figure II.3.2.1.4. Block diagram of dual-sensing amplifier for single sensing area. Source: Newport Sensors, Inc.	467
Figure II.3.2.1.5. Block diagram of dual-sensing amplifier for multiple sensing areas. Source: Newport Sensors, Inc.	467
Figure II.3.2.1.6. Developed dual-sensing amplifier for three sensing areas. Source: Newport Sensors, Inc.	467
Figure II.3.2.1.7. Small-scale model of SLIC bumper beam design. Source: Newport Sensors, Inc.	468
Figure II.3.2.1.8. SLIC specimen test setup. Source: Newport Sensors, Inc.....	468
Figure II.3.2.1.9. Tensile test result. Source: Newport Sensors, Inc.	469
Figure II.3.2.1.10. Bending test result. Source: Newport Sensors, Inc.	469
Figure II.3.2.1.11. Ball drop impact test result. Source: Newport Sensors, Inc.....	470
Figure II.3.2.1.12. Fabricated bumper beam compression mold. Source: Newport Sensors, Inc. ...	470
Figure II.3.2.1.13. Fabricated small-scale bumper beam. Source: Newport Sensors, Inc.....	470
Figure II.3.2.2.1. Proposed AUTO-SMART system. Source: Acellent Technologies, Inc.....	473
Figure II.3.2.2.2. SMART Layer® sensors. Source: Acellent Technologies, Inc.	474
Figure II.3.2.2.3. System test setup. Source: Acellent Technologies, Inc.	475
Figure II.3.2.2.4. System usage of PPS. (a) System architecture and (b) system algorithm development. Source: Acellent Technologies, Inc.	476
Figure II.3.2.2.5. Voltage impulse received upon an impact with a golf club. Source: Acellent Technologies, Inc.	477

Figure II.3.2.2.6. Impact signals from (a) a PVC pipe and (b) a wooden board. Source: Acellent Technologies, Inc.	477
Figure II.3.2.2.7. Impact signals from (a) a stone and (b) a wooden dowel rod. Source: Acellent Technologies, Inc.	478
Figure II.3.2.2.8. Voltage impulse received upon an impact with a prosthetic leg. Source: Acellent Technologies, Inc.	479
Figure II.3.2.2.9. The dimensions (in inches) and design of the MESC skateboard. Source: Acellent Technologies, Inc.	481
Figure II.3.2.2.10. (a) Schematics of the guided wave inspection setup on an indicative Li-ion battery, showing piezoelectric transducers used for pitch-catch guided wave propagation, as well as different internal layers of the battery and constituent materials. (b) Representative signals at two SoC, illustrating changes in the receiving signal amplitude and time of flight, as a result of changing SoC during charge. Source: Acellent Technologies, Inc.	481
Figure II.3.2.2.11. Cycling and HPPC test of the fabricated MESC cells in the battery cycler Source: Acellent Technologies, Inc.	482
Figure II.3.2.2.12. (a) Voltage obtained from the cyclic test of the MESC pouch cells up to 200 cycles. (b) A zoomed in view of a part of the voltage cycling. It takes about 500 hr. to perform 63 cycles. Source: Acellent Technologies, Inc.	482
Figure II.3.2.2.13. (a) Current obtained from the cyclic test of the MESC pouch cells up to 200 cycles. (b) A zoomed in view of a part of the current cycling. It takes about 500 hr. to perform 63 cycles. Source: Acellent Technologies, Inc.	483
Figure II.3.2.2.14. (a) Capacity obtained from the cyclic test of the MESC pouch cells up to 200 cycles. (b) A zoomed in view of a part of the capacity cycling. It takes about 500 hr. to perform 63 cycles. Notice how capacity decreases with the increasing number of cycles. Source: Acellent Technologies, Inc.	483
Figure II.3.2.2.15. (a) The current pulse and (b) corresponding voltage response obtained from the HPPC test. It takes about 20 hours to complete one HPPC test. Source: Acellent Technologies, Inc.	484
Figure II.3.2.2.16. Ultrasonic data collection from the skateboard using the SMART PZT layer while the skateboard was undergoing charging and discharging activities. Source: Acellent Technologies, Inc.	484
Figure II.3.2.2.17. (a) The collected ultrasonic signals are shown when the skateboard was charging and discharging for a different path; however, no specific trend is found. (b) After performing an autoregressive analysis on the same signals, the baseline, charging, and discharging phase is clearly separated. Source: Acellent Technologies, Inc.	485
Figure II.3.2.3.1. (a) Covalent surface functionalization of rCF with carbon nanofiller to form highly stable NMCF. SEM images of (b) freshly prepared NMCF and (c) recycled NMCF from NMVC-R ² . Due to the strong covalent bonding between CF micro-fillers and carbon-based nanofillers, NMCFs are stable even after a series of solution and solid-state processing under heat. Source: RockyTech Ltd.	487
Figure II.3.2.3.2. Tensile properties of various vitrimers. Source: RockyTech Ltd.	488

Figure II.3.2.3.3. (a) Comparison graph of tensile properties of various composites consisting of rCF. (b) Comparison graph tensile modulus and conductivity of composites made of rCF and NMCF. (c) Tensile stress-strain curve of CFRP consisting of V4 and unidirectional CFs. (d). SEM image of the CFRP consisting of V4 and woven CFs. (e) SEM image of NMVC-R ² . Source: RockyTech Ltd.	489
Figure II.3.2.3.4. (a) Repairing of NMVC-R ² composite under heat and pressure. (b) Tensile stress-strain curves of repaired NMVC-R ² composite in comparison with the original sample. (c) Reshapability of NMVC-R ² composite. Source: RockyTech Ltd.....	490
Figure II.3.2.3.5. (a) Closed-loop recycling of NMVC-R ² through solution-phase depolymerization and repolymerization. (b) Tensile stress-strain curves of recycled NMVC-R ² in comparison with the original sample. Source: RockyTech Ltd.....	491
Figure II.3.2.4.1. TEM image demonstrating a good dispersion of silane-functionalized multiwall CNTs in a SSBR-BR-silica-silane EV tread compound. CNTs circled in green. Source: MRD.	494
Figure II.3.2.4.2. A simplified block flow diagram showing the primary four unit operations to create a polymer “masterbatch” of silane-functionalized MR, with sub-operations also identified. Source: MRD.	495
Figure II.3.2.4.3. Spider graph demonstrating materials property changes to an EV tire tread compound with silane-MR from the masterbatch product form. Source: MRD.....	496
Figure II.3.2.4.4. A simplified piping and instrumentation diagram of the barrel-scale production system in use at MRD to produce silane-MR masterbatch for Objective #3 activities. Source: MRD.	497
Figure II.4.1.1.1. (a) Microhardness identification and (b) material classification results using the weld structure image and numerical data provided for Al-steel RSW joints. Source: PNNL.....	509
Figure II.4.1.1.2. Important process variables for producing quality AA6022-LCS and X626-LCS welds. Source: PNNL.....	510
Figure II.4.1.1.3. Partial effects plots with 95% confidence intervals from the GAM fitted for PC1 (top) and PC2 (bottom). Source: PNNL.	510
Figure II.4.1.1.4. Hardness curves, mean curves, and five rFPCs for each stack-up. Source: PNNL.....	511
Figure II.4.1.1.5. Information flow for developing the ensemble model. Source: PNNL.	512
Figure II.4.1.1.6. Example images in the dissimilar steel/steel data set. Optical .csv files contain the top-view weld images. Height .csv files contain the depth-of-weld images. Met .jpg files contain the metallurgic cross-sectional weld images. Weld .jpg files contain the top-view welds with measurements. The *.stl files contain the 3D-rendering of welds. Source: PNNL.....	513
Figure II.4.1.1.7. Extend the input data stream of process conditions into the unified ML for process - performance relationship. Source: ORNL.....	514
Figure II.4.1.1.8. ML model provided quantitative prediction for joint peak load average and its range (minimum, maximum) for a variety of material combinations. Source: ORNL.	515
Figure II.4.1.1.9. ML model-predicted weld performance under a variety of materials and welding conditions. Source: ORNL.....	515
Figure II.4.1.1.10. (a) Influence of welding current on joint peak load identified by DNN model. (b) DNN model predicted the process map for button vs. interfacial failure welds. Source: ORNL. .	516

Figure II.4.1.1.11. The fully trained DNN model applied for weld design to identify welding process conditions for meeting joint target performance for two example weld stack-ups of 0.8 mm X626 – 0.9 mm HDG LCS and 1.2 mm 6022 – 2.0 mm HDG LCS. Source: ORNL.	517
Figure II.4.1.1.12. Integrate the inline signals into ORNL’s expandable ML framework for inline weld quality monitoring. Source: ORNL.	518
Figure II.4.1.1.13. Initial model prediction of weld nugget size based on inline signals: (a) an average of more than 90% prediction accuracy and (b) error of prediction for 10-fold cross validation. Source: ORNL.	518
Figure II.4.1.2.1. (a) Load-displacement curves and (b) LSS of AA6061-CFRPPA joints. (c) Enhanced chemical bonding at the substrate-adhesive interface. (d) Percentage of void defects at the CFRPPA-adhesive interface. (e) Surface morphology of AA6061 substrates. Source: PNNL.	522
Figure II.4.1.2.2. (a) Load-displacement curves. (b) LSS of AA6061-CFRPA66 joints. Cases #1–4 represent: #1 non-treated adhesive and substrates; #2 non-treated adhesive and plasma-treated substrates; #3 plasma-treated adhesive and non-treated substrates; and #4 plasma-treated adhesive and substrates, respectively. Source: PNNL.	523
Figure II.4.1.2.3. (a) 3D profile of laser crater. (b) Variation of laser crater size with laser pulse energy. (c) Morphology of AA6061 surface at different overlap ratio. (d) Variation of LSS of AA6061-AA6061 joints at different overlap ratio and laser pulse energy. (e) Comparison of fracture surface morphology of as-received and laser-treated AA6061 substrates, demonstrating transformation from interfacial failure to more cohesive failure after laser treatment. Source: PNNL.	523
Figure II.4.1.2.4. (a) Lap-shear behaviors of dissimilar materials (AA6061-CFRPA66) with laser-surface modifications. (b) The cross-sectional images of lap-shear joint with and without vacuum-assisted manufacturing process shows void reduction. (c) The LSS comparison between the as-received and laser-pattern samples. (d) Failure morphologies of the lap-shear joints. Source: PNNL.	524
Figure II.4.1.2.5. (a–b) Normalized nominal shear-strength as a function of the interfacial void area fraction for two different ratios of $\sigma_{ins}/\sigma_{aus}$, representing different interfacial bonding behavior. Equivalent plastic strain at 1 μm away from substrate surface at the peak loads of two joints: (c) $A_{ivf} = 0\%$ and (d) $A_{ivf} = 6\%$. Source: PNNL.	525
Figure II.4.1.2.6. The LSS results for an ABL-based adhesive using aluminum as the adherent (a) with different loading of TA and (b) with different loading of reinforcing fillers. The control sample in (a) is ABL, and the control sample in (b) is the best ABL-TA sample from (a). Source: ORNL.	526
Figure II.4.1.2.7. SEM images for cryogenically fractured surfaces of selected adhesives: (a) ABL, (b) ABL-TA, and (c) ABL-TA-reinforcing filler. Source: ORNL.	526
Figure II.4.1.2.8. (a) Molecular dynamics simulations of Al-Al interfaces interacting at various normal and transverse velocities. Varying degrees of mixing can be seen along with the predicted temperature profiles. (b) Predicted cooled molecular dynamic microstructure exhibiting submicron grains and the observed microstructure through TEM. Source: PNNL.	527
Figure II.4.1.2.9. Interfacial properties generated from the APS at ANL. Both similar and dissimilar metal stacks are shown along with the internal lattice strains, material texture (integrated intensity), and crystallite size (peak width) mappings. Source: ANL.	528

Figure II.4.1.2.10. (a) Long-term fatigue testing of Al-Al HiVe joints showing increased performance at higher loadings than commercially available clinch/SPR. Typical fracture surfaces of Al-Al joints indicating common neck failure mode. (b) 3T DP980-AA6061-DP980 stack cross-section with embedded rivet. Subsequent lap-shear performance of 3T HiVe rivet stacks. Source: PNNL.	528
Figure II.4.1.2.11. Finite element simulations of new backing die configurations. (a) Half axisymmetric model of die with 2T DP1180 1.15 mm plates and corresponding (b) damage, (c) pressure, and (d) temperature profiles. Source: PNNL.	529
Figure II.4.1.2.12. (a) Maximum LSS obtained in HFR Al-steel joints after various surface modifications and comparisons made with FDS Al-steel joints from the literature. (b) Comparison of fatigue test results of the joint AA6061-DP590 with and without surface modification. Source: PNNL.	529
Figure II.4.1.2.13. Joint cross-section and corresponding load vs. displacement curves of 3T configurations: (a) DP590-AA6061-DP590 and (b) AA6061-DP780-AA6061. Source: PNNL.....	530
Figure II.4.1.2.14. (a) SPH model setup for friction-riveting and (b) processing parameter. Source: PNNL.	530
Figure II.4.1.2.15. Central cross-sectional images of friction-riveted joint from (a) experiment and (b) process modeling. Source: PNNL.	531
Figure II.4.1.2.16. SPH modeling predicted temperature distributions for isometric view (top row) and central cross-sectional view (bottom row) after 10 seconds (a and d), 20 seconds (b and e), and 30 seconds (c and f) processing time. Source: PNNL.....	531
Figure II.4.1.2.17. Validation of SPH model using experimental data: (a) plunge force and (b) multi-point temperature. Source: PNNL.	532
Figure II.4.1.2.18. Central cross-sectional distribution of equivalent plastic strain at (a) 10 seconds, (b) 20 seconds, and (c) 30 seconds of processing time. Source: PNNL.....	532
Figure II.4.1.3.1. Material arrangements for the four material stacks to be joined and characterized. Source: PNNL.	537
Figure II.4.1.3.2. Overview of project approach. Source: ORNL.....	537
Figure II.4.1.3.3. (a) Load per unit width vs. crosshead displacement for all four stack-ups (e.g., the FSLW stack shown in Figure II.4.1.3.1) upon lap-shear testing. Dashed lines are indicative of top two sheets being dissimilar Al. (b) Column chart showing a summary of repeatability of LSS values for the four stack-ups along with error bars showing standard deviations. Source: PNNL....	538
Figure II.4.1.3.4. (a) Load per unit weld width vs. crosshead displacement plotted for three samples each made with baseline tool (51-1) and coarser thread tool (51-8) in the Stack 3. (b) Load per unit weld width vs. crosshead displacement plotted for three samples each made with baseline tool (51-1) and coarser thread tool (51-8) in the Stack 4. Representative transverse cross-section is also shown for each case. Fractured sample for Stack 3 that broke out in the base metal is also shown. (c) Load vs. crosshead displacement for T-peel joints for Stack 1 using two tool designs are shown. Source: PNNL.....	539

Figure II.4.1.3.5. Multiple lines of FSLW in 3T configurations that were run for the tool like study in Stack 1 (top left). Top-view of FSLW tool at various weld length of 3T FSLW for H13 and MP19 tooling. The color map on the bottom three pictures represent the Z height from the lower feature providing a snapshot of wear over the weld length. Note that at 9.3 mm, the pin was sheared off for H13. Example images of side view of the tooling is also shown. Source: PNNL..... 541

Figure II.4.1.3.6. Several geometric features tracked during the tool life study are shown on the left. The bar chart for H13 and MP19 tool provides a snapshot of total wear measured in this study. Source: PNNL. 541

Figure II.4.1.3.7. Screen shots from XRT videos revealing the joint cross-section of Stack 2 at 1m/min. made at two different rpm containing (a) a large AS defect, and (b) a small defect. (c–d) Frequency domain plots of Z-force time series data showing peaks at two distinct frequencies. Source: PNNL. 542

Figure II.4.1.3.8. Simulated load-displacement plots compared with experimental results from strength testing of U-Peel/KSII samples with FSW Seam Configuration (a) #1 and (b) #2. Inset figures show the weld configurations. Source: PNNL. 543

Figure II.4.1.3.9. Simulated stresses on the surface of the tool pin are obtained by applying (a) just the surface tractions and (b) just the pressure distributions normal to the surface. Source: PNNL. 544

Figure II.4.1.3.10. (a) A macrograph of the FS-PR joint cross-section with the overlaid microhardness map. The key regions are also indicated on the joint cross-section (i.e., BM, HAZ, and TMAZ). (b) Microhardness profile corresponding to the locations marked by the blue dashed line in (a) and the representative locations, in which the USAXS and WAXS were analyzed and are marked in black circles. (c) USAXS+SAXS+WAXS setup in transmission mode at beamline 20-ID-B. The X-ray beam path is marked in white with a solid line showing the incident beam and dashed line showing a couple of scattered beams. Source: ORNL and ANL..... 545

Figure II.4.1.3.11. (a) WAXS patterns from measurement locations marked, with the peak positions of the major phases (Al, MgZn₂) marked below the patterns. (b) I(q) vs. q plots from the USAXS analysis for measurement locations with “knees” in spectra, which correspond to a precipitate/dispersoid population indicated using arrows. Note that a precipitate population “knee” in the lower q value corresponds to a higher value of mean precipitate size. Source: ANL.. 545

Figure II.4.1.3.12. Summary of averaged lap-shear and cross-tension joint strength of F-SPR AA7055 in 2T and 3T with different stacking orders. Source: ORNL. 546

Figure II.4.1.3.13. A new integrated welding system includes C-frame welding head, multi-axis motion stages, and fixture for scale-up part-level joining with multiple joints. Source: ORNL..... 547

Figure II.4.1.3.14. (a) Overview of scale-up 7xxx Al – 7xxx Al part joining using the newly integrated welding system, (b) demonstration of Al-Al and CFRC-Al part joining with multiple joints. Source: ORNL..... 548

Figure II.4.1.3.15. Practice FSLW runs on an experimental stamping of AA7055 sheet. Several lines of short and long linear welds are shown along with corresponding joint cross-sections with varying degrees of weld defects. Source: ORNL. 548

Figure II.4.1.4.1. Summary of measured surface energy for various lightweight materials after open-air plasma treatment. Source: ORNL. 553

Figure II.4.1.4.2. Summary of lap-shear tensile strength of different material combinations with different surface conditions. (a) Al7075-thermoset (TS) CFRP and (b) Al7075-Zn-coated DP980. Source: ORNL.	554
Figure II.4.1.4.3. Summary of LSS for the thermoplastic lignin-nitrile rubber (ABL) adhesive joints with various material combinations and fractography before and after open-air plasma treatment. Source: ORNL.....	554
Figure II.4.1.4.4. Summary of lap-shear tensile testing for before and after 500 hours corrosion exposed Al7075 and Zn-coated DP980 with different surface conditions. Source: ORNL.....	555
Figure II.4.1.4.5. (a) Schematic of galvanic corrosion mechanism due to galvanic current paths for CFRP-metal joint. (b) An illustration of galvanic corrosion mitigation approach to minimize galvanic current paths using an electrical insulated rivet. Source: ORNL.	556
Figure II.4.1.4.6. Examples of (a) representative cathodic polarization curves from steel, untreated, bare AFA and 850 °C pre-oxidized AFA, and (b, c) impedance-spectra of 850 °C pre-oxidized AFA and steel. The cathodic polarization curves in (a) were initiated at natural corrosion potentials of rivet materials in 0.1M NaCl and scanned down to -1.5 V _{SCE} with the rate of 0.5 mV/s. Impedance-spectra was collected at -1.5 V _{SCE} with the amplitude of ±10 mV and the frequency range of 200 kHz to 7 mHz. Source: ORNL.	557
Figure II.4.1.4.7. Individual (symbols) and average (numbers) values of (a) resistance against cathodic reaction, and (b) cathodic current at -1.5 V _{SCE} from steel and AFA with and without pre-oxidation. Source: ORNL.....	557
Figure II.4.1.4.8. STEM-EDS element maps for thermal processed AFA at 800°C, showing formation of dense Al-oxide layer. Source: ORNL.	558
Figure II.4.1.4.9. 0.1M NaCl solution immersion tested CFRP-Mg joints by F-SPR using steel rivet (control), thermal process AFA. Galvanic current for both cases was calculated based on measured corrosion volume of Mg. Source: ORNL.....	558
Figure II.4.1.4.10. Microbeam XRD patterns as a function of depth from the top surface of the oxide with the peak positions of the expected oxide phases above the patterns for (a) open-air plasma-treated, (b) laser-treated (75 W) and corroded samples. Source: ANL.....	559
Figure II.4.1.4.11. (a) Moisture absorption plot, (b) and (c) ATR-FTIR spectra of XP0012 and XP5005 adhesives before and after moisture absorption test. Source: PNNL.	560
Figure II.4.1.4.12. Moisture absorption plot of as-received and plasma-treated (a) Al6061, (b) Al5052, and (c) DP590 vs. the square root of exposure time to moisture. Source: PNNL.....	561
Figure II.4.1.4.13. ATR-FTIR spectra for as-received and plasma-treated (a) Al6061, (b) Al5052, and (c) DP590 before and after exposure to moisture at 35 °C and 98% RH for 3 months. Source: PNNL.	561
Figure II.4.1.4.14. (a) Moisture absorption plot and (b–c) ATR-FTIR spectra of the as-received and plasma-treated CFRP-PA66 before and after exposure to 98% RH and 35 °C. Source: PNNL.....	561
Figure II.4.1.4.15. (a–c) Load-displacement curves and (d–f) the average Mode I fracture energies of adhesively bonded Al6061/Al6061, Al6061/DP590, and Al5052/CFRP-PA66 joints after exposure of 1400 hours in a condition of 98% RH and 35 °C. Source: PNNL.....	562

Figure II.4.1.4.16. Surface morphologies of (a) Al6061 in Al6061/Al6061 joint, (b) DP590 in Al6061/DP590 joint, and (c) Al5052 in Al5052/CFRP-PA66 joint after DCB failure. Sample were tested after 1400 hours of exposure in a condition of 98% RH and 35 °C. Source: PNNL..... 563

Figure II.4.1.4.17. (a–c) Load-displacement curves and (d–f) average Mode I fracture energies of adhesively bonded Al6061/Al6061, Al6061/DP590, and Al5052/CFRP-PA66 joints after exposure of 800 and 1400 h at 5% salt fog condition of 98% RH and 35 °C. Source: PNNL..... 564

Figure II.4.1.4.18. Plots of corrosion-induced absolute % weight change vs. surface processing conditions in HiVe rivet and HiVe clinch samples of Al6061 joined to an Al6061 plate. Source: PNNL..... 565

Figure II.4.1.4.19. X-ray computed tomography of the virtual cross-sections show corrosion progress after 1400 hours accelerated salt fog corrosion test: (a) Al6061-Al6061 HiVe rivet without adhesive and (b) Al6061-Al6061 HiVe rivet with adhesive. Source: PNNL..... 566

Figure II.4.1.4.20. (a) Sequence of corrosion progress in the HiVe joints over 1400 h of corrosion. (b) Cross-section of a HiVe rivet joint showing the locations of corrosion progress after 1400 h of corrosion. Corrosion is restricted to the exposed face in the form of pits. The gap between the top-plate and rivet head shows corrosion products that prevent further solution ingress. Source: PNNL..... 566

Figure II.4.1.4.21. Absolute weight change (%) results of the salt fog tests and COMSOL multiphysics modeling results for Al6061-Al6061 sample with steel rivet. Source: PNNL..... 567

Figure II.4.1.5.1. Schematics and apparatus of URJ. Source: ORNL..... 573

Figure II.4.1.5.2. Sonotrode displacement curve showing three stages of the URJ process. Source: ORNL..... 573

Figure II.4.1.5.3. (a) Single-joint lap-shear sample welded by URJ and (b) lap-shear tensile results. Source: ORNL..... 573

Figure II.4.1.5.4. Cross-section of the joint interface showing the formation of voids in the CFRP adjacent to the rivet. Source: ORNL..... 574

Figure II.4.1.5.5. (a) Cross-section of the URJ joint interface. (b–d) Electron backscatter diffraction maps showing a grain refinement zone through the joint interface. Source: ORNL..... 574

Figure II.4.1.5.6. (a) Large CFRP-Al coupons consisting of five URJ joints. (b) Peak lap-shear load of each individual URJ joint and the comparison with single-joint coupon. Source: ORNL..... 575

Figure II.4.2.1.1. Systems approach with multiple simulation-validation loops at various component scales. (Figure for illustrative purposes only and not intended to show details.) Source: Clemson University..... 579

Figure II.4.2.1.2. Structural requirements benchmarking and design conceptualization. (Figure for illustrative purposes only and not intended to show details.) Source: Clemson University..... 580

Figure II.4.2.1.3. (a-b) CAD Concept 1 focused on the roof and subframe. (c) CAD Concept 2 focused on the side assemblies [6]. Source: Clemson University..... 580

Figure II.4.2.1.4. Displacement plots showing the static structural analysis of Iteration 1 of the two design concepts. Source: Clemson University..... 581

Figure II.4.2.1.5. (a) Dynamic (linear) structural analysis showing the force vs. displacement and displacement contour plots. (b) Stiffness of the design concepts compared to the baseline. Source: Clemson University.....	581
Figure II.4.2.1.6. Factors considered in the development of the parametric cost model [6]. Source: Clemson University.....	582
Figure II.4.2.1.7. Initial cost analysis for Iteration 1 of CAD Concepts 1 and 2 [6]. Source: Clemson University.....	583
Figure II.4.2.1.8. (a) CAD Concept Iteration 2 based on FEA and cost assessment finding. (b) Composite optimization approach and problem formulation [6]. Source: Clemson University.....	584
Figure II.4.2.1.9. (a-c) Optimization results for composite components. (d) Optimized concept performance. (e) Weight-reduction through iterative optimization (units for mass are proprietary) [6]. Source: Clemson University.....	585
Figure II.4.2.1.10. FMVSS 214 quasi-static side-pole impact simulation with non-linear material response to understand deformation behavior. Source: Clemson University.....	586
Figure II.4.2.1.11. Side impact crashworthiness evaluation simulation with non-linear material response to understand deformation behavior. Source: Clemson University.....	586
Figure II.4.2.1.12. Front-quarter-overlap impact simulation with non-linear material response to understand deformation behavior. Source: Clemson University.....	587
Figure II.4.2.1.13. Rear-quarter-overlap impact simulation with non-linear material response to understand deformation behavior. Source: Clemson University.....	587
Figure II.4.2.1.14. UAM process modifications: (a) the spindle-speed increaser, (b) the fiber alignment device, and (c) the runway welding surface. Source: The Ohio State University.....	588
Figure II.4.2.1.15. UAM implemented modifications: (a) the spindle-speed increaser, (b) the fiber alignment device, and (c) the runway welding surface. Source: The Ohio State University.....	588
Figure II.4.2.1.16. Methodology for coupon-level simulations to develop, calibrate, and validate the MAT 221 material card using experimental results for the CFRP-AI transition joint [6]. Source: Clemson University.....	589
Figure II.4.2.1.17. Complex geometries to be used for transition joint validation. (a) Top-hat section. (b) Double-hat structure. Source: Clemson University.....	590
Figure II.4.2.1.18. (a) Experimental force vs. displacement for four-point bending [7]. (b) Simulated experimental force vs. displacement for four-point bending. Source: Clemson University.....	590
Figure II.4.2.1.19. Fabrication of GF-AI transitions. Source: Source: The Ohio State University.....	591

List of Tables

Table I.1.1.1.1. Composition of Alloys (wt.%) Fabricated and Tested in this Study, as Verified by ICP-OES	8
Table I.1.1.2.1. Vickers Hardness and Roughness of Tested Alloy Rotors	17
Table I.1.1.4.1. Nominal Chemical Compositions of Aluminum Alloys Used in this Task	28
Table I.1.1.4.2. Summary of Average Electrochemical Corrosion Data for AM Al Alloys.....	29
Table I.1.1.6.1. Nominal Composition (wt.%) of Aluminum Alloys Used in this Task.....	41
Table I.1.1.7.1. Wear-testing Results of the Cast-Iron and Composite Brake Rotors	49
Table I.1.2.2.1. Nominal Composition (wt.%) of Commercial Gear Steels 16MnCr5 and AISI 8620 in Use in Europe and the United States	66
Table I.1.2.2.2. Alloys ORNL-52100 and PCS-52100 Hardness and Wear Volume Obtained After Testing	70
Table I.1.2.3.1. Five types of CNTs with Different Diameters and Lengths	76
Table I.1.2.4.1. Thermal Impedance Results Showing Substantially Reduced Thermal Impedance by Either Using the CNT Coating as a Standalone TIM or Using CNT Particles to Enhance a Conventional TIM	81
Table I.1.3.3.1. Candidate Dispersants for the Dispersion of Ni _{0.5} Zn _{0.5} Fe ₂ O ₄ Powder.....	112
Table I.1.3.4.1. Comparison of the Properties of Single Walled CNTs versus Cu.....	115
Table I.1.3.6.1. Component, Demonstration Dimensions, and Allowed Property Variability	128
Table I.1.3.8.1 Composition of Commercial Steels Used for Dies and Other Tooling (wt.%)	139
Table I.1.4.1.1. Thrust 4A1 Funded Advanced Characterization Projects in FY 2023.....	146
Table I.1.4.1.2. APT Measured Matrix Compositions for Al-6Ni-0.4Zr, Al-6Ni-0.3Ti, Al-6Ni-0.3V, and Al-6Ni-0.5Fe Alloys Subjected to a 400 °C, 200 H Heat-Treatment	148
Table I.1.4.1.3. CNT Dimensional Properties, Diameters, Lengths, and Raman Signatures Used in the Study.....	150
Table I.1.4.2.1. Improvement in Thermal Impedance for CNT-Coated Interface Materials.....	158
Table I.1.4.5.1. Task 4B1 Funded Advanced Computation Projects in FY 2023	178
Table I.1.4.6.1. Round-Robin Sample Densities Measured at ORNL for Al Wires	188
Table I.1.4.6.2. Round-Robin Sample Densities Measured at ORNL for Cu Wires.....	188
Table I.1.4.6.3. Round-Robin Sample Densities Measured at ORNL for Al Plates	188
Table I.1.4.6.4. Round-Robin Sample Densities Measured at ORNL for Cu Plates.....	188
Table I.1.4.7.1. Critical Materials Identified in LD and MD/HD Vehicles	191
Table I.2.1.1. Mass Comparison of Key Engine Components in Phase 2 and Baseline Engines.....	197
Table II.1.1.1. Composition of the Alloys Used, As-specified by the Manufacturer	218
Table II.1.1.2. Summary of Measured Material Properties	221

Table II.1.3.1. Summary of the Process Parameters for the Plasma-Assisted Organosilicon Deposition Performed at ORNL and Described in Figure II.1.3.2(a). Two Processes are Designated as P01 and P08. The Coating Thickness on a Si Wafer was Reported for Initial Process Evaluation.....	260
Table II.1.3.2. Summary of Four Treatment Conditions Using Different Solution Concentrations of NaHCO ₃ and LiNO ₃ Before the Thermal CO ₂ Treatments Performed at ORNL and Described in Figure II.1.3.2(b) for AZ91D and AM60	261
Table II.1.3.3. Summary of R_2 and $R_f + R_2$ Values from the Impedance-Data Fitting Conducted at ORNL.....	266
Table II.1.3.4. Summary of ORNL and Literature Corrosion-Evaluation Data and Technical Notes to Compare the Different Surface Modification and Coating Approaches for Mg-Alloys.....	267
Table II.1.3.5. Wear Properties of Substrate and Cold-sprayed Surface.....	272
Table II.1.4.1. Thrust 4 – Characterization, Modeling, and Life Cycle Projects Funded in FY 2023.	283
Table II.1.4.2. Composition Ranges of the Alloys Used in Thrust 1.1B and Thrust 2.2C in wt.% and with Single Values Indicating Maximums	296
Table II.1.4.3. FSP Parameters of the Characterized Samples.....	303
Table II.2.1.1. Die-Casting Alloys, Compositions, and Mechanical Properties.....	315
Table II.3.1.1.1. Phased Approach to HTC Project.....	320
Table II.3.1.1.2. S_{11} Versus Reflected Power	321
Table II.3.1.1.3. Line Speed Combinations of Samples for HTC6	325
Table II.3.1.1.4. Top Three Mechanical Results From HTC6 Where the Hexcel AS4 Data Are Shown Only For Reference (It Was Not Processed with EM Equipment).....	325
Table II.3.1.1.5. FY 2023 and Milestones Expected to Complete Early in FY 2024	326
Table II.3.1.5.1. FY 2023 Milestone Summary	352
Table II.3.1.8.1. Summary of CF Produced for Panel Testing.....	377
Table II.3.1.9.1. Alternative Precursor and Advanced Conversion Processing Estimated Reduced Cost and Embodied Energy	381
Table II.3.1.9.2. Task 3 Milestones, Task Descriptions, and Status	384
Table II.3.1.10.1. FY 2023 Milestones.....	392
Table II.3.1.11.1. Mechanical Testing Results for Various Spinning Conditions.....	413
Table II.3.1.13.1. PECAN-CFRC Properties Relative to Epoxy-Amine CFRCs.....	427
Table II.3.1.13.2. Techno-economic and Supply-Chain Analyses Results for the PECAN-CFRCs Across Multiple Lives	429
Table II.3.1.14.1. Project Milestones and Status	433
Table II.3.1.15.1. Milestone for Task 1 Work Stream Activities.....	437
Table II.3.1.16.1. Correlation Between Measured and Predicted Resistance Values	453
Table II.3.2.2.1. Peak Frequency due to Various Object Impacts.....	479

Table II.3.2.5.1. Mechanical Analysis of Vitrimax/Flax Fiber and Vitrimax/Glass Fiber Composites 503

Table II.3.2.5.2. Comparison of the Mechanical Properties of the Vitrimax Resin to the Standard Epoxy..... 504

Table II.3.2.5.3. Short Beam Shear and Three Point Bend Mechanical Data Comparing T130 Vitrimax RTM and RTM-6 505

Table II.3.2.5.4. Comparison of the Mechanical Properties of the Vitrimax/Flax to Other Materials 505

Table II.4.1.3.1. Summary of Mechanical Joint Strengths of Multi-Materials to Validate Weldability of New System..... 547

Table II.4.2.1.1. Project Partner Organizations..... 578

Table III.1.1.1. Average Curb Weight and Footprint for Model Year 2012 and 2017 Vehicles by Vehicle Type. Source: EPA 595

(This page intentionally left blank)

Vehicle Technologies Office Overview

Vehicles move our national economy. Each year in the United States (U.S.), vehicles transport 18 billion tons of freight—about \$55 billion worth of goods each day¹—and move people more than 3 trillion vehicle miles.² Growing our economy requires transportation, and transportation requires energy. The transportation sector accounts for approximately 30% of total U.S. energy needs³ and the average U.S. household spends over 15% of its total family expenditures on transportation,⁴ making it, as a percentage of spending, the costliest personal expenditure after housing. Transportation is critical to the overall economy, from the movement of goods to providing access to jobs, education, and healthcare. The transportation sector has historically relied heavily on petroleum, which supports over 90% of the sector’s energy needs today,⁵ and, as a result, surpassed electricity generation to become the largest source of CO₂ emissions in the country.⁶ The U.S. Department of Energy–Office of Energy-Efficiency and Renewable Energy (DOE-EERE) Vehicle Technologies Office (VTO) will play a leading role in decarbonizing the transportation sector and address the climate crisis by driving innovation and deploying clean-transportation technologies, all while maintaining transportation service quality and safety.

VTO funds research, development, demonstration, and deployment (RDD&D) of new, efficient, and clean mobility options that are affordable for all Americans. VTO leverages the unique capabilities and world-class expertise of the National Laboratory system to develop new innovations in vehicle technologies, including: advanced battery technologies; advanced materials for lighter weight vehicle structures and better powertrains; energy-efficient mobility technologies—including automated and connected vehicles, as well as innovations in efficiency-enhancing connected infrastructure; innovative powertrains to reduce greenhouse gas (GHG) and criteria emissions from hard to decarbonize off-road, maritime, rail, and aviation sectors; and integration that helps demonstrate and deploy new technology at the community level. Across these areas and in partnership with industry, VTO has established aggressive technology targets to focus RDD&D efforts and ensure there are pathways for technology transfer of federally supported innovations into commercial applications.

VTO is uniquely positioned to accelerate sustainable transportation technologies due to strategic public–private research partnerships with industry (e.g., U.S. DRIVE, 21st Century Truck Partnership) that leverage relevant expertise. These partnerships prevent duplication of effort, focus DOE research on critical RDD&D barriers, and accelerate progress. Working closely and in collaboration with DOE-EERE’s Bioenergy Technologies and Hydrogen and Fuel Cell Technologies Offices, VTO advances technologies that assure affordable, reliable mobility solutions for people and goods across all economic and social groups; enable and support competitiveness for industry and the economy/workforce; and address local air quality and use of water, land, and domestic resources.

Annual Progress Report

As shown in the organization chart (below), VTO is organized by technology area: Batteries research and development (R&D); Electrification R&D; Materials Technology R&D; Decarbonization of Off-Road, Rail, Marine, and Aviation; Energy-Efficient Mobility Systems; Technology Integration; and Analysis. Each year, VTO’s technology areas prepare an Annual Progress Report (APR) that details progress and accomplishments during the fiscal year. VTO is pleased to submit this APR for FY 2023. The APR presents descriptions of each active project in FY 2023, including funding, objectives, approach, results, and conclusions.

¹ Bureau of Transportation Statistics, DOT, Transportation Statistics Annual Report 2020, Table 4-1, <https://www.bts.gov/tsar>.

² Davis, Stacy C, and Robert G Boundy. Transportation Energy Data Book: Edition 40. Oak Ridge, TN: Oak Ridge National Laboratory 2022. <https://doi.org/10.2172/1878695>. Table 3.09 Shares of Highway Vehicle-Miles Traveled by Vehicle Type, 1970-2019.

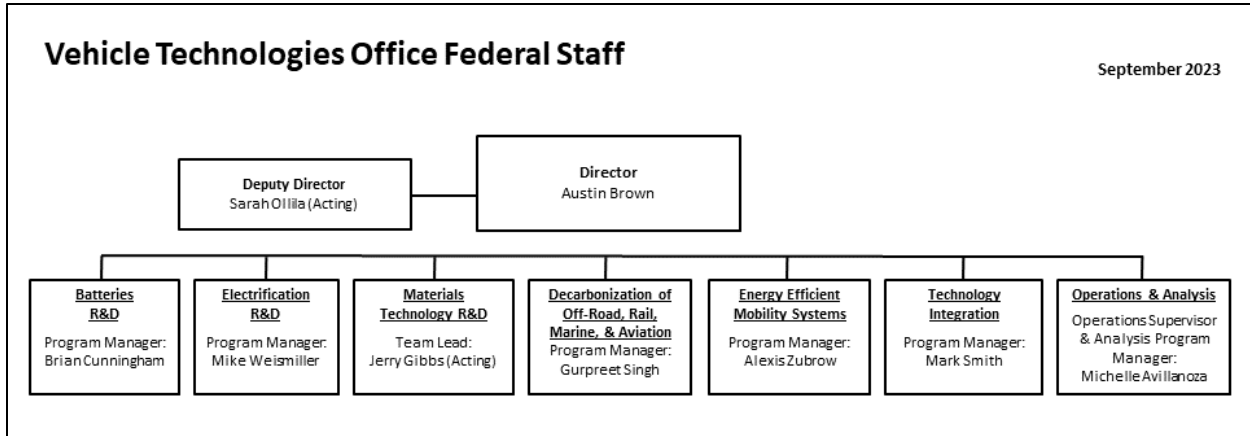
³ Ibid. Table 2.02 U.S. Consumption of Total Energy by End-use Sector, 1950-2021.

⁴ Ibid. Table 11.1 Average Annual Expenditures of Households by Income, 2020.

⁵ Ibid. Table 2.03 Distribution of Energy Consumption by Source and Sector, 1973 and 2021.

⁶ Environmental Protection Agency, Draft U.S. Inventory of Greenhouse Gas Emissions and Sinks, 1990-2019, Table 2-11. Electric Power-Related Greenhouse Gas Emissions and Table 2-13. Transportation-Related Greenhouse Gas Emissions.

Organization Chart



Materials Technology Program Overview

Program Introduction

The Materials Technology subprogram supports the VTO goal of achieving net-zero GHG emissions by 2050 through the reduction of weight, cost, and life cycle emissions using advanced lightweight materials. This ambitious goal will be realized through the increased deployment of electric and hydrogen fuel cell vehicles. Materials play an important role in increasing the efficiency of electric vehicles (EVs) through reduction of weight as well as enabling additional functionality such as faster charging and new sensing technologies. Lighter weight vehicle structures and electric drivetrains will require fewer batteries to achieve the same range, which in turn reduces battery cost, material needs, and reduces the GHG emissions from battery production. Functional materials with improved properties such as electrical conductivity, thermal conductivity, and unique sensing capabilities will enable innovations in charging and autonomous vehicles. Manufacturing methods used to make vehicles also contribute to GHG emissions. The Materials Technology subprogram supports research, development, and deployment to improve manufacturability, increase recyclability, and reduce the overall embodied energy of vehicle manufacturing. The Materials Technology subprogram accomplishes its technical objectives through research programs with academia, national laboratories, and industry.

The Powertrain Materials Core Program (PMCP) portfolio is closely aligned with other VTO subprograms to identify critical materials needed for next generation high-efficiency powertrain components for both HD and light-duty (LD) EVs. Strategies for achieving high-efficiency powertrains include addressing key challenges in electrical conductivity, thermal conductivity, magnetic materials, and high-temperature operation currently limiting advances in electric powertrains and wireless charging. The PMCP is a national laboratory consortium that targets critical powertrain components based on thermal loading, structural, and electrical requirements and utilizes an ICME approach to link advanced characterization to high-performance computing methods to accelerate development of new material families. The PMCP previously partnered with the Electrification subprogram to focus new materials development for challenges facing power electronics for EVs and in FY 2023, partnered with the Batteries, Charging, and Electric Vehicles subprogram to address lightweighting of battery enclosures.

The Lightweight Materials team works closely with industry through the U.S. DRIVE partnership to understand LD vehicle structural weight-reduction goals and to identify technical challenges that prevent the deployment of lightweight materials. The most promising and likely approach for lightweighting is a multimaterial structure, which focuses on the use of the most effective material for the application. The Lightweight Materials research portfolio addresses significant technology gaps for each family of structural materials: Mg, AHSS, Al, CF, and polymer composites. Gaps include raw material costs, formability, manufacturing cycle time, ability to model and predict failure, corrosion mitigation, incorporation of new materials into manufacturing plants, and materials life cycle and recyclability. In addition, research efforts investigate dissimilar material joining to enable the reliable assembly of these multimaterial systems.

Program Goals

The Materials Technology subprogram supports the VTO's mission to accelerate the deployment of clean energy technology toward achieving net-zero GHG emissions in the transportation sector by 2050. Lighter vehicles with more-efficient powertrains reduce energy use, decrease GHG emissions, and save consumers money. The structural and powertrain systems that are targeted for improvement are limited by materials performance. By improving the properties of powertrain and structural materials, a significant improvement in energy efficiency can be enabled for future vehicles. Increasing the thermal and electrical conductivity of low-

cost materials will enable increased EV efficiency while improving properties in structural materials, such as stiffness, strength, joinability, and crash-energy absorption—all with lower cost— will accelerate the deployment of lightweight materials in the automotive market. The specific performance and cost targets for the Materials Technology subprogram are to enable a 25% glider weight reduction for LD vehicles which includes body, chassis, and interior at less than \$5 per kilogram (kg) cost savings by 2030 compared to 2021 Mustang Mach E or a 2021 Chevrolet Suburban.

State-of-the-Art

Automakers are seeking to improve fuel economy, increase EV range, or reduce battery size while improving or maintaining vehicle performance and safety. Lighter weight vehicle structures and electric drivetrains will require fewer batteries to achieve the same range, which in turn reduces battery cost, material needs, and reduces the GHG emissions from battery production. Functional materials with improved properties such as electrical conductivity, thermal conductivity, and unique sensing capabilities will enable innovations in charging and autonomous vehicles. For structural components, the market is shifting from traditional steel components to lighter weight materials such as AHSSs, Al-alloys, Mg-alloys, and polymer composites.

To support the transition to all electric LD vehicles by 2035, research is needed to increase efficiency and decrease manufacturing cost of electrified powertrains. Development of new alloys with improved electrical/mechanical properties and enhanced resistance to corrosion/oxidation of components operating in harsh environments such as electrical bus bars, lightweight gears, underbody suspension, and brakes will address the needs for future properties of electric and hydrogen fuel cell vehicles. Expanded development and characterization of materials supporting electrification such as lightweight conductors, ferrites, and high-silicon steels are also important for challenging components such as inverters, motors, and the gear-train. However, inadequate databases, modeling, and design tools are significant barriers for further development of new materials. By evaluating existing computational tools and identifying gaps that must be overcome to achieve seamless integration across multiple-length scales and increasing understanding of the basic behavior of the material (effects of solute at the atomistic level, microstructural development, microstructure/property relationships, fracture and failure mechanisms, durability, temperature-dependent behavior, etc.), more accurate design tools and predictive models can be established. Characterization and multiscale computational materials methods will accelerate discovery and early-stage development of cutting-edge materials and innovative production techniques like AM for lighter and more-efficient powertrains.

AHSS is the most mature lightweight material in terms of widespread use in the automotive industry due to its compatibility with existing manufacturing infrastructure and vehicle materials. Application of third-generation high-strength steel has the potential to reduce component weight by up to 25%, particularly in strength-limited designs. However, the technical challenges that remain to improve weldability and weight reduction are dependent on the ability to maintain stiffness at reduced gauges. Al continues to see steady growth in market share in the automotive industry⁷ despite issues of material cost, room temperature (RT) formability, and limitations within the existing manufacturing infrastructure. This is due to the 40% weight-savings that can be achieved with Al along with the well-established domestic supply-chain. Mg has the potential to significantly reduce vehicle component weight by 55% or greater; however, there are several significant technical barriers preventing increased use of this material in vehicle designs. Mg has high raw material costs and price volatility, relatively low specific stiffness, difficulty in forming sheet at low temperatures, low ductility of finished components, and a limited alloy set, among other challenges. CF and other polymer composites have the potential to reduce component weight by more than 60%. The main barriers to widespread use are the high-cost to manufacture the CF, lack of high-volume composite manufacturing methods, and a need for reliable predictive tools for both part design and performance prediction.

7. Giampieri, A., J. Ling-Chin, Z. Ma, A. Smallbone, and A. P. Roskilly, 2020, "A review of the current automotive manufacturing practice from an energy perspective," *Appl. Energy*, Vol. 261, Art. 114074.

When combinations of the above lightweight materials are used, the resulting multimaterial structures have challenges of their own. Traditional joining methods used in automotive assembly, such as resistance spot-welding (RSW) and riveting, are inefficient for joining dissimilar metals and infeasible for some combinations. In the near-term, friction-stir scribe welding and resistance spot riveting are showing promising advances for the joining of AHSS and Al (the more mature lightweight metals). An additional challenge posed by multimaterial structures is the increased risk of corrosion due to galvanic coupling. As the barriers to introduction of Mg and CF are overcome, breakthroughs in joining technology will also be necessary.

Program Organization Matrix

Activities within the Materials Technology subprogram include the following:

- Powertrain Materials focuses on:
 - Materials for EV Powertrain Components (Jerry L. Gibbs) that includes addressing key challenges in electrical conductivity, thermal conductivity, magnetic materials, and high-temperature operation.
- Lightweight Materials consists of three research portfolios:
 - Light Metals (Christopher Schooler) that includes research on property improvement and processing advances for AHSS, Al, and Mg.
 - Carbon Fiber and Polymer Composites (H. Felix Wu) that includes research on low-cost production of CF, novel processing methods for polymer composites, and predictive performance models of CF and other fiber-reinforced or hybrid composites.
 - Joining of Dissimilar Materials (Christopher Schooler) that includes research on solid-state, mechanical, and chemical joining methods, as well as galvanic corrosion mitigation.

All the activities within the Materials Technology subprogram utilize computational methods for material discovery, prediction of structure, understanding failure mechanisms including corrosion, and the effects of processing on properties.

(This page intentionally left blank)

I Powertrain Materials

I.1 Powertrain Materials Core Program (PMCP)

I.1.1 Thrust 1: Lightweight Alloys for Electric Vehicle Propulsion

I.1.1.1 Task 1A. Fundamental Studies of Al-Ni Alloys for Improved Electrical Propulsion (Oak Ridge National Laboratory)

Dongwon Shin, Principal Investigator

Oak Ridge National Laboratory
Materials Science and Technology Division
1 Bethel Valley Rd.
Oak Ridge, TN 37830
E-mail: shind@ornl.gov

J. Allen Haynes, PMCP Consortium Manager

Oak Ridge National Laboratory
Materials Science and Technology Division
1 Bethel Valley Rd.
Oak Ridge, TN 37830
E-mail: haynesa@ornl.gov

Jerry L. Gibbs, DOE Technology Development Manager

U.S. Department of Energy
E-mail: Jerry.Gibbs@ee.doe.gov

Start Date: November 1, 2021

End Date: September 30, 2023

Project Funding: \$220,000

DOE share: \$220,000

Non-DOE share: \$0

Project Introduction

This task investigated the fundamental effects of two critical factors on the electrical conductivity and high-temperature stability in cast-aluminum-nickel (Al-Ni) alloys, specifically: (1) the volume fraction of the key intermetallic phase of nickel aluminide (Al_3Ni), and (2) the associated interfacial structure (Al/ Al_3Ni). The volume fraction of Al_3Ni was varied with different amounts of Ni, and select minor alloying elements (e.g., zirconium [Zr], titanium [Ti], vanadium [V], iron [Fe]) were added to investigate their propensity to segregate at the Al/ Al_3Ni interface, as well as their influence on aluminide formation. This task utilized advanced characterization (e.g., atom probe tomography [APT]/scanning tunneling electron microscopy) and computation (e.g., first-principles density functional theory calculations) to correlate experimentally measured electrical conductivity and hardness with the observed distribution of key intermetallic and Al/ Al_3Ni interface structures.

Objectives

This task aimed to understand the effect of the volume fraction of key intermetallic (Al_3Ni) and interfacial (Al/ Al_3Ni) structures on the electrical conductivity and high-temperature stability of cast-Al-Ni alloys.

Approach

Experiments were designed to systematically investigate the effect of interfacial structures (Al/ Al_3Ni) and the amount of Al_3Ni in Al-Ni alloys on electrical and thermal properties. Four different microalloying elements (e.g., Zr, Ti, V, Fe) were added to Ni-containing Al alloys to modify the Al/ Al_3Ni interface structures. These microalloying elements were anticipated to segregate at the Al/ Al_3Ni interface based on previously observed results for Zr and scandium (Sc). The prepared alloys contain 5–6 wt.% of Ni, near the Al-rich eutectic

composition in binary Al-Ni. Contents of Ni between 2 and 6 wt.%, compositions within the hypoeutectic region in the Al-Ni binary system, were used to vary the amount/density of the Al₃Ni intermetallic phase.

Once the alloys were synthesized, heat treatments were conducted at 300, 350, 400, and 450°C for 200 hours. Microstructure analysis and physical property measurements were completed using a suite of advanced characterization facilities at Oak Ridge National Laboratory (ORNL). We used the Vickers hardness test with a 5 kilogram-force (kgf) load for the microhardness measurements, the eddy current method for the electrical conductivity measurements, and laser flash analysis for the thermal diffusivity measurements. The microstructure and evolution of the intermetallic microfibers were analyzed by scanning electron microscopy (SEM). Atomic-scale composition analysis was carried out by APT to investigate the segregation of microalloying elements at the interface between the microfiber and the Al matrix. The APT investigations were accessed via a proposal and support through Thrust 4A, ‘Advanced Characterization,’ of the PMCP. The thermal and electrical properties measurements were conducted at ORNL via Task 4A3.

Results

All alloys were prepared by the electric arc melting method under an argon atmosphere, followed by casting into chilled copper molds. The bulk compositions were then analyzed by an inductively coupled plasma-optical emission spectrometer (ICP-OES). The results of the ICP-OES alloy compositions that were tested in this work are summarized in Table I.1.1.1.1.

Table I.1.1.1.1. Composition of Alloys (wt.%) Fabricated and Tested in this Study, as Verified by ICP-OES

System	Al	Ni	Zr	Ti	V	Fe	Si
Al-Ni	Balance	1.92	0	0	0.01	0.03	0.01
Al-Ni	Balance	3.76	0	0	0	0.03	0.02
Al-Ni	Balance	4.68	0	0	0	0.033	0.022
Al-Ni-Zr	Balance	2.09	0.45	0	0	0.03	0.02
Al-Ni-Zr	Balance	3.73	0.40	0	0	0.03	0.02
Al-Ni-Zr	Balance	5.70	0.41	0	0	0.032	0.02
Al-Ni-Ti	Balance	5.98	0	0.31	0	0.034	0.021
Al-Ni-V	Balance	5.69	0	0	0.30	0.032	0.2
Al-Ni-Fe	Balance	4.89	0	0	0	0.52	0.02

The relationship between microstructure evolution and two experimental factors (i.e., the Ni content and the microalloying elements) was investigated by SEM and APT. The Al₃Ni morphology with additions of Fe, Ti, V, and Zr in the Al-Ni alloys was investigated for the as-cast and heat-treated conditions of 300, 350, 400, and 450°C for 200 h. Figure I.1.1.1.1 shows representative SEM-secondary electron (SE) images of the intermetallic microfibers in the Al-5Ni, Al-6Ni-0.4Zr, Al-6Ni-0.3Ti, Al-6Ni-0.3V, and Al-5Ni-0.5Fe (wt.%) alloys. The microstructures show various degrees of spheroidization and coarsening of the Al₃Ni phase as a function of heat-treatment temperature. The Al₃Ni morphology in the as-cast condition is presented in Figure I.1.1.1.1(a). The Al₃Ni forms a long and fiber-like structure that is uniform in shape and evenly spaced across the eutectic phase. After heat-treatment at 350 and 450°C for 200 h, all alloys showed a significant spheroidization compared to the as-cast condition. Whereas the degree of spheroidization and coarsening of Al₃Ni microfiber is proportional to the heat-treatment temperature, the effect of the various microalloying elements on microstructure appears insignificant based on the comparison between different alloys at identical heat-treatment conditions.

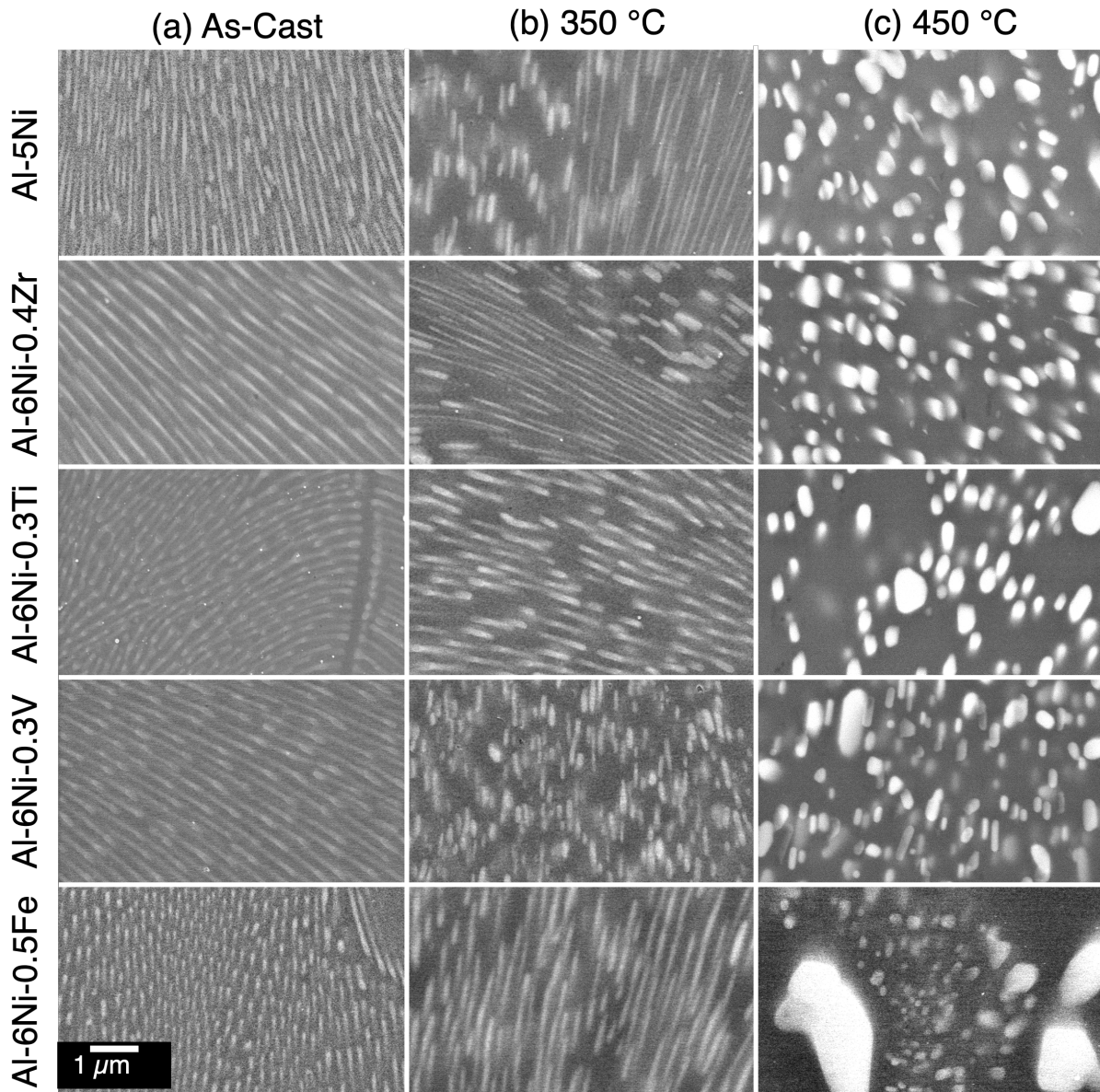


Figure I.1.1.1.1. SEM-SE micrographs of Al₃Ni microfibrils in Al-6Ni alloys with the addition of Zr, Ti, V, and Fe by wt.% for (a) as-cast alloys and alloys heat-treated at (b) 350 °C and (c) 450 °C for 200 h. Source: ORNL.

The direct observation of precipitate formation in the Al matrix was conducted by APT for alloys with the addition of Zr, Ti, V, and Fe. Figure I.1.1.1.2 shows the three-dimensional (3D) reconstruction of Al matrices in the four alloys after heat-treatment at 400 °C for 200 h. The formation of Al₃Zr precipitates was confirmed for the Al-6Ni-0.4Zr wt.% alloys. The average Al₃Zr precipitate size was 6.4 ± 0.9 nm in radius, determined by using sphere equivalent volume. The number density and average distance of precipitates were identified as $7.3 \times 10^{-6} \text{ nm}^{-3}$ and 40.1 ± 11.2 nm, respectively. No precipitates were observed for the other three alloys containing Fe, Ti, and V microalloying elements, while they are expected to form thermodynamically. Since these are 200 h. heat treatments at 350/450 °C, it is reasonable to assume the samples have reached or are near equilibrium. Perhaps these fine precipitates are not visible in the SEM images with low resolution; however, we have further investigated their microstructure via APT.

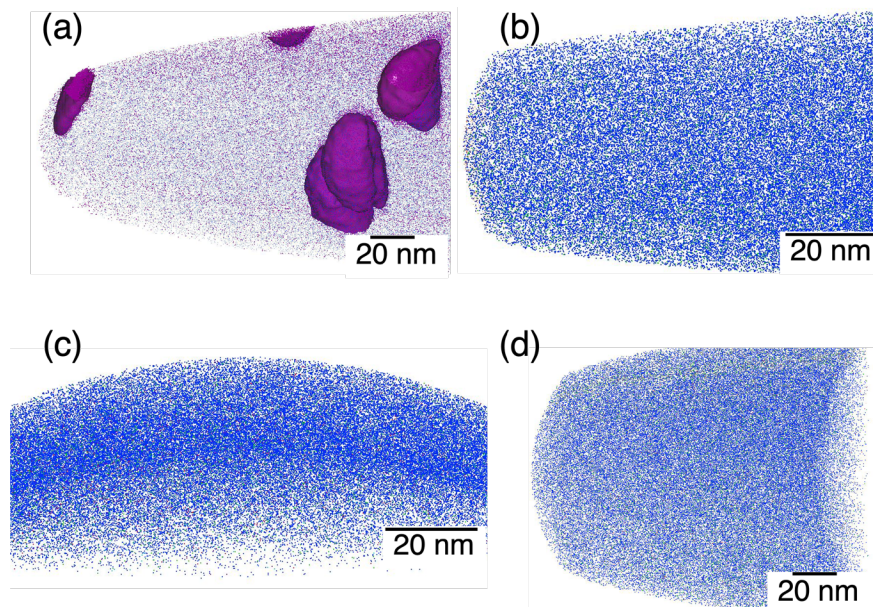


Figure I.1.1.1.2. 3D reconstruction of Al matrix by APT analysis: (a) Al-6Ni-0.4Zr, (b) Al-6Ni-0.3Ti, (c) Al-6Ni-0.3V, and (d) Al-6Ni-0.5Fe alloys heat-treated at 400 °C for 200 h. Source: ORNL.

APT also investigated the segregation of microalloying elements at the Al/Al₃Ni interface for the four alloys, which contained minor additions of Zr, Ti, V, and Fe after heat-treatment at 400°C for 200 h. Figure I.1.1.1.3(a) provides an example of APT analysis (e.g., the atom map of the Al-6Ni-0.3V wt% alloys) reconstructed in three dimensions. The blue- and green-colored dots represent Al and Ni atoms, respectively. The shaded area represents the interface between the Al matrix and the Al₃Ni phase. The concentration of a microalloying element (i.e., Zr, Ti, V, or Fe) and other impurities across the Al/Al₃Ni interface were analyzed for each alloy. Figure I.1.1.1.3(b) shows the proximity histograms of microalloying elements and impurities for all alloys. We confirmed the enrichment of Zr at the Al/Al₃Ni interface for Al-6Ni-0.4Zr wt.% alloys after heat-treatment at 400°C, as was previously reported by Pandey et al. [1]. On the contrary, no evident segregation was observed at the interface for other microalloying elements (i.e., Fe, Ti, and V). The enrichment of Si impurity (maximum ~1 at.%) was observed notably at the Al/Al₃Ni interface for all analyses, indicating that the segregation is uniform across the specimen.

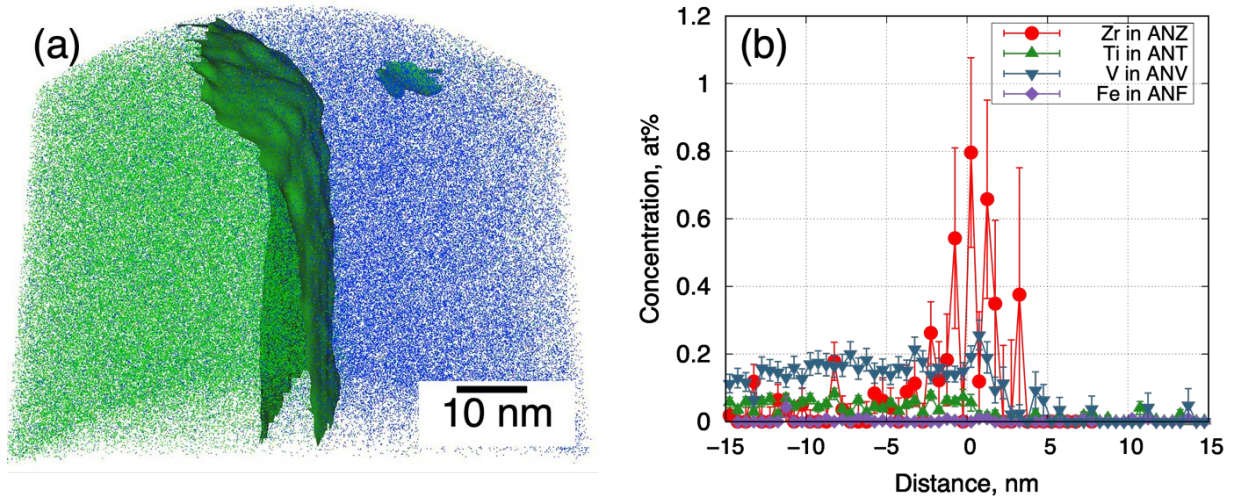


Figure I.1.1.1.3. APT analysis for Al/Al₃Ni interface after heat-treated at 400 °C for 200 h. (a) 3D construction showing Zr segregating at the Al/Al₃Ni interface, and (b) concentration profiles for Zr, Ti, V, and Fe. Source: ORNL.

Thermal conductivities of various alloys are present in Figure I.1.1.1.4 with respect to heat-treatment temperature and Ni content. A similar trend was anticipated between the thermal and electrical conductivities in metals because free electrons are the dominant charge carriers. Figure I.1.1.1.4 shows the crossover between Fe- and Zr-containing alloys with increasing heat-treatment temperature.

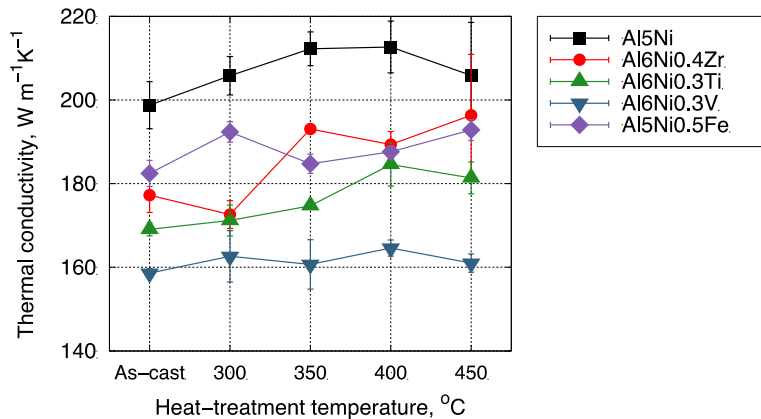


Figure I.1.1.1.4. Effect of various microalloying elements on the thermal conductivity of Al-Ni alloys heat treated at various temperatures for 200 h. Source: ORNL.

The evolution of Al₃Ni morphology in the Al-Ni and Al-Ni-Zr alloys was analyzed over various heat-treatment temperatures based on SEM images. Figure I.1.1.1.5(a) shows that the average fiber length of the Al₃Ni phase in both alloys has a similar decreasing trend with respect to increasing heat-treatment temperatures, indicating that slow diffusing elements may not be the rate-controlling factor for spheroidization. Similarly, the average radius of Al₃Ni microfibers analyzed for the two alloys is presented in Figure I.1.1.1.5(b). Overall, the fibers in the Al-Ni-Zr alloys have a shorter average radius than those in the Al-Ni alloys, reflecting a slow coarsening rate during heat-treatment. However, the difference is smaller than the radius variation within a specimen. As such, the analyses indicate the influence of Zr segregation at the Al/Al₃Ni interface is not significant for retaining Al₃Ni morphology when a long heat-treatment of 200 h is applied as seen in Figure I.1.1.1.5(c).

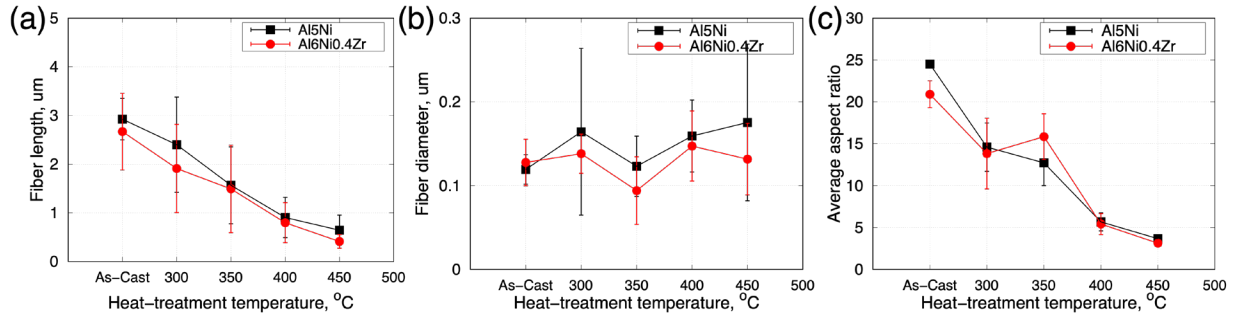


Figure I.1.1.1.5. Effect of microalloying elements on the Al_3Ni microfiber morphology evolution across various heat-treatment temperatures: (a) average fiber length, (b) average fiber diameter, and (c) average aspect ratio. Source: ORNL.

The effect of interface segregation on retaining hardness can be assessed by the load transfer model given by Nardone and Prewo [2]:

$$\Delta\sigma_{LT} = 1/2\sigma_m V_f (s + 2) \quad (1)$$

where $\Delta\sigma_{LT}$ is the yield strength (YS) increment by load transfer, σ_m is the YS of the Al matrix, V_f is the volume fraction of Al_3Ni microfibers, and s is the aspect ratio (fiber length/diameter). For the interface segregation of a slow diffusing element to enact in retaining hardness, a substantial difference in aspect ratio (s) should be observed. The assessed results indicate that the interface segregation effect of a slow diffusing element is insignificant in retaining hardness via the load transfer mechanism.

The dominant thermal carriers are free electrons whose behavior can be measured by electrical conductivity. Figure I.1.1.1.6 shows the thermal and electrical conductivities of all alloys investigated in this study with various heat-treatment conditions. The black solid line is a thermal conductivity prediction based on electrical conductivity through the empirical formula suggested by Smith and Palmer [3]. Figure I.1.1.1.6 shows the Smith-Palmer-based prediction for Al alloys also agrees with our experimental data for Al-Ni alloys, indicating that electrical conductivity measurement can be used as a surrogate for thermal conductivity.

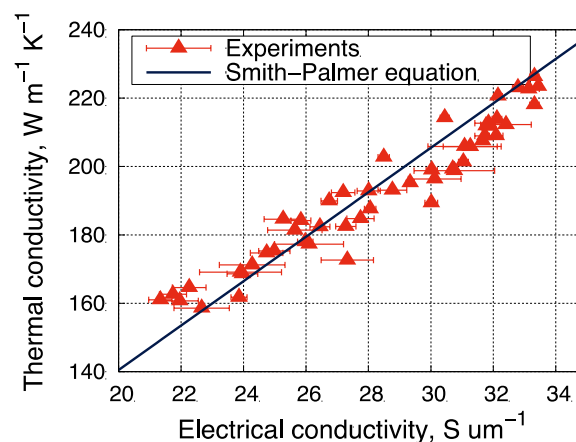


Figure I.1.1.1.6. The relationship between electrical conductivity and thermal conductivity is characterized for all alloys. Source: ORNL.

Conclusions

An experimental study was performed to investigate the effect of slow diffusing elements (e.g., Fe, Ti, V, Zr) on the microstructure features and physical properties of a series of Al-Ni alloys. APT confirmed Zr segregation at the Al/Al₃Ni interface and Al₃Zr precipitate formation in the Al matrix; however, no evidence of interface segregation or precipitation was observed for the Al-Ni alloys with Fe, Ti, and V after heat-treatment at 400°C. The morphology analysis of Al₃Ni revealed that interface segregation of Zr has little effect on Al₃Ni evolution with respect to heat-treatment temperature, which indicates that a design strategy aiming to retain fiber enforcement by interfacial segregation of a slow diffusing alloy may not be a practical approach.

References

1. Pandey, P., S. K. Makineni, B. Gault, and K. Chattopadhyay, 2019, “On the origin of a remarkable increase in the strength and stability of an Al-rich Al-Ni eutectic alloy by Zr addition,” *Acta Mater.*, 170, 205–217. <https://doi.org/10.1016/j.actamat.2019.03.025>.
2. Nardone, V. C., and K. M. Prewo, 1986, “On the strength of discontinuous silicon carbide reinforced aluminum composites,” *Scr. Metall.*, 20(1), 43–48. [https://doi.org/10.1016/0036-9748\(86\)90210-3](https://doi.org/10.1016/0036-9748(86)90210-3).
3. Smith, C. S. and E. Palmer, 1935, “Thermal and electrical conductivities of copper alloys,” *Trans. Am. Inst. Min. Metall. Eng.*, 117, 225–243.

Acknowledgements

The authors would like to thank R. Michi, K. Hanson, T. Muth, D. McClurg, J. Poplawsky, and H. Wang of ORNL for contributing to the experimental work.

I.1.1.2 Task 1B. Higher Temperature Aluminum Alloys and Composites for Lightweight Brake Systems (Oak Ridge National Laboratory)

Amit Shyam, Principal Investigator

Oak Ridge National Laboratory
Materials Science and Technology Division
1 Bethel Valley Rd.
Oak Ridge, TN 37830
E-mail: shyama@ornl.gov

J. Allen Haynes, PMCP Consortium Manager

Oak Ridge National Laboratory
Materials Science and Technology Division
1 Bethel Valley Rd.
Oak Ridge, TN 37830
E-mail: haynesa@ornl.gov

Jerry L. Gibbs, DOE Technology Development Manager

U.S. Department of Energy
E-mail: Jerry.Gibbs@ee.doe.gov

Start Date: November 1, 2021

End Date: September 30, 2023

Project Funding: \$270,000

DOE share: \$270,000

Non-DOE share: \$0

Project Introduction

This task focuses on development and implementation of lightweight alloys and lightweight metal-matrix composites (MMCs) for rear brake systems in electric vehicles (EVs). A suite of properties and testing schemes that are applicable for brake systems were evaluated for new compositions and existing higher temperature lightweight alloys. The wear resistance and temperature limit of lightweight Al brakes are lower than their cast-iron counterparts. The thermal conductivity and specific heat are also different. If the wear resistance and upper-temperature limit of Al alloys can be pushed higher, these alloy systems could be useful for brake-rotor applications, especially rear brakes for EV powertrains, which typically experience less severe conditions than front brakes. EV powertrains have hybrid mechanical and regenerative braking options; therefore, the mechanical braking material demands are expected to be less severe, and the lightweight-alloy systems are expected to have potential to displace higher density cast-iron in some scenarios. Lightweight-alloy brake rotors could reduce up to 25 lbs. per vehicle or more, considering there are at least four brake rotors on each vehicle. Also, since brake rotors are reciprocating mass, the impact is even more significant than in the lightweighting of stationary components. Along with reduced demand on mechanical braking in EVs, new generations of Al alloys with improved temperature capability provide renewed possibilities for lightweighting of brake rotors for EVs, as either monolithic alloys or as the matrix for composite brake materials. The work conducted in FY 2022 for this task focused on evaluating lightweight alloys under the most severe conditions, which involved combining monolithic Al alloys with brake testing under heavy-duty (HD) truck-braking conditions. Cast-Al-copper (Cu) and Al-cerium (Ce)-Ni additives were the primary alloys tested for these brake-rotor applications. For the FY 2023 reporting period, these alloys were evaluated for lower demand—medium-duty (MD) and light-duty (LD)—braking conditions as well.

Objectives

Task 1B will aid in the understanding and development of higher temperature Al alloys and related composites for lightweight brake systems that can be deployed in EVs. The long-term objective for the task is to apply Al alloys and MMCs as one or more components within lightweight brake systems.

Approach

Understanding the brake requirements of lightweight disk materials for EVs—where regenerative braking is possible—is the driving force for this task. The subscale brake-testing capability that can measure friction co-efficient, wear behavior, and temperature of the brake-disk specimen during simulated brake testing was re-established at ORNL. In FY 2022, a suite of monolithic high-temperature lightweight alloys with different heat treatments, along with baseline cast-iron specimens, was identified for brake testing under HD truck-braking conditions (e.g., the most severe conditions). The wear resistance, temperature limit, thermal conductivity, and specific heat of lightweight Al brakes are different from their cast-iron counterparts. If the wear resistance and upper-temperature limit of Al alloys can achieve an adequate threshold, those alloys could be useful for lightweighting of rear brake rotors for EVs, as either monolithic brake-rotor materials or higher temperature matrices for MMC rotors. Improvements in the testing methods and alloys were identified based on the FY 2022 results. New alloys and testing conditions were implemented in FY 2023, along with a refined understanding of EV brake requirements. In particular, the choice of brake-pad material is critical for determining the correct alloys that can serve as brake-rotor materials.

Results

Work completed in FY 2022 described a subscale brake-testing facility along with the method applied for testing. Specimen discs were 5 in. in diameter with a thickness of 0.5–0.625 in. A Jurid® 539 brake-pad material for HD vehicles was applied at a load level that results in 1 MPa contact pressure. Five repetitive drags at 20 s each were applied for each test speed at constant load in the following sequence of speeds: 2 m/s → 6 m/s → 9.6 m/s → 15 m/s → 9.6 m/s → 6 m/s → 2 m/s. Temperature of the test specimen was measured *in-situ* with an infrared sensor. Friction coefficient was measured during the test, and wear-tracks on the specimen were quantified with laser profilometry. Work conducted during FY 2023 consisted of two parts: (i) the development of suitable high-temperature alloys for brake testing, and (ii) the application of a suite of cast and additive lightweight Al alloys to test under automotive braking conditions. We start by discussing activities in alloy development.

Cast-Al alloys with creep resistance in the 300–400°C temperature range offer lightweighting solutions for increased energy-efficiency in weight critical automotive and aerospace applications by replacing heavier iron (Fe) and titanium (Ti) alloys. High-temperature Al alloys are strengthened by a fine distribution of coherent or semi-coherent precipitates in grain bulk and the creep resistance reduces above temperatures where precipitates coarsen rapidly. ORNL, with industry collaboration, has previously developed and patented Al-Cu-manganese (Mn)-zirconium (Zr)—or ACMZ—alloys in which metastable θ' -Al₂Cu precipitates within the grain bulk are stabilized by Mn and Zr interfacial segregation at temperatures up to 350°C, which is much higher compared to commercial AlCu alloys whose θ' -Al₂Cu stability is limited to temperatures below 250°C. Further research by the current team has provided new insights into the creep deformation mechanisms in ACMZ alloys. ACMZ alloys, like other precipitation-hardened Al alloys, exhibit precipitate free zones (PFZs) near grain boundaries (GBs) that are devoid of θ' -Al₂Cu precipitates. The PFZs develop during heat-treatment and continue to grow during creep due to growth and coarsening of GB θ -Al₂Cu precipitates at the expense of nearby θ' -Al₂Cu precipitates. We have found that creep deformation in ACMZ alloys localizes inside the PFZs due to the absence of strengthening θ' -Al₂Cu precipitates while the grain bulk with abundant θ' -Al₂Cu precipitates experiences much less creep [1]. This observation suggests that designing new variants of ACMZ alloys with coarsening-resistant GB precipitates that minimize PFZs would further enhance creep resistance.

Ni, cobalt (Co), or Fe were added to the ACMZ alloy because they form GB precipitates that are coarsening-resistant due to low solid solubility of these elements in an α -Al matrix. In contrast, Cu has high-solid solubility and diffusivity in an α -Al matrix due to the θ -Al₂Cu precipitates along the GBs that rapidly coarsen in the ACMZ alloy. The coarsening-resistant Ni/Co/Fe-rich GB precipitates minimize the PFZs and enhance creep resistance of the modified alloys compared to the unmodified ACMZ alloy with large PFZs because of rapidly coarsening θ -Al₂Cu GB precipitates. Ni/Co/Fe-rich GB precipitates are also good for creep resistance, because unlike θ -Al₂Cu GB precipitates, they do not grow by dissolving strengthening θ' -Al₂Cu precipitates.

Creep is a property important for lightweight brake-rotor materials so that dimensional tolerance during elevated-temperature exposure is not lost. The newly developed ACMZ alloy variants were tested in compression-creep at 300°C, as observed in Figure I.1.1.2.1. The ACMZ-Ni and ACMZ-Co alloys have higher creep resistance ($\sim 25\%$ higher at 10^{-9} s^{-1} strain-rate) than the more complex and expensive commercial cast-Al alloy RR350 with combined additions of Ni, Co, Ti, and antimony (Sb). The ACMZ-Fe alloy has a slightly better creep resistance than RR350 at lower stresses, but it is weaker at higher stresses. The advantage of the ACMZ-Ni alloy is that it provides better creep performance than RR350 and eliminates Co, which is 3–5 \times more expensive than Ni and vulnerable to supply-chain interruptions. ACMZ-Fe is the most cost-effective alloy due to only Fe (e.g., the least expensive of these transition elements) being added. Although creep resistance of ACMZ-Fe is lower than RR350 at higher strain rates (or stresses), similar or better creep performance can be achieved by increasing the Cu concentration in ACMZ-Fe because that will increase the volume fraction of strengthening θ' -Al₂Cu precipitates. Unfortunately, the coarsening-resistant GB precipitates that provide superior creep properties to the commercial RR350 alloy also reduce the hot-tearing resistance of the alloy. This tradeoff can be balanced in modified ACMZ alloys by varying Ni, Co, or Fe concentrations such that an optimal volume fraction of GB precipitates is present for creep and hot-tearing resistance. Higher Fe in some of the new ACMZ alloy variants also makes these new compositions more sustainable.

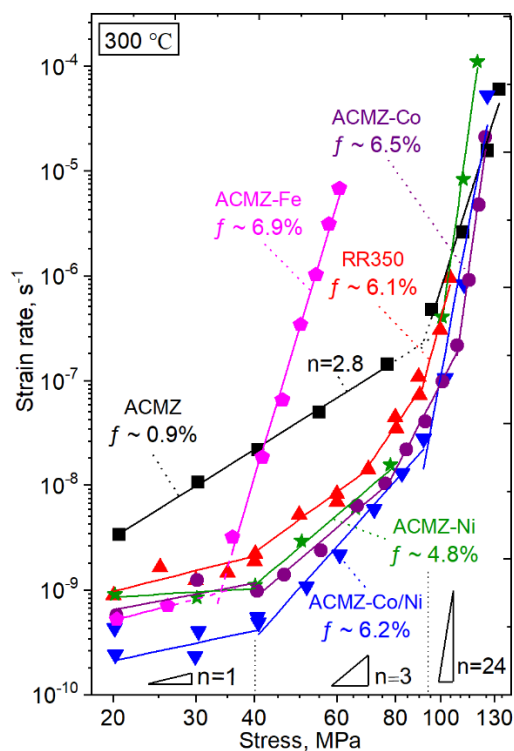


Figure I.1.1.2.1. Strain-rate vs. applied stress during compression-creep experiments at 300 °C for a variety of ACMZ alloys. Source: ORNL.

In addition to new ACMZ alloy variants, a new concept alloy was fabricated, which was predicated on recently published new work [2]. The concept demonstrated that in a cast-AlCuMgAg alloy, Sc atoms can infiltrate the well-known ω -phase (Al₂Cu) and transform it to the so-called V-phase having a thermal stability up to 400°C. An ORNL team followed the exact procedure detailed in the article, but was unable to reproduce the stability in 400°C hardness that was reported in that manuscript, as indicated in Figure I.1.1.2.2(a) with data from the manuscript, while Figure I.1.1.2.2(b) provides the ORNL data with Vickers microhardness (HV). One possibility is that the compositions are sensitive to impurity levels that were not reported in the original manuscript, which could be a topic for future research.

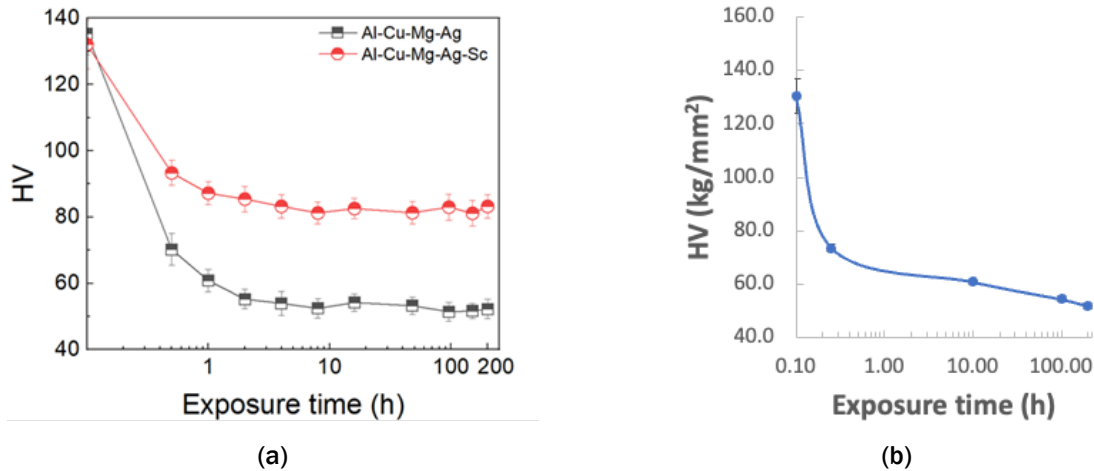


Figure I.1.1.2.2. A comparison of microhardness stability at RT due to 400 °C exposure for an AlCuMgAgSc alloy from (a) Xue et al. [2] and (b) the ORNL work reported here. The ORNL data is notably similar to the alloy without the Sc addition in the original work, which indicates a lack of thermal stability. Source: ORNL.

In FY 2023, the brake performance experiments of cast ACMZ alloy rotors with 6 and 9 wt.% Cu content were evaluated. Note that these were not the new Fe- or Ni-containing variants discussed earlier. The experiments were carried out for as-cast and as-aged alloys. The surface roughness (R_a) and Vickers hardness of the tested alloys were determined prior to testing and reported in Table I.1.1.2.1. ACMZ brake-rotor performance experiments were performed on a custom-built subscale brake tester. In these experiments, a brake-pad specimen (Jurid® 539) was loaded against the alloy rotor at a normal force of 161 N (1 MPa contact pressure). Alloy rotor brake performance was again tested at 2, 6, 9.6, and 15 m/s rotor speeds (increasing and decreasing order) with five 20 s repetitive drags at each speed, resulting in a total of 700 s of testing.

Table I.1.1.2.1. Vickers Hardness and Roughness of Tested Alloy Rotors

Alloy	ACMZ 6 wt% Cu (as-cast)	ACMZ 9 wt% Cu (as-cast)	ACMZ 6 wt% Cu (as-aged)	ACMZ 9 wt% Cu (as-aged)
Vickers Hardness (kg/mm ²)	87.7 ± 10.2	99.1 ± 16.3	100.9 ± 15.0	114.8 ± 12.1
Roughness, R_a (μm)	0.75 ± 0.10	0.85 ± 0.10	0.66 ± 0.09	0.71 ± 0.05

The brake performance testing revealed that all the tested lightweight alloys had poor wear behavior. Although the alloy rotors were supposed to be tested for a total of 700 s, only the 9% Cu as-cast alloy completed one of the two tests, although with a significant wear loss on both the rotor and the brake pad. The tests of all other alloys, including the second test of the 9% Cu as-cast alloy, were stopped prematurely for safety reasons due to excessive wear of the rotors and the pad. Figure I.1.1.2.3 compares images of worn brake-pad surfaces, brake-pad height loss, average friction coefficient, and cross-sectional profiles of the worn surfaces of the rotors for the tests that were conducted only at the 2 m/s speed. The 9% Cu as-cast rotors had somewhat lower wear rate than the 6% Cu rotors. The wear of the pad material was also lower with the 9% Cu disc. Aging appeared to improve the wear properties of the rotors and decreased the damage to the brake pad. Overall, lower wear rates of both the rotor and the pad were achieved with the 9% Cu composition. The frictional performance of all alloy rotors met the minimum friction coefficient requirement for braking greater than 0.35. The semi-metallic brake-pad material (Jurid 539) showed evidence that it is not compatible with the Al alloy rotors. Therefore, in the next evaluation, we tested the rotors with ceramic and organic brake pad materials that were designed for Al rotors.

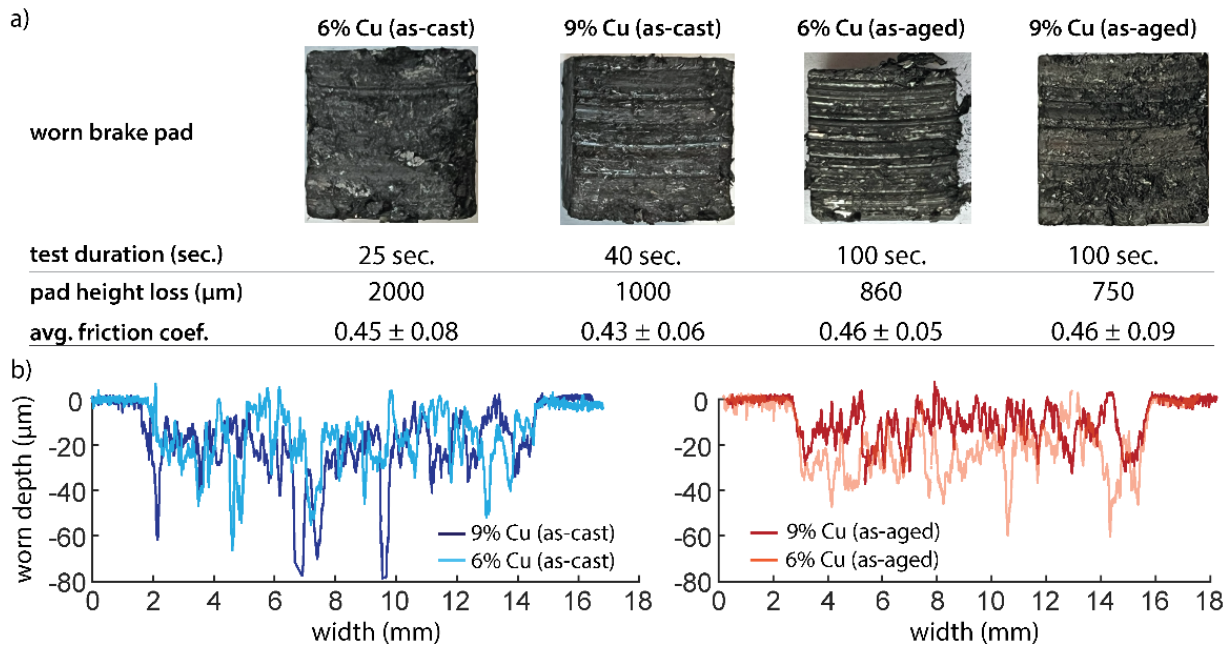


Figure I.1.1.2.3. Brake performance testing results: (a) Images of the worn surfaces of the pads, pad height loss, and average friction coefficient; and (b) average cross-sectional worn surface profile of the rotors. Source: ORNL.

Through the research performed in FY 2023, an improved brake-pad material for lightweight Al alloys was found in a material called Wilwood purple (Wilwood, Camarillo, CA). This material was tested with a number of Al alloys and a baseline cast-iron; the results are summarized in Figure I.1.1.2.4. Overall, the cast-iron still performed the best, and a 3D-printed DuAlumin-3D (AlCeNiMnZr) had an improved brake performance when compared with cast-AlCu alloys. The final FY 2023 tests were conducted on brake-pad materials recommended by other organizations, but also resulted in suboptimal brake performance. All results will be summarized in a journal article to be submitted in FY 2024.

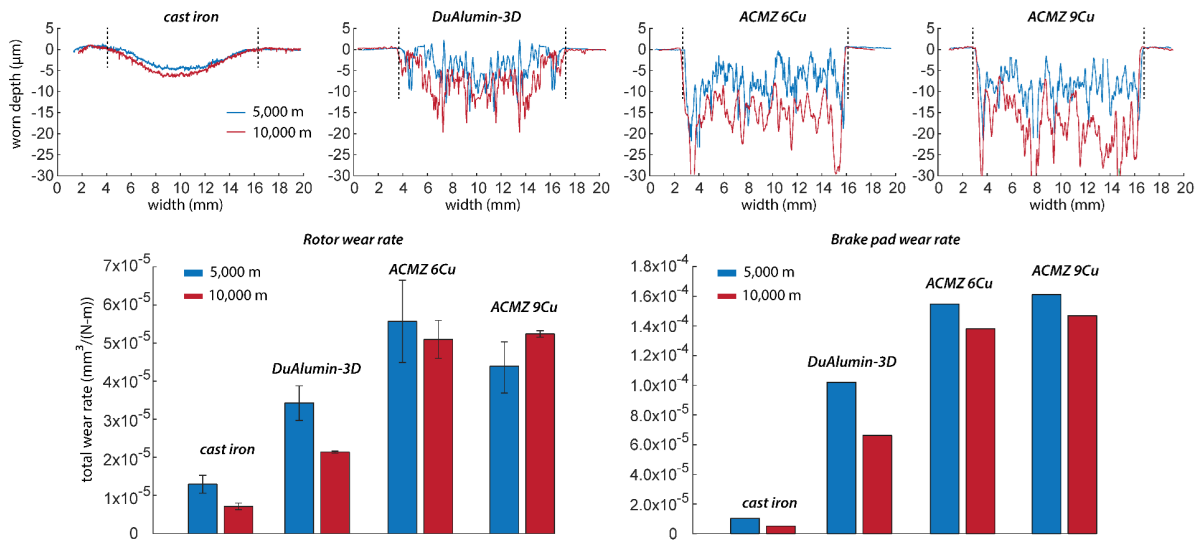


Figure I.1.1.2.4. A number of lightweight alloys were tested with an improved brake pad material, namely Wilwood purple. None of the Al alloys had improved performance relative to cast-iron. 3D-printed DuAlumin-3D had improved brake performance compared to the cast Al-Cu alloys. Source: ORNL.

Conclusions

The following conclusions were drawn based on FY 2023 activities in this task:

- New compositions that improve the creep performance and sustainability of potential lightweight-alloy rotor materials were explored. The ACMZ alloy with the addition of Ni, Co, and Fe led to promising improvements in creep resistance.
- Brake performance of AlCu based materials was suboptimal when measured with pad materials that were optimized for HD engines with cast-iron rotors. In general, the choice of pad material was very important for getting optimal brake performance from lightweight alloys.
- The 3D-printed DuAlumin-3D alloy (AlCeNiMnZr) had superior performance as compared to all other lightweight alloys tested in terms of brake performance.

Key Publications

1. Bahl, S., J. U. Rakhmonov, C. Kenel, D. C. Dunand, and A. Shyam, 2022, “Effect of grain boundary θ -Al₂Cu precipitates on tensile and compressive creep properties of cast-AlCuMnZr alloys,” *Mater. Sci. Eng. A*, 840, 142946. <https://doi.org/10.1016/j.msea.2022.142946>.
2. Rakhmonov, J. U., B. Milligan, S. Bahl, D. Ma, A. Shyam, and D. C. Dunand, 2023, “Progression of creep deformation from grain boundaries to grain interior in AlCuMnZr alloys,” *Acta Mater.*, 250, 118886. <https://doi.org/10.1016/j.actamat.2023.118886>.

References

1. Rakhmonov, J. U., B. Milligan, S. Bahl, D. Ma, A. Shyam, and D. C. Dunand, 2023, “Progression of creep deformation from grain boundaries to grain interior in AlCuMnZr alloys,” *Acta Mater.*, 250, 118886. <https://doi.org/10.1016/j.actamat.2023.118886>.
2. Xue, H., C. Yang, F. De Geuser, P. Zhang, J. Zhang, B. Chen, F. Liu, Y. Peng, J. Bian, G. Liu, A. Deschamps, and J. Sun, 2023, “Highly stable coherent nanoprecipitates via diffusion-dominated solute uptake and interstitial ordering.” *Nat. Mater.*, 22, 434–441. <https://doi.org/10.1038/s41563-022-01420-0>.

Acknowledgements

The authors acknowledge T. Grejtak, J. Qu, J. Rakhmonov, S. Bahl, A. Haynes, D. McClurg, A. Plotkowski, and J. Meier of ORNL for their contribution to this effort. They also acknowledge J. Qi, C. Kenel, and D. Dunand of Northwestern University for their help with the creep testing results and collaboration.

I.1.1.3 Task 1C. Fundamentals of Fatigue and Creep in Advanced Lightweight Alloys: Cost-Effective Lightweight Alloys for Electric Vehicle Propulsion (Oak Ridge National Laboratory)

Sumit Bahl, Principal Investigator

Oak Ridge National Laboratory
Materials Science and Technology Division
1 Bethel Valley Rd.
Oak Ridge, TN 37830
E-mail: bahls@ornl.gov

J. Allen Haynes, PMCP Consortium Manager

Oak Ridge National Laboratory
Materials Science and Technology Division
1 Bethel Valley Rd.
Oak Ridge, TN 37830
E-mail: haynesa@ornl.gov

Jerry L. Gibbs, DOE Technology Development Manager

U.S. Department of Energy
E-mail: Jerry.Gibbs@ee.doe.gov

Start Date: November 1, 2021

End Date: September 30, 2023

Project Funding: \$265,000

DOE share: \$265,000

Non-DOE share: \$0

Project Introduction

Creep and fatigue are important failure modes in lightweight materials. A fundamental understanding of creep and fatigue failure mechanisms is required to develop high-performance lightweight Al alloys for both structural and functional applications in EVs. The structural applications of interest include lightweight brake rotors, ultra-large high-pressure die-castings for vehicle-glider components, battery and transmission housings, suspension components, etc. The functional applications of interest include lightweight electrical conductors and thermal management devices, such as heat sinks. Emerging EV-related applications demand: (1) the development of new Al alloys, and (2) the use of advanced manufacturing methods that will lead to unique microstructures with unique deformation and failure mechanisms. The goal of this task is to establish the fundamental microstructure-processing-property relationships in Al alloys for EV applications to inform future alloy-design concepts for enhanced materials performance and sustainability.

Objectives

This task will aid in the understanding and development of creep and fatigue-resistant Al alloys for deployment in EV applications. Specific objectives are as follows:

- Apply *in-situ* creep under neutron diffraction for deeper understanding of creep mechanisms in cast-Al alloys for brake-rotor application.
- Characterize creep properties of novel cast-Al alloys for electrical-conductor applications and benchmark the performance against baseline-conductor Al alloys.
- Characterize fatigue properties of an Al alloy additively manufactured with liquid-metal jetting for heat-sink applications.

Approach

Al-6.6 Cu-0.45 Mn-0.2 Zr (ACMZ) wt.% is a new high-temperature cast-Al alloy that exhibits thermal stability up to 350°C, comparable to commercial cast-Al alloys, most of which evidence poor thermal stability above 250°C [1]. RR350 Al-5 Cu-1.5 Ni-0.2 Co-0.2 Mn-0.2 Zr-0.2 Ti-0.15 antimony (Sb) wt.% is a

commercial cast-Al alloy that is similar to ACMZ alloys but is more creep-resistant [2]. However, RR350 has poor castability and contains more expensive and strategic elements, such as Ni and Co, than ACMZ, which is more castable and based on a simpler, lower cost composition. A deeper understanding into creep mechanisms of ACMZ and RR350 alloys by using *in-situ* creep under neutron diffraction would inform development of more-creep-resistant variants of ACMZ and other alloy families.

Al-2Ni-0.5Zr (Al-Ni-Zr) is a dilute cast-Al alloy being developed for electrical-conductor applications. The Al-Ni-Zr alloy is strengthened by secondary L_{12} -Al₃Zr nanoscale precipitates, as well as Al₃Ni fibers, that form during solidification. The creep properties of this alloy have been characterized within this task at an intermediate temperature of 200°C, which is relevant for electrical-conductor applications, and alloy behavior is compared to the benchmark AA1350 commercial-conductor Al alloy.

Liquid-metal jetting (LMJ) is a new AM method whereby a part is 3D-printed by depositing liquid-metal droplets in a highly controlled manner [3]. LMJ offers high-throughput fabrication rates with the ability to print complex geometries, which makes it an attractive method for manufacturing advanced heat sinks for EVs. Cast-Al-7Si-0.3Mg (Al-Si-Mg) alloy, commercially known as A356, is one of the alloys used to manufacture heat sinks. The same alloy has been additively manufactured in this task with LMJ. RT high-cycle-fatigue (HCF) properties of the LMJ Al-Si-Mg alloy are characterized in the T6-aged condition (e.g., 530°C/5 h solution treatment followed by aging at 160°C for 5 h) and subsequently compared to that of T6 cast-Al-Si-Mg alloy.

Results

In-situ Neutron Diffraction Creep of ACMZ and RR350 Alloys

Figure I.1.1.3.1 shows minimum strain-rate vs. applied stress during *ex-situ* compression and *in-situ* tensile-creep tests at 300°C. The figure exhibits that RR350 has higher creep resistance than ACMZ at 300°C. Both alloys exhibit three creep regimes, defined by stress exponent $n = 1$ at stresses lower than ~20–30 MPa, $n=3$ for stresses higher than 20–30 MPa, and lower than 75–80 MPa, and $n = 24$ for stresses higher than 75–80 MPa. Only the $n = 3$ and 24 creep regimes were analyzed with *in-situ* neutron-creep testing.

Figure I.1.1.3.2 shows lattice strain evolution in α -Al matrix and strengthening θ' -Al₂Cu precipitates for ACMZ and RR350 alloys at various stresses during *in-situ* creep at 300°C. At higher applied stresses, in the $n = 24$ regime, lattice strain in the α -Al matrix decreases and in θ' precipitates increases with creep time. This load transfer from the matrix to the precipitates suggests that Orowan looping of dislocations around the precipitates is the active creep deformation mechanism. At lower stresses, in the $n = 3$ region, lattice strain in the α -Al matrix and θ' precipitates remain constant with creep time. This indicates that Orowan looping is inactive in the grain bulk.

The transmission electron microscopy (TEM) images of two regions—one away from and one near a grain boundary (GB), in a RR350 sample exposed to creep testing ($n = 3$ regime) at 300°C—are shown in Figure I.1.1.3.3. The dislocation density is significantly higher near GBs whereas only few dislocations are observed away from GBs into the grain bulk. The presence of a much lower population of dislocations in the grain bulk is consistent with *in-situ* neutron-creep results, which predict that Orowan looping is inactive in an $n = 3$ regime. Instead, the creep deformation mechanism in the $n = 3$ regime is expected to be grain boundary sliding, controlled by localized pipe diffusion and/or dislocation flow in PFZs surrounding the GBs. PFZs are the softest region in the microstructure because they are devoid of the strengthening θ' precipitates, resulting in susceptibility to strain localization. PFZs are narrower in RR350 due to this alloy's containing coarsening-resistant (Ni, Co)-rich grain boundary precipitates which makes the alloy more creep-resistant than ACMZ, which contains rapidly coarsening Cu-rich GB precipitates, wider PFZs, and lower creep resistance [2]. This work highlights the importance of coarsening-resistant GB precipitates in enhancing creep resistance of cast-Al alloys. Developing ACMZ variants with improved creep resistance without compromising their cost-

effectiveness and superior castability would require searching for inexpensive and non-strategic alloying alternatives to the Ni or Co that form coarsening-resistant GB precipitates.

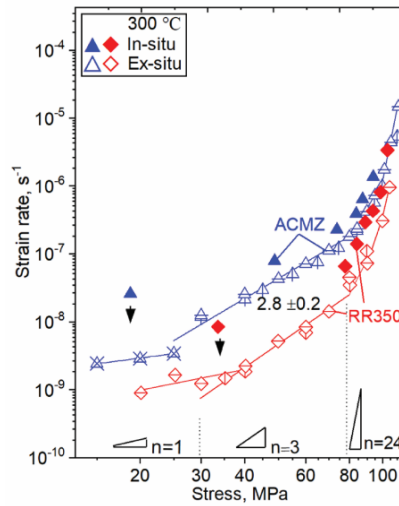


Figure I.1.1.3.1. Minimum creep strain rate vs. applied stress during *in-situ* (tensile) and *ex-situ* (compression) creep tests at 300 °C. Source: ORNL.

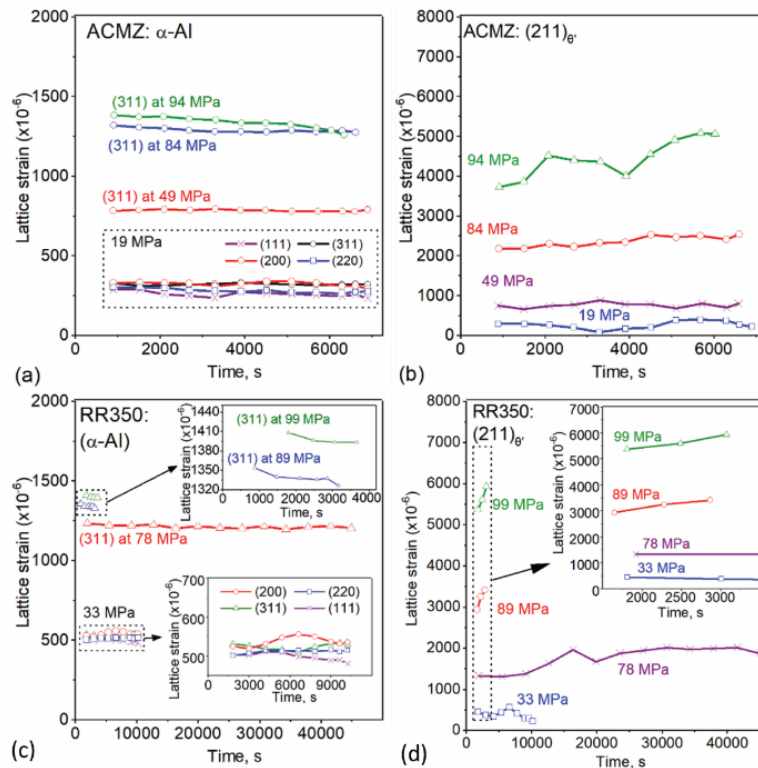


Figure I.1.1.3.2. Crystal plane (hkl) specific lattice strain evolution in (a, c) α -Al matrix and (b, d) θ' precipitates during 300 °C in situ creep tests in ACMZ and RR350 alloys. Source: ORNL.

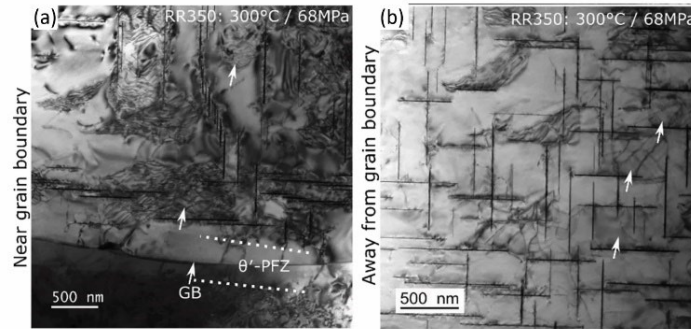


Figure I.1.1.3.3. TEM images of a 300 °C/68 MPa crept RR350 sample showing dislocation structure (a) near and (b) away from GBs. Arrows indicate dislocations. Source: ORNL.

Creep Properties of Al-Ni-Zr Electrical-Conductor Alloy

The as-cast-Al-Ni-Zr alloy was aged—in one case at 300°C for 200 h and, in the other case, at 450°C for 200 h—to induce nanoscale $L1_2$ - Al_3Zr precipitation. The 300°C/200 h aging leads to higher hardness of 69 ± 2 kg/mm² and lower electrical conductivity of $50.6 \pm 0.2\%$ International Annealed Copper Standard (IACS). The 450°C/200 h aging leads to a significantly lower hardness of 37 ± 2 kg/mm², but notably higher electrical conductivity of $55.4 \pm 0.3\%$ IACS. The lower hardness in the 450°C/200 h aged condition is due to greater coarsening of Al_3Ni fibers and $L1_2$ - Al_3Zr precipitates. The higher aging temperature of the 450°C/200 h condition should accelerate $L1_2$ - Al_3Zr precipitation, resulting in the α -Al matrix's being leaner in dissolved Zr than in the 300°C/200 h aging condition, and this may explain the higher electrical conductivity in the former condition. However, further work is required to confirm this hypothesis. Figure I.1.1.3.4 shows minimum creep strain rate versus applied compressive stress at 200°C for the Al-Ni-Zr alloy in the two aging conditions. The creep strain rate at a given applied stress is several orders of magnitude slower in the 300°C/200 h aged condition, which is consistent with hardness higher than in the 450°C/200 h aged condition, with its lower hardness and resultant more rapid creep rate. This work shows the tradeoff between creep resistance and electrical conductivity; aging treatment that leads to higher creep resistance (i.e., 300°C/200 h) exhibits reduced conductivity and vice versa. Figure I.1.1.3.4 compares the creep properties of Al-Ni-Zr alloy to those of commercial AA1350-H19 conductor Al alloy wire. Compositionally, AA1350 is a minimum of 99.5% Al, with small additions of Si, Cu, iron, and other elements. The H19 temper designates extra strain-hardened (cold-wire-drawn) condition. Figure I.1.1.3.4 shows that the 300°C/200 h aged Al-Ni-Zr alloy has higher creep resistance than 1350 Al alloy wire at stresses up to 30 MPa whereas creep resistance of the two alloys is similar at higher stresses.

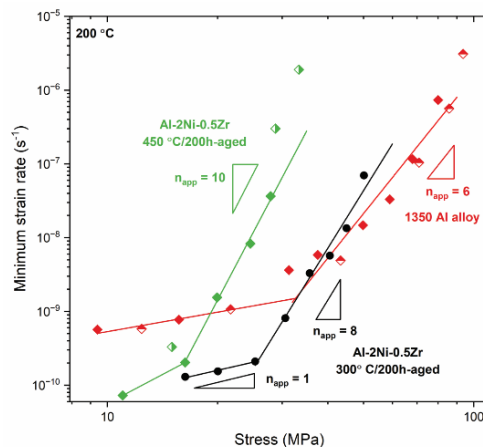


Figure I.1.1.3.4. Minimum creep strain rate vs. applied stress at 200 °C for Al-Ni Zr and commercial AA1350 conductor Al alloys. Source: ORNL.

Fatigue Behavior of LMJ Al-Si-Mg Alloy

Figure I.1.1.3.5(a, b) shows EBSD and SEM images of AF LMJ Al-Si-Mg alloy, respectively. The AF alloy consists of fine equiaxed grains of a few tens-of-microns size, as shown in the EBSD grain map in Figure I.1.1.3.5(a). The SEM image in Figure I.1.1.3.5(b) shows spheroidized Si particles present inside the grains and at GBs. The Si particles have spheroidized due to a high build temperature of 475°C in the LMJ process. The AF alloy was subjected to the same T6 heat-treatment that is applied to cast-Al-Si-Mg-alloys. Heat-treatment coarsens the Si particles, as shown in Figure I.1.1.3.5(c) and is expected to cause nanoscale precipitation of Mg-Si based precipitates; however, this needs to be confirmed with future TEM characterization. Figure I.1.1.3.5(d) shows tensile stress-strain curves of AF and T6 aged LMJ Al-Si-Mg alloy, measured parallel and perpendicular to the build direction and designated vertical and horizontal samples, respectively. The YS is similar, but ductility is lower in the vertical direction relative to the horizontal for both AF and T6 conditions. The YS increases from ~110 MPa in the AF condition to ~250 MPa in the T6 condition whereas the ductility reduces from ~18 to ~6% in the vertical direction and from ~21 to ~9% in the horizontal direction. Note that one of the AF vertical sample shows less than 5% ductility, likely due to a large printing defect, and it is excluded from the calculation of average ductility. The YS of the cast-Al-Si-Mg alloy (not shown in Figure I.1.1.3.5) is slightly lower than the printed alloy at ~230 MPa, and ductility is slightly higher at ~8% relative to the vertical direction of the LMJ Al-Si-Mg alloy.

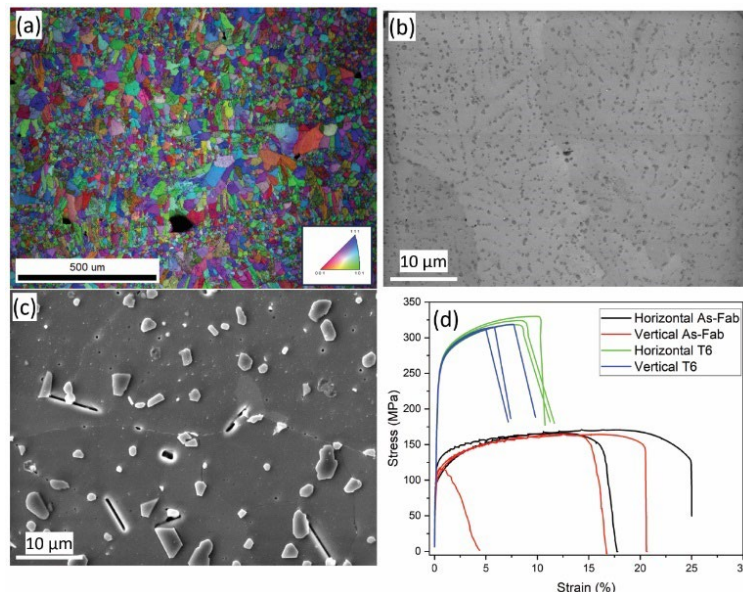


Figure I.1.1.3.5. (a) EBSD grain map of AF LMJ Al-Si-Mg alloy. SEM image of (b) AF and (c) T6 aged alloy. The build direction is vertical upwards. (d) Tensile stress-strain curves. Source: ORNL.

HCF tests of the LMJ printed Al-Si-Mg-alloys were performed in the weaker vertical direction as the most-conservative measurement of fatigue strength. These were compared to cast-Al-Si-Mg alloy with both in the T6 condition. Figure I.1.1.3.6(a) shows maximum cyclic stress versus cycles to failure for HCF tests. The fatigue strength, defined by specimen runout at 10^7 cycles (indicated by arrows), is lower in the LMJ Al-Si-Mg alloy (at 60 MPa) as compared to that in the cast alloy (90 MPa). Figure I.1.1.3.6(b) shows the fracture surface of an LMJ Al-Si-Mg sample tested at 75 MPa. Fatigue cracks initiated and propagated in two separate printed layers (marked 1 and 2); however, it is difficult to identify a particular crack-initiation site or the corresponding microstructural feature (e.g., a pore) that may have been responsible for crack-initiation. The droplet boundaries, as outlined in Figure I.1.1.3.6(b), are clearly visible on the fracture surface, suggesting that these boundaries are the preferred path for crack propagation and may be responsible for fatigue strength of the LMJ Al-Si-Mg alloy's being lower than the cast-Al-Si-Mg alloy, despite similar YS and ductility. Developing a fundamental understanding of weak droplet boundaries in the LMJ Al-Si-Mg alloy would inform future

alloy- and/or process design concepts to enable future fatigue-resistant LMJ Al alloys. The advantage of high-quality LMJ alloys would be high rates of deposition for 3D-printing and flexibility in feedstock configurations.

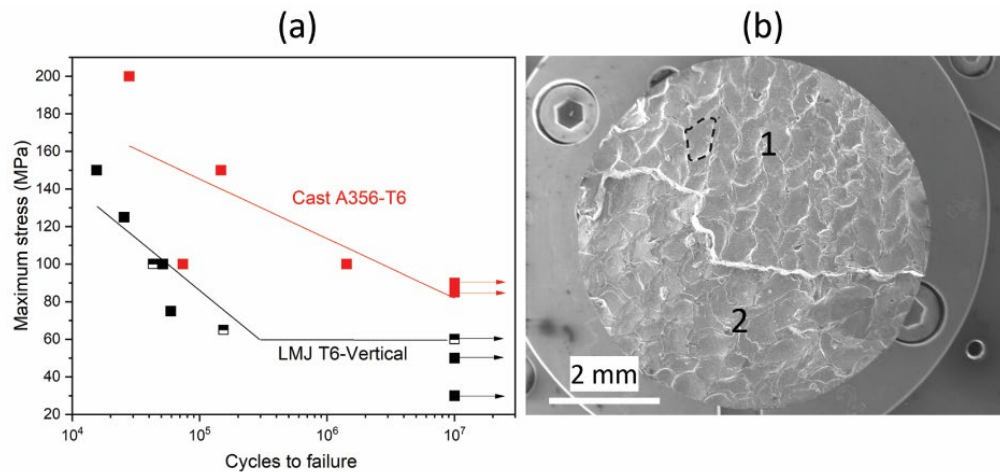


Figure I.1.1.3.6. (a) Maximum stress vs. cycles to failure in HCF tests of T6-aged LMJ (vertical) and cast-Al-Si-Mg (or A356) alloys. (b) Fractograph of an LMJ Al-Si-Mg sample fractured at 75 MPa. Source: ORNL.

Conclusions

Based on the results of this work, the following conclusions can be drawn:

- The creep mechanisms in ACMZ and RR350 high-temperature cast-Al alloys were determined with in-situ creep under neutron diffraction. In-situ results reveal that Orowan looping is active at $n = 24$, but inactive in the $n = 3$ creep regimes. The creep mechanism in the $n = 3$ regime is expected to be grain boundary sliding controlled by localized pipe diffusion and/or dislocation flow in PFZs. This is supported by TEM observation of high-dislocation density in the GB region.
- The creep properties of an Al-Ni-Zr alloy for conductor applications were characterized at 200°C in two aging conditions, including 300°C and 450°C for 200 h, with the former exhibiting higher hardness, but lower electrical conductivity than latter. Creep resistance is higher in the 300°C/200 h condition, consistent with its higher hardness. This result highlights an important challenge of understanding and designing for the tradeoff between creep resistance and electrical conductivity for advanced lightweight conductors intended for very high electrical current densities.
- The HCF properties of the T6-aged LMJ printed Al-Si-Mg alloy were measured parallel to the build direction at RT and compared to the cast version of the same alloy. The fatigue strength was lower in the LMJ Al-Si-Mg alloy (60 MPa) than in the cast-Al-Si-Mg alloy (90 MPa) despite similar YS and ductility. The presence of weak droplet boundaries in the LMJ Al-Si-Mg alloy is hypothesized to be responsible for lower fatigue resistance of the alloy.

Key Publications

1. Michi, R. A., S. Bahl, C. M. Fancher, K. Sisco, L. F. Allard, K. An, D. Yu, R. R. Dehoff, A. Plotkowski, and A. Shyam, 2023, "Load shuffling during creep deformation of an additively manufactured AlCuMnZr alloy," *Acta Mater.*, 244, 188557. <https://doi.org/10.1016/j.actamat.2022.118557>.
2. Michi, R. A., J. J. Simpson, S. Bahl, Q. Campbell, P. Brackman, A. Plotkowski, R. R. Dehoff, J. A. Haynes, Q. Wang, and A. Shyam, 2023, "Additively manufactured AlCeNiMn alloy with improved elevated-temperature fatigue resistance," *Addit. Manuf.*, 66, 103477. <https://doi.org/10.1016/j.addma.2023.103477>.

3. Rakhmonov, J. U., B. Milligan, S. Bahl, D. Ma, A. Shyam, and D. C. Dunand, 2023, “Progression of creep deformation from grain boundaries to grain interior in AlCuMnZr Alloys.” *Acta Mater.*, 250, 118886. <https://doi.org/10.1016/j.actamat.2023.118886>.

References

1. Shyam, A., S. Roy, D. Shin, J. D. Poplawsky, L. F. Allard, Y. Yamamoto, J. R. Morris, B. Mazumder, J. C. Idrobo, A. Rodriguez, T. R. Watkins, and J. A. Haynes, 2019. “Elevated-temperature microstructural stability in cast AlCuMnZr alloys through solute segregation,” *Mater. Sci. Eng. A*, 765, 138279. <https://doi.org/10.1016/j.msea.2019.138279>.
2. Rakhmonov, J. U., S. Bahl, A. Shyam, and D. C. Dunand, 2022, “Cavitation-resistant intergranular precipitates enhance creep performance of θ' -strengthened AlCu based alloys,” *Acta Mater.*, 228, 117788. <https://doi.org/10.1016/j.actamat.2022.117788>.
3. Simonelli, M., N. Aboulkhair, M. Rasa, M. East, C. Tuck, R. Wildman, O. Salomons, and R. Hague. 2019. “Towards digital metal AM via high-temperature drop-on-demand jetting.” *Addit. Manuf.*, 30, 100930. <https://doi.org/10.1016/j.addma.2019.100930>.

Acknowledgements

All team members—including R. Michi, J. Rakhmonov, B. Milligan, D. Ma, D. C. Dunand, J. Qi, C. M. Fancher, K. Sisco, L. F. Allard, K. An, D. Yu, R. R. Dehoff, A. Plotkowski, A. Shyam, J. J. Simpson, Q. Campbell, P. Brackman, J. A. Haynes, Q. Wang, G. Knapp, and A. Gomez—are acknowledged for their technical contributions. D. McClurg is acknowledged for technical support. The research was co-sponsored by the VTO under the PMCP and Advanced Materials & Manufacturing Technologies Office. A portion of this research used resources at the Spallation Neutron Source, a U.S. Department of Energy-Office of Science User Facility operated by ORNL.

I.1.1.4 Task 1D. Fundamentals of Corrosion Behavior in Advanced Lightweight Alloys for Electric Vehicle Propulsion (Oak Ridge National Laboratory)

Jiheon Jun, Principal Investigator

Oak Ridge National Laboratory
Materials Science and Technology Division
1 Bethel Valley Rd.
Oak Ridge, TN 37830
E-mail: junj@ornl.gov

J. Allen Haynes, PMCP Consortium Manager

Oak Ridge National Laboratory
Materials Science and Technology Division
1 Bethel Valley Rd.
Oak Ridge, TN 37830
E-mail: haynesa@ornl.gov

Jerry L. Gibbs, DOE Technology Development Manager

U.S. Department of Energy
E-mail: Jerry.Gibbs@ee.doe.gov

Start Date: November 1, 2021

End Date: September 30, 2023

Project Funding: \$185,000

DOE share: \$185,000

Non-DOE share: \$0

Project Introduction

High-performance cast and additively manufactured (AM)-Al alloys for EV applications were developed at ORNL under the PMCP [1], [2], [3], [4]. For developed Al alloys, an evaluation of aqueous-corrosion resistance was performed under Task 1D in FY 2023. Comparing the determined corrosion resistance with laboratory testing and understanding corrosion behaviors allows these new Al alloys to be considered for the next generation of lightweight powertrain materials to produce EV structural components, battery enclosures, or brake systems.

Objectives

This task aims to provide and compare electrochemical corrosion and post-corrosion characterization data for AM Al alloys with new and commercial compositions. Comprehensive evaluation of this data for the Al alloys supports the prediction of corrosion performance and aids relevant industries in the United States to identify advanced alloys potentially suitable for future EV applications.

Approach

Three AM Al alloys, with and without additional heat treatments, were used for the FY 2023 corrosion task. The baseline alloy was a commercial AM alloy composition (Al10SiMg), while the other two were new high-performance printable Al alloys, recently developed by ORNL (AlCeNiMn and AlCeNiMnZr). The nominal chemical compositions and heat-treatment conditions for these Al alloys are summarized in Table I.1.1.4.1. Corrosion resistance was assessed by two electrochemical techniques—electrochemical impedance spectroscopy (EIS) and polarization—in 3.5 wt% sodium chloride (NaCl) for short-term immersion (<3 h). Figure I.1.1.4.1 shows a schematic description of an electrochemical measurement setup, summaries of EIS and polarization conditions, and two equivalent circuit models used for impedance-data fitting. To investigate longer term corrosion behavior, all alloys were immersed in 3.5 wt% NaCl, open to air at RT for 168 h, and post-immersion characterization of cross-sectioned alloy samples were performed. The characterization techniques used in this task were SEM and EDS.

Table I.1.1.4.1. Nominal Chemical Compositions of Aluminum Alloys Used in this Task

AM Al Alloys [Process History]	Weight Percents							
	Ce	Mn	Ni	Zr	Si	Mg	Al	
Commercial Compositions	A10SiMg [as-printed by ORNL]							
ORNL-Developed	AlCeNiMn (ACNM450) [450 °C for 2 h after printing]	~9	~1	~4	-	-	-	Balance
	AM-AlCeNiMnZr (ACNMZ) [Three conditions: as-printed, 350 °C for 8 h after printing, 450 °C for 2 h after printing]	~9	~0.5	~4	~1	-	-	

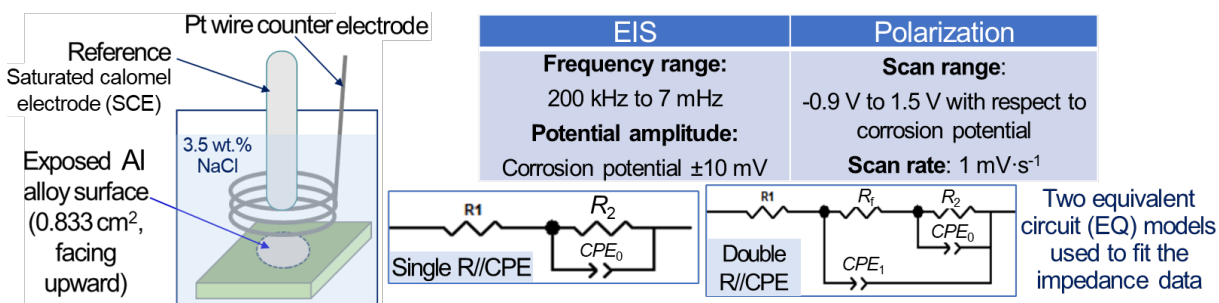


Figure I.1.1.4.1. Schematic description of electrochemical cell—EIS and polarization conditions—and two circuit models for impedance-data fitting. R_1 is solution resistance, R_2 is charge-transfer resistance, and R_f is permeable-film resistance. CPE_0 and CPE_1 account for non-ideal capacitive behavior associated with R_2 and R_f , respectively. Source: ORNL.

Results

Figure I.1.1.4.2 presents comparison of typical impedance-spectra and representative polarization curves from AM Al alloys. As-printed A110SiMg and ACNMZ showed greater impedance values than the other alloys tested, as indicated in Figure I.1.1.4.2(a), implying the corrosion rates would be lower in these two alloys. In the polarization curves, pitting or passivity-breakdown behavior, where anodic currents sharply increase at local Al dissolution spots, was captured, and the potential associated with pitting was determined as pitting potential (E_p), as designated by arrows in Figure I.1.1.4.2(b). Impedance-data fitting using two circuit models was performed, and the values of R_2 or $R_f + R_2$ were compared for semiquantitative evaluation of corrosion resistance. Higher R_2 or $R_f + R_2$ can be interpreted as higher corrosion resistance.

In Figure I.1.1.4.3(a), the values of R_2 or $R_f + R_2$ are plotted as a function of corrosion potential (E_{corr}). Average resistance values, which are designated as $\langle \rangle$ in the plot, support that as-printed A110SiMg and ACNMZ would be more resistant to corrosion than heat-treated ACNM (ACNM450) and heat-treated ACNMZ (ACNMZ350 and ACNMZ450). E_p , as a function of E_{corr} , is plotted in Figure I.1.1.4.3(b). As the difference of E_p and E_{corr} increases (i.e., the greater y distance between the data point and $E_p = E_{\text{corr}}$ line), it means that a passive state (from protective Al₂O₃ layer) was more persistent. Thus, the values of $E_p - E_{\text{corr}}$ can be considered as another factor to assess corrosion resistance. Overall, as-printed A110SiMg and ACNMZ exhibited high E_p values, which are also associated with greater $E_p - E_{\text{corr}}$, implying higher corrosion resistance.

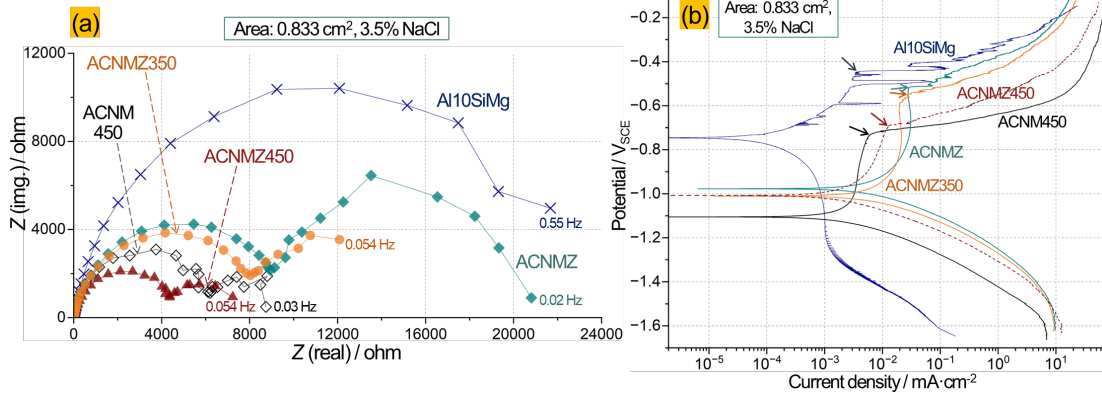


Figure I.1.1.4.2. (a) Typical Nyquist-impedance-spectra and (b) representative polarization curves of AM Al alloys with arrows designating pitting potential (E_p) values. Source: ORNL.

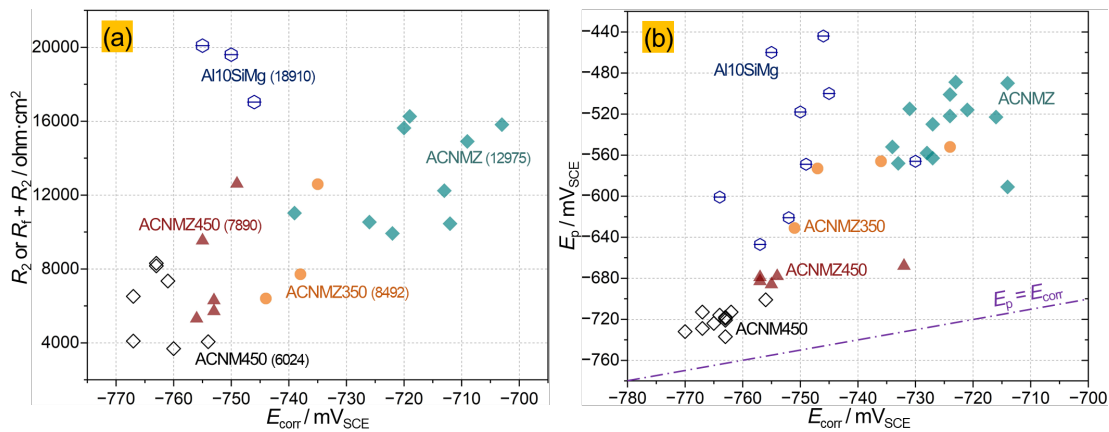


Figure I.1.1.4.3. (a) R_2 or $R_f + R_2$ and (b) E_p as a function of E_{corr} . In (b), $E_p = E_{corr}$ line is presented as a guide to assess the difference between E_p and E_{corr} data. Source: ORNL.

The average values of R_2 , $R_f + R_2$ and $E_p - E_{corr}$ data, with their standard deviations, are summarized in Table I.1.1.4.2 to aid the comparison of corrosion resistance between AM Al alloys for short-term immersion in 3.5 wt% NaCl. As noted, Al10SiMg and ACNMZ exhibited high average values associated with higher corrosion resistance. ACNM450 showed lower average values, which suggests greater susceptibility to corrosion. ACNMZ450 showed slightly lower resistance than ACNMZ350, suggesting a more detrimental effect of heat-treatment at a higher temperature on the alloy corrosion resistance.

Table I.1.1.4.2. Summary of Average Electrochemical Corrosion Data for AM Al Alloys

	A10SiMg	ACNM450	ACNMZ	ACNMZ350	ACNMZ450
Average R_2 (for A10SiMg) or $R_f + R_2$ (others)/ohm-cm ² [No. of data]	18910 [3 data]	6024 [7 data]	12975 [9 data]	8492 [4 data]	7890 [5 data]
Std. dev. of above	±1340	±1883	±2486	±2411	±2791
Average ($E_p - E_{corr}$)/mV	202 [9 data]	44 [11 data]	192 [13 data]	159 [4 data]	72 [5 data]
Std. dev. of above	±65	±8	±30	±23	±5
Note	High Resistance	Low Resistance	Decreased Resistance after 350 & 450 °C Treatments		

Cross-sectional characterization results were used to compare the corrosion-depth and chemical features associated with corrosion attacks. In the observed cross-sections of the samples, relatively shallow corrosion attacks were observed, along with localized deeper corrosion attacks. Figure I.1.1.4.4, Figure I.1.1.4.5, Figure I.1.1.4.6, Figure I.1.1.4.7, and Figure I.1.1.4.8 present rather shallow corrosion attacks in the cross-sectioned AM Al alloys after 168 h immersion in 3.5 wt.% NaCl. In Al10SiMg, shown in Figure I.1.1.4.4, an approximate 13- μm -deep attack with Si-rich oxide was observed. In ACNM450, depicted in Figure I.1.1.4.5, Al-rich outer- and inner-oxide layers formed a boundary where Ce, Mn, and Ni were enriched. The depth of inner-oxide, in this case, leached to $\sim 10\ \mu\text{m}$. In ACNMZ, indicated in Figure I.1.1.4.6, the inner- and outer-oxide layers separated by Ce, Mn, Ni, and Zr enriched boundaries were observed, and the depth of inner-oxide reached to $\sim 10\ \mu\text{m}$ in the characterized cross-section. In ACNMZ350, shown in Figure I.1.1.4.7, and ACNMZ450, observed in Figure I.1.1.4.8, the corrosion attack showed similar outer- and inner-oxide layer structures, but the enrichment of Ce, Ni, and Mn appeared within the inner-oxide layer. The depth of attacks in the observed locations of ACNMZ350 and ACNMZ450 were ~ 3 and $\sim 13\ \mu\text{m}$, respectively.

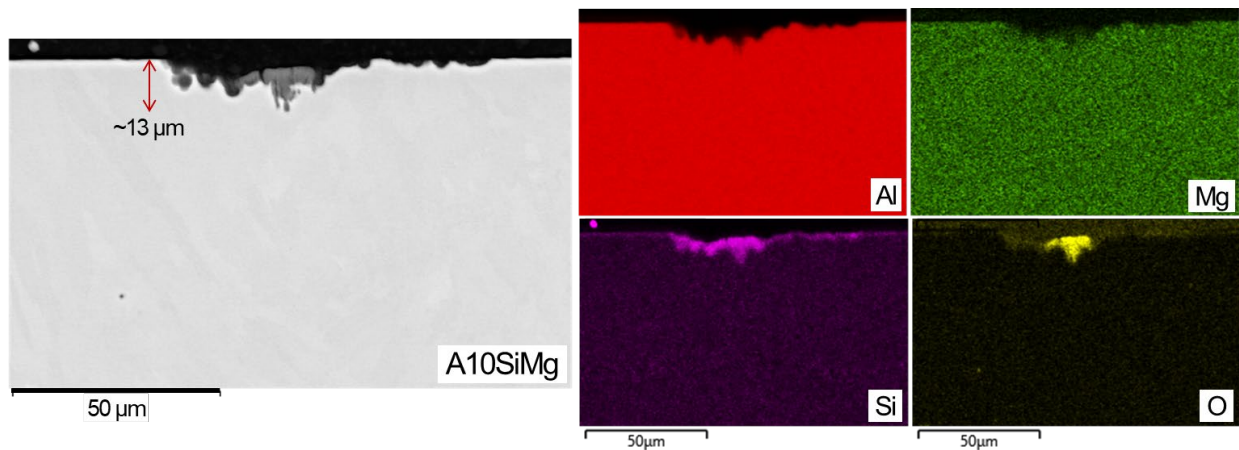


Figure I.1.1.4.4. Cross-sectional SEM image and EDS characterization maps (Al, Mg, Si, and O) of Al10SiMg after 168 h in 3.5 wt.% NaCl. Source: ORNL.

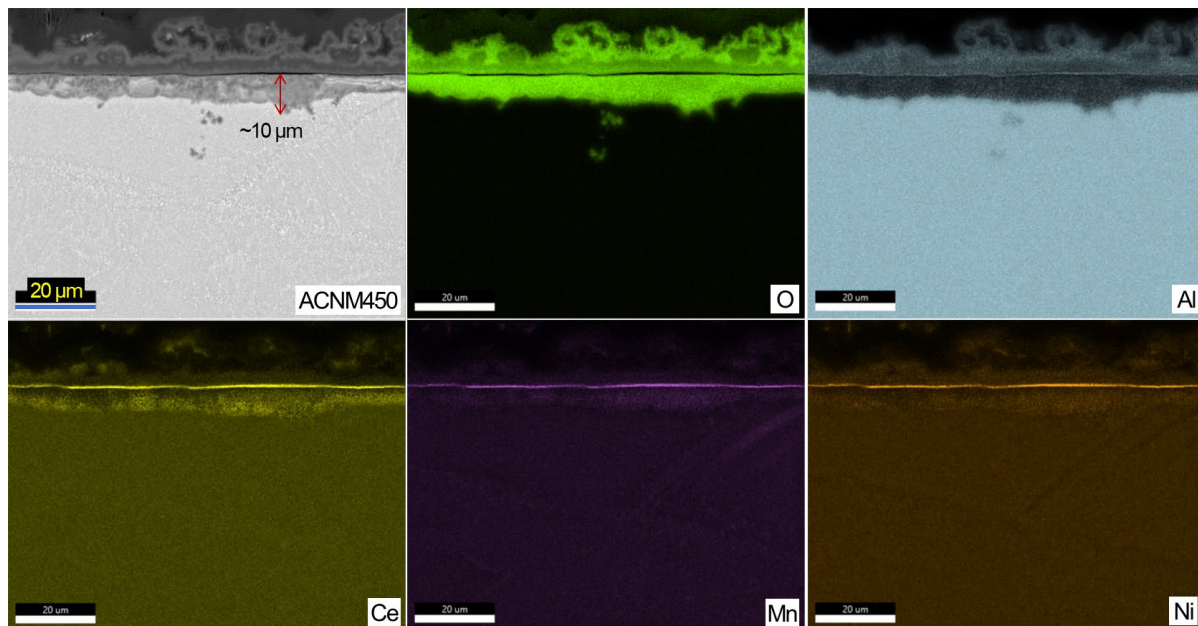


Figure I.1.1.4.5. Cross-sectional SEM image and EDS characterization maps (Al, Ce, Mn, Ni, and O) of ACNM450 after 168 h in 3.5 wt.% NaCl. Source: ORNL.

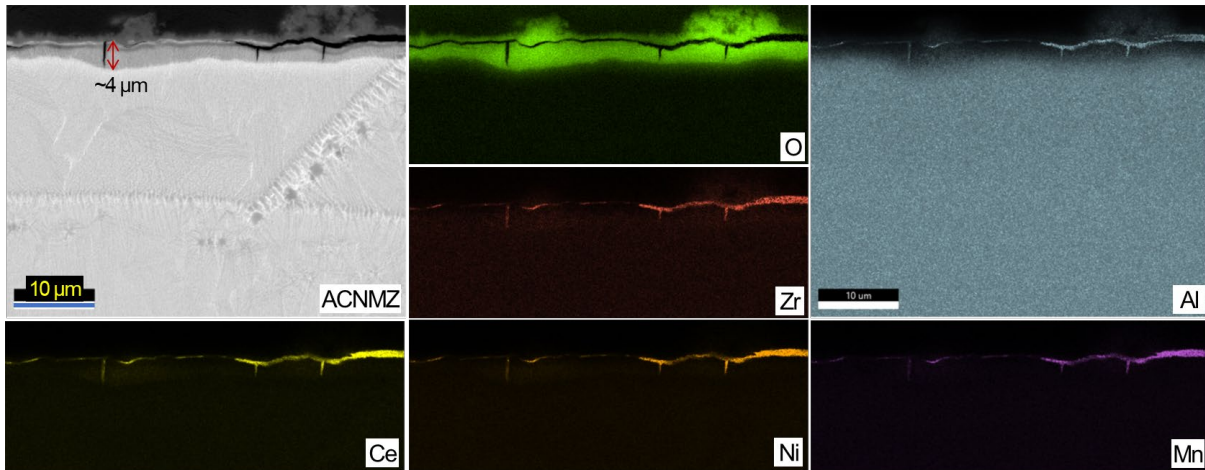


Figure I.1.1.4.6. Cross-sectional SEM image and EDS characterization maps (Al, Ce, Mn, Ni, Zr, and O) of ACNMZ after 168 h in 3.5 wt.% NaCl. Source: ORNL.

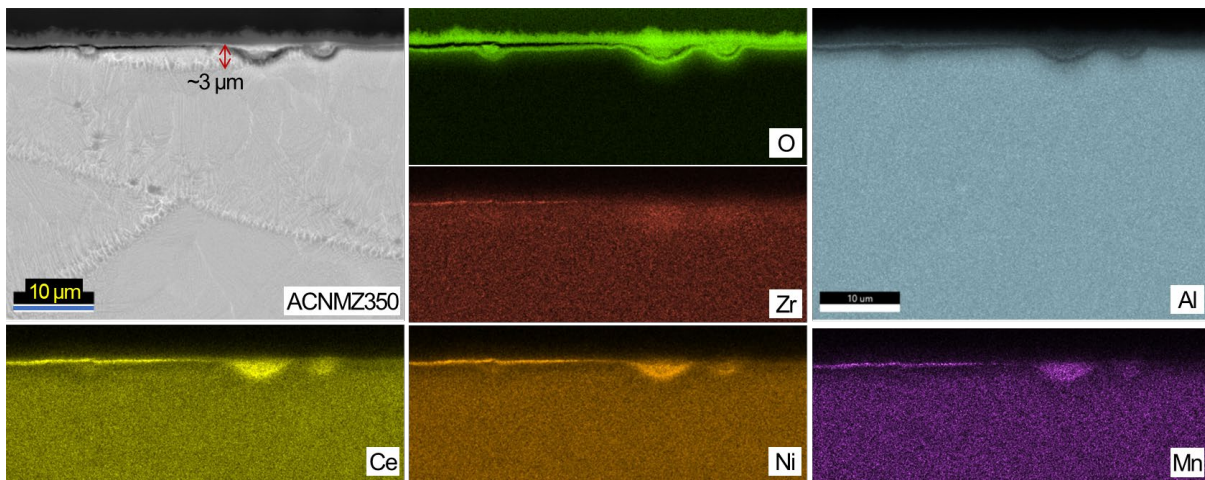


Figure I.1.1.4.7. Cross-sectional SEM image and EDS characterization maps (Al, Ce, Mn, Ni, Zr, and O) of ACNMZ350 after 168 h in 3.5 wt.% NaCl. Source: ORNL.

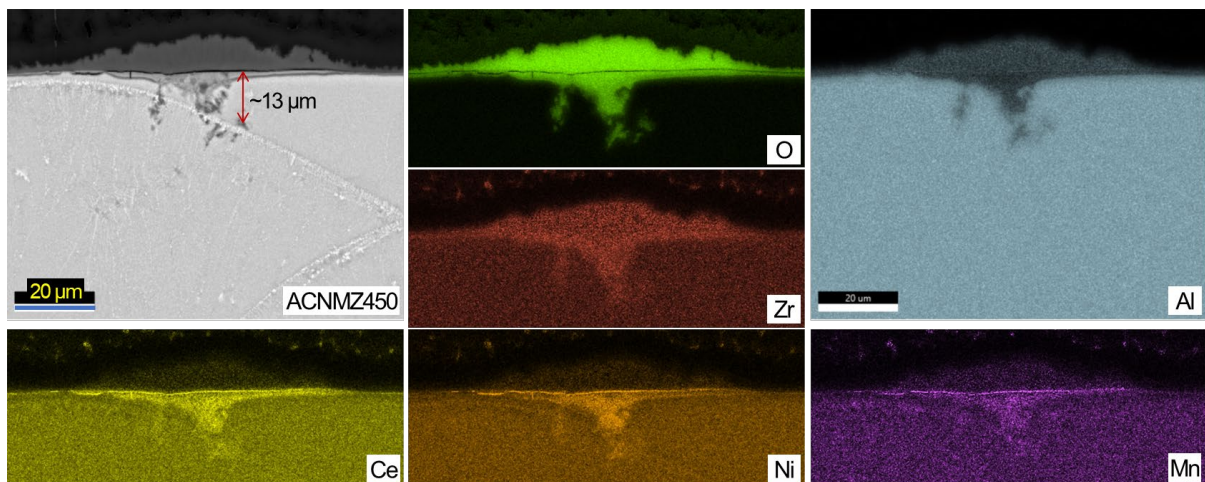


Figure I.1.1.4.8. Cross-sectional SEM image and EDS characterization maps (Al, Ce, Mn, Ni, Zr, and O) of ACNMZ450 after 168 h in 3.5 wt.% NaCl. Source: ORNL.

Meanwhile, the characterization of the ACNM450 and ACNMZ cross-sections revealed deeper corrosion attacks as observed in Figure I.1.1.4.9. In ACNMZ, O-rich corrosion attacks grew within the solidification domain and melt pool boundaries and reached to $\sim 52\ \mu\text{m}$. In ACNM450, pitting attacks with irregular boundaries and volume loss were observed and reached to $\sim 59\ \mu\text{m}$. Based on these results, it can be predicted that a long-term NaCl solution exposure causes more corrosion attacks in ACNM450 and ACNMZ than in Al10SiMg. However, it should also be emphasized that Al10SiMg may have deep corrosion attacks that were not found through the cross-sectional characterization performed in FY 2023. Therefore, it is recommended that more cross-sectional characterization be performed for corroded AM Al alloys in a future task to capture more corrosion attacks (including deep ones) and clearly understand the mode of key corrosion attacks.

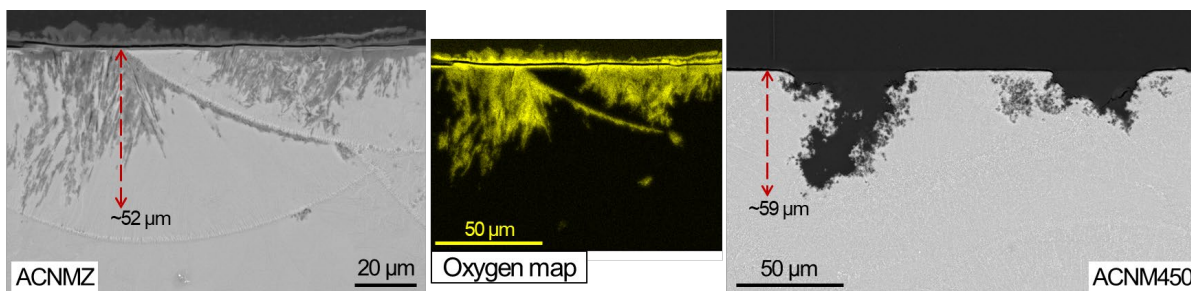


Figure I.1.1.4.9. Cross-sectional SEM image and EDS characterization maps of deeper corrosion attacks in ACNMZ (left and center) and ACNM450 (right) after 168 h in 3.5 wt% NaCl. Source: ORNL.

Conclusions

Based on the results of this work, the following conclusions can be drawn:

- Among the tested AM Al alloys, Al10SiMg and ACNMZ showed higher corrosion resistance than the others (including ACNM and heat-treated ACNMZ) in short-term (<3 h) immersion in 3.5 wt% NaCl, as revealed by electrochemical corrosion data.
- Cross-sectional characterization of AM Al alloys, except Al10SiMg, after 168 h corrosion immersion showed relatively shallow corrosion attacks where outer- and inner-oxide layer appeared with Ce-, Ni-, and Mn-enriched locations. In Al10SiMg, a shallow attack ($\sim 13\ \mu\text{m}$) with a Si-rich oxide remnant was observed.
- Relatively deep corrosion attacks (up to $\sim 59\ \mu\text{m}$) were found in both ACNM450 and ACNMZ in other characterized cross-sections. In ACNMZ, the corrosion growth was found within the solidification domain and melt pool boundaries while irregular pits associated with volume loss were found in ACNM450.
- This corrosion data suggests that Al10SiMg (with commercially available composition) and ACNMZ could exhibit comparable resistance to each other in short-term corrosion exposure, but ACNMZ could develop deeper attacks for longer immersion ($\sim 168\ \text{h}$). However, further post-corrosion characterization would be necessary to capture more corrosion attacks that may not have been identified in the current characterization results.

Key Publications

1. Jun, J., 2023, "Task 1D-22: Fundamentals of Corrosion Behavior in Advanced LW Alloys for EV Propulsion," presented at the PMCP VTO Mid-Year Program Review, April 5, 2023, Virtual.
2. Jun, J., A. Shyam, J. A. Haynes, and Y. Su, 2023, "Corrosion Behavior of Additively Manufactured Al-Ce-X and Al-10SiMg Alloys in 3.5 wt% NaCl Solution," presented at an invited oral presentation at TMS 2023, March 2023, San Diego, CA, USA.

3. Jun, J., A. Shyam, S. Bahl, Y.F. Su, and J.A. Haynes, 2023, “Corrosion-Evaluation of AlCuMnZr Cast Alloys in 3.5% NaCl Solution,” drafted for a journal paper submission, November 2023.

References

1. Bahl, S. X. Hu, E. Hoar, J. Cheng, J. A. Haynes, and A. Shyam, 2020, “Effect of copper content on the tensile elongation of AlCuMnZr Alloys: Experiments and finite element simulations,” *Mater. Sci. Eng. A*, 772, 138801. <https://doi.org/10.1016/j.msea.2019.138801>.
2. Bahl, S., J. Rakhmonov, C. Kenel, D. Dunand, and A. Shyam, 2022, “Effect of grain boundary θ -Al₂Cu precipitates on tensile and compressive creep properties of cast-AlCuMnZr alloys,” *Mater. Sci. Eng. A*, 840, 142946. <https://doi.org/10.1016/j.msea.2022.142946>.
3. Shyam, A., S. Roy, D. Shin, J. D. Poplawsky, L. F. Allard, Y. Yamamoto, J. R. Morris, B. Mazumder, J. C. Idrobo, A. Rodriguez, T. R. Watkins, and J. A. Haynes, 2019, “Elevated-temperature microstructural stability in cast AlCuMnZr alloys through solute segregation,” *Mater. Sci. Eng. A*, 765, 138279. <https://doi.org/10.1016/j.msea.2019.138279>.
4. Michi, R. A., K. Sisco, S. Bahl, Y. Yang, J. D. Poplawsky, L. F. Allard, R. R. Dehoff, A. Plotkowski, and A. Shyam, 2022, “A creep-resistant additively manufactured AlCeNiMn Alloy,” *Acta Mater.*, 227(1), 117699. <https://doi.org/10.1016/j.actamat.2022.117699>.

Acknowledgements

The authors thankfully acknowledge contributions and support from A. Shyam, A. Plotkowski, S. Bahl, D. McClurg, and J. Wade at ORNL.

I.1.1.5 Task 1E. Lightweight Materials for Improved Electrical Properties (Oak Ridge National Laboratory)

Amit Shyam, Principal Investigator

Oak Ridge National Laboratory
Materials Science and Technology Division
1 Bethel Valley Rd.
Oak Ridge, TN 37830
E-mail: shyama@ornl.gov

J. Allen Haynes, PMCP Consortium Manager

Oak Ridge National Laboratory
Materials Science and Technology Division
1 Bethel Valley Rd.
Oak Ridge, TN 37830
E-mail: haynesa@ornl.gov

Jerry L. Gibbs, DOE Technology Development Manager

U.S. Department of Energy
E-mail: Jerry.Gibbs@ee.doe.gov

Start Date: November 1, 2021

End Date: September 30, 2023

Project Funding: \$275,000

DOE share: \$275,000

Non-DOE share: \$0

Project Introduction

Conduction of electricity in a battery electric vehicle (BEV) is dominated by copper (Cu) components. The EV motor itself may have more than a mile of Cu wire in the stator windings. Overall, a BEV can have hundreds of pounds of Cu in various components. Compared to Cu wires, aluminum (Al) wires are a lower cost and lighter option for transportation conductors, such as wiring, stators, busbars, and connectors. Al (2.70 g/cm³) has only one-third the density of Cu (8.96 g/cm³). At the same time, Al wires are susceptible to galvanic corrosion, non-conductive oxide formation, and creep (particularly at higher currents), and have lower strength and higher electrical resistivity than Cu. This task will focus on designing Al alloy compositions with an improved balance of properties in wire form than is seen in Cu wires. A fundamental conflict exists between electrical and mechanical properties of wires because microstructural features that improve one are often detrimental to the other, and vice versa. In this task, we will pursue co-optimization of the mechanical and electrical properties of Al alloys for BEV automotive and freight applications through compositional, processing, and heat-treatment innovations.

Objectives

This task will develop new Al alloy compositions with a balance of properties in wire form that make them more competitive with Cu wires. Specific objectives from the second year of this task are as follows:

- To develop Al-conductor families of alloys capable of replacing Cu for EV applications by delivering economic and weight-saving opportunities.
- To develop fundamental understanding of microstructure electrical- and mechanical property relationships that help to guide development of such Al alloys.

Approach

A conflict exists between mechanical and electrical properties of Al alloys [1]. In this task, we started in FY 2022 by identifying microstructural features that help break the tradeoff in mechanical and electrical properties in Al alloys. Dilute binary and ternary alloys are of interest, such as Al-Zr, Al-tin (Sn), and Al-Sn-Zr alloy systems. Fundamental understanding of the microstructure electrical- and mechanical property relationships and tradeoffs were emphasized in the first year of the project, and an alloy-design framework was

established. Electrical resistivity measurement equipment was purchased and calibrated for Al alloys of interest. Advanced computational and characterization efforts towards understanding the favorable properties of the Al-Sn-Zr alloy system (and corresponding binary alloys) were initiated. In FY 2023, the team focused on generating a fundamental understanding of the mechanisms that lead to nucleation of aging precipitates that help break the tradeoff between electrical and mechanical properties. Longer term, this task will focus on designing Al alloy compositions with improved balance of properties for BEV applications in Al wire form than in Cu wire form.

Results

In FY 2022, a new capability was established to measure electrical conductivity (EC) in Al alloys through eddy current-based instrumentation. Alloy ingots were cast for evaluation of mechanical and electrical properties. Binary AlZr, AlSn, and AlZrSn alloys were examined after a variety of heat treatments. The concentration of Sn was designed to be low, at ~200 ppm (0.02 at.%). All alloys were homogenized at 640°C for 24 h and water quenched, and then a series of isochronal treatments were provided on individual specimens for 3 h each from 150 to 550°C in 25°C increments, followed by a water quench. Following each isochronal treatment, Vickers-microhardness (HV) and EC values were measured. In FY 2023, isothermal treatments were also performed to understand the mechanisms behind microstructural changes that lead to evolution of mechanical and electrical properties.

Figure I.1.1.5.1(a) shows the isothermal age-hardening response of the ternary Al-Zr-Sn alloy at 400°C (black dashed line) and 425°C (red solid line). Figure I.1.1.5.1(b) shows the isothermal age-hardening response of the Al-Zr-Sn (red) and Al-Sn (light blue) alloys at 200°C. The binary Al-Sn alloy shows an increase in hardness from 19.3 ± 0.8 HV5 (i.e., VH measured at 5 kg load) in the as-homogenized condition to 26.8 ± 0.5 HV5 after 8 h aging at 200°C. The addition of Zr to the Al-Sn alloy increases the hardness slightly during aging at 200°C. There is a strong age-hardening response of the ternary Al-Zr-Sn alloy at 400°C, with an increase from 20.9 HV5 in the as-homogenized condition to 38.1 HV5 in the peak aged condition after 100 h. Aging at 425°C results in an accelerated age-hardening response between 4 h and 16 h, and a lower peak hardness of 34.3 HV5 at 125 h.

The accompanying changes in EC are shown in Figure I.1.1.5.1(c) and Figure I.1.1.5.1(d). At 200°C, the Al-Sn and Al-Zr-Sn alloys have consistent EC values, and the EC of the Al-Sn alloy is higher on average: 58.6% IACS compared to 52.2% IACS for the Al-Zr-Sn alloy. At higher temperatures, there is an increase in EC with aging time for the Al-Zr-Sn alloy. The ternary Al-Zr-Sn alloys exhibit a dramatic increase in EC during aging at these higher temperatures, an important finding. At 400°C, the EC increases from 51 to 59% IACS for the Al-Zr-Sn alloy after 150 h. At 425°C, the EC of the Al-Zr-Sn alloy increases from 53 to 60.5% IACS after 175 h, with the 425°C condition exceeding the measured EC of the commercially pure (CP) feedstock Al used to make all three alloys, as indicated in Figure I.1.1.5.1(d). The increase in EC for the ternary Al-Zr-Sn alloy is accompanied by an increase in hardness. There is notably a tradeoff between hardness and EC between the two heat-treatment conditions because the 425°C condition obtains a slightly higher EC, but slightly lower hardness, than the 400°C condition.

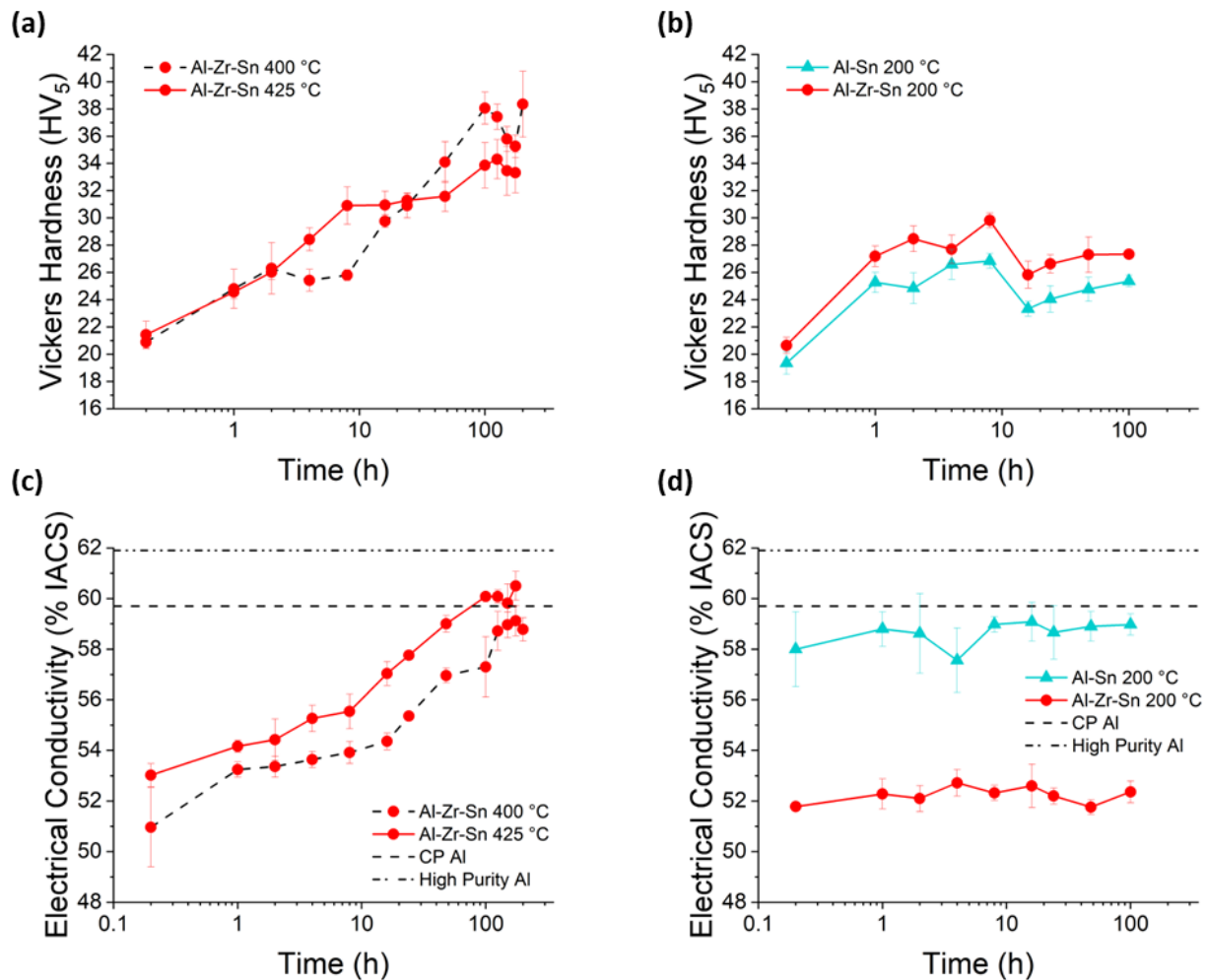


Figure I.1.1.5.1. Plots showing the effect of isothermal aging on the (a) hardness and (c) EC of the Al-Zr-Sn alloy at 400 °C (dashed lines) and 425 °C (solid lines). Plots showing the effect of isothermal aging on the (b) hardness and (d) EC of the Al-Sn (light blue triangles) and Al-Zr-Sn (red circles) at 200 °C. The measured EC values of the CP-Al feedstock material and high-purity (99.9999 wt%) Al are shown in (c) and (d).

Source: ORNL.

Figure I.1.1.5.2(a) shows the isochronal age-hardening response of the Al-Zr, Al-Sn, and Al-Zr-Sn alloys. While these results were presented in FY 2022, they are presented again to clearly identify specimens that were characterized further. Notably, isochronal aging provides insight into the behavior of an alloy over a wide range of temperatures without needing long-term isothermal aging exposure at each temperature. Throughout isochronal aging, the Al-Zr alloy shows a relatively consistent hardness until a small increase from 21.2 HV₅ at 400 °C to 26.5 HV₅ at 500 °C. The Al-Zr-Sn composition exhibits two peaks during isochronal aging. The first, smaller peak is 28.9 HV₅ at 200 °C and decreases to 21.1 HV₅ at 325 °C. The second peak occurs at 425 °C with a hardness of 46.2 HV₅ and decreases again as the temperature continues to increase. The addition of Sn increases the peak hardness, from 26.6 HV₅ in the binary Al-Zr alloy, to 46.2 HV₅ in the ternary Al-Zr-Sn alloy. Similar isochronal aging was performed on a number of other concept alloys and the results were reported in the quarterlies and not reproduced here.

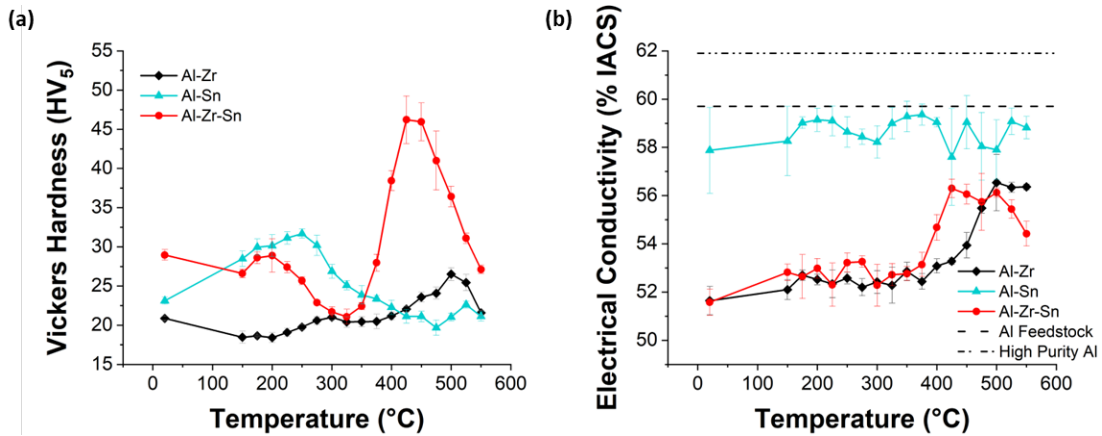


Figure I.1.1.5.2. Plots showing the effect of isochronal aging on (a) hardness and (b) EC for Al-0.34Zr wt.% (black diamonds), Al-0.09Sn wt.% (blue triangles), and Al-0.34Zr-0.09Sn wt.%. Source: ORNL.

After isochronal aging up to 200°C, Sn precipitates can be observed in both the Al-Sn alloy, as indicated in Figure I.1.1.5.3(a), and the Al-Zr-Sn alloy, as shown in Figure I.1.1.5.3(c). APT proximity histograms using the displayed 3 at.% Sn isoconcentration surfaces for the Al-Sn and Al-Zr-Sn alloys show the average Sn-composition profiles around the precipitate/Al matrix interface. The APT measured Sn-precipitate elemental concentrations are not reliable because the precipitate size is below the interfacial resolution limit, and the aberrations caused by the local magnification effect create artificial intermixing of the Sn-precipitate atoms with the Al matrix [2]. The smaller Sn-precipitate sizes in the Al-Sn alloy exaggerate this effect; therefore, the Sn contents are measured to be lower. These are β -Sn particles based on scanning transmission electron microscopy (STEM) measurements. The proximity histogram of the 3 at.% Sn isoconcentration surfaces in Figure I.1.1.5.3(b) is displayed in Figure I.1.1.5.3(c). The dashed-purple line is the background-corrected weighted-average Zr concentration inside the Sn isoconcentration surfaces, calculated from three APT datasets. The Zr content is higher in the Sn particles than the matrix. The average number of Sn atoms per Sn-precipitate is estimated to be 270 ± 110 (i.e., 11 precipitates) and $2,470 \pm 1,220$ (9 precipitates) for the Al-Sn and Al-Sn-Zr samples, respectively. Figure I.1.1.5.3(d) shows a bright-field TEM image of the ~ 5 nm β -Sn precipitates in the Al-Zr-Sn alloy. One of these precipitates is shown at higher magnification in Figure I.1.1.5.3(e).

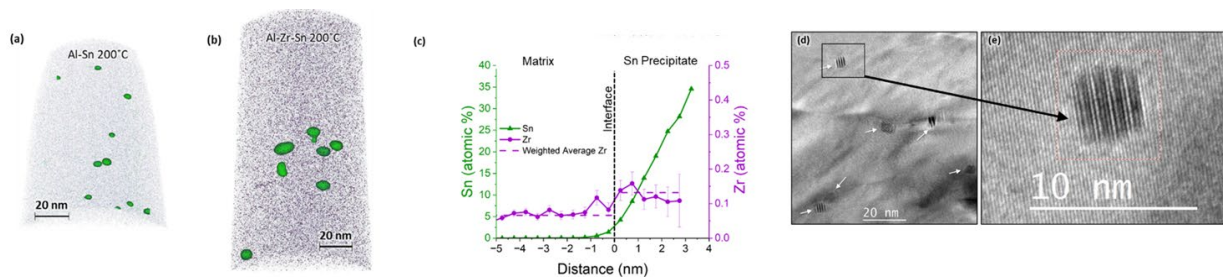


Figure I.1.1.5.3. APT reconstructions highlight the Sn precipitates with green 3 at.% Sn isoconcentration surfaces for the 200°C isochronally aged (a) Al-Sn and (b) Al-Zr-Sn alloys. Zr atoms are shown in purple, and Sn atoms in green. A proximity histogram (c) showing the average Sn (green triangles) and Zr (purple circles) concentrations across the interface, at 0 nm between the matrix and the Sn precipitates for the Al-Zr-Sn alloy. The weighted-average Zr concentration in the Al matrix and the Sn precipitates for all Sn precipitates from three APT datasets is shown as a dashed-purple line in (c) for the Al-Zr-Sn alloy. Bright-field TEM images along the $\langle 110 \rangle$ zone axis of the Sn precipitates (indicated by arrows) showing Moiré fringes at (d) lower and (e) higher magnification. Source: ORNL.

Through research performed in FY 2023, the role of Sn in simultaneously improving electrical and mechanical properties of Al has been clarified. Sn and other low-melting-point elements play a role in heterogeneously nucleating precipitates and dispersoids that can reduce the solute content in the matrix, thus increasing EC. Nucleation of precipitates, in turn, increases the strength of alloys through reduction of interparticle spacing. This mechanism has been demonstrated and clarified for nucleation of L1₂-structured Al₃Zr precipitates that form in a dilute Al-Zr alloy, microalloyed with Sn. The role of Sn in nucleating precipitates can be summarized through a multistep process:

- Al-Zr-Sn alloy leads to the formation of Sn-Zr-Vacancy (Vac) clusters during homogenization. Such clusters are energetically favorable according to first-principle calculations reported earlier.
- Sn-Zr-Vac clusters were experimentally observed through analysis of APT data represented as a radial-distribution function around an Sn atom for an alloy in the as-homogenized state as shown in Figure I.1.1.5.4(a).
- Sn clusters form during aging at 200°C as shown in Figure I.1.1.5.4(b) (STEM image) that lead to modest hardening in the alloy.
- Because Zr has zero solubility in Sn below the melting point of Sn at 230°C and, because Sn is at a homologous temperature of 0.95 at 200°C, the Zr atoms diffuse out of the Sn cluster.
- Zr atoms around the Sn clusters find fertile ground for heterogeneous-nucleation of the energetically preferred Al₃Zr precipitate on specific interfaces of Sn clusters as shown in Figure I.1.1.5.4(b).

Specifics of the identified heterogeneous-nucleation mechanism will be reported in a journal article that is under preparation.

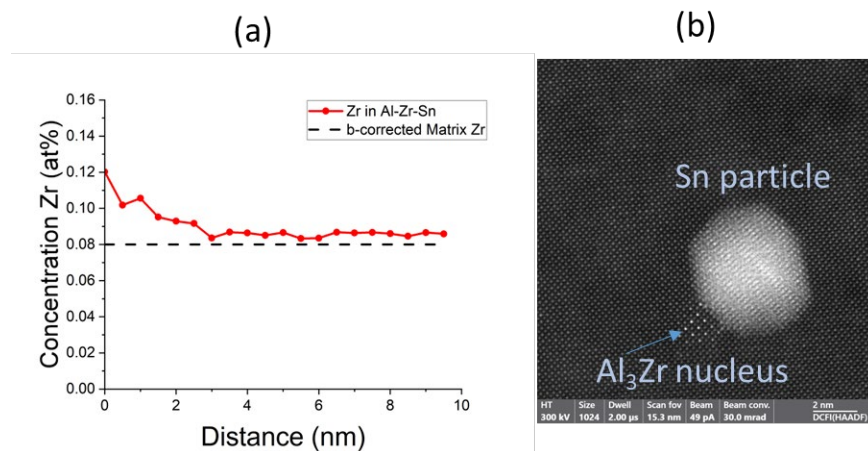


Figure I.1.1.5.4. (a) Sn-centered radial-distribution function (RDF) analysis showing a tendency of Zr atoms to cluster with Sn relative to the weighted-average bulk composition of Zr in the matrix. RDF function derived from APT analysis. (b) High-resolution annular dark-field image showing Al₃Zr precipitate nucleus next to an Sn particle. Source: ORNL.

Conclusions

Task 1E studied the fundamental effects of microalloying additions of 0.09 wt.% Sn to a dilute Al-0.24Zr (wt.%) alloy. In FY 2023, the effect of Sn additions in simultaneously improving the strength and EC of Al-0.24Zr alloy was clarified. The Sn addition results in an accelerated age-hardening response and increased EC after isochronal aging up to 425°C, a phenomenon that is not observed in the Al-Zr binary alloy. The peak hardness achieved during isochronal aging was higher and occurred more quickly than isothermal aging at 400°C or 425°C. However, extended isothermal aging was able to recover the EC of the alloy to the EC of the commercial purity Al used as a feedstock material.

The improved age-hardening response of isochronal relative to isothermal aging for the Al-Zr-Sn alloy is attributed to the heterogeneous nucleation of small Al_3Zr L_{12} precipitates that form adjacent to Sn precipitates that form at 200°C. A mechanism for the presence of these small precipitates at 200°C when Zr cannot diffuse effectively is proposed based on a combination of computational and characterization results. APT results show Zr and Sn atoms cluster during homogenization. Density functional theory calculations presented in FY 2022 suggest this clustering is due to the very favorable binding energy between Zr-Sn-vacancy triplets. During isochronal aging up to 200°C, Sn precipitates form on the Zr-Sn clusters. Small Zr L_{12} precipitates were observed to form adjacent to the Sn precipitates in APT and STEM. The average number of Zr atoms contained in the clusters after homogenization is large enough to form the small Zr L_{12} precipitates observed at 200°C. The overall mechanism suggests the Sn precipitates are serving as heterogeneous nucleation sites that help lower the nucleation barrier for the precipitation of L_{12} - Al_3Zr in Al.

For the small L_{12} precipitates to form, the Zr atoms need to diffuse out of the Sn precipitates. The diffusion of Zr is much faster in Sn than Al at 200°C due to a combination of the high Sn homologous temperature of 0.94 at 200°C, the high thermodynamic driving force due to the negligible solubility of Zr in Sn, and the higher vacancy concentration due to the binding of Sn with vacancies. At higher temperatures, the Sn precipitates dissolve and leave behind the small Al_3Zr L_{12} precipitates that can grow into larger L_{12} - Al_3Zr at an elevated aging temperature of 400 to 425°C. The overall result of the dilute Zr and Sn additions is an accelerated age-hardening response that can reach a higher hardness with improved EC due to precipitation of solute atoms.

References

1. Wang, Y., L. Zhu, G. Niu, and J. Mao. 2021. "Conductive Al alloys: The contradiction between strength and EC," *Adv. Eng. Mater.*, 23(5), 2001249. <https://doi.org/10.1002/adem.202001249>.
2. Vurpillot, F., A. Bostel, and D. Blavette. 2000. "Trajectory overlaps and local magnification in three-dimensional atom probe," *Appl. Phys. Lett.* 76(21), 3127–3129. <https://doi.org/10.1063/1.126545>.

Acknowledgements

The authors gratefully acknowledge N. Vo from NanoAl (now a part of Steel Dynamics, LLC) for his collaboration on this task. In addition, J. Meier, D. Shin, J. Poplawsky, A. J. Haynes, L. Allard, S. Bahl, and D. McClurg of ORNL are acknowledged for their contributions. Thermofisher Scientific is acknowledged for its use of microscopy results. APT research was conducted as a part of a user project at the Center for Nanophase Materials Sciences, which is a DOE Office of Science User Facility at ORNL.

I.1.1.6 Task 1G. Fundamentals of Thermal Properties in Lightweight Alloys for Electric Vehicle Propulsion (Oak Ridge National Laboratory)

Dongwon Shin, Principal Investigator

Oak Ridge National Laboratory
Materials Science and Technology Division
1 Bethel Valley Rd.
Oak Ridge, TN 37830
E-mail: shind@ornl.gov

J. Allen Haynes, PMCP Consortium Manager

Oak Ridge National Laboratory
Materials Science and Technology Division
1 Bethel Valley Rd.
Oak Ridge, TN 37830
E-mail: haynesa@ornl.gov

Jerry L. Gibbs, DOE Technology Development Manager

U.S. Department of Energy
E-mail: Jerry.Gibbs@ee.doe.gov

Start Date: November 1, 2021

End Date: September 30, 2023

Project Funding: \$270,000

DOE share: \$270,000

Non-DOE share: \$0

Project Introduction

This task aims to achieve optimal thermal conductivities of cast lightweight alloys for BEVs via T5 heat-treatment processes while maintaining or exceeding mechanical properties targets. Chill casting was used as a surrogate fabrication method for die-casting, which is currently used for manufacturing many housing and heat-transfer components for BEVs. Various T5 heat-treatment routes from the design-of-experiments approach are being performed in a (semi) high-throughput manner within the context of data analytics. Electrical conductivities of heat-treated samples were measured as a surrogate property to thermal conductivity. The hardness of all the samples is being measured to rapidly screen mechanical properties. Machine learning (ML) models are being trained to predict the electrical conductivities and hardness of Al alloys as a function of T5 heat-treatment. A large number of hypothetical heat-treatment conditions have been considered, and corresponding electrical conductivities and hardnesses have been predicted via trained ML models. Promising new T5 heat-treatment conditions of the commercial A380 alloy have been identified and experimentally validated.

Objectives

This project aims to establish an integrated workflow that combines experimental measurements and ICME to optimize heat-treatment conditions of cast lightweight alloys to improve thermal conductivities while maintaining or exceeding target mechanical properties.

Approach

A semi-high-throughput experimental campaign was conducted to reveal the effect of various process parameters on microhardness and thermal conductivity in high-silicon (Si) Al alloys that are widely used in high-pressure die-casting (HPDC). The A380 alloy, a common commercial die-cast composition, was chosen to investigate three process parameters: cooling rate in the mold during casting, heat-treatment temperature, and heat-treatment duration. A low-carbon steel step-mold with four thicknesses (i.e., 4, 10, 20, and 40 mm) was used to vary the cooling rate of each step section during casting. Five different temperatures (i.e., 100, 150, 200, 250, and 530°C) and several different durations (i.e., 0.5, 1.5, 3, 5, 6, 10, 24, 100, and 200 h) were considered for T5 heat-treatment conditions. Four additional high-Si commercial alloy compositions

commonly used for die-casting have also been evaluated in FY 2023, and their nominal compositions are presented in Table I.1.1.6.1.

Table I.1.1.6.1. Nominal Composition (wt.%) of Aluminum Alloys Used in this Task

Alloy	Al	Si	Fe	Cu	Mg	Sn	Ni	Zn	Mn	Sr	Ti
A380	Bal.	8.50	1.30	3.50	0.10	0.35	0.50	3.00	0.50	0.00	0.00
A383	Bal.	10.50	1.30	2.50	0.10	0.15	0.30	3.00	0.50	0.00	0.00
Aural 5	Bal.	7.12	0.09	0.00	0.23	0.00	0.00	0.00	0.62	0.02	0.07
Castasil-21	Bal.	8.50	0.60	0.02	0.03	0.00	0.00	0.07	0.01	0.02	0.01
Castaman-35	Bal.	10.25	0.20	0.03	0.35	0.00	0.00	0.10	0.65	0.00	0.15

After casting and heat-treatment, all samples were subjected to physical property (i.e., hardness and EC) measurement. Vickers hardness with 5 kgf load was used to measure microhardness. The eddy current method was used for EC measurements because Al is a non-magnetic material. The overall workflow of the study is presented in Figure I.1.1.6.1.

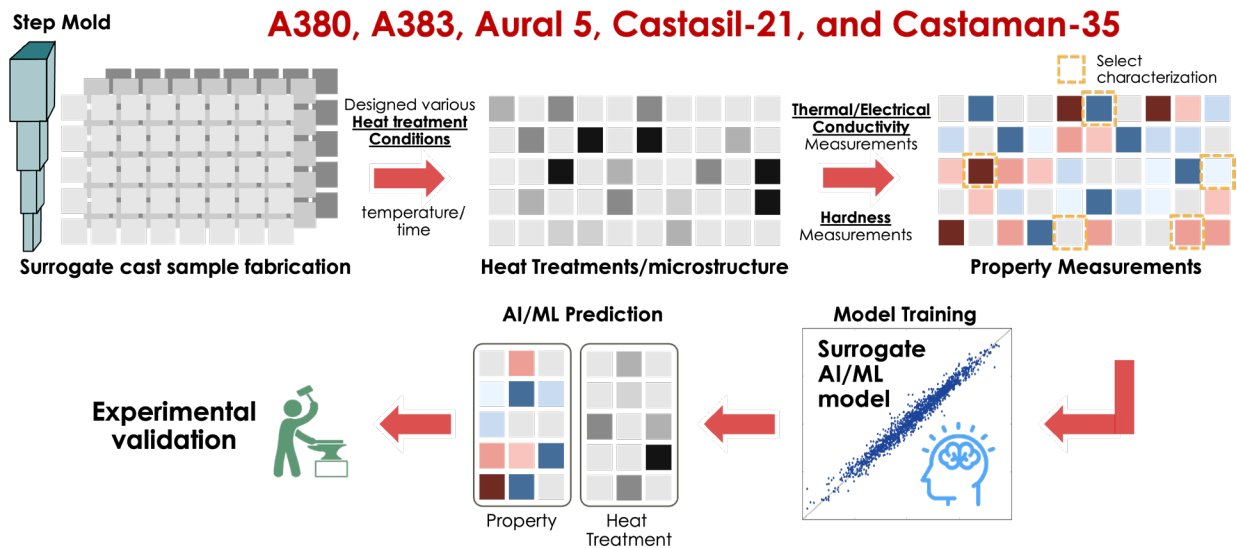


Figure I.1.1.6.1. A schematic of overall workflow to predict thermal properties (via surrogate EC) in lightweight alloys via the data analytics approach. Source: ORNL.

Results

From the large amount of collected experimentally measured data, an extensive correlation analysis was performed to identify the relationship between processing parameters (input features) and physical properties (target). We have used two different algorithms to numerically analyze the correlation: the Pearson correlation coefficient (PCC), which measures both the strength and direction of linear relations, and the maximal information coefficient (MIC), which can measure non-linear strength. Correlation analysis results are presented in Figure I.1.1.6.2.

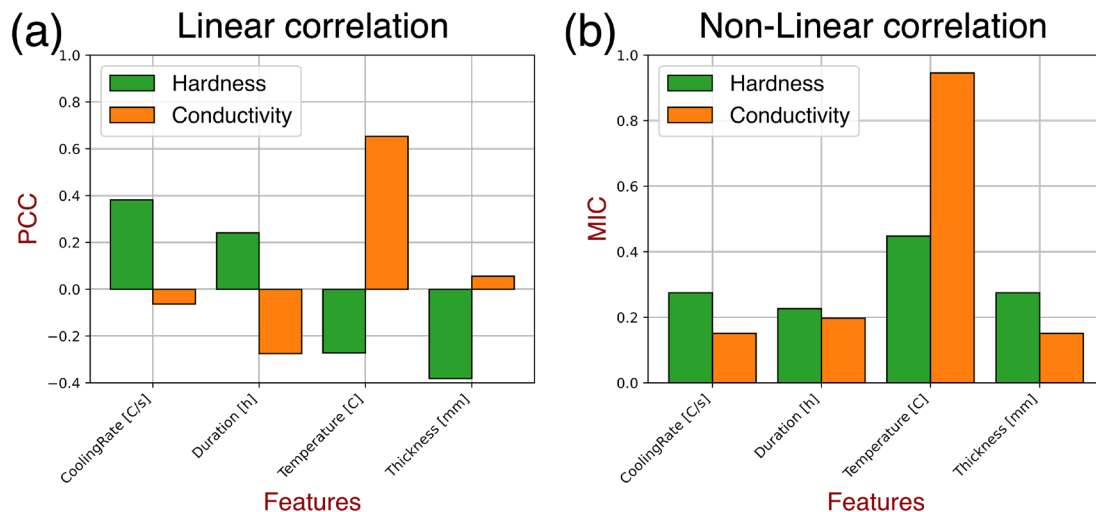


Figure I.1.1.6.2. Correlation analysis between input features (i.e., cooling rate of step-mold, duration, and temperature of T5 heat-treatment, and thickness of samples) and EC and hardness of A380 alloy. Two different algorithms, linear and non-linear, were used: (a) PCC and (b) MIC. Source: ORNL.

The step thickness negatively correlates with hardness, consistent with the qualitative analysis with as-cast samples, where a thinner step yields higher hardness. Different cooling rates contribute to differences in key microstructural features such as microsegregation and grain and/or intermetallic particle size. Notably, the heat-treatment temperature has the highest correlation score for EC in both PCC and MIC. In addition, PCC analysis in Figure I.1.1.6.2 shows that heat-treatment temperature has a favorable effect on EC while it is the opposite effect on hardness. As the heat-treatment temperature increases, the precipitates coarsen; thus, hardness will decrease. Simultaneously, the concentration of alloying elements in the Al matrix will decrease as temperature increases. Consequently, the leaner Al matrix will have higher EC. Although it is a relatively simple correlation analysis between any single input feature and the target property, it is encouraging that numerical analysis successfully captures underlying microstructural evolution phenomena.

Next, surrogate ML models were trained to predict the EC and hardness of A380 alloys as a function of T5 heat-treatment conditions and cooling rate/sample thickness. We have used the random-forest model as implemented in the ORNL-developed open-source data analytics frontend, ASCENDS [1]. A total of 1,280 experimental data points were used in the ML model training, and hyperparameters were optimized with 5,000 sampling values. The trained accuracies, represented as R^2 values, coefficient of determination, and parity plots that compare the actual with predicted values are presented in Figure I.1.1.6.3. Overall, good agreement between experimentally measured and predicted values is obtained while the training error is more significant in the hardness than in EC. This larger uncertainty could be attributed to the porosity formed during the casting, which is reflected by the hardness results. Thus, we performed detailed porosity morphology and distribution analysis via SEM and XCT.

The validity of the step-mold method to replicate the HPDC process was tested by comparing the microstructure and porosity distribution of both die-cast and step-mold cast Aural 5 alloy using SEM and XCT analyses. The result is shown in Figure I.1.1.6.4. Both samples have notable porosities and measured porosity volumes of the HPDC, and step-mold samples are 0.034 and 0.065 vol.%, respectively. The pores within the HPDC samples have larger sizes and more-irregular morphologies than step-mold casting, attributed to the more rapid cooling rate in die-casting. To further investigate the formation of porosity, we performed extensive XCT analysis of various as-cast T5 heat-treatment (0.5 and 6 hours at 150 and 250°C) conditions and solution-treated (530°C at 5 hours) A380 samples. The analysis is shown in Figure I.1.1.6.5.

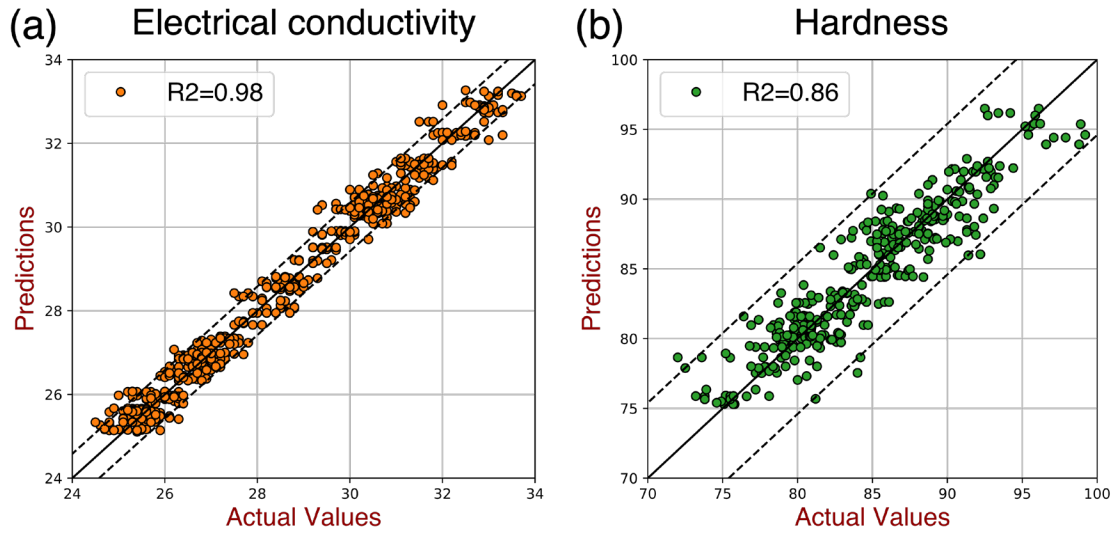


Figure I.1.1.6.3. Accuracy of trained random-forest ML models for (a) electrical conductivities and (b) hardness of A380 alloy with various T5 heat-treatment conditions. Source: ORNL.

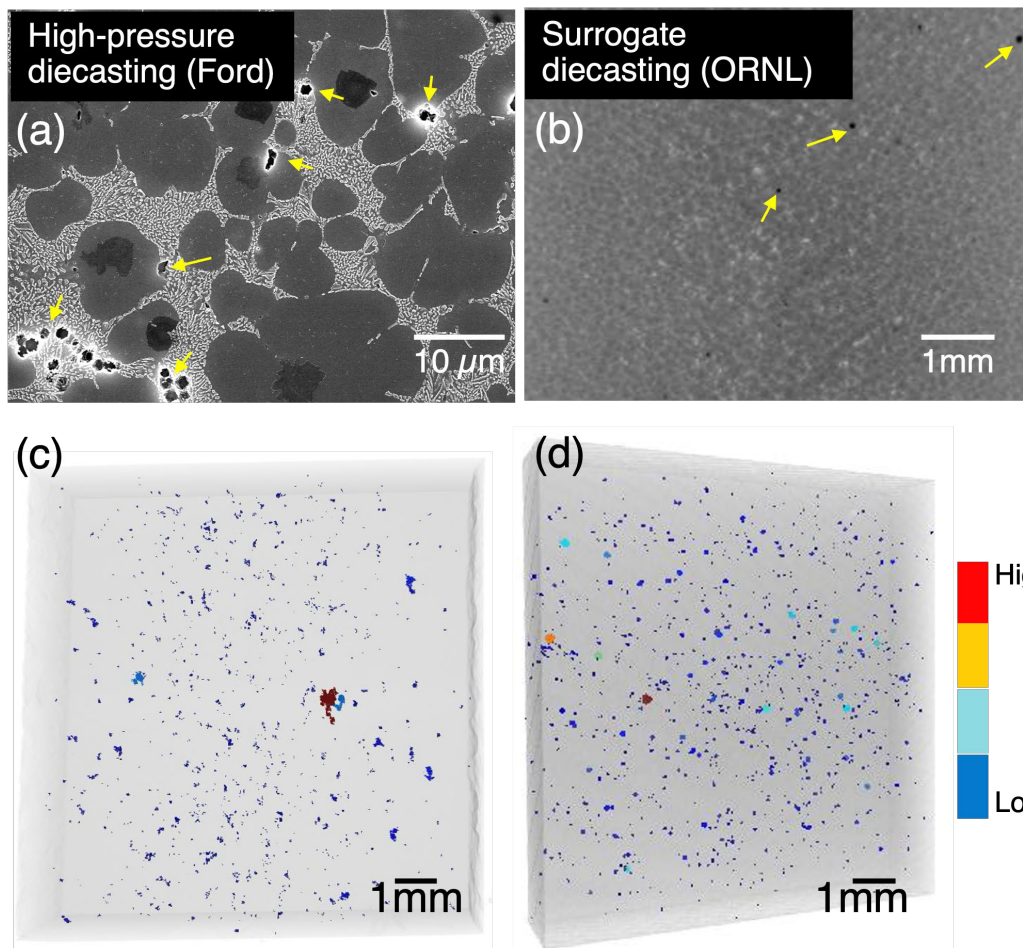


Figure I.1.1.6.4. SEM micrographs and XCT analysis of Aural 5 alloys from two different fabrication techniques: (a) and (c) HPDC sample provided by Ford; (b) and (d) 4 mm step-mold from ORNL. The color profile for (c) and (d) represents the volume of porosity. Source: ORNL.

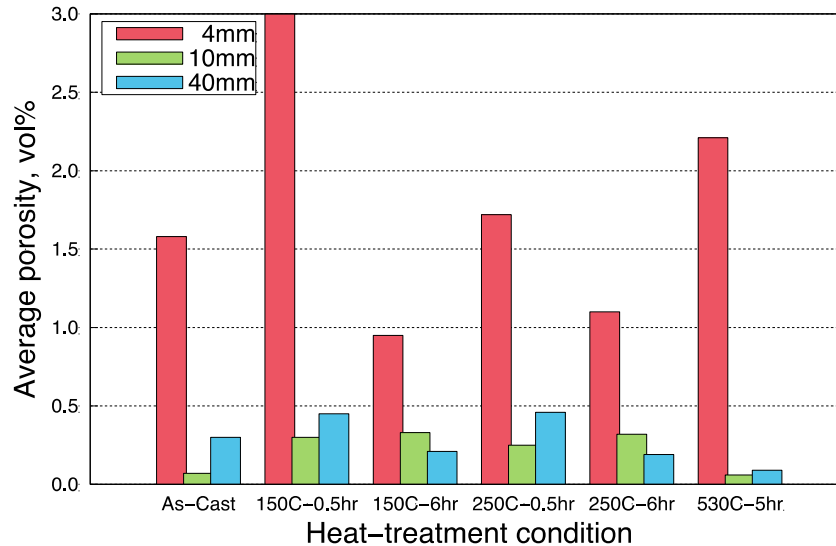


Figure I.1.1.6.5. Average volume percentages of A380 as a function of various T5 heat-treatment conditions. Source: ORNL.

Large and irregular pores are common for the 4 mm samples, regardless of the heat-treatment. The pores observed in the 4 mm samples are also large, connected, and significantly more lamellar. The lamellar and large pores are likely casting defects whereas the spherical pores are trapped-gas porosity. The molten metal may be cooling too fast for the pour rate in the 4 mm samples. This could lead to inconsistent filling, freezing, etc., resulting in elevated population and size of irregular-shaped pores. The more irregularly shaped pores and voids likely occur due to incomplete filling during casting. This systematic appearance could be associated with the process. For instance, one explanation could be related to the thermal properties of this casting route, where the liquid could solidify prematurely, before the mold is completely filled. (Note that there is no pressure applied during casting in step molds, leading to a slower fill rate vs. HPDC). This could then block the flow of molten metal and lead to large cavities. At 10 mm, this effect is significantly reduced; nevertheless, large, although fewer voids are seen. At 40 mm, the pores are mostly of a gas porosity type.

The porosity values between the 10 and 40 mm samples are similar. The heat treatments are not expected to change the porosity distribution but could significantly affect the microstructures. This is particularly prominent for the solution-treated samples that showed precipitate coarsening. Other microstructural changes were not within the detection resolution of the XCT system.

Ultimately, from these trained ML models, we have predicted T5 heat-treatment conditions that could achieve improved properties in both EC and hardness of the A380 alloy. A total of 130,000 hypothetical T5 conditions were considered, and their corresponding electrical conductivities and hardness values were predicted. As shown in Figure I.1.1.6.6, experimentally measured EC and hardness of A380 are in a reciprocal relationship. A set of ML-identified T5 conditions for step-cast A380 were predicted to have better EC and hardness. These specific predictions were then experimentally validated, as shown in Figure I.1.1.6.6. Because the features used in the present study are limited to superficial heat-treatment conditions that do not inform any underlying microstructural evolution, it is not possible to further interpret the predicted results. Nevertheless, it is encouraging that this task completed the entire workflow of integrating high-throughput data population because the data analytics followed the experimental validation outlined in Figure I.1.1.6.1. Further remaining efforts will be focused on combining the experimental data of all Al alloys, then performing data analytics to develop a design capability for T5 heat-treatment conditions as well as alloy chemistry.

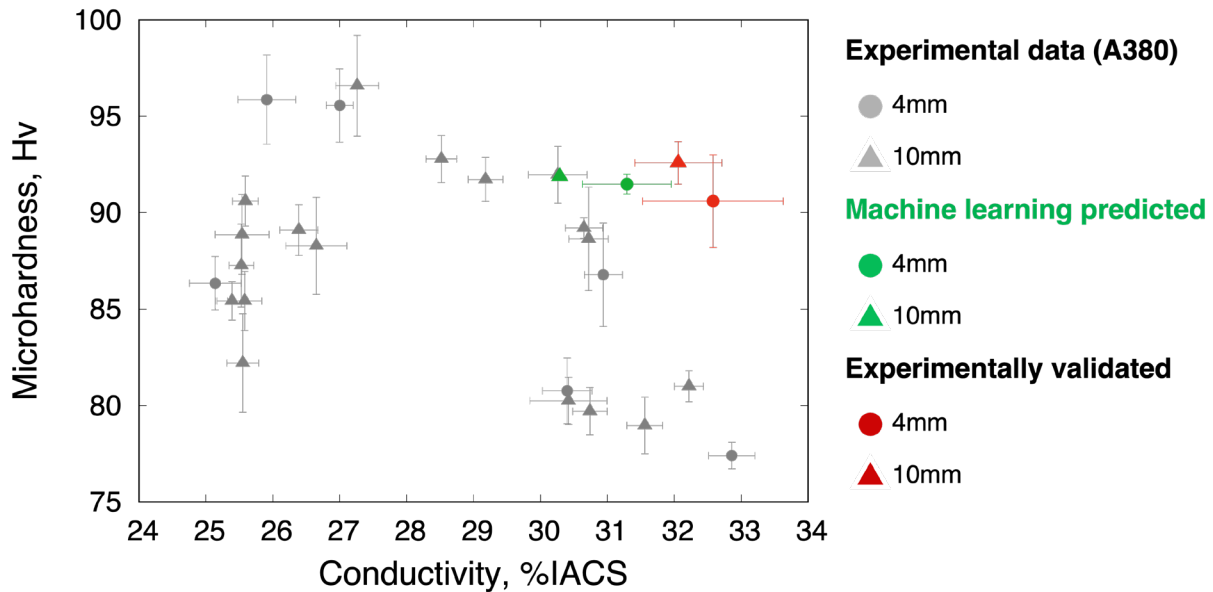


Figure I.1.1.6.6. Experimentally validated ML-identified T5 heat-treatment conditions of A380 alloy with improved EC and hardness. Source: ORNL.

Conclusions

Task 1G started from an experimental campaign to collect EC and hardness of high-Si Al alloys commonly used for HPDC—A380, A383, Aural 5, Castasil-21, and Castaman-35—as a function of T5 heat-treatment conditions, using a surrogate step-mold with different thicknesses (4, 10, 20, and 40 mm), which varies the cooling rate. The goal was to develop a predictive capability for heat treatments based on an emerging data analytics approach. Extensive correlation analysis of collected data was able to reproduce the known relationships between the heat-treatment process and physical properties such as higher heat-treatment temperatures reducing hardness but increasing the EC of Al alloys. A large number of highly consistent experimental data were demonstrated to successfully train surrogate ML models with high accuracy. The random-forest ML model adopted in the present study predicted new T5 heat-treatment conditions that could improve both EC and hardness. These conditions were subsequently validated experimentally. The demonstrated feasibility of the novel workflow developed in this task will be expanded to develop a predictive capability based on data analytics in accelerated-design alloy chemistries and heat-treatment conditions to simultaneously optimize thermophysical properties of a range of die-cast lightweight alloys required in advanced EVs.

References

1. Lee, S., J. Peng, A. Williams, and D. Shin, 2020, “ASCENDS: Advanced data SCiENce toolkit for non-data scientists,” *J. Open Source Softw.*, 5(46), 1656. <https://doi.org/10.21105/joss.01656>.

Acknowledgements

The authors would like to thank K. Hanson, T. Muth, D. McClurg, E. Cakmak, and H. Wang of ORNL for contributing to the experimental work.

I.1.1.7 Task 1H. Hybrid Dispersion-Strengthened Aluminum-Matrix Composites for Higher Efficiency Electric Vehicle Powertrains: Cost-Effective Lightweight Alloys for Electric Vehicle Propulsion (Pacific Northwest National Laboratory)

Mert Efe, Principal Investigator

Pacific Northwest National Laboratory
Energy Processes and Materials Division
900 Battelle Blvd.
Richland, WA, 99352
E-mail: mert.ef@pnl.gov

J. Allen Haynes, PMCP Consortium Manager

Oak Ridge National Laboratory
Materials Science and Technology Division
1 Bethel Valley Rd.
Oak Ridge, TN 37830
E-mail: haynesa@ornl.gov

Jerry L. Gibbs, DOE Technology Development Manager

U.S. Department of Energy
E-mail: Jerry.Gibbs@ee.doe.gov

Start Date: November 1, 2021

End Date: September 30, 2023

Project Funding: \$310,000

DOE share: \$310,000

Non-DOE share: \$0

Project Introduction

Al MMCs offer several advantages in powertrain applications over their cast-iron or steel counterparts. Weight-savings—particularly the reduction of unsprung weight—and the mass-compounding effect on adjacent components, such as suspension arms and springs with lighter designs, are among the most significant benefits. Lower wear and corrosion rates are also possible with Al MMCs. Despite these advantages, commercial applications of Al composites in internal-combustion-engine vehicle powertrains have been very limited [1]. Higher cost of materials and processing, difficulty in machining, non-uniform microstructures, higher heat-transfer to the adjacent components, and limited strength have been challenges limiting widespread application [1], [2].

The landscape has radically changed with the growth of EV use in recent years. In a modern EV powertrain, the differential and transmission are the second heaviest component after motors and inverters; and brake systems are the fourth heaviest component after the wheels and tires. Forty percent weight-saving is possible when steel gears and cast-iron rotors in these components are replaced by Al-MMC parts. This could translate into ~26 km range increase in a typical 1800 kg-560 km range EV, assuming 10% weight-savings corresponds to a 7% increase in range [3]. Moreover, lower wear and corrosion rates of Al-MMC reduce non-exhaust particle emissions from the brake system, which constitutes 59% of road-particulate-matter emissions [4]. The lower corrosion rate of Al also correlates well with the longer maintenance interval of EVs because cast-iron brake rotors are prone to rust. In addition, energy harvesting in EVs and hybrid vehicles decreases the amount of energy that must be dissipated by the mechanical brakes by as much as 40%. Lower brake temperatures can enable the use of Al-MMC brake rotors. Benefits of Al alloys and composites in EV powertrains also confirmed by a recent interest from the automotive industry, demonstrated by multiple research studies and applications [2], [5], [6].

This project addresses the challenges associated with the use of Al MMCs and investigates sustainable, lower cost MMCs with matching performance to cast-iron or steels. Titanium boride (TiB₂) was chosen as the

reinforcement particles for its lower cost and better wettability with Al matrix. TiB₂ is used as a grain refiner of Al alloys, which potentially enables recyclability of Al-TiB₂ composites for use as a grain refiner master alloy. Lower cost is also achieved by novel, near net-shape processing routes, where distributing submicron- and micron-sized TiB₂ particles in the Al matrix and shaping of the component happen simultaneously.

Objectives

The main objectives of the project are:

- Develop an Al-MMC containing micron-sized particles for wear resistance and submicron-sized particles for strengthening
- Develop a near-net-shape processing method for simultaneous compositing and shaping.

To achieve the objectives, the project investigates two processing methods to produce the composites: (1) squeeze casting for the application, such as brake rotors, requiring a cast product; and (2) solid-phase, friction-consolidation for applications, such as gears, motor rotors, shafts, requiring a wrought product. The project deliverable is a disc-shaped Al-MMC component that contains at least 8 vol.% micron- and submicron-sized reinforcing particles with < 2% porosity. Wear rates of the cast composites are benchmarked against cast-iron, with a target wear rate < 10⁻⁴ mm³/Nm. For the wrought application, the mechanical property target is > 600 MPa tensile strength in the matrix.

Approach

In FY 2023, Al A206-TiB₂ MMC brake rotors were produced by squeeze casting at Loukus Technologies, Inc. (Calumet, MI), with materials supplied by Pacific Northwest National Laboratory (PNNL). The cast composites were produced by halide-salt reactions with molten Al, which is a well-known process for the *in-situ* formation of submicron-sized TiB₂ particles inside an Al matrix [7]. Al A206 alloy was selected for the matrix due to its high-temperature strength. In some composites, the matrix was further reinforced with micron-sized TiB₂ particles to enhance wear resistance. The molten composite was then squeeze-cast into a disc-shaped 10-cm-diameter steel mold at 90 MPa pressure. The cast discs were then machined to the subscale brake-rotor dimensions and heat-treated to T7 temper. Overall, five brake rotors were produced with varying TiB₂ fractions: A206 control, A206 5 vol.% *in-situ* TiB₂, A206 5 vol.% *in-situ* TiB₂ + 5 vol.% powder TiB₂, A206 2 vol.% *in-situ* TiB₂ + 8 vol.% powder TiB₂, A206 1 vol.% *in-situ* TiB₂ + 9 vol.% powder TiB₂.

Wear-testing of the cast composites is performed by mounting the subscale rotors in an instrumented brake-testing rig capable of rotating the pad holder and applying clamping loads appropriate for automotive braking conditions. This rig is a reduced-scale brake dynamometer, available at PNNL. In this setup, the pad holder rotates, and the rotor is stationary. Temperature can be controlled by adjusting the test speed and contact pressure. Several energy profiles can be investigated, including low-temperature, low-load continuous-torque tests and high-load, high-temperature transients. Low-temperature (~150°C), low-load continuous-torque conditions were chosen for the purpose of benchmarking with cast-iron. Three phenolic pads with dimensions 8.7 mm × 8.7 mm were used as a counter-face. The pads and rotors were burnished at varying loads and temperatures prior to the wear tests. The wear tests were conducted in ambient air (~40% relative humidity) under a normal load of 111 N (~0.5 MPa initial contact pressure on each pad), which was chosen to be below the YS of the material. The sliding speed was fixed at 4.6 m/s. A total of 5520 m sliding distance was traveled to observe steady-state friction behavior. The coefficient of friction (CoF), the ratio of tangential load to normal load, was recorded for the entire test duration, as indicated in Figure I.1.1.7.1(a). The average CoF during the steady-state regime was reported. In addition, the temperature was also recorded using a thermocouple just under the wear-track during the test. A Keyence profilometer (Model VR 5000) was used to measure the wear area and wear depth inside each wear-track, as indicated in Figure I.1.1.7.1(b) and Figure I.1.1.7.1(c), respectively. A minimum of four profilometry traces were taken across each wear-track. The wear rate was calculated by dividing the wear volume by the normal load and total sliding distance, expressed in mm³/Nm. The average CoF and wear rates for the various alloys are shown in Figure I.1.1.7.1(d).

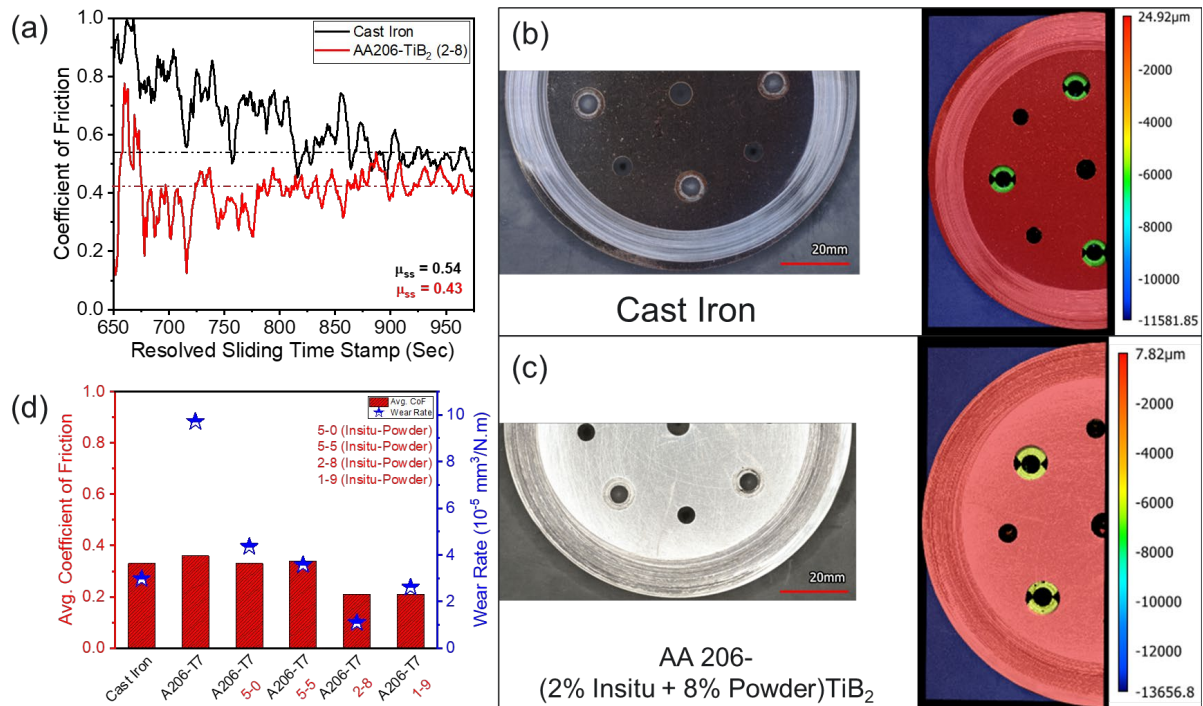


Figure I.1.1.7.1. (a) CoF evolution during the brake test. (b) Worn cast-iron rotor with the wear-track and profilometry results from the wear-track. (c) Worn Al composite rotor with the wear-track and profilometry results from the wear-track. (d) Average CoF and wear rates for the cast-iron and composite rotors.

Source: PNNL.

FY 2023 friction-consolidation efforts focused on increasing the volume fraction and dispersion of TiB₂ particles. AA7075 Al alloy powder (procured from Atlantic Equipment Engineers), with particle size ranging from 50 to 150 μm , was used as the precursor. TiB₂ powder (procured from US Research Nanomaterials, Inc.) was used as strengthening particles. The TiB₂ feedstock contained both submicron- and micron-sized particles (0.2–15 μm , with an average size of 5.2 μm). Three powder mixtures were prepared: 0, 12 vol.% (18.0 wt.%), and 24 vol.% (33.7 wt.%) of TiB₂. The powders were poured into a plastic bottle and mixed on a roller mixer for 2 h. The mixed powders were then loaded into a ring-shaped H13 tool steel container and cold compacted into a precursor billet. The billet was then subjected to friction-consolidation. Details of the friction-consolidation were provided in the FY 2022 report [8].

The friction-consolidated composite discs were heat-treated to a T6 condition—solutionized at 480°C for 1 h and water quenched, followed by a 24 h aging treatment at 120°C—to achieve maximum strength. The heat-treated samples were sectioned into halves along the diameter and Vicker's hardness measurements were recorded along the cross-section using 200 gf and 12 s dwell time. Gauge-length 4.3-mm and 1-mm-thick tensile specimens were cut from the top of the consolidated discs. Tensile tests were performed using 0.08 mm/min displacement rate. Digital image correlation (DIC) was used to record the strain during testing. Detail microstructural characterization with SEM, EDS, and EBSD were performed to determine the size and distribution of TiB₂ particles and correlate them with the enhanced mechanical properties.

Results

The melting and casting route achieved up to 10 vol.% TiB₂ fraction in the composites, which consists of up to 9 vol.% TiB₂ powder of a size ranging from 700 nm to 10 μm . This is possible when the powdered TiB₂ is combined with the *in-situ* TiB₂ and potassium fluortitanate (K₂TiF₆) and potassium borofluoride (KBF₄) salts, which help with wetting. The viscosity of the melt starts to increase around 10 vol.% of total TiB₂ and above, when dross removal becomes difficult, and fluidity of the melt is poor. Based on the microstructural

characterization, the cast composites contained <2% porosity due to the high-pressures achieved during casting. The TiB₂ phase fractions were confirmed by EBSD image analysis. Production of composite brake rotors with the target microstructures completed the project deliverable.

Figure I.1.1.7.2 shows the microstructure of the A206-1 vol.% *in-situ* TiB₂ + 9 vol.% powder TiB₂ composite. TiB₂ particles are uniformly distributed in the A206 matrix, with an average grain size of ~42 μm, as indicated in Figure I.1.1.7.2(a). Particles formed by the *in-situ* reaction are submicron-sized whereas the bigger particles are the powdered TiB₂ added to the molten Al, as observed in Figure I.1.1.7.2(b) and Figure I.1.1.7.2(c), respectively. As is evident from the microstructure, the composite is almost porosity-free. Other microstructures (not shown here) taken from random locations of the billet at various magnifications confirm this observation.

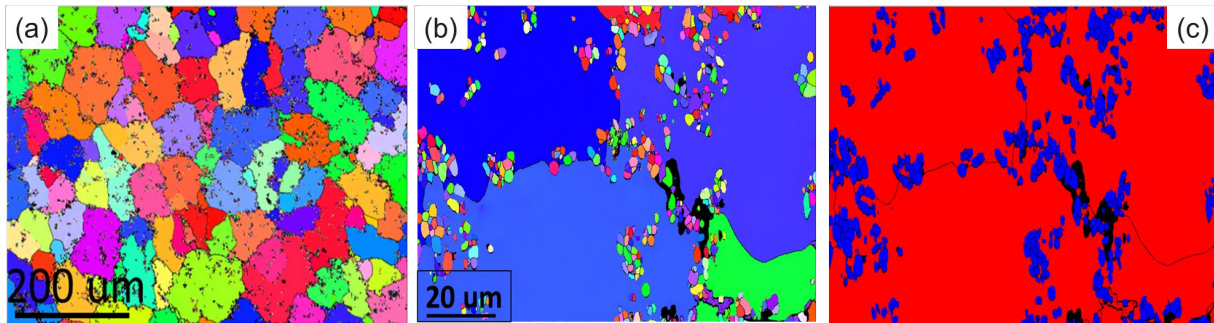


Figure I.1.1.7.2. (a) and (b) EBSD orientation maps of the A206-1 vol.% *in-situ* TiB₂ + 9 vol.% powder TiB₂ composite. (c) EBSD phase map of the composite. Source: PNNL.

Table I.1.1.7.2 and Figure I.1.1.7.1(d) above summarize wear-testing results for the benchmark cast-iron and composite brake rotors. The composite rotors had slightly higher wear rates than the cast-iron benchmark. However, A206-2% *in-situ* + 8% powder composite had 2.7× lower wear rate than the cast-iron, with its wear rate of 1.1×10^{-5} mm³/Nm. This was well below the project target of <10⁻⁴ mm³/Nm. The composite rotor initially showed a higher wear rate during the burnishing step; however, the wear rate was stabilized after a transfer layer was formed between the pads and the rotor. Figure I.1.1.7.1(b) and Figure I.1.1.7.1(c), respectively, show surface profiles after the formation of a transfer layer. Both materials had similar wear-tracks and depths. The overall net-volume loss (wear – burnishing) was lower in the composite, leading to lower wear rates. CoF in the composite rotors were also lower than in cast-iron rotors. The CoF of both materials stabilized towards the end of the test, with less scatter, as indicated in Figure I.1.1.7.1(a), which confirms the formation of a stable friction pair.

Table I.1.1.7.1. Wear-testing Results of the Cast-Iron and Composite Brake Rotors

	Net-volume loss (mm ³)	Average CoF	Wear rate (10 ⁻⁵ mm ³ /Nm)	Hardness (HRB)
Cast-Iron	18.25	0.37	2.98	90.8 ± 0.6
A206	59.53	0.36	9.72	75.3 ± 0.9
A206-5% In-situ	26.67	0.33	4.35	70.0 ± 0.6
A206-5% In-situ + 5% Powder	21.93	0.34	3.58	76.4 ± 0.8
A206-2% In-situ + 8% Powder	6.72	0.21	1.09	69.8 ± 1.0
A206-1% In-situ + 9% Powder	25.97	0.21	2.61	72.8 ± 1.9

Compared to the melting and casting route, the friction-consolidation process achieved volume fractions of up to 24 vol.% TiB₂ in a matrix Al 7075. The high TiB₂ volume fraction is attributed to intense plastic (shear) deformation, which is similar to the stir zone in friction-stir welding. The Al and TiB₂ are severely deformed, refined, mixed, and consolidated into a porosity-free composite. The processing temperature was ~550°C. Previous studies suggest that the maximum effective strain falls within the range of 10–20 mm/mm, accompanied by a maximum effective strain-rate of 5–15 s⁻¹ [9]. The friction-consolidation process was shown to achieve near-net shapes, such as gears, in the FY 2022 annual report [8].

Low- and high-magnification SEM images of the processing zones of 7075 and 7075 + 24 vol.% TiB₂ samples after T6 heat-treatment are presented in Figure I.1.1.7.3. The baseline sample has a well-consolidated, typical 7075-T6 microstructure where Mg-rich precipitates are identified from high-magnification images. EDS elemental mapping confirms homogenized distribution of submicron- and micron-sized TiB₂ particles across the composite matrix. EBSD imaging (not shown here) showed equiaxed grains with uniform size in the processing zone of all samples. This is typical of friction-stir based processes. The particles were more uniformly distributed across the matrix in the case of the 24 vol.% sample as opposed to the 12 vol.% sample. The TiB₂ particles were randomly distributed across the grains and along the grain boundaries. The addition of 12 and 24 vol.% TiB₂ reduced average grain size in 7075 from 6.2 to 3.9 and 2 μm, respectively. The particle size of TiB₂ was also refined about 2× in the friction-consolidation processes. This is because the high-shear deformation facilitated the refinement of TiB₂ particles while uniformly dispersed them throughout the matrix.

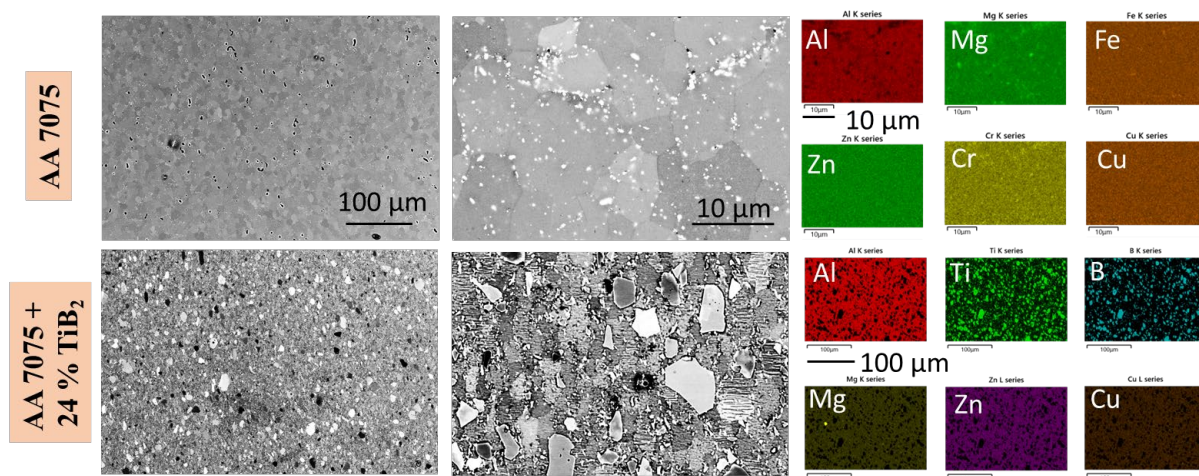


Figure I.1.1.7.3. SEM and EDS images of friction-consolidated AA 7075 composites with 0% (top) and 24 vol.% (bottom) of TiB₂. Source: PNNL.

Tensile and hardness properties of the friction-consolidated samples are presented in Figure I.1.1.7.4. The baseline sample without TiB₂ exhibits slightly lower strength than standard, wrought 7075-T6, but higher ductility, as observed in Figure I.1.1.7.4(a). The strength of the MMC samples is significantly enhanced as compared to the baseline sample and a standard, wrought 7075-T6. Both the yield and ultimate strengths of 12 vol.% TiB₂ are 10% higher than the baseline. The 24 vol.% TiB₂ sample reach to the yield and ultimate tensile strength of ~579 MPa and ~672 MPa, which are 30% higher than the baseline sample and 20% higher than the standard. Similar improvements are also obtained in the elastic modulus. The samples showed features of brittle fracture without necking, as shown in Figure I.1.1.7.4(b), indicating the failure was controlled by defects. Therefore, the composites can reach even higher strength with effective defect control through-process optimization. The microhardness results of 7075, 7075 + 12 vol.% TiB₂, and 7075 + 24 vol.% TiB₂ samples at both the as-processed and T6 conditions are presented in Figure I.1.1.7.4(c). For the as-processed condition, the hardness of the 12 and 24 vol.% samples increased by 33 and 75%, respectively, compared to the baseline sample. For the T6 condition, the hardness of the 12 and 24 vol.% samples increased by 20 and 50%, respectively, compared to the baseline sample.

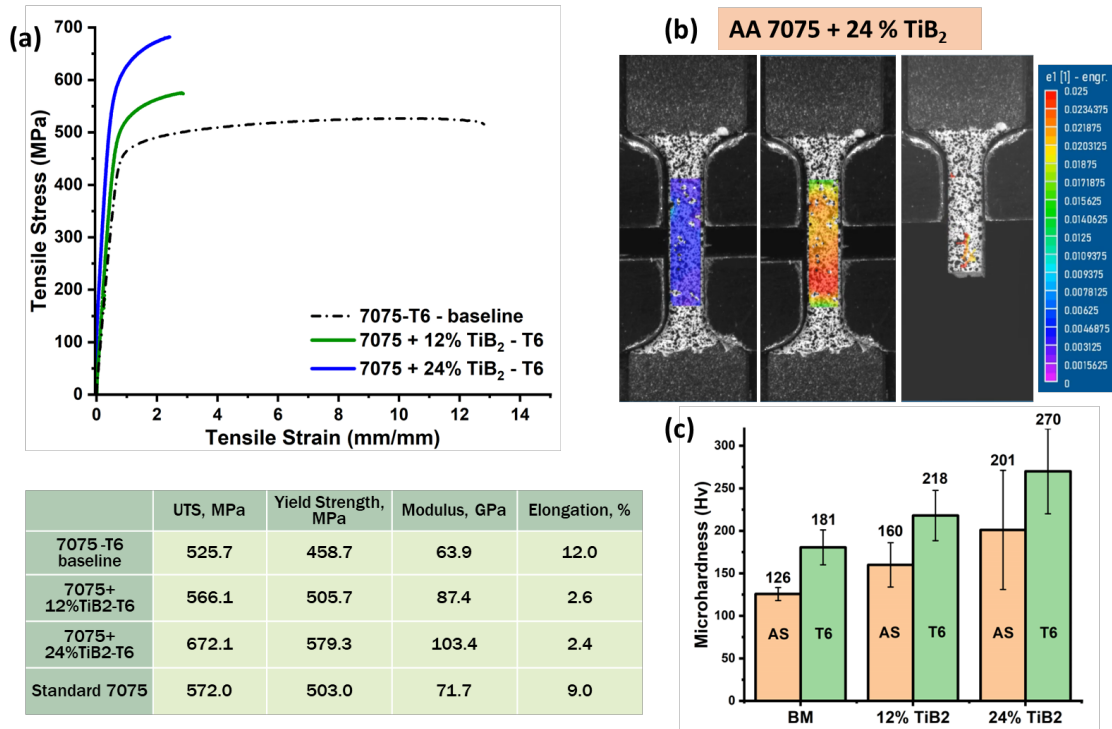


Figure I.1.1.7.4. (a) Engineering stress-strain curves and mechanical properties (inset table) of T6 heat-treated friction-consolidated samples with 0, 12, and 24 vol.% TiB₂. (b) DIC shows the strain distributions on the 24 vol.% sample during tensile tests, (c) average microhardness results for the samples in their as-processed and T6 conditions. Source: PNNL.

The friction-consolidation process itself does not change mechanical properties significantly; the baseline sample has similar hardness and slightly lower strength than the standard 7075. Therefore, the enhancement of mechanical properties in the Al-TiB₂ composites are mainly because of the addition of uniformly distributed submicron- and micron-sized TiB₂ particles. The refined grain structure of Al matrix also contributed to improved mechanical performance. This is because: (a) the severe plastic deformation during the friction-consolidation process refined the grain structure of the Al matrix, and (b) the incorporation of TiB₂ powder concentrated the strains in the Al matrix.

Conclusions

The project reached its objectives and goals in FY 2023. Melting and casting route delivered composite brake rotors with significantly better wear resistance than the project target. The wear rates were also comparable or better than the cast-iron benchmark. The friction-consolidation route demonstrated composites with up to 24 vol.% TiB₂ and strength well above the project targets. The TiB₂ powder was successfully mixed with the Al 7075 powder and consolidated into void-free solid material. Compared to the typical wrought-7075 values, the addition of 24-vol.% TiB₂ increased strength and modulus by ~20%, showing potential uses in applications requiring high-strength, wrought products. Both processing routes achieved near-net-shaped composites with desirable microstructures, <2% porosity, and are shown to be viable in producing lightweight, recyclable Al-TiB₂ composites.

Key Publications

1. Das, H., X. Li, L. Li, B. J. Schuessler, N. Overman, J. T. Darsell, P. Upadhyay, A. Soulami, D. Herling, V. V. Joshi, and M. Efe, 2023, “An innovative and alternative approach toward gear fabrication,” *J. Manuf. Process.*, 102, 319–329. <https://doi.org/10.1016/j.jmapro.2023.07.050>.

References

1. Rohatgi, P. K., N. Gupta, and A. Daoud, 2008, “Synthesis and Processing of Cast MMCs and Their Applications,” in: Viswanathan, S., et al. (eds.), *ASM Handbook, Volume 15: Casting*, ASM International, Materials Park, OH, USA, pp. 1149–1164.
<https://doi.org/10.31399/asm.hb.v15.a0005339>.
2. Carney, D., 2020, “Lightweight Aluminum Brakes for EVs are Continental’s Aim,” DesignNews website. Available at: <https://www.designnews.com/automotive/lightweight-aluminum-brakes-evs-are-continentals-aim> (accessed 6 December 2023).
3. Bull, M., 2011, “Mass Reduction Performance of PEV and PHEV Vehicles,” *Proceedings of 22nd International Technical Conference on the Enhanced Safety of Vehicles (ESV)*, Paper 11-0346, Washington, D.C., USA, 13–16 June 2011.
4. Air Quality Expert Group, 2019, “Non-exhaust emissions from road traffic,” Report prepared for Department for Environment, Food and Rural Affairs. Available at: https://uk-air.defra.gov.uk/assets/documents/reports/cat09/1907101151_20190709_Non_Exhaust_Emissions_ty_peset_Final.pdf (accessed 6 December 2023).
5. Rettig, M., et al., 2020, “Aluminum brake disc,” *Proceedings of EuroBrake 2020*, 16–19 June 2020, Online, Paper EB2020-MDS-010.
6. Shrestha, S., R. Francis, and A. Smith, 2020, “RELIABLE: Wear-resistant lightweight aluminium brakes for vehicles,” *Proceedings of EuroBrake 2020*, 16-19 June 2020, Online, Paper EB2020-EBS-032.
7. Pramod, S. L., S. R. Bakshi, and B. S. Murty, 2015, “Aluminum-based cast *in-situ* composites: A review,” *J. Mater. Eng. Perform.*, 24(6), 2185–2207. <https://doi.org/10.1007/s11665-015-1424-2>.
8. Efe, M., J. A. Haynes, and J. L. Gibbs, 2023, “I.1.1.7 Task 1H. Hybrid Dispersion-Strengthened Aluminum-Matrix Composites for Higher Efficiency EV Powertrains: Cost-Effective Lightweight Alloys for EV Propulsion,” In: Ollila, S., J. L. Gibbs, C. Schooler, and H. F. Wu (Eds.), *Materials FY 2022 APR*, VTO, DOE/EE-2731, August 2023, pp. 46–52.
9. Li, X., M. Reza-E-Rabby, A. Guzman, G. Grant, S. Mathaudhu, M. Hinton, and A. Reynolds, 2022, “Strain and strain-rate in friction extrusion,” *J. Mater. Res. Technol.*, 20, 882–893.
<https://doi.org/10.1016/j.jmrt.2022.07.116>.

Acknowledgements

The authors would like to commend Dr. X. Li and Dr. H. Das of PNNL for their leadership and help in the friction-consolidation tasks, and Dr. M. Pole of PNNL for leadership and help in characterizing the composites. Mr. M. Blazon and Mr. A. Ortiz of PNNL are acknowledged for their help in the metallography-sample preparation and hardness testing. Cast composites were manufactured by Loukus Technologies, Inc. (Calumet, MI, USA). We also thank Dr. A. Loukus and Mr. S. Kastamo of Loukus Technologies for their collaboration and technical discussions.

I.1.1.8 Task 1I. Design of Sustainable Lightweight Cast Alloys for Electric Vehicles (Oak Ridge National Laboratory)

Sumit Bahl, Principal Investigator

Oak Ridge National Laboratory
Materials Science and Technology Division
1 Bethel Valley Rd.
Oak Ridge, TN 37830
E-mail: bahls@ornl.gov

J. Allen Haynes, PMCP Consortium Manager

Oak Ridge National Laboratory
Materials Science and Technology Division
1 Bethel Valley Rd.
Oak Ridge, TN 37830
E-mail: haynesa@ornl.gov

Jerry L. Gibbs, DOE Technology Development Manager

U.S. Department of Energy
E-mail: Jerry.Gibbs@ee.doe.gov

Start Date: October 1, 2022
Project Funding: \$175,000

End Date: September 30, 2023
DOE share: \$175,000

Non-DOE share: \$0

Project Introduction

Extraction of primary Al from its ore is an energy-intensive process that accounts for ~3% of all greenhouse gas emissions [1]. In contrast, recycling scrap Al (or secondary Al) reduces associated energy consumption and GHG emissions by more than 90% of primary Al production. The use of lightweight Al alloys is projected to increase in the automotive industry, with a key driving force being the lightweighting of EVs for extended driving range [2]. An emerging application of interest for cast-Al alloys in EVs is ultra-large HPDC for structural applications. One of the challenges in utilizing secondary Al for structural applications is that higher impurity content in secondary (i.e., scrap) Al, particularly post-consumer scrap, leads to formation of intermetallic phases that can deteriorate mechanical properties—in particular, severely reducing the ductility of an alloy. Alloy-design can solve this problem by identifying robust composition and processing windows that control microstructure and phase selection in higher secondary content alloys. The goal of this one-year task was to develop an understanding of key fundamentals of designing impurity-tolerant, sustainable Al alloys with high-strength and high-ductility for structural EV applications.

Objectives

The overarching goal of this task is to design sustainable Al alloys using increased proportions of recycled scrap Al with high-strength and ductility for structural EV applications. Specific objectives within the task are as follows:

- Understand the physical metallurgy of a commercial HPDC Al alloy made using primary Al as a baseline material
- Evaluate the effect of controlled, increased impurity concentration on microstructure and tensile properties of the selected alloy
- Identify potential alloy-design pathways to use increased scrap and impurity content without compromising mechanical properties.

Approach

Al-4.3Mg-1.6Fe in wt.% is an HPDC Al alloy commercially known as Castaduct-42 that is used for automotive structural applications [3]. The alloy exhibits high-ductility, typically in the 10–22% range, with a modest 120–150 MPa YS. This ductility range makes it attractive for structural EV applications, particularly for components where energy absorption is important. Its high-ductility requires the Si impurity level in the alloy to remain lower than 0.2 wt.%, which precludes the use of most scrap Al because mixed-source post-consumer secondary Al is typically rich in Si content, which varies but is typically significantly greater than 0.2 wt.% due to the prevalence of Al-Si-based alloys. The effect of Si content on microstructure of Al-4.3Mg-1.6Fe alloy and the resultant mechanical properties is largely unknown. A fundamental understanding of the physical metallurgy of the Al-4.3Mg-1.6Fe-xSi alloy system would help guide alloy-design pathways for more sustainable variants of the Al-4.3Mg-1.6Fe alloy. In this work, Al-4.3Mg-1.6Fe alloys with 0.2, 0.5, 1.0 and 1.6 wt.% Si were prepared by vacuum arc melting followed by drop-casting in a water-cooled copper mold, as a laboratory-scale surrogate method for HPDC. The baseline Al-4.3Mg-1.6Fe alloy contains less than 0.05 wt.% Si and is referred to as the 0Si alloy. The other alloys are referred to by their nominal Si content, such as 0.2Si, 0.5Si, 1.0Si, and 1.6Si alloys, containing 0.2, 0.5, 1.0, and 1.6 wt.% Si, respectively. The effect of Si content on as-cast microstructures were analyzed with SEM. Tensile tests were performed at RT in the as-cast state to determine the change in strength and ductility with Si content. Cross-section microstructures of fractured tensile specimens were analyzed to determine failure mechanisms in the alloys.

Results

A BSE-SEM image of as-cast-Al-4.3Mg-1.6Fe alloy (0Si) is shown in Figure I.1.1.8.1(a). The microstructure is characterized by primary Al dendrites and an inter-dendritic, brighter-contrast eutectic phase. EDS elemental maps in Figure I.1.1.8.1(b) show the eutectic phase is Fe-rich, which is consistent with the expected formation of $\text{Al}_{13}\text{Fe}_4$ eutectic phase in the alloy [3]. The EDS maps also indicate increased Mg concentration in the interdendritic regions. However, poor contrast in the BSE-SEM images makes it difficult to determine whether the observed Mg enrichment is due to segregation of elemental Mg or formation of a Mg-rich intermetallic phase.

The BSE-SEM image of as-cast-Al-4.3Mg-1.6Fe alloy with the highest Si content of 1.6 wt.% (1.6Si alloy) is shown in Figure I.1.1.8.2(a). Compared to the baseline Al-4.3Mg-1.6Fe alloy with no Si, addition of Si impurity increases the volume fraction of interdendritic eutectic phases in the microstructure. Figure I.1.1.8.2(b) shows a higher magnification view of the microstructure where three different eutectic phases are observed. The corresponding EDS elemental maps shows that the eutectic phase marked 1 is Fe-rich with some Si partitioning. The first phase is likely the $\text{Al}_{13}\text{Fe}_4$ that is also present in the baseline alloy. The second eutectic phase is (Mg, Si)-rich, which could potentially be the Mg_2Si phase. The third eutectic phase is enriched in all three alloying elements (Mg, Si, and Fe). The Si addition also leads to the formation of coarse primary intermetallic phases, typically with a high-aspect ratio, as shown in the microstructure from a different region of the as-cast 1.6Si alloy in Figure I.1.1.8.3 (marked by arrows) and also visible in Figure I.1.1.8.2(a). The primary phase is identified as $\text{Al}_{13}\text{Fe}_4$, based on spot EDS analysis, and is qualitatively shown as such in the elemental maps. The $\beta\text{-Al}_5\text{FeSi}$ is a particularly detrimental intermetallic phase that is generally known to form in Al alloys containing Fe and Si together. However, evidence of the β phase was not observed in this study, despite the presence of 1.6 wt.% each of Fe and Si in the 1.6Si alloy.

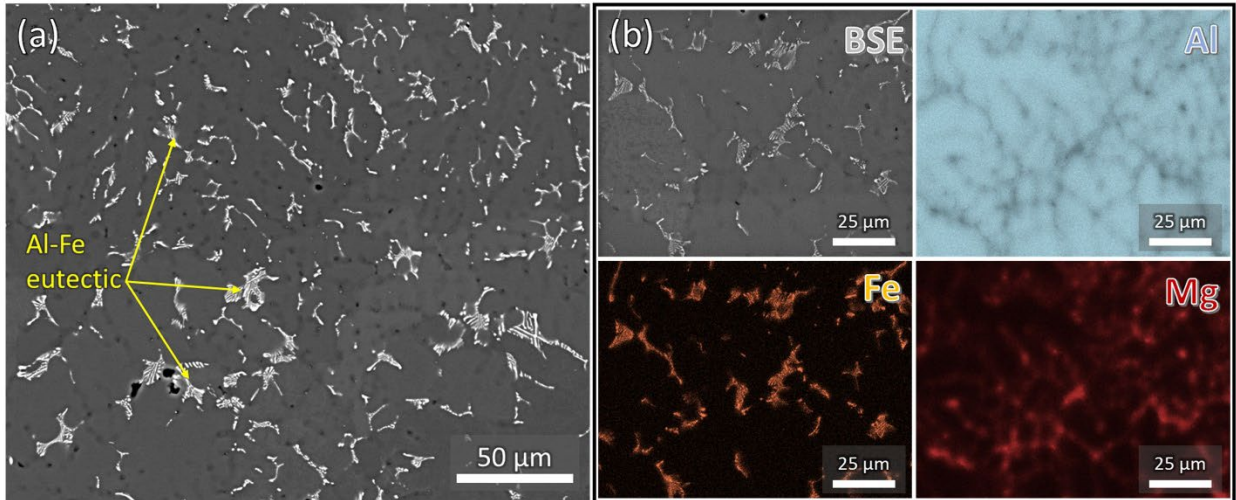


Figure I.1.1.8.1. (a) BSE-SEM image and (b) BSE-SEM image with corresponding EDS elemental maps of as-cast-Al-4.3Mg-1.6Fe alloy. Source: ORNL.

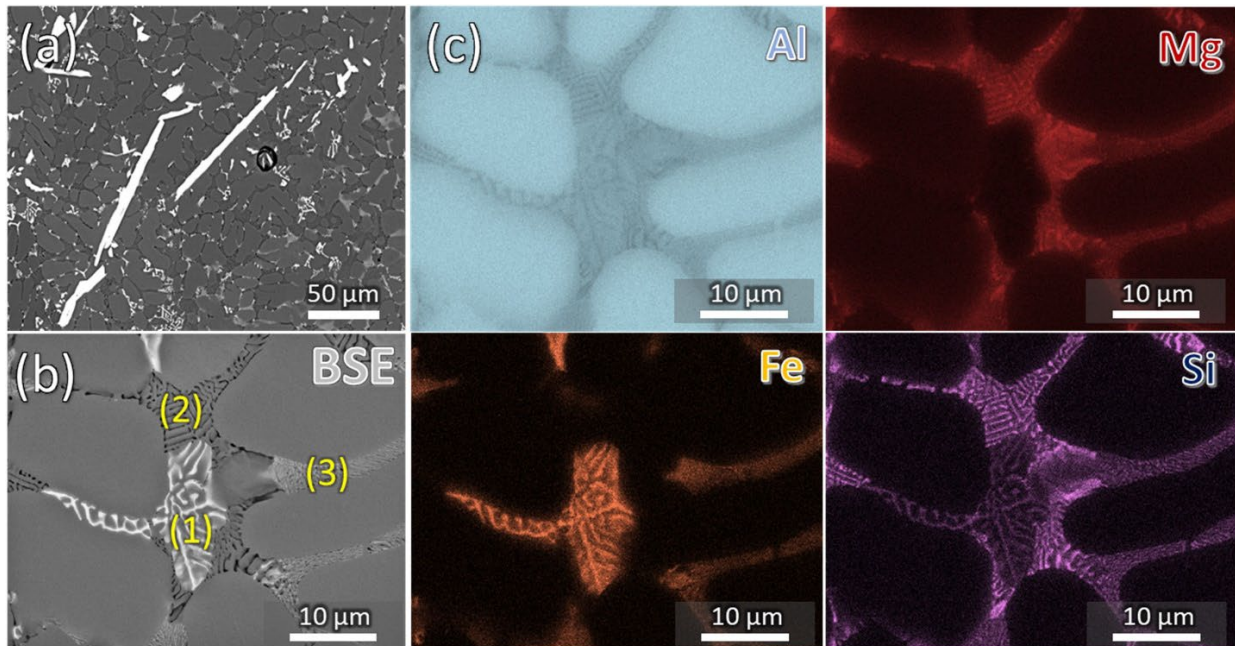


Figure I.1.1.8.2. (a) Lower- and (b) higher magnification BSE-SEM images of as-cast 1.6Si alloy. (c) EDS elemental maps corresponding to the SEM image in (b). Source: ORNL.

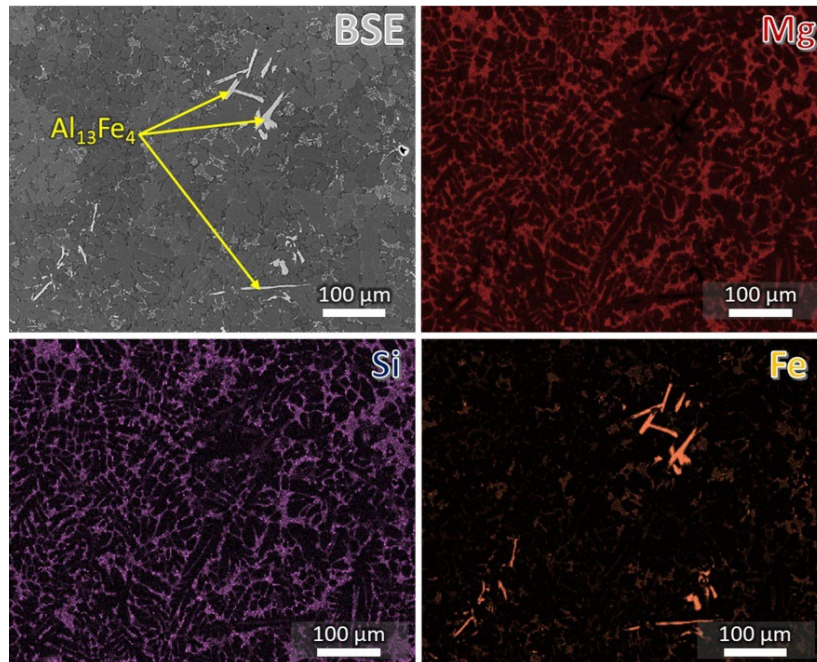


Figure I.1.1.8.3. BSE-SEM image and corresponding EDS elemental maps of as-cast 1.6Si alloy showing primary $\text{Al}_{13}\text{Fe}_4$ phase, as indicated by arrows. Source: ORNL.

Figure I.1.1.8.4 shows BSE-SEM images of 0.2Si and 1.0Si alloys with intermediate Si content. Primary $\text{Al}_{13}\text{Fe}_4$ intermetallic phase is observed in the 0.2Si alloy, indicating that a small Si addition of only 0.2 wt.% is sufficient to form this phase in the Al-4.3Mg-1.6Fe alloy. The 0.2Si alloy primarily contains one type of eutectic phase ($\text{Al}_{13}\text{Fe}_4$), while the 1.0Si alloy contains three eutectic phases, similar to that observed in the 1.6Si alloy. Comparing the microstructures of 0.2Si and 1.0Si alloys confirms the trend that higher Si addition leads to solidification of multiple eutectic phases, with an increase in their total volume fraction.

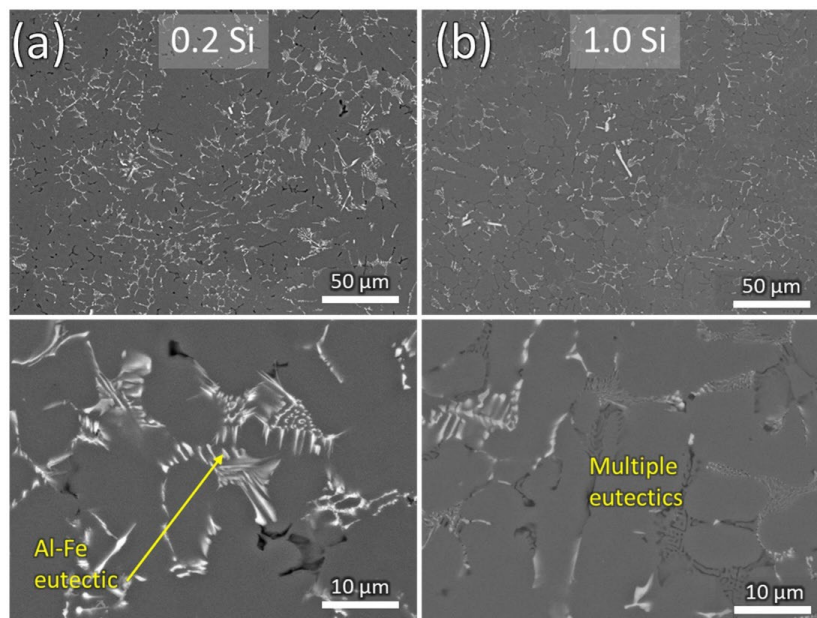


Figure I.1.1.8.4. BSE-SEM images at (top) lower and (bottom) higher magnifications of as-cast (a) 0.2Si and (b) 1.0Si alloys. Source: ORNL.

Tensile properties of as-cast alloys were measured at RT, and a minimum of three samples were tested for each alloy. Figure I.1.1.8.5(a) and Figure I.1.1.8.5(b) shows engineering stress-strain curves and summary of YS, ultimate tensile strength, and ductility of the different Si-containing alloys. The baseline Al-4.3Mg-1.6Fe (0Si) alloy exhibits YS of 116 ± 1 MPa and $14.3 \pm 1.4\%$ ductility, which are consistent with the properties reported for the commercially available HPDC version of this alloy [3]. The ductility decreases sharply whereas the YS increases slightly with increased Si content. The 1.6Si alloy has a substantially lower ductility of $2.2 \pm 1\%$ compared to $14.3 \pm 1.4\%$ in the 0Si alloy, which clearly highlights the powerful negative impact that Si impurities have on ductility of Al-4.3Mg-1.6Fe alloy. All of the Si-containing variants exhibited $<9\%$ ductility.

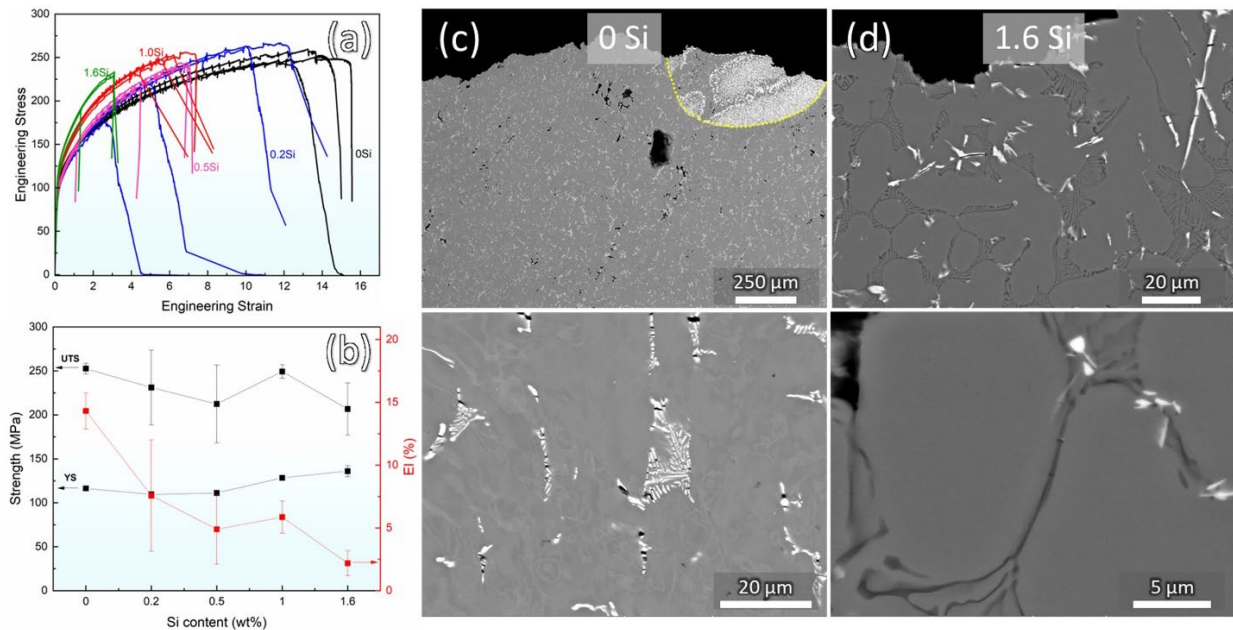


Figure I.1.1.8.5. (a) Tensile stress-strain curves of as-cast alloys and (b) summary of tensile properties. Cross-section BSE-SEM images at (top) lower and (bottom) higher magnifications of (c) 0Si and (d) 1.6Si fractured tensile samples. The yellow outline in (c) indicates an inhomogeneity in the as-cast alloy. Source: ORNL.

Cross-sections of fractured tensile samples were analyzed to identify the ductility-limiting microstructural features in as-cast alloys, and the results are shown in Figure I.1.1.8.5(c) and Figure I.1.1.8.5(d) for 0Si and 1.6Si alloys, respectively. The cross-section of 0Si alloy shows an Fe-rich region in the microstructure, as outlined in Figure I.1.1.8.5(c), that is likely due to insufficient melting and mixing of Al-Fe master alloy during vacuum arc melting. The 0Si alloy exhibits high-ductility despite the inhomogeneous microstructure. A high-magnification image of the sample shows cracked particles of Al_3Fe_4 in the eutectic phase, suggesting that these particles are potential sites for fracture initiation. The cross-section images of the 1.6Si alloy show that coarse particles of primary Al_3Fe_4 phase and the fine eutectic particles both cracked, acting as fracture initiation sites. Thus, a decrease in ductility with increase in Si impurity is attributed to increased volume fraction of the eutectic phases and occurrence of primary Al_3Fe_4 particles in the microstructure, an anticipated trend. This work has advanced our understanding of the effect of Si impurities on the microstructure and tensile properties of the cast-Al-4.3Mg-1.6Fe alloy and will assist in guiding future alloy-design pathways for developing sustainable variants of gravity-cast-Al-Mg-Fe-based alloys with greater impurity tolerance.

Conclusions

The effect of increased Si impurity levels (up to 1.6 wt.%) on microstructure and tensile properties of cast-Al-4.3Mg-1.6Fe alloy was investigated to anticipate the effects of future increased post-consumer secondary Al on this alloy family, and the following conclusions were drawn from the study:

- The as-cast-Al-4.3Mg-1.6Fe alloy microstructure comprises primary Al dendrites and the interdendritic Al₁₃Fe₄ eutectic phase.
- Addition of Si impurity (1) increases volume fraction of interdendritic eutectic phases, with three different types of eutectic phases identified in the alloy with the highest Si level of 1.6 wt.%, and (2) promotes solidification of primary Al₁₃Fe₄ particles.
- The often-reported detrimental β -Al₅FeSi phase was not observed in any of the alloy variants high in Si and Fe content.
- Si impurities significantly reduced ductility of the Al-4.3Mg-1.6Fe alloy, from 14.3 \pm 1.4% in the alloy without Si to 2.2 \pm 1% in the alloy with 1.6 wt.% Si. The YS increased only slightly with the Si addition. Cross-sectional examination of fractured tensile samples revealed that fine eutectic particles and coarse primary Al₁₃Fe₄ particles both crack under tension, which reduces the ductility of Si-containing alloys.

References

1. Raabe, D., D. Ponge, P. J. Uggowitzer, M. Roscher, M. Paolantonio, C. Liu, H. Antrekowitsch, E. Kozeshnik, D. Seidmann, B. Gault, F. de Geuser, A. Deschamps, C. Hutchinson, C. Liu, Z. Li, P. Prangnell, J. Robson, P. Shanthraj, S. Vakili, C. Sinclair, and S. Pogatscher, 2022, "Making sustainable aluminum by recycling scrap: The science of 'dirty' alloys," *Prog. Mater. Sci.*, 128, 100947. <https://doi.org/10.1016/j.pmatsci.2022.100947>.
2. Drive Aluminum, 2023, "Roadmap for Automotive Aluminum," The Aluminum Association webpage, Arlington, VA, USA. Available at: <https://drivealuminum.org/resources-post/roadmap-for-automotive-aluminum/> (accessed 8 December 2023).
3. Aluminum Rheinfelden Alloys GmbH, 2021, "Rheinfelden Alloys" webpage, Baden, Germany. Available at: www.rheinfelden-alloys.eu (accessed 8 December 2023).

Acknowledgements

The authors would like to thank Y. Yang, I. Roy, N. Richter, A. Plotkowski, A. Shyam, and G. Knapp for their research contributions. D. McClurg and K. Epps are acknowledged for their technical support. This research was sponsored by the VTO under the PMCP.

I.1.2 Thrust 2: Materials and Lubricants for Heavy-Duty Electric Vehicles and Electric Vehicle Propulsion

I.1.2.1 Task 2A. High-Performance Soft-Magnetic Materials for Motor Laminates (Fe-Si) via Shear-Rolling (Oak Ridge National Laboratory)

Govindarajan Muralidharan, Principal Investigator

Oak Ridge National Laboratory
Materials Science and Technology Division
1 Bethel Valley Rd.
Oak Ridge, TN 37830
E-mail: muralidhargn@ornl.gov

J. Allen Haynes, PMCP Consortium Manager

Oak Ridge National Laboratory
Materials Science and Technology Division
1 Bethel Valley Rd.
Oak Ridge, TN 37830
E-mail: haynesa@ornl.gov

Jerry L. Gibbs, DOE Technology Development Manager

U.S. Department of Energy
E-mail: Jerry.Gibbs@ee.doe.gov

Start Date: November 1, 2021

End Date: September 30, 2023

Project Funding: \$250,000

DOE share: \$250,000

Non-DOE share: \$0

Project Introduction

This task seeks to develop and demonstrate new FeSi steels that enable higher power density electric motors. The FeSi steels that are widely used to make motor laminates for EV motors typically contain 2.5–3.5 wt.% silicon. There is rapidly growing interest from motor manufacturers to increase motor speed to improve power density. High-speed motors incur losses in their magnetic cores due to changing magnetic fields. Widely used Fe-(2.5–3.5)Si steel must be rolled to extremely thin sheets of 0.35 mm or less and laminated into motor cores to reduce such losses. However, the use of thin sheets decreases the stacking factor and substantially increases manufacturing complexity and cost. Increasing the resistivity of FeSi steels is an alternate approach to achieve reduced losses in higher speed electric motors. Higher amounts of silicon in the steel increases its electrical resistance, improving magnetic properties, and reducing losses. For example, Si steels with 6.5% Si have a high-resistivity and permeability, low-eddy current losses and hysteresis losses (especially at higher frequencies), and almost zero magnetostriction [1]. However, as the Si content increases, the material becomes extremely brittle and is very difficult to cold roll into thin sheets. This embrittlement has been the primary deterrent in the use of higher silicon FeSi steels in motor laminates. The availability of an FeSi steel with a higher Si content that can be cold-rolled and stamped will facilitate its use in motor core laminates, thereby increasing the efficiency and power density of electric motors, and hence, the range of EVs.

Objectives

The objective of Task 2A is to develop higher Si steels (5–6.5 wt.% Si) that can be produced using traditional manufacturing routes, to include warm-shear-rolling and cold-rolling, and which can be stamped to form laminates that enable higher power density electric motors for EVs.

Approach

The limited ductility of FeSi steels with higher Si content is primarily due to ordering reactions that occur in FeSi alloys with higher Si levels, as shown in the phase diagram in Figure I.1.2.1.1. One or more ordered phases designated as B2 (FeSi type) and DO₃ (Fe₃Si type) can form in Fe-(6–6.5 wt.%) Si alloys depending on alloy composition, temperature, and processing history. The vertical line shown in the figure represents the alloy composition for Fe-6.5 wt.% Si. As shown in Figure I.1.2.1.1, this alloy is likely to show the presence of A2 (disordered body-centered cubic [bcc] structure), B2, or B2 + DO₃ at equilibrium, depending on the temperature and thermal-mechanical processing history [1], [2]. The types of intermetallic phases and the degree of ordering present in the alloys determines strength and ductility. In particular, it has been shown that the formation of the DO₃ phase during cooling can be responsible for the brittle behavior of Fe-6.5 wt.% Si alloy at RT.

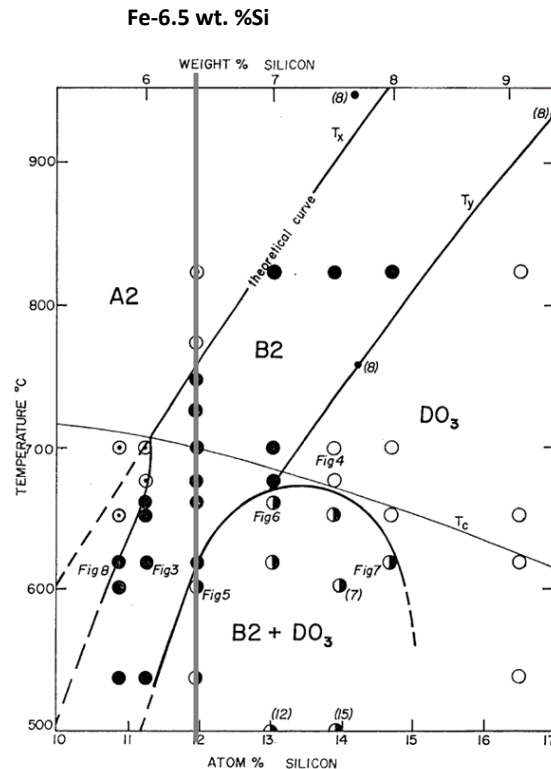


Figure I.1.2.1.1. FeSi phase diagram. Source: ORNL [2].

Several approaches have been used to improve RT ductility in Fe-6.5 wt.% Si alloys [1]. Previous work has shown rapid or splat quenching can suppress the formation of the DO₃ phase, thereby making the alloy more ductile. However, splat quenching can be achieved only in very thin and narrow ribbons, making it difficult and expensive to subsequently fabricate larger components. Other techniques, such as chemical vapor deposition to siliconize or hot-dipping of a ductile Fe-3.2 wt.% Si sheet followed by diffusion annealing, have been used to make thin sheets of high-Si steel, but these approaches can be complex and expensive.

This project uses two parallel and potentially synergistic approaches to enable the development of higher Si Fe Si steels. The first approach aims to develop a thermal-mechanical processing route, consisting of hot and warm rolling, which can be effective in softening Fe-6.5 wt.% Si alloys, thereby increasing RT ductility and enabling cold-rolling [3]. ORNL has a unique mill that employs heated rolls that can reach ~300°C and perform both symmetric and asymmetric shear-rolling. Shear-rolling has been shown to result in grain refinement, improving uniformity of microstructure, and texture modification in steels, Al alloys, titanium, and magnesium alloys; hence, it is attractive for this application [4]. The use of heated rolls eliminates the

potentially detrimental roll-quenching effect that happens when preheated sheets are cold-rolled. Results on the effect of shear-rolling were reported in the previous annual report [5].

The second approach used in the project is the addition of various alloying elements (X) to modify the stability of the intermetallic phases in FeSiX alloys. Recent work has shown that the addition of certain elements, including some rare earths, can reduce the degree of intermetallic ordering, thereby increasing RT ductility. Selection of alloying elements was initially guided by previous work in the literature and was refined using first-principles calculations [5]. For FY 2023, we report on the progress achieved in the processing of these new alloys and their magnetic properties.

Results

Alloy Processing

Two major aspects of processing were emphasized in FY 2023:

- Evaluating the effect of alloy composition on the ability to fabricate sheets < 1-mm-thick
- Fabricating alloy sheet of the required length, width, and thickness to complete magnetic-core-loss measurements.

Several experimental Fe-(5–6.5) wt.% Si-X alloys, where X denotes alloying elements such as chromium (Cr), were arc-melted and fabricated in the form of drop castings of typical size (0.5–1-in. square and 3–4-in. long), as observed in Figure I.1.2.1.2(a). Alloying elements were selected from previous first-principles modeling work performed in this project. These ingots were homogenized at 1,100°C, followed by hot-rolling to a thickness of ~2 mm, as indicated in Figure I.1.2.1.2(b). A hot-rolled plate of one alloy was successfully rolled at RT to a final thickness ~0.4 mm after an intermediate anneal, as shown in Figure I.1.2.1.2(c), thereby completing a major project milestone. From an initial batch of five developmental alloys, two higher Si alloy compositions could be successfully rolled at RT while the other alloys cracked when RT rolling was attempted. Both alloys were selected for further development in FY 2024.

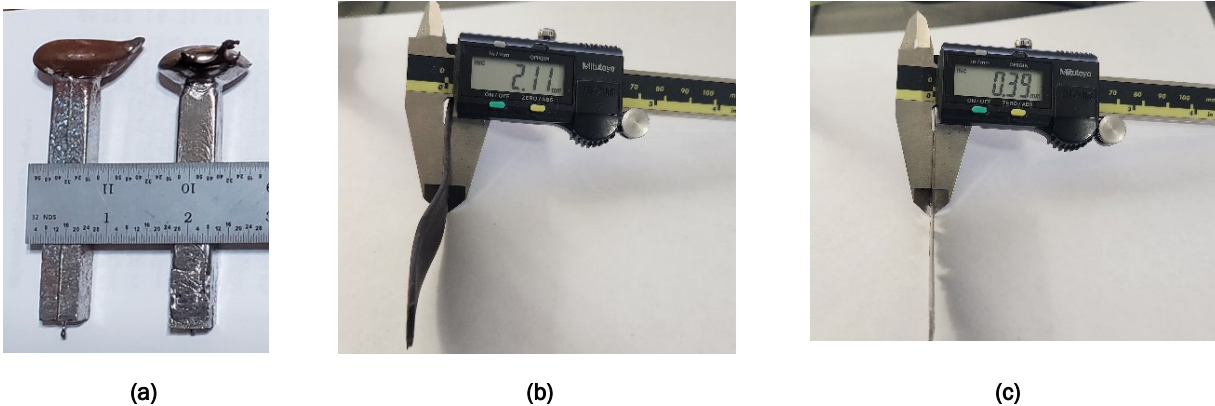


Figure I.1.2.1.2. (a) As-cast developmental Fe-(5–6.5) wt.% Si-X alloys. (b) Hot-rolled plate of one developmental alloy rolled to a thickness of ~2 mm. (c) Sheet rolled to a thickness of ~0.4 mm at RT from plate shown in (b). Source: ORNL.

Evaluation of Magnetic Properties

In the previous annual report, saturation magnetic moments were measured using squid magnetometry in a Quantum Design MPMS3 cryostat. This year, primary emphasis was placed on measuring core losses in developmental alloys. Core-loss measurements were performed using two different types of samples: a ring-sample and a strip-sample. All tests were conducted using the Brockhaus MPG-200 electrical steel tester.

The first set of measurements was performed on a ring-sample. This ring-sample, as observed in Figure I.1.2.1.3(a), was obtained from a rolled sheet. Ring samples were fabricated using electrical discharge machining. The Brockhaus electrical steel tester shown in Figure I.1.2.1.3(b) was used to conduct the test which determines the magnetic properties of rings, ring cores, strips, punched parts, etc. In all cases, a magnetic flux is created inside the sample when it is exposed to a defined magnetic field within a measuring coil. The current to establish the magnetic field is supplied by a power amplifier and measured using a temperature-stable and induction-free precision resistor or alternatively, by field coils. Polarization is estimated by measuring induced voltage, followed by conversion and integration [6].

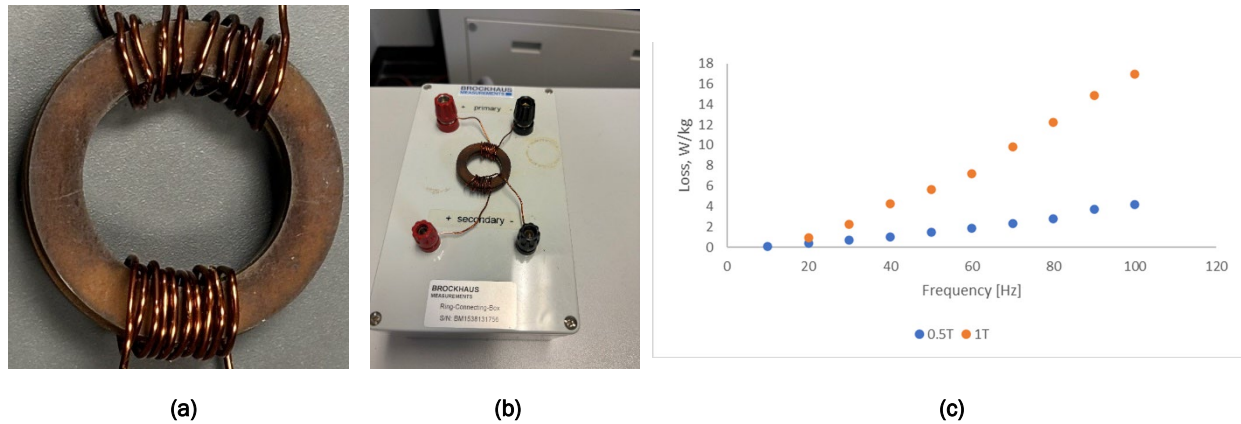


Figure I.1.2.1.3. (a) Ring-sample fabricated from rolled Fe-(4-6.5)Si-X alloys. (b) Image of the Brockhaus MPG-200 electrical steel tester. (c) Core-loss values as a function of frequency at flux densities of 0.5 and 1.0T. Source: ORNL.

The ring-sample test requires the test sample to be wound with primary and secondary coils [7], [8]. The primary winding is used to create the magnetic field, H , given by:

$$H = \frac{N_p I}{l_m} \quad (1)$$

where N_p is the number of turns on the primary coil, I , the current in the primary, and l_m , the magnetic path length. The voltage induced on the secondary coil, V , is given by:

$$H = \frac{N_p I}{l_m} \quad (2)$$

$$V = A_e N_s \frac{dB}{dt} \quad (3)$$

where A_e is the core area, N_s is the number of turns on the secondary and B is the flux density. The flux density is determined by measuring the secondary voltage and integrating it. The core geometric data and number of turns are provided as inputs to the tester. The B-H loops can thus be determined. In this experiment, the sample had an outer diameter of 28 mm and an inner diameter of 25 mm. Its lamination thickness was 1.3 mm, and the stack had a total height of 6 mm. The ring samples were wound with 10 primary and 9 secondary turns. Loss measurements were conducted at two flux densities—i.e., 0.5T and 1T over a 10–100Hz frequency range and the results are in Figure I.1.2.1.3(c). Measured loss at 50 Hz, 1T, was 5.9 W/Kg. While reference losses from an Fe-3Si alloy

currently commercially available using the same setup and identical thickness is not available, the max loss in W/Kg at 50 Hz, 1T, for standard D20 grade available from Arcelor Mittal has indicative core-loss of 2.6–5.8 W/Kg at a thickness of 1.0 mm and is expected to increase with increasing thickness. Work is ongoing to obtain data from a reference material using an identical testing technique and evaluating the effect of heat-treatment on core losses. The trends of increasing core-loss with increasing frequency are in line with expectations [9].

Core-loss measurements were also conducted on single strip samples 280 mm × 10.8 mm × 0.27 mm. Measurements were conducted on the Brockhaus SST 280 mm × 300 mm test fixture at 0.5T, 1T, 1.5T, and 1.9T with frequency sweeps between 10–100Hz. Similar to the observations with the ring-sample measurements, the trends of increasing core-loss with flux density and frequency were consistent with expectations. As part of future work, calibration of the measurement systems on ring and single strip samples fabricated from baseline alloys is planned.

Computational Modeling

Understanding the stabilities of the disordered (A2) and the ordered phases (B2 and D0₃) as a function of alloy composition and temperature in FeSiX alloys, as shown in Figure I.1.2.1.1, is critical in designing alloy compositions and processing steps to achieve alloys that have sufficient RT ductility and the required magnetic properties. However, only limited phase diagram information is available to predict the complex order-disorder transition beyond the FeSi binary system. Most previous bcc modeling of FeSi was focused on the A2/B2 order-disorder transition, without consideration of the D0₃ phase. Only recently, has a comprehensive thermodynamic description of D0₃ become available [10]. These newly available data, as observed in Figure I.1.2.1.4, show the computed order-disorder transition of the FeSi bcc phase, which agrees well with the experiments. The latest FeSi binary model can serve as a basis to expand the thermodynamic description of the bcc phase to predict order-disorder transition in FeSiX ternaries and higher order systems.

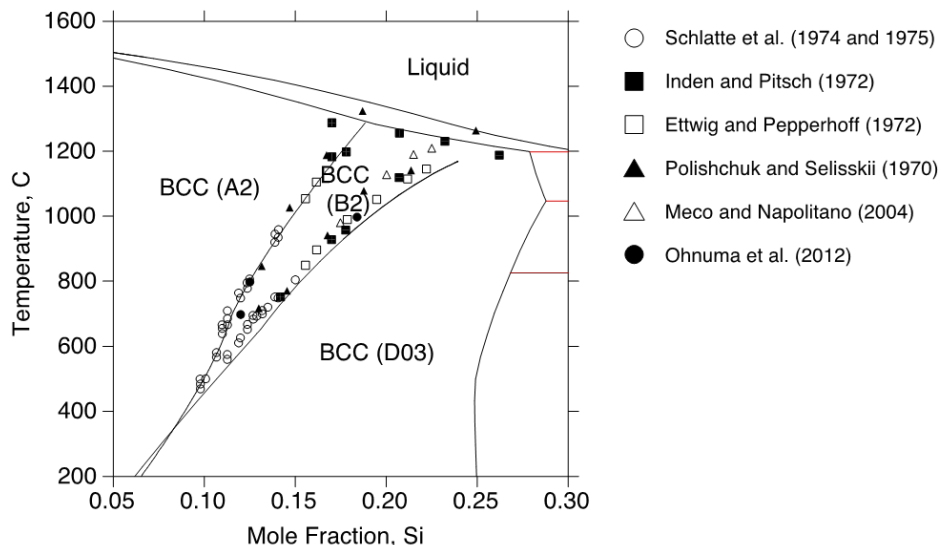


Figure I.1.2.1.4. Calculated thermodynamic phase diagram for the Si-rich portion of the FeSi phase diagram based on [10]. Source: ORNL.

Conclusions

The following are major conclusions from the work performed in FY 2023:

- New Fe-(4-6.5)Si-X alloys were successfully rolled to thicknesses less than 0.5 mm using a combination of hot- and cold-rolling
- Samples were successfully fabricated for the first-time to enable core-loss measurements

- Techniques were developed to perform core-loss measurements using ring samples and a single sheet of FeSi alloy
- Core-loss measurements show that the measured losses were within the approximate expectations for alloys of this composition and had the potential to be improved with subsequent heat-treatment
- Thermodynamic modeling was initiated to assist in further development of Fe-(4-6.5)Si-X alloys.

References

1. Ouyang, G., X. Chen, Y. Liang, C. Macziewski, and J. Cui, 2019, “Review of Fe-6.5 wt%Si high-silicon steel—A promising soft-magnetic material for sub-kHz application,” *J. Magn. Magn. Mater.*, 481, 234–250. <https://doi.org/10.1016/j.jmmm.2019.02.089>.
2. Swann, P. R., L. Grånäs, and B. Lehtinen, 1975, “The B2 and DO₃ ordering reactions in iron–silicon alloys in the vicinity of the curie temperature,” *Met. Sci.*, 9, 90–96. <https://doi.org/10.1179/030634575790445279>.
3. Fu, H., Z. Zhang, Q. Yang, and J. Xi, 2011, “Strain-softening behavior of an Fe–6.5wt%Si alloy during warm deformation and its applications,” *Mater. Sci. Eng. A*, 528(3), 1391–1395. <https://doi.org/10.1016/j.msea.2010.10.093>.
4. Vincze, G., F. J. P. Simões, and M. C. Butuc, 2020, “Asymmetrical rolling of aluminum alloys and steels: A review,” *Metals*, 10(9), 1126. <https://doi.org/10.3390/met10091126>.
5. Yu, X., Z. Zhang, and J. Xi, 2016, “Effects of RE elements doping on ordered structures and ductility improvement of Fe–6.5 wt%Si alloy,” *Mater. Lett.*, 184, 294–297. <https://doi.org/10.1016/j.matlet.2016.08.074>.
6. Brockhaus Group, 2023, “Electrical Steel Tester C 510” webpage, Dr. Brockhaus Messtechnik GmbH & Co., Lüdenscheid, Germany. Available at: <https://www.brockhaus.com/measurements/products/softmagnetic/est-series/c-510/?lang=en> (accessed 8 December 2023).
7. Hein, H., S. Yue, and Y. Li, 2019, “Comparative core-loss calculation methods for magnetic materials under harmonics effect,” *IOP Conference Series: Material Science and Engineering, 2019 4th Asia Conference on Power and Electrical Engineering (ACPEE 2019), 28–31 March 2019, Hangzhou, China*, 486, 012019. <https://doi.org/10.1088/1757-899X/486/1/012019>.
8. Hilton, G., 2003, “IEC Magnetic Materials 60404-Part 6: Methods of measurement of the magnetic properties of magnetically soft metallic and powder materials at frequencies in the range 20 Hz to kHz by the use of ring specimens,” International Electrotechnical Commission, Geneva, Switzerland.
9. Lee, S., J.-T. Park, and S.-J. Kim, 2022, “Examination of magnetic properties of non-oriented electrical steels using ring-type specimens,” *J. Magn. Magn. Mater.*, 557, 169471.
10. Cui, S., and I. H. Jung, 2017, “Critical reassessment of the FeSi system,” *CALPHAD*, 56, 108–125. <https://doi.org/10.1016/j.calphad.2016.11.003>.

Acknowledgements

The authors would like to acknowledge the following ORNL staff: Dr. D. Shin for thermodynamic modeling; Dr. V. Rallabandi for core-loss measurements; K. Hanson, R. Dalton, and C. Taylor for processing; and K. Hedrick and I. Stinson for mechanical testing. The authors also wish to acknowledge Dr. T. Ros from Cleveland Cliffs for guidance in this work.

I.1.2.2 Task 2B. Ferrous Alloys for Fatigue-Resistant, Lightweight Geartrains for Heavy-Duty Electric Vehicle Systems (Oak Ridge National Laboratory)

Dean Pierce, Principal Investigator

Oak Ridge National Laboratory
Materials Science and Technology Division
1 Bethel Valley Rd.
Oak Ridge, TN 37830
E-mail: piercedt@ornl.gov

J. Allen Haynes, PMCP Consortium Manager

Oak Ridge National Laboratory
Materials Science and Technology Division
1 Bethel Valley Rd.
Oak Ridge, TN 37830
E-mail: haynesa@ornl.gov

Jerry L. Gibbs, DOE Technology Development Manager

U.S. Department of Energy
E-mail: Jerry.Gibbs@ee.doe.gov

Start Date: November 1, 2021

End Date: September 30, 2023

Project Funding: \$200,000

DOE share: \$200,000

Non-DOE share: \$0

Project Introduction

This task aims to develop new steel alloys for applications in drivetrain components like gears and bearings in future HD EVs. The goal of this project will be to develop steels that cost-effectively reduce the weight of components or increase the efficiency of power transmission in electrified drive trains, particularly in HD vehicles. These would lead to fuel- and freight-efficiency increases and reductions in GHG emissions. The task focuses on steel due to the durability and longevity demands on the drivetrains of HD vehicles, vehicles that are often required to operate up to 1,000,000 miles. Materials development is focused on improving certain key manufacturing and performance attributes over existing low-alloy commercial gear and drivetrain steels, such as AISI 8620 (used in the United States) and 16MnCr5 (used in Europe), which contain low amounts of carbon (C), manganese (Mn), chromium (Cr), and/or nickel (Ni). Some of the key attributes of gear and bearing steels are (1) surface hardness and wear resistance (after carburizing or nitriding for gears), (2) HCF resistance, (3) low-mass, (4) surface tribological properties to reduce friction or damage, (5) thermal transport properties that can influence temperature at the contacting surfaces, and (6) gear core strength and toughness.

Objectives

The objectives of this task are to develop new and innovative steels and processing pathways that can reduce weight and increase the efficiency of power transmission in drivetrains of HD EVs in a cost-effective manner, leading to fuel- and freight-efficiency increases. The lean-alloy compositions of the baseline materials AISI 8620 and 16MnCr5, listed in Table I.1.2.2.1, make them cost-effective materials for gears. Furthermore, 52100 steel is the current baseline for bearing steels in the United States. Alloy 52100 is a high-C steel, which develops very high hardness after heat-treatment to provide wear resistance.

Table I.1.2.2.1. Nominal Composition (wt.%) of Commercial Gear Steels 16MnCr5 and AISI 8620 in Use in Europe and the United States⁸

	Steel Class	Mn	Cr	Si	C	Ni	Al	Mo	Fe
Carburizable Gear Steels									
16MnCr5	Martensitic Carburizing	1.15	0.95	0.25	0.16	-	-	-	Bal.
8620	Martensitic Carburizing	0.8	0.5	0.25	0.205	0.55	-	0.2	Bal.
ORNL 16MnCr5	Martensitic Carburizing	1.15	0.95	0.25	0.16	-	-	-	Bal.
ORNL 16MnCr5+5Al	Martensitic Carburizing	X	X	X	0.16	X	5	X	Bal.
High-C Bearing Steels									
PCS-52100	Martensitic High-C	0.35	1.45	0.225	1.05		0	-	Bal.
ORNL 52100	Martensitic High-C	0.35	1.45	0.225	1.05		0	-	Bal.
ORNL 52100+5Al	Martensitic High-C	X	X	X	1.05	X	5	X	Bal.
ORNL 52100+5Al+C	Martensitic High-C	X	X	X	1.2	X	5	X	Bal.

Approach

Developmental steels have been designed using computational thermodynamics with several objectives:

- Achieve properties that enable reduced gear weight
- Enable increased rolling sliding-contact fatigue (RSCF) strength over existing gear and bearing steels
- Incorporate an affordable alloying strategy reducing the barrier for industry adoption of new materials.

Initially, 16MnCr5 gear and 52100 bearing steels were modified by addition of Al and small amounts of other elements, in lieu of developing entirely new alloys, to evaluate the effect of Al on the baseline steels to provide technical understanding for further future alloy development. The developmental alloys include a modified version of 16MnCr5 with 5 wt.% Al addition (ORNL 16MnCr5+5Al) and two Al-modified variants of 52100 (ORNL 52100+5Al and ORNL 52100+5Al+C), with compositions listed in Table I.1.2.2.1. Al addition to steel can help meet Objective 1. Al reduces the density of steel by lattice-parameter expansion and also by replacement of iron (Fe) atoms with lower-atomic-weight Al atoms [1]. At moderate Al additions, Al can reduce the density of ferritic steel by 1.25% per wt.% of Al-added [1], resulting in a 6.7% density reduction of steel with 5 wt.% Al-added. In addition, a 5 wt.% addition of Al can reduce the Young's modulus of the steel from 200 to 180 GPa. While the overall impact of reducing Young's modulus in gear applications is not fully understood at this time, decreasing the Young's modulus will reduce peak Hertzian contact stresses, which are one of the causes of failure. Alternatively, reducing the Young's modulus from 200 to 180 GPa could also enable reducing gear width by approximately 10%, while maintaining equivalent maximum Hertzian contact stresses. Assuming 200 lb. of gears in a HD truck drivetrain, a 16.7% (10 + 6.7%) reduction in gear weight results in 33 lb. saved.

⁸. Developmental gear steel ORNL 16MnCr5+5Al, developmental bearing steels ORNL 52100+5Al and ORNL 52100+5Al+C, and commercial bearing steel 52100. Wear coupons of 52100 steel manufactured by ORNL (ORNL-52100) and also procured from PCS instruments (PCS-52100) to the same nominal composition. "X" indicates the amount of element can be disclosed upon request.

Al is also a solid-solution strengthening element [1], [2] and slightly increases the martensite start temperature of steel [2], such that high additions of Al may not result in additional quantities of soft retained austenite in the microstructure. These factors have the potential to increase the RSCF resistance of Al-modified steels (Objective 2). However, Al is also a strong ferrite stabilizer in steel, and at high enough levels in typical steels, it suppresses the austenite phase, making it impossible to form the hard martensitic microstructure needed for wear-critical applications without the addition of C or austenite stabilizing elements like Ni or Mn. This will cause the core of a gear steel to have a dual-phase ferrite and martensite microstructure, which has not yet been evaluated in forged gear steels to date. In addition, a fully martensitic microstructure is desired at the surface for wear resistance. Our hypothesis is that, in these Al-added gear steels, the carburizing process can overcome the ferrite stabilizing effect of Al because C is a strong austenite stabilizer. This enables a fully austenitic microstructure to be obtained at the surface during carburizing, which will result in a fully martensitic microstructure near the surface upon quenching. Similarly, the high-bulk-C content of bearing steels like 52100 can enable accommodation of relatively high levels of Al without destabilizing the austenitic phase, thereby making a fully martensitic microstructure possible. Thus, these alloys are potentially good candidates for Al addition.

In Objective 2, above, we hypothesize that significantly increasing RSCF resistance of the gear or bearing may have the potential for additional performance and endurance benefits. These additional benefits may include improved efficiency by enabling the use of lower viscosity gear oil to reduce churning losses. Thus, improved overall vehicle efficiency increases may be realized through lighter weight gears (Objective 1) and reduced drivetrain losses (Objective 2). To confirm the hypothesis outlined above, the developmental bearing steels with 5 wt% Al additions have been fabricated into RSCF specimens (roller and ring), and RSCF testing at ORNL to simulate gear contact began in Year 2 of this task (i.e., FY 2023). The workflow schematic for this task is depicted in Figure I.1.2.2.1. The developmental alloys are being compared to the baseline gear steels under typical gear simulation conditions previously developed by the tribology-research team at ORNL [3]. In parallel, ORNL conducts modeling simulations and characterization of the carburizing process of the new developmental gear steel, ORNL 16MnCr5+5Al, and experimental carburizing trials have been conducted to validate these simulations. Core properties of the developmental gear steels are also under investigation.

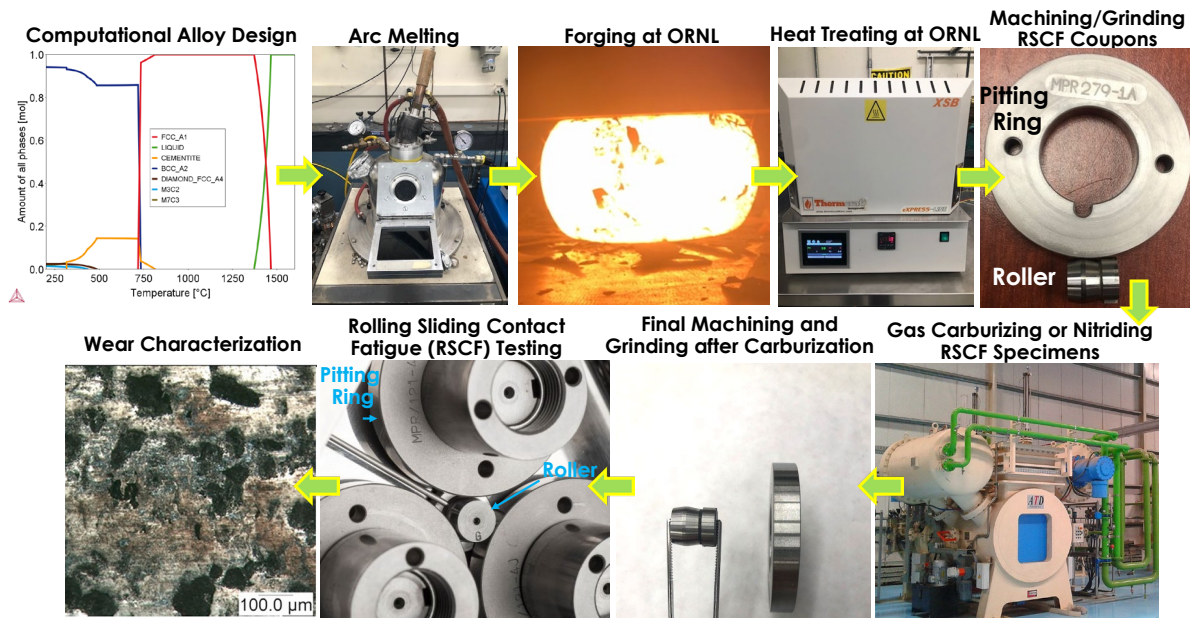


Figure I.1.2.2.1. Manufacturing route and activities for design and fabrication of developmental alloys and subsequent machining, testing, and evaluation of RSCF specimens. Source: ORNL.

Results

Results from simulations of the carburizing process on 16MnCr5 (baseline) and ORNL 16MnCr5+5Al are shown in Figure I.1.2.2.2(a) and Figure I.1.2.2.2(b), which show the predicted C content as a function of depth from the surface for different carburizing times at 930°C for baseline gear steels 16MnCr5 and ORNL 16MnCr5+5Al. The developmental alloy exhibits different predicted C diffusion kinetics. Figure I.1.2.2.2(c) and Figure I.1.2.2.2(d) show the predicted phase fractions as a function of depth from the surface for carburizing for 12 h at 930°C for the baseline gear steel 16MnCr5 and also ORNL 16MnCr5+5Al. The simulations reinforce the hypothesis, showing that carburizing of ORNL 16MnCr5+5Al at 930°C for 12 h can enable a fully austenitic microstructure near the surface to a depth of approximately 500 μm , after which a dual-phase ferrite and austenite microstructure is present.

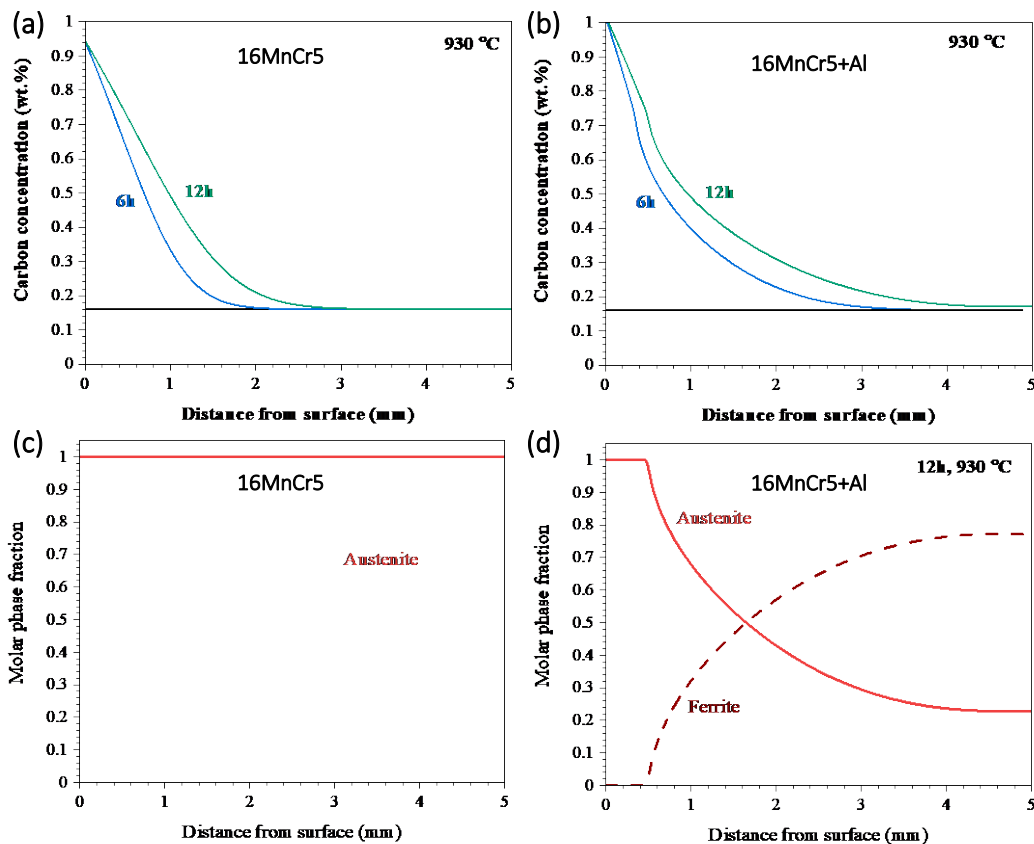


Figure I.1.2.2.2. Carburizing simulations show C content as a function of distance from the surface and time for (a) 16MnCr5 and (b) 16MnCr5+5Al. Phase fractions predicted after 12 h of carburizing at 930°C in (c) 16MnCr5 and (d) 16MnCr5+5Al. Source: ORNL.

Hardness traverses as a function of depth from the carburized surface, core tensile properties, and average core-impact toughness obtained from 1/2-scale miniaturized Charpy v-notch (MCVN) specimens (using ASTM E2248-15) from 16MnCr5 and 16MnCr5+5Al are shown in Figure I.1.2.2.3(a, b, and c), respectively. Optical micrographs of the microstructure of ORNL 16MnCr5 and ORNL 16MnCr5+5Al near the carburized surfaces and from the core region of ORNL 16MnCr5+5Al are shown in Figure I.1.2.2.3(d, e, and f), respectively. The hardness of 16MnCr5 is greater than the core hardness to a depth of approximately 3 mm, which is approximately consistent with the depth of carburization predicted in Figure I.1.2.2.2(a). The carburized depth of ORNL 16MnCr5+5Al is about 1 mm, based on the hardness traverses, and the difference between the predicted depth of approximately 4 mm in Figure I.1.2.2.2(b) is under investigation. The hardness of ORNL 16MnCr5+5Al at the surface is approximately 15% greater than that of ORNL 16MnCr5, which may

be beneficial for wear resistance and due to increased C content at the surface, as predicted in Figure I.1.2.2.2(b), or to the solid-solution strengthening influence of Al. The optical micrograph in Figure I.1.2.2.3(d) shows the fully martensitic microstructure of ORNL 16MnCr5 (top surface in micrograph was the exposed surface during carburization). The optical micrograph in Figure I.1.2.2.3(e) shows a fully martensitic microstructure within about 200 μm from the surface of 16MnCr5+5Al. This finding indicates the carburizing treatment was successful in fully stabilizing an austenitic microstructure during the carburizing process at 930°C; thus, it enables a hard and wear-resistant fully martensitic structure to form upon quenching. In gear steels, the core microstructure and properties, including strength and toughness, are also important. The typical microstructure of 16MnCr5+5Al in the core is shown in Figure I.1.2.2.3(f). Due to the addition of relatively high levels of Al, the core in this steel is dual-phase, predominately ferrite, with a smaller volume fraction of hard martensite islands at ferrite grain boundaries. Tensile and MCVN specimens were extracted from the core (away from the carburized surface) of the samples of ORNL 16MnCr5 and ORNL 16MnCr5+5Al that went through the carburizing process. The strength and ductility of ORNL 16MnCr5+5Al is substantially lower than ORNL 16MnCr5, as observed in Figure I.1.2.2.3(f). The impact toughness of ORNL-16MnCr5+5Al is also significantly lower than ORNL 16MnCr5. Investigation is ongoing to determine the root cause of the relatively low core strength and toughness in ORNL 16MnCr5+5Al, and particularly to identify modifications to the dual-phase microstructure. Al-containing dual-phase steels are not inherently weak or brittle, with some exhibiting exceptional toughness after specific hot-working process routes to introduce laminated-type microstructures [4]. Many processing and alloying modification strategies are under consideration to significantly improve the strength toughness.

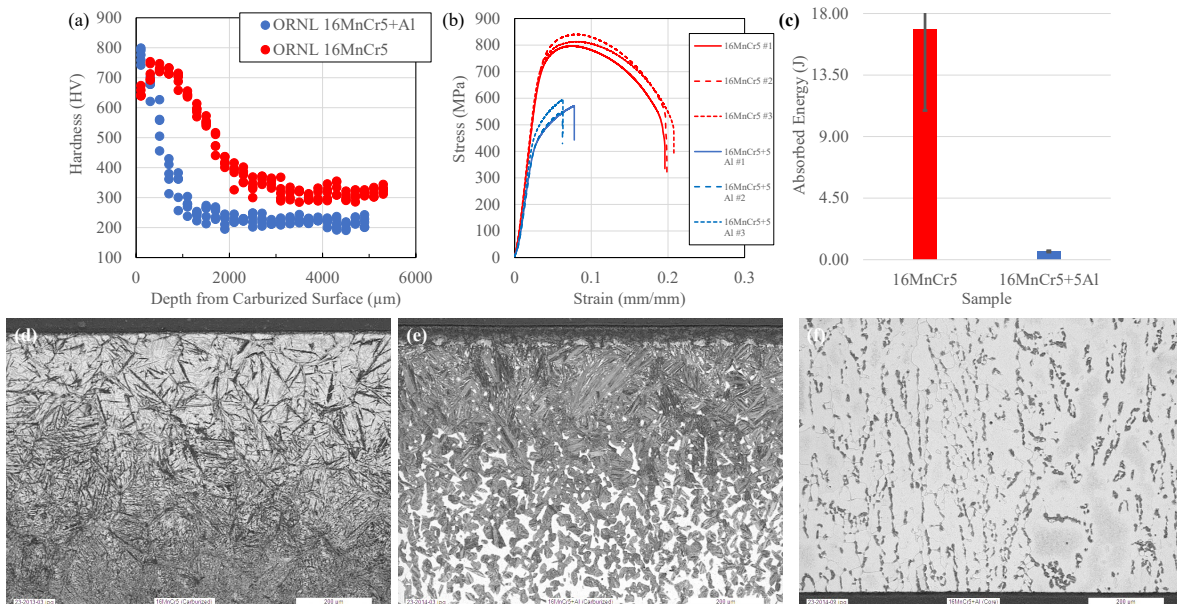


Figure I.1.2.2.3. (a) Hardness traverses for ORNL 16MnCr5 and ORNL 16MnCr5+5Al after carburizing for 12 h at 930°C, quenching, and tempering at 200°C for 1.5 h. (b) Core strength and (c) toughness for ORNL 16MnCr5 and ORNL 16MnCr5+5Al after carburizing process. Microstructure near carburized surface of (d) ORNL 16MnCr5 and (e) ORNL 16MnCr5+5Al. (f) Core microstructure of ORNL 16MnCr5+5Al. In (e) and (f), dark regions are martensite, and light regions are ferrite. Source: ORNL.

Initial RSCF testing has been conducted on 52100 steel produced by ORNL (ORNL-52100) and procured from PCS Instruments (PCS-52100). While the nominal composition of the two different variants is essentially equivalent, the hardness values differ significantly—at 979.1 \pm 11.9 for ORNL 52100 and 879.7 \pm 51.4 for PCS 52100—indicating the thermal processing of the samples was different, as indicated in Table I.1.2.2.2. The wear volume of the ORNL 52100 sample was approximately an order of magnitude less than for PCS 52100, suggesting hardness is playing an important role in the wear behavior. SEM images of the wear surfaces shown

in Figure I.1.2.2.4(a) and Figure I.1.2.2.4(b) for PCS 52100 and ORNL 52100, respectively, show the harder ORNL 52100 clearly has less surface damage. An initial RSCF test was performed on ORNL 52100+5Al+C, and the results are promising, showing low wear volumes, but further interpretation of the data and additional wear-testing are ongoing.

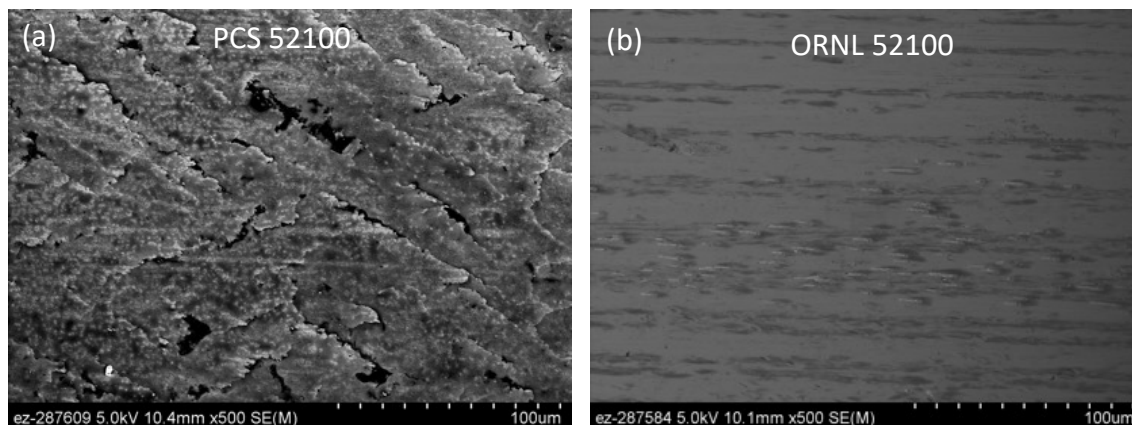


Figure I.1.2.2.4. SEM images of the wear surfaces of (a) PCS-52100 and (b) ORNL 52100 after wear-testing in accordance with the protocol in [3]. Source: ORNL.

Table I.1.2.2.2. Alloys ORNL-52100 and PCS-52100 Hardness and Wear Volume Obtained After Testing

Alloy	Vickers Hardness (HV)	Wear Volume (mm ³)
PCS 52100	879.7 ±51.4	0.69
ORNL 52100	979.1 ±11.9	0.088

Conclusions

Task 2B evaluates the potential for low-density Al-added steels in wear applications such as gears and bearings as a means to reduce drivetrain mass and potentially increase drivetrain efficiency. In this work, a standard commercial gear steel, 16MnCr5, was modified with 5 wt% Al (16MnCr5+5Al) and two variants of the standard bearing steel, 52100, were made, one to which 5 wt% Al was added (52100+5Al) and one to which Al and additional C were added (52100+5Al+C). Carburizing trials of the baseline gear steel (16MnCr5) and 16MnCr5+5Al were performed at an industrial facility. The trials demonstrated that 16MnCr5+5Al, which has a dual-phase microstructure, can be successfully carburized, and that a fully austenitic microstructure can be stabilized at the surface during carburizing, resulting in a hard martensitic microstructure after quenching. The high surface hardness of 16MnCr5+5Al, which is even higher than carburized 16MnCr5, may aid in good surface-wear characteristics, which will be further investigated. However, the core material of 16MnCr5+5Al exhibited low strength and impact toughness. The core of 16MnCr5+5Al leverages a dual-phase microstructure as a new approach to gear steel design; thus, additional thermomechanical processing or alloy chemistry optimization is needed to improve strength and toughness to make this alloy more attractive for gear applications. RSCF testing has begun on bearing steels, with most initial testing focused on the baseline 52100 material at different hardness values, clearly demonstrating the importance of greater hardness in reducing material loss due to wear. An Al and C added variant (52100+5Al+C) showed early promise of greater wear resistance in RSCF testing, and further evaluation and testing of these Al-modified bearing steels are ongoing.

Key Publications

1. Pierce, D. T., 2023, "Carburized Steel for Lightweight Wear Resistance Structures," Invention disclosure reference 202205250, Oak Ridge National Laboratory, Oak Ridge, TN, USA.

References

1. Chen, S., R. Rana, A. Haldar, and R. K. Ray, 2017, “Current state of Fe-Mn-Al-C low-density steels,” *Prog. Mater. Sci.*, 89, 345–391. <https://doi.org/10.1016/j.pmatsci.2017.05.002>.
2. Bhat, M. S., 1977, “Microstructure and mechanical properties of AISI 4340 steel modified with aluminum and silicon,” Ph. D Dissertation, University of California Berkely, Berkely, CA, USA. <https://doi.org/10.2172/7215788>.
3. Stump, B. C., Y. Zhou, M. B. Viola, H. Xu, R. J. Parten, and J. Qu, 2018, “A rolling sliding bench test for investigating rear axle lubrication,” *Tribol. Int.* 121, 450–459. <https://doi.org/10.1016/j.triboint.2018.01.058>.
4. Cao, W., M. Zhang, C. Huang, S. Xiao, H. Dong, Y. Weng, 2017, “Ultra-high Charpy impact toughness (~450J) achieved in high-strength ferrite/martensite laminated steels,” *Sci. Rep.*, 7, 41459. <https://doi.org/10.1038/srep41459>.

Acknowledgements

The following ORNL staff are acknowledged and thanked for their important contributions to this task: R. Pillai for performing carburizing simulations, J. Qu and W. Wang for rolling sliding contact fatigue guidance and testing, K. Hanson for rolling, A. Guajardo for impact testing, and C. Taylor for tensile testing.

I.1.2.3 Task 2C. New Lubricant Strategies for Advanced Thermal Management of Heavy-Duty Electric Vehicles (Oak Ridge National Laboratory)

Jun Qu, Principal Investigator

Oak Ridge National Laboratory
Materials Science and Technology Division
1 Bethel Valley Rd.
Oak Ridge, TN 37830
E-mail: qujn@ornl.gov

J. Allen Haynes, PMCP Consortium Manager

Oak Ridge National Laboratory
Materials Science and Technology Division
1 Bethel Valley Rd.
Oak Ridge, TN 37830
E-mail: haynesa@ornl.gov

Jerry L. Gibbs, DOE Technology Development Manager

U.S. Department of Energy
E-mail: Jerry.Gibbs@ee.doe.gov

Start Date: November 1, 2021

End Date: September 30, 2023

Project Funding: \$240,000

DOE share: \$240,000

Non-DOE share: \$0

Project Introduction

The electric motor in an EV rotates at 15,000 rpm currently, potentially going up to 30,000 rpm in the future. The copper winding on the e-motor gets very hot and is cooled by a lubricant. Increasing heat-transfer efficiency is currently the Number 1 challenge for e-motor oils to allow higher current for higher torque output. Excellent thermal conductivity (2,800–6,000 W/mK, 10× higher than copper) and self-lubricating of carbon nanotubes (CNTs) presents an opportunity for them to be used as oil additives for thermal and friction management. However, CNTs have poor oil suspendability and tend to aggregate and precipitate, thus losing heat-transfer enhancement. This task is to covalently functionalize CNTs using organics to enable stable suspension of CNTs in e-motor oils for improved heat-transfer. The organics on the CNT surfaces are expected not only to avoid CNTs' aggregation, but also to improve their oleophilicity for uniform oil dispersion. In addition, self-lubricating CNTs are expected to provide effective friction reduction and wear protection to allow the use of lower viscosity fluids for more rapid convection (more-efficient heat-transfer) and lower hydrodynamic drag (energy savings). A significant portion of this task is committed to a Cooperative Research and Development Agreement with Valvoline (NFE-22-09129), which started in June 2022.

Objectives

Task 2C intends to gain a fundamental understanding and develop new lubricant strategies—specifically organically modified CNTs and ionic liquids—as novel additives for EV fluid and grease lubricants to enable superior lubricity, heat-transfer, and sustainability for HD EVs.

Approach

The heat-transfer capability of a fluid can be evaluated using the Mouromtseff Number (Mo):

$$Mo = \rho^a \kappa^b C_p^d / \mu^e \quad (1)$$

where ρ , k , C_p , and m represent the density, thermal conductivity, specific heat capacity, and dynamic viscosity of the fluid, respectively.

The most-straightforward way to increase heat-transfer capacity is by reducing oil viscosity. However, lower viscosity would inevitably increase the risk of wear. Another approach is to use additives with higher thermal conductivity. Here, we aim to use covalently surface-functionalized multiwall CNTs as potential additives for lubricating oils to improve both the heat-transfer efficiency and tribological performance.

CNTs are ideal for heat-transfer applications because they have exceptional thermal conductivity (2,800–6,000 W/mK), which is one order of magnitude higher than that of metallic copper (385 W/mK) [1], and specific heat capacity of 0.7 J/gK, twice as that of copper. Previous researchers observed that multiwall CNTs provided more enhancement than single-wall CNTs. CNTs have been explored as additives to heat-transfer fluids [2], [3]. Unfortunately, CNTs have difficulties in remaining suspended in lubricating oils; as a result, the experimentally measured thermal conductivity of a fluid containing CNTs is significantly lower than the theoretical value. Our approach is to apply organic functionalization to the CNT surface for stable suspension in EV fluids, as illustrated in Figure I.1.2.3.1.

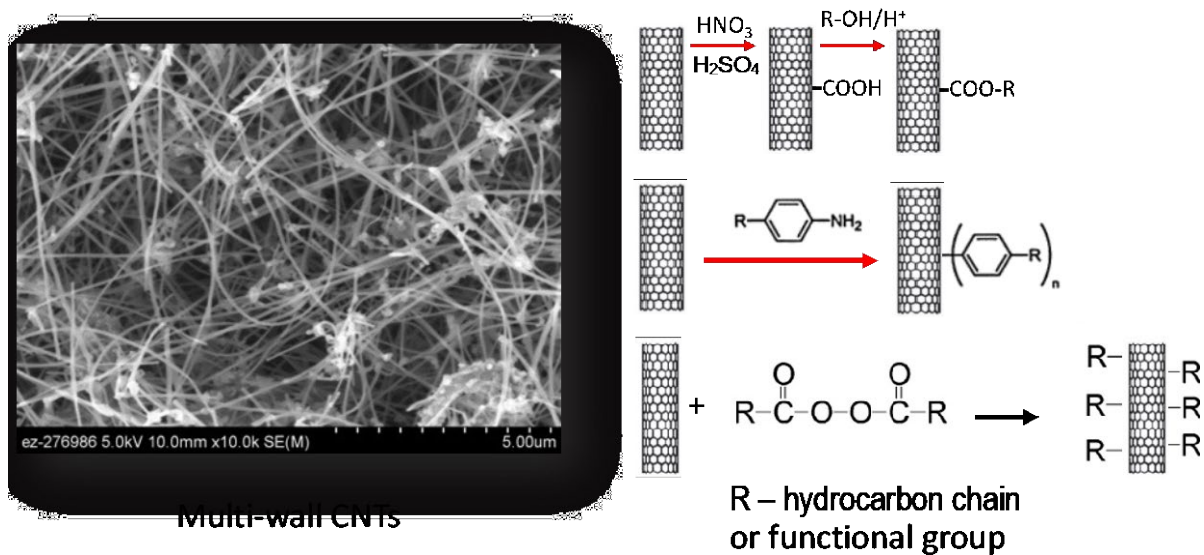


Figure I.1.2.3.1. Organic modifications for improving the oil suspendability of CNTs (R – hydrocarbon chain).
Source: ORNL

Results

ORNL has been developing surface modifications for CNTs to enable stable suspension in both polar and non-polar fluids. Figure I.1.2.3.2 shows two modifications, 1 and 6, for suspending CNTs in water and polyalkylene glycol (PAG), respectively, and their effectiveness is clearly demonstrated in Figure I.1.2.3.3. For the non-polar oils widely used in EV lubricants, five unsuccessful methods were tried before Modification 8, as observed in Figure I.1.2.3.2, provided a stable suspension of CNTs in a Valvoline EV d4 base oil at RT, as shown in Figure I.1.2.3.4(a). However, the addition of 1% dispersant, polyisobutylene succinimide dispersant (PIBSI), is still required to maintain stable suspension of CNTs at elevated temperatures like 100°C, as indicated in Figure I.1.2.3.4(d). Further development is ongoing.

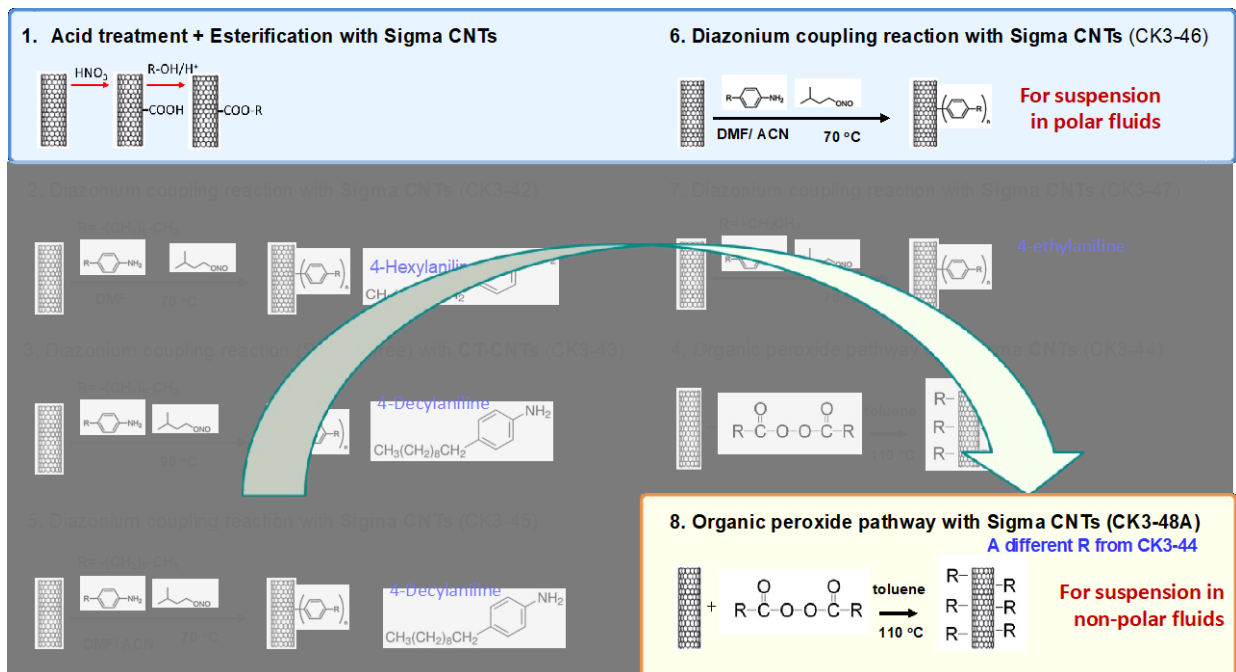


Figure I.1.2.3.2. ORNL's surface modifications for CNTs for stable suspension in both polar and non-polar fluids. Source: ORNL.

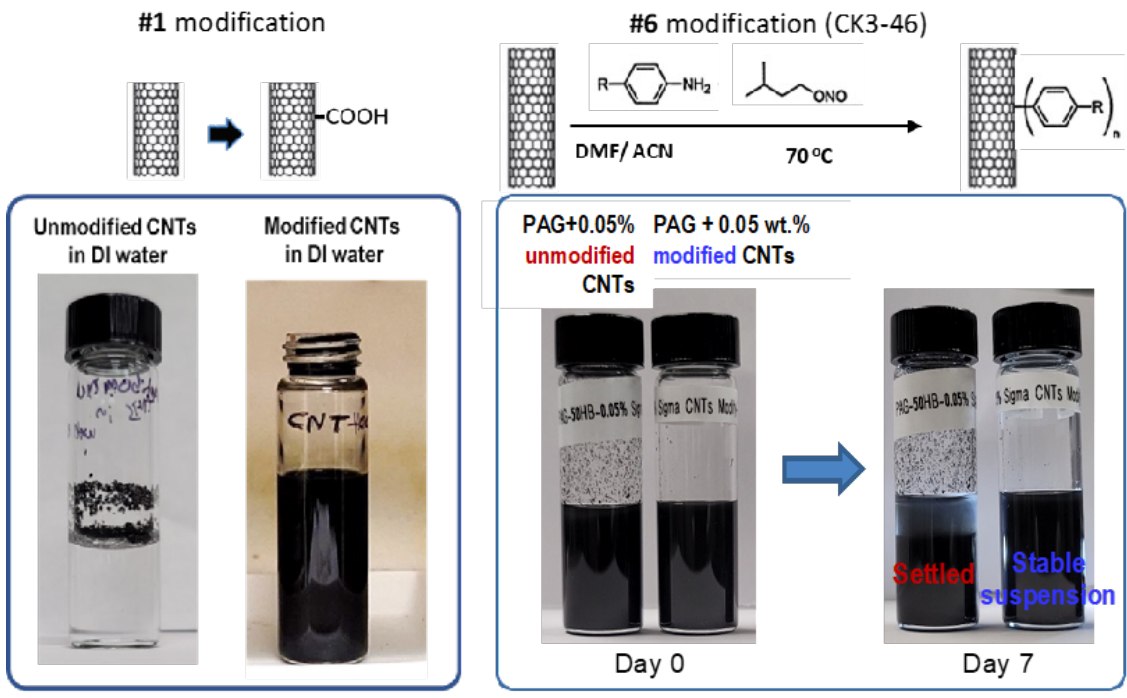


Figure I.1.2.3.3. Images of surface-modified CNTs show stable suspension in water and a polar oil (PAG). Source: ORNL.

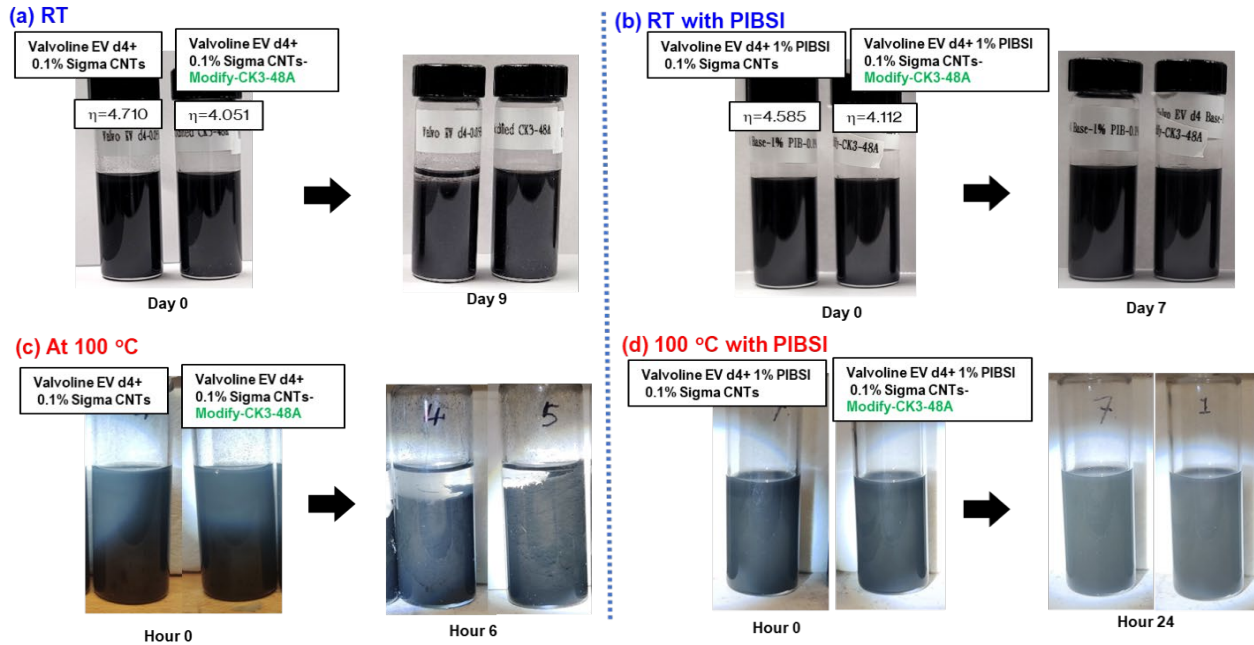


Figure I.1.2.3.4. Surface-modified CNTs showing: (a) stable suspension without a dispersant such as PIBSI in a non-polar oil (Valvoline EV base oil) at RT, (b) stable suspension with PIBSI in Valvoline EV base oil at RT, (c) unstable suspension without PIBSI in Valvoline EV base oil at 100 °C, and (d) stable suspension with PIBSI in Valvoline EV base oil at 100 °C. Source: ORNL.

For higher heat-transfer capability (i.e., Mouromtseff number) in a fluid, the increase in fluid viscosity should not overshadow the increase in the fluid’s thermal conductivity. Therefore, the impact of the addition of CNTs on oil viscosity was investigated. Unmodified CNTs were found to significantly increase oil viscosity. In the polar PAG base oil, 0.1 wt.% CNTs increase oil viscosity by 55–60%, depending on oil temperature. In the non-polar Valvoline EV d4 base oil, 0.1 and 0.25 wt.% CNTs increase oil viscosity by 13–20% and 45–410%, respectively. In contrast, organic modifications effectively mitigate the oil viscosity increases resulting from the addition of CNTs. In the polar PAG base oil, Modification 6 CNTs (CK3-46) at 0.1 wt.% increases oil viscosity by only 6–7% compared with 55–60% by unmodified CNTs. In the non-polar Valvoline EV d4 base oil, Modification 8 CNTs (CK3-48A) at 0.1 and 0.25 wt.% increase the oil viscosity by 0–4% and 22–61%, respectively, again much less than that which occurred with unmodified CNTs. Results are compared in Figure I.1.2.3.5, clearly showing that surface modification is effective in mitigating oil thickening upon the addition of CNTs.

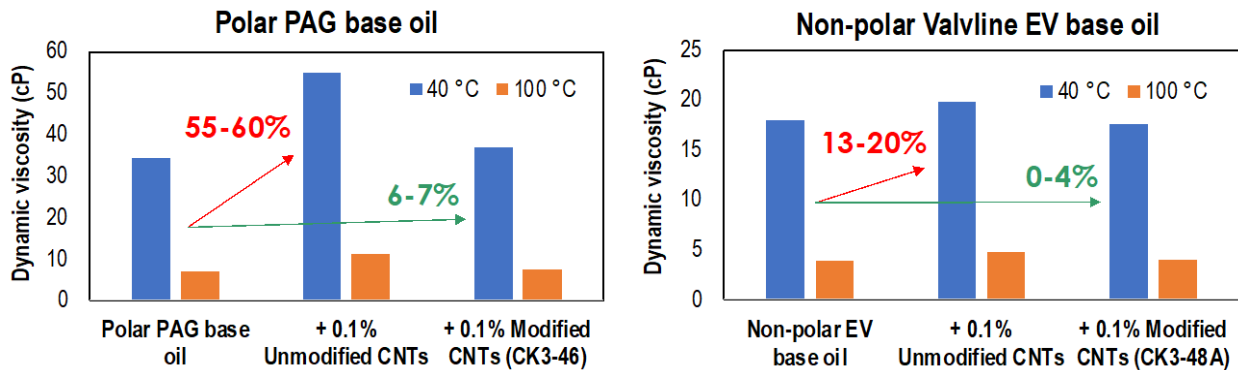


Figure I.1.2.3.5. Surface modification effective in mitigating oil thickening upon the addition of CNTs. (a) Polar oil (PAG) and (b) non-polar oil (Valvoline EV d4 base). Source: ORNL.

Surface modification of CNTs has demonstrated improved thermal conductivity (TC) when added into the Valvoline EV base oil. The TC of oils containing five types of CNTs of different diameters and lengths from Sigma, as listed in Table I.1.2.3.1, were measured using the standard hot-wire technique. At least four heating and cooling cycles were conducted with temperature ramping from 20° to 100°C. Initial TC tests were conducted by adding 0.1 wt.% of CNTs and later confirmed 0.025-0.05 wt.% as the optimal concentration range to minimize the viscosity rise. The Sigma CNTs Type 1 (length 10-20 µm and outer diameter of 50-90 nm) were found to be the most effective. As shown in Figure I.1.2.3.6, the TC of the oil containing Type 1 CNTs increased along with the number of heating and cooling cycles, and eventually reached a plateau of 11.5% improvement after 15 cycles. This could indicate CNTs are aligned to construct a CNT network, during the heating-cooling cycling, to provide more-efficient heat-transfer pathways. The addition of CNTs of Type 5 increased the oil TC by 5% in the first cycle but had no further improvement in the follow-on heating-cooling cycles. In addition, CNTs Type 2, 3, and 4 added oils showed little impact on the oil TC. No correlation between the TC improvement and the CNT size was observed.

Table I.1.2.3.1. Five types of CNTs with Different Diameters and Lengths

CNTs (from Sigma)	Diameter (nm)	Length (µm)
Type 1	50-90	10-20
Type 2	10	1.5
Type 3	6-13	2.5-20
Type 4	110-170	5-9
Type 5	10-40	500-1500

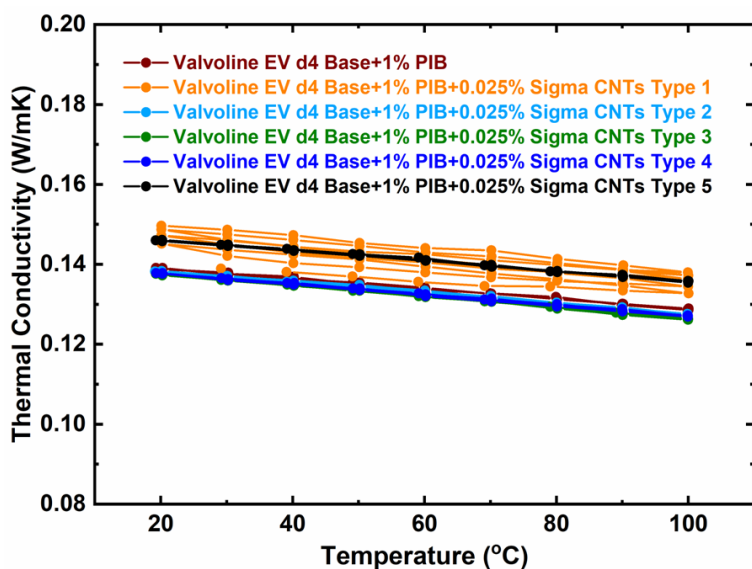


Figure I.1.2.3.6. Distinct impact of various types of CNTs on the oil TC. Source: ORNL.

Conclusions

This task explored the feasibility of using organically modified CNTs as additives for EV fluids to improve heat-transfer efficiency. The key technical challenge was to improve the oil's TC while also controlling oil viscosity. Various surface modifications were developed for suspending CNTs in both polar and non-polar fluids. As a result, an 11.5% improvement in TC of organically modified CNTs has been achieved by adding 0.025 wt.% into an EV base oil. Surface modification of CNTs also effectively reduced the oil viscosity increase from 13 to 60% down to 0 to 7%.

Key Publications

1. Qu, J., C. Kumara, H. Wang, H. M. Meyer, M. Lance, 2023, “Materials, lubricants, and cooling for heavy-duty EVs,” Project ID MAT237, DOE VTO Annual Merit Review, 13–15 June 2023, Washington, D.C., USA.
2. Qu, J., 2022, “CNTs for EV friction and thermal management,” The 2nd STLE Tribology and Lubrication for E-Mobility Conference, 30 November–2 December 2022, San Antonio, TX, USA.
3. Qu, J., 2022, “Ionic and nano lubricant additives for ICE, rear axle, and e-motor,” Valvoline International R&D Annual Meeting, 31 October–2 November 2022, Lexington, KY, USA (Invited Keynote).

References

1. Muratov, V. B., O. O. Vasil’ev, L. M. Kulikov, V. V. Garbuz, Y. V. Nesterenko, and T. I. Duda, 2012, “Thermodynamic properties of multiwalled carbon nanotubes,” *J. Superhard Mater.*, 34(3), 173–178. <https://doi.org/10.3103/S1063457612030045>.
2. L. Chen, and H. Xie, 2009, “Silicon oil based multiwalled carbon nanotubes nanofluid with optimized TC enhancement,” *Colloids Surf. A: Physicochem. Eng. Asp.*, 352(1–3), 136–140. <https://doi.org/10.1016/j.colsurfa.2009.10.015>.
3. Nanda, J., C. Maranville, S. C. Bollin, D. Sawall, H. Ohtani, J. T. Remillard, and J. M. Ginder, 2008, “TC of single-wall carbon nanotube dispersions: Role of interfacial effects,” *J. Phys. Chem. C*, 112(3), 654–658. <https://doi.org/10.1021/jp711164h>.

Acknowledgements

The author acknowledges the co-PI, C. Kumara, and the following key personnel from ORNL: W. Wang, H. Wang, and H. Meyer. The author also acknowledges our CRADA partner, Valvoline, with the following key personnel: J. Bonta, N. Ren, E. Murphy, and R. England.

I.1.2.4 Task 2D. Carbon Nanotube Coatings for Superlubricity and Thermal Management of Heavy-Duty Electric Vehicles (Oak Ridge National Laboratory)

Jun Qu, Principal Investigator

Oak Ridge National Laboratory
Materials Science and Technology Division
1 Bethel Valley Rd.
Oak Ridge, TN 37830
E-mail: qujn@ornl.gov

J. Allen Haynes, PMCP Consortium Manager

Oak Ridge National Laboratory
Materials Science and Technology Division
1 Bethel Valley Rd.
Oak Ridge, TN 37830
E-mail: haynesa@ornl.gov

Jerry L. Gibbs, DOE Technology Development Manager

U.S. Department of Energy
E-mail: Jerry.Gibbs@ee.doe.gov

Start Date: November 1, 2021

End Date: September 30, 2023

Project Funding: \$230,000

DOE share: \$230,000

Non-DOE share: \$0

Project Introduction

Parasitic frictional loss in EVs consumes 6% of the energy. Critical EV components—including the electric motor (e-motor), inverter, and battery—require more-efficient cooling to allow higher power output. This project aims to develop a CNT coating for potential applications to EV powertrains for friction and thermal management. This CNT coating possesses superlubricity (e.g., friction coefficient < 0.01) in macroscale sliding under minimum quantity lubrication in an ambient environment; thus, the coating is a very promising candidate for e-motor bearings and electric axle (e-axle) gears for improved mechanical efficiency. Potentially, this CNT coating also could be used to improve the heat dissipation in EV systems by taking advantage of the exceptionally high-TC of CNTs (e.g., $> 10\times$ higher than Al) and much increased surface area by $> 100\times$. One potential application is as a thermal-interface material (TIM) for enhanced heat-transfer. Another is as a surface coating for heat exchangers. This study develops these CNT coatings specifically for EV powertrain alloys to determine the sustainability of superlubricity, demonstrate the feasibility of enhanced heat-transfer capacity, and gain fundamental understanding for further improvements.

Objectives

This task focuses on gaining fundamental understanding and developing CNT-based coatings for EV powertrain components to enable enhanced frictional and thermal management.

Approach

Task 2D aims to develop novel coatings composed of CNTs for friction and thermal management of EVs. The coating process is based on the chemical vapor deposition (CVD) method and uses a low-cost precursor (e.g., ethanol). Thus, it has few geometric restrictions and is low-cost and readily scalable.

Unlike the superlubricity (defined as a CoF less than 0.01) reported in the literature, which is generally limited to the microscopic scale and often requires an ultra-high vacuum or inert environment to function (meaning it has limited practical use), the new ORNL CNT coating exhibits superlubricity behavior in macroscale sliding under an ambient environment [1]. A steady-state CoF less than 0.005 was observed in bench friction testing of the ORNL coatings. Such nearly frictionless behavior is achievable and sustainable at a proof-of-concept scale, even with minimum quantity lubrication. Basically, the CNT coating is “sacrificial” in running *in-situ* to

produce a thin graphene-containing tribofilm on the contact area that generates a graphene-graphene easy-to-shear interface, leading to the near frictionless behavior. A CNT superlubricity coating of this type could potentially be applied to the e-motor bearings and e-axle gears for improved mechanical efficiency. In addition to friction reduction, the superior wear protection of the CNT coating is also expected to enable the use of lower viscosity e-motor and e-axle lubricants, leading to a higher heat-transfer capacity.

The CNT coating can also be used for EV cooling, particularly the e-motor and inverter, by taking advantage of the exceptionally high-thermal-conductivity of CNTs (2,800–6,000 W/mK, compared with 88–251 W/mK for aluminum alloys), as well as the much increased surface area of the coatings (by 100–1,000×). For example, a CNT array used in our work was estimated to contain about 5 billion CNTs on a 1 cm² surface area. For CNTs of 50 nm diameter and 25 μm length each, the total surface area of the CNTs on the 1 cm² surface is 200 cm², a 200× increase.

These CNT coatings have the potential to function as an ideal TIM, such as between the e-motor stator and cooling jacket or between the inverter and cold plate. The thermal-interface accounts for almost 50% of total heat loss. Thin, high-thermal-conductivity interface materials are desired. A thermally conductive paste is often used to fill the roughness-induced gaps at the contact interface, but the TC of such commercial pastes is in the range of 0.1–8 W/mK. Our proposed approach is to coat CNTs on the cooling jacket or cold plate. When assembled under pressure, the CNT array at the high plateaus would be crushed and removed while the CNTs at the valleys would be deformed to interconnect and fill the gaps, resulting in a reduced thermal contact resistance. The CNT coating may be used together with a thermally conductive paste for combined contributions. Alternatively, premixing CNT segments into a thermally conductive paste would enhance the paste's TC. Another application of the CNT coating is heat exchangers. Growing CNTs on the fins of the e-motor heat exchanger or radiator is expected to improve the air-to-fin or liquid-to-solid heat-transfer.

Results

A Type 316 stainless-steel (SS) disk (10 or 12.7 mm in diameter) and SS foil (0.025-mm-thick) were used as substrates to deposit CNTs using a catalyst-free CVD process [1], [2]. The SEM images in Figure I.1.2.4.1 show top and side views of the CNTs grown on Type 316 SS disc and foil surfaces. The substrate surfaces appear to be black after the CVD process, which indicates good CNT coating coverage. The CNTs are vertically aligned to the substrate surface and have typical lengths and diameters of 10–25 μm and 40–60 nm, respectively. These CNT-coated SS disks (12.7 mm) and foils were used to examine the heat-sink properties, and 10 mm disks were used for the tribological testing.

A modified version of the ASTM D5470-17, “Standard Test Method for Thermal Transmission Properties of Thermally Conductive Electrical Insulation Materials,” was established at ORNL. Tests were set up with an infrared camera (FLIR SC7600 InSb), instead of the thermocouples suggested in the ASTM standard, to monitor the temperatures at critical locations. The experimental setup is shown in Figure I.1.2.4.2. A Type 316 SS cylinder of 1/2 in. diameter and 1/4 in. thickness was heated from the top and seated on an aluminum 6061 alloy cylinder of 1/2 in. diameter and 1 in. thickness, which stood on a water-cooled plate controlled at 18°C. The electric heater on the top of the stainless cylinder was used to control the mean temperature of the interface between the stainless and aluminum cylinders to ~38°C. The load frame was a servo-motor-driven system, and a 380 N (85 lb.) load was applied from the top to achieve a ~3 MPa contact pressure at the interface.

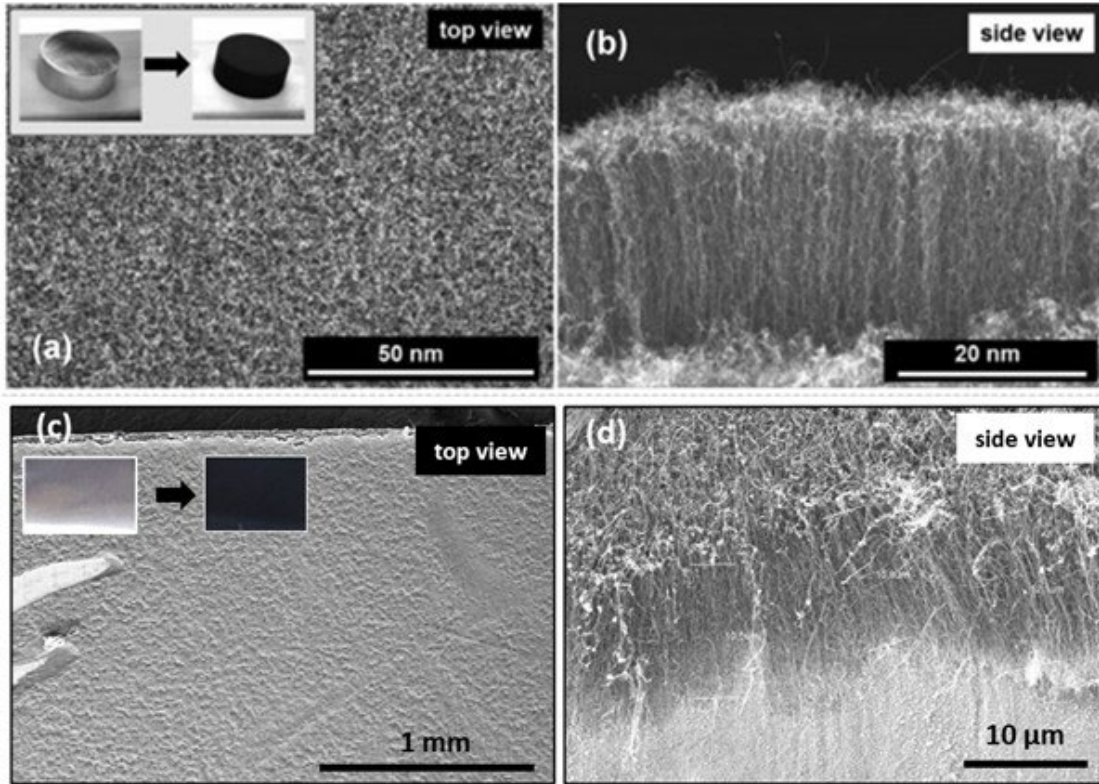


Figure I.1.2.4.1. CNT coating on Type 316 stainless disk (a and b) and stainless foil (c and d). Source: ORNL.

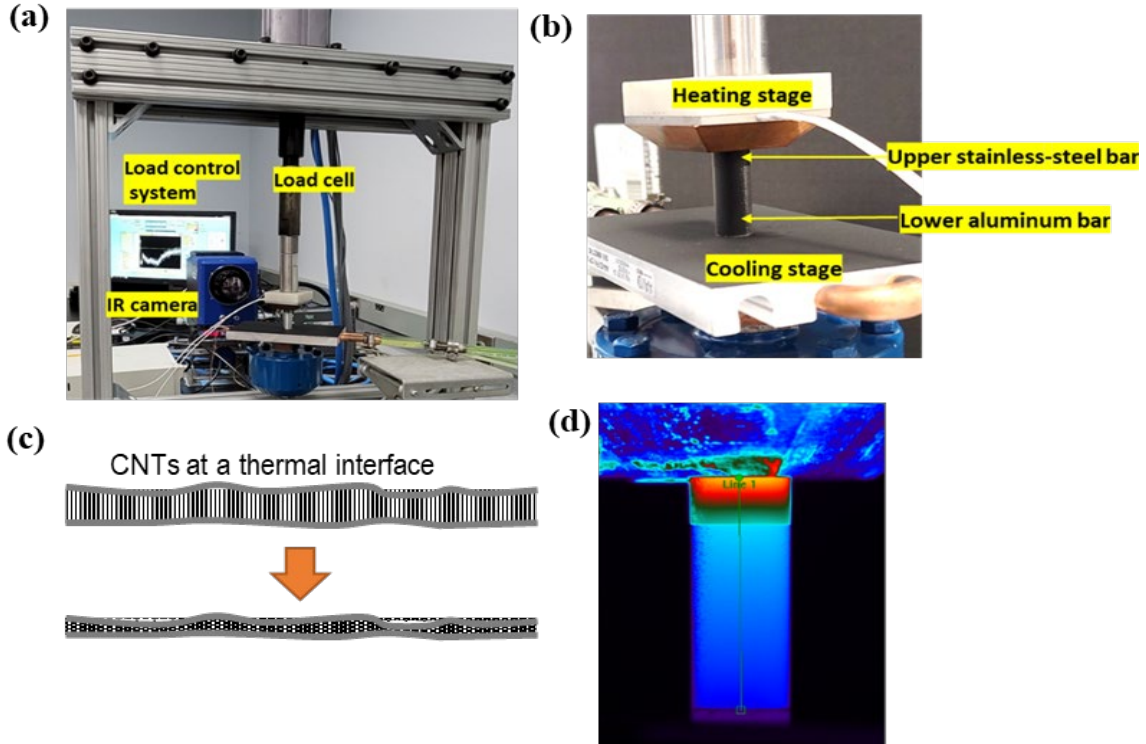


Figure I.1.2.4.2. A modified ASMT D5470-17 standard test to quantify the impact of the CNTs as thermal-interface materials. (a, b) Experimental setup, (c) schematic showing the compacted CNT coating at the thermal-interface, and (d) infrared image of the contact pair. Source: ORNL.

An array of CNTs was grown on the end surface of the SS cylinder and then tested as a candidate TIM at the contact interface against the aluminum cylinder. Under the contact load, CNTs may be compressed, creating a compact interface layer, as illustrated in Figure I.1.2.4.2(c). The CNT coating was then removed, and the same SS cylinder was put back into the setup with exactly the same orientation and alignment to ensure the same interface-contact geometry. No TIM was used between the stainless and aluminum cylinders in this case. Thus, thermal-interface impedance was measured without CNTs. Figure I.1.2.4.2(d) shows a representative thermal image of the contact pair, and the temperature profiles for tests with and without the CNT coating are compared in Figure I.1.2.4.3(a) and Figure I.1.2.4.3(b). The temperature profile was then used to determine the thermal impedance using Equations (1-7) in ASTM D5470-17. The calculated thermal impedances of the two tests are compared in Table I.1.2.4.1. The CNT coating demonstrated 40% reduced thermal-interface impedance compared to the bare interface.

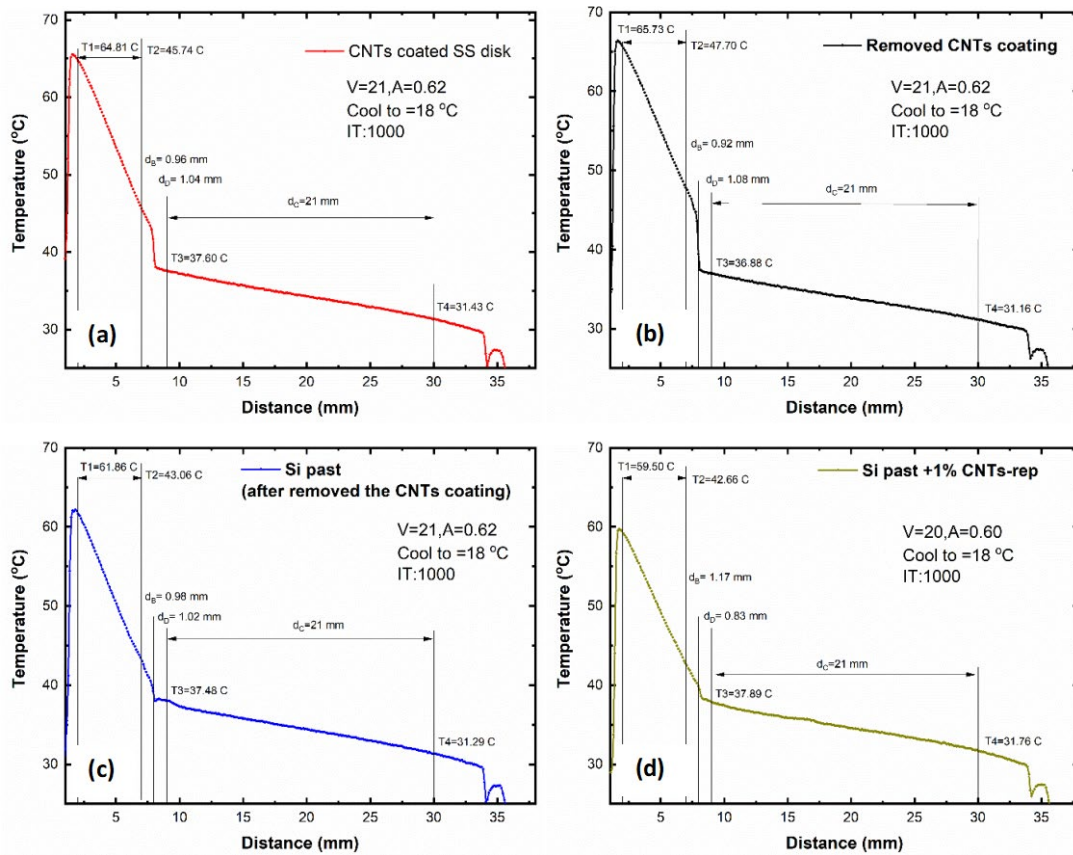


Figure I.1.2.4.3. Temperature profiles captured by the IR camera (a) with the CNT coating, (b) without the CNT coating, (c) using silicone paste, and (d) using silicone paste containing 1 wt% CNT particles. Source: ORNL.

Table I.1.2.4.1. Thermal Impedance Results Showing Substantially Reduced Thermal Impedance by Either Using the CNT Coating as a Standalone TIM or Using CNT Particles to Enhance a Conventional TIM

TIM	Thermal impedance ($\times 10^{-5} \text{ K m}^2/\text{W}$)	Impedance reduction by CNTs (%)
N/A (baseline 1)	6.75	-
CNT coating	4.06	40% vs. baseline 1
Silicone paste (Baseline 2)	1.45	-
Silicone paste + 1 wt% CNTs	0.62	57% vs. baseline 2

Additionally, a commercial silicone paste, Chemplex 1381 DE, was tested in its neat version and mixed with 1 wt.% CNTs (Vendor: Sigma-Aldrich, diameter 50–90 nm, length ~10–25 μm). The temperature profiles for the tests with and without the CNT particles are compared in Figure I.1.2.4.3(c) and Figure I.1.2.4.3(d). Table I.1.2.4.1 compares the calculated thermal impedances. The addition of 1 wt.% CNT particles reduced the thermal impedance by 57%. The proof-of-concept results suggest that the CNT coating could be used either as a standalone TIM for interfaces where pastes are not suitable due to temperature limitation (CNTs alone can sustain up to 400°C versus the 200°C limit for polymer-based pastes) or together with thermally conductive paste to further enhance the heat dissipation.

Because the CNT coating possesses both a very high TC and a large surface area, it could be an ideal coating for heat exchangers or heat sinks. In the initial trials, an SS foil was used as the substrate. The bare and CNT-coated samples were first heated and allowed to cool while researchers monitored the temperature change. The cooling rate was analyzed to understand the heat-transfer behavior. Figure I.1.2.4.4 shows the trial test setup and preliminary results. A bare and a CNT-coated SS foils, as shown in Figure I.1.2.4.4(a) were used to wrap around thermocouples and heated on a hot plate. Once reached the desired temperature (>80°C), they were quickly removed from the heating stage and allowed to cool under a controlled airflow (~100 cfm) inside a fume hood. Figure I.1.2.4.4(b) compares the temperature profiles of the bare and CNT-coated SS foils. The increased heating and cooling rates by the CNT coating suggests the potential application for heat exchangers. Further study, including a full matrix of validation experiments and thermodynamic calculations, is planned for FY 2024.

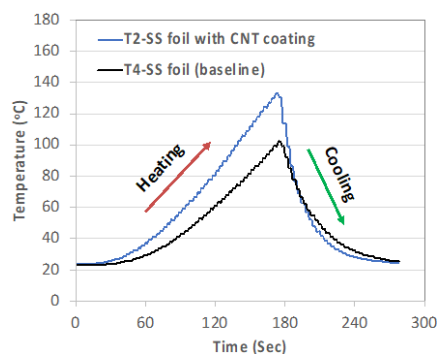
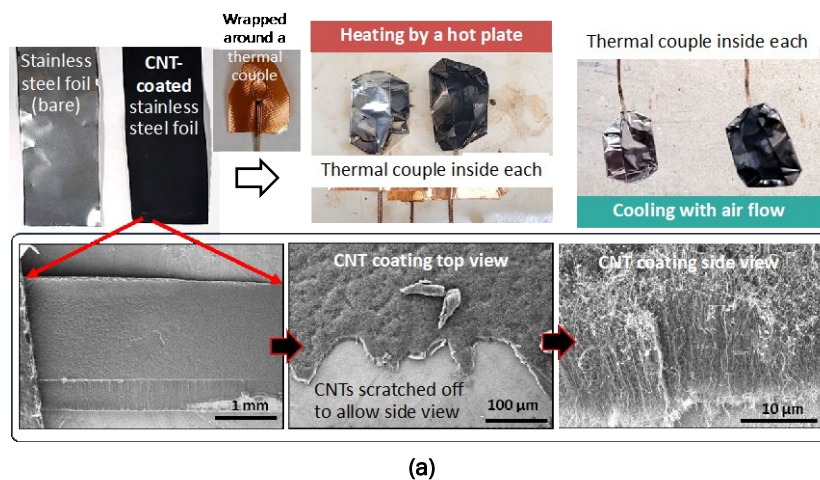


Figure I.1.2.4.4. Preliminary results suggest improved cooling efficiency by the CNT coating when applied to a stainless-steel foil. (a) Bare SS foil (silver) and CNT-coated SS foil (black) wrapping thermocouples first heated by a hot plate and then cooled by the airflow inside a fume hood; SEM images showing the CNTs. (b) Temperature profiles suggesting increased heating and cooling rates by the CNT coating. Source: ORNL.

Conclusions

In summary, under Task 2D, a coating composed of vertically aligned CNTs, deposited by CVD with ethanol precursor is being developed for frictional and thermal management for potential advanced EV components. The CNT coatings demonstrated superlubricity in an ambient environment as well as a 40% reduction in thermal-interface impedance. Adding 1% of CNT particles into a commercial silicone paste reduced the thermal-interface impedance by 57%. Preliminary feasibility tests of using the CNT coating on an SS foil have demonstrated improved cooling efficiency.

Key Publications

1. Kumara, C., M. J. Lance, and J. Qu, 2023, “Macroscale superlubricity by a sacrificial carbon nanotube coating,” *Mater. Today Nano*, 21, 100297. <https://doi.org/10.1016/j.mtnano.2022.100297>.
2. Qu, J., C. Kumara, and H. Wang, “CNT coating as a novel TIM,” U.S. Patent Application 63/432,435, 14 December 2022.
3. Qu, J., C. Kumara, H. Wang, H. M. Meyer, and M. Lance, “Materials, Lubricants, and Cooling for Heavy-Duty Electric Vehicles,” Project ID MAT237, *DOE VTO Annual Merit Review*, 13–15 June 2023, Washington, D.C., USA.
4. Qu, J., “CNTs for EV friction and thermal management,” *The 2nd STLE Tribology and Lubrication for E-Mobility Conference*, 30 November–2 December 2022, San Antonio, TX, USA.

References

1. Kumara, C., M. J. Lance, and J. Qu, 2023, “Macroscale Superlubricity by a Sacrificial Carbon Nanotube Coating,” *Mater. Today Nano*, 21, 100297.
2. Kumara, C., J. Qu, and P. A. Menchhofer. “Superlubricity coating containing carbon nanotubes,” U.S. Patent Application, 17/090,216, 5 November 2020.

Acknowledgements

The author acknowledges the assistance of the co-PI, C. Kumara, in addition to H. Wang and M. Lance.

I.1.2.5 Task 2E. Solid-Phase Joining and Processing Methods Towards Efficient, Heavy-Duty Electric Vehicle Motors (Pacific Northwest National Laboratory)

Piyush Upadhyay, Principal Investigator

Pacific Northwest National Laboratory
Energy Processes and Materials Division
900 Battelle Blvd.
Richland, WA 99354
E-mail: piyush.upadhyay@pnnl.gov

J. Allen Haynes, PMCP Consortium Manager

Oak Ridge National Laboratory
Materials Science and Technology Division
1 Bethel Valley Rd.
Oak Ridge, TN 37830
E-mail: haynesa@ornl.gov

Jerry L. Gibbs, DOE Technology Development Manager

U.S. Department of Energy
E-mail: Jerry.Gibbs@ee.doe.gov

Start Date: November 15, 2021

End Date: December 30, 2023

Project Funding: \$406,000

DOE share: \$406,000

Non-DOE share: \$0

Project Introduction

The purpose of this task is to develop solid-phase-based joining and processing technologies to produce high-performance dissimilar joints and materials to improve electric motors (e-motors) for EVs, resulting in lower cost, higher efficiency, and reduced weight. This task uses friction-stir derived joining and processing techniques to explore technical feasibility of producing (1) high-strength, high-conductivity AlCu joints; and (2) high-formability, high-resistivity, low-coercivity, and high-Si steel for rotor cores. These two subtasks are described below.

Subtask 1: AlCu Friction-Stir Welding (FSW) Joint Development

High-power induction-motor rotors are made entirely of either Al or Cu. The process of die-casting Al rotors is cost-effective and has gradually improved since first being developed a century ago. However, Al is 60% less electrically conductive than Cu. EV motors made from Cu can result in large efficiency improvements along with reduced motor package size and weight, which leads to a longer range between charging. However, the weight and cost of Cu and the high-cost of die-casting as compared to Al still represent challenges for the commercialization of Cu rotors. One approach is to replace the thick Cu end caps with lightweight Al, while retaining Cu shorting bars for improved conductivity throughout the steel core. Reduction of overall mass of the rotor (e.g., reduced inertia) can also increase durability, especially when operated at a higher revolutions per minute (rpms). However, significant challenges exist in manufacturing this hybrid assembly. The loss of EC and mechanical strength at the AlCu transition region/interface is a primary challenge. This challenge is due to vastly different melting points, high-temperature flow stresses, persistent oxide layers, and coefficient of thermal expansion mismatch. The AlCu interface created by both fusion and solid-state methods contains brittle intermetallic compounds that can negatively impact EC and mechanical strength at the joint. Proper control of thickness and composition of the intermetallic compound layer is critical for consistent mechanical and electrical performance. This task intends to leverage solid-phase, processing-based technological expertise at PNNL to enable low-weight AlCu hybrid rotors.

Subtask 2: : Friction-Stir Processing (FSP) of FeSi Steel

Rolled laminate sheets of ferromagnetic (Fe-2–3% Si) material is used as a magnetic core for induction rotors and stators. The current manufacturing technology begins with cold-rolling of hot-rolled strips, followed by

batch annealing and temper rolling. Subsequently, strip blanks are stamped, and the laminations are subjected to annealing treatments. These steps are followed to ensure that electrical and magnetic properties are optimized. The need is for high-magnetic permeability, high-saturation induction, low-coercivity, and low-eddy current loss. A roadblock to increasing efficiency is the gauge thickness of laminations. To minimize electrical conduction, and thereby minimize core-loss through maximizing magnetic flux density, the laminations are kept as thin as possible (e.g., 0.35 mm or thinner). This leads to increased manufacturing costs. One solution is to decrease resistivity by increasing the Si content of steel. Increased Si content has been shown to produce a good balance of high-saturation magnetization, high-electrical resistivity, and low Fe loss. However, conventionally manufactured high-Si steel is brittle and has poor formability, leading to higher rejection rates and blanking tool costs. Significant cost-savings could be achieved if high-Si steel can be produced with better formability.

Objectives

The goal of Task 1 is to mature friction-stir techniques to fabricate relevant AlCu coupons with co-optimized mechanical strength and EC for AlCu hybrid rotors. Experimental trials includes the fabrication of coupon and near component-level microstructural and mechanical characterization. Task 2 will develop FSP methods to produce high-Si steel from cast/rolled billet. The aim is to produce superior microstructures and heal any porosity present in high-Si steels towards increased resistivity and formability performance. Experimental trials will include coupon-level microstructural and mechanical property characterization.

Approach

Subtask 1: AlCu FSW Joint Development

Our approach for the second and final year will use novel AlCu interface geometries, tool design, and welding parameters to produce and study a large set of AlCu-bonded joints. End-cap construction is typically made of multiple stacks of thin sheets (as opposed to a single monolithic plate) in order to ensure hole tolerances are met during stamping and waterjet-cutting operation. For this rotor construction, five stacked Al sheets (2 mm each) are to be bonded to vertically arranged Cu shorting bars. Having proved the method at the linear coupon-level to join five stacked Al sheets to vertically configured copper shorting bars, the team set out to transfer the method to a mock rotor part. Mechanical and electrical testing of the joints are performed as the welding process is matured and benchmarked against the overcasting method. The overall construction of the induction-motor rotor is shown in Figure I.1.2.5.1.

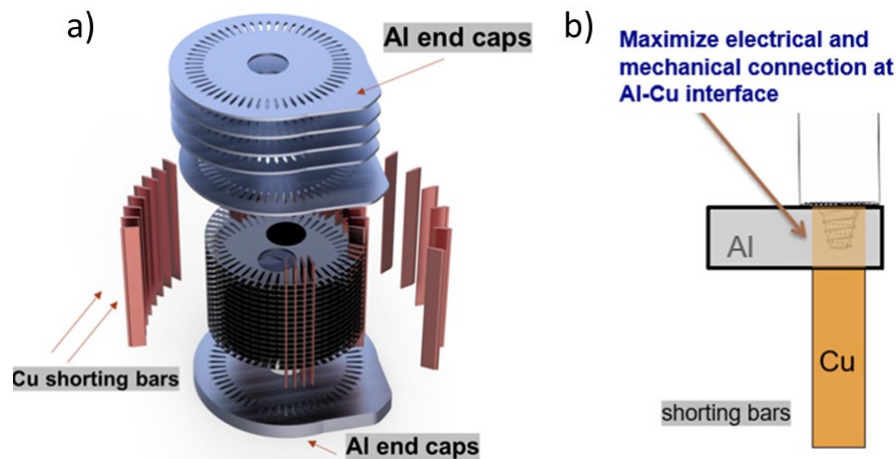


Figure I.1.2.5.1. Schematic of the (a) AlCu hybrid rotor, and (b) joining of Al to grooved Cu shorting bar.

Source: PNNL.

Subtask 2: AlCu FSP of FeSi Steel

This task will evaluate FSP of FeSi (5–6.5%). Process parameters, tooling, and thermal management will be optimized towards higher formability of high-Si electrical steels. This task will perform systematic

developmental work with microstructural, mechanical, and electrical characterization towards the goal of producing high-formability high-Si steel.

Results

Subtask 1: AlCu FSW Joint Development

Experimental process development was conducted towards the demonstration of viable joints between a five-sheet-stack of 2-mm-thick AA6101-T6 sheets with vertically configured Cu shorting in both simplified-linear and circular-rotor setups. Different tool geometries, welding schemes (e.g., double vs. single-pass, extent of pi tool engagement to copper shorting bars) were considered during the developmental runs. Once the linear coupons showed enough joint strength in static tensile testing, a welding path and clamping-fixture design for mock end-cap demonstrations were also performed. Copper shorting bars of the right dimension, with and without Ni-coating, and Al sheets for some trials were provided by General Motors, LLC (GM). Custom fixtures that are capable of appropriately reacting to the process loads while maintaining integrity of the shorting bar and end-cap assembly were designed and built in-house, as shown in Figure I.1.2.5.2(a).

Welds made using two passes of FSW lines each at the edge of the shorting bars yielded highest static strength. These mock end caps were produced for demonstration purposes for this condition. Figure I.1.2.5.2(b) shows the welding setup ready to be friction-stir welded affixed in a rotary table with clamping arrangements. A top and bottom view of the produced mock end-cap, containing ~4-in.-long Ni-coated copper shorting bars, are shown in Figure I.1.2.5.2(c) and Figure I.1.2.5.2(d), respectively. A welding-parameter combination, consisting of spindle-speed of 800 rpm at a welding speed of 100 mm/min was selected for this run. After welding, individual samples were extracted from several locations on the mock end-cap for metallography and tensile testing. Traverse and longitudinal weld sections at the joint interface show defect-free bonding between the Cu and Al interface, and a good bonding between the five layers of Al is also apparent, as indicated in Figure I.1.2.5.3(a–f). X-ray computed tomography was used to validate the bonding between the Al layers and Cu shorting bars, as shown in Figure I.1.2.5.3(g) and Figure I.1.2.5.3(h), respectively. Because the FSW tool is designed to minimally process the harder Cu while fully plasticizing Al matrix, a process akin to machining can occur in Cu. The result is distribution of Cu particles in the Al matrix and solid-state bonding of Cu to Al. Additionally, the intense local plasticization due to the FSW results in bulk deformation of the shorting bar, creating interlocking of the Cu with Al which may contribute to the overall strength of the joint.

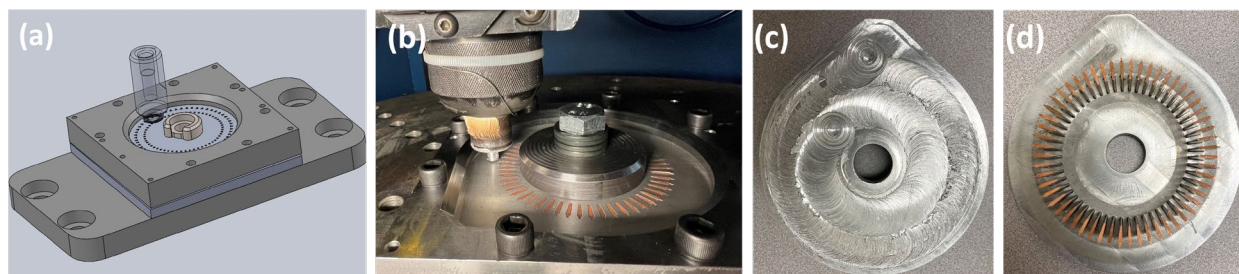


Figure I.1.2.5.2. (a) Schematic drawing showing isometric view of a mock end-cap setup. (b) Al to Cu shorting bar mock end-cap setup, ready to be welded in a rotary FSW system at PNNL. (c) Top-view of end-cap rotor. (d) Bottom view of end-cap rotor. Source: PNNL.

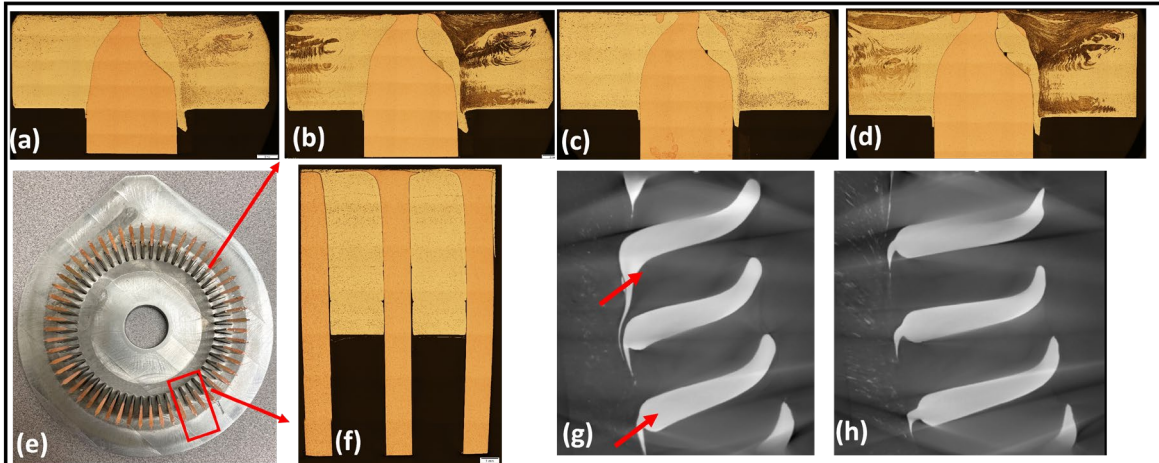


Figure I.1.2.5.3. (a–f) End-cap rotor back view with red arrows showing cross-sections for optical imaging. Unetched transverse cross-sections are shown in (a) and (c), while etched longitudinal cross-sections are provided in (b) and (d). (e) Bottom view of end-cap rotor. (f) Magnified view of the image highlighted by the red box in (e). (g–h) X-ray computed tomography of top-view from linear welds showing (g) Cu-interlocking (red arrows) and (h) distribution of Cu particles (white arrow) following FSW. Source: PNNL.

Process development was also performed towards establishing a single-pass fabrication route where the tool traverses at the center of the joint line such that Cu is minimally plasticized while Al was friction-stir welded. For this arrangement, a stack of Al sheets containing appropriate hole sizes made using laser cutting was used, as indicated in Figure I.1.2.5.4(a). After some iterative tool and process development, defect-free welds that suggest good bonding was obtained, as shown in Figure I.1.2.5.4(b). An intimate bond between the horizontal Al stacks and vertical shorting bars is apparent in the series of cross-sectional macrographs shown in Figure I.1.2.5.4(c).

To ensure the AlCu joint in the Cu rotor can perform well in service conditions that typically are at elevated temperatures, some high-temperature (HT) tensile testing on coupon-level linear joints were also performed. Before conducting the HT tests, baseline RT static tensile tests were carried out. The bar chart in Figure I.1.2.5.5(a) summarizes joint strength in tensile tests for various conditions. The load vs. crosshead displacement is also shown in Figure I.1.2.5.5(b). Pullout load of linear and end-cap rotor joints at RT are 3364 ± 64 N (six samples) and 2900 ± 300 N (five samples), respectively, whereas pullout load of linear joints at 100°C is 3070 ± 43 N (six samples), which is comparable to the end-cap rotors and slightly lower than the linear welds. However, pullout strength at both RT and HT is higher than the die-cast AlCu sample data provided by GM. Cu shorting bars fracture mostly at the interface during pullout tests. Sample-to-sample variation in the pullout load is minimal for linear-pass RT and HT samples. Limited fatigue testing was performed to understand the effect of cyclic loading in this dissimilar joint. The static joint strength for these samples was determined to be 3364 ± 64 N. For fatigue testing, samples were subjected to a load ratio of 0.1, with a maximum load of 2450 N, following a similar test based on data provided by GM. One of the samples achieved 455,000 cycles to failure (Nf), surpassing an overcasting sample based on data provided by GM (Nf = 402,650). A total of four samples were tested. The average of the four samples was approximately 241,000 Nf, with a standard deviation of about 130,000. To gain a deeper understanding of the intermetallic layer and its impact on fatigue properties, collaboration with the Thrust 4 Characterization team is ongoing.

Figure I.1.2.5.6 highlights two full rotors each containing a total of $4\times$ lines of circular welds to bond the Cu shorting bars to Al stacks that form the end caps. The full rotors, as observed in Figure I.1.2.5.6(a) were manufactured and tested until failure, as indicated in Figure I.1.2.5.6(c–f), respectively. Load vs. displacement curves obtained for the full rotor testing are shown in Figure I.1.2.5.6(b).

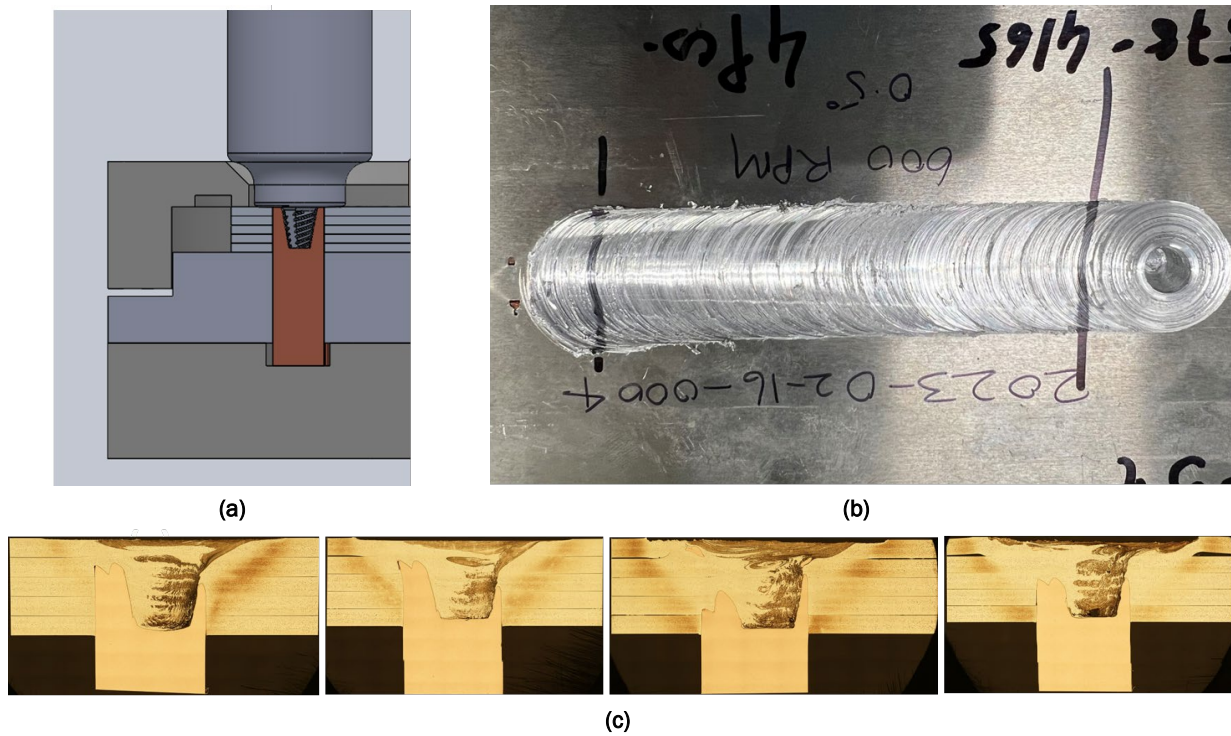


Figure I.1.2.5.4. (a) Cross-sectional view of mock end-cap setup for a single-pass FSW to join the Al end-cap to a Cu shorting bar. (b) Crown surface showing a linear FSW joint using single-pass. (c) A series of 4x lines of transverse cross-section images showing defect-free joints. Source: PNNL.

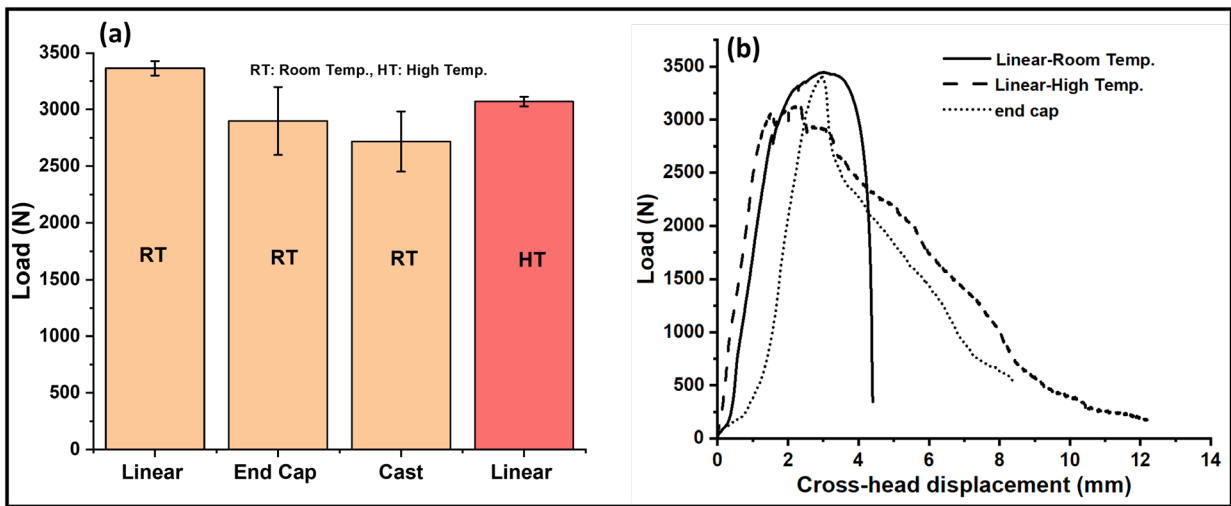


Figure I.1.2.5.5. (a) Pullout load comparison for (b) linear welds at RT and HT with end-cap welds and die-cast Al-Cu. Source: PNNL.

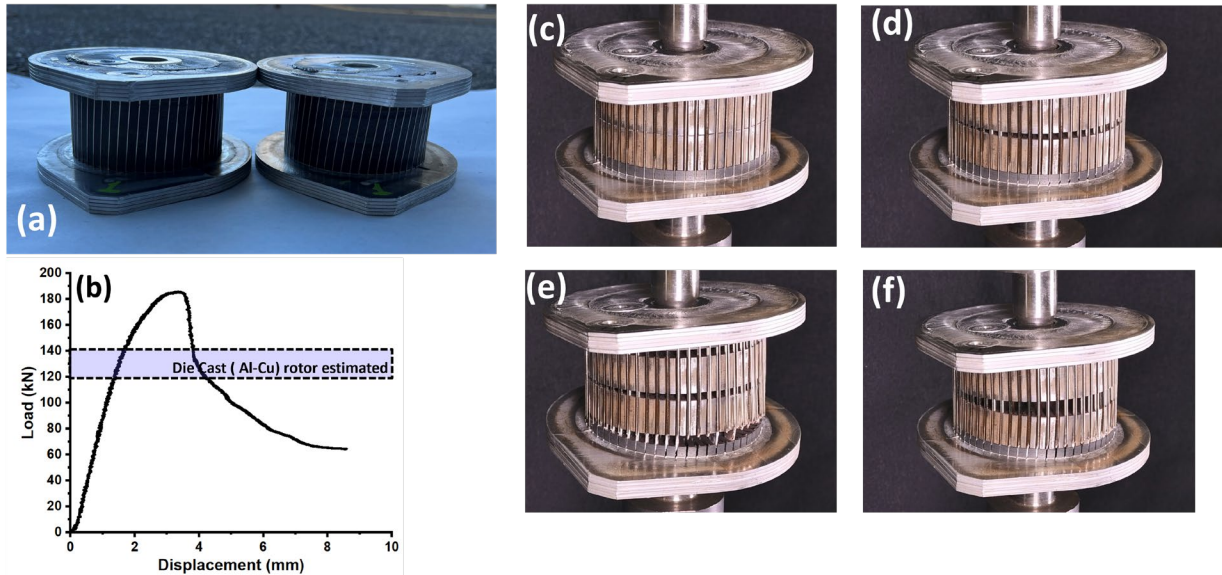


Figure I.1.2.5.6. (a) Two full-sized rotors made using the process developed in this work. (b) Load vs. displacement value obtained after full-size rotor testing and estimated die-cast rotor strength for benchmarking. (c–f) Al-Cu hybrid rotors being pull-tested. Source: PNNL.

Subtask 2: Al-Cu FSP of FeSi Steel

In FY 2023, our research pivoted towards advancing the process development of high-Si electrical steels, specifically in the 5.0–6.5 wt.% range. Building on the groundwork laid by the team’s task in FY 2022, our team has honed FSP techniques to enhance the formability of FeSi alloys, essential for high-performance electrical-motor laminates. Our investigation involved FSP at a lower processing temperature of 750°C, resulting in a favorable combination of processing techniques and resulting mechanical properties. The process temperature was measured using a thermocouple attached 5 mm from the tool shoulder. PNNL’s temperature control algorithm that modulates tool torque to maintain a set temperature was used for FSP.

Figure I.1.2.5.7(a) shows a typical FSP run on an electrical steel precursor. Argon gas was used to create a shielding atmosphere to avoid surface oxidation at HT. Figure I.1.2.5.7(b–e) show all FSP runs conducted at 750°C with temperature control highlighting excellent surface finishes in processed regions, even with high-Si-content steels, which are known to be highly brittle. With the increase in Si content, some hairline cracks were observed next to the edges of the friction-stir processed regions. It may be possible to reduce or eliminate hairline cracks with appropriate thermal management. In parallel, our wire-extrusion experiments on steels with 4 and 5% Si content resulted in fully consolidated extrudates, as shown in Figure I.1.2.5.7(f–g).

In the preceding FY, the team demonstrated that FSP of Fe-4%Si steel could achieve substantial grain refinement without detriment to ductility. This FY, the focus expanded to friction-stir extrusion to produce wires. After some process development, Fe-4%Si steel was extruded using a W-25%Re tool, resulting in the production of a 5-mm-diameter wire. Figure I.1.2.5.8(a) provides low-magnification backscattered electron (BSE)-SEM images of this Fe-4%Si steel, while Figure I.1.2.5.8(c) shows a low-magnification inverse pole figure (IPF) map of the corresponding region shown in Figure I.1.2.5.8(a). The microstructural characterization of the extruded wire revealed a bimodal grain distribution, with the wire’s core featuring larger grains up to 150 μm in diameter, and the edge exhibiting finer grains approximately 50 μm in diameter. This distribution is a characteristic byproduct of the extrusion process, which involves substantial shear forces. Moreover, the edge of the wire showed a uniform distribution of precipitates, with a lower contrast than the matrix, while the core did not display such features, as evidenced in the high-magnification BSE images in Figure I.1.2.5.8(b) and Figure I.1.2.5.8(d).

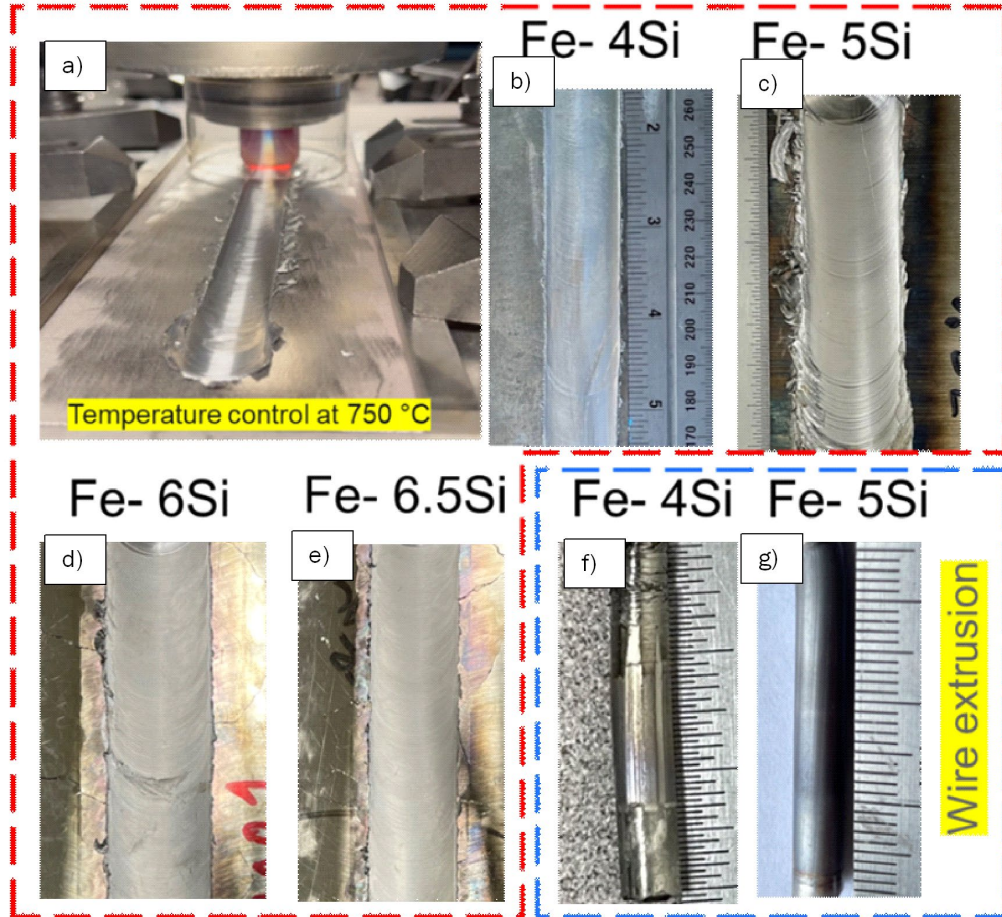


Figure I.1.2.5.7. (a) FSP of FeSi alloy. (b-e) FSP samples with 4–6% Si content. (f-g) Wire-extrusion samples with 4 and 5 wt.% Si. Source: PNNL.

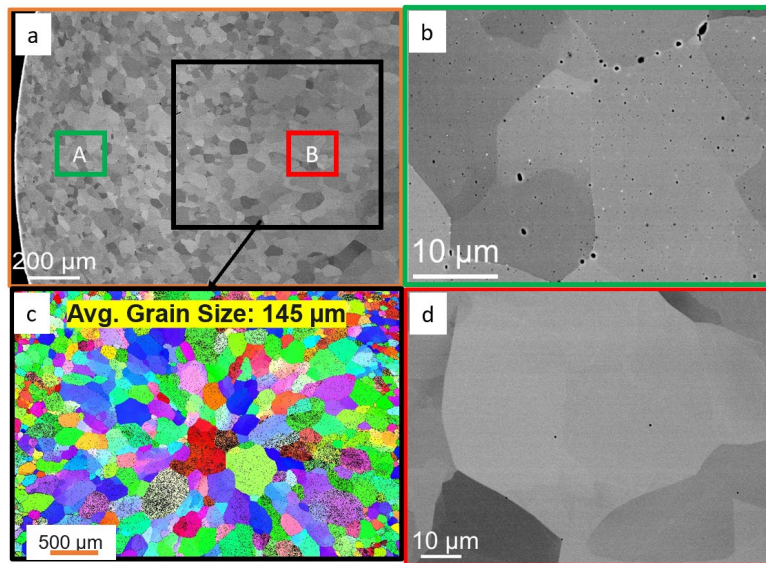


Figure I.1.2.5.8. (a) Low-magnification BSE-SEM images of Fe-4.0%Si. (b) High-magnification BSE images of edge region. (c) Low-magnification IPF map of the corresponding region shown in (a). (d) High-magnification BSE images of core region. Source: PNNL.

Our team extended our investigation to encompass FSP of electrical steels with Si content of 5, 6, and 6.5 wt.%. The intense plastic deformation and frictional heating intrinsic to FSP result in a distinctive basin-shaped nugget region. A montage of SEM images in Figure I.1.2.5.9(a) illustrates the processed region containing the FSP nugget in the transverse cross-section. The IPF, as observed in Figure I.1.2.5.9(b) and obtained through the EBSD analysis shown in Figure I.1.2.5.9(c), indicates an average grain size of 10 μm at the center of the nugget. Higher-resolution BSE images confirm the absence of large-scale precipitates in the nugget. Furthermore, electrical steel with 5 wt.% Si, post-FSP, retains a total elongation of approximately 22%, with a strength of around 700 MPa, as shown in Figure I.1.2.5.9(d). These findings provide valuable insights into the microstructural changes and mechanical performance of electrical steels with higher Si content subjected to FSP.

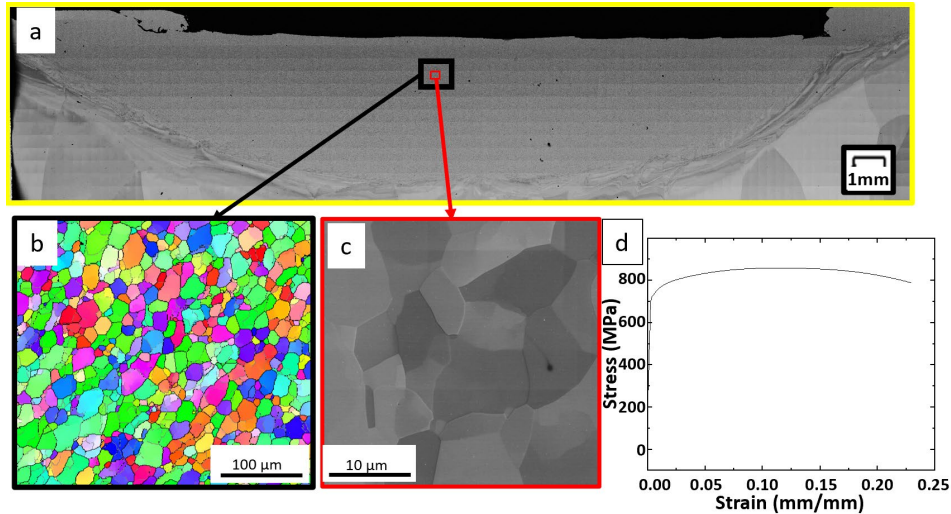


Figure I.1.2.5.9. (a) Low-magnification image showing the basin-shaped nugget after FSP of Fe-5%Si steel. (b) Higher magnification IPF map showing grain size and distribution in nugget. (c) High-magnification EBSD image showing absence of any large precipitate in nugget. (d) Stress-strain curve of the friction-stir processed Fe-5%Si steel. Source: PNNL.

A similar microstructural refinement was observed in FSP electrical steel with 6.5 wt.% Si, with the average grain size at the nugget's center measuring approximately 8 μm , as demonstrated in the IPF map shown in Figure I.1.2.5.10(a). The absence of visible precipitates was also noted in the higher magnification BSE image of Figure I.1.2.5.10(b). Ongoing studies under the Thrust 4 Characterization project using TEM and APT are expected to provide a more detailed characterization of the microstructural features. Furthermore, our team explored the mechanical properties through nanoindentation tests, as observed in Figure I.1.2.5.10(c), to gain insights into the compression response of the processed material. The ensuing section summarizes mechanical properties and draws comparisons with existing literature, enhancing our understanding of the material's behavior under these processing conditions.

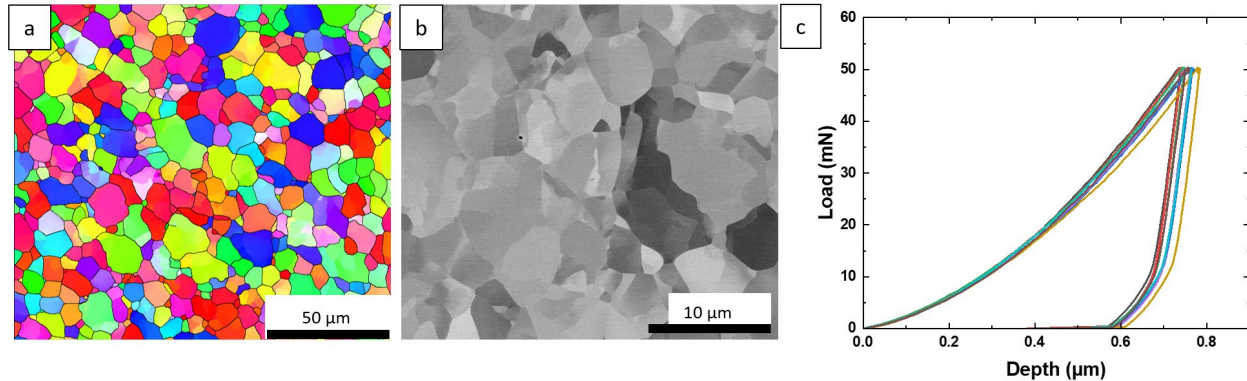


Figure I.1.2.5.10. (a) IPF map of the nugget region of the Fe-6.5%Si electrical steel, showing the fine grain microstructure and grain size distribution. (b) High-magnification BSE image of the same region. (c) Nanoindentation load vs. displacement curves. Source: PNNL.

The mechanical and magnetic properties of processed samples are summarized and compared with emerging and more mature methods to produce high-Si electrical steels in Figure I.1.2.5.11. FSP demonstrates a noteworthy equivalence to that achieved in high-Si electrical steels, which are manufactured through labor-intensive, multistep methods. The comparison includes methods such as melt-spinning (MS) and binder-jet additive manufacturing (BJAM). MS30 and MS5 refer to two cases of MS process done at high and low wheel speeds resulting in fast (smaller grains) and slow (larger grains) cooling rates, respectively [1]. On the other hand, the BJAM approach involves a series of steps, including curing, hold curing, vacuum-furnace sintering, and subsequent annealing, all preceding the measurement of hardness and coercivity [2]. When contrasting the FSP-processed and BJAM-formed samples, it is evident that, despite the grain size obtained after BJAM being approximately $5\times$ larger than that achieved through FSP, the hardness values are similar. Similarly, the MS-30 specimen exhibits higher hardness than the FSP sample. Overall, the comparison indicates that the hardness values for MS, BJAM, and FSP samples are comparable, highlighting the potential of FSP as a viable alternative with comparable performance. The hardness of the FSP samples is shown in Figure I.1.2.5.11(a), while the coercivity of the FSP samples is shown in Figure I.1.2.5.11(b). What sets FSP apart is its inherent promise—achieving comparable coercivity values straight from the production process. Moreover, the potential for further refinement exists, particularly through the reduction of grain size to the nanoscale. This anticipated reduction in grain size holds the prospect of not only maintaining parity with existing coercivity values, but potentially augmenting coercivity even further. FSP’s unique advantage lies in its capacity to enhance coercivity without necessitating additional elaborate post-processing steps, marking a significant advancement in the domain of electrical steel production.

Moreover, our team expanded our research to include the cold and hot-rolling of base material and FSP samples, specifically for Fe-4 wt.% Si, which are shown in Figure I.1.2.5.12. The samples chosen for rolling, extracted from the FSP nugget zone, were consistent in size—approximately $10 \times 5 \times 3$ mm. For hot-rolling, the samples were incrementally reduced from 3 to 1 mm and then to approximately 0.4-mm-thick. The cold-rolling process began at a thickness of 1 mm and aimed for a similar final thickness or continued until the material fractured. For hot-rolling, a 20% reduction in each step was obtained while for cold-rolling, ~ 7 –10% reduction was achieved in each step. Notably, the base material developed cracking by the third step of rolling and was completely bifurcated by the fourth. In contrast, the FSP material withstood up to seven rolling steps, successfully achieving the targeted thickness of approximately 0.4 mm. This enhanced ductility in the FSP samples emphasizes its superior performance and potential in simplifying the laminate-production process for electrical steel applications.

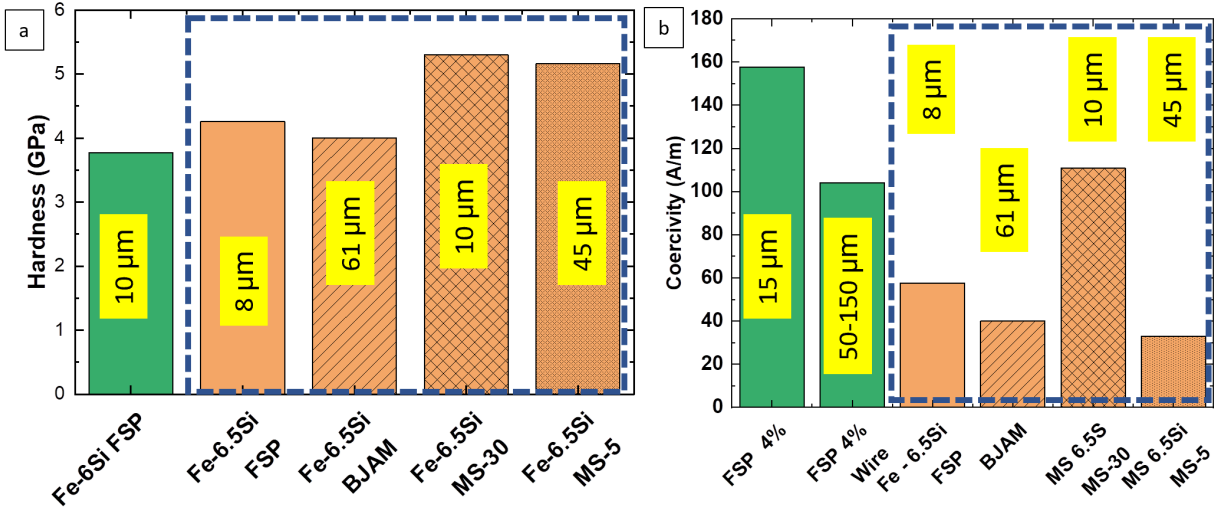


Figure I.1.2.5.11. (a) Hardness and (b) coercivity values of high-Si containing electrical steel produced by FSP, BJAM, and MS. Source: PNNL.

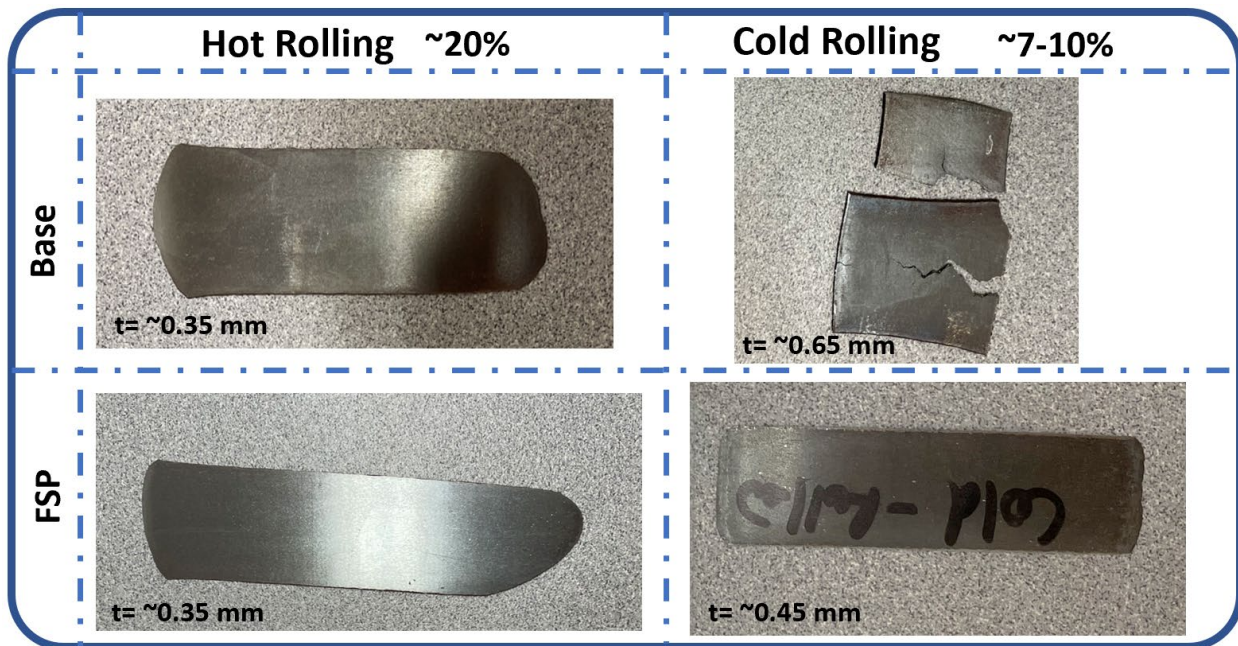


Figure I.1.2.5.12. Results of hot and cold-rolling on Fe-4%Si, showing comparison of performance between as-received and FSP conditions. Source: PNNL.

Conclusions

FSW enabled production of an induction-motor rotor that contained a lightweight Al end-cap connected to Cu shorting bars. Welding approach, tooling, fixturing to implement the assembly and manufacturing of dissimilar material was developed in Task 1 of this project. Joint cross-sections static and dynamic strength, as well as HT properties show promising results. Processes developed in this work enabled an ability to manufacture lightweight full-sized rotors of Al and Cu.

For the FeSi task in the last year of this project, our team explored the viability of solid-phase processing for high-Si electrical steel, specifically within the 5–6.5 wt% range, with a focus on producing laminates for

electrical-motor applications. This period saw the development of specialized tooling and the refinement of processing parameters tailored for FSP and extrusion techniques. Our team undertook a comprehensive characterization of mechanical, microstructural, and magnetic properties of the processed samples, benchmarking our findings against both emerging and established manufacturing methods.

In wire extruded Fe-4%Si steel, a bimodal grain distribution with distinct grain sizes at the core and edge was observed. A refined grain size in the nugget region, and mechanical properties of the processed materials, such as total elongation and strength, were outlined. In comparison to other emerging manufacturing methods like MS and BJAM, for work performed thus far, FSP achieves comparable hardness values and coercivity, offering a promising alternative with the added advantage of simplified processing routes. Additionally, preliminary hot- and cold-rolling experiments on FSP samples showed excellent rollability compared to unprocessed precursors. This indicates the strong potential of FSP in creating laminates through a more-efficient process, reducing the number of steps required by traditional manufacturing methods. These developments reinforce our anticipation that FSP can play a crucial role in the future of high-silicon electrical steel-laminate production.

References

1. Ouyang, G., B. Jensen, W. Tang, K. Dennis, C. Macziewski, S. Thimmaiah, Y. Liang, and J. Cui, 2018, "Effect of wheel speed on magnetic and mechanical properties of melt-spun Fe-6.5 wt.% Si high-silicon steel," *AIP Adv.*, 8, 056111. <https://doi.org/10.1063/1.5006481>.
2. Cramer, C. L., P. Nandwana, J. Yan, S. F. Evans, A. M. Elliott, C. Channasamy, and M. P. Paranthaman, 2019, "BJAM method to fabricate near-net-shape crack-free highly dense Fe-6.5 wt.% Si soft magnets," *Heliyon* 5(11), e02804. <https://doi.org/10.1016/j.heliyon.2019.e02804>.

Acknowledgements

At PNNL, welding, processing, and data analysis activities were supported by H. Das, S. Shukla, and M. Blocher, in association with M. Pole, T. Liu, and A. Devraj. Mechanical testing was performed by T. Roosendaal, R. Seffens, and E. Nickerson. Electrical and magnetic property testing were conducted by K. Kappagantula and A. Nittala. Metallography and hardness testing was completed by A. Guzman and M. Blazon. The rolling was performed by M. Rhodes and R. Seffens. The authors are thankful to B. Carlson and J. Agapiou for their material and technical support, as well as their valuable input during Task 1.

I.1.3 Thrust 3: Advanced Processing and Additive Manufacturing for Electric Vehicles

I.1.3.1 Task 3A. Fundamental Development of Additive Manufactured Lightweight Alloys for Electric Vehicle Propulsion (Oak Ridge National Laboratory)

Alex Plotkowski, Principal Investigator

Oak Ridge National Laboratory
Materials Science and Technology Division
1 Bethel Valley Rd.
Oak Ridge, TN 37830
E-mail: plotkowskij@ornl.gov

J. Allen Haynes, PMCP Consortium Manager

Oak Ridge National Laboratory
Materials Science and Technology Division
1 Bethel Valley Rd.
Oak Ridge, TN 37830
E-mail: haynesa@ornl.gov

Jerry L. Gibbs, DOE Technology Development Manager

U.S. Department of Energy
E-mail: Jerry.Gibbs@ee.doe.gov

Start Date: October 1, 2022

End Date: September 30, 2023

Project Funding: \$350,000

DOE share: \$350,000

Non-DOE share: \$0

Project Introduction

Al alloys are widely used in the automotive industry due to their high-specific strength. Emerging hybrid and electric vehicles (HEVs) in the automotive industry require applications possessing high-EC in addition to their high-strength. Pure Al has high-EC, but limited strength, whereas those with high-strength, such as Al-Si-based cast alloys widely used in the automotive industry, exhibit poor EC because Si has high-solubility in the Al matrix, which deteriorates the EC of the alloy. Designing new Al alloys with a combination of high-strength and EC allow for the replacement of more costly Cu alloys in various HEV systems and expands the application space of lightweight Al alloys. Alloying elements with limited solubility in the Al matrix, yet with a potential to improve alloy strength, may enable a combination of improved strength and EC. Zr and Ni are elements with limited solid solubilities, with Zr producing a precipitation-strengthening effect through formation of L1₂-structured Al₃Zr nanoprecipitates upon aging heat-treatment and Ni producing an additional strengthening effect by forming eutectic Al₃Ni fibers on solidification. The length-scale of the solidification microstructure in Al alloys with Zr and Ni additions determines the level of strength the alloy can gain. Higher cooling rates that refine the microstructure are therefore desirable and will also lead to more solute trapping in the Al matrix upon solidification, which, through subsequent aging, can be decomposed to precipitate out a higher fraction of strengthening precipitates. Additive manufacturing (AM) processes, such as laser powder bed fusion, offer several orders of magnitude higher solidification cooling rates compared to conventional casting processes (10⁵–10⁷°C/s vs. 10⁰–10³°C/s) [1]. Therefore, this process is well-suited for alloy compositions expected to synergistically improve both the strength and EC of Al alloys. This task investigates microstructural evolution, EC, and mechanical properties of two novel additively manufactured Al alloy compositions, Al-1Zr-0.09Sn (Sn) and Al-2Ni-1Zr (wt.%).

Objectives

This task aims to study microstructural evolution and its resultant effects on the EC and mechanical properties of two new Al alloy compositions, Al-1Zr-0.09Sn and Al-2Ni-1Zr (wt.%), produced by laser powder bed fusion processing. The objectives pursued within this task are to:

- Study the printability of both alloys
- Study the aging response of both alloys in terms of their strength (hardness) and EC
- Characterize microstructures, EC, and tensile properties of Al-1Zr-0.09Sn and Al-2Ni-1Zr alloys
- Establish the microstructure-property relationships and provide input for designing high-strength and high-EC Al alloys for AM.

Approach

The application space for alloys with a combination of high-strength and EC expands with the expected increase of the share of HEVs in the transportation industry. This necessitates research efforts aimed at designing new alloys and processing methods that provide a combination of enhanced strength and EC to applications used in HEVs. Zr and Ni are the two alloying elements with limited solid solubilities, yet significant potential to improve the strength and creep resistance of Al alloys with little degradation of their EC. High-cooling rates inherent to AM are expected to make this process suitable for such alloys. Two new Al alloy compositions, Al-1Zr-0.09Sn and Al-2Ni-1Zr (wt.%), were designed to produce strengthening effects by $L1_2$ - Al_3Zr nanoprecipitates and eutectic Al_3Ni precipitates, which are expected to strengthen the alloy without significantly affecting the EC of Al, given their low solid solubilities. Both alloys were fabricated using different processing parameters to determine the processing window for each alloy. Specimens free from pores and cracks were obtained for certain parameter sets for both alloys, and using the downselected process parameters, mechanical coupons were produced to study microstructural evolution and the resultant effects on tensile properties, creep resistance, and EC of both alloys. Microstructural characterization was performed using SEM, with an instrument equipped with EDS, EBSD, TEM, and APT. Phases in Al-1Zr-0.09Sn were identified via XRD measurements. Tensile properties were measured at both 20°C and 200°C. The creep resistance of alloys was investigated at 200°C in tension. EC of both alloys was measured in an AF state and after various isochronal aging heat treatments.

Results

Figure I.1.3.1.1(a–c) shows typical AF microstructures of the AM Al-1Zr-0.09Sn (wt.%) alloy. A representative lower magnification micrograph in Figure I.1.3.1.1(a) shows that the microstructure is free from pores and cracks, which indicates that the optimized process parameters allow us to fabricate crack-free Al-1Zr-0.09Sn with limited porosity. Higher magnification micrographs in Figure I.1.3.1.1(a and b) reveal fine, spherical-shaped precipitates distributed uniformly within the α -Al matrix, and such precipitates are identified as Al_3Zr , based on the peaks observed in the XRD spectra from this alloy, as indicated in Figure I.1.3.1.2. XRD spectra cannot distinguish $L1_2$ -structured from $DO_{22/3}$ -structured Al_3Zr , but based on their spherical morphology, these precipitates are likely of the $L1_2$ - Al_3Zr type. Ongoing in-depth microstructure characterization will address these phases in more detail. APT measurements of the matrix composition indicate that about half of the Zr (0.5 wt.%) and Sn (0.004 wt.%) added to the alloy is supersaturated in the α -Al matrix upon solidification; the other half is bound to the intermetallic particles formed on solidification. Elemental distribution maps obtained by APT measurements for a sample from this alloy comprise Figure I.1.3.1.1(d), which shows the uniform distribution of Sn and Zr in the Al matrix. In addition to Al_3Zr precipitates, a small fraction of pure Sn particles are also present in the as-solidified microstructure, as determined by the XRD measurements, as observed in Figure I.1.3.1.2.

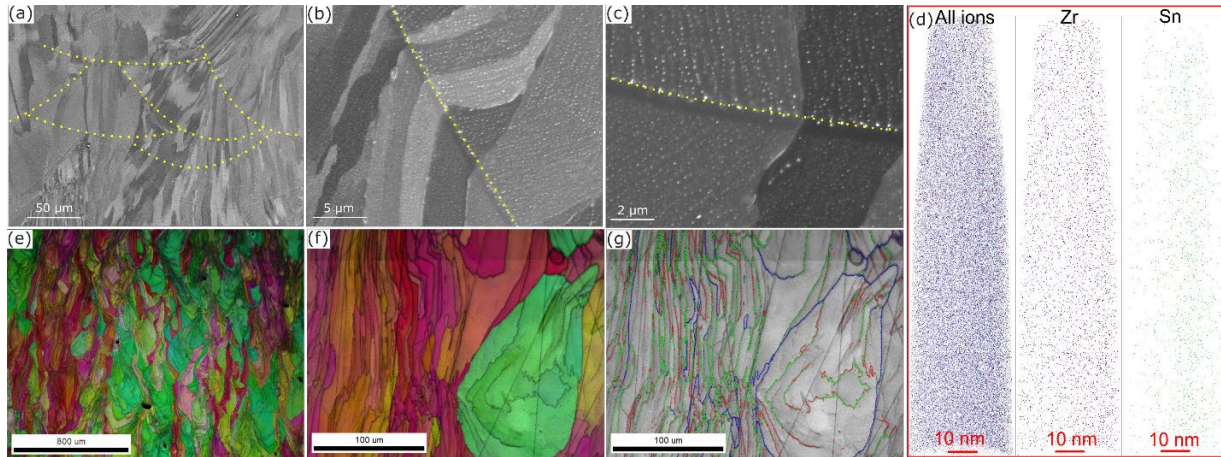


Figure I.1.3.1.1. A summary of AF microstructure of Al-1Zr-0.09Sn alloy: SEM micrographs showing the typical microstructures at (a) low and (b and c) high magnifications; (d) elemental distribution maps of all elements (Al, Zr and Sn) together, and individual Zr and Sn; (e and f) IPF colored maps, aligned along build direction, showing the typical grain structure; and (g) a map, corresponding to (f), showing the distribution of low-angle (red and green lines) and high-angle (blue lines) grain boundaries. Source: ORNL.

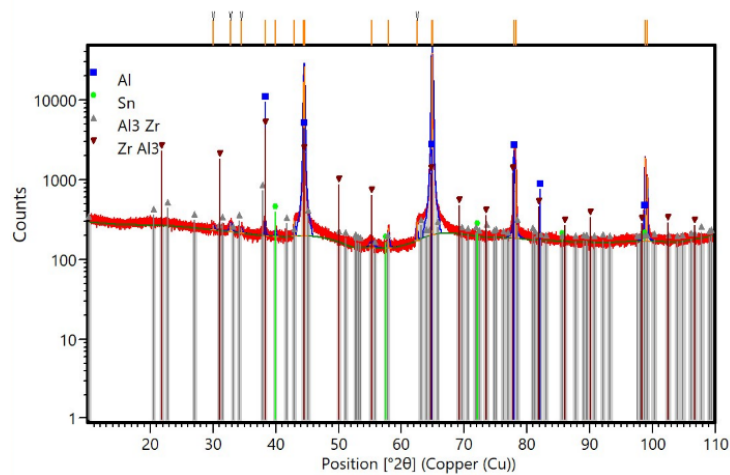


Figure I.1.3.1.2. XRD spectra obtained from AF Al-1Zr-0.09Sn alloy. Source: ORNL.

Figure I.1.3.1.1(e) shows the representative grain structure of AM Al-1Zr-0.09Sn (wt.%), which is composed of coarse grains elongated along the build direction, with most grains showing $\langle 001 \rangle_{\text{Al}}$ (red grains) and $\langle 011 \rangle_{\text{Al}}$ (green grains) orientations parallel to the build direction. Coarse-grain formation, resulting from a strong epitaxial growth, is also notable in SEM micrographs in Figure I.1.3.1.1(a) and Figure I.1.3.1.1(b) due to grain-orientation contrast. The presence of coarse grains is surprising given the high-Zr content in this alloy, which is known for its *in-situ* grain-refining effect. The high-cooling rates may suppress the formation of primary Al_3Zr to lower temperatures, at which Al_3Zr solidifies alongside $\alpha\text{-Al}$ via a eutectic reaction. The occurrence of a eutectic reaction has previously been observed in the Al-Zr system [2]. The EBSD map in Figure I.1.3.1.1(f) was acquired at a small (0.2 μm) step size to gain insight into the distribution of low-angle (green and red lines) and high-angle (blue lines) misorientations. The grain boundary distribution map in Figure I.1.3.1.1(g), which corresponds to Figure I.1.3.1.1(f), shows the presence of a high fraction of low-angle grain boundaries (green and red lines) in this alloy. Melt pool boundaries are outlined by dotted lines in (a–c). Build direction (BD) is vertically upwards. Microstructures correspond to the alloy produced at 370 W and 1100 mm/s scanning speed.

Figure I.1.3.1.3(a–c) shows typical microstructures of AM Al-2Ni-1Zr alloy in an AF state. Unlike Al-1Zr-0.09Sn which exhibited excellent printability, the printability of Al-2Ni-1Zr was found to be highly sensitive to the applied process parameters with some parameter sets leading to extensive cracking during printing. However, careful selection of process parameters resulted in the fabrication of the alloy with limited pores and cracks, as shown in Figure I.1.3.1.3(a). Higher magnification micrographs, as observed in Figure I.1.3.1.2(b–c), reveal a higher fraction of intermetallic particles in the microstructure of Al-2Ni-1Zr than in Al-1Zr-0.09Sn, as indicated in Figure I.1.3.1.1(a–c), consistent with the presence of additional Al₃Ni intermetallic particles that form during solidification in Al-2Ni-1Zr. Precipitates are more interconnected at the bottom regions of the melt pool, and they are more spherical at the top region, as can be seen in Figure I.1.3.1.2(b–c), which likely results from the variation of the growth rate and thermal gradient at different parts of the melt pool. Similar to Al-1Zr-0.09Sn, as shown in Figure I.1.3.1.1, Al-2Ni-1Zr also exhibits coarse grains elongated along the BD, as observed in Figure I.1.3.1.3(d), and the grain-orientation contrast seen in Figure I.1.3.1.3(a) points to a strong epitaxial growth during solidification. However, unlike Al-1Zr-0.09Sn, which exhibits strong $\langle 001 \rangle$ Al//BD and $\langle 011 \rangle$ Al//BD textures, as indicated in Figure I.1.3.1.1(d), the EBSD map of Al-2Ni-1Zr reveals no such textures, as can be seen in Figure I.1.3.1.3(d). Al-2Ni-1Zr also exhibits a high fraction of low-angle misorientations within the grains, as observed in Figure I.1.3.1.3(e–f). Melt pool boundaries are outlined by dotted lines in Figure I.1.3.1.3(a–c) where the BD is vertically upwards. Microstructures correspond to the alloy produced at 370 W and 2000 mm/s scanning speed.

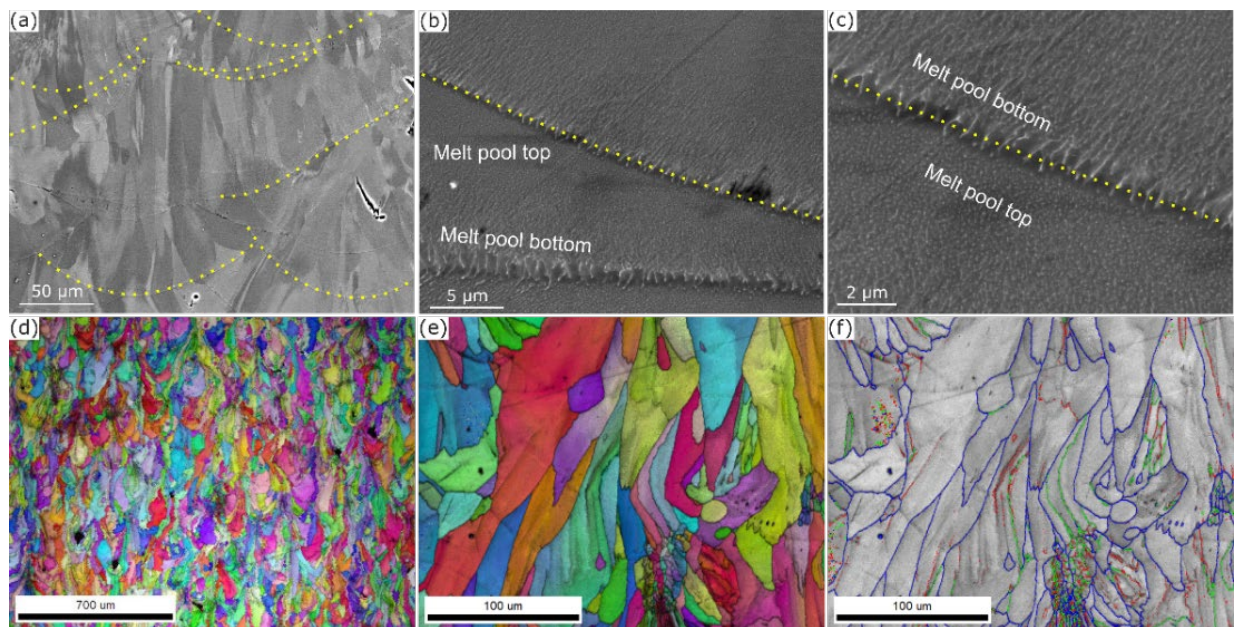


Figure I.1.3.1.3. (a) A summary of AF microstructure of Al-2Ni-1Zr alloy: SEM micrographs showing the typical microstructures at (a) low and (b–c) high magnifications; (d–e) IPF colored maps, aligned along the BD, showing the typical grain structure; and (f) a grain boundary distribution map, corresponding to (e), showing the distribution of low-angle (red and green lines) and high-angle (blue lines) grain boundaries. Source: ORNL.

Tensile properties of AF Al-1Zr-0.09Sn and Al-2Ni-1Zr are measured at both 20 and 200°C, as summarized in Figure I.1.3.1.4(a). At RT, Al-2Ni-1Zr has higher YS than Al-1Zr-0.09Sn (~136 vs. ~76 MPa), consistent with the higher fraction of reinforcements in this alloy. However, this improvement also results in the reduction of alloy ductility from ~22% for Al-1Zr-0.09Sn to ~13% for Al-2Ni-1Zr. Al-2Ni-1Zr exhibits higher strain-hardening capability than Al-1Zr-0.09Sn, leading to a higher ultimate tensile strength (UTS) of ~218 MPa for Al-2Ni-1Zr versus ~106 MPa for Al-1Zr-0.09Sn. By increasing the test temperature to 200°C, the YS of both alloys drops by ~10–20 MPa, but the drop in the UTS is much more pronounced for both alloys. While the UTS of Al-2Ni-1Zr is higher than its YS by ~23 MPa, the UTS of Al-1Zr-0.09Sn is very close to its YS, indicating that strain-hardening capability of these alloys, and particularly of Al-1Zr-0.09Sn, diminishes

significantly at 200°C. No apparent changes in the ductility of both alloys are observed with the increasing test temperature, to 200°C, because the measured elongation at break values for each alloy at two different temperatures is essentially the same, within the measurement error. Such high-tensile properties obtained in the AF state are very promising, and applying appropriate aging heat treatments to these alloys is expected to significantly improve the YS and UTS through solid-state precipitation of L_{12} - Al_3Zr nanoprecipitates.

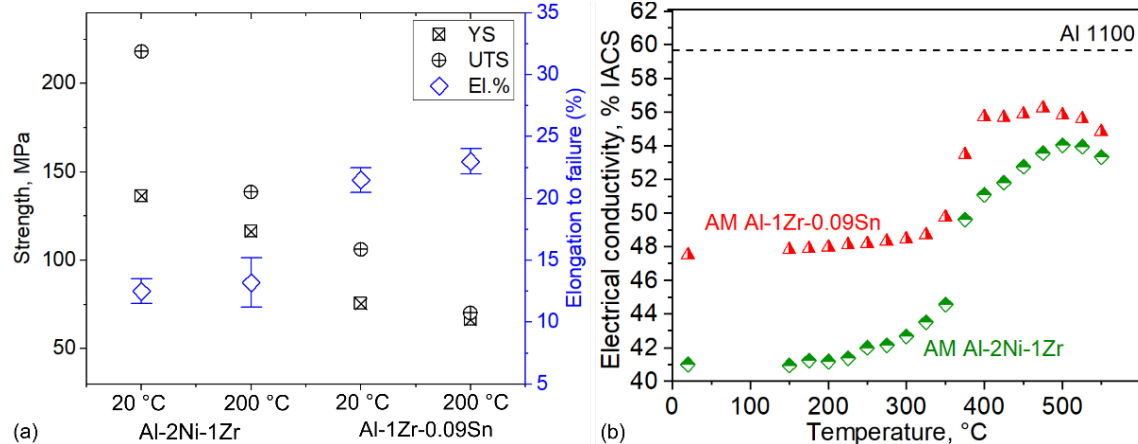


Figure I.1.3.1.4. (a) Tensile properties of AF Al-2Ni-1Zr and Al-1Zr-0.09Sn alloys at 20 and 200°C and (b) evolution of the EC of Al-2Ni-1Zr and Al-1Zr-0.09Sn alloys as a function of isochronal aging heat treatments. Source: ORNL.

The high-Zr solute trapping in Al matrix achieved by the AM-induced high-cooling rates is also expected to lead to the formation of this phase at much higher fractions than can be achieved in conventional processes. The EC of both alloys was measured in an AF state and upon isochronal aging at different temperatures and times, as summarized in Figure I.1.3.1.4(b). The EC of AA1100 is also included in Figure I.1.3.1.3(b) for comparison. The EC values are given relative to the IACS. In the AF state, both alloys exhibit relatively lower EC compared to Al 1100 (41% IACS for Al-2Ni-1Zr and 47.5 %IACS for Al-1Zr-0.09Sn versus 59.5 %IACS for Al 1100), which is primarily due to high solute content in the Al matrices of these two alloys. Heat-treatment causes these elements to form precipitates, reducing the solute content in the matrix and increasing conductivity. Given the low solid solubility of Ni, less Ni is expected to supersaturate in the Al matrix even at AM-induced high-cooling rates, and the presence of (interconnected) Al_3Ni intermetallic precipitates in the grain interiors is likely the main cause of relatively lower EC of Al-2Ni-1Zr relative to Al-1Zr-0.09Sn. Further ongoing in-depth microstructure investigations involving TEM and APT will address these points. With isochronal aging, a drastic change in EC is noted at ~350°C, at which L_{12} - Al_3Zr precipitation activates, and the EC of both alloys increases with the decomposition of Zr solute from the Al matrix to precipitate out L_{12} - Al_3Zr . For Al-1Zr-0.09Sn, a peak EC value of ~56% IACS is achieved at 400°C, which remains constant with further isochronal aging up to 475°C, after which it starts to slowly decline, reflecting a slight dissolution of coarsened L_{12} - Al_3Zr into the Al matrix. For Al-2Ni-1Zr, a drastic increase in EC is noted when increasing the temperature from 350° to 375°C, after which the EC value keeps increasing more slowly until reaching an isochronal aging temperature of 500°C, which gives the EC value of ~54% IACS. In Al-2Ni-1Zr, in addition to L_{12} - Al_3Zr precipitation, fragmentation, and coarsening of Al_3Ni intermetallic particles also contributes to the EC changes in the alloy, which explains why the aging curve of this alloy differs from that of Al-1Zr-0.09Sn. Overall, the aging curves of these two alloys indicate that their EC alongside their YS and UTS can be significantly improved with the decomposition of Zr solutes upon the appropriate aging heat-treatment.

Figure I.1.3.1.5 summarizes the tensile-creep data obtained for Al-1Zr-0.09Sn and Al-2Ni-1Zr at 200°C. The creep strain versus time curve obtained for Al-1Zr-0.09Sn at different stresses, displayed in Figure I.1.3.1.5(a), shows that the strain-rate at stresses below 60 MPa is extremely slow, and even at 60 MPa, which is very close to the YS of the alloy at 200°C (~66 MPa). The strain-rate is measured as $3.6 \times 10^{-10} \text{ s}^{-1}$, indicative of a

diffusional creep and no dislocation climb. When the stress level was increased to 70 MPa, which is higher than the YS of the alloy, the specimen failed immediately. The temporal creep strain-evolution curve for Al-2Ni-1Zr at different stresses, displayed in Figure I.1.3.1.5(b), shows that the strain-rate remains slow, varying within the 10^{-10} – 10^{-9} s⁻¹ range at stresses up to 100 MPa. When the applied stress is increased to 110 MPa, the strain-rate increases drastically, leading to the initiation of the tertiary creep and final failure of the specimen. Both AM alloys, when compared to cast, homogenized, and aged Al-0.34Zr-0.09Sn (wt.%) and cold-rolled AA1350 H19-type conductive Al alloys, exhibit much higher creep resistance, as shown in Figure I.1.3.1.5(c), and the creep resistance of these alloys is expected to further increase significantly upon the solid-state precipitation of L₂-Al₃Zr nanoprecipitates.

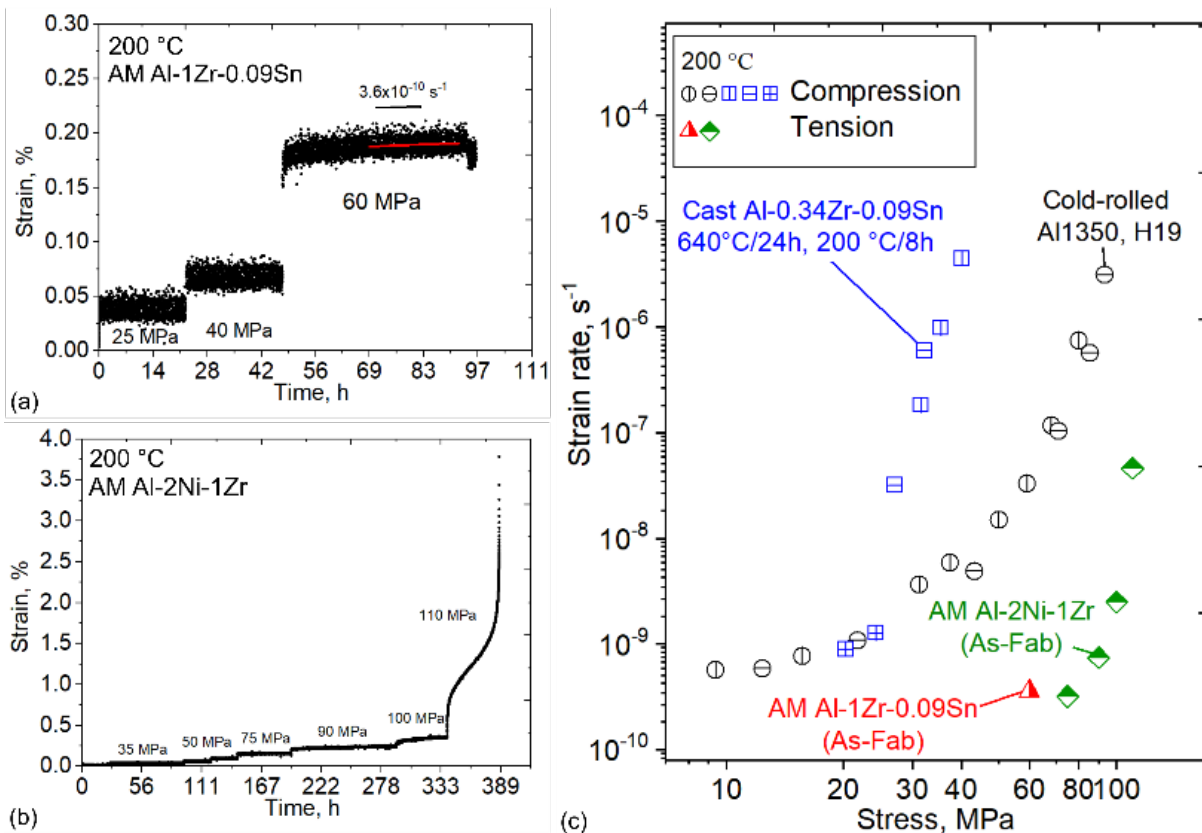


Figure I.1.3.1.5. Tensile properties of AF (a) Al-1Zr-0.09Sn and (b) Al-2Ni-1Zr alloys at 200 °C. (c) Evolution of the EC of Al-2Ni-1Zr and Al-1Zr-0.09Sn alloys as a function of isochronal aging heat-treatments compared to Al-0.34Zr-0.09Sn and Al1350. Source: ORNL.

Conclusions

The following conclusions were drawn based on FY 2023 activities in this task:

- Two Al alloys, Al-1Zr-0.09Sn and Al-2Ni-1Zr (wt.%), were successfully fabricated in a near-defect-free condition via AM. Both alloys exhibit coarse-grain structures resulting from strong epitaxial growth of α -Al grains at melt pool boundaries. While the microstructure of Al-1Zr-0.09Sn is composed of the spherical-shaped Al₃Zr precipitates distributed uniformly within the Al matrix, Al-2Ni-1Zr has a much higher fraction of reinforcement precipitates due to the additional presence of Al₃Ni intermetallic precipitates in this alloy.
- High-Zr solute trapping in the Al matrix upon solidification gives the alloys lower EC values of 41% IACS for Al-2Ni-1Zr and 47.5% IACS for Al-1Zr-0.09Sn. However, with isochronal aging which leads

to the solid-state precipitation of Al₃Zr, the EC increases, reaching a peak of ~56% IACS for Al-1Zr-0.09Sn and ~54% IACS for Al-2Ni-1Zr.

- Both alloys in an AF state showed a combination of high-strength and ductility, with Al-2Ni-1Zr, compared to Al-1Zr-0.09Sn, exhibiting relatively higher YS (~136 vs. ~76 MPa) but lower ductility (~13% vs. ~22%), consistent with the presence of a comparably higher fraction of reinforcements in the former alloy.
- Creep properties of both alloys are characterized by very low steady-state tensile strain rates up to their YS, with strain rates controlled by diffusional creep and no sign of dislocation climb occurring at these stresses. Both AM alloys exhibit much higher creep resistance compared to cast, homogenized, and aged Al-0.34Zr-0.09Sn (wt.%) and conventionally cold-rolled AA1350 H19 Al alloys.

References

1. DebRoy, T., H. L. Wei, J. S. Zuback, T. Mukherjee, J. W. Elmer, J. O. Milewski, A. M. Beese, A. Wilson-Heid, A. De, and W. Zhang, 2018, “AM of metallic components – Process, structure and properties,” *Prog. Mater. Sci.*, 92, 112–224. <https://doi.org/10.1016/j.pmatsci.2017.10.001>.
2. Wang, F., D. G. Eskin, A. V. Khvan, K. F. Starodub, J. J. H. Lim, M. G. Burke, T. Connolley, and J. Mi, 2017, “On the occurrence of a eutectic-type structure in solidification of Al-Zr alloys,” *Scr. Mater.*, 133, 75–78. <https://doi.org/10.1016/j.scriptamat.2017.02.027>.

I.1.3.2 Task 3B. Fundamentals of Non-Equilibrium Processing for Additive Manufacturing Alloys (Oak Ridge National Laboratory)

Ying Yang, Principal Investigator

Oak Ridge National Laboratory
Materials Science and Technology Division
1 Bethel Valley Rd.
Oak Ridge, TN 37830
E-mail: yangying@ornl.gov

J. Allen Haynes, PMCP Consortium Manager

Oak Ridge National Laboratory
Materials Science and Technology Division
1 Bethel Valley Rd.
Oak Ridge, TN 37830
E-mail: haynesa@ornl.gov

Jerry L. Gibbs, DOE Technology Development Manager

U.S. Department of Energy
E-mail: Jerry.Gibbs@ee.doe.gov

Start Date: November 1, 2021
Project Funding: \$210,000

End Date: September 30, 2023
DOE share: \$210,000

Non-DOE share: \$0

Project Introduction

Solidification processes (e.g., die-casting, welding, AM) play an important role in determining the microstructure, and consequently the physical and mechanical properties, of metallic alloys. The microstructure formed during solidification depends on both the alloy composition and the local thermal conditions [1]. Near eutectic alloys are desirable for solidification processing as their relatively low melting temperatures and narrow freezing range improve fluidity and help to avoid solidification cracking [2], [3]. However, for near eutectic compositions, the competition between dendritic and eutectic solidification modes under different cooling conditions profoundly affects the phase morphology, size, and distribution, leading to differences in material performance. Despite the advancement of manufacturing processes in the last decade, designing processing conditions to obtain desired microstructure is still mostly approached through a trial-and-error method. The ability to predict microstructural features based on alloy composition and processing conditions is essential for more effective computational design guidance of new materials [4], [5]. State-of-the-art manufacturing processes, such as AM, offer distinctly different microstructure than casting, primarily due to extremely high-heating and cooling rates during processing. Different regions of a given part produced through additive processing often show drastically different microstructures depending on thermal history during solidification [6]. As it is almost impossible to test all possible processing conditions to experimentally tune microstructure, robust computational models are necessary to understand the effect of process-controlling parameters on microstructure formation during solidification.

Objectives

The objective of this work is to develop a cellular automata (CA) model for understanding how thermodynamic (e.g., initial composition, partition coefficient, slope of liquidus line) and kinetic parameters (e.g., initial undercooling, cooling rate, thermal gradient, diffusion coefficient) affect microstructure evolution during solidification.

Approach

The approach used in this work is combining dendritic and eutectic solidification with consideration of nucleation and growth models within a CA framework assuming local equilibrium is maintained at the solid-liquid interfaces. The proposed approach begins with the development of a dendritic growth model, followed by a eutectic growth model. Subsequently, these two models are integrated to simulate the competitive growth of

dendrites and eutectic structures. To verify the accuracy of the dendritic and eutectic models, they are initially compared against well-established analytical solutions, such as Lipton-Glicksman-Kurz (LGK) [7] for isothermal dendritic growth and Jackson-Hunt (JH) [8] for eutectic coupled growth, respectively. Once the models demonstrate satisfactory performance individually, they are integrated to simulate the microstructure of a hypoeutectic Al-25 wt.% Cu alloy under varying cooling conditions. With the currently developed CA framework, as shown in Figure I.1.3.2.1, we can gain insight into the microstructural features observed for hyper- and hypoeutectic alloys, including dependence on processing conditions, such as increased eutectic volume fraction at high-cooling rates.

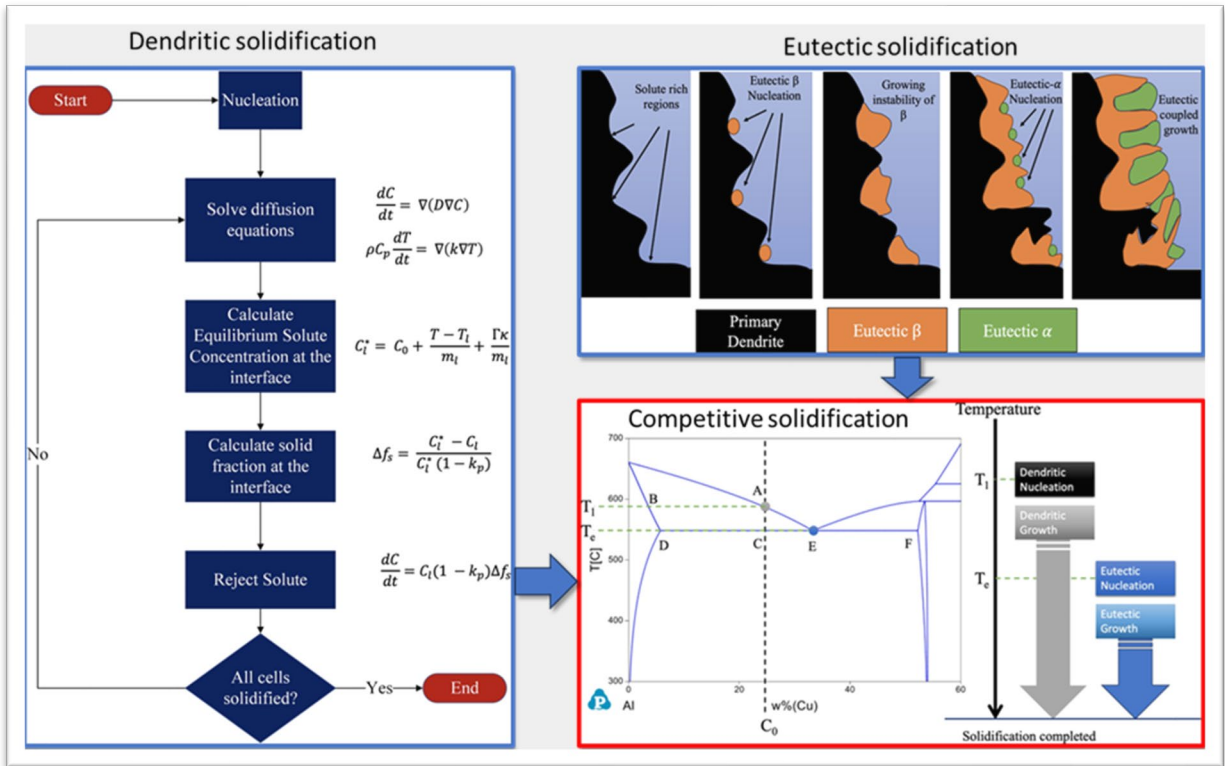


Figure I.1.3.2.1. Flowchart on developing the CA framework on modeling the nucleation and growth of dendritic solidification, eutectic solidification, and their competition under different cooling conditions. Source: ORNL.

Results

Dendritic Solidification

Here, the velocity of a single equiaxed dendrite growing in an isothermal undercooled melt was obtained from the CA model at eight different undercooling levels and compared to the LGK model [7]. The solidification community often uses comparison to the LGK model to verify numerical solutions, because it provides the analytical solution on the growth velocity of an isothermal dendrite tip in the absence of thermal gradient in the melt. Figure I.1.3.2.2(a) shows an example of dendritic growth of Al-4 wt.% Cu from the CA model at an undercooling of 4 K, where solidification proceeded preferentially along the dendrite tip directions where the solute concentration gradients are largest. Solute segregates into the liquid phase, piling up in the interdendritic regions where diffusion occurs less easily. The comparison of the CA modeled dendrite tip velocity at steady-state to the LGK solution is shown in Figure I.1.3.2.2(b); as the undercooling increases, the modeled dendrite tip velocity increases, which is consistent with the LGK solution at the various undercooling values.

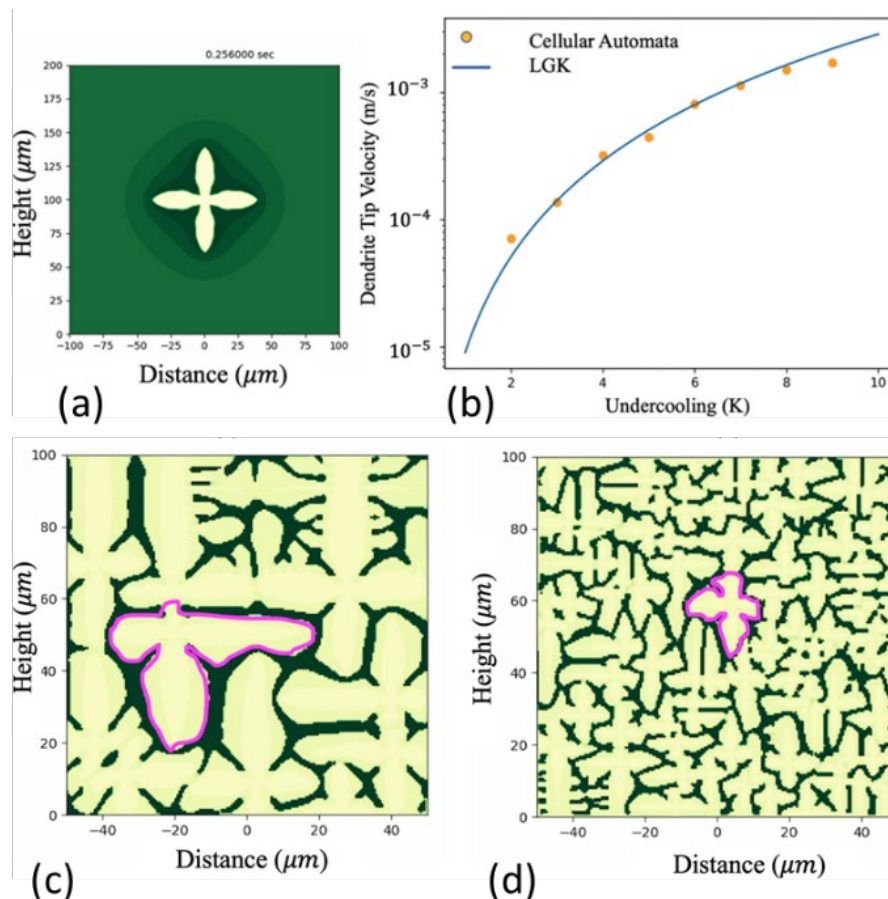


Figure I.1.3.2.2. (a) Growth of Al-dendrite of Al-4 wt.% Cu in 5 K undercooled melt after 0.256 s. (b) Comparison of CA simulated velocity of dendrite tip at steady-state with the analytical LGK solution vs. liquid undercoolings. (c–d) Effect of cooling rate on grain size for Al-4 wt.% Cu alloy in the isothermal field under 100 K/s and 1,000 K/s. The magenta highlight shows difference in dendrite size for two cooling rates. Source: ORNL.

In advanced manufacturing processes, such as AM, the cooling rate is orders of magnitude higher than conventional casting. To investigate the effect of a high-cooling rate on a hypoeutectic alloy, solidification of an Al-4 wt.% Cu alloy was simulated for two cooling conditions as shown in Figure I.1.3.2.2(c-d). For the purpose of simplicity, the thermal field was assumed to be isothermal at a given time. The cooling rates for two cases are: (1) fast cooling at 1,000 K/s; and (2) slow cooling at 100 K/s. At the beginning of the

simulation, the liquid alloy was set at the equilibrium liquidus temperature of the alloy. The temperature of the domain decreased uniformly with the applied cooling rate. Nucleation sites were distributed throughout the domain with a maximum density of $1.6 \times 10^{10}/\text{m}^3$, mean undercooling of 2 K, and standard deviation of undercooling of 0.1 K. For fast cooling, it is observed that the grain size is much smaller than the slow cooling case as evident from the magenta highlights in Figure I.1.3.2.3(c-d). The spacing between the dendrite arms also decreases with the increase in cooling rate. The grain refinement effect is due to increased activation of nucleation sites for faster cooling, even though the maximum nucleation density is the same for both cases. This is consistent with the literature results found by Sprague et al. [9].

Eutectic Solidification

The CA modeling results on stable lamella eutectic solidification are shown in Figure I.1.3.2.3. The relationship between eutectic solidification velocity and inter-lamellar spacing is analytically given using the JH theory [7], which was later modified by Magnin and Trivedi [10]. The growth pattern of the alternating phases in the form of lamella depends on species availability, which in turn is dictated by diffusion. If the initial lamella spacing is the same as that defined by the extremum point of the JH model, as observed by point (b-c) in Figure I.1.3.2.3(a), stable lamella growth occurs, as shown in the CA model results in Figure I.1.3.2.3(b-c). However, when the spacing is larger or smaller than the extremum point for the given velocity, instabilities are observed. Such instabilities help to form or eliminate lamella to maintain steady-state growth. Figure I.1.3.2.3(d-e) shows a case where the initial spacing was larger than that at the extremum point. In this case, solute builds up in front of the α -phase, as observed in Figure I.1.3.2.3(d), which increases the undercooling driving solidification of the β -phase to maintain stability. As new lamellas nucleate and grow, the width of the lamella is automatically adjusted to maintain steady-state growth. If the initial lamella spacing is less than that at the extremum point, faster growth of one phase over the other is observed, as indicated in Figure I.1.3.2.3(f-g). In this case, some of the lamellae are eliminated to maintain steady growth at the extremum spacing. The instability observed in Figure I.1.3.2.3(g) is because the steady-state has not been reached yet. These results verify the accuracy of the eutectic CA model.

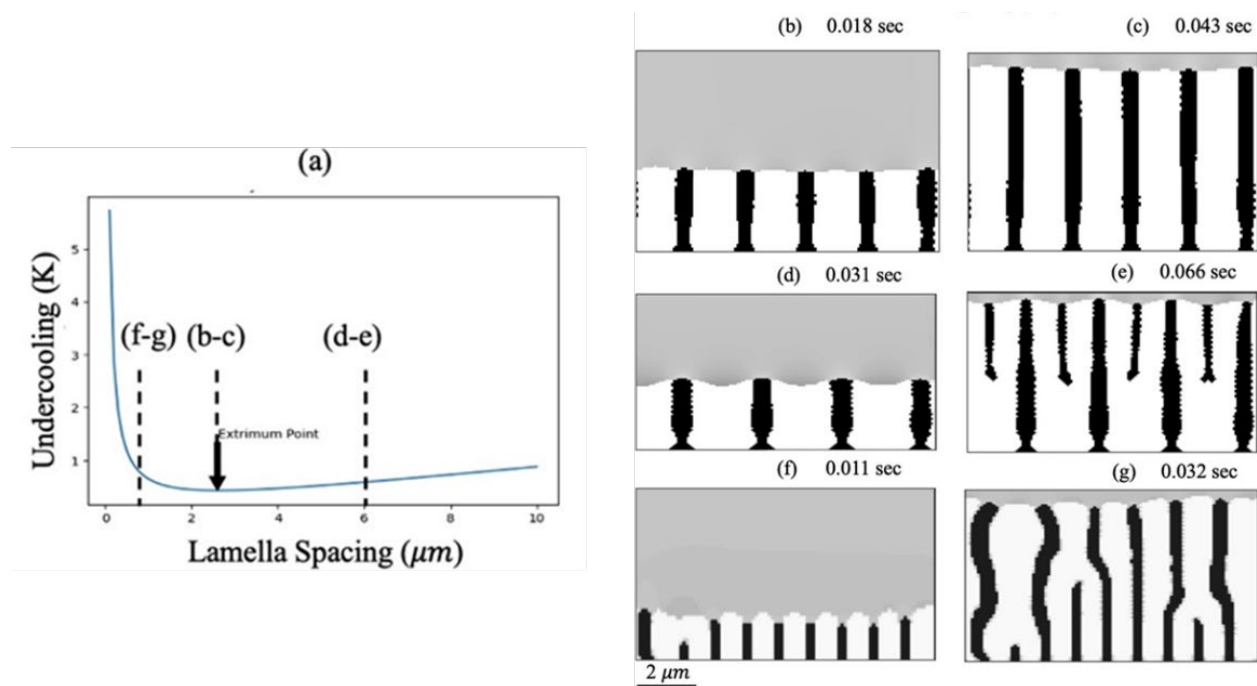


Figure I.1.3.2.3. Validation of the eutectic model: (a) Lamella spacing vs. undercooling relationship as obtained from the JH Model. Growth of lamella at two different times (b–c) with initial spacing equal to that at the extremum point, (d–e) with initial spacing larger than that at the extremum point, and (f–g) initial spacing smaller than that at the extremum point. Source: ORNL.

Combined Dendritic and Eutectic Solidification

After validating the dendritic and eutectic growth models separately, the models were combined to simulate a hypoeutectic Al-25 wt.% Cu alloy where both solidification modes were expected to be observed. Figure I.1.3.2.4 schematically represents the integration of the two models for simulating combined dendritic and eutectic solidification modes. For AlCu, the eutectic composition is 32 wt.% Cu. For a hypoeutectic Al-25 wt.% Cu alloy, dendritic solidification is expected when the temperature reaches the liquidus temperature, at which point the solid begins rejecting solute into the liquid. Primary dendritic growth of the α phase continues until the composition and temperature of the liquid trigger nucleation and growth of the θ phase, leading to eutectic growth of both phases. Because the solute diffusion in the liquid that affects undercooling for eutectic nucleation is rate dependent, the formation of the eutectic is expected to be dependent on cooling rate. To investigate the effect of solidification condition, three different cooling rates, 100 K/s, 1,000 K/s, and 10,000 K/s, were chosen to model the microstructure evolution of Al-25 wt.% Cu alloy. For the slowest cooling rate, large dendrites are observed. As the cooling rate increases from 100 K/s to 1,000 K/s, the area covered by the dendrites decreases while the eutectic area increases. Upon cooling at 10,000 K/s, the alloy mostly shows a eutectic microstructure and almost non-existent dendrites. It has been reported that AlCu shows a symmetric eutectic coupled zone [11]. Therefore, the complete eutectic transformation of Al-25 wt.% Cu is realistic from an experimental point-of-view. Note that due to the large differences in length-scale between the primary dendrites and the eutectic lamella, the grid size used for these simulations was selected to resolve the dendritic growth and eutectic nucleation behavior.

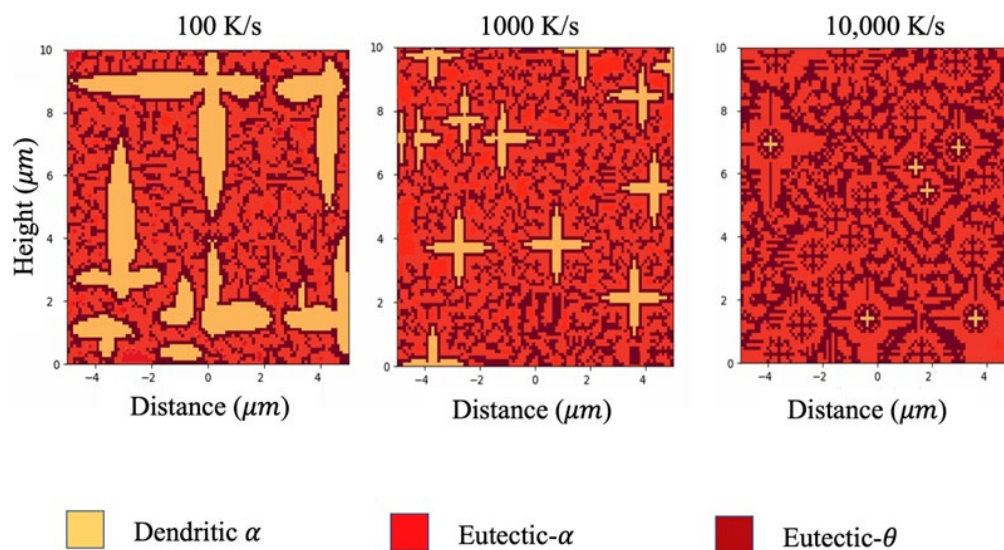


Figure I.1.3.2.4. Microstructure of Al-25 wt.% Cu after solidification at 100 K/s, 1000 K/s, and 10,000 K/s (left to right). Source: ORNL.

Conclusions

The microstructure of an alloy after solidification depends on the cooling condition. As the mechanical properties of any alloy are strongly correlated to the microstructural features, it is important to understand the solidification of different phases under different cooling conditions. Analytical approaches have been considered in the past to understand the competitive growth between different phases. This work developed a novel computational framework to understand the thermodynamic and kinetic effects on dendritic and eutectic solidification as well as their competition using CA. This physics-based model tracks the spatiotemporal evolution of the microstructure considering finite diffusion in the liquid for binary alloy. Dendritic or eutectic solidification models implemented in this work were individually validated with literature data. By solving the mass diffusion equation at every CA step, solute redistribution is appropriately captured in CA. Although some parameter optimization is needed for CA, such as for nucleation density and critical undercooling, the trends obtained from such modeling are very useful in understanding non-equilibrium effects during solidification.

Key Publications

1. Perrin, A., R. A. Michi, D. N. Leonard, K. Sisco, A. Plotkowski, A. Shyam, J. D. Poplawsky, L. Allard, and Y. Yang, 2023, “Effect of Mn on eutectic phase equilibria in Al-rich Al-Ce-Ni alloys,” *J. Alloys Compd.*, 965, 171455. <https://doi.org/10.1016/j.jallcom.2023.171455>.
2. Roy, I., M. Rolchigo, J. Coleman, S. Chen, A. Plotkowski, and Y. Yang, 2024, “Understanding solidification of near eutectic alloy using CA,” *Comput. Mater. Sci.*, 236, 112835. <https://doi.org/10.1016/j.commatsci.2024.112835>.
3. Sisco, K., A. Plotkowski, Y. Yang, L. Allard, C. Fancher, C. Rawn, J. D. Poplawsky, R. Dehoff, and S. S. Babu, 2023, “Heterogeneous phase transformation pathways in additively manufactured AlCeMn alloys,” *J. Alloys Compd.*, 938, 168490. <https://doi.org/10.1016/j.jallcom.2022.168490>.

References

1. Shabestari, S., and H. Moemeni, 2004, “Effect of copper and solidification conditions on the microstructure and mechanical properties of Al-Si-Mg-alloys,” *J. Mater. Process. Technol.*, 153, 193–198. <https://doi.org/10.1016/j.jmatprotec.2004.04.302>.
2. Roberts, C. E., D. Bourell, T. Watt, and J. Cohen, 2016, “A novel processing approach for AM of commercial aluminum alloys,” *Phys. Procedia*, 83, 909–917. <https://doi.org/10.1016/j.phpro.2016.08.095>.
3. Kotadia, H. R., G. Gibbons, A. Das, and P. D. Howes, 2021, “A review of laser powder bed fusion AM of aluminum alloys: Microstructure and properties,” *Addit. Manuf.*, 46, 102155. <https://doi.org/10.1016/j.addma.2021.102155>.
4. Suzuki, A., T. Miyasaka, N. Takata, M. Kobashi, and M. Kato, 2021, “Control of microstructural characteristics and mechanical properties of AlSi12 alloy by processing conditions of laser powder bed fusion,” *Addit. Manuf.*, 48, 102383. <https://doi.org/10.1016/j.addma.2021.102383>.
5. Spierings, A. B., K. Dawson, T. Heeling, P. J. Uggowitzer, R. Schäublin, F. Palm, and K. Wegener, 2017, “Microstructural features of Sc-and Zr-modified Al-Mg-alloys processed by selective laser melting,” *Mater. Des.*, 115, 52–63. <https://doi.org/10.1016/j.matdes.2016.11.040>.
6. Plotkowski, A., K. Sisco, S. Bahl, A. Shyam, Y. Yang, L. Allard, P. Nandwana, A. M. Rossy, and R. H. Dehoff, 2020, “Microstructure and properties of a HT AlCeMn alloy produced by AM,” *Acta Mater.*, 196, 595–608. <https://doi.org/10.1016/j.actamat.2020.07.014>.
7. Lipton, J., M. E. Glicksman, and W. Kurz, 1987, “Equiaxed dendrite growth in alloys at small supercooling,” *Metall. Mater. Trans. A Phys. Metall. Mater. Sci.*, 18, 341–345. <https://doi.org/10.1007/BF02825716>.
8. Jackson, K. A., and J. D. Hunt, 1988, “Lamellar and rod eutectic growth,” In: Pelcé, P. (ed.), *Dynamics of Curved Fronts*, Elsevier, Amsterdam, Netherlands, pp. 363–376. <https://doi.org/10.1016/B978-0-08-092523-3.50040-X>.
9. Sprague, E., J. Mazumder, and A. Misra, 2022, “Cooling rate and dendrite spacing control in direct metal deposition printed Cu-Fe alloys,” *J. Laser Appl.*, 34(2), 022013. <https://doi.org/10.2351/7.0000464>.
10. Magnin, P., and R. Trivedi, 1991, “Eutectic growth: A modification of the Jackson and Hunt theory,” *Acta Metall. Mater.*, 39(4), 453–467. [https://doi.org/10.1016/0956-7151\(91\)90114-G](https://doi.org/10.1016/0956-7151(91)90114-G).
11. Kurz, W., and D. J. Fisher, 1979, “Dendrite growth in eutectic alloys: The coupled zone,” *Int. Met. Rev.*, 24(1), 177–204. <https://doi.org/10.1179/imtr.1979.24.1.177>.

Acknowledgements

The authors are grateful to I. Roy, A. Plotkowski, M. Rolchigo, J. Coleman, S. Chen, D. Shin, A. Luo, A. Perrin, R. A. Michi, D. N. Leonard, K. Sisco, A. Shyam, J. D. Poplawsky, and L. Allard for their assistance.

I.1.3.3 Task 3C. Advanced Ceramics and Processing for Wireless Charging Systems (Ferrites) (Oak Ridge National Laboratory)

Beth Armstrong, Principal Investigator

Oak Ridge National Laboratory
Materials Science and Technology Division
1 Bethel Valley Rd.
Oak Ridge, TN 37830
E-mail: armstrongbl@ornl.gov

J. Allen Haynes, PMCP Consortium Manager

Oak Ridge National Laboratory
Materials Science and Technology Division
1 Bethel Valley Rd.
Oak Ridge, TN 37830
E-mail: haynesa@ornl.gov

Jerry L. Gibbs, DOE Technology Development Manager

U.S. Department of Energy
E-mail: Jerry.Gibbs@ee.doe.gov

Start Date: November 1, 2021

End Date: September 30, 2023

Project Funding: \$270,000

DOE share: \$270,000

Non-DOE share: \$0

Project Introduction

Wireless charging is a critical technology to enable a broader spectrum of the future transportation sector to transition to EVs. While wired charging works for plugging in cars at night or while not in use, wireless charging is needed for transportation applications like heavy vehicles, where on-road time needs to be maximized [1] and there can be localized high-load scenarios, such as very steep grades. Minimizing charging time is made possible through dynamic wireless charging, where vehicles are charged as they drive. While this concept has been shown for buses and delivery trucks, new materials are required for both on-road (transmitting) and on vehicle (receiving) wireless charging devices to improve the function, cost, relative mass, and durability of current systems [2], [3]. One major area for materials development is in the ferrite core as it is typically the heaviest component in a high-power wireless charging pad [4]. The tunability of this class of advanced ceramic materials provides a strong framework and opportunity for developing new chemistries to meet the variable electric drive design space. It also enables flexibility in the processing of unique and/or composite architectures. Current ferrite parts, with conventional ferrite materials, have been dominated by simple, planar geometries and are too heavy and cumbersome to be effectively utilized on the vehicle side of such charging systems.

By combining the suite of relevant capabilities and expertise at ORNL—including ceramic synthesis, processing, wireless charging system design, and characterization—new hybrid material systems and advanced architectures may be realized. A systematic approach is being utilized to evaluate and determine baseline property sets of the current state-of-the-art commercial ceramic materials. A new compositional array of materials is being designed and synthesized using guidance from computational predictions and targeted advancements over the baseline materials in the desired suite of processing, mechanical, physical, and magnetic properties.

Initial, simple geometries have been fabricated using traditional ceramic processing methods to begin developing architecture—property relationship baseline understanding that will better enable the design of potentially complex novel wireless structures that will require more advanced ceramic processing methods, such as AM. Materials and designs are being characterized by a diverse array of collaborators at ORNL, including the electric drive team at the National Transportation Research Center and the Basic Energy Sciences—Materials Sciences and Engineering Division team in the Materials Science and Technology Division, and the eventual more complex ceramic architectures will be printed in collaboration with the AM team at the Manufacturing Demonstration Facility.

Objectives

Task 3C aims to develop tunable and lighter weight advanced ceramic materials (ferrites), as well as the appropriate processing methods for fabrication of wireless charging systems for heavy vehicle applications. This project will utilize promising candidate ferrite-based ceramic powders identified in FY 2022 to further develop and characterize scalable processing methods to fabricate lightweight components for transportation based wireless charging systems.

Approach

This research task is taking place in three main subtasks: (1) Material Property Evaluation and Novel Component Design, (2) Fabrication of Test Samples, and (3) Magnetic Property Characterization and Testing.

In FY 2022 and during the first quarter of FY 2023, determining properties of interest and baselining commercially available materials provided a foundation to start investigating pathways to new, advanced ceramics for wireless charging systems. This foundation assisted in the identification of a selection of candidate material compositions to use for fabrication into preliminary simple shapes for testing. To begin fabrication and magnetic property characterization, further material characterization including zeta potential, particle size, sinterability, rheology, and magnetic structure (Mössbauer spectroscopy) were identified and carried out to further optimize composition and processing understanding to guide development of robust materials and fabrication techniques that are well-suited to make both simple and complex geometries and architectures for wireless charging. These materials will be further evaluated to ensure adequate performance and provide feedback for further optimization of both composition and processing.

Results

The focus of the work this year was divided between experimental activities and modeling to address the three subtasks to characterize and develop candidate materials and processes to fabricate simple geometries, as well as to begin to develop a framework for high-throughput computational and theoretical screening of potentially more complex ferrite compounds. Last year, the materials needs were defined by motor and power electronics designers, and from an initial literature review and several discussions with collaborators, the following key parameters were identified: (a) low-cost, (b) high-saturation flux density, (c) low-power loss, (d) operation at high-frequencies (85 – 150 kHz), (e) high-Curie temperature ($>100^{\circ}\text{C}$), and (f) low-relative permeability (1500 – 3000). Of these parameters, Curie temperature and relative permeability were selected as two key measurable parameters to benchmark materials. The spinel ferrites were chosen as the first material systems of interest as they have both high operational frequencies and Curie temperatures, as well as diverse chemical systems that would yield tunable compositions and properties.

The efforts developing the framework for high-throughput computation and screening were accomplished via a proposal and project award from Thrust 4, Task 4B, “Advanced Computational Materials,” within this program. This supporting project established the baseline standard operating procedure for predicting new compositions of ferrites that would be suitable for use in wireless charging and assisted the experimental advances made during FY 2023. The baseline standard operating procedures were broken into two discrete sections: (1) first-principles predictions of materials stability, and (2) corresponding magnetic properties and thermodynamic modeling, based on known experimental compositions, to narrow down the phase space of synthesizable compounds. Initial computational studies focused on first-principles, density functional theory (DFT) calculations of the substitutional stability and magnetic structure of doped ZnFe_2O_4 . These calculations

examined the doping of Ni and Mg on either Zn or Fe sites and will be the basis for the high-throughput examination of a wide range of dopants as determined from the thermodynamic calculations described below. These results demonstrated a strong tendency for Fe-site substitutions, which for Mg doping resulted in a significant decrease in the total magnetization with a corresponding 1.08% increase in the volume. Ni also exhibited a preference for the Fe-site doping but with a corresponding decrease in the volume of the unit cell. Most notable was that 50% Mg on the Fe sites had a density of 4.88 g/cm³ while 50% Ni on Fe sites had a density of 5.53 g/cm³. In all cases, Fe anti-site substitutions were unfavorable for Ni and Mg doping. Computed magnetization values for the Ni-doped ferrites compared qualitatively well with literature data; relative permeability values decrease with Mg substitution and increase with Ni doping. Using Ni_{0.5}Zn_{0.5}Fe₂O₄ as an example, the permeability was 200 for 50% Ni substitution, while the permeability value fell to 50 for 0% Ni substitution, which is bulk ZnFe₂O₄. These values were experimentally validated by data collected at Steward Advanced Materials, the powder supplier industrial partner.

Although the permeability goal of 1,500 was set at the beginning of FY 2023, that value is not only dependent upon dopant chemistry but is also dependent on grain size and domain orientation. DFT calculations of changes in magnetization upon doping is ongoing. Theoretical input suggested the use of Mössbauer as an experimental verification of the total magnetization changes due to Mg and/or Ni substitutions in the *A*- and *B*-sites, and work has been initiated. To further accelerate compositional development and to investigate potential dopants for ferrite spinels that can improve magnetic properties, detailed information for defect chemistry, as discussed above, is essential. However, given the large number of potential dopants and defects (i.e., vacancies, anti-site defects, etc.), it can be too computationally expensive to study this entirely with DFT. To complement the DFT calculations, Calculation of Phase Diagrams (CALPHAD) was employed. This approach uses experimental heats of formation to predict feasible compounds for further electronic structure calculations. These calculations allowed for the determination of which elements in the periodic table can be doped into the ferrite lattice structure. Initial efforts studied Zn and Ni-doped into Fe₃O₄ as a demonstration of the value of the approach. Indeed, it was able to determine that Zn would dope into the tetrahedral “*A*”-site to form ZnFe₂O₄, while Ni preferentially forms an anti-ferrite compound (i.e., doped on the octahedral site). Note, this model is agnostic to magnetism and is therefore used as a guide for further DFT studies involving other dopants. These results correlate well with the aforementioned DFT calculations that indicate a preference for Ni to dope on the Fe-site, thus confirming the formation of an inverse ferrite spinel phase.

Compositional optimization is one piece of the complex relationship to realizing lighter weight equivalent ceramic ferrite structures. In addition, the current state-of-the-art thin, dense, structures being utilized in electronic dynamic wireless charging applications need to be reimaged. This means new, revolutionary architectures, designs, and manufacturing methods need to be developed. Advanced manufacturing techniques lend themselves to this challenge. Advanced manufacturing techniques that utilize slurries provide the most flexibility in developing more complicated ceramic structures at a scale necessary for vehicle usage. A useful slurry must have a low enough viscosity to be castable, and not have significant agglomeration to maintain proper structural integrity and consistent density in the preform [5]. Another key characteristic that is typically necessary for the slurry is a high-content of solids (>50 vol.%) to minimize shrinkage during the sintering process and to maintain structural integrity [6]. The slurry must also be stable. One factor that impacts slurry stability is its zeta potential, essentially its charge at the interface between the particle and the solvent. Within this boundary, the particle and associated ions will move as a unit [7]. The amount of repulsion increases with higher absolute values of zeta potential due to the strength of charges from ions. Particles with absolute values of zeta potential above 30 mV are generally stable. The pH at which zeta potential is zero is called the isoelectric point and is the pH at which the powders are most unstable and likely to agglomerate and settle out of suspension [8]. Care must be taken to avoid this point in the development of the slurry. The zeta potential can be manipulated through static and/or steric forces (i.e., by altering the pH of the solvent and/or the use of a dispersant or organic additive). In FY 2023, this project focused on characterization of the candidate ferrites by determining zeta potential for each material with respect to the pH in an aqueous solvent. The project also analyzed the effect of dispersants on Ni_{0.5}Zn_{0.5}Fe₂O₄ colloidal stability. Select dispersants were used to form

slurries to test their ability to improve stability with higher amounts of solids present. Zeta potentials of a total of fourteen different ferrite compositions were carried out and evaluated for relative stability in dilute suspension; however, only the $\text{Ni}_{x-1}\text{Zn}_x\text{Fe}_2\text{O}_4$ samples, due to their magnetic permeability and curie temperature behavior as determined previously, will be highlighted here. Neutral pHs (6-8) were evaluated as the benchmark pH range for zeta potential stability as it is the working pH range for the slurry fabrication approach. Seven different $\text{Ni}_{x-1}\text{Zn}_x\text{Fe}_2\text{O}_4$ samples were studied to determine the effect of different concentrations of Ni and Zn on stability, as indicated in Figure I.1.3.3.1. As the Ni concentration increased in the $\text{Ni}_{x-1}\text{Zn}_x\text{Fe}_2\text{O}_4$ doped material, stability generally increased over the working pH range. Unfortunately, the stability of these selected ferrite compositions is still lower than desired in the working pH range ($< |30\text{mV}$). This highlighted the need for the use of a dispersant to increase the zeta potential and further stabilize the powders and prevent agglomeration during slurry formation. A series of dispersants were selected to evaluate the impact of dispersant type.

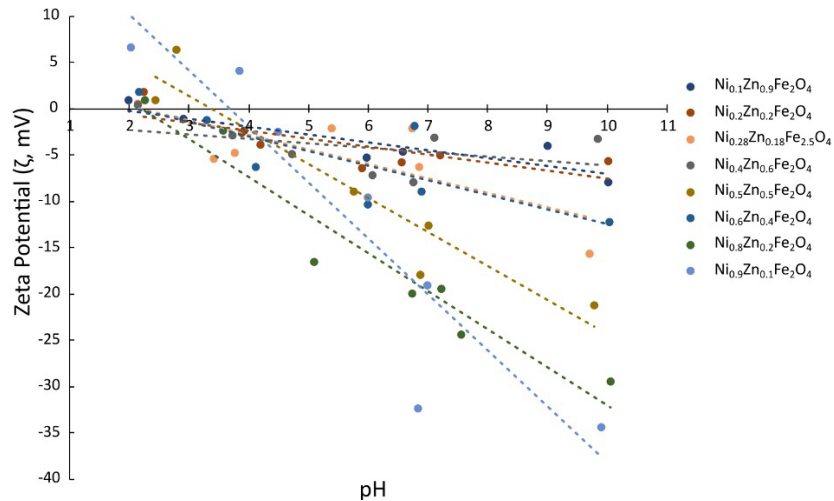


Figure I.1.3.3.1. Zeta potential as a function of pH for the $\text{Ni}_{x-1}\text{Zn}_x\text{Fe}_2\text{O}_4$ powder samples. Note, the dotted lines merely guide the eye. Source: ORNL.

For the preliminary evaluations of the effectiveness of dispersants with various ferrite compositions, $\text{Ni}_0.5\text{Zn}_0.5\text{Fe}_2\text{O}_4$ was selected due to its magnetic properties and low stability, which would make the effect of a dispersant more noticeable. Seven dispersants with varying chemistries were selected to be tested as documented in Table I.1.3.3.1. As $\text{Ni}_0.5\text{Zn}_0.5\text{Fe}_2\text{O}_4$ had an isoelectric point below a pH of 3, it was expected that a cationic dispersant would be the most effective for increasing stability due to the likelihood of optimum absorption. However, while polyethyleneimine (PEI) is a cationic dispersant and absorption was evident by the shift in zeta potential behavior, it was ineffective for providing long-term stability, even when employing varied molecular weights. Therefore, the effect of anionic and nonionic dispersants on stability was explored. Darvan CN, an anionic dispersant, did not increase the stability of $\text{Ni}_0.5\text{Zn}_0.5\text{Fe}_2\text{O}_4$ within the neutral pH range. Darvan 821A, also an anionic dispersant, was the most effective dispersant tested for $\text{Ni}_0.5\text{Zn}_0.5\text{Fe}_2\text{O}_4$ over moderate time scales (~12 hours) with a zeta potential value of -15 mV at its native pH of 6.9. Slurries were formulated using $\text{Ni}_0.5\text{Zn}_0.5\text{Fe}_2\text{O}_4$ and Darvan 821A. However, the highest stable solids loading was 26 vol.%, well below the 50 vol.% target. In general, the doped ferrite compositions had low stability ($< |30\text{ mV}$ at a pH 7) without the use of a dispersant. As increasing Ni concentration improved the stability of the ferrite powder, creating composite compositions may improve processing and still meet magnetic property requirements. Further optimization is required to achieve higher solids loading and longer processing time stability.

Table I.1.3.3.1. Candidate Dispersants for the Dispersion of Ni_{0.5}Zn_{0.5}Fe₂O₄ Powder

Dispersant	Molecular Weight (MW)	Concentration (wt.% in mother)	Dispersant Type	Supplier
PEI-2.5k	2,500 g/mol.	15	Cationic	Polysciences Inc.
PEI-25k	25,000 g/mol.	15	Cationic	Polysciences Inc.
PEI-40k	40,000 g/mol.	15	Cationic	Polysciences Inc.
PEI-70k	70,000 g/mol.	27	Cationic	Alfa Aesar
Darvan CN	10,000-16,000 g/mol.	11	Anionic	R. T. Vanderbilt Co.

Lastly, the ability to fabricate and utilize a reimagined ferrite structure relies on the ability to control the magnetic alignment and microstructure through sintering. The modeling work has expanded the compositional space and the substitution in both the *A*- and *B*-sites of the spinel structure to predict the relative magnetization of new ferrite compositions suitable for use in wireless charging. Modeling of the magnetic structure of the bulk ZnFe₂O₄ with Ni and Mg dopants, as well as magnetic characterization of the starting powders, identified that relative permeability values decreased with Mg substitution and increased with Ni doping. Thus, focus on building the foundation of composition-architecture (density) property control utilized the Ni-doped ZnFe₂O₄ material systems. To determine whether porous architectures can be utilized as an approach to lightweighting of ceramic ferrite structures, control of densification is paramount. Using simple, uniaxially pressed components, such as a disc or bar, densification behavior can be studied to promote control of processing conditions to optimize grain growth and density. Bars were pressed from the Ni_xZn_{1-x}Fe₂O₄ (where $x = 0.1, 0.2, 0.3, 0.4, 0.5, 0.6, 0.7, 0.8, 0.9$) as-received powders for dilatometry (linear shrinkage) and additional densification studies. Previous densification studies had showed that the Ni_{0.5}Zn_{0.5}Fe₂O₄ did not sinter to >95% below 1,500°C. The as-received Ni_{0.5}Zn_{0.5}Fe₂O₄ powder was ball-milled with and without addition of a sintering aide to determine whether reduced particle size and/or sintering aid would improve densification behavior at lower temperatures to enable more control of the component density, grain growth, and subsequent architecture. These ball-milled powders were also pressed into bars for dilatometric characterization. The results are still pending.

Conclusions

The efforts developing the framework for high-throughput computation and screening established the baseline standard operating procedure for predicting new compositions of ferrites that would be suitable for use in wireless charging and assisted the experimental advances made during FY 2023. The modeling work has expanded the compositional space and the substitution in both the *A*- and *B*-sites of the spinel structure to predict the relative magnetization of new compositions of ferrites suitable for use in wireless charging. Modeling of the magnetic structure of the bulk ZnFe₂O₄ with Ni and Mg dopants, as well as magnetic characterization of the starting powders, identified that relative permeability values decreased with Mg substitution and increased with Ni doping. Thus, focus on building the foundation of composition-architecture (density) property control utilized the Ni-doped ZnFe₂O₄ material systems. Zeta potential was characterized for the Ni_xZn_{1-x}Fe₂O₄ ferrite powders and was found to require the use of an additive to assist the stabilization of the powders in aqueous slurries. Fabrication studies were initiated on slurry-based techniques and magnetic characterization is in progress. Sintering studies continued on Ni_{0.5}Zn_{0.5}Fe₂O₄ powders that were ball-milled both with and without the addition of a sintering aide to determine whether reduced particle size and/or sintering aid would improve densification behavior at lower temperatures to enable more control of the component density, grain growth, and subsequent architecture.

Key Publications

1. Armstrong, B., M. P. Paranthaman, S. Bullock, and V. Rallabandi, 2023, "Pre-ceramic magnets," ORNL Invention Disclosure, 202305296 February 2023.
2. Armstrong, B., M. Kesler, R. McAuliffe, S. Bullock, and V. Cooper, 2022, "Aligned magnetic printing," ORNL Invention Disclosure 202205148, June 2022.

- Bullock, S. E., B. L. Armstrong, V. R. Cooper, M. S. Kesler, and R. D. McAuliffe, 2022, “Additive printing of ferrite magnetic structure for wireless charging,” ORNL Invention Disclosure 202205148, September 2022.

References

- Lukic, S., and Z. Pantic, 2013, “Cutting the cord: Static and dynamic inductive wireless charging of EVs,” *IEEE Electrific. Mag.*, 1(1), 57–64. <https://doi.org/10.1109/MELE.2013.2273228>.
- Jang, Y. J., Y. D. Ko, and S. Jeong, 2012, “Optimal design of the wireless charging EV,” *2012 IEEE International EV Conference*, 1–5. <https://doi.org/10.1109/IEVC.2012.6183294>.
- Thurston, A., 2022, “Magnetisable concrete’ trialed for non-stop charging of EVs,” *The Energyst*, 7 January 2022 [Online]. Available at: <https://theenergyst.com/magnetisable-concrete-trialled-for-non-stop-charging-of-evs/> (accessed 14 December 2023).
- Mohammad, M., S. Choi, and M. E. Elbuluk, 2019, “Loss minimization design of ferrite core in a DD-coil-based high-power wireless charging system for electrical vehicle application,” *IEEE Trans. Transp. Electrification*, 5(4), 957–967. <https://doi.org/10.1109/TTE.2019.2940878>.
- Tsetsekou, A., C. Agrafiotis, and A. Miliadis, 2001, “Optimization of the rheological properties of alumina slurries for ceramic processing applications, Part I: Slip-casting,” *J. Eur. Ceram. Soc.* 21(3), 363–373. [https://doi.org/10.1016/S0955-2219\(00\)00185-0](https://doi.org/10.1016/S0955-2219(00)00185-0).
- Chen, Z., Z. Li, J. Li, C. Liu, C. Lao, Y. Fu, C. Liu, Y. Li, P. Wang, and Y. He, 2019, “3D-printing of ceramics: A review,” *J. Eur. Ceram. Soc.*, 39(4), 661–687. <https://doi.org/10.1016/j.jeurceramsoc.2018.11.013>.
- McFadyen, P., and D. J. Fairhurst, 2008, “Zeta potentials of nanoceramic materials- measurement and interpretation,” *Semantic Scholar* [Online]. Available at: <https://www.semanticscholar.org/paper/Zeta-Potentials-of-Nanoceramic-and-Interpretation-Mcfadyen-Fairhurst/1eadd93457affc6b35f9326e6ddd8501d8a0a795> (accessed 14 December 2023).
- Anonymous, 2010, “Zeta potential: An introduction in 30 minutes,” *MalvernPanalytical Worldwide*, 4 November 2010 [Online]. Available at: <https://www.malvernpanalytical.com/en/learn/knowledge-center/technical-notes/tn101104zetapotentialintroduction> (accessed 14 December 2023).

Acknowledgements

The author would like to acknowledge Steward Advanced Materials for providing and characterizing the commercial ferrite powders. V. Cooper, S. Bullock, D. Shin, and S. Kwon are acknowledged for the DFT and CALPHAD development. A. May and R. McAuliffe are recognized for their assistance in measuring the magnetic properties of the ferrite powders. M. Mohammad is appreciated for his discussions on design requirements for the wireless charging pads. The authors would also like to acknowledge A. Haynes, T. Watkins, D. Shin, and J. Gibbs for their programmatic guidance on this project.

I.1.3.4 Task 3D. Novel, Ultra-High Conductivity Materials (Copper Tape + Carbon Nanotubes) for Electric Vehicles (Oak Ridge National Laboratory)

Tolga Aytug, Principal Investigator

Oak Ridge National Laboratory
Chemical Sciences Division
1 Bethel Valley Rd.
Oak Ridge, TN 37830
E-mail: aytugt@ornl.gov

J. Allen Haynes, PMCP Consortium Manager

Oak Ridge National Laboratory
Materials Science and Technology Division
1 Bethel Valley Rd.
Oak Ridge, TN 37830
E-mail: haynesa@ornl.gov

Jerry L. Gibbs, DOE Technology Development Manager

U.S. Department of Energy
E-mail: Jerry.Gibbs@ee.doe.gov

Start Date: May 1, 2022

End Date: September 30, 2023

Project Funding: \$330,000

DOE share: \$330,000

Non-DOE share: \$0

Project Introduction

This project focuses on the design, study, and evaluation of scalable and high-throughput synthesis approaches and material technologies for the fabrication of a new class of high-performance Cu-based tape conductors called ultraconductive Cu (UCC) composites. These advanced conductors have higher EC than pure Cu to enable significant improvement in the efficiency of most on- and off-board electrical conduction applications for EVs. The new concepts and methods developed within this project are expected to contribute to meeting the DOE VTO 2025 performance and EV cost targets. After over a decade of global research and development (R&D) efforts to develop other types of UCC composites elsewhere, the most promising of these are composed of one-dimensional (1D) CNTs and Cu, but the RT performance of these composites is inconsistent, and the synthetic processing methods are neither reproducible nor scalable to commercially viable levels.

The core problem being addressed in this effort is that power losses associated with the electrical resistance of Cu adversely impact and limit the efficiency and performance of all electric devices. The remarkable ballistic electrical transport characteristics offered by CNTs (the charge carriers can travel over approximately 500 nm in nanotubes without scattering) offer the opportunity to measurably improve the electrical and TC of a Cu matrix composite vs. pure Cu conductors, as well as imparting additional CNT-enabled benefits, including lower weight, better flexibility, and improved thermal management, as observed in Table I.1.3.4.1.

Table I.1.3.4.1. Comparison of the Properties of Single Walled CNTs versus Cu

	Cu	CNT
Electrical Conductivity (MS/m)	59.6	100
TC (W/m-K)	400	4,000
Current Density (A/cm ²)	106	108

To date, a few promising ultra-conducting Cu-CNT composites have been reported with conductivities increased by $\geq 30\%$ compared with the International Annealed Cu Standard and ampacities up to $\sim 100\times$ higher than Cu [1], [2], [3], [4]. However, all these technologies are only capable of being demonstrated on very short (i.e., μm -mm) sample sections and are not scalable to practically useful lengths. To our knowledge, there are presently no viable competing technologies commercially available to produce such advanced conductors to simultaneously provide consistently increased conductivity over Cu, higher current density, and improved mechanical properties in a scalable manner. Numerous processes have been explored to prepare Cu-CNT composites. The most common approaches to form layered Cu-CNT structures include powder metallurgical wire processing routes, such as spark plasma sintering, hot-pressing, deformation-based processing techniques, and electrochemical processing methods. All other technologies are based on either CNT-fibers, which do not enable conductivity levels comparable to pure Cu or involve covetic processes based on the introduction of carbon particles into a molten metal under forced convection and a high electric field [5], [6]. However, the field of covetic material is very new and results are controversial [7], [8]. To date, there have been very few reports on improved conductivity in covetic Cu materials. The issues related to fundamental understanding of the potential mechanism(s) of metal-carbon bonding and inconsistent performance characteristics have not been resolved for proposed covetic systems. Notably, the ORNL UCC materials reported here are not related to covetic concepts or technologies.

Some possible reasons for the weak performance for longer material lengths of UCC materials include the employment of low-quality/purity CNTs, a lack of controlled CNT alignment along the direction of the current flow, limited wettability, and inhomogeneous distribution of CNTs on and into the metal-matrix, and a poor fundamental understanding and control of Cu-CNT interactions affecting bulk electrical transport properties [2]. Furthermore, most of the previous UCC-type processing strategies have been unstable, with research either demonstrating inconsistent results, or being limited to unscalable laboratory processing techniques, rendering them unsuitable for large-scale commercial development into affordable, practical conductors.

Objectives

Cost and size are the key barriers to achieving the technical R&D targets of the Electrical and Electronics Technical Team 2025 electric traction drive system. This necessitates more energy-efficient power delivery through the development of improved conductors able to provide enhanced EC, higher current carrying capacity (i.e., ampacity), and better mechanical strength. Such conductors can improve energy utilization through reduced ohmic losses, transport power with a smaller size and/or lightweight wires/cables, and enable better thermal management across system components, potentially resulting in immense cumulative technological and economic value in all energy sectors ranging from on- and off-board components in electric drive vehicles to power grid systems, as well as interconnects to electronic devices and motors.

The overall objective of this project is to demonstrate a novel technological platform, designed around scalable, cost-effective, and commercially viable processing methods to produce UCC conductors that are suitable for most electrified powertrain components (i.e., converters, batteries, wiring, interconnects, busbars, charging systems, etc.) while enabling much needed reduced weight/volume, higher power density, and improved reliability and thermal characteristics. These UCC composites exhibit improved EC, ampacity, and mechanical strength, all exceeding that of pure Cu by as much as 10%. This new composite conductor couples the excellent properties of CNTs: lightweight, high-strength, and good conductivity. The R&D effort combines

ORNL's strengths in theory and simulations, nanomaterial research, electron microscopy, and scalable material processing with novel methods to produce scalable assemblies of Cu-CNT multilayer composites. Specific R&D efforts in FY 2023 included: (1) establishing critical design inputs to increase EC through improvements in processing protocols and increasing the volume percent of CNTs in the composite structure, (2) theoretical and computational modeling of the complex parameter spaces of CNTs and metal coatings to establish fundamentals and further improvements in electrical transport properties of UCCs, and (3) setting up key processing tools for prototype scale-up (> 50 cm).

Approach

Our overall approach is to couple theoretical and experimental efforts to enable the design, reproducible assembly, and scaling of CNT-Cu multilayer composites that have EC and ampacity exceeding that of pure Cu and other current Cu-CNT composites. To achieve this, two interrelated and equally important tasks are being pursued: (1) the development of controllable processing techniques for the design and scalable, reproducible fabrication of advanced multilayer Cu-CNT composites, and (2) theory-guided optimization for high-performance Cu-CNT multilayer composites. The second activity was supported through Thrust 4, "Advanced Characterization and Computational Thrust," via a project entitled "Materials by Design for Novel, Ultra-High Conductive Materials Using First-Principles Computational Approaches," led by ORNL staff member M. Yoon. Using first-principles atomistic calculations, the aim of the Thrust 4 project is to establish a fundamental understanding and structure-property relationship between materials parameters and macroscale performance, which will guide experimental efforts for improved electrical transport properties. With guidance from the Thrust 4 project, we have identified the pressure effect from CNT packing and the combination of Cu, N, and O doping on the electronic properties of semiconducting CNTs and have confirmed that the band gap of semiconducting CNTs can be reduced by pressure and eventually transform into metallic tubes through doping.

The unique fabrication approach begins with formulating stable CNT dispersions via solution methods for the deposition of a directionally aligned, uniform network of CNT coatings on the surface of commercial Cu tapes. Following CNT deposition via solution methods along the length of the Cu substrate tape, which can be scaled to a continuous manufacturing process, samples were heat-treated to remove all organic chemicals related to the solution binders from the CNT matrix and Cu surface. Subsequent deposition of thin Cu overlayers by industry-standard (i.e., high-volume capable) sputter deposition techniques, followed by thermal treatment processes, enables high-percolation conductivity of Cu throughout the entire CNT/metal-matrix ensemble, as shown in Figure I.1.3.4.1. The result is a thin continuous network of highly conductive CNTs embedded beneath the sputtered Cu, such that both external surfaces of the UCC tape are only Cu. The steps of the entire process are then repeated to integrate additional CNT and Cu layers to increase the volume percentage of CNTs in the composite structure for further improvement of the electrical and mechanical properties. Notably, a flexible substrate surface with low reactivity, such as a Cu tape, is necessary for these solution methods to successfully deposit and align a continuous network of CNTs along the desired axis. The sequence of manufacturing methods selected for this UCC technology is based on previously adopted methods and developed and used for commercial manufacturing of higher temperature superconducting tapes, which have been scaled to continuous manufacturing processes.

Samples were characterized by SEM for the investigation of microstructures. Cross-sectional microstructures of samples were studied by Z-contrast STEM. Specimen preparation was carried out by FIB methods, and STEM images were recorded using a Nion UltraSTEM operating at 200 kV. EC of the UCC composites was characterized in the temperature range from 4–400 K using a physical property measurement system. Ampacity measurements (i.e., defined as maximum current that a conductor can carry continuously under the conditions of use) were conducted using a custom-built 4-point transport probe under controlled vacuum in 1 atmosphere of ambient helium gas. Owing to its inertness and high-thermal-conductivity, helium was used as a heat-transfer medium to prevent heat-induced damage to spring-loaded voltage contacts during measurements. Although all dimensions of the test structures were carefully determined using an optical microscope and a micrometer, based on errors that may be associated with the equipment used to measure geometrical factors

(e.g., sample width, distance between the voltage contacts, substrate thickness), a generous estimation of uncertainty of 5% and 9% was calculated for the resistivity values on 28 μm and 12 μm Cu substrates, respectively.

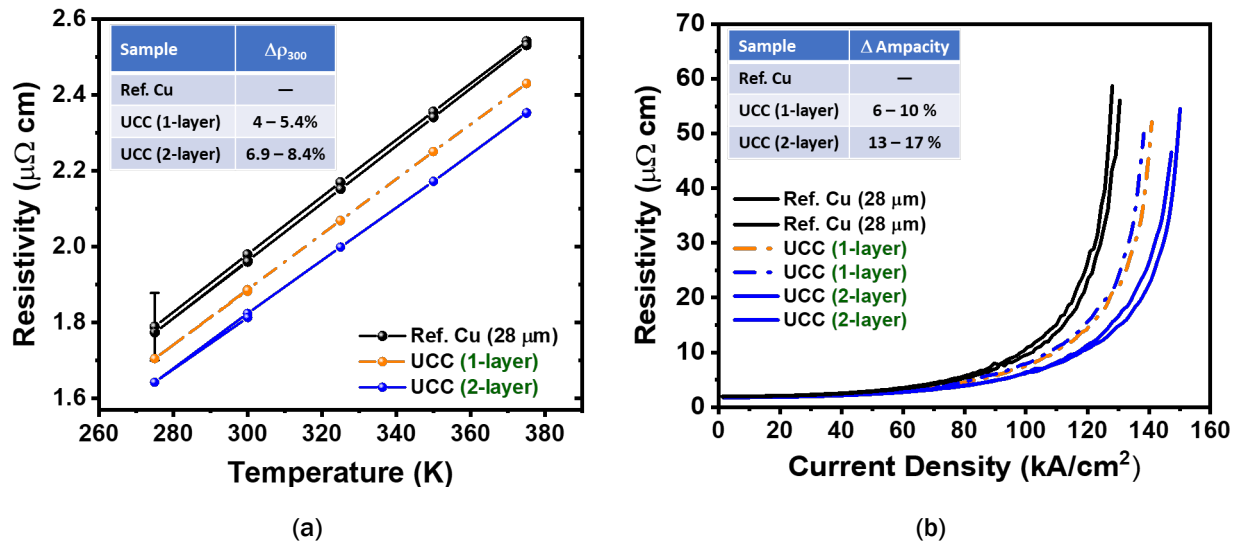


Figure I.1.3.4.1. (a) Comparison of resistivity as a function of temperature (275–375 K), and (b) current density for single and double CNT layer UCC architectures. Plots display significantly reduced resistivity and increased ampacity as compared to reference Cu substrates (see table insets). To demonstrate consistency and reproducibility, ampacity from two different pieces for each sample is shown. Source: ORNL.

Results

In addition to the benefits of CNT alignment, the improvement in electrical properties depends on the volume fraction of CNTs in the composite structure, as well as effective Cu diffusion into the deposited CNT matrix. To further improve the EC of the composites, our efforts in FY 2023 have concentrated on the integration of additional Cu/CNT stack(s) on the first Cu/CNT/Cu architecture to increase the volume fraction of CNTs within the composite assembly, as well as optimization of thermal processing protocols to achieve more-efficient Cu penetration into the CNT matrix. To enable high-percolation conductivity through the entire CNT/metal-matrix ensemble, special attention was paid to both the homogeneity and thickness of CNT and metal overlayer thicknesses. Employing a 4-probe physical property measurement system and current density set up, temperature-dependent electrical properties and the ampacity of the single and multilayer layer Cu/CNT/Cu samples that are processed at relatively optimized parameters were measured. Results shown in Figure I.1.3.4.1 verified reduction of electrical resistivity from > 5% to > 8% over the entire temperature range and increased current density from > 6% to > 13% in going from single-layer to the two-layer UCC architecture compared to that of the pure Cu reference samples. However, note that this performance does not scale linearly with the additional number of Cu/CNT stacks. That is, if compared to the observed ~5% decrease in resistivity for the single-layer UCC composite, it is expected that the decrease in resistivity of the two-layer counterpart should have exceeded 10%. We believe that the reason for this behavior is highly dependent on the uniformity and structural quality of each additional Cu and CNT layer.

To evaluate this, cross-sectional Z-contrast SEM investigations were conducted for select two-layer UCC samples, as shown in Figure I.1.3.4.2. Z-contrast STEM provides detailed information related to thickness, microstructural defects, and possible doping effects throughout the thickness of the samples. Note that the higher Z elements (Cu with $Z = 29$) appear brighter than the lower Z elements (C with $Z = 6$) when the cross-sectional images are taken in high-angle annular dark-field imaging mode. However, the results in Figure I.1.3.4.2 are presented in annular bright-field imaging mode shown in Figure I.1.3.4.2(b-c), in which the contrast was essentially reversed from the high-angle annular dark-field mode, thus revealing the brighter

CNT layers and darker regions of Cu. For analysis, UCC specimens were prepared using FIB technique and STEM images of the FIB sections, shown in Figure I.1.3.4.2(a) have also been collected to validate the spatial structural uniformity of the CNT and Cu layers. Both SEM and Z-contrast cross-sectional images display evenly dispersed CNT layers in between the two Cu layers, as well as dense, homogeneous Cu microstructures and good interfacial adhesion characteristics between the Cu and CNT layers. The annular bright-field imaging mode also clearly shows the diffusion of Cu inside the CNT matrix (i.e., dark regions infiltrating into the CNT layer). Diffusion of Cu is not only important to realize a high percolative conductive network throughout the entire CNT/metal-matrix ensemble, but also essential to facilitate modification of CNTs via Cu doping. Doping mainly serves (i) to improve charge transport across interparticle contacts by reducing tunneling barriers, or to provide conducting shunts around defective nonconducting regions, and (ii) affects the electronic structure of CNTs through charge-transfer doping. On the other hand, while cross-sectional images show relatively dense and homogeneous second Cu/CNT coverage over the first Cu/CNT layer, the thickness of the second CNT layer appears to be relatively less than the first layer; hence, possibly resulting in the non-linear improvement in conductivity that is observed with an increased number of Cu/CNT stacks. These results also underscore the importance of process optimization to obtain the best possible electrical performance characteristics of multilayer UCC prototypes.

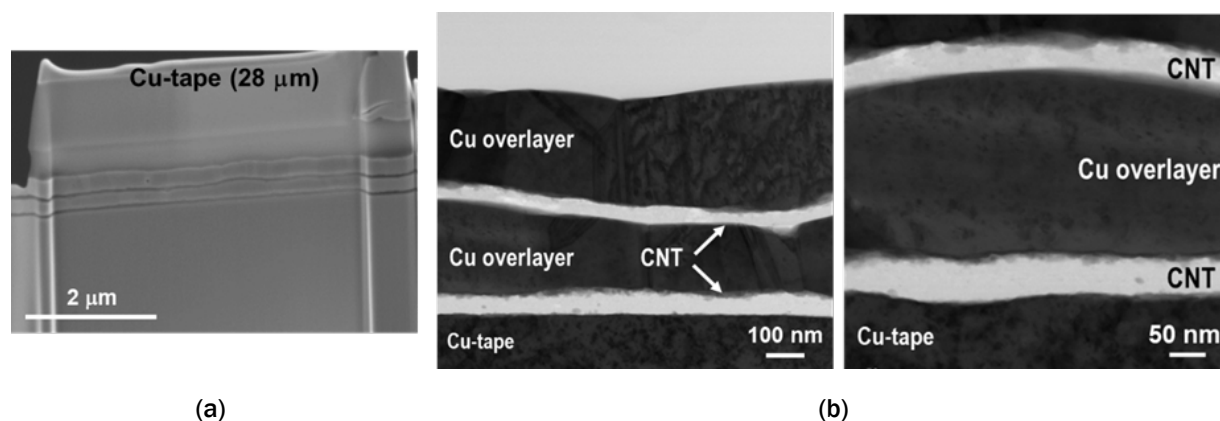


Figure I.1.3.4.2. (a) Cross-sectional STEM image of the FIB sample and (b, c) Z-contrast STEM images of the Cu/CNT/Cu/CNT/Cu double layer UCC sample on a 28 μm Cu substrate. Source: ORNL.

Next, a series of first-principles DFT calculations were conducted to understand the pressure effect from the CNT packing that mimics the real experimental UCC matrix and the influence of doping associated with Cu, N, and O. Through a series of computational calculations, we have identified mechanisms that explain the favorable influence of CNT-CNT interactions toward reducing the energy bandgap of semiconducting CNTs, as well as the combination of N, O, and Cu doping on the electronic properties of the semiconducting CNTs. Pressure exerted on CNTs together with dopants helps semiconducting CNTs to generate high electron density near the Fermi level, resulting in conversion of semiconducting CNTs into metallic tubes. Note that N doping of the CNTs is associated with the chemical nature of polyvinylpyrrolidone that is used in preparation for the electrospinning CNT solution. Cu doping is correlated with the vacuum-induced volatility and diffusion of Cu atoms from the underlying Cu substrate into the CNT matrix, and O doping is associated with the chemical modification of as-received CNTs. Hence, doping CNTs with N, O, and Cu (all electron donors) increases the electron density of the nanotubes and enhances their metallic properties. This is particularly important because the synthetic production methods of CNTs generally yield one-third of CNTs in metallic and two-thirds in semiconducting nature, rendering a high fraction of the as-received CNTs having a limited positive influence on the conductivity of the composites. Figure I.1.3.4.3(a) shows the density of states in undoped semiconducting CNTs as a function of doping and pressure, as well as compared to Cu-doped, as shown in Figure I.1.3.4.3(b); N- and O-doped, as indicated in Figure I.1.3.4.3(c); and a combination of both N/O and Cu/N/O of semiconducting tubes, as observed in Figure I.1.3.4.3(d). While semiconducting tubes show a large

energy bandgap around the Fermi level, which is denoted by a black dotted oval, a pressure effect on CNTs reduces the Fermi gap and, combined with doping either by N, O, or Cu, significantly enhances the density of states near the Fermi level, as indicated by the red dotted circles, which represent an increased number of conduction electrons and, hence, improved electronic transport properties of semiconducting CNTs. Thus, the processing methods also improve the electrical properties of the embedded CNTs.

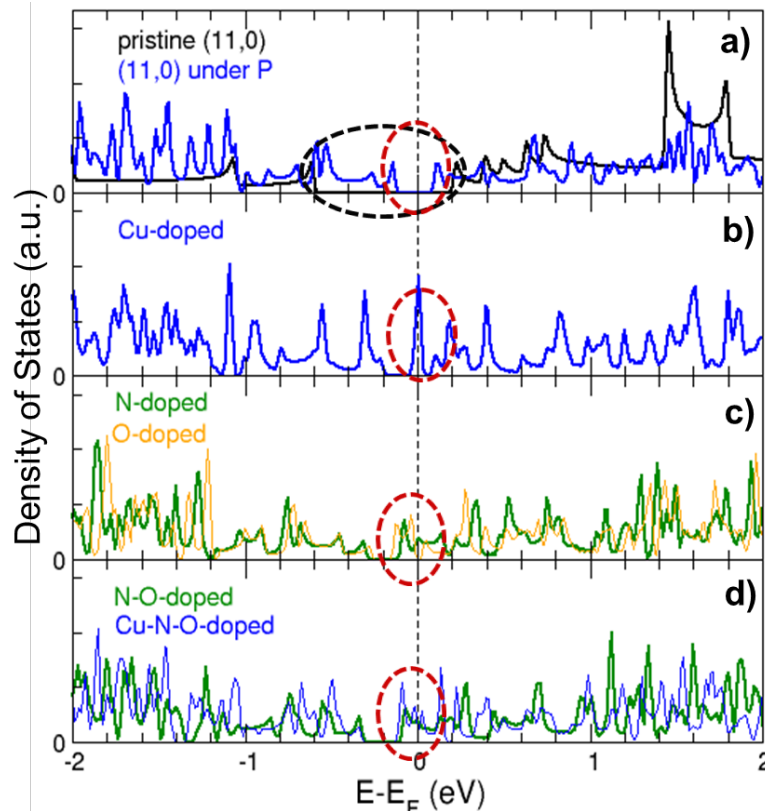


Figure I.1.3.4.3. (a) Density of states in electronic states of pressurized semiconducting (11,0) CNTs showing a reduced band gap due to CNT-CNT interactions. (b,c,d) N, O, and Cu doping help to significantly increase the electron density near the Fermi level, transforming semiconducting CNTs into metallic CNTs. Source: ORNL.

Conclusions

Advanced low resistive loss materials are needed to increase power density and reduce cost while improving efficiency and reliability of most on- and off-board electrical conduction applications for EVs. Under this multi-year project, using scalable, cost-effective, and commercially viable processing methods, we have demonstrated the feasibility of a novel materials processing/computational modeling platform that can facilitate the design and scalable fabrication of advanced ultra-conducting copper composite materials for a broad range of industrial applications. The benefits that will be gained from this research are expected to help meet the DOE VTO 2025 performance targets and can lead to reduced weight/volume, as well as improved reliability, efficiency, and thermal characteristics for all electrified power train components. Specific accomplishments include: (1) achieving step-wise further improvement in electrical performance ($\geq 8\%$ decrease in resistivity & $\geq 1\%$ increase in ampacity) through the integration of additional CNT layers over pure Cu; (2) completing the necessary hardware software design for scalable assembly of UCC composites; and (3) demonstrating the importance of theoretical modeling for the support, understanding, and guidance of experimental efforts and observations, with simulation efforts supported by a project in collaboration with the program's "Advanced Characterization and Computational Thrust."

Key Publications

1. Aytug, T., 2023, “Advanced Processing and AM for EV Propulsion: Novel, Ultra-High-Conductivity Composites for EVs,” presented at the 2023 DOE VTO Annual Merit Review, June 12, 2023, Washington, D.C., USA.

References

1. Stillman, H., and M. Burwell, 2013, “Ultraconductive Copper Wire: Overview of Worldwide R&D.” Presented at International Copper Association: Copper 2013 International Conference, December 1–4, 2013, Santiago, Chile.
2. Lee, D. F., M. Burwell, and H. Stillman, 2015, “Priority Research Areas to Accelerate the Development of Practical Ultraconductive Copper Conductors.” ORNL/TM-2015/403, Oak Ridge National Laboratory, September 2015, Oak Ridge, TN, USA. Available at: <https://info.ornl.gov/sites/publications/files/Pub58011.pdf> (accessed 20 January 2023).
3. Subramaniam, C., T. Yamada, K. Kobashi, A. Sekiguchi, D. N. Futaba, M. Yumura, and K. Hata, 2013, “One hundredfold increase in current carrying capacity in a carbon nanotube–copper composite,” *Nat. Commun.*, 4, 2202. <https://doi.org/10.1038/ncomms3202>.
4. Subramaniam, C., A. Sekiguchi, T. Yamada, D. N. Futaba, and K. Hata, 2013, “Nanoscale, planar, and multi-tiered current pathways from a carbon nanotube–copper composite with high-conductivity, ampacity, and stability.” *Nanoscale*, 8, 3888–3894. <https://doi.org/10.1039/C5NR03762J>.
5. Forrest, D. R., I. Jasiuk, L. Brown, P. Joyce, A. Mansour, and L. Salamanca–Riba, 2012, “Novel MMCs with integrally-bound nanoscale carbon,” Presented at Nanotech 2012, June 18, 2012, Santa Clara, CA, USA, CRC Press, Boca Raton, FL, USA.
6. Brown, L., P. Joyce, D. Forrest, and J. Wolk, 2011, “Physical and mechanical characterization of a nano-carbon-infused aluminum-matrix composite,” Proceedings of the SAMPE Fall Technical Conference, October 17–20, 2011, Ft. Worth, TX, USA.
7. De Groh III, H. C., and U. (Balu) Balachandran, 2018, “Conductivity of copper-carbon covetic composite,” NASA/TM—2018-219790, National Aeronautics and Space Administration, Hampton, VA, USA. Available at: <https://ntrs.nasa.gov/archive/nasa/casi.ntrs.nasa.gov/20180003330.pdf> (accessed December 14, 2023).
8. Bakir, M., and I. Jasiuk, 2017, “Novel metal-carbon nanomaterials: A review on covetics,” *Adv. Mater. Lett.*, 8, 884–890. <https://doi.org/10.5185/amlett.2017.1598>.

Acknowledgements

The author would like to acknowledge the support provided by J. Gibbs, DOE Technology Development Manager for the Electric Drive Technologies Program, DOE-EERE VTO. The author also recognizes and appreciates the support of J. A. Haynes, ORNL PMCP Manager. The significant contributions from K. Li, M. McGuire, M. Yoon, A. Lupini, and F. List to the project are also acknowledged.

I.1.3.5 Task 3E. Print Casting of Lightweight Metal-Matrix Composites for Battery Enclosures with Impact Resistance and Thermal Management (Oak Ridge National Laboratory)

Derek Splitter, Co-Principal Investigator

Oak Ridge National Laboratory
Buildings and Transportation Science Division
2360 Cherahala Blvd.
Knoxville, TN 37932
E-mail: splitterda@ornl.gov

Sebastien Dryepondt, Co-Principal Investigator

Oak Ridge National Laboratory
Materials Science and Technology Division
1 Bethel Valley Rd.
Oak Ridge, TN 37830
E-mail: dryepondtsn@ornl.gov

J. Allen Haynes, PMCP Consortium Manager

Oak Ridge National Laboratory
Materials Science and Technology Division
1 Bethel Valley Rd.
Oak Ridge, TN 37830
E-mail: haynesa@ornl.gov

Jerry L. Gibbs, DOE Technology Development Manager

U.S. Department of Energy
E-mail: Jerry.Gibbs@ee.doe.gov

Start Date: November 1, 2021

End Date: September 30, 2023

Project Funding: \$175,000

DOE share: \$175,000

Non-DOE share: \$0

Project Introduction

This task seeks to understand how a new materials architecture, involving the AM of a reinforcing metal network combined with metal casting and infiltration of lower melting temperature alloys such as Al, can be developed to create lightweight metal-metal composite structures that increase energy absorption with equal or improved TC and overall weight. This new process, developed by ORNL, has been termed PrintCasting (PC). A key advantage of the PC method is that it leverages AM control over the reinforcing phase mesostructure. Therefore, the geometry and spatial distribution of the reinforcing constituent can be precisely controlled to create composites with geometries that realize improved energy absorbing behavior, as well as other tailored mechanical and thermal properties, with capability for locally controlled and varied properties across a component. It has been demonstrated that high levels of energy absorption can be achieved by creating a reinforcement geometry that converts the applied tensile load into local compression of the more brittle, cast-Al matrix [1]. The printed reinforcement geometry is patterned with a topology designed to be bending dominated, which upon axial loading collapses the reinforcement mesh, thus compressing the lightweight-alloy matrix trapped between. The project has the potential to provide solutions to overcome key barriers related to lightweight battery containment, including impact absorption and thermal management. This novel architecture also offers significant crosscutting opportunities, as evidenced by its being licensed for non-transportation industries.

Objectives

This project aims to create AM metal-metal composites for battery enclosures with high-energy absorption and tailorable local mechanical, acoustic, and thermal properties. Potential broader applications include energy absorption under tensile loading for scenarios that include impulse loading, blast containment, and load-bearing structures, all of which are conditions relevant to battery containment in EVs. The objective is to understand the geometric factors, bonding, material selection, manufacturing, cost, and scaling aspects that enable development of multimaterial hybrid systems suitable to high-demand, long-duration EV battery containment applications, such as electric freight trucks.

Approach

A powerful feature of metal AM is the ability to directly print net-shaped structures with high levels of architectural complexity, but most additive processes are limited to a single feedstock resulting in monolithic materials. In the hybrid approach of PC materials developed by ORNL the capabilities of AM are leveraged with the lower cost and more rapid processing offered by conventional casting. Specifically, the local control over composition is achieved through the AM portions by changing the printed lattice size and/or geometry, enabling gradients in composition. Subsequently, the printed, complex, reinforcement lattice is overcast and melt-infiltrated with a lower melting point, lightweight-alloy—in this study a cast-Al alloy A356. The lightweight cast A356 alloys have lower ductility due to casting porosity and experience brittle failure under tension but can undergo very large plastic deformation under compression, whereas the AM reinforcement lattice (printed from stainless alloy 316L or Ti6Al4V) exhibits very high-strength and tensile ductility.

The A356/316L or Ti64/Al material systems are known to form brittle Fe-Al or Ti-Al intermetallic compounds when fused together [2], which motivated the design of the novel PC hybrid processing strategy. This approach combines AM of the higher melting point material lattice with casting of the lower melting point alloy to eliminate any liquid phase mixing of the two alloys during processing, and thus, avoids intermetallic formation, as highlighted in Figure I.1.3.5.1.

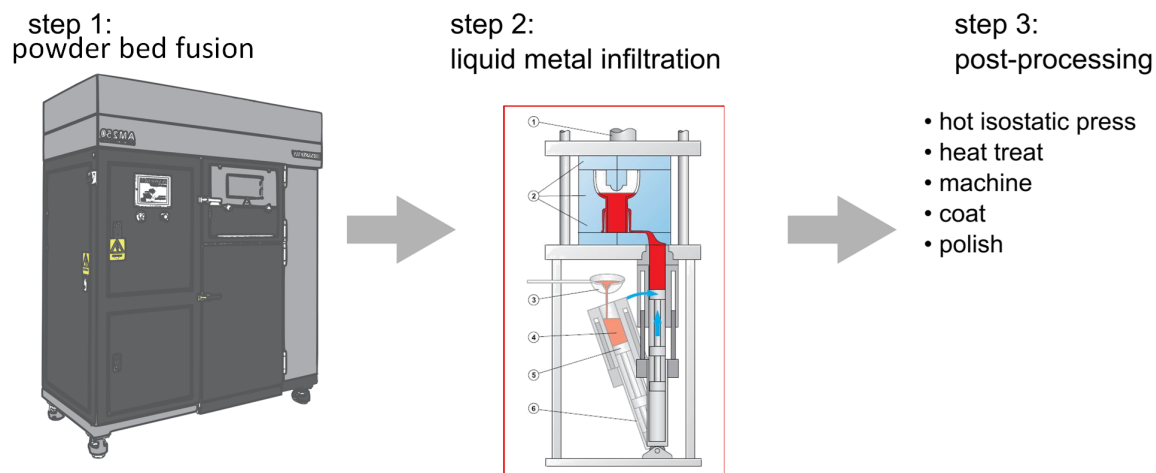


Figure I.1.3.5.1. Process for synthesizing interpenetrating phase composite materials using the PC technique.

The reinforcing lattice is printed using a laser powder bed fusion process, filled with liquid-metal using pressure die-casting, and then post-processed to optimize the properties. Source: ORNL.

The result of the PC process is an interpenetrating phase composite in which the two constituents form continuous and interconnected networks, but do not fuse and do not form Al-based intermetallics at the interfaces. It has been shown that an interpenetrating morphology can enable unique mechanical and thermal properties in a non-linear blending of the properties of the constituents [1], [3], [4], [5]. More specifically, it has been shown that fracture toughness can be increased by interconnecting the more ductile phase in a brittle/ductile system, which further improves energy absorption [1]. The goal of this project is to leverage

these unique properties of PC materials for EV battery containment systems, where PC materials can exceed the individual material energy absorption performance criteria of the individual PC constituents (monolithic Al or stainless-steel); yet the PC material can be nearly 50% thinner than monolithic Al members and more than 2× more thermally conductive than stainless-steel [6]. These properties not only improve impact resistance, but also allow for smaller EV battery assembly sizes and weight reductions from material properties alone, in addition to reducing cooling demand for the battery pack. The potential advantage of the PC approach to battery containment is highlighted in that a known critical technology gap in EV battery containment is weight management. The battery containment enclosure is often the single heaviest component in an EV, which typically can exceed 110–160 kilograms itself (compromising up to 6–10% of total LD EV vehicle mass). Therefore, improvement in structural performance and weight-savings afforded by optimizing material properties also has the potential to greatly reduce vehicle mass, thus demonstrating a pathway to improved vehicle energy-efficiency, lower battery demand, and/or improved vehicle range.

Results

The initial task effort centered around working with an external vendor to produce the HPDC infiltration of lattices. Falcon Lakeside Manufacturing designed a HPDC-specific mold for this project. During the process of casting these modeling tools, EKKcapcast software was used to develop intra-mold flow features to improve lattice infiltration from the previous approaches used, such as vacuum casting. The significant pressure increase (i.e., tons vs. previous vacuum casting at 1 atmosphere approach) is anticipated to improve infiltration and expand the dimensions of the cast structures from approximately $40 \times 40 \times 10$ mm prototypes to much larger and more challenging $228 \times 152 \times 25$ mm slabs. The purpose of the larger slabs is for demonstration purposes for highlighting infiltration capability at larger length scales required for better containment structures. To date, these length scales have been unproven with the PC approach.

ORNL-produced nine additively manufactured slabs of BCC lattice geometry with laser powder bed fusion AM. Some of the initial production samples of three slabs are seen in Figure I.1.3.5.2. Note that in the image two of the slabs show a grid pattern in the build while one is free of the grid pattern. The grid anomaly is an artifact of the production process that was resolved in this project (slab at left free of the grid).

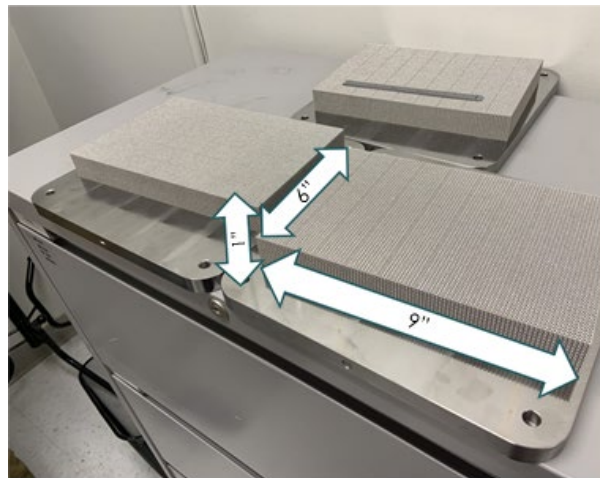


Figure I.1.3.5.2. A portion of the ORNL-produced AM lattices using 316L stainless-steel. Source: ORNL.

A significant barrier that was overcome in the scale-up of the lattice geometry was the computational cost and computing power required for the lattice files. Specifically, a unit cell geometry on the order of 2 mm was used. Figure I.1.3.5.3 displays the unit cell that was repeated in the X, Y, and Z directions to generate the lattice slab. However, directly generating the slab in its entirety results in file sizes beyond those that current AM software tools and machines can handle (e.g., requiring file sizes more than 10 GB and rendering times on the order of days). The tessellation of features at the upscaled size became far too computationally expensive

to be practical, so a solution needed to be developed. The first step in this process was to generate small “building block” size lattice configurations that could then be repeated in the AM software. The approach was to use 25 mm cell (~1 inch) or 10-unit cell cubes in the current unit cell configuration, as shown in Figure I.1.3.5.3. The approach downsized the file by over two orders of magnitude to file sizes of less than 100 MB (from greater than 10 GB for the full slab).

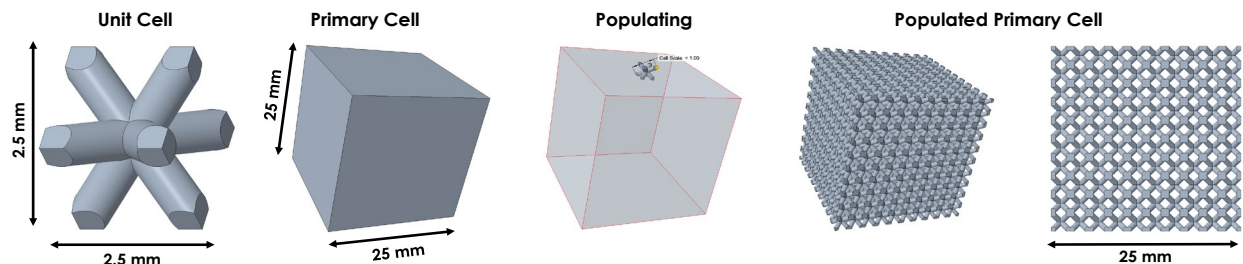


Figure I.1.3.5.3. Process of upscaling individual unit cell from 2.5 mm cube to a 10 × 10 unit cell populated cell block. Source: ORNL.

Using the 25 mm cell approach, the build volume was encompassed by a 9 × 6 cell layout, as shown in Figure I.1.3.5.4, which enabled complete fabrication. Once the physical dimensions of the approach were overcome, the last remaining file size challenges in the scale-up approach was some of the lattices had complex radius shapes, which exponentially increased the tessellation of the files.

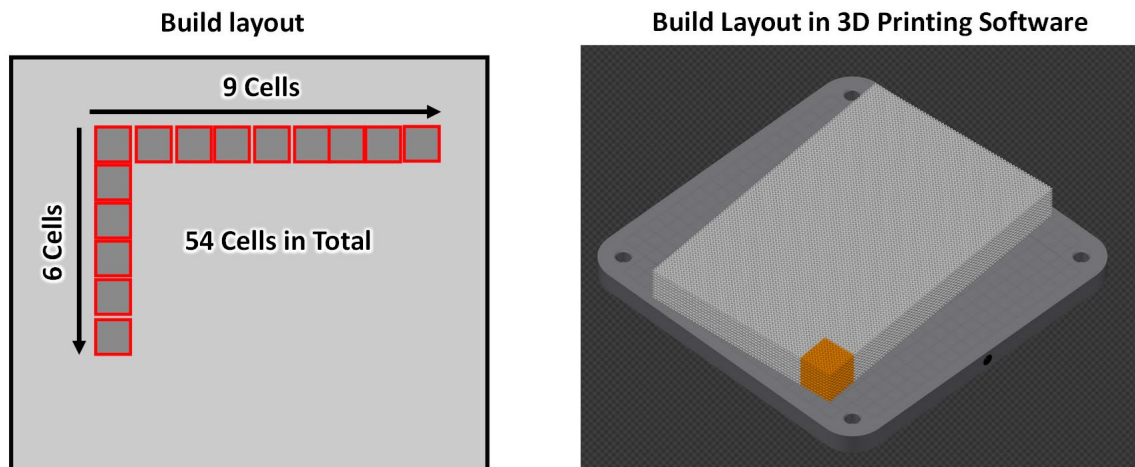


Figure I.1.3.5.4. Slab production process with 54 cell block repetitions. Source: ORNL.

Previous simulation work for the project in FY 2021 suggested that a filleted radius in the lattice structure may be beneficial to improving impact resilience and overall strength. By removing the stress concentrator at the junctions of ligaments in the lattice (the point called the node of the lattice), the lattice strength increased in the simulation. To validate these simulations, the current work physically produced the radiused lattices. To reduce file size and enable filleted lattice production, the resolution of the lattice was altered in the physical files and the renderings of them. When left unrendered, over 9 million triangles (tessellations) exist in the “best” condition for high-resolution of the 25 × 25 × 27 mm cell lattice; for a full build, that cell is repeated 54 times, resulting in over 500 million triangles. To prevent software crashes and associated file size issues, the tessellations were reduced to the granularity/resolution of the physical AM process, as shown in Figure I.1.3.5.5. In doing so, the tessellation count reduced by more than an order of magnitude. The reduction in unnecessary/unachievable precision in the computational domain is expected to have no translatable affect in the physical build, as the production methodology would not be able to achieve the resolution generated in the virtual environment.

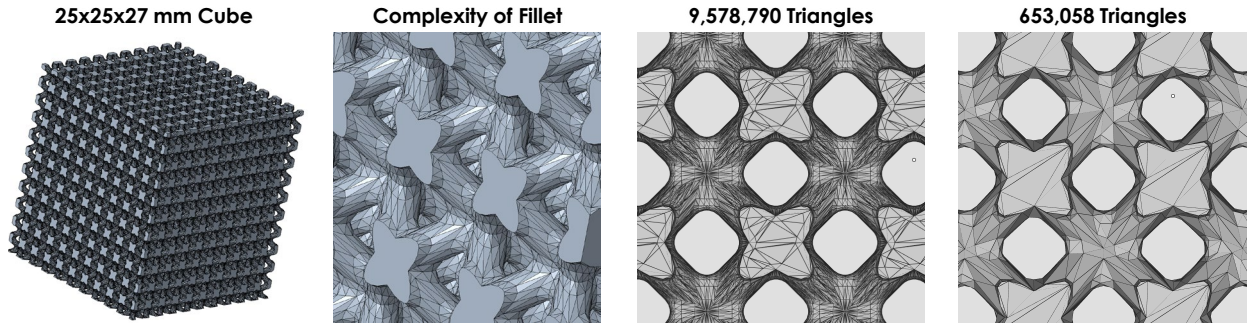


Figure I.1.3.5.5. Lattice tessellation reduction approach - over an order of magnitude reduction in surface geometry with no loss in physical build resolution. Source: ORNL.

Once the optimized physical lattices were produced, the associated die-casting tooling was produced and fitted to the physical lattice geometry. The physical molds for the HPDC matrix infiltration, as seen in Figure I.1.3.5.6, illustrate the spring-loaded ejector pins (right upper figure) are used to hold the ORNL-produced lattices in place during the infiltration process. These industrial scale molds, designed for high-pressure infiltration, will be used to infiltrate the combinations of lattices, both with and without fillets. The corresponding infiltration process was delayed due to subcontracting and production line setbacks but is on target to be completed before the end of calendar year 2023.

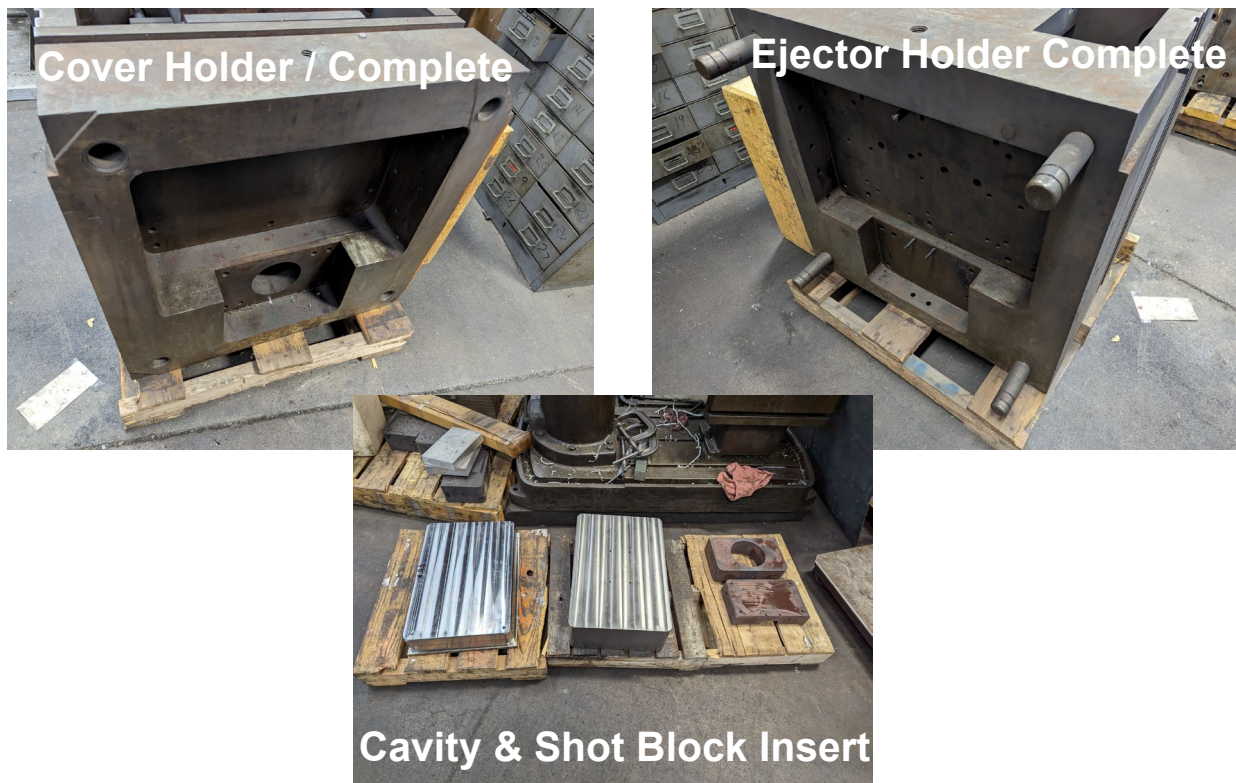


Figure I.1.3.5.6. The HPDC molds machined and ready for infiltration. Source: Falcon Lakeside Manufacturing.

Conclusions

Research and analysis of Task 3E has aimed to understand the properties and potential of novel, PC metal-metal composite architectures for EV battery containment. FY 2023 work focused on scale-up (e.g., greater than 100× the scale vs. our previous work) and the utilization of a HPDC approach to infiltrate the scaled-up lattices. A barrier to the production of the lattices was the physical scaling of the intricate geometry and coordinating printable computational models. Significant effort was made on this front where nearly two orders of magnitude reduction in file size was achieved, enabling more reasonable production/design rates and reduced computational cost. A U.S. supplier of high integrity die-castings was contracted, who has contributed to designing a prototype and in resolving known areas of materials performance improvements. The resulting scalable prototype from this effort is in the final production stages, targeting completion by the end of the calendar year. It is anticipated that significant performance and scalability of manufacturing improvements will be achieved using HPDC for matrix infiltration in PC metal-metal composite structures.

References

1. Cheng, J., M. Gussev, J. Allen, X. Hu, A. R. Moustafa, D. A. Splitter, and A. Shyam, 2020, “Deformation and failure of PrintCast A356/316L composites: DIC and finite element modeling,” *Mater. Des.*, 195, 109061. <https://doi.org/10.1016/j.matdes.2020.109061>.
2. Hofmann, D. C., J. Kolodziejska, S. Roberts, R. Otis, R. P. Dillon, J.-O. Suh, Z.-K. Liu, and J.-P. Borgonia, 2014, “Compositionally graded metals: A new frontier of AM,” *J. Mater. Res.*, 29(17), 1899–1910. <https://doi.org/10.1557/jmr.2014.208>.
3. Moustafa, A. R., R. B. Dinwiddie, A. E. Pawlowski, D. A. Splitter, A. Shyam, and Z. C. Cordero, 2018, “Mesostructure and porosity effects on the TC of additively manufactured interpenetrating phase composites,” *Addit. Manuf.*, 22, 223–229. <https://doi.org/10.1016/j.addma.2018.05.018>.
4. Pawlowski, A. E., Z. C. Cordero, M. R. French, T. R. Muth, J. K. Carver, R. B. Dinwiddie, A. M. Elliott, A. Shyam, and D. A. Splitter, 2017, “Damage-tolerant metallic composites via melt infiltration of additively manufactured preforms,” *Mater. Des.*, 127, 346–351. <https://doi.org/10.1016/j.matdes.2017.04.072>.
5. Poole, L. L., M. Gonzales, M. R. French, W. A. Yarberr III, A. R. Moustafa, and Z. C. Cordero. “Hypervelocity impact of PrintCast 316L/A356 composites,” 2020, *Int. J. Impact Eng.*, 136, 103407. <https://doi.org/10.1016/j.ijimpeng.2019.103407>.
6. French, M., W. Yarberr, A. E. Pawlowski, A. Shyam, D. A. Splitter, A. M. Elliott, K. Carver, and Z. Cordero, 2017, “Hypervelocity Impact of Additively Manufactured A356/316L Interpenetrating Phase Composites,” AC05-00OR22725, Oak Ridge National Laboratory, Oak Ridge, TN, USA.

Acknowledgements

The authors express their great thanks to H. Hyer of ORNL for his assistance in the AM computational optimization and production efforts.

I.1.3.6 Task 3F. Ultra-Conductor Development for Enhanced Electric Vehicle Performance (Pacific Northwest National Laboratory)

Keerti S. Kappagantula, Principal Investigator

Pacific Northwest National Laboratory
Energy Processes and Materials Division
900 Battelle Blvd.
Richland, WA 99354
E-mail: ksk@pnnl.gov

J. Allen Haynes, PMCP Consortium Manager

Oak Ridge National Laboratory
Materials Science and Technology Division
1 Bethel Valley Rd.
Oak Ridge, TN 37830
E-mail: haynesa@ornl.gov

Jerry L. Gibbs, DOE Technology Development Manager

U.S. Department of Energy
E-mail: Jerry.Gibbs@ee.doe.gov

Start Date: November 15, 2022
Project Funding: \$360,000

End Date: September 30, 2023
DOE share: \$360,000

Non-DOE share: \$0

Project Introduction

In this project, we are developing Al and Cu conductors with enhanced electrical performance for use as EV electrical components, such as motor windings, busbars, connectors, and cables in order to demonstrate the potential for reduced energy loss and greenhouse gas emissions, all while improving EV range. Electrical components in EVs are traditionally made using alloys with high-EC, such as electrolytic tough pitch Cu (C11000) and oxygen-free, high-conductivity Cu (C10100) alloys. Additionally, high-EC Al alloys, such as AA1350 or AA1100, are also used to promote vehicle lightweighting because of their low-density even though they demonstrate only ~60% of the EC of C11000. Enhancing EV performance through the use of materials with better electrical properties—in particular, higher EC and current density, as well as a lower temperature coefficient of resistance (TCR) compared to commercial alloys—will lead to significantly improved energy savings.

Recent work at PNNL shows that manufacturing metal composites with nanocrystalline additives such as graphene using a shear-based solid-phase processing technique called shear-assisted processing and extrusion (ShAPE™) can enhance EC both at RT and elevated operating temperatures, as well as at a lower TCR compared to commercial-conductor grade Cu and Al alloys [1]. Such composites, when demonstrating enhanced electrical properties compared to the base metals, are colloquially referred to as “ultra-conductors.” While demonstrating enhanced electrical performance in ShAPE™-synthesized metal-graphene composites is a significant step forward in ultra-conductor development, barriers exist in using these composites to manufacture commercial-scale EV electrical components. To motivate easy market adoption of ultra-conductors, performance metrics should be at least 10% higher than existing commercial conductors at operating temperatures. Additionally, the composite manufacturing process, ShAPE™, must be scaled-up to synthesize bulk metal composites at industrially significant volumes while preserving the enhanced EC.

At the beginning of the project, the Cu and Al composite samples were manufactured to have the largest dimensions of ~2-m-length and 2–3 mm diameter [2]. This must be extended to manufacturing bar-stock with dimensions and volumes matching those generally used by windings and component manufacturers in processing setups. Finally, there are several post-processing steps (e.g., rolling, stamping, annealing,

machining) used in manufacturing EV components using rod-, bar-, or sheet-stock, depending on the final product forms. Such thermomechanical processing can alter the microstructures of the ShAPE™ ultra-conductors and could be detrimental to electrical, mechanical, and corrosion behavior. There is a gap in ultra-conductor literature on the effects of machining and forming operations on composite performance. Understanding these effects of post-processing and accounting for them during component manufacturing is essential to ensure the performance enhancements developed in the bulk-scale ShAPE™ composite are preserved in the final parts manufactured from the ultra-conductor extrudates.

Objectives

Based on the gaps identified in the roadmap for adoption of ShAPE™ ultra-conductors at the commercial-scale, the following objectives were developed for the current project:

1. Demonstrate 10% enhanced electrical performance in Cu ultra-conductors and Al ultra-conductors manufactured using ShAPE™ technology.
2. Scale-up ultra-conductor manufacturing using ShAPE™ in sufficient quantities of 5-mm diameter rods that are necessary for making EV components, such as windings and cables.
3. Determine the effects of post-processing techniques (such as drawing and annealing) on the electrical and mechanical behavior of the bulk-scale ShAPE™-synthesized ultra-conductors.

Approach

This project is progressing along two simultaneous tracks encompassing three tasks. Track 1 focuses on Al and Cu ultra-conductor development using ShAPE™. Here, we are evaluating the effect of nanocrystalline carbon additives (e.g., graphene, reduced graphene oxide) on electrical and mechanical properties; namely EC, TCR, UTS, YS, and percent elongation of C10100, C11000, and AA1100. We are also identifying composite formulations demonstrating enhanced performance compared to market standards, apt for commercial applications in this track. Track 2 focuses on ultra-conductor component manufacturing process development. Here, we are determining optimal precursor configurations, ShAPE™ manufacturing parameters, tooling, product forms, and post-processing treatments required for making EV components, such as motor windings, wires, and cables using the ultra-conductors developed in Track 1. In this track, we are benchmarking scaled-up, ultra-conductor performance against commercial product performance by testing the electrical and mechanical performance of the ShAPE™ samples.

Results

The team previously identified there may be local variations in electrical properties of the three-dimensional ultra-conductors with graphene additives being developed in this effort. This is an anticipated outcome associated with any manufactured component, and especially with composite materials with local phase differences due to the discrete additives present in the material. However, across EV component applications, there is a requirement to maintain uniform properties within an error margin in order to ensure consistent long-term performance of the component. To identify the allowed variability in local properties in a component, the team conducted a series of discussions with several EV component manufacturers to understand the typically allowed variability in local properties, especially EC, tolerated in EV components. The team also determined the local variations in the electrical properties of ShAPE™ composites to understand the factors responsible and developed strategies to reduce local variability in electrical properties. Table I.1.3.6.1 provides the viable property variations as indicated by the EV component manufacturers for different baseline Cu and Al alloy-based components.

Table I.1.3.6.1. Component, Demonstration Dimensions, and Allowed Property Variability

Component	Demo Sample Sizes	Conductivity Variation
Motor wires	2 – 3 m long wires, 1 – 3 mm diameter	1 – 2% IACS along the length
Busbars	1 m long bars or wires, >2 mm diameter	2 – 3% IACS along the length
Contact Assemblies	1.5 m long wires, >1 mm diameter, measurement gauge-length of 300 mm at least	1 – 2% IACS along the length

Subsequently, we measured the EC of the ShAPE™ wires with and without additives that demonstrated lower TCR than AA1100. We noted that controlling temperature and pressure during ShAPE™ enables us to maintain uniform properties along the wires as a function of location, as seen in Figure I.1.3.6.1. It is interesting to note that even with the microstructural stochasticity induced by the inclusion of nanoscale additives, the variation in EC of the ShAPE™ wires was ~0.5–0.6% IACS, which is an order of magnitude less than industrial requirements.

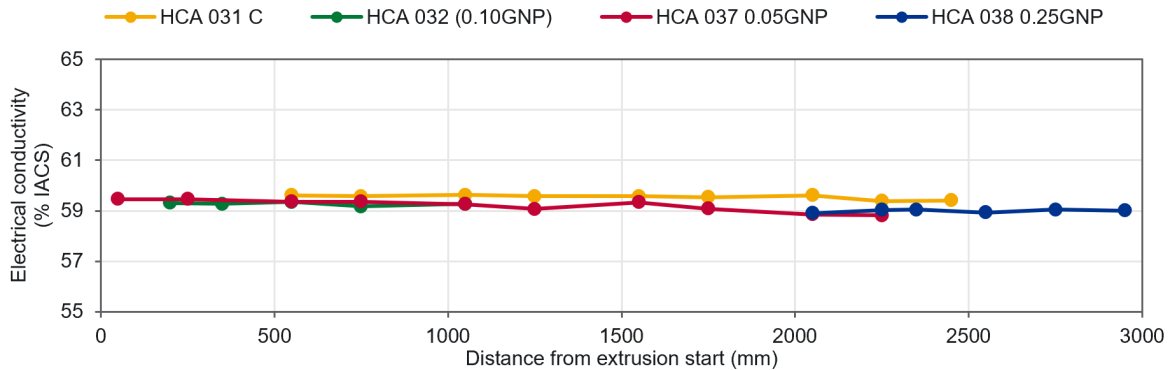


Figure I.1.3.6.1. EC of ShAPE™ AA1100-graphene composites with varying graphene content demonstrating lower TCR than AA1100 along the length of the wires showing <0.6% IACS variability. Source: PNNL.

In FY 2023, several samples were manufactured over the course of the task performance with varying material composition (graphene content) and process parameters (ShAPE™ pressure and temperature). Since mechanical properties of the conductors are relevant for the post-processing operation, namely drawing and annealing, UTS and percent elongation is reported for the ultra-conductors in their as-extruded condition. ShAPE™ Cu ultra-conductors with 6 ppm graphene show a conductivity of 104.8% IACS, while those with 12 ppm graphene show a TCR of $3.45 \times 10^{-3} \text{ }^\circ\text{C}^{-1}$. For comparison, Cu alloy EC is typically 100–101% IACS with a TCR of $3.96\text{--}4 \times 10^{-3} \text{ }^\circ\text{C}^{-1}$. This shows that ShAPE™ Cu ultra-conductors are >10% more conductive than commercial Cu alloys at operating temperatures beyond 200°C. ShAPE™ Al ultra-conductors with 0.1 wt.% reduced graphene oxide demonstrated an EC of 66% IACS, which is >8% higher than that of the corresponding control sample with a conductivity of 61% IACS. Please note that the control sample performance is similar to the AA1100 samples procured commercially as well. Additionally, the ShAPE™ Al ultra-conductors show a TCR of $4.04 \times 10^{-3} \text{ }^\circ\text{C}^{-1}$ while that of the ShAPE™ AA1100 manufactured at similar process parameters show a $4.55 \times 10^{-3} \text{ }^\circ\text{C}^{-1}$, which is in the range of the property reported for commercial AA1100 of $4.5\text{--}.6 \times 10^{-3} \text{ }^\circ\text{C}^{-1}$. This shows that ShAPE™ Al ultra-conductors are within 80% of C11000 performance since C11000 alloy has a temperature coefficient of $3.96 \times 10^{-3} \text{ }^\circ\text{C}^{-1}$. ShAPE™ Cu-graphene wires with 6 ppm graphene demonstrate a UTS of 240.9 MPa, which is higher than that of a comparable commercial Cu alloy (221.4 MPa). The ShAPE™ Cu ultra-conductors show a percent elongation of 51.2%, which is higher than Cu alloy wires at 42.4%. ShAPE™ Al-graphene wires with 0.1 wt.% additive showed a UTS of 101.6 MPa, which is slightly lower than seen for commercial AA1100 at 103.9 MPa. On the other hand, ShAPE™ Al ultra-conductors showed a percent elongation of 25.7%, which is higher than AA1100 at 20.8%. Finally, we subjected commercially procured AA1100, ShAPE™ AA1100, and ShAPE™ ultra-conductor wires to drawing to achieve 90% cold work imparted to the samples. Subsequently, the wires were annealed at 250°C and 400°C to evaluate the effect of temperature and duration on the electrical properties. We measured the EC of the as-ShAPE™-drawn and annealed wires and determined the change in conductivity with respect to the virgin as-ShAPE™ condition. Changes in the conductivity of the ShAPE™ samples post drawing and annealing are shown in Figure I.1.3.6.2. As can be seen, the reduction in conductivity after drawing ranged between 0.5–1% IACS for the commercially procured wire from McMaster Carr, while the ShAPE™ AA1100 wire showed a reduction in conductivity after drawing by ~1.1%. However, the ShAPE™ ultra-conductor wire with 0.1 wt.% graphene showed a reduction in conductivity by 0.8–1.7%, which is the greatest variation recorded among the samples. This is to be expected owing to the ultra-conductor being a

composite rather than a uniform alloy such as the commercial or ShAPE™ wire. Annealing the wires at 250°C increased the conductivity of the commercial and ShAPE™ AA1100 wires by 0.2% and 0.4%, as shown in Figure I.1.3.6.2(a). However, conductivity of the Al/graphene wire decreased by 0.1%. Contrarily, annealing to 400°C retained all the EC of the ShAPE™ ultra-conductor wires that was seen in the virgin condition, as seen in Figure I.1.3.6.2(b). Here we note that the conductivity of the commercial and ShAPE™ wires reduced by ~0.4% and 0.1% when annealed at 400°C.

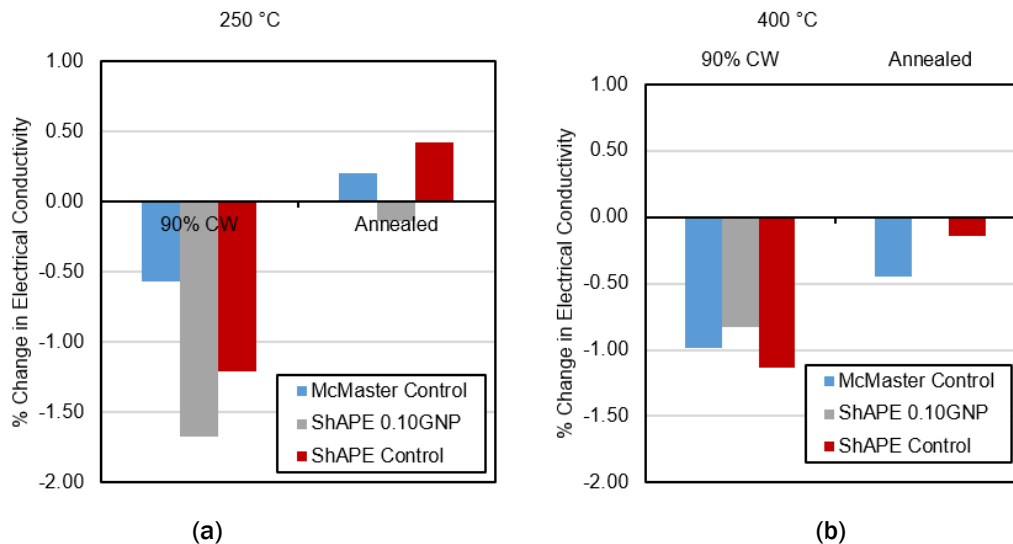


Figure I.1.3.6.2. Change in EC of commercially procured AA1100 wire from McMaster Carr, ShAPE™ AA1100 wire (ShAPE™ control), and ShAPE™ Al/graphene ultra-conductor wire with 0.1 wt.% graphene after cold drawing and annealing at (a) 250°C and (b) 400°C with respect to their as extruded or as-procured condition.

Source: PNNL.

Conclusions

In FY 2023, the team conducted a series of discussions with several EV component manufacturers to understand the typically allowed variability in local properties, especially EC, tolerated in EV components. The team also determined the local variations in the electrical properties of ShAPE™ composites to understand the factors responsible and developed strategies to reduce local variability in electrical properties. Additionally, ShAPE™ tooling, namely extrusion die and rings, were designed to scale-up conductors with a diameter of 5 mm. Since mechanical properties of the conductors are relevant for the post-processing operation, namely drawing and annealing, we determined UTS and percent elongation for the ultra-conductors in their as-extruded condition. The team subjected commercially procured AA1100, ShAPE™ AA1100, and ShAPE™ ultra-conductor wires to drawing to achieve 90% cold work imparted to the samples. Subsequently, the wires were annealed at 250°C and 400°C to evaluate the effect of temperature and duration on electrical properties. We measured the EC of the as-ShAPE™, drawn and annealed wires, and determined the change in conductivity with respect to the virgin (as-ShAPE™) condition increased by 0.2% and 0.4%.

Key Publications

1. Kappagantula, K. S., G. J. Grant, A. K. Nittala, X. Li, M. Reza-E-Rabby, W. J. Choi, B. Gwalani, and J. A. Silverstein, 2023, "Extrusion processes, feedstock materials, conductive materials and/or assemblies," US Nonprovisional Patent Application, iEdison No. 0685901-13-0018, IPID 30343-E, Patent Master ID 10706, March 2023.
2. Kappagantula, K. S., G. J. Grant, A. K. Nittala, X. Li, M. Reza-E-Rabby, W. J. Choi, B. Gwalani, and J. A. Silverstein, 2023, "Extrusion processes, feedstock materials, conductive materials and/or

assemblies,” Patent Master ID 10708, iEdison No. 0685901-13-0018, IPID 30343-E WO9, March 2023.

3. Kappagantula, K. S., G. J. Grant, A. K. Nittala, X. Li, M. Reza-E-Rabby, W. J. Choi, B. Gwalani, and J. A. Silverstein, 2023, “PCT: Aluminum/carbon composites with ultra-high conductivity,” Patent Master ID 10707, iEdison No. 0685901-20-0035, IPID 31815-E WO, March 2023.
4. Nittala, A., J. Smith, B. Gwalani, J. Silverstein, F. Kraft, and K. Kappagantula, 2023, “Simultaneously improved electrical and mechanical performance of hot-extruded bulk-scale aluminum-graphene wires,” *Mater. Sci. Eng. B*, 293, 116452. <https://doi.org/10.1016/j.mseb.2023.116452>.
5. Subedi, K. N., K. Nepal, C. Ugwumadu, K. Kappagantula, and D. A. Drabold, 2023, “Electronic transport in copper–graphene composites,” *Appl. Phys. Lett.*, 122(3), 031903. <https://doi.org/10.1063/5.0137086>.

References

1. Li, X., C. Zhou, N. Overman, X. Ma, N. Canfield, K. S. Kappagantula, J. Schroth, and G. Grant, 2021, “Copper-carbon composite wire with a uniform carbon dispersion made by friction extrusion,” *J. Manuf. Process.*, 65, 397–406. <https://doi.org/10.1016/j.jmapro.2021.03.055>.
2. Kappagantula, K., 2022, *CABLE Big Idea Workshop 2022*, 20–21 July 2022, Chicago, IL, USA.

Acknowledgements

The authors appreciate the efforts of M. R. E. Rabby on the ShAPE™ process design, A. Nittala for the conductor design and property characterization, P. Ottoni for the property testing, N. Overman and J. Escobar for the microstructural characterization efforts, and A. Guzman for the sample preparation efforts. PNNL is operated by the Battelle Memorial Institute for DOE under contract DE-AC06-76LO1830.

I.1.3.7 Task 3G. Design of Sustainable Aluminum Alloy Feedstock for Additive Manufacturing (Oak Ridge National Laboratory)

Sumit Bahl, Principal Investigator

Oak Ridge National Laboratory
Materials Science and Technology Division
1 Bethel Valley Road
Oak Ridge, TN 37830
E-mail: bahls@ornl.gov

J. Allen Haynes, PMCP Consortium Manager

Oak Ridge National Laboratory
Materials Science and Technology Division
1 Bethel Valley Rd.
Oak Ridge, TN 37830
E-mail: haynesa@ornl.gov

Jerry L. Gibbs, DOE Technology Development Manager

U.S. Department of Energy
E-mail: Jerry.Gibbs@ee.doe.gov

Start Date: October 1, 2022
Project Funding: \$360,000

End Date: September 30, 2023
DOE share: \$360,000

Non-DOE share: \$0

Project Introduction

Lightweight Al alloys are widely used in the automotive industry. Primary Al production is energy-intensive and leads to high greenhouse gas emissions. Recycling of secondary (or scrap) Al requires ~5% of the energy used for primary production, with much lower greenhouse gas emissions [1]. One of the main challenges with recycling is the pickup of various impurity elements, such as Fe, Cu, etc., that can negatively affect both the downstream processing and/or the mechanical properties of Al alloys due to formation of coarse intermetallic phases. Scrap recycling to achieve sustainability necessitates research into methods that can neutralize the harmful effects of undesirable impurities. The goal of this task is to evaluate AM as a method to process scrap-based Al alloy compositions. AM processes, such as laser powder bed fusion (LPBF), offer several orders of magnitude higher solidification cooling rates compared to conventional casting processes (e.g., $10^5 - 10^7$ °C/s vs. $10^0 - 10^3$ °C/s) that could be beneficial for the processing of scrap-utilizing Al alloys [2]. This task will investigate the effect of high AM cooling rates on microstructural refinement and the resultant effect on mechanical properties of Al alloy compositions with increased impurity content.

Objectives

This small one-year task, which focuses on identifying pathways toward the design of sustainable (higher secondary content) and printable Al alloys for future automotive AM, aims to study the effect of increased Fe concentration (0.75 wt.%) in an AM Al-Si-Cu-Mg-Fe (e.g., Al-7Si-0.5Cu-0.3Mg wt.%) alloy on its microstructure and mechanical properties. The specific objectives pursued within this task are as follows:

- To study the processability of the Al-Si-Cu-Mg-Fe alloy via LPBF AM.
- To characterize the microstructures and tensile properties of the AM Al-Si-Cu-Mg-Fe alloy.
- To determine the aging behavior of the alloy under T5 and T6 heat treatments.
- To establish the microstructure-property relationships and provide input for designing impurity-tolerant secondary Al alloys for AM.

Approach

Al-7Si-0.5Cu-0.3Mg (wt.%) is a cast-Al alloy (also known as A356+0.5Cu) used to manufacture internal combustion engines (ICEs) for passenger vehicles. The transition from ICE vehicles to EVs is expected to generate a significant amount of A356+0.5Cu Al alloy scrap in the coming years. The effect of increased Fe-impurity (0.75 wt.%) on the microstructure and mechanical properties of the Al-7Si-0.5Cu-0.3Mg alloy produced by LPBF is investigated. The Al-Si-Cu-Mg-Fe alloy was fabricated using various LPBF AM processing parameters to determine alloy processability. The alloy exhibited excellent processability within the investigated processing parameters range. Mechanical coupons were subsequently produced using four down-selected parameter sets where the laser power and scan speed were varied to study the effect of process variations on microstructure and tensile properties. Microstructural investigations were conducted using a SEM equipped with EDS, EBSD, and APT. Tensile properties were measured at RT and compared to those of other AM Al-Si-based alloys with a low Fe concentration.

Results

Figure I.1.3.7.1 shows the grain structure and microstructure of the AM Al-Si-Cu-Mg-Fe alloy. The electron backscatter diffraction map shown in Figure I.1.3.7.1(a) indicates that the grains are mostly columnar throughout, with a few fine, equiaxed grains observed only near the melt pool boundaries. The lower magnification SEM image in Figure I.1.3.7.1(b) shows very few porous defects and no cracks in the microstructure indicating excellent processability of the alloy with high Fe-impurity. The higher magnification SEM in Figure I.1.3.7.1(c) shows the typical solidification microstructure of this alloy, comprising eutectic α -Al channels and fine, interconnected Si particles. The region below melt pool boundaries, as indicated by the yellow dotted line in Figure I.1.3.7.1(c) is thermally cycled during melting of the subsequent layer; this region is known as a heat-affected zone (HAZ). A few needle-shaped precipitates are observed in the HAZ, which are likely to be an AlFeSi phase that is expected to form due to high-Si and high-Fe content in the alloy. The high AM cooling rates significantly refine the size of the AlFeSi phases, which are typically detrimental in cast secondary Al alloys due to their much larger size when solidified more slowly (casting). The APT results provided in Figure I.1.3.7.2 indicate the α -Al matrix is essentially devoid of Fe, but it is supersaturated with Si and Mg, which should allow direct aging heat treatments without the need for an intermediate solutionizing step.

The tensile properties of the Al-Si-Cu-Mg-Fe alloy in an AF state are summarized in Figure I.1.3.7.3(a). This alloy displays high YS (~250 MPa), UTS (~450 MPa), and high-ductility (~4-5%) despite the presence of 0.75 wt.% Fe, and the properties are independent of the process parameters investigated here. Figure I.1.3.7.3(b) compares the YS and elongation of the Al-Si-Cu-Mg-Fe alloy with those of other AM Al-Si-Mg based alloys that contain limited Fe. Significant variation exists among the literature data, which may reflect the effect of process and compositional variations in these alloys. Nevertheless, the ductility of the Al-Si-Cu-Mg-Fe alloy falls within the ductility range for lower-Fe containing AM Al-Si-Mg-alloys, which is an important finding since it indicates that rapid solidification conditions of this AM process effectively suppress the deleterious effects of intermetallics resulting from the higher Fe content in the alloy.

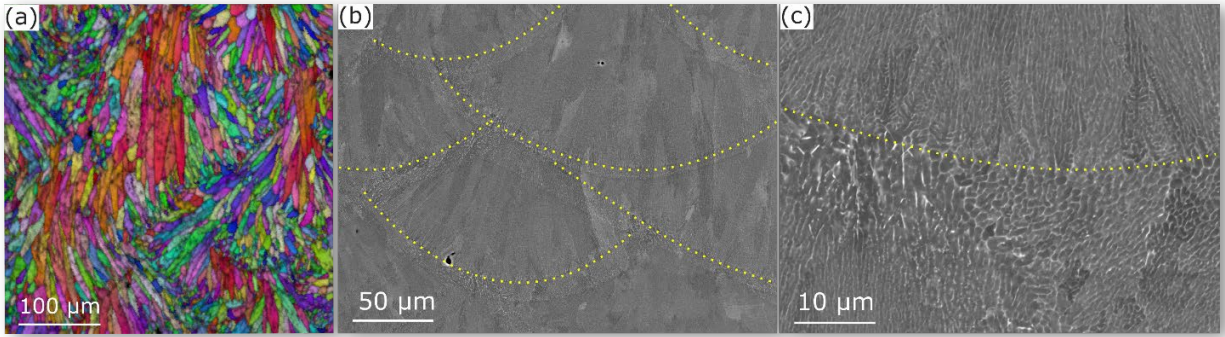


Figure I.1.3.7.1. A summary of the AF microstructure of the Al-Si-Cu-Mg-Fe alloy: (a) IPF colored map showing the grain structure; SEM micrographs showing microstructures at (b) lower and (c) higher magnifications. Melt pool boundaries are outlined by dotted lines in (b) and (c). The BD is vertically upwards. The microstructures correspond to the alloy produced at 370 W and 1,600 mm/s scanning speed. Source: ORNL.

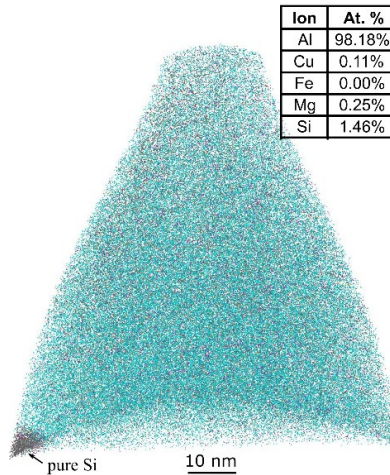


Figure I.1.3.7.2. APT results for the Al-Si-Cu-Mg-Fe alloy in an AF state. The table in the inset lists the matrix composition, excluding the Si-particle observed at the left bottom edge of the tip. Source: ORNL.

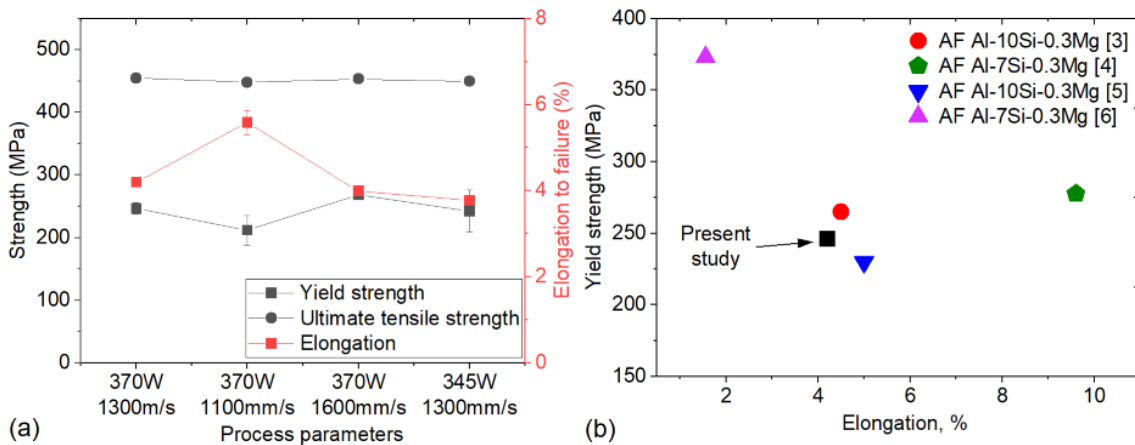


Figure I.1.3.7.3. (a) Tensile properties of the as-fabricated (AF) AlSiCuMgFe alloy processed with different processing parameters. (b) A comparison of tensile properties with other relevant AM Al-Si-Mg based alloys whose tensile data are reproduced from Refs. [3]–[6]. Source: ORNL.

The response of the as-fabricated (AF) AlSiCuMgFe alloy to T5 and T6 treatments was investigated. The T6 treatment first involves a solutionizing and quenching treatment to dissolve the maximum amount of solutes into the α -Al matrix followed by an aging step to induce nanoscale precipitation of strengthening phases. The high AM cooling rates promote solute trapping during solidification where a direct aging treatment (T5) without the solutionizing step can possibly be applied for precipitation-strengthening. Considering shorter diffusion distances in the refined AM AlSiCuMgFe alloy microstructure and the desire to avoid excessive coarsening of Si particles, a short solutionizing time of 1 h at 530°C was used instead of the 5–10 h typically used for cast A356 counterparts during a T6 treatment. The samples were quenched in water after solution treatment. The aging treatment for both T6 and T5 was performed at 180°C for various durations up to 24 h.

Figure I.1.3.7.4(a) shows the grain structure after 530°C for 1 h solutionizing, but before 180°C aging. As observed in Figure I.1.3.7.4(a), no apparent difference exists between the AF and solutionized grain structures, indicating that grains remain resistant to growth or coarsening. Figure I.1.3.7.4(b) and Figure I.1.3.7.4(c) show the microstructures in the melt pool interiors at lower and higher magnifications, respectively. While Si particles in the grain interiors only experience fragmentation, those at/near grain boundaries experience a notable coarsening, leading to the presence of much coarser precipitates at grain boundaries. Due to the grains being much finer near the melt pool boundaries, precipitate coarsening in these regions is more pronounced compared to the melt pool interiors, as indicated in Figure I.1.3.7.4(d). The EDS measurements in Figure I.1.3.7.4(e–g) of the area in Figure I.1.3.7.4(d) show that the coarser precipitates with globular morphology are Si particles, whereas those with a platelet morphology also contain Fe, which are suggested to be an Al₃FeSi phase based on their morphology.

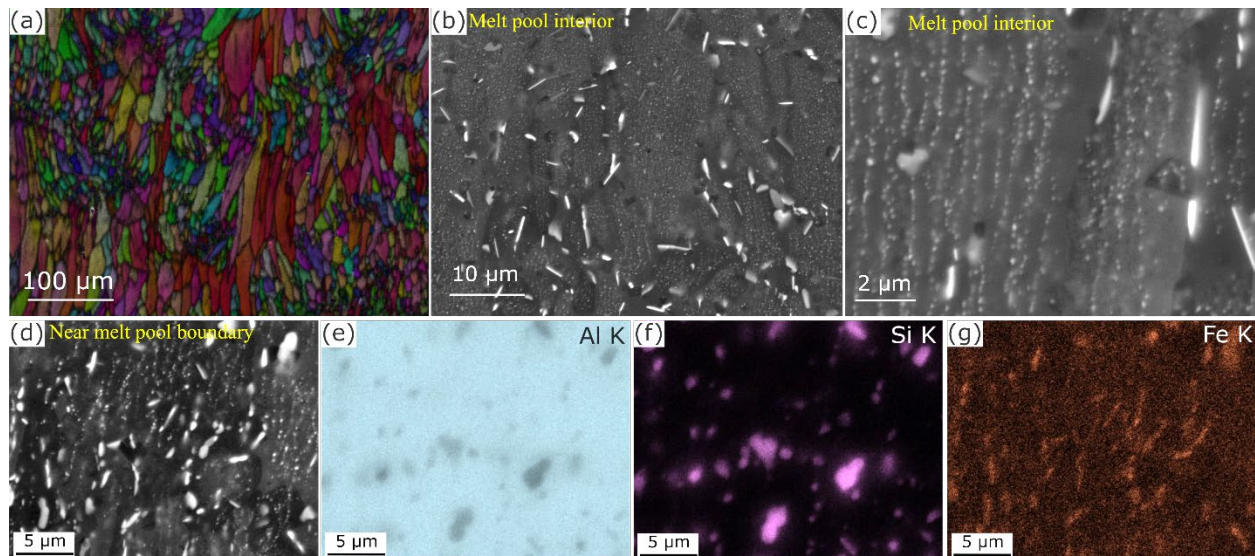


Figure I.1.3.7.4. A summary of the as-solutionized microstructures of the Al-Si-Cu-Mg-Fe alloy: (a) IPF colored map showing the grain structure; (b) and (c) SEM micrographs showing microstructures in melt pool interiors at (b) lower and (c) higher magnifications; (d) SEM micrograph showing microstructure near a melt pool boundary; and (e–g) EDS maps, corresponding to (d), showing elemental distributions of (e) Al, (f) Si, and (g) Fe. Source: ORNL.

Figure I.1.3.7.5(a) and Figure I.1.3.7.5(b) show hardness evolution with time during direct aging (T5) and aging after solutionizing (T6), respectively. When aged directly without solutionizing heat-treatment, the alloy shows no-age-hardening response up to 24 h, regardless of the process parameters used during alloy fabrication, as indicated in Figure I.1.3.7.5(a). This behavior could possibly be a result of the already completed *in-situ* precipitation of nanoscale strengthening phases due to the 150°C-heated build plate and/or thermal cycling during AM. However, this result contradicts the APT observation, as shown earlier in

Figure I.1.3.7.2, where Si, Cu, and Mg supersaturation should have led to a strengthening response. More APT characterization is required to determine possible sample-to-sample variations in the measured solute supersaturations. The hardness of the alloy decreases significantly from ~ 125 HV in the AF condition to ~ 85 HV after solutionizing due to the coarsening of Si particles. The hardness rises during subsequent aging due to precipitation of nanoscale strengthening phases. The peak hardness of 110 HV occurs at 7 h of aging, which remains constant with further aging up to 24 h; however, the peak hardness is still lower than the AF hardness. This result indicates that T6 heat-treatment which makes the AM Al-Si-Cu-Mg-Fe alloy more precipitation-hardenable, cannot produce a high enough strengthening effect that can compensate for the hardness loss due to Si-particle coarsening.

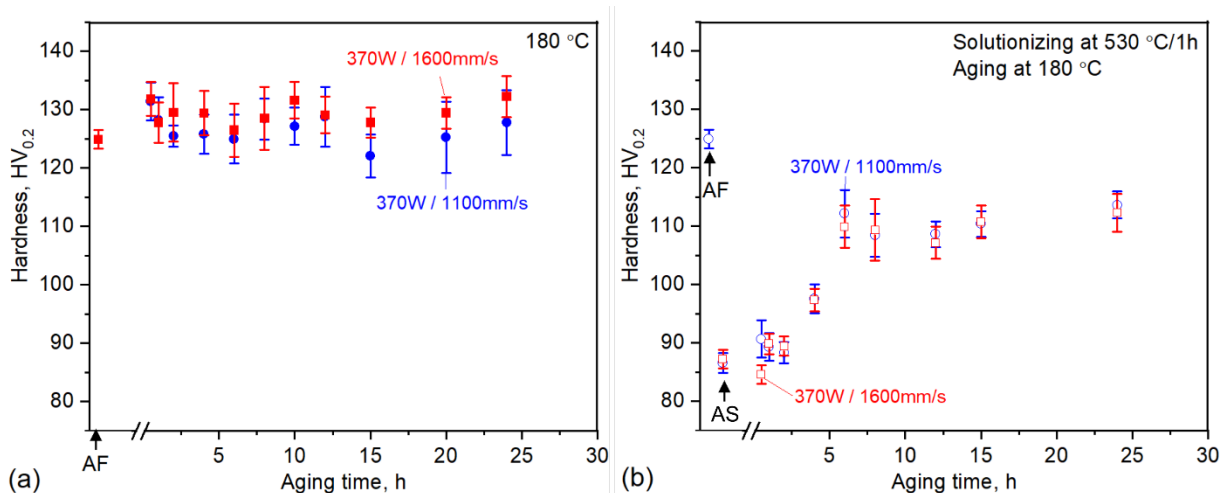


Figure I.1.3.7.5. Evolution of hardness as a function of aging time at 180 °C: (a) direct aging of the alloy after fabrication and (b) aging of the alloy after initially solutionizing at 530 °C for 1 h. AF stands for as-fabricated state, while AS refers to the solutionized and quenched state. Source: ORNL.

Conclusions

- An Al-7Si-0.5Cu-0.3Mg alloy (wt.%) contaminated with 0.75 wt.% Fe was additively manufactured successfully in a near-defect-free condition, implying this level of increased Fe-impurity had no negative effect on the alloy processability. The AF solidification microstructure primarily comprises eutectic α -Al channels and interconnected Si particles.
- Rapid cooling rates inherent to AM significantly refine the Fe-rich intermetallic phases forming during solidification. The thermal cycling during processing within the HAZs slightly coarsens the Fe-rich intermetallic; however, they are still finer in size compared to similar phases formed in cast-Al alloys. The refined solidification microstructure leads to high YS (~ 250 MPa) and good ductility ($\sim 4\%$) in the AF material, indicating the beneficial effect of rapid cooling on neutralizing or minimizing the deleterious effects, particularly on ductility, of Fe-rich intermetallics formed on solidification.
- Direct aging at 180 °C of the AF alloy does not produce a notable precipitation-strengthening effect. Initial solutionizing (530 °C for 1 h) prior to aging causes the Si particles to fragment and coarsen significantly, leading to a hardness reduction from ~ 125 HV to ~ 85 HV. Aging at 180 °C following solution heat-treatment leads to a notable hardness increase, although the peak hardness (~ 110 HV) remains lower than the AF hardness (~ 125 HV).

References

1. Raabe, D., D. Ponge, P. J. Uggowitzer, M. Roscher, M. Paolantonio, C. Liu, H. Antrekowitsch, E. Kozeschnik, D. Seidmann, B. Gault, F. de Geuser, A. Deschamps, C. Hutchinson, C. Liu, Z. Li, P. Prangnell, J. Robson, P. Shanthraj, S. Vakili, C. Sinclair, and S. Pogatscher, 2022, "Making

sustainable aluminum by recycling scrap: The science of ‘dirty’ alloys,” *Prog. Mater. Sci.*, 128, 100947. <https://doi.org/10.1016/j.pmatsci.2022.100947>.

2. DebRoy, T., H. L. Wei, J. S. Zuback, T. Mukherjee, J. W. Elmer, J. O. Milewski, A. M. Beese, A. Wilson-Heid, A. De, and W. Zhang, 2018, “AM of metallic components – Process, structure and properties,” *Prog. Mater. Sci.*, 92, 112–224. <https://doi.org/10.1016/j.pmatsci.2017.10.001>.
3. Li, W., S. Li, J. Liu, A. Zhang, Y. Zhou, Q. Wei, C. Yan, and Y. Shi, 2016, “Effect of heat-treatment on AlSi10Mg alloy fabricated by selective laser melting: Microstructure evolution, mechanical properties and fracture mechanism,” *Mater. Sci. Eng. A*, 663, 116–125. <https://doi.org/10.1016/j.msea.2016.03.088>.
4. Rao, J. H., Y. Zhang, X. Fang, Y. Chen, X. Wu, and C. H. J. Davies, 2017, “The origins for tensile properties of selective laser melted aluminium alloy A357,” *Addit. Manuf.*, 17, 113–122. <https://doi.org/10.1016/j.addma.2017.08.007>.
5. Takata, N., H. Kodaira, K. Sekizawa, A. Suzuki, and M. Kobashi, 2017, “Change in microstructure of selectively laser melted AlSi10Mg alloy with heat treatments,” *Mater. Sci. Eng. A*, 704, 218–228. <https://doi.org/10.1016/j.msea.2017.08.029>.
6. Wang, M., B. Song, Q. Wei, Y. Zhang, and Y. Shi, 2019, “Effects of annealing on the microstructure and mechanical properties of selective laser melted AlSi7Mg alloy,” *Mater. Sci. Eng. A*, 739, 463–472. <https://doi.org/10.1016/j.msea.2018.10.047>.

Acknowledgements

The authors acknowledge J. U. Rakhmonov, J. D. Poplawsky, A. Shyam, and A. Plotkowski for their research contributions. D. McClurg is acknowledged for technical support. The research is sponsored by the VTO under the PMCP. APT research was supported by the Center for Nanophase Materials Sciences, which is a DOE Office of Science User Facility at ORNL.

I.1.3.8 Task 3H. Fundamentals of Printable Higher Temperature Steels for Die-Cast Tooling and Inserts (Oak Ridge National Laboratory)

Dean Pierce, Co-Principal Investigator

Oak Ridge National Laboratory
Materials Science and Technology Division
1 Bethel Valley Rd.
Oak Ridge, TN 37830
E-mail: piercedt@ornl.gov

Peeyush Nandwana, Co-Principal Investigator

Oak Ridge National Laboratory
Materials Science and Technology Division
1 Bethel Valley Rd.
Oak Ridge, TN 37830
E-mail: piercedt@ornl.gov

J. Allen Haynes, PMCP Consortium Manager

Oak Ridge National Laboratory
Materials Science and Technology Division
1 Bethel Valley Rd.
Oak Ridge, TN 37830
E-mail: haynesa@ornl.gov

Jerry L. Gibbs, DOE Technology Development Manager

U.S. Department of Energy
E-mail: Jerry.Gibbs@ee.doe.gov

Start Date: October 1, 2022
Project Funding: \$100,000

End Date: September 30, 2023
DOE share: \$100,000

Non-DOE share: \$0

Project Introduction

Al die-casting and stamping are critical manufacturing processes for making parts for automobiles and other equipment. Dies used for these processes conventionally manufactured from standard tool steels are low-volume, often have long-lead times, are exceedingly expensive, and are often sourced from overseas producers, which limits the responsiveness and efficiency of manufacturing lines in the U.S. LPBF AM and other techniques, such as wire arc additive manufacturing, have a high-potential for manufacturing of complex tooling and die components with intricate internal cooling channels. However, conventional tool steels, as observed in Table I.1.3.8.1, do not have acceptable printability for large dies and inserts. Further, the existing class of highly printable commercial maraging steels (e.g., M300) do not exhibit the necessary HT strength and resistance to softening needed for extended use in die applications. Both H13 tool steels and maraging steels have relatively low TC, which causes dies to cool more slowly and can increase cycle times for high-rate processes, such as die-casting. This limitation/gap in the combination of printability, microstructural stability during use, and TC causes a significant technical barrier to achieve the significant potential advantages of manufacturing large dies by AM.

Table I.1.3.8.1 Composition of Commercial Steels Used for Dies and Other Tooling (wt.%)

Alloy	Ni	Mn	C	Cr	Si	V	Mo	Co	Ti	Fe
H10 Modified	0	0.55	0.4	3.25	1	0.4	2.5	2	–	Bal.
H13	0	0.3	0.4	5	0.9	1	1.25	–	–	Bal.
1.2367	0	0.35	0.36	5.07	0.25	0.65	2.8	–	–	Bal.
DH31-EX	0.14	0.92	0.33	5.43	0.34	0.53	2.36	–	–	Bal.
M300	18	0.1 max	0.03 max	<0.3	0.1 max	–	4.9	9	0.6	Bal.

Objectives

The aim of Task 3 is to develop and evaluate novel printable HT steels for the manufacture of inserts and dies by AM. The steels will target good printability, high-elevated temperature strength, and good TC, to enable long-term durability and performance in Al die-casting and stamping operations. Achieving higher TC than current state-of-the-art die steels, in combination with conformal cooling channels enabled by AM, may also allow for more rapid cooling, enhanced microstructural refinement and solute trapping, and improved properties in die-cast Al parts.

Approach

To achieve an excellent combination of printability, high-elevated temperature strength, and good TC in the developmental steels, computational alloy-design, combined with ORNL’s expertise in the development of HT materials from prior projects, are being leveraged to identify appropriate compositions that meet targets. Targets for printability, post-printing processability, and in-service performance were identified. Targets for printability and post-printing processability are relevant to the intellectual property of the alloy-design strategy and are not listed in this brief report but can be discussed in detail upon request. Two targets for in service performance are:

- Strength: A minimum hardness of 44 HRC (438 HV) at RT, consistent with current hardness levels of H13 dies.
- Thermal Conductivity: The TC must be equal to or exceed that of H13 to enable faster cooling times, greater heat dissipation, and better durability.

Strength and TC were identified as two key properties that when enhanced, significantly reduce the propensity for heat-checking of dies [1], which is a form of fatigue-cracking that manifests on die surfaces and is one of the primary failure mechanisms of steel dies.

Alloy compositions are being evaluated from small lab-scale-testing of arc-melted ingots (700 g). The ingots have reduced C content relative to H13, since minimizing C content is a key feature to enable improved printability of steels. However, this feature creates challenges with both strengthening the steels at high-temperatures in the range of 500–600°C and having sufficient resistance to softening at these temperatures. The steels being developed in this task will develop strength through martensitic transformation, as well as subsequent age-hardening—the alloys will be solution-treated and quenched (STQ), followed by aging. Arc-melted ingots, which have been through the STQ process and aged have been used to evaluate the response to age-hardening (e.g., hardness increase with aging time and temperature), thermal properties, and microstructure. One of the promising alloys has been selected for laser track studies where the material is melted and rapidly solidified by a laser to simulate certain AM processes, as well as to evaluate a particular alloy composition’s resistance to cracking under such conditions. Since remelting and rapid solidification changes the microstructure relative to the cast plus STQ microstructure, the age-hardening response of the rapidly solidified microstructure are also being evaluated in promising alloys. Prior work conducted by Nandwana et al. [2] demonstrated that “direct aging” of the as-solidified microstructure produced by AM led to an improved balance of strength and ductility in M300 maraging steel.

Results

Ten low-C developmental die steels have been computationally designed and 700 g ingots have been cast of each alloy. The ingots were solution-treated and aged at 500°, 550°, 600°, or 650°C for 4 h. Figure I.1.3.8.1 shows (a) optical and (b) SEM images of the microstructure of Alloy 2 after solution-treating, water-quenching to mimic rapid cooling, and over-aging at 650°C to reveal precipitation in the SEM. Figure I.1.3.8.1(a) shows a lower magnification optical micrograph illustrating the grain and sub-grain structure of the martensite, whereas Figure I.1.3.8.1(b) shows a higher magnification SEM image of precipitation that occurred during aging. Precipitates of various sizes ranging from 50–500 nm are observed in Figure I.1.3.8.1(b). The type of the precipitates as inferred from EDS are consistent with the thermodynamic predictions (Thermocalc TCFE9) for specific compositions.

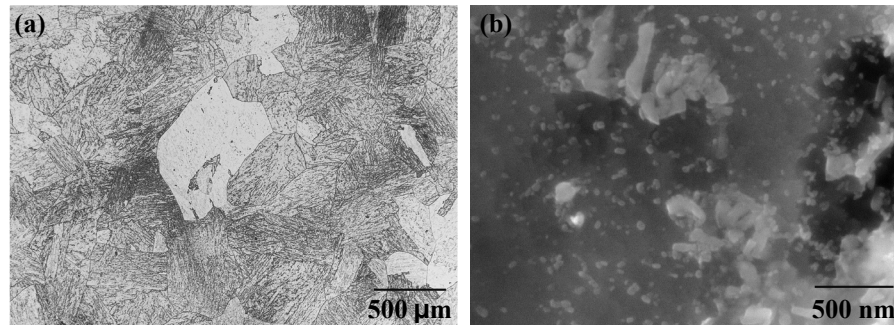


Figure I.1.3.8.1. (a) Low-magnification optical micrograph and (b) high-magnification SEM images of Alloy 2 after aging for 4 h at 650 °C. Source: ORNL.

Hardness testing in the solution-treated condition and after aging at 550°C for 4 h was conducted on the ten alloys to evaluate the age-hardening response of these low-C alloys. Figure I.1.3.8.2 shows the hardness in the solution-treated condition and after aging. Hardness ranging between 23–32 HRC in the STQ condition indicates a desirably soft martensitic microstructure is achieved to improve the resistance to cracking during printing. Age-hardening occurs in most of the alloys, with Alloys 4 through 10 showing an increase in hardness of 8–13 HRC after aging. The role of composition on the age-hardening response was identified. Alloy 7 demonstrated a hardness of 41 HRC in the aged conditions and was selected for further evaluation of printability by laser track studies and aging response after rapid solidification.

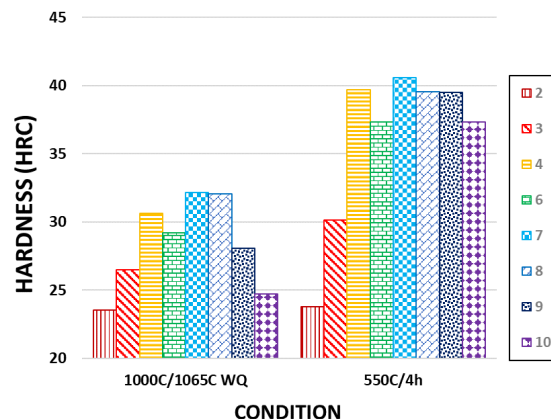


Figure I.1.3.8.2. Hardness of cast developmental die steels after STQ and then subsequent aging at 550 °C for 4 h. Source: ORNL.

An image of the top-view of three laser tracks on a sample of Alloy 7 are shown in Figure I.1.3.8.3. The numbering of the laser tracks correspond to how many times the laser traversed back and forth on a single track. Visual inspection revealed no cracking, but additional metallography is underway to confirm whether cracking has been uniformly suppressed. Each laser track was sectioned in the vertical direction (e.g., along the red dashed lines in Figure I.1.3.8.3) and metallography and microscopy were performed to understand how the remelted and rapidly solidified microstructure responded to aging. The remelted material extended approximately 2 mm underneath the surface, whereas the HAZ extended to greater depths.

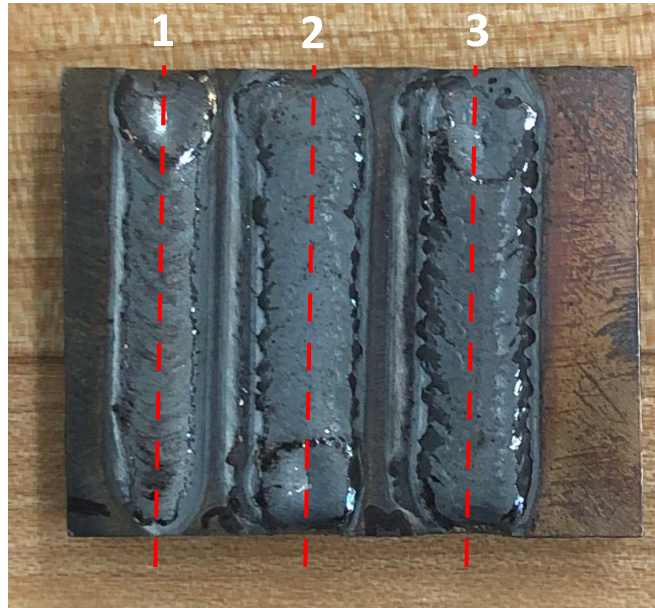


Figure I.1.3.8.3. Top-view of the Alloy 7 sample after laser track passes. On the track designated “1,” a single laser pass was made. On track “2,” two laser passes were made back and forth. On track designated “3,” three laser passes were made. Source: ORNL.

Figure I.1.3.8.4(a) shows hardness traverses performed on cross-sections of specimens where the surface was melted by a single laser track, as well as on specimens where the surface was laser melted, and the material was subsequently aged at 550°C for 4 h. The latter was performed to evaluate how differences in starting microstructure influence the age-hardening response. In the aged sample, the material that was remelted and rapidly solidified by the laser at a depth of approximately 2 mm exhibits a greater age-hardening response, exhibiting a hardness of 475 HV compared to about 425 HV in the HAZ. A hardness of 475 HV (~47 HRC) exceeds the target of 438 HV (~44 HRC), suggesting that dies laser-printed from Die Steel 7 and directly aged may achieve typical hardness values used in current conventionally manufactured H13 dies. The mechanism for enhancing the age-hardening response in the laser remelted region is under further investigation, but rapid solidification can often lead to greater microstructural refinement, greater dislocation density, and more nucleation sites for precipitation, which can lead to finer precipitates sizes with enhanced strengthening potential [2]. EBSD IPF maps in Figure I.1.3.8.4(b) and Figure I.1.3.8.4(c) are from the laser remelted material after aging and the HAZ region after aging, respectively. The maps suggest a finer prior-austenite grain structure may exist in the laser remelted and aged material, but further characterization is needed, particularly of the precipitate and dislocation structure, which is likely to have significant impact on the strength. STEM of the laser remelted and aged material will be performed to further understand how the aging mechanism may be assisted by laser remelting and rapid solidification of the material.

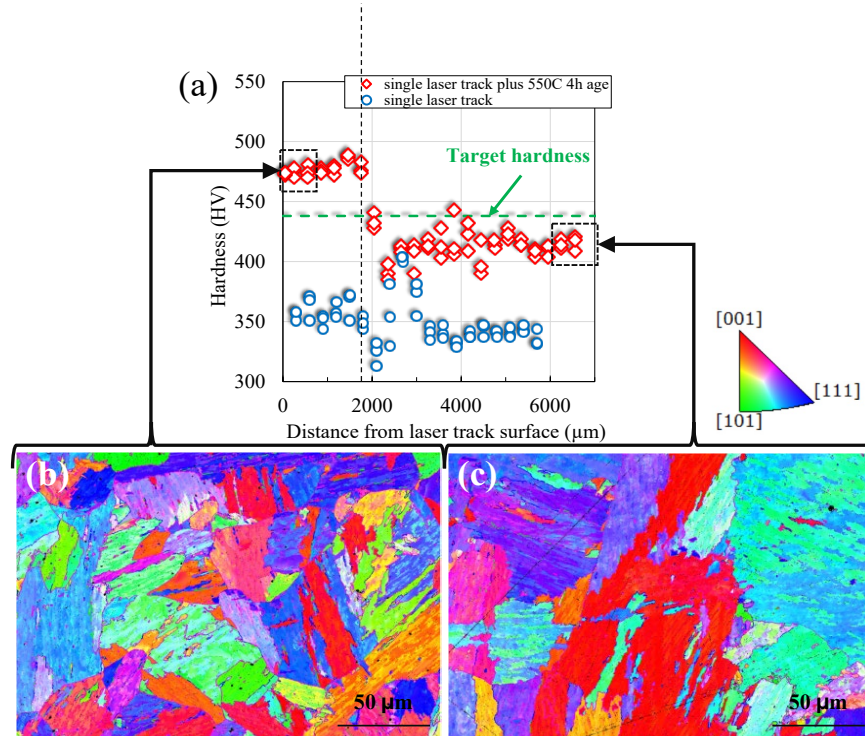


Figure I.1.3.8.4. (a) Hardness traverses as a function of distance from the laser remelted material of Alloy 7 after laser remelting and subsequent aging at 550°C for 4 h. EBSD IPF maps of the BCC phase/martensitic microstructure phase corresponding to a region of (b) laser remelted and aged material and (c) a region away from the laser remelted material in the HAZ after aging. Source: ORNL.

The TC of Alloy 7 in the cast+STQ and aged condition was measured along with H13 and is shown in Figure I.1.3.8.5. Also shown in Figure I.1.3.8.5 is the TC of M300 [3]. Die steel 7 exhibits approximately 15% and 54% increases in TC over H13 and M300, respectively. Alloy 7 meets the TC target of being greater than the TC of H13. Alloy-design modifications are under way to further increase the TC of the developmental die steels, since further increases will enable the dies to operate at lower temperatures with extended lifetimes.

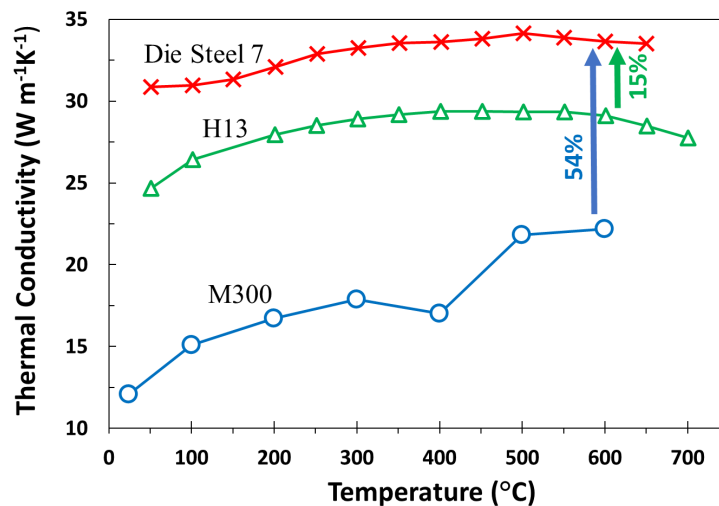


Figure I.1.3.8.5. Measured TC of Alloy 7 and H13. The TC of M300 is derived from [3]. Source: ORNL.

Conclusions

Currently, printable steels with a combination of robust HT strength and excellent TC for dies and inserts do not exist. This work aims to fill the gap in available materials for printable die steels to enable improved industrial efficiency of Al die-casting and stamping processes, increase the responsiveness and agility of manufacturing lines, and enable dies to be manufactured in the U.S. by AM. A novel alloy-design strategy was developed for steels with excellent printability, high-elevated temperature strength, and excellent TC. Ten alloys have been arc-melted and evaluated by measuring their strength after aging (hardness), TC, and for one downselected alloy (e.g., Alloy 7), the response to remelting and rapid solidification by laser processing. While the propensity for cracking under rapid solidification of Alloy 7 is still under investigation, no significant external cracking was observed after laser processing with multiple passes. In addition, Alloy 7 exceeded the strength target of 44 HRC after laser processing and rapid solidification followed by age-hardening, indicating this alloy likely has sufficient strength for die applications. This alloy also demonstrated a 15% and 54% increase in TC over H13 and maraging steel M300, respectively, which is a key parameter contributing to the in service durability of dies [1]. Additional compositional refinements are being explored to further enhance properties, and an improved understanding of the aging mechanisms after laser remelting is being sought by leveraging the advanced characterization resources available in Thrust 4. Industrial partners are being sought that can fabricate a die from one of the developed alloys in this project for field testing.

Key Publications

1. Pierce, D., and P. Nandwana, 2023, “Printable Steel with Good Balance of High-Elevated Temperature Strength, TC, and Oxidation Resistance,” ORNL Invention Disclosure 202305448, August 2023.

References

1. Umemori, N., M. Kawano, and T. Masuda (Daido Steel Co., Ltd.), 2021, “Evaluation of Heat-Checking of Molds through Flow and Solidification Simulation,” NADCA Die-Casting Congress & Exposition, Transaction No. T18-012. Available at: <https://www.daido.co.jp/common/pdf/pages/products/tool/technical-data/sd2106-d06e.pdf> (accessed 18 December 2023).
2. Nandwana, P., R. Kannan, and D. N. Leonard, 2020, “Leveraging solute segregation in LPBF to achieve superior strength and ductility via single-step heat-treatment in Ti-free grade 300 maraging steel,” *JOM*, 72(12), 4221–4231. <https://doi.org/10.1007/s11837-020-04435-7>.
3. Jarfors, A. E. W., T. Matsushita, D. Sifakas, and R. Stolt, 2021, “On the nature of the anisotropy of maraging steel (1.2709) in AM through powder bed laser-based fusion processing,” *Mater. Des.*, 204, 109608. <https://doi.org/10.1016/j.matdes.2021.109608>.

Acknowledgements

The authors acknowledge S. Graham for the metallography studies, A. M. Rossy for conducting the SEM, K. Epps for the mechanical testing, and C. Taylor for melting and heat-treating.

I.1.4 Thrust 4: Advanced Characterization and Computation

I.1.4.1 Task 4A. Advanced Characterization Coordination of Multi-Lab Characterization (Task 4A1) (Oak Ridge National Laboratory)

Thomas R. Watkins, Co-Principal Investigator

Oak Ridge National Laboratory
Materials Science and Technology Division
1 Bethel Valley Rd.
Oak Ridge, TN 37830
E-mail: watkinstr@ornl.gov

J. Allen Haynes, Co-Principal Investigator

Oak Ridge National Laboratory
Materials Science and Technology Division
1 Bethel Valley Rd.
Oak Ridge, TN 37830
E-mail: haynesa@ornl.gov

Jerry L. Gibbs, DOE Technology Development Manager

U.S. Department of Energy
E-mail: Jerry.Gibbs@ee.doe.gov

Start Date: October 1, 2022

End Date: September 30, 2023

Project Funding: \$390,000

DOE share: \$390,000

Non-DOE share: \$0

Project Introduction

This report describes the activities performed during the fifth year of Thrust 4 Task 4A1, Advanced Characterization under the PMCP consortium, occurring at ORNL. The report also covers the coordination of the Thrust 4 Multi-Lab Characterization efforts amongst the three consortium labs: ORNL, PNNL, and ANL. These activities are sponsored by the DOE-EERE VTO PMCP.

In FY 2023, which was the consortium's final year of a five-year program, the PMCP's mission completed the pivot from a focus on internal combustion engines to a focus on EVs. The three materials development thrusts were continued from last FY (with each thrust consisting of multiple development tasks): Thrust 1: "Lightweight Alloys for EV Propulsion," Thrust 2: "Materials & Lubricants for Heavy-Duty EVs," and Thrust 3: "Advanced and AM for EVs." The goal of the PMCP is to accelerate the design, development, demonstration, and deployment of new, cost-effective advanced materials solutions for EV powertrains via a modern ICME approach. The properties of these new materials are targeted to enable improvements in electric motor efficiency, component lightweighting, improved thermal management, and improved durability for future lightweight EVs with a longer range. To support this goal, Thrust 4, which includes both advanced characterization (Task 4A) and advanced computation (Task 4B), undergirds the development tasks within the three development thrusts (Thrusts 1, 2, and 3). It provides the tools and expertise from within the national laboratory consortium to acquire a deeper understanding of materials structure and properties, and thus, insight into the design and development of superior future materials for LD, MD, and HD EV powertrain applications. This unique programmatic support model was created within the PMCP and has since been adopted by other programs.

Objective

The overall objective for Thrust 4A is to provide advanced characterization support projects for Thrusts 1, 2, and 3 of the PMCP in order to obtain data and scientific understanding that will be applied to the development of new materials for future advanced EVs. Thrust 4A1 covers the advanced characterization activities at ORNL and also coordinates the Thrust 4 research activities across all three consortium labs.

Approach

Coordination of the multi-lab characterization activities are accomplished first with dedicated funding for advanced characterization after an internal proposal call, review, and awards of Thrust 4 projects to support specific development tasks from Thrusts 1–3, and second with ad hoc and regularly scheduled meetings amongst the PMCP task PIs and the Thrust 4 project researchers. These dedicated Thrust 4 research funds are intended to enable advanced characterization (and computation) to support the science and development objectives of the development tasks more effectively. Thus, any task PI from any lab within Thrusts 1, 2, and 3 can request advanced characterization support from defined Thrust 4 resources and staff at any of the three labs through a standardized multi-lab proposal review process. Therein, two-page proposals are submitted, reviewed, and ranked by a review committee, as indicated in the flow chart in Figure I.1.4.1.1. In FY 2023, nine Thrust 4A1 proposals were approved for advanced characterization projects across the three consortium labs—ORNL, ANL, and PNNL—as observed in Table I.1.4.1.1.

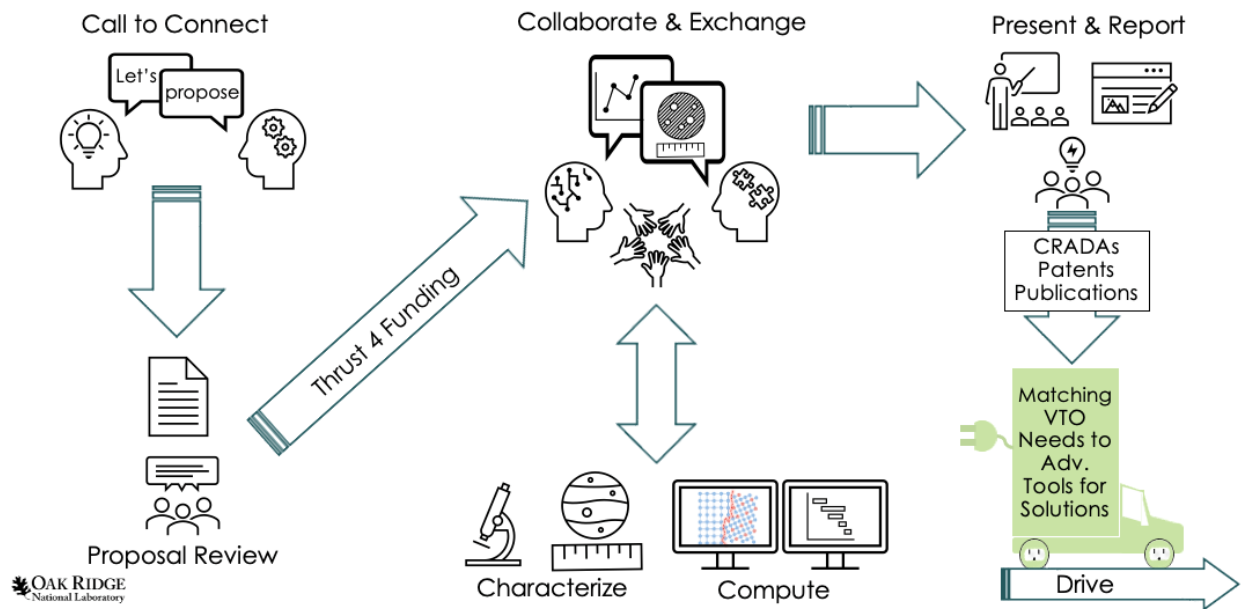


Figure I.1.4.1.1. Thrust 4 coordination of the multi-lab characterization. Researchers identify an EV material problem to be solved and propose work. Upon successful review and ranking, funds are awarded with advanced characterization (and computation) and analyses ensuing. Discussions and meetings occur often between researchers at the national laboratories through hybrid meetings and email. Results are converted into research products with the goal of their application within future EVs. Source: ORNL.

Table I.1.4.1.1. Thrust 4A1 Funded Advanced Characterization Projects in FY 2023

Thrust	Task Lab	Task	Thrust 4A1 Lab	Tool	Project Number and Description
1A*	ORNL	Fundamental Studies of Al-Ni Alloys for Improved Electrical Properties	ORNL	APT	23-4: Understanding Precipitation Mechanisms in Al-Ni-X Alloys (X=Zr, Ti, V, and Fe) using APT
1E	ORNL	LW Materials for Improved Electrical Properties	ORNL	STEM	23-12: Understanding Precipitation Mechanisms in Al-(Fe)-Zr-Sn Alloys using STEM
1G	ORNL	Fundamentals of Thermal Properties in Lightweight Alloys for EV Propulsion	ORNL	XCT	23-13: Investigating Porosity Distribution and Evolution of HPDC Al Alloys via XCT
2C**	ORNL	New Lubricant Strategies for Advanced Thermal Management of HD EVs (Valvoline CRADA)†	ORNL	Raman Spectroscopy	23-5: Raman Spectroscopic Analysis of Surface-Modified CNTs and Associated Tribofilm
2E	PNNL	Solid-Phase Joining and Processing Methods towards Efficient, HD EV Motors	PNNL	STEM & APT	23-16: Characterization of AlCu Interface for Improved Strength and Conductivity for EV Application
2A	ORNL	High-Performance Soft-Magnetic Steels for Motor Laminates via Shear-Rolling	ORNL	STEM & APT	23-15: STEM and APT of Fe-6Si Alloys
3A***	ORNL	Fundamentals of AM for EV Propulsion	ORNL	SAXS	23-9: Evolution of Clustering during Aging in Al-Sn-Based Alloys
3H	ORNL	Fundamentals of Printable Higher-Temp Steels for Die-Cast Tooling & Inserts	ORNL	STEM & APT	23-10: Microstructures of Rapidly Solidified Printable Steels for HT Applications
3A	ORNL	Fundamentals of AM for EV Propulsion	ANL	Advanced Photon Source (APS), Synchrotron SAXS	23-14: Evolution of Clustering during Aging in Al-Sn-Based Alloys

*1. Lightweight Alloys for EV Propulsion; **2. Materials & Lubricants for HD EVs; ***3. Advanced and AM for EVs.

The following are examples of the technical approach of two selected Thrust 4A1 projects from FY 2023. Briefly, **Project 23-4** uses APT to understand the distribution of microalloying elements within the precipitates, as well as the Al matrix, of a prototype lightweight conductor alloy. **Project 23-12** examines microstructural changes in a new Al-Tin(Sn) conductor alloy resulting from isochronal aging using STEM. **Project 23-5** uses Raman spectroscopy to characterize the surfaces of CNTs before and after functionalization for use within EV lubricants with advanced thermal management potential. **Project 23-9** qualifies laboratory SAXS with synchrotron-based ultra SAXS for understanding the precipitate mechanisms of an Al-Sn conductor alloy on the bulk-scale. Each of the four representative FY 2023 projects are described in more detail below.

Results

Project 23-4: Understanding Precipitation Mechanisms in Al-Ni-X Alloys (X=Zr, Ti, V, and Fe) using APT

Microalloying Al-Ni alloys with slow diffusing elements has been reported to improve their mechanical properties and thermal stability; however, little is known regarding how these elements affect the electrical and thermal conductivities of such alloys, which may have potential for high amperage applications within EVs and charging systems. To this end, Al-Ni alloys with Fe, Ti, V, and Zr additions were subjected to heat treatments from 300–450°C, and their mechanical, electrical, and thermal properties were measured. This task focused on using APT to measure the microalloying element matrix concentration and segregation tendencies to Al/Al₃Ni interfaces. The APT results were correlated to the mechanical, electrical, and thermal property measurements to identify the microstructural origins of these properties.

APT samples were prepared from four cast-Al-Ni alloys with different microalloying elements using a DB FIB/SEM. The samples were then loaded into a CAMECA local electrode atom probe (LEAP[®] 4000 XHR) for APT analysis. Figure I.1.4.1.2 displays an example of an APT reconstruction of the Al/Al₃Ni interface and the corresponding compositional profiles across these interfaces for the Al-6Ni-0.4Zr, Al-6Ni-0.3Ti, Al-6Ni-0.3V, and Al-6Ni-0.5Fe alloys, each subject to a 400°C, 200 h heat-treatment. In Figure I.1.4.1.2(a), the blue- and green-colored dots represent the Al and Ni atoms, respectively, while the green surface is a 5 at.% Ni isoconcentration surface that is located at the Al/Al₃Ni interface. The negative distance values on the left of Figure I.1.4.1.2(b) are within the Al matrix with 0 nm being the interface; the positive compositional profile distance values on the right of the figure are within the Al₃Ni precipitate. Only Zr was found to segregate to the Al/Al₃Ni interface. The matrix compositions of the above four alloys subject to a 400°C, 200 h heat-treatment are displayed in Table I.1.4.1.2. The absence of detected Ni and Fe in the matrices of the Al-6Ni-0.4Zr and Al-6Ni-0.5Fe alloys indicates the Ni and Fe must be segregated or bound to the precipitates. The lowest solute contents for the Al-6Ni-0.4Zr and Al-6Ni-0.5Fe alloys are consistent with the higher EC of these samples as compared to the Al-6Ni-0.3Ti and Al-6Ni-0.3V samples.

In summary, APT was used to detect solute segregation to Ni₃Al precipitates and the solute matrix contents in Al-6Ni-0.4Zr, Al-6Ni-0.3Ti, Al-6Ni-0.3V, and Al-6Ni-0.5Fe alloys subject to a 400°C, 200 h heat-treatment. The APT results show Zr segregation to the Ni₃Al/matrix interface for the Al-6Ni-0.4Zr, while no solute segregation was detected at this interface for the other three alloys. APT measured the lowest matrix solute contents in the Fe- and Zr-containing alloys, which is consistent with the highest EC measured in these alloys. Only the Zr-containing alloy contained additional intragranular precipitates besides the Al₃Ni precipitates. These APT results were critical for linking the mechanical, thermal, and electrical properties with the alloy microstructures.

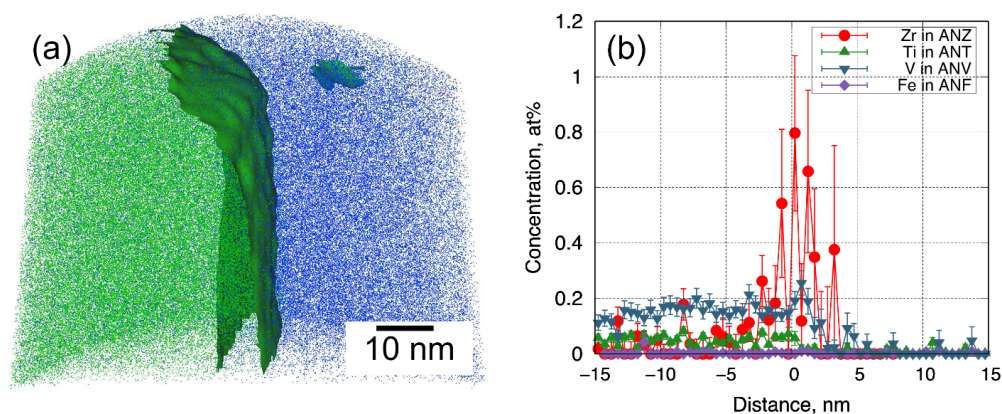


Figure I.1.4.1.2. Al-Sn blanks were prepared by wire electro-discharge machining (EDM) sheets that are sufficiently thin to mitigate the need for a post-EDM grinding as part of the metallographic preparation needed to achieve polished foils with ~150 micron thicknesses. Source: ORNL.

Table I.1.4.1.2. APT Measured Matrix Compositions for Al-6Ni-0.4Zr, Al-6Ni-0.3Ti, Al-6Ni-0.3V, and Al-6Ni-0.5Fe Alloys Subjected to a 400 °C, 200 H Heat-Treatment

Element (at.%)	Al-6Ni-0.4Zr	Al-6Ni-0.3Ti	Al-6Ni-0.3V	Al-6Ni-0.5Fe
Al	99.974%	99.926%	99.778%	99.952%
Ni	0.000% §	0.025%	0.101%	0.005%
Si	0.012%	0.011%	0.026%	0.034%
Zr	0.014%	-	-	-
Ti	-	0.038%	-	-
V	-	-	0.092%	-
Fe	-	-	-	0.000%

§ APTs sensitivity is ~10 ppm.

The Al matrix APT reconstructions for the four alloys heat-treated at 400°C for 200 h shown in Figure I.1.4.1.3 display no precipitation within the Al-6Ni-0.3Ti, Al-6Ni-0.3V, and Al-6Ni-0.5Fe matrices. The Al-6Ni-0.4Zr alloy contains Al₃Zr L₁₂ precipitates in the matrix, and the observation of L₁₂ precipitation is consistent with the age-hardening behavior found only in the Al6Ni0.4Zr alloy.

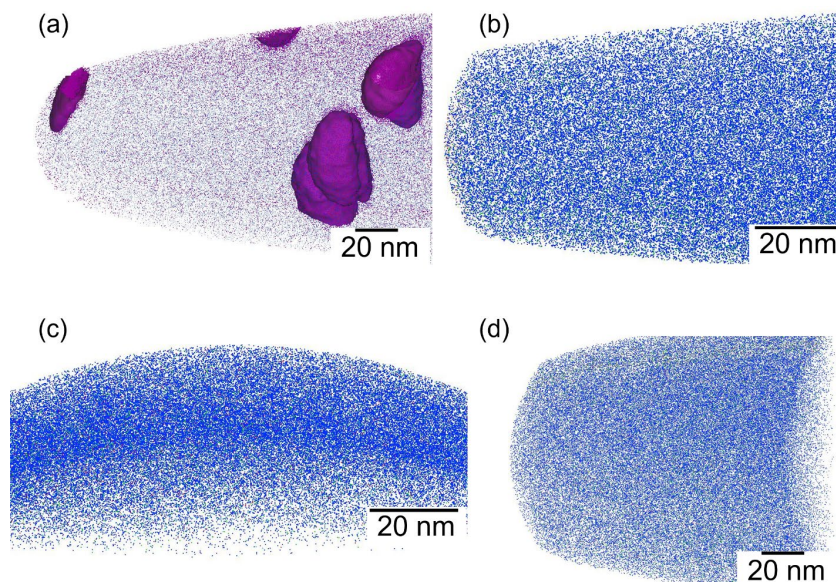


Figure I.1.4.1.3. APT maps of the Al matrix by for the (a) Al-6Ni-0.4Zr, (b) Al-6Ni-0.3Ti, (c) Al-6Ni-0.3V, and (d) Al-6Ni-0.5Fe alloys heat-treated at 400 °C for 200 h. The blue and purple dots are the Al and Zr atoms, respectively. 3 at.% Zr isoconcentration surfaces are displayed in (a) to highlight the Al₃Zr L₁₂ precipitates in the matrix. Source: ORNL.

23-12: Understanding Precipitation Mechanisms in Al-(Fe)-Zr-Sn Alloys using STEM

Within Development Task 1E-23, “Lightweight Materials for Improved Electrical Properties,” it was observed that isochronal aging resulted in accelerated age-hardening behavior and increased peak hardness relative to the samples that were isothermally aged at 425°C. This improvement was suspected to be associated with the formation of Sn nanoprecipitates around 200°C during isochronal aging that are not formed during isothermal aging at 425°C. A thorough investigation was undertaken to determine how the Sn nanoprecipitates affected the precipitation of a dispersion of Al₃Zr nanoprecipitates at higher temperatures. A sample suite comprising electropolished thin foils of Al-0.09Sn exposed to 200°C and 425°C isochronal heat treatments, and Al-0.03Zr-0.09Sn exposed to 200, 325, 375, and 425°C isochronal heat treatments, respectively, has been

prepared; imaging experiments on the 200° and 425°C samples of both sets have been conducted, with early results reporting primarily via bright-field imaging and microchemical analysis via EDS of phases observed on the JEOL 2100F STEM. An example of these results from the Al-Zr-Sn alloy are presented herein.

In the Al-0.03Zr-0.09Sn alloy isochronally aged at 200°C, a distribution of pure elemental β -Sn nanoparticles in the 5–7 nm size range was observed having several different crystallographic orientation relationships to the matrix Al. Associated with a large fraction of these nanoparticles were nanoclusters, just a few unit cells in size, which were consistent with the L12 structure of the Al_3Zr phase. Figure I.1.4.1.4(a) provides an example of the appearance of the Al_3Zr phase; the inset of a Al_3Zr crystal structure model matches the observed cluster structure. To further characterize the nanocluster, high-resolution EDS elemental “hypermaps” of a typical Sn-rich nanoparticle with an associated nanocluster were collected, as indicated in Figure I.1.4.1.4(b–e) [1], that shows individual spectra from Areas 1–3 in Figure I.1.4.1.4(f). In Figure I.1.4.1.4(c), the composite map of the Zr and Sn clearly shows the overlap of Zr concentration in the area of the nanocluster with only Sn in the area of the nanoparticle, further confirming the analysis of the microstructure. After isochronally aging the alloy at 425°C, we previously reported the microstructure showed a dispersion of 5–7 nm sized nanoparticles of Al_3Zr , but no evidence exists of the presence of residual Sn nanoparticles as observed in the 200°C sample. This observation of the Al_3Zr nanoclusters with Sn nanoparticles within the 200°C sample, therefore, has important implications for the mechanism of formation of the Al_3Zr nanoparticle dispersion after 425°C aging.

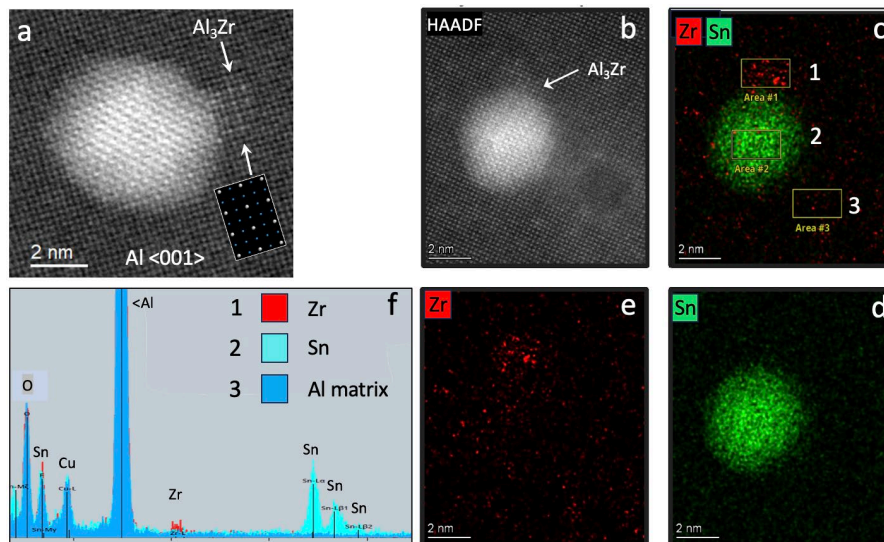


Figure I.1.4.1.4. (a) A high-angle annular dark-field image of a typical Sn-rich nanoparticle in an Al-Zr-Sn alloy, with an associated nanocluster consistent with the Al_3Zr phase. (b) A similar nanoparticle and Al_3Zr nanocluster. A hypermap of the elements was obtained showing the overlap of the Zr and Sn maps in (c); separate maps in (d) and (e) clearly differentiate the locations of Zr (Area 1) and Sn (Area 2), respectively. (f) Energy-dispersive x-ray spectra from Areas 1–3 in (c) also confirm only Sn in the nanoparticle and only Zr in the nanocluster. Source: (a) ORNL, (b–f) Thermo Fisher Scientific [1].

23-5: Raman Spectroscopic Analysis of Surface-Modified CNTs and Associated Tribofilm

Balancing the extent of surface functionalization of CNTs is critical to maintain high-TC in EV fluids, in addition to enabling stable suspension of CNTs. Raman analysis is a unique tool to nondestructively query the level of surface defects caused by functionalization by analyzing the I_G/I_D ratio, as defined below. Such information will provide insights for the formation of CNT tribofilm helping to optimize the extent of organic modification to the CNT surface. CNTs with optimized surface modifications are expected to have stable suspension in electric motor oil for improved thermal and frictional management.

Specifically, the objective of this project was to determine how surface modification influences the graphene structure of CNTs and their resultant lubricant and thermal properties. Here, CNT samples were obtained from a commercial vendor with varying diameter and lengths, as shown in Table I.1.4.1.3. Initial TC tests were performed to prescreen the TC performance to down-select which CNTs had the best potential for effective surface modification. Sigma CNTs Type 1 with a length of $<20\ \mu\text{m}$ and an outer diameter of 50–90 nm showed good TC in Valvoline base oil and, therefore, were selected for further surface modification trials. Several surface modification techniques were utilized to modify CNTs to improve oil suspensibility. Surface modification trial CK3-46 used nitrobenzene surface modification to suspend the Sigma CNTs Type 1 in polar PAG oil. Surface modification trial CK3-48A used phenyl and oleylamine surface modification to disperse the CNTs in non-polar EV oils. Since the surface modification process may alter the graphene structure of the CNTs, which could eventually affect the TC properties, Raman analysis examined any changes to the intensities of the graphene G and D peaks.

Table I.1.4.1.3. CNT Dimensional Properties, Diameters, Lengths, and Raman Signatures Used in the Study

CNT-Type	Diameter (nm)	Length (μm)	I_G/I_D Ratio
Sigma CNT-Type 1	50–90	10–20	12.2
Sigma CNT-Type 2	10	1.5	0.7
Sigma CNT-Type 3	6–13	2.5–20	2.0
Sigma CNT-Type 4	110–170	5–9	0.8
Sigma CNT-Type 5	10–40	500–1500	2.7
Sigma CNT-Type 1-Modify CK3-46	50–90	10–20	9.1
Sigma CNT-Type 1-Modify CK3-48A	50–90	10–20	9.2

Raman spectra were acquired using a Raman microprobe with a 532 nm Nd-YAG laser with a spot size of $\sim 2\ \mu\text{m}$. There are two Raman signature peaks for the CNT, as indicated in Figure I.1.4.1.5: CNTs defect/disorder peak at $1345\text{--}1360\ \text{cm}^{-1}$ (D) and graphitic peak at $1575\text{--}1580\ \text{cm}^{-1}$ (G). Second-order Raman peaks also appear between $2,600$ and $3,000\ \text{cm}^{-1}$. The intensity ratio of the G to D peaks (I_G/I_D) indicates the degree of disorder in the graphene structure of the CNTs. As shown in Table I.1.4.1.3 above, the I_G/I_D ratio of Type 1 CNTs is about ~ 12 , which indicates a very good graphene structure. After organic surface modification, the I_G/I_D ratio of surface-modified CNTs decreased $\sim 25\%$, which was regarded as a minimal change to the graphene structure. Sigma CNTs Types 2 through 5 showed broader peaks than Type 1. The CNTs Types 3 and 4 have a dominant G peak, whereas Types 2 and 4 have a dominant D peak. Due to the significantly reduced I_G/I_D ratio (<1), Types 2 and 4 seem to have a more disordered graphene structure. These results show the surface modifications are not significantly altering the graphene structure of the CNTs, which is desired for the next stage of sample testing in TC. The Raman data will be used later to correlate to the TC data.

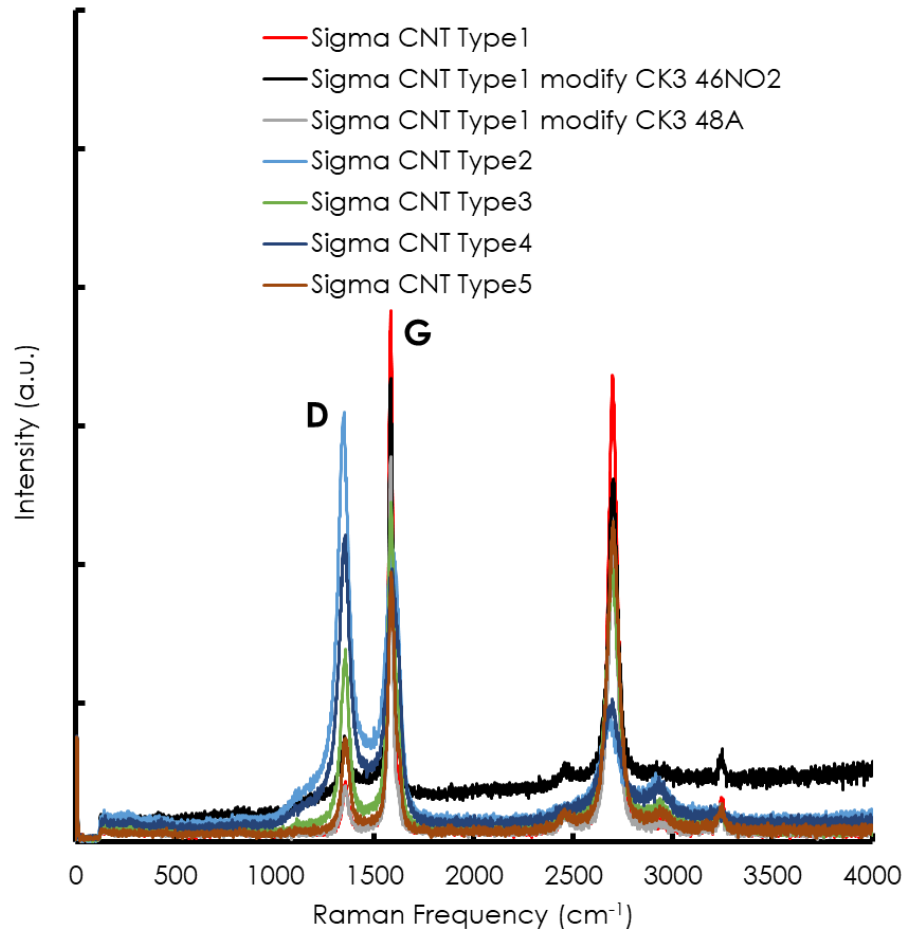


Figure I.1.4.1.5. Raman spectra from CNTs. Source: ORNL.

23-9: Evolution of Clustering during Aging in Al-Sn-Based Alloys

SAXS data provides insights into the shape and size of nano-scaled features. This data can help address open questions about the pathway for precipitation in Al-Sn-based alloys. *In-situ* observation of the evolution in precipitate size and shape will allow the development of a heat-treatment that optimizes aging. Further, this data will inform the pathway for precipitate clustering. The SAXS data analysis in this work relied on related APT and STEM analysis that was performed on the same system related to Development Task 1E-23. The STEM and APT results give physical meaning to the fitting parameters used for the SAXS data analysis. The SAXS results provide a bulk understanding of the alloy by evaluating a volume that is 15–20 orders of magnitude larger than that of STEM and APT. The objective of this task is to determine the feasibility of using a laboratory-scale SAXS instrument for effectively studying and understanding the precipitation behavior of very dilute Al-based alloys intended as lightweight conductors.

The test samples were fabricated by the arc-melt and drop-casting method followed by a homogenization at 640°C for 24 h, cut to size ($\sim 5 \times 5 \times 0.5$ mm) using an EDM, and polished to 0.05 microns following standard metallographic procedures to produce foils with ~ 150 μm thickness. Polished foils were isothermally heated at 200°C while measuring the SAXS data to monitor precipitate evolution. An example of a sample after final thinning is shown in Figure I.1.4.1.6. SAXS data were measured at the APS using the ultra SAXS instrument to obtain the best possible data that was normalized to allow for quantification. SAXS data were then measured at ORNL to determine the viability for achieving similar measurements locally, where access is simpler and there is more instrument time available.

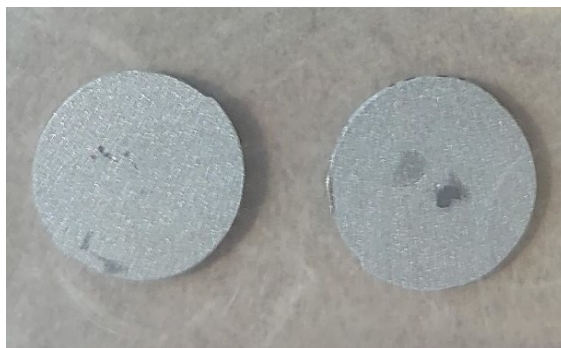


Figure I.1.4.1.6. Al-Sn blanks were prepared by wire EDM sheets that are sufficiently thin to mitigate the need for a post-EDM grinding as part of the metallographic preparation needed to achieve polished foils with $\sim 150 \mu\text{m}$ thicknesses. Source: ORNL.

SAXS data measured at the APS showed a great signal with changes over the Q range of $\sim 3 \times 10^{-1} \text{ \AA}^{-1}$. Figure I.1.4.1.7 shows the SAXS region of the measurement curve for reference. We note that the full range data, including the ultra SAXS data, extends to a lower Q of 10^{-4} \AA^{-1} and more completely captures the changes in the signal. However, the high-end region of the ultra SAXS (low Q of SAXS) has poor signal to noise and results in noisy data that are more difficult to interrupt. In contrast, SAXS data measured at the laboratory-scale at ORNL spans the Q range of interest ($\sim 5 \times 10^{-2} \text{ \AA}^{-1}$ to $\sim 3 \times 10^0 \text{ \AA}^{-1}$) needed to resolve the formation and evolution of precipitates of the size found in these samples. In summary, the region of interest is measured with good signal to noise and has been shown to agree with the APS data, giving confidence that the laboratory-scale SAXS system measures fully normalized data. Analysis is ongoing to extract the cluster evolution from the ORNL and APS data as a quality check. These preliminary results indicate that the SAXS system at ORNL is a viable tool for measuring precipitate evolution in at the scales associated with these very dilute Al-based alloys.

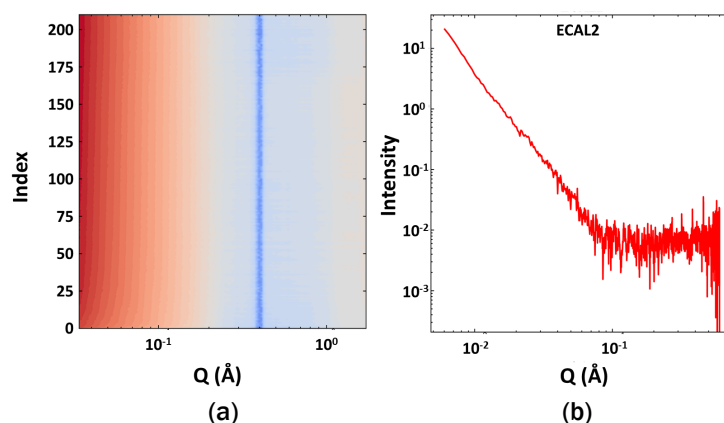


Figure I.1.4.1.7. (a) SAXS data measured during isothermal hold at the APS showing changes in the intensity at a small size ($\sim 3 \times 10^{-1} \text{ \AA}$). (b) Single scan of a previously heat-treated sample measured at ORNL showing a good signal over the range of interest. Source: ORNL.

Conclusions

Understanding the behavior of alloy systems under various processing and application conditions benefits tremendously from a suite of advanced materials characterization techniques to clarify chemical, microstructural, and phase changes as a function of time, elevated-temperature, pressure/loading, and other conditions. The coordination of this suite of advanced characterization capabilities and expertise across three national laboratories is managed through Thrust 4.

Examples of the FY 2023 Thrust 4A1 projects highlighted here are essential for accomplishing the mission of accelerated materials development for future advanced EVs under the PMCP. Here, APT, STEM, and SAXS allowed direct imaging of crystalline phases, precipitates, distributions, and chemical information in potential future EV alloys and have elucidated strengthening mechanisms. The STEM work is particularly revealing. Raman spectroscopy is a critical technique for accessing the surface condition of the CNTs to determine whether they retain thermal properties after treatment. The combination of advanced characterization tools from the national labs provides for these four examples of essential, unique, and timely discovery, as well as deeper scientific understanding, which enable more rapid development of the next generation of advanced powertrain materials for light-, medium-, and HD EVs.

Key Publications

1. Ajantiwalay, T., R. Michi, C. Roach, A. Shyam, A. Plotkowski, and A. Devaraj, 2022, "Influence of microstructural heterogeneities on small-scale mechanical properties of an additively manufactured Al-Ce-Ni-Mn alloy," *Addit. Manuf. Lett.*, 3, 100092. <https://doi.org/10.1016/j.addlet.2022.100092>.
2. Bahl, S., A. Plotkowski, T. R. Watkins, R. A. Michi, B. Stump, D. N. Leonard, J. D. Poplawsky, R. Dehoff, and A. Shyam. "3D-printed eutectic aluminum alloy has facility for site-specific properties," *Addit. Manuf.*, 70, 103551. <https://doi.org/10.1016/j.addma.2023.103551>.
3. Gwalani, B., J. Liu, S. Lambeets, M. Olszta, J. Poplawsky, A. Shyam, and A. Devaraj, 2022, "Rapid assessment of interfacial stabilization mechanisms of metastable precipitates to accelerate HT Al alloy development," *Mater. Res. Lett.*, 10(12), 771779. <https://doi.org/10.1080/21663831.2022.2102947>.
4. Harsha Gunda, N. S., R. A. Michi, M. F. Chisholm, A. Shyam, and D. Shin, 2023, "First-principles study of Al/Al₃Ni interfaces," *Comput. Mater. Sci.*, 217, 111896. <https://doi.org/10.1016/j.commatsci.2022.111896>.
5. Jang, G. G., S. Yeom, J. K. Keum, M. Yoon, H. Meyer III, Y.-F. Su, and J.-H. Jun, 2023, "Formation of carbon and oxygen rich surface layer on high-purity magnesium by atmospheric carbon dioxide plasma," *J. Magnes. Alloy*, 11(1), 88–99. <https://doi.org/10.1016/j.jma.2022.10.008>.
6. Kannan, R., Y. Lee, D. Pierce, K. Unocic, B. Fillingim, T. Feldhausen, A. Marquez Rossy, H. Wang, and P. Nandwana, 2023, "AM as a processing route for steel-aluminum bimetallic structures," *Mat. Des.*, 231, 112003. <https://doi.org/10.1016/j.matdes.2023.112003>.
7. Knapp, G. L., M. Gushev, A. Shyam, T. Feldhausen, and A. Plotkowski, 2022, "Microstructure, deformation, and fracture mechanisms in Al-4043 alloy produced by laser hot-wire AM," *Addit. Manuf.* 59, 103150. <https://doi.org/10.1016/j.addma.2022.103150>.
8. Kumara, C., M. J. Lance, and J. Qu, 2023, "Macroscale superlubricity by a sacrificial carbon nanotube coating," *Mater. Today Nano*, 21, 100297. <https://doi.org/10.1016/j.mtnano.2022.100297>.
9. Michi, R. A., S. Bahl, C. M. Fancher, K. Sisco, L. F. Allard, K. An, D. Yu, R. R. Dehoff, A. Plotkowski, and A. Shyam, 2023, "Load shuffling during creep deformation of an additively manufactured AlCuMnZr alloy," *Acta Mater.*, 244, 118557. <https://doi.org/10.1016/j.actamat.2022.118557>.
10. Michi, R. A., J. J. Simpson, S. Bahl, Q. Campbell, P. Brackman, A. Plotkowski, R. R. Dehoff, J. A. Haynes, Q. Wang, and A. Shyam, 2023 "Additively manufactured AlCeNiMn Alloy with improved elevated-temperature fatigue resistance," *Addit. Manuf.*, 66, (2023): 103477. <https://doi.org/10.1016/j.addma.2023.103477>.

11. Perrin, A., S. Bahl, D. N. Leonard, R. A. Michi, K. Sisco, A. J. Plotkowski, A. Shyam, R. Dehoff, D. Shin, and Y. Yang, 2022, “Phase stability in cast and additively manufactured Al-rich AlCuCe alloys,” *J. Alloys Compd.*, 926, 166984. <https://doi.org/10.1016/j.jallcom.2022.166984>.
12. Perrin, A. E., R. A. Michi, D. N. Leonard, K. D. Sisco, A. J. Plotkowski, A. Shyam, J. D. Poplawsky, L. F. Allard, Jr., and Y. Yang, 2023. “Effect of Mn on eutectic phase equilibria in Al-rich Al-Ce-Ni alloys,” *J. Alloys Compd.*, 965, 171455. <https://doi.org/10.1016/j.jallcom.2023.171455>.
13. Poplawsky, J. D., R. A. Michi, L. F. Allard, S. Bahl, A. J. Plotkowski, and A. Shyam, 2022, “Using theta prime interfaces as templates for L12 precipitation in AlCuMnZr alloys,” *Addit. Manuf. Lett.*, 3, 100086. <https://doi.org/10.1016/j.addlet.2022.100086>.
14. Qu, J., C. Kumara, and H. Wang, 2022, “CNT coating as a novel TIM,” U.S. Patent Application 63/432,435, 14 December 2022.
15. Rakhmonov, J. U., B. Milligan, S. Bahl, D. Ma, A. Shyam, and D. C. Dunand, 2023, “Progression of creep deformation from grain boundaries to grain interior in AlCuMnZr alloys,” 2023, *Acta Mater.*, 250, 189223. <https://doi.org/10.1016/j.actamat.2023.118886>.
16. Romedenne, M., S. Lambeets, M. Song, C. Roach, A. Devaraj, and R. Pillai, 2023, “Revealing the elusive role of water vapor on the oxidation of a Mn-Si-containing NiCr alloy at 950°C,” *Corros. Sci.*, 221, 111348. <https://doi.org/10.1016/j.corsci.2023.111348>.
17. Romedenne, M., B. Pint, M. Lance, and S. Dryepondt, 2023, “Oxidation behavior of heat-resistant type HK steel (HK30Nb) at 800°C,” *HT Corrosion of Mater.*, 100, 157–176. <https://doi.org/10.1007/s11085-023-10168-0>.
18. Sisco, K. D., A. Plotkowski, Y. Yang, L. Allard, C. Fancher, C. Rawn, J. D. Poplawsky, R. Dehoff, and S. S. Babu, 2023, “Heterogeneous phase transformation pathways in additively manufactured AlCeMn alloys,” *J. Alloys Compd.*, 9238, 168490. <https://doi.org/10.1016/j.jallcom.2022.168490>.
19. Wang, Y., K. Sebeck, M. Tess, E. Gingrich, Z. Feng, J. A. Haynes, M. J. Lance, G. Muralidharan, R. Marchel, T. Kirste, and D. Pierce, 2023, “Interfacial microstructure and mechanical properties of rotary inertia friction welded dissimilar 422 martensitic stainless-steel to 4140 low-alloy steel joints,” *Mater. Sci. Eng. A*, 885, 145607. <https://doi.org/10.1016/j.msea.2023.145607>.
20. Zhang, S. H., Y. Li, A. Frederick, Y. L. Wang, Y. Y. Wang, L. F. Allard, Jr., M. Koehler, S. Shin, A. Hu, and Z. Feng, 2023, “*In-situ* formation of Al₃Ni nano particles in synthesis of Al 7075 alloy by FSP with Ni powder addition,” *J. Mater. Process. Technol.*, 311, 117803. <https://doi.org/10.1016/j.jmatprotec.2022.117803>.

References

1. Dr. H. Cheng, Thermo Fisher Scientific, Hillsboro, OR, for EDS scans in Figure I.1.4.1(b-f).

Acknowledgements

The authors gratefully acknowledge the effort and contributions of L. F. Allard, J. D. Poplawsky, J. M. Meier, M. J. Lance and C. Fancher. This research was supported by the DOE-EERE VTO Propulsion Materials Program. The APT research was supported by the Center for Nanophase Materials Sciences (CNMS), which is a DOE Office of Science User Facility at ORNL. The authors also would like to thank J. Burns for their assistance in performing the APT samples preparation and running the APT experiments. This research used the resources of the APS, which is a DOE Office of Science User Facility that is operated for DOE by ANL under Contract No. DE-AC02-06CH11357. The authors also gratefully acknowledge S. Graham for the metallographic preparation, L. Kearny for the SAXS measurements at ORNL, and J. Illovsky for the SAXS measurements at APS.

I.1.4.2 Task 4A. Advanced Characterization of PMCP Research Samples: Characterization of Thermal, Electrical, and Magnetic Properties (Task 4A3) (Oak Ridge National Laboratory)

Hsin Wang, Co-Principal Investigator

Oak Ridge National Laboratory
Materials Science and Technology Division
1 Bethel Valley Rd.
Oak Ridge, TN 37830
E-mail: wangh2@ornl.gov

J. Allen Haynes, Co-Principal Investigator

Oak Ridge National Laboratory
Materials Science and Technology Division
1 Bethel Valley Rd.
Oak Ridge, TN 37830
E-mail: haynesa@ornl.gov

Jerry L. Gibbs, DOE Technology Development Manager

U.S. Department of Energy
E-mail: Jerry.Gibbs@ee.doe.gov

Start Date: October 1, 2021

End Date: September 30, 2023

Project Funding: \$165,000

DOE share: \$165,000

Non-DOE share: \$0

Project Introduction

Understanding of electrical and thermophysical properties of materials used in EV powertrains is important to further advancements because they: (1) provide key materials processing quality controls and performance parameters, and (2) are used in vehicle design, modeling, and simulation of components. Task 4B2 focused on test setup and validation of state-of-the-art methods for the characterization of electrical and thermal properties of key EV-related materials. Testing standards and metrology are emphasized, especially for advanced conductors and new alloys produced by modern-casting and AM processes.

Objectives

There are two main objectives for this task. The first is supporting the various materials development tasks within Thrusts 1–3 by characterizing the thermal and electrical properties of baseline and new materials being studied and developed in those tasks. The second objective is contributing to the integral materials development strategies of the PMCP via the scientific and technical understanding developed in these characterization studies.

Approach

The FY 2023 approach to this characterization task included the following:

- Presented highlights of Year 1 support to the multi-lab team and made new testing capabilities available to the Thrust 1–3 PIs
- Worked with the Thrust 1 through Thrust 3 PIs to establish appropriate testing protocols, specimen specifications, and baseline materials properties for each related task
- Performed testing of electrical and thermal properties of Thrust 1 through Thrust 3 materials, conducted data analysis, and prepared reports and publications.

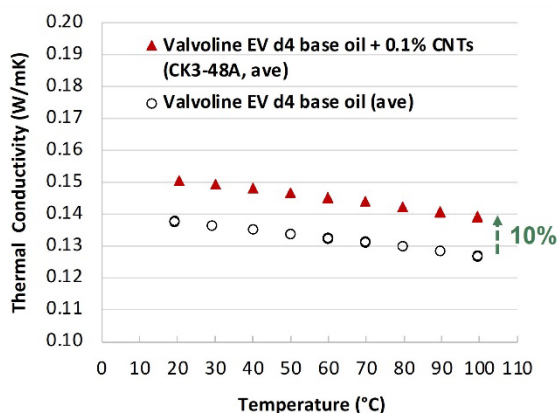
Results

Selected Results Supporting Task 2C-23: Thermal Conductivity of Lubricants

Improvement in TC in EV lubricants can enhance heat-transfer and has the potential to enable better temperature control of vehicle components, such as motors and other rotating parts. In FY 2023, Task 2C-23 continued to evaluate the addition of surface-modified CNTs to EV lubricants to improve the thermal management capabilities of those fluids. The Thermtest transient hot-wire TC system was used for this study. The system follows the methods of American Society for Testing and Materials (ASTM) D7896-19 [1] to measure liquid TC over the temperature range 35°C to 350°C. During FY 2023, over 70 measurements were made on this system for Task 2C. Two selected results are shown in Figure I.1.4.2.1 indicating significant improvement in TC of polar PAG 4cSt base oil and non-polar Valvoline EV d4 base oil. More details can be found in Report No. I.1.2.3, “Task 2C: New Lubricant Strategies for Advanced Thermal Management of Heavy-Duty EVs.”

Non-polar Valvoline EV d4 base oil

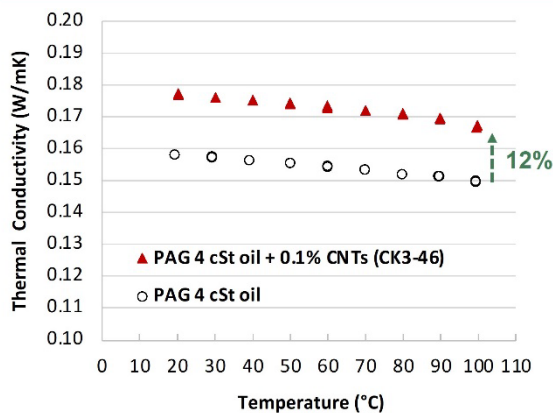
(0.1% CNTs → 10% improved thermal conductivity and 10% volumetric heat capacity)



(a)

Polar: PAG 4 cSt base oil

(0.1% CNTs → 12% improved thermal conductivity and 16% volumetric heat capacity)



(b)

Figure I.1.4.2.1. Selected results of Task 2C-23 on TC improvement: (a) non-polar Valvoline EV d4 base oil; and (b) polar PAG 4 cSt base oil. Source: ORNL.

Selected Results Supporting Task 2D-23: Thermal-Interface Impedance Measurements

Interface thermal resistance is a very important property that affects heat-transfer and removal from numerous EV-related components and devices. Task 2D, “Carbon Nanotube (CNT) Coatings for Superlubricity and Thermal Management of Heavy-Duty EVs,” has a very specific requirement for this measurement between an Al and stainless-steel interface. A thermal resistance measurement system was designed and built at ORNL and is shown in Figure I.1.4.2.2(a-b). The system incorporates a servomotor driven mechanical load frame, following ASTM D5470-17 [2], to apply constant load to compress the samples. A forward-looking infrared camera, FLIR SC7000, was used to monitor the temperature of the specimens and the interface. The system uses an Al nitride heater to apply heat from the top and an Al cooling plate at the bottom to remove the heat. A major improvement to the system in FY 2023 was the addition of a chiller cold plate at the bottom. The Al plate is connected to a chiller and placed above the load cell, as shown in Figure I.1.4.2.2(b). A CNT-coated sample and CNT schematic at the thermal-interface is shown in Figure I.1.4.2.2(c-d).

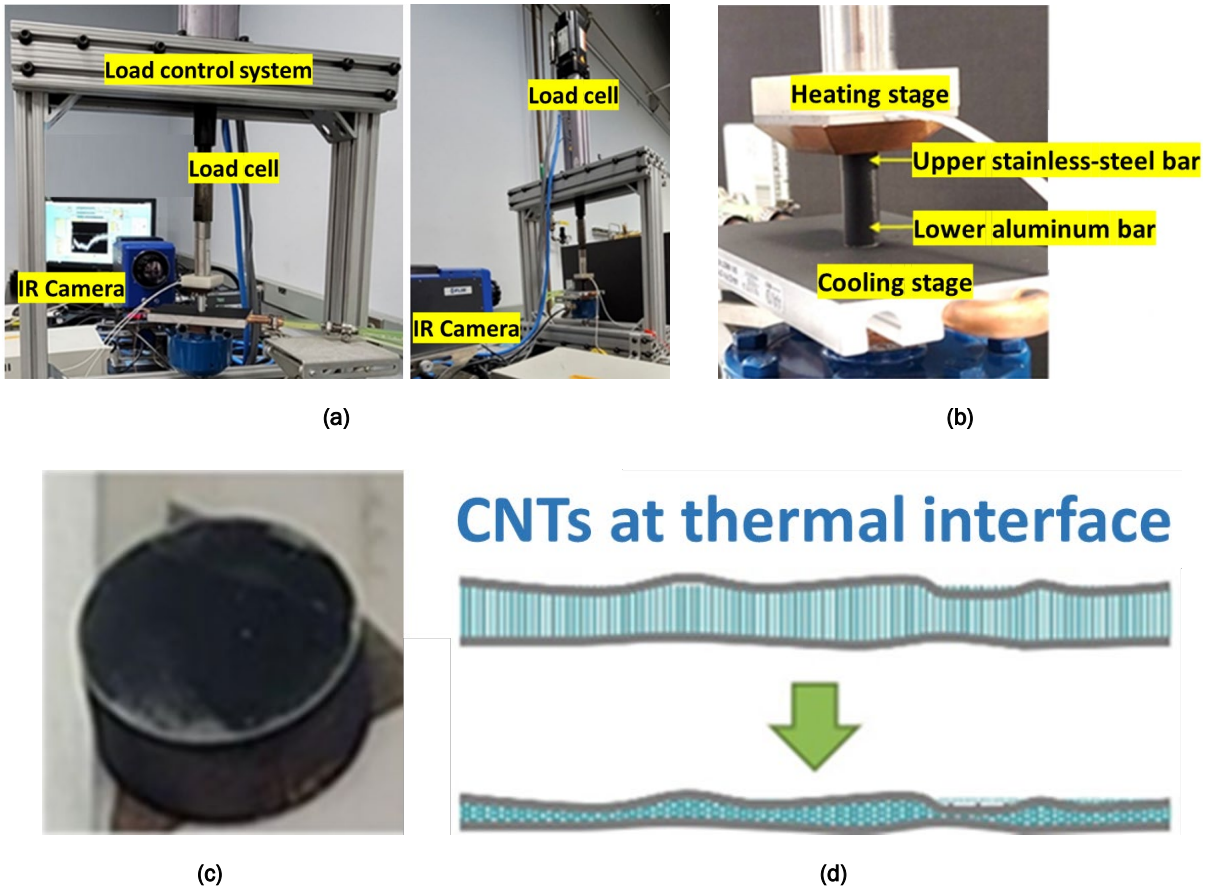


Figure I.1.4.2.2. Improved thermal impedance measurement system: (a) Location of the load cell and the infrared (IR) camera, (b) stainless-steel and Al bar between the heating and cooling stage, (c) a CNT-coated sample, and (d) its interface relationship. Source: ORNL.

An IR image captured during a measurement is shown in Figure I.1.4.2.3(a). A line profile showed the temperature gradient through the 316 steel and Al cylinders, and a clear temperature drop indicated interface resistance, as shown in Figure I.1.4.2.3(b). This method was used to evaluate the thermal impedance of ORNL’s recently developed CNT coatings and silicone plates with 1 wt.% CNT. Results for improvement in the thermal impedance are given in Table I.1.4.2.1. More details can be found in Report No. I.1.2.4, “Task 2D: Carbon Nanotube (CNT) Coatings for Superlubricity and Thermal Management of Heavy-Duty EVs.”

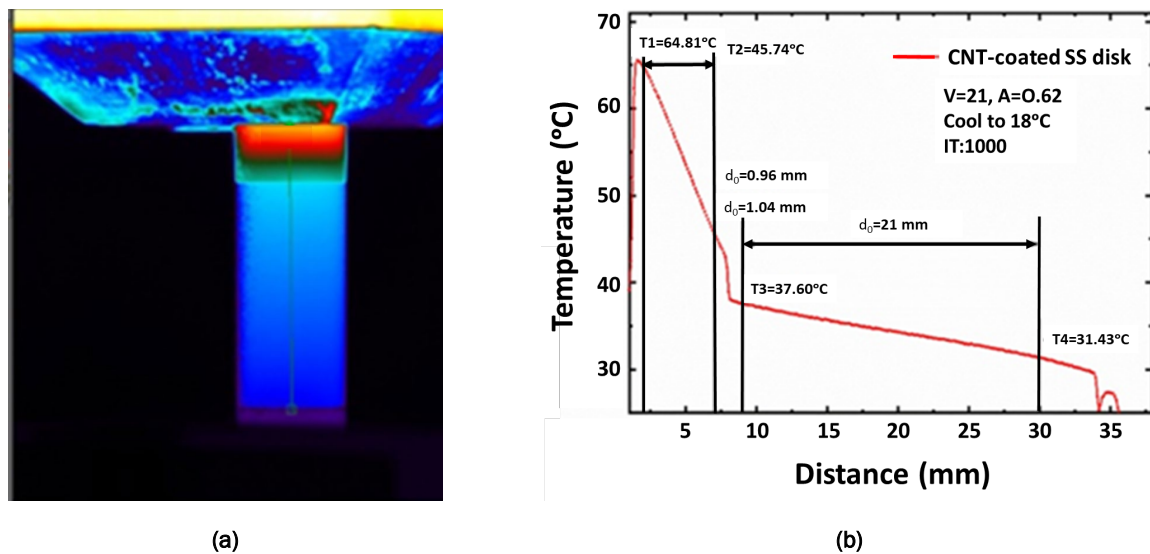


Figure I.1.4.2.3. (a) Infrared image showing temperature gradient and interface resistance. Source: ORNL.

Table I.1.4.2.1. Improvement in Thermal Impedance for CNT-Coated Interface Materials

Thermal-Interface Material	Thermal Impedance (x105 K-m ² /W)	Improvement Using CNTs (%)	Temperature Range in Applications
Baseline 1	6.75	-	Up to 400°C
CNT-Coated	4.06	40	
Baseline 2 (silicone paste)	1.45	-	Up to 200°C
Silicone past +1 wt% CNTs	0.62	57	

Selected Results Supporting Task 1A-23: EC Measurements

Electrical conductivity/resistivity is also a focus of the PMCP, and related measurements were requested by multiple development tasks across Thrusts 1–3. Two techniques were used: (1) the 4-point probe method for electrical resistivity using ULVAC ZEM-3; and (2) the Eddy current probe method for non-magnetic materials, particularly Al. The eddy current method [3] employs a probe, and EC is measured using various appropriate known standards for calibration. Figure I.1.4.2.4 is an example of a pure Al ingot that was cast in 4-step thicknesses. The cooling rate was different and affected the microstructure formation. EC measurement clearly showed a decreasing trend as a function of thickness. This ingot was used in more detailed measurements and subsequent annealing steps were also added. Specimens for thermal diffusivity, specific heat, and thermal expansion testing were prepared for this task. These are typically thermophysical properties following ASTM E1461 [4], E831 [5], and E1269 [6]. One of the goals of this task was to generate a large amount of data from consistently collected properties to enable a property database for ML and the optimization of future cast-Al alloys. A database of hundreds of properties' measurements is being built under Task 1A. One of the functions is to optimize mechanical properties associated with thermal and/or electrical properties. Details can be found in the main Task 1A-23 report.

Pure Aluminum Ingot in 4 Step-Thicknesses



Electrical Conductivity by Eddy Current Probe (60 kHz)

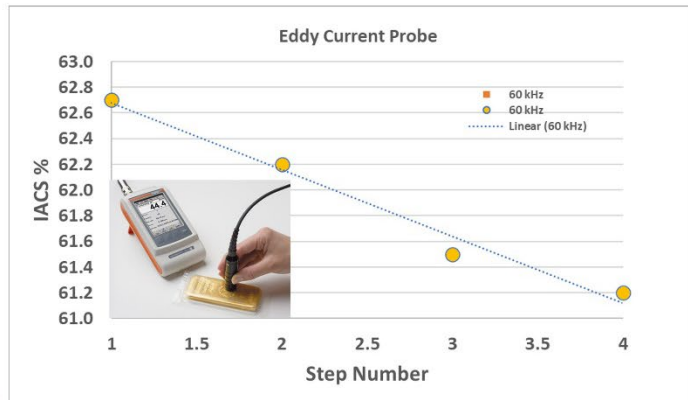


Figure I.1.4.2.4. Pure Al ingot with 4-step thickness and EC indicating the effect of cooling rate.
Source: ORNL.

Selected Results Supporting Task 3G-23: Thermal Properties of Al Alloys

Thermal properties of 3D-printed Al alloys were investigated under Tasks 3 and 5. In this study, the Al alloys that were tested were (1) AF and (2) T6 annealed. Two types of specimens were prepared—one in the horizontal direction of the print and one in vertical direction of the print. Three properties were measured to 500°C: (1) thermal diffusivity, (2) thermal expansion, and (3) specific heat. As shown by the series of TC graphs in Figure I.1.4.2.5(a-b), the AF materials showed a small hysteresis in thermal diffusivity and no noticeable change in thermal expansion. In the specific heat scan, a big difference between the first heat and cooling was observed. For the T6 annealed samples, the hysteresis in thermal diffusivity was much larger with the onset of changes at 300°C. The change in coefficient of thermal expansion measurement was also noticeable at 300°C upon heating. Similarly, a larger difference was observed in specific heat. These results were consistent with a previous study of the same alloy prepared by traditional casting. An interesting observation was that there is no clear difference between the horizontal and vertical specimens, indicating these 3D-printed materials have isotropic thermal properties. More details can be found in Report No. I.1.3.7, “Task 3G: Design of Sustainable Al Alloy Feedstock for AM.”

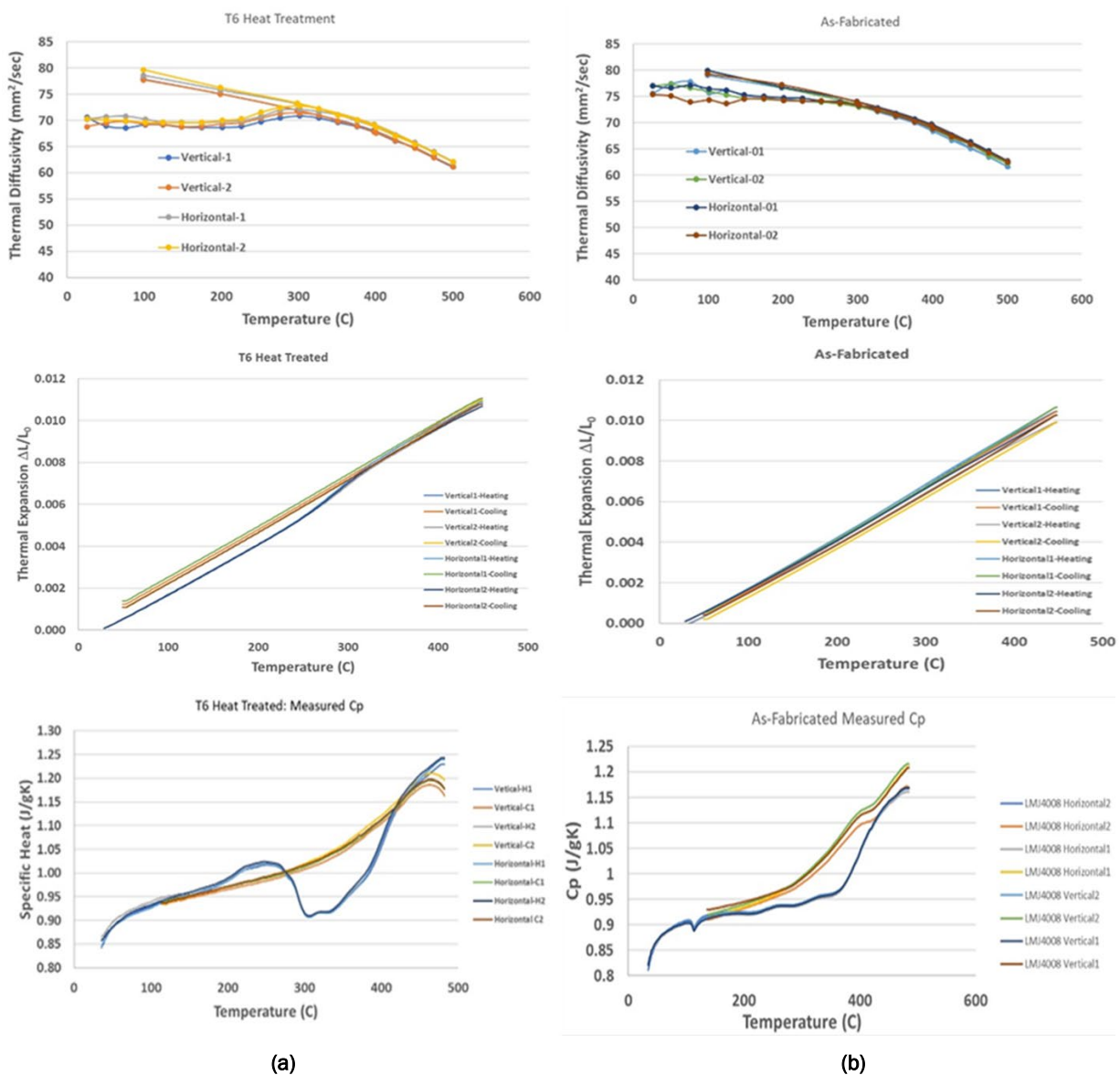


Figure I.1.4.2.5. Thermal diffusivity, thermal expansion, and specific heat of 3D-printed Al alloys for (a) T6 heat-treated and (b) AF conditions. Source: ORNL.

Selected Results Supporting Task 3C-23: Sintering Study of Ferrites

Ferrites are prepared under Task 3C-23 for more-efficient EV charging applications. The sintering behavior of these oxides can be studied using a dilatometer. The Netzsch Dil 402, dual pushrod system was used. The 25 mm long as-pressed specimens were loaded into an alumina fixture in a furnace with silicon carbide heating elements. Two specimens were loaded at each test. The system thermal expansion was calibrated using a sapphire standard. The samples were heated to 1500°C in the air. As shown in Figure I.1.4.2.6, three as-pressed ferrites showed the onset of shrinkage at 600°C and 900°C, respectively. This information is used to design ceramic processing pathways that deliver ferrites with higher density and improved mechanical properties. Details can be found in the main Task 3C-23 report.

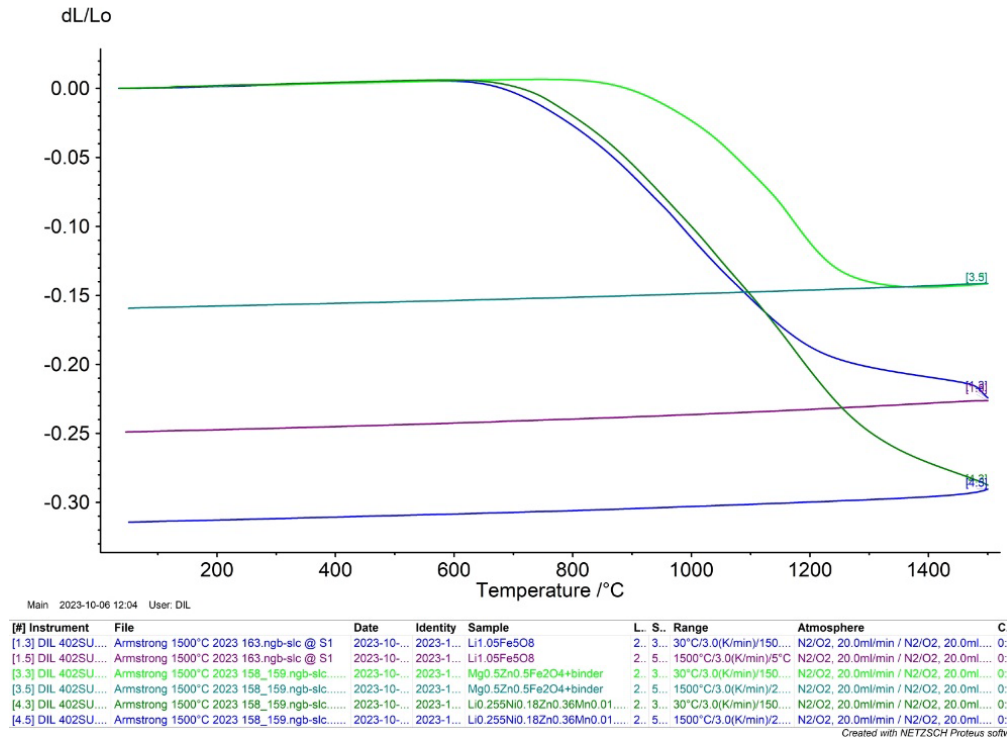


Figure I.1.4.2.6. Sintering of three ferrites up to 1500 °C with the onset of shrinkage at 600 °C and 900 °C. Source: ORNL.

Selected Results Supporting Task 3H-23: Fundamentals of Printable Higher Temperature Steels for Die-Cast Tooling and Inserts

Thermal properties of tool steels, such as 4140 and X35, are being studied under Project I.1.3.8, Task 3H, “Fundamentals of Printable Higher Temperature Steels for Die-Cast Tooling and Inserts.” The ULVAC ZEM-3 system was used to obtain the electrical resistivity of the materials. As shown in Figure I.1.4.2.7, there were no changes in the resistivity of both materials upon heating to 600°C. The Seebeck coefficient of the samples was also measured. Both materials showed slightly positive Seebeck coefficient over the temperature range indicating holes as the dominate carriers. For pure metals, the Wiedemann-Franz law is used to calculate electron contribution to TC. For alloys, especially steels, EC is lower and the Lorenz number L0 needs to be corrected by subtracting the square of the Seebeck coefficient. The TC of X35 shown in Figure I.1.4.2.8 indicated lattice (phonon) and electric contributions. More details can be found in Report No. I.1.3.8, “Task 3H: Fundamentals of Printable Higher Temperature Steels for Die-Cast Tooling and Inserts.”

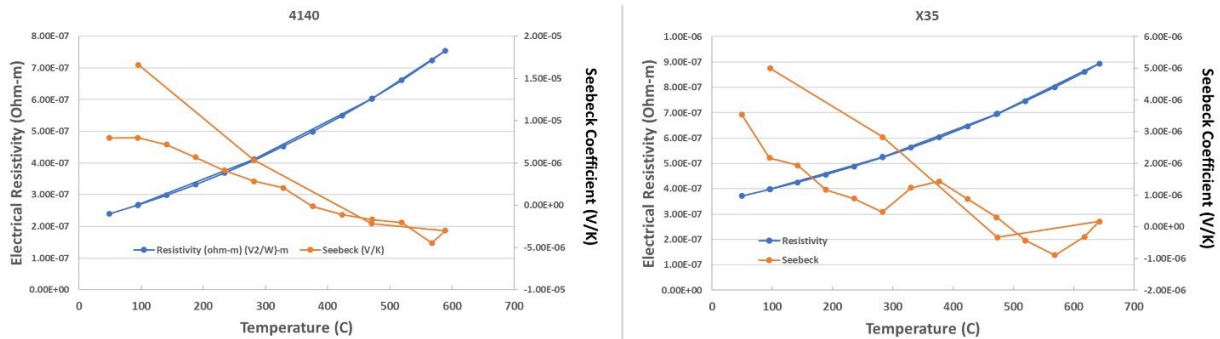


Figure I.1.4.2.7. Electrical resistivity and Seebeck coefficient of 4140 and X35 tool steels to 600 °C. Source: ORNL.

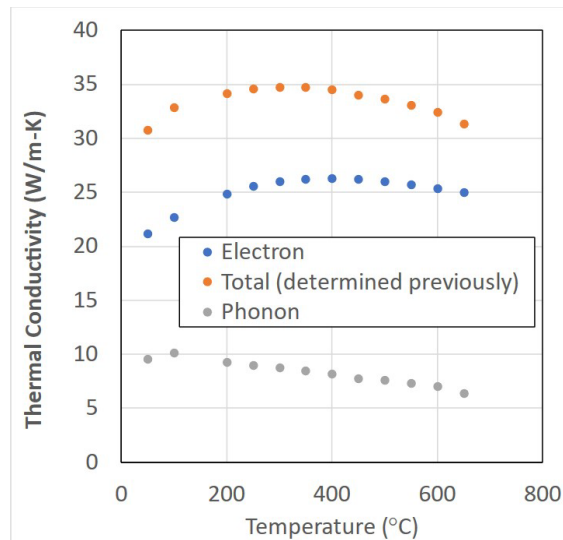


Figure I.1.4.2.8. Total TC of X35 with electron and phonon contributions. Source: ORNL.

Conclusions

In FY 2023, Task 4A3 supported a number of developmental tasks at ORNL within Thrusts 1–3 to characterize and understand the thermal and electrical properties of a wide variety of materials classes being pursued within the program team for future EV powertrains. In addition to the materials properties, a collaborative relationship with the task PIs was established whereby the understanding developed in these characterization studies was applied to support the materials design goals.

References

1. ASTM D7896-19, 2019, “Standard Test Method for TC, Thermal Diffusivity, and Volumetric Heat Capacity of Engine Coolants and Related Fluids by Transient Hot-Wire Liquid TC Method,” ASTM International, West Conshohocken, PA, USA.
2. ASTM D5470-17, 2017, “Standard Test Method for Thermal Transmission Properties of Thermally Conductive Electrical Insulation Materials,” ASTM International, West Conshohocken, PA, USA.
3. ASTM E1004, 2017, “Standard Test Method for Determining EC Using the Electromagnetic (Eddy Current) Method,” ASTM International, West Conshohocken, PA, USA.
4. ASTM E1461-13, 2022, “Standard Test Method for Thermal Diffusivity by the Flash Method,” ASTM International, West Conshohocken, PA, USA.
5. ASTM E831-19, 2019, “Standard Test Method for Linear Thermal Expansion of Solid Materials by Thermomechanical Analysis,” ASTM International, West Conshohocken, PA, USA.
6. ASTM E1269-11(2018), 2018, “Standard Test Method for Determining Specific Heat Capacity by Differential Scanning Calorimetry,” ASTM International, West Conshohocken, PA, USA.

Acknowledgements

The authors gratefully acknowledge collaboration with the following Thrust 1–3 researchers: S. Kwon, A. Shyam, D. Shin, J. Qu, C. I. Gamaralalage, S. Bahl, D. Pierce, and B. Armstrong. Thanks also go out to S. Curlin and D. McClurg for their support in accomplishing electrical and thermal properties measurements.

I.1.4.3 Task 4A. Advanced Characterization: Argonne Advanced Characterization (Task 4A4) (Argonne National Laboratory)

Dileep Singh, Principal Investigator

Argonne National Laboratory
Applied Materials Division
9700 South Cass Ave.
Lemont, IL 60439
E-mail: dsingh@anl.gov

J. Allen Haynes, PMCP Consortium Manager

Oak Ridge National Laboratory
Materials Science and Technology Division
1 Bethel Valley Rd.
Oak Ridge, TN 37830
E-mail: haynesa@ornl.gov

Jerry L. Gibbs, DOE Technology Development Manager

U.S. Department of Energy
E-mail: Jerry.Gibbs@ee.doe.gov

Start Date: October 1, 2022
Project Funding: \$290,000

End Date: September 30, 2023
DOE share: \$290,000

Non-DOE share: \$0

Project Introduction

As part of our Thrust 4 PMCP support, this report entails the synchrotron x-ray characterizations performed during FY 2023 for two specific projects:

- *FeSiX alloys* are one of the best candidates for use as cores in EV motors due to their excellent soft-magnetic properties. While Fe-6.5wt.%Si is found to be an ideal candidate with regards to the magnetic properties, it is highly brittle at RT, and therefore, not amenable to conventional processing techniques, such as rolling. This brittleness in Fe-6.5wt.%Si is caused due to the presence of deleterious intermetallic phases—B2 (FeSi) and D0₃ (Fe₃Si). While the cause for the brittleness is attributed to the above intermetallic phases in previous studies [1], the detailed literature on the phase diagram is still lacking. Our goal is to address this knowledge gap using *in-situ* high-energy synchrotron x-ray diffraction and further enable better selection of process parameters (e.g., cooling rate, process temperature, alloy composition) to minimize the intermetallics formed in the microstructure of soft-magnetic FeSiX alloys.
- *Understanding the structure and strain state of solid-phase processed nanocarbon in bulk metal (Cu, Al) by synchrotron x-ray characterizations.* Samples under investigation are composites produced by the shear-assisted processing and extrusion (ShAPE™) process developed at PNNL. ShAPE™-processed ultra-high-conductivity materials, also known as ultra-conductors, contain minute amounts of nanoscale crystalline carbon additive, such as graphene or CNTs incorporated into base metal (Cu or Al) matrix via ShAPE™. ShAPE™ ultra-conductors exhibit enhanced electrical properties when compared to their parent materials. Synchrotron characterization can provide an explanation on the mechanism for enhanced performance in transport properties.

Several nanocarbon features of interest in ShAPE™-processed ultra-conductors' nanocomposites, such as nanocarbon morphology, topology, defect density, and interfacial integration, with the surrounding metal can affect the electrical properties of the conductors. Previous modeling work has shown that these features are crucial in developing high-mobility charge carrier pathways in ultra-conductors [2]. Since the nanocarbon infused into metal-matrix by ShAPE™ is in a far-from-equilibrium condition, the ultra-conductor composites and nanocarbon structures dispersed in them are rather unique. Laboratory x-ray diffraction systems provide insufficient signal to noise resolution for probing nanocarbon structures. Thus, it requires a high-intensity synchrotron x-ray source to resolve structural fingerprints of these carbon nanostructures infused in the metals for developing a comprehensive understanding of the nanostructure formation/distribution in the material. Previously, our team utilized the high-intensity focused beam synchrotron x-ray available at beamline Sector 33-ID at the APS at ANL for the investigation of nanocarbon structures infused in both the Cu and Al ShAPE™-processed ultra-conductors.

Objectives

The objective of this investigation is to utilize the high-intensity focused beam synchrotron x-rays at APS to carry out diffraction studies to understand the structural characteristics of: (a) the minor intermetallic phase constituents in FeSiX alloys for improved processing, and (b) the distribution of nanocarbon structures infused into metal matrices in the ShAPE™-processed ultra-conductors.

Approach

The approach for the two specific synchrotron x-ray characterizations performed during FY 2023 are as follows:

- FeSiX alloys: High-energy x-ray diffraction (HE-XRD) was used to determine the presence of minor intermetallic phases (B2-FeSi and D03-Fe3Si) as a function of composition and cooling rate. Four sample buttons were obtained from ORNL with a combination of two compositions (Fe-6Si and Fe-6Si-2Cr) and two cooling rates (slow-cooled for 30 min and quenched from 1100°C). 2D Debye-Scherrer diffraction patterns were obtained using a transmission geometry at beamline 1-ID-E and 6-ID-D at the APS. The beamline setup is shown in Figure I.1.4.3.1. The energy of the monochromatic x-ray probe was about 71.676 keV with a probe size of 100 mm × 100 mm and an exposure time of about 0.5s. A CeO2 calibrant was used to calibrate the detector distance (~ 900 mm) of the setup. The diffraction measurement involved a 360° rotation of the sample while being exposed to the x-ray beam to acquire several 2D diffraction patterns and a summed diffraction pattern from the 45 frames was used for the analysis in the GSAS-II software. This step was performed to ensure sufficient information about the minor phases is captured for the analysis.
- ShAPETM-processed Al ultra-conductors were investigated by both transmission and surface micro-diffraction characterizations utilizing a high-intensity synchrotron X-ray beamline at Sector 33-ID at APS for the focused beam diffraction studies. Circular disk-ShAPETM samples of ≈2-mm-diameter and 200-μm-thick were cut from bulk samples by focused ion beam and used for our study at Sector 33-ID beamline at APS. Sample arrangements for transmission diffraction and surface diffraction are illustrated in Figure I.1.4.3.2.

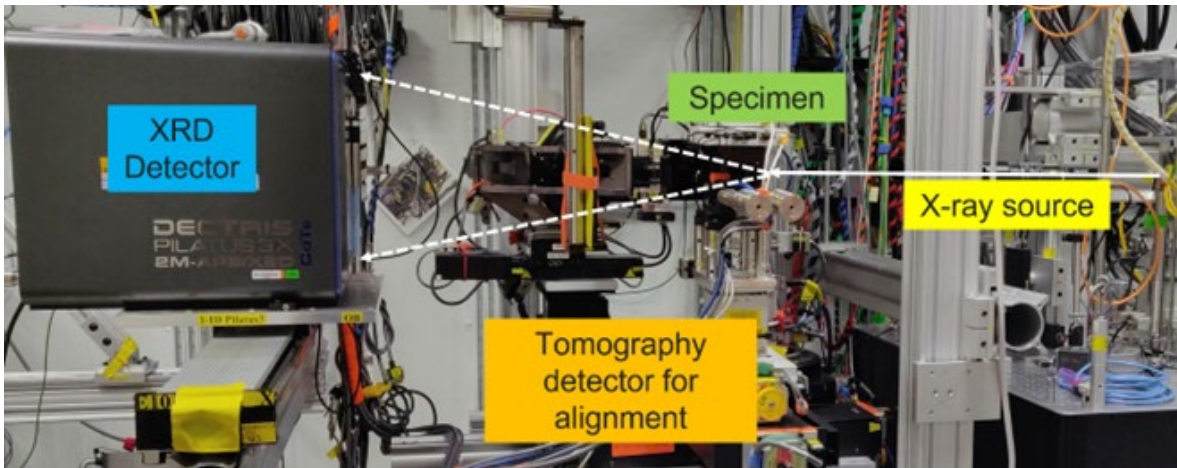


Figure I.1.4.3.1. The transmission geometry x-ray diffraction setup at beamline 1-ID-E in the APS, where the x-ray beam path is marked in white with solid line showing the incident beam and dashed lines showing transmitted/diffracted beams. Source: ANL.

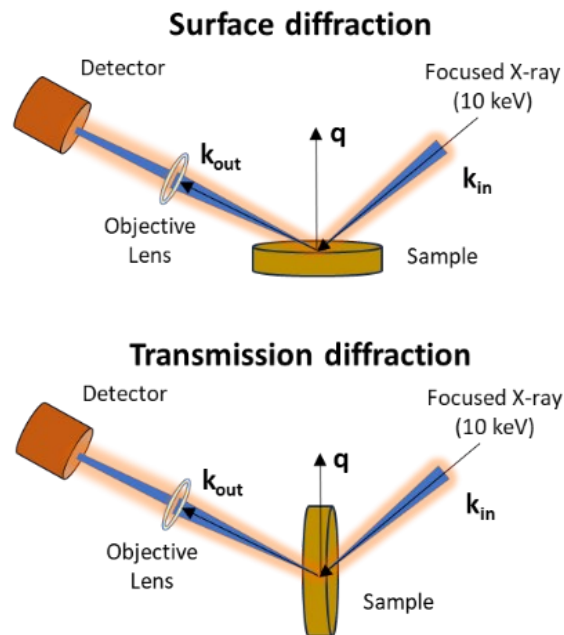
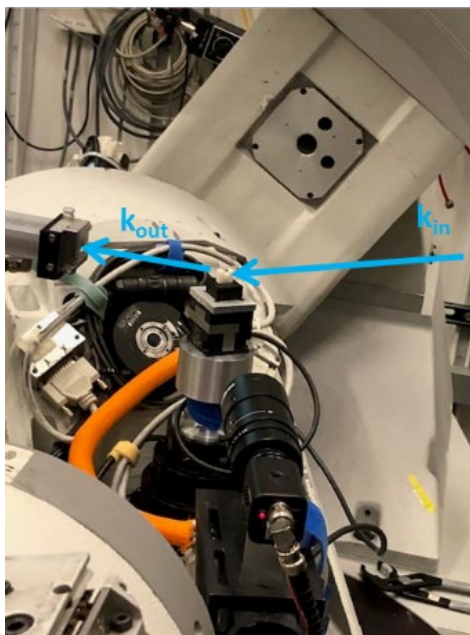


Figure I.1.4.3.2. Photograph and schematic drawings of synchrotron x-ray diffraction arrangements for the study of SHAPETM-processed Al specimens received from PNNL. Source: ANL.

Results

The results for the two specific synchrotron x-ray characterizations performed during FY 2023 are as follows:

- FeSiX alloys: The sample buttons received from ORNL were observed to have large grains (~ 0.1 mm) that resulted in a “spotty” 2D diffraction pattern. Therefore, an initial effort to obtain finer particulates from the sample buttons was conducted using a hammering + mortar/pestle route and a drilling route. As can be seen from Figure I.1.4.3.3(a), the drilling route resulted in full Debye-Scherrer rings in the diffraction pattern as opposed to the spots/arcs seen on the diffraction pattern for the hammering + mortar/pestle route, as observed in Figure I.1.4.3.3(b). This optimization effort prompted us to use the drillings from the sample buttons for subsequent x-ray experiments. The 1D diffraction patterns obtained from the azimuthal integration of the 2D diffraction patterns are shown in Figure I.1.4.3.4. As can be seen

in the figure, all sample conditions mostly contain the BCC-Fe phase (marked using blue diamonds). Additionally, low intensity peaks are seen to occur at similar relative locations to the crystal structures corresponding to the intermetallic phases but are slightly displaced from the locations listed on current standard crystallographic database files. The intermetallic peaks are marked using black circles (B2) and red squares (D03) in Figure I.1.4.3.4. A comparison between Figure I.1.4.3.4(a) showing the slow-cooled Fe-6Si, and Figure I.1.4.3.4(b) showing the slow-cooled Fe-6Si-2Cr, indicates that alloying suppresses the intermetallic phases effectively, as expected, even during slow cooling. A similar comparison between Figure I.1.4.3.4(a), showing the slow-cooled Fe-6Si, and Figure I.1.4.3.4(c), showing the quenched Fe-6Si, indicates that the cooling rate used is insufficient to suppress the formation of intermetallics. The sample with a high-cooling rate and alloying as indicated in Figure I.1.4.3.4(d) showing the quenched Fe-6Si-2Cr unexpectedly shows the presence of intermetallics. More detailed in-situ experiments are necessary to explain this observation. The ex-situ experiments and results have laid out the foundation for future in-situ experiments planned at the APS after upgrade. It is planned that in-situ experiments with the drillings in inert quartz ampoules will be conducted as a function of temperature, cooling rate, and alloy composition to map out the phase diagram.

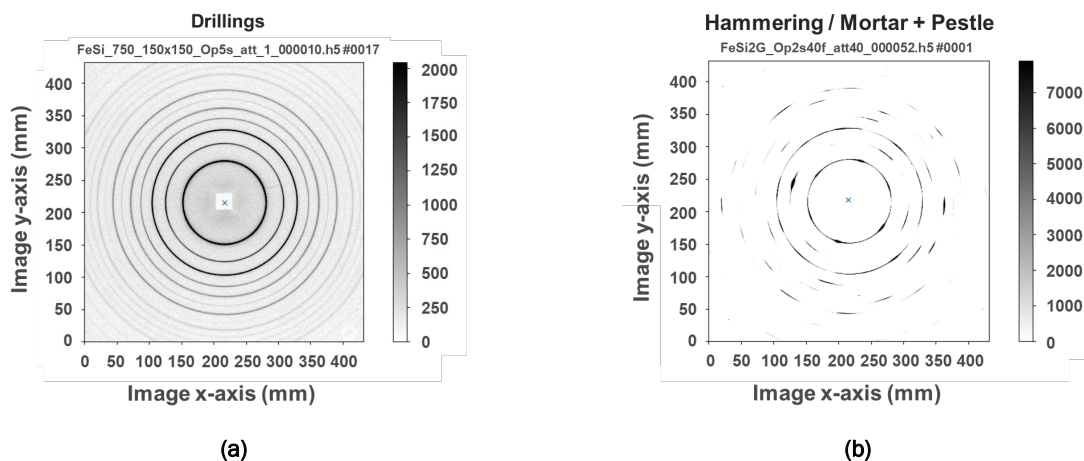


Figure I.1.4.3.3. 2D-transmission Debye-Scherrer patterns obtained for (a) drilling and (b) hammering / mortar + pestle routes. Source: ANL.

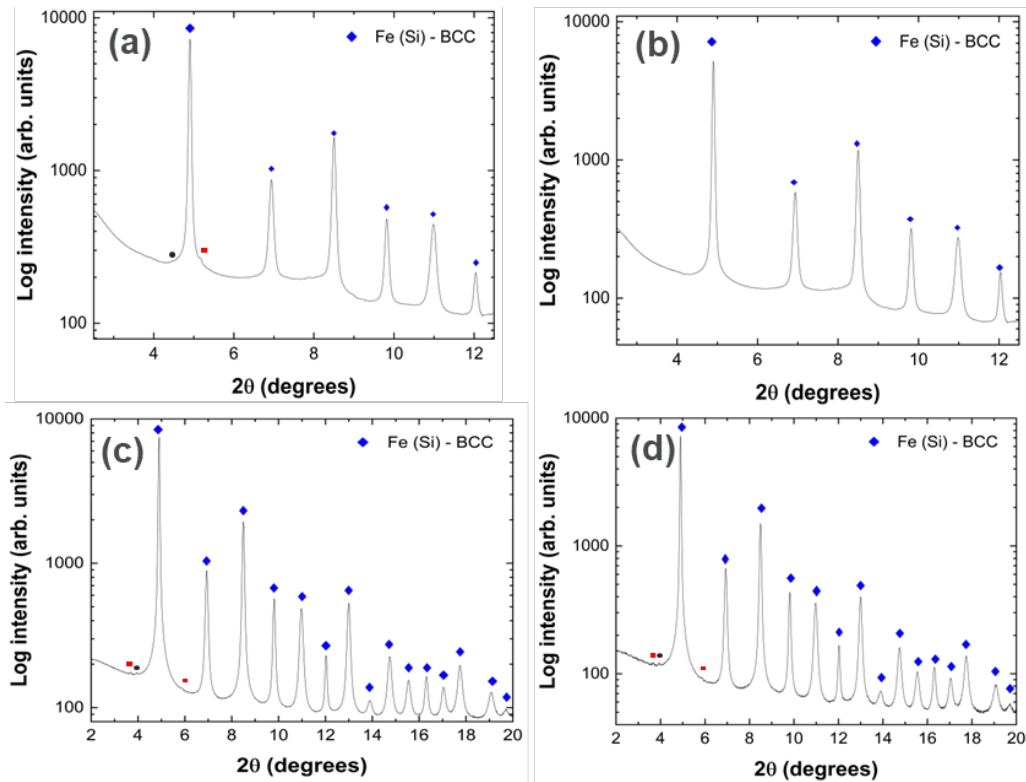


Figure I.1.4.3.4. Integrated and indexed 1D-patterns of the various sample conditions: (a) Fe-6Si slow-cooled for 30 min from 1100 °C, (b) Fe-6Si-2Cr slow-cooled for 30 min from 1100 °C, (c) Fe-6Si quenched from 1100 °C, and (d) Fe-6Si-2Cr quenched from 1100 °C. The peaks indexed using blue diamonds are signatures of BCC-Fe major phase. The peaks corresponding to the crystal structures of minor intermetallic phases, B2 and DO₃, are marked using black circles and red squares, respectively. Source: ANL.

- ShAPETM-processed Al ultra-conductors: Two samples received from PNNL were investigated. They are: (1) ShAPETM AA1100 sample; and (2) ShAPETM AA1100/0.1 wt.% graphene sample extruded at high-speed. For this work, we intend to investigate small features of carbon utilizing a finely focused synchrotron beam. As illustrated by the plot shown in Figure I.1.4.3.5(a), sample size is ≈ 2.4 mm in diameter. Using finely focused beam micro-diffraction, we successfully resolved structural features with peak intensities that are three orders of magnitude weaker when compared to the prime diffraction peaks of aluminum. As shown in Figure I.1.4.3.5(b), both the transmission and surface diffraction patterns were measured on Sample 1, which is the ShAPETM AA1100 sample, without an additional incorporation of graphene. Only transmission diffraction measurement was performed in Sample 2. Surface diffraction investigation was not performed due to the lack of beam time. We plan to continue our investigation after the APS upgrade.

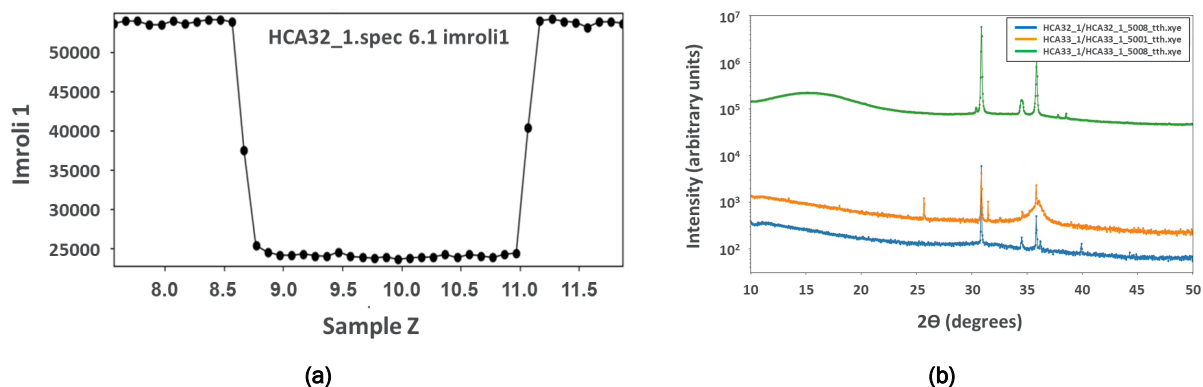


Figure I.1.4.3.5. (a) Beam profile scan at center = 9.85, width \approx 2.4 mm. (b) Micro-diffraction patterns measured two ShAPETM-processed Al specimens received from PNNL measured with a 10 keV beam.

Source: ANL.

Conclusions

FeSiX alloys were characterized using high-energy x-ray diffraction. *Ex-situ* diffraction experiments indicated that alloying was more effective than fast cooling in suppressing the intermetallics. Based on the *ex-situ* results, detailed *in-situ* experiments as a function of alloying, cooling rate, and temperature are planned to be conducted after the APS upgrade.

Synchrotron x-ray diffraction is effective in characterizing nanocarbon structures and their distribution in the ShAPETM-processed Al and Cu ultra-conductors. Transmission diffraction characterization of Al ultra-conductors produced by the ShAPETM process revealed tiny peaks likely associated with intermetallic phases in the specimens. Future studies are necessary and will be conducted after the APS upgrade.

Key Publications

1. Watkins, T., Muralidharan, G., Kamath, R., Singh, D., 2023, "Phase Study within the FeSi System," poster presentation, ORNL, Denver X-ray Conference, 7–11 August 2023, Denver, CO, USA.

References

1. Ouyang, G., B. Jensen, C. R. Macziewski, T. Ma, F. Meng, Q. Lin, L. Zhou, M. Kramer, and J. Cui, 2019, "Characterization of ordering in Fe-6.5%Si alloy using X-ray, TEM, and magnetic TGA methods," *Mater. Charact.*, 158, 109973. <https://doi.org/10.1016/j.matchar.2019.109973>.
2. Gwalani, B., M. Pole, K. E. Whalen, S. Li, B. T. O'Callahan, J. Tao, A. K. Nittala, and K. Kappagantula, 2021, Evaluating Effects of Shear Processing on 2D Crystalline Materials in 3D Metal Matrices, PNNL-32102, September 2021, Pacific Northwest National Laboratory, Richland, WA, USA. Available at: https://www.pnnl.gov/main/publications/external/technical_reports/PNNL-32102.pdf (accessed 18 December 2023).

Acknowledgements

Task leads for the ultra-conductors and FeSiX alloys projects were K. Kappagantula (PNNL) and G. Muralidharan (ORNL), respectively; their valuable insights and providing samples is greatly appreciated. Contributions by B. Ma and Z. Zhang (ultra-conductors) and, R. R. Kamath and A. Chuang (FeSiX alloys) at ANL in conducting the APS experiments and data analysis is acknowledged. Helpful discussions with T. Watkins (ORNL) are appreciated. This research used the resources of the APS, a DOE Office of Science user facility operated for the DOE Office of Science by ANL under Contract No. DE-AC02-06CH11357.

I.1.4.4 Task 4A. Advanced Characterization: PNNL Advanced Characterization (Task 4A5) (Pacific Northwest National Laboratory)

Arun Devaraj, Principal Investigator

Pacific Northwest National Laboratory
Energy Processes and Materials Division
900 Battelle Blvd.
Richland, WA 99354
E-mail: arun.devaraj@pnnl.gov

J. Allen Haynes, PMCP Consortium Manager

Oak Ridge National Laboratory
Materials Science and Technology Division
1 Bethel Valley Rd.
Oak Ridge, TN 37830
E-mail: haynesa@ornl.gov

Jerry L. Gibbs, DOE Technology Development Manager

U.S. Department of Energy
E-mail: Jerry.Gibbs@ee.doe.gov

Start Date: October 1, 2019
Project Funding: \$340,000

End Date: September 30, 2023
DOE share: \$340,000

Non-DOE share: \$0

Project Introduction

This report summarizes the progress on advanced microstructural characterization of materials conducted at PNNL for the PCMP during FY 2023, as follows:

- Project 1: Advanced Characterization of Aluminum-Graphene Composites. Al-graphene nanoparticle (GNP) composites were fabricated using solid-phase processing by shear-assisted processing and extrusion (ShAPETM) technology. This project focused on the microscopic characterization of Al-GNP composites using advanced microstructural characterization—namely TEM and APT.
- Project 2: AlCu Interface Analysis of Dissimilar Joints for Rotor Application: Joining Al end caps with different Cu short bars with and without an Ni-coating by FSP for rotor applications shows enhanced mechanical joint strength without compromising the electrical properties. The microstructure of such joints needs to be understood in detail and correlate with the property evaluation for better engineering applications. This project focuses on revealing the advanced characterization of the Al/Cu interfacial joints using TEM and APT.
- Project 3: Advanced Characterization of AA206-TiB₂ Composites: For cost-effective lightweight alloys for EV propulsion, hybrid dispersion-strengthened Al matrix (AA206)-TiB₂ composites were produced through in-situ reactions of Ti and B containing halide salts and TiB₂ powders with the molten AA206 alloy. The microstructure of such in-situ formed composites needs to be understood and optimized to best engineer these composites and achieve optimum mechanical properties. This task is focused on revealing the microstructure of in-situ AA206-TiB₂ composites using advanced characterization by SEM and TEM.
- Project 4: Advanced Characterization of Friction-Stir Processed FeSi Alloys: Rolled sheet (laminates) of ferromagnetic (Fe-2-3 wt% Si) material is used as a magnetic core for induction rotors and stators. However, the current manufacturing technology for FeSi steels is costly and leads to high rejection rates due to the low formability of high-Si-containing alloys. Significant cost-savings could be achieved if high-Si steel can be produced with better formability. Therefore, solid-phase processing-based manufacturing technologies are being explored at PNNL to produce high-performance FeSi steels for

low-cost, efficient, and lightweight EV motors. The focus of this task is to use advanced characterization by TEM and APT to analyze the microstructure of friction-stir processed FeSi alloys for high-formability, high-resistivity, and low-coercivity high-Si steel for a rotor core.

Objectives

The overall objective for Thrust 4A5 is to provide advanced characterization support for Thrusts 1, 2, and 3 of the PMCP to obtain data and scientific understanding that will be applied to the development of new materials for future advanced EVs.

Approach

Specific approaches for each task are described in the sections that follow.

Project 1: Advanced Characterization of Al-Graphene Composites.

This project focused on the microscopic characterization of Al-GNP composites fabricated using ShAPE™ technology. GNP, in the form of GNP/isopropanol ink, was introduced during ShAPE™ through holes drilled in Al billets. The Al/GNP billets are then transformed into composite wires via the friction extrusion method using ShAPE™. During Al/GNP extrusion in this study, the tool transverse rate was maintained at 1 mm/min while the tool-rotation rate was adjusted to maintain extrusion temperatures at 450°C. This process allows the production of 1.5–2.5mm Al/GNP wires that present an EC enhancement >7%. This characterization work aimed to uncover the relationship between the microstructure and the EC improvement that was observed.

Metallographically polished cross-sections of Al-GNP composites were imaged first using SEM to identify the regions of interest. Samples for TEM and APT were then prepared through a site-specific lift-out process using dual-beam FIB SEM [1]. Detailed TEM and APT analyses were conducted to analyze the structure and composition of the GNP/Al interface. The APT measurements were carried out using a local electrode atom probe system equipped with a 355 nm wavelength ultraviolet laser. Analyses were performed using the Integrated Visualization and Analysis Software.

Project 2: AlCu Interface Analysis of Dissimilar Joints for Rotor Application.

Al/Cu dissimilar joints prepared using high-speed FSP for rotor applications under Task 1H was metallographically polished. The microstructure was characterized by SEM and EDS. Based on the SEM-EDS results, specific regions were selected for preparing TEM and APT samples using a FIB microscope. Subsequent TEM and APT analysis was targeted to reveal the structural and compositional analysis of the Al-Cu interfaces.

Project 3: Advanced Characterization of Al206-TiB2 Composites.

Composites containing 10 vol.% *in-situ* formed TiB₂ dispersions in AA206 alloy obtained from Task 1H at PNNL were metallographically polished. The microstructure was characterized by SEM and EDS. Based on the SEM-EDS results, specific regions were selected for preparing TEM and APT samples using a FIB microscope. The TEM and APT analysis targeted revealing the detailed microstructure of these composites.

Project 4: Advanced Characterization of Friction-Stir Processed FeSi Alloys.

Sectioned samples of Fe-5Si, Fe-6Si, and Fe-6.5Si wt.% alloys were obtained from the Task 2E team members at PNNL after FSP, which was performed at a constant temperature of 750°C. All samples were metallographically polished. SEM-based EBSD and micro-XRD analysis was conducted to analyze the variation in microstructure in the shear zone (SZ) as a function of Si content. Specific regions from the microstructure were identified for FIB-based sample preparation for TEM and APT analyses.

Results

Project 1: Advanced Characterization of Al-Graphene Composites.

TEM bright-field images and EDS maps are shown on Figure I.1.4.4.1(a) depicting the interface between a graphene domain and Al matrix. The EDS maps clearly show the presence of an oxide layer between the Al

matrix and main graphene domain, and scandium (Sc) traces in the graphene. This oxide layer is shown in a bright yellow color in the O-K EDS map and magnified on Figure I.1.4.4.1(b) and Figure I.1.4.4.1(c), respectively. Electron energy loss spectroscopy measurements were performed in zones covering the different phases and the interface. As expected, Al is mainly found in the matrix phase, but weaker signals are also found at the oxide layer and graphene phase. C-K signals are strongly found in the graphene phase and slightly less in the oxide phase. Finally, the O-K signal is only found in the oxide layer and remains absent from the other phases. More interestingly, smaller isolated grains of C graphene of few hundreds of nanometer size are found embedded in the Al matrix near the main grain and pointed on the C-K EDS map in Figure I.1.4.4.1(a), and unlike the main graphite grain, those isolated grains do not show a surrounding oxide layer.

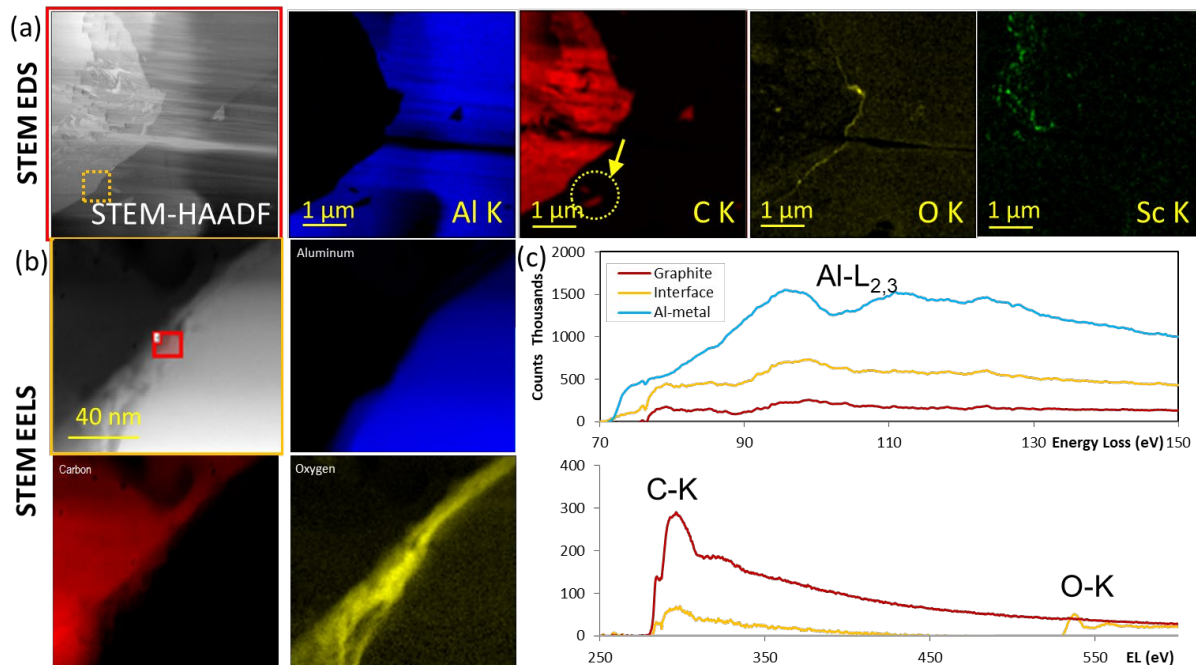


Figure I.1.4.4.1. (a) TEM bright-field images and EDS maps of Al, C, O, and Sc. (b) STEM-HAADF and EDS maps of the Al-oxide layer found between the C graphene grain and the Al. (c) Electron energy loss spectroscopy plots of the different zones probed across the oxide layer. Source: PNNL.

The APT reconstruction of the Al-GNP composite is given in Figure I.1.4.4.2(a), which displays the atomic map of the specimen probed at the interface between a C grain and the Al. The overall volume of the reconstruction is $30 \times 30 \times 140 \text{ nm}^3$. The main ions species that were collected are presented in separate maps in Figure I.1.4.4.2(b). Al represents more than 99% of the ions collected, under the form of Al^{n+} (9, 13.5 and 27 Da), and can be found in the entirety of the specimen. C atoms, detected in the form of C^{n+} (6 and 12 Da) and C_2^+ (24 Da), are mainly found on the top of the specimen. Finally, Al oxides and oxygen (O) atoms were found in the form of Al_2O^{n+} (23.3, 35, 35.5 and 36 Da), AlO^{n+} (21.5 and 43 Da), AlO_2^+ (59 Da) and O^+ (16 Da). We can distinguish two regions as depicted on Figure I.1.4.4.2(c) with the iso-volume of C that encapsulates the regions with at least 0.5 at.% C. A region of interest is isolated, as shown in red on Figure I.1.4.4.2(c), along which the composition is plotted. The atomic concentration plot, as indicated in Figure I.1.4.4.2(d) along the region of interest, establishes a clear correlation between the presence of O and C atoms in the C-enriched zone extended over 3 nm, while the ionic concentration plot shows that most of the O atoms are found in the form of Al oxides.

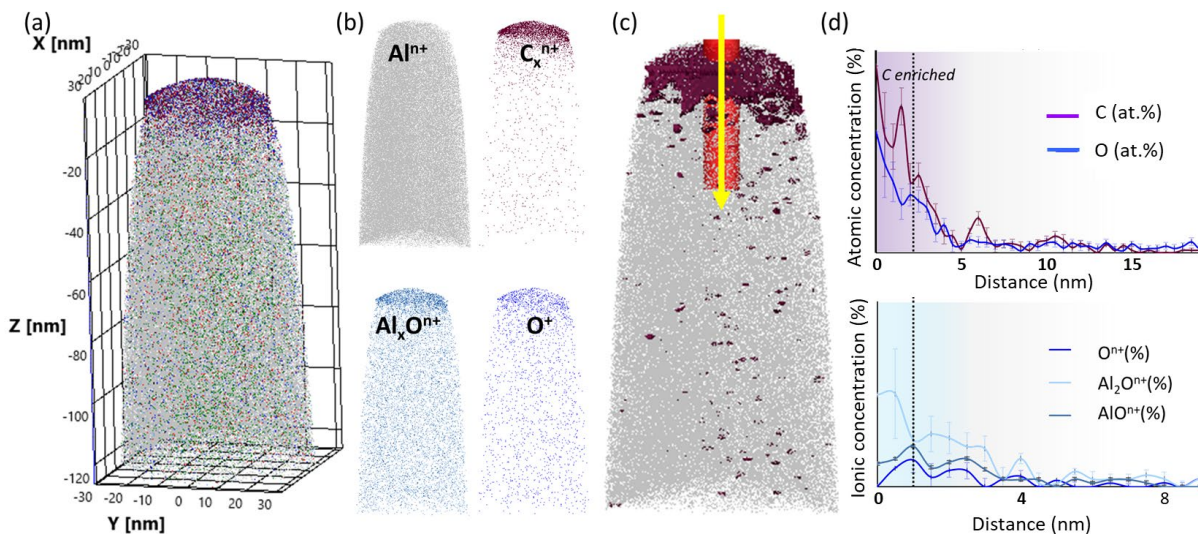


Figure I.1.4.4.2. (a) 3D reconstruction of the Al-GNP specimen with (b) individual maps of different ionic species. (c) 3D atomic map of the Al-GNP with the iso-volume enclosing the region with a minimum of 0.5 at.% of C. (d) Concentration (atomic and ionic) plots of the region of interest found in (c). Source: PNNL.

Such a detailed comparison of TEM and APT results from the interaction zone between the GNP and its Al matrix displays a presence of an Al-oxide layer that encapsulates the GNP. However, the TEM-EDS images also reveal the presence of smaller GNP fragments of a few hundreds of nm radius-free from oxides. Those observations must be considered to improve the accuracy of theoretical models and deepen our understanding of the effects of GNP on Al EC.

Project 2: Al-Cu Interface Analysis of Dissimilar Joints for Rotor Application.

The investigation of the microstructural characteristics in hybrid Al/Cu joints designated for rotor applications encompasses a meticulous analysis across three distinct regions of interest. In the initial region, SEM and EDS examinations, as depicted in Figure I.1.4.4.3(a) and Figure I.1.4.4.3(b), respectively, elucidate the microstructure resulting from high-speed FSP. The SEM image highlights disparate contrasts in fragmented zones, indicative of diverse phases generated during FSP. EDS analysis corroborates the Cu and Al enrichment in these fragmented regions, further identifying sporadic Mg and Si precipitates.

Moving to the core of the Al/Cu joint, which remains uncoated as shown in Figure I.1.4.4.3(c) and Figure I.1.4.4.3(d), the microstructure exhibits uniform layers of approximately 700 nm width with discernible contrasts. EDS maps of this core joint unveil a gradient shift in Al and Cu concentrations across the interface. This gradient suggests the potential development of intermetallic layers, such as Al_2Cu , Al_2Cu_3 , or Al_4Cu_9 , accompanied by the presence of Mg_2Si precipitates.

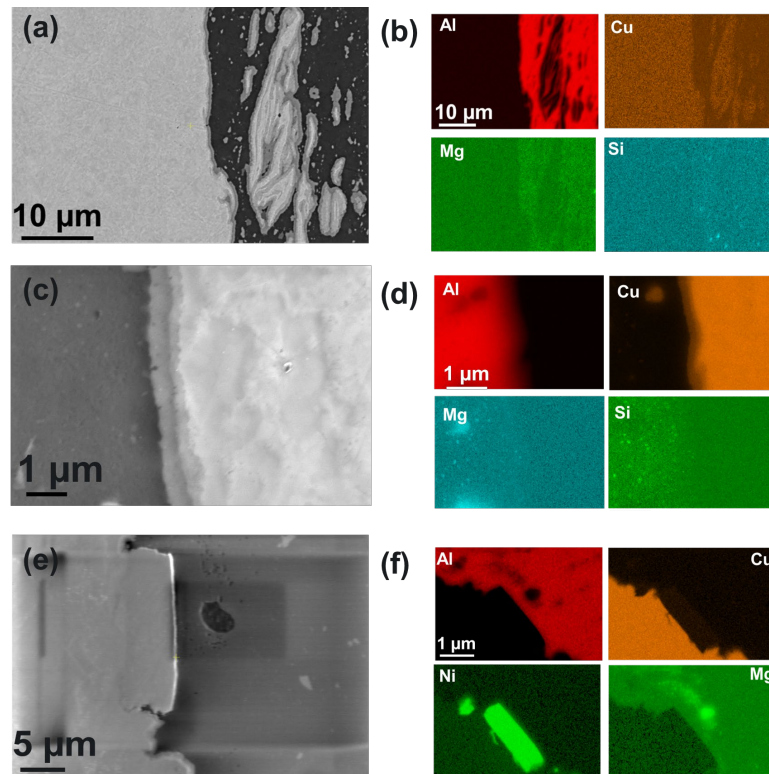


Figure I.1.4.4.3. (a) SEM image of the fragmented Cu in the Al matrix. (b) EDS of the fragmented Cu and Al in the matrix reveals the mixing of Al and Cu. (c) SEM image of the Cu/Al interface showing different contrasts from regions rich in Al and Cu elements along with precipitates rich in Mg and Si, as shown in (d). (e–f) SEM and EDS of the hybrid joint of the Al/Cu interface coated with Ni. Source: PNNL.

The final region of the Al/Cu interfacial joint with a Ni-coating, are illustrated in Figure I.1.4.4.3(e) and Figure I.1.4.4.3(f). The SEM images portray the interfacial joint with a Ni-coating, revealing a harmonious integration with the Al matrix. Concurrent EDS analysis indicates the prevalence of Cu, Ni, Al, and Mg elements, signifying the formation of ordered structures, including Ni_3Al with an L1_2 structure, and various intermetallic compounds. These structures contribute significantly to the enhancement of joint strength in the rotor application. Detailed TEM and APT analysis of all these three regions are currently under progress to understand the structure and compositions of these phases in atomic-scale spatial resolution.

In summary, this detailed microstructural investigation, employing SEM, and EDS analyses, provides a refined understanding of the hybrid Al/Cu joints. The observations of distinct phases, elemental gradients, and precipitates in specific regions contribute vital insights for optimizing manufacturing processes and tailoring mechanical properties to meet the stringent requirements of rotor applications.

Project 3: Advanced Characterization of Al206-TiB₂ Composites.

The overall microstructure of the squeeze-cast AA206 alloy with 10 vol.% TiB_2 composite is shown by the low-magnification BSE image in Figure I.1.4.4.4(a). It exhibits minimal dross, indicating a well-controlled casting process. Notably, TiB_2 particles are predominantly situated at the grain boundaries, suggesting a potential strengthening mechanism at these locations. At higher magnification, the BSE image reveals intricate details of the microstructure, as shown in Figure I.1.4.4.4(b). The presence of the Al_2Cu phase within the matrix is identified. Additionally, the distinction between in-situ TiB_2 (bright contrast) and powder TiB_2 (dull contrast) phases becomes apparent, indicating a differentiation in morphology and chemical composition between the two types of TiB_2 . EDS confirmed the elemental composition at the grain boundaries. These regions are found to be rich in Ti, B, and Cu while being relatively lean in Al, providing insight into the distribution of these elements across the microstructure, as shown in Figure I.1.4.4.4(c).

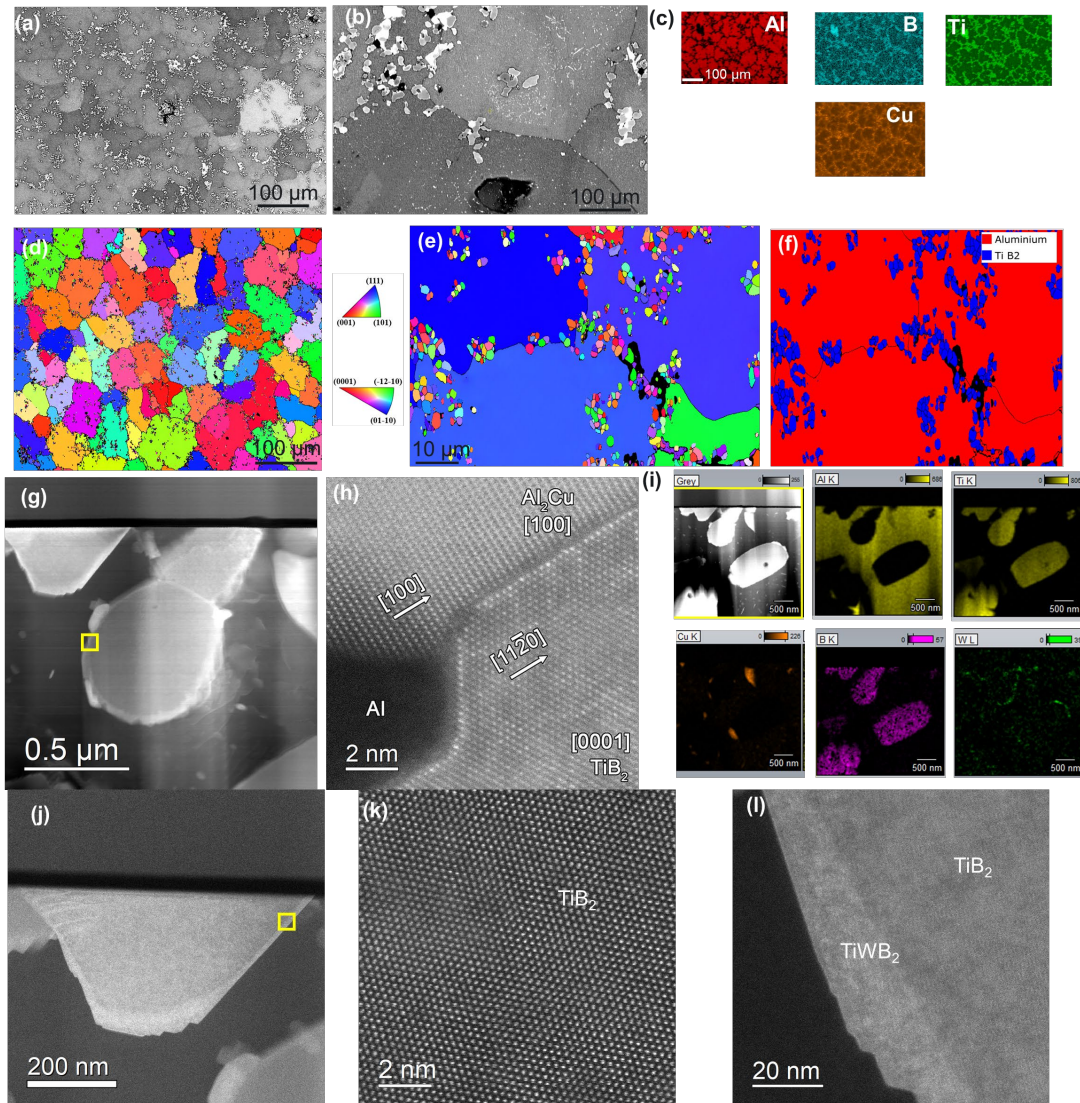


Figure I.1.4.4.4. (a-c) BSE images and EDS maps of the AA206- AA206- 10 vol.% TiB₂ (1% *in-situ* + 9% powder). (d-f) IPF-z map on the composite at low and high-magnification showing the grain size variation of Al and TiB₂ along with phase map evolution. (g-h) STEM and HAADF images of the composite showing different phases such as TiB₂, Al₂Cu, and TiWB₂ within the Al matrix. Source: PNNL.

Figure I.1.4.4.4(d) and Figure I.1.4.4.4(e) present the EBSD inverse pole figures (IPF-z) at low- and high-magnification depicting the overall grain structure. The average grain size is determined to be 42 μm , with the TiB₂ phase exhibiting a grain size of approximately 1.6 μm . This information is crucial for understanding the mechanical properties of the material. The phase map confirms the presence of TiB₂ as a secondary-phase with a hexagonal crystal structure, as shown in Figure I.1.4.4.4(f). The distribution of this phase aligns closely with the anticipated amount of powder added during the casting process, demonstrating the effectiveness of the manufacturing method in controlling phase formation.

In conclusion, the comprehensive microstructural analysis employing various advanced techniques provides detailed insights into the composition, morphology, and distribution of phases within the AA206-TiB₂ composite material. These findings are instrumental in understanding the properties and performance of the material, contributing to advancements in the field of composite materials and casting techniques.

Project 4: Advanced Characterization of Friction-Stir Processed FeSi Alloys.

Linear friction-stir processed Fe-5Si, Fe-6Si, and Fe-6.5Si alloys at a constant temperature of 750°C were metallographically polished to analyze the microstructure. The EBSD IPF maps in the middle of the SZ are shown in Figure I.1.4.4.5(a-c). Equiaxial grains are obtained after FSP. Low-angle grain boundaries are also observed, indicating the dynamic recrystallization is partially completed during FSP. The weighted-average grain size in equivalent circle diameter is presented in the Figure I.1.4.4.5(d), which shows $11.9 \pm 4.3 \mu\text{m}$, $14.0 \pm 5.1 \mu\text{m}$, and $11.0 \pm 4.1 \mu\text{m}$ for Fe-5Si, Fe-6Si, and Fe-6.5Si, respectively. Micro-XRD was performed in the middle of the SZ using 300 μm spot size X-ray beam. The XRD patterns are shown in Figure I.1.4.4.5(e) and indexed with A2, B2, and D0₃ structures. Only the A2 structure is found in the friction-stir processed Fe-5Si alloy. With increasing Si, superlattice diffraction peaks of the B2 structure is observed in the friction-stir processed Fe-6Si alloy. The presence of the higher order superlattice diffraction peaks indicate the formation of the D0₃ phase in the friction-stir processed Fe-6.5Si alloy.

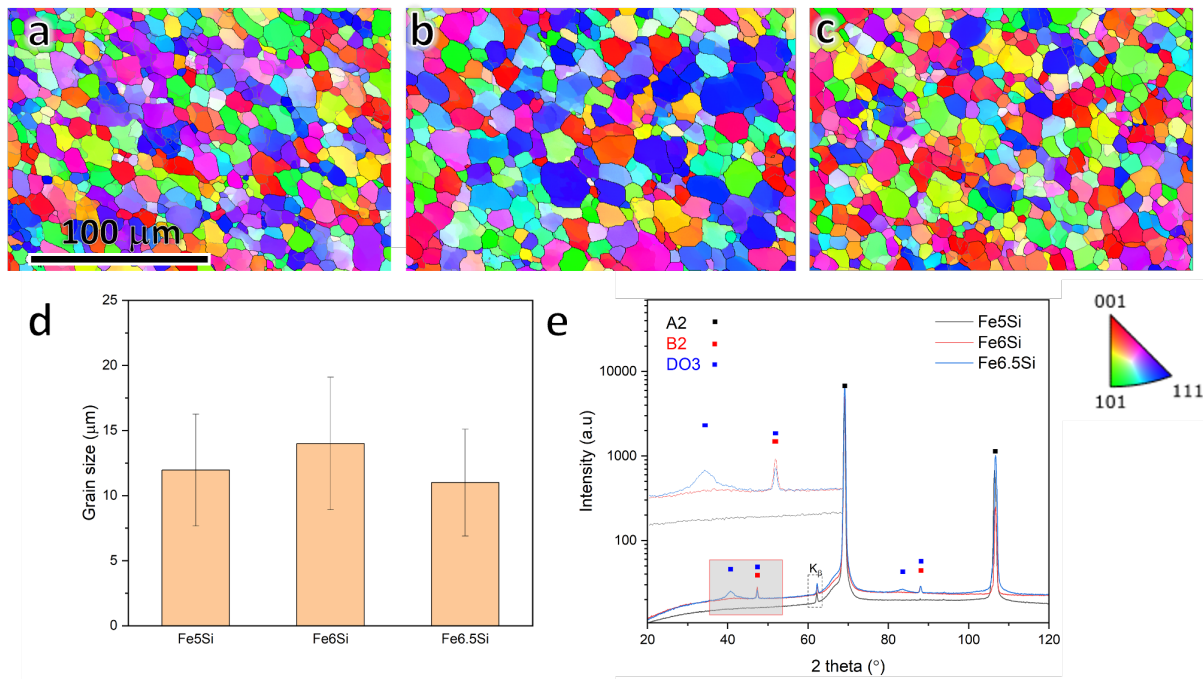


Figure I.1.4.4.5. EBSD IPF images of (a) Fe-5Si, (b) Fe-6Si and (c) Fe-6.5Si in the center of SZ. (d) Histogram plot of the average grain size. (e) XRD patterns in the center of SZ. Source: PNNL.

The detailed microstructure is characterized by using high-resolution TEM. In Figure I.1.4.4.6(a), nano-sized D0₃ phase are observed in the Fe-6.5Si alloy as evident in the TEM dark-field image using $[1\bar{1}1]$ superlattice reflection circled in the electron diffraction pattern. High-resolution TEM image of the Fe-6.5Si alloy along the $[110]$ zone axis is shown in Figure I.1.4.4.6(b). D0₃ domains with 1–2 nanometers size are highlighted in the corresponding inverse fast Fourier-transform image obtained by masking four $\langle 111 \rangle$ reflections in the FFT pattern in Figure I.1.4.4.6(c). In addition, APT will be conducted in the friction-stir processed Fe-6.5Si alloy to show the 3D morphology and the composition of the D0₃ phase.

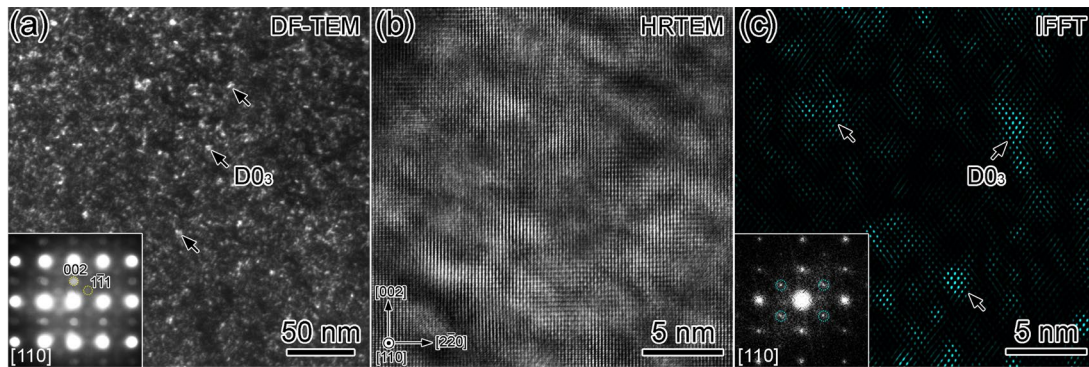


Figure I.1.4.4.6. (a) TEM dark-field image of the Fe-6.5Si alloy using the $[1\bar{1}1]$ superlattice reflection circled in the electron diffraction pattern. (b) High-resolution TEM image of the Fe-6.5Si alloy along the $[110]$ zone axis, and (c) the corresponding inverse fast Fourier-transform image obtained by masking four (111) reflections in the fast Fourier-transform pattern. Source: PNNL.

Conclusions

Across all four tasks, advanced microstructural characterization is revealing key atomic-scale insights on processing-microstructure-mechanical or electrical or magnetic property relationships for materials relevant to the PMCP. This synergy between advanced characterization conducted under Thrust 4 and material development activities conducted in Thrusts 1 to 3 can help design next generation materials with extraordinary properties for future EVs.

Key Publications

1. Gwalani, B., J. Escobar, M. Song, J. Thomas, J. Silverstein, A. Chihpin Chuang, D. Singh, M. P. Brady, Y. Yamamoto, T. R. Watkins, and A. Devaraj, 2023, "Mechanisms for high creep resistance in alumina-forming austenitic (AFA) alloys," *Acta Mat.*, 263, 119494. <https://doi.org/10.1016/j.actamat.2023.119494>.
2. Romedenne, M., S. Lambeets, M. Song, C. Roach, A. Devaraj, and R. Pillai, 2023, "Revealing the elusive role of water vapor in the oxidation behavior of a Mn-Si-containing NiCr alloy at 950°C," *Corros. Sci.*, 221, 111348. <https://doi.org/10.1016/j.corsci.2023.111348>.

References

1. Devaraj, A., D. E. Perea, J. Liu, L. M. Gordon, T. J. Prosa, P. Parikh, D. R. Diercks, S. Meher, R. P. Kolli, Y. S. Meng, and S. Thevuthasan, 2018, "Three-dimensional nanoscale characterization of materials by APT," *Int. Mater. Rev.*, 63(2), 68–101. <https://doi.org/10.1080/09506608.2016.1270728>.

Acknowledgements

For Project 1, the key contributors were S. Lambeets, T. Liu, M. Pole, S. Tripathi, and A. Devaraj from PNNL. For Project 2, the key contributors were M. Pole, S. Tripathi, and A. Devaraj from PNNL. For Project 3, the key contributors were M. Pole, M. Olszta, and A. Devaraj from PNNL. For Project 4, the key contributors were T. Liu, Z. Li, M. Pole, S. Lambeets and A. Devaraj at PNNL. For T4 coordination in PMCP, the contributions from T. Watkins and A. Haynes from ORNL and D. Herling from PNNL are acknowledged.

I.1.4.5 Task 4B. Advanced Computation: Advanced Computational Materials (Task 4B1) (Oak Ridge National Laboratory)

Dongwon Shin, Principal Investigator

Oak Ridge National Laboratory
Materials Science and Technology Division
1 Bethel Valley Rd.
Oak Ridge, TN 37830
E-mail: shind@ornl.gov

J. Allen Haynes, PMCP Consortium Manager

Oak Ridge National Laboratory
Materials Science and Technology Division
1 Bethel Valley Rd.
Oak Ridge, TN 37830
E-mail: haynesa@ornl.gov

Jerry L. Gibbs, DOE Technology Development Manager

U.S. Department of Energy
E-mail: Jerry.Gibbs@ee.doe.gov

Start Date: November 1, 2021

End Date: September 30, 2023

Project Funding: \$325,000

DOE share: \$325,000

Non-DOE share: \$0

Project Introduction

This report describes FY 2023 activities in Task 4B1 within the VTO PMCP. The PMCP aims to rapidly develop and deliver new materials and manufacturing solutions via an ICME framework that enables both powertrain efficiency advancements and weight reductions over the full range of on-road vehicle classes. The program pivoted all research from an original focus on internal combustion engines to a new focus on EVs in FY 2022.

Thrust 4 is a unique programmatic research strategy initiated in FY 2019 at the launch of the five-year PMCP consortium and is intended and structured to elevate emphasis and access to the unique world-class computational and characterization capabilities of the PMCP's three national labs. Task 4A focuses on advanced characterization, while Task 4B1 has an emphasis on advanced computational materials/ICME. Development tasks within the PMCP's three materials development Thrusts (e.g., Thrusts 1–3) submit proposals for Thrust 4 projects annually to compete for Thrust 4 capabilities and resources to support specific research objectives or to address specific scientific problems within the development tasks.

Task 4B1, "Advanced Computational Materials," is designed to provide ICME research capabilities to the development tasks within the PMCP's three development thrusts. Once Thrust 4 project awards are made, the Task 4B1 project staff are integrated into their sponsoring development tasks and provide a range of computational capabilities within these teams, including computational thermodynamic and kinetic simulation approaches (such as CALPHAD), high-throughput first-principles DFT calculations, phase-field, finite element, crystal plasticity, cellular automata, finite element method, and modern data analytics.

Objectives

The objective of Task 4B1 is to integrate computational materials capabilities within an ICME framework to foundationally undergird materials design subtasks within Tasks 1–3. The goal is to apply advanced ICME methodologies, combining predictive and advanced characterization tools of alloy behavior to accelerate materials design from technology readiness levels (TRLs) 1 to 4.

Approach

Task PIs within Thrusts 1–3 request support from Thrust 4 projects at the three labs through a standardized brief, proposal form, after which a small committee reviews, ranks, and awards the Thrust 4 projects. Thrust 4 provides funding for each project, with some defined fraction of cost-sharing from the sponsoring task. Thrust 4 projects are typically intended as one-year support efforts with specifically defined goals and are funded anywhere from \$25,000 – \$50,000. The FY 2023 project awards are provided in Table I.1.4.5.1.

Table I.1.4.5.1. Task 4B1 Funded Advanced Computation Projects in FY 2023

T4 Project	Dev. Tasks	Dev. Task PI	T4 Project PI	Task 4B1 Project Title
23-01*	3D-23	T. Aytug	M. Yoon	Materials by design for novel, ultra-high conductive materials using first-principles computational approaches.
23-02*	1E-23	A. Shyam	M. Yoon	Materials by design for lightweight materials with improved electrical properties using first-principles theoretical approaches.
23-03	1D-23	J. Jun	D. Shin	Computational thermodynamic investigation of aqueous-corrosion resistance of Al-Cu-Ce alloys via Pourbaix diagrams.
23-06	1I-23	S. Bahl	Y. Yang	High-throughput CALPHAD prediction of solidification microstructure in dirty aluminum alloys.
23-07	3E-23	D. Splitter	J Cheng	Simulation prediction of laminated vs. continuous Print Cast composite reinforcement.
23-08*	2B-23	Y. Yang	I. Roy	CA modeling on solidification microstructure in Al alloys.
23-11*	1A-23	D. Shin	Y. Lee	Finite element simulations combined with a ML approach to predict thermal conductivities of Al alloys.

Selected example results (denoted as an * in Table I.1.4.5.1) from specific projects within Task 4B1 are presented as brief vignettes on the following pages to provide examples of progress and results in FY 2023.

Results

Project 4B-23-1: Materials by Design for Novel, Ultra-High Conductive Materials using First-Principles Computational Approaches (Project PI: M. Yoon, ORNL)

Development task supported: *Task 3D-23: Novel, Ultra-High-Conductivity Materials (Cu tape + CNTs) for EVs (Task PI: T. Aytug, ORNL)*

This project aims to support the development of Task 3D in designing and manufacturing ultraconductive Cu-CNT composites with significantly improved electrical conduction properties by providing first-principles atomistic calculations that support the explanation of experimental results in the parent development task. In particular, the energetics, electronic properties, and transport properties of Cu-CNT composites functionalized with nitrogen have been investigated.

Molecular dynamics (MD) simulations were performed to guide experimental efforts to achieve better Cu coatings on CNT networks. MD simulations of a single Cu nanoparticle (NP) melting at two substrates have been studied and compared with bare Cu-NP melting. The embedded atom method potential is used for the Cu-NP and Cu substrate, while the AIREBO interaction potentials (e.g., force-fields) are used for CNT and

graphene. The cross-interactions are modeled using Lennard-Jones potential parameters. The main results are shown in Figure I.1.4.5.1.

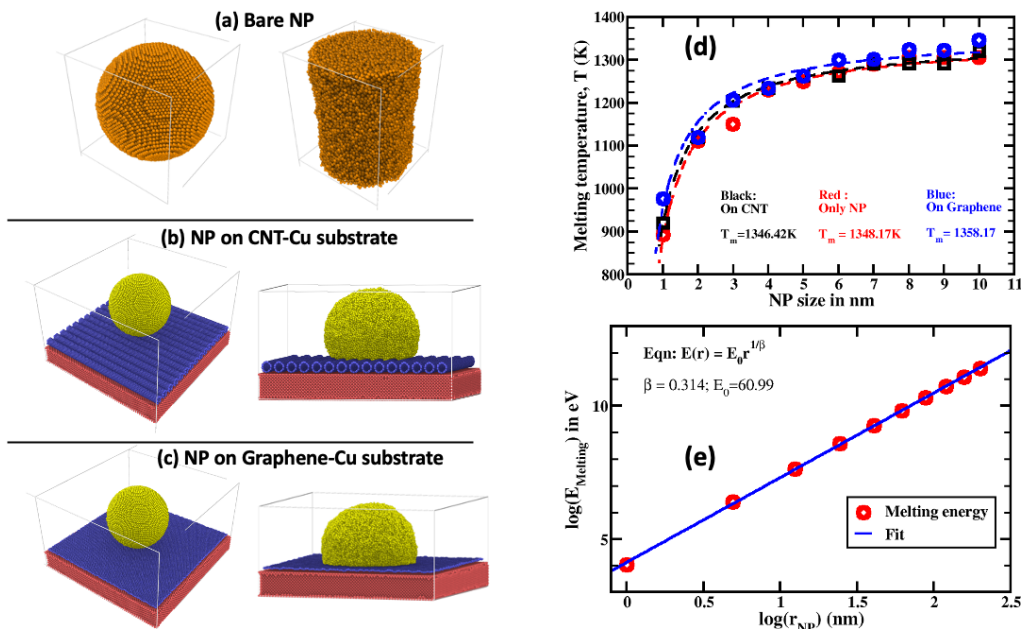


Figure I.1.4.5.1. (a), (b), and (c) melting of bare Cu-NP on CNT-infused Cu substrate and graphene-infused Cu substrate; (d) melting temperature as a function of NP sizes; and (e) scaling of melting temperature.

Source: ORNL.

The snapshot of Cu-NP melting on different substrates, including the bare Cu-NP melting, is shown in Figure I.1.4.5.1(a), (b), and (c). In the left panel of Figure I.1.4.5.1(a), (b), and (c), the pristine face-centered cubic structures of Cu-NP on different substrates are observed, while the right panel shows the melted state. The pristine face-centered cubic structure breaks down at the melted states (right panel). Figure I.1.4.5.1(d) shows the melting temperature as a function of NP sizes where the melting temperature (T_m) increases with the NP sizes.

Project 4B-23-2: Materials by Design for Lightweight Materials with Improved Electrical Properties using First-Principles Computational Approaches (Project PIs: M. Yoon and G. Samolyuk, ORNL)

Development task supported: *Task 1E-23: Lightweight Materials for Improved Electrical Properties (Task PI: A. Shyam, ORNL)*

The ultimate goal of this project is to systematically explore the material parameter space of Al-based alloys by combining material synthesis, characterization, and first-principles modeling to improve their electrical transport properties. In this first phase of the project, we aim to understand the electrical transport properties of Al-based $Al_{1-x}Zr_x$ alloys. Specifically, we have performed atomistic first-principles calculations and solved the Boltzmann transport equation to characterize their electronic properties and EC. These calculations explore parameters such as binary compositions and doping densities.

By evaluating the energetics of binary compounds and analyzing their electronic band structures, we have been able to extrapolate electronic wave functions. These are essential for evaluating the electron-phonon coupling and allow us to tackle the Boltzmann transport equation. The results of these calculations have provided EC values that are compared to actual experimental measurements, providing a robust comparison and guidance for future experimental efforts. In particular, our work has focused on Al-based compounds with pronounced

structural stabilities. Using first-principles calculations, we have addressed the Boltzmann transport equation to derive EC values comparable to experimental metrics.

A key achievement was demonstrated in the $\text{Al}_{1-x}\text{Zr}_x$ alloys, where our first-principles approach, integrating electronic structure calculations via DFT and the Wannier function technique, allowed us to determine temperature-dependent resistivity. The results, shown in Figure I.1.4.5.2, show a remarkable agreement between the theoretical calculations and the experimental results, especially in the 300–700 K temperature range, with discrepancies of less than 10% for pure Al. The total resistivity of $\text{Al}_{1-x}\text{Zr}_x$ alloys as a function of Zr concentration, x , is obtained as shown in the inset, with the doping rate close to the experimental setting. The resistivity increases with Zr doping. We can further extract the total resistivity at a finite temperature using Matthiessen's rule as the sum of the residual resistivity and the temperature-dependent component.

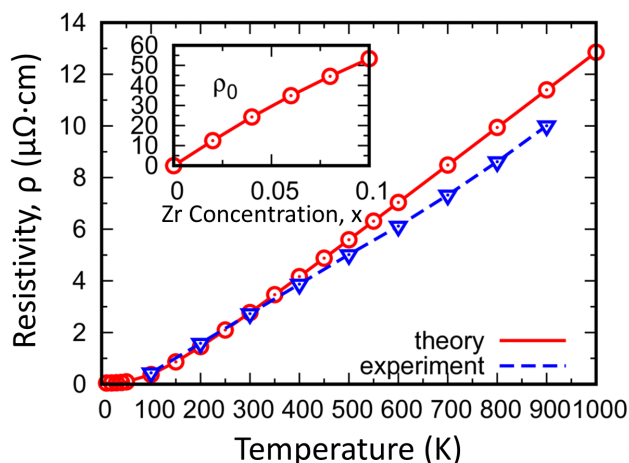


Figure I.1.4.5.2. Calculated (red) and experimental (blue) Al resistivity as a function of temperature; inset: $\text{Al}_{1-x}\text{Zr}_x$ calculated residual resistivity as a function of Zr concentration, x . Source: ORNL.

This comprehensive investigation not only provides insight into the electrical properties of Al-based alloys but also sets the stage for refined alloy-design in the future. We will extend this methodology to investigate a wide range of alloys, including ternary and binary with different dopant densities, and guide experimental efforts to optimize the electronic properties of Al-based alloys.

Project 4B-23-8: CA Modeling on Solidification Microstructure in Al Alloys (Project PI: I. Roy, ORNL)

Development task supported: *Task 3B-23: Fundamental of Non-equilibrium Processing for AM Alloys (Task PI: Y. Yang, ORNL)*

Recycling Al scrap alloys has a great potential to reduce greenhouse gas and energy costs, which prompted the International Aluminum Institute to raise the usage of scrap Al alloys from the current 1/3 to 1/2 by 2050. However, increased usage of scrap materials also means high impurity levels, such as iron (Fe) and silicon (Si) in the final products, which can lead to the formation of a significant amount of faceted and coarse detrimental intermetallics, such as $\beta\text{-Al}_5\text{FeSi}$, and degrades mechanical performance due to reduced ductility and fatigue resistance. A critical route to promote the fine-scale and uniformly distributed eutectic $\beta\text{-Al}_5\text{FeSi}$ phases instead of forming the coarse and faceted primary $\beta\text{-Al}_5\text{FeSi}$ phase is to form these intermetallic phases through eutectic solidification by a rapid solidification-favored eutectic couple zone. The goal of Development Task 3B-23 is to develop a complete CA framework to understand how thermodynamic (e.g., initial composition, partition coefficient, slope of liquidus line) and kinetic parameters (e.g., initial undercooling, cooling rate, thermal gradient, diffusion coefficient) affect microstructure evolution during solidification. This supporting task under Thrust 4 focused on developing the CA model on the Open-Source Field Operation and

Manipulation (OpenFOAM) framework, which will enable future coupling with additiveFOAM solver, a custom thermal solver built on OpenFOAM, to simulate heat transport during beam-based melting and solidification. This will facilitate solidification microstructure simulation under the non-uniform and non-equilibrium thermal conditions expected during the AM process.

In this work, the velocity of a single equiaxed dendrite growing in an isothermal undercooled melt was obtained from the currently developed CA model at eight different undercooling levels and compared against the Lipton-Glicksman-Kurz (LGK) solution, as observed in Figure I.1.4.5.3(a) and (b). The LGK model is an analytical model that describes the growth velocity of an isothermal dendrite tip without a thermal gradient in the melt. The solidification community often compares to the LGK model to verify numerical solutions. Figure I.1.4.5.3(a) shows an example of dendritic growth of Al-4 wt% Cu from the CA model at an undercooling of 4K, where solidification proceeded preferentially along the dendrite tip directions where the solute concentration gradient is most significant. As per the phase diagram for AlCu, solute segregates into the liquid phase, piling up in the interdendritic regions where diffusion occurs less easily. The comparison of the CA modeled dendrite tip velocity at steady-state to the LGK solution is shown in Figure I.1.4.5.3(b); as the undercooling increases, the modeled dendrite tip velocity increases, which is consistent with the LGK solution at the various undercooling values. The validated two-dimensional dendritic growth model was then built into the OpenFOAM framework. Figure I.1.4.5.3(c) shows the three-dimensional growth of a dendrite in the AlCu system at the same cooling condition but in different periods. This work has successfully developed a dendritic CA model and implemented the CA mode into the OpenFOAM framework.

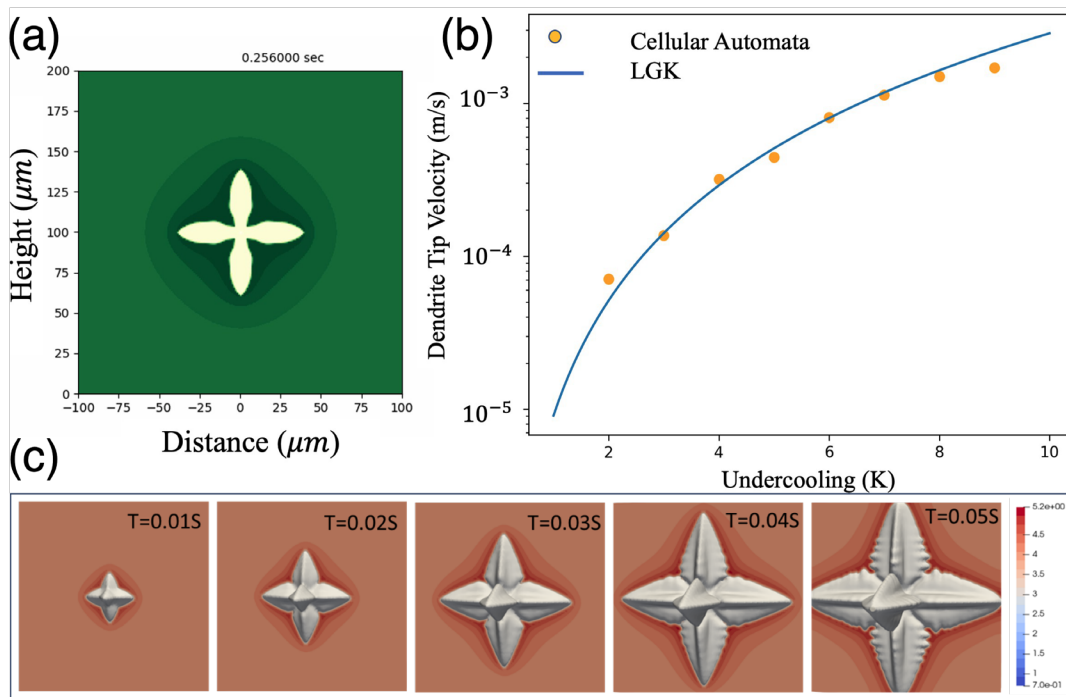


Figure I.1.4.5.3. (a) Two-dimensional growth of Al-dendrite of Al-4 wt.% Cu in a 5K undercooled melt after 0.256 seconds. (b) Comparison of CA simulated velocity of dendrite tip at steady-state with the analytical LGK solution at multiple liquid undercooling values. (c) Snapshots of three-dimensional growth of Al-dendrite simulated on OpenFOAM. Source: ORNL.

Project 4B-23-11: Finite Element Simulations Combined with ML to Predict Thermal Conductivities of Al Alloys (Project PI: Y. Lee, ORNL)

Development task supported: *Task 1A-23-Fundamentals Studies of Al-Ni Alloys for Improved Electrical Propulsion (Task PI: D. Shin, ORNL)*

Measuring TC over various microstructural features of precipitates (e.g., fraction, morphology) is difficult, costly, and time-consuming. However, a comprehensive numerical tool for TC prediction is not yet established for cast-Al-alloys due to uncertainties of input parameters, largely stemming from measurement uncertainties. To investigate this problem, we first developed a modeling methodology to address uncertainty within these modeling inputs. Then, the model was validated with experimentally measured thermal conductivities of Al-3-nickel(Ni) and Al-3Ni-0.45Zr. Lastly, we performed a statistical analysis of microstructures to provide a quantitative understanding of the correlation between microstructure and TC that can be used as an input for physics-based simulations to enable ML studies.

The sources of uncertainties causing prediction error were investigated and identified: (1) multiphase composite features of eutectic microstructures; and (2) local microstructure inhomogeneity. Measuring the TC of each eutectic composition is not only difficult but also impractical, such that the TC of eutectics is typically known to be in the range of 40–80 W/m-°C in the literature. Therefore, the eutectic conductivity of Al-3Ni and Al-3Ni-0.45Zr alloys was initially assumed in finite element method simulations to be the same. Although the prediction captures the trend in Figure I.1.4.5.4(a), the reversed values are found in N7 (Al-3Ni) and N8 (Al-3Ni-0.45Zr) (i.e., N8 marked in red should be lower than N7 in black). Reportedly, Zr has a lower TC than Ni (i.e., Zr: 18 W/m-°C, Ni: 60 W/m-°C, and Al: 240 W/m-°C), such that the different values of TC should be applied for eutectics of N7 and N8. After iterative calibrations of elemental TC, the reversal trend was corrected in Figure I.1.4.5.4(b).

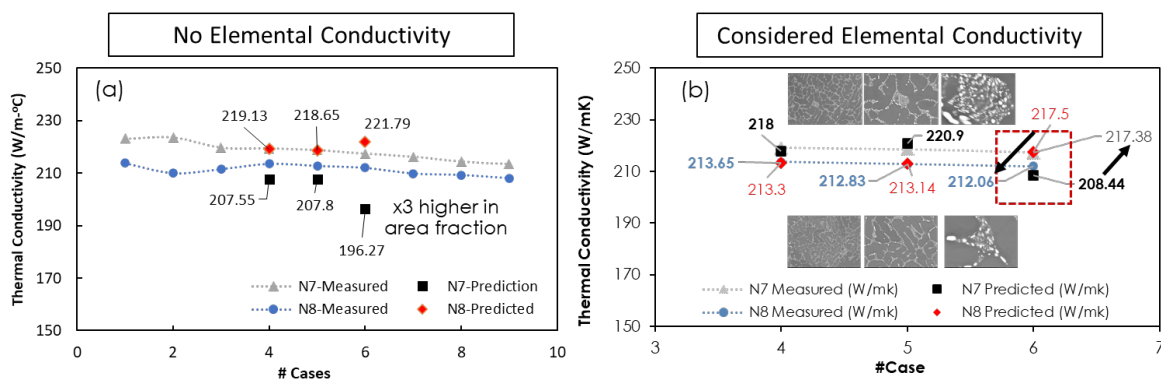


Figure I.1.4.5.4. Comparison of the predicted TC with the measured values. (a) The predicted trend agrees well with the measured values. (b) Elemental conductivity should be considered for correct prediction of Al-3Ni and Al-3Ni-0.45Zr. Source: ORNL.

Conclusions

Utilizing advanced computation to generate simulated data can provide insight into a deeper understanding of the behavior of alloy systems under various compositional, processing, and operating conditions relevant to automotive applications. A suite of ICME methods in projects sponsored by Task 4B1 has been coordinated to address specific questions or phenomena to accelerate understanding and progress in various PMCP development tasks.

The examples of FY 2023 Task 4B1 projects highlighted here are essential steps for accomplishing the mission of accelerated development of advanced materials for improved EVs under the PMCP. This report has provided brief glimpses of the approach and results of several selected projects, which include MD simulations to guide experimental efforts to achieve better Cu coating on CNT (Project 4B23-1), DFT calculations to investigate the electrical transport properties of Al-Zr alloys (Project 4B-23-2), a CA framework to understand how thermodynamic and kinetic parameters affect microstructure evolution during solidification (Project 4B-23-8), and finite element method simulations to predict thermal conductivities of Al-Ni alloys as a function of microstructures (Project 4B-23-11). Combined with Task 4A1 advanced characterization projects, the advanced modeling and simulation projects within Task 4B1 support Thrusts 1–3 tasks to elucidate underlying mechanisms and accelerate the discovery and development of advanced materials for future EVs.

Acknowledgements

This research used resources from the Oak Ridge Leadership Computing Facility at ORNL, supported by the Office of Science of the U.S. Department of Energy under contract DE-AC05-00OR22725.

I.1.4.6 Task 4B. Advanced Computation: Analysis of EVs for the International Energy Agency (Task 4B2) (Oak Ridge National Laboratory)

Hsin Wang, Principal Investigator

Oak Ridge National Laboratory
Materials Science and Technology Division
1 Bethel Valley Rd.
Oak Ridge, TN 37830
E-mail: wangh2@ornl.gov

J. Allen Haynes, PMCP Consortium Manager

Oak Ridge National Laboratory
Materials Science and Technology Division
1 Bethel Valley Rd.
Oak Ridge, TN 37830
E-mail: haynesa@ornl.gov

Jerry L. Gibbs, DOE Technology Development Manager

U.S. Department of Energy
E-mail: Jerry.Gibbs@ee.doe.gov

Start Date: October 1, 2021
Project Funding: \$100,000

End Date: September 30, 2023
DOE share: \$100,000

Non-DOE share: \$0

Project Introduction

Task 4B2 supports the International Energy Agency (IEA) Advanced Materials for Transportation (AMT) activity and focuses on testing and validation of state-of-the-art methods for characterization of electrical and thermal properties of key EV-related materials. Electrical and thermophysical properties of materials used in EV powertrains provide key materials processing quality controls and performance parameters, and are used in vehicle design, modeling, and simulation of components. Internationally recognized testing standards and metrology are emphasized, especially for advanced electrical conductors used to achieve more-efficient conduction and transmission of electric energy.

Objectives

There are two main objectives for this task. The first is to understand common practice and international standards used for the characterization of electrical and thermal properties. The second objective is contributing to the integral materials development strategies of the PMCP via international round-robin studies and standards development.

Approach

The FY 2023 approach to supporting the IEA task included a virtual workshop that was organized and hosted with the topic of ultra-high conductivity materials with participants from industry, government labs, and universities. The current state-of-the-art electric conductor materials and testing methods were reviewed, and common issues were identified.

ORNL resumed the leadership role in the IEA-AMT Annex VIII after a three-year pause due to the COVID-19 pandemic. A new focus on EV-related materials was identified and agreed upon by the member countries. An international round-robin on high-EC materials was initiated and started, using materials provided by industry (Southwire, Carrolton, GA). Twelve labs from six countries are participating in the round-robin.

Results

ORNL organized a one-day virtual workshop on EC measurements. Topics included:

- Overview of the issue: DOE perspective

- Subject matter expert review: NIST (Dr. J. Matin)/ University of Texas (UT)–Austin (Prof. M. Tehrani)
- Test standards on electrical conductivity/current density
- Active DOE projects: ORNL and PNNL on ultra-high-conductivity materials
- Applications: GM, Southwire, and other industry end users
- Panel discussion on challenges in ultra-high-conductivity materials and testing
- Other topics: Theory/model to explain and predict ultra-high EC.

The workshop speakers and their title pages are shown in Figure I.1.4.6.1. Although EC measurement has been a very routine test at most laboratories, challenges for ultra-high-conductivity (e.g., low electrical resistivity) materials have been identified. The critical issue of sample size was raised when the samples of new materials are significantly smaller. In the case of conductor wires, a 1-meter-long wire is specified, and much shorter samples have been tested and reported in the literature. The following issues were discussed during the panel session:

- Measurements of ultra-high-conductivity materials
- Ampacity: Definition, industry, laboratory experiment
- Al: CTE, strength, “don’t forget aluminum”
- Southwire: The ultimate target is all about high-current, low-temperature rise, reduce I²R loss
- GM: Current collectors of batteries, insulators (e.g., Al and Cu foils)
- Megawatt charging station: Materials and contact issues.

The final consensus of the workshop was to carry out an international round-robin to understand the measurement uncertainties of EC. The goal was to compare uncertainties on EC measured by different test methods and using different sample geometries. Previous international round-robin experiences have shown that measurement issues could be identified, and better test procedures and test standards can be developed as an outcome of the round-robin.

The round-robin plan was presented to IEA-AMT during the semi-annual executive committee meeting in January 2023. ORNL resumed the leadership role in Annex VIII, which previously focused on thermoelectric conversion materials. The round-robin plan was presented and endorsed by the member countries. The following 12 laboratories in six countries agreed to participate:

- **USA:**
 - ORNL (round-robin lead, H. Wang)
 - Southwire (R. Landry and V. Rundquist)
 - PNNL (K. Kappagantula)
 - UT-Austin (Prof. M. Tehrani)
 - GM Corporate R&D (J. Salvador)
 - Army Research Laboratory (ARL) (P. Taylor)
 - NIST (J. Martin).
- **Canada:** CanmetMATERIALS (Y. Tseng).
- **Germany:** Bundesanstalt für Materialforschung (BAM) (Ö. Özcan).

- **Austria:** Technical University (TU)- Wien (C. Gachot).
- **China:** Shanghai Institute of Ceramics, Chinese Academy of Sciences (SICCAS) (S. Bai).
- **Korea:** Hanbat National University (HNU) (M.-W. Oh).

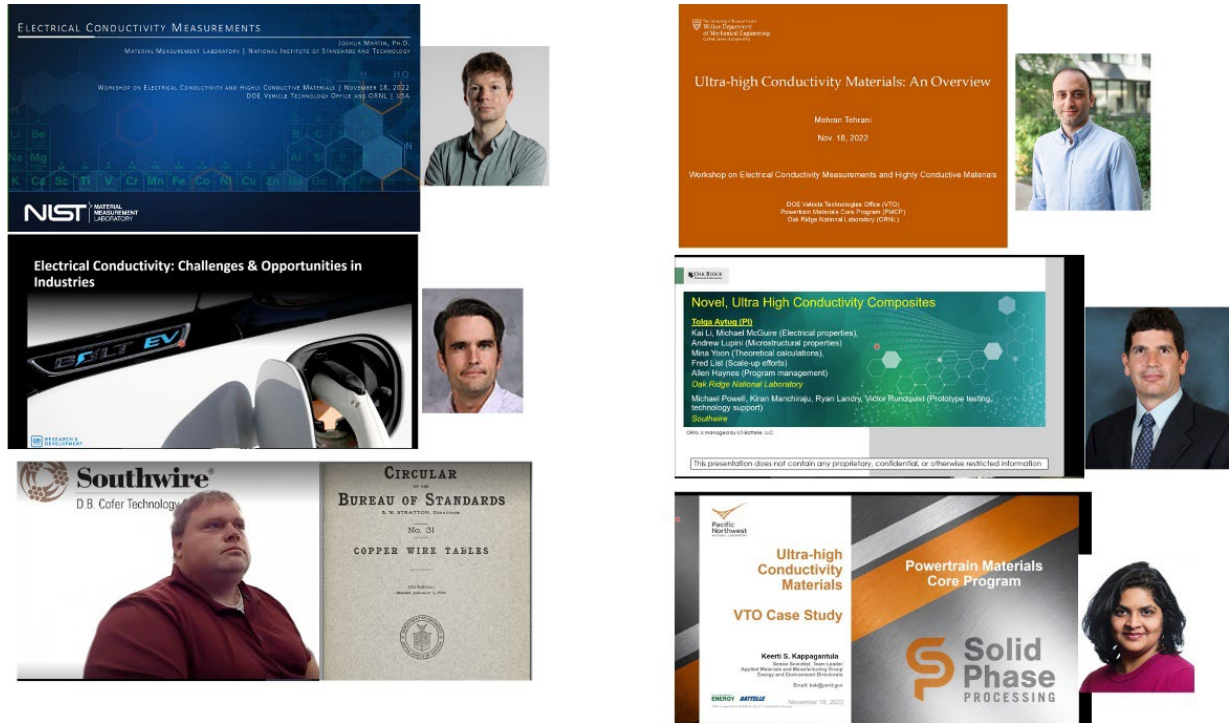


Figure I.1.4.6.1. DOE-ORNL virtual workshop speakers. Source: ORNL.

The round-robin samples were prepared and tested at Southwire. Four sets of samples were made available for the round-robin, as shown in Figure I.1.4.6.2:

- 12AWG Annealed C11000 ETP Cu Wire (3 wires and a 4th 8 mm sample for the Physical Property Measurement System)
- 12AWG Annealed 1350 Al Wire (3 wires and a 4th 8 mm sample for Physical Property Measurement System)
- 0.05-in. Thick Annealed C10100 OFE Cu Sheet (2 samples)
- 0.04-in. Thick Annealed AA1100 Al Sheet (2 samples).



Figure I.1.4.6.2. Four sets of samples were made available for the DOE-ORNL round-robin. Source: ORNL.

The density of each sample was measured at ORNL using mass and geometric volume. Table I.1.4.6.1 gives the results for the Al wires. Table I.1.4.6.2 provides the results for the Cu wires. Table I.1.4.6.3 presents the results for the Al plates. Table I.1.4.6.4 delivers the results for the Cu plates. Due to the small sample sizes, there were sample-to-sample variations. The uncertainties were mainly from the diameter measurements of the wire and thickness measurements of the plates. However, the densities are consistent with expected values for Al and Cu alloys. The round-robin samples were tested using standard industry-accepted methods at Southwire in August 2023 and shipped to ORNL for initial testing. The following instructions were sent along with the sample sets:

- Use your current lab measurement system(s) to test as many samples as you can.
- Use your current test procedures and there are no specific procedures to follow from the group.
- Record the following data:
- RT EC
- Test temperature: Laboratory temperature or specimen temperature if applicable
- Temperature of coefficient of resistance: This is optional if you can make this measurement on any sample. Maximum temperature is 60°C (please notify the organizer if overheating occurs).
- Reporting: Send your results ORNL in Excel spreadsheet format. You can attach notes about test conditions, system calibrations, and any notes of your analysis.
- Data management: Data received will not be shared with other labs during the round-robin. At the end of the study, each lab will be identified as Lab 1, Lab 2, etc., in our report and publications.

As of 30 September 2023, two labs (Southwire and ORNL) had completed testing, and the samples were sent to PNNL. As of 31 October 2023, the current testing lab is the University of Texas at Austin. The remaining round-robin testing labs include GM, ARL, CanmetMATERIALS, BAM, TU Wien, SICCAS, and HNU.

Table I.1.4.6.1. Round-Robin Sample Densities Measured at ORNL for Al Wires

Sample ID	Diameter (mm)	Length (mm)	Mass (g)	Density (g/cc)
Al Wire #1	2.055	12.248	0.10878	2.678
Al Wire #2	2.053	24.636	0.219	2.685
Al Wire #3	2.056	50.78	0.4537	2.691
Al Wire #4	2.055	151.65	1.3594	2.703

Table I.1.4.6.2. Round-Robin Sample Densities Measured at ORNL for Cu Wires

Sample ID	Diameter (mm)	Length (mm)	Mass (g)	Density (g/cc)
Cu Wire #1	2.041	12.642	0.3673	8.880
Cu Wire #2	2.045	25.309	0.7339	8.828
Cu Wire #3	2.041	50.26	1.462	2.691
Cu Wire #4	2.049	152.10	4.4227	8.818

Table I.1.4.6.3. Round-Robin Sample Densities Measured at ORNL for Al Plates

Sample ID	Diameter (mm)	Length (mm)	Thickness (mm)	Mass (g)	Density (g/cc)
Al Plate #1	12.446	12.291	1.034	0.41029	2.594
Al Plate #2	25.247	25.169	1.031	1.72568	2.634

Table I.1.4.6.4. Round-Robin Sample Densities Measured at ORNL for Cu Plates

Sample ID	Diameter (mm)	Length (mm)	Thickness (mm)	Mass (g)	Density (g/cc)
Cu Plate #1	12.618	12.468	1.275	1.74328	8.691
Cu Plate #2	25.223	25.341	1.274	7.17756	8.814

Test results are being held until every laboratory has completed testing. This is by design, so no given target is available. The goal of the round-robin is not to make the most accurate measurements but to use current laboratory practices. The smaller samples are expected to give larger measurement uncertainties and we intend to identify the causes and begin to address how to improve the testing procedures for smaller, very low-resistivity specimens.

Conclusions

Task 4B2 was able to host a virtual workshop and conduct a survey of current state-of-the-art testing methods for EC. An international round-robin of high-conductivity materials was initiated under the International Exchange Agreement - AMT, Annex VIII. The round-robin of twelve laboratories in six countries is expected to be completed in FY 2024.

Acknowledgements

In addition to being funded by DOE, this work is supported by in-kind contributions of effort from the IEA under the implementing agreement for the AMT. Annex VIII is under a cost-share structure in which all members contribute time and efforts. Special thanks to Southwire for providing materials and PNNL, University of Texas at Austin, NIST, GM, ARL, CanmetMATERIALS, BAM, TU Wein, SICCAS, and HNU for participating in the round-robin.

I.1.4.7 Task 4B. Advanced Computation: Life Cycle Analysis (LCA) of EVs, GREET® (Task 4B4) (Argonne National Laboratory)

Christopher P. Kolodziej, Co-Principal Investigator

Argonne National Laboratory
Energy Systems & Infrastructure Analysis Division
9700 S. Cass Ave.
Lemont, IL 60439
E-mail: ckolodziej@anl.gov

Jared Kelly, Co-Principal Investigator

Argonne National Laboratory
Energy Systems & Infrastructure Analysis Division
9700 S. Cass Ave.
Lemont, IL 60439
E-mail: jckelly@anl.gov

Michael Wang, Co-Principal Investigator

Argonne National Laboratory
Energy Systems & Infrastructure Analysis Division
9700 S. Cass Ave.
Lemont, IL 60439
E-mail: mqwang@anl.gov

J. Allen Haynes, PMCP Consortium Manager

Oak Ridge National Laboratory
Materials Science and Technology Division
1 Bethel Valley Rd.
Oak Ridge, TN 37830
E-mail: haynesa@ornl.gov

Jerry L. Gibbs, DOE Technology Development Manager

U.S. Department of Energy
E-mail: Jerry.Gibbs@ee.doe.gov

Start Date: October 1, 2022
Project Funding: \$135,000

End Date: September 30, 2023
DOE share: \$135,000

Non-DOE share: \$0

Project Introduction

On April 12, 2023, the U.S. Environmental Protection Agency (EPA) announced a target of 67% of LD vehicle sales and 46% of MD vehicle sales to be BEVs by Model Year 2032 [1]. The objective is the widespread adoption of BEVs to significantly reduce GHG emissions; however, some barriers exist to obtaining this goal. The Greenhouse gases Regulated Emissions and Energy use in Technologies (GREET®) model that has been developed at ANL with DOE support can analyze the impact of various materials used in vehicle production on lifecycle GHG emissions. The influence of substituting lightweight materials to reduce vehicle weight, and thus vehicle battery demand, is of particular interest in this study and addresses a key barrier to widespread EV adoption. In addition, the use of critical materials in electric MD/HD vehicles is of interest.

ANL has been developing the GREET® model since 1994 with an initial focus on energy production and consumption in the transportation sector. From the beginning, the vehicle cycle (i.e., life cycle burden of materials used within the vehicle and vehicle production), as well as the fuel-cycle, were included to have a complete, cradle-to-grave view of the vehicle life cycle. The vehicle cycle analysis is included in GREET2, as GREET1 is primarily used for fuel-cycle analysis. In GREET2, ANL characterized the energy and material

inputs associated with many important vehicle materials and identified the composition of the components associated with powertrains across multiple vehicle classes. ANL has since updated and expanded those material characterizations, as well as the vehicle powertrain options.

Objectives

The following are the primary objectives of this effort:

- Assess component and material weight composition of LD vehicles and MD/HD vehicles using GREET®
- Identify which critical materials could impact the success of on-road transportation fleet electrification
- Evaluate mass of critical materials per vehicle for LD vehicles and MD/HD vehicles using GREET®
- Determine vehicle sales potentials of LD vehicles and MD/HD vehicles found in GREET®
- Calculate potential critical material demand of new LD and MD/HD vehicle sales
- Identify important critical materials for new electric LD and MD/HD vehicle sales.

Approach

There are six types of vehicles in GREET® that have full cradle-to-grave analytical frameworks available. This allows for a vehicle cycle analysis of energy and water consumption and GHG and criteria pollutant emissions from vehicle manufacturing, use, and end-of-life. The three LD vehicles detailed in GREET® include a mid-size passenger car, a small sport-utility-vehicle (SUV), and a pickup truck (PUT), while the three MD/HD vehicles are a Class 6 box truck, a Class 8 regional day-cab truck, and a Class 8 long-haul sleeper-cab truck. The bill of materials of these vehicles in GREET® were used to estimate the quantity of critical materials per vehicle for conventional internal-combustion-engine vehicles (ICEVs) and BEVs. Combined with an average of historical vehicle sales numbers from 2015 to 2019 from the U.S. Energy Information Administration for LD vehicles and the Transportation Energy Data Book for MD/HD vehicles, an estimate of U.S. critical material demand for the new vehicle fleet was calculated [2], [3]. The supply of critical materials was provided by the U.S. Geological Survey (USGS) mineral commodity summaries for existing material supply [4]. To consider how this current supply could meet a prospective but counterfactual current demand, three scenarios of EV adoption were evaluated: (1) a hypothetical 0% EV sales (100% ICEV sales), (2) a 50% EV sales (50% ICEV sales), and (3) a 100% EV sales (0% ICEV sales) for the present day. Figure I.1.4.7.1 shows a schematic of the critical materials analysis workflow.

To explore reductions in LD vehicles critical material demands per EV, vehicle materials lightweighting and a different battery chemistry was investigated. The vehicle lightweighting was provided by replacing 50% of the steel in the vehicle body with wrought Al and 40% of the steel in the chassis with cast-Al (each with a 0.6 mass substitution ratio between Al and steel). These substitution ratios were based on Kelly et al., 2015 [5]. The battery energy capacity was reduced to maintain a constant range of 300 miles. The battery energy capacity reduction due to lightweighting was assessed based on a fuel reduction value of 0.075 liters gasoline equivalent per 100 km per 100 kg of reduced weight (0.65 kWh/100 km/100 kg) per the findings of Kim and Wallington, 2016 [6]. The effect of changing the battery chemistry from nickel-manganese-cobalt (NMC)622 to lithium-iron phosphate (LFP) on the critical materials per vehicle was also evaluated.

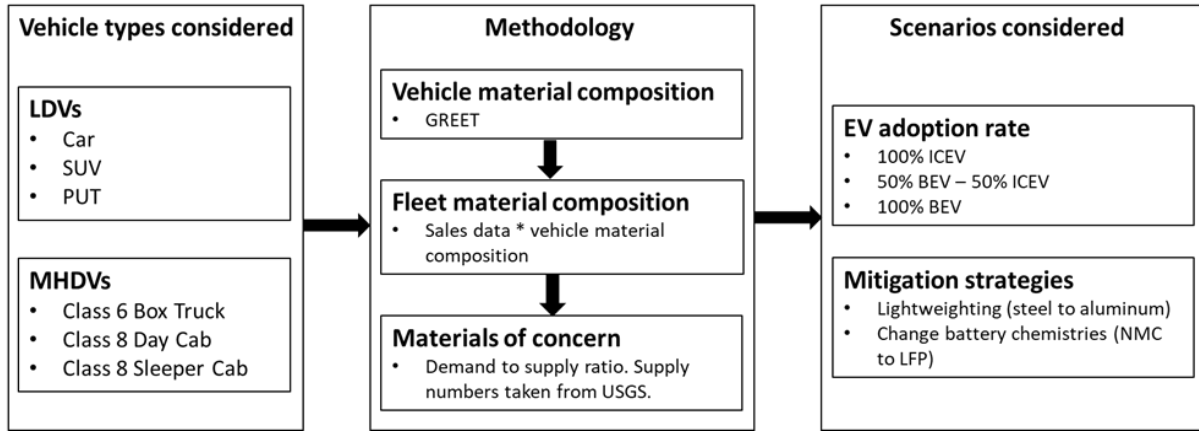


Figure I.1.4.7.1. Critical materials analysis workflow. Source: ANL.

Results

Table I.1.4.7.1 shows the vehicle components and critical materials from each vehicle component for EVs and ICEVs of LD vehicles and MD/HD vehicles, respectively. Note that while Cu and phosphorus (P) were not listed among the critical materials included in the list of critical materials by Nassar et al., 2020 [7], Cu is included in the DOE Critical Materials Assessment, while P is included in the list of critical materials by the European Commission (EU) [8], [9], [10]. As such, those materials are included in this analysis.

Table I.1.4.7.1. Critical Materials Identified in LD and MD/HD Vehicles

Vehicle Technology	Component	LD Vehicle Materials	MD/HD Vehicle Materials
EV	Body	Al, Cu	Al, Cu, Graphite
	Powertrain	Al, Cu	Al, Cu
	Transmission	Cu, Mg, Al	Al, Cu, Nd
	Chassis	Al, Cu, Mg	Al, Cu
	Traction Motor	Al, Cu, Nd, Ni, Zn	Al, Cu, Nd, Ni, Zn
	Electric Controller	Al, Cu, Ni, Zn	Al, Cu, Ni, Zn
	Battery (NMC622, LFP)	Al, Cu, Li, Ni, Mn, Co, Graphite, P	Al, Cu, Li, Ni, Mn, Co, Graphite, P
	Van/Box	-	Al, Cu
ICEV	Body	Al, Cu	Al, Cu, Graphite
	Powertrain	Al, Cu, Pt, Pd, Rh	Al, Cu, Graphite, Pt, Pd, Rh
	Transmission	Al	Al, Cu
	Chassis	Al, Cu, Mg	Al, Cu
	Van/Box	-	Al, Cu

Figure I.1.4.7.2 shows the percentage of U.S. critical materials demand, based on the bill of materials of the six vehicle types in GREET2022 and average U.S. sales numbers during 2015 to 2019, of global critical materials supply, based on the USGS mineral commodity summaries. The analysis is performed for each critical material identified in Table I.1.4.7.1 for LD vehicles. In this first set of results, only LD vehicles were considered. The scenarios were 100% ICEV (0% BEV), 100% BEV (conventional vehicle materials and NMC battery chemistry), 100% BEV (lightweighted vehicle materials and NMC battery chemistry), and 100% BEV (conventional vehicle materials and LFP battery chemistry). The 100% ICEV scenario did not show any materials with higher than 30% U.S. vehicle critical material demand of the global critical material supply.

However, several materials with greater than 30% demand were identified in the 100% BEV scenario with conventional vehicle materials and NMC battery chemistry, being cobalt, graphite, lithium, magnet, and nickel.

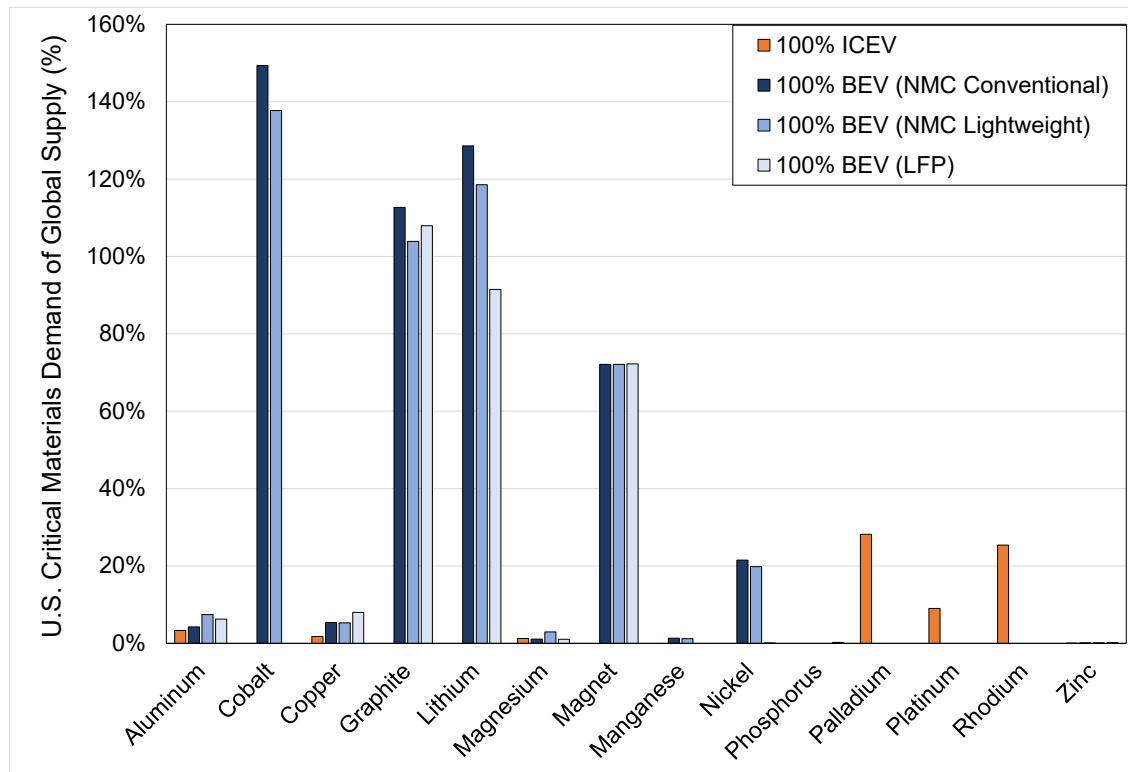


Figure I.1.4.7.2. U.S. critical materials demand of global supply for LD vehicles only, by material, for 0% and 100% electric vehicle adoption rates, as well as scenarios with 100% EVs with lightweighting or alternative LFP battery chemistry. Source: ANL.

By lightweighting the BEVs, the energy consumption rate is reduced, and the size of the battery can be smaller while still maintaining the same driving range. This slightly increased the demand of Al and Mg, since Al was the key lightweighting material explored; however, Al and Mg demand were still much lower. Battery materials were notably reduced by 5–10% due to lightweighting, but the same materials of concern are present. In this work, reductions to electric motor magnet materials were not explored, but it is possible that some magnet materials could also be reduced with vehicle lightweighting and electric motor downsizing. When the NMC battery chemistry was changed to the lower energy density LFP battery chemistry, some of the materials of concern were nullified, including cobalt and nickel. Lithium demand was significantly reduced, but still a material of concern. Phosphorus demand was well met by global supply. Graphite demand increased with LFP battery chemistry and was a result of the lower energy density requiring a larger battery to achieve the same driving range as the NMC battery chemistry.

Figure I.1.4.7.3 displays the combined U.S. demand of global critical material supply for both LD vehicles and MD/HD vehicles in scenarios of 100% ICEV (0% BEV), 50% ICEV-50% BEV, and 100% BEV. In the 100% ICEV scenario, demand for all critical materials is met by supply, and MD/HD vehicle demand is such a small portion relative to LD vehicle demand that it is hardly visible. Similarly for the 100% BEV scenario, LD vehicles composed the majority of the critical material demand. Under a 50% BEV adoption rate, similar materials were of concern (cobalt, graphite, lithium, and magnet) had demands representing a significant portion of global supply. Nickel was a material of concern under a 100% BEV scenario, but not under a 50% BEV scenario.

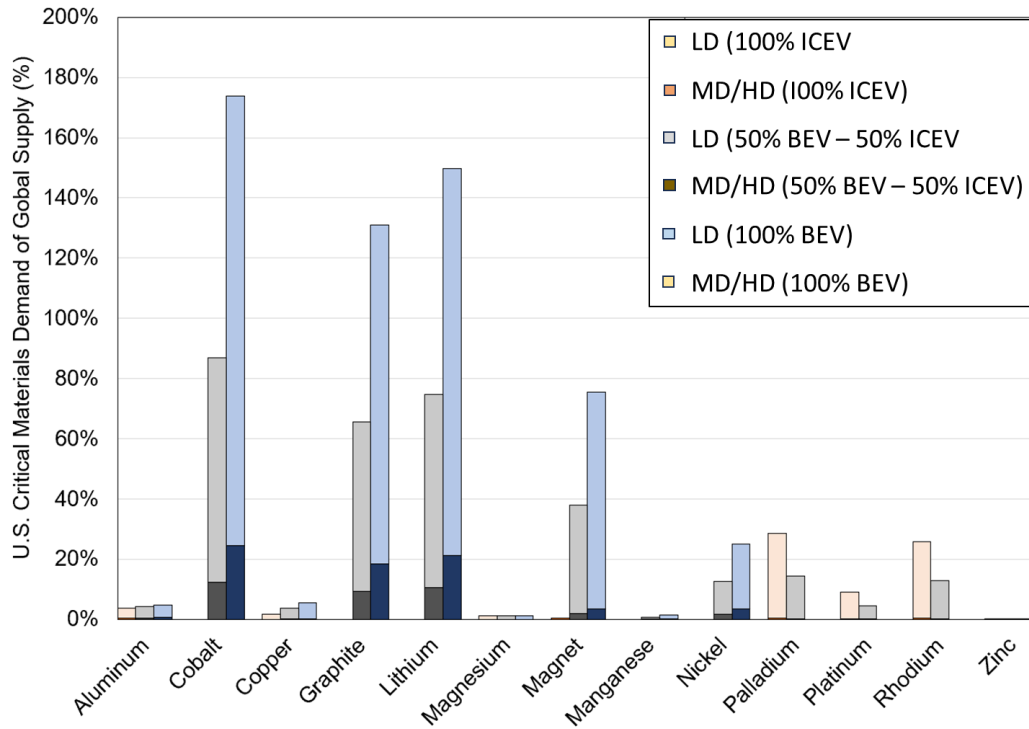


Figure I.1.4.7.3. U.S. critical materials demand of global supply for LD vehicles and MD/HD vehicles, by material, for 0%, 50%, and 100% EV adoption rates. Source: ANL.

Conclusions

This analysis shows that in order for the U.S. to reach its target BEV sales of 67% LD vehicles and almost half of MD/HD vehicles by 2032, an increased supply of cobalt, graphite, lithium, magnet, and potentially nickel would likely be required. Battery materials were notably reduced by 5–10% due to vehicle material lightweighting. Advances in alternative battery chemistries that do not use cobalt, graphite, lithium, or nickel, and electric motors requiring less magnetic material would also be useful in curtailing demand. At the same time, advances in recycling of these critical materials could benefit by increasing supply. The analysis of LD vehicles and MD/HD vehicles showed the majority of on-road critical material demand is coming from LD vehicles, since the sales volume and materials demands were higher for LD vehicles than for MD/HD vehicles.

References

1. EPA, 2023, “Biden-Harris Administration Proposes Strongest-Ever Pollution Standards for Cars and Trucks to Accelerate Transition to a Clean-Transportation Future,” EPA website, Washington, D.C., USA. April 12, 2023. Available at: <https://www.epa.gov/newsreleases/biden-harris-administration-proposes-strongest-ever-pollution-standards-cars-and-trucks> (accessed 19 December 2023).
2. U.S. Energy Information Administration (EIA), 2023, “Independent Statistics and Analysis,” EIA website, Washington, D.C., USA. Available at: <https://www.eia.gov/outlooks/aeo/data/browser/#/?id=48-AEO2023®ion=1-0&cases=ref2023&start=2021&end=2050&f=A&linechart=&map=ref2023-d020623a.5-48-AEO2023.1-0&ctype=linechart&sourcekey=0> (accessed 7 August 2023).
3. Davis, S. C., and R. G. Boundy, 2022, “Transportation Energy Data Book: Edition 40,” ORNL/TM-2022/2376, ORNL, Oak Ridge, TN, USA. Available at: https://tedb.ornl.gov/wp-content/uploads/2022/03/TEDB_Ed_40.pdf (accessed 19 December 2023).

4. U.S. Geological Survey (USGS), 2023, “Mineral Commodity Summaries 2023,” USGS website, Reston, VA, USA. Available at: <https://pubs.usgs.gov/periodicals/mcs2023/mcs2023.pdf> (accessed 19 December 2023).
5. Kelly, J. C., J. L. Sullivan, A. Burnham, and A. Elgowainy, 2015, “Impacts of vehicle weight-reduction via material substitution on life cycle greenhouse gas emissions,” *Environ. Sci. Technol.*, 49(20), 12535–12542. <https://doi.org/10.1021/acs.est.5b03192>.
6. Kim, H. C., and T. J. Wallington, 2016, “Life cycle assessment of vehicle lightweighting: A physics-based model to estimate use-phase fuel consumption of electrified vehicles,” *Environ. Sci. Technol.*, 50(20), 11226–11233. <https://doi.org/10.1021/acs.est.6b02059>.
7. Nassar, N. T., J. Brainard, A. Gulley, R. Manley, and S. M. Fortier, 2020, “Evaluating the mineral commodity supply risk of the U.S. Manufacturing sector,” *Sci. Adv.*, 6(8), eaay8647. <https://doi.org/10.1126/sciadv.aay8647>.
8. U.S. Department of Energy (DOE), 2023, “Critical Materials Assessment,” DRAFT REPORT, DOE/GO-000000-0000, DOE, Washington, D.C., USA. Available at: <https://www.energy.gov/sites/default/files/2023-05/2023-critical-materials-assessment.pdf> (accessed 19 December 2023).
9. European Commission (EU), 2023, “Study on the Critical Raw Materials for the EU 2023 Final Report,” EU website, Luxembourg City, Luxembourg. <https://doi.org/10.2873/12230>.
10. U.S. Defense Logistics Agency (DLA), 2023, “Strategic Materials,” DLA website, Washington, D.C., USA. Available at: <https://www.dla.mil/Strategic-Materials/Materials/> (accessed 1 August 2023).

Acknowledgements

The authors would like to thank their ANL colleague, Dr. R. Iyer, of ANL’s Systems Assessment Center and T. Maani, who is a Purdue University PhD Candidate and ANL research aide, for providing the analytical support that informed the present study.

I.2 Legacy Internal-Combustion-Engine (ICE) Powertrain Materials

I.2.1 Low-Mass and High-Efficiency Engine for Medium-Duty Truck Applications (General Motors)

Qigui Wang, Co-Principal Investigator

General Motors, LLC.
30003 Fisher Brothers Rd.
Warren, MI 48093
E-mail: qigui.wang@gm.com

Ed Keating, Co-Principal Investigator

General Motors, LLC.
28755 Louis Chevrolet Rd.
Warren, MI 48093
E-mail: ed.keating@gm.com

Jerry L. Gibbs, DOE Technology Development Manager

U.S. Department of Energy
E-mail: Jerry.Gibbs@ee.doe.gov

Start Date: October 1, 2019
Project Funding: \$1,919,099

End Date: March 31, 2024
DOE share: \$955,202

Non-DOE share: \$963,897

Project Introduction

Today's transportation vehicle customers are demanding that manufacturers produce engines with lower weight and improved efficiency to reduce fuel consumption, emissions, and costs associated with vehicle use, while maintaining or even increasing engine performance. Developing the next generation of high-efficiency, very low-emission ICEs requires a combination of new combustion strategies, advanced materials, and new materials processing techniques to further increase engine efficiency and reduce weight.

Objectives

The objective of this collaborative project between GM, ORNL, The Ohio State University (OSU), Michigan Technological University (MTU), and Eck Industries Inc. (ECK) is to develop an advanced MD truck engine equipped with advanced materials and combustion technologies capable of achieving $\geq 10\%$ fuel-efficiency improvement and $\geq 15\%$ engine weight-reduction when compared to the 2015 Model Year GM L96 VORTEC 6.0L V8 engine compliant with applicable EPA emission standards with performance demonstrated via simulation coupled with an engine dynamometer test.

Approach

This project was proposed as a large-scale engine design and demonstration enabled by an advanced materials and manufacturing development program, with a comprehensive plan spanning a period of four years in two phases. The project began with engine architecture design and analysis activities, advanced materials and manufacturing process development, and downselection. It culminated in an engine test cell evaluation with optimal materials and manufacturing solutions supporting final vehicle simulation. The final engine test will verify engine weight-reduction and performance to the objectives of the Funding Opportunity Announcement (FOA) [1].

Several advanced combustion technologies will be investigated, including enhanced mixture motion and rapid combustion, increased compression ratio, combustion charge dilution through cooled exhaust gas recirculation, and ultra-high-pressure fuel injection. High-strength and heat-resistant materials are developed and incorporated with novel metal casting and AM processes to produce highly durable engine structures to maximize performance of the materials and systems with minimum mass and cost. The opportunity to include

advanced materials and manufacturing in conjunction with high-potential combustion system and engine technologies also creates the chance to revisit the most appropriate engine specification to realize the desired efficiencies while reducing engine weight cost-effectively. A point of focus is the most cost-effective solution to promote wide-market acceptance using the right materials in the right place and the right process for the right parts. Single- and multimaterial solutions for key engine components will be investigated. ICME [2], [3] and computer-aided engineering tools will be utilized fully to accelerate both engine design and material and manufacturing solution development and optimization.

Results

Based on Phase 1 R&D, advanced combustion and materials technologies have been developed and downselected for the proposed MD truck engine capable of meeting requirements.

Task 3.1 Design and Build Engines to Facilitate Test Cell Evaluation of Proposed MD Truck Solution Incorporating Components

The Phase 2 engine shown in Figure I.2.1.1 was designed and built to demonstrate fuel economy performance, and contains the following key features: (1) two spark plugs/cylinder with supporting ignition system; (2) ultra-high-pressure direct inject fuel system design integrated with cylinder head; (3) active charge motion control valve integrated into intake assembly; (4) high-pressure exhaust gas recirculation system; (5) cast-Al block; (6) fabricated tubular exhaust manifolds; (7) plastic rocker covers and valley tray; and (8) split cooling with valve bridge drilling.

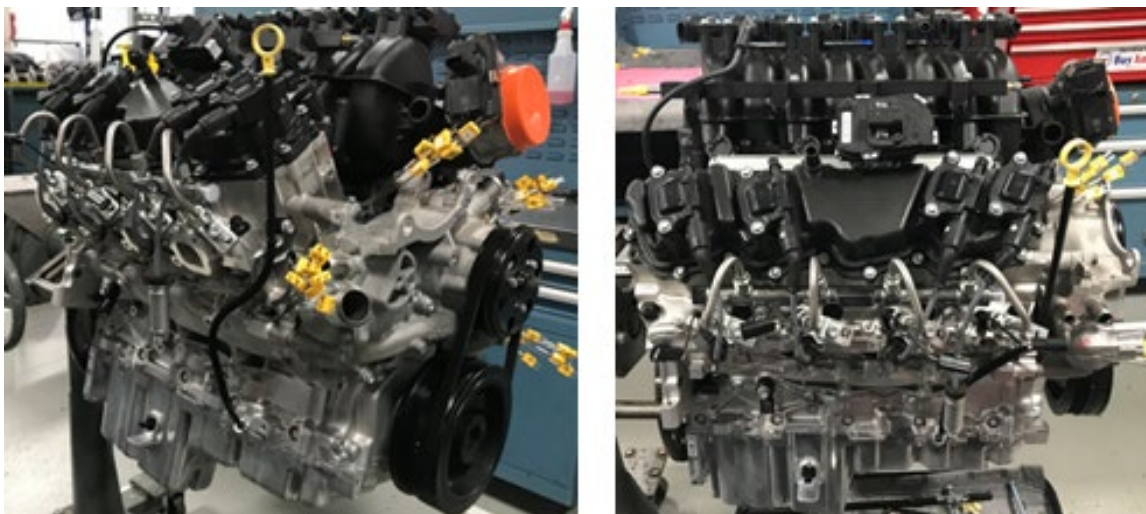



Figure I.2.1.1. Completed Phase 2 fuel economy test engine build (front and side views). Source: GM.

Task 3.2 Demonstration of the Highest-Payoff Materials and Manufacturing Solutions for Key Engine Components for the Proposed MD Truck Engine

With the materials solutions developed in Phase 1, the overall Phase 2 engine weighs 200 kg, which is >17.7% lighter than the L96 baseline engine, while engine displacement has increased from 6L to 6.6L, as indicated in Table I.2.1.1. A significant mass-savings was achieved by replacing the cast-iron block in the baseline engine with a high-performance cast-Al block (saving mass >56%). Hollow cast-steel and ductile iron crankshafts have saved the mass by 1% and 3%, respectively, compared with the forged steel crank. AM Al pistons also have saved the mass by 3% after replacing the cast-Al pistons. The Phase 2 cast-Al head, however, has increased the mass by 31% in comparison with the baseline head due to the integration of two spark plugs/cylinder with a supporting ignition system, ultra-high-pressure direct inject fuel system design, and an active charge motion control valve integrated with the cylinder head.

Table I.2.1.1. Mass Comparison of Key Engine Components in Phase 2 and Baseline Engines

DOE FOA Baseline Engine		Phase 2 – Validation and Demonstration
Key Parts	L96 6.0L V8 Engine	DOE New 6.6L V8 Engine
Engine Block	Cast-Iron	Cast-Al (saving mass by 56%)
Cylinder Head	Cast-Al	Cast-Al (increasing mass by 31% due to new combustion)
Crankshaft	Ductile Iron	Cast-Steel (saving mass by 1%) Cast-Iron (saving mass by 3%)
Camshaft	Hollow Steel	Austempered Ductile Iron (saving mass by 9%)
Piston (Each)	Cast-Al	AM-Al (saving mass by 3%)
Total Engine Weight	243.1	200.0
Overall Engine Mass Reduction		-17.7%

A novel low-pressure precision sand casting (LPPSC) process has been developed for casting high-quality Al cylinder heads and engine blocks through a comprehensive casting process simulation and multiscale defect and microstructure modeling, gating, and riser system, as well as LPPSC process parameter optimization. The Phase 2 cast-Al engine blocks are shown in Figure I.2.1.2(a), while the cylinder heads are shown in Figure I.2.1.2(b). Both were cast using the LPPSC.

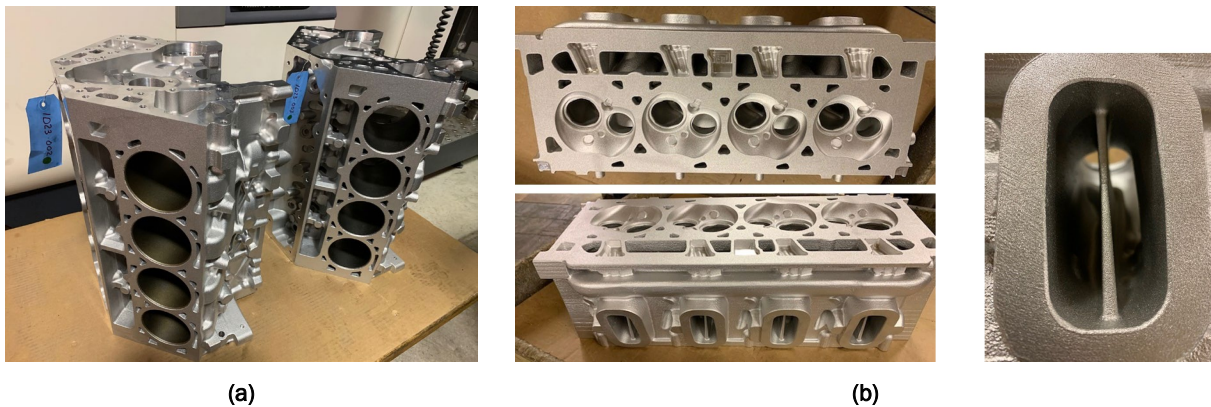
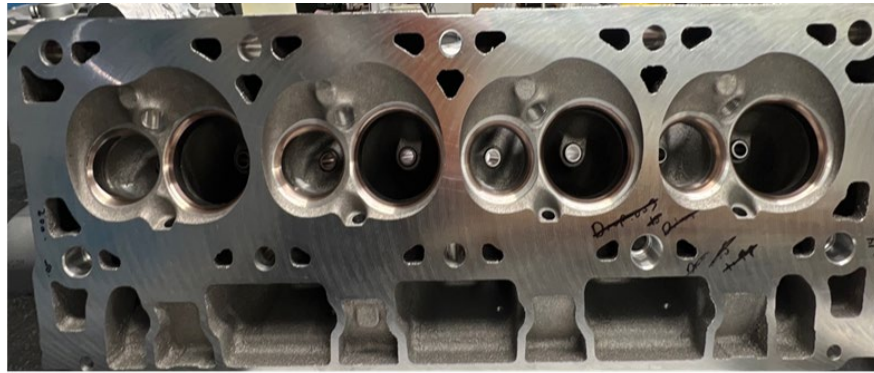


Figure I.2.1.2. (a) Phase 2 cast-Al engine blocks. (b) Cylinder heads. Source: GM.

Figure I.2.1.3(a) shows tensile properties of the cylinder heads made by LPPSC process with different alloys. Figure I.2.1.3(b) compares the fatigue properties for the baseline and the LPPSC cylinder heads. For the same alloy (i.e., A319), the LPPSC process has improved fatigue properties of the heads by at least 20% compared with baseline heads. ORNL’s ACMZ alloy demonstrated a very high potential of improving both tensile and fatigue properties of the cylinder heads at elevated temperatures.

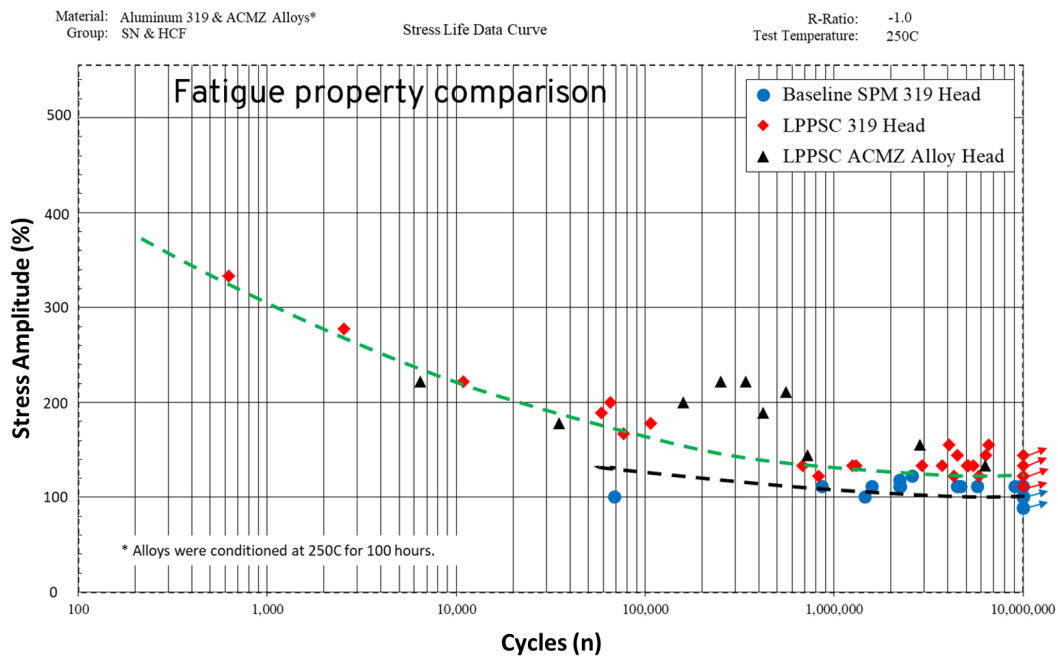
Figure I.2.1.4(a) shows the bulkhead sampling locations for fatigue testing. Fatigue properties of engine blocks made by the developed LPPSC process are shown in Figure I.2.1.4(b). Similar to the findings with cylinder heads, the engine blocks made by ORNL’s ACMZ alloy also demonstrated improved fatigue strength by at least 25% compared with cast-Al engine blocks made of A319 alloy.



Tensile strength (UTS) comparison

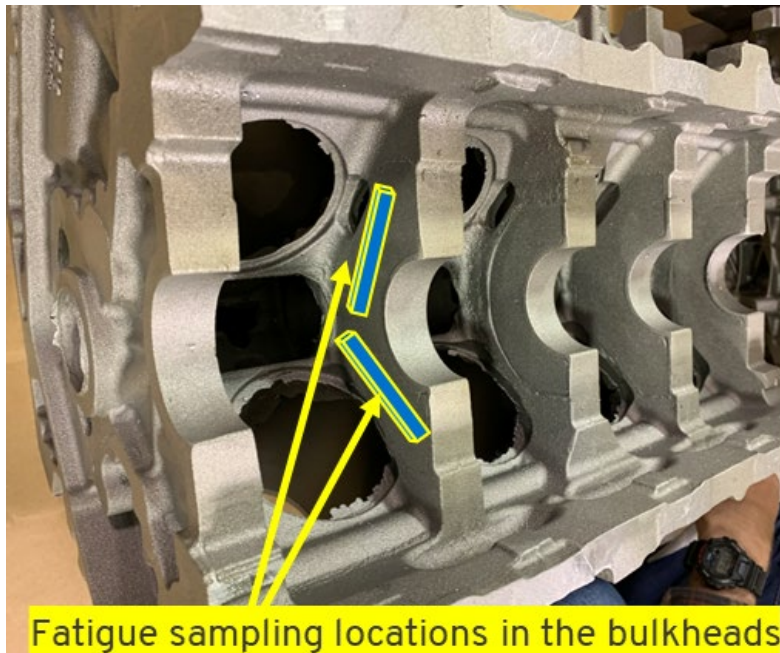
Location	Test Temperature (°C)	Baseline 319 Head Tensile Strength (MPa)	LPPSC 319 Head Tensile Strength (MPa)	LPPSCACMZ Head Tensile Strength (MPa)
Deck Face	250	98	104	184

(a)

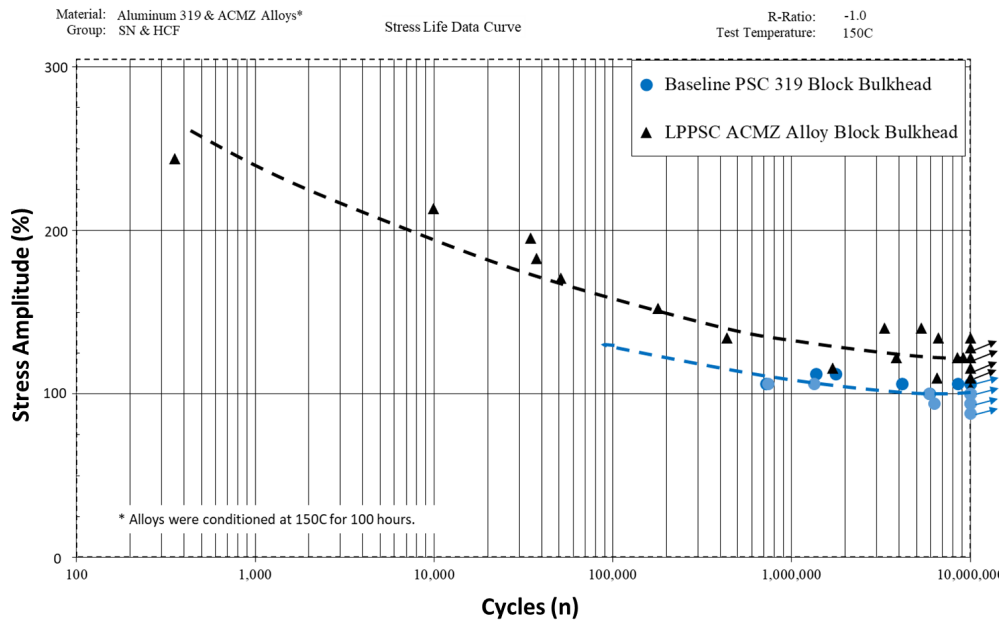


(b)

Figure I.2.1.3. (a) Tensile strength comparison and (b) fatigue properties comparison of cylinder heads made by the developed LPPSC process. Source: GM.



(a)



(b)

Figure I.2.1.4. (a) Fatigue sampling locations in the bulkhead and (b) properties of engine blocks made by the developed LPPSC process. Source: GM.

AM-printed pistons from ORNL’s Al-cerium (Ce)-based DuAlumin-3D alloy have been comprehensively evaluated and compared with cast-Al production pistons. Figure I.2.1.5 and Figure I.2.1.6 show the tensile and fatigue properties of the AM pistons together with cast-Al production pistons, confirming that the DuAlumin-3D alloy exceeds the cast alloy on every metric. At RT, the DuAlumin-3D alloy has significantly higher tensile strength of 443 MPa, but also more than twice the ductility compared with a cast-Al piston alloy. The comparative advantages of the DuAlumin-3D alloy are even more pronounced at 300°C. Tensile strength of

the DuAlumin-3D alloy is roughly twice that of the cast-Al piston alloy, with more than a 50% improvement in elongation to failure [4]. On fatigue, the DuAlumin-3D alloy AM piston samples also display a remarkably superior fatigue performance compared to the cast-Al alloy piston samples, as well as AM AISi10Mg materials. The HCF strength at 10^7 cycles of the DuAlumin-3D alloy AM pistons at 300°C is 105 MPa, which is a remarkable 50% improvement over the cast-Al alloy pistons of 70 MPa. The improvement of fatigue properties in low cycle fatigue region at $<100,000$ cycles for the DuAlumin-3D AM pistons is even more pronounced due to the extremely refined AM microstructure, as observed in Figure I.2.1.6. As expected, the fatigue strength of AISi10Mg AM piston samples at 300°C is much lower than that of cast-Al pistons.

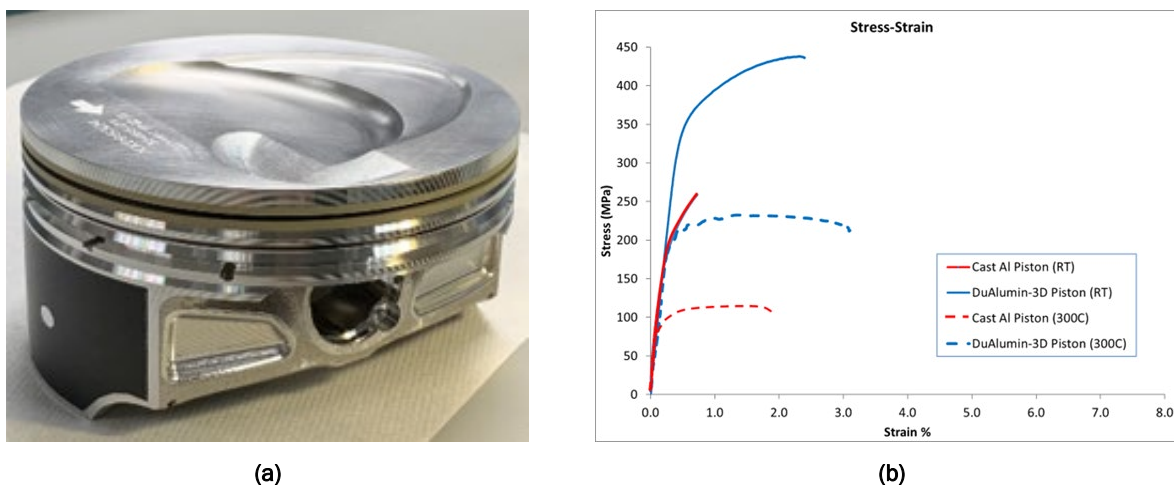


Figure I.2.1.5. (a) AM DuAlumin-3D alloy piston and (b) its tensile properties compared with cast-Al pistons. Source: GM.

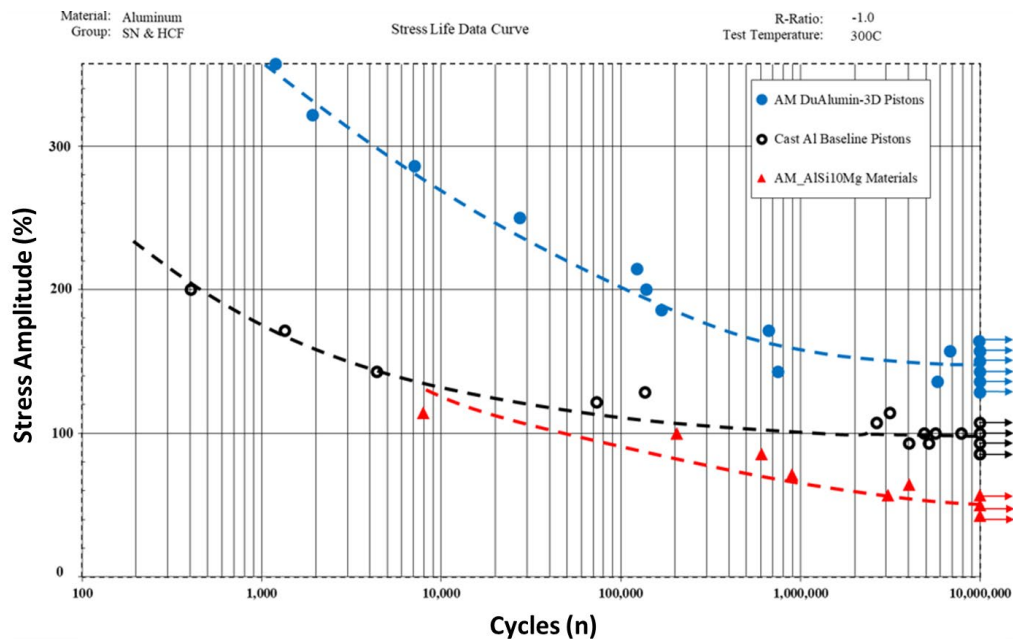
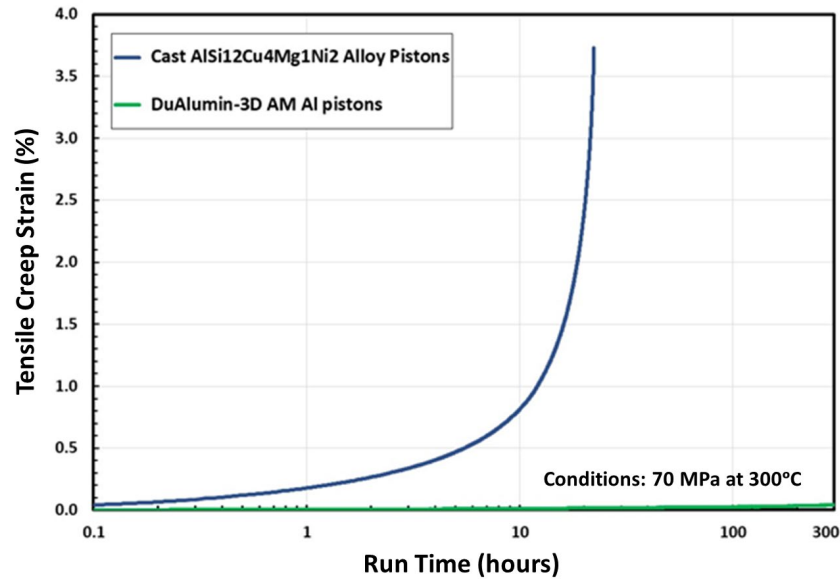


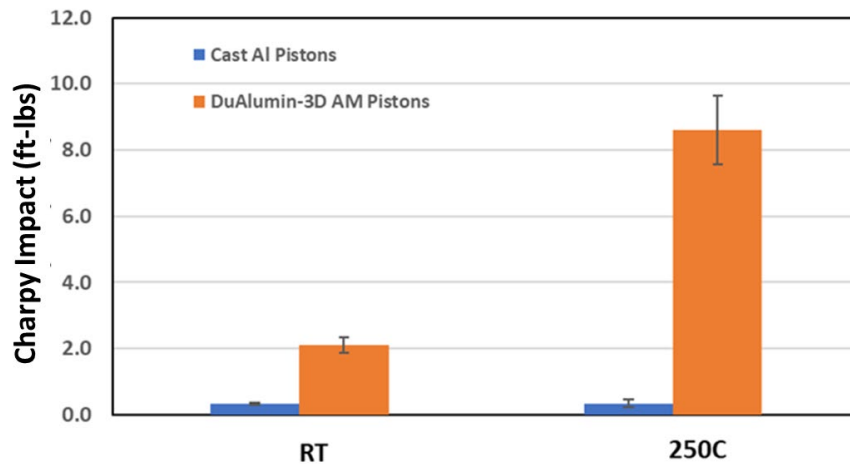
Figure I.2.1.6. Fatigue properties of AM DuAlumin-3D alloy pistons, cast-Al production pistons, and AM AISi10Mg piston sample. Source: GM.

Figure I.2.1.7(a) shows the creep strain as a function of exposure time for both DuAlumin-3D alloy and cast-Al piston alloy tested at 300°C and 70 MPa. At the stress and temperature tested, DuAlumin-3D alloy is

clearly superior to high-performance cast-Al piston alloy, particularly with the increase in exposure time. The cast-Al piston alloy sample ruptured around 20 hours, while DuAlumin-3D had little creep even at 300 hours. Figure I.2.1.7(b) shows the Charpy impact test results of the DuAlumin-3D alloy AM pistons at both RT and 250°C. The Charpy impact energy of the DuAlumin-3D alloy piston samples at 250°C and 8.6 ft-lbs. is more than three times better than their impact energy at RT (2.1 ft-lbs.). In comparison with cast-Al pistons, the DuAlumin-3D AM piston samples are very superior at both RT and 250°C. The Charpy impact energy of the notched cast-Al piston samples is only 0.34 ft-lbs. at both RT and 250°C. The high Charpy impact energy of the DuAlumin-3D AM pistons is mainly attributed to the refined nanoscale solidification eutectic phase particles.



(a)



(b)

Figure I.2.1.7. (a) Creep curves (ϵ - t) of the DuAlumin-3D alloy and the cast-Al piston alloy tested at 300°C and 70 MPa and (b) Comparison of Charpy impact energy of notched specimens between the DuAlumin-3D AM pistons and cast-Al alloy pistons. Source: GM.

High-quality cast-steel cranks with minimum microporosity shown in Figure I.2.1.8(a) were produced using newly designed chills, gating, and riser system. The fatigue properties of cast-steel cranks after short hipping

treatment are better than the forged steel baseline cranks as shown in Figure I.2.1.8(b). The detailed fatigue-property comparison can be found in [5]. High-modulus and high-strength ductile iron cranks have been developed using an innovative low-carbon alloy and two-step inoculation process. Tensile properties of the developed hollow ductile iron crank exceed the tensile property requirement and particularly the modulus of the low-carbon alloy ductile iron crank is increased by >10% because of the refined graphite nodules, increased nodularity, and matrix strength, as shown in Figure I.2.1.8(c). The microstructure of the low-carbon alloy crank is shown in Figure I.2.1.8(d).

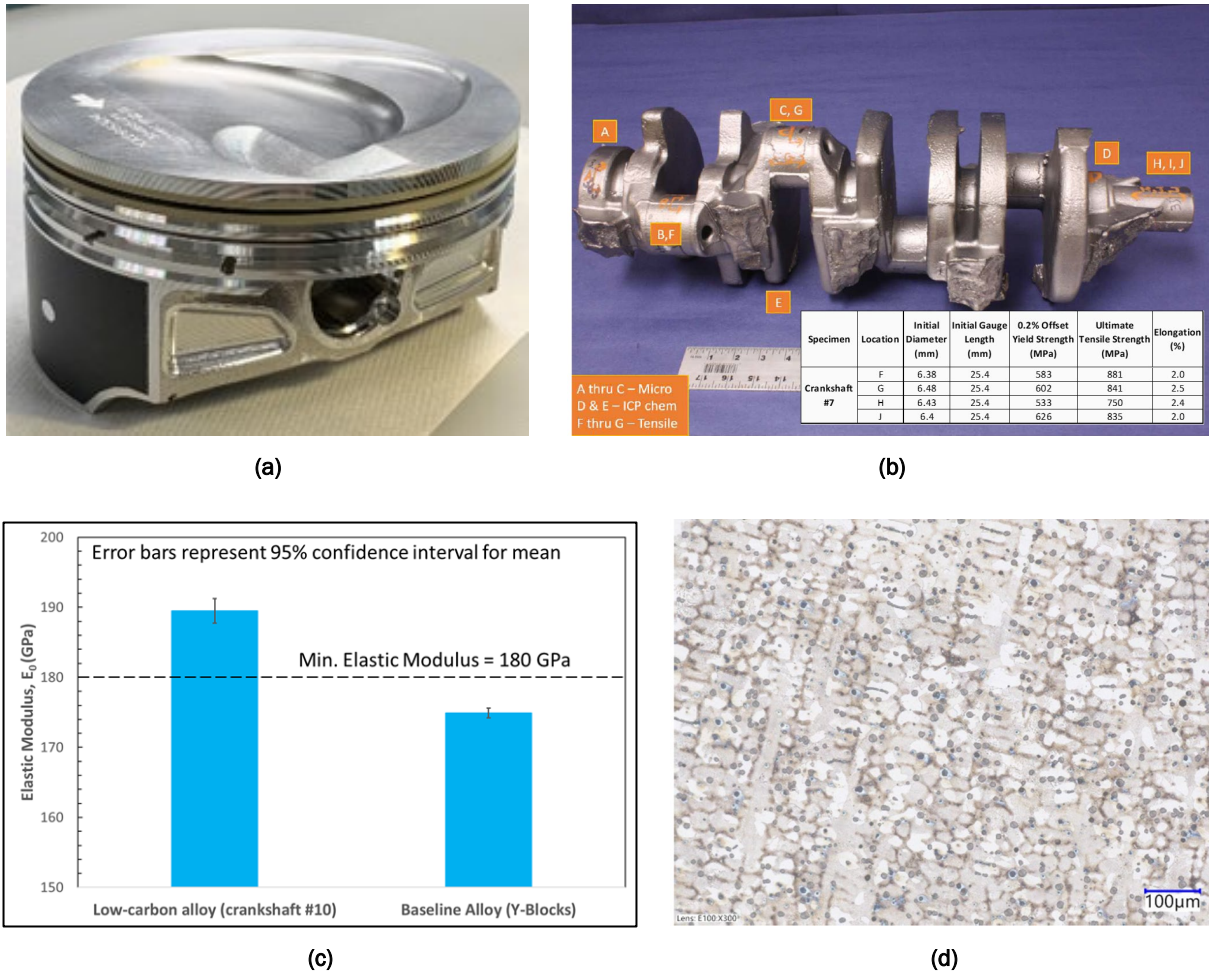


Figure I.2.1.8. (a) In-mold inoculation for ductile iron crank. (b) Nodular iron crank with tensile and micro-sampling locations and tensile properties. (c) Modulus comparison of the developed low-carbon alloy crank with baseline alloy. (d) Microstructure of the low-carbon alloy crank. Source: GM.

High-performance austempered ductile iron (ADI) camshafts have also been developed. Figure I.2.1.9 shows the stress vs. number of cycles fatigue data of the ADI camshafts developed in both Phase 1 and Phase 2. In comparison with the camshafts developed in Phase 1, the Phase 2 camshafts show better fatigue properties, and the high-cycle (10^7 cycles) fatigue strength is increased by 10~15%. Figure I.2.1.10 compares the surface and subsurface residual stresses between the camshafts made in both phases. The camshafts made in Phase 2 show lower subsurface tensile residual stresses in comparison with the Phase 1 camshafts. The combination of the increased fatigue strength and the reduced subsurface tensile residual stresses shall improve the camshaft performance and durability.

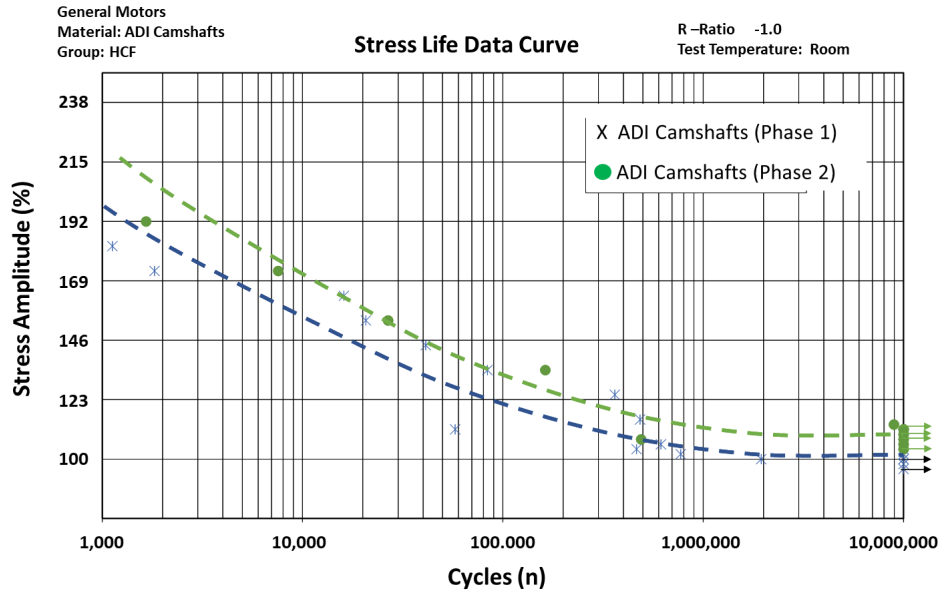


Figure I.2.1.9. Stress vs. number of cycles fatigue data of ADI camshafts. Source: GM.

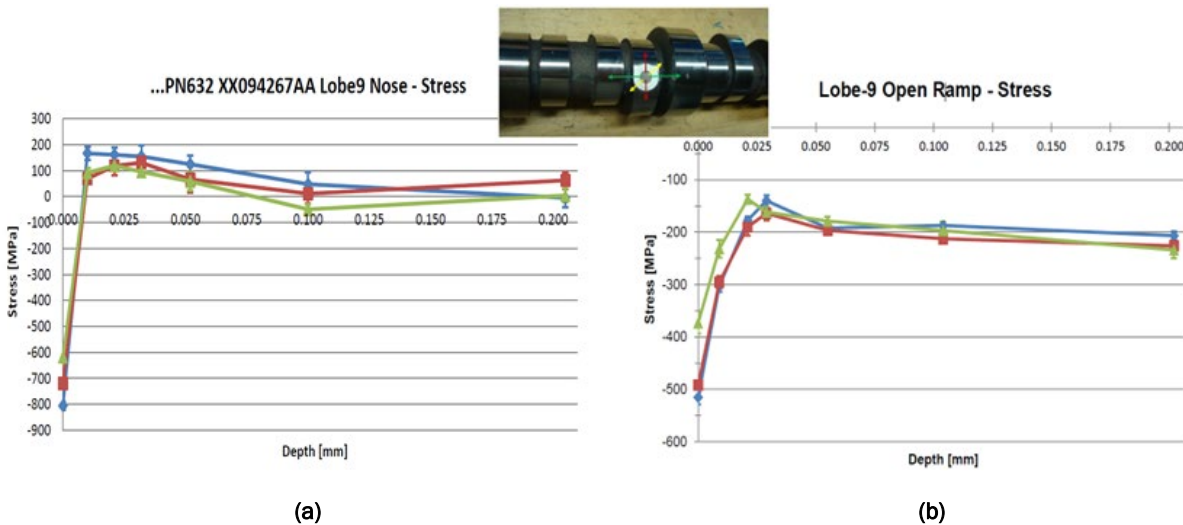


Figure I.2.1.10. Residual stress comparison between Phase 1 and Phase 2 ADI camshafts. Source: GM.

The ICME approach and through-process modeling method has been applied to key engine component development in Phase 2, such as the cast-Al cylinder head and engine block, cast-steel crankshaft, nodular iron crank, ADI camshaft, and cast- and AM Al pistons to ensure their designs and quality to meet performance and durability requirements. Figure I.2.1.11 shows an example of through-process modeling and durability analysis flow for the Phase 2 cast-Al engine block development using the ICME capability at GM. After a comprehensive casting process simulation, the local microstructure, such as secondary dendrite arm spacing (DAS), and the defect population, such as porosity and oxides, can be simulated throughout the entire block casting. Based on the simulated defects and microstructure from the casting process modeling, location-specific material properties (e.g., tensile and fatigue properties) can then be predicted and incorporated into the computer-aided engineering performance and durability analysis of the block casting.

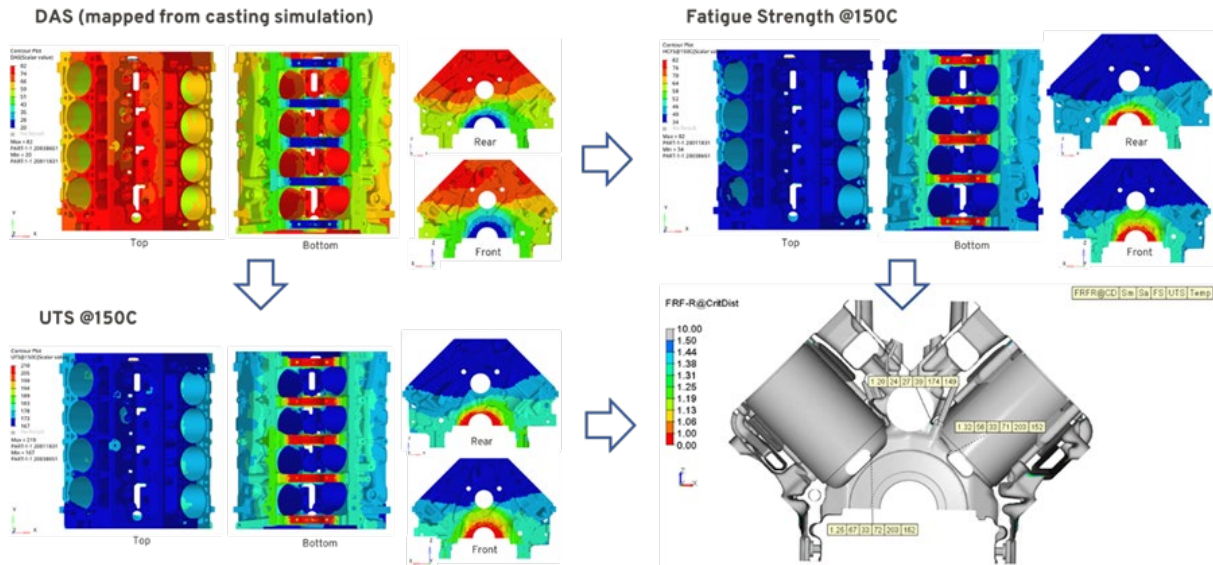


Figure I.2.1.11. An example of through-process modeling and durability analysis flow for Phase 2 cast-Al engine block development. Source: GM.

The current cellular automaton (CA) model used for casting process simulation was improved at OSU to better predict the columnar to equiaxed transition (CET) in conventional casting processes. The model is based on the sharp interface method, which assumes local equilibrium at the solid to liquid interface. The Rappaz random nucleation model was adopted to simulate the random nucleation of grains ahead of the solidifying dendrites. Figure I.2.1.12 shows a good agreement between the experimental and simulated CET microstructure.

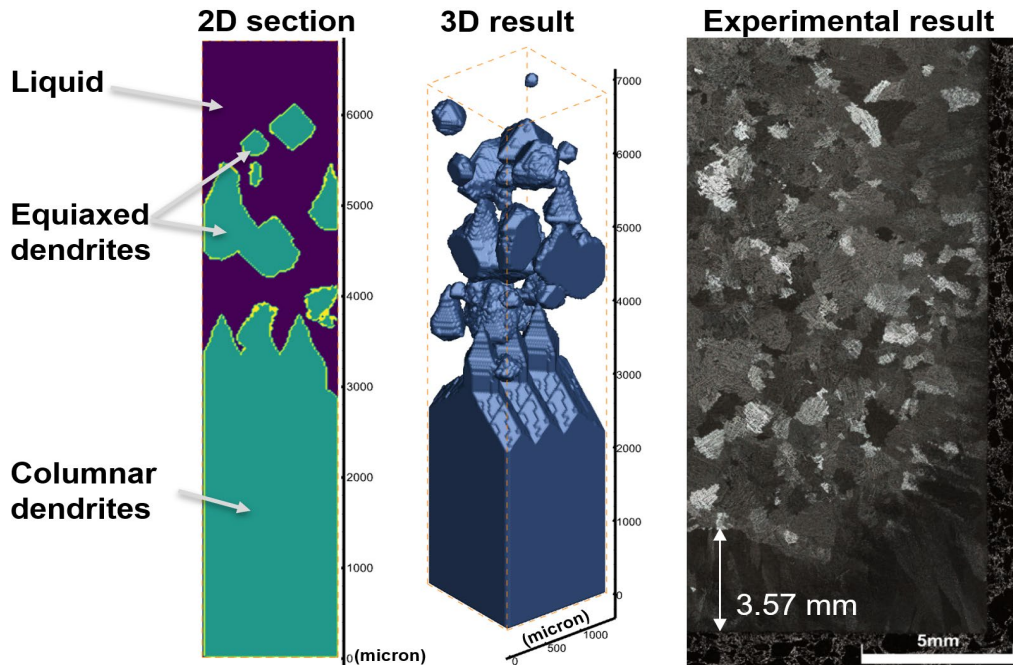


Figure I.2.1.12. CA modeling of CET structure and comparison with experimental microstructure. Source: OSU.

The CA casting model was further updated to incorporate the effect of hydrogen porosity. In the CA model, the diffusion of hydrogen in the domain (e.g., solid, liquid, solid/liquid cells) is calculated to simulate the hydrogen concentration. The nucleation and growth of hydrogen pores is also considered. Figure I.2.1.13 shows a simulation example of a HPDC process. Figure I.2.1.13 provides a look at the phases (top left), hydrogen concentration field (bottom left), 3D grain and pore structure (top right), and 3D pore structure (bottom right). From Figure I.2.1.13, it is possible to see that the hydrogen content in the liquid decreases around the porosity as it is absorbed into the growing pore. The hydrogen porosity model is also coupled with the metal pressure during the solidification process, which impacts the pore shape. The updated casting CA model is suitable for simulating hydrogen porosity in the casting conditions ranging from sand casting to HPDC.

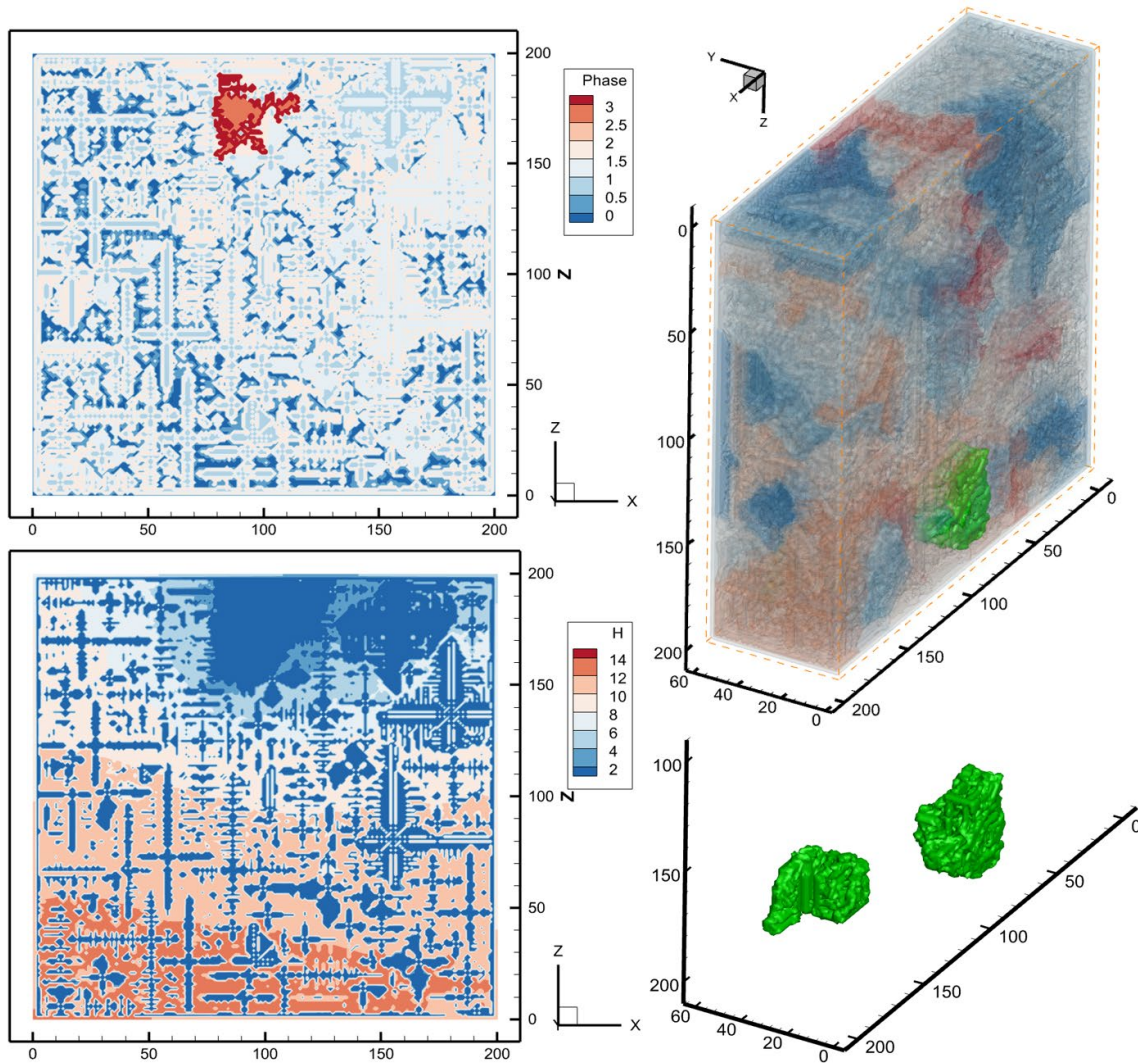


Figure I.2.1.13. Casting CA simulation results for HPDC process showing simulated hydrogen porosity.
Source: OSU.

The AM-CA model has undergone enhancements to include functions related to the prediction of hydrogen pores. The model adheres to Sievert's law, assuming a local equilibrium of hydrogen concentration at the hydrogen pore interface. A boundary flux is computed, and this, in turn, contributes to the net flux of the pore, which is further applied to the growth calculations. The outcomes reveal the presence of hydrogen pores within the melt pool, exhibiting a range of sizes, as seen in Figure I.2.1.14.

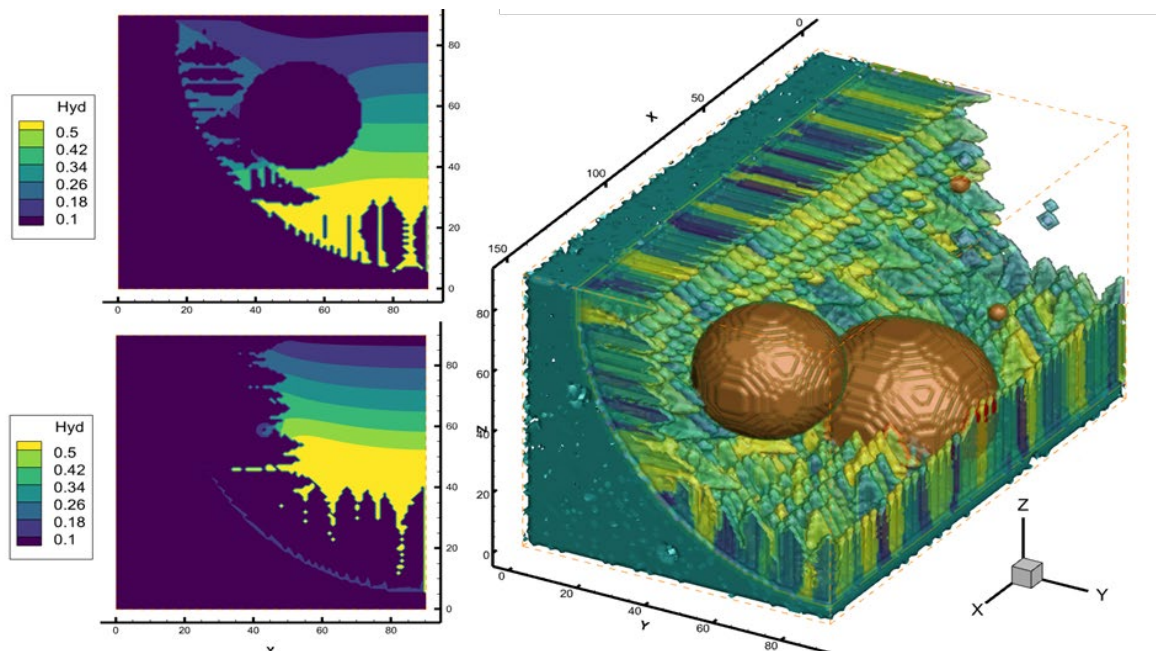


Figure I.2.1.14. The AM-CA model shows a hydrogen concentration map at two YZ planes (large and small pores, left) of the solid 3D model (pores shown in brown color, right). Source: OSU.

Task 3.3 Test Cell Installation and Initial Evaluation of Proposed MD Truck Solution

Performance testing of the Phase 2 fuel economy engine and control system is underway. Figure I.2.1.15 provides the setup in the test cell.

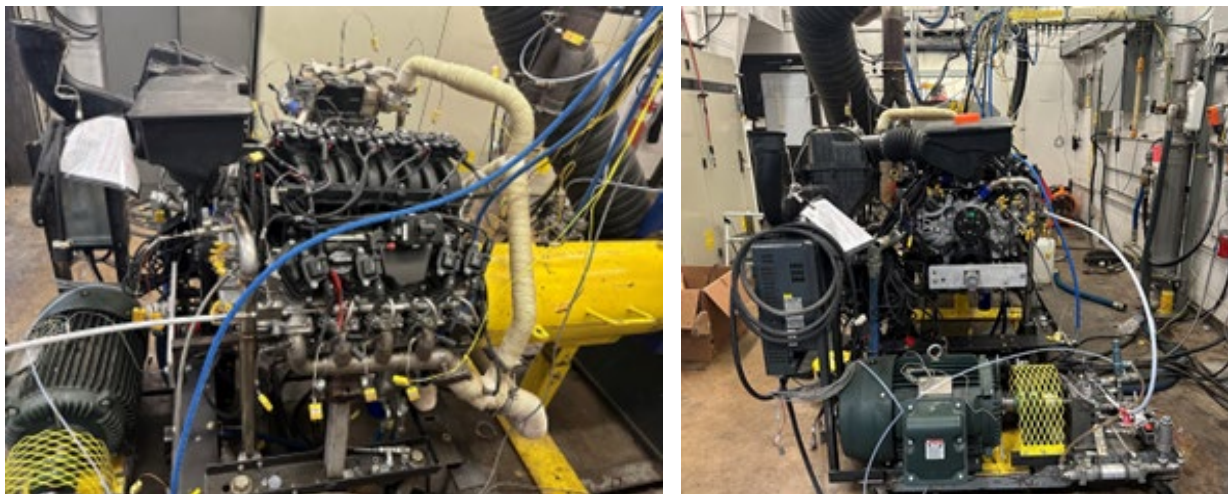


Figure I.2.1.15. Phase 2 fuel economy engine setup in test cell. Source: GM.

Conclusions

The Phase 2 engine has been assembled and is being tested, incorporating the advanced combustion and materials technologies developed in Phase 1. The overall mass of the Phase 2 engine is 200 Kg, 17.7% lighter than the baseline engine, therefore achieving the project mass reduction goal of 15%. Based on the combustion technology development and verification, conducted both computationally and experimentally, GM is confident the developed Phase 2 engine will achieve the FOA objective of 10% fuel economy improvement.

The ICME approach has been used in the project to link materials, manufacturing, and system design into a holistic computational framework to enable the design and manufacturing of key engine parts with location-specific microstructure and material property modeling. The tools have helped achieve robust design and development of the key engine components with the desired mechanical properties.

Key Publications

1. Anderson, S., P. Sanders, Q. Wang, and J. Yang, 2023, “Strategy for developing a castable, high-strength ductile iron alloy with improved stiffness for a lightweight crankshaft application,” *Proceedings of the 7th Keith Mills Symposium on Ductile Iron*, 16–20 October 2023, Atlanta, GA, USA.
2. Michi, R. A., J. J. Simpson, S. Bahl, Q. Campbell, P. Brackman, A. Plotkowski, R. R. Dehoff, J. A. Haynes, Q. Wang, and A. Shyam, 2023, “Additively manufactured AlCeNiMn alloy with improved elevated-temperature fatigue resistance,” *Addit. Manuf.*, 66, 103477. <https://doi.org/10.1016/j.addma.2023.103477>.
3. Wang, Q., A. Wang, R. Ricchi, R. Petrus, D. Wilson, A. Plotkowski, A. Shyam, and A. Haynes, 2023, “Mechanical properties of additively manufactured DuAlumin-3D alloy pistons,” *Proceedings of the PowderMet2023 and AMPM2023*, 18–21 June 2023, Las Vegas, NV, USA.
4. Wang, Q., A. Wang, A. Park, J. Yang, D. Wilson, and D. Gerard, 2023, “Microstructure and mechanical properties of cast-aluminum pistons,” *AFS Transaction*, April 2023.

References

1. DOE-EERE, 2019, “FY 2019 Advanced Vehicle Technologies Research Funding Opportunity Announcement,” FOA Number DE-FOA-0002014, Washington, D.C., USA. Available at: <https://eere-exchange.energy.gov/FileContent.aspx?FileID=25f7a4dd-9874-4aee-9606-2ab52fe9cc18> (accessed 21 December 2023).
2. Pollock, T. M., et al., 2008, *ICME: A Transformational Discipline for Improved Competitiveness and National Security*. National Academies Press, Washington, D.C., USA.
3. Wang, Q. G., P. Jones, Y. Wang, and D. Gerard, 2011, “Advances in computational tools for virtual casting of aluminum components,” *Proceedings of the 1st World Congress on ICME*, Chapter 30, pp. 217-222. <https://doi.org/10.1002/9781118147726.ch30>.
4. Wang, Q., A. Wang, R. Ricchi, R. Petrus, D. Wilson, A. Plotkowski, A. Shyam, and A. Haynes, 2023, “Mechanical properties of additively manufactured DuAlumin-3D alloy pistons,” *Proceedings of the PowderMet2023 and AMPM2023*, 18–21 June 2023, Las Vegas, NV, USA.
5. DOE-EERE, 2022, “2022 Annual Merit Review, VTO, Results Report,” DOE/EE-2662, November 2022. Available at: https://www.energy.gov/sites/default/files/2022-2/2022_VTO_Annual_Merit_Review_Results_Report.pdf (accessed 21 December 2023).

Acknowledgements

The project team would like to thank our DOE project managers and directors, K. Howden (retired), G. Singh, J. Gibbs, S. Khan, R. Nine, and M. Ursic for their great support for the project. The team also like to thank S. Campbell (contract manager at GM), E. Keating (Co-PI, retired), J. Coryell, D. Wilson (retired), D. Gerard (retired), M. Wood, M. Gonzalez Delgado, R. Baker, A. Rodrigues, C. Gough (retired), J. Jocsak, S. Dixon, and J. Lee at GM for their support and advice to the project. Editing of the report by F. Crowson and G. Holt is greatly appreciated.

I.2.2 Lightweight and Highly Efficient Engines Through Al and Si Alloying of Martensitic Materials (Oak Ridge National Laboratory)

Dean Pierce, Co-Principal Investigator

Oak Ridge National Laboratory
Materials Science and Technology Division
1 Bethel Valley Rd.
Oak Ridge, TN 37830
E-mail: piercedt@ornl.gov

J. Allen Haynes, PMCP Consortium Manager

Oak Ridge National Laboratory
Materials Science and Technology Division
1 Bethel Valley Rd.
Oak Ridge, TN 37830
E-mail: haynesa@ornl.gov

Jerry L. Gibbs, DOE Technology Development Manager

U.S. Department of Energy
E-mail: Jerry.Gibbs@ee.doe.gov

Start Date: May 1, 2021

End Date: February 28, 2024

Project Funding: \$300,000

DOE share: \$300,000

Non-DOE share: \$0

Project Introduction

The reliable, rapid, and efficient movement of on-road freight over long distances is essential to the health and well-being of people and economies across the globe. There were over 13 million Class 8 HD trucks from 33,001 to 80,000 lbs. gross vehicle weight that were registered in the U.S. in 2019. These trucks accounted for 11% of the 2.9 trillion U.S. vehicle miles driven in 2020. Long-haul freight vehicles are classified as difficult to electrify due to extreme range, weight, and delivery time demands. Thus, the HD truck sector is extremely challenging to decarbonize. Although battery electric and hydrogen fuel cell technologies are under development and are experiencing limited early deployment in semi-trucks, it is widely agreed that decades of further development, including more robust electric power infrastructure, are necessary to scale BEV HD transportation technologies to affordable, effective market impact within the logistics of the long-haul freight market.

Today, large reciprocating diesel engines are used to power long-haul, HD freight trucks, which collectively use approximately 20% of U.S. transportation petroleum per year. Consequently, there is an increasingly urgent need for advanced HD engines offering improved efficiency and decreased emissions and which also can rapidly transition to the use of lower-carbon fuels, such as natural gas, biofuels, or green hydrogen. The efficiency of reciprocating engines is closely associated with the intensity of combustion, simplistically meaning that higher operating temperatures and pressures can enable increased efficiency. Life cycle emissions also decrease for higher efficiency engines, with proper controls and exhaust treatment, as well as increasing use of lower-carbon fuels. However, the more severe operating conditions of higher efficiency engines, which are designed for more than a million miles of freight operation, place increasing burdens on engine materials. Thus, there is increasing demand for affordable, higher temperature alloys that also offer improved fatigue resistance. A key materials barrier that has limited further engine efficiency improvements has been the <500°C temperature limits of the medium-carbon commercial steels used to manufacture HD piston crowns, namely 4140 martensitic steel and microalloyed steel (MAS) grade 38MnSiVS5.

A key technical challenge for alloy designers in developing affordable steels for temperatures greater than 500°C is the tradeoff between mechanical, thermal, and oxidation properties. Typically, as the HT strength of

an alloy increases, a corresponding decrease in the TC often results. Similarly, improving HT oxidation resistance through alloying additions like chromium (Cr) usually results in a decrease in TC. Thus, as elements are added to strengthen or increase the oxidation resistance of an alloy, the TC will often degrade. These oft observed tradeoffs have made it difficult to design affordable (i.e., low-alloy content), higher strength, higher temperature steels providing effective thermal management to engine components that must be aggressively oil-cooled with pistons. For these pistons, oil sprayed into a cooling gallery extracts heat to keep the piston from overheating and exceeding the material temperature limit.

In this project, started in May 2019, Cummins and ORNL collaborated to develop a cost-effective medium-carbon steel for piston crowns, designated as eXtreme HT Strength (3Cr-XHTS), which offer significant improvement in peak-temperature capability over 4140 or MAS. In 4+ years, the team went from conceptualizing the alloy-design strategy to completing a successful Peak Power Output (PPO) engine test on a 15 L engine of a piston made from the new alloy in FY 2023.

Objectives

The objective of this work was to design a new alloy for piston crowns of advanced HD ICEs for long-haul freight applications. The new alloy must be affordable, machinable, and weldable by solid-state processes, and offer greater strength and oxidation resistance than the current alloys, 4140 martensitic steel, and MAS.

Approach

The approach of this project was to combine the expertise in ICEs and component development at Cummins with the expertise in HT alloy development at ORNL. Computational alloy-design tools and an existing suite of HT materials testing and characterization facilities at ORNL, along with technical input from Cummins, were utilized to design and develop a new piston crown alloy for HD engines in the first two years of the project. Five main criteria were used to develop the alloy: (1) HT strength; (2) oxidation resistance; (3) TC; (4) manufacturability; and (5) affordability, as illustrated in Figure I.2.2.1.

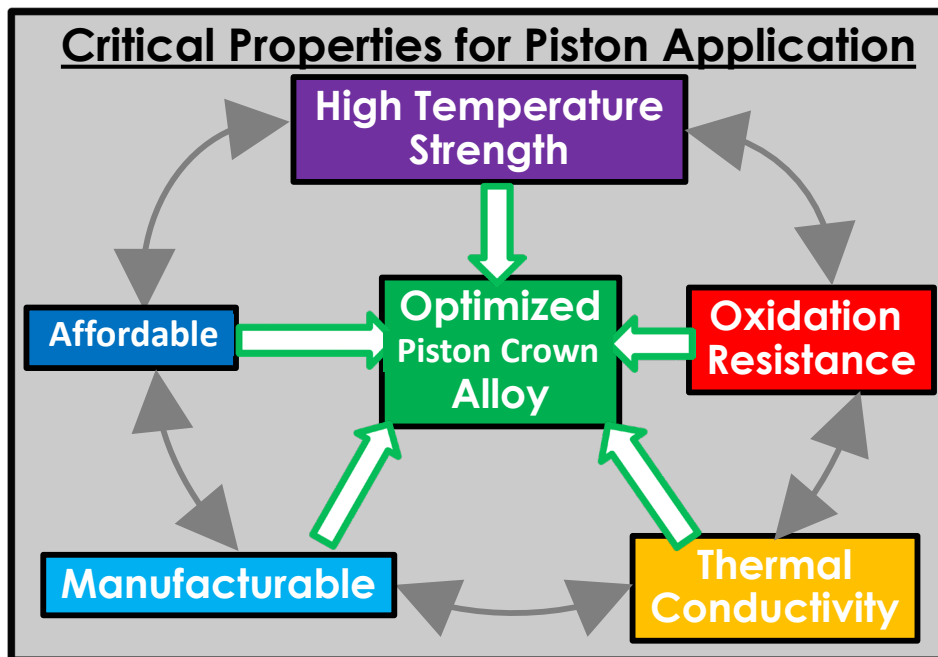


Figure I.2.2.1. Diagram of important criteria for piston crown design for next generation ICEs. Source: ORNL.

At the end of Year 2, an alloy composition with a balance of the aforementioned properties that was superior to 4140 was downselected. In Years 3 and 4, the Cummins and ORNL team worked with outside vendors, including melting and forging shops, heat-treatment facilities, and a piston supplier, to melt and forge a 1600

lb. ingot of the desired composition and subsequently fabricate prototype pistons from the new alloy, then successfully completed a 500 h enhanced severity PPO engine test of the new pistons in FY 2023. The team is currently performing final project tasks associated with characterization of the engine tested pistons and evaluating whether any improvements to the alloy should be considered based on the engine test results.

Results

Prototype pistons were fabricated from a 3Cr-XHTS steel crown and an MAS skirt and are shown in Figure I.2.2.2. The skirt and crown were successfully joined by rotary friction welding. The ring grooves in the 3Cr-XHTS were successfully machined as shown in Figure I.2.2.2(a). Figure I.2.2.2(b) shows a piston with 3Cr-XHTS crown installed in the test cell prior to engine testing. Figure I.2.2.2(c) shows the crown of a 3Cr-XHTS/MAS piston.

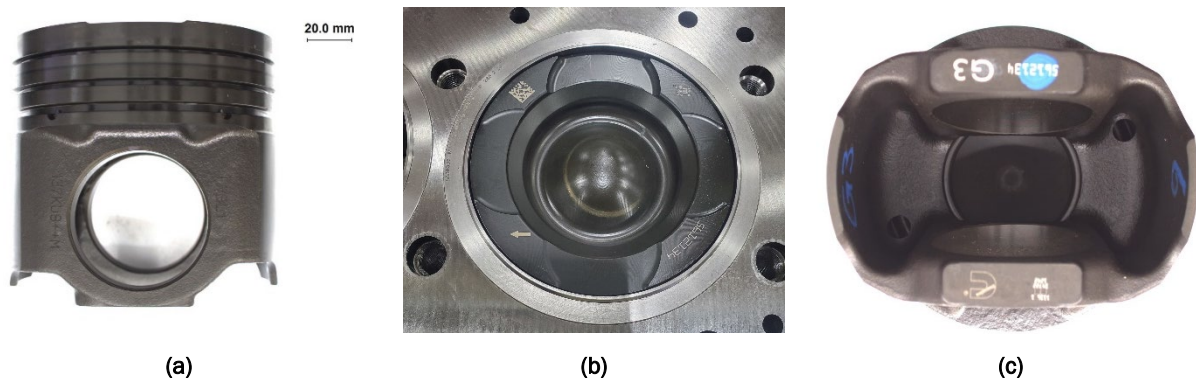
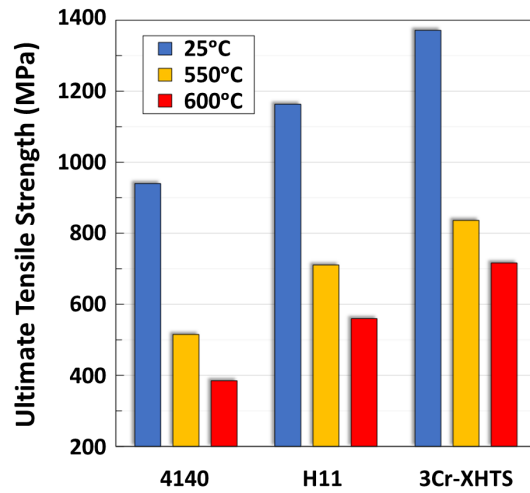
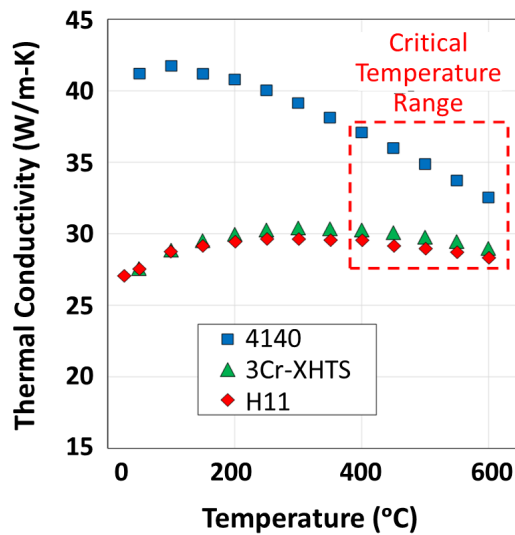


Figure I.2.2.2. Steel pistons for Cummins 15 L HD engine, with the piston crown manufactured from 3Cr-XHTS steel friction welded to a MAS steel skirt. (a) Front of piston showing ring grooves in the 3Cr-XHTS crown and the pin bore in the skirt. (b) Crown of a 3Cr-XHTS/MAS piston visible in cylinder during engine assembly. (c) Bottom of 3Cr-XHTS/MAS piston showing cooling gallery holes. Source: ORNL.

3Cr-XHTS offers significantly improved tensile and yield strengths over the full range of operating temperatures, while also maintaining suitable ductility. Figure I.2.2.3(a) compares the UTS of 3Cr-XHTS steel to 4140 and H11 at 25°C, 550°C, and 600°C. The 4140, 3Cr-XHTS, and H11 were exposed to similar final tempering temperatures of 620°C, 650°C, and 650°C for an appropriate evaluation of their respective strengths. Remarkably, the UTS of the 3Cr-XHTS steel is 86% and 28% greater than 4140 and H11 at 600°C, respectively. The significant improvement in strength over H11 is particularly noteworthy, given that H11 has greater alloying content and is more expensive. Figure I.2.2.3(b) compares the TC of 3Cr-XHTS to 4140 and H11. The TC of 3Cr-XHTS is slightly greater than that of H11. The combination of substantially higher elevated-temperature strength and modestly higher TC of 3Cr-XHTS, relative to H11, illustrates the improvement of two critical materials properties, which are often in competition with one another, as described previously. While the 3Cr-XHTS TC is slightly lower than 4140 in the critical temperature range 400–600°C, as observed by the red dashed box in Figure I.2.2.3(b), the TC of 3Cr-XHTS is more than sufficient to allow effective piston oil cooling for HD engines, particularly considering the high-strength of 3Cr-XHTS can enable thinner piston walls to enhance heat flow.



(a)



(b)

Figure I.2.2.3. Comparisons of 3Cr-XHTS medium-carbon steel, 4140 medium-carbon steel, and H11 tool steel for (a) tensile properties at 25, 550, and 600 °C, and (b) TC from 25–600 °C. Source: ORNL.

This improvement in strength, as well as microstructural stability at higher temperatures, was accomplished by a unique alloying strategy and novel heat-treatment that work synergistically to generate a fine martensitic microstructure with exceptionally HT strength. The microstructure, after quenching and tempering, is shown in the dark-field STEM micrograph in Figure I.2.2.4 and a higher magnification energy-dispersive spectroscopy map for vanadium (V) in the inset. These ultra-fine, intra-lath carbides, which are stable to at least 600°C, result from a unique alloying strategy that relies on synergistically optimizing the amounts of carbon and other carbide forming elements. Finally, a unique heat-treatment tailored to the alloy's chemistry, followed by rapid cooling, was developed to unlock the full strengthening potential of the alloy and enable precipitation of the fine carbide structure.

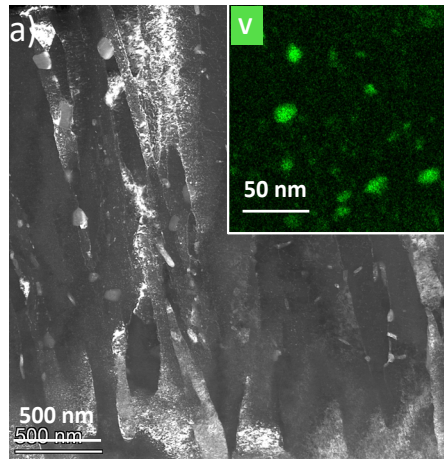
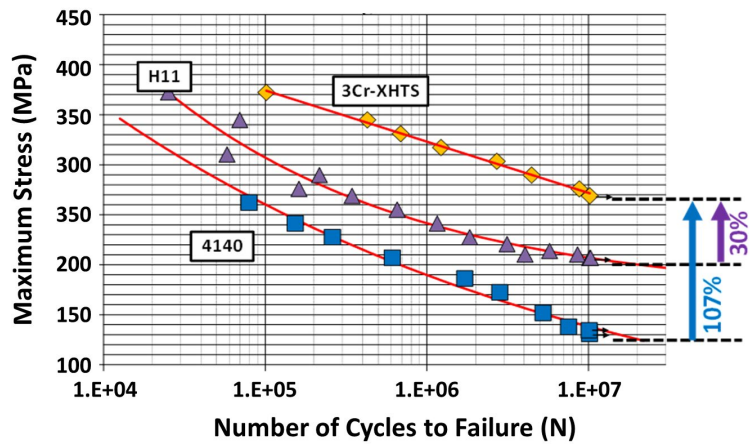


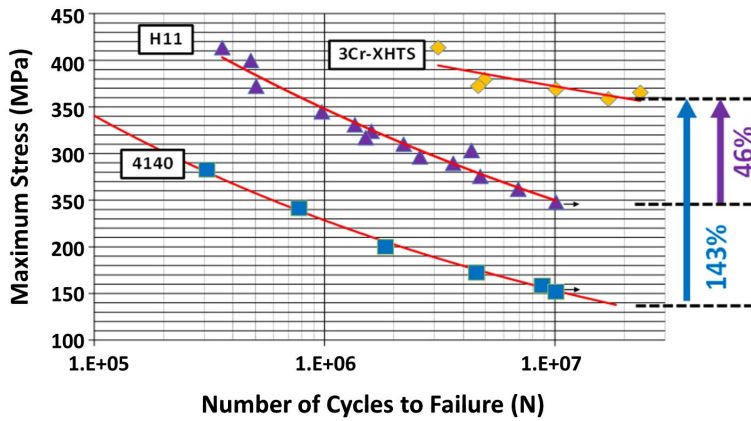
Figure I.2.2.4. Dark-field STEM images of the microstructure of 3Cr-XHTS steel with EDS elemental map of V inset. Source: ORNL.

The metallurgical design and thermal processing strategy of 3Cr-XHTS results not only in exceptional elevated-temperature tensile properties and microstructural stability to 600°C, but also best-in-class HT fatigue resistance. Rotating beam fatigue (RBF) testing concluded that 3Cr-XHTS at laboratory-scale heat exhibited a 40% increase in fatigue limit at 600°C in the as-tempered condition compared to commercial vacuum arc remelted (VAR) H11 tool steel, as shown in Figure I.2.2.5(a). The VAR process greatly reduces impurity elements like sulfur (S) and phosphorus (P) to improve fatigue properties, making the 40% enhancement of fatigue strength of 3Cr-XHTS over the H11 steel even more remarkable. The 147% increase in fatigue strength for 3Cr-XHTS over 4140, as indicated in Figure I.2.2.5(a) is also notable. Further, the 3Cr-XHTS steel maintains its remarkable fatigue advantages over H11 and 4140 even after all materials were exposed to a long-term thermal soak at 600°C for 500 h prior to fatigue testing. Figure I.2.2.5(b) shows the RBF data from an industrial heat of 3Cr-XHTS and the same commercial 4140 and VAR H11 at 600°C after thermal soaking. The industrial produced 3Cr-XHTS alloy still exhibits a 30% increase in fatigue strength over the VAR H11 steel, despite the intentional addition of 0.025 wt.% S and 0.02 wt.% P to the 3Cr-XHTS steel to further enhance machinability for the piston application. For comparison, the H11 VAR steel contains an order of magnitude lower values of S (0.003 wt.%) and P (0.004 wt.%). This comparison confirms the higher temperature thermal stability of the previously described strengthening mechanisms in the 3Cr-XHTS alloy.

3Cr-XHTS is designed to provide a level of oxidation resistance at 575°C that is equivalent to or better than that of 4140 piston steels at 500°C, which is the oxidation limit of 4140, in combustion environments that include water vapor. Figure I.2.2.6 shows the mass gain due to oxidation during cyclic oxidation testing in air plus 10% water vapor to simulate combustion conditions for the 3Cr-XHTS steel at 600°C compared to 4140 at 600°C. Mass gain due to oxidation is an important criterion for determining the oxidation resistance of an alloy at a specific temperature. The 3Cr-XHTS alloy exhibits a 38% reduction in oxidation mass gain at 600°C relative to 4140 after 1,000 h of cyclic oxidation testing. The oxidation mass gain of 3Cr-XHTS at 600°C is only slightly greater than that of 4140 at 500°C, which is not shown in figure for clarity, suggesting the oxidation limiting temperature of 3Cr-XHTS is likely near 575°C—at least a 75°C increase over 4140.



(a)



(b)

Figure I.2.2.5. RBF comparison at 600°C of 3Cr-XHTS medium-carbon steel, 4140 medium-carbon steel, and H11 tool steel: (a) quench and tempered condition, and (b) after 500 h thermal soak at 600°C. Source: ORNL.

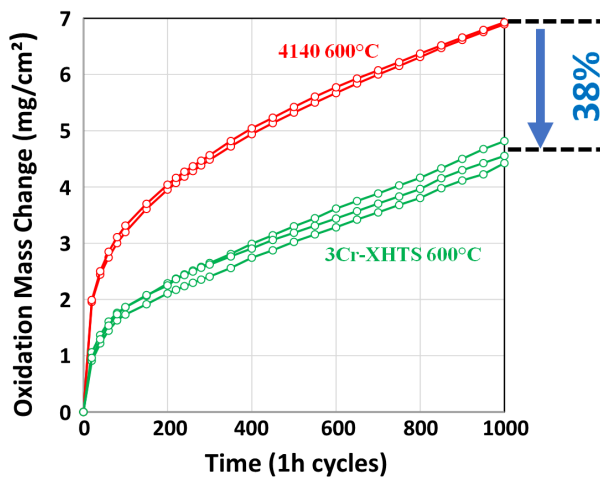


Figure I.2.2.6. Oxidation mass change during cyclic oxidation testing (1 h cycles) in air plus 10% water vapor for 3Cr-XHTS and 4140 at 600°C. The 3Cr-XHTS steel exhibits approximately 38% less oxidation mass gain at 600°C compared to 4140 after 1000 cycles. Source: ORNL.

Conclusions

ORNL and Cummins, Inc., have developed and rigorously tested the new 3Cr-XHTS steel, a higher temperature medium-carbon steel with an unprecedented combination of mechanical and thermal performance advantages for this class of steel operating at $>500^{\circ}\text{C}$. The alloy's martensitic structure is designed to form nanoscale, intra-lath strengthening carbides, providing superior and stable mechanical properties to $>600^{\circ}\text{C}$. The alloying strategy provides good oxidation resistance to 575°C while still maintaining necessary thermal properties for severe environments. The alloy offers best-in-class HT fatigue performance at temperatures up to 600°C . 3Cr-XHTS steel has been demonstrated successfully in a 500 h PPO engine test. The alloy can also be tempered to intermediate strengths, while maintaining other key properties, creating opportunities for durable pistons for green hydrogen fuels. The powerful combination of superior higher temperature mechanical performance, thermal properties, and environmental resistance of 3Cr-XHTS steel offers new opportunities for affordable, impactful product design and advancement across a range of industries, including freight, tooling, automotive, industrial, energy, and defense. A joint international patent application has been filed by Cummins and ORNL.

Key Publications

1. International Joint Patent Application from Cummins Inc., International Publication Number WO 2022/265639 A1: "Steel Alloy and Method of Manufacture Exhibiting Enhanced Combination of HT Strength, Oxidation Resistance, and Thermal Conductivity," Cummins Inc., UT-Battelle, LLC, Yong-Ching Chen, Quancang Ma, Howard S. Savage, Dean T. Pierce, Govindarajan Muralidharan, James Allen Haynes, International Publication Date: December 22, 2022.

Acknowledgements

The authors acknowledge the following who were instrumental in support of this project: G. Muralidharan and J. A. Haynes for technical guidance; K. Unocic for STEM; J. Poplawsky for APT; K. Hanson, R. Dalton, and C. Taylor for melting and heat-treating of alloys; K. Epps for mechanical testing; G. Garner for oxidation testing; T. Lowe for microscopy; and S. Curlin for thermal properties measurement.

II Lightweight Materials

II.1 Lightweight Metals Core Program

II.1.1 Thrust 1. Selective Processing of Al Sheet Materials (Tasks 1A, 1B, and 1C) (Pacific Northwest National Laboratory and Oak Ridge National Laboratory)

Darrell Herling, Principal Investigator

Pacific Northwest National Laboratory
Energy Processes and Materials Division
900 Battelle Blvd.
Richland, WA 99354
E-mail: darrell.herling@pnnl.gov

Scott Whalen, Co-Principal Investigator (Project 1A)

Pacific Northwest National Laboratory
Energy Processes and Materials Division
900 Battelle Blvd.
Richland, WA 99354
E-mail: scott.whalen@pnnl.gov

Alex Plotkowski, Co-Principal Investigator (Project 1B)

Oak Ridge National Laboratory
Materials Science and Technology Division
1 Bethel Valley Rd.
Oak Ridge, TN 37830
E-mail: plotkowskij@ornl.gov

Mert Efe, Co-Principal Investigator (Project 1C1, Thrust 1 Lead)

Pacific Northwest National Laboratory
Energy Processes and Materials Division
900 Battelle Blvd.
Richland, WA 99354
E-mail: mert.ef@pnnl.gov

Govindarajan Muralidharan, Co-Principal Investigator (Project 1C2)

Oak Ridge National Laboratory
Materials Science and Technology Division
1 Bethel Valley Rd.
Oak Ridge, TN 37830
E-mail: muralidhargn@ornl.gov

Chris Schooler, DOE Technology Development Manager

U.S. Department of Energy
E-mail: Christopher.Schooler@ee.doe.gov

Start Date: October 1, 2020
Project Funding: \$1,300,000

End Date: September 30, 2023
DOE share: \$1,300,000

Non-DOE share: \$0

Project Introduction

The Lightweight Metals Core Program (LMCP), led by PNNL, is an integrated effort between PNNL, ORNL, and ANL. The overall program aims to develop and demonstrate scalable, cost-effective processing methods to

locally enhance the properties of Al- and Mg-alloys to enable broader implementation of lightweight alloys in vehicles. Focused collaborative research thrusts have been established to develop local property modification strategies for each targeted metal system: (1) high-strength Al sheet and tube (Thrust 1); (2) Al castings (Thrust 2); and (3) Mg castings (Thrust 3). Figure II.1.1.1 provides a brief description of these thrusts and how the principal manufacturing methodologies interact with each other and the support thrusts on characterization and modeling, as well as the transition to higher TRLs.

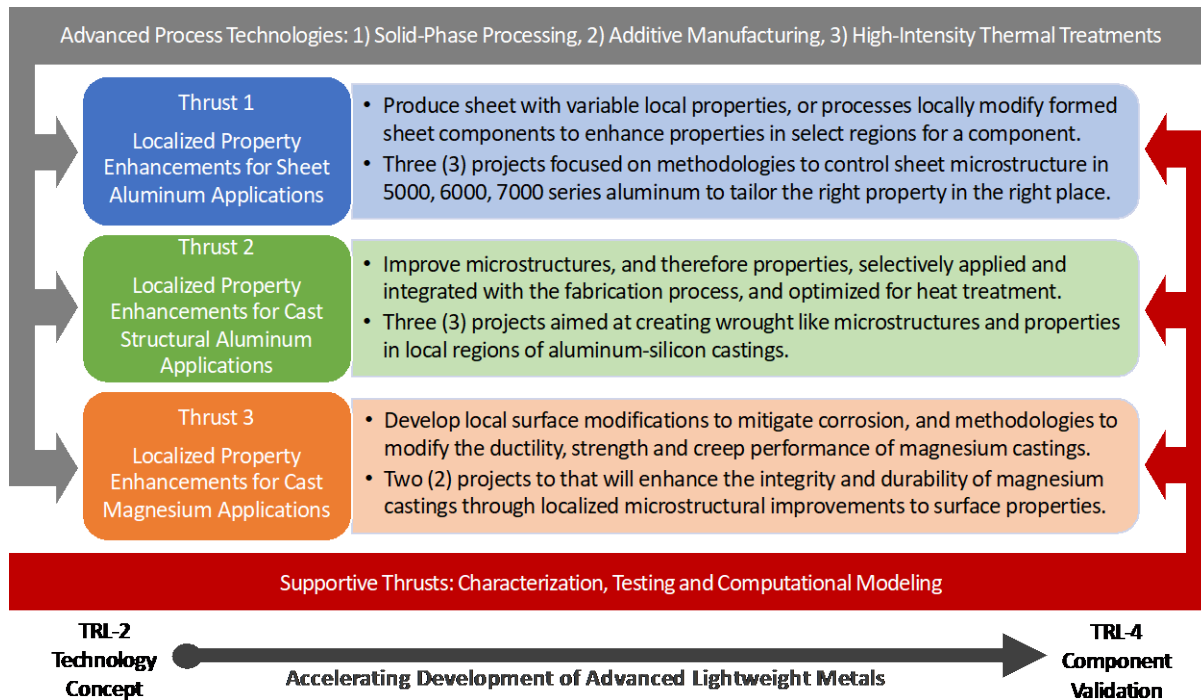


Figure II.1.1.1. Thrust and project structure of the LMCP. Source: PNNL.

The technical goal of the program is to demonstrate that components and assemblies composed of commercially available alloys can be selectively modified to exhibit locally enhanced properties and deliver high materials performance in the most needed locations. This approach allows for significant improvements in manufacturability, structural efficiency, and weight-savings in next generation vehicles. Furthermore, the approach enables the right properties in the right locations and provides the opportunity to decrease the number of metal alloys required for new vehicle manufacture, reducing the challenges that automakers face today in managing supply chains, assuring sufficient materials sustainability, and efficiently recycling scrap metal.

The following report describes the FY 2023 technical efforts and results of Thrust 1, “Localized Property Enhancements for Sheet Aluminum Applications.” Wrought Al that is stamped or formed into components represent a material category making up the largest percentage of the glider in most designs. High-strength Al sheets and extrusions offer the opportunity to significantly reduce the weight of the glider through down-gauging and steel structure replacement. However, multiple science and engineering challenges prevent more widespread high-strength Al use. These challenges include the natural tradeoffs between high-strength, ductility, stiffness, joining, and durability. High-strength Al can suffer from low ductility, which leads to poor RT formability, joinability, and energy absorption during crash deformation. Aligning with the overarching LMCP consortium goal, Thrust 1 seeks to address these challenges by developing cost-effective and scalable methodologies to locally modify Al sheets and extrusions so the right property is in the right place.

Objectives

The main objective of Thrust 1 is to solve challenges associated with high-strength Al by local improvements in the properties and/or geometry. Thrust 1 has three projects, as shown in Figure II.1.1.2. Project 1A (PNNL)

aims to demonstrate the potential of using PNNL’s shear-assisted processing and extrusion (ShAPE™) technology [1] for producing automotive components with locally modified properties and thickness variations along the length. Components are envisioned to be in the form of tubular extrusions. Project 1B (ORNL) aims to improve the understanding of additively manufactured Al features on wrought Al alloys and to demonstrate that local properties and functionality of Al sheet can be enhanced using the form-and-print process. Projects 1C1 (PNNL) and 1C2 (ORNL) have the common goal of improving local formability in the processed regions of age- or work-hardened Al sheet. Targeted applications for all the projects include such energy transfer structures as the A-B-C pillars or cross-body structures, and inner and outer closure panels and their reinforcement members.

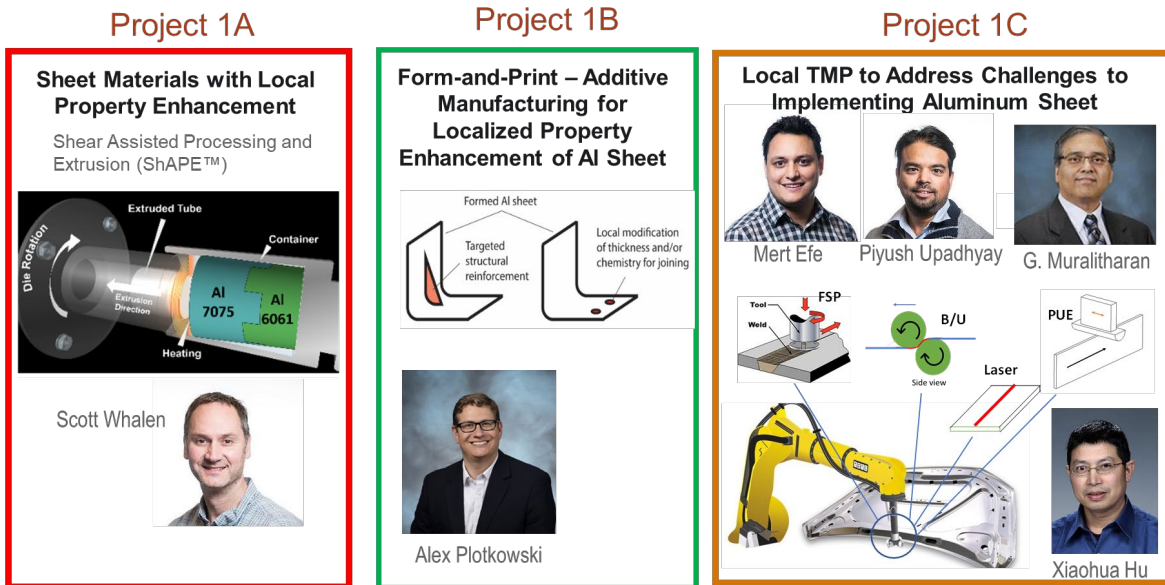


Figure II.1.1.2. Thrust 1 and project structure of the LMCP. Source: PNNL.

Approach

Project 1A: Sheet Materials with Local Property Enhancements

This project includes development of the ShAPE™ technology and associated post-processing techniques for fabricating Al components with material properties that vary along the component’s length. Figure II.1.1.3 shows the primary tasks that were pursued in FY 2023 and are described in detail below. Feedstock materials investigated include AA6082 for variable wall thickness and AA6111 for locally modified strength and toughness. These materials were identified during conversations with Tier 1 and original equipment manufacturer (OEM) companies. General advantages of ShAPE™ over conventional extrusion include *in-situ* homogenization of as-cast billets, extreme microstructural refinement, variable hardening response to heat-treatment, and ability to tune thermomechanical conditions (such as temperature and strain) at specific locations during the extrusion process.

Task 1. Variable Wall Thickness.

Develop tooling, fixtures, and process parameters to demonstrate variable wall thickness extrusion, as shown in Figure II.1.1.3(a).

Task 2. Locally Modified Properties.

Control thermomechanical conditions during extrusion to create regions with a different precipitation-hardening response, as shown in Figure II.1.1.3(b).

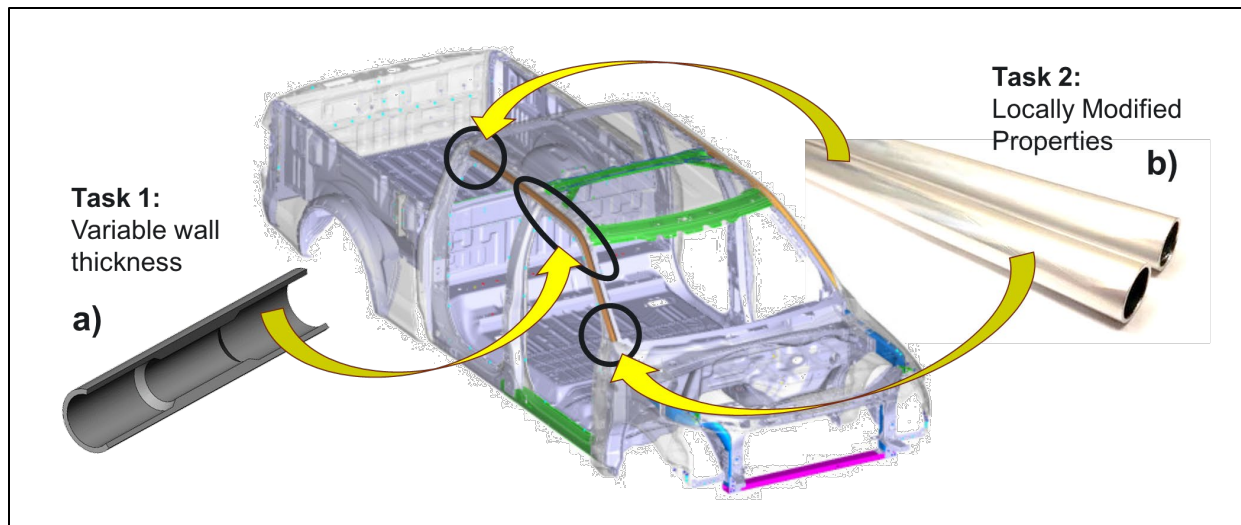


Figure II.1.1.3. (a) Variable wall thickness (Task 1). (b) Locally modified properties (Task 2). Source: PNNL.

Project 1B: Form-and-Print – AM for Localized Property Enhancement for Al Sheet

The form-and-print process aims to combine the high-throughput approach of sheet forming with the ability of AM to locally deposit material with a high-degree of geometric freedom and potential microstructural and properties advantages. In FY 2023, the task focused on the demonstration of sheet modification for a variety of applications relevant to the automotive industry, with a specific goal of modification without deforming or marring the opposite face of the modified sheet. A wire-based directed-energy-deposited system, the Mazak VTC-800G, was used for material deposition, as well as for subtractive machining using the system’s multi-axis milling head. Based on the analysis of processability and characterization of material properties from previous years of the task, the commercially available wire-feedstock alloys used for deposition were AA4043, AA4047, and AA5356. The compositions of these alloys are shown in Table II.1.1.1.

Table II.1.1.1. Composition of the Alloys Used, As-specified by the Manufacturer

Alloy	Al	Si	Mg	Fe	Cu	Cr	Mn	Zn	Ti
AA4043	Remainder	4.5–6.0	0.05	0.8	0.3	-	0.05	0.1	0.2
AA4047	Remainder	11–13	0.1	0.8	0.3	-	0.15	0.2	-
AA5356	Remainder	0.25	4.5–5.5	0.4	0.1	0.05–0.2	0.05–0.2	0.1	0.06–0.2

All compositions are in wt.%. Single values indicate maximums.

Based on discussions with an automotive manufacturer, three subtasks were selected to demonstrate the local modification of an Al sheet. First, the form-and-print process was used to deposit and machine material to close and stiffen hemmed sheets of a 6xxx-series alloy. Hem-closure can improve the acoustic properties of the panel to reduce road noise [2]. Second, AA6111 sheets were bonded in a lap-joint configuration, with the intent of joining the sheets without affecting the surface finish of the outer sheet face. Last, a dissimilar lap-joint between AA6111 sheet and stainless-steel (SS) 304 was made with a similar goal of not affecting the surface finish of the outer sheet face. This was done with the intent of easing the joining challenges between such dissimilar materials as Al sheet and structural-steel members. Characterization of each demonstration was performed to understand how the substrates were affected by the deposited material.

Project 1C: Local Thermomechanical Processing (TMP) to Address Challenges to Implementing Al Sheet

This joint project aims to develop new thermomechanical processing methods for improving the local formability of commercial Al sheets relevant to body-in-white and closure applications. The approach is to start with an age- or work-hardened sheet and improve its formability only where needed, without losing high-strength elsewhere. In FY 2023, research work focused on AA6111-T4 and T6, AA6451-T4 and T6, and AA7075-T6 alloys. The 6xxx series were selected for their use in closure panels and support members whereas 7xxx series were selected for their potential application in structural frame members. The AA6111-T4 and T6, AA6451-T4 sheets were provided as courtesy of OEMs and their suppliers. The AA6451-T4 sheets were heat-treated to T6 temper at PNNL. The AA7075-T6 sheets were purchased through commercial vendors.

PNNL investigated two methods for the local formability improvements. The first method is FSP. The intense plastic deformation and heating during FSP results in dynamically recrystallization and refined grains that results in local softening at certain processing parameters [3]. FY 2023 efforts focused on high-speed robotic FSP at process speeds > 2.5 m/min.

The second PNNL method is roller bending/unbending (B/U) process. This process employs rollers that clamp to a sheet and travel along its length to bend and unbend the sheet without changing its final shape and thickness locally and continuously. Spacing between the rolls can be adjusted to accommodate different sheet thicknesses and to vary the amount of deformation during bending. A compact apparatus was developed for this method, which can be integrated into a robot as an end-effector. In FY 2023, a four-roller design was assembled and tested to produce sheets flatter and straighter than did the three-roller design developed in FY 2022. A 5-kW-capacity commercial induction-heating (IH) system was integrated into the four-roller design to enable simultaneous heating during B/U.

ORNL investigated two approaches: local heat-treatment to induce softening via laser heating, and localized modifications using power ultrasonic edge (PUE) processing. The purpose of laser heating is to heat regions of interest to a temperature that would coarsen or dissolve strengthening precipitates, thereby reducing local strength, increasing ductility, and improving formability in the treated zones to better enable bending or shearing operations of high-strength sheet alloys within those treated zones. Heat-transfer models were developed to predict the temperature profile of the laser heating of AA7075-T6 and AA6061-T6 sheets. Experimentally measured temperature profiles were used to calibrate the thermal models of laser processing.

Power ultrasonic actuators, when pressed on a metallic material, can induce acoustic plastic softening, reduce the contact-friction coefficient, and promote phase transformation and recrystallization. Recent research at ORNL on ultrasonic-assisted indentation and self-piercing riveting has demonstrated up to 50% localized softening. The current work aims to increase the edge quality of trimmed Al sheet alloys by burr smoothing and damage elimination of edge surface and subsurface through pretreatment with a power ultrasonic actuated hemispherical probe. The edge formability will also be significantly improved by this edge quality enhancement. It has been suggested by the previous high-fidelity simulations by Hu et al. [4] that the edge formability can also be improved by removing plastic strains introduced during local heating of the deformed area. In this work, laboratory-scale shearing of AA6111-T6 sheets was performed, and ultrasonic edge modification was conducted on the edges of the sheared samples using different processing conditions (e.g., variations in ultrasonic power).

Testing efforts were coordinated between PNNL and ORNL to measure and benchmark the performance of the processed sheets. This year's testing efforts focused on sharp-radius bend testing according to the Verband der Automobilindustrie (VDA)-238-100 standard [5] and edge stretchability testing [4]. These were done in consultation with a collaborating automotive OEM that use VDA data to assess material formability. For the VDA tests, 25-mm-wide samples were sheared from as-received and processed sheets, with the processed region at the center of the samples. The samples were bent with a fixed radius (either 0.2 mm or 0.4 mm, depending on the sheet thickness) and a knife-edge-type punch until the load during testing dropped by 70% of

the maximum load. Displacement at this 70% load-drop and bend angles after testing are reported. For edge stretchability tests, the as-received and processed AA6111 sheets were sheared with a pneumatic shear at controlled clearances of 5, 10, 20, 30, and 40% sheet thickness. Shearing was along the processed zone of the sheets. Clearance values were checked and confirmed by microscopy on the sheared cross-section of the sheets. Half-dog-bone-shaped tensile test samples were then waterjet cut from the sheared sheets. Edge stretchability was measured by pulling the tensile test samples until failure and reporting the tensile elongation at rupture values. Higher elongation values indicate higher stretchability of the sheared edge under tension. At least three sample were tested for each processing condition and clearance to get repeatable results.

Results

Project 1A: Sheet Materials with Local Property Enhancements

Task 1 Progress: Variable Wall Thickness.

Building upon the variable wall thickness capability developed in FY 2023 for 12-mm outer diameter (OD) extrusions, the tooling and fixtures were modified to extrude 20-mm diameter tubing. To control wall thickness during ShAPE™ extrusion, the position of a tapered mandrel must be precisely controlled within the die throat as the rotating die plunges into the billet, as shown in Figure II.1.1.4. A thin wall is created by positioning the larger diameter region of the mandrel within the die throat, while a thick wall is created by positioning the smaller region of the mandrel within the die throat.

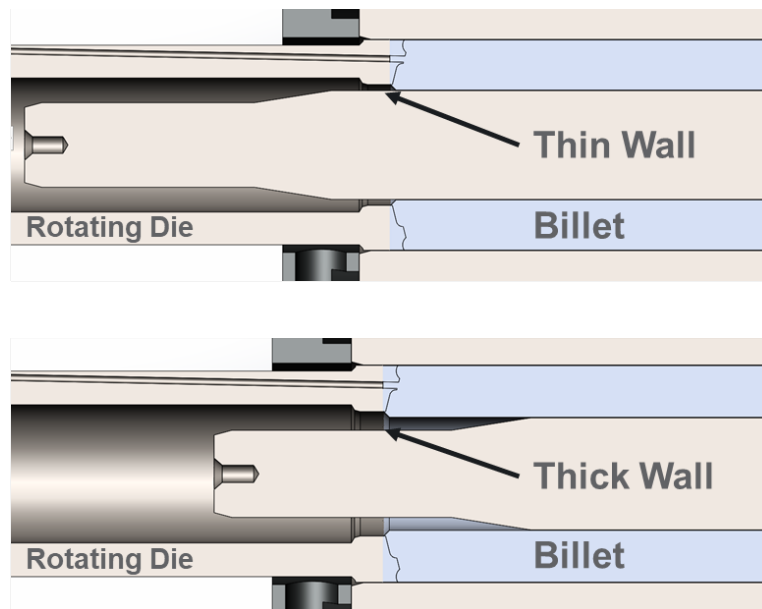


Figure II.1.1.4. The position of the mandrel during ShAPE™ extrusion to create locally modified wall thickness. Source: PNNL.

The approach shown in Figure II.1.1.4 was used to extrude AA6082 with 20-mm OD and wall thickness that transitioned from 1 mm to 2 mm, and back to 1 mm along the length of the extrusion. Figure II.1.1.5(a) shows longitudinal cross-sections of tubing fabricated with mandrel translation velocities of 2.5 m/min (top) and 1.25 m/min (bottom). Necking of the OD was observed as the extrusion transitioned from constant wall thickness (i.e., stationary mandrel) to a different wall thickness (i.e., moving mandrel). The necking effect was more pronounced at high-velocity (e.g., 0.8 mm @ 2.5 m/min vs. 0.4 mm @ 1.25 m/min). We hypothesize the complex material flow induced during mandrel insertion and retraction, as indicated in Figure II.1.1.5(a–b), leads to flow instabilities that manifest as necking. To test this hypothesis, additional mandrels were fabricated with longer taper lengths of 20 mm and 40 mm, as observed in Figure II.1.1.6, in comparison to the 10 mm taper length used in Figure II.1.1.5. A shorter taper length of 5 mm was also fabricated to elucidate the expected trend.

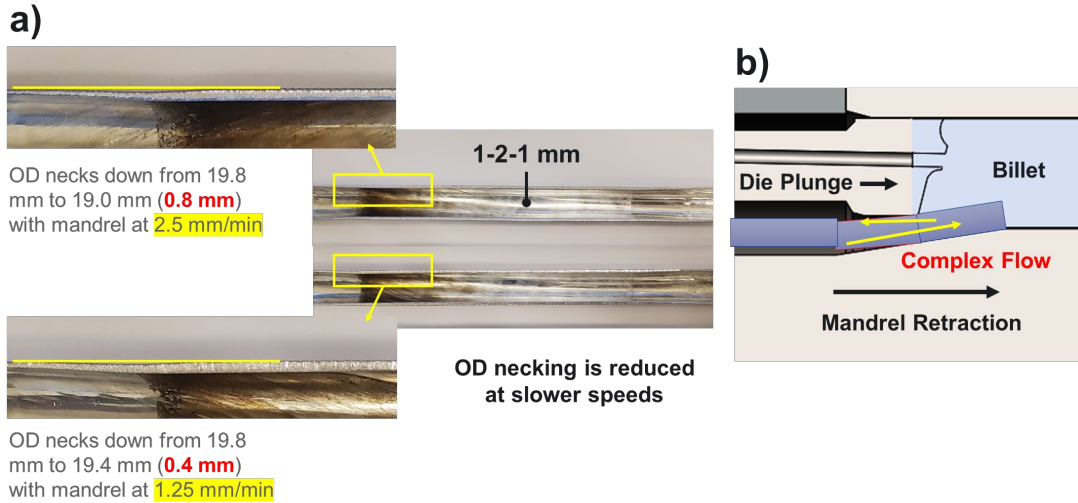


Figure II.1.1.5. (a) Longitudinal cross-sections showing necking in the wall thickness transition zone. (b) Schematic of the die plunge and mandrel retraction process. Source: PNNL.

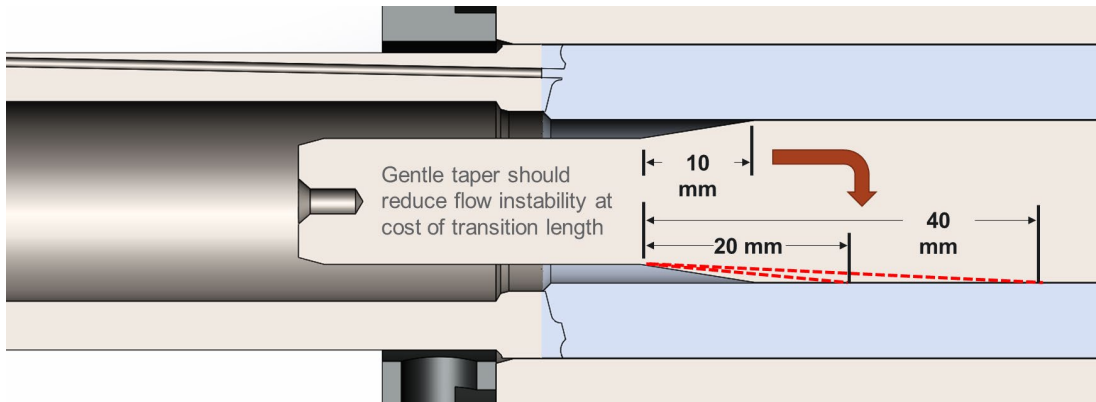


Figure II.1.1.6. Longer mandrel taper lengths of 20 mm and 40 mm were used to reduce flow instability and necking. Source: PNNL.

Extrusion of AA6082 was performed with wall thickness varying from 1 mm to 2 mm, and back to 1 mm at a fixed mandrel velocity of 1.25 mm/min for the four different mandrel taper lengths shown in Table II.1.1.2. Results for necking (i.e., OD reduction) are shown in Figure II.1.1.7 with a somewhat linear relationship noted between taper slope and OD reduction. It was also observed that necking is more pronounced when the mandrel is being retracted (i.e., wall thickness transitioning from 1 to 2 mm). For a taper slope of 0.025 mm/mm, the OD reduction was approximately 0.1 mm, which is only 0.5% of the OD. This suggests that fabricating variable wall thickness tubing may be possible without significant impact on OD dimensional stability.

Table II.1.1.2. Summary of Measured Material Properties

Mandrel Taper Length (mm)	Mandrel Taper Slope (mm/mm)
5	0.2
10	0.1
20	0.05
40	0.025

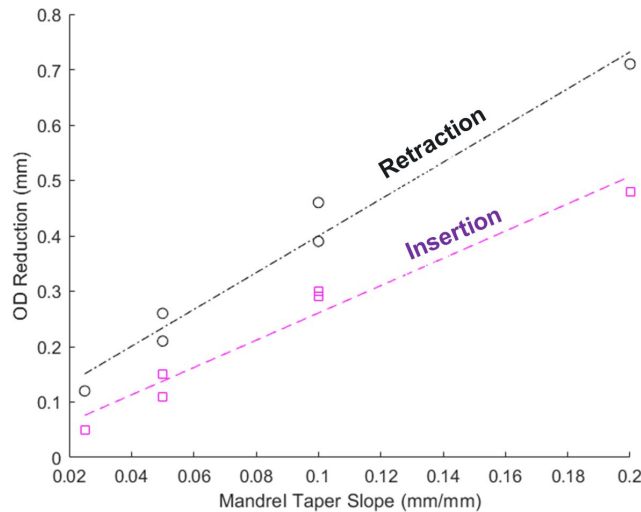


Figure II.1.1.7. Necking of OD reduces as mandrel taper slope decreases. Source: PNNL.

Task 2 Progress: Locally Modified Properties.

A unique feature differentiating ShAPE™ from conventional extrusion is the ability to prescribe process temperature by controlling rotational velocity (i.e., RPM) of the billet. For 6xxx alloys, this affects the extent of second-phase solutionization during extrusion which, in turn, impacts Mg_2Si precipitation in different regions of the extrudate during artificial aging. The ability to control ram speed and RPM independently and complementarily enables sharp temperature transitions at precise locations within the extrudate. Building upon the variable-property capability developed in FY 2023, research this year focused on achieving large differences in strength and toughness within the same extrudate. Figure II.1.1.8 shows stress-strain curves for two different regions of a single AA6111 extrudate.

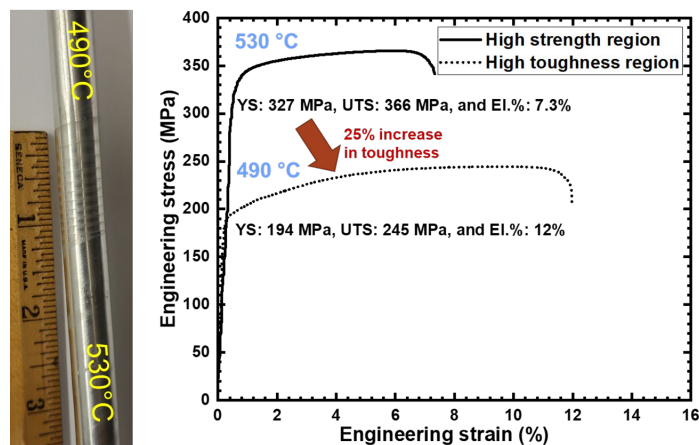


Figure II.1.1.8. AA6111 tubing manufactured by ShAPE™ with regions processed at different temperatures to locally modify strength and toughness in a single extrudate. Source: PNNL.

Research was conducted to explore how sharp the temperature transitions could be made and whether multiple transitions could be achieved in rapid succession. Two methods were employed to obtain the processing temperature variability with single and multiple transitions. The first method was to change the rotational speed from 30 RPM to 110 RPM, at a constant ram speed of 120 mm/min. The second method was to change the extrusion rate from 20–120 mm/sec, at a constant rotational speed of 100 RPM. Both single and double transitions were obtained via this method, as displayed in Figure II.1.1.9(a) and (d), respectively. Single

transition involved an increase in the spindle-speed to obtain two steady-state processing temperatures in the tube while in double transition, the spindle-speed was increased followed with reduction in speed to obtain three steady-state processing temperatures. In the second method to minimize the transition length between the low- and HT processing regions, the ram speed was reduced to 20 from 120 mm/min during the spindle-speed change, as shown in Figure II.1.1.9(b) and (e). To change the processing temperature as quickly as possible, during the transition, the spindle-speed was briefly changed beyond the steady-state rotational speed required to maintain the new-temperature steady-state. In this method as well, both single and multiple transitions can be obtained, as presented in the Figure II.1.1.9(e). Figure II.1.1.9(c) and (f) shows the magnified view of ram speed and spindle-speed during the transition. There was a 64% difference in toughness achieved for different regions of a single strip.

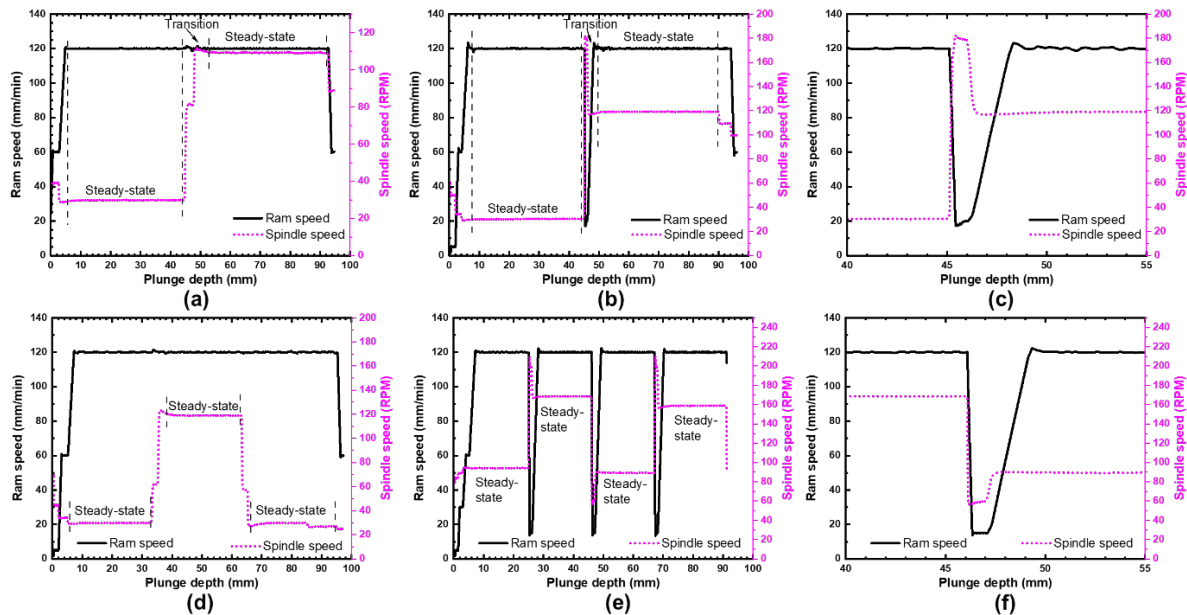


Figure II.1.1.9. (a-f) AA5182 strip-rolled to a uniform thickness of 0.9 mm from a tube having variable wall thickness of 1 mm and 2 mm. Sixty-four percent difference in toughness is achieved for different regions of a single strip. Source: PNNL.

Project 1B: Form-and-Print—AM for Localized Property Enhancement for Al Sheet

Work on this task during FY 2021 and FY 2022 focused on deposition on 6xxx wrought substrates in bulk/billet form. Transitioning to deposition on thin sheet substrates required iterative process development to identify process parameters that did not melt through the thin sheet substrates. The deposition parameters were found to be sensitive to the thickness of the plate; therefore, process parameter development was necessary for each demonstration.

The first demonstration of hem sheet closures involved the clamping of the hemmed sheets of 6xxx-series alloy on the rotary table in the system, followed by deposition and machining of material at the hem line. Figure II.1.1.10 shows hemmed sheets at different stages of the process (unmounted from the rotary table). Notably, different samples had different surface conditions due to pre-straining of the sheet, such as the matte surface finish of the samples in (a) and (c) compared to the mill finish of sample (b). This had some effect on the laser's coupling efficiency with the substrate because highly reflective surfaces absorb less power, which requires process parameter tuning. Ultimately, a primary goal of process development was to leave the bottom surface of the hemmed sheets unaffected by the processing. This was accomplished.

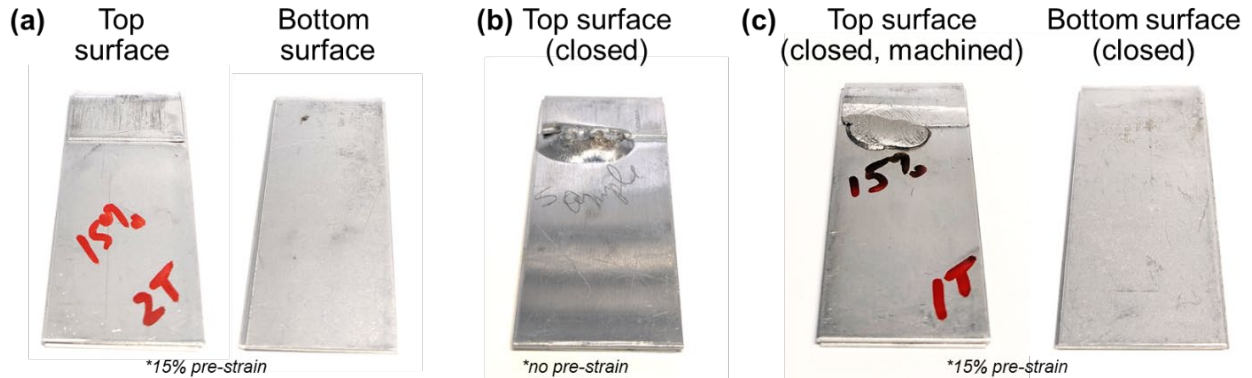


Figure II.1.1.10. Photographs of hemmed sheet samples (a) before processing, (b) after deposition, but before machining, and (c) after deposition and machining showing no deformation of the bottom surface of the sheet. Source: ORNL.

Inspection of the resultant hem closures was done by sectioning the samples through the deposited material and imaging using optical microscopy. Figure II.1.1.11 shows the optical micrograph of one of the specimens, annotated to show the various features of the cross-section. Notably, there is a gap between the middle sheet and the outer hem sheet. This is hypothesized to be the main reason for the ability to fuse the thin sheet without melting all the way through because the air gap provides some thermally insulating behavior.

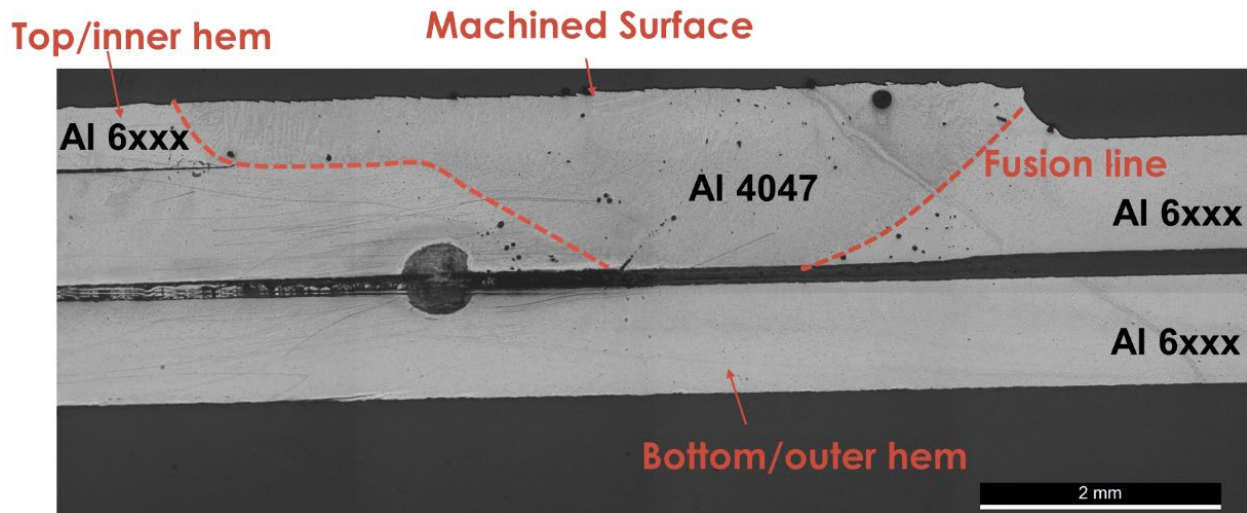
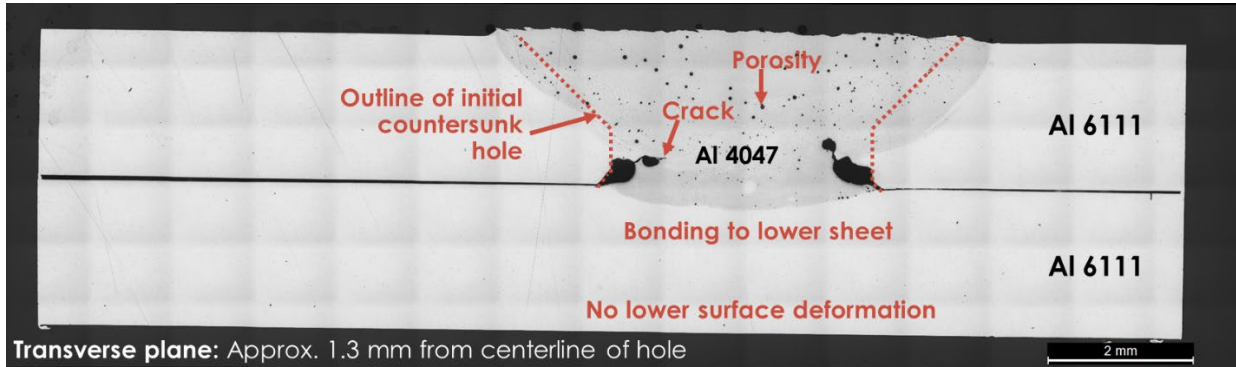


Figure II.1.1.11. Annotated optical micrograph of a cross-section of the hemmed sheet after deposition and machining. Notably, the fusion zone does not cross the gap between the middle and outer sheets. Source: ORNL.

The second demonstration of the form-and-print process was to join two similar AA6111 sheets. A countersunk hole was pre-drilled through one of the sheets and then the sheets were mounted on the steel rotary stage in lap-joint configuration. The hole was then filled with AA4047 to bond the two sheets together. A parameter-development campaign was undertaken by visually inspecting the deposition for melt through of the bottom sheet, as well as testing whether the sheets could be separated by hand. Figure II.1.1.12 shows a cross-section near the centerline of the hole for the sample at the best parameters from this development campaign. Dotted lines show the approximate initial geometry of the hole, showing that there was fusion bonding to both the lower sheet and the walls of the hole. However, some gas porosity was observed, as was cracking due to incomplete filling of the hole volume. Anecdotally, the oxygen content of the atmosphere under the shielding gas was found to have over 3% oxygen, which explains the gas porosity and possibly some

of the larger pores in the corners. Overall, this initial demonstration indicated that it was indeed possible to additively deposit material in a manner that did not deform the lower sheet. It is likely that most of the observed porosity could be reduced or eliminated with improved shield-gas strategies and further process optimization.



Transverse plane: Approx. 1.3 mm from centerline of hole

Figure II.1.1.12. Annotated optical micrograph of the transverse cross-section of locally deposited material to bond similar AA6111 sheets. Source: ORNL.

The third demonstration was to attach two dissimilar AA6111 and SS 304 sheets. Like the similar-sheet experiment, a countersunk hole was drilled through the top SS 304 sheet, and then the sheets were mounted to the rotary table in lap-joint configuration. Then, the AA4047 was deposited into the holes to fuse to the bottom sheet. After testing a wide range of material parameters, fusion bonding between the AA4047 and SS 304 was not achieved. This was an expected result due to the large difference in melting points. However, the deposited material mechanically fastened the plates to prevent translation motion while rotation was still possible. Therefore, two holes were drilled to fully restrict the motion of the plates. Figure II.1.1.13(a) shows the top-view of one sample, while Figure II.1.1.13(b) shows the corresponding cross-section. The deposited AA4047 was shown to be fusion-bonded to the lower AA6111 sheet, but a noticeable gap can be seen between the deposited AA4047 and SS 304 plate. This confirms that no metallurgical bonding occurred between the deposited Al and the steel plate. Again, the lower plate was not deformed on the outer surface, which is desirable if the lower plate is an externally facing body panel. However, the lack of metallurgical bonding may present issues with vibration of the sheets.

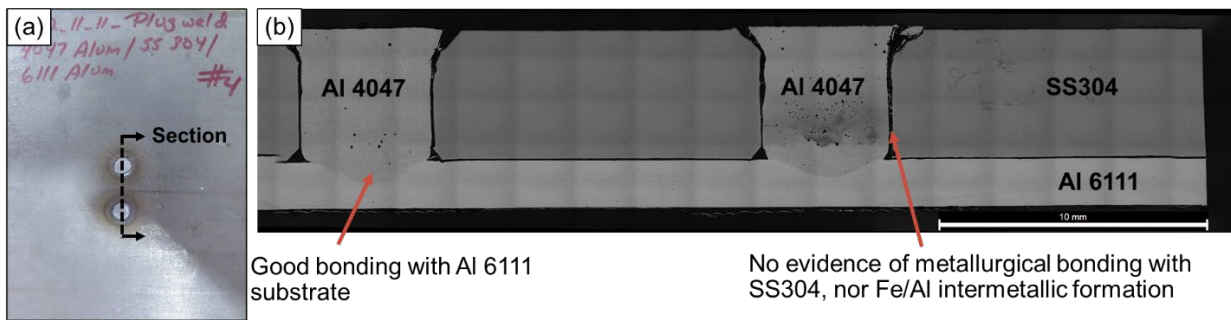


Figure II.1.1.13. Annotated optical micrograph of (a) the top-view showing the sectioned area and (b) the transverse cross-section of locally deposited material to bond dissimilar AA6111 and SS 304 sheets. Source: ORNL.

Project 1C: Local Processing to Address Challenges to Implementing Al Sheet

Project 1C1 Progress (PNNL)

To further improve processing speed and enhance local formability, FSP in FY 2023 focused on further widening processing windows for AA7075 and AA6111 sheets. Figure II.1.1.14 summarizes the formability of several Al sheets, as measured by compressive head displacement at 70% load-drop during VDA testing and bend angle measured following the test. For AA6111-T6, FSP up to a process speed of 4 m/min resulted in formability nearly identical to samples subjected to a T4 (i.e., the most formable) temper. At a lower speed of 0.5 m/min, no cracks were observed on the specimens at the end of the bend test, demonstrating significantly greater formability improvement beyond the T4 value. For AA7075-T6, both the bend angle and displacement after 70% load-drop were higher after FSP in comparison to the initial T6 condition, indicating better bendability. However, AA7075-T6 with FSP demonstrated formability slightly lower than that for T4 temper.

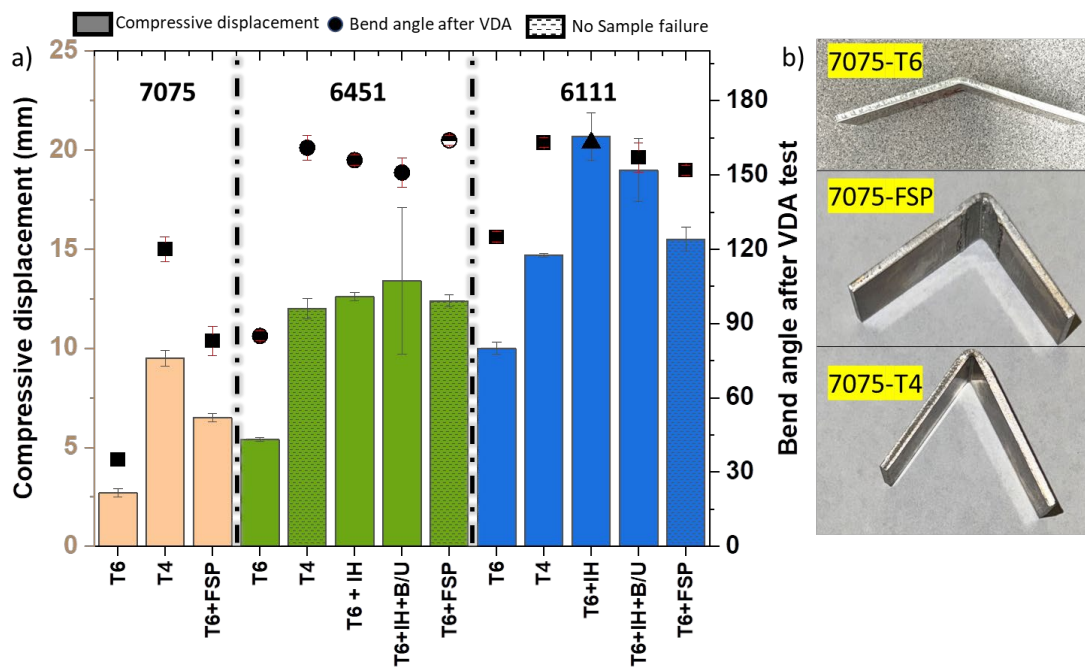


Figure II.1.1.14. (a) Bar chart showing formability comparison of several cases of Al sheets as measured by displacement and bend angle (represented by solid symbols) after VDA testing. Shaded bar graphs correspond to the cases that do not show any cracking after 70% peak load-drop. (b) Example pieces showing VDA bend samples of AA7075 T6, FSP, and T4 samples. Source: PNNL.

A large process window was explored to establish processing parameters that result in the highest level of formability, as indicated in Figure II.1.1.15. A range of tool speeds from 300 RPM to 1700 RPM was used to vary peak process temperature from 300–500°C at welding speeds of 0.5 m/min for AA7075-T6 and 2.5 m/min for AA6111-T6. Figure II.1.1.15(a–b) show the temperature during processing measured using a thermocouple attached to the tool shoulder, as observed in Figure II.1.1.15(d). Peak-temperature extracted from Figure II.1.1.15(a–b) are plotted against the tool rotational speed in Figure II.1.1.15(c). Approximate peak temperatures that have yielded the most formable samples are shown by red and black boxes for respective alloy systems. Select samples and their associated data sets were shared with corresponding Thrust 4 efforts in the topic of advanced characterization and finite element modeling. This work is discussed separately in the Thrust 4 annual report in a later section.

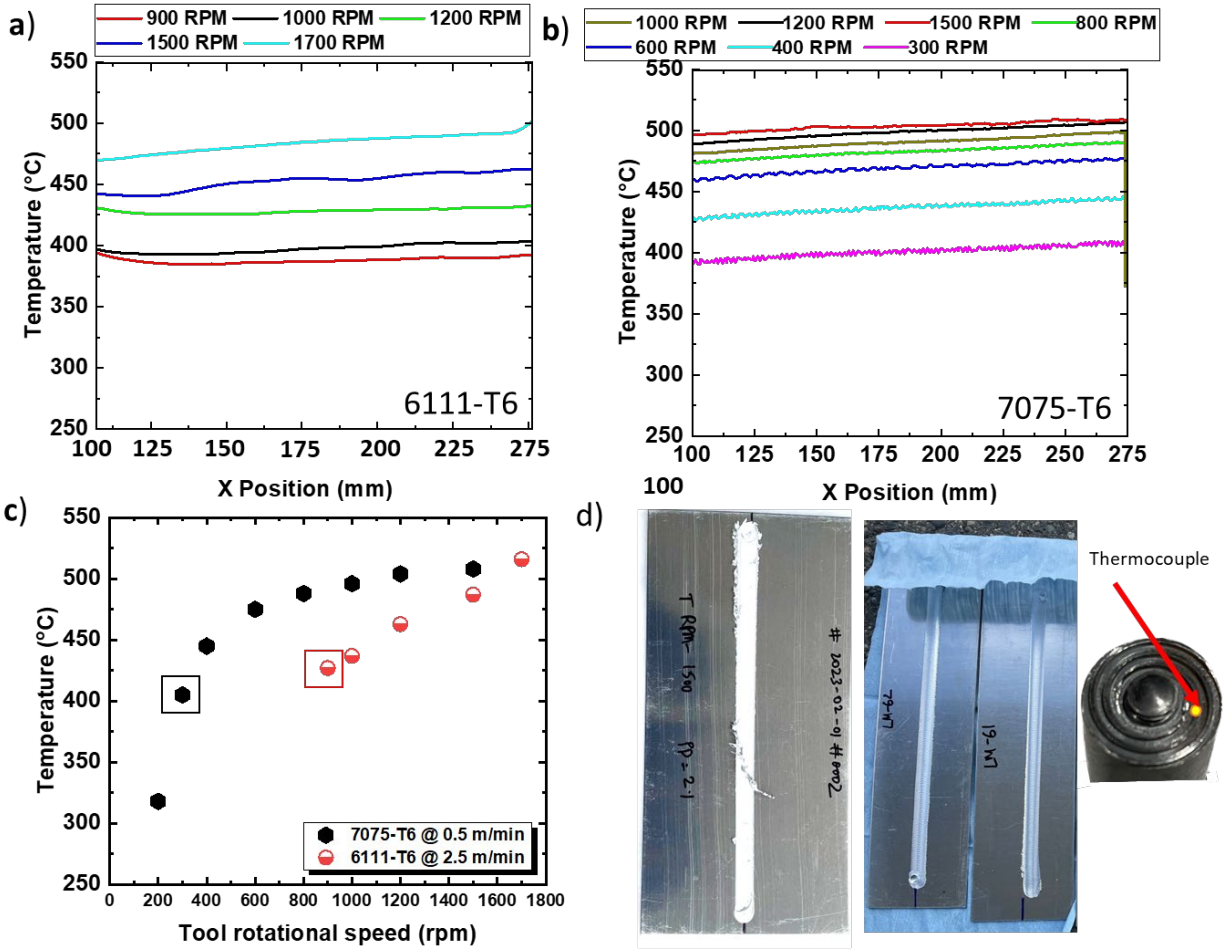


Figure II.1.1.15. Temperature profile in the steady-state processing of (a) AA6111-T6 and (b) AA7075-T6. (c) Peak temperature during processing vs. tool rotational speed for AA6111-T6 and AA7075-T6. (d) Example processed samples of AA7075 and AA6111 and FSP tool with thermocouple placement. Source: PNNL.

Progress was made this year in developing FSP at high-speed using the ABB Robotics platform. Processing speeds of 4, 5, and 6 m/min were demonstrated, as indicated in Figure II.1.1.16(a). Thermocouples attached to the shoulder of the FSP tool were used to measure temperature during processing, as observed in Figure II.1.1.16(b). Sheets processed at speeds of up to 4 m/min using the robotic platform have formability similar to sheets processed at slower speeds using the Gantry machine. This demonstrates that a robotic arm could be a viable method for integrating FSP in the automotive industry. A LightMAT seed proposal with an OEM partner is exploring the possibility of using high-strength Al alloys to a potential battery tray application with the use of press brake for 90-degree bends at sharp radii, enabled using local thermomechanical processing.

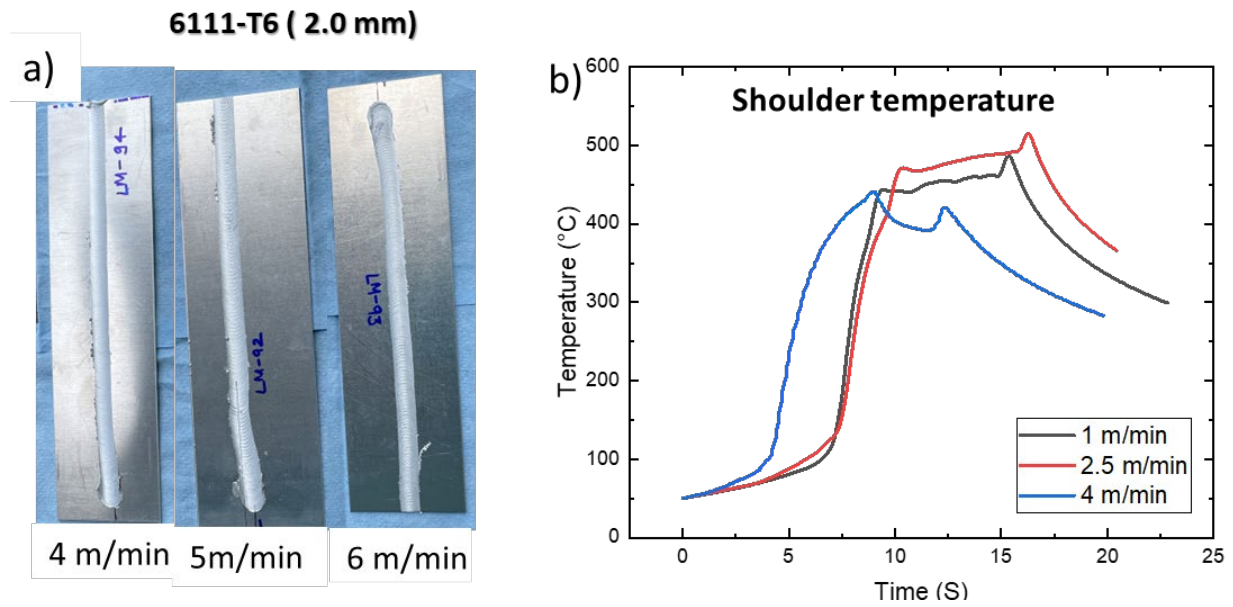


Figure II.1.1.16. (a) Samples processed at 4, 5, and 6 m/min speed using a robotic platform. (b) Shoulder temperature at the shoulder tip of the FSP tool. Source: PNNL.

Figure II.1.1.17 summarizes the edge stretchability results for the as-received and processed AA6111-T6 sheets sheared using different clearances. Edge stretchability, as measured by the tensile elongation, decreases with increasing clearance across all tested materials. This is an expected result, as the ductility of the samples will suffer with increasing clearance due to burr formation and increased deformation at the sheared edges. Among the materials, those in the T4-temper exhibit superior edge stretchability at varying clearances, attributable to their inherently greater ductility. Conversely, the T6 sheet demonstrates the least stretchability due to its inherently lower ductility. However, applying FSP enhances the local ductility of T6-temper sheets within the processed zones, which in turn improves edge stretchability. This is illustrated in Figure II.1.1.17, where the AA6111-T6 with FSP samples outperform T6-temper samples in edge stretchability across all clearances, with enhancements ranging from 27% to 73%. Notably, while FSP significantly elevates the formability of T6 to meet or surpass the T4 levels, the edge stretchability values for T4 are still unmatched.

As part of the B/U process approach, the four-roller B/U system introduced in FY 2023 represents a significant enhancement over the three-roller design, yielding sheets that are flatter and straighter, as depicted in Figure II.1.1.18. The first pair of rollers form a bend across the width of the sheets. The severity of this bend can be controlled by adjusting the vertical spacing between the rollers.

Three levels of bending are possible: low, medium, and high. The second pair of rollers unbends the sheet by flattening it, also shown in Figure II.1.1.18. For this pair of rollers, the roller gap is equal to the processed-sheet thickness. The process was either performed at RT or at 500°C using IH. A continuous processing speed of 1 m/min was used for RT runs. For the processing runs conducted at HT, sheets were processed intermittently to ensure a uniform temperature profile along the sheet, which was measured with a thermal camera. However, a sufficiently powerful IH supply and optimum coil design can allow continuous operation at higher speeds. To separate the impact of heating from mechanical deformation, controlled experiments would involve IH without the B/U steps.

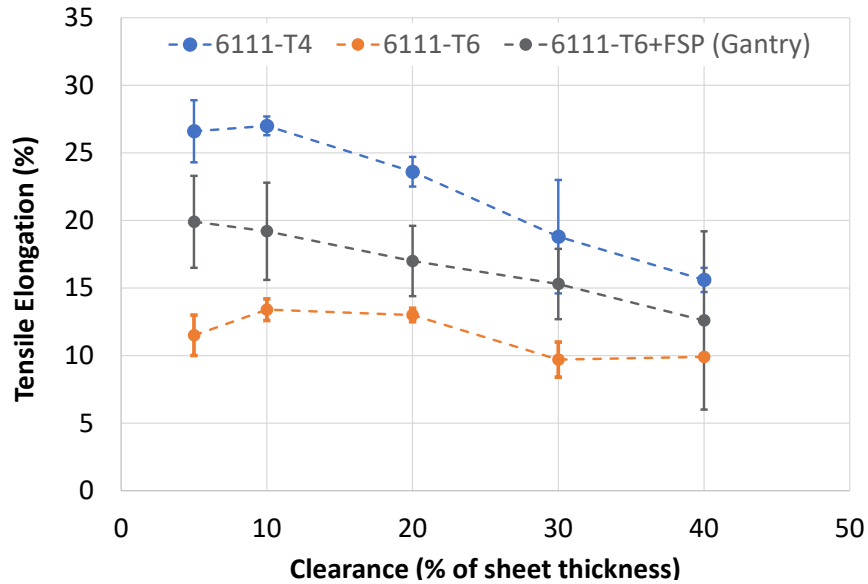


Figure II.1.1.17. Tensile elongation vs. clearance plot summarizing the results of the edge stretchability tests. Source: PNNL.

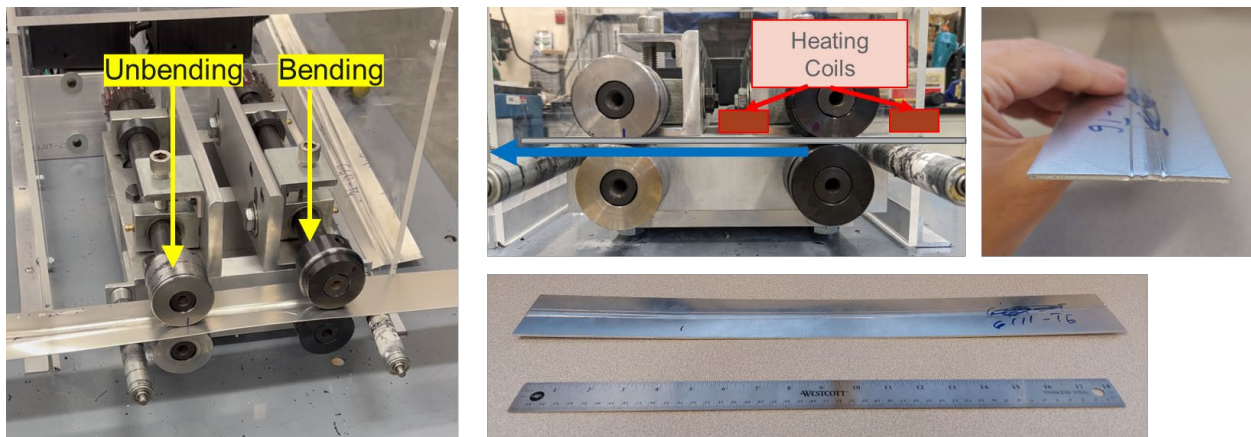


Figure II.1.1.18. Pictures of the B/U setup, heating coils, and processed sheets. Source: PNNL.

The process was either performed at RT or at 500°C using IH. A continuous processing speed of 1 m/min was used for runs at RT. For the processing runs conducted at HT, sheets were processed intermittently to ensure a uniform temperature profile along the sheet, which was measured with a thermal camera. However, a sufficiently powerful IH supply and optimum coil design can allow continuous operation at higher speeds. To separate the impact of heating from mechanical deformation, controlled experiments would involve IH without the B/U steps.

Figure II.1.1.18 above summarizes the formability improvements obtained by IH only or simultaneous IH during B/U (IH+B/U). IH and IH+B/U yielded similar formability improvements in T6 tempers of AA6451 and AA6111 sheets. It was possible to obtain T4 or better levels of formability within the processed zones of both sheets. VDA testing indicates that, compared to heating only, the added deformation during B/U resulted in greater scatter in both measures of formability (displacement at 70% load-drop during bending and bend angle after testing), and slightly lower formability.

Finite element simulations of B/U performed in collaboration with Thrust 4 researchers predicted the equivalent strain profiles through the thickness of AA6451 sheets for the different levels of bending (low to high), as shown in Figure II.1.1.19. The strains are largest at the bottom surface, where the sheet is in tension during the initial bending. The strains gradually decrease and reach nearly zero at the center then increase towards the top surface. Microhardness tests on the sheet cross-sections confirms the simulation predictions and shows trends similar to the strain distributions. Despite the relatively low equivalent strains predicted in the finite element simulations, B/U at RT was still able to increase hardness in the T4 sheets to T6 levels (~108 HV), and further increase hardness in the T6 sheets by 18% to ~128 HV.

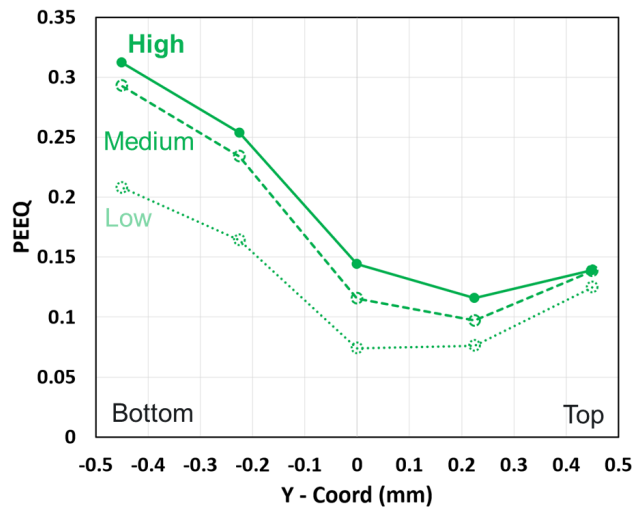


Figure II.1.1.19. Finite element simulation results of the equivalent strains across the sheet thickness for low, medium, and high B/U levels. Source: PNNL.

The low equivalent strains produced by B/U do not cause a significant change in grain size in the processed zones, even at high-process temperatures, as indicated by the EBSD images in Figure II.1.1.20. Therefore, it is possible to conclude that precipitate dissolution and/or over-aging from exposure to HTs are the main cause of softening and formability improvements in the sheets, rather than dynamic recrystallization. However, as predicted by the simulations, B/U results in gradual deformation in the microstructure, where the greatest rotation of the grains is observed near the bottom surface. The rotation of the grains results in weakening of the initial cube texture of the as-received T6-temper sheets. Processing at high-temperature further contributes to texture weakening, as observed in Figure II.1.1.20. Therefore, the main benefit of IH plus B/U over simple IH is heterogeneous deformation and texture weakening, which may be useful for some forming operations and other mechanical properties.

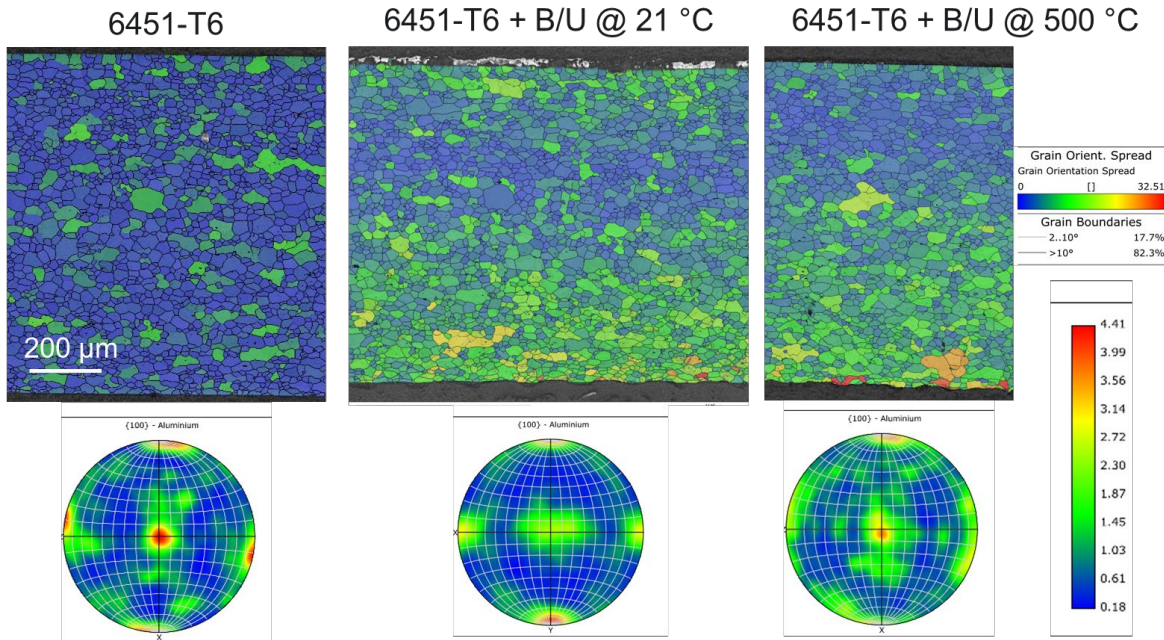


Figure II.1.1.20. EBSD characterization of the as-received and processed AA6451-T6 sheets. The top row of images are the grain misorientation maps. The bottom row is {100} pole figures. Source: PNNL.

To conclude the project activities and to obtain feedback on the feasibility of approaches developed in the core program, locally processed FSP and B/U Al sheets were shared with an OEM collaborator to test the local formability improvements in production-relevant applications. Project 1C1 will conclude with the feedback received and application of the processes on newly developed 6xxx sheets with even more significant formability challenges.

Project 1C2 Progress (ORNL)

For the approach using laser modification of local microstructure, localized laser processing was performed using a TRUMPF laser system. The laser was programmed to traverse along a straight-line path on the top surface of the sample. Laser power, travel speed, and the number of passes of the laser were process variables that were used to control the localized heating along a line profile of the sample. In contrast to work during FY 2023, where temperature profiles were monitored using one or more thermocouples placed in contact with the bottom side of the sample along the path of the laser, temperatures achieved on the bottom side of the sample were monitored using an infrared camera. Figure II.1.1.21(a) shows a view of the laser head and a view of the top surface of the sample exposed through an Al alloy frame used to isolate the region to be processed. Figure II.1.1.21(b) shows a view of the setup from the bottom side. The FLIR brand infrared camera shown in the image is used to monitor the temperatures achieved on the bottom side of the sample at the laser location and in adjacent regions during laser treatments.

Several trials were completed using local laser processing at different power levels and laser travel velocities. Figure II.1.1.22(a) shows an infrared image obtained of the bottom surface of the sample at one instant during the laser processing. The color profiles show temperatures at different locations from the instantaneous position of the laser. Figure II.1.1.22(b) shows the maximum temperature in the field of view as a function of frames elapsed (time is proportional to the frames elapsed) and number of passes at a power level of 200 W. Note that the average temperature and the time at higher temperatures increases with the number of passes.

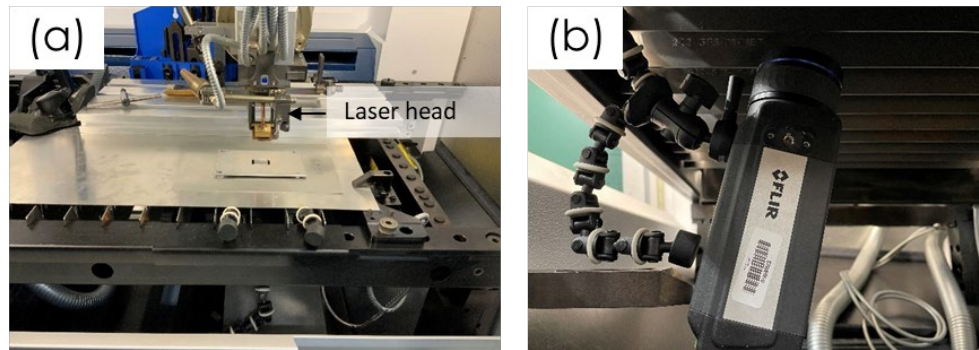


Figure II.1.1.21. (a) Top-view of the setup used for laser modification. (b) The infrared camera placed on the bottom side for measuring the temperature of the sample. Source: ORNL.

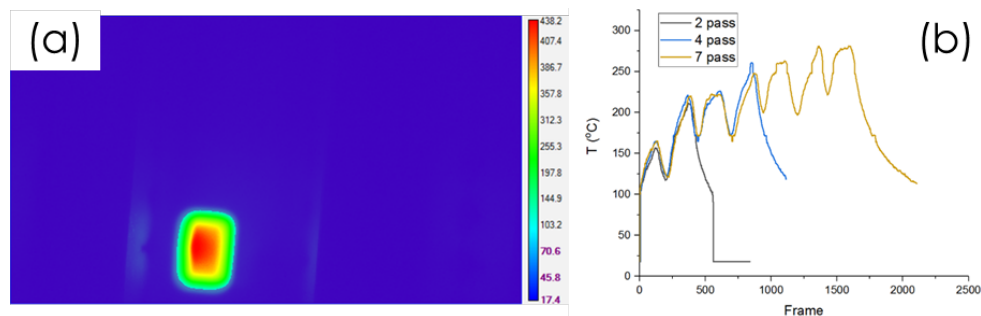


Figure II.1.1.22. (a) Image captured by the infrared camera showing the spatial variation of temperatures achieved at the bottom surface of the sample (temperature scale is in °F). (b) Maximum temperatures (°C) achieved as a function of the number of passes at a power of 200 W. Source: ORNL.

Local heating experiments were carried out on 2.5-mm-thick AA7075-T6 sheet at typical power levels of 200, 350, and 400 W. Samples treated at a power level of 400 W were selected for bend tests because these showed the greatest reduction in YS. Bend tests were performed using punch radii of 2.35, 1, 0.762, and 0.2 mm. Figure II.1.1.23(a) shows load-displacement curves obtained in three-point bend testing (support spacing = 25 mm, specimen width ~12.7 mm) for a punch radius 0.2 mm (radius-to-thickness ratio = 0.08) of the untreated and 400-W-treated specimens. Improvements in bendability were characterized by evaluating punch displacements at which the load dropped to 70% of the maximum load at the same radius-to-thickness ratio. Measurements show an improvement from ~26% at a punch radius of 0.762 mm to 34% at a punch radius of 0.2 mm, both exceeding improvements of 25%, validating the use of laser processing for modifying bendability. Figure II.1.1.23(b) shows images of the two samples tested using a punch radius of 0.2 mm. Testing was stopped once the load dropped to similar levels in both cases. Figure II.1.1.23(b) clearly shows that the treated sample accommodated a larger bend angle, indicative of the improved bendability. Further work is needed to evaluate the variations in process conditions, in particular the effect of temperature and time on the improvement achieved in bendability.

For the shearing of AA6111-T6 sheets using the PUE-processing approach, 2-mm-thick AA6111-T6 alloy sheets were sheared into samples with planar dimensions of 10×2.5 cm². The sheared edges showed obvious presence of unevenness and burrs. As discussed in the Approach section previously, PUE modification was performed by applying ultrasonic power through a sonotrode to the sheared edges of the samples. It was shown that the samples could be effectively modified with the low ultrasonic power for 4 seconds with a rather small load of 200 N, resulting in measurable improvements on edge stretchability and tensile elongations. Improvements in elongation of 27–75% were achieved in samples that were modified using the PUE modification process when compared to samples tested in the as-sheared condition.

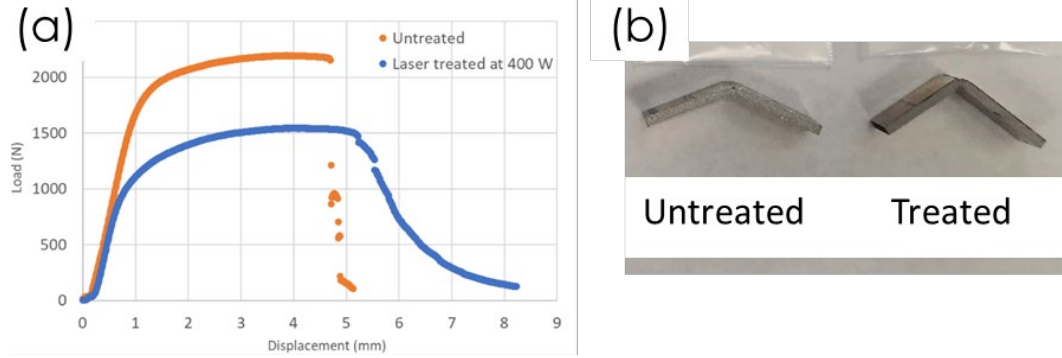


Figure II.1.1.23. (a) Load-displacement curve of the untreated and laser-treated at 400 W samples using a punch radius of 0.2 mm. (b) Images of bent untreated and treated specimens. Source: ORNL.

The mechanisms of this improvement can be related to (a) better edge quality (smoother surface) and (b) removal of edge defects due to PUE and is a subject of the work that was pursued in FY 2023. Figure II.1.1.24(a) is an optical image of short cross-section of the sheet showing the microstructure of the sheared edge in the as-sheared condition, and Figure II.1.1.24(b) shows a similar region after PUE. The difference is clear: there are many shear-induced defects in the as-sheared condition, including elongated pores and surface cracks and notches due to shearing, as shown in Figure II.1.1.24(a). On the other hand, the surface is observed to be significantly smoother with almost no shearing induced cracks at the sheared surface after the successful application of PUE. High-resolution SEM and EBSD of the microstructure in the sheared region shows the presence of rather fine grain structure suggesting that dynamic recrystallization occurred during the PUE modification process, as shown in Figure II.1.1.25.

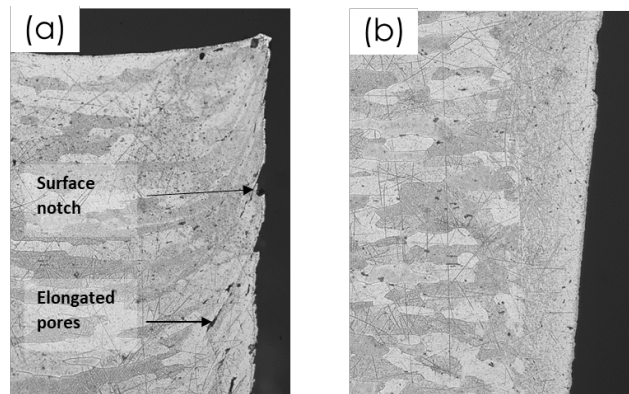


Figure II.1.1.24. Optical image of cross-section of the sheets showing the microstructure of the sheared edge in the (a) as-sheared condition and (b) after PUE. Source: ORNL.

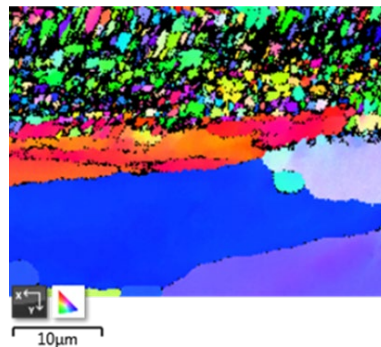


Figure II.1.1.25. Fine grains are observed near the surface after PUE. Source: ORNL.

Conclusions

In FY 2023, each project in Thrust 1 achieved its goals in selectively modifying an Al sheet and tube properties and geometries. Project 1A demonstrated that selective modification of stiffness (variable wall thickness), strength, and toughness (locally modified properties) could be achieved during ShAPE™ extrusion with the following accomplishments:

- AA6082 extrusions with 20 mm OD and wall thickness varying from 1 to 2 mm and back to 1 mm were achieved with less than 1% necking of the OD in the transition region.
- AA6111 extrusions were achieved with selectively modified regions differing by 69% for YS, 49% for ultimate strength, and 25% for toughness.
- Techniques for balancing spindle RPM and ram speed were explored to sharpen temperature transitions, reduce transition length, and allow for multiple transitions in rapid succession.
- The project accomplishments were awarded one of six “Project Team Awards” at the 2003 DOE VTO Annual Merit Review. <https://www.energy.gov/eere/vehicles/articles/2023-vto-amr-plenary-and-awards#:~:text=Each%20year%2C%20VTO%20presents%20awards,deployment%20achievements%20in%20specific%20areas.>

Project 1B demonstrated the objective of locally modifying 6xxx-series Al sheet without deforming the opposing face in three distinct experimental configurations. The directed energy of the laser hot-wire process allowed for deposition of material with significant heat accumulation in the substrate. Additionally, in the case of the hem-closure demonstration, the gap within the geometry of the formed substrate contributed to preventing melting through. Overall, it was demonstrated that material could be deposited on thin sheets without deforming the bottom sheet surface in a variety of configurations.

Project 1C showed feasibility of various techniques in improving the local formability and edge stretchability of the high-strength Al sheets in their T6 temper with the following accomplishments:

- Both FSP and B/U achieved T4-level formability within the processed zones AA6451-T6, AA6111-T6, and AA7075-T6 sheets, as confirmed by the VDA test displacements and bend angles.
- FSP achieved 27–73% improvements in edge stretchability of the T6 sheets; however, values for T4 are still unmatched.
- Bend test results and the processed sheets were shared with an automotive OEM for their feedback on the feasibility of the processes in production-relevant applications.
- Laser heating caused local softening and bending experiments show that laser processing allows improvements of 25% or more in the bendability of AA7075-T6.
- A significant reduction of near-surface porosity and improvement of edge quality was achieved in AA6111-T6 sheets using PUE. This contributed to the substantial enhancement of edge stretchability of the ultrasonic edge modified sheets after shearing in comparison with edges that were not modified.

Key Publications

Project 1A

1. Komarasamy, M., B. S. Taysom, M. Milligan, B. Schuessler, G. Grant, D. Herling, and S. A. Whalen, 2024, “Aluminum Tubing with Locally Modified Properties by ShAPE™),” Extrusion Technology 2024 Conference, Orlando, FL, April 30 - May 2, 2024. (Accepted).
2. Komarasamy, M., L. Li, B. S. Taysom, A. Soulami, G. Grant, D. Herling, and S. Whalen, 2024, “Co-extrusion of dissimilar Al. alloys via ShAPE,” *Coatings*, 14(1), 42. <https://doi.org/10.3390/coatings14010042>.

3. Komarasamy, M., S. Whalen, G. Grant, and S. Taysom, 2024, “Manufacturing components with variable properties via solid-phase processing.” (Pending).
4. Komarasamy, M., S. Whalen, and B. Milligan, 2024, “Shear-assisted extrusion assemblies and methods.” (Pending).
5. Milligan, B. K., B. S. Taysom, X. Ma, and S. A. Whalen, 2023, “Solutionization via severe plastic deformation: Effect on natural aging in an Al-Mg-Si-(Mn) alloy,” In: Broek, S. (ed.), *Light Metals, 2023*, TMS 2023. The Minerals, Metals, and Materials Series. Springer, Cham, Switzerland. pp. 333–338. https://doi.org/10.1007/978-3-031-22532-1_46.
6. Milligan, B. K., L. Li, M. Komarasamy, T. Roosendaal, A. Soulam, and S. Whalen, 2023, “Cladding and butt-joining dissimilar Al alloys simultaneously via ShAPE,” *JOM*, 75, 3033–3040. <https://doi.org/10.1007/s11837-023-05855-x>.
7. Milligan, B. K., X. Ma, B. S. Taysom, and S. A. Whalen, 2023, “Solutionization via severe plastic deformation: Effect of temperature and quench method in a ShAPE™-processed Al-Mg-Si alloy,” *Metall. Mater. Trans. A Phys.*, 54, 2576–2584. <https://doi.org/10.1007/s11661-023-07034-8>.
8. Taysom, B. S., and S. Whalen, 2024, “Extrusion with specifiable or variable wall thickness.” (Pending).
9. Whalen, S., Md. Reza-E-Rabby, and M. Komarasamy, 2023, “Devices and Methods for Performing Shear-Assisted Extrusion, Extrusion Feedstocks, Extrusion Processes, and Methods for Preparing Metal Sheets,” US 11,684,959, (Granted).

Project 1B

1. Kannan, R., G. L. Knapp, P. Nandwana, R. Dehoff, A. Plotkowski, B. Stump, Y. Yang, and V. Paquit, 2022, “Data mining and visualization of high-dimensional ICME data for AM,” *Integr. Mater. Manuf. Innov.*, 11, 57–70. <https://doi.org/10.1007/s40192-021-00243-2>.
2. Knapp, G., D. Brown, M. Paramanathan, T. Feldhausen, and A. Plotkowski, 2023, “Local modification of cast-Al alloys via the cast-and-print process,” ORNL/TM-2023/3174, Oak Ridge National Laboratory, Oak Ridge, TN, USA. <https://doi.org/10.2172/2224157>.
3. Knapp, G. L., M. Gussev, A. Shyam, T. Feldhausen, and A. Plotkowski, 2022, “Microstructure, deformation, and fracture mechanisms in Al-4043 alloy produced by laser hot-wire AM,” *Addit. Manuf.*, 59(A), 103150. <https://doi.org/10.1016/j.addma.2022.103150>.

Project 1C

1. Balusu K., K. S. Choi, H. Das, A. Samanta, P. Upadhyay, S. Jana, and A. Soulam, 2023, “On the utility of the thermo-pseudo-mechanical model’s residual stress prediction capability for the development of FSP,” *Int. J. Adv. Manuf. Technol.*, 126, 1775–1788. <https://doi.org/10.1007/s00170-023-11199-2>.
2. Nasim, W., H. Das, P. Upadhyay, and M. Efe, 2022, “Improving local formability of 6xxx and 7xxx Al alloy sheets using FSP,” *Int. J. Adv. Manuf. Technol.*, 124, 2957–2967. <https://doi.org/10.1007/s00170-022-10569-6>.
3. Nasim, W., H. Das, S. S. Kulkarni, A. Rohatgi, D. R. Herling, G. J. Grant, P. Upadhyay, and M. Efe, 2022, “Local thermomechanical processing for improving formability of high-strength Al sheets,” SAE Technical Paper 2022-01-0244. <https://doi.org/10.4271/2022-01-0244>.

References

1. Taysom, B. S., N. Overman, M. Olszta, Md. Reza-E-Rabby, T. Skaszek, M. DiCiano, and S. Whalen, 2021, “ShAPE of high-strength aluminum alloy tubing,” *Int. J. Mach. Tools Manuf.*, 169, 103798. <https://doi.org/10.1016/j.ijmachtools.2021.103798>.
2. Talay, E., and A. Altinisik, 2019, “The effect of door structural stiffness and flexural components to the interior wind noise at elevated vehicle speeds,” *Appl. Acoust.*, 148, 86–96. <https://doi.org/10.1016/j.apacoust.2018.12.005>.
3. Ma, Z. Y., 2008, “FSP technology: A review,” *Metall. Mater. Trans. A Phys.*, 39, 642–658. <https://doi.org/10.1007/s11661-007-9459-0>.
4. Hu, X. H., X. Sun, and S. F. Golovashchenko, 2014, “Predicting tensile stretchability of trimmed AA6111-T4 sheets,” *Comput. Mater. Sci.*, 85, 409–419. <https://doi.org/10.1016/j.commatsci.2014.01.015>.
5. Noder, J., A. Abedini, C. Butcher, 2020, “Evaluation of the VDA 238–100 tight radius bend test for plane strain fracture characterization of automotive sheet metals,” *Exp. Mech.*, 60, 787–800. <https://doi.org/10.1007/s11340-020-00597-2>.

Acknowledgements

PNNL, ORNL, and ANL thank the DOE-EERE VTO for their support through the LMCP. The Project 1A PNNL staff members M. Komarasamy (locally modified properties) and B. S. Taysom (variable wall thickness) are commended for their excellent task leadership on this project. Project 1B acknowledges the contributions of the ORNL team members: G. Knapp, T. Feldhausen, A. Shyam, D. Brown, M. Paramanathan, S. Graham, and A. Haynes. The authors would also like to thank Ford Motor Company for supplying the hemmed sheets and Mazak Corporation and Lincoln Electric for their support with the Mazak VTC-800G system. P. Upadhyay was co-PI of the PNNL Project 1C1, while X. Hu was co-PI of the ORNL Project 1C2. Project 1C1 also thanks past and current PNNL staff members S. Shukla, H. Das, K. Rader, A. Ortiz, and K.-S. Choi for their excellent contributions. Project 1C2 acknowledges ORNL staff members K. Faraone and R. Miller for the laser modification experiments, J. Chen for assistance with the ultrasonic experiments, and K. Hedrick and S. Hawkins for the mechanical testing.

II.1.2 Thrust 2. Selective Processing of Aluminum Castings (Tasks 2A1, 2A2, 2B, and 2C) (Pacific Northwest National Laboratory and Oak Ridge National Laboratory)

Glenn J Grant, LMCP Program Manager, Principal Investigator (Thrust 2)

Pacific Northwest National Laboratory
 Energy Processes and Materials Division
 900 Battelle Blvd.
 Richland, WA 99352
 E-mail: glenn.grant@pnnl.gov

Saumyadeep Jana, Co-Principal Investigator (Project 2A1)

Pacific Northwest National Laboratory
 Energy Processes and Materials Division
 900 Battelle Blvd.
 Richland, WA 99352
 E-mail: saumyadeep.jana@pnnl.gov

Zhili Feng, Co-Principal Investigator (Project 2A2)

Oak Ridge National Laboratory
 Materials Science and Technology Division
 1 Bethel Valley Rd.
 Oak Ridge, TN 37830
 E-mail: fengz@ornl.gov

Aashish Rohatgi, Co-Principal Investigator (Project 2B)

Pacific Northwest National Laboratory
 Energy Processes and Materials Division
 900 Battelle Blvd.
 Richland, WA 99352
 E-mail: aashish.rohatgi@pnnl.gov

Alex Plotkowski, Co-Principal Investigator (Project 2C)

Oak Ridge National Laboratory
 Materials Science and Technology Division
 1 Bethel Valley Rd.
 Oak Ridge, TN 37830
 E-mail: plotkowskij@ornl.gov

Chris Schooler, DOE Technology Development Manager

U.S. Department of Energy
 E-mail: Christopher.Schooler@ee.doe.gov

Start Date: October 1, 2020
 Project Funding: \$1,450,000

End Date: September 30, 2023
 DOE share: \$1,450,000

Non-DOE share: \$0

Project Introduction

The LMCP, led by PNNL, is an integrated effort between PNNL, ORNL, and ANL. The overall program aims to develop and demonstrate scalable, cost-effective processing methods to locally enhance the properties of Al- and Mg-alloys to enable broader implementation of lightweight alloys in vehicles. The technical goal is to demonstrate that components and assemblies composed of commercially available alloys can be selectively modified to exhibit locally enhanced properties and deliver high materials performance in the most needed locations. This approach allows for significant improvements in manufacturability, structural efficiency, and weight-savings in next generation vehicles. Furthermore, the approach enables the right properties in the right

locations and provides the opportunity to decrease the number of metal alloys required for new vehicle manufacture, which reduces the challenges automakers face today in managing supply chains, assuring sufficient materials sustainability, and efficiently recycling scrap metal.

New processing methodologies could allow high-strength Al sheet materials over 450 MPa yield stress to reach ductility over 15% or forming bend radii $< 2 \times$ thickness. Local processing of cast parts can produce regions on a casting that will show $> 5 \times$ fatigue life or doubling of the endurance limit stress. Inherent to the research plan is an underpinning science theme to understand the behavior of microstructure evolution during manufacturing and the resulting material performance in service. Recognizing metal microstructures are process dependent, controlling and optimizing the right microstructure will lead to desired property (ductility, strength, fatigue, corrosion resistance, etc.) in the right location of the components. Focused collaborative research thrusts have been established to develop local property modification strategies for each targeted metal system: high-strength Al sheet, Al castings, and Mg castings. Figure II.1.2.1 provides a brief description of these thrusts and how the principal manufacturing methodologies interact, as well as transition to higher TRLs. Within those thrusts, individual projects explore and develop the science and process engineering to create spatially tailored properties in alloys and assemblies of target metal systems. A fourth, crosscutting thrust provides overarching support in testing, characterization, and modeling.

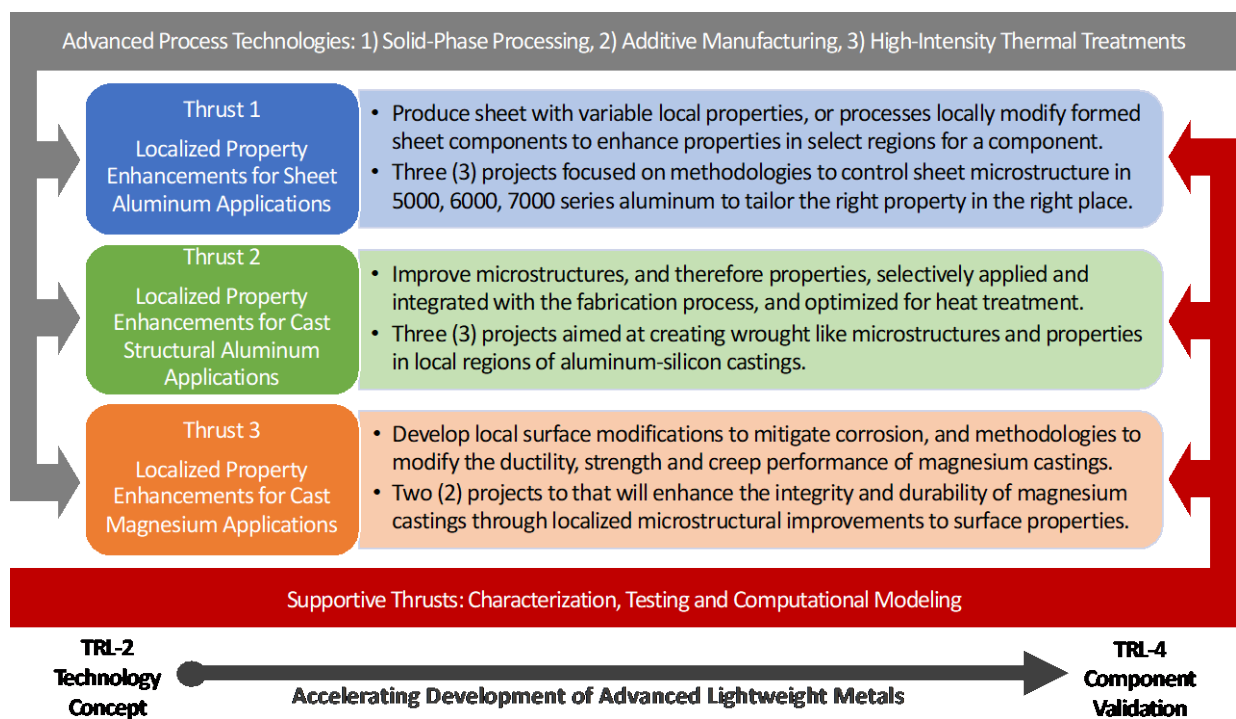


Figure II.1.2.1. Thrust and project structure of the LMCP. Source: PNNL.

The following report describes the FY 2023 technical efforts and results of Thrust 2, “Selective Processing of Aluminum Castings.” Al-cast parts offer excellent opportunities for vehicle lightweighting, a reduced part count, and lowered assembly costs. However, there are science and engineering challenges with the application of castings in automotive body/chassis structures, including local ductility in the regions where castings are attached to other structures; fatigue in stressed members; and the sometimes-inverse relationship between castability (fluidity) and strength. To enable further integration of lightweight castings into the body-in-white (BIW), this thrust proposes to develop processes to locally modify cast parts so single castings can satisfy the varying property requirements at different locations of the component.

Cast microstructures are inherently less homogeneous than the wrought materials, and their properties (e.g., fatigue, fracture performance, ductility, strength) are usually defined by local microstructural characteristics, such as porosity; second-phase distribution and morphology; and dendrite size and morphology. Castings are especially prone to durability challenges due to near-surface microstructural inhomogeneities. Through the development of manufacturing approaches to locally customize, optimize, and/or repair microstructures in the component to meet specific application performance requirements, it will become possible to consider Al castings for a much wider range of applications and to reduce wall thicknesses in existing cast parts to enable additional weight-savings. In addition, local thermomechanical processing (TMP) may be able to bring alloys with high impurity content, like those with a high-content of recycled feedstock, back to high property levels needed by designers.

HPDC Al alloys provide a potential route to achieve lightweighting by using a large, thin wall and intricately shaped castings as structural members in a car body, replacing multiple joined structures and assemblies with single complex castings. However, for HPDC components to reliably perform as structural members, they need to demonstrate a good combination of strength, ductility, fracture toughness, and in certain situations, energy absorption and/or high-fatigue properties. Most general purpose HPDC Al alloys contain a dendritic microstructure, acicular Si particles, and intermetallic compounds (β -FeSiAl (FeSiAl₅), Al₁₅(MnFe)₃Si₂, etc.) that negatively impact the strength and ductility of HPDC Al alloys, hampering their acceptance as structural car body components [1], [2]. Work in Thrust 2 addresses these challenges by investigating TMP techniques, such as FSP and power ultrasonic surface processing (PUSP) to locally alter the microstructure of HPDC components, remove casting defects, and help achieve better mechanical properties.

In recent DOE-funded research, the front and rear subframes in a multimaterial lightweight vehicle were designed to be produced from cast-Al welded to extruded Al sections [3]. In the same work, the rear control arms were designed to be made of cast-Al [4]. However, as-cast microstructures are typically dendritic, are inherently less homogeneous, and may contain porosity resulting in lower mechanical performance when compared to wrought materials. Some enhancement in the as-cast properties can be achieved through microstructural refinement by increasing the local cooling rate (e.g., by using chills) and/or enhancing the nucleation rate in the melt (e.g., by adding grain refiners). However, the use of chills is not always practical and grain refiners are limited in how small of a grain size they can efficiently produce. Furthermore, castings are often heat-treated to achieve high-strength. However, heat treatments that require solutionizing at elevated temperatures are not always feasible in cases where the presence of entrapped gas porosity can create blistering, such as in HPDC.

AM offers unique advantages compared to the casting of components, including generally faster cooling rates to achieve more refined microstructures and improved properties, as well as a broader range of geometric freedom. However, using AM to create a large quantity of monolithic structures would be significantly more costly and time-consuming compared to casting the same parts. The Thrust 2 Cast-and-Print project looks to combine the economic benefits of casting with AM by selectively using AM to locally modify geometry or chemistry of cast parts. This approach is significantly different from existing additive techniques, because the ‘substrate’ for the AM process is not discarded after printing due to being an actual part. Thrust 2 endeavors to overcome many of the challenges limiting greater use of Al castings in automotive structures. While Al casting technology is well-developed, many scientific and technical challenges remain, and performance improvements are possible that can enable greater weight-savings, fewer separate parts, more recycled content, and lower embedded carbon in vehicle manufacturing and end-use.

Objectives

Thrust 2 will seek to enhance the local properties in cast-Al components through three projects: (1) using FSP or PUSP to create local regions of an improved microstructure that exhibit better fatigue performance, and to fix locally defected microstructures at cold shots or in locations where die filling is challenging; (2) using an integrated high-intensity thermomechanical approach that combines ultrasonics, Joule-heating, and high-pressure water jet peening (WJP) to modify local microstructures for enhanced strength, fatigue resistance, and

ductility; and (3) using an AM cast-and-print process to locally improve microstructures and/or add structural features.

Thrust 2 consists of three individual projects, as shown in Figure II.1.2.2. Project 2A is a collaborative project between PNNL and ORNL (e.g., 2A1, 2A2) investigating FSP and PUSP to locally improve the strength, ductility, and fatigue performance of HPDC Al alloys in thin-walled castings. Project 2B (PNNL) focuses on high-intensity thermomechanical and thermal treatments to improve the properties of thicker wall (e.g., > 2 mm) Al structural castings, and Project 2C (ORNL) focuses on using AM to make cast parts with local AM additions.

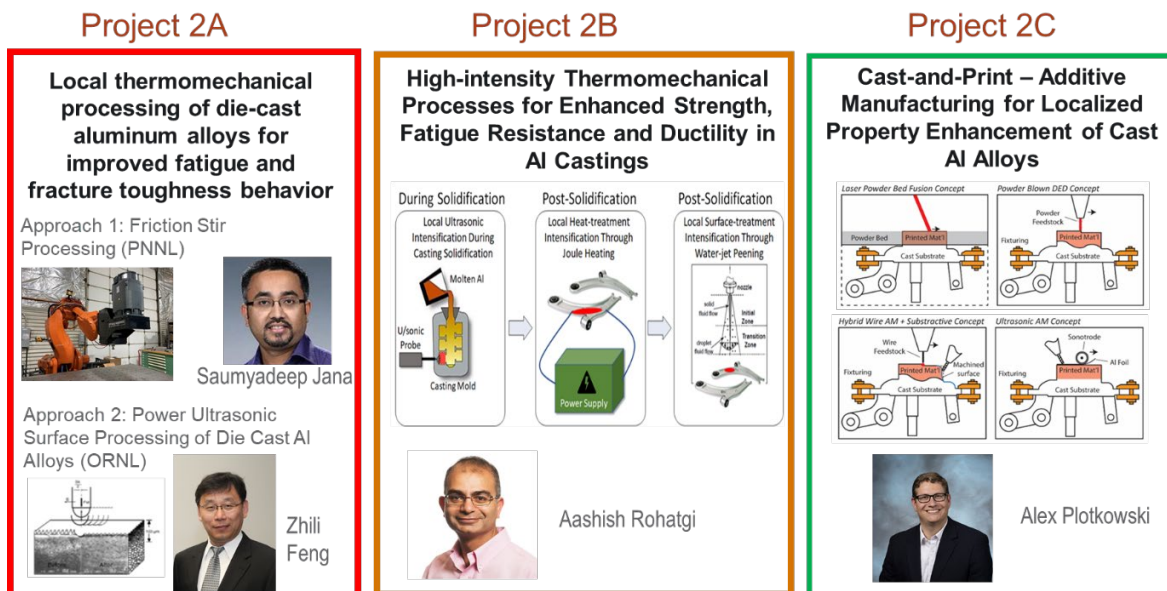


Figure II.1.2.2. Three projects within the LMCP Thrust 2. Source: PNNL and ORNL.

Project 2A1 – Solid-Phase Processing of Al Castings (PNNL)

This research investigates the effectiveness of FSP, a thermomechanical processing method that can be applied at the areas of interest in a cast component to locally modify the microstructure of thin-walled HPDC Al alloy plates. FSP can efficiently modify the microstructural properties of cast-Al alloys [5]. During FSP, a rotating tool imparts severe plastic deformation on the workpiece material resulting in complex material flow and mixing [6] that helps to eliminate porosity, refines the cast microstructure, and elevates the performance of cast materials. An FSP method has been developed for thin wall (e.g., 2.5–3.5 mm thickness) HPDC Al alloys, and mechanical performance has been determined through coupon-level testing. Two kinds of HPDC Al alloys were used in this study: (i) high-iron (Fe) containing A380, and (ii) low Fe containing Aural-5, respectively.

The overall objective of this research is to demonstrate that FSP can be an effective material processing method that can help in improving mechanical performance at the areas of interest, and thus, can enable the use of HPDC Al alloy cast components as structural members in a car body.

Project 2A2 – Power Ultrasonic Surface Processing of Die-Cast-Al Alloys (ORNL)

The goal of Task 2A is to explore and develop PUSP technology to enhance surface properties of cast-Al alloys for autobody structures. Specifically, R&D activity focuses on: (1) near-surface local property enhancement at critical regions, such as load transfer locations, high-stress locations, and stress concentration points within complex die-cast components; and (2) lower-load, one-sided surface processing to improve the local microstructure of thin wall complex geometries, such as difficult to reach locations in die-cast components.

Project 2B – High-intensity Thermomechanical Processes (PNNL)

The goal of this work is to develop approaches to locally modify and enhance the mechanical performance of Al castings. The project objectives are (1) to improve the local tensile strength and ductility of cast-Al alloys, and (2) to increase the local fatigue life of cast-Al alloys.

Project 2C – Cast-and-Print - AM for Localized Property Enhancement of Al Castings (ORNL)

The objective of the cast-and-print task is to develop processing capabilities and understanding of process-property-structure relationships for AM material deposited to locally modify surfaces of cast-Al parts.

Theoretically, established high-throughput casting manufacturing processes can be used to make the bulk of a cast-structure, with AM being used to add value to parts by manufacturing complex geometries or locally enhanced properties due to relatively high-cooling rates of AM. Because there have been limited practical demonstrations of such an approach [7], [8], [9], this task aims to demonstrate the associated possibilities and challenges. Specifically, the deposition and testing of “rivet tabs” (e.g., material deposited as surface to use for joining via riveting) on a thick HPDC plate was demonstrated.

Approach***Project 2A1 – Solid-Phase Processing of Al Castings (PNNL)***

In FY 2021 and FY 2022, FSP was performed in a gantry system on a flat plate geometry for two HPDC alloys (i.e., one recyclable grade high Fe A380 alloy and one premium grade low Fe Aural-5 alloy). Our research demonstrated the effectiveness of FSP in a gantry system by generating a porosity-free wrought microstructure with the refinement of detrimental phases. FSP-driven microstructure refinement demonstrated improvement in tensile ductility and YS for both materials. A simultaneous increase in strength and ductility led to better fatigue performance and fracture toughness, thereby enabling better crashworthiness.

In FY 2023, the project goal was to extend this process to a robotic platform to enable the processing of a 3D geometry to be effectively included in an automotive assembly line. Initially, 1-pass and 2-pass FSP trials were performed on HPDC A380 alloy on flat plate geometry to show the feasibility of FSP on a robotic platform, as indicated in Figure II.1.2.3. Those trials used an ABB Robotics IRB 7600 industrial robot to demonstrate a combination of linear welds and corner welds with two different curvature radii of 50 mm and 30 mm. During the weld traverse direction change, the robot head was able to adjust the tilt angle. The microstructure at the corner regions was consistent with the linear segments without any additional line defect or flash formation. Later, the focus was to demonstrate FSP on an actual HPDC 3D-profiled part with a complex geometry. A profiled automobile structural HPDC Aural-5 alloy component was acquired from Magna International, Inc. The front and back side of the 3D component is shown in Figure II.1.2.4. Small rim structures (1,2,3,4) were machined off for more accessible backing plate support. After machining, the part was sand-blasted for a good surface finish.

Multiple front and back grooves and rim structures have limited the accessibility of the backing plate. In addition, the locations for clamping were not flat, which made it difficult to secure the part before processing. Several small pieces of the metals were placed intricately to ensure the desired processing location has backing plate support and the cast-structure does not bend during processing. A small tilting is applied to the whole cast-structure to ensure the desired processing location is flat. Multiple clamps were employed to flatten the process location. FSP trials were performed using a 12-mm shoulder diameter tool with a 2-mm tool pin length. After a few trials, successful FSP regions were fabricated (FSP 4,5,6,7) on the 3D-profiled part at 1200 revolutions per minute and a 0.1 m/min welding speed. No visible line defect or significant flash formation was observed in the processed regions.

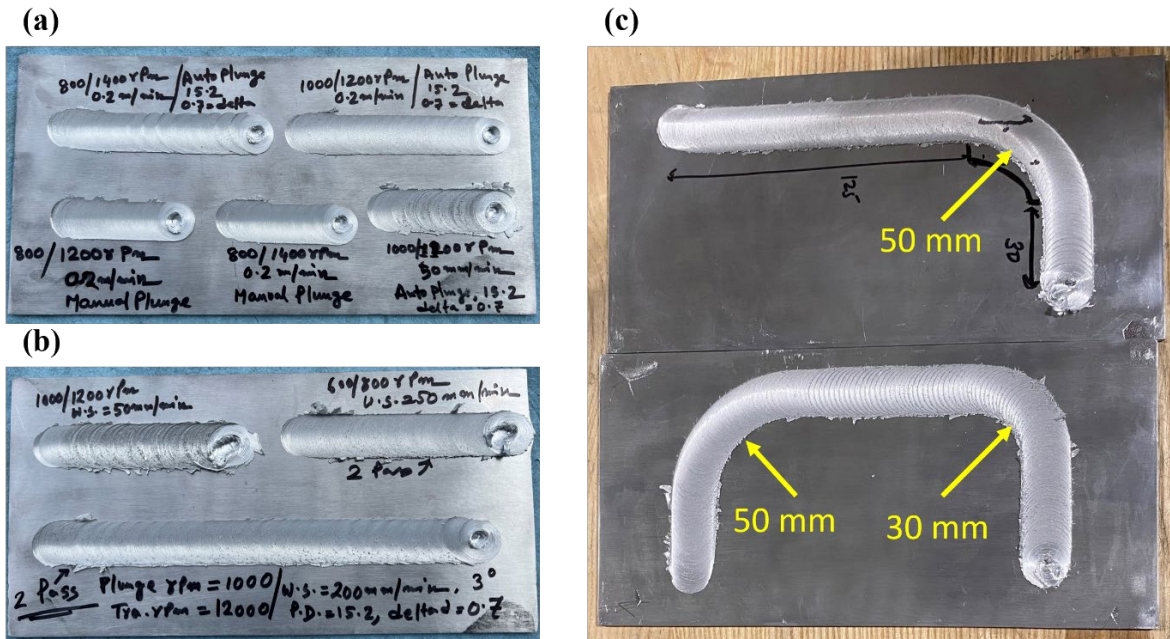


Figure II.1.2.3. FSP trials on the ABB industrial robot: (a) 1-pass; (b) 2-pass; (c) corner FSP with a different radius. Source: PNNL.

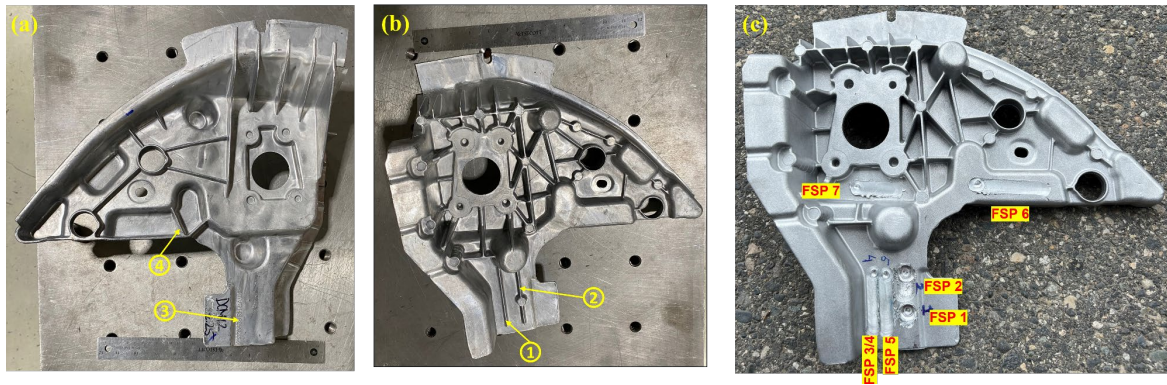


Figure II.1.2.4. HPDC 3D profiled part (Aural-5) from Magna: (a) front side, (b) back side, and (c) seven different FSP regions. Source: PNNL.

An X-ray based technique was developed for nondestructive detection of defects within an HPDC 3D-profiled part. X-ray radiography was performed to detect underlying defects within a location in an HPDC part before and after FSP to show the defects were eliminated by FSP.

Project 2A2 – Power Ultrasonic Surface Processing of Die-Cast-Al Alloys (ORNL)

The PUSP method is a relatively new concept that is in the preliminary stages of development. The underlying physics of PUSP suggest it has the potential to achieve local near-surface microstructural modifications at low normal loads to the part surface, which will be essential for single-side processing in some complex-shaped automotive body components, particularly thin wall die-cast components that may be prone to deformation at higher normal loads. The second potential advantage of PUSP is its ability to create compressive surface residual stresses. It is well-known that compressive surface residual stress induced by laser shot peening has led to significant improvement of fatigue life of Al alloy structures for aerospace applications. The advantage of PUSP over shot or laser peening is that it also significantly modifies the subsurface microstructure, including porosity.

The purpose of this task is to explore and develop PUSP technology to improve local properties of cast-Al alloys for auto-body structures. Specifically, the task is pursuing understanding of how surface property enhancements of die-cast Al imposed by surface treatment with power ultrasonics can enable increased durability and fatigue life. During PUSP of the surface, highly localized heating and severe plastic deformation occur, which closes solidification porosity, refines the microstructure, and generates compressive residual stresses within a specific volume determined by processing conditions and material properties. In addition, the acoustic plastic softening effect is being investigated to reduce the required process load for one-side processing of thin wall or difficult to reach surfaces, thus enabling integration with robotic auto-body structure-assembly systems.

This subtask employs both experimental process development and physics-based computational simulation methods. The multiscale modeling effort is designed to support process development by simulating heat generation, plastic deformation, and residual stresses, as well as the resulting microstructure, residual stress affected by PUSP, and enhanced durability or fatigue life of body-structure components.

The physics-based computational modeling framework integrates three types of analyses leading to the prediction of the fatigue life of parts that have been locally treated by PUSP. First, a previously developed ultrasonic joining process model [10] was refined and applied to ultrasonic processing by means of the thermomechanical finite element method (FEM). The process model is being applied to determine the effects of sonotrode geometry and processing conditions to impart surface deformation and vibrational heating. Transient temperature, plastic strain, and stresses from the process model are used as inputs for future recrystallization and microstructure simulations. Fatigue performance simulations are being used to connect the process, microstructure changes, and residual stresses to the improvement in fatigue life by ultrasonic processing.

Project 2B – High-intensity Thermomechanical Processes (PNNL)

This project is divided into three main tasks where each task will develop a different processing approach that may be used to improve the local properties of cast-Al automotive components at various stages of the manufacturing process. The first task will enhance the initial casting stage by applying local ultrasonic intensification during casting with the goal of refining the as-cast microstructure. Ultrasonic-induced microstructural refinement has been attributed to mechanisms such as enhanced heterogeneous-nucleation and the fracture of dendrites [11], [12], [13], [14] and the ultrasonically refined microstructure is expected to improve the as-cast strength, ductility, and fatigue life of the casting [15]. The second task will enhance the heat-treatment stage by applying local thermal intensification with the goal of strengthening the as-cast microstructure. Thermal intensification will be applied through Joule-heating and is expected to accelerate atomic-scale diffusion processes, which will decrease the time and/or temperatures required for post-solidification heat treatments. The third task will enhance the surface-treatment stage by applying local WJP to impart deep residual compressive stresses, which are expected to improve the fatigue life of the casting. In industrial practice, one or more of these three techniques could be applied to produce high-performance Al castings where the local properties have been enhanced to meet the local property requirements.

During FY 2023, the primary focus of this work was to demonstrate how the techniques being developed in this work could be applied in industrial practice. Accordingly, the goal of Task 1 was to demonstrate casting in a preheated steel mold with a simultaneous application of ultrasound. In Task 2, the goal was to demonstrate a local Joule-heating approach on a production cast-Al component. Finally, the goal of Task 3 was to demonstrate an improvement in fatigue life through local WJP of an HPDC Al plate.

For Task 1, the ultrasonication approach during casting was initially developed in this project using graphite molds, which are relatively cheap, easy to use, and simulate cooling rates associated with preheated permanent steel molds used in commercial casting. This initial developmental work was expanded to demonstrate the application and suitability of the ultrasonic casting approach to preheated steel molds as well. A356 Al was melted and heated to 725°C and cast in a cylindrical steel mold preheated to 350–400°C. Samples were cast

with and without ultrasound. The resulting microstructures and ultrasonic-induced refinement were characterized using OM. EBSD was used to quantify grain size.

Task 2 efforts in FY 2022 on coupon-scale samples had demonstrated the ability of Joule heat-treatment to increase the local strength in an HPDC Al plate by ~13% (relative to the as-cast) [16]. Efforts in FY 2023 focused on the demonstration of local Joule-heating on an actual size cast-Al part. An Al alloy control arm casting, as observed in Figure II.1.2.5, was provided by Eck Industries for the demonstration experiments. The casting was clamped between graphite electrodes at a location adjacent to the bushing holes. This region was selected due to its potential to be a region of stress concentration in actual use of the control arm and the ease of making an electrical connection due to its flat surface. The entire casting was coated with a HT black paint for thermal camera temperature measurements, except the locations where electrodes touch the sample. The casting was electrically connected by the electrodes from either side as shown and then Joule heated by passing electrical current. The temperature over the casting surface was measured using a Fluke Ti480-Pro infrared thermal camera.

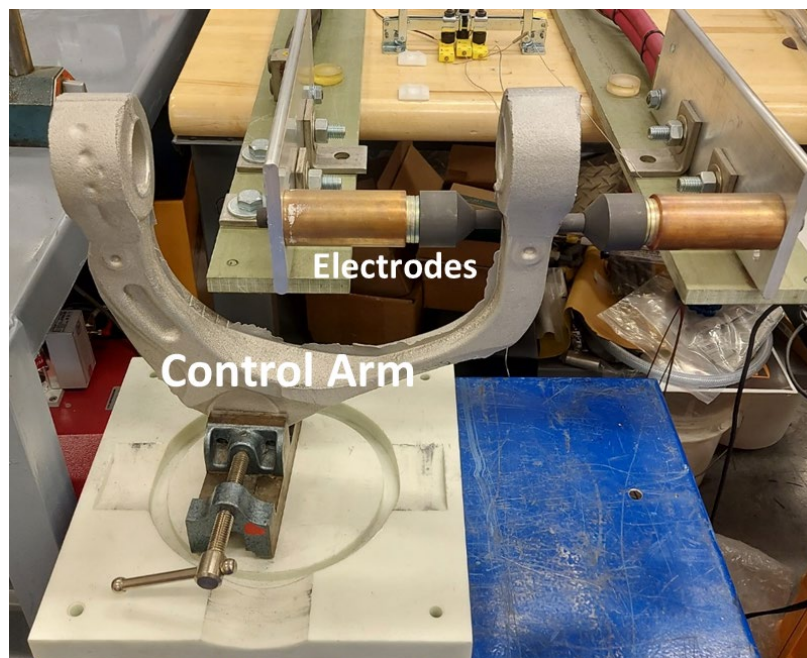


Figure II.1.2.5. Photo of the Joule-heating setup and Al control arm held between the electrodes.
Source: PNNL.

In Task 3, HPDC A380 plates were processed by WJP, and their fatigue life evaluated in a 4-point bend test configuration. The plates, peened identically on both sides via three peening conditions labeled A, B, and C, were used that qualitatively corresponded during peening to fast, medium, and slow traverse speed, respectively. Rectangular fatigue specimens were machined out from the untreated and peened plates and fatigue testing was performed at three stress levels at 10 Hz frequency and a stress ratio of $R = 0.1$. Notably, the fatigue specimens were tested with an as-peened surface finish (i.e., their surface was not polished after peening). In addition, through-thickness residual stresses in the HPDC plates were measured using the hole-drilling method on a Stresstech Prism 3 system.

Project 2C – Cast-and-Print - AM for Localized Property Enhancement of Al Castings (ORNL)

To manufacture parts, a laser hot-wire AM system, the Mazak VTC-800G, was used to deposit wire-feedstock. Because the Mazak VTC-800G is a hybrid manufacturing system, the machining capabilities of the system were also used for achieving a machined surface finish on the final geometries.

After discussions with Ford Motor Company, the deposition of a locally modified geometry and composition to use for rivet joining of thick HPDC plates was found to be a useful demonstration. Due to the relatively high-strength of HPDC alloys compared to other cast materials, riveting through thick regions can be difficult to accomplish without the formation of defects. The characterization of various deposited alloys was completed in FY 2021 and FY 2022, and the results were used to select a material to use for deposition on the HPDC substrate. Figure II.1.2.6 shows the stress-strain curves of three tested alloys—Al 4043, Al 4047, and Al 5356—as compared to measurements of HPDC Aural-5S from Guo et al. [17]. The Al 5356 alloy had the highest ductility, which was determined to be a benefit for subsequent processability via riveting [18]. Therefore, the rivet tabs were manufactured using Al 5356 wire deposited on a 4.4-mm-thick Aural-5S plate in an as-cast condition.

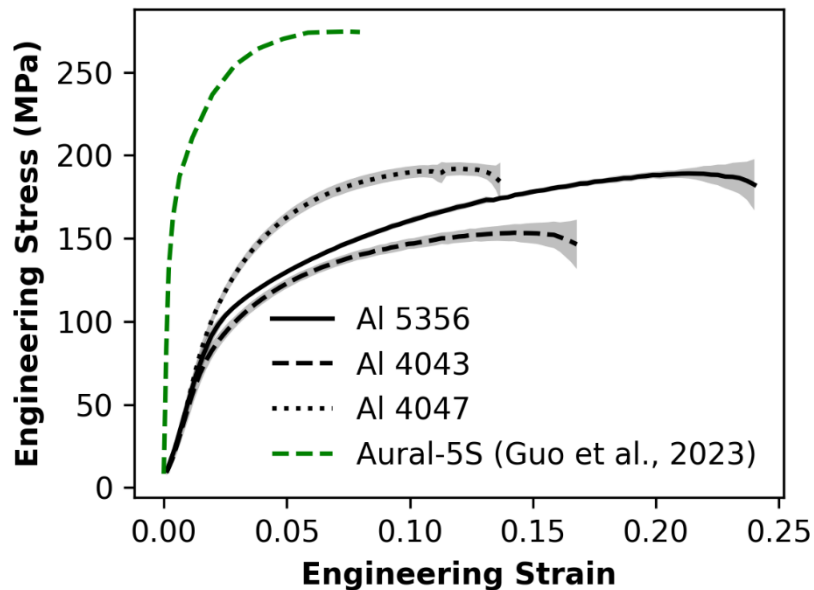


Figure II.1.2.6. Stress-strain curves from five SS-J3 subscale tensile tests with black lines showing the average and the gray regions showing one standard deviation. Aural-5S data from Guo et al. [17] is overlaid. Reproduced from Knapp et al. [20]. Source: ORNL.

Results

Project 2A1 – Solid-Phase Processing of Al Castings (PNNL)

A microstructural examination was conducted at the FSP-6 region to check for porosity and other microstructural features (Si-particle size, shape, etc.). Figure II.1.2.7 captures various aspects of the microstructural changes in HPDC- and FSP-processed regions. Typical dendritic structures bounded by Al-Si eutectic colonies were apparent in HPDC regions. The presence of shrinkage porosity was evident, especially in the middle section of the HPDC region. FSP resulted in wrought microstructure with the closure of casting porosity in the processed region. Refinement and uniform redistribution of Si particles and other phases were evident in the advancing side and middle section. Slight differences in the size and number density of Si particles could be noticed between the advancing side and middle section.

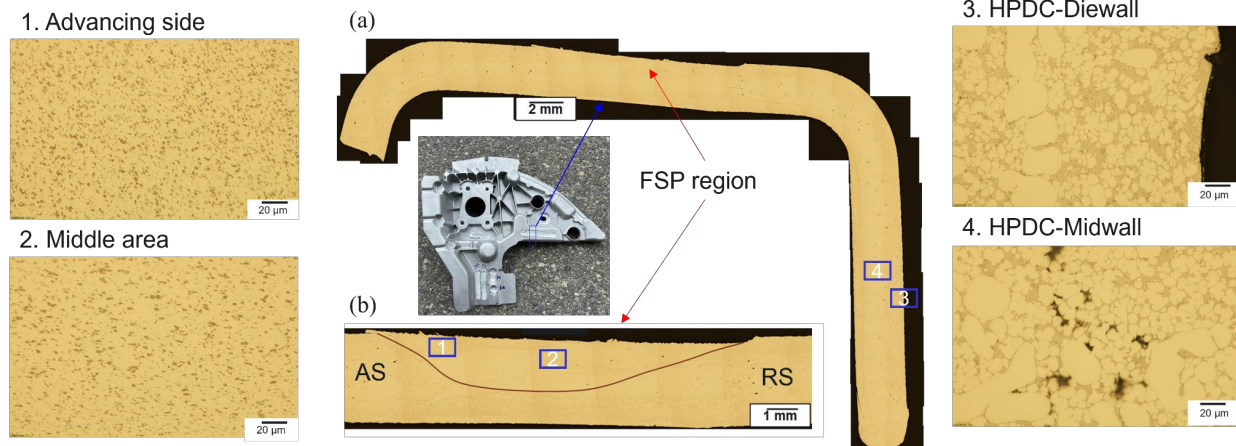


Figure II.1.2.7. Optical images of (a) a HPDC 3D-profiled part in the as-received and (b) FSP-processed conditions in different regions for the advancing side (AS) and retreating side (RS). Source: PNNL.

A specific area of the FSP-processed location was cut from the HPDC Aural-5 part to extract miniature tensile specimens from both the HPDC- and FSP-processed region, as illustrated in Figure II.1.2.8(a). Three miniature-sized tensile specimens were extracted from the process zone along the thickness to locally compare the mechanical properties. After FSP, the percent elongation to failure in the FSP-processed region with specimens from both the die-wall and mid-wall was $16.0 \pm 2.7\%$, whereas the percent elongation to failure in the HPDC die-wall and mid-wall were $10.2 \pm 1.4\%$ and $6.2 \pm 2.9\%$, respectively, as indicated in Figure II.1.2.8(b) and Figure II.1.2.8(c). This corresponds to a 57% enhancement of ductility with respect to the HPDC die-wall and a 160% enhancement with respect to the HPDC mid-wall. However, the YS and UTS has dropped in the FSP-processed regions after processing. Heat-treatment investigation is ongoing to reinstate the YS and UTS at their original values of HPDC and maintaining improved ductility.

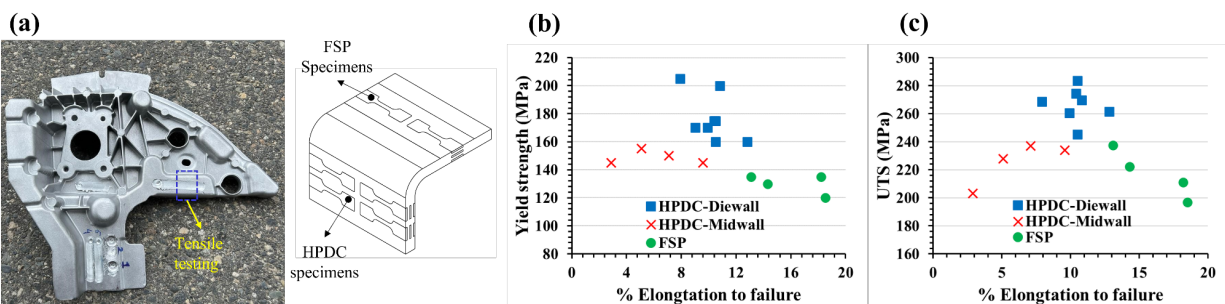


Figure II.1.2.8. Mechanical property characterization on an HPDC 3D-profiled part. (a) Miniature tensile specimen cut from the FSP-processed region. Variation of (b) YS and ductility and (c) UTS and ductility at distinct locations of the HPDC and FSP-processed regions. Source: PNNL.

X-ray radiography was performed on an HPDC 3D-profiled part to detect underlying porosity defects within a specific location, as illustrated in the yellow marked area in Figure II.1.2.9(a). A low-magnification radiograph is illustrated in Figure II.1.2.9(b). Some high-magnification images in location 1,2,3 show bright porosity defects with a size ranging from 300–1300 μm size, as shown in Figure II.1.2.9(c–e).

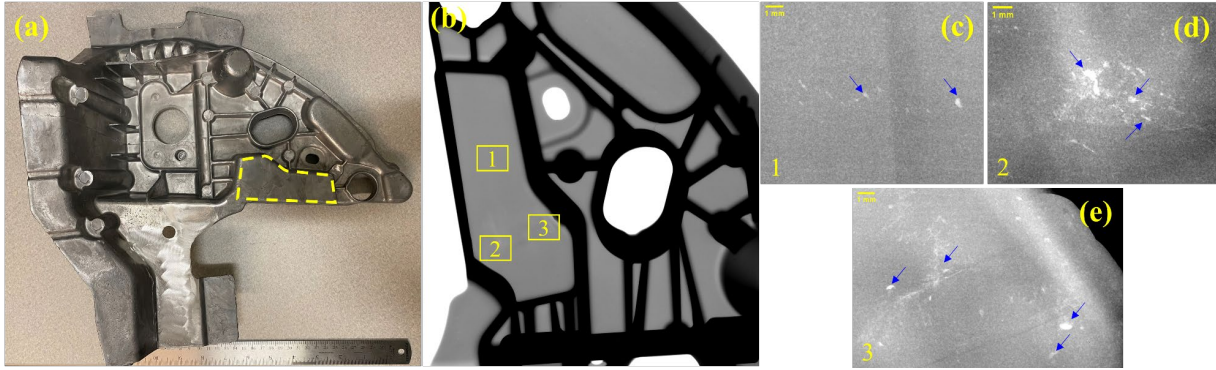


Figure II.1.2.9. Nondestructive defect analysis of the HPDC Aural-5 part. (a) HPDC 3D-profiled part from Magna with location indicating for nondestructive radiography. (b) Low-magnification radiography image of the locations. (c-e) High-magnification image of location 1,2,3 showing the defects. Source: PNNL.

Following FSP, a cut-off sample shown in Figure II.1.2.10(a) from the same location was subjected to radiography analysis. High-magnification radiography images did not show similar bright porosity defects as the HPDC parts, as illustrated in Figure II.1.2.10(b) and Figure II.1.2.10(c). This shows that FSP can eliminate the porosity defects from the HPDC parts. However, there are some black marks detected in the FSP-processed region, as marked by yellow arrows. Further investigation is ongoing to characterize those marks.

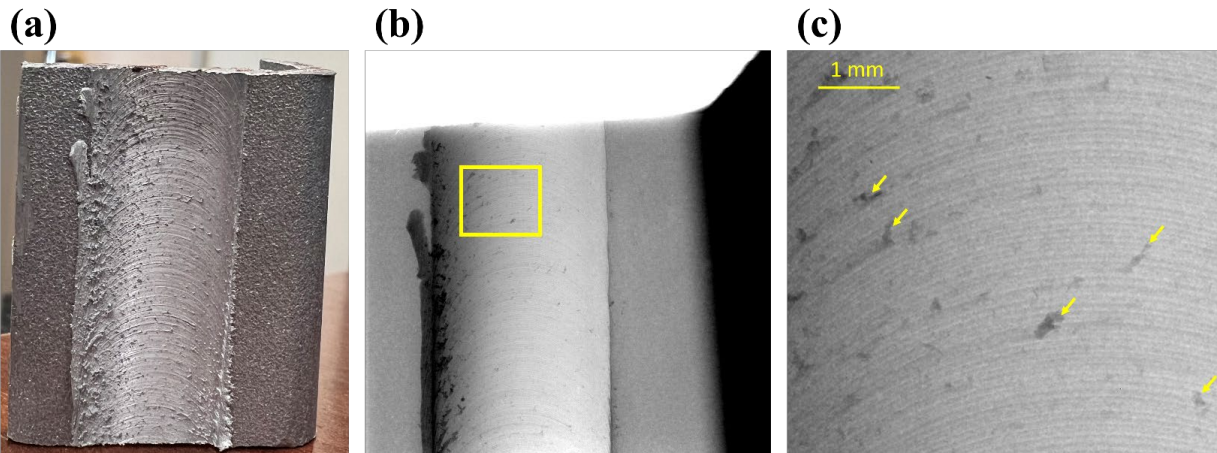


Figure II.1.2.10. Radiography analysis of FSP-processed location. (a) FSP-processed location. (b) Low-magnification radiography. (c) High-magnification images of the location. Source: PNNL.

Project 2A2 – Power Ultrasonic Surface Processing of Die-Cast-Al Alloys (ORNL)

The R&D in FY 2021 and FY 2022 demonstrated the promising benefits of PUSP to improve the fatigue life and durability of thin-walled HPDC Al alloy A380 and Aural 5 through: (1) significant near-surface microstructure refinement, and (2) introducing compressive surface residual stresses. More importantly, we were able to reduce the PUSP process load to only 250–300 lbs. This is essential for future single-side localized processing of thin wall complex-shaped cast-Al component surfaces with a robotic system. The R&D in FY 2023 focused on: (1) further reducing the process load for industry robotic applications, and (2) demonstrating the process on an actual complex geometry automotive die-cast body component donated by GM.

Figure II.1.2.11 shows the HPDC autobody component received from GM. This was a rail cast from Aural 5, which was one of the Al-cast alloys selected for study in this Task. As shown in Figure II.1.2.11, the large piece is approximately 4-ft-long and 2.5-ft-wide, with several intricate details. The wall thickness of the part is

3–5 mm, which would be a reference prototypical component for our R&D. We selected three locations that would benefit from local property improvements (e.g., the stress concentration locations or stress transfer pieces). We note that all these locations would be processed by one-side PUSP, without any backside support, due to the low-load levels of PUSP.

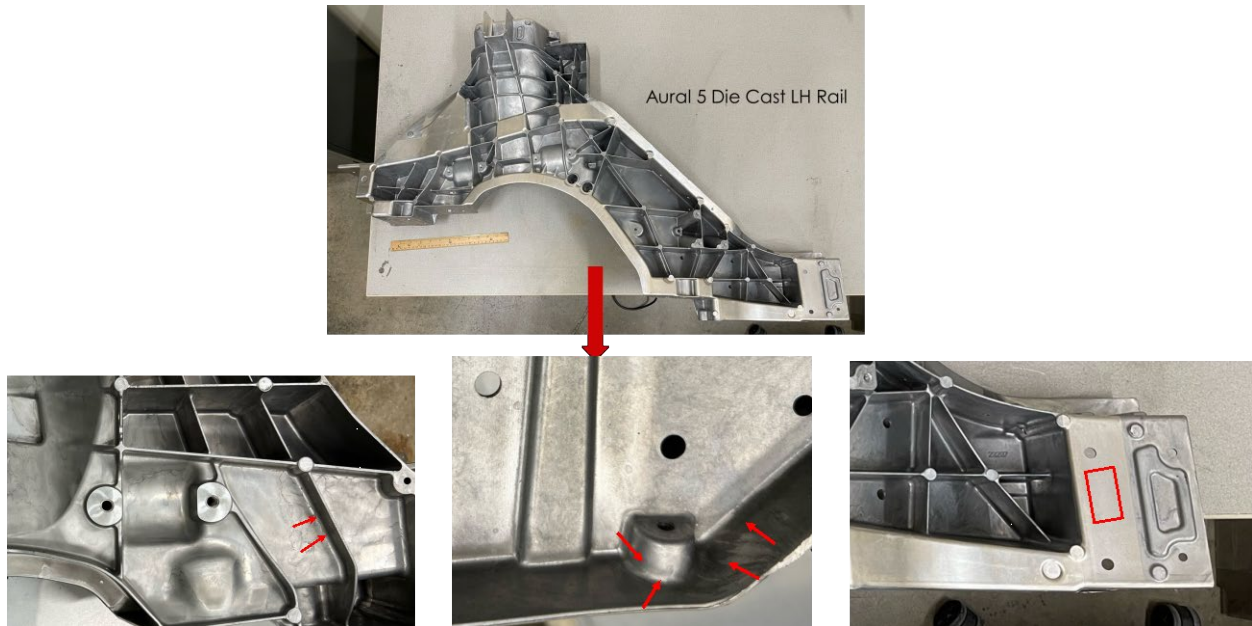


Figure II.1.2.11. A HPDC auto-body component for demonstration of single-sided PUSP for local property improvement. Source: ORNL.

We then conducted FEM simulations of the PUSP on these three identified locations on the cast rail to determine the PUSP process conditions necessary to achieve the benefits of compressive surface residual stress and near-surface microstructure refinement.

Figure II.1.2.12 shows one of the FEM models used to simulate the PUSP process and understand the associated load requirements. This model corresponds to the flat flange location of the component. The modeling results show it is possible to process the identified region with a relatively low downward processing load at 100 lbs., and process power in the range of 100–300 W. Under these processing conditions, the structural rigidity would be sufficient to sustain the process load without additional backside support.

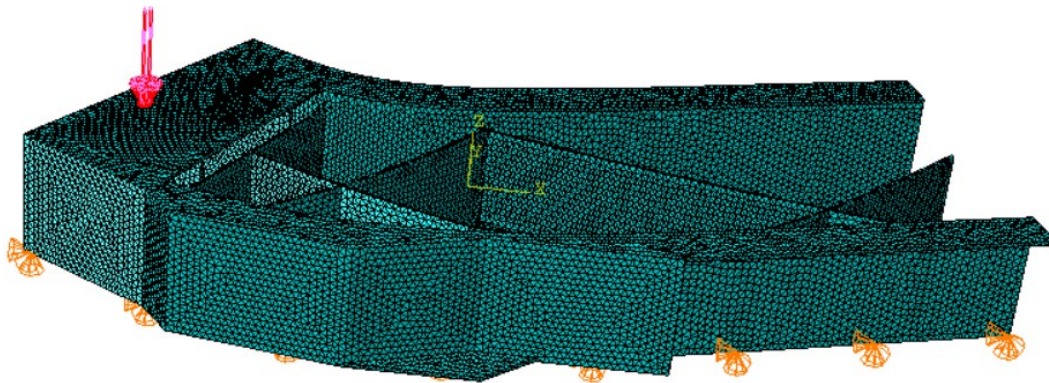


Figure II.1.2.12. A FEM model showing the simulation results for the prototypical HPDC part with a load transfer location as marked by the red arrow on its flange. Source: ORNL.

We then conducted more detailed PUSP simulations to further optimize the process conditions with the goal of single-sided processing. The results are given in Figure II.1.2.13. We applied ORNL's in-house Dr-Weld high-performance computing code, which explicitly enables simulation at every vibration cycle of the 20 kHz PUSP over the entire process. The results suggested it is possible to reduce the process load to a static load of 18 N (4 lbs.) with a dynamic load range less than 600 N (140 lbs.) that still enabled significant compressive residual stresses in the stress concentration region of the part.

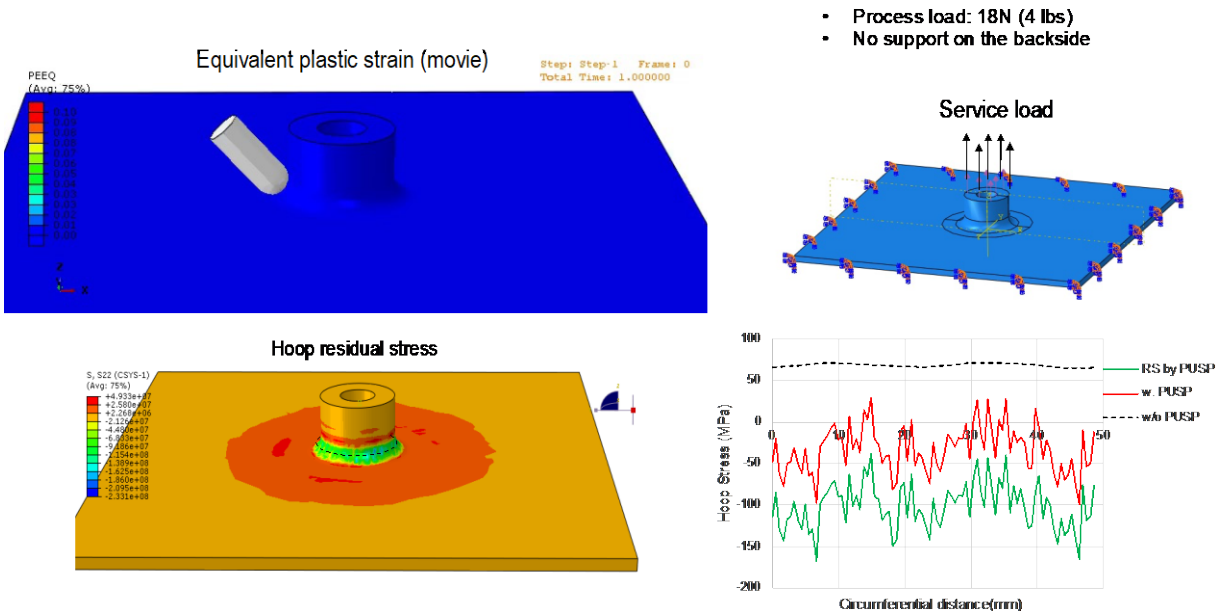


Figure II.1.2.13. A detailed FEM model to simulate PUSP to locally process the stress concentration region and results for the hoop stress as a function of the circumferential distance. Source: ORNL.

Accordingly, it was decided to build a fixture to support the entire component in Figure II.1.2.11 and allow one-side access and processing of the three representative locations. The fixture system is being fabricated with delivery delayed to Q1 FY 2024. The revised projected completion date for completing the PUSP demonstration on the prototype part is anticipated to be December 2023.

Project 2B – High-intensity Thermomechanical Processes (PNNL)

Task 1: The average cooling rate during casting in a preheated steel mold was $\sim 1^\circ\text{C/s}$, which is similar to the cooling rates associated with permanent mold casting techniques (~ 0.1 to 1°C/s) and is slightly slower than the average cooling rates when casting in a graphite mold [19]. As reported previously for experiments in graphite molds [16], the application of ultrasound transformed the microstructural morphology from dendritic to non-dendritic, which is also referred to as globular in the literature [13], [14], during casting in the steel mold as well, as shown in Figure II.1.2.14.

The primary Al grains of the globular microstructure (area-weighted mean diameter = $56\ \mu\text{m}$) are 97% smaller than the primary Al grains of the dendritic microstructure (area-weighted mean diameter = $1800\ \mu\text{m}$). Furthermore, the globular grains of the ultrasonicated casting were observed throughout the entire cross-section of the casting, at distances up to 2 in. away from the ultrasound probe. This is an improvement over previous experiments that cast in a graphite mold, where non-dendritic grains were only observed at distances up to 6 mm away from the ultrasound probe in an alloy with a similar composition. We hypothesize that reducing the cooling rate during solidification, by casting in a preheated steel mold rather than in a RT graphite mold, allowed the ultrasonic field to affect a larger volume of the solidified microstructure. Thus, these results demonstrate the suitability of the ultrasonic technique to improve industrially produced automotive castings that typically utilize preheated steel molds.

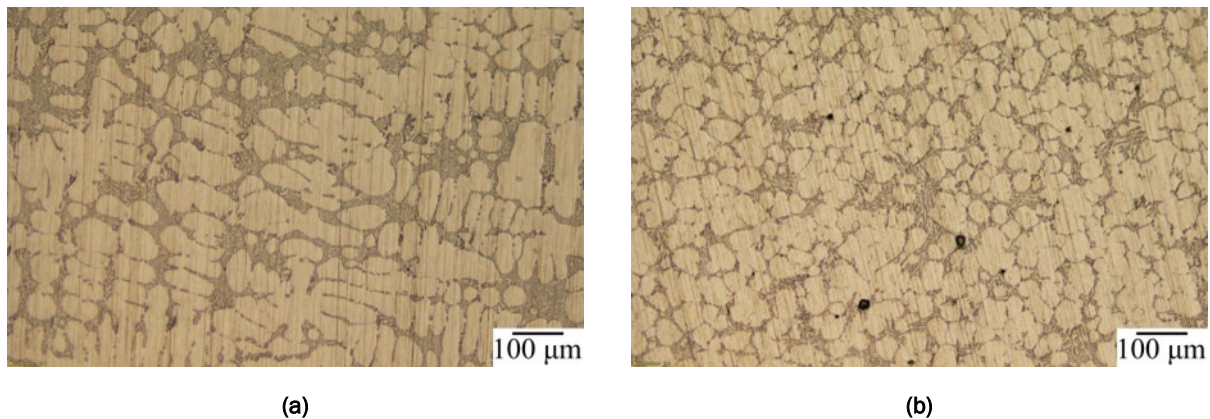


Figure II.1.2.14. Optical micrographs from steel mold castings depict: (a) the dendritic microstructure of the control casting, and (b) the globular microstructure of the ultrasonicated casting. Specimens are etched so the Si phase appears darker than the Al phase. Source: PNNL.

Task 2: Figure II.1.2.15 shows thermal camera images from the locally heated Al control arm. When the current is turned on, a distinctive hot spot develops with almost a comparable size to the electrode contact surface. The temperature distribution on the sample once it had reached the target temperature of 520°C shows the extent of the hot spot and the thermal gradient, as evident by a temperature of ~360°C a few millimeters away from the hot spot. A temperature that is lower by ~160°C from the target location temperature, just a few millimeters away from the hot spot, implies a steep temperature gradient and demonstrates the “local” nature of the Joule-heating approach. The local temperature at the spot, where electrodes were touching the sample, was maintained within +/- 1°C by adjusting the power supply. At the edges of the control arm, the temperature was 294°C at the heated arm and 44°C at the unheated arm. The hot spot disappears instantly when the current is turned off, showing the effectiveness of the Joule-heating approach to rapidly heat/cool a component, and thus, control the local temperature and thermal profile. The temperature around the electrodes and neighboring areas equilibrates to ~350°C. This is likely due to the high-thermal-conductivity of Al, which also helps in obtaining a well-defined local hot spot when the current is flowing.

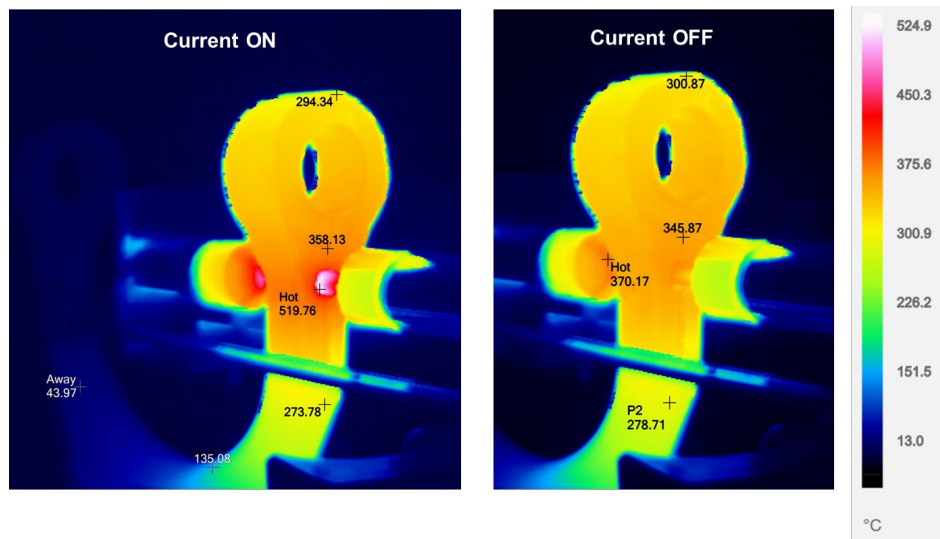


Figure II.1.2.15. Thermal camera images of the temperature distribution on the control arm during and right after Joule-heating. Source: PNNL.

Task 3: Figure II.1.2.16(a) shows fatigue performance, expressed as the number of cycles to failure, for WJP-treated specimens compared to untreated HPDC A380 alloy specimens. The data shows that at an applied stress level of 200 MPa, the WJP-C-treated specimens demonstrated a ~3.4-fold increase in fatigue life as compared with their untreated counterparts. In contrast, the fatigue lives of the WJP-A and WJP-B specimens remained similar to the untreated HPDC A380 alloy. Moreover, the WJP-C specimens, which were assessed at two additional higher stress levels (225 MPa and 250 MPa), consistently displayed improvements ranging from 1.6–2.8 × increase in fatigue life. This increase in fatigue life is attributed to the compressive residual stresses introduced in the HPDC plates by the WJP treatment. As shown in Figure II.1.2.16(b), the WJP-treated specimens exhibited significant compressive residual stresses in the traverse direction (σ_{xx}), with values of 93 MPa for WJP-A, 94 MPa for WJP-B, and 146 MPa for WJP-C. On the other hand, the untreated HPDC A380 material displayed minimal (~20 MPa) to no residual stresses. Irrespective of the peening conditions in A, B, or C, the compressive residual stresses were primarily confined to a depth of approximately 400 μm below the surface. The data, therefore, provides guidance on the level of residual stresses needed to improve fatigue life in HPDC A380 alloy.

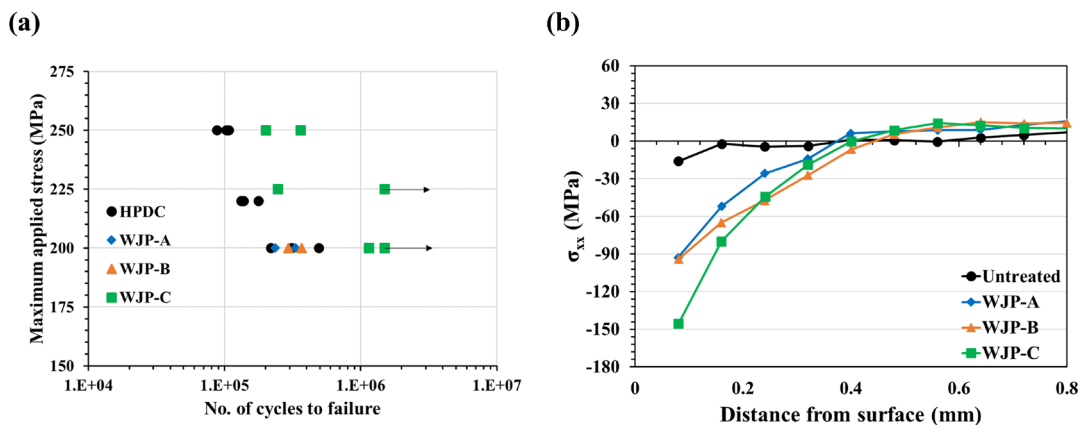


Figure II.1.2.16. Comparison of (a) fatigue life and (b) through-thickness residual stress distribution for three conditions of WJP and untreated HPDC A380 alloy. In (a), the right-pointing arrows next to the WJP-C data points at 1.5e06 cycles imply the test was stopped and the actual number of cycles to failure is greater than 1.5e06 cycles. Source: PNNL.

Project 2C – Cast-and-Print - AM for Localized Property Enhancement of Al Castings (ORNL)

The deposition of the rivet tabs consisted of several stages: an initial process parameter development campaign, deposition with machining of the final rivet tab geometry, characterization of a subset of the rivet tab samples, and finally a test rivet using a friction-stir rivet system. For the process parameter development, work in FY 2022 identified functional deposition parameters for Al 5356 alloy on bulk substrates that were used as a starting point. It was found that additional testing was needed to find a reasonable parameter set based on the change in the substrate. Consequently, the final parameters were slightly different for depositing material on the relatively thin Aural-5S 4.4-mm-plate as compared to the approximately 50-mm-thick A365.2 ingot sections that were used as a substrate in previous experiments.

Notably, the interlayer machining method described in the FY 2022 task report was needed to address oxide formation between layers. The build environment is shielded by an argon gas flow; however, persistent cases of a thin white layer on the surface of the Al, confirmed by energy-dispersive spectroscopy measurements to be a combination of Al and Mg oxides, indicated the shield-gas did not fully prevent exposure of the melt pool to oxygen. Therefore, to overcome this limitation within this preliminary demonstration, between each layer, the milling head in the Mazak VTC-800G system was used to remove a section of the top-most material to have a consistent layer thickness and provide a relatively clean surface for the deposition of the next layer. Without the interlayer machining step, a significant lack of fusion defects was observed.

After a reasonable set of process parameters were found, rivet tabs that were 50-mm-long, 10-mm-tall, and 2-mm-thick were deposited and machined. Two samples were sectioned through the middle of the wall length and metallographic specimens were prepared for the cross-section. Figure II.1.2.17 shows the resulting optical microscopy and HV testing results for the two specimens. In both specimens, the hardness of the deposited material was between 64-72 HV, which was comparable to the base plate hardness of approximately 70 HV. Figure II.1.2.17(a) shows a sample that is largely defect-free, except for a horizontal lack of fusion defect in the wall approximately 1 mm above the top of the substrate. Due to the planar nature of the defect and its vertical location being equal to the offset for interlayer machining, it was likely related to the interlayer machining operation. Figure II.1.2.17(b) shows a sample that had internal lack of fusion porosity that was not visible from the outside of the wall in addition to a similar horizontal lack of fusion defect in the wall just above the top of the substrate. Both the planar lack of fusion defect and the internalized lack of fusion defect indicate that the interlayer machining approach was not able to fully mitigate the detrimental effects of excess oxygen in the shielding gas.

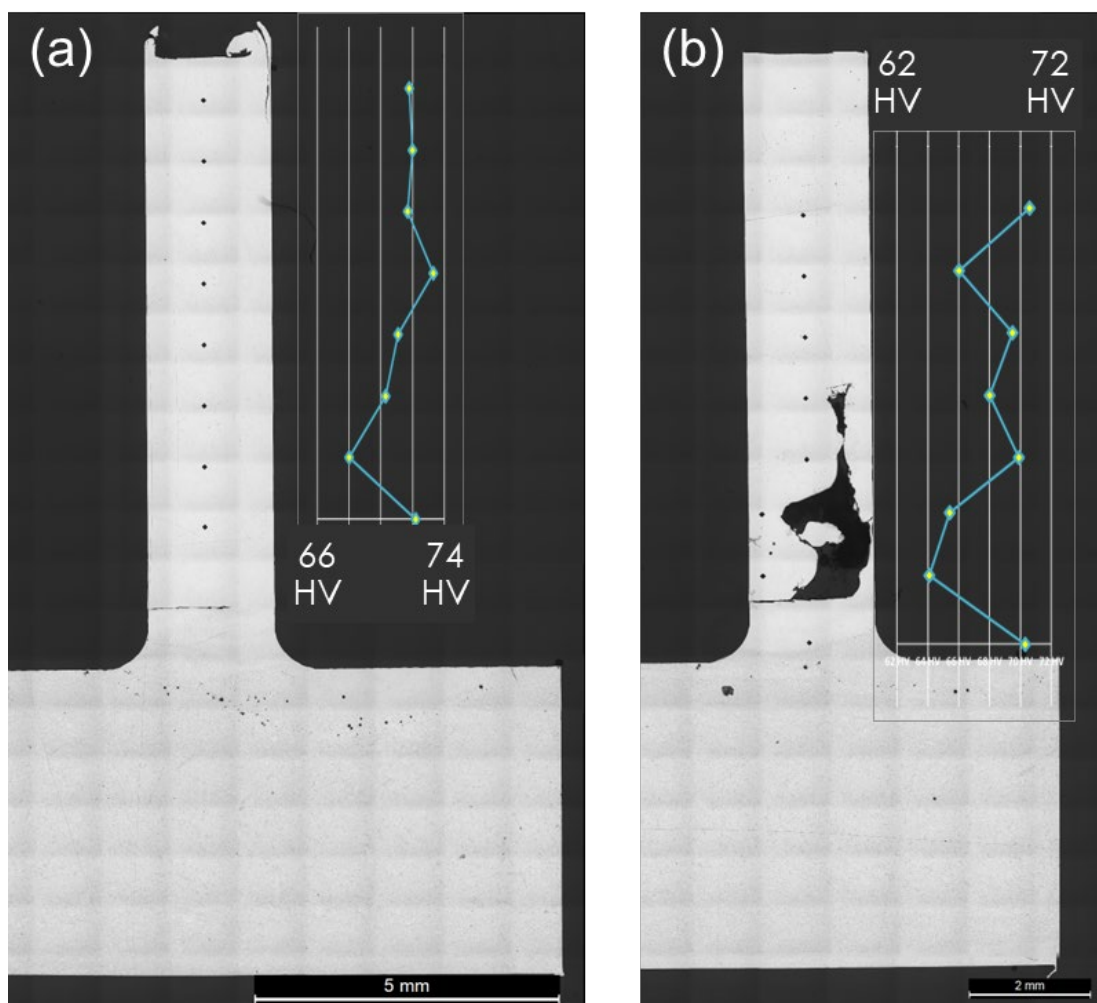


Figure II.1.2.17. Optical micrographs of the cross-section of two rivet tabs made from deposited Al 5356 on a 4.4-mm-thick Aural-5S plate with hardness measurements throughout the height of the wall overlaid.

(a) A sample that is largely defect-free, except for a horizontal lack of fusion defect in the wall approximately 1 mm above the top of the substrate. (b) A sample that had an internal lack of fusion porosity and was not visible from the outside of the wall just above the top of the substrate. Reproduced from Knapp et al. [20].

Source: PNNL.

The remainder of the samples were prepared for riveting in the configuration shown in Figure II.1.2.18(a). The friction-stir rivet system operated by ORNL's Welding and Joining Laboratory was set up using the configuration of the Aural-5S sheet on top of the Al 5356 rivet tab. The rivet tool then lowered, pierced, and stirred the rivet through the Aural-5S into the rivet tab. A result of the riveting process is shown in Figure II.1.2.18(b), which shows several interactions of the defects in the wall with the riveting process. First, the horizontal lack of fusion defect shown in Figure II.1.2.18(b) is fully separated in the location marked by the "interface crack" annotation. Second, the larger lack of fusion porosity, akin to that shown in Figure II.1.2.18(b), appeared to flow around the edge of the zone affected by the stir rivet. Though friction-stir riveting can assist in closing some porosity due to the material flow, in this case the inherent porosity was too significant to be mitigated.

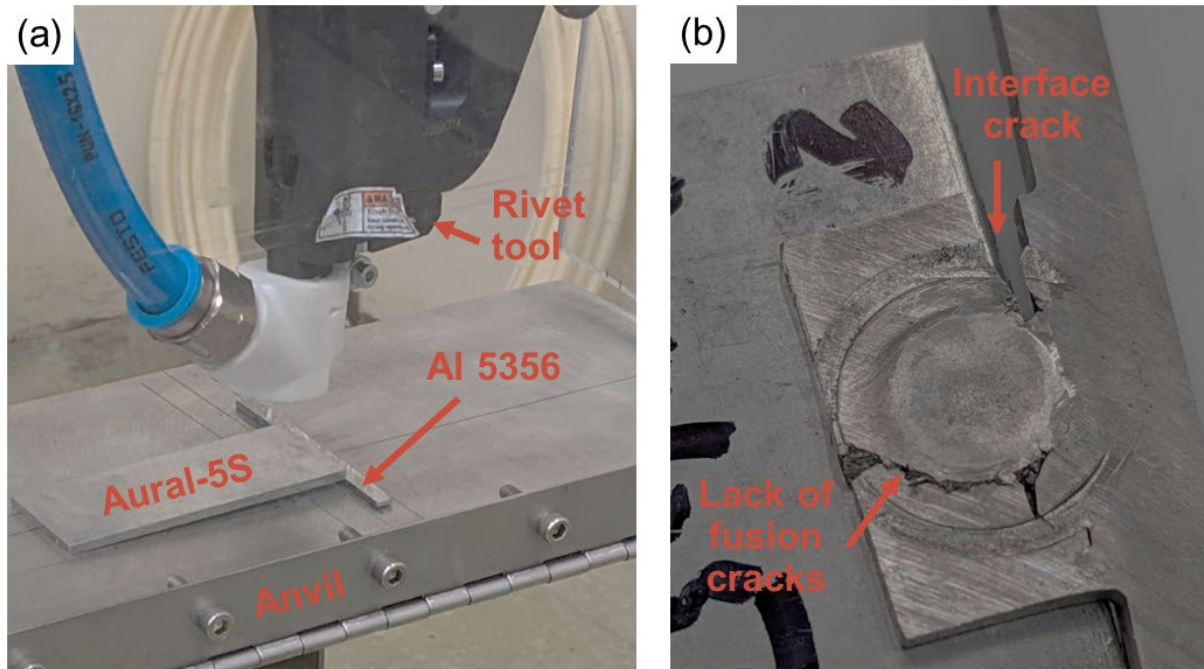


Figure II.1.2.18. (a) Annotated photograph of the set up for rivet testing. (b) Annotated image of the damaged sample after riveting. Modified from Knapp et al. [20]. Source: ORNL.

Conclusions

Project 2A1 – Solid-Phase Processing of Al Castings (PNNL)

During FY 2023, robot-based FSP was developed to process HPDC 3D-profiled parts to enhance their mechanical properties. An ABB Robotics IRB 7600 industrial robot was used for local FSP trials on a flat plate, as well as complex 3D parts. Although successful FSP trials were performed on HPDC 3D-profiled part, there are several challenges that need to be addressed in the future. The following conclusions were reached:

- It is feasible to create linear and curved FSP zones with consistent microstructure, negligible line defect, or flash formation using the robot system.
- To process a complex 3D part, an appropriate backing plate design should be performed to reduce part-bending. Proper clamping needs to be performed to secure the part before processing.
- When FSP is applied to HPDC 3D-profiled parts, improvement in tensile ductility is noted. Microstructural examination of the FSP condition reveals refinement and homogeneous distribution microstructural phases, which enhanced tensile ductility.
- Nondestructive x-ray-based radiography can be a valuable tool to detect defects in complex 3D castings to provide information about the locations where FSP needs to be performed.

Project 2A2 – Power Ultrasonic Surface Processing of Die-Cast-Al Alloys (ORNL)

The following accomplishments have been made in FY 2023:

- Advanced the PUSP for single-sided processing of complex thin wall HPDC autobody components.
- Optimized the process conditions, resulting in anticipated significant process load reductions that are readily manageable for the robotic systems typically used in autobody assembly lines.

Project 2B – High-intensity Thermomechanical Processes (PNNL)

Ultrasonic, Joule-heating, and WJP-based high-intensity processing techniques are being developed to enhance the mechanical performance of Al castings. Local ultrasonication processing was performed on an Al alloy cast in a preheated steel mold; local Joule-heating was demonstrated on an actual size control arm casting; local WJP was performed on an HPDC Al plate. The following conclusions were reached:

- The applicability of local ultrasonic processing and resulting microstructural refinement was successfully demonstrated for casting in a permanent steel mold.
- Ultrasound, applied in a preheated permanent steel mold, reduced grain size by 97% (~56 μm grain size using ultrasound vs. ~1800 μm) at distances up to 2 in. away from the ultrasound probe. Thus, reasonably “large” portions of automotive castings could be improved through this approach.
- Joule-heating, with an appropriate electrode design, is a suitable technique to rapidly heat-treat a local area in a casting. In the present work, the locally heated region had well-defined boundaries with its area similar to the electrode area and it was possible to control the local temperature within +/- 1°C of the target temperature by controlling the electrical current.
- WJP treatment was demonstrated to improve the fatigue life of HPDC A380 alloy, compared to the untreated HPDC material, by 1.6–3.4 \times in tension-tension 4-point bending tests with a stress ratio of 0.1. The beneficial effect of WJP was predominantly confined to a depth of ~400 μm below the material’s surface where substantial compressive residual stresses were measured.

Project 2C – Cast-and-Print - AM for Localized Property Enhancement of Al Castings (ORNL)

Task 2C deposited Al 5356 rivet tabs on an as-cast Aural-5S substrate. Characterization of the rivet tabs indicated defects that were related to oxide formation due to poor shielding of the Al melt pool during processing. The defects were shown to be too significant to overcome with mitigation measures, such as using friction-stir riveting, and ultimately no successful rivet was demonstrated. The control of oxygen during the deposition process, within the current deposition system, is a key limiting factor in understanding the effectiveness of this technique. It would require significant modification of this particular AM system, but oxygen control during processing is an engineering hurdle that could be overcome. If oxygen control during the melt and solidification process can be corrected, the laser hot-wire deposition approach does produce bulk material out of commercial welding wire, such as Al 5356, that would have desirable properties for rivet tabs or other features where local ductility is important to enable joining or improved functionality of large cast-Al structures.

Key Publications**Project 2A1 – Solid-Phase Processing of Al Castings (PNNL)**

1. Balusu, K., K. S. Choi, H. Das, A. Samanta, P. Upadhyay, S. Jana, and A. Soulam, 2023, “On the utility of the thermo-pseudo-mechanical model’s residual stress prediction capability for the development of FSP,” *Int. J. Adv. Manuf. Technol.*, 126, 1775–1788. <https://doi.org/10.1007/s00170-023-11199-2>.
2. Samanta, A., H. Das, G. J. Grant, and S. Jana, 2022, “Effect of tool design and pass strategy on defect elimination and uniform, enhanced tensile properties of friction-stir processed HPDC A380 alloy,” *Mater. Sci. Eng. A*, 861, 144388. <https://doi.org/10.1016/j.msea.2022.144388>.

Project 2A2 – Power Ultrasonic Surface Processing of Die-Cast Al Alloys (ORNL)

1. Jana, S., and Z. Feng, 2022, “LMCP P2A – Solid-Phase Processing of Aluminum Castings,” *DOE-EERE VTO 2022 Annual Merit Review Meeting*, 21–23 June 2022, Washington D.C., USA.

Project 2B – High-intensity Thermomechanical Processes (PNNL)

1. Rader, K., A. S. Sabau, and A. Rohatgi, 2023, “Microstructural refinement in ultrasonically modified A356 Al castings,” *J. Mater. Sci.*, 58(1–4). <https://doi.org/10.1007/s10853-023-08999-y>.
2. Rader, K., J. Darsell, J. Helgeland, N. Canfield, T. Roosendaal, E. Nickerson, A. Denny, and A. Rohatgi, 2023, “Improving the mechanical properties of cast-aluminum via ultrasonication-induced microstructural refinement,” In: Broek, S. (ed.), *Light Metals 2023*. Springer, New York, NY, USA. pp. 422–428.
3. Rohatgi, A., 2023, “Fabrication of castings with local application of ultrasound during solidification,” Provisional patent application # 63/521,392, 16 June 2023.

Project 2C – Cast-and-Print - AM for Localized Property Enhancement of Al Castings (ORNL)

1. Kannan, R., G. L. Knapp, P. Nandwana, R. Dehoff, A. Plotkowski, B. Stump, Y. Yang, and V. Paquit, 2022, “Data mining and visualization of high-dimensional ICME data for AM,” *Integr. Mater. Manuf. Innov.*, 11, 57–70. <https://doi.org/10.1007/s40192-021-00243-2>.
2. Knapp, G. L., M. Gushev, A. Shyam, T. Feldhausen, and A. Plotkowski, 2022, “Microstructure, deformation, and fracture mechanisms in al-4043 alloy produced by laser hot-wire AM,” *Addit. Manuf.*, 59(A), 103150. <https://doi.org/10.1016/j.addma.2022.103150>.
3. Knapp, G., D. Brown, M. Paramanathan, T. Feldhausen, and A. Plotkowski, 2023, “Local modification of cast-Al alloys via the cast-and-print process,” ORNL/TM-2023/3174, Oak Ridge National Laboratory, Oak Ridge, TN, USA. <https://doi.org/10.2172/2224157>.

References

1. Sigworth, G. K., and R. J. Donahue, 2021, “The metallurgy of aluminum alloys for structural high-pressure die-castings,” *Int. J. Met.*, 15, 1031–1046. <https://doi.org/10.1007/s40962-020-00535-x>.
2. Hartlieb, M., 2013, “Aluminum alloys for structural die-casting,” *Diecast. Eng.*, 57(3), 40–43. Available at: https://www.mercalloy.com/site_media/pdfs/NADCA_-_Aluminum_Alloys_for_Structural_Die_Casting.pdf. (last accessed 13 February 2024).
3. Zaluzec, M., D. Wagner, T. W. Skrzek, and J. Conklin, 2015, “MMLV: Project overview,” SAE Technical Paper 2015-01-0407, *SAE 2015 World Congress & Exhibition*, SAE International, Warrendale, PA, USA. <https://doi.org/10.4271/2015-01-0407>.
4. Betrancourt, S., X. Chen, J. Wallace, C. Flanigan, D. A. Wagner, V. Kiridena, J. L. Conklin, R. M. Carpenter, and J. Logsdon, 2015, “MMLV: Chassis design and component testing,” SAE Technical Paper 2015-01-1237, *SAE 2015 World Congress & Exhibition*, SAE International, Warrendale, PA, USA. <https://doi.org/10.4271/2015-01-1237>.
5. Nakata, K., Y. G. Kim, H. Fujii, T. Tsumura, and T. Komazaki, 2006, “Improvement of mechanical properties of aluminum die-casting alloy by multi-pass FSP,” *Mater. Sci. Eng. A*, 437(2), 274–280. <https://doi.org/10.1016/j.msea.2006.07.150>.
6. Jana, S., R. S. Mishra, J. B. Baumann, and G. Grant, 2009, “Effect of stress ratio on the fatigue behavior of a friction-stir processed cast-Al-Si-Mg alloy,” *Scr. Mater.*, 61(2), 992–995. <https://doi.org/10.1016/j.scriptamat.2009.08.011>.

7. Yang, D. Y., M. Bambach, J. Cao, J. R. Duflou, P. Groche, T. Kuboki, A. Sterzing, A. E. Tekkaya, and C. W. Lee, 2018, “Flexibility in metal forming,” *CIRP Ann.–Manuf. Techn.*, 67(2), 743–765. <https://doi.org/10.1016/j.cirp.2018.05.004>.
8. Bambach, M., A. Sviridov, A. Weisheit, and J. H. Schleifenbaum, 2017, “Case studies on local reinforcement of sheet metal components by laser AM,” *Metals*, 7(4), 113. <https://doi.org/10.3390/met7040113>.
9. Meiners, F., J. Ihne, P. Jürgens, S. Hemes, M. Mathes, I. Sizova, M. Bambach, R. Hama-Saleh, and A. Weisheit, 2020, “New hybrid manufacturing routes combining forging and AM to efficiently produce high-performance components from Ti-6Al-4V,” *Procedia Manuf.*, 47, 261–267. <https://doi.org/10.1016/j.promfg.2020.04.215>.
10. Huang, H., J. Chen, Y. C. Lim, Z. L. Feng, X. H. Hu, J. H. Cheng, and X. Sun, 2019, “Heat generation and deformation in ultrasonic welding of magnesium alloy AZ31,” *J. Mater. Process. Tech.*, 272, 125–136. <https://doi.org/10.1016/j.jmatprotec.2019.05.016>.
11. Wang, F., D. Eskin, J. Mi, C. Wang, B. Koe, A. King, C. Reinhard, and T. Connolley, 2017, “A synchrotron X-radiography study of the fragmentation and refinement of primary intermetallic particles in an Al-35 Cu alloy induced by ultrasonic melt processing,” *Acta Mater.*, 141, 142–153. <https://doi.org/10.1016/j.actamat.2017.09.010>.
12. Zhang, Z., Wang, C., Koe, B., Schlepütz, C. M., Irvine, S., and Mi, J. 2021. “Synchrotron X-ray imaging and ultrafast tomography *in-situ* study of the fragmentation and growth dynamics of dendritic microstructures in solidification under ultrasound,” *Acta Mater.*, 209, 116796. <https://doi.org/10.1016/j.actamat.2021.116796>.
13. Khalifa, W., Tsunekawa, Y., and Okumiya, M. 2008. “Effect of ultrasonic melt treatment on microstructure of A356 aluminum cast alloys,” *Int. J. Cast Met. Res.*, 21(1–4), 129–134. <https://doi.org/10.1179/136404608X361819>.
14. Puga, H., J. Barbosa, S. Costa, S. Ribeiro, A. M. P. Pinto, and M. Prokic, 2013, “Influence of indirect ultrasonic vibration on the microstructure and mechanical behavior of Al-Si-Cu alloy,” *Mater. Sci. Eng. A*, 560, 589–595. <https://doi.org/10.1016/j.msea.2012.09.106>.
15. Eskin, G. I., 2001, “Broad prospects for commercial application of the ultrasonic (cavitation) melt treatment of light alloys,” *Ultrason. Sonochem.*, 8, 319–325. [https://doi.org/10.1016/S1350-4177\(00\)00074-2](https://doi.org/10.1016/S1350-4177(00)00074-2).
16. Grant, G. J., S. Jana, Z. Feng, A. Rohatgi, and A. Plotkowski, 2023, “II.1.2, Light Metals Core Program: Thrust 2 – Selective Processing of Al Castings,” In: Kleinbaum, S., J. L. Gibbs, C. Schooler, and H. F. Wu (Eds.), *Materials FY 2022 APR*, VTO, DOE/EE-2615, August 2022, pp. 234–258.
17. Guo, Y., S. Shankar, M. K. Jain, L. Baenen, A. Lombardi, and G. Byczynski, 2023, “Self-piercing riveting of high-ductility Al–ZnMg casting alloy (Nemalloy HE700) in F temper,” *Proceedings of the 61st Conference of Metallurgists, COM 2022*. pp. 492–501. https://doi.org/10.1007/978-3-031-17425-4_64
18. Zhao, X., D. Meng, J. Zhang, and Q. Han, 2020, “The effect of heat-treatment on die-casting Al to apply self-pierce riveting,” *Int. J. Adv. Manuf. Technol.*, 109(9), 2409–2419. <https://doi.org/10.1007/s00170-020-05833-6>.

19. Grant, G. J., S. Jana, Z. Feng, A. Rohatgi, and A. Plotkowski, 2022, “II.1.8, Light Metals Core Program: Thrust 2 – Selective Processing of Al Castings,” In: Kleinbaum, S., J. L. Gibbs, and H. F. Wu (Eds.), *Materials FY 2021 APR*, VTO, DOE/EE-2236, June 2022, pp. 240–259.
20. Knapp, G. L., D. J. Brown, M. Paramanathan, T. A. Feldhausen, and A. J. Plotkowski, 2023, “Local Modification of Cast-Al Alloys via the Cast-and-Print Process,” ORNL/TM-2023/3174, October 2023, Oak Ridge National Laboratory, Oak Ridge, TN, USA. <https://doi.org/10.2172/2224157>.

Acknowledgements

Project 2A1 – Solid-Phase Processing of Al Castings (PNNL)

The technical contributions of the PNNL staff supporting this research are gratefully acknowledged. We are grateful to Dr. A. Samanta for leading the experimental tasks of FSP and characterization. Dr. Samanta was assisted by Drs. H. Das and S. Shukla in the friction-stir experiments. R. J. Seffens assisted with the mechanical testing, M. L. Blazon and I. L. Brown assisted with the metallography, and Dr. A. Lall aided with the microscopy. We also acknowledge T. Skszek pertaining to Al casting practice and approaches to implement new processing techniques in industrial applications.

Project 2A2 – Power Ultrasonic Surface Processing of Die-Cast Al Alloys (ORNL)

We acknowledge contributions from Dr. J. Chen, H. Huang, J. Wang, Y. Li, Y. C. Lim, J. Cheng, X. Hu, and J. Allen of the ORNL project team. We also acknowledge the support from GM and Ford in providing die-cast materials and prototype die-cast body-structure components.

Project 2B – High-intensity Thermomechanical Processes (PNNL)

This project, and the LMCP program, is a collaborative effort across several DOE national labs. We are thankful for technical discussions with Drs. A. Sabau, A. Plotkowski, and T. Watkins at ORNL and Drs. D. Singh, J. Thomas, A. Chaung, P. Kenesei, K. Fezzaa, and A. Deriy at ANL. The technical contributions of the PNNL staff supporting this research are gratefully acknowledged. In particular, we express appreciation to Drs. K. Rader, M. Efe, and A. Samanta for leading the experimental tasks on ultrasonic processing, heat-treatment, and fatigue testing, respectively. Dr. Rader was assisted by J. Helgeland and Dr. J. Darsell in the ultrasonic process development and casting experiments. Dr. K. Balusu and A. Soulami led the thermal modeling and residual stress measurement efforts. T. McAllister assisted with fabrication of the steel mold, R. J. Seffens assisted with fatigue testing, Dr. X. Ma contributed to the overall project coordination, and A. Guzman and N. Canfield assisted with the metallography and microscopy. We are grateful to A. Tsuji and his team at Sugino Corp. (Wixom, Michigan) for conducting WJP. We also acknowledge discussions with D. Weiss at Eck Industries (Manitowoc, Wisconsin) and T. Skszek pertaining to Al casting practice and approaches to implement new processing techniques in industrial applications.

Project 2C – Cast-and-Print - AM for Localized Property Enhancement of Al Castings (ORNL)

The authors acknowledge Dr. Y. C. Lim in the ORNL Welding and Joining Laboratory for facilitating the rivet tests. The authors also acknowledge the cooperation and support of the Mazak Corporation and Lincoln Electric, as well as Ford Motor Company for supplying HPDC plates.

II.1.3 Thrust 3. Selective Processing of Magnesium Castings (Tasks 3A1, 3A2, and 3B) (Pacific Northwest National Laboratory and Oak Ridge National Laboratory)

Darrell Herling, Thrust Lead

Pacific Northwest National Laboratory
Energy Processes and Materials Division
900 Battelle Blvd.
Richland, WA 99354
E-mail: darrell.herling@pnnl.gov

Jiheon Jun, Co-Principal Investigator (Project 3A1)

Oak Ridge National Laboratory
Materials Science and Technology Division
1 Bethel Valley Rd.
Oak Ridge, TN 37830
E-mail: junj@ornl.gov

Vineet V. Joshi, Co-Principal Investigator (Project 3A2)

Pacific Northwest National Laboratory
Energy Processes and Materials Division
900 Battelle Blvd.
Richland, WA 99354
E-mail: vineet.joshi@pnnl.gov

Mageshwari Komarasamy, Co-Principal Investigator (Project 3B)

Pacific Northwest National Laboratory
Energy Processes and Materials Division
900 Battelle Blvd.
Richland, WA 99354
E-mail: mageshwari.komarasamy@pnnl.gov

Chris Schooler, DOE Technology Development Manager

U.S. Department of Energy
E-mail: Christopher.Schooler@ee.doe.gov

Start Date: October 1, 2020

End Date: September 30, 2023

Project Funding: \$1,100,000

DOE share: \$1,100,000

Non-DOE share: \$0

Project Introduction

The high-pressure die-casting process (HPDC) is generally used to fabricate cast-magnesium (Mg) components. Almost 90% of the cast-Mg components are currently manufactured via the HPDC process. The main advantages of the process are that it is fast and economical and can produce complex components. However, the cast components have about 1.5–4% porosity area fraction in AZ91 and AM60 Mg-alloys. The presence of pores negatively affects static-, cyclic-, and damage-tolerant properties. The current solution is to employ vacuum-assisted HPDC or the super-vacuum die-casting process, which have been shown to reduce porosity. In the current project, local thermomechanical processing will be employed to locally modify the microstructure and properties. Furthermore, corrosion is a major hindrance to widespread Mg usage [1], [2]. More robust corrosion protection approaches for Mg castings will result in increased adoption in vehicle components that require their corresponding lightweighting benefits. Automotive manufacturers and Tier-1 suppliers will not increase the adoption of lightweight Mg alloy castings without more robust corrosion resistance, as well as improved mechanical properties. The development of processes to locally enhance such properties in cast surfaces is a highly challenging fundamental- and applied-research topic with strong academic, national laboratory, and industry interest. National laboratories have world class advanced

characterization facilities, combined with cutting-edge materials and processing-science capabilities beyond that available at a given company.

Objectives

This project has two main objectives: (1) the improvement of localized corrosion properties (e.g., Project 3A); and (2) the improvement of localized mechanical properties (e.g., Project 3B), as shown in Figure II.1.3.1.

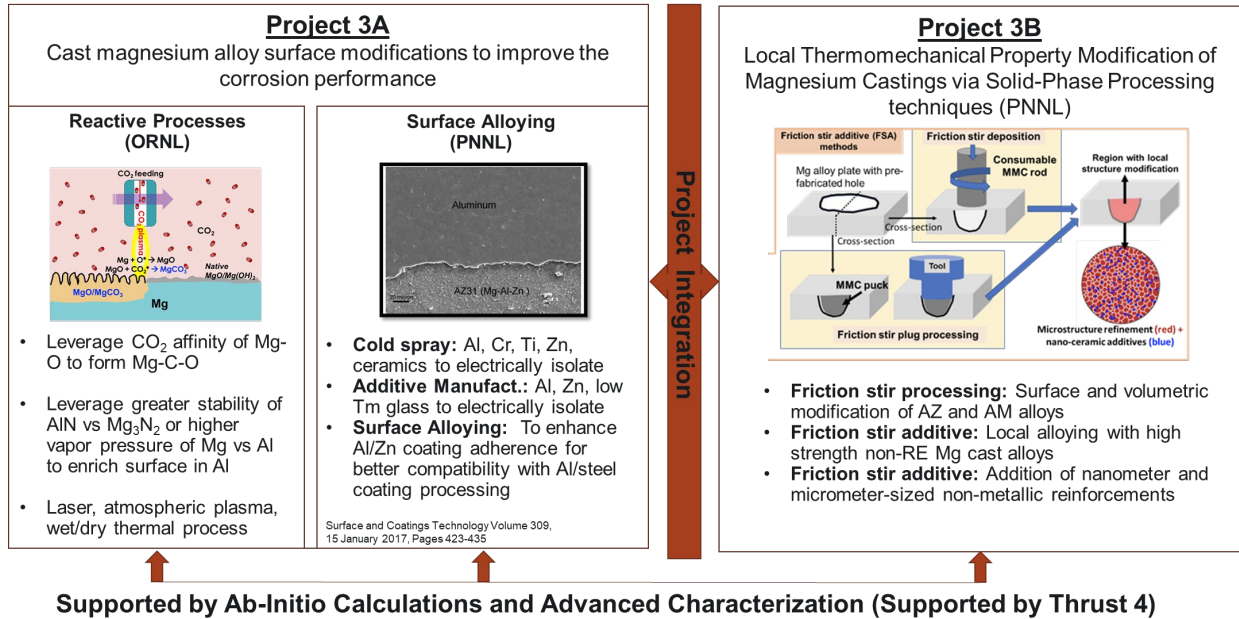


Figure II.1.3.1. Primary thrust areas for Project 3A, “Surface Modification for Improving Corrosion Properties,” and Project 3B, “Improving Local Thermomechanical Treatments for Improving Mechanical Behavior of Mg-Alloys.” Source: PNNL.

Projects 3A1 (Reactive Processes – ORNL) and 3A2 (Surface Alloying – PNNL)

The objective is to perform localized surface modification in cast-Mg components that will improve their overall corrosion performance. The end goal of the project is to improve corrosion resistance, eliminate or minimize corrosion-induced fatigue, minimize galvanic coupling for faying surfaces, and if needed, improve surface receptivity for subsequent top-coating processes on Mg castings. In this multi-laboratory collaborative effort, we plan to accomplish these goals by employing a multifaceted approach that relies on replacing the corrosion-susceptible MgO-Mg(OH)₂ native film—either directly or indirectly—by modifying the alloy’s surface composition. To accomplish this, processing strategies and techniques are being developed that are guided by improved fundamental understanding of the underlying mechanisms using *ab-initio* methods, advanced electrochemical potential measurement, and microstructural characterization techniques. The effort will focus on HPDC AM60 and AZ91 alloy families and may also consider additional processes or alloys based on automotive manufacturer and Tier-1 supplier inputs.

Projects 3B (Thermomechanical Property Modification – PNNL)

The objective of this project is to locally enhance such mechanical properties as ductility, strength, and fatigue properties of HPDC Mg components using FSP and friction-stir additive methods. This project will develop methods for localized microstructure modification and local alloying, measure the change in resultant properties, and demonstrate the property modification on either AZ91 or AM60 cast-Mg components, as shown in Figure II.1.3.1. The focus of the work in FY 2023 is to improve fatigue performance of Ca-modified AM60 and FSP of curved plates.

Approach

Project 3A1

In FY 2023, two developmental reactive-surface processes were further optimized for improved corrosion and wear resistance, building on the research from the prior year: (1) plasma-assisted organosilicon coatings, and (2) lithium(Li)-salt-assisted thermal CO₂ treatments. Schematic descriptions of these two processes are presented in Figure II.1.3.2. These coatings pursue two distinct surface modification strategies. Unlike plasma-assisted organosilicon coatings, which are deposition of precursor materials, the thermal CO₂ treatment is classified as a surface modification because Mg participates in the chemical reactions that form the surface layer. Table II.1.3.1 and Table II.1.3.2 summarize process parameters associated with the two reactive-surface processes. Two HPDC Mg-alloys, AZ91D (Mg-9Al-1Zn-0.5Mn) and AM60 (Mg-6Al-0.5Mn-0.2Zn), were used as the alloy substrates for surface processing.

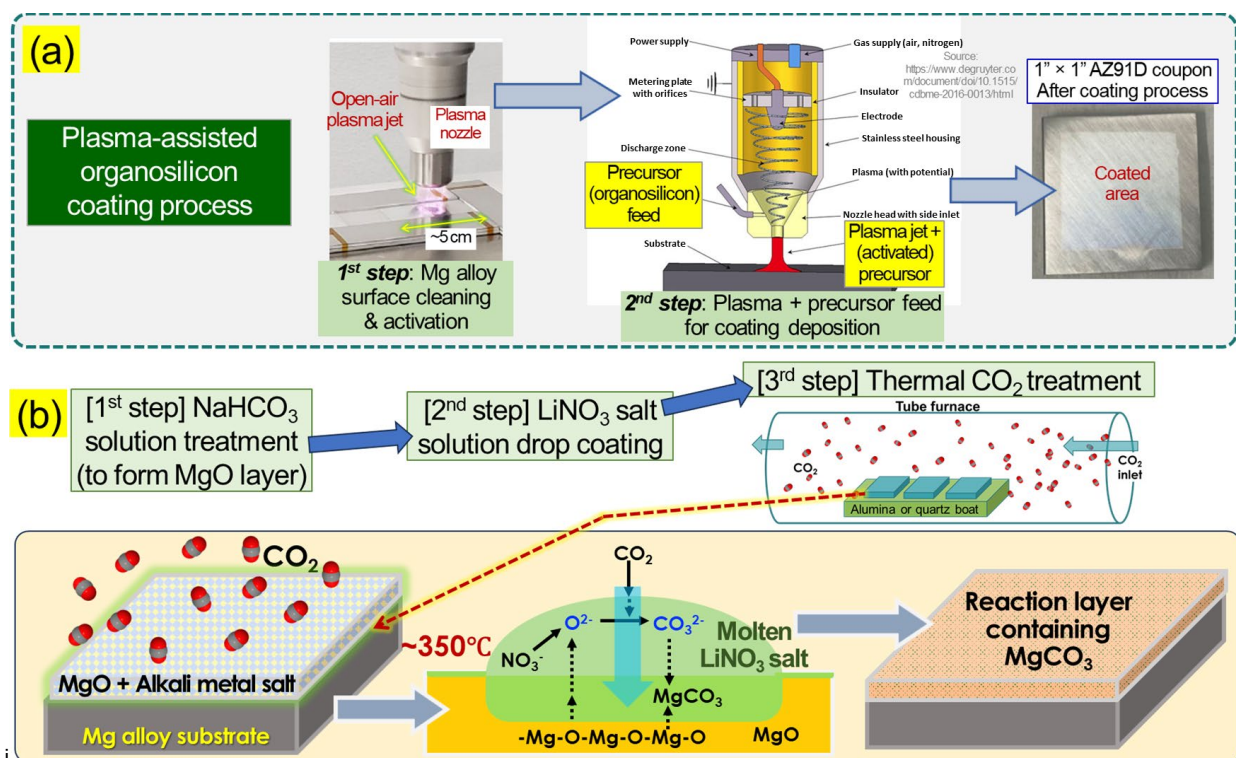


Figure II.1.3.2. Reactive-surface-processing illustration for Mg-alloys. (a) Plasma-assisted organosilicon-coating in collaboration with Plasmatreat USA. (b) Thermal CO₂ treatment with Li-salt preloading. Source: ORNL.

Table II.1.3.1. Summary of the Process Parameters for the Plasma-Assisted Organosilicon Deposition Performed at ORNL and Described in Figure II.1.3.2(a). Two Processes are Designated as P01 and P08. The Coating Thickness on a Si Wafer was Reported for Initial Process Evaluation

Process ID	Ionization Gas (1 st and 2 nd Steps)	Precursor Carrier Gas (2 nd Step)	Plasma Nozzle Rastering Speed (2 nd Step) / mm s ⁻¹	Precursor Flow Rate / g h ⁻¹	Deposition Thickness on Si Wafer by Reflectometry
P01	Clean Dry Lab Air	N ₂	166	50	~220 nm
P08	Clean Dry Lab Air	N ₂	50	25	~320 nm

Table II.1.3.2. Summary of Four Treatment Conditions Using Different Solution Concentrations of NaHCO₃ and LiNO₃ Before the Thermal CO₂ Treatments Performed at ORNL and Described in Figure II.1.3.2(b) for AZ91D and AM60

Treatment ID	NaHCO ₃ Concentration	LiNO ₃ Concentration	Thermal CO ₂ Concentration
Li-0.5-1.0 for AZ91D	0.5 wt.%	10 wt.%	at 350 °C for 8 h
Li-2.5-2.5 for AZ91D	2.5 wt.%	25 wt.%	at 350 °C for 8 h
Li-2.5-2.0 for AM60	2.5 wt.%	40 wt.%	at 310 °C for 6 h
Li-2.5-4.0 for AM60	2.5 wt.%	40 wt.%	at 310 °C for 6 h

To assess corrosion resistance of the coated or treated Mg alloy samples, typical EIS and H₂ collection measurements were conducted in 3.5 wt.% NaCl solutions, which were open to air at RT. A schematic description of these measurements with a summary table is presented in Figure II.1.3.3. For EIS measurements, an SCE and Pt-wire counter electrode were used with an insulation-tape-masked sample surface (i.e., a working electrode with a 0.833 cm² area) to complete a three-electrode configuration. For the fitting of impedance-spectra data, single and double resistance constant phase element (*R*//*CPE*) models as described at the bottom left in Figure II.1.3.3 were used, and the *R*₂ or *R*₂ + *R*_f values were compared for corrosion resistance in the short-term (i.e., < 3 h). For H₂-collection measurement, the volume of H₂ (i.e., stoichiometrically correlated with Mg corrosion [3]) was compared over the immersion in 3.5 wt.% NaCl up to 500 h. Advanced multiscale characterization techniques were employed for microstructural and chemical analyses, including SEM, STEM, and X-ray EDS.

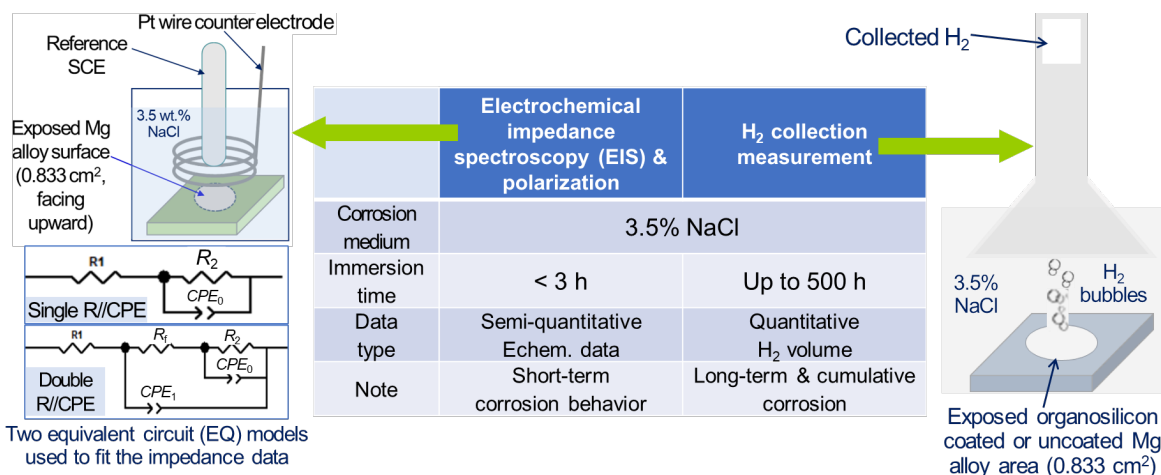


Figure II.1.3.3. A schematic description of the electrochemical and H₂-collection experimental setup for corrosion-evaluation with a summary table for the measurement conditions. Also included at the bottom left are the equivalent circuit models used for impedance-data fitting. *R*₁ is solution resistance, *R*₂ is charge-transfer resistance, and *R*_f is permeable-film resistance. *CPE*₀ and *CPE*₁ account for non-ideal capacitive behavior associated with *R*₂ and *R*_f, respectively. Source: ORNL.

Project 3A2

A surface modification technique, namely cold-spray, was used to surface-coat/alloy Mg with Al and Zn, respectively. Commercially procured (CP) Zn and Al 6061 are coated on top of cast-Mg alloys using the cold-spray method. Successfully performing this coating process will completely change the corrosion characteristics of the alloy. This will also make it more amenable to conventional conversion or plasma-electrolytic and epoxy electro-coat techniques, as well as mitigation of the challenges associated with joining cast-Mg components with Al or steel components. To evaluate corrosion properties of coating Al 6061 and Zn with respect to the substrate, electrochemical properties were measured on surface-modified cast-Mg alloys at

the microscopic as well as the macroscale levels. Electrochemical and long-term corrosion tests were also performed using an immersion-test method, and corrosion progress was tracked by collecting H₂ gas. Mechanical properties of the coatings were evaluated by performing wear and adhesion test of the coating. The optimized coating process parameter was finally utilized on a section of an actual AZ91D HDPC cast part.

Additionally, we employed smooth-particle hydrodynamics (SPH) to model single-particle cold-spray impacts on AZ91 substrate material to understand temperature and pressure evolution during the impact process. Using SPH, we have also successfully modeled the ideal velocity range for particle impact onto the substrate and compared modeling and experimental results to understand the nature of bonding. Knowledge of the process parameters most ideal for bonding will help improve bonding quality and coating density of future sprays.

Project 3B

Prior work within this program established a method to generate high-strength Ca-added AM60 through FSP and friction surfacing, which led to a tensile YS of ~270 MPa against 100 MPa in the base AM60 alloy. In FY 2023, the fatigue performance of the Ca-added AM60 alloy was investigated following FSP.

Friction-Stir Processing and Friction Surfacing of Ca-Added AM60

For FSP of the Ca-added AM60, the key processing parameters were the tool-rotation rate in RPM and the traverse velocity (mm/min). The ideal tool-rotation rate was found to be in the range of 800–1600 RPM, and the optimal traverse velocity was 150 mm/min. Figure II.1.3.4(a) shows the Ca-added AM60 after FSP, with a high-quality processed surface. Microstructures are shown in Figure II.1.3.4(b–f). Notably, the Al₂Ca that was present in the Figure II.1.3.4(c) base material is heavily refined and solutionized in the stir zone shown in Figure II.1.3.4(e) and in the thermally affected zone shown in Figure II.1.3.4(d). Samples for fatigue testing were fabricated from the double-pass FSP at 1200 RPM and double-pass FSP at 1600 RPM. These runs showed promising elimination of defects and improvement in mechanical properties compared to the base material. Fatigue-property analysis in a stress-controlled configuration with the fatigue ratio (i.e., the ratio of maximum to minimum stress) of 0.1 was completed in the as-cast and as-processed conditions.

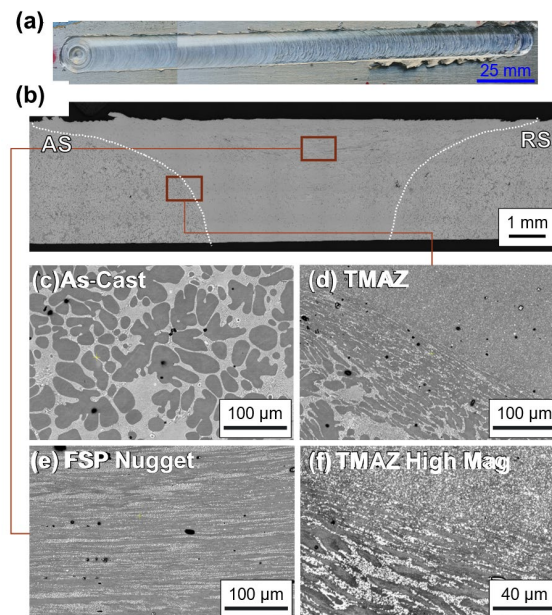


Figure II.1.3.4. (a) The surface of FSP Ca-added AM60. OM of the cross-section is shown in (b) with a higher magnification of (c) the base material, (d) the thermomechanically affected zone, (e) the stir zone, and (f) the transition between the weld and the base material. Source: PNNL.

Friction-Stir Processing of Curved Surfaces

A robotic FSW system, as shown in Figure II.1.3.5(a), was used to perform FSP on curved surfaces. AZ31 plates with a ~3 mm thickness were bent using a press-break to angles of 45° and 65° and an inner radius curvature of 12.7 mm. The tool and an example of a processed curved plate with a 65° curvature can be seen in Figure II.1.3.5(b) and Figure II.1.3.5(c), respectively. A custom-backing block, as shown in Figure II.1.3.5(d) was machined to match the change in angle and radius of curvature for both angles, as observed in Figure II.1.3.5(e). The optimized processing condition for linear processing was 900 RPM, a 500 mm/min traverse velocity, and a 5° tool tilt angle. Optical microscopy of the curved region was performed to observe consolidation of casting defects and microstructure evolution after FSP.

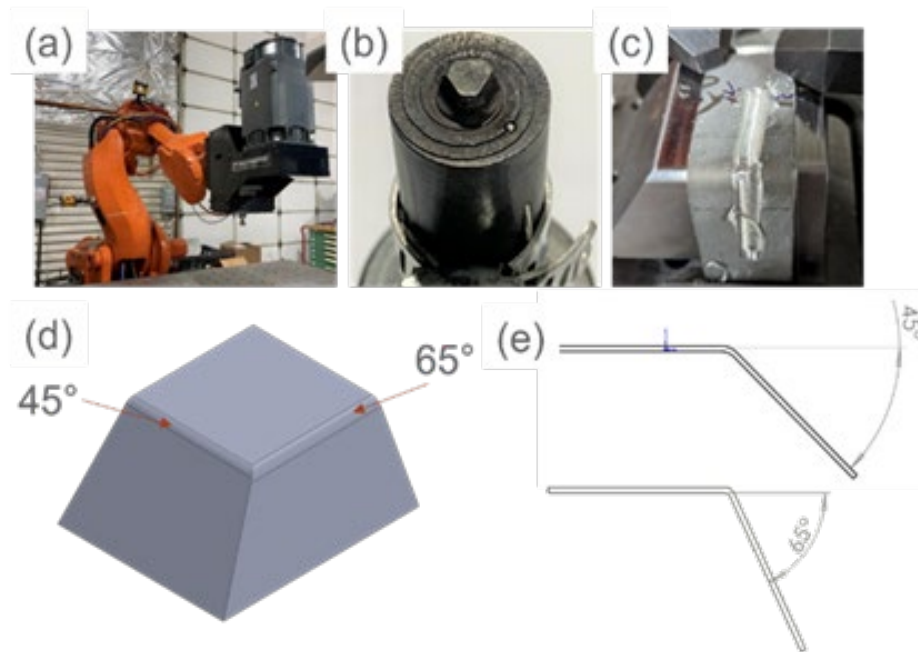


Figure II.1.3.5. Experimental approach for the FSP of curved surfaces. (a) The FSW robot used for this work. (b) The FSW tool used for this work. (c) A fixtured plate after FSP. (d) A computer-aided drawing (CAD) schematic of the anvil used for this work. (e) A CAD sideview of the curved surface plates. Source: PNNL.

Results

Project 3A1

Plasma-assisted organosilicon coatings, which were evaluated on commercial Mg alloy AZ91D in FY 2022, were applied to commercial Mg alloy AM60 in FY 2023 using the P01 and P08 processes described in Table II.1.3.1 above.

STEM images and EDS line-scan profiles are presented in Figure II.1.3.6 and Figure II.1.3.7, for the P01- and P08-coated AM60 cross-sectional samples prepared by focused ion beam (FIB) milling, respectively. In both the P01 and P08 coated samples, two layers were identified; a submicron-thickness external coating and a very thin intermediate layer adjacent to the alloy substrate. The chemical composition and thickness were 55Si-37O-8C and ~140 nm in the P01 coating and 52Si-42O-6C and ~250 nm in the P08 coating on AM60. Between the coating and alloy substrate, an intermediate layer, as characterized by a gradient composition—indicative of interdiffusion phenomenon—was observed to be ~130 nm and ~80 nm thick in the P01 and P08 coatings, respectively. Overall, no defects were observed in the coating layers or the interfaces in the sampled cross-sections, suggesting that this newly developed plasma-assisted organosilicon-coating process is compatible with the AM60 Mg alloy.

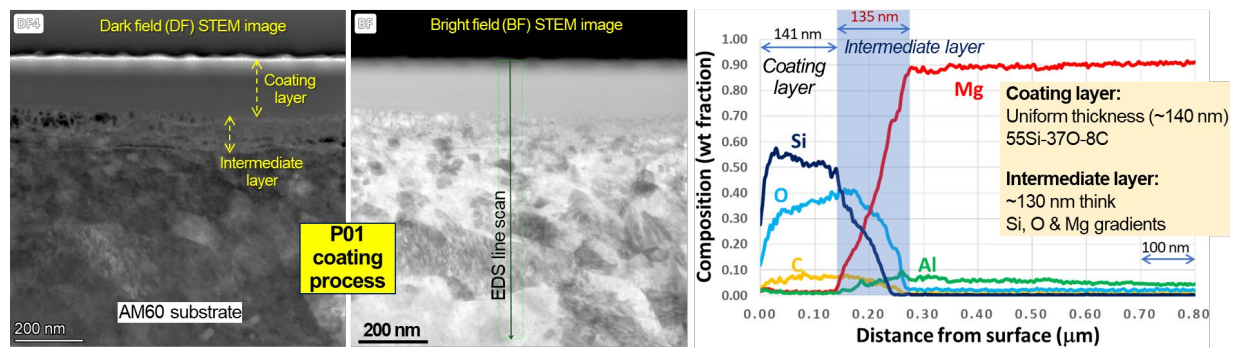


Figure II.1.3.6. STEM and EDS line-scan characterization results of organosilicon-coated AM60 Mg alloy sample by P01 process. Source: ORNL.

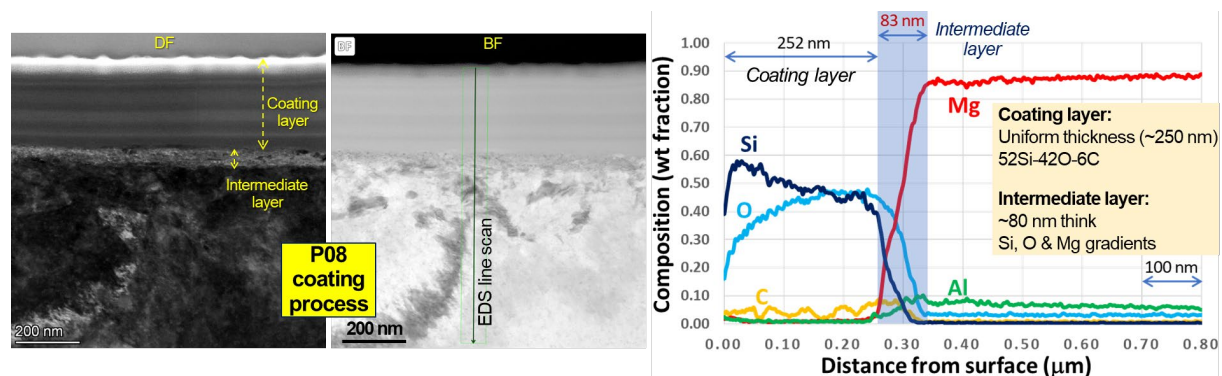


Figure II.1.3.7. STEM and EDS line-scan characterization results of organosilicon-coated AM60 Mg alloy sample by P08 process. Source: ORNL.

A tilted-view SEM image of FIB milled Li-0.5-1.0 treatment on AZ91D is presented along with the EDS point-analysis results in Figure II.1.3.8. The treated layer was $\sim 2\text{--}3\ \mu\text{m}$ thick and uniform over the surface as observed in the figure. The top and mid-sections of the layer were enriched in Mg, O, and C, which could be associated with the formation of MgCO_3 .

Typical impedance-spectra of uncoated and organosilicon-coated AM60 samples are compared in Figure II.1.3.9(a). The impedance scale was greater in the coated samples than in the uncoated one, implying the P01 and P08 organosilicon-coating decreased the rate of corrosion reaction. As summarized in Table II.1.3.3 and Table II.1.3.4, the fitted corrosion resistance values were approximately 760% and 1600%, respectively, for the P01 and P08 coatings on AM60 with respect to the uncoated AM60. The H_2 -collection volumes of uncoated and organosilicon-coated AM60 are plotted as a function of immersion time in Figure II.1.3.9(b). The volumes of H_2 , accounting for long-term and cumulative corrosion behavior, were lower in P01- and P08-coated AM60 than for the uncoated specimen, indicating the coating layer suppressed Mg corrosion for relatively long immersion periods (e.g., at least 500 h). For the designated H_2 volume data around 260 and 310 h in Figure II.1.3.9(b), P01 and P08 coating resulted in -73% and -69% reduction of Mg corrosion volumes, respectively, with respect to the uncoated AM60.

Impedance-data-fitting results from short-term immersion EIS measurements are summarized in Table II.1.3.3 for AZ91D and AM60 alloy samples with and without reactive-surface processing (e.g., plasma-assisted organosilicon-coating and LiNO_3 -assisted thermal CO_2 treatment). It is clearly noted that the developed surface coating and modification processes increased corrosion resistance, as supported by higher R_2 and $R_f + R_2$ values.

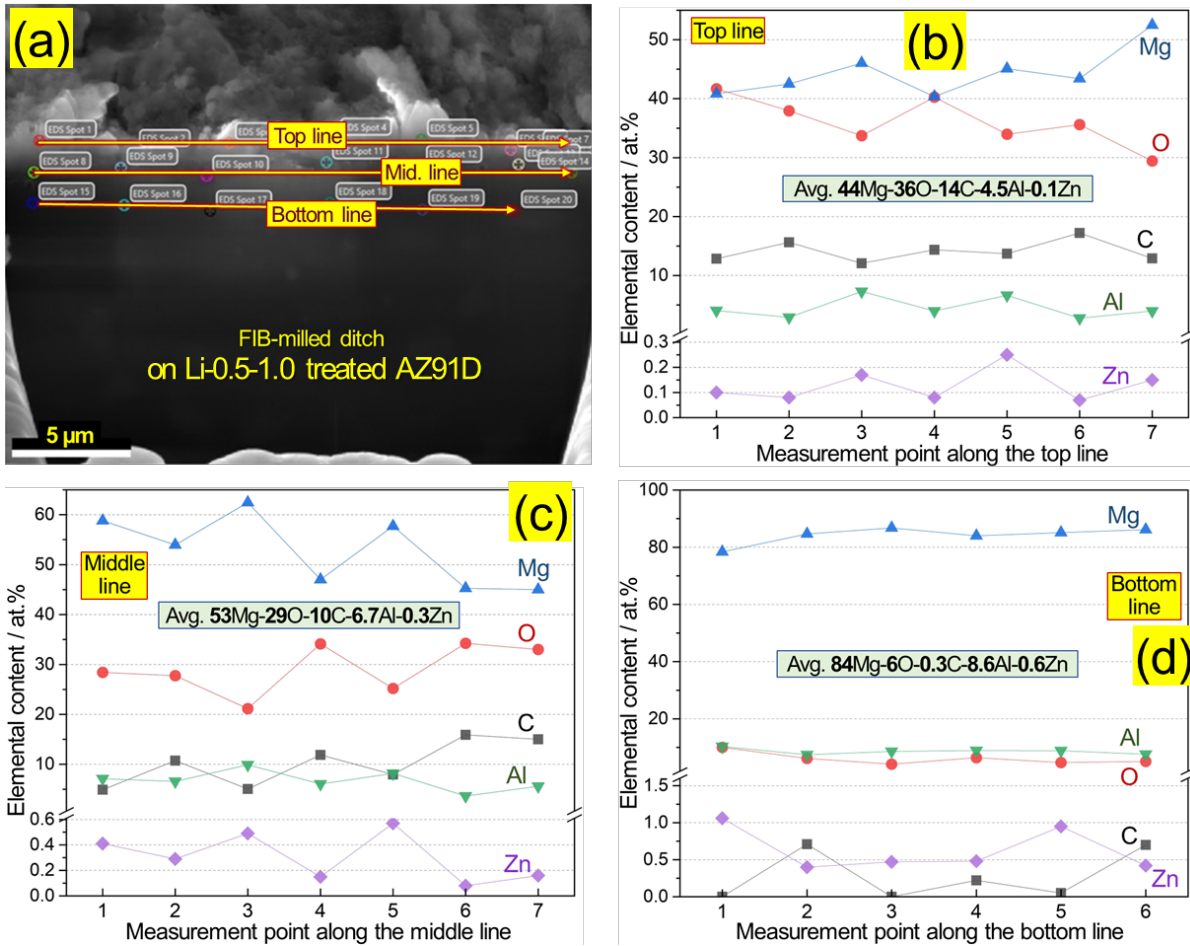


Figure II.1.3.8. Chemical composition characterization of thermal CO₂-treated AZ91D after solution pretreatment by 0.5 wt.% NaHCO₃ and 10 wt.% LiNO₃ solutions (Li-0.5-1.0). (a) FIB milled ditch to reveal a local cross-section for the chemical composition analysis in the top, mid, and bottom sections of the treated surface layer. (b-d) The compositions in atomic percents for the top, mid, and bottom lines, respectively, with the average compositions designated in each plot. Source: ORNL.

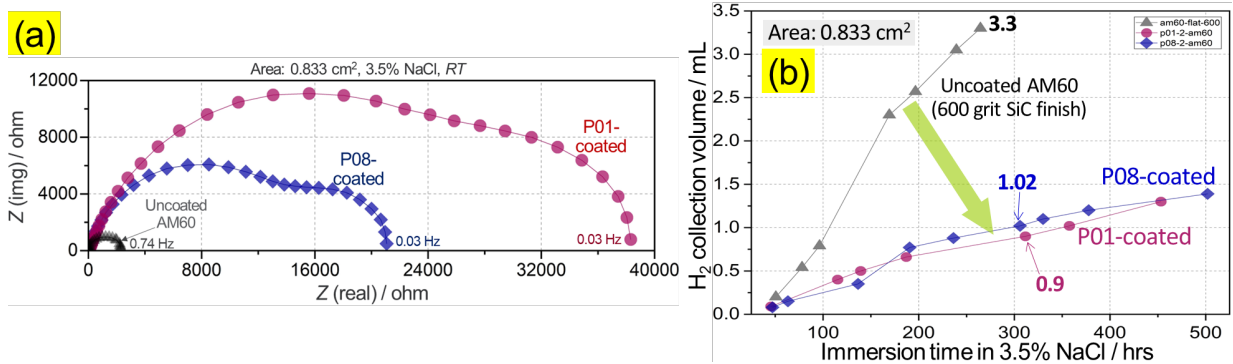


Figure II.1.3.9. (a) Comparison of impedance-spectra. (b) H₂ collection volume between uncoated (e.g., 600 grit SiC finished) vs. P01 and P08 organosilicon-coated AM60 Mg alloy samples. Source: ORNL.

Table II.1.3.3. Summary of R_2 and $R_f + R_2$ Values from the Impedance-Data Fitting Conducted at ORNL

Mg Alloy Substrate	Surface Coating or Treatment	R_2 or [$R_f + R_2$] / ohm-cm ²
AZ91D	Bare alloy (baseline)	2536 (avg. of 6 data)
	P01 organosilicon*	[~23000], [~22110] (2 data)
	P08 organosilicon*	[~48700], [~43900] (2 data)
	Li-2.5-2.5	[~31330], [~34950], [~49550] (3 data)
AM60	Bare alloy (baseline)	3041 (avg. of 6 data)
	P01 organosilicon	[~31690], [~20110] (2 data)
	P08 organosilicon	[~22350], [~17370] (2 data)
	Li-2.5-2.0	~24190
	Li-2.5-4.0	~35230

*Data previously reported in the FY 2022

Table II.1.3.4 summarizes the quantitative comparison of corrosion-evaluation data from this task and the literature with technical notes on the samples and industrial applicability. For the AZ91D Mg alloy, both plasma-assisted organosilicon (P08) and Li-salt-assisted thermal CO₂ treatment showed corrosion resistance (~1810% and ~1954%, respectively, compared to the baseline AZ91D) higher than plasma-electrolytic oxidation (PEO) coating (~1160% compared to the baseline AZ91D). Note that the comparison of corrosion data is not made for the tests in the same condition. For the AM60 Mg alloy, corrosion resistance improvement by PEO (from literature data) is greater than the improvement estimated for the organosilicon-coating and CO₂ treatments developed by this task.

Recent modification of plasma-assisted organosilicon coatings produced thicker layers on AM60, which was estimated to be ~500–990 nm. STEM/EDS characterization on the thicker organosilicon coatings is underway. Meanwhile, preliminary wear-track tests on the coated AM60 samples with thicker organosilicon layers showed the wear volume was reduced by 43% with respect to uncoated AM60. Further wear-performance evaluation is underway. For LiNO₃-assisted thermal CO₂ treated AZ91D samples, the wear rate was reduced by 22% with respect to uncoated AZ91D, as reported previously for this task in FY 2022. Overall, the reactive-surface processing developed under this task demonstrated higher corrosion and wear resistances for AM60 and AZ91D Mg-alloys, supporting the key technical goals of the LMCP.

Table II.1.3.4. Summary of ORNL and Literature Corrosion-Evaluation Data and Technical Notes to Compare the Different Surface Modification and Coating Approaches for Mg-Alloys

Item	Uncoated/Untreated (Baseline)		Open-Air Plasma-Assisted Organosilicon-Coating		Li-salt-Assisted Thermal CO ₂ Treatment		PEO	
	AZ91D	AM60	AZ91D	AM60	AZ91D	AM60	AZ91D	AM60
Mg Alloy Substrate	AZ91D	AM60	AZ91D	AM60	AZ91D	AM60	AZ91D	AM60
Note	<ul style="list-style-type: none"> The Mg-alloys were produced by HDPC. These samples were tested at ORNL. 						<ul style="list-style-type: none"> Literature data. PEO process conditions were different for each alloy. 	
Corrosion Medium	3.5 wt.% NaCl						0.5 M NaCl (~2.9 wt.% NaCl)	
EIS or Polarization Corrosion Data (avg. or max. values, short-term)	2536 ohm cm ²	3041 ohm cm ²	For P01 – 22000 ohm cm ² For P08 – 45900 ohm cm ²	For P01 – 23000 ohm cm ² For P08 – 48700 ohm cm ²	For Li-2.5-2.5 – 49549 ohm cm ²	For Li-2.5-2.0 – 24910 ohm cm ² For Li-2.5-4.0 – 35230 ohm cm ²	29423 ohm cm ²	272000 ohm cm ²
% Value of Above Data with Respect to the Baseline	100%	100%	For P01 – ~ 868% For P08 – ~ 1810%	For P01 – ~ 756% For P08 – ~ 1601%	For Li-2.5-2.5 – ~ 1954%	For Li-2.5-2.0 – ~ 819% For Li-2.5-2.0 – ~ 1159%	~ 1160%	~ 89440%
Reference	-		This task's FY 2022 Annual Report	-	[4]	-	[5]	[6]
Scale-up and Other Notes	Open-Air Plasma-Assisted Organosilicon-Coating		<ul style="list-style-type: none"> Possible by modification of existing industrial plasma treatment systems for local and bulk areas. Can avoid wet-chemical process. Long-term protection under galvanic configurations (e.g., dissimilar joint sections) need to be investigated. 					
	Li-salt-Assisted Thermal CO ₂ Treatment		<ul style="list-style-type: none"> Most suitable for bulk area batch process. Utilization of excessive CO₂ for beneficial corrosion protection. Long-term protection under galvanic configurations to be investigated. 					
	PEO		<ul style="list-style-type: none"> Most commonly found in literature for corrosion protection. Needs wet chemicals and high electric current (for scale-up, large volume chemicals & more power consumption). Mostly applicable for bluk area of Mg-alloys. 					

Project 3A2

In FY 2022, we demonstrated that optimized coatings of Zn showed porosities less than 1% by area. A similar exercise was performed for optimized Al 6061 coatings in FY 2023 to demonstrate low porosity. Cold-spray was performed on HDPC AZ91 cast coupons. Surfaces were polished to a 600-grit finish before performing the cold-spray coating. Coatings were performed with varying temperature and pressure to obtain coating porosity less than 1% without bond coating. The first pass was sprayed at a 45° angle to clean the surface, followed by 10 passes at a 90° angle.

Figure II.1.3.10(a–c) depicts the microstructures of coatings deposited at 500°C while varying the nitrogen gas pressure from 2.5 to 6.5 MPa. The microstructures reveal a decrease in porosity fraction with increasing gas pressure. At 2.5 MPa pressure, the microstructure exhibits numerous interparticle pores, whereas very few isolated pores were observed at 6.5 MPa gas pressure. No significant interface pores were observed with the coatings; porosity was typically noticed only within the coatings. As gas pressure increases, porosity reduces significantly as particle velocity increases resulting in coatings with less than 1% porosity. Figure II.1.3.10(d) shows the microstructure of the as-cast HPDC AZ91 alloy displaying a network-like distribution of the $Mg_{17}Al_{12}$ secondary-phase within the matrix.

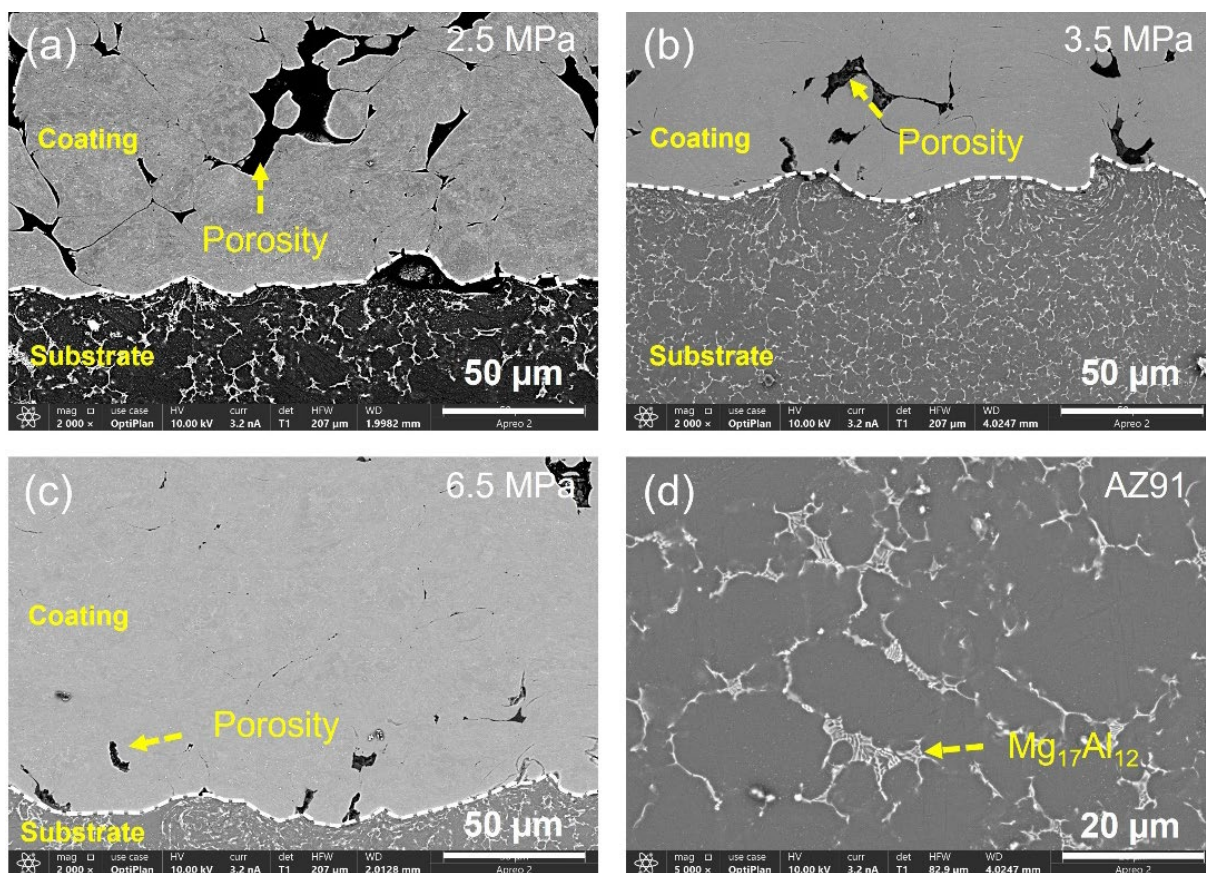


Figure II.1.3.10. SEM microstructures of Al 6061 coatings deposited at 500 °C and gas pressures of (a) 2.5, (b) 3.5, and (c) 6.5 MPa, respectively. (d) Microstructure of the as-cast HPDC AZ91 substrate. Source: PNNL.

In Figure II.1.3.11(a), the percentage of coating porosity is correlated with the wear rate for samples coated with different gas temperatures and pressures. A clear trend is observed in which the wear rate increases significantly with increasing coating porosity. The data indicate the wear rate is lower than that of the wrought Al 6061 alloy for coating with porosities below 3%. Dense coating deposited at high-temperatures and high-pressures significantly improved wear properties due to accumulation of high plastic strain during high-

velocity impact of particles on the substrate. The wear rate of the HDPC and wrought Al 6061 alloys is also included in Figure II.1.3.11(a). The data show a significant improvement in wear properties compared to the wrought Al 6061 alloy and cast AZ91 substrate, with wear rates in the optimized coatings approximately 44% and 62% lower than those of wrought Al 6061 and HDPC AZ91 alloy, respectively. In Figure II.1.3.11(b), the average CoF is shown for the samples coated at gas temperatures ranging from 400–500°C and gas pressures from 2–6.5 MPa. The data displays a similar level of average CoF for all the coatings, and the values are close to the CoF of the wrought Al 6061 alloy.

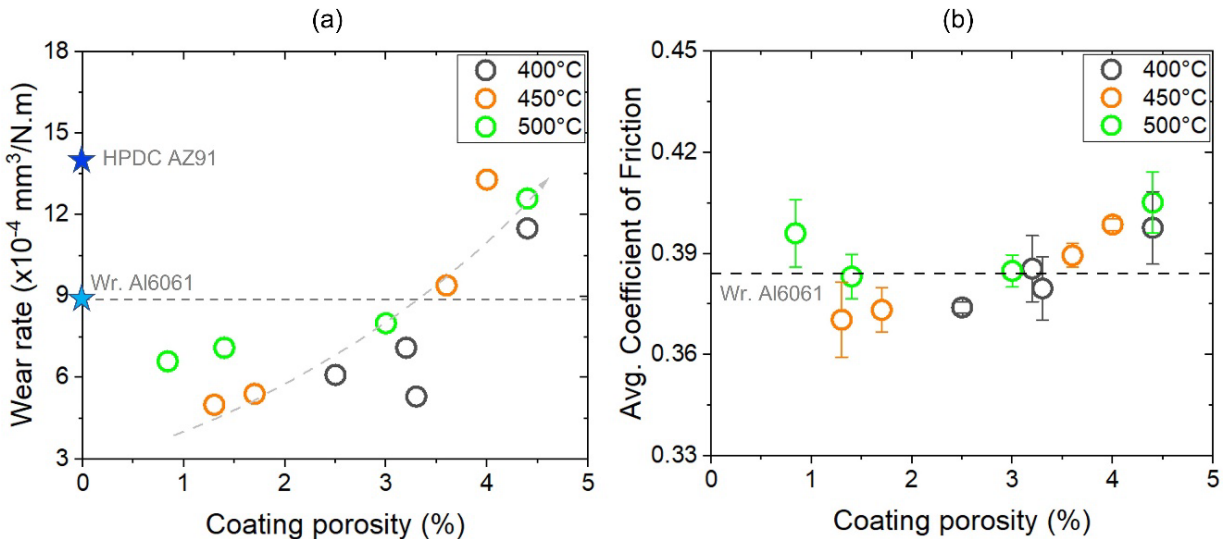


Figure II.1.3.11. (a) Coating porosity vs. wear rate for coatings deposited at different gas temperatures and pressures. The wear rate of wrought Al 6061 and HDPC AZ91 alloys is also included in the figure for comparison purposes. (b) Corresponding coating porosity vs. average CoF. Source: PNNL.

The bond strength of the coatings was evaluated using adhesion testing following the ASTM D4541 method. Testing was conducted on samples coated at gas temperatures ranging from 400–500°C with pressure variation from 2–6.5 MPa. Figure II.1.3.12(a) illustrates the adhesion strength as a function of temperature and pressure. At a low-pressure of 2.0 MPa, the average bond strength was 10.8 and 10.3 MPa, respectively for coatings deposited at 400°C and 500°C, respectively.

It is important to note that adhesion strength increases with increasing gas pressure at gas temperatures above 400°C. The maximum adhesion strength was observed at 6.5 MPa pressure, with strengths of 30.3 MPa, 33.8 MPa, and 33.4 MPa, respectively, for temperatures of 400°C, 450°C, and 500°C, respectively. A strong linear correlation between coating porosity (%) and adhesion strength was identified where the strength decreases significantly with increasing porosity. Figure II.1.3.12(b) illustrates the relationship between adhesion strength and porosity for samples coated at various gas temperatures and pressures. Adhesion strength decreased from 33.4–10.3 MPa as the coating porosity increased from 0.84–4.4%. Porosity also has some detrimental effects on other properties, including elastic modulus, cohesion strength, hardness, fatigue, and corrosion resistance, among others. In most of the recent samples, cohesive-type coating failure was observed; the coating failed at the interface between the coating and the substrate. For representative purposes, the fracture surface for a sample coated at 500°C and 5 MPa is shown in Figure II.1.3.12(c). The results suggest that the better quality bonding at high-temperatures and high-pressures was attributed to mechanical interlocking and metallurgical bonding. In the present study, high adhesive strength was achieved without peening media, possibly due to more plastic deformation of Al 6061 particles at the interface at high-gas temperatures and pressures.

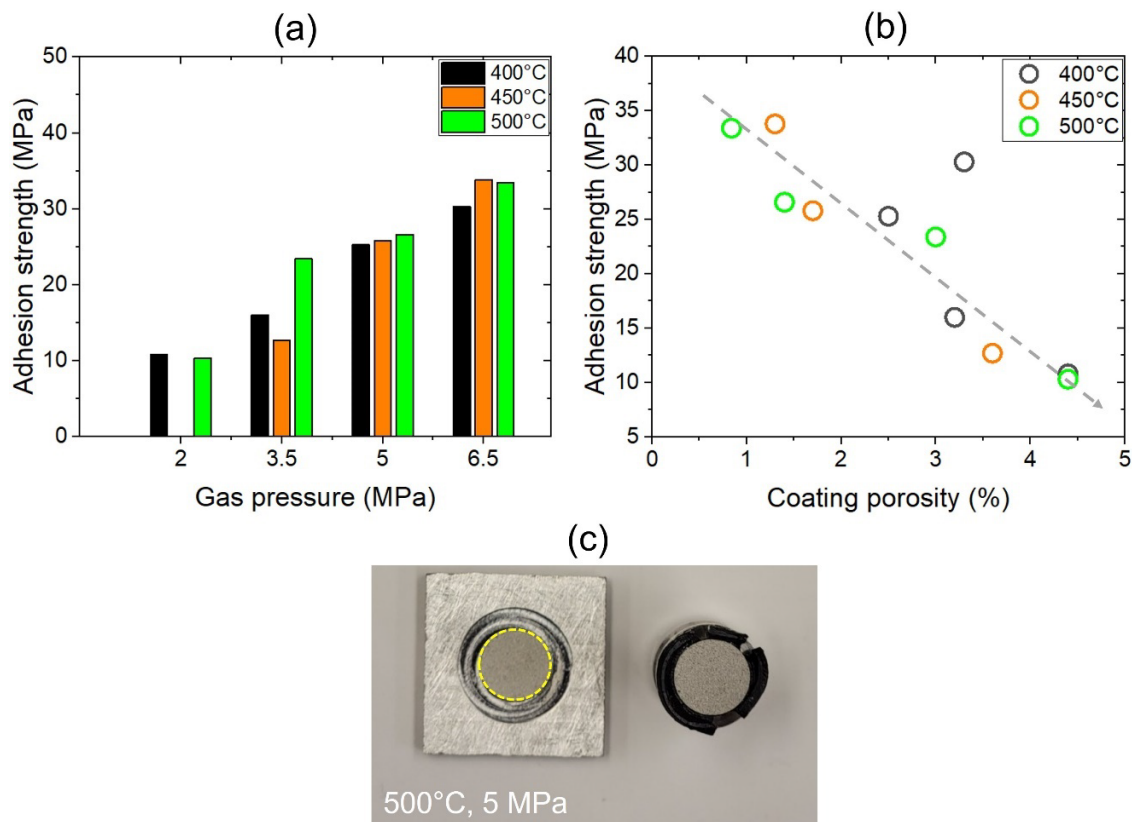
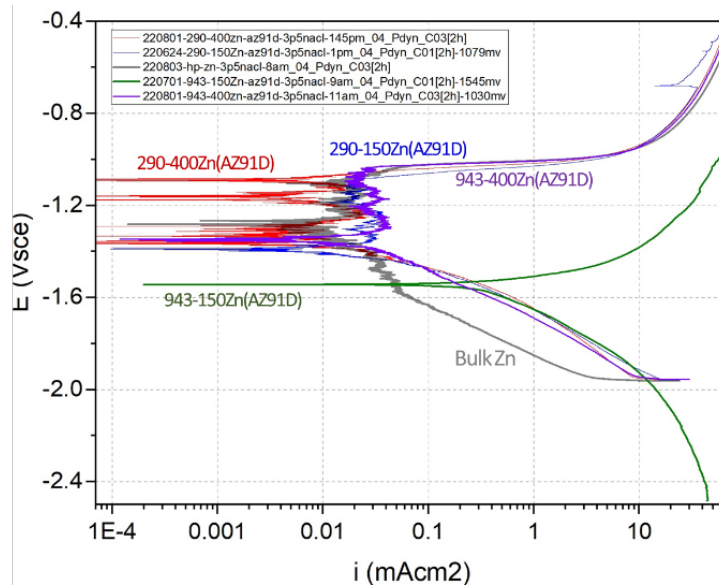


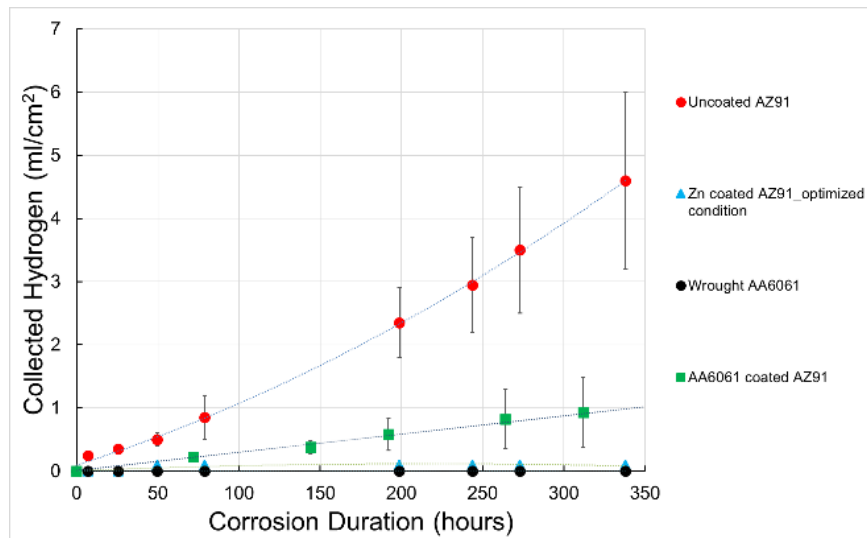
Figure II.1.3.12. (a) Adhesion strength as a function of gas pressure and temperature. (b) Al 6061 coating porosity vs. adhesion strength for the samples coated with different temperatures and pressures. (c) A representative adhesion-tested sample showing cohesion-type failure for a sample coated at 500 °C temperature and 5 MPa gas pressure. Source: PNNL.

Potentiodynamic polarization tests were conducted on several samples of Zn coatings coated on AZ91 substrate and compared with uncoated AZ91. A 0.6-wt.% NaCl solution was used as the corrosive medium, an SCE as the reference electrode, and graphite as the counter electrode. The corrosion results shown in Figure II.1.3.13(a) indicate that Zn-coated AZ91 samples exhibit more noble behavior compared to uncoated AZ91. Hydrogen-evolution tests were conducted on both optimized Zn and Al 6061 coatings coated on AZ91 substrates. In the case of the Zn-coated samples, the coating process was carried out at temperature of 400°C and a pressure of 3.5 MPa with a nozzle distance of 25 mm to achieve a coating porosity of less than 1%. In the case of the Al 6061-coated samples, three spray parameters with gas pressures and temperatures of 3.5 MPa and 300°C, 6.5 MPa and 450°C, and 6.5 MPa and 425°C were immersed. The initial pass in all of these samples was conducted at a 45° spray angle followed by 10 passes at a 90° spray angle. Corrosion performance was evaluated on (i) AZ91 substrate and (ii) AZ91 substrate coated with Zn. Square-shaped samples, both the substrate and the coating with dimensions of 15 mm × 15 mm (2.25 cm²), were polished with 1200-grit paper before the corrosion test. Corrosion performance was assessed using a standardized immersion-test method in which corrosion progress was monitored by collecting evolved H₂ gas. NaCl solution, with a concentration of 0.6 wt.%, served as the corrosion medium. Figure II.1.3.13(b) illustrates the relation between immersion time and the total volume of H₂ gas collected. The long-term corrosion tests were conducted with H₂-gas collection extending to 338 hours (~14 days) of immersion time. Significantly higher volumes of H₂ gas were collected from the bare AZ91 substrate compared to the Zn-coated substrate. The data on H₂ collection suggests a substantial reduction (4500%) in H₂-gas evolution in the Zn-coated sample compared to the bare substrate and a reduction in H₂-gas evolution of at least 300% when the substrate is

coated with Al6061. This indicates a significant improvement in the corrosion properties of the coated substrates.



(a)



(b)

Figure II.1.3.13. (a) Potentiodynamic polarization-accelerated corrosion tests to evaluate the corrosion performance of several coated Zn-coated AZ91 samples as compared with uncoated AZ91. (b) Hydrogen collection data of bare AZ91 and AZ91 coated with Zn for up to 338 hours (e.g., 2 weeks) immersion time. Wrought Al 6061 and Al 6061 coated on AZ91 samples data are also included in the plot. Source: PNNL.

Wear tests were performed on (i) an AZ91 substrate, (ii) an optimized Zn-coating on AZ91, (iii) an optimized Al 6061 coating with a CP-Al bond coat on top of AZ91 substrate, and (iv) an optimized Al 6061 coating on AZ91 substrate. Wear volume and wear rate of the substrate and coating are calculated and shown in Table II.1.3.5. Relatively higher wear volume and wear rate were observed in the uncoated substrate material. The data display 72% improvement in wear resistance (or decreased wear rate) in Zn-coated AZ91 compared with substrate material. The data also show improvement of wear resistance (or decrease in wear rate) in the Al

6061 top-coating and Al 6061 with bond coating by 63 and 25.2%, respectively, compared with AZ91 substrate material.

Table II.1.3.5. Wear Properties of Substrate and Cold-sprayed Surface

Sample	Wear Rate (mm ³ /nm)	Decrease in Wear Rate with Respect to Uncoated AZ91
Zn-coated AZ91 (3.5 MPa, 300 °C)	3.64×10^{-4}	72%
Al 6061 coating with CP-Al bond coat on AZ91	1.006×10^{-3}	25%
Al 6061-only optimized coating (6.5 MPa, 450 °C)	5.0×10^{-4}	63%
Uncoated AZ91D	1.345×10^{-3}	-

Meshfree Modeling of Cold-Spray: Single Zn-Particle Impact into AZ91D Substrate

The aim is to develop a high-fidelity process model for cold-spray to help understand the *in-situ* impact conditions, material morphologies, and bonding mechanism, which are challenging to observe experimentally. To this end, the Lagrangian meshfree SPH method was used, which is well-suited to handling the extreme condition during cold-spray. Single Zn-particle impact into a mismatched AZ91D substrate was particularly studied with experimental validation.

First, an SPH particle size sensitivity study was carried out on a case with a 26 μm diameter (d) particle impact with 600 m/s speed. The temperature and plastic strain results at 56 ns with SPH particle sizes ranging from 1000 nm ($d/26$) to 200 nm ($d/130$) are given in Figure II.1.3.14. Material jetting was captured only if the SPH particle size is smaller than 650 nm, and the model-predicted temperature and plastic strain results are almost identical when the SPH particle size is around 200 nm. As a result, 200 nm was used as the default SPH particle size for the following modeling and analysis. Figure II.1.3.14 shows that the maximum temperature occurs along the bottom interface of Zn particles (left half of each image), while the maximum plastic strain occurs near the jetting forming location (right half of each image). This is the free surface where the impact shock waves from the Zn-particle and AZ91 substrate detach, and where the pressure is released to form a tensile load that leads to the material jetting.

The SPH model was then used to simulate a 10 μm Zn-particle impacting AZ91 with 450 m/s and 650 m/s, and a 26 μm particle impacting with 600 m/s. The particle sizes and speeds were selected according to the experimental data and setting. Figure II.1.3.15(a, c, e) display the final material morphology for each case, whose shapes agree well with the cross-sectional SEM images on the corresponding cold-spray sample. When the particle size is small (10 μm) with lower speed (450 m/s), the kinetic energy is less to barely deform the particle, as shown in Figure II.1.3.15(a–b). When the speed is increased to 650 m/s, the kinetic energy is also increased to help the particle deform horizontally and become “flat,” as shown in Figure II.1.3.15(c–d). When the particle size is large (26 μm) and the speed is high (600 m/s), the kinetic energy is very large. However, there are redundant material in the top half of the Zn-particle deforming horizontally to form a cap-like morphology, as shown in Figure II.1.3.15(e–f).

To understand the forming mechanism of this cap-like morphology for large Zn particles, the pressure distribution in the particle at different times are shown in Figure II.1.3.16. Here, high-pressure is indicated with red, medium pressure with green, and tension with blue. In the initial impact stage ($t = 3$ ns), a small high-pressure zone is formed immediately at the particle-substrate contact surface, as shown in Figure II.1.3.16(a). This zone expands rapidly as the impact continues and the particle flattens to create large interfacial surface at $t = 5$ ns in Figure II.1.3.16(b). The velocity of the high-pressure zone (free surface) expansion is initially faster than the shock (pressure) wave speed and then becomes slower with time, enabling the shock waves to detach from the particle’s edge. At this moment, the high-pressure zone is in contact with a free surface with nearly zero pressure. Such a high-pressure gradient leads to a localized tension in a small

material region to form an incipient “jet lip,” as shown in Figure II.1.3.16(b). At $t = 17$ ns in Figure II.1.3.16(c), the bottom half of the particle remains under compression while the pressure wave reaches to the top particle surface and gets released there to expose a large area with tension. This pressure release and tension force further promotes the jet forming. Because of the mismatched material properties for Zn and AZ91, the free surfaces of particle and substrate expand at *different* speeds. The tension in the top particle surface cannot get released quickly and, thus, forms a cap-like particle shape.

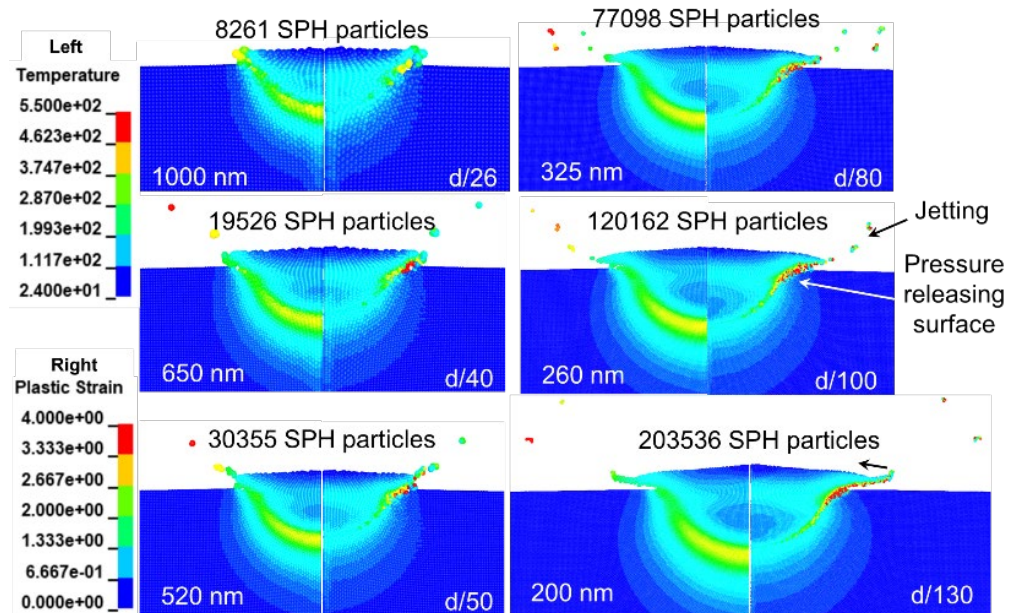


Figure II.1.3.14. SPH particle size sensitivity analysis on cold-spray temperature and plastic strain at 56 ns.
Source: PNNL.

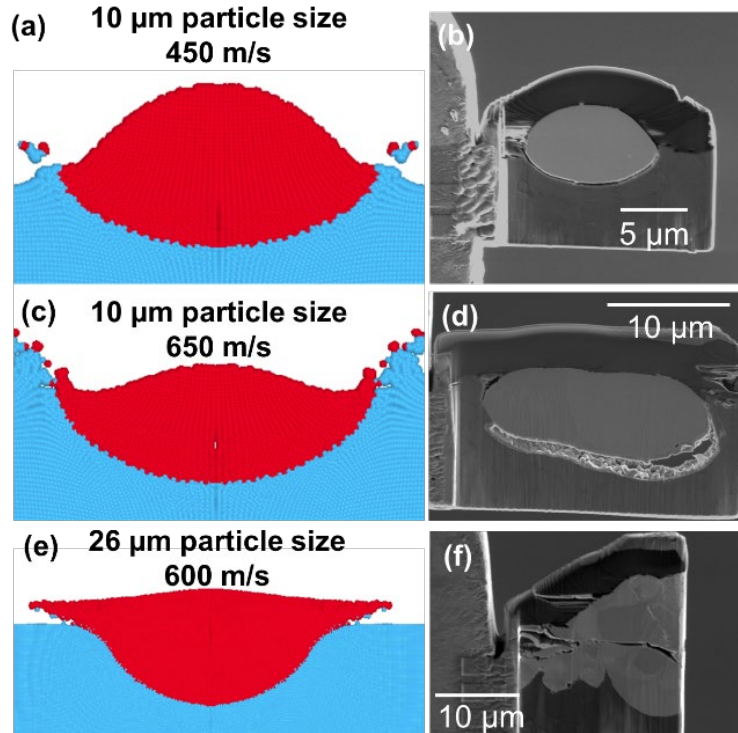


Figure II.1.3.15. (a, c, e) Model-predicted morphologies compared to (b, d, f) experimental results with various particle sizes and speeds. Source: PNNL.

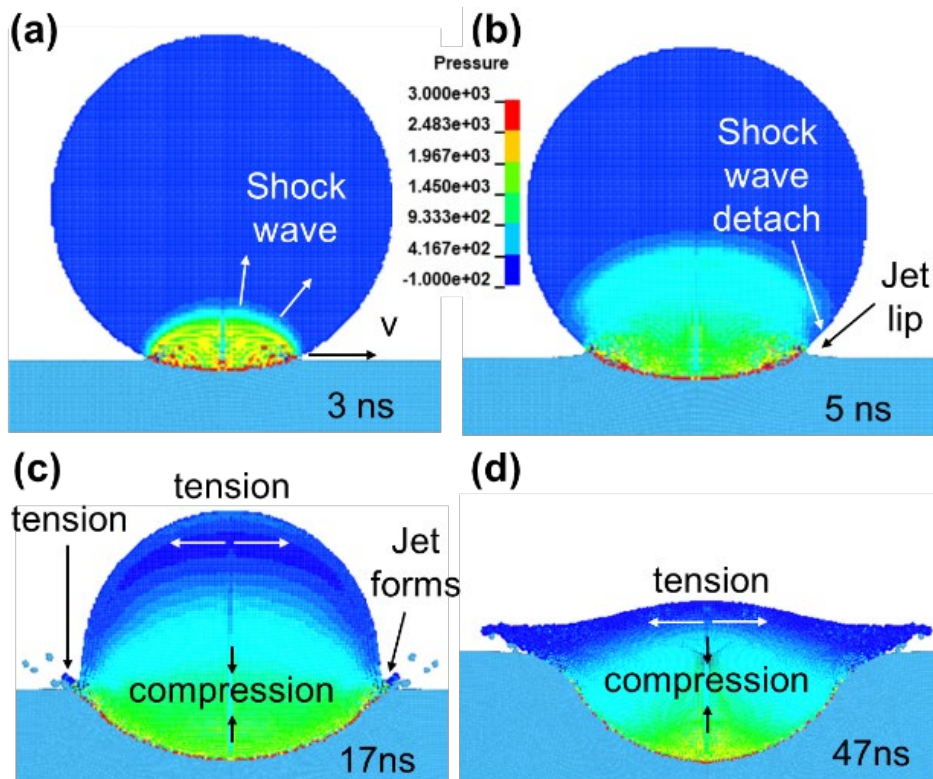


Figure II.1.3.16. (a, c, e) Model-predicted morphologies compared to (b, d, f) experimental results with various particle sizes and speeds. Source: PNNL.

Project 3B

Fatigue Life of FSP Ca-Added AM60

The key results presented in this FY 2023 report are from fatigue life of the Ca-added AM60 after local property modification using FSP and FSP curved coupons. The results are presented for these conditions.

As previously shown in Figure II.1.3.4(a) and the mechanical testing results from FY 2022, improved mechanical properties result from several microstructural changes. FSP leads to direct refinement of grains and refinement of the secondary phases (Al_2Ca for the Ca-added AM60). Furthermore, there is consolidation of casting porosity due to high-temperatures and shear experienced during FSP. The combination of these factors can lead to a simultaneous increase in strength and ductility of the alloy as shown in Figure II.1.3.17(a). Two double-pass FSP conditions were selected for further mechanical testing through the exploration of fatigue life at $R = 0.1$. The testing results and a schematic of the fatigue coupon are shown in Figure II.1.3.17(b). Note that the y-axis is the tensile average stress as fraction of the material YS. The Ca-added AM60 was tested at nominally higher average tensile stress than the cast AM60. Even at higher average tensile stress, the FSP material greatly outperforms the non-FSP material by an order of magnitude. The double-pass at 1600 RPM condition has a $\sim 2\times$ improvement in fatigue life, while the double-pass at 1200 RPM has a $\sim 10\times$ improvement in fatigue life. The differences in fatigue performance for these two processing conditions is likely a result of the energy input during FSP. Further investigation of the strengthening mechanisms at various processing conditions will be performed in FY 2024. The key factor for improved fatigue life is likely the refinement of the Al_2Ca phase and consolidation of casting defects. Large secondary-phase particles can act as crack-initiation sites during fatigue and casting defects act as pre-cracks during fatigue testing.

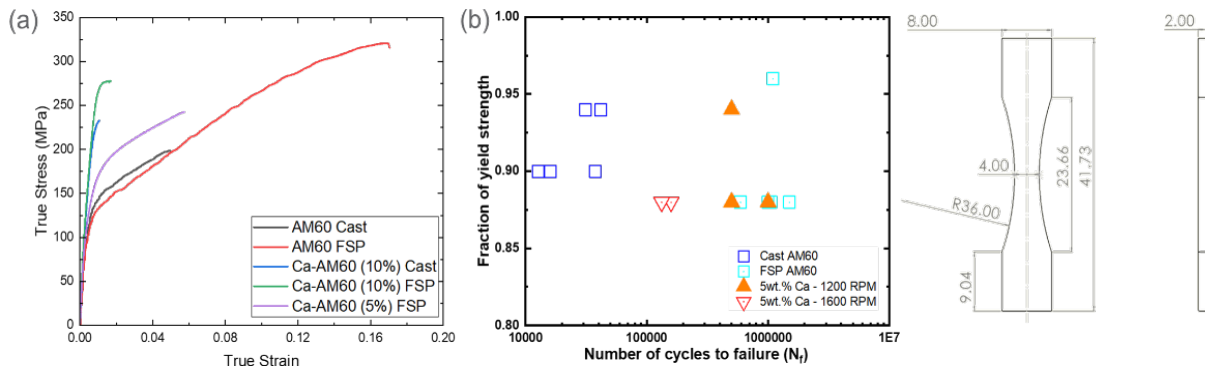


Figure II.1.3.17. (a) Plots showing stress-strain data for selected FSP samples at various processing Ca wt.%. (b) The cycles to failure as a fraction of the YS and fatigue sample geometry. Source: PNNL.

Friction-Stir Processing of 45° and 65° Curved Surfaces

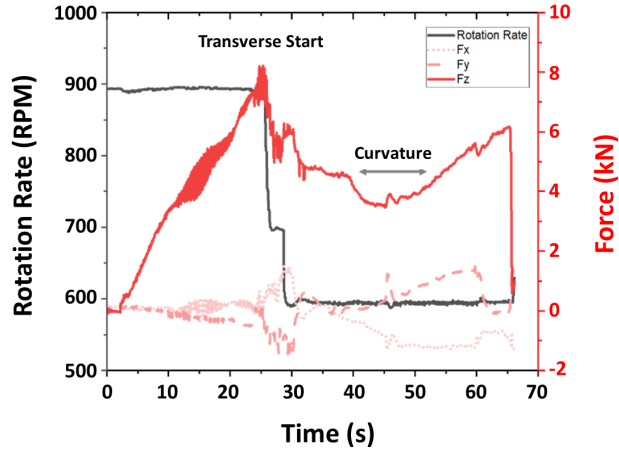
FSP of curved surfaces with 45° and 65° angles and an inner curvature radius of 12.7 mm was successfully performed in this program. This geometry was chosen because it is representative of common features on automotive components made from HPDC Mg-alloys. Several challenges had to be overcome to achieve FSP in such a small radius, which are highlighted in Figure II.1.3.18.

One key challenge in FSP of curved surfaces is the temperature management during the reorientation of the robot posture on the curved surface. There is a large energy input while processing the curved region, which is a direct result of the time required for the robot to reorient itself. During this change in robot positioning, there is very little forward-traverse motion. This leads to over-softening of the plate material. The FSW robot has automated force control during FSP to accommodate for the compliance of the robot arm. However, due to the softening of the material, the robot plunges deeper into the plate, which can lead to tearing if the heat is not managed properly. This is accommodated by reducing the rotation rate during FSP of the curved surface to 600 RPM, as shown in Figure II.1.3.18(a). Even when accounting for this with a reduced RPM, there is still a

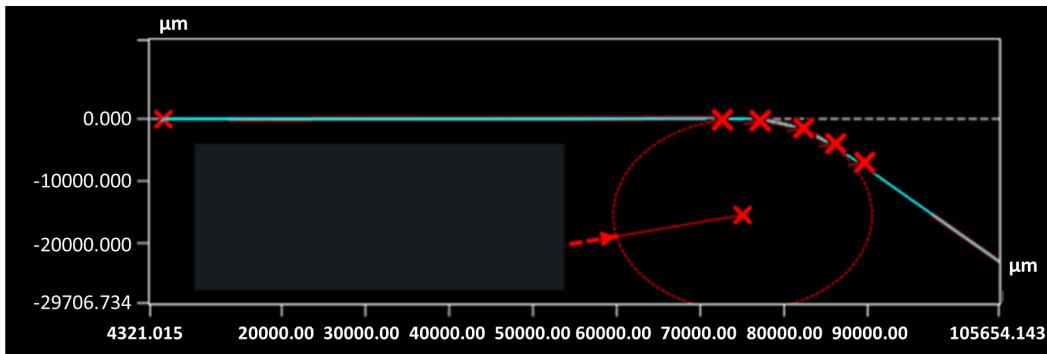
reduction in the forging force of ~ 1 kN; however, the material retains enough strength to prevent excessive plunge depth and tearing. Figure II.1.3.18(c) demonstrates the challenges with the tool-rotation over such a small curvature radius. It appears to lead to negative traverse motion of the pin during the change in posture of the FSW robot.

Another key challenge was proper description of the robot planning and identification of the surface geometry. Minor variations in the plate and curvature geometry existed due to the way the curvature was manufactured (manual press-break). This led to variations in the start position of the curve relative to the plate edge and an error in curvature of $\pm 2^\circ$. Incorrect input of the correct geometry into the FSP robot program led to either excessive or insufficient plunge depth during FSP of the curved region. To account for this, a Keyence VR-5000 3D scanner was used to measure the surface contours of every plate. This allowed for correct identification of the radius start position, the radius of curvature, and the angle change for each plate.

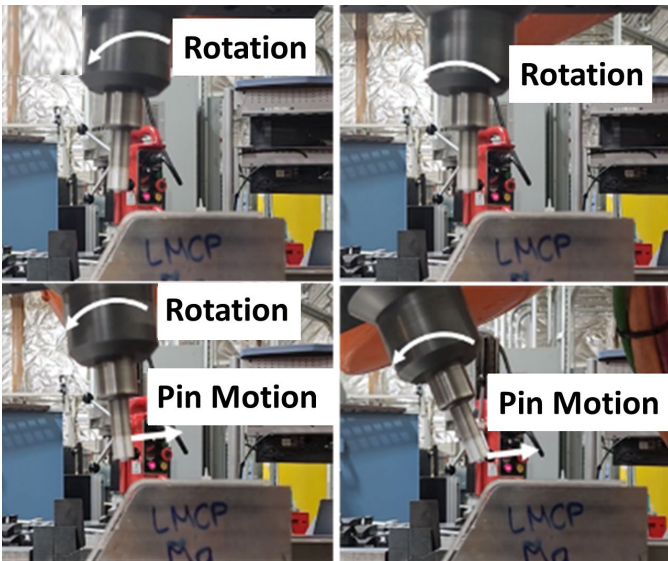
An example of the linear profile obtained for a plate with 45° curvature is shown in Figure II.1.3.18(b). Improper alignment of the FSP robot with the target geometry can also lead to insufficient plunge depth in the linear region following the curvature. The highlighted area in Figure II.1.3.18(d) where the tool appears to retract from the surface and the pin of the tool leaves a groove defect on the surface of the plate. This was also corrected through adjustments based on the 3D surface reconstruction.



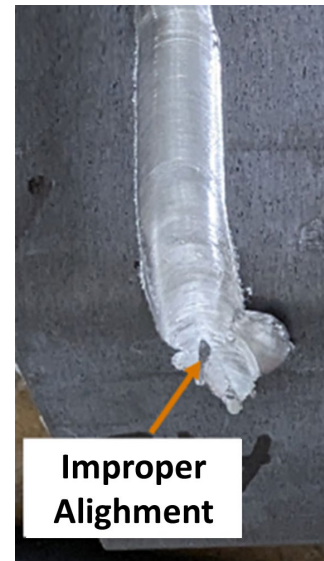
(a)



(b)



(c)



(d)

Figure II.1.3.18. (a) A plot showing the processing forces and rotation rate during processing of the 65° curved plate. (b) A 3D reconstruction of the curved-plate surface used to approximate the path of the tool during curved-plate FSP. (c) Pictures of the curved-plate FSP demonstrating a key challenge in FSP of a small radius of curvature sample. (d) A common defect resulting from improper alignment of the plate and FSW robot system. Source: PNNL.

Optical micrographs of the curved region for both the 45° and 65° curvatures are shown in Figure II.1.3.19. Notably, the cast material has a large quantity of voids and casting defects, as shown in Figure II.1.3.19(a). After FSP, the porosity is reduced from ~2% in the base material to ~0.04% and ~0.1% in the 45° and 65° curvatures, respectively. In the 45° macroscopic image, as indicated in Figure II.1.3.19(b), a unique change in geometry is observed that can result from improper alignment with the target geometry. Here, the plate appears to undergo substantial thinning of the geometry; however, no processing defect is produced in this sample. This was addressed through improved alignment of the robot and the plate geometry. For the 65° curvature, minor surface roughness is in the processed region. Similarly, there is no processing defect that results in the 65° curvature case, as observed in Figure II.1.3.19(c).

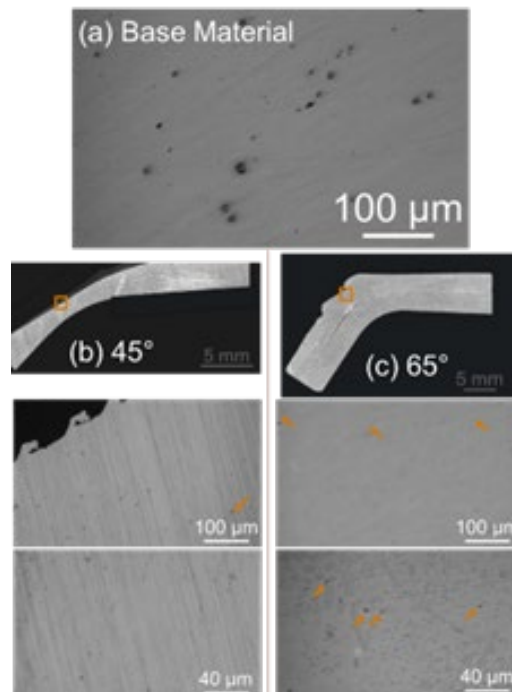


Figure II.1.3.19. Optical micrographs of (a) the base material, (b) the FSP curved surface at 45°, and (c) the FSP curved surface at 65°. Source: PNNL.

Conclusions

Project 3A1

At the completion of Project 3A1 in FY 2023, the following conclusions can be drawn:

- The reactive-surface-processing methods developed under this task (both plasma-assisted organosilicon and Li-salt-assisted thermal CO₂) successfully demonstrated their capability to form thin, uniform surface layers on Mg alloy AM60, resulting in increased corrosion and wear resistance.
- Plasma-assisted organosilicon-coating (P01 and P08) processes formed sound coating layers containing Si, O, and C with uniform thicknesses of 140 and 250 nm. The organosilicon-coated AM60 samples showed corrosion resistance higher than uncoated AM60 (~760% and ~1600% greater based on fitted resistance data in 3.5 wt.% NaCl) as revealed by short-term EIS and long-term H₂ collection results.
- LiNO₃-assisted thermal CO₂ treatment of AZ91D resulted in an Mg-, O-, and C-enriched surface layer, suggesting the formation of MgCO₃ within the layer. As revealed by EIS data, LiNO₃-assisted thermal CO₂ treatment can increase corrosion resistance of AZ91D and AM60 Mg alloy surfaces (up to 1950% greater than the untreated surface as evaluated by fitted resistance data for short-term immersion in 3.5 wt.% NaCl).

Project 3A2

At the conclusion of Project 3A2 in FY 2023, the following conclusions can be drawn:

- The ability to successfully deposit coatings of both pure Zn and Al 6061 powders onto AZ91 substrates that result in very low porosity (less than 1% by area) were demonstrated.
- Cold-spray coatings show significantly better wear resistance as compared to uncoated AZ91. The wear rate is 72% lower in Zn coatings and 63% lower in Al 6061 coatings.
- Electrochemical tests and long-term corrosion results show that the coatings are substantially more noble to corrosion than the uncoated AZ91 material.
- Adhesion tests reveal high-strength values, greater than 30 MPa., increasing with the increase in gas pressure and decrease in porosity.
- SPH modeling has provided excellent insight into the pressure, temperature and velocity range distribution ideal for bonding between substrate and particles and is shedding light on the mechanism of bonding in the materials being investigated.

Project 3B

At the conclusion of Project 3B in FY 2023, the following conclusions can be drawn:

- FSP of Ca-added AM60 leads to a notable increase in the mechanical properties and fatigue life compared to the base AM60 alloy.
- YS is improved from 100 MPa to up to 270 MPa, while fatigue life is improved by a factor of 10.
- Several challenges in FSP of curved regions were addressed, including overheating and alignment issues that helped eliminate common processing defects.
- Curved regions with a curvature of 45° and 65° were successfully processed via FSP. The porosity was substantially reduced in the FSP region from ~2% in the cast condition to 0.04% and 0.1% in the 45° and 65° curvatures, respectively.

Key Publications

1. Garcia, D., H. Das, X. Ma, T. Roosendaal, V. Joshi, D. Herling, M. Komarasamy, and G. Grant, 2022, "Exploring the microstructure-property relationship of Mg-Al-Mn alloys enhanced via FSP," In: Maier, P., S. Barela, V. M. Miller, and N. R. Neelameggham (eds.), *Magnesium Technology 2022*, The Minerals, Metals & Materials Series, Springer, Cham, Switzerland. https://doi.org/10.1007/978-3-030-92533-8_33.
2. Jang, G. G., S. Yeom, J. K. Keum, M. Yoon, H. Meyer III, Y.-F. Su, and J. Jun, 2023, "Formation of carbon and oxygen rich surface layer on high-purity magnesium by atmospheric carbon dioxide plasma," *J. Magnes. Alloy.*, 11(1), 88–99. <https://doi.org/10.1016/j.jma.2022.10.008>.
3. Jun, J., Y. C. Lim, Y.-F. Su, A. Sy, R. Robinson, and D. Pappas, 2023, "Open-air plasma-assisted Si-O-C layer deposition on AZ91D Mg alloy for corrosion mitigation," In: Barela, S., A. Leonard, P. Maier, N. R. Neelameggham, and V. M. Miller (eds.), *Magnesium Technology 2023*, The Minerals, Metals & Materials Series, Springer, Cham, Switzerland. https://doi.org/10.1007/978-3-031-22645-8_13.
4. Jun, J., Y. F. Su, J. Wade IV, D. Pappas, R. Robinson, A. Sy, and Y. C. Lim, 2024, "Open-air plasma-assisted deposition of organosilicon-coating for corrosion protection of AZ91D Mg alloy," *J. Coat. Technol. Res.*, in press. <https://doi.org/10.1007/s11998-023-00876-2>.
5. Niverty, S., R. Kalsar, R. J. Seffens, A. D. Guzman, T. J. Roosendaal, L. E. Strange, and V. V. Joshi, 2023, "Probing corrosion using a simple and versatile *in-situ* multimodal corrosion measurement system," *Sci. Rep.*, 13, 16695. <https://doi.org/10.1038/s41598-023-42249-0>.

6. Niverty, S., M. Pole, R. Kalsar, G. Grant, D. Herling, and V. V. Joshi, 2024, “Cold-spray process optimization and performance of commercial AA6061 coated on HPDC AZ91 Mg alloy,” (in preparation).
7. Niverty, S., R. Kalsar, A. J. Naccarelli, T. J. Eden, X. Ma, N. Overman, R. Prabhakaran, G. Grant, D. Herling, and V. V. Joshi, 2024, “Bond coat-assisted enhancement in microstructural, mechanical, and corrosion behavior of AZ91 Mg alloy cold-spray coated with Al alloys,” (in preparation).
8. Niverty, S., R. Kalsar, G. Grant, D. Herling, and V. V. Joshi, 2024, “Cold-sprayed coatings of CP Zn for enhancing the corrosion performance of Mg-alloys,” (in preparation).

References

1. Lim, Y. C., J. Jun, D. N. Leonard, Y. Li, J. Chen, M. P. Brady, and Z. Feng, 2022, “Study of galvanic corrosion and mechanical joint properties of AZ31B and carbon-fiber-reinforced polymer joined by friction self-piercing riveting,” *J. Magnes. Alloy*, 10(2), 400–410. <https://doi.org/10.1016/j.jma.2021.05.003>.
2. Jun, J., V. V. Joshi, A. Crawford, V. Viswanathan, D. N. Leonard, J. Chen, P. Updadyay, Y. C. Lin, and Z. Feng, 2023, “Galvanic corrosion of AZ31B joined to dual-phase steel with and without Zn layer by ultrasonic and friction stir welding,” *J. Magnes. Alloy*, 11(2), 462–479. <https://doi.org/10.1016/j.jma.2023.01.016>.
3. Song, G., A. Atrens, and D. St. John, “A hydrogen evolution method for the estimation of the corrosion rate of magnesium alloys,” In: Hryn, J. N. (ed.), *Magnesium Technology 2001*, 255–262. <https://doi.org/10.1002/9781118805497.ch44>.
4. Jang, G., et al., 2024, “Alkali metal salts facilitated CO₂ absorption for formation of corrosion barrier layer on AZ91D magnesium alloy,” *J. Magnes. Alloy*, (drafted for submission).
5. Aljohani, T. A., S. Aljadaan, M. T. Bin Rubayan, and F. Khoshnaw, 2021, “Impact of processing parameters in plasma electrolytic oxidation on corrosion resistance of magnesium alloy type AZ91D,” *Eng. Rep.*, 4(2), e12459. <https://doi.org/10.1002/eng2.12459>.
6. Alateyah, A., T. A. Aljohani, M. O. Alawad, S. Elkatatny, and W. H. El-Garaihy, 2021, “Improving the corrosion behavior of biodegradable AM60 alloy through plasma electrolytic oxidation,” *Metals*, 11(6), 953. <https://doi.org/10.3390/met11060953>.

Acknowledgements

The authors from PNNL recognize D. Garcia, X. Ma, H. Das, A. Guzman, T. Roosendaal, R. Seffens, M. Rhodes, R. Kalsar, S. Niverty, V. Prabhakaran, C. B Smith, D. Graff, and G. G. Neuenschwander for their processing and/or characterization activities for this project. The authors from ORNL acknowledge Y. C. Lim, G. G. Jang, A. Plotkowski, and J. Wade.

II.1.4 Thrust 4. Characterization, Modeling, and Life Cycle (Tasks 4A1, 4A2, 4A3, 4C1, and 4C2) (Pacific Northwest National Laboratory, Oak Ridge National Laboratory, and Argonne National Laboratory)

Arun Devaraj, Co-Principal Investigator (Project 4A1)

Pacific Northwest National Laboratory
 Energy Processes and Materials Division
 900 Battelle Blvd.
 Richland, WA 99354
 E-mail: arun.devaraj@pnnl.gov

Thomas Watkins, Co-Principal Investigator (Project 4A2)

Oak Ridge National Laboratory
 Materials Science and Technology Division
 1 Bethel Valley Rd.
 Oak Ridge, TN 37830
 E-mail: watkinstr@ornl.gov

Dileep Singh, Co-Principal Investigator (Project 4A3)

Argonne National Laboratory
 9700 South Cass Ave.
 Lemont, IL 60439
 E-mail: dsingh@anl.gov

Jeffrey S Spangenberg, Co-Principal Investigator (Project 4C1)

Argonne National Laboratory
 9700 South Cass Ave.
 Lemont, IL 60439
 E-mail: jspangenberg@anl.gov

Ayoub Soulami, Co-Principal Investigator (Project 4C2)

Pacific Northwest National Laboratory
 Energy Processes and Materials Division
 900 Battelle Blvd.
 Richland, WA 99354
 E-mail: ayoub.soulami@pnnl.gov

Chris Schooler, DOE Technology Development Manager

U.S. Department of Energy
 E-mail: Christopher.Schooler@ee.doe.gov

Start Date: October 1, 2020
 Project Funding: \$1,150,000

End Date: September 30, 2023
 DOE share: \$1,150,000

Non-DOE share: \$0

Project Introduction

This report describes the activities performed during FY 2023 within the DOE VTO LMCP in the Characterization, Computation, and Life Cycle activity under Thrust 4. The goal of the LMCP, which was launched in October 2020, is to combine multiscale modeling, rapid measurement of properties (i.e., high-throughput testing), and novel processing technologies (i.e., solid-phase processing, AM, and high-intensity thermal treatment) to locally control material properties. Three materials development thrusts are included in the LMCP: Thrust 1 – Selective Processing of Al Sheet; Thrust 2 – Selective Processing of Al Castings; and Thrust 3 – Localized Property Enhancement for Cast-Mg Alloys. Thrust 4 supplements and supports the advanced characterization, computational modeling, and life cycle needs of the various tasks within the three materials development thrusts. Advanced characterization activities include STEM, APT, synchrotron x-rays, neutron scattering, and other capabilities. The advanced characterization is a multi-laboratory effort involving ANL, PNNL, and ORNL. In FY 2023, PNNL conducted the STEM and APT studies. Beamline proposals have been submitted to ANL’s APS for accessing synchrotron x-rays for diffraction experiments. The modeling task includes HPC, DFT, SPH, multiscale modeling for understanding solidification, thermodynamic models, process models, and micro-macro FEM for bendability. Modeling tasks have been conducted both at PNNL and ORNL; residual stress characterization, prediction, and optimization tasks have been conducted at PNNL; and material life cycle studies have been conducted at ANL. This report will cover the results from the Thrust 4 efforts conducted at PNNL, ORNL, and ANL across all three of the following tasks: (1) advanced characterization and modeling; (2) residual stress characterization, prediction, and optimization; and (3) material life cycle in FY 2023 of this project.

Objectives

The objectives of this project are to (1) bring together advanced microstructural characterization, local mechanical testing, and predictive modeling to help establish processing-microstructure-property/performance relationships; (2) characterize, predict, and optimize residual stresses introduced by the local processing approaches used to achieve intentionally heterogeneous microstructure; and (3) study recyclability of intentionally heterogeneous Al- and Mg-alloys.

Approach

The approach in this thrust is to leverage the unique combinations of experimental and computational science capabilities and expertise at these three national laboratories in advanced characterization, modeling, residual stress studies, and material life cycle assessments. The LMCP PIs from Thrusts 1–3, all propose, compete, and obtain access to advanced characterization capabilities and modern computational tools and expertise through an internal proposal review process, issued twice in each financial year. During the review process of the Thrust 4 requests, emphasis is placed on cross-national laboratory collaborations, especially integrating advanced characterization with computational studies from PNNL, ORNL, and ANL.

The access to advanced characterization and computation—as well as residual stress studies and material life-cycle expertise enabled through Thrust 4—provides a unique opportunity to accelerate the development of Al- and Mg-based lightweight alloys with an intentionally heterogeneous microstructure. Table II.1.4.1 provides all the advanced characterization, computation projects, residual stress, and life cycle projects funded and executed in FY 2023. The “Results” section focuses on describing the progress of selected subprojects from each of the three primary projects.

Table II.1.4.1. Thrust 4 – Characterization, Modeling, and Life Cycle Projects Funded in FY 2023

Project	Sub-project Title	Relevant Thrust and Project	Lab Ownership
Advanced Characterization and Modeling	Conducting thermodynamic and process modeling to understand factors affecting the melting and solidification of Al alloys during AM processing. This work was funded in FY 2022 with work continuing in FY 2023.	1B & 2C	ORNL
	<i>In-situ</i> transmission electron microscopic analysis Al6111-T6 at ORNL.	1C1	PNNL & ORNL
	Understanding the composition, size, and spatial distribution of strengthening precipitates formed after local thermal treatments of Al Alloy 6111.	1C3	ORNL
	Understanding the composition, size, and spatial distribution of strengthening precipitates formed after local thermal treatments of Al Alloy 7075.	1C3	ORNL & PNNL
	Developing the multi-spatial and time-resolution finite element heat-transfer model.	1C3	ORNL
	Understanding the microstructure evolution and chemical mixing along the interface of a CP Al/Al6061 cold-sprayed coating on Mg-AZ91 substrates.	3A2	PNNL
	Understanding localized surface corrosion behavior of cold-sprayed Al6061 and CP Zn on AZ91 alloy using scanning kelvin probe force microscopy and correlate with <i>ab-initio</i> simulation results.	3A2	PNNL
	Quantifying the magnitude and distribution of residual stresses in cold-spray samples using microbeam x-ray diffraction and the micro-hole-drilling method.	3A2	PNNL
	Meshfree modeling of cold-spray for mismatched metals: Single Zn-particle impact into AZ91D substrate.	3A2	PNNL
	Modeling the forming of friction-stir processed wrought Al alloys.	1C3	PNNL
Residual Stress Characterization, Prediction, and Optimization	Studying the effect of FSP parameters on the three-dimensional residual stresses distribution in Al alloys.	4	PNNL
	Calculating the residual stresses from WJP and laser peening.		
	Calculating the residual stresses from bending and unbending.		
Material Life Cycle	Performing the material life cycle studies.	4	ANL

Results

Project 1 – Advanced Characterization and Modeling

This task brought together the capabilities and expertise in advanced microstructural characterization and computational modeling at PNNL, ORNL, and ANL for supporting requests under various subprojects from Thrusts 1–3. Results from a subset of these projects are described in the sections that follow.

Project 1.1 – Advanced Characterization of Microstructure-Mechanical Property Relationship in Friction-Stirred Processing of 6111-T6 Al Alloy

This project focused on elucidating the microstructural alterations induced by the FSP of Al 6111-T6 alloy commercial rolled sheets. The FSP led to a 30% reduction in hardness and a 70% enhancement in bending ductility within the stir zone compared to the base Al 6111-T6 alloy. The primary objective of this advanced characterization project was to establish a correlation between the microstructure and mechanical properties within the stir zone. Advanced microstructural characterization techniques, specifically APT at PNNL, was utilized.

For the base Al 6111-T6 alloy, observations included elongated grains with a weak texture in BSE imaging and EBSD inverse pole figure (IPF-Z) images, as shown in Figure II.1.4.1(a) and Figure II.1.4.1(b). APT-reconstructed data showing elemental maps of Al, Cu, Mg, and Si, facilitated an understanding of individual element partitioning among diverse precipitates, as shown in the 3D atom maps in Figure II.1.4.1(c). The APT reconstruction and 1D composition profile from Figure II.1.4.1(d) and Figure II.1.4.1(e) highlighted the precipitates were abundant in Mg and Si, approximating a Mg_2Si stoichiometry. In the friction-stir processed Al 6111-T6 alloy, recrystallized grains with a pronounced texture along 110 were evident in the BSE and IPF-Z images, as shown in Figure II.1.4.1(f) and Figure II.1.4.1(g). Figure II.1.4.1(h) and Figure II.1.4.1(i) show the APT reconstruction of friction-stir processed Al 6111-T6 alloy, highlighting solute-enriched regions. Figure II.1.4.1(j) shows the frequency distribution histograms of second-order nearest neighbor (2NN) distance obtained from the selected region of interest. The 2NN distribution shows the peak frequency of the Mg-Si pairs shifts to a small distance as compared to the random curve, indicating the formation of Mg-Si clusters in the friction-stir processed Al 6111 alloy. Figure II.1.4.1(k) illustrates calculations with an average Mg/Si ratio of approximately 0.96 and a number density of Mg-Si clusters at $4.8 \times 10^{24} m^{-3}$. This pointed to solute clusters within the matrix of the friction-stir processed Al 6111-T6 alloy. Thus, this study, employing APT, provided intricate insights into the microstructural transformations associated with FSP and their implications on mechanical properties of Al 6111-T6 alloy before and after FSP.

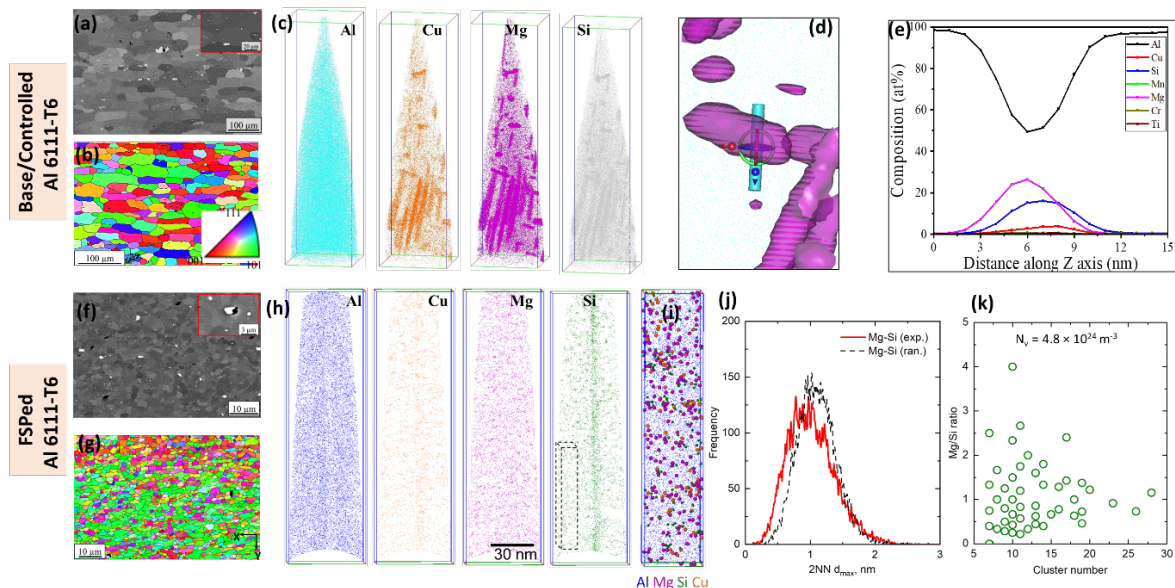


Figure II.1.4.1. (a) BSE image and (b) IPF-Z image of the Al 6111-T6 base alloy. (c-e) The APT reconstruction reveals the element distribution and the composition of the precipitates before FSP. (f) BSE image and (g) IPF-Z image of the friction-stir processed alloy. (h-i) The APT reconstruction reveals the element distribution and composition of the precipitates after FSP. (j) Frequency distribution of Mg-Si obtained from APT and the random distribution. (k) Graph showing the average Mg/Si ratio-to-density of Mg-Si clusters.

Source: PNNL.

Project 1.2 – Specimen Preparation using the Plasma FIB for In-situ TEM Heating Experiment of Al6111 Alloy

This PNNL project contributed to the preparation of samples for the *in-situ* TEM heating experiments conducted at ORNL, which were targeted to understand the microstructural evolution of the Al6111 alloy during FSP. For this task, PNNL performed site-specific lift outs using the PFIB/SEM for the *in-situ* TEM heating experiments to be conducted at ORNL. PFIB utilizes a Xe ion beam, which enables clean, contamination-free machining of specific regions of Al6111. The lift-out strategy is shown in Figure II.1.4.2(a-b). Electropolished 3-mm discs were first characterized in the TEM to identify specific grain orientations in Al6111. These grains were marked and lift-out was completed by making smaller cuts in the foil using PFIB. An Easylift micromanipulator was then used to lift-out the lamella from the 3-mm disc and a cut section was then attached on the Si protochip while making sure the thinner regions aligned with the circular holes on the protochip, as indicated in Figure II.1.4.2(b). W deposition was then used to attach the lamella on the protochip at a low current. The entire process was performed with minimal exposure to a plasma Xe-beam to ensure minimal contamination. EDS mapping was performed on the lamella, as shown in Figure II.1.4.2(c), which revealed minimum W and Xe contamination, while most of the signal came from the Al Alloy and the Si chip. Site-specific mapping at the locations marked by the white boxes in Figure II.1.4.2(b) revealed only 0.23 at.% and 0.08 at.% of W at the areas of interest for heating, as can be seen in Figure II.1.4.2(d). Likewise, minimal traces of Xe are seen at both locations, as observed in Figure II.1.4.2(c). This technique thus enabled a clean, contamination-free TEM lamella, which was shipped to PNNL for further characterization using the *in-situ* TEM heating experiments discussed below.

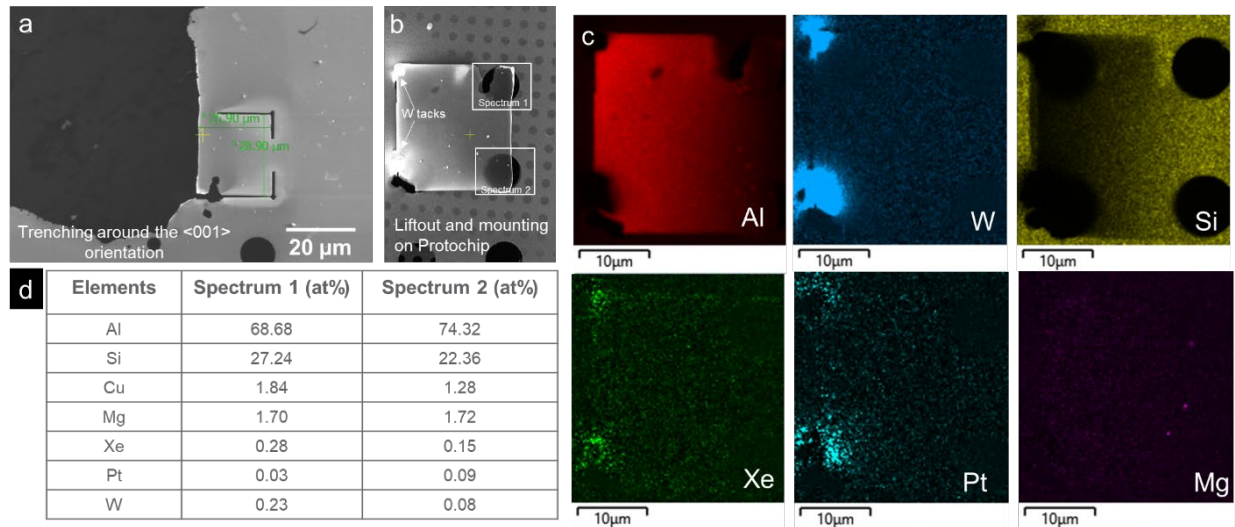


Figure II.1.4.2. (a) SEM image showing cuts made around the area of interest <001> orientation. (b) The lift-out placed on a Si protochip designed for *in-situ* TEM heating experiments. (c) The EDS mapping of the entire lift-out reveals the signals from Al, W, Si, Xe, Pt, and a weak Mg signal. (d) The at.% composition at the two thin areas marked by white boxes in (b). Source: PNNL and ORNL.

Project 1.3 – In-situ TEM analysis Al 6111-T6

ORNL researchers assisted their PNNL counterparts with an LMCP Thrust 1, Task 1C, Approach 1 Project where ORNL employed an *in-situ* HT STEM to monitor the microstructural changes at high-temperatures. Quantifying the associated kinetics will be key in designing the process parameters and understanding the role of microstructural features that control the mechanical behavior. Previously, the ORNL protocols were developed for mounting delicate samples onto the micro-electromechanical system-fabricated Protochips Co. heater devices (e.g., “E-chips”) used in the double-tilt heating holder for an aberration-corrected electron microscope. The first successful mount is shown in Figure II.1.4.3(a), where a secondary electron image from a SEM showing a thin $20 \times 30 \mu\text{m}$ lamella of the Al 6111-T6 alloy is positioned such that the electron-

transparent edge of the lamella subtended two of the holes in the 3×3 hole array in the E-chip. Figure II.1.4.3(b) shows a higher magnification SEM image of the inset in Figure II.1.4.3(a), with another inset showing a low-magnification high-angle annular dark-field (HAADF) image in Figure II.1.4.3(c). An *in-situ* heating protocol was conducted involving sequential pulsing of the temperature of the lamella from 100–200°C and back to 100°C for subsequent imaging, then a repeat up to 300–400°C. Figure II.1.4.3(c) shows a precipitate “ball” (P), which was used as a fiducial marker to relocate the imaging areas following the pulse to 200°C. With the next pulse step (e.g., 100–300°C in 3 s with a 1 s “soak” and an immediate quench to 100°C), a remarkable change in the structure was observed, as seen in the HAADF image shown in Figure II.1.4.3(d). In addition to the ball precipitate, P, a number of additional precipitates appeared, which were determined to contain AlCu (likely the Al_2Cu or “theta” phase); the three elemental maps of the area illustrate the Cu-rich new precipitates, along with the Fe-Mn (and also Cr, not shown) composition of the ball precipitate P. Not shown here was the final pulse step from 100–400°C, which surprisingly caused large areas of the thin region to melt and evaporate, leaving behind the residual nascent thin Al-oxide layer that coats the surface of the Al samples. Also not shown here are high-resolution images of changes in nanoscale precipitates and defects in the alloy structure that were taken. In future work, we plan to use the remarkable capabilities of today’s *in-situ* heating technology to better control the pulse heating process so we can capture the steps of microstructural changes that occur during these heating cycles in greater detail. We have determined that holding the alloy sample at 100°C during the imaging process apparently does not cause significant changes in the microstructure; therefore, we will be able to study all the microstructural details during heating of the alloy lamella to better understand the mechanisms of microstructure development during the applied thermal process.

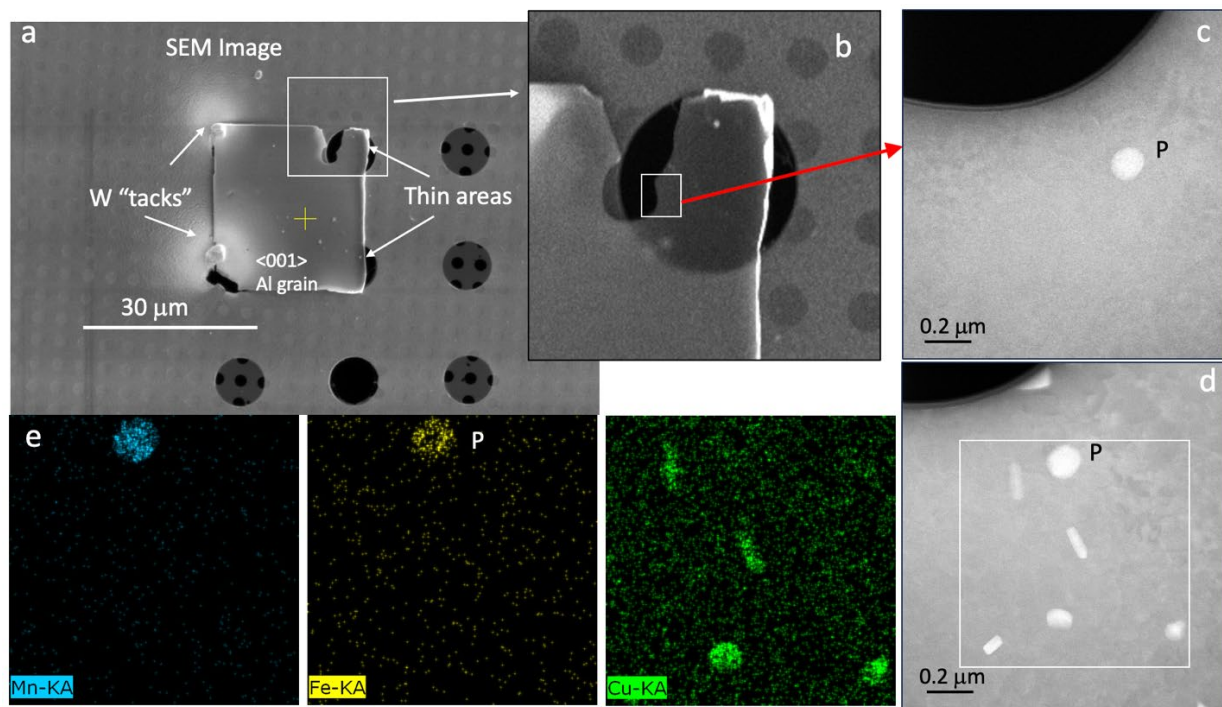


Figure II.1.4.3. (a) SEM image showing the mounted Al lamella with W “tacks” to secure the lamella to the heater membrane. (b) Higher magnification of the thin area over the upper hole in the heater. (c) HAADF-STEM image of the area of the inset in (b) but rotated 90° CW, showing a “ball” precipitate, P, after a 200 °C heating pulse. (d) The same area is shown after a subsequent heating pulse to 300 °C, which created a number of new precipitates. The elemental “maps” in (e) show the Cu-rich composition of the new precipitates along with the Fe-Mn composition of the fiducial ball P. Source: ORNL.

Project 1.4 – Understanding Bond Strength in the Interface of Zn-Zn Particles and Zn-AZ91 Substrate after Cold-Spray using In-situ RT Micropillar Compression and Micro-tension Test

During cold-spray, the spray powder particles undergo severe plastic deformation due to the impact on the substrate. A metallurgical bond is formed at the coating-substrate interface; the microstructure of which consists of pancake shaped grains and some porosity. The focus of this task was to estimate the local bond strength of Zn-coating on Mg AZ91 substrate material to study the overall role of these microstructural features on the coating performance. Figure II.1.4.4(1a-4a and 1b-4b) shows the SEM images of the pillars milled at the coating-substrate interface; the Z-contrast imaging shows the bright contrast areas as Zn-coating and the darker contrast regions as the Mg-substrate. Pillars 1, 2, and 3 show the fracture occurred at the ZnMg interface region. The interface bond strength for Pillars 1, 2, and 3 was calculated to be approximately 194 MPa, 145 MPa, and 135 MPa, respectively. Pillar 1 shows a mixed mode of fracture with the presence of several dimples and river marks. On the left side, a bigger Zn-particle was present where delamination occurred and shows up as a taller surface as compared to the adjacent grain. Similar behavior is observed in Pillar 2, where the crack-initiation site is at the porous interfacial region, and as loading progresses, the fracture occurs along the crack. Pillar 2 also shows several dimple-like features along with intermittent porosity in the coating areas. As we compare these results to pure-Mg, the maximum strength achieved in Pillar 4 is ~200 MPa, which is lower than the UTS of conventional AZ91 Mg at 240 MPa, as shown in Figure II.1.4.4(c). While a size effect is expected in micromechanical testing, in this case, the strength obtained is slightly lower than the bulk alloy. The deformation occurred via slipping mechanism, the slip steps can be seen on the side of the pillar and as the sharp load drops on the stress vs. strain curves. In conclusion, in this work, we were able to calculate the bond strength of ZnMg interface using site-specific micromechanical testing and observe the fracture mechanisms.

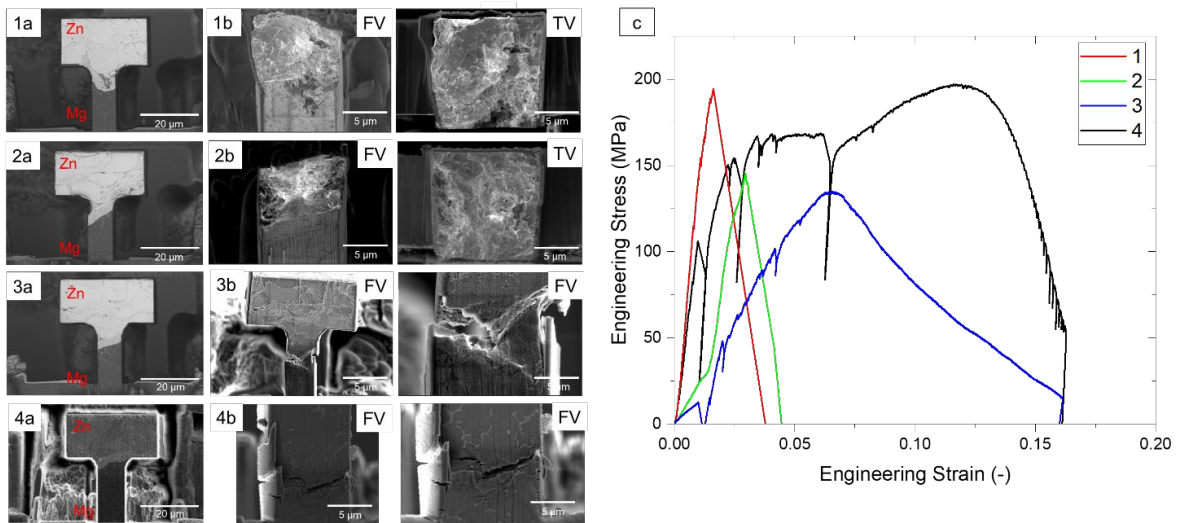


Figure II.1.4.4. SEM images of micro-tensile pillars fabricated at the cold-spray interface (1a–4a) before- and (1b–4b) after-deformation. The after-deformation images are taken at the fracture surface (front-view [FV] and top-view [TV]). (c) The corresponding engineering stress vs. strain curves from the micro-tensile tests.

Source: PNNL.

Project 1.5 – Advanced Characterization of Al Alloy 7075 before and after Friction-Stir Processing

PNNL researchers in Thrust 1, Project C, successfully processed Al 7075 alloys using high-speed FSP. The microstructure in stir zones after FSP is known to reduce the load to the yield point in the bend tests. The focus of this subtask was to characterize the microstructure of Al 7075 base and FSP alloys using aberration-corrected STEM and APT at PNNL to establish the FSP-microstructure-mechanical property relationships.

Figure II.1.4.5(a–b) shows the HAADF-STEM image and the 3D atom maps of Zn, Mg, Cu, and Cr of the T6-treated Al 7075 base sample near the grain boundary (GB). A high-density of η' ($\sim 1.19 \times 10^{24} \text{ m}^{-3}$) and string-like η precipitates are observed in the grain interior and along the GB, respectively. A solute-depletion region (i.e., precipitation free zone [PFZ]) of $\sim 60 \text{ nm}$ width also forms around the GB, as evident in the 3D atom maps. The corresponding 1D compositional profile along the arrow in Figure II.1.4.5(b) reveals $\sim 9.4 \text{ at.}\%$ Zn, $7.4 \text{ at.}\%$ Mg, and $\sim 0.8 \text{ at.}\%$ Cu enrichment in the GB, while the average concentration of Zn and Mg of ~ 1.1 and $0.8 \text{ at.}\%$ in the PFZs is lower than the grain interior, which is $\sim 2.6 \text{ at.}\%$, as observed in Figure II.1.4.5(c). Contrary to the base sample, the FSP stir zone shows almost no η' and η precipitate in the grain interior or GB, as shown in Figure II.1.4.5(d), indicating the significant dissolution of precipitates during FSP. The 3D atom maps show a small number of Guinier–Preston zones (e.g., $\sim 7.23 \times 10^{22} \text{ m}^{-3}$) enriched with Zn and Mg formed in the grain interior, as can be seen in Figure II.1.4.5(e), which results from the natural aging after FSP. The GB of the FSP sample shows lower Zn, Mg, and Cu concentrations of ~ 1.9 , 4.1 , and $1.2 \text{ at.}\%$, respectively, compared to the base sample, as shown in Figure II.1.4.5(f). The width of PFZ around the GB is also reduced to $\sim 30 \text{ nm}$. This reduction in the precipitate number density and PFZ width leads to an increase in bendability of the Al 7075 alloy locally at the friction-stir processed zone.

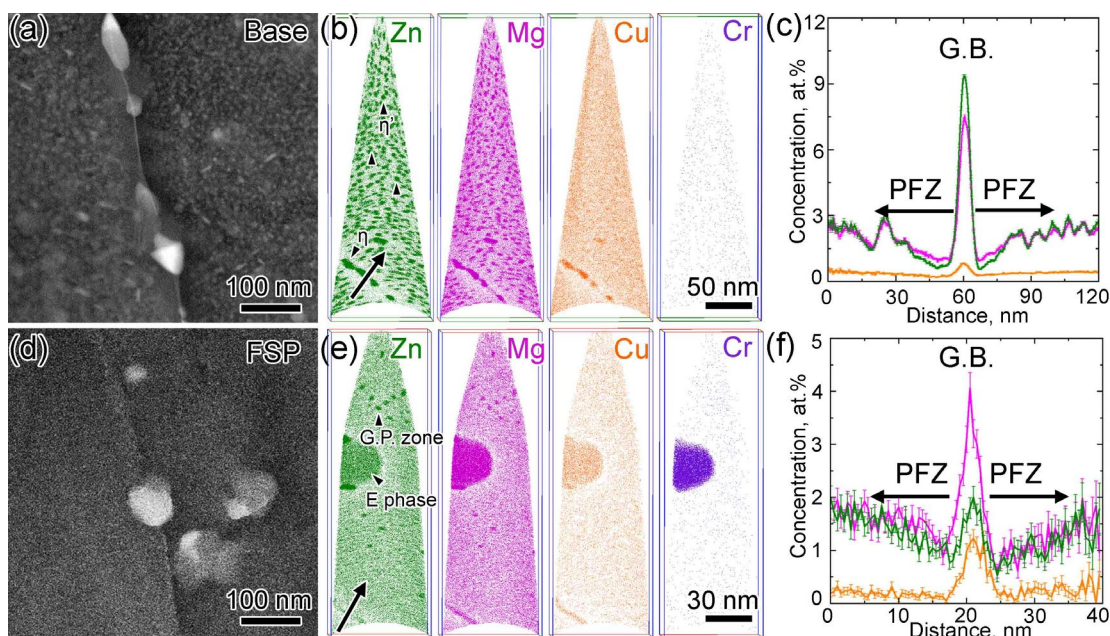


Figure II.1.4.5. HAADF-STEM images, 3D atom maps of Zn, Mg, Cu, and Cr, and the corresponding 1D compositional profiles across the GBs of (a–c) the T6-treated Al 7075 base alloy, and (d–f) the friction-stir processed stir zone. Source: PNNL.

Project 1.6 – Characterization of Precipitate Size Distribution in FSP Al Alloys using Small Angle X-ray Scattering

With the aim of improving local formability, FSP was performed on 2.5-mm-thick Al 7085-T6, Al 7055, and Al 7075 alloy sheets. It was observed that certain combinations of thermomechanical variables resulted in a higher bendability by tests conducted at PNNL [1]. One of the key factors that determine the formability in the Al-7xxx alloy system is the nature of the precipitates/dispersoids present [2]. Therefore, small angle x-ray scattering (SAXS) experiments in transmission mode were conducted at beamline 20-ID-B, APS [3] to characterize the volume fraction/number density and size distribution of the precipitates/dispersoids in a statistically significant sample volume. An x-ray beam of size $0.5 \text{ mm} \times 0.5 \text{ mm}$, with an energy of 21 keV , was used to perform the measurements on samples extracted from the stir zone of Al 7085-T6 plates with FSP process temperatures varying from $400\text{--}480^\circ\text{C}$. The experimental setup at the beamline is shown in Figure II.1.4.6. Ultra-small angle x-ray scattering (USAXS), SAXS, and wide-angle x-ray scattering (WAXS)

measurements were performed sequentially using three separate detectors to cover at least four decades in q (reciprocal space vector), translating to a feature size range of angstrom to μm in real space. The data was pre-processed and stitched (USAXS+SAXS) to obtain a single intensity ($I(q)$) vs. q for a given sample using the Nika and Indra software packages in an Igor Pro environment. WAXS analysis was performed using the Irena software package in an Igor Pro environment.

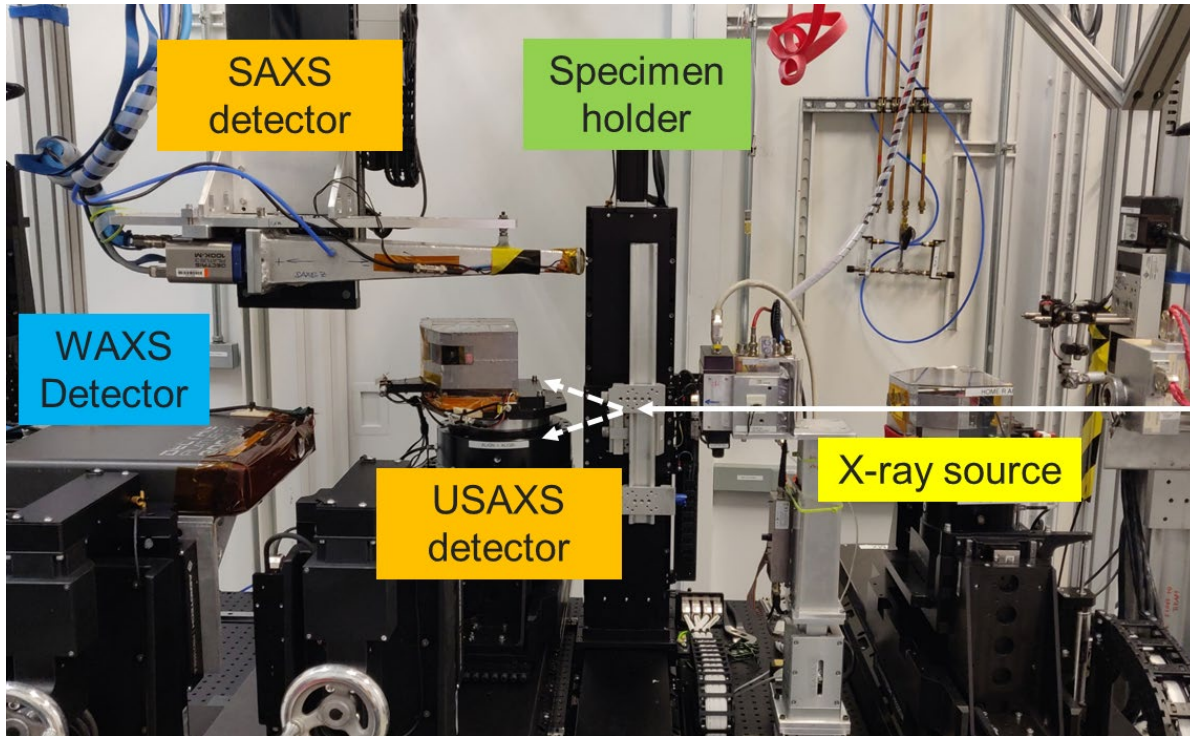


Figure II.1.4.6. USAXS+SAXS+WAXS setup in transmission mode at beamline 20-ID-B. The x-ray beam path is marked in white with a solid line showing the incident beam and a dashed line showing two scattered beams. Source: ANL.

Figure II.1.4.7(a) shows representative WAXS patterns for two boundary cases—the sample with low formability at a process temperature of 400°C and the sample with high-formability at a process temperature of 465°C for the Al 7085-T6 alloy. The WAXS patterns show the presence of Al_3Zr dispersoid and MgZn_2 precipitate peaks along with the prominent Al matrix peaks. This corroborates the TEM/APT observations from the same alloy at PNNL shown above in Project 1.5. Further, each diffraction peak corresponding to the precipitates show different peak intensities when compared across the two conditions, qualitatively indicating a different phase fraction of the precipitates that can be further quantified using the USAXS and SAXS results.

A representative USAXS+SAXS spectrum corresponding to the high-formability sample is shown in Figure II.1.4.7(b). On the $I(q)$ vs. q plots, the larger mean feature sizes of the precipitates/dispersoids are seen as “knees” in the lower q region. The “knees,” labeled in Figure II.1.4.7(b), were able to fit well to a Gaussian distribution of one Al_3Zr sphere and two MgZn_2 disk/cylinder populations—one at the grain interior and the other at the grain boundary. The average feature sizes that were extracted were similar to those observed in the microscopy results—further supporting the statistically representative SAXS results. The volume fraction and precipitate size, as indicated in Figure II.1.4.7(c–d), respectively, of the major strengthening MgZn_2 disk/cylinder-shaped precipitates from the grain interior were found to be the lowest for the samples with a process temperature of 465°C and the highest for the samples with a process temperature of 400°C . This correlates well with the observed trends in bendability (i.e., samples with lowest strengthening precipitate fraction and size show the highest bendability). Note that the “error bar” in Figure II.1.4.7(d) spans the range

of the Gaussian distribution fit, while the symbol indicates the mean size of the precipitate disk. Also, note that three datapoints for the same process temperature correspond to samples extracted from different locations along the weld line.

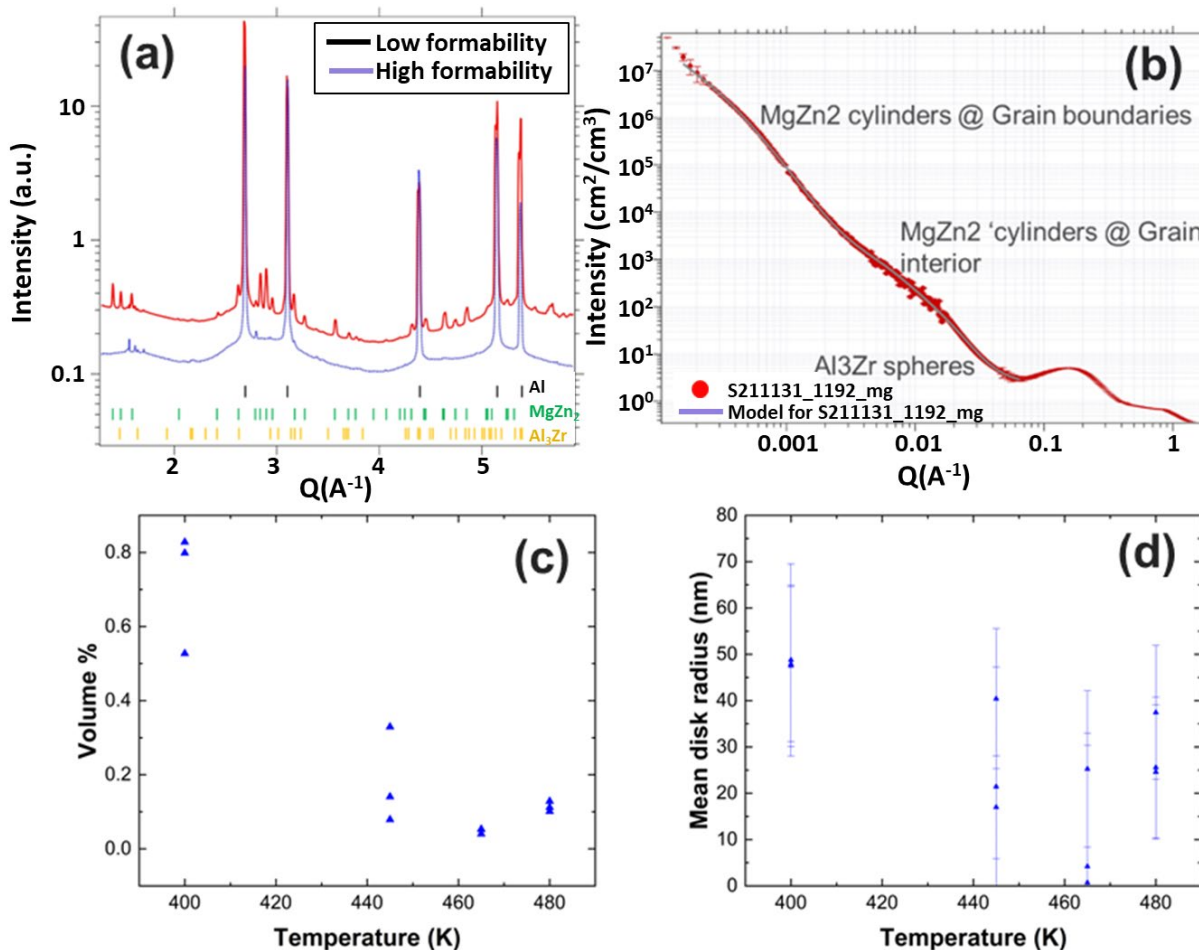


Figure II.1.4.7. (a) WAXS patterns from representative Al 7085-T6 samples, showing the highest and lowest formability, with the peak positions of the precipitates/dispersoids/matrix marked below the patterns. (b) $I(q)$ vs. q plots from the USAXS+SAXS analysis corresponding to the high-formability condition shown in (a) with the “knees” in spectra corresponding to the labeled precipitate/dispersoid populations. Note that a precipitate population “knee” in the lower q value corresponds to a higher value of mean precipitate size. (c) Volume fraction and (d) mean disk radius of the MgZn₂ precipitates present in the grain interior as a function of FSP process temperature for three locations along each weld line (i.e., similar process temperature). Source: ANL.

In summary, FSP Al-7xxx alloys were characterized using USAXS-SAXS-WAXS. The WAXS results showed precipitate (MgZn₂) and dispersoid (Al₃Zr) species present in the stir zone of the FSP Al 7085-T6. The quantitative USAXS+SAXS results show the size and number density of the major strengthening precipitate population (i.e., MgZn₂ in the grain interior) is lower for samples with higher formability. A journal manuscript, led by ANL, is currently being drafted based on this work.

Project 1.7 – Characterization of FSP Al Alloys using the APS

FSP was performed on a 2.5-mm-thick Al 7075 alloy sheet to improve local formability. It was observed that certain combinations of thermomechanical variables resulted in a higher bendability by tests conducted at PNNL [1]. To probe the fundamental deformation mechanisms resulting in the higher formability, tensile tests

with *in-situ* high-energy XRD were carried out in beamline 11-ID-C, APS dog-bone samples from the FSP region of Al 7075 and compared with similar tests on samples from the base material (BM). A tensile load was applied on the BM and FSP samples at a strain-rate of 10^{-4} s $^{-1}$, while simultaneously collecting 2D Debye-Scherrer patterns in transmission mode at a frequency of 1 Hz.

A photograph of the measurement setup in the beamline, as well as an example 2D diffraction pattern, are shown in Figure II.1.4.8(a–b), respectively. Both samples were loaded to a strain of 0.2, well into the plastic region. The measured force and applied strain were used to obtain the engineering stress-strain curves presented in Figure II.1.4.8(c). Further, the 2D patterns were azimuthally integrated (e.g., “caked”) for a total of 20° around the tensile (north) direction to obtain 1D diffraction patterns for analysis. The 1D diffraction patterns obtained were fit using Gaussians in the “single-peak fitting” module of the General Structure Analysis System (GSAS)-II software to extract the peak attributes (e.g., position, width, integrated intensity) of the key peaks in both the matrix and precipitate phases as a function of applied strain. The modified Williamson-Hall method was used to deconvolute the size and microstrain contributions from the peak width.

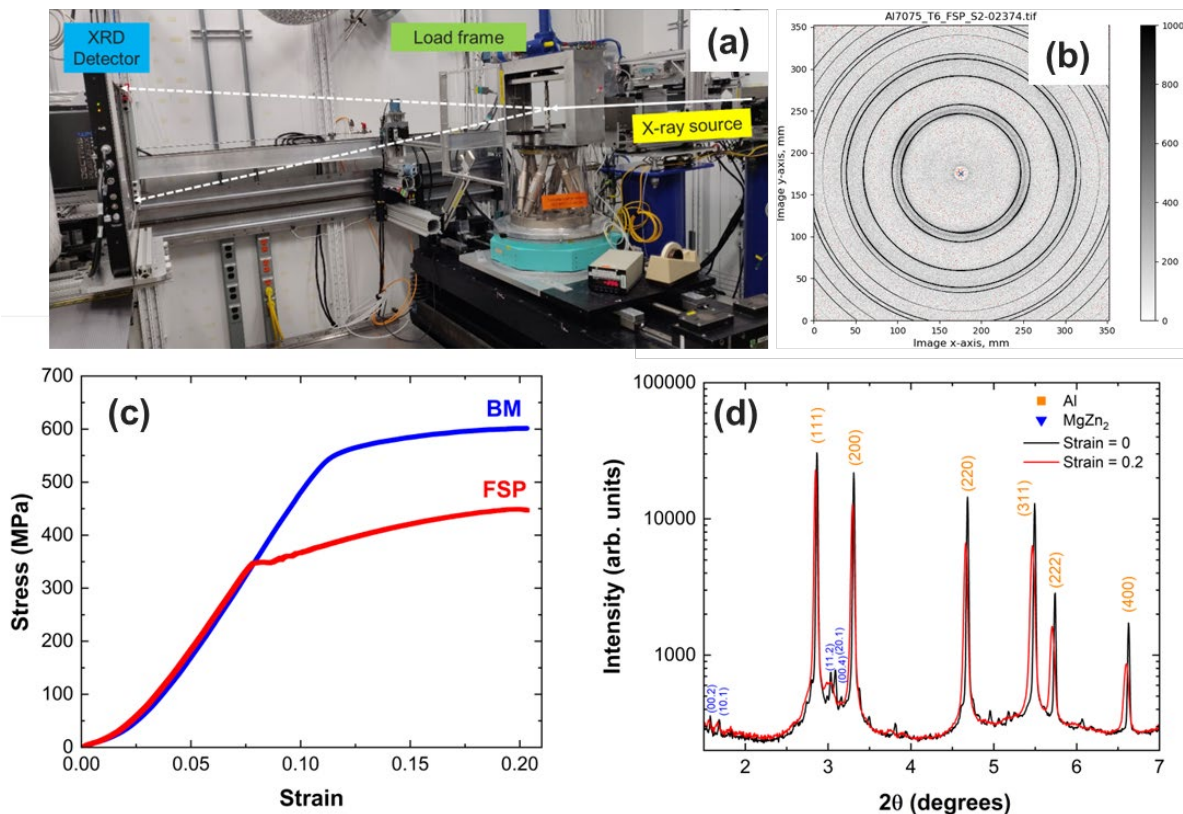


Figure II.1.4.8. (a) Diffraction setup in transmission mode, along with the loading frame, at beamline 11-ID-C, APS. The x-ray beam path is marked in white with a solid line showing the incident beam and a dashed line showing two diffracted beams. (b) An example 2D Debye-Scherrer diffraction pattern recorded at strain = 0 for the FSP sample. (c) The engineering stress-strain data for both samples. (d) Example 1D diffraction patterns at the start (strain = 0) and end (strain = 0.2) of the experiment for the FSP sample showing select indexed peaks from the matrix and precipitate. Source: ANL.

The specific objective of this effort was to help elucidate the fundamental deformation mechanisms in the BM and FSP zones of Al 7075 to help explain the observed increase in formability after FSP. This was achieved by probing the evolution of peak position, width, and integrated intensity during tensile loading of Al 7075 to extract the lattice strain response, crystallite size/dislocation density, and texture.

Figure II.1.4.8(d) shows two example 1D diffraction patterns for the FSP sample obtained from the 2D diffraction patterns recorded at the start (strain = 0) and end (strain = 0.2) of the *in-situ* experiment. The major phases present were the Al matrix and MgZn₂ precipitates, as can be seen in Figure II.1.4.8. The elastic lattice strain (calculated using peak position) as a function of applied stress for different lattice planes in the Al matrix are shown for the BM and FSP in Figure II.1.4.9(a–b), respectively. As has been commonly observed for alloys with a face-centered cubic (FCC) crystal structure [4], the (200) plane accommodates the most and the (111) plane accommodates the least elastic strain for any applied stress in both BM and FSP samples.

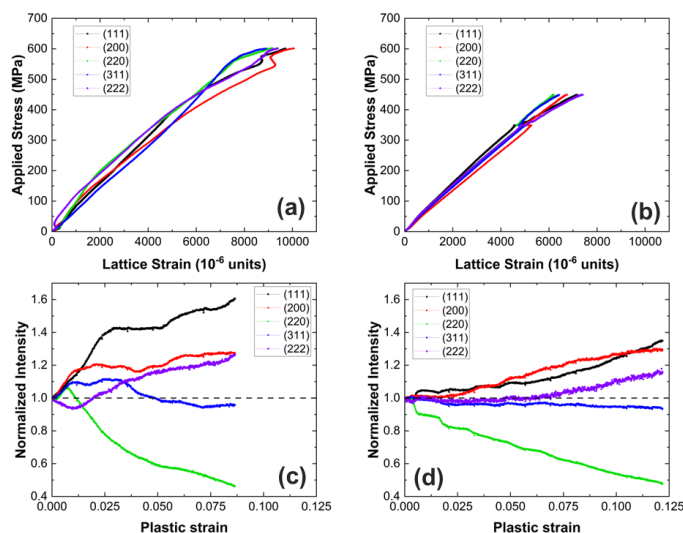


Figure II.1.4.9. Lattice strain as a function of applied stress for different lattice planes in the Al matrix for (a) BM and (b) FSP samples. Normalized integrated intensity as a function of plastic strain for different lattice planes in the Al matrix for (c) BM and (d) FSP samples. Source: ANL.

The normalized integrated intensity—indicative of a change in crystallographic texture during deformation—as a function of plastic strain for different lattice planes in the Al matrix are shown for the BM and the FSP in Figure II.1.4.9(c–d), respectively. The normalized intensity of the (111) plane increases as a function of plastic strain while that of (220) decreases for both the samples. This trend also agrees with previous observations [4] in deformation studies of FCC alloys.

The crystallite size and microstrain in the Al matrix as a function of applied plastic strain for the BM and FSP samples are shown in Figure II.1.4.10(a–b), respectively. The crystallite size is similar and does not change much with increasing plastic strain. The dislocation density, calculated from the microstrain using the formulations in the modified Williamson-Hall method, in the Al matrix for the BM and FSP samples are presented in Figure II.1.4.10(c–d), respectively. The dislocation density in the BM sample is markedly higher (2–5 ×) than the FSP sample at any given value of plastic strain suggesting dislocation slip being a more prominent deformation mechanism in BM than in FSP sample.

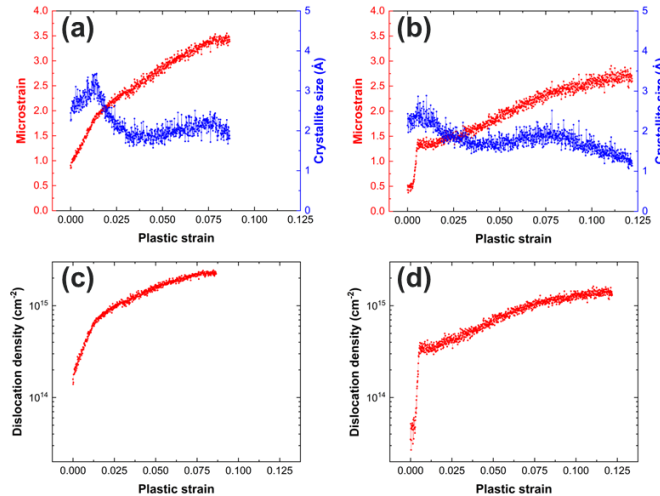


Figure II.1.4.10. Lattice strain as a function of applied stress for different lattice planes in the Al matrix for (a) BM and (b) FSP samples. Normalized integrated intensity as a function of plastic strain for different lattice planes in the Al matrix for (c) BM and (d) FSP samples. Source: ANL.

In summary, the microscopic changes during deformation in FSP and BM Al 7075 were characterized using *in-situ* high-energy XRD. The change in elastic lattice strain and integrated peak intensity with the progression of deformation is similar to previous studies on FCC alloys. The dislocation density was found to be markedly higher in the BM than the FSP indicating dislocation slip being a more prominent deformation mechanism in BM than in FSP sample. A journal manuscript, led by PNNL, is currently being drafted based on this work—also supported by extensive pre- and post-deformation microstructural characterization.

Project 1.8 – Understanding the Composition, Size, and Spatial Distribution of Strengthening Precipitates Formed after Local Thermal Treatments of Al Alloy 7075

The overall focus of Thrust 1 is to use processing techniques to locally alter the microstructure, properties, and edge quality, thereby enhancing the formability and performance of high-strength Al Alloy sheets. At ORNL, a project for LMCP's Thrust 1, Task 1C, Approach 3 investigated the application of thermomechanical and laser processing to improve the formability of high-strength Al sheets. Laser heating can heat localized regions of interest to a temperature that coarsens or dissolves strengthening precipitates, thereby reducing strength, increasing ductility, and improving formability in these regions prior to bending or shearing operations of high-strength sheet alloys in those zones. The objective of this supporting Thrust 4 Project is to understand the composition, size, and spatial distribution of strengthening precipitates formed after local thermal treatments of Al 7075 to enable the correlations with tensile properties and bendability. In this sub-project, Al 7075-T6 samples were laser-treated and then prepared for imaging and elemental microanalysis on multiple TEM/STEM measurements. APT samples were also prepared. Figure II.1.4.11(a–d) compares five passes of the microstructures of the untreated and laser-treated Al 7075-T6 samples. In Figure II.1.4.11(a), the bright-field (BF)-TEM image shows fine and blocky precipitates indicated by the red and yellow arrows, respectively. The majority of fine precipitates were identified as η' phases, contributing significantly to the high-strength of the untreated material. In Figure II.1.4.11(b), the HAADF-STEM image and associated EDS elemental maps of a similar area show the distribution of Zn, Mg, and Cr. The region marked with a red square was identified as the $\text{Al}_{18}\text{Mg}_3\text{Cr}_2$ phase, while the yellow square denotes the η (eta) phase, which is attached to the $\text{Al}_{18}\text{Mg}_3\text{Cr}_2$ phase. Figure II.1.4.11(c) displays APT data for the untreated sample. The Al, Mg, Cu, and Zn atom maps are displayed in the middle, and a proximity histogram of the gray 5 at.% Zn iso-concentration surfaces is displayed on the right. The APT data shows the alloy contains a fine distribution of η' phases.

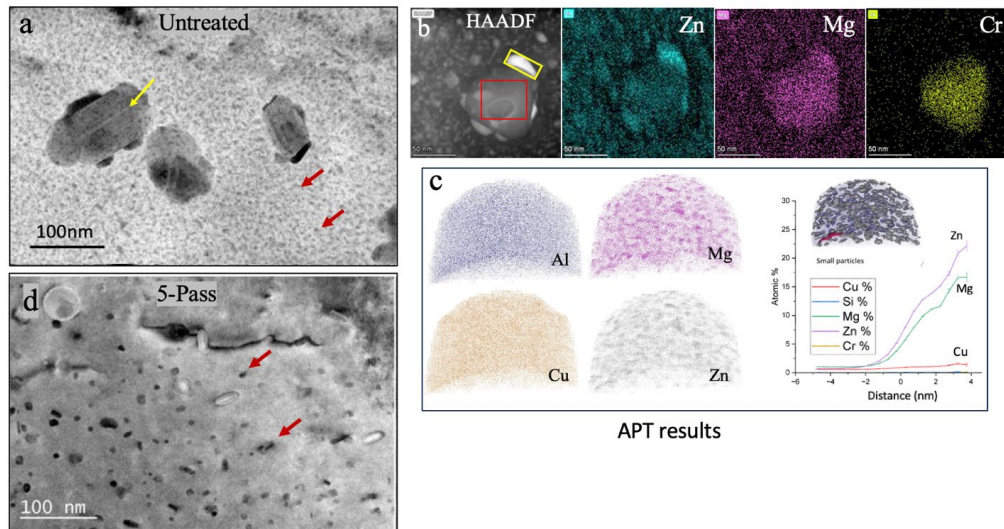


Figure II.1.4.11. (a) BF-TEM image of the untreated AA 7075-T6 alloy, showing the fine precipitates (red arrows) and large blocky precipitates identified as $\text{Al}_{18}\text{Mg}_3\text{Cr}_2$ (yellow arrow). (b) Elemental maps showing the composition of typical blocky precipitates confirm the $\text{Al}_{18}\text{Mg}_3\text{Cr}_2$ composition. (c) APT results confirm the composition of the fine precipitates in the untreated sample. (d) Typical laser-processed region after five laser passes showing the coalescence of the fine precipitates into larger, well-dispersed particles.

Source: ORNL.

Figure II.1.4.11(d) presents a TEM image of the five-pass sample revealing that, in comparison to the untreated sample, the precipitates were more widely spaced, and the $\text{Al}_{18}\text{Mg}_3\text{Cr}_2$ and η phases have grown substantially by 146% and 118%, respectively. This transition in precipitate types observed in different laser pass treatments highlights the profound impact of laser treatment on the material's microstructure, which significantly impacts the material's physical properties, particularly its strength, as these precipitates serve as dislocation barriers that resist deformation during processing steps that involve sheet deformation. These results confirm the Task 1C hypothesis that controlled, localized laser treatments can significantly coarsen a very fine alloy microstructure, reducing strength in the treated zone only, to enable more effective bending within that zone during processing of very high-strength Al sheet alloys.

Project 1.9 – Characterization of Precipitates in Friction-Stir Processed Cast-Mg-alloys using SAXS and WAXS

Two cast-Mg-alloys (AZ91 and AM60) were friction-stir processed at PNNL with the aim of locally modifying the microstructure to obtain desirable properties at specific locations. Certain combinations of thermomechanical variables and post-process heat treatments were seen to produce a local increase in the mechanical properties. One of the key contributors to changes in mechanical properties in AZ91 and AM60 is the nature of the precipitates/dispersoids present, which are in turn dependent on the thermal history experienced. Therefore, to obtain the precipitate/dispersoid characteristics in a statistically representative volume ($\sim\text{mm}^2$), SAXS experiments in transmission mode were conducted at beamline 20-ID-B, APS [3]. An X-ray beam measuring $0.5\text{ mm} \times 0.5\text{ mm}$, with an energy of 21 keV, was used to perform measurements in the center of the stir zone for samples subject to various friction-stir and post-process heat-treat conditions. The experimental setup at the beamline is shown in Figure II.1.4.6 above. For each measurement location, sequential acquisition of USAXS, SAXS, and WAXS was performed using three separate detectors to cover at least four decades in q (reciprocal space vector), translating to a feature size range of angstrom to μm in real space. The data was pre-processed and stitched (USAXS+SAXS) to obtain a single $I(q)$ vs. q for a given sample using the Nika and Indra software packages in an Igor Pro environment. WAXS analysis was performed using the Irena software package in an Igor Pro environment.

The specific objective of this effort was to characterize the size distribution and number density of the precipitates/dispersoid species present in the stir zone of FSP cast-Mg-alloys (AZ91 and AM60) to help explain the observed enhancement in mechanical properties.

The WAXS patterns shown in Figure II.1.4.12(a) were used to identify the phases present in the stir zone of AM60 for three different FSP conditions. In addition to the major Mg matrix phase, the peaks corresponding to precipitate species, β -Mg₁₇Al₁₂ and Al₆Mn (icosahedral quasicrystalline), were also identified in the WAXS patterns. Each diffraction peak corresponding to the precipitates show different peak intensities when compared across the three FSP conditions, implying a different phase fraction of the precipitates that can be further quantified using USAXS and SAXS results.

The corresponding USAXS results for the three FSP conditions are shown in Figure II.1.4.12(b). On the I(q) vs. q plots, the larger mean feature sizes of the precipitates/dispersoids are seen as “knees,” which are marked using arrows, in the lower q region. The marked “knees” in Figure II.1.4.12(b) point to at least two precipitate populations, differing in composition and/or mean feature size, and show significant differences even qualitatively. Further, an initial input of approximate particle size and shape is required for the quantitative SAXS analysis to obtain the precipitate size distributions for each population and will be investigated in detail following microscopy studies at PNNL.

In conclusion, FSP Mg-alloys that were characterized using USAXS-SAXS-WAXS. The WAXS results showed two precipitate species, β -Mg₁₇Al₁₂ and Al₆Mn, are present in the stir zone of the FSP AM60. The USAXS results show a qualitative difference in the size and number density of these precipitate populations. A more quantitative analysis will be conducted leveraging the microscopy studies at PNNL.

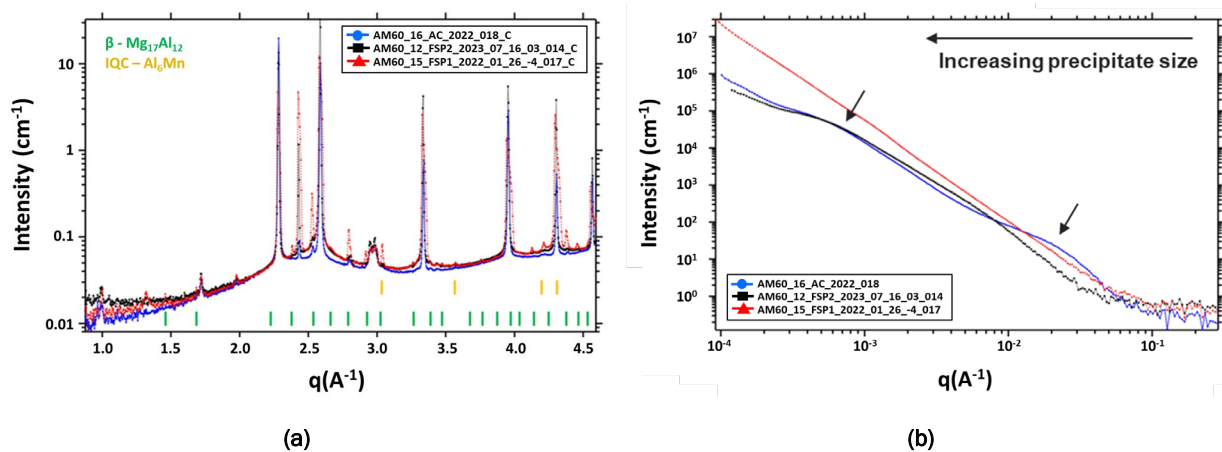


Figure II.1.4.12. (a) WAXS patterns from AM 60 subject to three FSP conditions with the peak positions of the precipitates marked below the patterns. (b) I(q) vs. q plots from the USAXS analysis corresponding to the conditions shown in (a) with “knees” in spectra, each of which correspond to a precipitate/dispersoid population, which are indicated using the arrows. Note that a precipitate population “knee” in the lower q value corresponds to a higher value of mean precipitate size. Source: ANL.

Project 1.10 – Thermodynamic and Process Modeling to Understand Factors Affecting the Melting and Solidification of Al Alloys during AM Processing

This project supports tasks 1.1B (Form-and-Print) and 2.2C (Cast-and-Print), which both involve the localized deposition of 3D-printed material to locally modify composition and properties of wrought/formed and cast parts, respectively. The deposition of material on dissimilar substrates creates a dilution region with a mixed composition between the substrate alloy and the deposited wire-feedstock alloy. It is relatively straightforward to characterize the mechanical properties of the as-deposited bulk deposited material and the bulk substrate

material. However, understanding the properties of the interface and the heat-treatment response of as-deposited materials is more intensive. The objective of this sub-project is to leverage computational tools to assist in understanding the development of alloy properties as a function of heat-treatment and composition.

A thermodynamic database for Al alloys was developed at ORNL for other applications [5]. The database was leveraged in this project for thermodynamic prediction of phases in the relevant Al alloys. Heat-transfer simulations using AdditiveFOAM [6] were done to approximate the thermal cycling that additively deposited material experiences during manufacturing. The resulting thermal cycles were used as input to a precipitation simulation using the software Pandat, developed by CompuTherm, to estimate the change in precipitate nucleation and size after the manufacturing process and because of various heat treatments.

A separate effort aimed to characterize the precipitates in the Al matrix under various heat-treatment conditions was conducted in parallel with this project. Because kinetic properties of the Al-Si-Mg system were needed to predict precipitation behavior in addition to the existing thermodynamic database, an initial validation of precipitation model results was done based on experiments of the aging behavior of cast alloy A356. The alloys of interest are largely part of the Al-Si-Mg system, as indicated by the list of Al Alloy compositions for substrates and wire feedstocks, as included in Table II.1.4.2.

In a previous support task, the thermodynamic database was compared with and agreed well with the simulation and experimental data from Povoden-Karadeniz et al. [7] for phase fractions in an Al-Si-Mg alloy system. For the objectives of the current task, a kinetic database for the alloys also had to be developed and optimized in addition to the previous validation of the thermodynamic database.

Table II.1.4.2. Composition Ranges of the Alloys Used in Thrust 1.1B and Thrust 2.2C in wt.% and with Single Values Indicating Maximums

Alloy	Al	Si	Mg	Fe	Cu	Cr	Mn	Zn	Ti
A356.2 Substrate	Balance	6.5–7.5	0.3–0.45	0.12	0.1	-	0.05	0.05	0.2
Al 6111 Substrate	Balance	0.7–1.1	0.5–1	0.4	-	0.1	0.15–0.45	0.15	0.1
Al 4043 Feedstock	Balance	4.5–6.0	0.05	0.8	0.3	-	0.05	0.1	0.2
Al 4047 Feedstock	Balance	11–13	0.1	0.8	0.3	-	0.15	0.2	-
Al 5356 Feedstock	Balance	0.25	4.5–5.5	0.4	0.1	0.05–0.2	0.05–0.2	0.1	0.06–0.2

Figure II.1.4.13(a) shows the results of Pandat simulations using the developed kinetic parameters for the Al-Si-Mg system considering the formation of β' and β'' precipitates in a solutionized matrix. Tuning of the kinetic parameters for the precipitate phases allowed for reasonable agreement with experimentally observed precipitate volume fractions from Du et al. [8] for an A12 alloy sample undergoing aging at 250°C. Figure II.1.4.13(b) shows the results of the estimated YS from Pandat simulations for A356 T6 heat-treatment at 150°C for 15 hours, starting at the solutionized state. The YS increases over time due to the precipitation of the β' and β'' phases in the matrix. The estimated strength increase is shown to match well with the experimental results of Carniero et al. [10], indicating that the kinetic model parameters are reasonable for an Al-Mg-Si alloy.

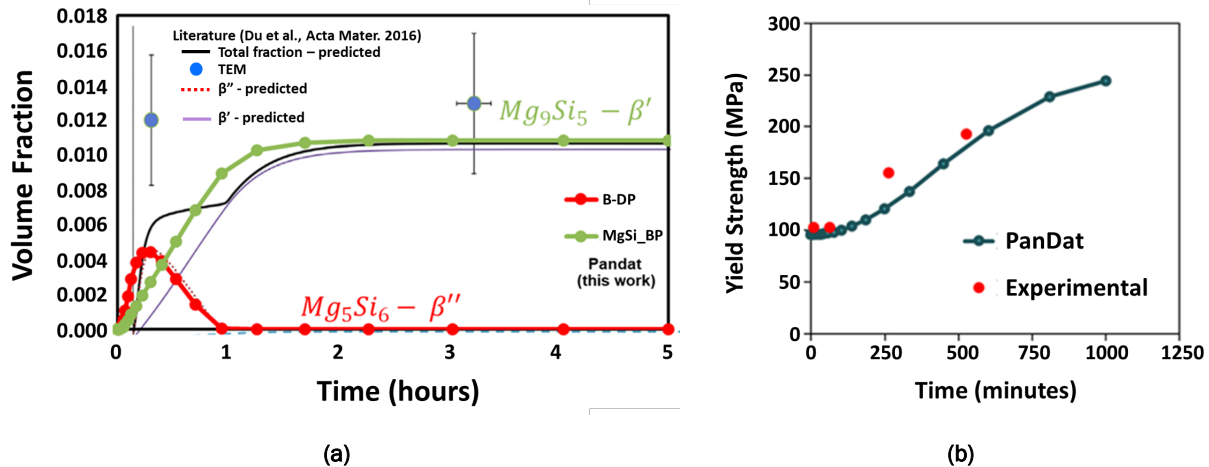


Figure II.1.4.13. (a) Validation of Pandat simulations and kinetic database for phase fraction of β' and β'' in A12 alloy compared to simulations and experiments of Du et al. [8]. (b) A356 YS as a function of T6 aging time at 150 °C based on precipitation simulations via comparison against experiments from Carniero et al. [9]. Source: ORNL.

Further validation and extension of the approach for the dilution region of deposited Al 5356 (Al-Mg alloy) with cast-A356 (Al-Si-Mg alloy) will be done once results can be analyzed from a parallel task applying APT to characterize the matrix in the deposit and dilution region. The APT data is expected to estimate the observed precipitate volume fraction that can be used to validate the precipitation model. Once validated, the precipitation model can be used to better understand optimal heat treatments for the deposited material and the dilution region.

Project 1.11 – Multi-spatial and Time-Resolution Finite Element (MUST-FE) Heat-transfer Model

In the supported development task (ORNL Task 1C), local heating using laser and ultrasonics was used to modify the microstructure at a designated location and locally increasing the formability of Al sheets alloys including AA7075-T6, AA6111-T4. The FY 2023 task goal was to achieve an optimum bendability through optimum process control. The modification of local microstructure of these Al alloys is highly sensitive to local temperature control. During heating and cooling of the heat-treatable alloys, microstructures can undergo changes in precipitates dissolving and re-precipitation, or recrystallization. The precise control of temperature distribution in the sample is therefore the most critical for controlled microstructure modification at designated locations. Non-ideal process conditions could lead to lower than desired properties or unexpected microstructure modification over too large a volume of material. To avoid the trial-and-error approach in this Thrust 4 Project, a recently developed MUST-FE concurrent thermal-mechanical modeling scheme to accurately predict the temperature distribution with high-resolution during local thermal laser treatment processing of Al sheets was applied. The goal is to use this model to determine the optimum processing parameters (e.g., laser power, spot size, travel speed) that will result in the target temperature and microstructure necessary to provide the targeted bendability enhancement.

A temperature history was measured using a single thermocouple placed directly beneath the laser at “b,” as shown in Figure II.1.4.14(a). Based on the local laser heating geometry, an Abaqus heat-transfer model was developed for an Al sheet of nominally $100 \times 12.7 \times 2$ or 2.5 mm^3 . A ring heat source model with an inside diameter of 1.98 mm and an outside diameter of 0.7 mm, respectively, was used. The heat (q) input per unit area was assumed to be homogeneously distributed within the ring: $q = aP/A$, where P is the laser power, A is the area of the ring, and a is the laser absorption rate. To reduce computational time, only half of the model was considered, which assumed mirror symmetry with reference to the width \times thickness plane of the sheet. Eight node hexahedral thermal elements were used with the meshing being denser at the top surface and mid-

plane of the sheet, which are directly under the laser illumination, as observed in Figure II.1.4.14(a). Simulations were performed for both AA7075T6 alloy of 2.5-mm-thickness and AA6111T6 alloys of 2-mm-thickness with the use of two absorption rates ($a=0.12$ or 0.16). Figure II.1.4.14(b) shows a comparison between the predicted temperature histories and measured temperatures at the bottom of the sheet. The predicted temperature history is within 10% accuracy as compared to that of the measurements when the absorption rate is chosen to be 0.12. In the future and once refined, the temperature portion of the MUST-FE model will be calibrated with infrared thermography.

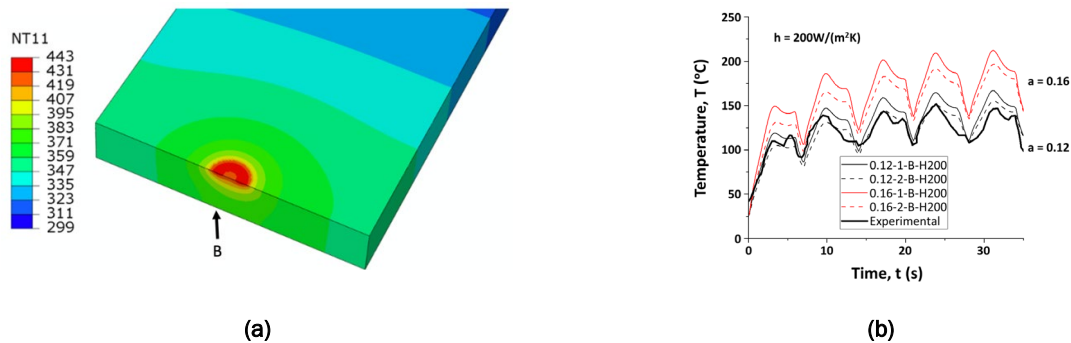


Figure II.1.4.14. Half of the sheet used in the laser heating model. (a) Predicted temperature distribution (K) within the sheet. (b) The predicted temperature histories (solid line) of AA7075-T6 alloy with $P=350 \text{ W}$ are compared with actual measured temperatures (black bold curve) for the identical process conditions at point, B, at the bottom center of the sample shown in (a). Here, $P=350 \text{ W}$, a laser scan speed of $125 \text{ mm}/\text{minute}$ and laser waiting time = 1 s between laser scans. A convective heat-transfer of the sheet surface with the ambient air (25°C) is considered for cooling. The convection coefficient, h , of $200 \text{ W}/(\text{m}^2 \cdot \text{K})$ is used to lump sum the effect of air cooling and cooling from the clamps. The thermal parameters for the AA6111-T6 and AA7075-T6 alloys, such as the heat-transfer coefficient and heat capacity, were taken from the literature.

Source: ORNL.

Project 1.12 – Meshfree Modeling of Cold-Spray for Mismatched Metals: Single Zn-Particle Impact into the AZ91D Substrate

This task aims to develop a high-fidelity process model for cold-spray (CS) to help understand its *in-situ* impact conditions, material morphologies, and bonding mechanism, which are challenging to observe experimentally. To this end, the Lagrangian meshfree SPH method was used, which is well-suited to handling the extreme condition during CS. Single Zn-particle impact into mismatched AZ91D substrate was particularly studied with experimental validation.

First, a SPH particle size sensitivity study was carried out on a case with a $26\text{-}\mu\text{m}$ diameter particle impact and 600 m/s speed. The temperature and plastic strain results at 56 ns with SPH particle sizes ranging from 1000 nm ($d/26$) to 200 nm ($d/130$) are given in Figure II.1.4.15. Material jetting was captured only if the SPH particle size is smaller than 650 nm , and the model-predicted temperature and plastic strain results are almost identical when the SPH particle size is around 200 nm . As a result, 200 nm was used as the default SPH particle size for the following modeling and analysis. It can be seen from Figure II.1.4.15 that the maximum temperature occurs along the bottom interface of Zn-particle, while the maximum plastic strain occurs near the jetting forming location. This is the free surface where the impact shock waves from Zn-particle and AZ91 substrate detach, and where the pressure is released to form a tensile load that leads to the material jetting.

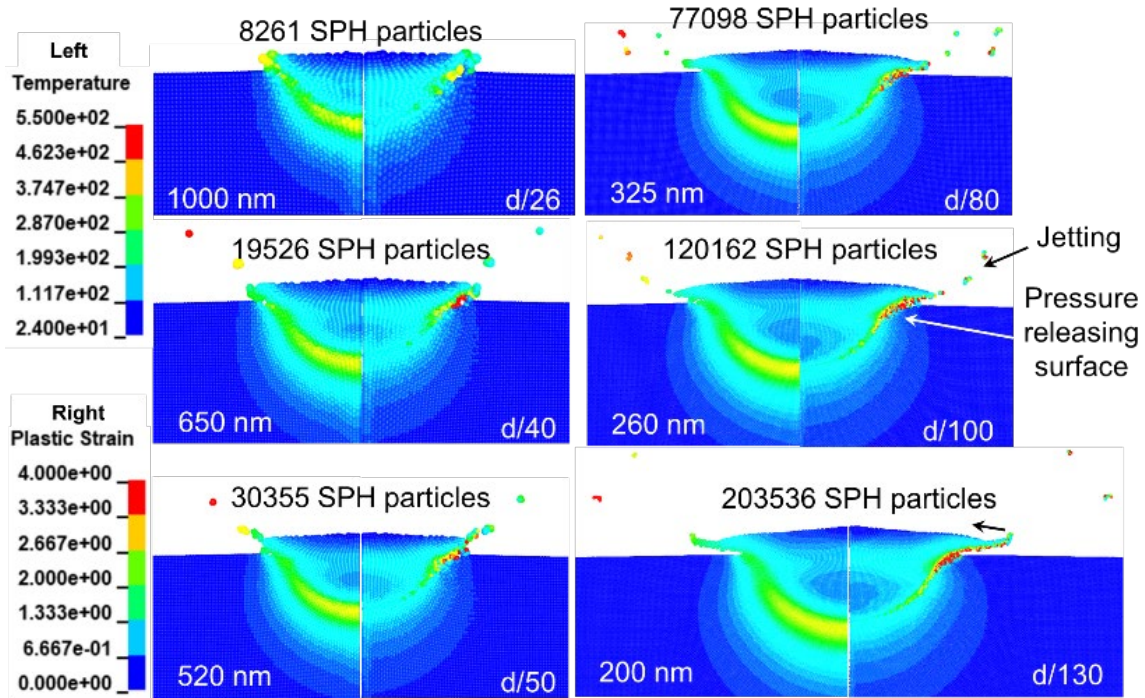


Figure II.1.4.15. SPH particle size sensitivity analysis on (left) CS temperature ($^{\circ}\text{C}$) and (right) plastic strain at 56 ns. Source: PNNL.

The SPH model was then used to simulate 10- μm Zn-particle impacting AZ91 with 450 m/s and 650 m/s, and 26- μm particle impacting with 600 m/s. The particle sizes and speeds were selected according to the experimental data and setting. Figure II.1.4.16(a), (c), and (e) display the final material morphology for each case, whose shapes agree well with the cross-sectional SEM images on the corresponding CS sample. When the particle size is small (10 μm) with a lower speed (450 m/s), the kinetic energy is less to barely deform the particle, as shown in Figure II.1.4.16(a–b). When the speed is increased to 650 m/s, the kinetic energy is also increased to help the particle deform horizontally and become “flat,” as shown in Figure II.1.4.16(c–d). When the particle size is large (26 μm) and the speed is high (600 m/s), the kinetic energy is very large. However, there are redundant material in the top half of the Zn-particle deforming horizontally to form a cap-like morphology, as shown in Figure II.1.4.16(e–f).

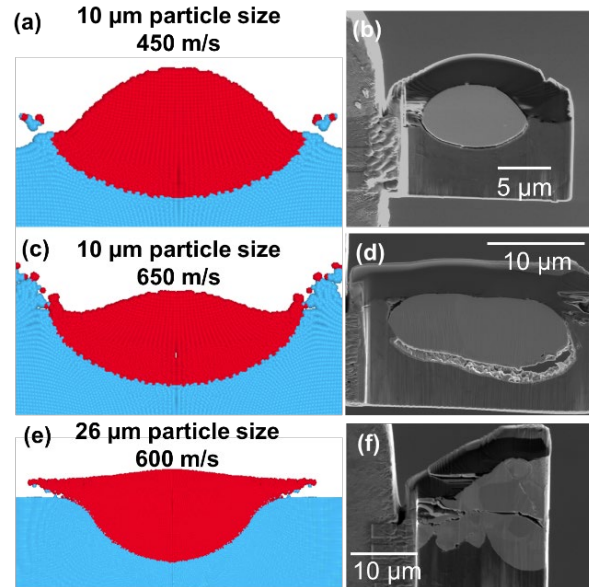


Figure II.1.4.16. (a, c, and e) Model-predicted morphologies compared to (b, d, and f) experimental result with various particle sizes and speed. Source: PNNL.

To understand the forming mechanism of this cap-like morphology for large Zn particles, the pressure distribution in the particle at different times are snapshotted in Figure II.1.4.17. Here, the high-pressure is demonstrated with red, medium pressure with green, and tension with blue. In the initial impact stage ($t = 3$ ns), a small high-pressure zone is formed immediately at the particle-substrate contact surface, as shown in Figure II.1.4.17.(a). This zone expands rapidly as the impact continues and the particle flattens to create large interfacial surface at $t = 5$ ns in Figure II.1.4.17(b). The velocity of the high-pressure zone (free surface) expansion is initially faster than the shock (pressure) wave speed and then becomes slower with time, enabling the shock waves to detach from the particle's edge. At this moment, the high-pressure zone is in contact with a free surface with nearly zero pressure. Such a high-pressure gradient leads to a localized tension in a small material region to form an incipient "jet lip," as shown in Figure II.1.4.17(b). At $t = 17$ ns in Figure II.1.4.17(c), the bottom half of the particle remains under compression, while the pressure wave reaches to the top particle surface and gets released there to expose a large area with tension. This pressure release and tension force further promotes the jet forming. Because of the mismatched material properties for Zn and AZ91, the free surfaces of particle and substrate are expanding with different speeds. The tension in the top particle surface cannot get released quickly and thus form a cap-like particle shape.

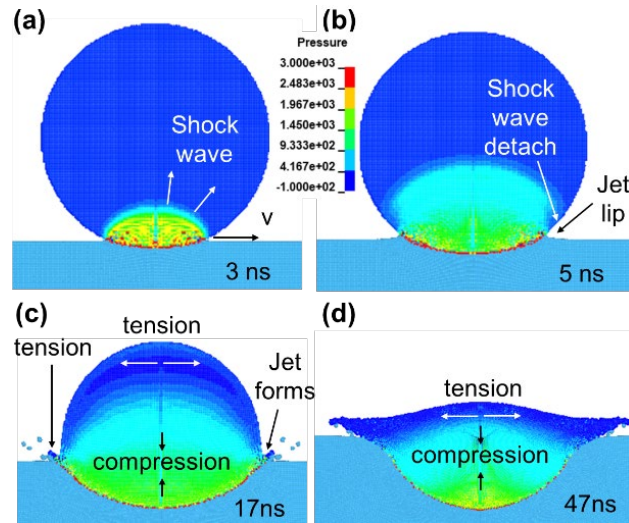


Figure II.1.4.17. Deformation and pressure distribution (GPa) for 26 μm particle size and 600 m/s at different times. Source: PNNL.

Project 1.13 – Modeling Forming of FSP-Wrought Al Alloys

Under project 1C1, FSP has improved the local ductility and bendability of wrought Al alloys [1]. This ability to enhance local formability can enable high and complex strain loading without fracture in automotive forming processes, including stamping parts. However, there is a need to understand specific FSP paths (linear and/or curvilinear) that would allow taking advantage of improved local bendability. Therefore, modeling work has been performed in this task to capture the local material properties of various FSP plate regions and then to design optimal FSP paths toward using the process for improved formability of high-strength Al.

FEM has been performed to simulate coupon-level uniaxial tensile and bending (i.e., VDA) tests. Figure II.1.4.18 shows the force-displacement plot for the FSP AA7075 alloy sheet, derived from both experimental tests and simulations incorporating calibrated material properties. As Figure II.1.4.18 shows, bendability is better when the processed zone’s root is under tension as opposed to the crown under tension. The calibration process revealed that this phenomenon is not because of the difference in hardness/yield stress between the crown and tension. It was because the heat-affected zone (HAZ), which is at the root, is more ductile than the stir zone, which is at the crown. Note that hardness distributions have been considered by using the nanoindentation data. The excellent match with the tests implies that the properties of all the regions in the FSP plate have been accurately incorporated into the models.

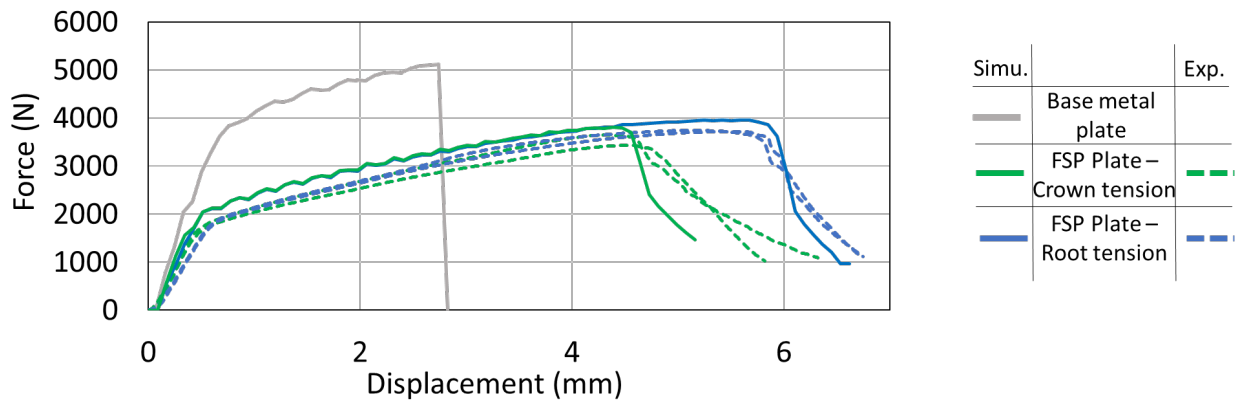


Figure II.1.4.18. Force-displacement plot from bending tests of the FSP A7075 plates. Results from both simulation and experiments have been shown. Source: PNNL.

For the next step, simulations have been used to recreate the limiting dome height test. This test involves a larger scale component and more complex loading. The predicted fracture locations for unprocessed and processed AA7075 alloy plates are shown in Figure II.1.4.19(a-b). As also observed in experimental tests, the base metal plate fails at the center, and the processed plate fails in the HAZ, just outside the stir zone. HAZ being softer leads to plastic strain localization, and regardless of the higher HAZ ductility, the overall ductility of the processed plate was lower. This underscores the need for modeling to design such an FSP path so that strain localization in the HAZ is prevented.

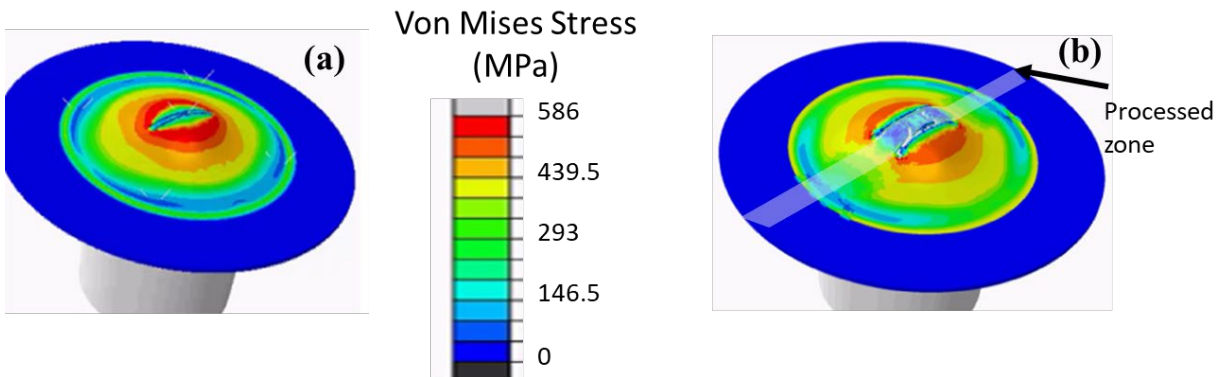


Figure II.1.4.19. Simulated fracture during the limiting dome height test of (a) an unprocessed AA7075 alloy plate and (b) an AA7075 alloy plate FSP along a line in the center. Source: PNNL.

Project 2 – Residual Stress Characterization, Prediction, and Optimization for Hybrid Property Assemblies

The objective of this task is to investigate residual stresses resulting from local microstructure modification processes and provide support to the projects in Thrusts 1–3. The approach taken in this project combines the continuum-level models to predict the residual stresses and dimensional instabilities with experimental measurements of residual stress distributions. During FY 2021, predictive modeling tools to simulate residual stresses from FSP of Al alloys were developed and validated. FY 2022 focused on upgrading the FSP simulation tools, and the development of models for ShAPE™ and other processes. In FY 2023, an in-house comprehensive campaign to characterize the 3D residual stress distributions in many of the processes in the program was undertaken.

Project 2.1. – Effect of FSP Parameters on the 3D Residual Stresses Distribution in Al Alloys

Residual stresses are influenced by the FSP process parameters, such as weld speed, tool-rotation speed, and the number of passes. Developing mitigation strategies requires understanding how changes in process parameters affect the residual stresses and their distributions on the surface of the component and through its thickness, too. For this purpose, characterization of processed wrought Al 7075 and cast-Al 380 alloy samples at different process parameters was carried out.

A total of five FSP samples, whose process parameters are shown in Table II.1.4.3, were characterized. The samples include three HPDC A380 alloy samples and two wrought A7075 alloy samples, all at different process conditions. Residual stress characterization was carried out using the hole-drilling electronic speckle pattern interferometry. Through-thickness in-plane residual stress distributions at selected locations on the sample surfaces were determined using this technique. Figure II.1.4.20(a–b) show the through-thickness distribution of residual stresses at the edge of the processed zone in the cast A380 alloy two-pass Sample #3 and wrought A7075 alloy Sample #4, respectively. The stress distributions in both these samples share a few similarities. The residual stresses in the longitudinal/process direction (σ_{xx}) are tensile and always larger than the stresses in the transverse direction (σ_{yy}). For this reason, longitudinal stresses will mainly be discussed. The magnitude of the largest stress value as a fraction of yield in both samples is similar at around 25–30%. The obvious dissimilarity is in the variation with respect to depth. In this wrought Al sample and all other wrought Al samples, the stresses are the largest on the top/processed surface and decrease monotonically, with

respect to the depth, and are the lowest at the bottom surface. However, in all cast-Al samples, the stresses at the bottom surface are likewise large. Only in the middle of the sample, the residual stresses are lower by around 20 MPa.

Table II.1.4.3. FSP Parameters of the Characterized Samples

No.	Name	Material	Rotations per minute (RPM)	WS (m/min)	Tool diameter (mm)	Process Temperature (°C)
1	Cast-Al 1 Pass	HPDC A380	1200	0.2	20	448
2	Cast-Al 1 Pass - High temp.	HPDC A380	450	0.05	20	481
3	Cast-Al 2 Pass	HPDC A380	450	0.05	20	478.9 & 476.2
4	Wrought Al	Al 7075 - T6	500	0.5	12.7	445
5	Wrought Al - High temp.	Al 7075 - T6	1000	0.5	12.7	498

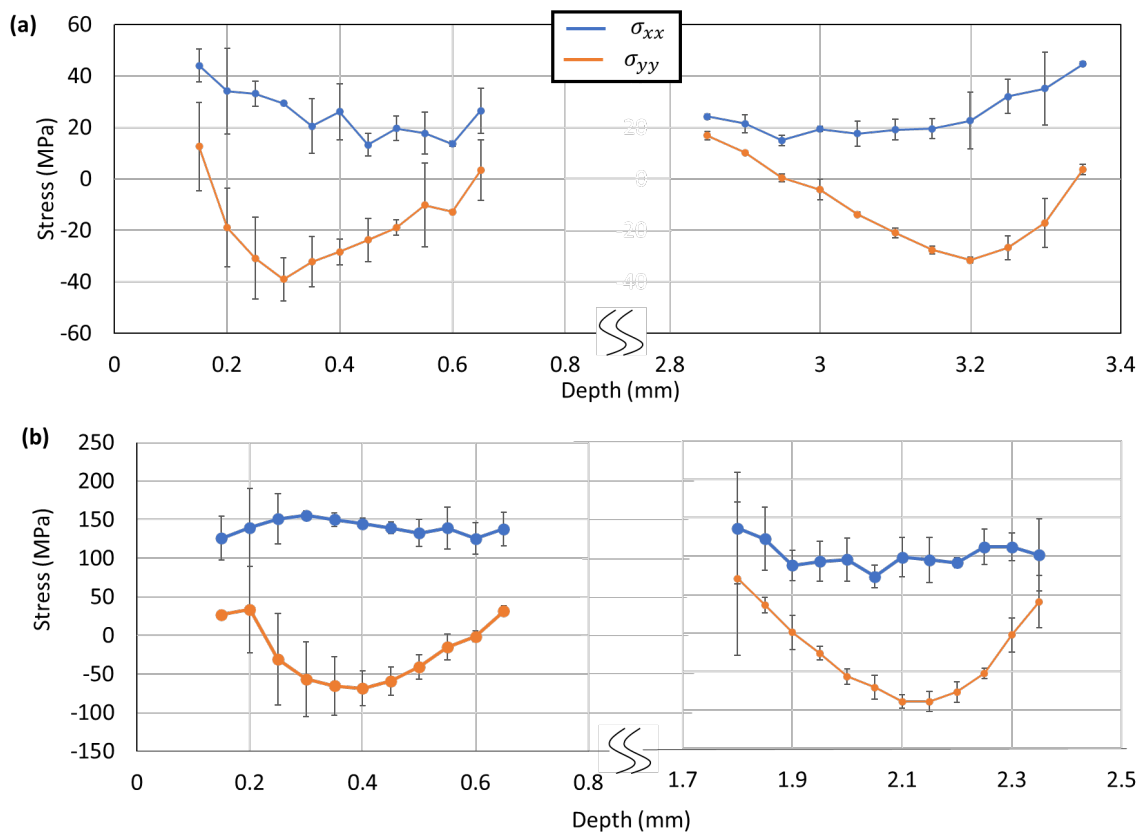


Figure II.1.4.20. Through-thickness distributions of residual stresses in the longitudinal/weld (σ_{xx}) and transverse (σ_{yy}) directions at the center of the processed zone in (a) the cast-A380 alloy two-pass Sample #3 and (b) the wrought Al 7075 alloy FSP Sample #4. Source: PNNL.

Residual stress variation with location in a sample and variation with process parameters in the rest of the samples was studied by averaging the through-thickness data. Figure II.1.4.21 shows the residual stresses averaged over a depth of 0.65 mm below the top surface from all five samples and at a few locations on each sample. The shape of the longitudinal residual stress distribution is M-shaped or plateau-shaped as expected, with the stresses near the processed zone being tensile and stresses everywhere else being slightly compressive

or stress-free. Figure II.1.4.21(a) shows the stresses from the cast A380 alloy samples. Here, the one-pass FSP Sample #1 displays the highest stress magnitude. The stresses from the HT one-pass FSP Sample #2 are lower by around 10–15 MPa and are the smallest. The stresses at the same temperature but with two FSP passes (i.e., Sample #3) are larger by around 5–8 MPa. Figure II.1.4.21(b) shows the stresses from the wrought Al 7075 alloy samples. Here, the stresses in the HT FSP Sample #5 are larger by around 15–35 MPa when compared to the lower temperature FSP Sample #4. These observations not only directly advocate stress mitigation strategies but also validate the simulations, thereby contributing to the ongoing development of more effective stress mitigation approaches.

These observed stress variations with location and process parameters are expected and were predicted by the thermo-pseudo-mechanical (TPM) model [10]. The only unexpected observation is that in cast A380 alloys, the through-thickness residual stress variation with depth is not monotonically decreasing from the top surface, but residual stresses at both the top and bottom surface are greater than stresses in the interior of the sample.

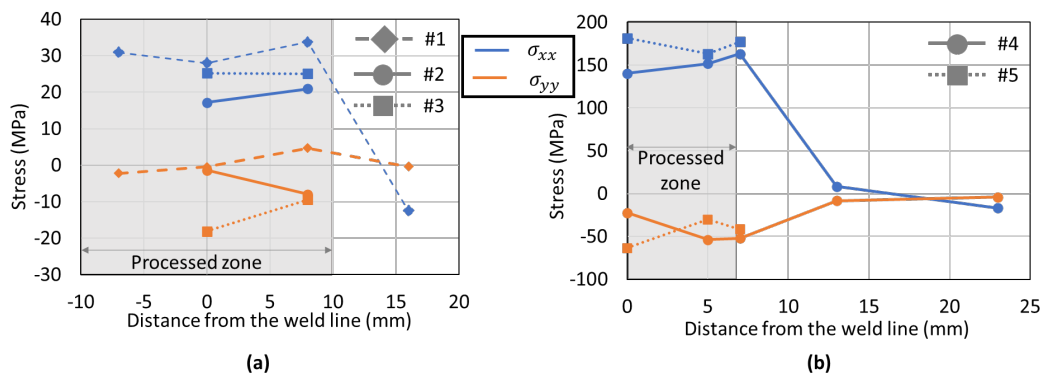


Figure II.1.4.21. Residual stresses in the longitudinal/weld (σ_{xx}) and transverse (σ_{yy}) directions, at a few selected locations specified as distance from the weld line. (a) Cast A380 alloy Samples #1, #2, and #3 and (b) wrought Al 7075 alloy Samples #4 and #5. Source: PNNL.

The hypothesis of this phenomenon is that it comes from the skin effect [11], which is the observation that cast-Al alloys are harder at the surface. To test the hypothesis, the TPM model was used to simulate the FSP-cast A380 Sample #2 with and without a 15% harder 0.5-mm-thick skin. The resulting through-thickness residual stresses at the edge of the processed zone from the two kinds of simulations are shown in Figure II.1.4.22. Figure II.1.4.22(a) shows that assuming uniform material properties results in monotonically decreasing stresses. Figure II.1.4.22(b) shows the results from the simulation where the skin effect was considered. In this case, the stresses close to both surfaces are more prominent. The simulated longitudinal stresses at the top surface match well with experimental results. For a better match elsewhere, the exact microstructure has to be considered in future simulations. Nevertheless, the results prove the hypothesis that through-thickness material property variation in cast-Al influences the residual stresses developed after FSP.

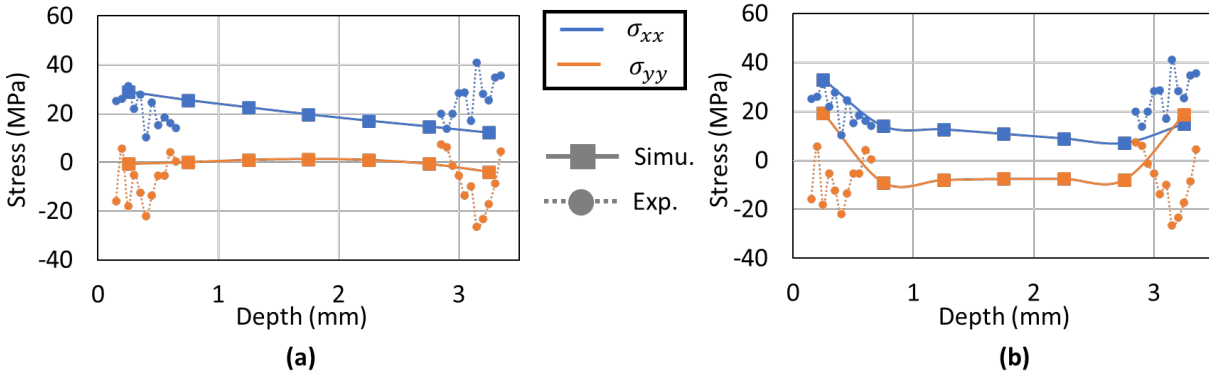


Figure II.1.4.22. Simulated and characterized through-thickness residual stresses in the longitudinal/weld (σ_{xx}) and transverse (σ_{yy}) directions at the edge of the processed zone in the high-temperatures. FSP cast A380 Sample#2. Simulated results from (a) assuming uniform material properties and (b) hardened skin. Source: PNNL.

Project 2.2. – Residual Stresses from WJP and Laser Peening

Peening metal surfaces induces compressive residual stresses through plastic deformation. The magnitude and location of the stresses influences the degree of improvement in mechanical properties. Therefore, to achieve the optimum material properties, the influence of the peening process parameters must be known. In this section, the results of residual stress characterization of the water jet and laser peened samples are presented. The details of the process parameters that were used were mentioned in the section on Thrust 2.

Figure II.1.4.23 shows the residual stresses in the three-water jet peened samples, both in the water jet travel direction and in the direction normal to it. The stress distributions are compressive, and similar in the two directions, with stresses in the travel direction being 20–30 MPa larger. In all samples, the largest stresses are at the surface, which gradually decrease with depth and are negligible beyond 0.4 mm. Surface residual stresses in Sample C, at 150 MPa, are the largest. The peak residual stresses in both Sample A and Sample B are lower at 90 MPa. This explains the observation that fatigue performance of Sample C was the most improved.

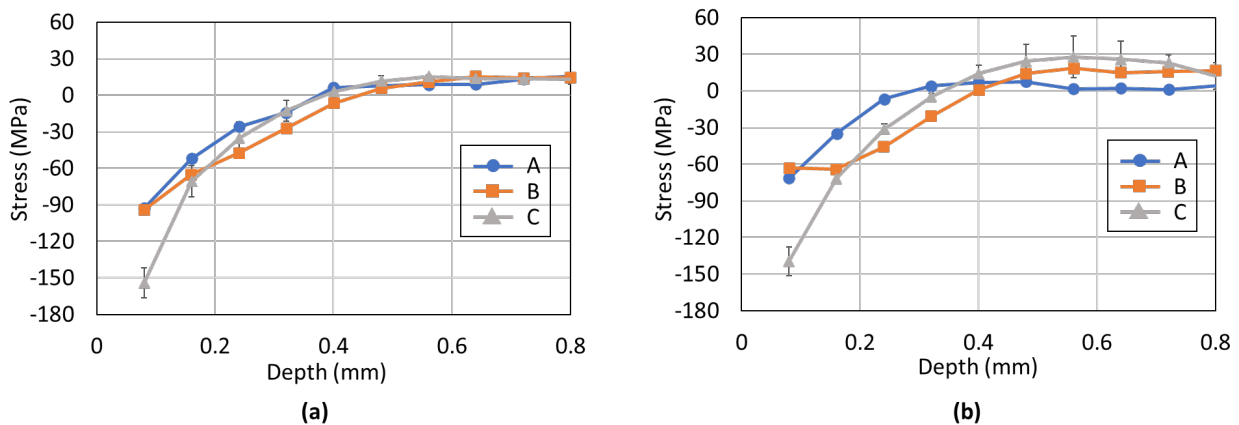


Figure II.1.4.23. The through-thickness residual stresses in the water jet peened A380 alloy samples. Stresses in the (a) longitudinal/travel and (b) transverse directions. Source: PNNL.

Figure II.1.4.24 shows the residual stresses in the three laser peened samples, both in the laser travel direction and in the normal direction. All measurements were made in the center of the laser spot. The stress distributions are mostly compressive, and similar in the two directions, with stresses in the travel direction being 10–20 MPa larger. In Region 2, the compressive stresses are smaller than 17 MPa and are the smallest

among all the other regions. In Region 3, the stresses are the largest and the peak stress is 77 MPa and found close to the surface. In Region 1, the stresses on the surface are negligible. The peaks stress of 36 MPa is found at a depth of 0.2 mm. Combining these observations with insights into microstructure modifications can elucidate the enhancements in the mechanical properties.

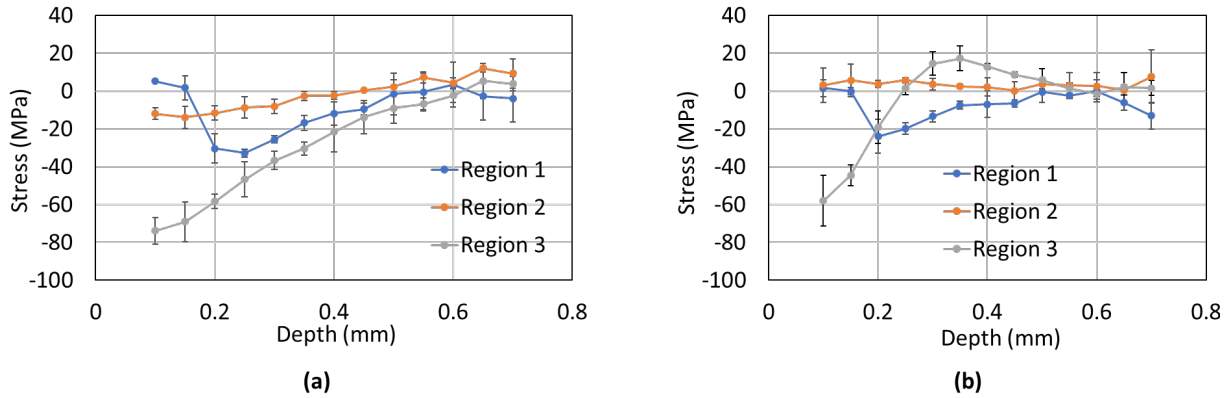


Figure II.1.4.24. The through-thickness residual stresses in the laser peened A380 alloy samples. Stresses in the (a) longitudinal/travel and (b) transverse directions. Source: PNNL.

Project 2.3. – Residual Stresses from Bending and Unbending

The bending and unbending process induces residual stresses through uneven plastic deformation. Understanding their relationship to the process parameters is critical to optimize the mechanical performance. An approach using both simulations and experimental characterization has been chosen. Residual stresses have been studied for two AA6451 alloy samples processed at almost the same conditions. Only the temperatures differ. One sample was processed at RT and the other at 500°C. More details are mentioned in the Thrust 1 section of this report. Figure II.1.4.25 shows both simulated and characterized surface residual stresses at multiple locations on the two samples. Substantial residual stresses, even those exceeding the yield stress of the BM, can be observed in both samples.

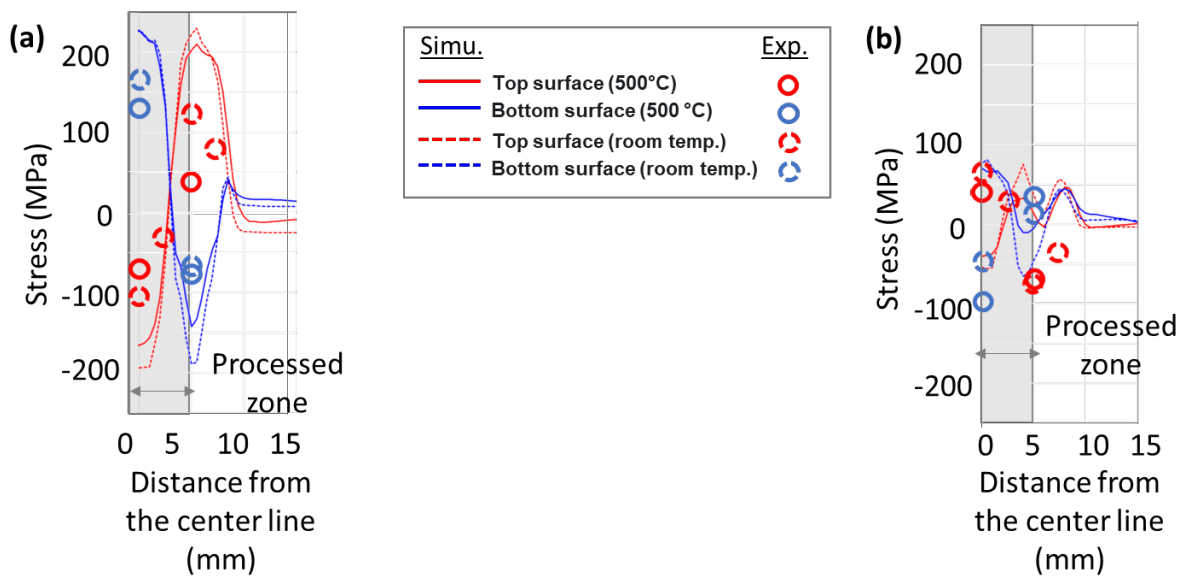


Figure II.1.4.25. Simulated and experimentally characterized residual stresses in two samples. The results were extracted from the top and bottom surfaces at multiple locations and a depth of 0.115 mm. (a) Longitudinal (σ_{zz}) and (b) transverse (σ_{xx}) stresses. Source: PNNL.

Longitudinal stresses in Figure II.1.4.25(a) (σ_{zz}), which are the stresses in the travel direction, are significantly greater than the transverse stresses (σ_{xx}) shown in Figure II.1.4.25(b). The variation of residual stress with in-plane locations and depth is noteworthy. For instance, longitudinal stresses on the top surface are compressive, reaching their lowest point at the center and highest tensile stress at the roller's end (e.g., 5 mm from the center line). Remarkably, stresses on the top and bottom surfaces are similar in magnitude but exhibit a sign change; if the top surface is compressive, the bottom surface is tensile, and vice versa. These patterns are consistent in both simulation and experimental data. However, the simulation data tends to overestimate the magnitude of longitudinal stresses and inaccurately predicts the direction of lower-magnitude transverse stresses.

Figure II.1.4.26 shows through-thickness residual stresses in the center of the processed region. Both simulations and experimental results show there is significant variation of stress with depth. Transverse stresses vary significantly with respect to depth. Multiple peaks and troughs exist in the stress distributions, both on the surface and in the interior too. In these stresses, a significant discrepancy between the simulation and the experiment—not in the magnitude, but in the distributions—has been observed. However, longitudinal stresses monotonically increase with depth and simulation predicts this satisfactorily. To conclude, this study advances the understanding of residual stresses formation and helps design residual stress mitigation strategies.

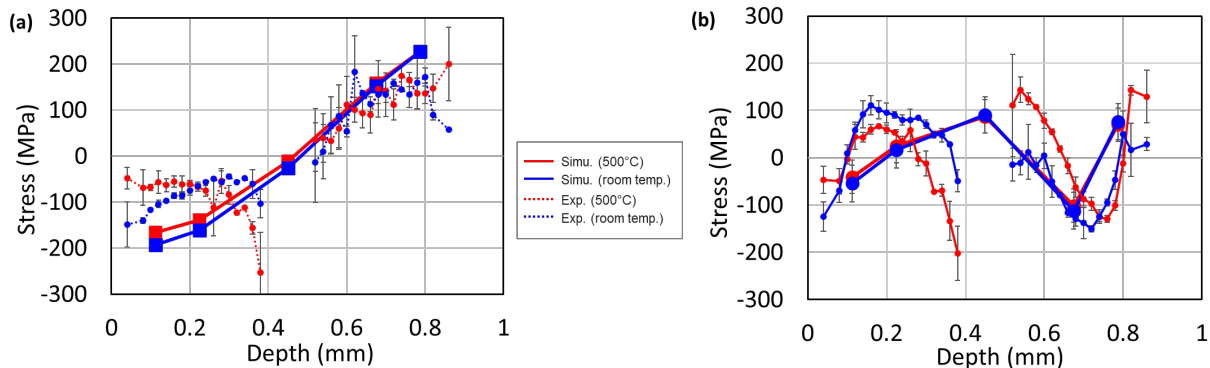


Figure II.1.4.26. The through-thickness residual stresses at the center of the processed zone in the bent-untent A6451 alloy samples. Stresses in (a) the longitudinal/travel and (b) the transverse directions.

Source: PNNL.

Project 3 – Material Life Cycle

This project focuses on developing a spreadsheet model that can estimate the cost and environmental impacts related to the work conducted for the LMCP program and can be used by LMCP researchers to inform R&D.

In FY 2023, we developed an alpha version of the model, tentatively named EverLightMat. Figure II.1.4.27 describes the framework of EverLightMat, which examines the manufacturing phase, use-phase, and end-of-life separation phase, which includes the recycling of vehicle components made of lightweight materials and estimates the cost and environmental impacts pertaining to each stage, as well as the entire life cycle of the component. The goal of EverLightMat is to ensure that vehicle lightweighting efforts under LMCP will not cause unintended consequences when it comes to end-of-life management (e.g., using a material or joining technology that poses challenges to recycling) and promote closed-loop recycling of Al alloys. The current version of EverLightMat focuses on Al alloys, but the framework of the model should be readily expanded to cover other lightweight materials, such as Mg-alloys. EverLightMat will be reviewed by the stakeholders and then released in Q2 FY 2024.

In FY 2023, we also used the still in-development EverLightMat model to evaluate life cycle greenhouse gas (GHG) emission reduction achievable through local thermomechanical processing (LTP) and HPDC. The results are shown in Figure II.1.4.28.

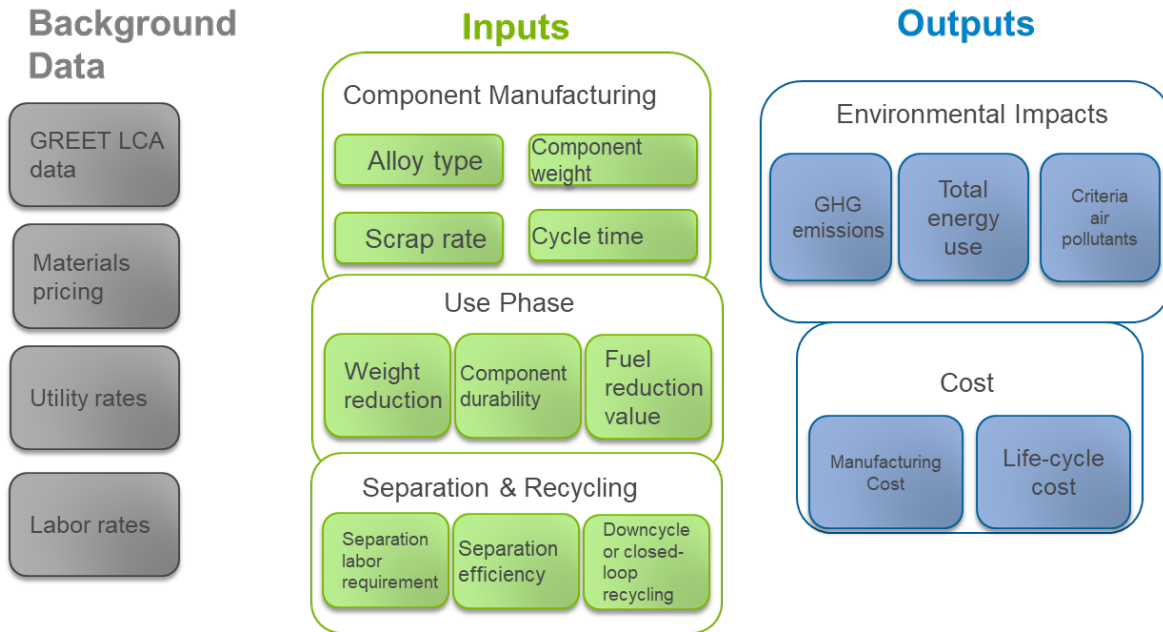
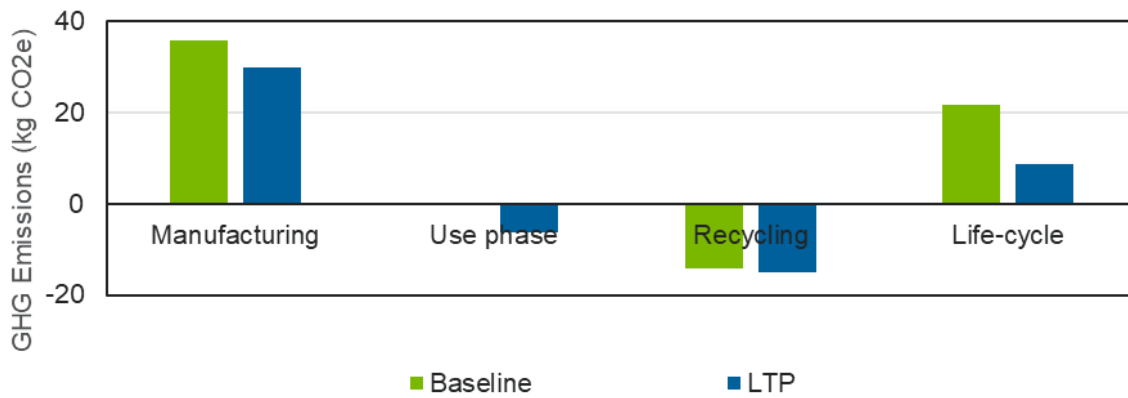
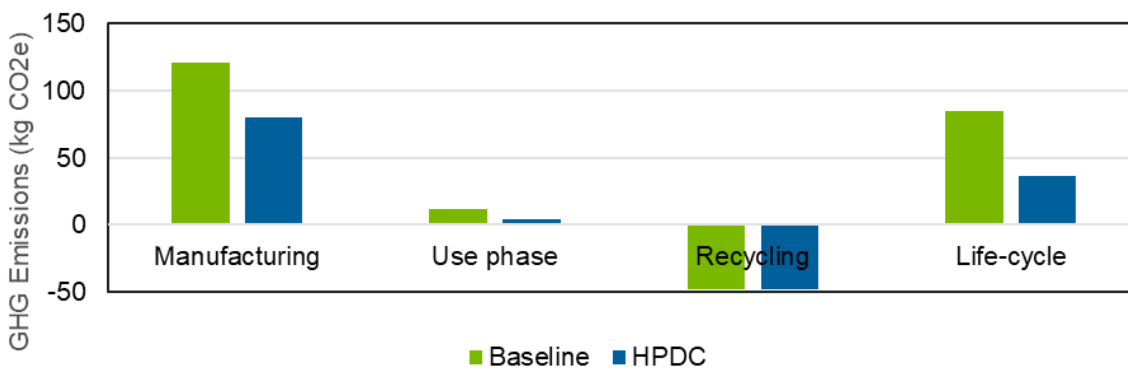


Figure II.1.4.27. EverLightMat framework. Source: ANL.



(a)



(b)

Figure II.1.4.28. GHG emissions results for (a) LTP and (b) HPDC analysis. Source: ANL.

LTP is proposed for the manufacturing of narrow, local zones in the closure panels. It can achieve 17% down-gauging and enable closed-loop recycling by replacing high-Cu 6xxx alloy with low-Cu 6xxx alloy. For closure panels, our analysis shows that from the component life cycle perspective, recycling represents the best opportunity for GHG emissions reduction, followed by fuel-saving during vehicle operation through lightweighting. Using LTP to manufacture local areas of vehicle closure panels (e.g., assumed to account for 10 wt.% of all panels) can lead to a net life cycle GHG emissions reduction of 13 kg CO₂e per vehicle thanks to down-gauging. Benchmarking LTP against the baseline, the net GHG emissions reduction is primarily achieved through component lightweighting, which leads to substantial reductions during both the use-phase and manufacturing stage.

HPDC has the potential to replace stamping for the manufacture of BIW components. Our analysis shows that completely replacing a 9-kg body stamping component with an HPDC one can lead to a GHG emissions reduction of 48 kg CO₂e per vehicle. Over 80% of the net reduction can be attributed to the manufacturing stage, because manufacturing of wrought Al components is more GHG-intensive than that of HPDC ones due to a higher scrap rate and higher Al content in the alloy. In addition to specific technologies, in FY 2023, we evaluated the implications of wrought-to-wrought Al recycling and whether it could contribute to a more sustainable future. We find that enabling wrought-to-wrought Al will become increasingly important, as the content of wrought Al in vehicles is expected to grow from 152 pounds per vehicle in 2020 to 239 pounds in 2030. As of 2022, an Al sheet has 0% post-consumer recycled content, and Al extrusion only has 16%. If we can achieve 100% wrought-to-wrought Al throughout the U.S. LD fleet by 2030, we will be able to avoid the production of 1,330 thousand metric tons of primary Al, and also avoid 8,960 thousand metric tons of GHG emissions. In FY 2024, we will continue to improve EverLightMat, and use it to inform R&D under LMCP.

Conclusions

Across all subprojects under Project 1, advanced microstructural characterization and computational simulations are revealing key atomic-scale insights on processing-microstructure-mechanical property relationships for Al- and Mg-alloys relevant to the LMCP. This synergy between advanced characterization and computation conducted under Thrust 4 and the material development activities conducted in Thrusts 1 to 3 can help design the next generation of lightweight metals with an intentionally heterogeneous microstructure having extraordinary properties for automotive applications.

Under Project 2, key modeling capabilities—such as the TPM model, SPH, and FEMs, as well as the experimental methods—have now been developed to predict and evaluate residual stresses in friction-stir processed alloys.

Finally, the material life cycle task under Project 3, is ensuring that various thrusts from 1–3 have a positive impact on energy and environment. There are a lot of factors that come into play when determining this impact. The team has—and will continue—to communicate and learn from the many stakeholders.

Key Publications

1. Balusu, K., K. S. Choi, H. Das, A. Samantha, P. Upadhyay, S. Jana, and A. Soulami, 2022, “On the utility of the thermal-pseudo-mechanical model’s residual stress prediction capability for the development of FSP,” *Int. J. Adv. Manuf. Technol.*, 126, 1775–1788. <https://doi.org/10.1007/s00170-023-11199-2>.
2. Jang, G. G., S. Yeom, J. K. Keum, M. Yoon, H. Meyer III, Y-F. Su, and J. Jun, 2023, “Formation of carbon and oxygen rich surface layer on high-purity magnesium by atmospheric carbon dioxide plasma.” *J. of Mg and Alloys*, 11(1), 88–99. <https://doi.org/10.1016/j.jma.2022.10.008>.
3. Knapp, G. L., M. Gussev, A. Shyam, T. Feldhausen, and A. Plotkowski, 2022, “Microstructure, deformation and fracture mechanisms in Al-4043 alloy produced by laser hot-wire AM,” *Addit. Manuf.*, 59(A), 103510. <https://doi.org/10.1016/j.addma.2022.103150>.

References

1. Nasim, W., H. Das, P. Upadhyay, and M. Efe, 2022, “Improving local formability of 6xxx and 7xxx aluminum alloy sheets using FSP,” *Int. J. Adv. Manuf. Technol.*, 124(7-8), 2957–2967. <https://doi.org/10.1007/s00170-022-10569-6>.
2. Marlaud, T., A. Deschamps, F. Bley, W. Lefebvre, and B. Baroux, 2010, “Evolution of precipitate microstructures during the retrogression and re-ageing heat-treatment of an AlZnMgCu alloy,” *Acta Mater.*, 58(14), 4814–4826. <https://doi.org/10.1016/j.actamat.2010.05.017>.
3. Ilavsky, J., F. Zhang, R. N. Andrews, I. Kuzmenko, P. R. Jemian, L. E. Levine, and A. J. Allen, 2018, “Development of combined microstructure and structure characterization facility for *in-situ* and *operando* studies at the APS,” *J. Appl. Crystallogr.*, 51(3), 867–882. <https://doi.org/10.1107/S160057671800643X>.
4. Liu, T., Y. Gao, H. Bei, and K. An, 2018, “*In-situ* neutron diffraction study on tensile deformation behavior of carbon-strengthened CoCrFeMnNi high-entropy alloys at room and elevated temperatures,” *J. Mater. Res.*, 33(19) (2018) 3192–3203. <https://doi.org/10.1557/jmr.2018.180>.
5. Du, Y., Y. A. Chang, S. Liu, B. Huang, F.-Y. Xie, Y. Yang, and S.-L. Chen, 2005, “Thermodynamic description of the Al-Fe-Mg-Mn-Si system and investigation of microstructure and microsegregation during directional solidification of an Al-Fe-Mg-Mn-Si alloy,” *Int. J. Mater. Res.*, 96(12), 1351–1362. <https://doi.org/10.3139/146.101185>.
6. Coleman, J., K. Kincaid, G. L. Knapp, B. Stump, A. Plotkowski, and S. T. Reeve, 2023, “AdditiveFOAM v1.0,” Oak Ridge National Laboratory, Oak Ridge, TN, USA. Available at: <https://github.com/ORNL/AdditiveFOAM> (accessed 31 January 2024).
7. Povoden-Karadeniz, E., P. Lang, P. Warczok, A. Falahati, W. Jun, and E. Kozeschnik, 2013, “CALPHAD modeling of metastable phases in the Al-Mg-Si system,” *CALPHAD*, 43, 94–104. <https://doi.org/10.1016/j.calphad.2013.03.004>.
8. Du, Q., K. Tang, C. D. Marioara, S. J. Andersen, B. Holmedal, and R. Holmestad, 2017, “Modeling over-ageing in Al-Mg-Si alloys by a multiphase CALPHAD-coupled Kampmann-Wagner Numerical model,” *Acta Mater.*, 122, 178–186. <https://doi.org/10.1016/j.actamat.2016.09.052>.
9. Carneiro, V. H., H. Puga, and J. Meireles, 2018, “Heat-treatment as a route to tailor the yield-damping properties in A356 alloys,” *Mater. Sci. Eng. A*, 729, 1–8. <https://doi.org/10.1016/j.msea.2018.05.042>.
10. Balusu, K., K. S. Choi, H. Das, A. Samanta, P. Upadhyay, S. Jana, and A. Soulam, 2023, “On the utility of the thermal-pseudo-mechanical model’s residual stress prediction capability for the development of FSP,” *Int. J. Adv. Manuf. Technol.*, 126, 1775–1788. <https://doi.org/10.1007/s00170-023-11199-2>.
11. Yang, K. V., C. H. Cáceres, and M. A. Easton, 2013, “A microplasticity-based definition of the skin in HPDC Mg-Al alloys,” *Mater. Sci. Eng. A*, 580, 355–361. <https://doi.org/10.1016/j.msea.2013.05.018>.

Acknowledgements

For the advanced characterization and computation projects conducted at PNNL, the PIs gratefully acknowledge the contributions of M. Pole, Z. Li, T. Liu, S. Lambeets, T. Ajantiwalay, M. Olszta, and A. Devaraj at PNNL. Some of the research utilized the advanced microstructural characterization facility housed at the Environmental Molecular Sciences Laboratory (EMSL), which is a DOE Office of Science National User Facility located at PNNL and funded by the DOE Office of Biological and Environmental

Research office. For the advanced computational projects conducted at PNNL, the PIs gratefully acknowledge the contributions of K. Balusu, L. Li, and A. Soulami.

For the advanced characterization and computation projects performed at ORNL, the PIs gratefully acknowledge the effort and contributions of L. F. Allard, J. D. Poplawsky, P. A. Thisera, X. Hu, G. Muralidharan, I. Roy, Y. Yang, G. Knapp, and A. Plotkowski. The PIs also acknowledge the research conducted as part of a user project at the CNMS, which is a DOE Office of Science National User Facility located at ORNL.

For all three advanced characterization tasks performed at ANL, the PIs gratefully acknowledge the contributions from R. R. Kamath, J. Ilavsky, K. Beyer, and J. Thomas at ANL to conduct the APS experiments and data analysis is acknowledged. This research used the resources of APS, which is a DOE Office of Science National User Facility located at ANL under Contract No. DE-AC02-06CH11357.

For Project 2, the residual stress contributions from K. Balusu, L. Li, and A. Soulami are acknowledged.

Finally, for Project 3, the life cycle assessment contribution from J. Spangenberg is acknowledged.

II.2 Light Metals

II.2.1 Developments of a Novel Magnesium Alloy for Thixomolding® of Automotive Components – LightMAT (Oak Ridge National Laboratory)

Govindarajan Muralidharan, Co-Principal Investigator

Oak Ridge National Laboratory
Materials Science and Technology Division
1 Bethel Valley Rd.
Oak Ridge, TN 37830
E-mail: muralidhargn@ornl.gov

Bryan Macek, Co-Principal Investigator

Fiat Chrysler Automobiles U.S. Limited Liability Company
1000 Chrysler Dr.
Auburn Hills, MI 48326
E-mail: bryan.macek@stellantis.com

Nathan Sanko, Co-Principal Investigator

Leggera Technologies
87 Northe pointe Dr.
Orion Township, MI, 48359
E-mail: nathan@leggeratech.com

Christopher Schooler, DOE Technology Development Manager

U.S. Department of Energy
E-mail: Christopher.Schooler@ee.doe.gov

Start Date: February 1, 2020

End Date: September 30, 2023

Project Funding: \$200,000

DOE share: \$100,000

Non-DOE share: \$100,000

Project Introduction

Mg alloy die-castings are increasingly used in the automobile industry to achieve cost-effective mass reduction, especially in systems where multiple components can be integrated into a single thin wall die-casting. However, there is only one die-caster in North America capable of producing die-castings of the size needed for components, such as instrument panel structures, liftgate inner panels, swing gate inner panels, and similar components, thus making it difficult to negotiate competitive pricing and creating a supply-chain risk. Furthermore, there are several component quality restrictions in thin-walled Mg die-castings, including variability in dimensional accuracy, part-to-part variation in mechanical properties, and porosity in the final part, which has limited the continued growth of die-cast components in the automobile industry.

An alternative to die-casting is the process of thixomolding. Widely used in the electronics industry, the thixomolding process has begun to make inroads into the automobile industry (e.g., 2018 Jeep Wrangler spare tire carrier) as a competing process to die-casting for producing complex thin wall Mg components.

While the thixomolding process is similar to the die-casting process in that hot metal is injected into a die, it differs in at least one significant aspect. While the die-casting process relies on filling a mold at high speeds with the alloy in the completely molten state, the thixomolding process fills a mold with a thixotropic alloy in a semi-solid slurry state at a temperature between the liquidus and solidus temperatures. Ideally, the material should be ~30–65% solid rather than being completely liquid at the beginning of the injection process. Advantages of the thixomolding process over die-casting include a finer grain structure, lower porosity, improved dimensional accuracy, improved part-to-part consistency, improved mechanical properties

(particularly ductility in the component), the ability to reduce wall thickness for mass-savings, and longer tool life due to lower process temperatures.

Although thixomolding offers improved mechanical properties over die-cast Mg components, the mechanical properties obtained in the thixomolded parts are still not sufficient to broadly enable application in components where both strength and ductility are key requirements (e.g., crash critical components exposed to high-impact velocities and powertrain or chassis components subjected to high levels of cyclic loading). Currently, the mechanical properties are limited by the alloys being used, which are the same alloys used in the die-casting process. Thus, there is a need for the development of new alloys, which can achieve high-strength with improved ductility for use in components fabricated by the thixomolding process.

Objectives

The objective of this project is to develop one or more novel Mg-alloys more suitable for thixomolding automotive structural components than the current die-casting alloys used for this process. For this project, ORNL will assist Fiat Chrysler Automobiles U.S. LLC (FCA US LLC) and Leggera Technologies in the development of up to two new Mg-alloys optimized for the thixomolding process with improved mechanical properties when compared to current die-casting alloys. The primary interest is in improving ductility and fatigue strength, as these are properties that are critical for use in body and chassis structural applications. Since good corrosion resistance is also desirable for this application, this property will also be considered when evaluating promising alloy compositions. Additionally, suitability for heat-treatment to further improve YS, UTS, and corrosion performance is of interest, since this capability is not available in current die-casting alloys.

Approach

In consultation with Leggera Technologies, FCA US LLC will establish the desired thixomolding processing parameters, target strength, ductility, and corrosion performance requirements of the new alloy. To understand the relationship between thixomolding process conditions, alloy composition, microstructure, and properties of the current alloys, ORNL will perform a baseline study of two industry-standard Mg-alloys suitable for thixomolding in collaboration with industrial partners. ORNL has initiated microstructural characterization of an existing thixomolded component fabricated with AM60 using OM, SEM, and X-ray microchemical analysis to understand the effect of alloy composition and processing conditions on the microstructural evolution during the thixomolding process and its effect on strength and ductility. The goal of this work is to determine which alloying element additions will result in microstructural modifications that increases both the strength and ductility in the final thixomolded product.

Based on correlations developed in this part of the work, the team will initiate new alloy development by identifying favorable microstructural characteristics for the target mechanical properties. ORNL will establish the feasibility of using computational thermodynamic models to predict the observed microstructure and to simulate the effect of selected alloying element additions on the solidification behavior. ORNL will also identify alloy compositions that have the potential to be successfully fabricated using the thixomolding process, while having the desired microstructure in the final thixomolded component. Laboratory-scale heats will be fabricated at ORNL, and the as-cast microstructure and tensile properties of the alloys will be evaluated to identify the required type and amount of alloying element additions. One or two alloys will be downselected for alloy ingot and chip production for use in the thixomolding process, and a prototype component will be produced by Leggera Technologies. FCA US LLC will coordinate and complete the material characterization tests for one new material from samples excised from the component produced by Leggera Technologies and will supervise computer-assisted engineering (CAE) card development to support component modeling. Finally, FCA US LLC will conduct simulated component structural evaluation using the new properties developed for the CAE card. Figure II.2.1.1 provides a schematic of the approach used in the project.

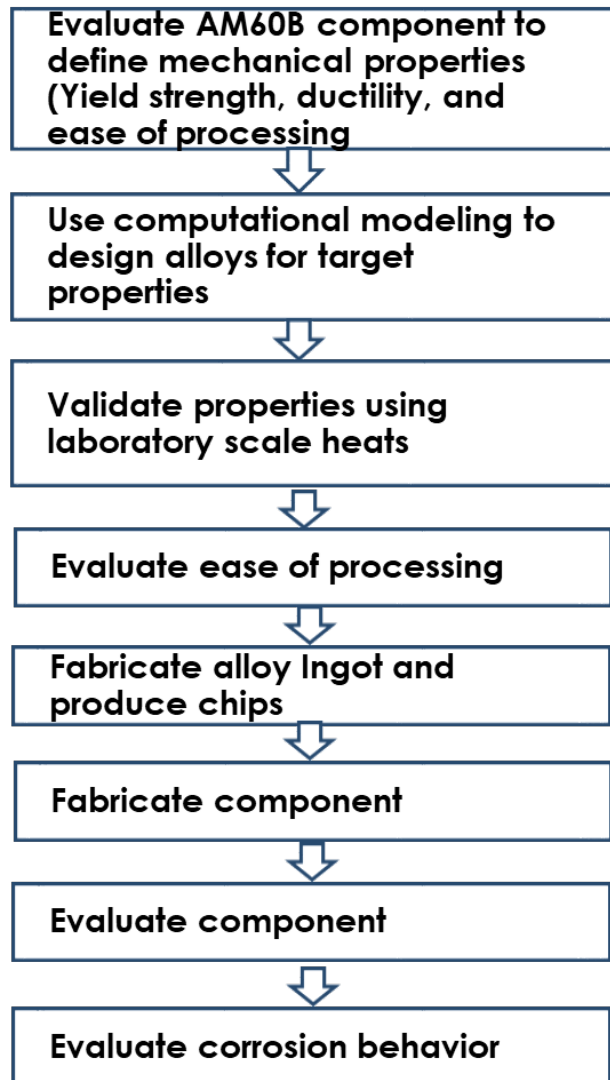


Figure II.2.1.1. Schematic of the approach used in the project. Source: ORNL.

The aim of the alloy development effort used in this project was to develop new alloys for use in the thixomolding process that balance three major characteristics: (1) ease of processing; (2) strength; and (3) ductility. An alloy such as AZ91D exemplifies ease of processing, but at the cost of ductility. AM60B has good ductility and strength, but better processing characteristics are desirable for use in the thixomolding process. Table II.2.1.1 shows the nominal compositions of the alloys, their RT YSs, and ductilities [1], [2], [3], [4]. Figure II.2.1.2 schematically shows the three required characteristics of the alloys and the current status of properties of AM60B and AZ91D. For the alloy development effort, ease of processing was characterized by the liquidus, solidus, and melting range (e.g., defined as the difference between the liquidus and solidus) [5]. AZ91D has a significantly greater melting range and lower solidus when compared to AM60B, which was associated with ease of processing. Hence, a lower solidus and wider melting range were targeted for the new alloys.

Table II.2.1.1. Die-Casting Alloys, Compositions, and Mechanical Properties

Alloy	Mg	Al	Zn	Mn	Sr	YS (MPa)	% Elongation
AM60B	Bal.	6	0.2	0.3	0	121	16
AZ63A	Bal.	6	3	0.15	0	130	5
AJ52	Bal.	5	0	0.4	2	126	9
AZ91D	Bal.	9	0.7	0.3	0	158	6

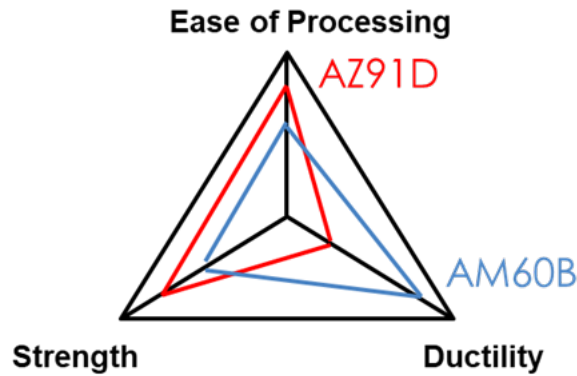


Figure II.2.1.2. Schematic showing the three characteristics of interest for alloys used in the thixomolding process. Source: ORNL.

Results

In previous years of this project, two promising alloys, Alloy #1 and Alloy #6 as shown in Figure II.2.1.3, were identified based on their liquidus, solidus, and melting range, and were scaled-up in industrial scale heats. Extrusions were fabricated and chips were manufactured for the thixomolding trials. Figure II.2.1.4 shows an image of the thixomolded parts fabricated from Alloy #1. It was not possible to converge to good experimental parameters for the thixomolding components using Alloy #6 with the amount of feedstock that was produced with available funds and time required in this project. Further work of process parameter refinements is needed to successfully produce components using Alloy #6.

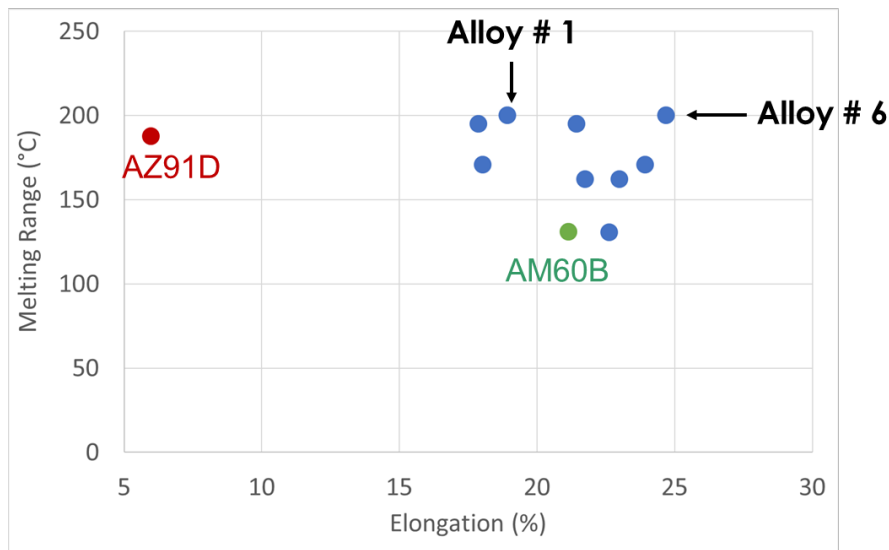


Figure II.2.1.3. Melting range and percent elongation of experimental alloys. Source: ORNL.



Figure II.2.1.4. Prototype components were successfully produced using Alloy #1. Source: ORNL.

Figure II.2.1.5 shows a comparison between the microstructure of thixomolded AM60B and Alloy #1. Note that the grain size in the part fabricated using Alloy #1 was observed to be ~ 25% smaller than in AM60B. This is also reflected in higher yield and tensile strengths in Alloy #1, as observed in Figure II.2.1.6(a), and in improved ductility, as indicated in Figure II.2.1.6(b). Further improvement in properties can be achieved in Alloy #1 by optimizing the thixomolding process to obtain a higher volume fraction of primary α -Mg nodules in the cast alloy.

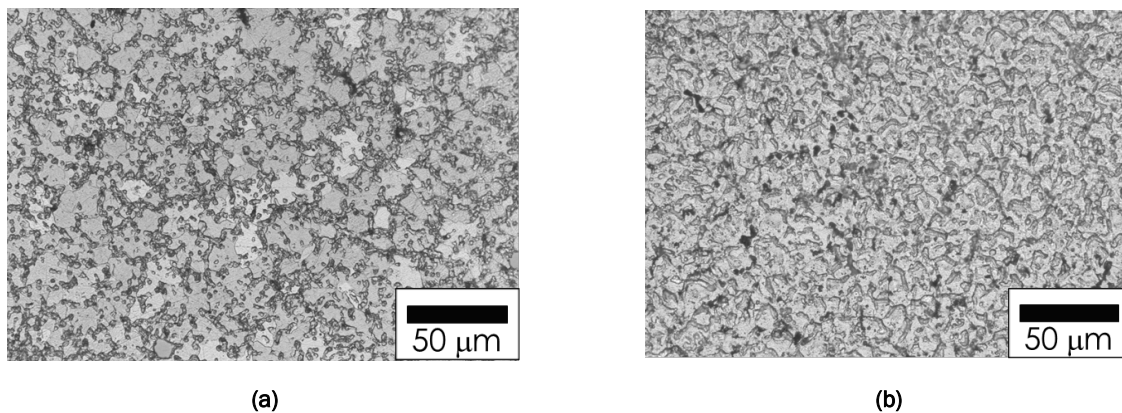


Figure II.2.1.5. Optical micrographs from comparable regions in components fabricated using (a) AM60B and (b) Alloy #1. Source: ORNL.

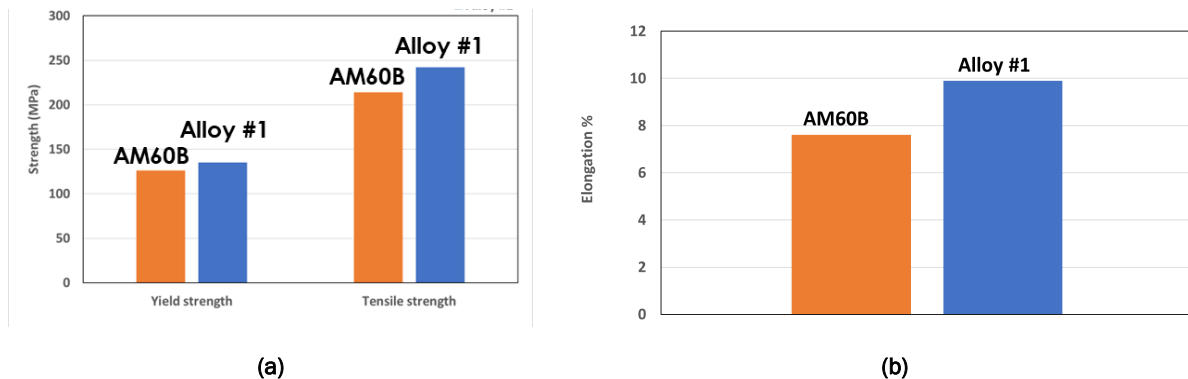


Figure II.2.1.6. (a) YS, UTS, and (b) elongations measured from material obtained from thixomolded components fabricated using AM60B and Alloy #1. Source: ORNL.

New alloys required for thixomolding applications have to balance ease of processing, strength, and ductility. Computational modeling was used to identify promising alloys that would have better processing characteristics than the current baseline alloy, AM60B, while retaining strength and ductility. Two promising alloy compositions were identified and scaled-up for thixomolding. A tire carrier was successfully thixomolded using one alloy. It was determined that further work would be needed to identify appropriate thixomolding conditions for the second alloy. An increase in strength and ductility was observed in the thixomolded component fabricated from the newly developed alloy when compared to the properties of AM60B. Microstructural characterization showed that further improvement in properties can be achieved in the properties of the new alloy by optimizing the thixomolding process to obtain a higher volume fraction of primary Mg nodules in the thixomolded component.

Conclusions

New alloys required for thixomolding applications have to balance ease of processing, strength, and ductility. Computational modeling was used to identify promising alloys that would have better processing characteristics than the current baseline alloy AM60B while retaining strength and ductility. Two promising alloy compositions were identified and scaled-up for thixomolding. A tire carrier was successfully thixomolded using one alloy; it was determined that further work would be needed to identify appropriate thixomolding conditions for the second alloy. An increase in strength and ductility was observed in the thixomolded component fabricated from the newly developed alloy when compared to the properties of AM60B. Microstructural characterization showed that further improvement in properties can be achieved in the properties of the new alloy by optimizing the thixomolding process to obtain a higher volume fraction of primary Mg nodules in the thixomolded component.

Key Publications

1. Muralidharan., G., B. Macek, and N. Sanko, 2023, “New magnesium alloys for thixomolding applications,” Nonprovisional Patent Application 18/375,301, filed 29 December 2023.
2. Muralidharan., G., B. Macek, and N. Sanko, 2023, “Development of a novel magnesium alloy for thixomolding of automotive components,” final CRADA report, ORNL/TM-2023/3095, Oak Ridge National Laboratory, Oak Ridge, TN, USA. <https://doi.org/10.2172/2001375>.

References

1. Luo, A. A., 2013, “Magnesium casting technology for structural applications,” *J. Magnes. Alloy*, 1(1), 2–22. <https://doi.org/10.1016/j.jma.2013.02.002>.
2. Patel, H. A., D. L. Chen, S. D. Bhole, and K. Sadayappan, 2010, “Microstructure and tensile properties of thixomolded magnesium alloys,” *J. Alloys Compd.*, 496(1–2), 140–148. <https://doi.org/10.1016/j.jallcom.2010.02.042>.
3. Avedesian, M. M., and H. Baker (eds.), 1999, *Magnesium and Magnesium Alloys*, ASM International, Materials Park, OH, USA.
4. Moosbrugger, C. (ed.), 2017, *Engineering Properties of Magnesium Alloys*, ASM International, Materials Park, OH, USA.
5. Czerwinski, F., 2004, “Processing features of thixomolding magnesium alloys,” *Die-Casting Engineer*, 48(6), 52–58. Available at: https://www.researchgate.net/profile/Frank-Czerwinski-2/publication/288473936_Processing_features_of_thixomolding_magnesium_alloys/links/57d2955c08ae5f03b48cab30/Processing-features-of-thixomolding-magnesium-alloys.pdf (accessed 1 December 2023).

Acknowledgements

The authors would like to acknowledge Dr. R. Davies, Dr. A. Haynes, and Dr. T. Skszek (LightMAT) for their support, S. Hawkins, and K. Hedrick for their assistance with the mechanical property evaluation, and Dr. J. Caris and N. Farkas from Magnesium USA (Terves) for their help with the Mg alloy scale-up.

II.3 Carbon Fiber and Polymer Composites

II.3.1 Composites Core Program

II.3.1.1 High-Temperature Carbon Fiber Carbonization via Electromagnetic Power (Oak Ridge National Laboratory)

Eng Felix L. Paulauskas, Principal Investigator

Oak Ridge National Laboratory
Chemical Sciences Division
1 Bethel Valley Rd.
Oak Ridge, TN 37830
E-mail: paulauskasfl@ornl.gov

Rich Davies, Composites Core Program Manager

Oak Ridge National Laboratory
Materials Science and Technology Division
1 Bethel Valley Rd.
Oak Ridge, TN 37830
E-mail: daviesrw@ornl.gov

H. Felix Wu, DOE Technology Development Manager

U.S. Department of Energy
E-mail: Felix.Wu@ee.doe.gov

Start Date: November 17, 2020

End Date: June 30, 2023

Project Funding: \$4,536,349

DOE share: \$4,536,349¹

Non-DOE share: \$0

Project Introduction

HTC of polymer-fiber via EM power is a project that aims to develop an innovative and scalable process for the final stage of CF conversion by reaching sufficiently high coupling and temperature elevation of the material. This project is the continuation of a previous effort dedicated to LTC² that will complete the portfolio of technologies developed by ORNL and 4XTechnologies, which were funded by DOE and intended to replace the conventional carbonization technology used in the CF industry. This is a joint development research project carried out by ORNL and 4XTechnologies (formerly RMX Technologies) that is fully funded by DOE. Preliminary work on EM carbonization was initiated at ORNL with the Microwave Assisted Plasma (MAP) project;³ efforts have since jointly continued with 4XT since 2013. This report covers the progress made on the HTC project during FY 2023.

ORNL and 4XTechnologies recently completed the development of a new LTC technique for the manufacture of CF. This successful LTC project demonstrated that Close Proximity Electromagnetic Carbonization (CPEC)⁴ technology is feasible, scalable,⁵ and produces CF with the tensile strength meeting or exceeding 500 kilopound per square inch (ksi)⁶ after subsequent conventional HTC processing [1]. This novel technology has the potential to significantly reduce the cost of manufacturing CF by reducing energy consumption and processing time, and decreasing maintenance, capital, and labor requirements as well. This new method

¹ This amount includes additional funding for the acquisition and installation of a wet spinning line at ORNL, in collaboration with 4XTechnologies, LLC. Contributions also were received from Mr. Pol Grappe and Dr. Truman Bonds.

² The Low Temperature Carbonization (LTC) project was a project jointly conducted by ORNL and 4XTechnologies (FY 2016–FY 2020).

³ Microwave assisted plasma carbonization was a one stage carbonization project conducted solely by ORNL (FY 1997–FY 2007). This technology required vacuum.

⁴ CPEC: Close Proximity Electromagnetic Carbonization is the given name to the technology developed for the EM-powered LTC stage.

⁵ The last prototype built with the CPEC technology (LTC project) was rated to 1.0 annual metric ton of CF.

⁶ Details about the mechanical performances of the CF produced with the CPEC technology can be seen the third quarterly progress report of the LTC FY2020 covering the performance period of April–June 2020 (issued in July 2020) as well as the final report.

utilizes an EM heating technique that operates at atmospheric pressure. Nevertheless, this process still requires a final HTC stage to produce completed CF, which itself is highly energy-intensive and requires high maintenance. The recent achievements and need for cost-reduction in CF production justifies the pursuit of this HTC project.

EM processing is, in general, characterized by direct deposition of energy into the material by dielectric coupling. This leads to faster and more-efficient energy deposition than conventional processing, provided the dielectric properties are adequately aligned with the coupling requirements. This was the case with the LTC project. However, with HTC, the feedstock material shows unfavorable dielectric properties, since the polymer has already been exposed to a thermal treatment, thus making the fiber electrically conductive. This critical difference must be considered in the design for the HTC process. The progress with EM LTC has already reduced the residence time to less than one minute as compared to 90 seconds or more for conventional processing. Fiber processed by EM LTC and then conventionally carbonized at HT produces CF with tensile properties above 500 ksi. Related to energy-efficiency deposition per unit mass in the EM LTC, the experimental work showed it is possible to decrease the energy consumption compared to the lowest value of a benchmark⁷ by approximately 40% under certain conditions [2]. These conditions include the limitation of the control volume to the applicator⁸ only.

The goal of this new project is to develop an EM-based technology to replace the conventional HTC stage while producing CF with comparable mechanical properties. The scope of this project is limited to HT carbonization and will capitalize on the knowledge and experience gained from former successful projects, such as EM LTC and MAP. The HTC apparatus operates at a higher power density level as compared to the devices built for LTC. The primary mechanism for the HTC applicator is a hybrid of the two different configurations explored at LTC, thereby providing a novel pattern of radiation while still operating at atmospheric pressure. The ultimate goal is to make EM HTC technology more-efficient than conventional technology and increase its scalability for use in industrial production lines.

Objectives

The objective of the HTC project is to develop a faster and more-efficient carbonization process than the current conventional process. The concept is to focus the energy deposition on the material and limited parts of the furnace with the goal of reducing the unit energy consumption (in kWh/kg) by approximately 20%, while producing the same (or better) CF quality. This achievement would represent about a 5% cost-reduction of the overall CF manufacturing process. The HTC furnace is designed to treat at least four tows of 24,000 filaments each.

Approach

The HTC project is split into four phases over a two-year effort. The first three phases were dedicated to the design and construction of the experimental setup. The final phase was dedicated to the experimental work, which will include testing, as well as all needed upgrades. The four phases are summarized and described in Table II.3.1.1.1. The HTC technology was co-developed by ORNL and 4XTechnologies.

⁷ Details about benchmarks can be found here: Ellringmann, T., C. Wilms, M. Warnecke, G. Seide, and T. Gries. 2016. "Carbon fiber production costing: a modular approach," *Text. Res. J.*, 86(2), 178–190. <https://doi.org/10.1177/0040517514532161>.

⁸ If the controlled volume is extended to include the generator and its cooling system, the energy yield per unit mass of the experimental setup becomes greater than the lowest value of the benchmark; this is mostly because the generator has a low energy conversion yield, with only around 41% of consumed electric power being converted into EM energy.

Table II.3.1.1.1. Phased Approach to HTC Project

Phase	Name	Year	Status	Description
1	Modeling and Design	FY 2021	Completed	Evaluation, modeling, design, and sourcing.
2	Construction	FY 2021	Completed	Construction of the setup with all subsystems.
3	Commissioning	FY 2021	Completed	Performance test and adjustment of each subsystem. This phase includes the safety evaluation, system modification, and improvements.
4	Operation	FY 2022/FY 2023	Completed	Testing, upgrade, and energy evaluation of the setup.

Results

Summary for FY 2021 and FY 2022

As of September 30, 2021, the system design, procurement, construction, and commissioning were completed for this project. The HTC applicator and all its ancillary equipment were declared ready for operation, validating Milestone M3.⁹ At this point, the project accrued approximately three months of delay compared to the initial schedule proposed in the annual operating program (AOP) for FY 2021, and Milestone M4¹⁰ related to material production had to be rescheduled to FY 2022. The three-month delay was due to the following factors:

- The project effectively began in the second half of November 2020 because of an administrative delay¹¹
- Some critical parts were delivered with a five-week delay in the final quarter
- The research team had been contaminated by the COVID-19 virus in the final quarter.

Therefore, the milestone schedule in the AOP of FY 2022 was amended. In this new schedule, the production of fiber (e.g., Milestone M4) was moved to 30 December 2021, and the three following milestones were rescheduled, keeping the overall timeline and resources of the project unchanged. As of 30 September 2022, the work that was conducted led to the following achievements:

- Testing and commissioning of the equipment previously built.
- Production of CF from a 300,000 filament ribbon of commodity-grade oxidized precursor fiber (OPF), matching the property requirements of milestone M4 only. The mechanical properties achieved were: 260 ksi ≤ tensile strength ≤ 380 ksi and 27.5 Msi ≤ modulus ≤ 29.5 Msi.
- Production of CF from 50,000 filament tows from spools of commodity-grade OPF. All property requirements were exceeded (milestones M5, M6, and M7). The mechanical properties achieved were: 427 ksi ≤ tensile strength ≤ 595 ksi and 23.5 Msi ≤ modulus ≤ 33 Msi.

Those achievements demonstrated the relevance of the process. However, due to a significant hardware failure, the last few milestones were not completed (e.g., Milestones M8–M10) on-schedule. Several parts of the system were irreparably damaged and needed replacements. Some spare parts were already on hand, but some required multiple months of lead time for delivery. Consequently, the project needed a no-cost extension. A new milestone schedule, factoring potential delays from the suppliers, was issued in the AOP for FY 2023.

⁹ Milestone M3: Commissioning of HTC hardware and demonstration of stable/proper operation of all subcomponents for 15 min.

¹⁰ Milestone M4: Successfully carbonize material on a continuous basis in the HTC process with carbonized material achieving a minimum density of 1.6g/cc, a minimum mechanical properties of 300 ksi tensile strength, and a 25 Msi modulus.

¹¹ The contract between the two main project participants (ORNL and 4XTechnologies, LLC) was signed on 18 November 2020.

Summary for FY 2023

Operational Restoration

As a result of the equipment failures in FY 2022, the HTC system would no longer function until the damaged parts were replaced. The reason for the failure was investigated and documented, and the system was redesigned to prevent such a failure in the future. While some spare parts were already on hand, others had to be ordered. Most of the missing parts had to be custom-made. The most complex part was quoted with an initial 10-week lead time. The part was delivered during the first week of December 2022, with a delay of approximately two additional months.

In the meantime, all other parts were collected, tested, assembled, and the full system was commissioned under restricted conditions (e.g., at limited power). The final part was tested and mounted on the setup. At this point, the commissioning of the equipment at low-power was completed using a vector network analyzer (VNA) for the return loss measurement, which is a measurement of the incident power ratio injected into the system to the power reflected back to the generator. The most important parameter was the measurement of the reflection coefficient, S_{11} , which is in units of decibels (dB) or one-tenth of a bel. These units are typically the ratio of two power measurements on a logarithmic scale. The reflection coefficient is also commonly referred to as return loss, but for historical reasons, they are actually the negative of each other, which sometimes leads to confusion between the two terms:

$$RL_{dB} = -S_{11} \quad (1)$$

where

$$S_{11} = (\text{Reflected Power})/(\text{Incident Power}) \quad (2)$$

The project team had a goal of achieving an S_{11} of -10 dB or less. To give the reader an idea of what this means in terms of reflected power back to the generator, Table II.3.1.1.2 is provided. In essence, the target was 10% reflected power or less. A power supply that can produce up to 4 kilowatts (kW) of power was essential to minimize reflections for optimal performance and to prevent equipment and part damage. An example of the S_{11} measurements using the VNA is shown in Figure II.3.1.1.1.

Table II.3.1.1.2. S_{11} Versus Reflected Power

S_{11} , dB	Reflected Power, %
-5	31.6
-8	15.8
-10	10.0
-13	5.0

Figure II.3.1.1.1 and Figure II.3.1.1.2 both show examples of return loss measurements using different configurations and probing systems. In both cases, the measurements show an unacceptable high value of potential risk of failure.

With the necessary equipment finally in hand, efforts then were focused on equipment tuning at low-power (1-10W). Two major issues were encountered:

- The overall average reflection in the system was relatively high (ca. -9 dB = 12.6% reflected power).
- The reflection in certain areas of the transmission system was higher than the average, preventing normal and safe operation.

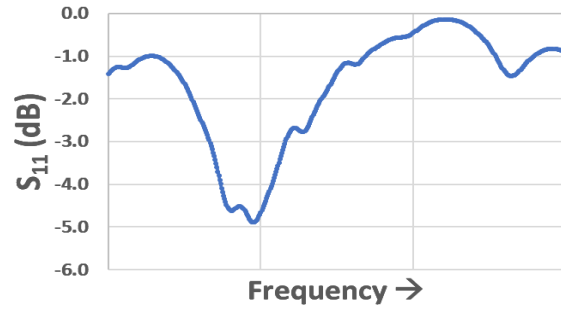


Figure II.3.1.1.1. Example of VNA cavity measurement. The band of operation of the generator covers only the central delimited by the vertical marker on this plot. This measurement shows a very high reflection, which is not desirable. Source: ORNL.

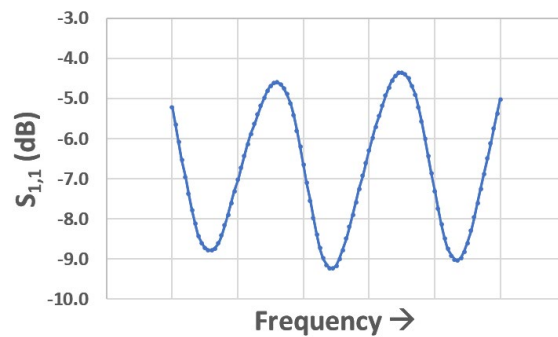


Figure II.3.1.1.2. Example of return loss measurement evaluated with the generator at low-power over its full band of operation. The return loss value is lower than in Figure II.3.1.1.1, but still unacceptable. Source: ORNL.

Figure II.3.1.1.3 shows the return loss measurement from the power supply, which is an example of the reflection pattern where the limitation described in the first point can be observed: the value of the reflection coefficient remains greater than the targeted -10 dB. Processing in this condition may induce additional equipment failure. In addition to this unfavorable pattern of reflection, the maxima might not always be at a constant frequency across the system. This complicates the process of selecting a frequency for operation.

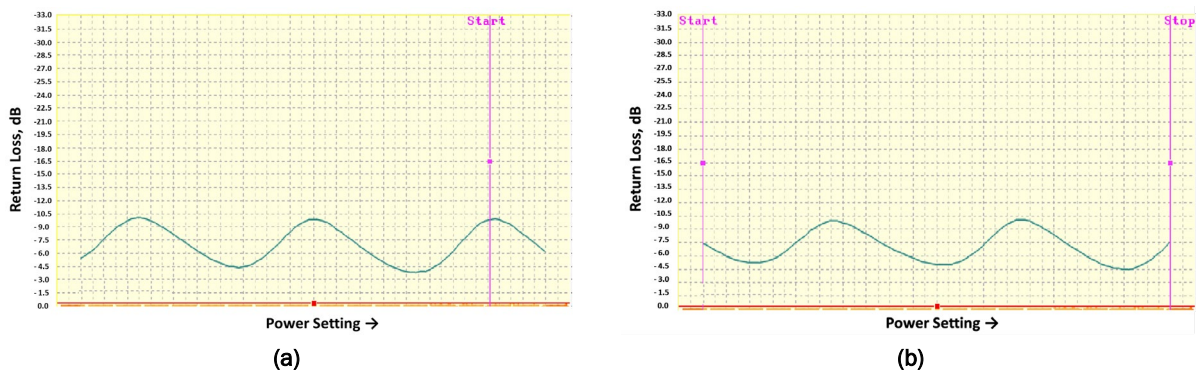


Figure II.3.1.1.3. (a) Typical pattern of reflection measured across the full band of operation with the generator at low-power. The center of the band of operation is marked by an orange dot, in the middle of the “power set” line. The return loss value is greater than the minimal acceptable value of -10 dB. (b) An example of an inconsistent pattern of reflection. The value of the reflection is similar but shifted. The vertical line (purple) indicates the selected frequency of operation, which is different in both examples. Source: ORNL.

For testing purposes, the transmission line was replaced by a simplified fixture allowing for connection of the generator to the reactor, just like with the original transmission line, but with the transmissible power severely reduced. This fixture cannot be used for normal operation. However, it does allow the reflection measurement with the generator, as seen in Figure II.3.1.1.4. The measurements demonstrate the system has three narrow bands of tuning opportunity in the band of operation for the generator, which indicates the following:

- The tuning capability of the cavity is as good as predicted by previous computer modeling.
- The problems are due to the transmission line. The resolution is described below.



Figure II.3.1.1.4. Measurement of the return loss with the generator using simplified transmission line. The best tuning-point can be as good as -22.5 dB (0.6% reflection). Source: ORNL.

After all the received parts were measured and verified, the system was reassembled, tested, and commissioned. Previously, the transmission line was identified as being the subsystem causing damage. Efforts then focused on the transmission line and equipment tuning. Subsequently, four major issues were addressed and resolved as follows:

1. A portion of the transmission displayed an unusual frequency shift in return loss measurements across the entire band of generator operation. The parts responsible for this unexpected observation were identified and replaced, which solved this issue.
2. Another critical part of the transmission line was still introducing more reflection than specified and anticipated. Despite this part being replaced and multiple configurations tested, the transmission line was still presenting a relatively high-level of reflection. This level was comparable to the one observed at the time the damage occurred during the previous FY. Only approximately 50% of the tuning span was tested and measured. Eventually, a good tuning setting was found.
3. When parts of the transmission line were replaced and tested, a substantial discrepancy between the reflection measured by the generator and S1,1 measured with a VNA was observed, as can be seen in Figure II.3.1.1.5. However, subsequent testing showed this was not the case.
4. On 25 May 2023, a subsystem of the generator was damaged, which temporarily reduced its power to ~75% of normal operation. The power output of the generator will stay reduced until repaired. The damaged parts have been shipped to the manufacturer. This incident was due to a human mistake. Low-power was involved, however, so no injury or exposure occurred. While the damaged part was returned to the manufacturer for repair, it was deemed unrepairable due to obsolete parts used in its construction. This reduced the team's available power supplies from two to one. The consequence was that LTC and HTC processing could no longer be performed inline simultaneously. Each had to be performed one at a time, slowing down progress even more.

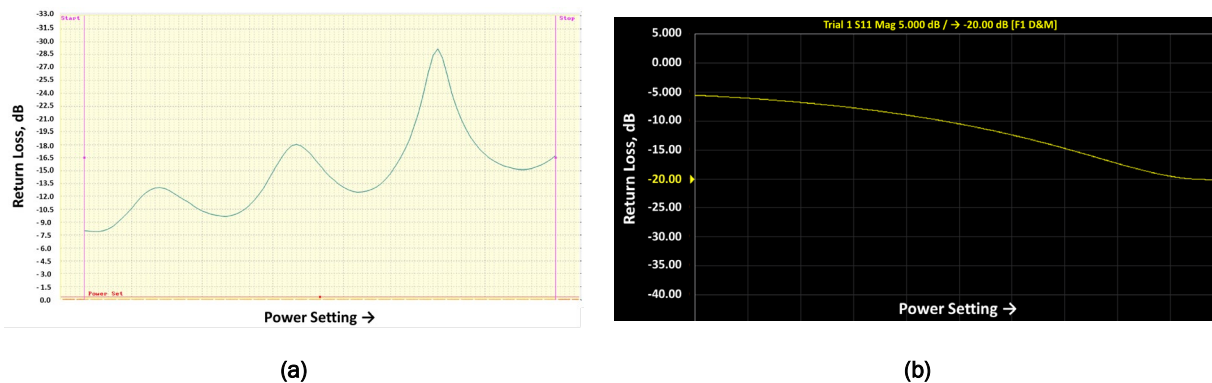


Figure II.3.1.1.5. (a) Pattern of reflection measured across the full band of operation with the generator at low-power. The presence of three peaks can be seen, with the two best values observed at -16 dB and -29 dB (Note: on this instrument, the Y-axis is inverted). (b) Pattern of reflection ($S_{1,1}$) measured with the VNA across the same span of frequencies. Only one broad peak at -20 dB is measured. Both measurements are performed on the HTC reactor using a simplified transmission line. Source: ORNL.

Carbon Fiber Processing

All the above-listed technical issues were resolved. The return losses at full power then ranged from -14.5 dB to -33.5 dB (3.5 – 0.04 % reflection), well exceeding the requirements. With the HTC system fully operational, the team commenced experimental work. Since the LTC and HTC had to be performed separately, different line speeds for the two steps could be explored. Again, $4 \times 50,000$ tows of OPF were utilized for this run. Figure II.3.1.1.6 shows the inline configuration using four tows in prior runs such as HTC4, but as stated above, for HTC6, the LTC and HTC steps were performed separately.

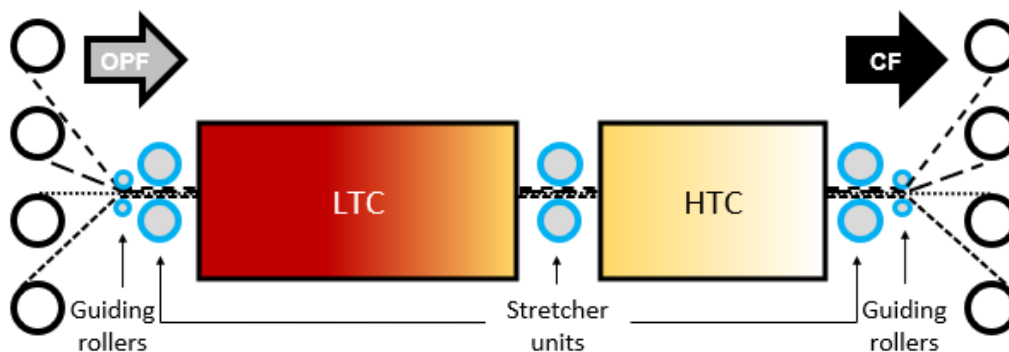


Figure II.3.1.1.6. Carbonization in one step of four tows of 50,000 filaments of commodity-grade OPF using two EM powered furnaces setup inline. One process condition corresponds to one assigned color identification (COLOR ID). Source: ORNL.

In the next round of testing, labeled HTC6, new low-temperature fiber was produced using the EM LTC system from the previous project, at two different line speeds. HTC6 represents a preliminary broad sweep of process conditions to explore the parameter space. Final, optimized results will be presented in the final report. Then, this material was used to produce CF with the EM HTC system at four different line speeds. Four tows were processed simultaneously at the same process conditions. The speed combinations are shown in Table II.3.1.1.3. All other process conditions were held constant.

Table II.3.1.1.3. Line Speed Combinations of Samples for HTC6

Color ID	LTC Line Speed in/min	HTC Line Speed in/min	HTC Residence Time sec
White	30	20	33.75
Purple	30	30	22.50
Green	30	40	16.88
Blue	40	20	33.75
Orange	40	30	22.50
Brown	40	40	16.88
Yellow	40	50	13.50

Table II.3.1.1.4 shows the three samples with the best mechanical properties. The top row shows a common commercial fiber for comparison, and the bottom row shows this project's milestones for this material. The "Color ID" represents the different line speeds as shown.

Electrical resistivity, as indicated in Table II.3.1.1.4, is a good predictor of final mechanical properties. However, the density of the "White" and "Purple" samples was unusually high, yet the electrical resistivity was also high. Normally, as density increases, electrical resistivity decreases. The result of these samples shows that the energy density in the process area was too high, which possibly led to morphological damage of the material. Subsequent processing took this into account. These densities are more typical of graphitized fiber, which sees much higher temperatures than the typical HTC process.

During all testing, power consumption data was recorded for use in the final cost-savings analysis. This information will be presented in the final report.

Table II.3.1.1.4. Top Three Mechanical Results From HTC6 Where the Hexcel AS4 Data Are Shown Only For Reference (It Was Not Processed with EM Equipment)

Color ID	Break Stress (ksi)	Modulus (Msi)	Density (g/cc)	Electrical Resistivity (Ohm-cm)
Hexcel AS4	643	33.5	1.78	0.00156
Blue	528	28.9	1.87	0.00433
White	443	25.2	1.94	0.01479
Purple	323	18.3	1.84	0.28459
Milestone 11 Target	550	29	N/A	N/A

Note: As a reference, the Hexcel AS4 properties are listed in the first row. The mechanical properties are from the Hexcel specification sheet. The electrical resistivity was measured by the same system used in the analysis of the project fiber.

Ancillary Tasks – Wet Spinning Line

ORNL requires precursor materials to conduct a wide variety of current research. Unfortunately, there is no open market of such materials in the United States, especially for polyacrylonitrile (PAN) fiber, from which 95% of all-CF is made. Even globally, only textile and commodity-grade acrylic fiber can be purchased, and even this is difficult and costly. No aerospace quality precursor is available for purchase. Currently, ORNL cannot autonomously produce quantities of precursor, which represents ~50% of the cost of CF, at the level needed to fully and cost-effectively demonstrate new CF approaches in composite test articles. For multiple reasons, such as the restricted number of manufacturers, their fear of reverse engineering is a real challenge, even sometimes impossible, to get a supply of PAN precursors on the open market. ORNL encountered this difficulty multiple times over the past decades, frequently delaying or even compromising some of its projects.

A spinning line is one of the last pieces of equipment ORNL needs to cover the entire production stream of PAN fiber. Therefore, a wet spinning line was identified that would provide an appropriate scale to match CF conversion development and demonstration capabilities already at ORNL. The acquisition of this industrial line at reasonable cost is an exceptional opportunity. This will allow ORNL to support multiple future projects with custom material at different levels of processing, without having to rely on external suppliers. This will significantly increase its capacity to develop new technologies of precursors for future material generations. To expediently acquire this unique capability, ORNL worked with DOE to modify the AOP of the HTC project for FY 2022 by adding a task focused on the acquisition of the wet spinning line. The equipment will be supplied by Dienes Corporation (Mülheim, Germany). Some upgrades were specified to meet ORNL's needs and bring it to the current state-of-the-art. Specifications were submitted before 30 September 2022.

The process of purchasing a refurbished wet spinning line, initiated in June 2022, was then finalized. This acquisition required substantial effort due to the nature of the equipment, i.e., foreign origin (Germany), the work that must be accomplished for customization prior to shipping, and its high-cost. The purchase order was eventually approved and issued. The vendor was able to initiate the specified modifications and prepare the shipment. As of September 30, 2023, most of the equipment was delivered to ORNL and is being held on-site in temporary storage. With respect to Milestone 12, shown in Table II.3.1.1.5, conformity has been confirmed through documentation only, since testing is not yet possible. Laboratory infrastructure upgrade work is also underway. These include electrical power, compressed air, nitrogen, water, and exhaust distribution to the large system. These facility upgrades are anticipated to be completed in the first quarter of FY 2024 so that equipment installation can begin very late in the first quarter or early in the second quarter. The balance of the wet spinning line equipment is anticipated to be delivered from Dienes in the second quarter of FY 2024, coincident with availability of the laboratory space for installation. Commissioning of all installed equipment is expected to take place in FY 2024.

Table II.3.1.1.5. FY 2023 and Milestones Expected to Complete Early in FY 2024

Milestone	Due Date	Description	Status
M10	02/28/2023	M10: Reach at least S1,1 lower -10dB on each port, with appropriate hardware modification (cavity with load).	Completed
M11	04/30/2023	M11: optimization of the process condition. Evaluation of the windows and limitation of processability. Reach a minimum baseline of 550 ksi tensile strength, 29 Msi modulus with 4 tows of 24k filaments. Energy balance data acquisition.	In Progress <i>Exp. Completion November</i>
M12	04/30/2023	M12: Check conformity and acceptancy of all devices of the spinning line upon receiving at ONRL.	In Progress
M13	05/31/2023	M13: Demonstrate HTC at least 5% cost-savings versus conventional carbonization.	In Progress <i>Exp. Completion December</i>
M14	06/30/2023	M14: Final report with discussion about further technology implementation/scale-up.	In Progress <i>Exp. Completion December</i>

Conclusions

The work conducted in FY 2023 led to the following achievements:

- The EM HTC system was restored to full power operation.
- A new round of testing was performed that nearly met the mechanical targets of Milestone M11, as shown in Table II.3.1.1.5. Subsequent rounds of testing will be performed in the final quarter of this project to meet this milestone. Note that all mechanical results are produced using single-filament testing, which typically can be 10% lower than full tow testing that is standard in the industry.

- The work needed to complete this project is as follows:
- The techno-economic analysis will be completed.
- The final report will be completed.
- Final fiber-processing will be performed.

Key Publications

1. An invention disclosure on this work will be finalized and submitted for patent filing consideration.

References

1. *FY 2022 Materials APR*, 2022, https://www.energy.gov/sites/default/files/2023-10/FY2022%20VTO%20Materials%20Consolidated%20Report_FINAL_compliant-min.pdf
2. Ellringmann, T., C. Wilms, M. Warnecke, G. Seide, and T. Gries. 2016. "Carbon fiber production costing: a modular approach," *Text. Res. J.*, 86(2), 178–190. <https://doi.org/10.1177/0040517514532161>.

Acknowledgements

This research was sponsored by DOE-EERE VTO, performed at ORNL, and managed by UT-Battelle, LLC, for DOE under AOP project contract DEAC05-00OR22725. The experimental work was performed under subcontract with 4XTechnologies, LLC in Knoxville, TN, with primary support from Mr. Pol Grappe and Dr. Truman Bonds.

II.3.1.2 Additive Manufacturing for Property Optimization for Automotive Applications (Oak Ridge National Laboratory)

Seokpum Kim, Principal Investigator

Oak Ridge National Laboratory
Materials Science and Technology Division
1 Bethel Valley Rd.
Oak Ridge, TN 37830
E-mail: kimsp@ornl.gov

Rich Davies, Composites Core Program Manager

Oak Ridge National Laboratory
Materials Science and Technology Division
1 Bethel Valley Rd.
Oak Ridge, TN 37830
E-mail: daviesrw@ornl.gov

H. Felix Wu, DOE Technology Development Manager

U.S. Department of Energy
E-mail: Felix.Wu@ee.doe.gov

Start Date: October 1, 2020

End Date: September 30, 2024

Project Funding: \$500,000

DOE share: \$500,000

Non-DOE share: \$0

Project Introduction

This project is aimed at using advanced manufacturing methods for developing property-optimized structures for applications in passenger vehicles. The primary objective of this project is to develop lightweight structures with tailored mechanical responses by utilizing multiple technologies associated with polymer and composites AM. The primary AM technologies developed in this work include multimaterial printing using a material extrusion AM process, out-of-plane printing (OPP) using a multi-axis robotic arm printer, and toolpath optimization associated with printing systems. In addition to material selection and optimization, design flexibility offered by the AM process will be leveraged in this project by developing novel lattice structures with tailored responses in AM parts. Some of the key steps towards attaining these goals include lattice structure optimization, ML for design selection, toolpath optimization, multi-axis robot arm control, and part fabrication/testing.

Objectives

With the primary focus being on developing tailored structures with high-performance for applications in passenger vehicles, two target parts/components have been chosen in this project, in collaboration with Ford Motor Company (Ford). The first part is a front bumper, while the second is a door panel arm rest.

To develop a front bumper that meets the performance requirements, research will be conducted on fabricating parts with multimaterial printing. Therefore, our studies involve printable material properties and optimizing material combinations. In the design space, novel 2.5D lattice structures with tailored mechanical responses will be developed in collaboration with the University of California—Berkeley (UCB) using ML techniques. The final printed bumper will be aimed to incorporate both material and design-optimized structures, thereby being a customized lightweight structure with high-performance.

In the case of a door arm rest, research will be conducted with the OPP technique using a robotic arm printer. Extrusion and control techniques in the OPP system require R&D in this project, including slicing technology development, toolpath planning and optimization, robotic arm control and extrusion control optimization, and material property evaluation and optimization. For OPP technology development, a single material with optimized structures will be explored to obtain lightweight high-performance components.

Approach

The proposed work is divided into three major tasks, with various subtasks for each. Task 1 will provide a large-scale structure optimized for structural design and multimaterial placement printed using AM. In Task 2, an OPP control technique will be developed, and the subcomponent of a vehicle will be fabricated. The third task will focus on the ML algorithm development for a subcomponent structure with tailored energy absorption characteristics in collaboration with Prof. Rayne Zheng at UCB. Here is the list of tasks and subtasks that were completed in FY 2023:

Task 1. Multimaterial large-scale printing of optimized structures (bumper):

Subtask 1.1. Conduct print trials on full-scale bumper with property-optimized material blends with inputs from Task 3.

Task 2. OPP printing of optimized structures (arm rest):

Subtask 2.1. Generate a new door armrest design with less support structures.

Subtask 2.2. Develop robotic arm control and extrusion control for the multi-axis system.

Subtask 2.3. Demonstrate printing of an out-of-plane property-optimized structure.

Task 3. Tailored lattice structures using ML:

Subtask 3.1. Training of the ML framework using simulation data acquired to predict a property-optimized lattice design.

Subtask 3.2. Generation of tailored lattice structures and evaluation (small-scale).

Results

Task 1. Multimaterial large-scale printing of optimized structures (bumper).

Subtask 1.1. Conduct print trials on full-scale bumper with property-optimized material blends.

The full-scale bumper was printed using a three-dimensional printing (3DP) 3D Platform™ printer, as shown in Figure II.3.1.2.1(a). The printer has a print volume of 4 ft × 8 ft × 3 ft. Filament spools with different materials blends were manufactured by Push Plastic from the material in the form of pallets. For the initial printing, the chosen material was carbon fiber-reinforced acrylonitrile-butadiene-styrene (CF-ABS) for the bottom portion of the bumper, and a blend of CF-ABS and thermoplastic polyurethane (TPU) in a ratio of 85:15, respectively, for the top portion of the bumper. Before printing, the filament spools were dried in an oven for eight hours. After multiple attempts for printing calibration and changes in the design of filament feeding inlet, a bumper was successfully printed with the chosen materials as shown in Figure II.3.1.2.1(b).

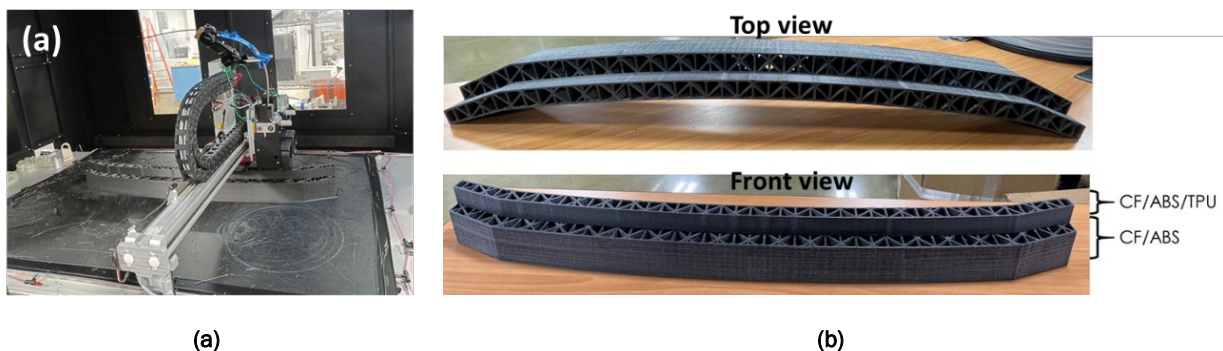


Figure II.3.1.2.1. (a) A multimaterial bumper being printed on the 3DP 3D Platform™ printer using filament-based feedstock. (b) 3D-printed multimaterial bumper structure. Source: ORNL.

Task 2. OPP of optimized structures (armrest).

Subtask 2.1. Generate a new door armrest design with less support structures.

The previously designed OPP armrest required supporting blocks during printing and their removal once printing is completed. To minimize the support structures and automate overall armrest printing, a new supportless structure needed to be designed to satisfy the design constraints. A new 3D supportless armrest structure was designed, as shown in Figure II.3.1.2.2(a). This supportless armrest structure consists of constructs in the 3D space with angles less than 45° vertical to enable 3D-printing in a vertical orientation, as shown in Figure II.3.1.2.2(a). It also includes some curved struts with varying curvature connecting between different parts of the armrest for effective load transfer. The CAD model of the armrest was then imported into the commercial finite element software ABAQUS for meshing, as shown in Figure II.3.1.2.2(b). The side of the armrest that would be mounted on to the door was prescribed with a fixed boundary condition, as observed in Figure II.3.1.2.2(c). The armrest can be subjected to two different loading conditions (i.e., a vertical and horizontal load), as illustrated in Figure II.3.1.2.2 (c). Simulations were performed on the armrest for both loading conditions. A maximum deflection of 9.4 mm occurs for a vertical load of 670 N. This design satisfied the criteria as the maximum deflection was within 15 mm. The armrest was analyzed for a vertical load acting at a different (non-centric) location. Even for this loading configuration, maximum displacement within the armrest was less than 15 mm, which satisfied the design criteria.

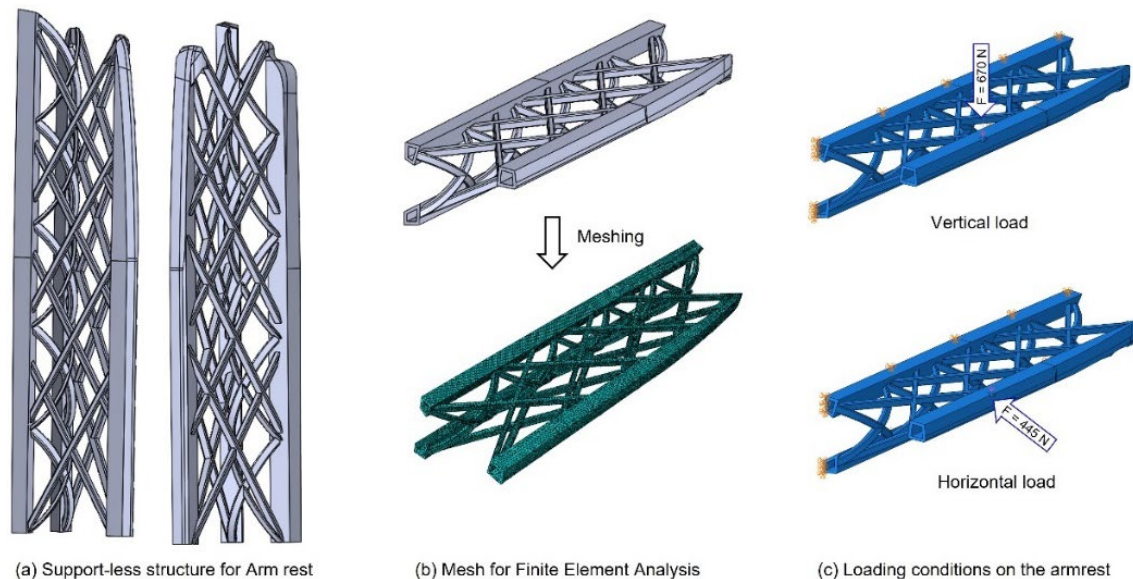


Figure II.3.1.2.2. Supportless armrest structure design for OPP. Source: ORNL.

Subtask 2.2. Develop robotic arm control and extrusion control for the multi-axis system.

The critical challenge in OPP of the previously designed armrest is due to the robotic arm and extrusion control on the out-of-plane surface. Programming was performed for extrusion control on the curved surface of the armrest, as well as for the wrapping of the entire armrest. Figure II.3.1.2.3 shows the printing of the armrest and robotic arm control for the OPP on the curved surface followed by the wrapping. Once the robotic arm control was programmed for the Kuka robotic arm mounted on the Orbital Composites 3D-printer, our team printed the designed armrest in four steps, as shown in Figure II.3.1.2.4: (1) the base structure of the armrest was printed with carbon fiber-reinforced polyethylene terephthalate glycol (PETG) in a layer-by-layer fashion; (2) support blocks that would fit into the holes in the armrest design were printed separately and inserted while the armrest was being printed; (3) once the armrest printing with support blocks was completed, the armrest was wrapped with a thin sheet of PETG with the help of a heat gun to conform the shape of the armrest; and (4) OPP on the curved surface and wrapping of the armrest on top of the PETG film. The support blocks made up of soluble material can be dissolved by immersing the printed structure into the solvent, and thus obtain the armrest design with OPP.

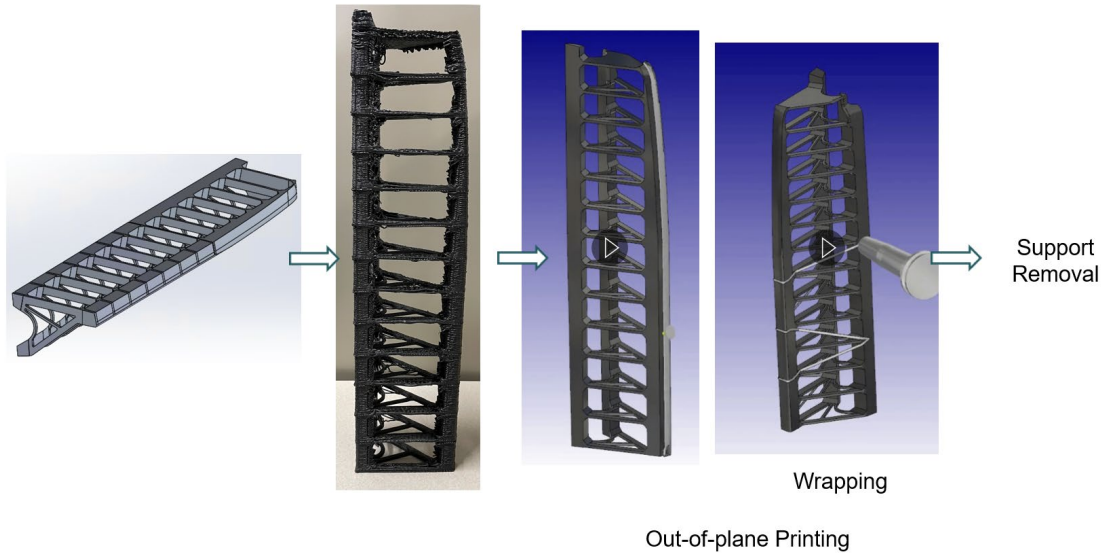


Figure II.3.1.2.3. Robotic arm control for the OPP (wrapping) on the armrest design. Source: ORNL.

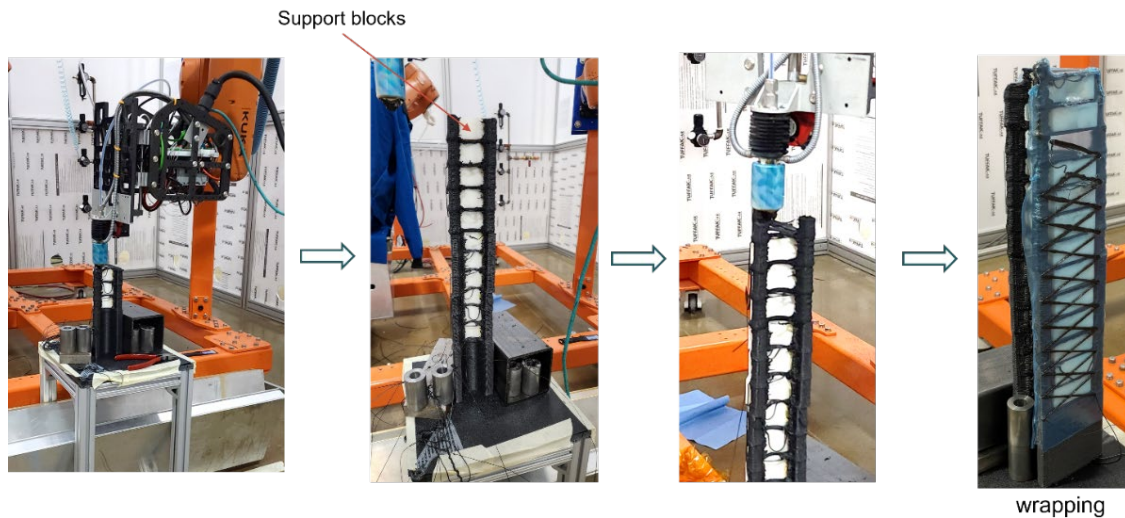


Figure II.3.1.2.4. OPP with inserted support blocks in the armrest design. Source: ORNL.

Subtask 2.3. Demonstrate printing of an out-of-plane property-optimized structure.

One of the challenges in OPP of the previously designed armrest was the support blocks that were inserted at regular intervals requiring the printing to be interrupted. As described in Section 2.1, support structures in the next iteration of the armrest design have been eliminated in preference of the redesigned structure, shown previously in Figure II.3.1.2.2(a). The overall shape of the armrest design was still retained; however, the internal struts were designed such that they can be printed without any additional supports. The supportless armrest design was subsequently printed using a Fortus 450 3D-printer using ABS. The printed armrest design was depicted in Figure II.3.1.2.5.

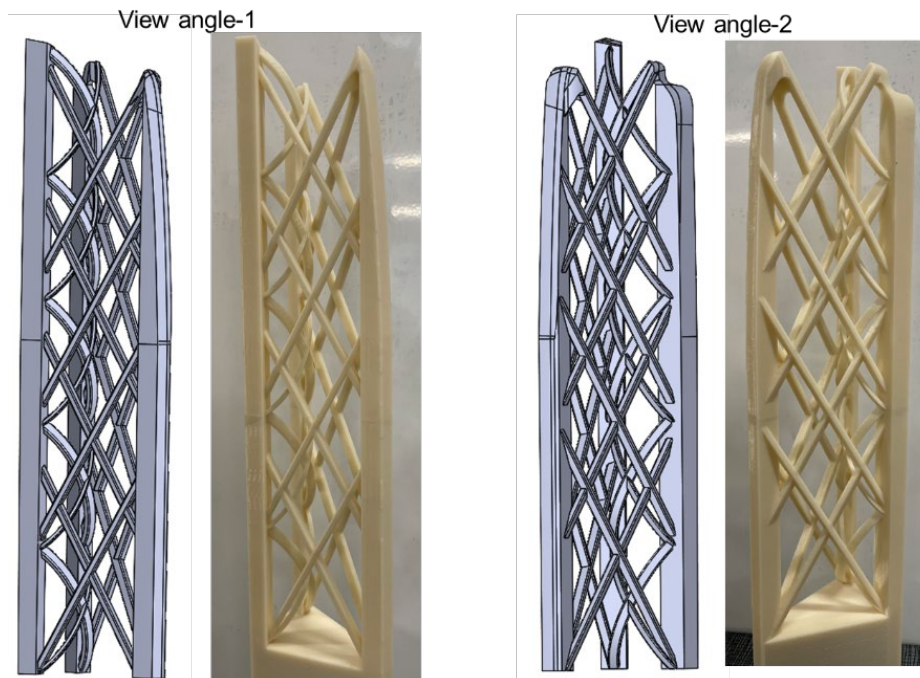


Figure II.3.1.2.5. Optimized supportless armrest structure.. Source: ORNL.

Task 3. Tailored lattice structures using ML.

Subtask 3.1. Training of the ML framework using simulation data acquired to predict property-optimized lattice design.

In the ML framework, the target mechanical properties were used as the input to inverse design lattices to satisfy design requirements. Numerical simulations were performed via finite element analysis on a representative volume element consisting of $3 \times 2 \times 2$ -unit cells using periodic boundary conditions. The workflow of the ML framework for inverse lattice design is shown in Figure II.3.1.2.6. The architectural genes consist of seven distinct type of unit cells based on internal strut member angles. Five different material blend ratios were also used for the choice of material. The full design space of attainable properties by combining lattice topologies and material combinations was first analyzed. The sequential integrated ML strategy takes mechanical properties as inputs and outputs for the lattice gene type and material combinations. Once the tailored lattice was determined, a full-scale computer- aided design model can be obtained followed by slicing, by toolpath optimization using an ORNL slicer, and by 3D-printing in a 3DP filament-based printer.

The integrated ML model with sequential prediction strategy, as shown in Figure II.3.1.2.7, was developed. Given the target mechanical properties, the inverse model outputs design parameters of the lattice via a two-stage prediction process. These predicted parameters are then passed to a set of forward models for the evaluation of corresponding mechanical properties of an inversely-designed lattice structure.

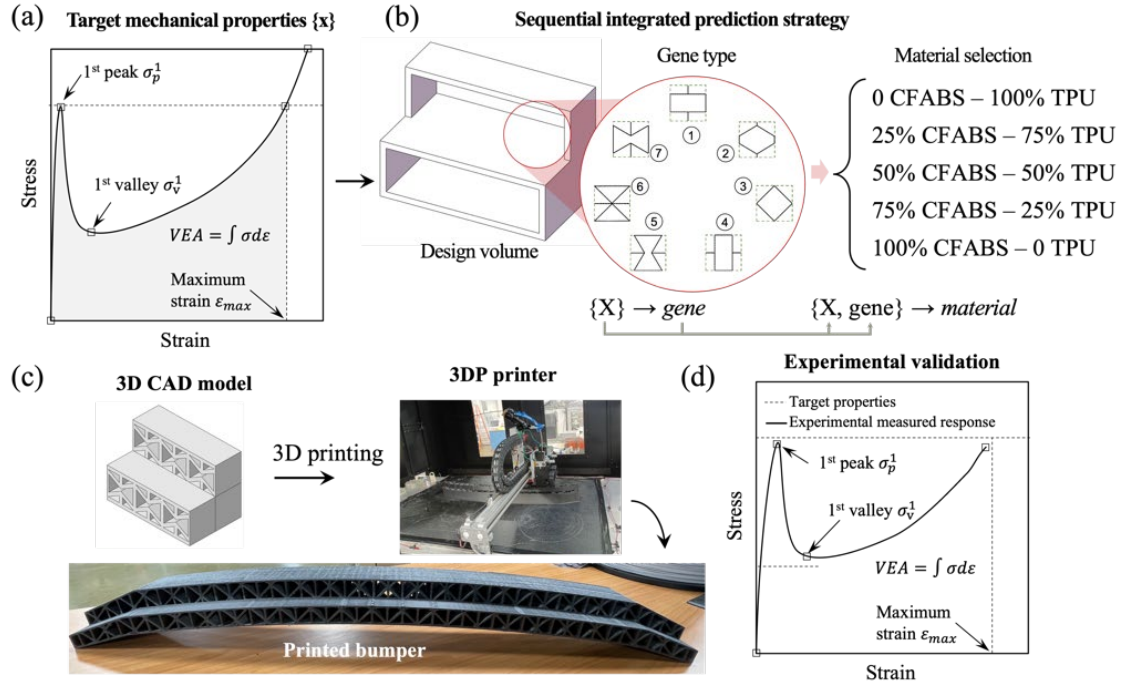


Figure II.3.1.2.6. Workflow of the ML-based inverse design framework. Source: UCB.

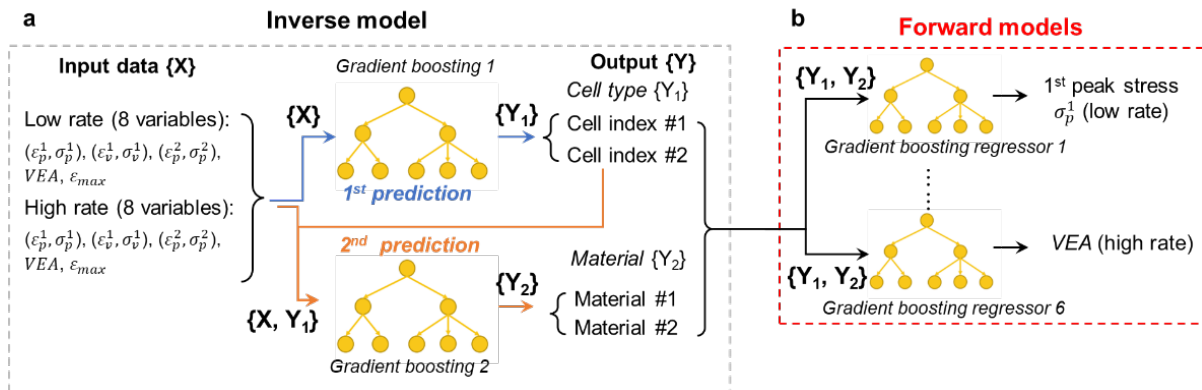


Figure II.3.1.2.7. Workflow of the integrated ML model. (a) The inverse model takes 16 mechanical properties as an input and predicts the design parameters of the lattice in a sequential manner. (b) The forward models evaluate the mechanical properties of the designed lattice. Source: UCB.

The input data $\{X\}$ for the inverse model consists of 16 critical mechanical properties for both loading cases consisting of peak stress and volumetric energy absorption (VEA) as shown in Figure II.3.1.2.7(a). The output data $\{Y\}$ consists of a lattice cell type $\{Y_1\}$ and a material index $\{Y_2\}$ in the upper and lower section of the bumper, respectively. The inverse model first takes the mechanical properties $\{X\}$ as the input to predict the cell types of the lattice $\{Y_1\}$. The predicted cell type $\{Y_1\}$, along with the input mechanical properties $\{X\}$, forms the new input for the evaluation of material combination $\{Y_2\}$ in the lattice structure, as indicated in Figure II.3.1.2.7(a).

The design parameters $\{Y\}$ (e.g., $\{Y_1, Y_2\}$) are then passed to six forward models. Each model estimates a single mechanical property of the design lattice, such as the peak stresses and VEA for each loading-rate case. These predicted mechanical properties are compared with the target properties to evaluate the prediction accuracy of the inversely-designed lattice structure.

For ML framework training, our team first trained six individual forward models with the augmented dataset. The forward models were implemented using a Gradient Boosting regressor and a random-forest regressor in an open-source package, Scikit-learn. Each forward model was trained with 70% of the augmented dataset and then tested with the other 30% of the dataset, which is not used in the training process. The hyperparameters of the forward models were optimized using Scikit-learn's GridSearchCV function for a maximum testing score. We observed over 90% prediction accuracy for all forward models. Prediction accuracy of a forward model is presented in Figure II.3.1.2.8(a) for a low-loading rate and Figure II.3.1.2.8(b) for a high-loading rate. These results validate the forward models effectively act as a surrogate model that replaces conventional simulations used to evaluate the responses of a lattice design.

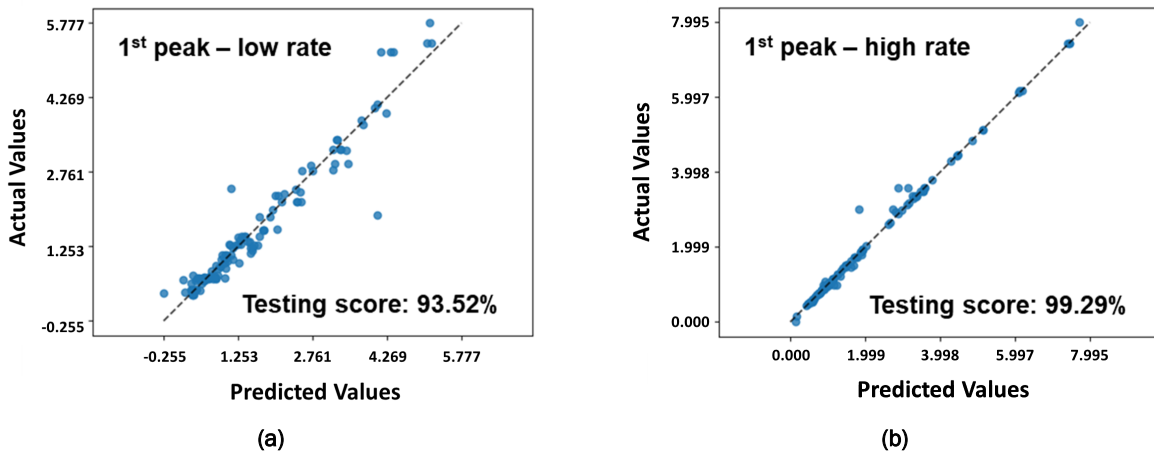
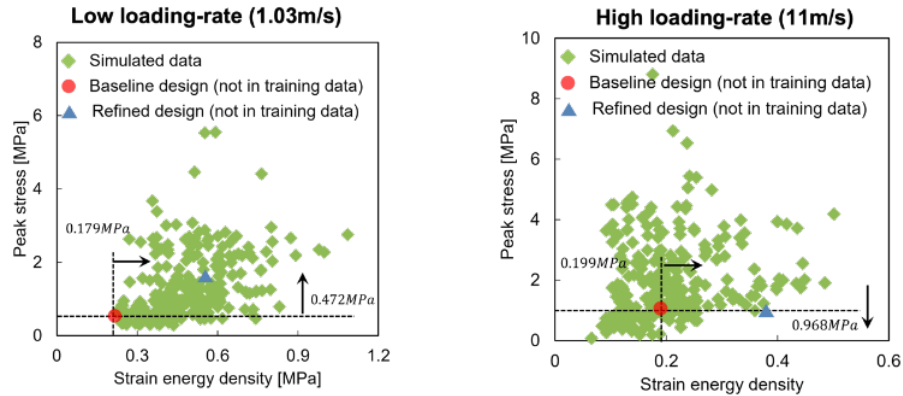


Figure II.3.1.2.8. Prediction accuracy of forward models for (a) a low rate and (b) a high-rate. Source: UCB.

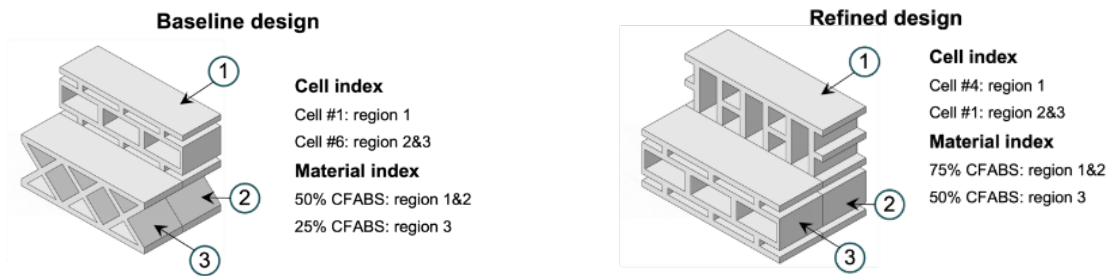
Once the forward models were trained, these models were kept frozen (i.e., the hyperparameters of all forward models were fixed) and were then used to train the inverse model with the pristine training dataset. The inverse model was implemented using MultiOutputClassifier in the open-source package, Scikit-learn. Due to the low number of data points in the pristine dataset, we used 10% of the pristine dataset as the testing set (not used in training) for the evaluation of the prediction accuracy. In this training process, the prediction accuracy of all mechanical properties, as output from the forward models, was used to optimize the hyperparameters of the inverse model. The testing accuracy of the inverse model was found to be more than 75% on average.

Subtask 3.2. Generation of tailored lattice structures and evaluation (small-scale).

We have previously obtained a lattice from the inverse design framework that was referred to as our baseline design. Here, we utilized the ML framework to further optimize the mechanical behaviors of the bumper. The team used a higher peak stress and higher strain energy density performance as an input for the low-loading rate case. For the high-loading-rate case, a lower peak stress and higher strain energy density were prescribed. The selected targeted property set was mapped onto the design space for the low- and high-loading rate cases, as shown in Figure II.3.1.2.9(a). For the new target property set, the refined design with the geometrical and material combination, as shown in Figure II.3.1.2.9(b), was predicted by the ML framework. The baseline design is also shown in the figure for comparison purposes.



(a)



(b)

Figure II.3.1.2.9. (a) Training data and selected target property set mapped onto the design space for low- and high-loading rate tests, and (b) the refined design with the geometrical and material combination
Source: UCB.

Conclusions

In FY 2023, print trials were successfully performed using the optimized material blends of TPU and CF-ABS for Task 1. A full-scale bumper was printed using a 3DP mid-scale printer. The printing of the bumper with an optimized lattice structure is in progress. For Task 2, first, an armrest design was updated to eliminate the support structures, thus easing the printing process. Additionally, to achieve the printing of out-of-plane curved surfaces in the armrest, the robotic arm control and extrusion controls are programmed accordingly. The redesigned armrest printing was performed using a Fortus 450 3D-printer using ABS. In the case of Task 3, the developed ML framework was trained for forward and inverse models. More than 75% of accuracy was observed in the validation exercise performed on the test cases. Using this framework, optimized lattice structures were obtained for the bumper as per the targeted property set.

Key Publications

1. S. Kim, A. Nasirov, D. K. Pokkalla, V. Kishore, T. Smith, C. Duty, and V. Kunc, 2023, "Compression and energy absorption characteristics of short-fiber-reinforced 2D composite lattices made by material extrusion," *Eng. Rep.*, 5(12), e12701. <https://doi.org/10.1002/eng2.12701>.

Acknowledgements

The work performed in this project in FY 2023 involve contributions from teams at ORNL, UCB, and Ford. The key personnel who contributed to project progress in the past year include S. Kim, D. Pokkalla, N. Garg, S. Simunovic, T. Smith, A. Hassen, V. Kunc, T. Feldhausen from ORNL; X. Zheng and D. Yao from UCB; and E. Lee, I. Farooq, R. Baccouche, S. Chowdhury, Z. Pecchia, and M. Rebandt from Ford.

II.3.1.3 3D-Printed Hybrid Composite Materials with Sensing Capability for Advanced Vehicles (Oak Ridge National Laboratory)

Rigoberto C. Advincula, Principal Investigator

Oak Ridge National Laboratory
Materials Science and Technology Division
1 Bethel Valley Rd.
Oak Ridge, TN 37830
E-mail: advincularc@ornl.gov

Rich Davies, Composites Core Program Manager

Oak Ridge National Laboratory
Materials Science and Technology Division
1 Bethel Valley Rd.
Oak Ridge, TN 37830
E-mail: daviesrw@ornl.gov

H. Felix Wu, DOE Technology Development Manager

U.S. Department of Energy
E-mail: Felix.Wu@ee.doe.gov

Start Date: November 1, 2020
Project Funding: \$500,000

End Date: June 30, 2024
DOE share: \$500,000

Non-DOE share: \$0

Project Introduction

The project has been extended at no-cost for nine months beyond the original end date of 30 September 2023 to 30 June 2024. ORNL and collaborators at the University of North Texas (UNT) have pursued research on 3D-printed CF composites for vehicle lightweighting with sensing functionality. The objectives are (1) the enhanced organic-inorganic interface for long-term performance via covalent bonding between CF and a polymer matrix, and (2) the real-time evaluation of material properties with embedded sensors. The group has targeted AM and synchronous sensor fabrication/embedding towards next generation vehicle structures and materials as follows:

1. Synthesis, modification, and characterization of CF/polymer composites using low-cost CFs, surface modifiers, and optimized resin formulations and chemistry.
2. Dynamic studies of curing control and characterization guided by simulations on multifunctional polymer-based composites with feedback loop materials development protocol.
3. Advanced AM- and 3D-printing of continuous CF/polymer composite geometries.
4. Assembly of sensor-embedded CF/polymer composites via multimaterial 3D-printing.

Specific developments for this FY 2023 period involved detailed studies and results on the following: (1) the development of polyvinylidene fluoride (PVDF) sensors with various concentrations of molybdenum disulfide (MoS₂) and other MXene two-dimensional nanomaterials boosting the piezoelectric response, (2) the extension of interfacial chemistry modification with dendron and hyperbranched amine functionality to understand their effect on reaction kinetics and surface adhesion, (3) the measurement of the adhesion properties of CF with the epoxy using extensional rheology and universal tensile testing, and (4) the development of continuous CF 3D-printing apparatus, which is the main subject of the extension period. There are several publications for this year, including plans for several reports and presentations.

Objectives

The project's overall objective is to focus on enhancing the interfacial interaction between CF and polymer and to enable monitoring of the material's performance [1]. To meet these objectives, the group has pursued the following specific objectives:

1. Investigate chemical reactions at CF-polymer interface and long-term thermomechanical performance to achieve mechanical properties with Young's modulus > 15 GPa and tensile strength > 250 MPa.
2. Conduct simulation and computational studies to establish structure-process-property relationships and evaluate interfacial failure mechanisms with finite element analysis (FEA).
3. Fabricate 3D-printed composite parts with controlled fiber orientation, multi-axis capabilities, and enhanced fiber-polymer interfacial adhesion at various test geometries and parts design.
4. Incorporate and test sensor-embedded CF/polymer composites with 3D-printing to embed piezoelectric sensor layers [2] in-situ with designed vehicle component geometries that can be monitored for stress and fatigue with time.

Specifically for this extension period, the group will pursue the following objectives: (1) to optimize continuous fiber extrusion and 3D-printing, (2) to optimize epoxy and thermoset materials blends closer to the curing behavior for continuous CF printing with surface amine modification, and (3) to demonstrate a sandwiched sensor device and a fabricated composite layer. The last objective has yet to be met. In the final period, an objective will be to demonstrate AM 3D-printing and structural monitoring through embedded sensors verified by simulation studies for robust materials and process design.

Approach

The ORNL PI (R. C. Advincula) and co-PI (Z. Demchuk) bring strengths in synthetic chemistry, composite materials, and AM. The UNT Co-PIs (W. Choi and Y. Jiang) enabled simulations and embedded sensors using nanomaterials and 3D-printing capabilities. Originally, the project was divided into four tasks, as indicated in Figure II.3.1.3.1 and described as follows:

Task 1. Precise Chemical Reaction Control in Resin Materials.

Objective: Develop CF/polymer with enhanced inorganic-organic interface covalent interaction.

End-of-project Goal: Achieve composites with optimum chemistry, processability, and high-performance.

Task 2. Computational Studies of Interfacial Interaction between Polymer Matrix and CF.

Objective: Simulation of interfacial properties and optimum reactive chemical species.

End-of-project Goal: Achieve a high-correlation of printed components with predictive tools.

Task 3. 3D-Printing of Continuous CF/Epoxy Composite with Enhanced Fiber-Polymer Adhesion.

Objective: 3D-printing of continuous CF-epoxy matrix with optimal fabrication parameters.

End-of-project Goal: Achieve AM process and materials combination for high-performance.

Task 4. Continuous Sensor-Embedded Polymer/CF Composite 3D-Printing.

Objective: 3D-print continuous CF/polymers with embedded sensor geometries and testing.

End-of-project Goal: Achieve sensing capability in continuous CF/epoxy 3D-printed parts.

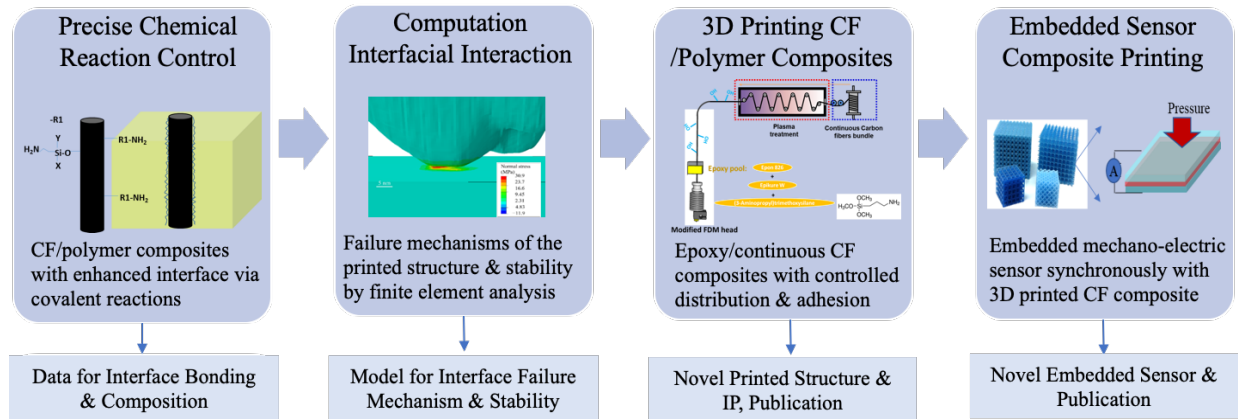


Figure II.3.1.3.1. Schematic of the tasks for enhanced organic-inorganic interface between the CF and polymer matrix and real-time evaluation of material properties with embedded sensors. Source: ORNL.

Four tasks were on-schedule in the short-term (FY 2022), and the path for the final phase (FY 2023) was considered by a cohesive team between ORNL and UNT that met every two weeks. The technical accomplishments for this FY included:

1. We conducted a comprehensive study of epoxy/chopped CFs based on establishing the reproducible methods of surface functionalization and curing kinetics [3]. The ability to functionalize the surface was extended beyond silanes and single amines into hyperbranched and dendrimeric structures. The study on crown ether coordinated surface functionalization is almost finished. Preparation of optimized epoxy resins with optimized protocols for grafting surface functional groups in CFs was completed. We completed the original goals for FY 2022 but extended this work with new goals in FY 2023.
2. We have established data-driven ML models to predict the interface adhesion properties, precisely identified imperfections from the FEA, and developed algorithms for material programming. We were on-schedule for completing this work in FY 2023.
3. We have achieved 3D-printing of epoxy-CF composite using a viscous solution printing (VSP)-based method, including some success in continuous CF 3D-printing. However, CF embedment and the continuous printing demonstration to form larger objects or parts still need to be completed. Due to difficulties in machine development, the demonstration is delayed until FY 2023, and will be concluded during FY 2024.
4. We have achieved sensor capabilities with PVDF and developed a protocol and 3D-printing ink for embedded sensors and fabrication with epoxy/CF composite. This phase was on-schedule for FY 2023; however, fabrication has to await embedment on more significant parts or concept composites with continuous CF 3D-printing.

Results

Results and accomplishments are described per task in the following sections:

Task 1. Precise Chemical Reaction Control in Resin Materials.

- Prepared CF/epoxy composites with different content of CFs (1, 5, 10, 20 wt.%) in the epoxy matrix (3:1 epoxy: amine ratio) at 100°C for 3 h. Optimized: 3:1 epoxy: amine ratio at 5 wt.% CF loading and cured at 100°C for 3 h.
- Established a protocol for silane-amine functional modification and discovery of new CF surface enhancement strategies together with graphene oxide, crown ether derivatives, and dendrimeric amines, as illustrated in Figure II.3.1.3.2.

- Kinetics of curing for epoxy is established. The mechanical strength of the polymer resin improves when the temperature rises from 80–180°C, up to 3 h, with isothermal differential scanning calorimetry studies.
- Initiated characterization of a CF/epoxy matrix interface using atomic force microscopy (AFM) to probe the mechanical properties of the interfacial layer and make contact resonance measurements with force-distance mapping of Young’s modulus on the nanoscale.
- Confirmed the de-sizing and effect of CF chemical treatment on the surface roughness as evidenced by AFM or AFM probe measurements.
- The kinetics of the curing and thermal cycling were studied. This enabled us to compare the extent of tensile strength deterioration on the various epoxy composites resulting in optimized matrix curing methods. Then, we utilized Raman spectroscopy to map the differences in s-CF/epoxy composites optimized with pristine-CF.

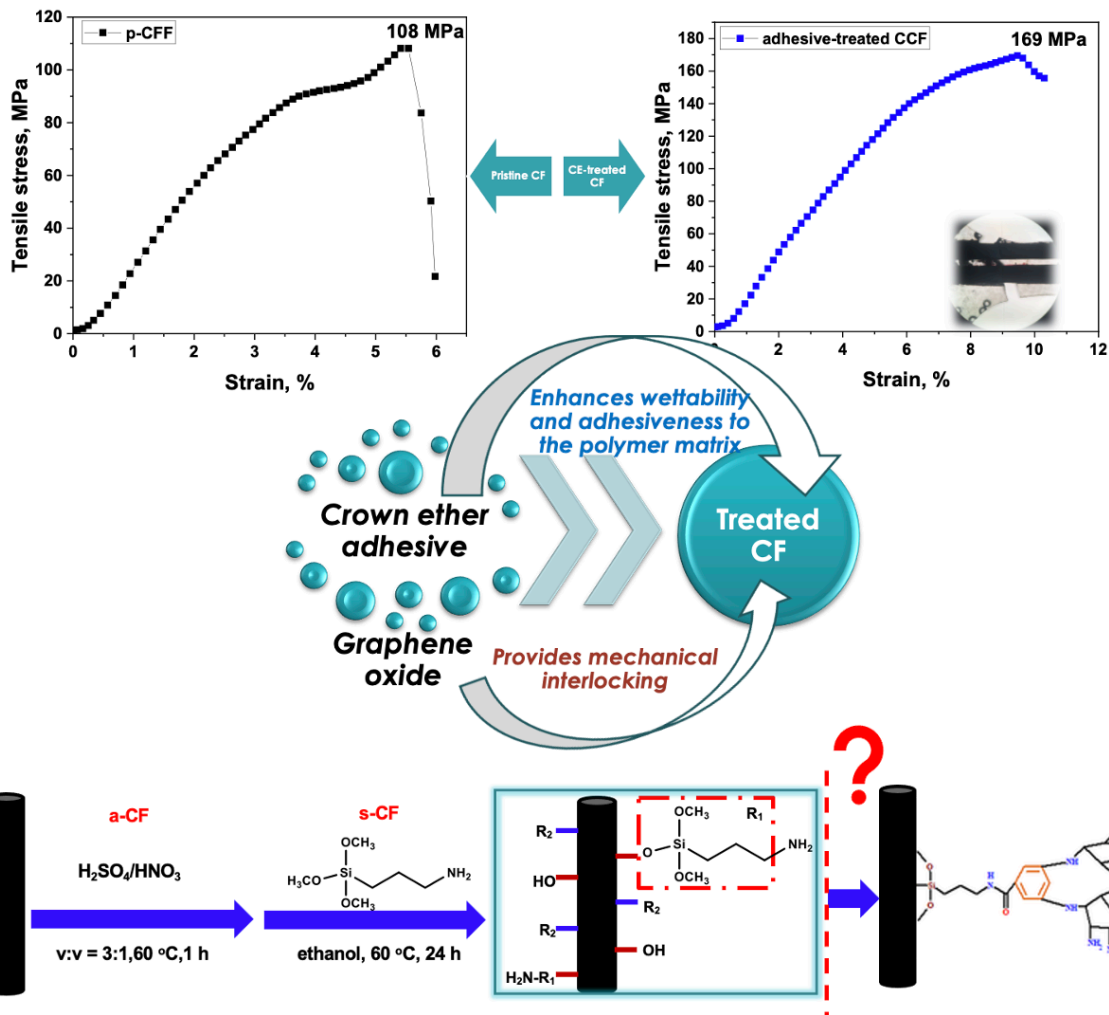


Figure II.3.1.3.2. Mechanical test results showing the tensile properties of an unmodified vs. modified surface of CF with crown ether silanes, which improves adhesion properties and enhances wettability. A schematic representation of the surface modification scheme with the addition of dendrimeric amines is also shown. Source: ORNL.

Task 2. Computational Studies of Interfacial Interaction between Polymer Matrix and CF.

- We have developed and optimized data-driven ML models to precisely predict the interface adhesion properties and identify imperfections along interfaces from FEA and standard experiments using a Python-Abaqus customized program. These specific activities included: (a) a comparison of the stress-strain curves from experimental tests and FEA simulations, (b) measurement of interfacial strength and toughness for 5 wt.% p-CF, a-CF, and s-CF/epoxy composites, and (c) determination of the first-principle stress contours for s-CF/epoxy composite.
- We have developed the FEA simulation protocol. We used Python script – Abaqus for determining the elastic (isotropic and anisotropic), piezoelectric, and dielectric (isotropic and anisotropic) properties with PVDF. We determined the MoS₂ sensor layers with inverse fit from experimental data, as observed in Figure II.3.1.3.3.
- We will further develop the data-driven method based on FEA, ML, and experiments that characterize interfacial properties without pre-determined model forms as a composite 3D-printed object. These properties include Elastic, Piezoelectric, and Dielectric (isotropic and anisotropic). PVDF nanocomposites by 3D-printing for process-property relationships. We will validate experimental and FE simulations using prediction tools for piezoelectric composite design [4].

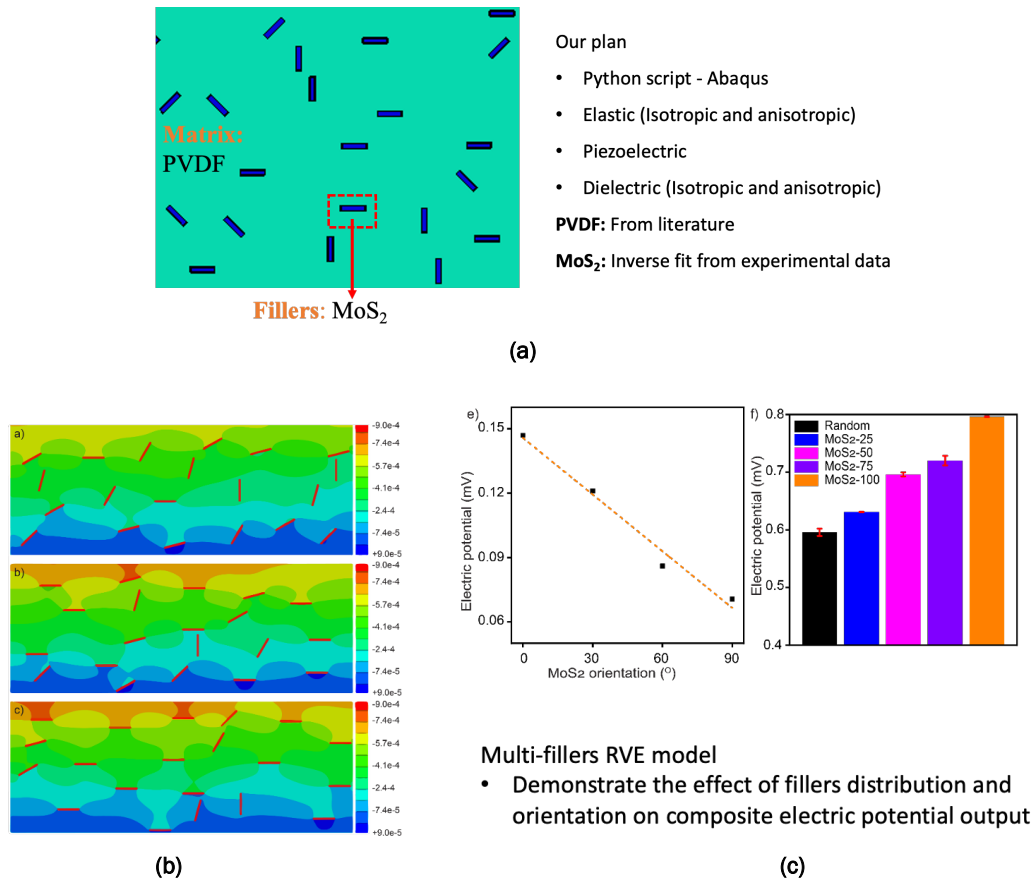


Figure II.3.1.3.3. FEA simulations. (a) Schematic of the data-driven method based on FEA and ML experiments that characterize interfacial properties without pre-determined model forms for PVDF as a matrix and MXenes (MoS₂) as the filler showing elastic, piezoelectric, and dielectric (isotropic and anisotropic) properties. PVDF nanocomposites were fabricated by 3D-printing for process-property relationships. (b) The distribution of stress with similar composition via FEA simulation of a 3D-printed sandwich structure. (c) The electric potential output as a function of increasing MoS₂ orientation (angle). Source: ORNL.

Task 3. 3D-Printing of Continuous CF/Epoxy Composite with Enhanced Fiber-Polymer Adhesion

- As reported above, the 3D-printing of the epoxy-milled CF composite was achieved using a VSP-based method. The wt.% composition was studied from 5–40%. The rheology and mixing of a commercial-based epoxy and chopped CF were used to demonstrate the upscalability of this process.
- Continuous CF 3D-printing was initially achieved but needed further optimization with fast-curing and a new machine design to print larger objects and control the embedment of the CF with fine control of the curing kinetics:
 - Previous design: Continuous CF inside a hermetically sealed chamber with back pressure compensation.
 - New design: A second pressure regulator for the filament chamber with the ability to disassemble easier, as indicated in Figure II.3.1.3.4 and a fully pneumatic system that is more direct for adjusting extrusion velocities. We demonstrated ultraviolet light curing with the addition of an acrylate resin blend. This will be further pursued. We used infrared light curing of the epoxy ink with carbon black to drive thermal crosslinking. The composite was heated to temperatures greater than 300°C with the reaction occurring in ~ 0.1 second. This process is the most feasible in terms of time and feasibility for continuous CF.

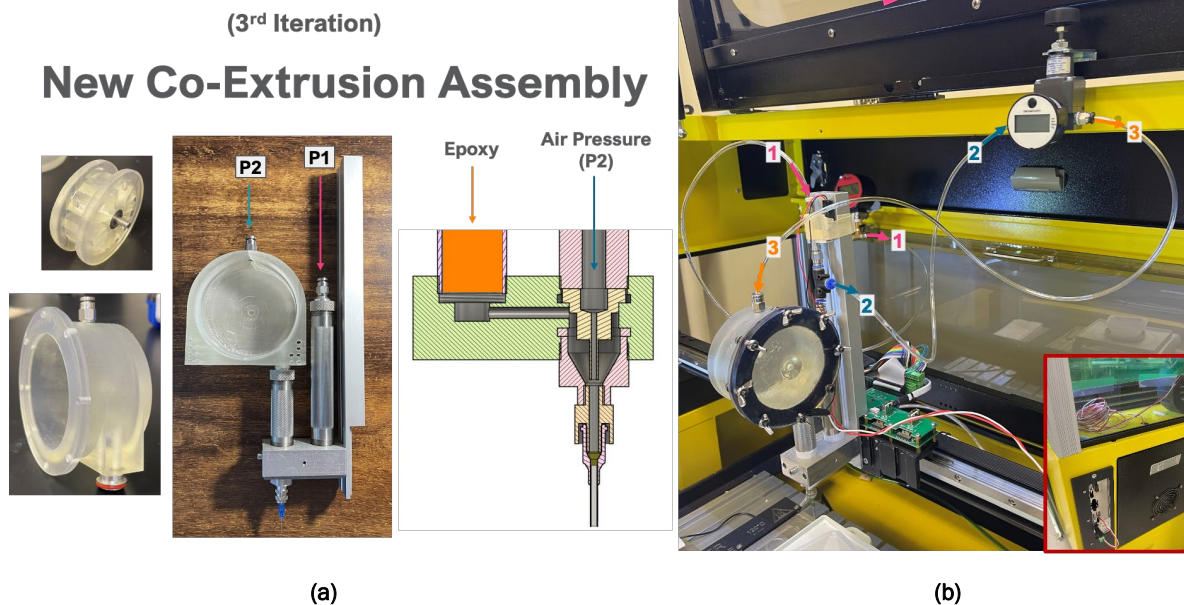
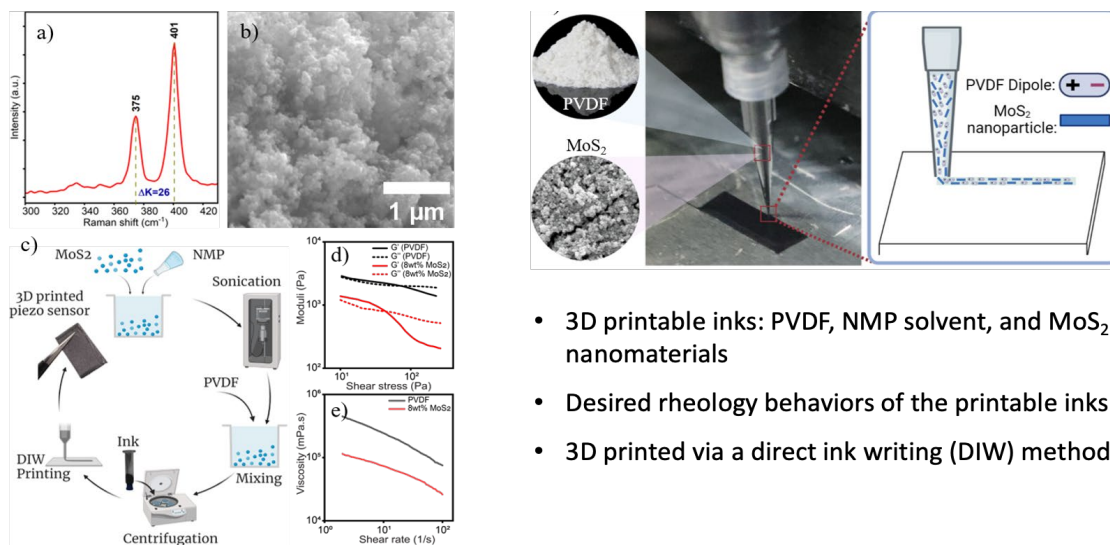


Figure II.3.1.3.4. (a) A new co-extrusion assembly was designed to have both the fiber and the epoxy matrix under the same pressure environment. (a) 3D-printing of epoxy and continuous CF was initially achieved with the modified Hyrel attachment. Source: ORNL.

Task 4. Continuous Sensor-Embedded Polymer/CF Composite 3D-Printing.

- The goal is to design and demonstrate multimaterial 3D-printing to incorporate in-situ embedded sensors with the concept of printing vehicle components that can be monitored with stress over time.
- We developed a protocol and 3D-printing inks for embedded sensors: PVDF-MoS₂ composite: 8% PVDF solution. In a recent paper, we reviewed the important developments in this field [5].
- We have designed and fabricated porous structures of a Zn-anode having a high surface area for increased efficiency with a high-specific capacity of 650mAh/g [2].
- We have introduced 3D-printing/polishing with a PVDF-MoS₂ composite for a more significant piezoelectric effect (i.e., concentration and the shear-stress effect).

- Raman and SEM characterization of 2-11% MoS₂ in PVDF was completed. The output voltage and current decreased when more than 8% MoS₂ was added. The next step is making samples with post-electrical poling and dispersion of MoS₂ with finer MoS₂ particles.
- For the 3D-printed anodes, optimized formulation and composition effects were demonstrated. This was also confirmed with the rheological studies.
- We utilized an electro spray film of PVDF-MoS₂ composite as another control that provides around 10× the enhancement of piezoelectric output for shear-stress of 8% MoS₂ PVDF and around 3× the enhancement for pristine PVDF.
- Other characterization:
 - X-ray studies and infrared mapping: Beta phase presence was observed with the XRD analysis. Beta phase enhancement was observed with Fourier-transform infrared spectroscopy (FTIR) imaging analysis with increasing shear-stress and concentration. Figure II.3.1.3.5 provides the results of the tests.



- 3D printable inks: PVDF, NMP solvent, and MoS₂ nanomaterials
- Desired rheology behaviors of the printable inks
- 3D printed via a direct ink writing (DIW) method

Figure II.3.1.3.5. (a) Raman spectroscopy data together with (b) SEM imaging confirmed the distribution and effect of the MoS₂ on the PVDF matrix and morphology. (c) The protocol for preparation of the 3D-printable ink and (d-e) the rheological (storage and loss modulus) and shear-thinning viscosity properties of the ink comparing the 8% MoS₂ composition with pristine PVDF. The scheme for 3D-printing is shown on the right. Source: ORNL.

Conclusions

- We have demonstrated a comprehensive study of epoxy/chopped CFs and optimized epoxy resins with optimized protocols for grafting surface functional groups in CFs.
- We have established data-driven ML models to predict the interface adhesion properties precisely, identified imperfections from FEA, and developed algorithms for material programming.
- We achieved 3D-printing of epoxy-CF composite using a VSP-based method, including continuous CF 3D-printing. However, large area printing and an embedded sensor demonstration has been delayed.
- We have developed a protocol and 3D-printing inks for embedded sensors and epoxy/CF composite fabrication.
- Future work:
 - Investigate long-term thermomechanical properties of CF/polymer composites in tandem with simulations using FEA and genetic algorithms for optimized 3D-printing methods.

- Investigate other modes of surface modification of CF including use of other sizing and surface modifiers (hyperbranched silanes, graphenes, crown ethers, etc.) with various wt.% CF/epoxy composites in a continuous CF/epoxy 3D-printing system.
- Investigate the possibility of sandwiching 3D-printed sensors (MXenes, etc.) and develop a high-resolution sensor with the epoxy/CF composite as the final goal.

Key Publications

1. Choi, W., R. C. Advincula, H. F. Wu, and Y. Jiang, 2023, “Artificial intelligence and ML in responsive composites’ design and AM,” *MRS Commun.* 13, 714–724. <https://doi.org/10.1557/s43579-023-00473-9>.
2. Ferdousi, S., R. Advincula, A. Sokolov, W. Choi, and Y. Jiang, 2023, “Investigation of 3D-printed lightweight hybrid composites via theoretical modeling and ML,” *Compos. B Eng.*, 265, 110958. <https://doi.org/10.1016/j.compositesb.2023.110958>.
3. Islam, M. N., R. H. Rupom, P. R. Adhikari, Z. Demchuk, I. Popov, A. P. Sokolov, H. F. Wu, R. C. Advincula, N. Dahotre, Y. Jiang, and W. Choi, 2023, “Boosting piezoelectricity by 3D-printing PVDF-MoS₂ composite as a conformal and high-sensitivity piezoelectric sensor,” *Adv. Funct. Mater.*, 2302946. <https://doi.org/10.1002/adfm.202302946>.
4. Jiang, Y., M. N. Islam, R. He, X. Huang, P.-F. Cao, R. C. Advincula, N. Dahotre, P. Dong, H. F. Wu, and W. Choi, 2023, “Recent advances in 3D-printed sensors: materials, design, and manufacturing,” *Adv. Mater. Technol.*, 8, 2200492. <https://doi.org/10.1002/admt.202200492>.

References

1. Sun, J., F. Zhao, Y. Yao, Z. Jin, X. Liu, and Y. Huang, 2017, “High efficient and continuous surface modification of carbon fibers with improved tensile strength and interfacial adhesion,” *Appl. Surf. Sci.*, 412, 424–435. <https://doi.org/10.1016/j.apsusc.2017.03.279>.
2. Stephen, A., S. Bhoyate, P. Cao, R. Advincula, N. Dahotre, Y. Jiang, and W. Choi, 2022, “3D-printed flexible anode for high-performance zinc ion battery,” *MRS Commun.*, 12, 894–901. <https://doi.org/10.1557/s43579-022-00267-5>.
3. Demchuk, Z., J. Zhu, B. Li, X. Zhao, N. M. Islam, V. Bocharova, G. Yang, H. Zhou, Y. Jiang, W. Choi, R. C. Advincula, and P.-F. Cao, 2022, “Unravelling the influence of surface modification on the ultimate performance of carbon fiber/epoxy composites,” *ACS Appl. Mater. Interfaces*, 14(40), 45775–45787. <https://doi.org/10.1021/acsami.2c11281>.
4. Zhang, J., S. Ye, H. Liu, X. Chen, X. Chen, B. Li, W. Tang, Q. Meng, P. Ding, H. Tian, X. Li, Y. Zhang, P. Xu, and J. Shao, 2020, “3D-printed piezoelectric BNTs nanocomposites with tunable interface and microarchitectures for self-powered conformal sensors,” *Nano Energy*, 77, 105300. <https://doi.org/10.1016/j.nanoen.2020.105300>.
5. Jiang, Y., M. N. Islam, R. He, X. Huang, P.-F. Cao, R. C. Advincula, N. Dahotre, P. Dong, H. F. Wu, and W. Choi, 2023, “Recent advances in 3D-printed sensors: materials, design, and manufacturing,” *Adv. Mater. Technol.*, 8, 2200492. <https://doi.org/10.1002/admt.202200492>.

Acknowledgements

The authors gratefully acknowledge the technical support they received from Hyrel on the fabrication of the 3D-printing attachment, as well as the Sokolov Group at the Chemical Sciences Division, ORNL.

II.3.1.4 New Frontier in Polymer Matrix Composites via Tailored Vitrimer Chemistry (Oak Ridge National Laboratory)

Tomonori Saito, Principal Investigator

Oak Ridge National Laboratory
Materials Science and Technology Division
1 Bethel Valley Rd.
Oak Ridge, TN 37830
E-mail: saitot@ornl.gov

Rich Davies, Composites Core Program Manager

Oak Ridge National Laboratory
Materials Science and Technology Division
1 Bethel Valley Rd.
Oak Ridge, TN 37830
E-mail: daviesrw@ornl.gov

H. Felix Wu, DOE Technology Development Manager

U.S. Department of Energy
E-mail: Felix.Wu@ee.doe.gov

Start Date: October 1, 2020
Project Funding: \$500,000

End Date: September 30, 2023
DOE share: \$500,000

Non-DOE share: \$0

Project Introduction

Carbon-fiber-reinforced polymers (CFRPs) are critical structural materials for achieving net-zero carbon goals because of their lighter weight. Likewise, their utilization in transportation can lower fuel consumption and carbon emissions. For example, the incorporation of lightweight materials in passenger vehicles can improve fuel-efficiency by 6–8% by reducing overall vehicle weight by 10%. The demand for lightweight CFRPs is rapidly growing in various industries ranging from transportation to sporting goods, even though the cost of CFs is comparatively higher than that of metals. However, the increasing production and rapid adoption of CFRPs are accompanied by numerous challenges, including weak interfacial adhesion, easy delamination, poor polymer-fiber miscibility, and waste management. The epoxy-based permanently crosslinked thermoset polymers are typically used to make CFRPs due to their high-structural properties, but those conventional thermoset-based CFRPs suffer from a long manufacturing process time, relatively high costs, poor malleability, lack of repairability, recyclability, and frequent fiber-polymer delamination caused by inadequate interfacial adhesion. Consequently, a large amount of CFRP waste is generated after their service life, which typically ends up in landfills. While some advances have been made in recycling CFRPs through mechanical, thermal, and chemical approaches, most of them involve high-energy consumption with difficulty in recovering both fiber and resin, as well as resulting in lower-value material properties. Therefore, developing energy-efficient, ecological-friendly closed-loop recycling of CFRPs with minimum impact on the strength of the fibers while enhancing interfacial compatibility are critically needed for establishing carbon neutrality and circular manufacturing of lightweight materials for automotive and other applications.

Objectives

In response to the challenges inherent in conventional CFRPs, this groundbreaking study ventures into uncharted territory by harnessing cutting-edge “vitrimer” materials. The primary aim of the project is to transform the production of recyclable CFRPs through the introduction of an innovative vitrimer chemistry approach. The overall goal of this project is to develop fast-processable, repairable, recyclable, and affordable CFRP composites while exhibiting superior mechanical properties by incorporating vitrimer chemistry into the fibers and resins. Our vision is to infuse dynamic covalent chemistry into both the fibers and resins to create CFRPs that are exceptionally robust, environmentally responsible, and affordable. Our innovative solution involves designing and synthesizing vitrimer-based resins that leverage fast and robust dynamic exchange

chemistry, which allows for the creation of crosslinked networks that are both reprocessable and closed-loop recyclable. By introducing dynamic covalent bonds in the fiber and the matrix, our methodology enables rapid manufacturing, akin to the efficiency of thermoplastic resins, while upholding the mechanical strength and remarkably improving the fiber-matrix interfacial adhesion. Overall, we have designed a tough and closed-loop recyclable carbon-fiber-reinforced vitrimer (CFRV) with exceptional interfacial adhesion through the synergy of using a boronic ester-modified commodity polymer, a multi-diol crosslinker, and a diol-functionalized CF.

Approach

Nature has utilized dynamic interfaces to provide various tough materials like nacre or superior adhesion seen in marine mussels. They have sophisticated structures with complex hierarchical designs of the hard-soft dynamic interface, allowing outstanding strength and energy dissipation mechanisms. Inspired by these examples, we hypothesize that mastering the interfacial chemistry between the CF and polymer matrix not only enhances the interfacial adhesion, but also improves the toughness of the CFRP. In addition, the incorporation of dynamic functional groups on the CF surface significantly improves the CF recyclability and dispersion with the polymer matrix, while preserving or even enhancing their mechanical properties. Herein, we report a nature-inspired molecular design of high-performance CFRVs with a tailored interface, which addresses the aforementioned challenges. We have utilized a boronic ester functionalized triblock commodity thermoplastic elastomer, polystyrene-*b*-poly(ethylene-co-butylene)-*b*-polystyrene or styrene-ethylene-gutylene-styrene (SEBS), and a dynamic multi-diol crosslinker to prepare vitrimer resin [1]. To master the interfacial interaction between CFs and the polymer matrices, we have functionalized the CF surface using dynamic diol functional groups, which can form dynamic covalent bonds with the boronic ester group on the polymer matrices. The prepared CFRV composites demonstrate significantly improved interfacial adhesion and toughness, as evidenced by enhanced tensile properties, interlaminar shear-strength, and Raman mapping. Moreover, the reversible crosslinked nature of the boronic ester exchange reaction not only allows thermal reprocessing, but also offers the opportunity for facile closed-loop recycling of both CFs and polymer matrices. These findings provide insights into mastering the interface of CF using a dynamic functional group to enhance the fiber-matrix interfacial adhesion for the design of exceptionally tough and closed-loop recyclable CFRPs for many lightweight material applications, including the automotive, aerospace, wind-turbine blade, and construction industries.

Results

To design a tough vitrimer that can dynamically bind to CFs, we chose a microphase-separated SEBS triblock commodity polymer, where the soft block participates to dissipate energy and the hard styrene block is modified to interact with sized CF and a dynamic crosslinker for achieving high-strength and toughness. The borylated SEBS triblock copolymer (S-Bpin) was synthesized from 30 mole percent (mol%) styrene containing commodity thermoplastic elastomer SEBS (MW 118,000 g/mol) via an aromatic C-H borylation reaction following our recently reported method [2]. Dynamic boronic ester containing vitrimer resin was subsequently synthesized from S-Bpin reacting with a dynamic multi-diol crosslinker, as observed in Figure II.3.1.4.1(a). The dihydroxyl group on the multi-diol crosslinkers could react with the boronic ester groups on S-Bpin to produce dynamic boronic ester-based vitrimers. The team envisioned that the varied architecture of the crosslinker can tune the mechanical properties of the vitrimers [1]. Three different multi-diol crosslinkers, including diglycerol, bisphenol A diol, and tris-diol (3,3',3''-((methanetriyltris(benzene-4,1-diyl))tris(oxy))tris(propane-1,2-diol)), were chosen to prepare the dynamic crosslinked vitrimer and the resultant vitrimers are denoted as diglycerol_S-Bpin, bisphenol-diol_S-Bpin, and tris-diol_S-Bpin, respectively, also shown in Figure II.3.1.4.1(a). The multi-diol with two and three arms was selected to investigate the consequence of the diol spacer length, flexibility, network density, and mechanical properties of the vitrimer. The tetrahydrofuran (THF) solution of S-Bpin and 5 mol% (5 mol% of boronic ester group in S-Bpin) of multi-diol crosslinker were mixed at RT and dried under reduced pressure at 120°C to obtain partially crosslinked networks. Then, they were hot-pressed at 200°C for 30 min under ~1 ton pressure to result in fully cured resin films. Temperature, time and pressure can be lowered by adjusting the degree of functionalization of boronic ester and amount of crosslinker which makes them scalable.

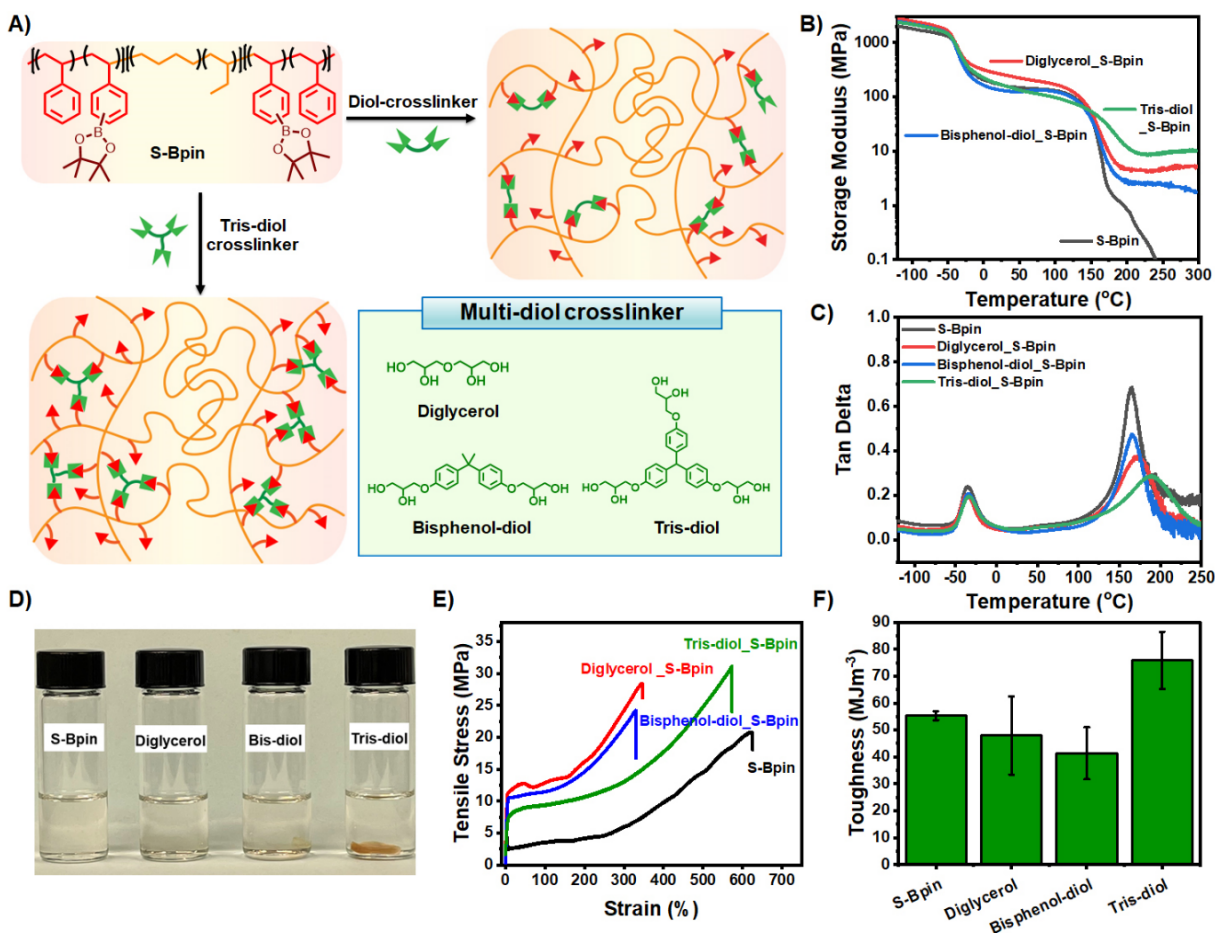


Figure II.3.1.4.1. The design of dynamic boronic ester crosslinked vitrimers and their tailored mechanical and thermomechanical performance. (a) Schematic illustration of the synthesis of multi-diol-crosslinked vitrimer from modified SEBS (S-Bpin), and chemical structures of multi-diol crosslinkers. The dynamic mechanical properties of neat S-Bpin, crosslinked diglycerol, bisphenol-diol, and tris-diol resins are demonstrated by (b) storage modulus as a function of temperature, and (c) tan delta versus temperature for S-Bpin and multi-diol_S-Bpin resins. (d) The solvent resistance test of dynamic boronic ester crosslinked resins in THF at RT for 24 hrs., demonstrating their crosslinking nature. (e) Representative tensile stress-strain curves from uniaxial elongation until failure and (f) toughness. The error bars indicate standard deviations from at least triplicate measurements. Source: ORNL.

The presence of the constant second rubbery plateau at high-temperatures above 160°C in dynamic mechanical analysis curves, as indicated in Figure II.3.1.4.1(b), further confirms the formation of dynamic covalent crosslinking between the multi-diol crosslinker and S-Bpin polymer. The increased storage modulus at the second rubbery plateau region of tris-diol_S-Bpin clearly indicates a higher network stiffness and crosslinked density than the two-arm diol-crosslinked resin, in part due to higher functionality of the former (e.g., three functional group in tris-diol instead of two). The $\tan \delta$ curve from the dynamic mechanical analysis, as shown in Figure II.3.1.4.1(c) indicates a significant shift in the glass transition temperature (T_g) of the borolated polystyrene block from ~165°C of S-Bpin to ~190°C of tris-diol_S-Bpin, while the T_g of ethylene butylene containing midblock remains constant at -40°C). The T_g is closely dependent on both network stiffness and crosslinking density, thus, tris-diol_S-Bpin exhibited the highest T_g at 190°C as compared to the diglycerol_S-Bpin at 175°C and bisphenol-diol_S-Bpin at 167°C. The crosslinking nature of multi-diol_S-Bpin was further demonstrated via a solvent resistance study, where a universal solvent was chosen for this system, THF, as it was used to make all S-Bpin-based resins. The multi-diol_S-Bpin films were submerged in THF for 24 hours at RT and the solubility was monitored. As illustrated in Figure II.3.1.4.1(d), S-Bpin, diglycerol_S-Bpin, and bisphenol_S-Bpin films were dissolved in THF, while tris-diol_S-Bpin remained intact even after 24 hrs. soaking under THF. Thus, the excellent THF solvent resistance of tris-diol_S-Bpin, compared to the other two-arm diol crosslinkers, also confirms its higher crosslinking density and resulting enhanced property.

The mechanical properties of multi-diol_S-Bpin resins exhibited significant improvement in stiffness, yield point, and UTS, as well as toughness compared to uncrosslinked S-Bpin, as observed in the uniaxial tensile stress-strain curves, as shown in Figure II.3.1.4.1(e), at RT. In contrast to the uncrosslinked S-Bpin polymer, the crosslinked tris-diol_S-Bpin resulted in a 48% and 40% increase in UTS and toughness, respectively. The tensile properties of the tris-diol_S-Bpin exhibited the highest UTS at 31 MPa as compared to the other diol-crosslinked resins. The toughness of tris-diol_S-Bpin (e.g., 76 MJ·m⁻³) is 58% higher than that of the diglycerol_S-Bpin (e.g., 48 MJ·m⁻³) and 85% higher than that of bisphenol-diol_S-Bpin, as observed in Figure II.3.1.4.1(f). The tris-diol crosslinker consists of three aromatic diol arms that offer extra mechanical reinforcement to the polymeric network. In comparison to the other two crosslinkers, the tris-diol crosslinker's additional diol group likely allows the formation of more dynamic covalent bonds with boronic ester groups, ultimately leading to an increase in crosslink density and network density, as observed in the determined crosslinked density.

We functionalized CFs with the diol group and the diol-CF can interact with vitrimer resin not only via covalent bonding, but also via physical (H-bonding) bonding to increase the fiber-matrix interfacial adhesion. Tough multiphase composite was developed by combining the tris-diol_S-Bpin vitrimer with diol-CFs. The diol group in the CFs is covalently bonded with the vitrimer resin through dynamic boronic ester bonding, as shown in Figure II.3.1.4.2(a). The CFRVs are fabricated by *in-situ* reaction of impregnating three layers of woven diol-CF mats in THF solution of S-Bpin and tris-diol and dried of solvent under a high vacuum at 120 °C overnight. The dry composite samples are cured and hot-pressed at 200 °C for 30 minutes under 1-ton pressure. The mechanical properties of diol-CF-reinforced tris-diol_S-Bpin vitrimer (diol-CFRV) composites were investigated at a vitrimer resin content of approximately ~30 wt% and compared with the composites made from conventional epoxy (Control-1) and pristine-CF reinforced tris-diol_S-Bpin vitrimer (Control-2) composites. As shown in Figure II.3.1.4.2(b), the unidirectional tensile strengths of each CF composite were measured at a crosshead speed of 1 mm·min⁻¹. Importantly, the UTS and modulus of diol-CFRV composites reached 731±89.15 MPa and 22.37±1.39 GPa respectively, which are 49%, and 55% higher than that of the conventional epoxy-based CFRP (Control-1). We attribute this to the increased interfacial adhesion between the vitrimer resin and the fiber, while epoxy groups have minimal to no covalently bound functional groups with the fiber surface, as observed in Figure II.3.1.4.2(c). The unmodified CFRV (Control-2) showed 26% lower tensile strength as compared to the diol-CFRV, suggesting that fiber functionalization with diols plays a vital role in increasing mechanical properties. Moreover, the application of diol-functionalization on CFs leads to a remarkable enhancement in the toughness of diol-CFRVs.

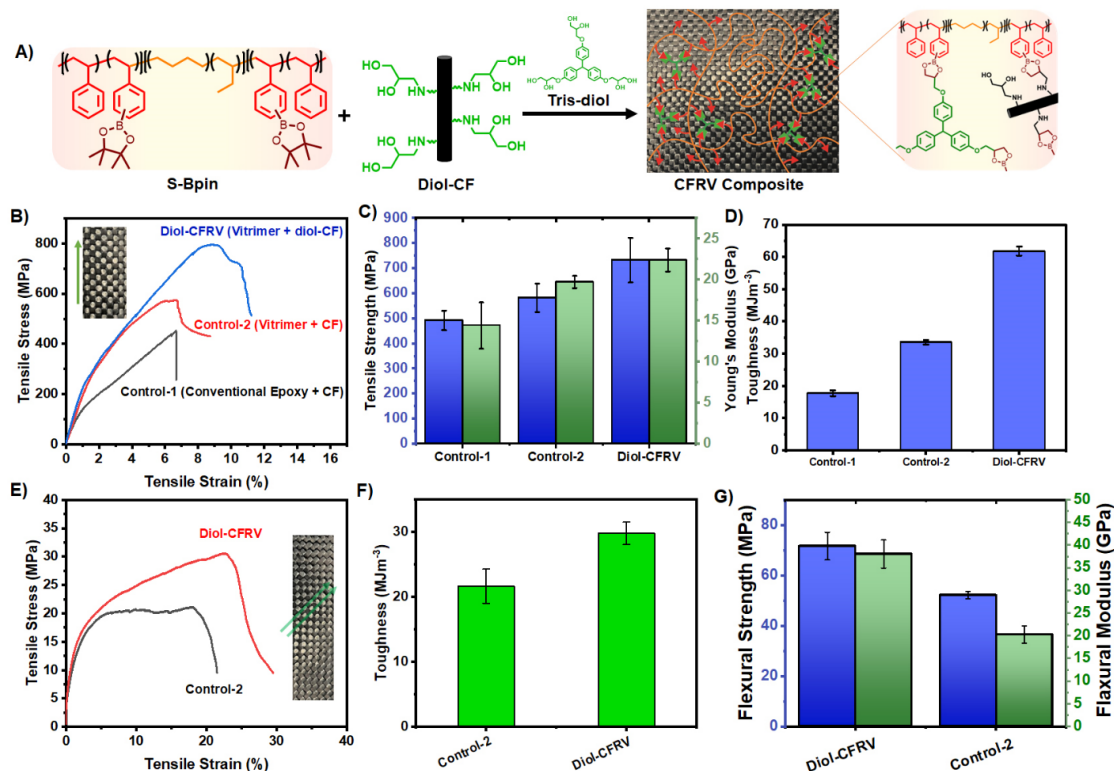


Figure II.3.1.4.2. Synthesis and mechanical properties of CFRPs. (a) Synthetic pathways of diol-CFRV composite, where the diol-functionalized CF was used not only as a reinforcing agent, but also as a dynamic crosslinker. (b) Tensile stress-strain curves of conventional CFRP and CFRV composites. (c) Comparison of tensile and Young's modulus among controls and diol-CFRV composites. (d) Toughness. (e) Tensile stress-strain curves of 45°-oriented CF composites to demonstrate the fiber-matrix interactions. (f) Comparison of interfacial toughness calculated from the area underneath the curve of the tensile stress-strain plots (e). (g) Comparison of tensile and Young's modulus for Control-2 and diol-CFRV composites. The error bars indicate standard deviations from at least triplicate measurements. Source: ORNL.

Specifically, when compared to Control-2, the toughness of the diol-functionalized CFRVs increases by 84%, and the increase in toughness reaches a staggering 248% when compared to control-1, as indicated in Figure II.3.1.4.2(d). The diol-CFRVs also exhibited a significant improvement at 45° in interlaminar shear-strength compared to the pristine CFRV, indicating that the incorporation of diol to CFs and their interaction with the vitrimer matrix has a significant impact on the interlaminar shear-strength of the composite material. To assess the interfacial adhesion between the fiber and matrix, the uniaxial tensile strength of 45°-fiber-oriented CFRVs was tested, and the resulting tensile stress and strain data, as shown in Figure II.3.1.4.2(e), clearly indicate a significant (~43%) increase in interfacial strength for the diol-CFRV as compared to the Control-2 composite, thus validating the effectiveness of the functionalization process. The strong interfacial adhesion between fiber and matrix is also confirmed by the 38% higher toughness (the area underneath the tensile stress-strain curve) of diol-CFRV compared to Control-2, as indicated in Figure II.3.1.4.2(f). Moreover, the diol-CFRV composite exhibited notable enhancements in both flexural strength and modulus, with a remarkable increase of 37.4% and 87.5%, respectively, in comparison to Control-2, as can be seen in Figure II.3.1.4.2(g). These superior properties, along with the heightened tensile strength and interlaminar shear-strength, emphasize the exceptional robustness and strength of the diol-CFRV composite.

One of the advantages of vitrimer-based CFRV composites over thermosets is the thermoforming ability. As demonstrated in Figure II.3.1.4.3(a), the rectangular composite sample was thermally deformed into a “V” shape at 200°C. The structural integrity of the “V” shape was maintained at RT until it was reformed into its initial rectangular shape. Dynamic boronic ester interaction in CFRV composites also offers self-

joining/adhesive capability, as shown in Figure II.3.1.4.3(b). The two composite samples were then hot-pressed at 200°C for 10 minutes and subjected to lap-shear testing to analyze the extent to which they can be performed as self-adherents. The maximum lap-shear strength was 2 MPa, which is comparable with the literature data and making them a good candidate for applications requiring self-bonding. Such self-joining ability of CFRV provides an attractive option for many industries including automotive, where the replacement of mechanical fasteners and metals with lightweight materials can eliminate the use of adhesives and fasteners. As mentioned above, the tris-diol_S-Bpin vitrimer resin is chemically recyclable, while the polymer and crosslinker can be recovered separately.

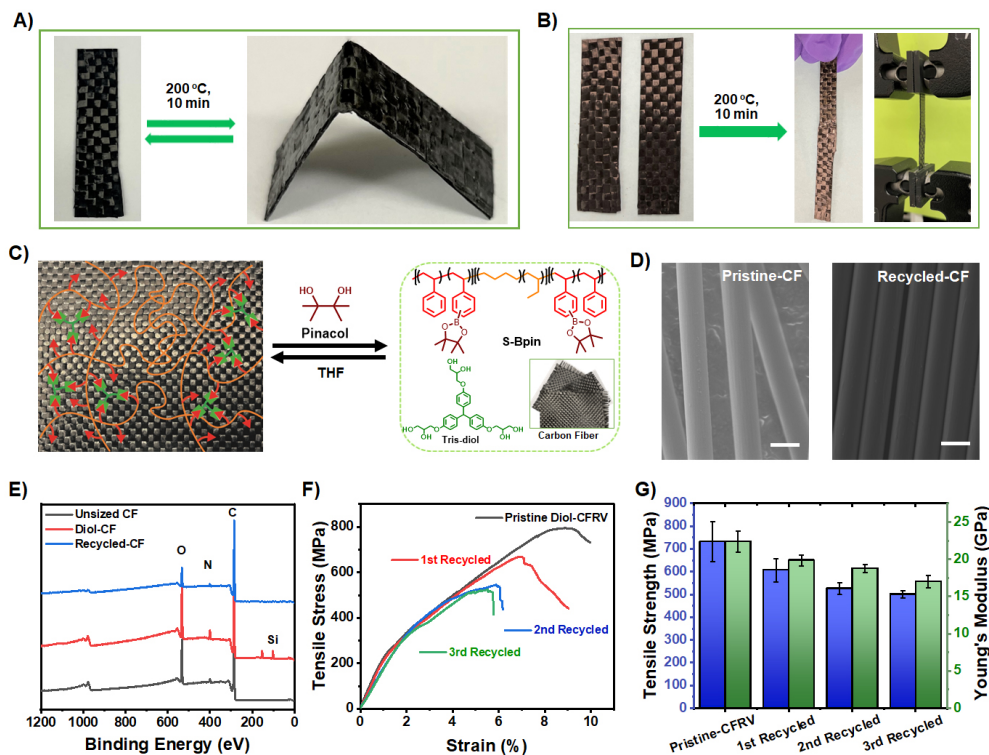


Figure II.3.1.4.3. The thermofforming capability of cured CFRV. (A) Rectangular CFRV composite heated to 200 °C deformed into a “V” shape, which was retained at RT; heating the “V”-shaped composite to 200 °C restored its rectangular shape. (B) Photographs of CFRV composites before and after the self-adhering tests. (C) Chemical recycling of CF from the CFRV composite in the presence of pinacol and THF at 65 °C. (D) SEM images of the pristine and recycled CF of the tris-diol-CFRV. (E) The full scan of x-ray photoelectron spectroscopy spectra of unsized, diol-CF, and recycled CF composite. (F) Uniaxial tensile properties of diol-CFRV and chemically recycled CF. (G) Comparison of UTS and Young’s modulus of pristine CFRV and recycled CFRV composites. The error bars indicate SDs from at least triplicate measurements. Source: ORNL.

Similar to the chemical recycling of tris-diol_S-Bpin, the CFRV composites can be chemically recycled in the presence of pinacol and THF, as shown in Figure II.3.1.4.3(c). The composites were soaked in pinacol-THF solution at 65°C overnight, where the vitrimer resin participates in exchange reactions with diol groups of pinacol, subsequently dissolving the polymer network. Therefore, introducing dynamic hydroxyl groups onto the fiber surface completely recovered the resin-free fiber. In addition, the SEM images clearly illustrate no visible mechanical damage in either of the two CFs, as indicated in Figure II.3.1.4.3(d). In the x-ray photoelectron spectroscopy data, as observed in Figure II.3.1.4.3(e), it is evident the silicon peak intensity has diminished in the recycled CF. The hydroxyl groups present in pinacol have the capacity to react with the silicon-oxygen bonds, displacing the silane-containing diol groups and effectively restoring the pristine state-of-the-CF. To demonstrate CF reusability, the CFs obtained after the chemical recycling were re-functionalized with diol and refabricated as CFRVs. After each cycle, the uniaxial tensile strength was remeasured, as can be seen in Figure II.3.1.4.3(f). The tensile strength and modulus were roughly maintained over at least three

cycles, as shown in Figure II.3.1.4.3(g). Although visible mechanical damage in the individual fibers was not observed, the fiber alignments of the woven mats could be changed during experimental handling. Thus, the slight decline in the tensile values may be attributed to the fiber misalignment of the woven CFRP composites. These findings are encouraging as they suggest the deconstruction, separation, recycling, and (re)processing of the CF from the CFRVs did not cause any serious damage to the mechanical properties. Therefore, the closed-loop recycling of the CF from the composites was successfully achieved, without compromising its strength and modulus. Such closed-loop recycling of CF from composites has the potential to significantly reduce the environmental impact of the composites industry, by diverting waste from landfills and reducing the need for virgin materials.

Conclusions

In conclusion, our study marks a significant breakthrough in the development of a mechanically resilient and entirely recyclable CFRV through a biomimetic hierarchical design approach. By drawing inspiration from the intricate dynamics of tough natural materials, we have engineered a vitrimer resin based on a common thermoplastic reinforced with diol-functionalized CF. This CFRV exhibits exceptional mechanical properties, including remarkable strength, toughness, wide temperature stability, and excellent resistance to solvents. The introduction of dynamic diol functional groups to the CFs has notably improved the compatibility and wetting between the fibers and the matrix, resulting in vastly enhanced interfacial adhesion. This unique fiber-matrix interaction in diol-CFRV is achieved through dynamic boronic ester covalent bonds and crosslinking with a multi-diol crosslinker, as well as diol-functionalized CF. As a result, it delivers superior interfacial adhesion and tensile strength when compared to unmodified CFRV and conventional epoxy-based CFRP. The utilization of dynamic boronic ester exchange not only facilitates the reparability, swift thermoformability, and self-adhesion of the CFRV, but also allows for the recovery and reuse of the modified fiber without a significant loss in mechanical properties, ensuring a complete closed-loop circularity for CFRV. This groundbreaking approach offers an innovative and sustainable solution for recycling both the fiber and the matrix in the CFRPs while addressing the longstanding issue of poor interfacial adhesion between the fiber and the polymer matrices. Our biomimetic CFRV design, distinguished by its exceptional mechanical attributes and recyclability, has the potential to bring about a paradigm shift in the realm of advanced composites, offering transformative possibilities for a wide array of applications.

Key Publications

1. Rahman, M. A., M. S. Karunarathna, C. C. Bowland, G. Yang, C. Gainaru, B. Li, S. Kim, V. Chawla, N. Ghezawi, H. M. Meyer III, A. K. Naskar, D. Penumadu, A. P. Sokolov, and T. Saito, 2023, “Tough and recyclable carbon-fiber composites with exceptional interfacial adhesion via tailored vitrimer-fiber interface,” *Cell Rep. Phys. Sci.*, 4(12), 101695. <https://doi.org/10.1016/j.xcrp.2023.101695>.
2. Rahman, M. A., M. Koralalage, and T. Saito, 2023, “Tough and recyclable carbon-fiber composites with ultrastrong interfacial adhesion enabled by tailored vitrimer and carbon fiber,” U.S. provisional Patent Application Serial No. 63/467,026, filed on May 17, 2023.

References

1. Rahman, M. A., M. S. Karunarathna, C. C. Bowland, G. Yang, C. Gainaru, B. Li, S. Kim, V. Chawla, N. Ghezawi, H. M. Meyer III, A. K. Naskar, D. Penumadu, A. P. Sokolov, and T. Saito, 2023, “Tough and recyclable carbon-fiber composites with exceptional interfacial adhesion via tailored vitrimer-fiber interface,” *Cell Rep. Phys. Sci.*, 4(12), 101695. <https://doi.org/10.1016/j.xcrp.2023.101695>.
2. Rahman, M. A., C. Bowland, S. Ge, S. R. Acharya, S. Kim, V. R. Cooper, X. C. Chen, S. Irle, A. P. Sokolov, A. Savara, and T. Saito, 2021, “Design of tough adhesive from commodity thermoplastics through dynamic crosslinking,” *Sci. Adv.*, 7(42), eabk2451. <https://doi.org/10.1126/sciadv.abk2451>.

Acknowledgements

This research was sponsored by the DOE-EERE VTO. The authors thank the team members of this project: Drs. A. Rahman, M. S. Karunarathna, C. Bowland, and A. Naskar; Mr. B. Li; and Ms. N. Ghezawi.

II.3.1.5 Adopting Heavy-Tow Carbon Fiber for Repairable, Stamp-Formed Composites (Oak Ridge National Laboratory)

Amit Naskar, Principal Investigator

Oak Ridge National Laboratory
Materials Science and Technology Division
1 Bethel Valley Rd.
Oak Ridge, TN 37830
E-mail: naskarak@ornl.gov

Rich Davies, Composites Core Program Manager

Oak Ridge National Laboratory
Materials Science and Technology Division
1 Bethel Valley Rd.
Oak Ridge, TN 37830
E-mail: daviesrw@ornl.gov

H. Felix Wu, DOE Technology Development Manager

U.S. Department of Energy
E-mail: Felix.Wu@ee.doe.gov

Start Date: October 1, 2020
Project Funding: \$500,000

End Date: June 30, 2024
DOE share: \$500,000

Non-DOE share: \$0

Project Introduction

This project focuses on interface engineering and high-throughput manufacturing methods for heavy-tow CF having > 100,000 filaments in a single bundle and tailoring its bonding and interactions with thermoplastic matrices to develop new stamp-formed layered structures. This involves the integration of fundamental understanding, the application of structure characterization tools, and high-performance computation to achieve the rational molecular level design and control of the mechanical properties in thermoplastic composites. State-of-the-art automotive parts produced from thermoplastic composites at a high-production rate (> 250,000 parts/year) cost more than \$50/kg. This project will develop technology that enables a 30–50% cost-reduction in composite parts, such as roofs, hood inner-liners, and inner door panels (\$20–\$30/kg in parts). Research will eliminate several processing steps, multiple shipments, and storage requirements for composite intermediates. In addition, it will deliver repairable low-cost thermoplastic composites with a multilayered stamp-formed structure containing 40–60 vol.% fiber and outstanding mechanical performance (e.g., 0.8–1.4 GPa tensile strength, 50–100 GPa Young's modulus, ~10% failure strain). Researchers will use thermoplastics, including low-cost commodity-grade polypropylene (PP) plastic, to develop automotive composite structures with broad end-use potentials. ORNL has successfully produced low-cost, heavy-tow CFs from textiles; however, the brittle nature of the carbonized fibers precludes complex handling. In addition, uniform application of sizing on such a large number of filaments remains a challenge. Current surface treatment methods are developed for epoxy matrices and are not applicable for thermoplastics with less polarity than epoxies.

To address these challenges, this project envisions a sizing-free, direct-calendaring process for the matrix immobilization on the fiber surface. With minimal unit operations, direct manufacturing of heavy-tow CFs into reinforced intermediates enables subsequent stamp-forming to a structure. Unlike thermosets, thermoplastic-matrix-infused intermediates are easy to store, enabling repair or remolding of the parts and restoration of the embodied energy in the structures after end-of-life.

Objectives

The objective of this research is to develop and commercialize new interfacial engineering methods for the efficient reinforcement of thermoplastic matrices by heavy-tow CFs and demonstrate composition chemistry

and processing that allow the formation of multilayer laminate structures rivaling the rapid stamping rate of metals. The project will deliver repairable low-cost thermoplastic composites with a multilayered stamp-formed structure containing 30–60 vol.% fiber and outstanding mechanical performance (e.g., 0.8–1.4 GPa unidirectional UTS, 50–100 GPa Young’s modulus). High-throughput processing technologies for thermally recyclable or repairable CF composites of thermoplastic matrices will enable a new paradigm toward cost-competitive lightweight materials for automotive fuel-efficiency without compromising their mechanical performance and crashworthiness.

Approach

The overarching goal of this research is to connect the key physicochemical relationships at different length scales—including surface adsorption or bonding, polymer interfacial dynamics, and fiber-fiber interactions—to the key process engineering considerations, along with macroscopic rheological and mechanical properties of thermoplastic polymer matrix composites. To this end, we combine polymer and interfacial chemistry, x-ray scattering, rheology, intermediate thermomechanical characterization, and formed samples and spectroscopy (on the experimental side) with molecular dynamics simulations (on the high-performance computation side). Specifically, the project team is: (1) developing new interfacial interactions to optimize the polymer-fiber interaction, (2) revealing the interplay of the interfacial interactions on the processability and composites’ response to load by using mechanical testing and thermal analysis, and (3) elucidating the relationship between CF volume fraction, matrix morphology, and the performance of the stamp-formed multilayered structures.

Results

The following summary includes the work performed in FY 2023 for the completion of project milestones listed in Table II.3.1.5.1 at ORNL.

Table II.3.1.5.1. FY 2023 Milestone Summary

Milestone Name/Description	Criteria	End Date
Exhibit polymer matrix CFRPs with 0.75 GPa composites tensile strength.	Mechanical testing of intermediates delivers the expected properties.	12/31/2022
Demonstrate polymer matrix intermediates containing 35 vol.% fiber exhibiting 10% elongation.	Mechanical testing of intermediates delivers the expected properties.	03/31/2023
Develop fiber pullout test method to estimate fiber-matrix bond strength and establish baseline data for CF/PP and CF/epoxy and compare with new data after new interfacial bonding.	Micromechanical testing delivers the data.	06/30/2023
Demonstrate remolding/re-stamping of structures and deliver the final report.	Sample-making process is demonstrated.	09/30/2023

Work completed in FY 2022 demonstrated that composites based on unidirectional fiber-reinforced thermoplastic PP laminates reaching > 0.5 GPa UTS encouraged the team to enhance the performance of PP composites and properties for other thermoplastic matrix-based reinforced composites. Therefore, the work has been expanded to include other polymer-coating methods in FY 2023. A plasticized ABS matrix was prepared to impregnate unidirectional woven mats comprised of 24,000 CF tows. The mats were then quickly dried to produce tow-preg, preform, or tape equivalent samples. The ABS-CF composite preforms were thermoformed under 5,000 psi pressure in a conformal mold. Composite parts were sectioned and tabbed to eliminate damage in the grips, as shown in Figure II.3.1.5.1. The tensile specimens were tested on an electromechanical 100 kN frame (Instron 5982, Norwood, MA) at a deformation rate of 1 mm/min. Each of the tested composites failed within the gauge section, which is consistent with the composite failure mode. The average peak stress value for the testing set was 1096 ± 134.5 MPa, as seen in Figure II.3.1.5.2, thus exceeding the targeted milestone of 750 MPa. Composites technology development continued through FY 2023 to deliver a robust framework for processing thermoplastic composites from both amorphous and semicrystalline polymer morphologies.

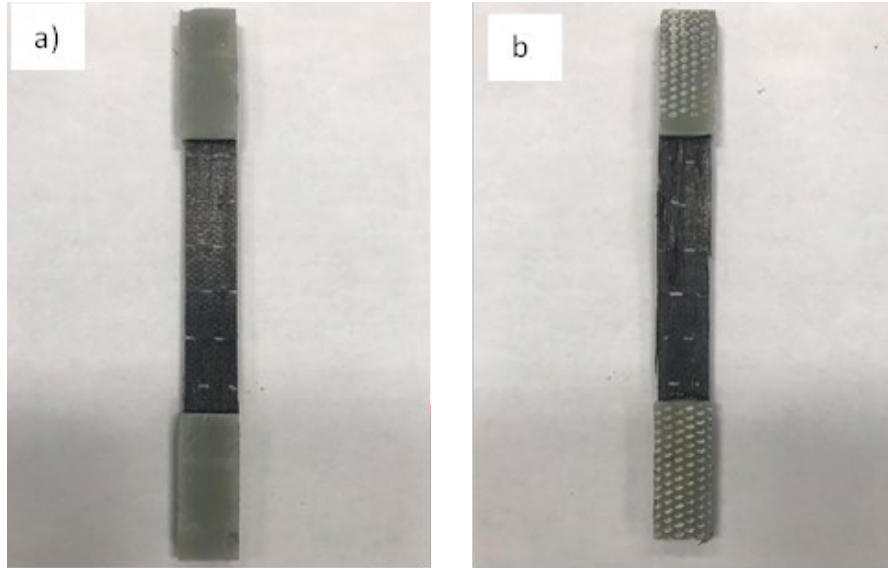


Figure II.3.1.5.1. Fabricated composite tensile specimen (a) before and (b) after tensile testing. Source: ORNL.

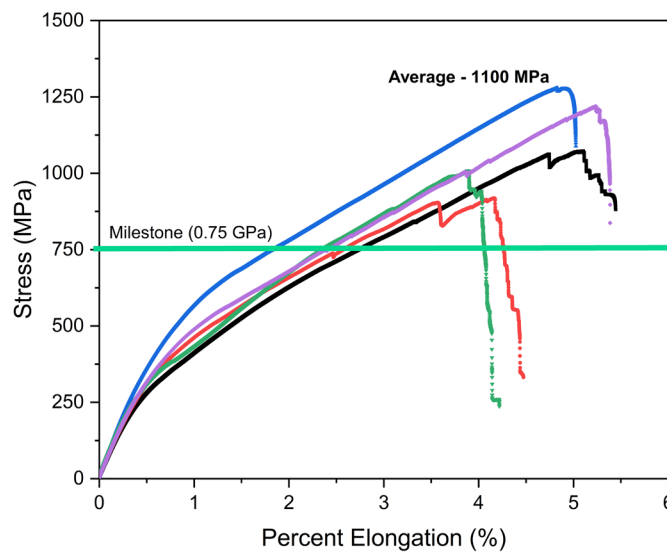


Figure II.3.1.5.2. Stress vs. elongation plot summarizing the tensile performance of the five composite specimens. Source: ORNL.

Interfaces play an important role in determining the bulk properties and performance during the service life of filled polymers. The utilization of unidirectional specimens in fabrication can also serve to investigate the interfacial interactions present in composite materials. Researchers reproduced the laminate composite preform fabrication at a volume fraction of 40% by employing sequential stacks of unidirectional CF tape comprised of five layers and PP sheets comprised of seven bilayers. The preform was pressed at 185°C and 5000 psi of pressure. To prevent shrinkage of the polymer matrix, the composite was allowed to cool under pressure. Tensile specimens underwent testing using a tensile tester. The control PP composite group, without fiber-matrix bonding, had 6-8% ultimate elongation. The ultimate strain increased from 6-8% to ~24% after surface immobilization. The interaction between the fiber and the polymer has been observed to significantly increase the ductility of the composite material. Subsequently, researchers translated the same concept with discontinuous CFs dispersed in an ABS matrix where appropriate immobilization of the matrix on the fiber enhanced composite ultimate elongation occurred, as observed in Figure II.3.1.5.3.

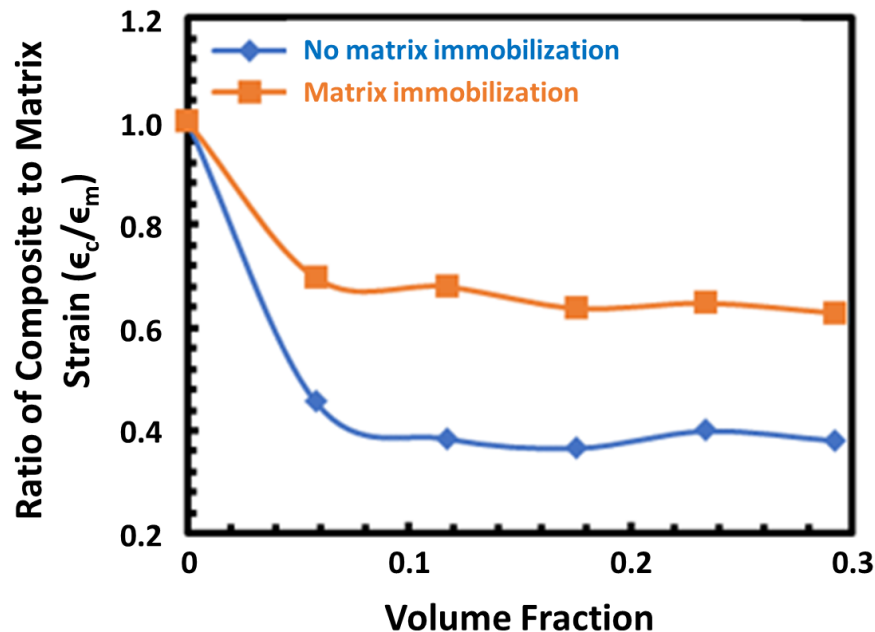
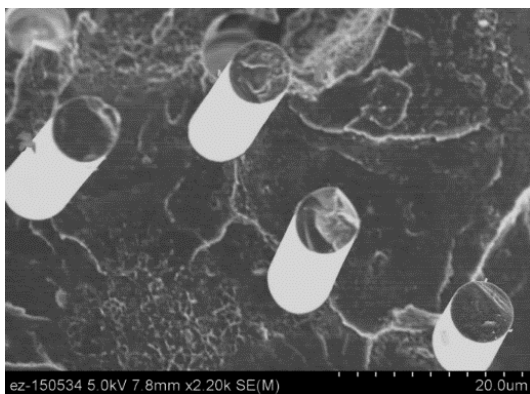
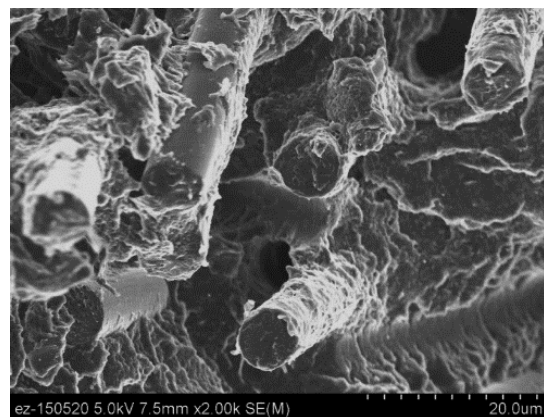


Figure II.3.1.5.3. About 30–40% improved ultimate elongation of the composites was demonstrated when the polymer matrix was immobilized on the fibers. Y-axis data shows the ratio of ultimate elongations in the composites to the neat matrix at different discontinuous CF volume fractions. Source: ORNL.

Images of the composite surfaces were also captured using SEM. A layer of gold particles with a thickness of 10 nm was applied to the samples to enable SEM imaging to analyze the surface of the CF/PP composites. As shown in Figure II.3.1.5.4(b), the CF is well-adhered with the polymer matrix than the CF shown in Figure II.3.1.5.4(a). Matrix adhesion on the CF surfaces improves matrix wetting, facilitating better interfacial interaction within the composite. Composites technology research will continue through FY 2024 to provide a robust framework for manufacturing thermoplastic composites from both amorphous and semicrystalline polymers.



(a)



(b)

Figure II.3.1.5.4. SEMs of fracture surfaces of CF-reinforced thermoplastic composites show (a) a lack of fiber-matrix adhesion and (b) an appropriate fiber-matrix adhesion that minimizes early fiber pullout, leading to increased strength and ultimate elongation. Source: ORNL.

Direct interrogation of the interfacial properties of composite materials is a challenging task. Previously, researchers utilized calorimetry to simulate process relevant conditions and studied the resulting impacts on the morphology of CF laden isotactic polypropylene (iPP) composites. From these studies, researchers ascertained the key relationships between the temperature profile-induced crystallization dynamics and began to make connections to the bulk properties of the composites, which now routinely meet or exceed their epoxy counterparts. Mechanical tensile testing is an essential tool but is dependent on many intertwined co-factors. Researchers have been seeking techniques that can more directly determine the interfacial properties between CFs and our model polyolefin matrix material. Utilizing modifications to ORNL's existing filament testing equipment, researchers have devised a protocol that introduces a single CF filament to a melt pool of polymer, as indicated in Figure II.3.1.5.5, at a known insertion depth of 4 mm. Following a solidification process, which can be adjusted to replicate varying isothermal cooling profiles, the embedded fiber can be extracted, and the resulting force recorded.

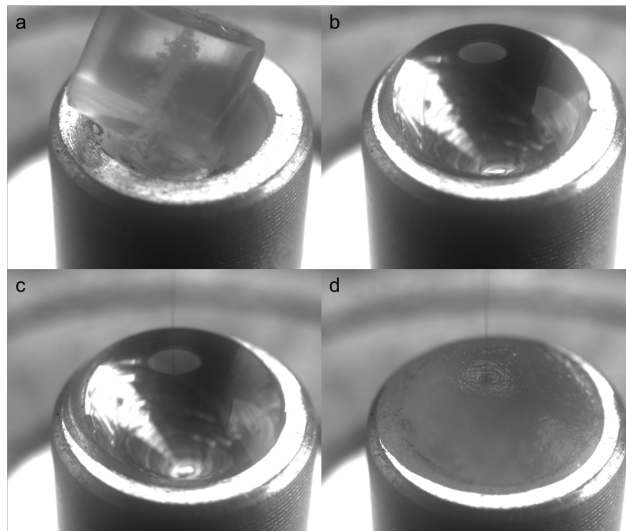


Figure II.3.1.5.5. Time series of standardized interfacial characterization study. (a) An iPP pellet in a sample environment. (b) Conformal melt pool of the iPP prior to CF insertion. (c) CF insertion in the center of the melt pool. (d) Solidified polymer sample with opaque microstructure resulting from crystallite scatter ready for pullout testing. Source: ORNL.

The application of corrections for frictional forces and the apparent laminar shear-stress (τ_{app}) can be directly calculated. Figure II.3.1.5.6 summarizes the distribution of τ_{app} GPa across multiple thermal conditioning. An iPP sample with a sufficiently low-melt-index was required to facilitate consistent results for the iPP-CF systems. In addition to thermoplastic composites, researchers also applied these methodologies on a more traditional thermoset composite for comparison. Researchers selected a common commercial epoxy-hardener system based on the Epon 828 formulation. Following a curing step, the fiber pullout achieved 0.014 GPa, which was approximately double what was observed in the iPP system. In contrast with the Epon-based resin system, iPP interfacial properties are dictated by physical interactions alone. Furthermore, higher molecular weight iPP, which are valued for their higher strength and used in our composite systems, would likely produce higher interfacial shear values resulting from more deeply entangled networks, but they could not be reliably tested in this configuration. The development of this toolkit as a high-throughput method for directly assessing the interfacial characteristics will complement the mechanical testing routines—tensile, short-beam shear, and v-notch to build robust connections between the thermoplastic morphology and composite properties.

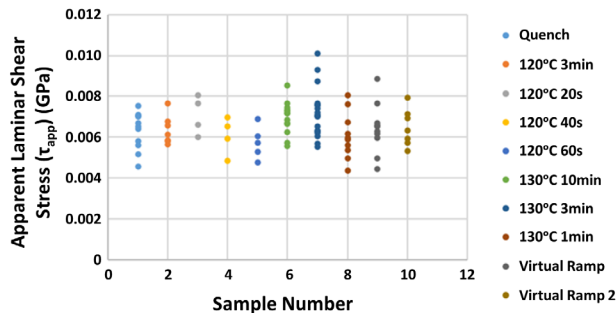


Figure II.3.1.5.6. Apparent interfacial shear-stress across a library of thermal envelopes for crystallization. A refinement of the preparation methods leads to consistent values for interfacial properties for the challenging iPP-CF system. Source: ORNL.

Earlier, researchers demonstrated a polymer matrix recycling method by solvent fractionation. The method allowed the separation of fibers from a PP matrix. PP/CF composites were refluxed with xylene for two hours to ensure the xylene thoroughly infiltrated the composite and dissolved the PP chains that were not strongly bonded to CF surfaces. Following the reflux process, the composite sample was removed from the reflux vessel and washed with hot xylene to remove any traces of dissolved PP that might have settled on the fiber surface. Finally, the composite sample was dried to remove the solvent and weighed to obtain the remaining weight. The sample weight after reflux and solvent washing indicated the PP fraction was immobilized on the CF surface and did not get separated from the surface. These fibers were used with a raw PP matrix for repurposed composite fabrication.

Researchers also showed PP/CF composites could be reprocessed by simple extrusion. During extrusion, researchers noticed that CF alignment was caused by flow. Four different samples were investigated: (1) neat PP (PP_{neat}); (2) 40 wt% CF in PP (PP40C, control sample); (3) 40 wt% CF in PP followed by processing that leads to partial matrix degradation (PPD40); and (4) 40 wt% CF with thermally immobilized PP matrix on the fiber surface (PP40S). Among these samples, the current approach with physical immobilization of PP on a CF surface via crystallization delivers the least viscosity composition that allows (re)processability. Here, CFs act as nucleating agents for PP during extrusion/thermal reprocessing of discontinuous composite. The composites of CFs with PP did not change the chemical signature of the PP matrix, evidenced by the FTIR and XRD data, as shown in Figure II.3.1.5.7(a–b), respectively. However, researchers found that the presence of CFs in the CF-PP composites significantly contributed to PP crystallinity improvement. Herein, the four selected samples were investigated by the differential scanning calorimetry (DSC) technique. Three cycles of heating and cooling from -80°C to 220°C with a ramp rate of $10^{\circ}\text{C}/\text{min}$ were employed. The samples were first melted to remove all the PP crystalline fraction in the first heating cycle and then cooled at $10^{\circ}\text{C}/\text{min}$ to recrystallize. The second and third heating cycles were also measured to determine PP crystallinity in the corresponding composites, as shown in Figure II.3.1.5.8.

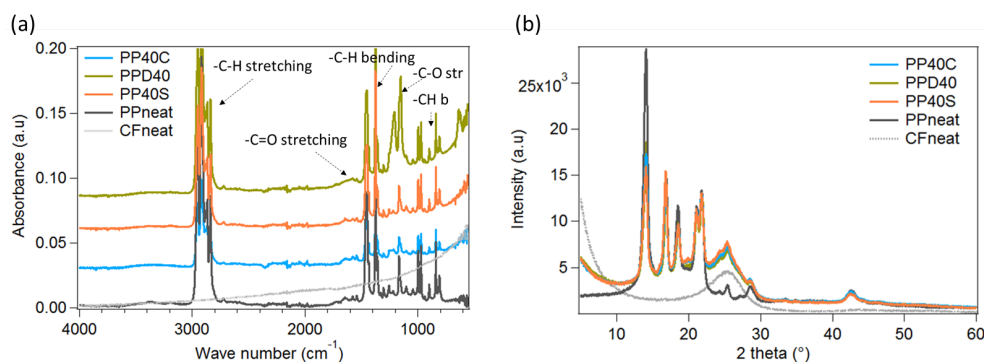


Figure II.3.1.5.7. (a) FTIR and (b) x-ray data of different CF-PP composites. Source: ORNL.

The DSC data of the first heating cycle Figure II.3.1.5.8(a) revealed an increasing trend of the melting temperature, T_m , from 157.3°C to 159.5°C, 161.4°C, and then 164.2°C of PP40C, PPD40, PP neat, and PP40S, respectively. Interestingly, the same trend was observed in both the second and third heating cycles as well, as shown in Figure II.3.1.5.8(b–c). A higher melting point and the sharp melting peak of PP_{neat} suggest a larger and more uniform crystal structure presented in pristine PP in comparison to the CF-PP composites, including PP40C and PPD40. However, the CF surface immobilized PP matrix composite, PP40S, exhibited the highest T_m (164.2°C) and the sharpest melting peak in all three cycles. Researchers anticipate that the polymer immobilization on the surface of CF created a more uniform layer of PP on CFs; hence, they provided more crystal growing sites. Therefore, uniform crystals could be formed.

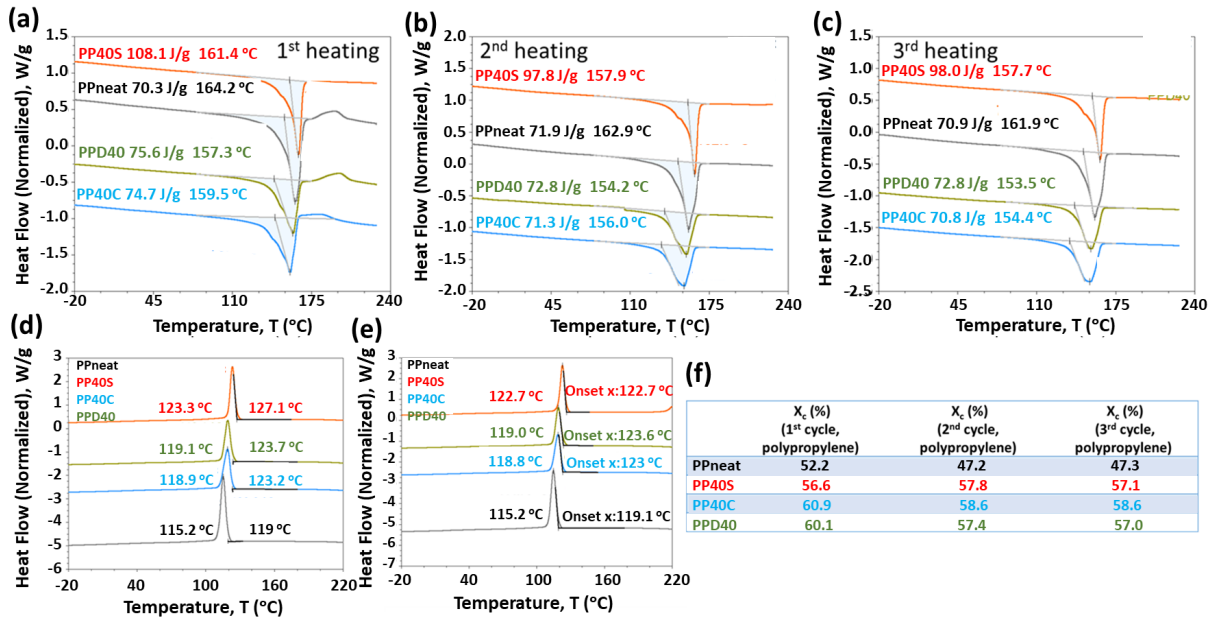


Figure II.3.1.5.8. Nucleation of PP crystals in the presence of CF. (a–c) The DSC data of the studied samples. The first, second, and third heating cycles were presented correspondingly. (d–e) The first and second cooling cycles, respectively. (f) The measured crystallinity of PP in the CF-PP composites by wt.%. Source: ORNL.

To quantify the amount of PP crystallinity in the studied samples, the enthalpy of fusion and the integrated area under the melting curve were measured. The weight fraction of PP crystallinity was computed using Equations 1 and 2.

$$X_c = \frac{\Delta H^*}{\Delta H_{\infty}} \times 100 \quad (1)$$

$$\Delta H = \Delta H^* \times f_{pp} \quad (2)$$

where X_c is the PP crystallinity weight fraction (%), f_{pp} is the PP weight fraction in composites (60 wt%), ΔH^* is the heat of fusion of PP only, and ΔH_{∞} , 207 (J/g) is the heat of the fusion of 100 % PP crystalline [1].

The X_c data were measured and presented in Figure II.3.1.5.8(f). In all cases (e.g., first, second, third cycles), a considerable increase in PP crystallinity was revealed. After removing the sample thermal history, the second and third cycles indicated similar results. An increase of more than 20% PP crystallinity in the CF-PP composites in comparison to the neat PP was determined. For example, X_c of neat PP in the second cycle is 47.2%, whereas the X_c of PP in the PP40S sample is 57.8%, as indicated in Figure II.3.1.5.8(f). The computed X_c data demonstrated considerable improvement of PP crystallinity in the presence of CFs, supporting our argument that CFs nucleate and promote PP crystallization. To verify this conclusion, after heating to remove all the PP crystals, the cooling process at 10°C/min was utilized to recrystallize the melted PP. Data shown in the first and second (identical with the third) cooling cycles, as shown in Figure II.3.1.5.8(d–e), exhibited an

increased trend in PP recrystallization temperature (T_c) in the presence of CFs. The neat PP recrystallized at the lowest temperature, *ca.* 115°C, while PP40S indicated a higher T_c , *ca.* 123°C, which was 8°C higher than that of the neat PP.

Conclusions

ORNL achieved all FY 2023 milestones toward the development of rapidly processable thermoplastic composites via the processing of thermoformable or compression moldable laminates. Researchers developed a fiber-processing method to engineer the interface in polymer matrix composites, observing significantly higher strength and stiffness as compared to control composites. An in-depth study of the crystallization behavior, along with nanoscale and microscale morphology of the composites, revealed that crystallization rates increase with CF loading, as CF surfaces provide an abundance of nucleation sites for semicrystalline matrix crystal growth. Researchers developed a fiber pullout test protocol to estimate fiber-matrix bond strength, established baseline data for CF/PP and CF/epoxy, and compared with new data after new interfacial engineering of the formed composites. Researchers also observed that the matrix forms a transcrystalline region at the fiber surfaces with an abundance of abundant individualized crystals on the surface since it offers an excellent nucleation site. In addition to understanding interfacial morphology, researchers developed and demonstrated compression molding and thermoforming processes and successfully fabricated multilayered composite structures with good fiber wetting and resin penetration. Nearly void-free microstructure of the composites delivered high-performance (> 1 GPa tensile strength) that is suitable for applications in vehicle structures.

Key Publications

1. Allen, K., L. T. Kearney, S. Datta, and A. K. Naskar, 2023, “Tuning crystallization in isotactic polypropylene–carbon fiber composites for rapid composite manufacturing” (in preparation).
2. Jana, A., N. Ferralis, J. C. Grossman, L. T. Kearney, and A. K. Naskar, 2023, “Effect of methyl groups on formation of ordered or layered graphitic materials from aromatic molecules,” *Small*, 19(43), 2302985. <https://doi.org/10.1002/sml.202302985>.
3. Sharma, J., Z. Demchuk, N. Kanbargi, J. Li, A. K. Naskar, G. Polyzos, and R. Tao, 2023, “Aligned carbon fibers-carbon nanotube-polymer-based composite as lithium-ion battery current collector,” *J. Mater. Process. Technol.*, 318, 118015. <https://doi.org/10.1016/j.jmatprotec.2023.118015>.
4. Yu, Z., X. Zhou, C. C. Bowland, H. E. Hinton, L. T. Kearney, S. S. Rohewal, and A. K. Naskar, 2023, “A sustainable route to control interfacial properties of carbon fiber composites” (article in journal review).

References

1. Van der Wal, A., R. J. Gaymans, and J. J. Mulder, 1998, “Fracture of polypropylene: The effect of crystallinity,” *Polymer*, 39(22), 5477–5481. [https://doi.org/10.1016/S0032-3861\(97\)10279-8](https://doi.org/10.1016/S0032-3861(97)10279-8).

Acknowledgements

The authors would like to acknowledge K. Allen, L. Kearney, C. Bowland, Z. Yu, N. Kanbargi, and S. Gupta of ORNL and former ORNL colleagues N. Nguyen, K. Akato, and S. Datta.

II.3.1.6 Multimaterial Functional Composites with Hierarchical Structures (Oak Ridge National Laboratory)

Christopher Bowland, Principal Investigator

Oak Ridge National Laboratory
Materials Science and Technology Division
1 Bethel Valley Rd.
Oak Ridge, TN 37830
E-mail: bowlandcc@ornl.gov

Rich Davies, Composites Core Program Manager

Oak Ridge National Laboratory
Materials Science and Technology Division
1 Bethel Valley Rd.
Oak Ridge, TN 37830
E-mail: daviesrw@ornl.gov

H. Felix Wu, DOE Technology Development Manager

U.S. Department of Energy
E-mail: Felix.Wu@ee.doe.gov

Start Date: October 1, 2020
Project Funding: \$500,000

End Date: September 30, 2023
DOE share: \$500,000

Non-DOE share: \$0

Project Introduction

This project is developing approaches to modify fiber surfaces with nano- and microstructures to improve composite strength through better fiber-matrix adhesion. Stronger composites require less material to meet strength specifications, thus leading to better vehicle efficiency. As reported by DOE, a 10% reduction in vehicle weight equates to a 6–8% increase in vehicle efficiency [1]. To further enhance efficiency, this work is enhancing the mechanical properties of fiber-reinforced composites by at least 10–20% using hierarchical structures with different fiber-matrix combinations. Based on DOE estimates, this 10–20% increase of the composite strength-to-weight ratio leads to a 12–16% increase in vehicle efficiency.

Fiber surface modification via added functional groups or nanomaterials has shown promising laboratory-scale results in the literature for enhancing the fiber-matrix interface, but few approaches have been successful in going beyond laboratory-scale demonstrations. Process scalability is one key aspect of fiber production and composites manufacturing that limits a good deal of research from making the transition from laboratory-scale demonstrations to commercial-scale applications. The fibers in this project are processed using different scalable methods and integrated into both thermosets and thermoplastics, covering a wide performance range to meet specifications for both semi-structural and structural automotive applications with added functional properties. Specifically, the structural automotive components of interest for the thermoset matrix are the frame components, such as A-, B-, and C-pillars and roof rails, where high-specific strength and stiffness are paramount. The thermoplastic composites will be used in semi-structural composites on the automobile's exterior, such as the door panels, bumpers, pickup truck bed, and trunk lid/deck lid.

Objectives

The tasks laid out for this research offer routes toward vehicle lightweighting by increasing the strength of the composites. The overall goal is to present versatile methods to deposit nanostructures and microstructures on the fiber surface for both high-performance structural composites and low-cost, high-volume, semi-structural composites. Beyond mechanical performance enhancements, the high-performance structural composites will be capable of being embedded *in-situ* sensing and structural health monitoring, owing to the design of the added structures. Even though the main focus of this research is to increase the strength of fiber-reinforced composites to meet VTO's vehicle lightweighting goal, there are other functional properties that the surface-adhered structures can provide to the composites.

Approach

Previous efforts in this project developed a method to deposit nanoparticles on the surface of basalt fiber to create an electromechanically coupled composite with enhanced mechanical performance and passive sensing capabilities. While this method was versatile regarding fiber and nanoparticle compositions, it lacked the ability to deposit high-aspect ratio nanoparticles. Therefore, this final year of the project explored an alternative method for depositing high-aspect ratio nanoparticles on the surface of fiber via electrospinning. PAN and ABS were selected as the nanofiber and matrix materials, respectively. The hypothesis was that these two materials would undergo crosslinking at appropriate thermal conditions, thus enhancing the mechanical properties of the fiber-reinforced composite. This was a model system that could be applied to any nitrile-containing matrices.

Results

This work began with the deposition of PAN nanofibers on the surface of carbon fiber (CF). The general configuration of the process is shown in Figure II.3.1.6.1(a). A PAN dope was prepared with PAN in dimethylformamide and placed in a syringe mounted in a syringe pump that pumped the PAN dope through a metal needle. The metal needle had a high-voltage applied to it that caused the nanofibers to accelerate to a grounded drum with a unidirectional CF fabric. The resulting PAN nanofibers on the CF are shown in the SEM images in Figure II.3.1.6.1(b)-(d). Overall, it was shown that this process homogeneously deposited randomly dispersed PAN nanofibers with an average diameter of approximately 350 nm.

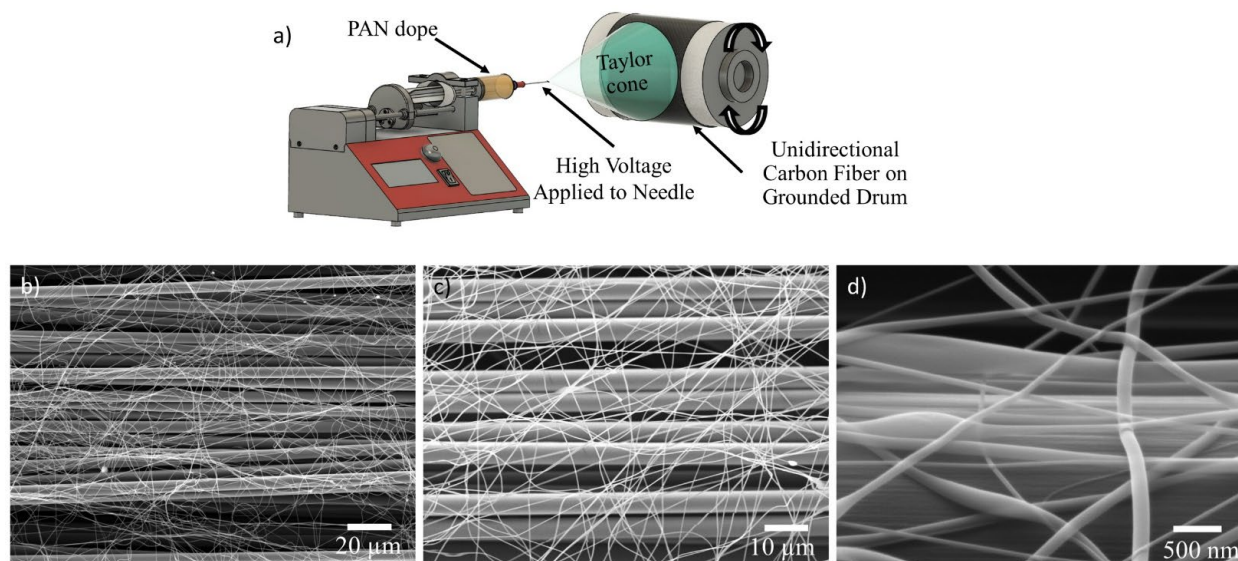


Figure II.3.1.6.1. (a) A schematic of the electrospinning setup with the PAN dope pumped by a syringe pump and connected to a high-voltage power supply to deposit the nanofibers on a unidirectional CF fabric on a rotating grounded drum. (b)-(d) SEM images of the resulting nanofibers on the CF. Source: ORNL.

After demonstrating the success of the electrospinning process on CF, the next step was to verify the hypothesized reaction between PAN and ABS. This was approached by looking at an ABS and PAN

composite without nanofibers. This was fabricated by melt-mixing ABS pellets and PAN nanofibers, as shown in Figure II.3.1.6.2(a). Using this composite blend, the ABS/PAN crosslinking was studied under thermal treatment. The chemical structure schematics shown in Figure II.3.1.6.2(b) depict the hypothesized ABS/PAN crosslinking, which is similar to the well-known PAN cyclization process. Figure II.3.1.6.2(c) illustrates the four different characterization techniques used to validate the crosslinking. These consist of rheology, mechanical, solubility, and solid-state nuclear magnetic resonance (NMR) experiments.

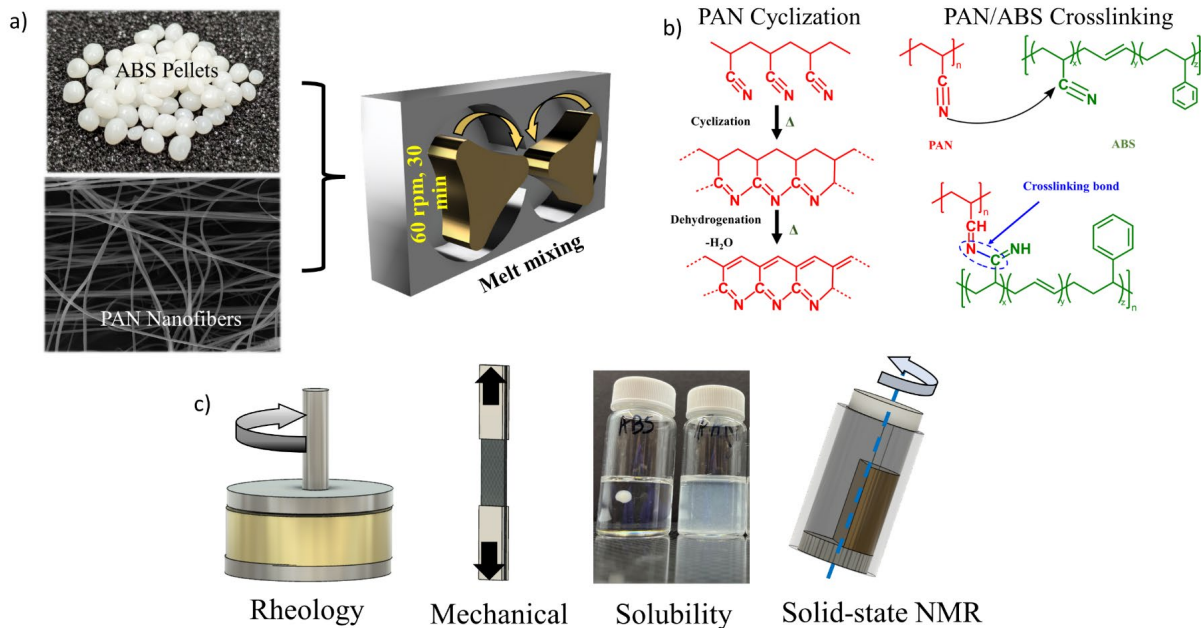


Figure II.3.1.6.2. (a) A picture and SEM image of the ABS pellets and PAN nanofibers with a schematic of the melt-mixing process. (b) Two chemical structures showing the PAN cyclization process and PAN/ABS crosslinking. (c) Four schematics showing the different experiments that were run to validate PAN/ABS crosslinking. Source: ORNL.

The results from these four tests are shown in Figure II.3.1.6.3. The rheological responses during the frequency sweep for the PAN-ABS specimens and neat ABS heat-treated at different temperatures are shown in Figure II.3.1.6.3(a). Compared to neat ABS, the PAN/ABS composites exhibit dramatic improvement in complex viscosity (η) and storage modulus (G'). This observation could indicate more PAN/ABS crosslinking with increasing heat-treatment temperature. The neat ABS rheological properties were also observed to not change with heat-treatment temperature. As an ultra-low concentration of PAN was maintained (0.01 wt.%), the reinforcing effect due to the self-cyclization of PAN could be neglected. Hence, these observed trends in the rheological properties of the PAN-ABS composites could be an indicator of PAN-ABS crosslinking. The solubility tests were performed for 48 hours at 60°C with a dimethyl sulfoxide/chloroform (1:1 by weight) solvent blend. As shown in Figure II.3.1.6.3(b), the ABS, PAN, and (ABS-PAN)_{150°C} all dissolved, but the (ABS-PAN)_{220°C} did not dissolve due to its crosslinked structure. To determine the mechanical effects of this composite, uniaxial tensile tests were performed on ABS, PAN powder-ABS, and PAN nanofiber-ABS, all heat-treated at 220°C. The PAN powder sample displayed similar mechanical properties as the ABS.

In contrast, the PAN nanofiber sample showed ~60% higher Young's modulus and ~20% higher tensile strength than the ABS and PAN powder samples, as shown in Figure II.3.1.6.3(c). In the solid-state NMR results in Figure II.3.1.6.3(d), peak-broadening was observed for the ABS-PAN sample heated to 220°C, as compared to the ABS-PAN sample heat to 150°C, indicating crosslinking. These four experiments validated the ABS and PAN crosslink under appropriate heat-treatment temperatures.

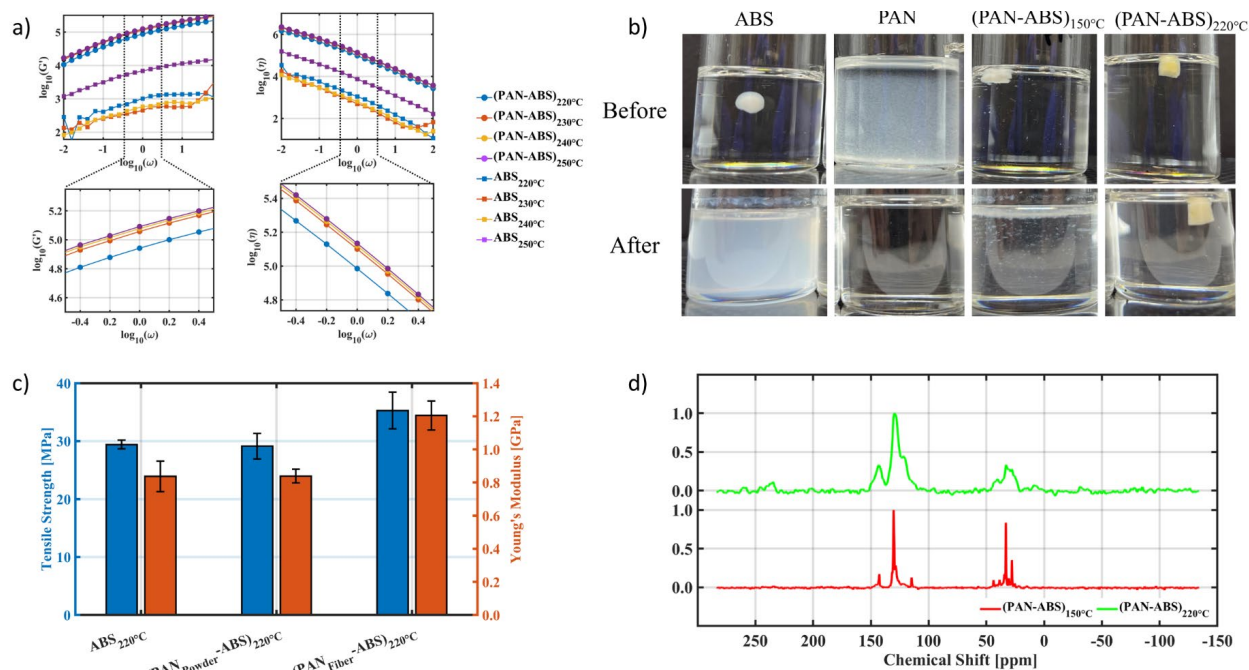


Figure II.3.1.6.3. (a) Rheology results for ABS and ABS/PAN composites heat-treated at various temperature. (b) Pictures of the composites before and after the solubility tests. (c) The tensile test results for the ABS compared to ABS/PAN samples made with PAN nanofiber versus PAN powder. (d) Solid-state NMR results showing peak-broadening after heat-treatment indicating crosslinking between ABS and PAN. Source: ORNL.

After confirming evidence of crosslinking without CF, the PAN nanofibers were electrospun on unidirectional CF sheets to evaluate their effect on the fiber-reinforced composite. The composites were fabricated by combining two CF sheets with the PAN nanofiber-coated sides joined together, as schematically illustrated in Figure II.3.1.6.4(a). The composites were infiltrated with ABS and hot-pressed at two different temperatures (150°C and 220°C) to create samples before and after crosslinking. The optical microscopy image of the cross-section of these samples is shown in Figure II.3.1.6.4(b). The composites were polished to interrogate the cross-section of the fibers using an AFM, as shown in Figure II.3.1.6.4(c). Using the AFM, an indentation test was performed at every pixel within the mapped region. The slope of the force vs. the indentation distance, as shown in Figure II.3.1.6.4(e), was calculated and mapped across the composite cross-section, as shown in Figure II.3.1.6.4(d). The slope represents the material stiffness and reveals an extended and stiffer interphase region for only the sample that was heated to 220°C, which could lead to better stress transfer between the fiber and the matrix.

Three maps showing the slope of the force versus displacement curves from the AFM are shown in Figure II.3.1.6.5. The tested samples are CF with no nanofibers in ABS, nanofibers on the CF in ABS heated to 150°C, and nanofibers on the CF in ABS heated to 220°C. Overall, the 220°C sample shows significant increases in the stiffness of the matrix at longer distances from the fiber surface, indicating crosslinking of PAN nanofibers with the ABS matrix at the CF-matrix interphase region.

The final experiment demonstrates the competence of the PAN fibers crosslinking at the CF-ABS matrix interphase to enhance the toughness of the bulk composites. Laminates with symmetric unidirectional CF sheet laid up at $[+45^\circ/-45^\circ]_2$, as shown in Figure II.3.1.6.6(a), were prepared through different heat-treatment temperatures and their in-plane shear-strength (τ_{IPST}) was characterized as a direct measure of CF-matrix interfacial strength. Tensile tests were performed according to ASTM D3518 with the configuration shown in Figure II.3.1.6.6(b). The average τ_{IPST} of the composites is displaced in Figure II.3.1.6.6(c). Using appropriate thermal treatments, electrospun nanofibers significantly improved the composite's mechanical performance. The 250°C sample was the best-performing specimen with ~60% improvement in in-plane shear-strength.

Above 250°C, the mechanical properties began to degrade due to ABS degradation. An optical image of the fractured tensile specimen is shown in Figure II.3.1.6.6(d), with additional SEM images of the fracture surfaces for the composites with different heat treatments shown in Figure II.3.1.6.6(e)-(h). Fracture surface images revealed increasing amounts of residual matrix on the fibers above 220°C, indicating a better fiber-matrix adhesion.

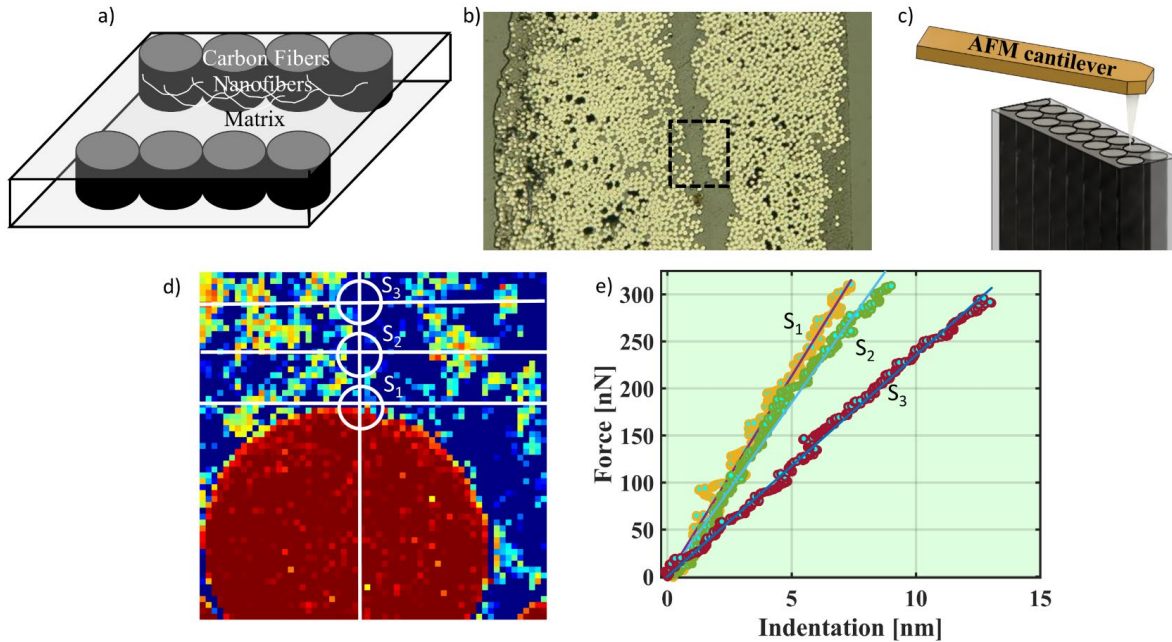


Figure II.3.1.6.4. (a) A schematic showing how the composites were fabricated for the AFM studies. (b) OM image showing the cross-section of two CF plies with the area of interest for AFM studies highlighted with the dashed line box. (c) A schematic showing the cross-section of a CF composite and an AFM cantilever on top probing the cross-section of the composite. (d) A map of the slope of the force vs. displacement curve from the indentation tests. (e) A plot showing the force vs. displacement for the indentation tests.

Source: ORNL.

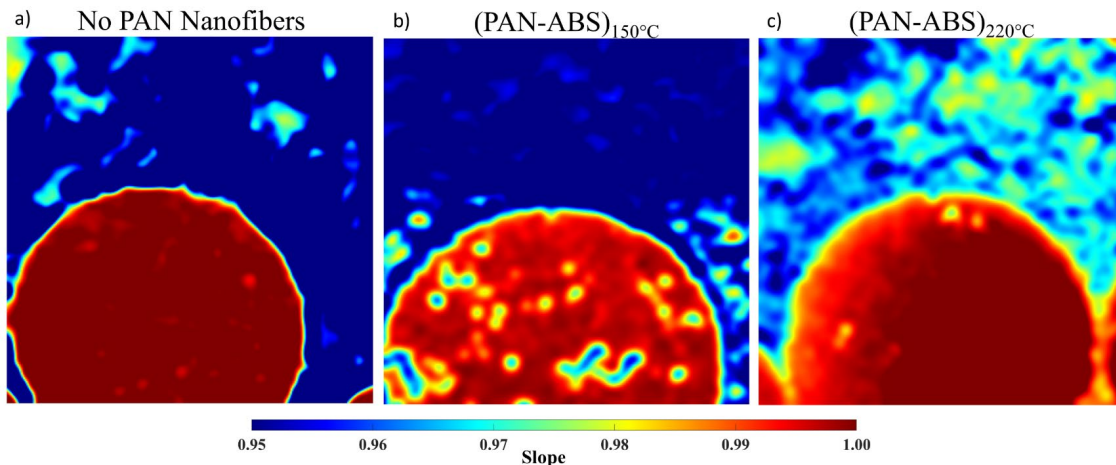


Figure II.3.1.6.5. Three maps with the slope of the force versus displacement curves from the AFM tests: (a) CF with no nanofibers in ABS, (b) nanofibers on the CF in ABS heated to 150°C, and (c) nanofibers on the CF in ABS heated to 220°C. Source: ORNL.

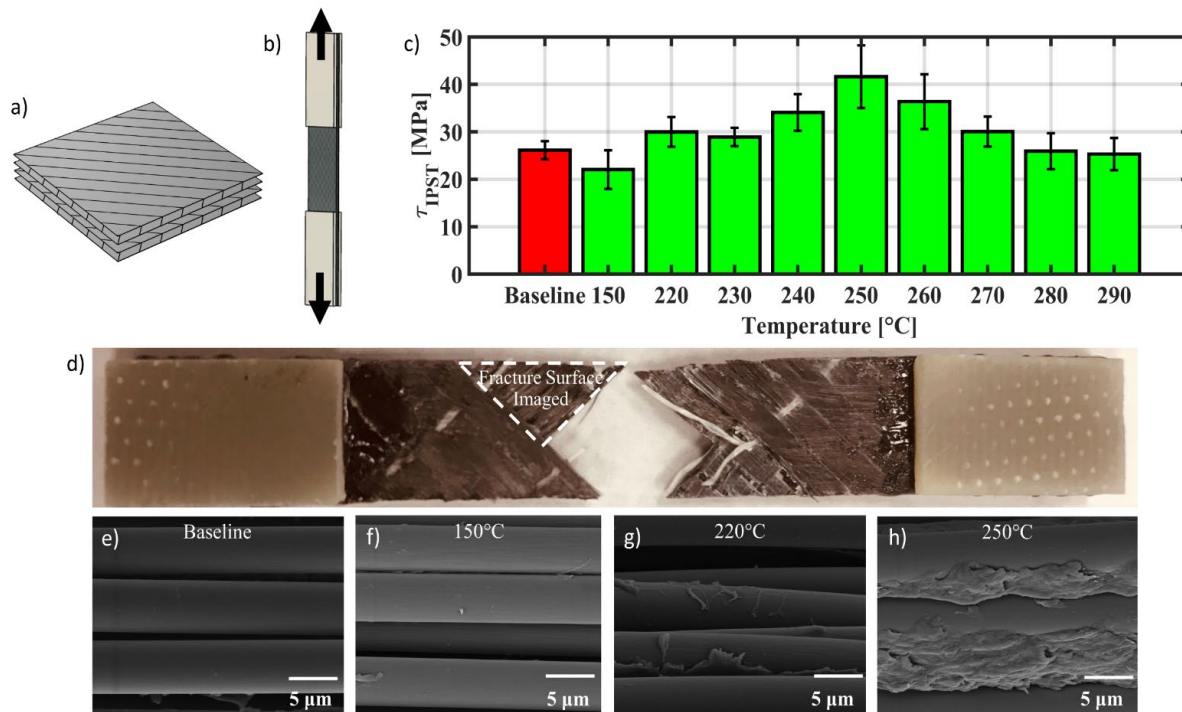


Figure II.3.1.6.6. (a) A schematic showing the composite stacking sequence of +45 and -45°. (b) A schematic of the uniaxial tensile tests performed. (c) A bar plot showing the in-plane shear-strength of the tensile tests samples at different heat-treatment temperatures. (d) A photo of the fracture surface from the tensile tests. Four SEM images of the fiber surface at the fracture surface are shown for (e) the baseline sample with no nanofibers, (f) the sample with the nanofibers at 150 °C, (g) the sample with nanofibers at 220 °C, and (h) the sample with nanofibers at 250 °C. Source: ORNL.

Conclusions

Within this work, a route was developed to significantly enhance the composite's mechanical performance using electrospun PAN nanofibers. The crosslinking behavior between the ABS and PAN in the absence of CF was thoroughly characterized using mechanical, solubility, rheology, and solid-state NMR tests. When integrated at the fiber-matrix interphase of a fiber-reinforced composite, these nanofibers crosslinked with ABS and created an interphase with intermediate stiffness, as found through an AFM indentation study. Such interphases serve as a co-continuous network at discontinuous-type fiber-matrix interphases, offering a better fiber-matrix load-transferring pathway. Composites were then fabricated to assess the bulk composite properties improvements. By optimizing the processing conditions, it was found that by utilizing a low concentration of nanofibers (0.025 wt.%) in the composite, a ~60% improvement in in-plane shear-strength could be achieved. This work established the fundamental understanding of nanofiber scaffolding and its crosslinking with the polymer matrix to result in a composite with outstanding fiber-matrix interfacial strength and toughness.

Key Publications

1. Bowland, C. C., S. Gupta, S. M. Rankin, and A. K. Naskar, 2021, "Passive sensing of a microparticle modified hybrid, fiber-reinforced composite," *Nondestructive Characterization and Monitoring of Advanced Materials, Aerospace, Civil Infrastructure, and Transportation XV*, 11592, 115920B. Preprint available at: <https://www.osti.gov/servlets/purl/1817516> (accessed 9 November 2023).
2. Bowland C. C., S. Gupta, and A. K. Naskar, 2022, "Passive sensing fiber-reinforced composite," U.S. Nonprovisional Patent Application No. 17/690,432.

3. Bowland C. C., A. K. Naskar, and S. Gupta, 2023, “Polyacrylonitrile fiber reinforcement for polymers and fiber-reinforced composites,” U.S. Provisional Patent Application No. 63/458,217.
4. Gupta, S., A. K. Naskar, and C. C. Bowland, 2022, “Multifunctional fiber-reinforced composites for passive sensing and energy harvesting with enhanced mechanical performance,” *Nondestructive Characterization and Monitoring of Advanced Materials, Aerospace, Civil Infrastructure, and Transportation XVI*, 12047, 120470F. Preprint available at: <https://www.osti.gov/servlets/purl/1881133> (accessed 9 November 2023).
5. Gupta S., A. K. Naskar, and C. C. Bowland, 2022, “Model-enabled design of multifunctional composites for passive self-sensing and energy harvesting with improved mechanical strength,” *ASME 2022 Smart Materials, Adaptive Structures, and Intelligent Systems*, 93821, Preprint available at: <https://www.osti.gov/servlets/purl/1881133> (accessed 9 November 2023).
6. Gupta, S., A. K. Naskar, and C. C. Bowland, 2022, “An engineered multifunctional composites for passive sensing, energy harvesting, and *in-situ* damage identification with enhanced mechanical performance,” *Adv. Mater. Technol.*, 7(9), 2101549. <https://doi.org/10.1002/admt.202101549>.
7. Gupta S., A. Mahapatra, P. X. Angelopoulou, L. T. Kearney, Z. Yu, A. K. Naskar, and C. C. Bowland, 2023, “A versatile fiber coating process for efficient fabrication of multifunctional composites,” *Nondestructive Characterization and Monitoring of Advanced Materials, Aerospace, Civil Infrastructure, and Transportation XVII*, 12487, 124870I. Preprint available at: <https://www.osti.gov/servlets/purl/1817516> (accessed 9 November 2023).
8. Rohewal, S. S., S. Gupta, L. T. Kearney, A. K. Naskar, and C. C. Bowland, 2023, “A recyclable self-healing composite with advanced sensing property,” *ASME 2023 Smart Materials, Adaptive Structures, and Intelligent Systems*.

References

1. Joost, W. J., 2012, “Reducing vehicle weight and improving U.S. energy-efficiency using ICME,” *JOM*, 64(9), 1032–1038. <https://doi.org/10.1007/s11837-012-0424-z>.

Acknowledgements

The authors would like to acknowledge S. Gupta, who is working as an R&D staff member on this project, and A. K. Naskar for his supervision and assistance with this research. The authors would also like to acknowledge the research assistance received from other members of the Carbon and Composites Group, including L. T. Kearney, N. Kanbargi, J. T. Damron, M. D. Toomey, and S. S. Rohewal for assisting with the nanofiber-coated CF analysis. The authors acknowledge the support from L. Collins and M. Checa at ORNL’s CNMS for their contributions to the AFM experiments.

II.3.1.7 Ultra-Lightweight, Ductile Carbon Fiber-Reinforced Composites (Oak Ridge National Laboratory)

Vlastimil Kunc, Principal Investigator

Oak Ridge National Laboratory
Materials Science and Technology Division
1 Bethel Valley Rd.
Oak Ridge, TN 37830
E-mail: kuncv@ornl.gov

Rich Davies, Composites Core Program Manager

Oak Ridge National Laboratory
Materials Science and Technology Division
1 Bethel Valley Rd.
Oak Ridge, TN 37830
E-mail: daviesrw@ornl.gov

H. Felix Wu, DOE Technology Development Manager

U.S. Department of Energy
E-mail: Felix.Wu@ee.doe.gov

Start Date: October 1, 2020
Project Funding: \$500,000

End Date: September 30, 2023
DOE share: \$500,000

Non-DOE share: \$0

Project Introduction

CFRP composites are known for their high-stiffness-to-weight ratio, and hence, are of great interest in diverse modern engineering fields. CFRP metamaterials with rationally designed architectures can be realized through AM technologies. Among the many additive fabrication approaches, the light-based technique is most suitable for micro-architected metamaterials due to their high-resolution and robust mechanical properties of photopolymers. In the previous project phase, we developed a multimaterial optical AM technique for multiphase materials, which enabled the production of a group of CFRP microlattice that simultaneously exhibited high-stiffness and high-structural damping. Most high-precision AM techniques are limited by the tradeoff between printing area and resolution. The projection stereolithography process, in particular, is capable of achieving unmatched feature sizes below 100 μm , but the overall dimension is limited to a few centimeters. This limits their application to produce critical components that require high-surface-finish and precision multiscale feature sizes over large volumes.

Last FY, we designed and constructed a novel 3D printer capable of printing a large structure with a fine resolution and demonstrated a part with a 50-cm overall length and 50-mm minimum feature size. We also integrated a custom extrusion system with an optical scanning system for controlling fiber alignment. This FY, we performed parametric studies for optimal printing using the 3D printer we developed last year. The parameters studied include cure depth, fiber length, fiber amount, and processibility (i.e., extrusion from syringe and deposition via viscosity analysis). This work was performed in collaboration with the University of California–Berkeley (UC-B).

Objectives

This work aims to enable high-speed, large area, and high-resolution printing of CFRP composites. The objective for this FY was to focus on parametric analysis for optimal 3D printing. The following milestones were proposed and accomplished:

- **Milestone 1.** Synthesis CF fiber materials with carbon nanotubes and optimized cure depth.
- **Milestone 2.** Rheology and ultraviolet (UV) curing study of matrix material and CF of various sizes.

- **Milestone 3.** UV curing depth study of matrix material and CF of various loadings.
- **Milestone 4.** Processability study with various fiber loadings.

Approach

A large area high-resolution UV curing printer integrated with an infinity-corrected projection system was designed and constructed in FY 2022, as shown in Figure II.3.1.7.1. Light rays emitted from the light engine, which is equipped with a digital micromirror device chip, pass through a collimating lens and enter as an infinity parallel beam in the focusing lens, thus forming an intermediate image. This intermediate image is then relayed and forms an image with the prescribed resolution through a projection lens. In contrast to a conventional projection lens in digital light processing printing technology where the focused image will be out of focus as soon as the lens moves, our infinity-corrected projection system allows the translation of a projected image over a large distance while keeping the focus and intensity.

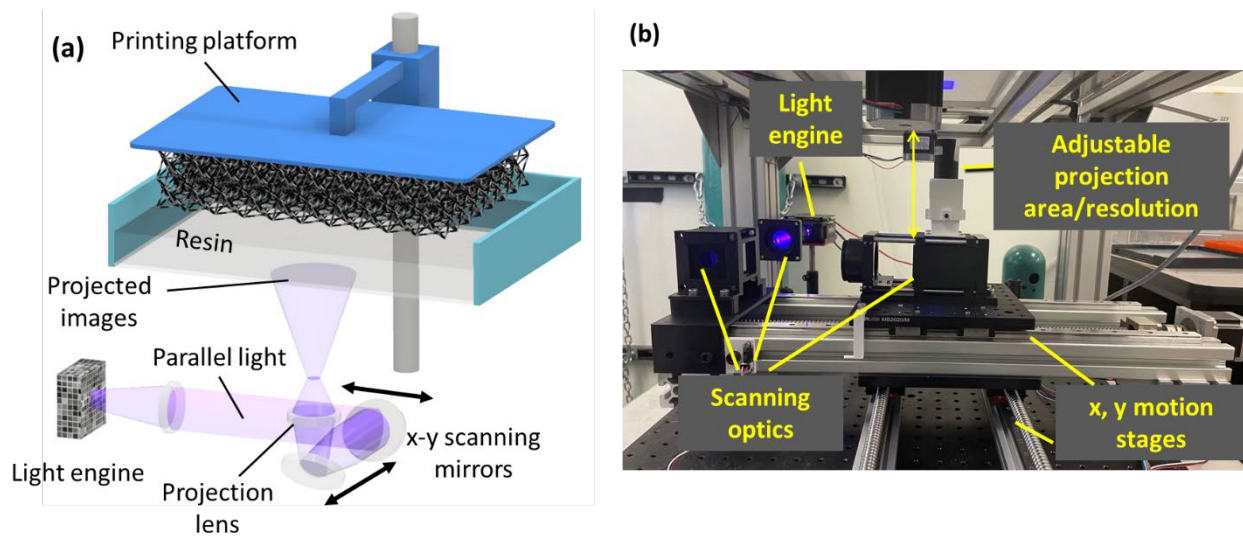


Figure II.3.1.7.1. (a) Schematic of the large area high-resolution projection stereolithography system. (b) Large area high-resolution projection stereolithography 3D printing system with a large format printing vat the team developed. Source: ORNL.

Our 3D-printing method combines the advantage of direct ink writing and projection stereolithography. The nozzle extrudes resin in the vat with predefined toolpaths, enabling localized two-dimensional fiber alignment. Unlike regular direct ink writing that uses extruded beads to compose the structure directly, our approach is to solidify the extruded resin onto the printing platform through moving optics. Therefore, the resolution of the printed feature depends on the optical system involved rather than the nozzle size, which makes the smallest printable feature size less than $50\ \mu\text{m}$. With the developed printing technique, the team successfully demonstrated printing a large-size high-resolution Voronoi vase, as shown in Figure II.3.1.7.2(a), in FY 2022. The vase is made of a CFRP material with a maximum length of 50 cm and a minimal strut thickness of $50\ \mu\text{m}$. The team also successfully fabricated a car bumper model with a size of 110 cm, as shown in Figure II.3.1.7.2(b). Each half ($\sim 55\ \text{cm}$) was printed separately, and then the halves were bonded together.

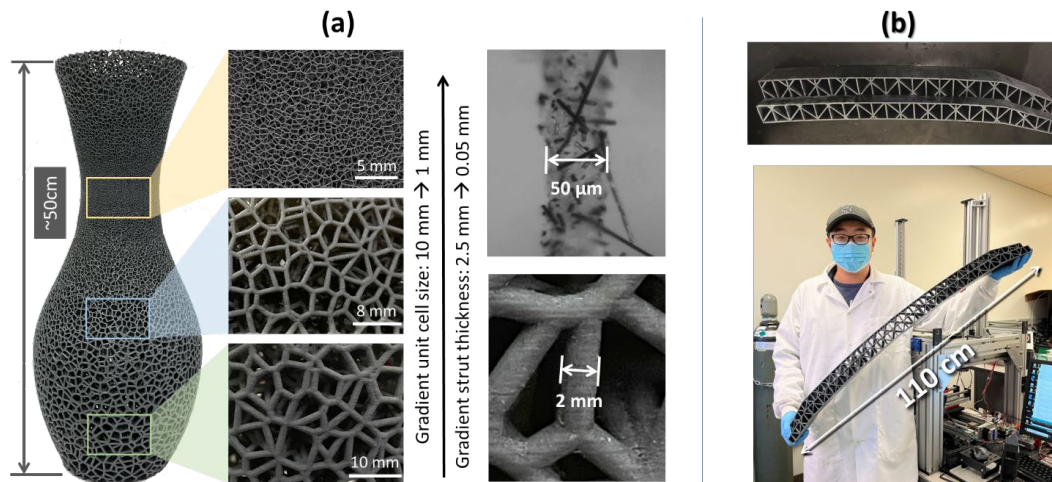


Figure II.3.1.7.2. (a) 3D-printed large-size high-resolution Voronoi vase made of CFRP. The vase is designed to have gradient unit cell size and strut thickness varying from 50 μm to 2 mm. (b) 3D-printed hollowed car bumper. Each half (~55 cm) was printed separately and bonded together to make a full-size (110 cm) bumper. Source: ORNL.

After successful demonstration of a large-size 3D-printed part with fine minimum feature size using the 3D printer the team developed, our focus in FY 2023 shifted to optimization of the 3D-printing process through parametric analysis of processing conditions. We analyzed cure depth, fiber length, fiber amount, and processibility. For the cure depth measurement, a test pattern is projected onto a piece of transparent Teflon fluorinated ethylene propylene film where CFRP resin sits. The UV exposure dose is controlled by the exposure time with predefined light intensity. After exposure, the uncured suspension was rinsed away using ethanol. The cured layer is cut through the middle, and the thickness is measured by an optical camera (Dino-lite Inc.).

Results

Effect of Fiber Amount

Figure II.3.1.7.3 shows the measured cure depth of the CFRP resins with a range of different fiber loadings. Each value is averaged over five measurement points. Here, we varied the loading from 0–15 wt.%, while maintaining the fiber type and other parameters to be the same. For a specific fiber loading, we observed the cure depth shows an exponential relation with the exposure energy. For example, for the resin without any CF, the trendline approaches an asymptotic value of the cure depth to be approximately 600 μm when the exposure energy is larger than 25 mJ/cm^2 . Similar cases can be found for other resins. Moreover, we found that adding CF significantly reduces the cure depth even for a fiber loading of only 5 wt.%. With the same exposure energy, the cure depth of 5 wt.% CFRP resin is only ~100 μm , while the resin without any fiber can be as large as 600 μm . When the fiber loading increases further, the cure depth continues to decrease. This finding implies that curing of CFRP resin requires sophisticated, well-calibrated curing conditions, and one needs to optimize the printing parameters carefully before printing.

Adding CF to the matrix can add functionality to the resin while posing challenges for UV curing because the fiber suspensions can have very high turbidity due to radiation scattering. The scattering-induced turbidity limits the distance of penetration into the resin and largely reduces the cure depths. The obtained diagram can be used as a guide map for selecting printing parameters for specific resin. For example, when dealing with 5 wt.% resin, a cure depth of 100 μm with an exposure energy of 21.25 mJ/cm^2 can be found from the plot. Then, one could define the exposure of each layer time-based on the system's light intensity. Usually, higher light intensity is preferred as it can reduce the curing time. For example, our system has a maximum light intensity of 1.2 mJ/cm^2 , and an exposure time of ~18 s can be used to achieve a cure depth of 100 μm for the 5 wt.% CFRP resin. To ensure the bounding between adjacent layers, a layer thickness of 50 μm , half of the cure depth, can be set for the printing.

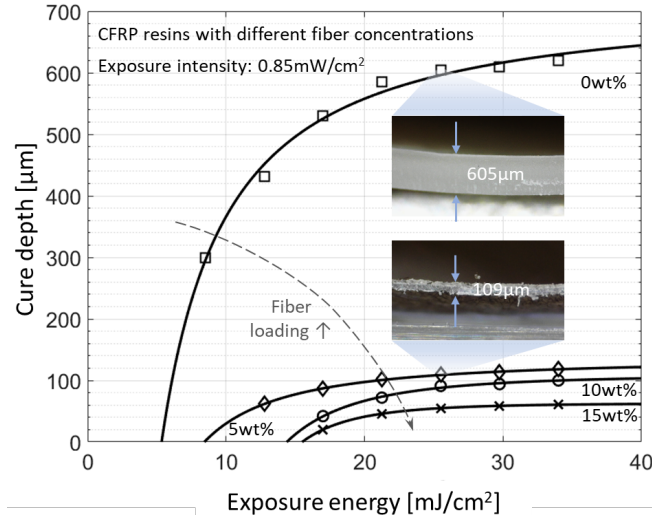


Figure II.3.1.7.3. Cure depth as a function of energy density for CFRP resin with different fiber concentrations. As the resin has a greater amount of fibers, the curing depth decreases. Source: ORNL.

Effect of Fiber Length

To determine their influence on curing behavior, we compared two types of fibers. The evaluation of the fiber length distribution with their relative frequency is shown in Figure II.3.1.7.4. The evaluation was performed using Fiji imaging software, based on optical images from a microscope, and a minimum of 350 fibers in each fiber class were used for the evaluation. By using the same fiber weight fraction, the two types of fiber differ in terms of the total number of fibers.

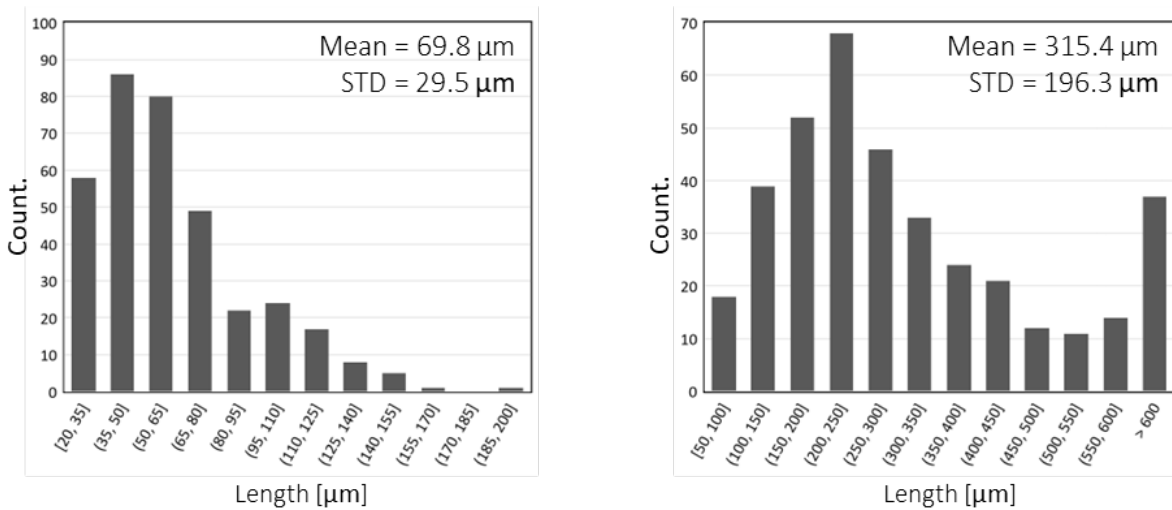


Figure II.3.1.7.4. Measured fiber length distribution histogram of two types of CFs. Source: ORNL.

Figure II.3.1.7.5 shows the depth of the layer required for cure from the two classes of fibers—315 μm and 70 μm—as a function of UV exposure energy. The resin loaded with 70 μm fibers requires more exposure energy than that loaded with 315 μm. This is consistent with the results obtained by Badev et al. [1], who found a lower degree of polymerization can be triggered due to increased scattering with an increased number of particles. The resin with 70 μm fibers is more dispersed, causing more scattering and less polymerization than the resin with 315 μm fibers.

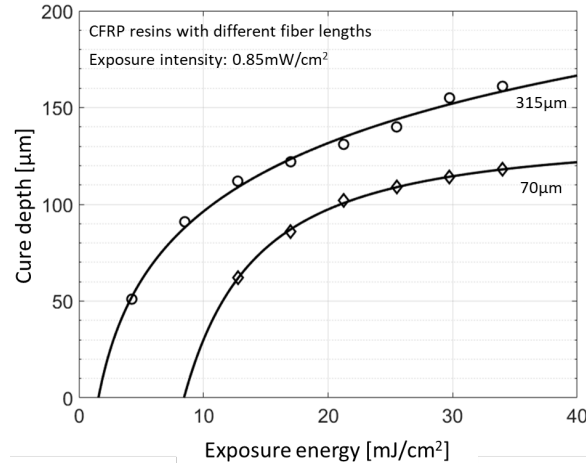


Figure II.3.1.7.5. Cure depth as a function of energy density for CFRP resin with two different fiber lengths: 70 μm and 315 μm . Source: ORNL.

Effect of Initiator Concentrations

Notably, when the fiber loading is as high as 15 wt.%, the cure depth is only $\sim 60 \mu\text{m}$, even if the exposure time is over 40 s, according to Figure II.3.1.7.3. Such a long exposure time is not desired as it will prolong the printing process. The CFRP resin was determined to not be very active to UV light when CFs are present in the resin, although the matrix material already contains a photoinitiator. We found that adding more photoinitiator makes the resin more sensitive to UV light and thus allows for an increased depth of cure at the same exposure energy.

The results of cure depth and the effect of the initiator are presented in Figure II.3.1.7.6. The initiator, Irg 819 (0, 1, 2 wt.%), was added to 15 wt.% CFRP for the measurements. The result shows the curing depth of the resin is significantly increased when 1 wt.% initiator is added. For example, for an exposure energy of 20 mJ/cm^2 , we can see the cure depth increase from $40\text{--}80 \mu\text{m}$, doubled for resin without an initiator. While when further increasing the concentration to 2 wt.%, the increase is not much from 1 wt.%. Nevertheless, this result shows that the initiator plays an important role in the curing process, and one could manipulate the initiator's concentration to control such a process.

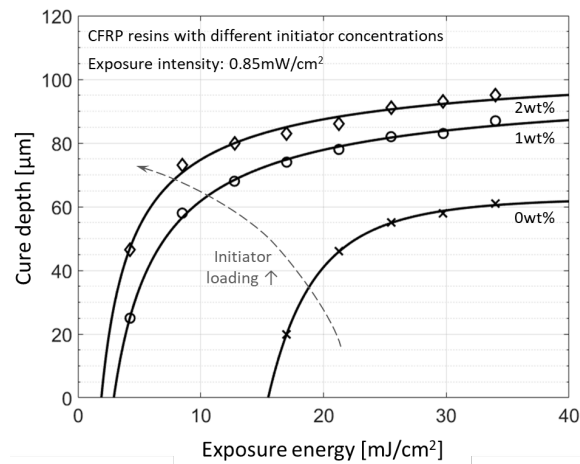


Figure II.3.1.7.6. Cure depth as a function of energy density for CFRP resin with different initiator concentrations. Source: ORNL.

Viscosity Analysis for Processibility

CFRP resin viscosity was measured with respect to shear-rate for different fiber loadings. Viscosity is an important parameter for a projection SLA process. Two configurations exist for the projection SLA process: top-

down and bottom-up. For a top-down system, the UV light projects from the top onto the surface of the resin. While for the bottom-up approach, the UV light projects from beneath to a vat with a transparent bottom to solidify resin onto the printing stage, as observed in Figure II.3.1.7.7(a). After curing, the stage elevates to allow new resin replenishment. A separation interface made of non-stick materials like polydimethylsiloxane (PDMS) and fluorinated ethylene propylene is used to help with separation [1]. Such a process is called the “recoating process,” which is highly related to resin viscosity. For both configurations, thin resins are always desired because they can be recoated via gravity, while viscous resin usually is hard to be recoated efficiently. Although the bottom-up approach is less demanding on resin viscosity than the top-down method, it still requires the resin to settle down in a reasonable time. Therefore, it is necessary to study CFRP rheology to understand the printing process and further expand the range of printable materials. When fiber concentration increases, viscosity increases, and the resin with 25 wt.% CFs show a shear-thinning behavior, as observed in Figure II.3.1.7.7(b). The resulting resin has a high-viscosity at low-shear rates and a low viscosity at high-shear rates, making it flow only upon pressure. To process such viscous resin, a tape-casting method was proposed and applied. Such a method utilizes the shear-thinning effect of the resin to recoat each layer efficiently.

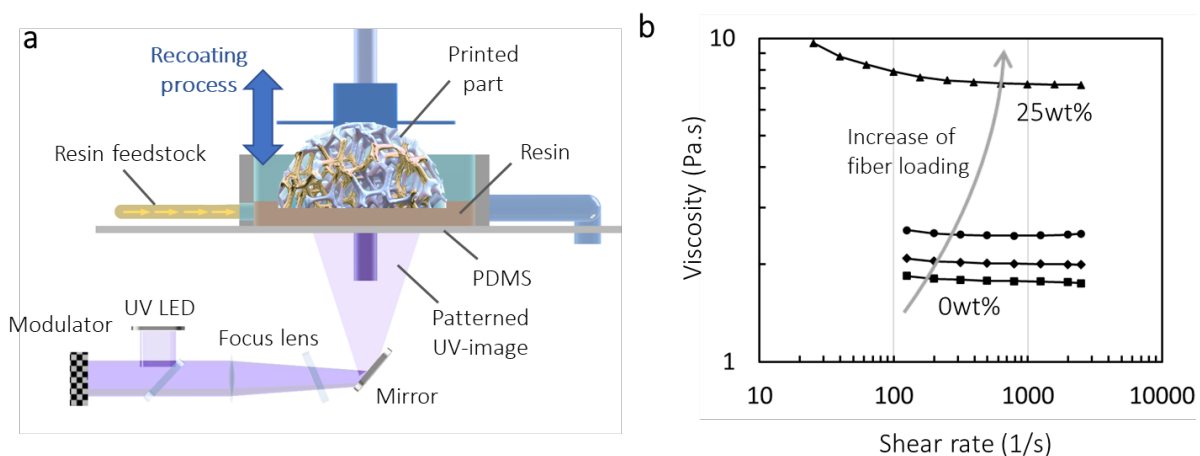


Figure II.3.1.7.7. (a) Schematic of a typical bottom-up projection SLA system. (b) Measured viscosity of CFRP resin with different fiber concentrations (e.g., 0, 5, 10, 25 wt.%) in shear-rate domain. Source: ORNL.

Conclusions

This work systematically shows the different influences of short CFs on the curing behavior of photopolymers. CFRP resins show limitations in the achievable cure depth compared with pure monomers. By adding more initiators, the cure depth can be increased. Resin with shorter fibers is harder to cure due to scattering than for longer fibers. We also studied the rheology and printability of these CFRP resins and proposed several methods to resolve recoating issues caused by high-viscosity. The presented results help to find optimal printing parameters and have implications for other work.

Key Publications

- Xu, Z., H. Lu, Q. Chen, S. Kim, V. Kunc, and X. R. Zheng, 2023, “AM of self-sensing carbon fiber composites,” *Adv. Eng. Mater.*, 2301249. <https://doi.org/10.1002/adem.202301249>.

References

- Badev, A., Y. Abouliatim, T. Chartier, L. Lecamp, P. Lebaudy, C. Chaput, and C. Delage, 2011, “Photopolymerization kinetics of a polyether acrylate in the presence of ceramic fillers used in stereolithography,” *J. Photochem. Photobiol., A*, 222(1), 117–122. <https://doi.org/10.1016/j.jphotochem.2011.05.010>.

Acknowledgements

This work was performed in collaboration with the University of California–Berkeley, specifically Prof. R. Zheng’s group.

II.3.1.8 Low-Cost, High-Throughput Carbon Fiber with Large Diameter (Oak Ridge National Laboratory)

Felix Paulauskas, Principal Investigator

Oak Ridge National Laboratory
Chemical Sciences Division
1 Bethel Valley Rd.
Oak Ridge, TN 37830
E-mail: paulauskasfl@ornl.gov

Robert E. Norris, Co-Principal Investigator

Oak Ridge National Laboratory
Chemical Sciences Division
1 Bethel Valley Rd.
Oak Ridge, TN 37830
E-mail: norrisrejr@ornl.gov

Rich Davies, Composites Core Program Manager

Oak Ridge National Laboratory
Materials Science and Technology Division
1 Bethel Valley Rd.
Oak Ridge, TN 37830
E-mail: daviesrw@ornl.gov

H. Felix Wu, DOE Technology Development Manager

U.S. Department of Energy
E-mail: Felix.Wu@ee.doe.gov

Start Date: October 1, 2020
Project Funding: \$500,000

End Date: September 30, 2023
DOE share: \$500,000

Non-DOE share: \$0

Project Introduction

ORNL and its partners are demonstrating and evaluating the effects of combining textile PAN fibers produced via dry-spinning at substantially larger diameters and oxidized with atmospheric plasma-oxidation (APO) to produce CF that meets automotive requirements at significantly lower costs while also enhancing processing characteristics. CF composites (CFCs) have been gaining interest from automotive designers due to the potential benefits offered by their high-stiffness and low-density. It has been projected that CFCs could possibly reduce the weight of vehicle structures by greater than 50% and that fuel economy can be increased by as much as half of the percentage of weight-savings. The excessive cost of the fiber remains the largest hurdle for production implementation of CFCs as a vehicle structural material. Automotive vehicle manufacturers have consistently indicated that fiber costs approaching \$5/lb. are necessary to achieve substantial inroads into automotive utilization in mass-marketed vehicles where fuel economy can significantly affect national petroleum usage. The costs to produce industrial-grade CF with properties like those of interest to these automotive applications have been estimated at \$7–10/lb., which is almost equally split between the cost of the precursor itself and the cost of the conversion. To achieve the necessary cost-reduction of 30% or greater, most industry insiders concede that a combination of precursor and conversion cost reductions must be implemented. Fortunately, automotive engineers indicate they are willing to give up some performance to achieve this cost-reduction as well. This initiative intends to take advantage of all these factors to achieve the necessary cost-reduction.

Essentially, all PAN-based CF is currently produced from precursors manufactured expressly for CF production. While acrylic fiber produced for a CF precursor is similar chemically to acrylic fiber produced for textile applications, textile acrylics have not been involved in widespread CF manufacturing. ORNL has made

considerable progress in demonstrating pathways to CF production utilizing textile products, and that approach is being exploited further in this project. It is also worth noting that although PAN fibers are commonly utilized in textile applications worldwide, all acrylic fibers produced for CF conversion and most PAN fibers produced for textiles are solution-spun. Dry-spinning is a more challenging approach and an infrequently used variant in textile acrylic fiber production. However, dry-spinning utilizes significantly less solvent in producing fiber and requires less equipment and energy to extract and recover the solvents. These differences allow for greater production speeds as well, meaning this approach is less costly than wet spinning, as described in the Institute for Advanced Composites Manufacturing Innovation (IACMI) Report #IACMI/R-0006-2020/6.061 [1]. The dry-spinning process is also being demonstrated and exploited in this project.

Conventional oxidation takes place in large open chamber ovens that heat PAN in air. This process typically takes ~90 minutes for commercial CFs—although CF manufacturers do not allow their exact residence times to be published. The APO was jointly invented by ORNL and 4X Technologies (4XT) and is currently being scaled and commercialized by 4XT and its commercialization arm, 4M Carbon Fiber Corporation. The process involves the indirect exposure of PAN to atmospheric plasma (AP) in an oven at temperatures like conventional oxidation. This has been shown to enhance the oxidation process in CF conversion, especially since it has been shown to be at least 3× faster than conventional approaches.

ORNL's acrylic fiber manufacturing partner, Dralon, has indicated that producing larger diameter fibers is not technically challenging and can significantly enhance production economics by up to 30% on their end. However, practical limitations in textile applications and/or the drastic time penalties associated with diffusion time requirements of large diameters in the oxidation process in CF conversion continue to be the limitations on acrylic fiber diameters until this approach is conclusively demonstrated for CF. Success in our approach has the major benefit of dramatically increasing the throughput of both precursor production and CF conversion, leading to significant cost decreases in both stages.

Objectives

The objective of this work is to demonstrate the effects of (a) combining textile PAN fibers (b) produced via dry-spinning (c) at substantially larger diameters and (d) oxidized with APO to produce lower cost CF that meet automotive requirements at significantly lower costs while enhancing processing characteristics. While several of these factors have been considered individually or in combination with a single factor in past DOE programs, this is the first-time all four approaches have been combined. Ultimately, we intend to demonstrate this approach can produce CF meeting mechanical performance minimums of 375 ksi, 30 Msi, and 1% strain, along with 25–30% or greater savings. Scaled-up CF production at ORNL for composite panel evaluation in the third year of this project will show the overall advantages of this approach, along with providing a more detailed assessment of cost/performance tradeoffs.

Approach

During Project Year 1, the team established a baseline for this approach with CF converted from the dry-spun textile precursor from Dralon along with a fiber effectively at least 25% larger in diameter. Note that since the dry-spun fibers are not round, as indicated in Figure II.3.1.8.1, it is more appropriate to cite the fiber dtex (or mass per unit length in g/10,000 m) rather than diameter. For example, the fibers of focus in this study at 3.3- and 5.5-dtex, would be equivalent in a cross-sectional area to round fibers of an approximate 18.8- and 24.3-micron diameter, respectively, whereas round precursor fibers traditionally of 11 microns in diameter would be a little over 1.1-dtex. Thus, all the fibers we are considering are at a significantly higher mass per unit length than the typical precursor as 3.3-dtex and 5.5-dtex represent 3× and 5× higher filament mass than 1.1-dtex. Additionally, it is worth noting that the dog-bone shape of the dry-spun precursor offers potential advantage of shorter pathway distances for oxygen diffusion into each filament that appears to also contribute to shorter oxidative stabilization times, which is the key production rate-limiting step in conversion.

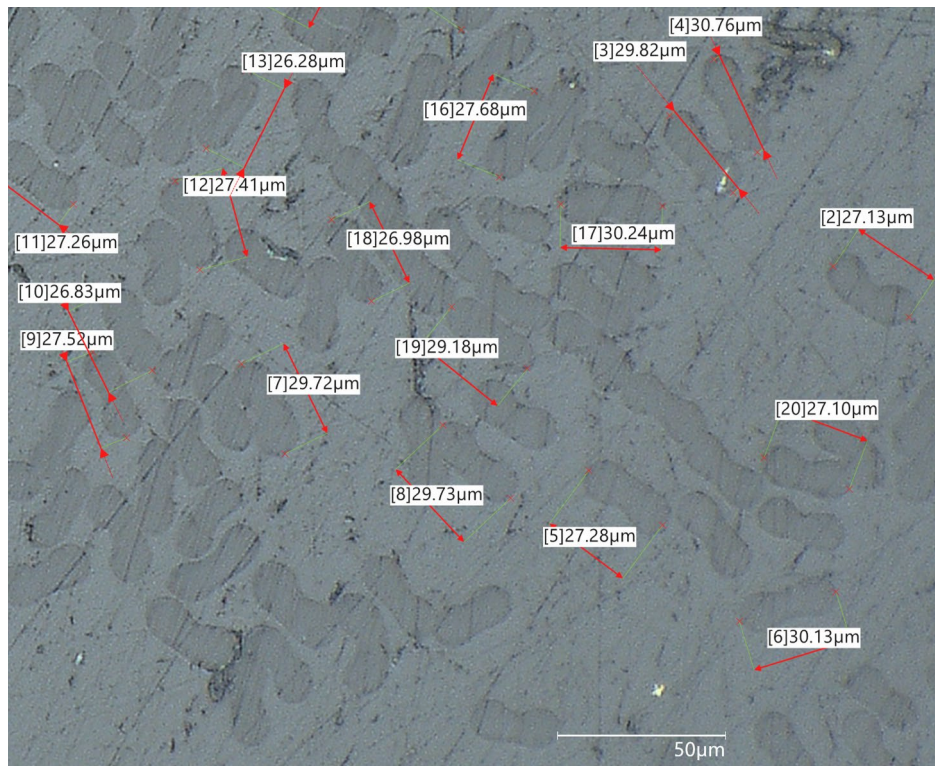


Figure II.3.1.8.1. Pronounced “dog-boned shape” of the dry-spun precursor. Source: ORNL.

Performance of these fibers has been assessed utilizing single-filament testing. The cost of the project baseline fiber will be compared with modeled commercial industrial fiber cost data and preliminary cost projections for larger diameter fiber trends to demonstrate cost-savings for this approach. To meet the Go/No-Go decision point for the project, the baseline fiber exceeded the DOE minimum performance standards established many years ago for the Low-Cost Carbon Fiber Program of 250 ksi strength, 25 Msi modulus, and 1% strain-to-failure. The ORNL team has met a higher requirement for this project Go/No-Go of 300 ksi strength, 30 Msi modulus, and 1% strain-to-failure, along with a projected cost-savings of 20% versus the modeled commercial fiber.

Year 2 has focused on producing fiber effectively at least 50% larger than the project baseline, along with performance minimums of 375 ksi, 33Msi, and 1% strain, while developing and scaling fiber post-treatment processes to pre-production level production. The cost target for Year 2 is to continue toward the demonstration that 25–30% or greater savings are potentially achievable with this approach and to project optimal diameter targets for scaled-up production in Project Year 3 for composite panel evaluation to demonstrate the overall advantages of this approach.

The Year 3 focus has been on completing the general material and process development and transitioning to demonstrating and evaluating the attractiveness of the product form selected for this purpose. The bulk of the effort has been expended on making and evaluating the fiber required to fully evaluate and define the advantages of this approach. The project team will utilize the results of this ongoing effort to compare the cost versus the performance benefits in combining the effects of the textile PAN fibers produced via dry-spinning and at substantially larger diameters and oxidized with APO to assess what is expected to be a major impact in the approach for making lower cost CF.

Our project partner, Dralon, had earlier produced a variety of precursor fiber sizes in quantities largely commensurate with our needs for this project utilizing their well established, world-class dry-spinning process. Steam-stretching is sometimes employed in CF production prior to either conventional or advanced oxidation

processes to enhance precursor fiber orientation as desired going into conversion. ORNL was responsible for the steam-stretching processes utilized for some of the samples. 4XT is responsible for all the advanced oxidative stabilization portions of the conversion of the dry-spun precursor. 4XT has been developing oxidation protocols specifically for the unique dry-spun precursors to oxidize the fiber and provide increments to ORNL for conventional oxidation used in some cases and carbonization of all samples along with test and evaluation of these variants in Years 1 and 2. Similar to capabilities in conversion, ORNL has, independently and in collaboration with others, established post-treatment capabilities at a variety of scales. Oxidized fiber from 4XT was provided to ORNL in Years 1 and 2 to (1) develop appropriate carbonization and post-treatment protocols for completing the CF process and (2) produce larger quantities of completely converted and post-treated CF for the composite demonstrations in Year 3.

Results

Due to a significant downturn in business conditions largely due to COVID-19 limitations, Dralon production over the last 2+ years was terminated pending the potential sale of this unique capability. Fortunately, Dralon had already produced samples that were adequate for our initial needs so that our other partner could utilize them for other purposes. We are now executing planned experimental activities utilizing that fiber, which was produced for 4XT. These plans include the experimental work to evaluate process conditions and associated economic/performance tradeoffs, as well as some equipment adaptations we believe will facilitate process control and overall production attractiveness.

During the first portion of this reporting period, the team finalized the general material and process development by comparing the 3.3- and 5.5-dtex fibers. Although we had several samples from the 5.5-dtex precursor that achieved >300ksi tensile strength, the typical tensile strength and modulus of CF made from that precursor was significantly lower and had greater variability than the CF made from the 3.3-dtex precursor. Since the 3.3-dtex fibers could consistently achieve >350ksi tensile strength and was available in larger quantities than the remaining stock of the 5.5-dtex precursor, the team chose the 3.3-dtex fiber for scaling-up production to make and evaluate the demonstration panels.

Since 4XT has the only established capability for performing the advanced APO oxidative stabilization process, as observed in Figure II.3.1.8.2, and also has the most advanced version of the plasma surface treatment system, which was also co-developed with ORNL and shown in Figure II.3.1.8.3, 4XT was the obvious choice for performing those portions of the sample production. 4XT has similarly scaled versions of carbonization, as indicated in Figure II.3.1.8.4, and sizing equipment, as can be seen in Figure II.3.1.8.5, from ORNL that work well in tandem with the more unique oxidation and surface treatment hardware—so all of the scale-up was performed there as well.

In scaling-up, several issues were encountered with needs to better control the processing parameters to optimize properties and resolve equipment issues, especially with the operation of the aging low- and HT carbonization furnaces. In addition, most of our work up to this point involved CF that had not been post-treated for use in composites, so the surface treatment, sizing materials, and processes needed for the development of this specific fiber and tow sizes could be utilized. At the conclusion of this reporting period, approximately six pounds of CF having the properties summarized in Table II.3.1.8.1 have been completed and are ready for delivery to the University of Tennessee on 13 individual spools. Our plan is to utilize this developmental product, along with at least one commercially available variant, to compare cost versus performance estimates.

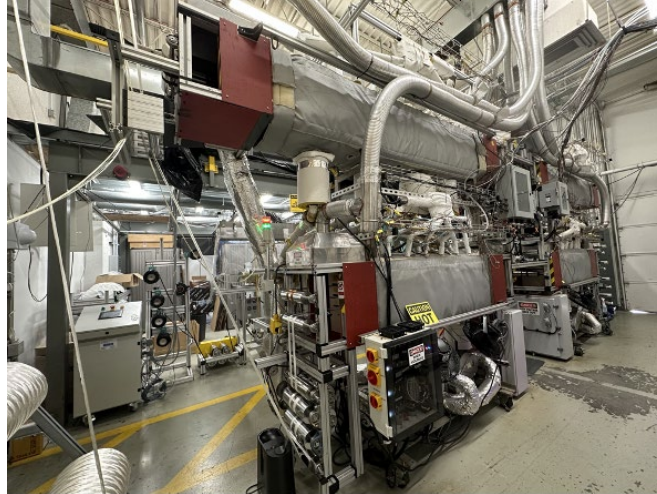


Figure II.3.1.8.2. Advanced plasma-oxidation system co-developed by 4XT and ORNL. Source: ORNL.



Figure II.3.1.8.3. Advanced surface treatment co-developed by 4XT and ORNL. Source: ORNL.



Figure II.3.1.8.4. Low (bottom) and high (top) temperature carbonization furnaces. Source: ORNL.



Figure II.3.1.8.5. Sizing application and dryer (foreground) integrated with surface treatment system (background). Source: ORNL.

ORNL continues to develop a relationship with Sudamericana de Fibras (SDF) in Peru as an alternative supplier for the dry-spun PAN precursor should Dralon not be able to return to production. The SDF products are manufactured from essentially the same dry-spun process, but the PAN is co-monomered at SDF with vinyl acetate instead of methyl acrylate, which will not achieve the same tensile strength as the Dralon fiber. During the previous period, SDF supplied a new variant that can be split more easily than in earlier forms and visually appears more robust in initial processing. Results from converting and evaluating this precursor show that while not yet equivalent to the PAN/methyl acrylate precursor from Dralon, the SDF fiber is approaching that of Dralon and may indeed be a long-term alternative to Dralon should the Dralon precursor continue to be unavailable.

Table II.3.1.8.1. Summary of CF Produced for Panel Testing

Spool	Diameter (µm)	Density (g/cc)	Break Stress (Ksi)	Modulus (Msi)	Strain (%)
1	8.01	1.7613	350.99	26.90	1.28
2	8.01	1.7588	376.46	26.58	1.38
4	7.86	1.7658	315.22	27.30	1.14
5A	7.86	1.7740	418.64	27.43	1.50
5B	7.67	1.7731	382.50	27.21	1.39
6	8.11	1.7595	406.45	27.71	1.43
7	8.07	1.7453	404.69	27.14	1.45
8	8.38	1.7514	374.04	24.10	1.51
10	8.11	1.7718	303.23	26.73	1.12
11	7.83	1.7801	332.53	27.68	1.17
12	8.07	1.7757	328.56	27.39	1.18
Average	8.00	1.7652	363.03	26.92	1.32
Std. Dev.	0.19	0.0109	39.39	1.00	0.15
Coef. of Variance (%)	2.4	0.6	10.9	3.7	11.3

Conclusions

In FY 2022 and FY 2023, significant technical progress has been achieved despite the severe impact of materials availability limitations due to COVID-19 and the resulting business impacts on our project partners. The project team has now largely caught up to schedules after more than six months of delay at project initiation and has identified both means for meeting our materials supply and composite article demonstration needs.

The fiber data presented in this report demonstrates the textile-based, dry-spun precursor clearly has the potential for broad commercial application in vehicles as defined by the long-running DOE goals of performance exceeding minimum targets of 250 ksi tensile strength, 25 Msi tensile modulus, and 1% strain-to-failure. Although not required to meet these minimum requirements, the team feels that further property improvements are likely with better optimized precursor and conversion processes, especially in better tailoring the advanced oxidation to match the very large diameters of the 5.5-dtex fibers. One potential approach postulated for the larger diameter fiber is to develop and implement a plasma treatment that varies in intensity as a function of the oxidation progression over time. In addition to making and testing composite articles during the final year of the project, areas needing more focus include modulus enhancement and completing more detailed techno-economic modeling. Typically, increasing the modulus is accomplished much more easily than increasing tensile strength or strain, which already meets the project targets, by increasing processing temperatures and/or conversion residence time. The techno-economic modeling has been delayed due to the uncertainty of materials availability and selection, as well as the larger width of the processing envelope than had been expected going into the project. However, the larger mass per unit length of the experimental product forms versus the conventional CF precursors and the rapidity of conversion processes that are being employed to get the resulting CF still portend well for substantial economic advantages of this approach.

References

1. Wego, A. J., 2020 “Development of a Lower Cost, High-Volume, Commercially Available, Precursor for Lower Cost Carbon Fiber for Automotive and Wind Blade Applications,” IACMI/R-0006-2020/6.06, Institute for Advanced Composites Manufacturing Innovation, Knoxville, TN, USA. Available at: <https://iacmi.org/wp-content/uploads/2022/01/IACMI-6.06-Final-Project-Report-for-Dralon-12.22.21-approved.pdf> (last accessed 15 January 2024).

Acknowledgements

The authors would like to recognize the technical contributions by D. McConnell and F. Xiong from ORNL; A. Wego from Dralon; and T. Bonds, J. Ford, D. Martin, and J. Nowak from 4XT.

II.3.1.9 Carbon Fiber Technology Facility (Oak Ridge National Laboratory)

Merlin Theodore, Co-Principal Investigator

Oak Ridge National Laboratory
Materials Science and Technology Division
1 Bethel Valley Rd.
Oak Ridge, TN 37830
E-mail: theodore@ornl.gov

Amit Naskar, Co-Principal Investigator

Oak Ridge National Laboratory
Materials Science and Technology Division
1 Bethel Valley Rd.
Oak Ridge, TN 37830
E-mail: naskarak@ornl.gov

Rich Davies, Composites Core Program Manager

Oak Ridge National Laboratory
Materials Science and Technology Division
1 Bethel Valley Rd.
Oak Ridge, TN 37830
E-mail: daviesrw@ornl.gov

H. Felix Wu, DOE Technology Development Manager

U.S. Department of Energy
E-mail: Felix.Wu@ee.doe.gov

Start Date: March 1, 2011
Project Funding: \$1,000,000

End Date: Project continuation is evaluated annually
DOE share: \$1,000,000 Non-DOE share: \$0

Project Introduction

In March 2009, DOE-EERE issued a competitive call for proposals to construct and operate a highly flexible, highly instrumented Carbon Fiber Technology Facility (CFTF) for demonstrating and evaluating low-cost carbon fiber (LCCF) and new low-cost manufacturing technologies at a pilot scale. Construction on the CFTF began in March 2011 and the facility was commissioned for operations in March 2013.

CFTF is a national treasure and the only open access state-of-the-art CF manufacturing research facility in the U.S. offering a unique, highly flexible, highly instrumented CF and melt-spinning precursor processing line with a capacity of 25 and 65 tons per year, respectively. CFTF is used for demonstrating advanced technology scale-up and producing market development volumes of prototypical advanced CFs. The unique capabilities provided by CFTF, including the flexibility to process a range of feedstocks and product forms, are unmatched anywhere in the U.S. CFTF fills a critical need for supporting industrial competitiveness in the manufacture of advanced fibers in this nation by serving as a national resource assisting industry in overcoming barriers associated with cost- and technology-scaling of low-cost advanced fibers and composites—including product and market development. CFTF allows new advanced fiber-related technologies to commercialize effectively by bridging R&D to demonstration, deployment, and validation of such technologies using low-cost precursors and energy-efficient advanced conversion processes at an industrial relevant scale. CFTF also serves as a conduit for testing and validating new technologies in digital and/or smart manufacturing.

ORNL operates the CFTF and works with leading companies to overcome technology barriers to reduce the cost and energy consumption of advanced fiber manufacturing to reveal the strength and energy saving benefits of these new materials. CF is one example of an advanced fiber. Due to its exceptional strength and

low-density, CF is an enabling material for many applications, such as fuel-efficient automobiles, large wind-turbine blades, and lightweight compressed hydrogen or natural gas tanks. DOE is interested in increasing the availability and affordability of CFs and CFCs to increase energy-efficiency and product performance. The major obstacles to CF and other advanced fibers are the availability in high-volume industries at a high-cost relative to materials currently used, limited availability or a lack of domestic sources, and the lack of compatible materials and processes for manufacturing its composites. For advanced fibers to achieve widespread use in vehicle and industrial markets, the cost of production of these advanced fibers must be reduced by 30% to 50%.

CF is a strong, stiff, and lightweight material used as a reinforcement for polymer-based composites to enable improved product performance in many applications. However, the use of CF in cost-sensitive, high-volume industrial applications is limited because of today's relatively high-cost of production. Half of the cost in manufacturing lies in the precursor material, as seen in Figure II.3.1.9.1. Current methods for manufacturing CF and CF-reinforced composite structures are time-consuming and energy-intensive. New, innovative manufacturing processes for low-cost precursor development and conversion technologies hold the key to reducing CF cost for energy applications.

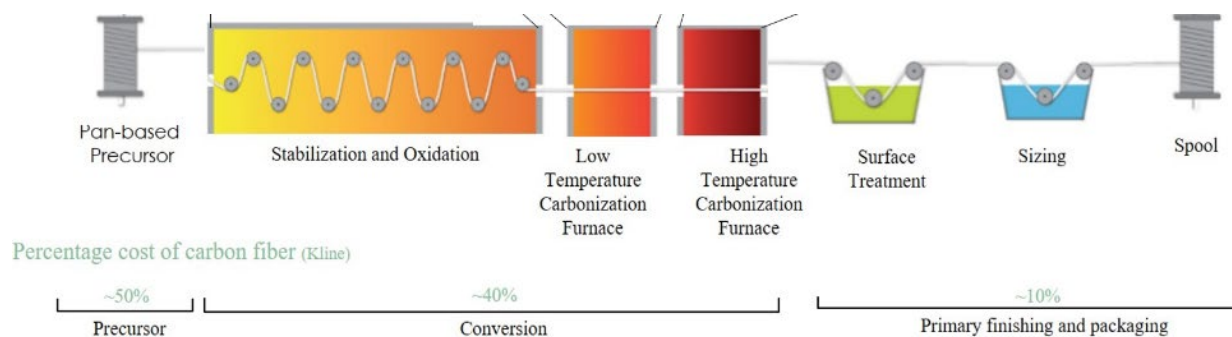


Figure II.3.1.9.1. CF manufacturing process and cost analysis. Source: ORNL.

The high-cost of commercially available CF is due largely to the high-cost of specialty precursor materials and the energy- and capital-intensive nature of the conversion process. ORNL was the successful proposer of a DOE-EERE competitive solicitation in 2009 for advanced research, development, and demonstration of CF production and build a semi-production-scale facility with capability to handle various feedstock materials, to integrate advanced energy-efficient conversion technologies, and to produce enough finished fiber to supply end users for R&D of improved composite manufacturing methods. The proposed capability was focused on four critical areas: (1) development of low-cost feedstocks (precursors); (2) development of more affordable feedstock conversion methods; (3) integration of developed technologies into an industry-scalable demonstration facility to reduce risk of investment; and (4) development of CF composite material and processing technologies. The project objective will be addressed through the third task in the CFTF annual operating plan..

The objective of this project is to accomplish the safe and reliable operation of CFTF and to further DOE objectives for large-scale LCCF commercialization. ORNL's Advanced Fibers Manufacturing Group functioning at CFTF supports DOE-EERE's efforts toward transitioning technologies to industry by focusing on developing scale-up science and technologies for advanced fiber manufacturing and associated fabrication of functional components for high-volume energy applications at the CFTF.

In FY 2023, ORNL continued its R&D efforts to further reduce the cost of CF using other alternative precursors or advanced processes. Table II.3.1.9.1 depicts a list of alternative precursors and advanced processes, along with their advantage and disadvantage for use and the estimated reduction in cost and embodied energy.

Table II.3.1.9.1. Alternative Precursor and Advanced Conversion Processing Estimated Reduced Cost and Embodied Energy

Precursor/Process	Advantage	Disadvantage	Conversion Yield	Cost-Reduction	Energy-Reduction
Standard Polyacrylonitrile (PAN) Precursor (baseline)	Strength, elongation, knowledge base, and fiber architecture.	Feedstock price, volatility, capital cost, energy, yield, and processing.	50%	-	-
Textile PAN Precursor	Properties and knowledge base comparable to standard PAN. Energy consumption and cost reduced.	Capital cost and yield comparable to standard PAN precursor.	50%	*Theoretical ~25% Actual ~54%	Theoretical ~30 Actual ~41%
Polyolefin/Polyamide Precursor	Feedstock price and stability, spinning, yield, and fiber architecture.	Conversion process and equipment, knowledge base, and capital cost.	65–75%	~20%	~50%
Pitch-Based Precursor	Feedstock price and stability, spinning, yield, knowledge base, properties develop w/o stretching, moderate capital. Pitch-based precursor offers the highest potential cost- and energy-reduction potential.	Elongation, compression strength, and fiber strength.	80–85%	~70%	~70%

Preliminary estimations depicted in Figure II.3.1.9.2 show a significant reduction potential in coal pitch CF embodied manufacturing from a lower raw material embodied energy and a higher process yield. Additionally, pitch CF potentially offers the lowest cost/stiffness among CF; hence, a compelling value in cost-sensitive, stiffness-driven, and high-volume applications. ORNL will initiate R&D efforts in other advanced fibers in the near future.

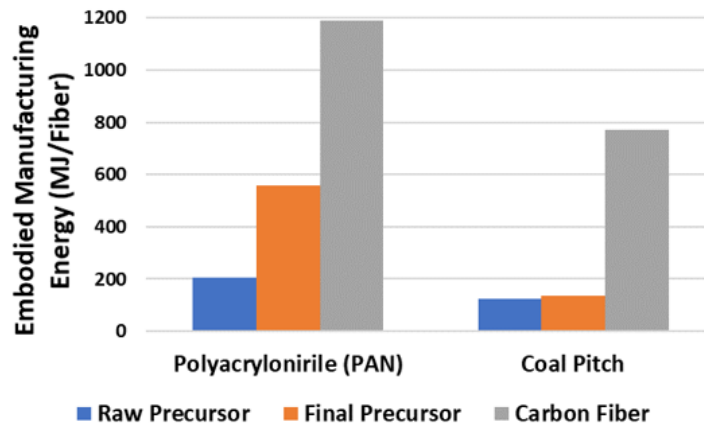


Figure II.3.1.9.2. Embodied energy for PAN and coal pitch precursor and CF manufacturing. Source: ORNL.

Objectives

The project's objective is to develop low-cost fibers from alternative precursors and accomplish safe and reliable R&D projects to further DOE objectives for large-scale commercialization of LCCFs. The tasks covered under these agreements are co-funded by the VTO and AMO in support of the efforts by DOE-EERE in transitioning technologies to industry. The CFTF serves as a national resource to assist industry in overcoming the barriers of CF cost, technology-scaling, and product and market development. The CFTF provides tours so that industry and others can see the technology and process science being developed to produce LCCF with industry-appropriate mechanical properties from alternative precursor materials.

The goal of this project is to develop the technology and support the commercial development of advanced fibers with a cost of production less than 50% of current practice and properties suitable for use in vehicle and other industrial applications. Additionally, work will be undertaken to further reduce the cost of production, energy consumption and environmental impact and increase the economic benefit of CF production in the U.S. This work will be directed toward precursors that can be produced via melt-spinning/blowing, which is an environmentally friendly process that lowers fiber generation cost significantly; however, questions remain whether the process can deliver a precursor fiber that can be processed at high-throughput through oxidation ovens and carbonization furnaces with the required properties. Pitch-based fiber offers the highest potential at 70% for cost- and energy-reduction in CF manufacturing. In FY 2023, we propose to investigate an innovative mesophase pitch process development for the downstream pitch precursors and CF manufacturing.

Approach

The ORNL team recently modified the strategic plan that resulted in a diverse and comprehensive multiscale integrated plan delivering impactful R&D efforts from basic-to-applied TRL research encompassing “conception to commercialization” or “precursor to part.”

Currently, no commercial manufacturer exists for LCCF, therefore, the CFTF shall identify cost-effective alternative sources of precursors based on availability, carbon yield, cost, and spinnability. Once the chemistry of the precursor is developed and baseline properties of 250 Ksi tensile strength and 25 Msi modulus are met, enough material will be produced for scaling-up to the next level. Results generated from the bench-scale studies are then used to develop a baseline condition or starting point for scaling to the next scale. The CFTF staff will then develop process conditions for converting the precursor material into LCCF that will exceed the baseline properties. The performance of the fibers will be characterized and evaluated in a variety of resins systems at a coupon-level utilizing various compositing methods. Enough CF will be produced for deployment to industry to evaluate, thereby showcasing the quality of LCCF on a multitude of end-user platforms. This work is intended to produce industry demand for the technology. The CFTF staff continues to hold discussions with industrial partners that are interested in scaling the processes being developed at CFTF. The financial investment for industry to scale-up the technology is significant and, thus, is not a subject for quick decision.

The CF that is integrated in the CFTF and its composites research portfolio, within the intricate ORNL ecosystem and shown in Figure II.3.1.9.3, was developed to maximize the impact in the U.S. economy. ORNL is the only national laboratory in the U.S. that can deliver a multiscale strategic approach from precursor to part with TRLs ranging from TRL 1 through TRL 7 at handoff to collaborating partners. The vision was developed to drive innovation in R&D from precursor to part for structural and non-structural applications across various technology areas, especially automotive.

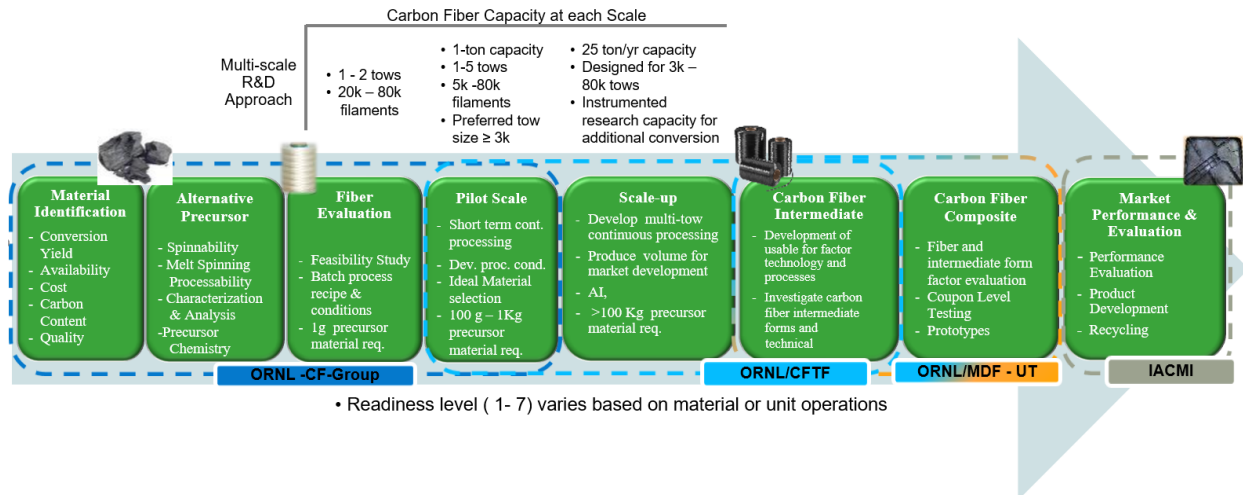


Figure II.3.1.9.3. Multiscale R&D approach. Source: ORNL.

CFTF’s mission is to transition technology to industry for scaling, but many technical challenges remain that must be overcome to further reduce the risk for industry to implement the technology. These technical challenges are being addressed in collaboration with industry to reduce the uncertainties and implementation risks associated with scaling technologies. These challenges include handling the various form factors of fibers processed from the alternative precursors and developing appropriate sizing for LCCFs for specific composite applications. The CFTF continues to be a training ground for any technical staff involved in CF production. Key strategies implemented by the project in FY 2022 supported by VTO were labeled under Task 3, entitled “Investigate Potential Alternative CF Precursors,” of the CFTF annual operating plan with defined milestones. The milestones and their status at the end of FY 2022, as shown in Table II.3.1.9.2, were to investigate potential alternative CF precursors. This will allow for the selection of a candidate precursor not previously studied and an investigation of supplier-to-supplier variation effects in precursor chemistry, physical characteristics on product variability, and performance.

Carbon-based materials are of utmost importance in modern society, enabling a remarkable amount of highly engineered applications from nuclear shielding, performance composites, and adsorbents. One of the most demanding is pitch-based CFs, which requires a molecularly ordered liquid “mesophase” to form highly oriented connected basal planes, which grant CFs their extraordinary stiffness and strength [1]. A critical limitation of pitch-based CFs is the formation of the mesophase, which is a mixture of polyaromatic hydrocarbons (PAHs) from common coal or petroleum-based hydrocarbon feedstocks. The synthesis of pitch from the hydrocarbon fractions of petroleum and coal have been previously demonstrated for the fabrication of pitch-based CF [2], [3]. The polydispersity and natural compositional variation in coal and petroleum grades resulting from the breakdown of plant and animal matter, coupled with an inability to reliably predict and separate mesogenic compounds from pitches have continued to present practical developmental challenges to the realization of highly graphitizable phases [4]. Prior efforts were focused on developing a *synthetic* mesophase pitch with a relatively well-controlled population of anisotropic PAHs that displayed optically active phase domains consistently above 90%. However, those efforts required toxic chemicals/catalysts [5]. While a process was commercialized for a short-time, it was ultimately discontinued over toxicity concerns and practical challenges with handling of highly corrosive chemicals at HT. As a result, there is a serious need to invent alternative approaches to form highly controlled mesophases from synthetic feedstocks without the use of legacy chemicals. The incorporation of metal ion catalysts with isotropic molecular precursors showed successful partial conversion to a thermotropic liquid crystal pitch [5], [6]. Those are not yet effective, as a separation of those reduced metals is necessary to produce defect-free carbon materials.

The alternative precursor and CF development task in CFTF’s annual operating plan will be undertaken under the VTO lightweight material development program with a focus on the development of a new method for

producing pitch material from different feedstocks to demonstrate relevant utilization of pitch as a precursor for CF manufacturing. Basic R&D shall be performed to develop and evaluate new pitch precursor materials and an advanced processing method not used before at the bench-scale. Upon evaluation, confirmation, and demonstration that the concept works, a scale-up plan will be developed later. The following subtasks listed in Table II.3.1.9.2 will be undertaken.

Table II.3.1.9.2. Task 3 Milestones, Task Descriptions, and Status

Milestone/Deliverable Name/Description	End Date	Type	Criteria
Design new continuous process and procure equipment for bench-scale studies.	12/31/2022	Quarterly Progress Measure (Regular)	The equipment set up is established and commercial isotropic material is processed.
Demonstrate conversion of hydrocarbon molecules to pitch material with a softening point >200 °C and with at least 30% mesophase content.	03/31/2023	Quarterly Progress Measure (Regular)	Convert pitch to mesophase and quantify mesophase content of the raw material prior to spinning.
Thermal characterization and analysis of pitch material with respect to its spinnability or ability to form fibers of 30 micrometer or smaller diameters.	06/30/2023	Quarterly Progress Measure (Regular)	Develop the process conditions for converting the pitch precursor material into pitch-based precursor fiber.
CFs show 250 Ksi strength and 25 Msi modulus is prepared.	09/30/2023	Quarterly Progress Measure (Regular)	Mechanical characterization and analysis of pitch CF and demonstrate in-house synthesized pitch-based CFs show 250 Ksi strength and 25 Msi modulus.

Results

Visitors/Tours

A total of 182 visitors from 68 organizations toured the CFTF in FY 2023. A significant decrease in visits was expected this year due to critical major upgrades on the CF line abatement equipment. This effort took 8 months. The CF line was brought back online in September 2023.

Alternative Precursor and CF Development

Innovative Pitch Synthesis Method

ORNL partnered with industry partners in FY 2022 who are in the process of developing and scaling a petroleum and/or coal-based pitch material process for producing a pitch precursor for pitch CF production. Two kinds of pitch existing today are isotropic and anisotropic (mesophase). However, all pitch begins as an isotropic pitch material that can be further processed through thermal processing to become a mesophase pitch material. Mesophase pitch has the potential to be an excellent precursor to produce high-quality CFs with a higher Young's modulus and substantially lower cost than using polyacrylonitrile (PAN). Pitch material has various forms with inconsistent qualities, such as a varying concentration of volatiles, granules/particles size, and texture within the same batch, as observed in Figure II.3.1.9.4. Each source of pitch material poses different challenges with processability in the melt-blowing process.

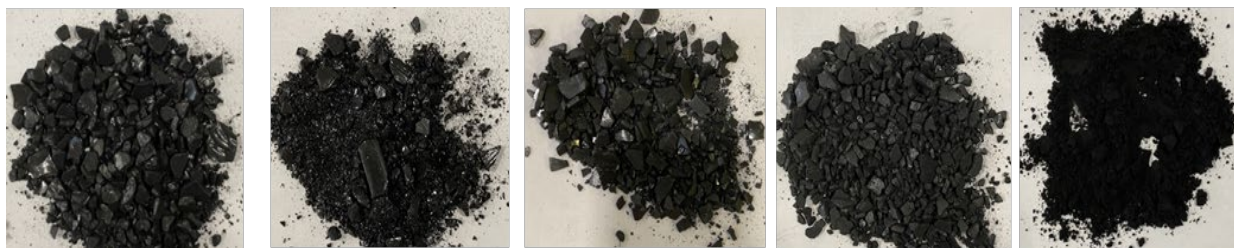


Figure II.3.1.9.4. Pitch material from different sources. Source: ORNL.

Addressing issues observed in FY 2022, we proposed to devise a first-of-its-kind flow-through mesophase pitch reactor and characterize the resultant polymerized products to establish the key process-reactivity relationships in FY 2023. This groundbreaking concept is in its infancy stages. The envisioned system would bring isotropic starting materials (i.e., mono- or poly-disperse), heated to melt-flow conditions, in contact with a supported metal catalyst bed positioned within the flow path of the molten reactant. This low TRL research can revolutionize pitch CF manufacturing dependence on the laborious, costly, and inconsistent production of mesophase pitch via slow (several hours or more) reactions in pressurized batch reactors. Circumvention of this process would enable the production of pitch from mono-disperse feedstocks. A laboratory-scale concept reactor was designed for converting various sources of isotropic pitch material to mesophase pitch material. The thermophysical and spectroscopic characterization of the resultant material was also analyzed.

Our approach was based on the low-temperature coking of small molecule hydrocarbon, as observed during our prior ICME project and graphite-based materials research by Klett [7] that utilized a solid-state catalytic bed at elevated temperatures. Our ability to control residence time and the reaction(s) for the first-time will demonstrate contamination-free pitch synthesis. Details of the concept design was submitted to the ORNL strategic partnership group as an invention disclosure. An invention disclosure (invention ID #81944342), entitled, “Catalytic flow reactor for valorization of polyaromatic hydrocarbon precursors to liquid crystal mesophases,” was submitted on the pitch concept, as shown in Figure II.3.1.9.5. The pitch concept consists of a stationary catalyst-based bed that can be used to enhance mesophase formation in a flow-through reactor.

In addition to extruding coal-tar-based isotropic pitches to qualify a simplified reactor flow path, we performed some small-scale polymerizations on naphthalene, due to its low carcinogenicity relative to higher PAH with iron chloride (FeCl_3). The stirred naphthalene melted quickly and transitioned from clear to brown and eventually to black during the reaction consistent with the extension of the electron distribution to a highly absorbing PAH. The crude products had evidence of an infusible coked chunks alongside an N-methyl pyrrolidone soluble fraction, which was isolated and dried as observed in Figure II.3.1.9.6, and the carbon mesophase content at low-, medium-, and high-loadings were determined, as shown in Figure II.3.1.9.7. Next, we explored other candidate precursors (e.g., methyl naphthalene, anthracene) and mixtures to target anisotropic mesogen synthesis.



Figure II.3.1.9.5. Reactor bed design. Source: ORNL.

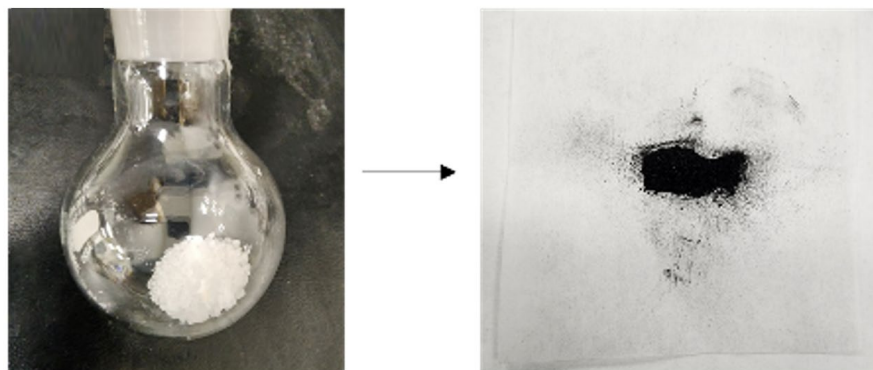


Figure II.3.1.9.6. Polymerization product of naphthalene precursor with FeCl_3 . Source: ORNL.

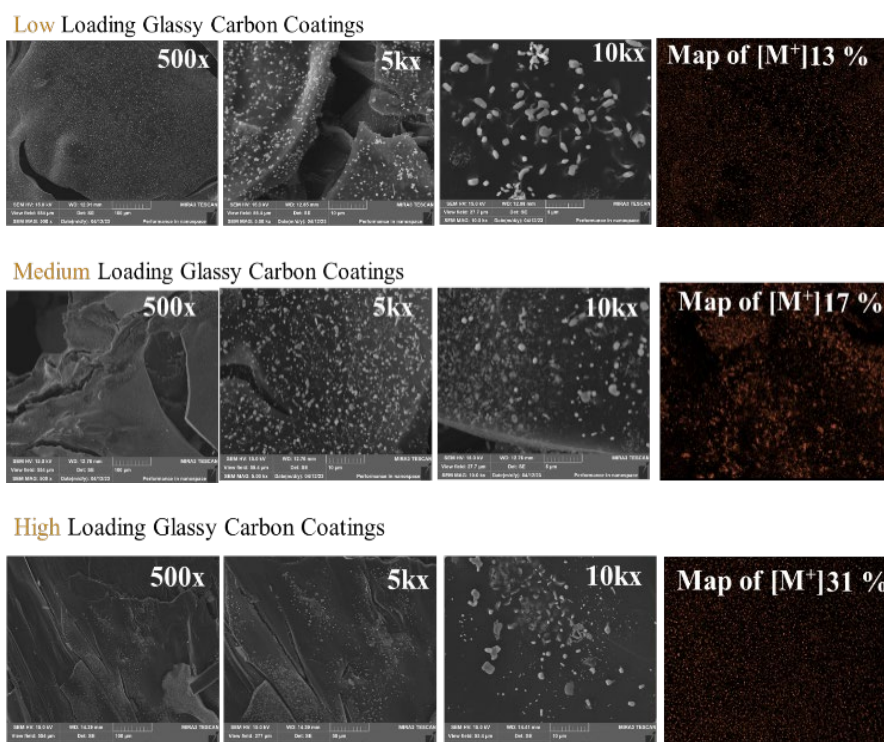


Figure II.3.1.9.7. Carbon mesophase content at low-, medium-, and high-loadings. Source: ORNL.

Major results were summarized and presented during the VTO Annual Merit Review in June 2023 [8]. Reviewer comments from industry and academia were highly positive and excited with the direction regarding scaling-up. Following the installation of the heating mantles, initial baseline experiments were performed. First, a trial run with a traditional glass-filled extruder cleaner was extruded through the reactor volume, without inserts, to ensure the heating mantle worked as expected. Based on the observed pressure and to reduce the possibility of backflow, an additional heating zone controller was installed enabling for the temperature of the reactor zone near the outlet to be set independently higher to accommodate anticipated increases in melt viscosity. Additionally, we observed large fluctuations in the applied power to the heating mantle by the controller as well as accompanying temperature fluctuations. To overcome this issue, we purchased insulation based on the recommendation of the ORNL instrumentation group and updated the design to the reactor, as shown in Figure II.3.1.9.8. We initiated reaction campaigns with two materials feedstocks: (1) a low softening point material (i.e., 170°C); and (2) dimer- and trimer-based fused aromatic hydrocarbons. We also must study the kinetics of catalyst deterioration and generation to inform future viability studies more accurately.

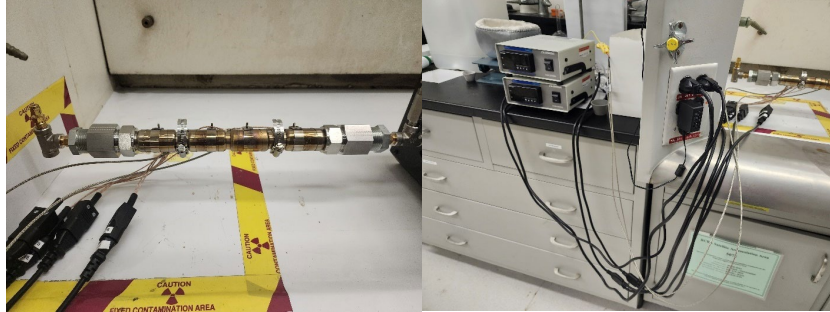


Figure II.3.1.9.8. Reactor bed design. Source: ORNL.

Supporting Data and Explanation

Lewis acid catalysts, such as FeCl_3 , are highly reactive and sparingly soluble in non-polar media. To perform the catalyst functionalization, we performed a wide study of organic solvents and found anhydrous alcohols to produce the best results. Figure II.3.1.9.9 summarizes pictorially the best solubility results for dissolution of the catalyst phase and co-solvation of the glassy carbon producing phenolic resin.

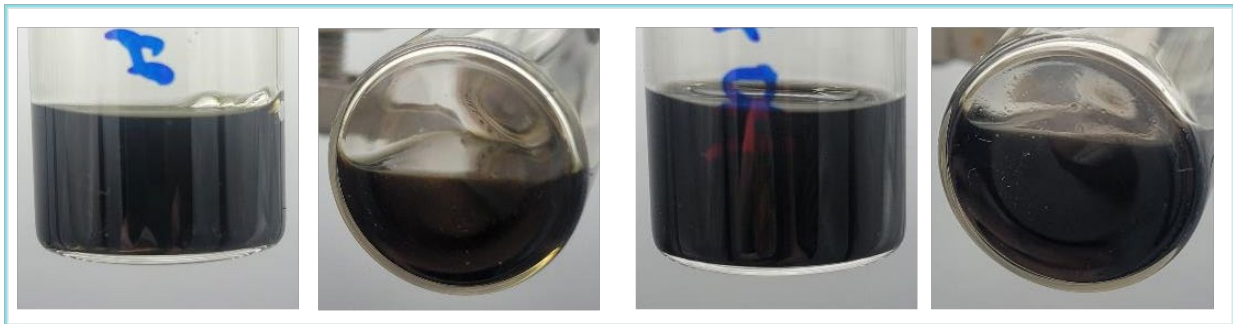


Figure II.3.1.9.9. Homogeneous solubility of metal catalyst in alcohols prior to contact with porous graphitic material. Source: ORNL.

Graphitic material pieces were sectioned to a consistent thickness of 1 in. and introduced to a reservoir containing the catalyst. A screening matrix was developed for 36 unique samples that were varied based on resin type, catalyst content, and final carbonization temperature. Batch carbonation was performed in an inert atmosphere at a ramp rate of $2^\circ\text{C}/\text{min}$ to the carbonization temperature, held for 30 minutes and allowed to cool to RT. Sample sets were sectioned and imaged with SEM. Energy-dispersive spectroscopy was performed alongside the generation of micrographs to map the elemental distribution and unambiguously established the spatial homogeneity of the catalyst following carbonization, as indicated in Figure II.3.1.9.10. To further quantify the metal atom catalyst present in the graphite material following attachment x-ray photoelectron spectroscopy, as observed in Figure II.3.1.9.11, was performed on various surfaces. The open cell core was confirmed to contain 7.2 at.% of Fe and only trace amounts of Cl following carbonization. Surface-directed metal atom centers will serve as the sites for heterogeneous catalysis of the pitch condensation to high-order mesogens.

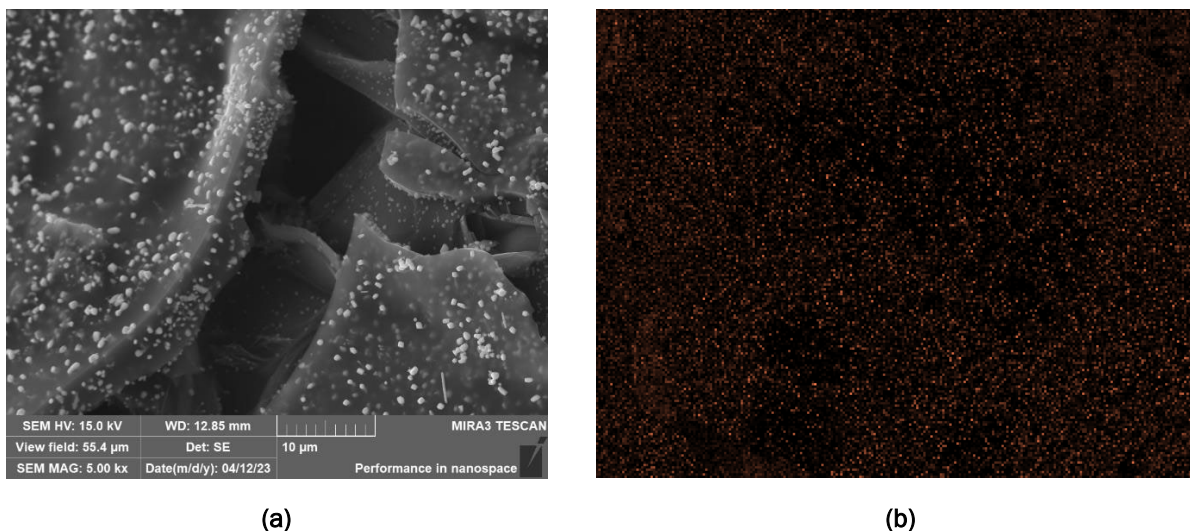


Figure II.3.1.9.10. (a) SEM showing the morphology of deposited surface catalyst. (b) EDS overlay suggesting a 13 at.% of Fe on the graphitic material. Source: ORNL.

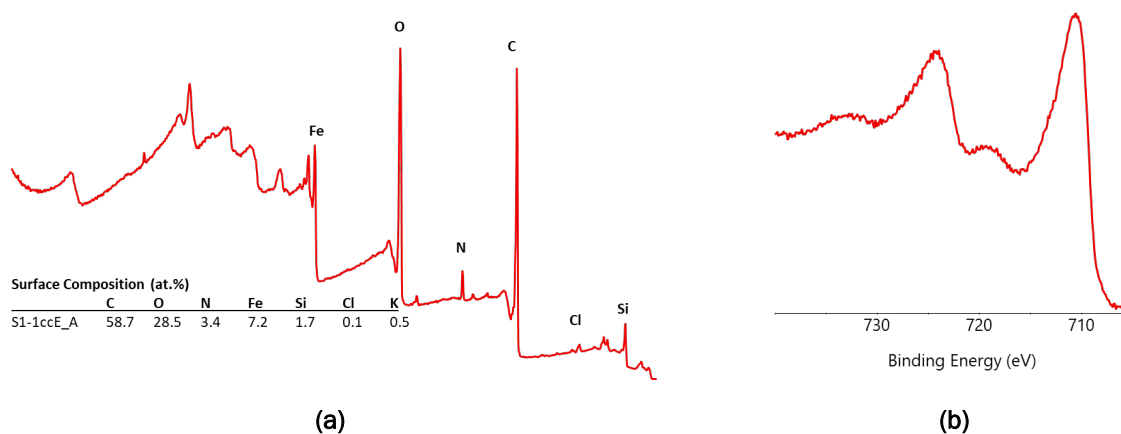


Figure II.3.1.9.11. (a) X-ray photoelectron wide-scan spectra quantifying the at.% of Fe at 7. (b) A high-resolution scan of the Fe 2p orbital bonding environment. Deconvolution of the high-resolution spectra will be performed to fully assign the Fe oxidation state and coordination state. Source: ORNL.

During this initial phase of the project, various design considerations were established for future scale-up. First, the feed consistency of the powdered pitch materials slightly above their softening points was problematic. Future work will consist of working with flake or pelletized materials, as shown in Figure II.3.1.9.12, to ensure the molten pitch charge is uniformly introduced into the catalytic environment. Even without the catalyst present, PAHs can react to higher molecular weights or coke at temperatures where dehydrogenation is possible. Unlike in melt-spinning where the pitch is expected to have negligible changes in viscosity while in the extrusion path, the viscosity rise during conversion to a mesophase pitch is likely to cause backflow of the pitch as flow becomes restricted. This was experienced in several of the initial trials and was overcome with more aggressive temperature offsets near the exit and will be a major consideration for future scaled-up reactor design.



Figure II.3.1.9.12. Binder pitch feedstock for next trials in pellet/flakes form to avoid issues associated with feed instability from caking events. Source: ORNL.

Conclusions

The pitch-processing concept was proven to work. However, improvements shall be taken into consideration for modification and scale-up of the unit to overcome challenges discussed in the project. Additionally, trials, evaluation, characterization, and analysis of more pitch sources shall be executed. Future upgrades for easier processability shall consist of the capability for material re-feed to extend reactor bed contact time will be added via a valve control in a second-generation design.

Key Publications

1. Klett, J., A. Naskar, L. Kearney, A. Clarke, and M. Theodore, 2023, “Catalytic flow reactor for valorization of polyaromatic hydrocarbon precursors to liquid crystal mesophases,” ORNL invention disclosure #81944342.
2. Theodore, M., and A. Naskar, 2023, “Carbon Fiber Technology Facility,” VTO Annual Merit Review, 12–15 June 2023, Virtual Event.

References

1. Mochida, I., S.-H. Yoon, and Y. Korai, 2002, “Mesoscopic structure, and properties of liquid crystalline mesophase pitch and its transformation into carbon fiber,” *Chem. Rec.*, 2(2), 81–101. <https://doi.org/10.1002/tcr.10016>.
2. Mochida, I., K. Kudo, K. Takeshita, R. Takahashi, Y. Suetsugu, and J. Furumi, 1974, “Modifying carbonization properties of pitches: 1. Conversion of benzene-insoluble matter of coal-tar pitch into graphitizable carbon,” *Fuel*, 53(4), 253–257. [https://doi.org/10.1016/0016-2361\(74\)90045-3](https://doi.org/10.1016/0016-2361(74)90045-3).
3. Lee, S. H., S. M. Lee, U.-S. Im, S.-D. Kim, S.-H. Koon, B.-R. Lee, D.-H. Peck, Y.-G. Shul, and D.-H. Jung, 2019, “Preparation and characterization of high-spinnability isotropic pitch from 1-methylnaphthalene-extracted low-rank coal by co-carbonization with petroleum residue,” *Carbon*, 155, 186–194. <https://doi.org/10.1016/j.carbon.2019.08.061>.
4. Zhang, W., J. T. Andersson, H. J. Räder, and K. Müllen, 2015, “Molecular characterization of large polycyclic aromatic hydrocarbons in solid petroleum pitch and coal-tar pitch by high-resolution MALDI ToF MS and insights from ion mobility separation,” *Carbon*, 95, 672–680 (2015). <https://doi.org/10.1016/j.carbon.2015.08.057>.

5. Kislov, V. V., A. I. Sadovnikov, and A. M. Mebel, 2013, “Formation mechanism of polycyclic aromatic hydrocarbons beyond the second aromatic ring,” *J. Phys. Chem. A*, 117(23), 4794–4816. <https://doi.org/10.1021/jp402481y>.
6. Kumar, S., and M. Srivastava, 2018, “Enhancement of mesophase formation in paraffinic-rich clarified oil using transition metal catalysts (Cr and Cu),” *Appl. Petrochem. Res.*, 9(1), 23–33. <https://doi.org/10.1007/s13203-018-0224-7>.
7. Klett, J., R. Hardy, E. Romine, C. Walls, and T. Burchell, 2000, “High-thermal-conductivity, mesophase-pitch-derived carbon foams: Effect of precursor on structure and properties,” *Carbon*, 38(7), 953–973. [https://doi.org/10.1016/S0008-6223\(99\)00190-6](https://doi.org/10.1016/S0008-6223(99)00190-6).
8. DOE-EERE, 2023, “Meet clean energy champion Merlin Theodore,” 28 February 2023. <https://www.energy.gov/eere/articles/meet-clean-energy-champion-merlin-theodore>.

Acknowledgements

The CFTF team would like to acknowledge our DOE sponsor; Dr. H. F. Wu, DOE VTO Technology Development Manager; and the ORNL Management/Team. Specific thanks go out to V. Kunc, L. Kearney, A. Clarke, D. Webb, F. Crowson, R. Strong, and R. Davies for their sponsorship, contributions, and/or support of the ORNL CFTF program.

II.3.1.10 Ultra-Lightweight Thermoplastic Polymer/Polymer-Fiber Composites for Vehicles (Pacific Northwest National Laboratory and Oak Ridge National Laboratory)

Kevin Simmons, Co-Principal Investigator

Pacific Northwest National Laboratory
Energy Processes and Materials Division
900 Battelle Blvd.
Richland, WA 99352
E-mail: kl.simmons@pnnl.gov

Amit Naskar, Co-Principal Investigator

Oak Ridge National Laboratory
Materials Science and Technology Division
1 Bethel Valley Rd.
Oak Ridge, TN 37830
E-mail: naskarak@ornl.gov

Rich Davies, Composites Core Program Manager

Oak Ridge National Laboratory
Materials Science and Technology Division
1 Bethel Valley Rd.
Oak Ridge, TN 37830
E-mail: daviesrw@ornl.gov

H. Felix Wu, DOE Technology Development Manager

U.S. Department of Energy
E-mail: Felix.Wu@ee.doe.gov

Start Date: August 17, 2020
Project Funding: \$375,000

End Date: September 30, 2023
DOE share: \$375,000

Non-DOE share: \$0

Project Introduction

PNNL and ORNL teamed up to develop ultra-lightweight, thermoplastic polymer-fiber and thermoplastic polymer matrix composites to reduce vehicle component mass. The approach is built on the fact that the mechanical properties of plastic materials, such as polypropylene (PP) and polyethylene (PE) (density ~ 0.9 g/cm³), can be improved by introducing a structural alignment of polymer chains and crystals during solid-phase processes like uniaxial stretching. The resulting enhanced polymer fibers with highly oriented morphology can then be mixed with common thermoplastic polymers and formed into high-performance PFRPs suitable for passenger vehicles. As a result, lightweighting and cost-reduction can be attained due to the removal of higher density fibers (e.g., CFs ~ 1.6 g/cm³, glass fiber ~ 2.6 g/cm³) with lower density fibers and matrices. In addition, using PFRPs can have several advantages over traditional glass-reinforced and CF-reinforced thermoset and thermoplastic polymers due to their high-specific strength and stiffness ratios,, impact performance, recyclability, and elimination of galvanic corrosion with Al and Mg joints.

Objectives

The project objective is to develop an all thermoplastic composite using polymer fibers to reduce the weight by 30%, have a < 3-minute cycle time, meet the broad cost penalty target of < \$5/kg-saved, and feature higher specific properties as described in the milestones below. The research aims to exploit melt- and solution-spun high-performance polymer fibers that have unique mechanical properties, chemical resistance, and thermal stability. With a new composite that is more recyclable due to the use of polymer fibers, the project will also demonstrate a scalable, adaptable approach for recycling these materials into new products with lower cost and higher manufacturing efficiency.

Approach

This project leverages existing processing methods and commercially available materials, promising lower cost and a short path to commercialization. The concept uses fiber-spinning capabilities at ORNL for solid-phase uniaxial fiber-processing to improve mechanical properties of performance polymers by inducing molecular alignment during the forming process. The project objectives will be met by developing ultra-high-strength, low-cost, lightweight polymer fibers from commodity plastics such as PP and polyester, and their highly drawn controlled crystallinity product with > 700 MPa strength. A major challenge in manufacturing polymer-polymer composites is avoiding dimensional instability during fabrication caused by shrinkage force from misorientation/relaxation of fiber polymers. To achieve this, partial crosslinking in fibers will be induced and new chemistries will be developed.

PNNL will develop fabrication techniques with high-quality temperature controls for controlling the rheological behavior of the polymer matrix and cooling for development of polymer morphology to minimize void fractions and maximize material property performance while achieving continuous compression molding or injection-molding under three-minute cycle times.

Results

The following summary includes the work for the completion of the project milestones for both PNNL and ORNL teams in FY 2023 listed in Table II.3.1.10.1. While PNNL focused on using commercial polymeric fibers available at an industrial-manufacturing scale for ultra-lightweight composite manufacturing, ORNL directed the in-house manufacturing of polymeric fibers followed by bench-scale fabrication of reinforced composites.

Table II.3.1.10.1. FY 2023 Milestones

Milestone Name/Description	Criteria	End Date
PM1: Demonstrate thermoplastic fiber-matrix injection mold compound	Retain at least 50% of the original fiber length.	12/31/2022
PM2: Investigate the mechanical performance of PFRPs	Achieve ~200 MPa composite strength at 5 GPa modulus made by < 3 min. molding cycle.	03/31/2023
PM3: Demonstrate the recyclability of PFRP wastes	Recycle and mold the wastes into 4 in. × 4 in. plaques and report material strength and modulus.	06/30/2023
PM4: Demonstrate the high mechanical performance of PFRPs	Deliver composite with > 500 MPa tensile strength, 10 GPa modulus, and > 5% elongation at break.	09/30/2023

Summary of PNNL Results

Project Milestone (PM)1, titled, “Demonstrate Thermoplastic Fiber-Matrix Injection Mold Compound Retaining at Least 50% of the Original Fiber Length,” was achieved by December 31, 2022. In this study, a woven fabric of PP fibers was cut into a rectangular shape. Longitudinal warp yarns were removed starting from the outer edge to obtain unidirectional fibers. A few warps remained to hold the shape during the composite curing process. HT tapes were placed at the ends of the wefts. The fibers were placed between low-density polyethylene films. The sandwiched plate was cured at 120°C for 20 minutes with a pressure of 1.38 MPa. The tapes and central warps were trimmed, and the remaining unidirectional PFRPs were collected. The PFRP plate manufacturing process is shown in Figure II.3.1.10.1. The final PP fiber length was set to 0.5 in. (12.7 mm). These unidirectional PFRPs and pure low-density polyethylene films were used as injection-molding compounds.

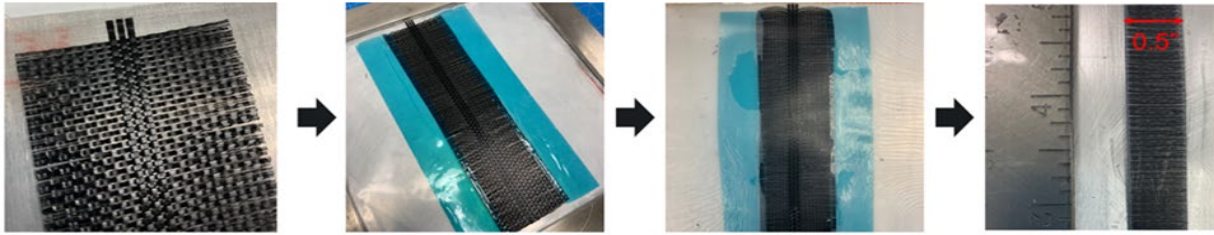


Figure II.3.1.10.1. PFRP plate manufacturing process with controlled unidirectional fiber length from a woven PP fabric. The PFRP plate was used for injection-molding to fabricate samples for the evaluation of fiber lengths. Source: PNNL.

An Electromatic 55E injection molder with custom-made molds was used to produce rectangular or square plates as shown in Figure II.3.1.10.2. The molding compounds were inserted through the feeding entrance at the top of the machine with a screw rotation speed of 60 revolutions per minute (rpm). The fiber composite compounds entered the barrel under controlled barrel temperatures. The barrel had three different temperature control systems: rear, front, and nozzle. For simplicity, the team set equal temperatures for the rear and front systems and set the nozzle system to a temperature set at 5°C higher. Two temperatures for the rear and front systems were selected: 132°C and 137°C. These temperatures were slightly higher than the onset of PP fibers (130°C) but lower than the peak-temperature of 149°C. The molten plastics were injected into the molds at two different injection speeds—0.3 in./s and 0.6 in./s (7.6 mm/s and 15.2 mm/s)—to observe the effect of the injection speed. A lower injection speed of 0.1 in./s (2.5 mm/s) was also investigated but did not lead to the successful modeling of the samples. In Figure II.3.1.10.2, the retained fiber lengths in the sample were measured using the ImageJ program, and the retained fiber lengths with various injection-molding parameters were summarized.

Out of three different injection-molding parameters in Figure II.3.1.10.2(c), two of them successfully retained the average fiber length above 50% of the original fiber length target for Identification number (ID) 1 at 70.2% and ID 2 at 51%. ID 3 retained an average fiber length of 48%, which was very close to the target percentage. Depending on the injection-molding parameters, some of the fibers increased their length due to the deformation during the injection-molding process.

Milestone PM2, titled “Investigate the Mechanical Performance of Polymer-Fiber-Reinforced Polymers (PFRPs),” was achieved by March 31, 2023. The objective of this milestone was to identify the combination of processing parameters in the composite fabrication process that can lead to the achievement of the criteria in PM2 and lay the foundation for achieving the high mechanical properties of PFRPs in PM4.

The investigated PFRPs are composed of ultra-high-molecular-weight polyethylene (UHMWPE) fibers as the reinforcement and high-density polyethylene (HDPE) in the polymer matrix. There is approximately a 20°C difference between the melting peak temperatures of the UHMWPE fiber and HDPE matrix, which ensures a wide processing temperature for the fabrication of the PFRPs without risking fiber strength degradation due to overshooting the temperature during molding.

Unidirectional UHMWPE-polymer-fiber-reinforced HDPE composites were used to demonstrate the composite strength and modulus required to meet the criteria outlined in PM2 above. The fabrication process involved two main steps: filament winding and compression molding. These steps are illustrated in Figure II.3.1.10.3(a-c). The entire composite fabrication process comprises five steps: (1) place HDPE films on a plate with a mandrel (127 mm × 152 mm), (2) wind UHMWPE fibers, (3) repeat the previous steps, (4) perform compression molding using a hot presser at a specific temperature and pressure, and (5) cool the composite down to RT at a rate of 5.5°C/min. Notably, the horizontal movement speed of the winder (v_h) varies with different fiber volume fractions (V_f).

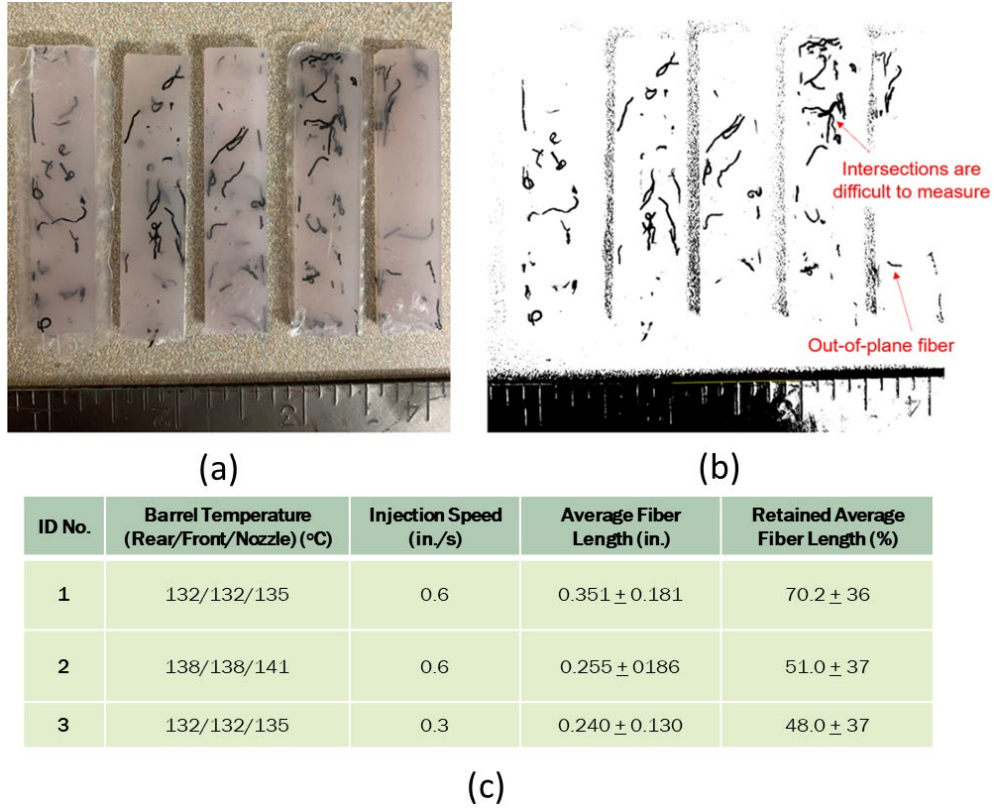


Figure II.3.1.10.2. (a-b) PFRP plates with controlled unidirectional fiber length from a woven PP fabric. The PFRP plate was used for injection-molding to fabricate samples for the evaluation of fiber lengths for (c) three different injection-molding parameters. Source: PNNL.

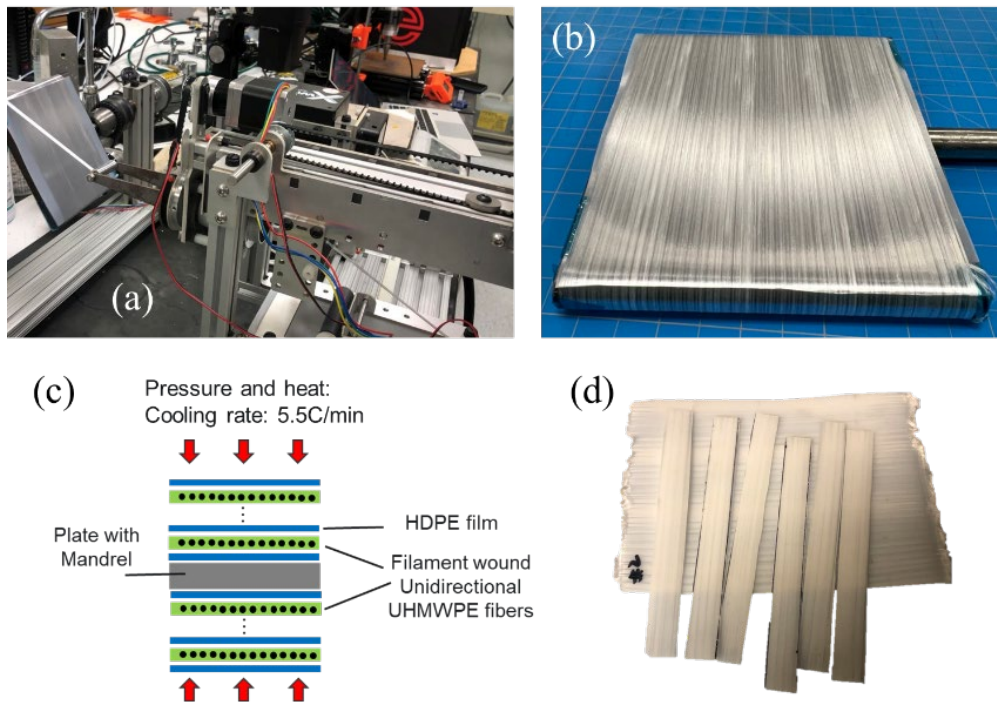


Figure II.3.1.10.3. (a-b) Filament winding of unidirectional UHMWPE fibers on HDPE films, (c) compression molding process of the composite, and (d) UHMWPE-fiber-reinforced HDPE composites. Source: PNNL.

During PM2, we investigated $V_f = 30\%$, with v_h set at 0.4 mm/s. We maintained the compression molding pressure (P) at 0.25 MPa, while we explored a range of processing temperatures. It is important to note that the investigation of different compression molding pressures was also conducted and is reported in the PM4 section. The investigated temperature range starts at 120°C and goes to 160°C, with an interval of 10°C. For the processing temperature at 120°C, UHMWPE fibers were not bonded with the HDPE matrix to form a composite, and intended mechanical tests were not performed to obtain the mechanical properties. For other processing temperatures, specimens with the dimension of 125 mm × 12.5 mm × 1.1 mm were cut from the composite panels, as shown in Figure II.3.1.10.3(d). Uniaxial tensile tests were performed by means of an electromechanical Instron 5582 load frame, and the displacement rate was about 2 mm/min. A digital imaging correlation technique was used to track the entire strain field of the composite in the gauge area of 65 mm × 12.5 mm to better understand the longitudinal failure behavior of the composites.

In Figure II.3.1.10.4, the longitudinal tensile strength and modulus of the investigated composites were plotted in red against the processing temperature. Additionally, the endothermic behavior of the individual material phases (e.g., UHMWPE fiber and HDPE matrix) in the composite was also plotted in black, as were the mechanical behaviors. It is evident from Figure II.3.1.10.4 that the composite with a fiber volume fraction (V_f) of 30% exhibited the longitudinal tensile strength and elastic modulus, measuring 420 MPa and 20 GPa, respectively, at processing temperatures of 130°C and 140°C. Notably, these temperatures are in proximity to the melting point of the HDPE matrix but significantly lower than the melting point of the UHMWPE fiber. However, the mechanical properties of the composites saw a dramatic decrease as the processing temperature increased up to 160°C. This phenomenon was attributed to fiber shrinkage and the melting of the reinforcing UHMWPE fibers, which began above 150°C, as observed in Figure II.3.1.10.5.

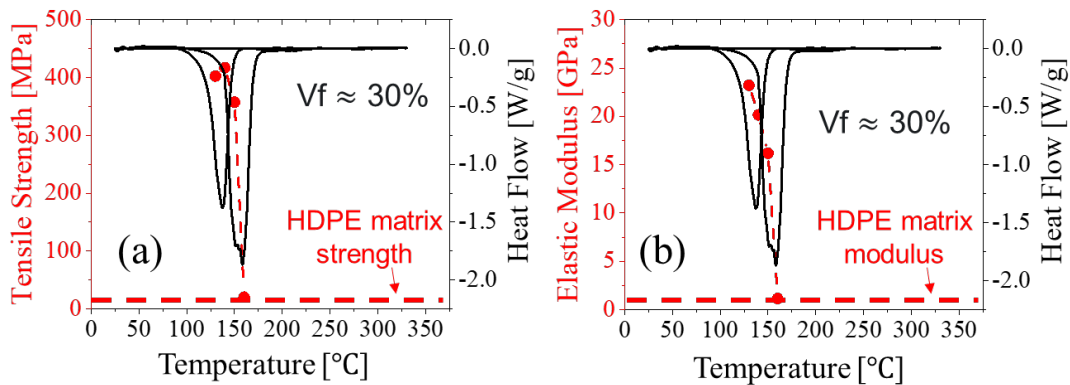


Figure II.3.1.10.4. (a) Longitudinal tensile strength and (b) modulus of unidirectional UHMWPE-polymer-fiber-reinforced HDPE composites ($V_f = 30\%$) as a function of processing temperature in compression molding. The results were plotted together with melting behaviors of UHMWPE fiber and HDPE matrix. Source: PNNL.

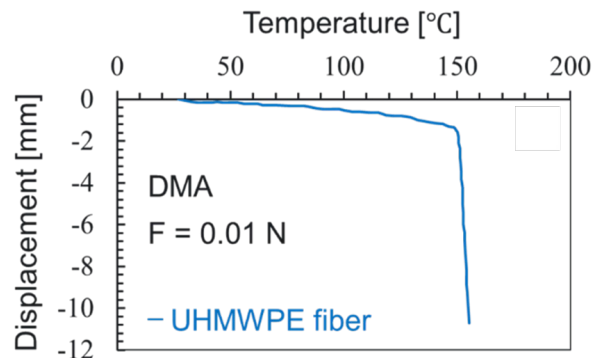


Figure II.3.1.10.5. Displacement as a function of temperature for UHMWPE fiber at a constant load of 0.01 N obtained from dynamic mechanical analysis. Source: PNNL.

Fracture morphologies and mechanisms of the composites ($V_f = 30\%$) fabricated at different temperatures were further investigated. As shown in Figure II.3.1.10.6(a), significant splitting cracks developed along the UHMWPE fiber direction when the unidirectional composite was loaded under tension right before the final failure at a processing temperature of 140°C , in addition to fiber breakage and delamination. However, at a processing temperature of 160°C , matrix yielding and necking due to strain localization dominated the failure behavior of the composite due to reinforcing UHMWPE fibers that were completely melted, losing oriented molecular chains, as observed in Figure II.3.1.10.6(b). This confirms the lower strength and modulus of the composite corresponding to a higher processing temperature, as previously discussed and shown in Figure II.3.1.10.4.

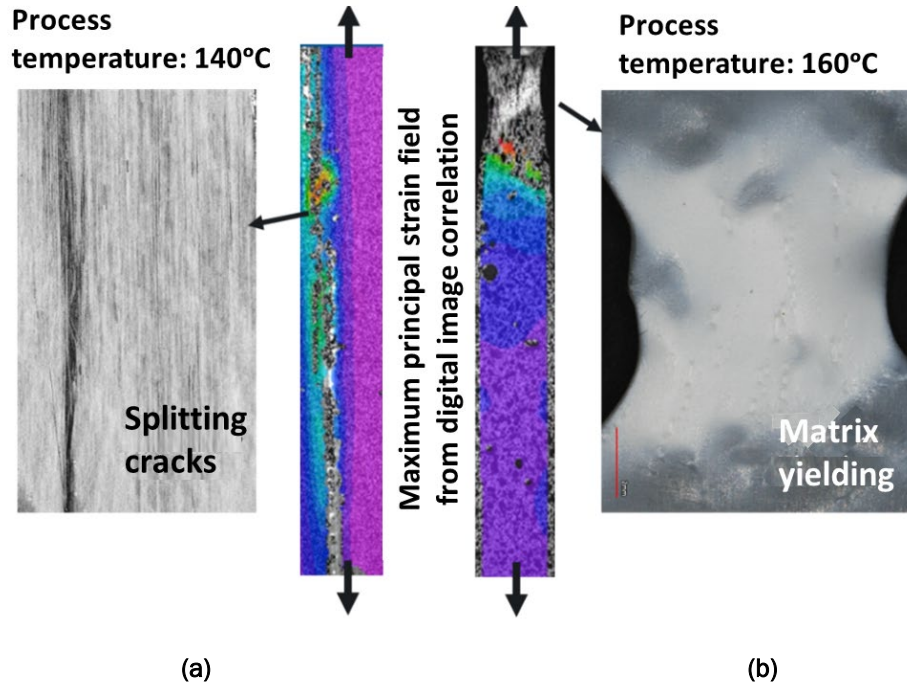


Figure II.3.1.10.6. Normalized maximum principal strain field and fracture morphologies of UHMWPE-polymer-fiber-reinforced HDPE composites fabricated at the temperature of (a) 140°C or (b) 160°C . This figure corresponds to the results almost at the peak load of the composite under uniaxial tension. Source: PNNL.

Milestone PM3, entitled “Demonstrate the Recyclability of PFRPs,” was achieved by June 30, 2023. The objective of this milestone was to explore recycling methods for PFRP waste, aiming to achieve the end-of-life use of the PFRPs. Self-reinforced PP woven composites were used as an example to demonstrate the mechanical recycling of the PFRPs via injection-molding using chopped composite materials, as shown in Figure II.3.1.10.7. In the injection-molding process, there are various processing parameters, including molding temperature (T), injection speed (V_i), screw drill speed (V_s), cooling rate (T_c), and composite chip size (C_s) for feeding into the molder. In this study, we focused on investigating the molding temperature and composite chip size on the tensile properties of recycled, self-reinforced PP woven composites.

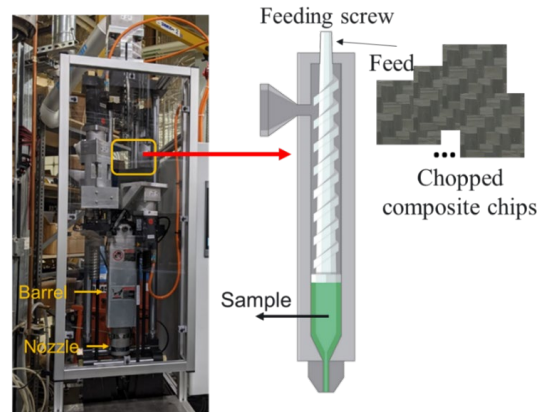


Figure II.3.1.10.7. Mechanical recycling of self-reinforced PP woven composites by injection-molding using chopped composite chips. Source: PNNL.

We investigated different sets of processing parameters in the injection-molding process: (1) $T = 165^{\circ}\text{C}$ and $C_s = 0.5 \text{ in.} \times 0.5 \text{ in.}$; (2) $T = 165^{\circ}\text{C}$ and $C_s = 0.25 \text{ in.} \times 0.25 \text{ in.}$; (3) $T = 170^{\circ}\text{C}$ and $C_s = 0.5 \text{ in.} \times 0.5 \text{ in.}$; (4) $T = 170^{\circ}\text{C}$ and $C_s = 0.25 \text{ in.} \times 0.25 \text{ in.}$; (5) $T = 180^{\circ}\text{C}$ and $C_s = 0.5 \text{ in.} \times 0.5 \text{ in.}$; and (6) $T = 180^{\circ}\text{C}$ and $C_s = 0.25 \text{ in.} \times 0.25 \text{ in.}$. The investigated processing temperature range was chosen based on the endothermic behavior of self-reinforced PP woven composite, as shown in Figure II.3.1.10.8, whereas the composite chip size was decided based on the representative unit cell size of the composite $\approx 0.5 \text{ in.} \times 0.5 \text{ in.}$. Regarding the first two sets, the molding temperature of $T = 165^{\circ}\text{C}$ is between the onset and peak melting temperatures of the self-reinforced PP woven composite, as observed in Figure II.3.1.10.8. As a result, the composite chips exhibited high-viscosity, which hindered successful injection-molding despite attempting various processing parameters. For sets (3) to (6), we successfully produced recycled composites using chopped composite chips. As for the other fixed processing parameters in this study, an injection speed of $V_i = 0.75 \text{ in./s}$, a screw speed of $V_s = 30 \text{ rpm}$, and a cooling process consistently controlled using the metal molds at RT. The mechanical properties of the recycled composites were evaluated by conducting quasi-static tensile tests under displacement control with a displacement rate of 10 mm/min . The specimens followed Type V dimensions as recommended in ASTM D638. The specimens were directly molded into tensile specimens instead of $4 \text{ in.} \times 4 \text{ in.}$ plaques to minimize the plaque location variation.

For the recycled PP composites using the same chip size but different molding temperatures, it is evident from Figure II.3.1.10.9 that the failure strain increases significantly as the molding temperature increases from 170°C to 180°C . For the chip size of $0.5 \text{ in.} \times 0.5 \text{ in.}$, as observed in Figure II.3.1.10.9(a–b), the failure strain can increase by approximately ten times. For a smaller chip size of $0.25 \text{ in.} \times 0.25 \text{ in.}$, as indicated in Figure II.3.1.10.9(c–d), the failure strain can increase by approximately 20 times. This phenomenon can be explained by the fact that a higher temperature leads to the melting of a greater amount of reinforcing PP fibers. Consequently, the recycled composites molded at higher processing temperatures exhibit much greater ductility compared to those molded at lower processing temperatures.

For the recycled PP composites using the same molding temperature but different chip sizes, it is observed from Figure II.3.1.10.9 that while chip size does not significantly change the tensile properties of the composites molded at 170°C , the chip size can noticeably affect the failure strain of the composites molded at a higher temperature, as indicated in Figure II.3.1.10.9(b–d). The explanation requires further investigation of microstructural morphology before conducting the tensile tests. However, the results clearly showed the dependency between processing temperature and chip size on the failure behavior of recycled composites. However, the investigated sets of parameters did not significantly affect the tensile strength and elastic modulus of the recycled composites. The tensile strength was approximately 40 MPa , while the elastic modulus was around 540 MPa . The differences among the investigated sets of parameters were within 10%. The tensile strength and elastic modulus of the recycled PP composites were $2\times$ and $1.4\times$ higher than that of the pure PP polymers, respectively.

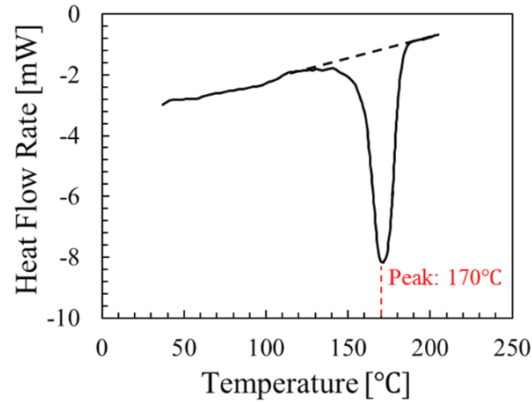


Figure II.3.1.10.8. Process conditions for the mechanical recycling of self-reinforced PP woven composites by injection-molding using chopped composite chips. Source: PNNL.

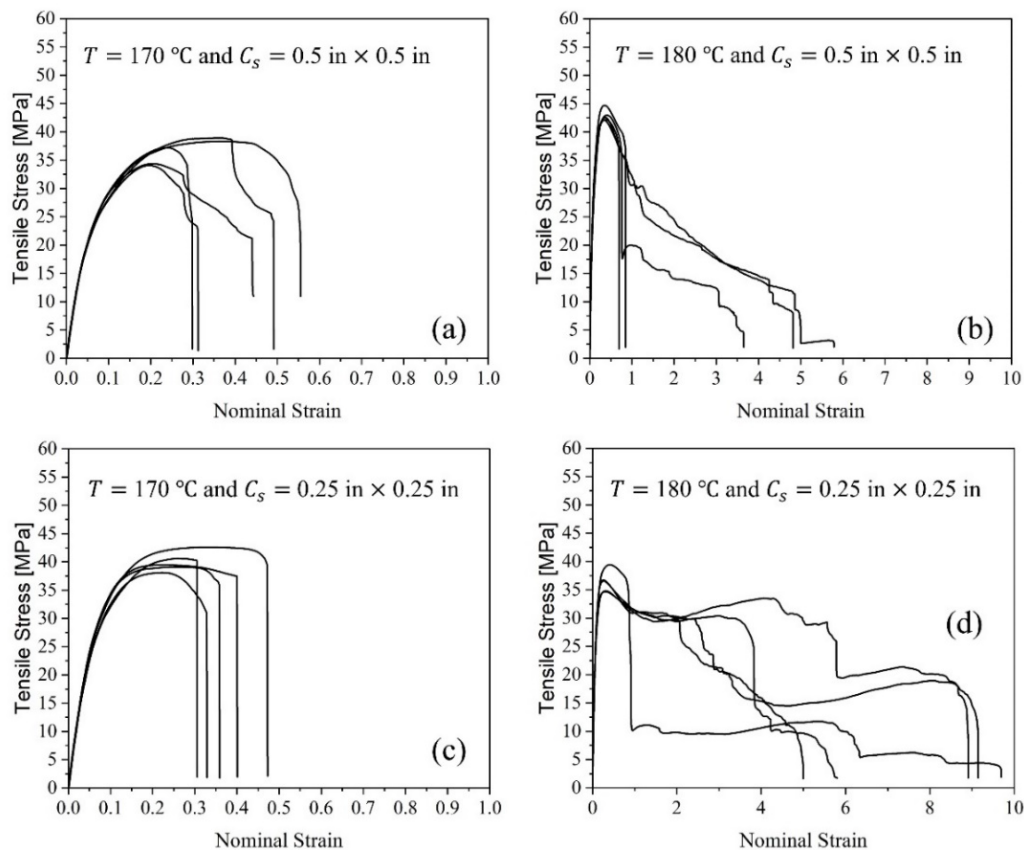


Figure II.3.1.10.9. Recycled PP composites via injection-molding with different sets of parameters: (a) $T = 170\text{ }^{\circ}\text{C}$ and $C_s = 0.5\text{ in.} \times 0.5\text{ in.}$; (b) $T = 180\text{ }^{\circ}\text{C}$ and $C_s = 0.5\text{ in.} \times 0.5\text{ in.}$; (c) $T = 170\text{ }^{\circ}\text{C}$ and $C_s = 0.25\text{ in.} \times 0.25\text{ in.}$; and (d) $T = 180\text{ }^{\circ}\text{C}$ and $C_s = 0.25\text{ in.} \times 0.25\text{ in.}$. Note: injection speed, screw speed, and the cooling process were all fixed. Details can be found in the report. Source PNNL.

Milestone PM4, entitled “Demonstrate the High Mechanical Performance of PFPRs with $>500\text{ MPa}$ Tensile Strength, 10 GPa Modulus, and $>5\%$ Elongation at Break,” was achieved by September 30, 2023. The milestone objective was to optimize all the processing parameters in the composite fabrication process of UHMWPE-fiber-reinforced HDPE polymers based on the studies in PM2, and to investigate different fiber volume fractions and compression molding pressures to reach the criteria of PM4.

The longitudinal tensile strength (S) and elastic modulus (E) of the composite as functions of T , P , and V_f were plotted in Figure II.3.1.10.10. Similar to the observation from the studies during PM2, T increases while P and V_f remain fixed. The mechanical behavior of the composite does not initially exhibit significant changes. However, it undergoes a sudden reduction as the processing temperature increases towards the melting onset temperature of the HDPE matrix and surpasses 150°C . This temperature-dependent behavior of UHMWPE fiber can also be directly observed from the cross-section of the composite obtained using optical microscopy. As illustrated in Figure II.3.1.10.11(a), the composite with $V_f = 38\%$ and $T = 140^\circ\text{C}$ shows that UHMWPE fibers are distributed and embedded in the HDPE matrix, with a significant fraction of the fibers bonded together because the process T was very close to the melting on-site temperature of the fiber.

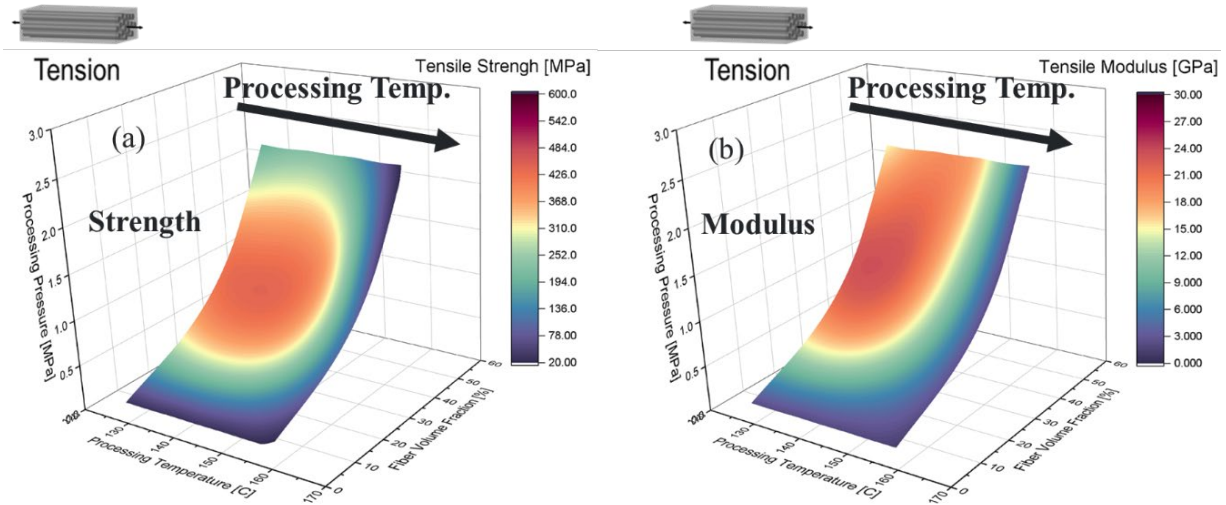


Figure II.3.1.10.10. (a) Longitudinal tensile strength and (b) elastic modulus of UHMWPE-fiber-reinforced HDPE composites as functions of processing temperature, processing pressure, and fiber volume fraction. Source: PNNL.

The bonded fibers did not noticeably affect the mechanical behavior of the composite since only the surface of the fiber was slightly melted, as can be seen in Figure II.3.1.10.11, and the fiber reinforcing capability was not significantly decreased, as indicated by the DSC and dynamic mechanical analysis results. In the case of the composite with the same V_f but a $T = 150^\circ\text{C}$, most UHMWPE fibers were melted and bonded completely, as shown in Figure II.3.1.10.11(b). Consequently, the reduced mechanical behavior of the fibers led to a reduction of the composite strength and modulus, as plotted in Figure II.3.1.10.10 above. The optimized S and E of the composite were 570 MPa and 30 GPa , respectively, with 8% elongation at failure. The properties reached the criteria of PM4, which was achieved under a combined condition of $T = 140^\circ\text{C}$, $P = 0.25\text{ MPa}$ to 1.25 MPa , and $V_f = 38\%$. In addition, using higher processing pressure in the composite fabrication process can lead to the misalignment of unstitched unidirectional fibers, while composites with a higher fiber volume fraction tend to have more defects, which reduces strength but enhances post-peak ductility. Future work in this project will focus on optimizing the composite fraction within the framework of compression molding to further improve the mechanical behavior of PFPRs in general with a higher fiber volume fraction.

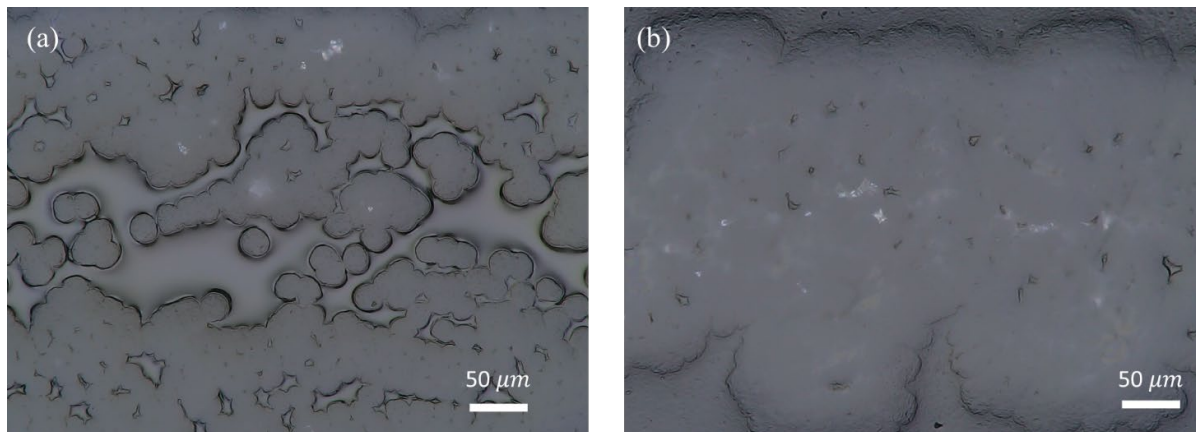
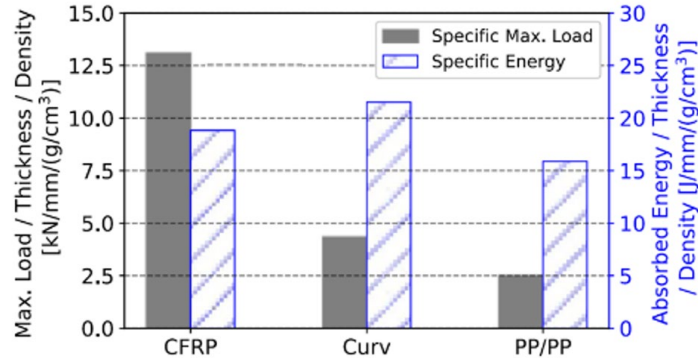


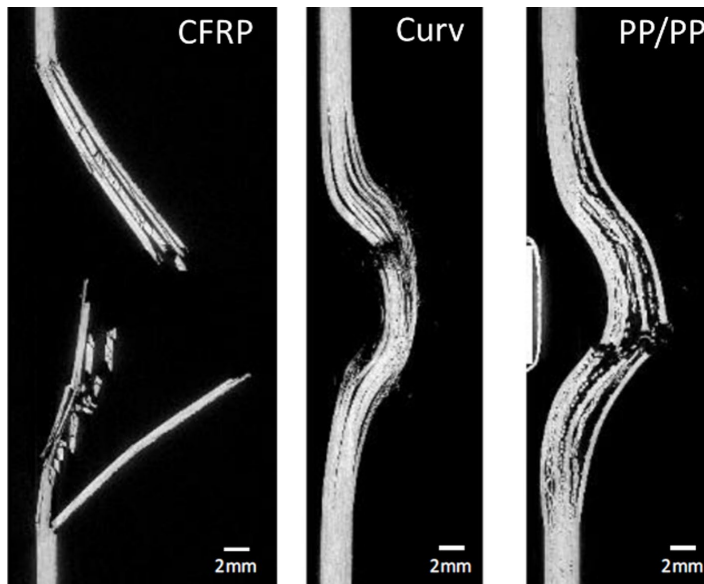
Figure II.3.1.10.11. UHMWPE-fiber-reinforced HDPE composites with the same $V_f = 38\%$ and $P = 1.25$ MPa but different temperatures: (a) $T = 140^\circ\text{C}$ and (b) $T = 150^\circ\text{C}$. Source PNNL.

Additionally, we conducted a research task to demonstrate the ductility of PFRPs by investigating their impact behaviors and comparing them with those of CFRPs. Three different polymer composites were tested. The first is a CFRP composite, manufactured using woven T700S fibers in combination with G-83C thermoset resin from Toray. The compression molding process was used to produce flat plates with an average thickness of 1.63 mm. Two types of PFRPs were manufactured. Both composites, referred to as Curv (a commercially available, self-reinforced PP woven composite from Propex) and PP/PP, were composed of PP fibers and a PP matrix. For Curv, eight layers were stacked to achieve an average thickness of 2.72 mm. The PP/PP was manufactured using PP fibers from Tencate and PP films. Three layers of woven fibers were combined with four films to create flat panels with an average thickness of 2.61 mm. Both Curv and PP/PP were manufactured using the compression molding technique with a hot press. Uncured laminates were pressed between two flat aluminum molds under a pressure of 2.75 MPa. The molds were heated to 170°C for Curv and 130°C for PP/PP, and the elevated temperatures were maintained for 20 minutes before gradually cooling to RT at a rate of 2.7°C per minute. After the curing process, each plate was trimmed to dimensions of 127 mm by 127 mm.

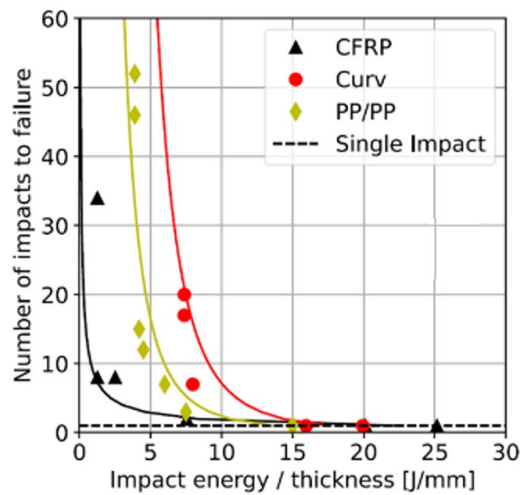
We used a simple drop-weight tower to apply low-velocity impacts following ASTM D7136 guidelines. The details for the testing configuration can be found in our publications. We conducted both single impact to perforation and multiple impacts to perforation to evaluate the ductility of the PFRPs. For single impact to perforation, Figure II.3.1.10.12(a) summarizes the results for the three different composites. In terms of specific absorbed energy (normalized by density), PFRPs is comparable to or even higher than that of CFRP. In the case of Curv, the specific absorbed energy is 25% higher than the CFRP, while PP/PP is 6% below the CFRP. Figure II.3.1.10.12(b) showcases representative failure images of three composites. The brittle failure mode of CFRP is clearly evident with delamination and fiber breakage. In contrast, PFRPs demonstrate elongated fibers that are plastically bent, which contrasts with the behavior of CFs. While CFRPs demonstrate higher energy absorption capability in a single impact, the opposite is observed for multiple impacts to perforation, as shown in Figure II.3.1.10.12(c). For example, when the applied impact energy per thickness is around 7.5 J/mm, the CFRP can only withstand two impacts, whereas Curv can withstand 20 impacts, and PP/PP can withstand three impacts. The differences become more pronounced as the applied impact energy decreases. At 5.98 J/mm, Curv remains unbroken even after 400 impacts, which is not shown in Figure II.3.1.10.12(c), while the CFRP can only withstand eight impacts at half the impact energy (e.g., 2.51 J/mm). By setting the number of impacts to failure equal to 200 and using the trend lines in Figure II.3.1.10.12(c), it is determined that Curv and PP/PP have impact endurance limits that are 370 and 200 times higher compared to CFRP. These findings highlight the remarkable impact resistance of PFRPs compared to CFRPs, demonstrating the ductility of PFRPs.



(a)



(b)



(c)

Figure II.3.1.10.12. (a) Summary of impact resistances of CFRP and PFRPs. (b) Through-thickness views of perforated CFRP and PFRPs using X-ray micro computed tomography scan. (c) Summary of the CFRP and PFRPs for low-energy, multiple impact performances. Source: PNNL.

Summary of ORNL Results

The goal of the first milestone, PM1, is to demonstrate that a thermoplastic fiber/thermoplastic matrix compression molding compound retains 50% of the original fiber length while maintaining mechanical properties. The self-reinforced polymer composite (SRPC) laminate was fabricated by incorporating 30 wt.% PP fiber reinforcement into a PP-compatible matrix through hot press, as shown in Figure II.3.1.10.13.

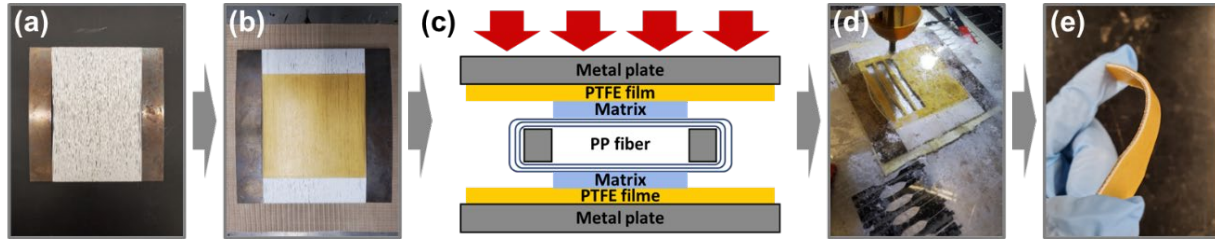


Figure II.3.1.10.13. The overall hot process to fabricate SRPC laminate using PP fiber reinforcement and PP-compatible matrix. (a) PP fiber wound on a stainless-steel frame. (b) PP fiber sandwiched by two PP-compatible matrix sheets. (c) Scheme of the hot press process. (d) Waterjet-cutting. (e) Dumbbell-shaped tensile specimen of SRPC laminate. Source: ORNL.

PP fiber reinforcement was uniaxially wound on a custom stainless-steel frame featuring a 10 cm × 10 cm window. The PP fibers were then sandwiched between two PP-compatible matrix sheets and compressed under high-temperatures using a laboratory press and two Teflon films. The SRPC laminate was cooled down to RT by circulating water under pressure. Six dumbbell-shaped tensile bars were prepared along the longitudinal direction for mechanical testing. No visible delamination or shrinkage of the fiber reinforcement was observed, indicating good adhesion between the matrix and fibers. Figure II.3.1.10.14 displays mechanical properties of PP fiber, PP-compatible matrix, and SRPC laminate, which contains 30 wt.% PP fibers, along with the properties of bulk PP as a reference.

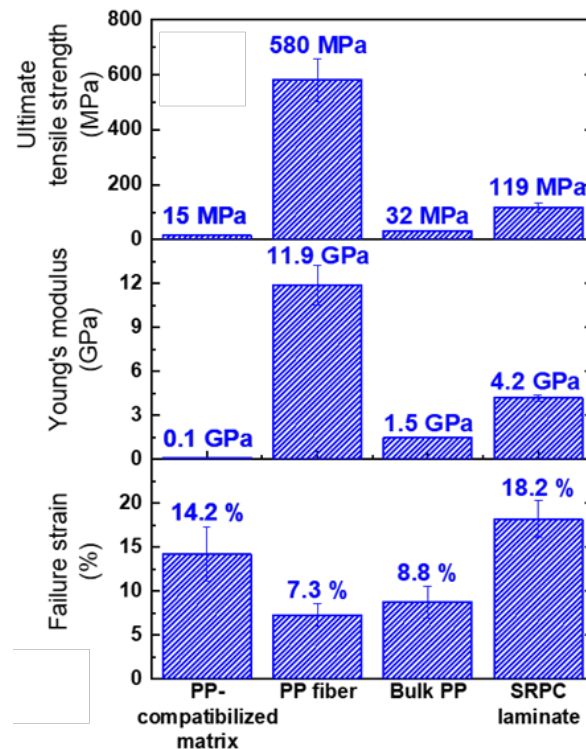


Figure II.3.1.10.14. Mechanical properties of PP fiber, PP-compatible matrix, and SRPC laminate containing 30 wt.% PP fibers along with those of bulk PP as a reference. Source: ORNL.

In the case of PP fiber drawn with a draw ratio of 18, the tensile strain-stress curve exhibited limited ductility until reaching a maximum stress of 580 MPa. The failure strain of the PP fiber (7-9%) was nearly identical to the strain at peak or UTS of the SRPC laminate. This was due to the fracture of the fiber reinforcements between the two matrix sheets. After the PP fiber reinforcements began to fracture at the UTS in the SRPC laminate, the load gradually dropped until the elongation at break of the PP-compatible matrix at 14.2%. The gradual decrease in tensile stress beyond the UTS is likely due to the individual failures of PP fibers with the support of the PP-compatible matrix. When compared to bulk PP, the SRPC laminate containing 30 wt.% unidirectional PP fibers shows a higher maximum tensile strength (32 → 119 MPa), Young's modulus (1.5 → 4.2 GPa), and even elongation at break (8.8 → 18.2%) due to the sequential fracture of the PP fiber reinforcements that are welded with PP matrix.

In the presented processing method, no fiber attrition occurred. So, the fibers retained original characteristics (e.g., 100% length retention). Furthermore, performance-wise with a 30% fiber fraction of the original PP fiber (e.g., 580 MPa strength), our goal was to demonstrate composite properties with high fiber performance retention. The fiber strength with 100% strength retention should have been 174 MPa. Instead, the best that could be achieved was ~120 MPa, which shows nearly ~70% fiber property retention via molding or thermal cycling process. Thus, we progressed significantly to meet part of our second performance goal or milestone. Going forward, our focus will be to increase the fiber fill fraction in the composites to further improve composite performance.

PM2 involves demonstrating a composite with ~200 MPa composite strength and 5 GPa modulus, produced via a < 10-minute molding cycle. Figure II.3.1.10.15 shows the fabrication process for the polymer-polymer composite, which involved melt-fiber-spinning and a subsequent drawing of a blend composed of 90 wt.% neat PP as a reinforcing material and a 10 wt.% PP-compatible matrix, followed by hot compaction.

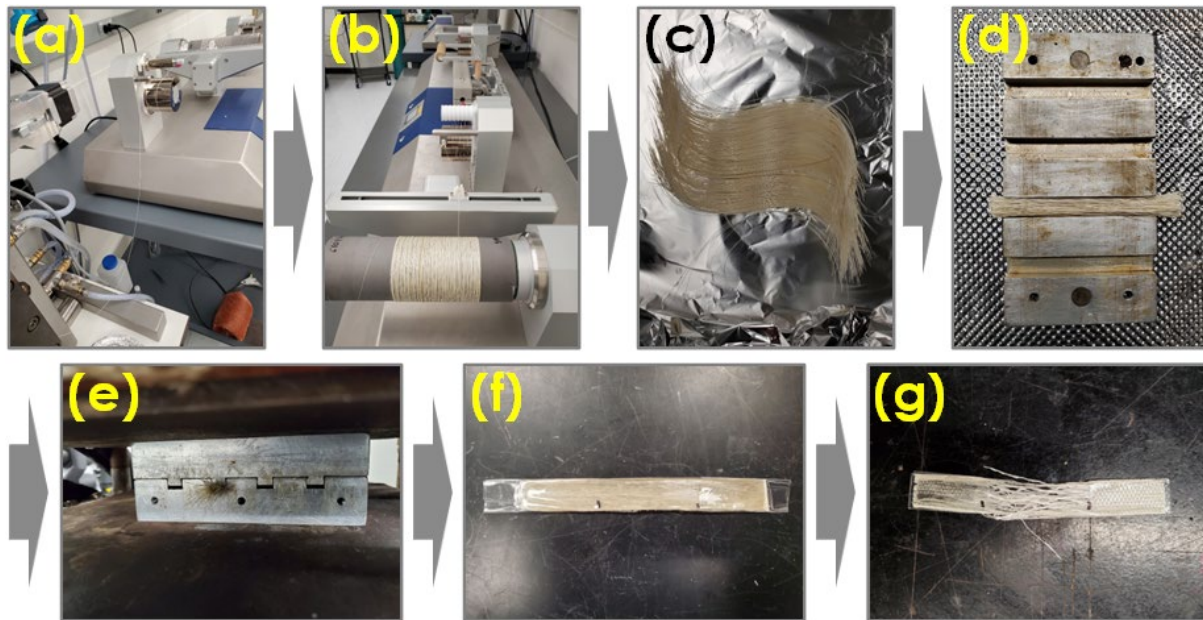


Figure II.3.1.10.15. (a) Melt-fiber-spinning. (b) Fiber drawing a fiber bundle in a custom-mold. (c) Before and (d) after hot compaction. (e) Digital image of compaction process. Strap specimen (f) before and (g) after tensile testing. Source: ORNL.

Initially, neat PP and PP-compatible matrix pellets were fed into a micro-compounder. The components were mixed for ~10 minutes with a screw speed of 100 rpm, and the resulting melt was extruded through a 0.5 mm die, as illustrated in Figure II.3.1.10.15(a). The as-spun PP fiber was collected and stretched through a two-stage fiber drawing process, as shown in Figure II.3.1.10.15(b). The degree of stretching was controlled by altering the speed differential between the feed and take-up rollers, resulting in the draw ratio of take-up speed

to feed speed. The first and second fiber drawings were carried out with a constant draw ratio of 10 and 1.4, respectively, resulting in a total draw ratio of 14. The stretched fibers were cut into 12-cm lengths, as shown in Figure II.3.1.10.15(c), and fibers were placed in a custom-made mold, as shown in Figure II.3.1.10.15(d). The bundle of fibers was compressed at various temperatures (i.e., 130°C, 140°C, 150°C, and 160°C) to assess the compaction temperatures under high-pressure (~150 MPa), as illustrated in Figure II.3.1.10.15(e). During the hot compaction, the PP-compatible matrix selectively melted and bonded PP fibers, as shown in Figure II.3.1.10.15(f), which were reinforced by fiber drawing. The strap specimen was subjected to mechanical testing, and the failure was predominantly observed between fibers because the tensile strength of the matrix was weaker than the reinforcing fibers. Figure II.3.1.10.16 shows the mechanical properties of PP fiber-reinforced PP composites fabricated at various compaction temperatures (i.e., 130°C, 140°C, 150°C, and 160°C) are presented. The optimal compaction temperature was found to be 140°C, where the matrix was selectively melted, while the crystals of reinforcing PP fiber were preserved. We demonstrated fabrication of composite with nearly 218 MPa strength at 5 GPa Young's modulus made via a < 10-minute molding cycle and met the second milestone (e.g., PM2).

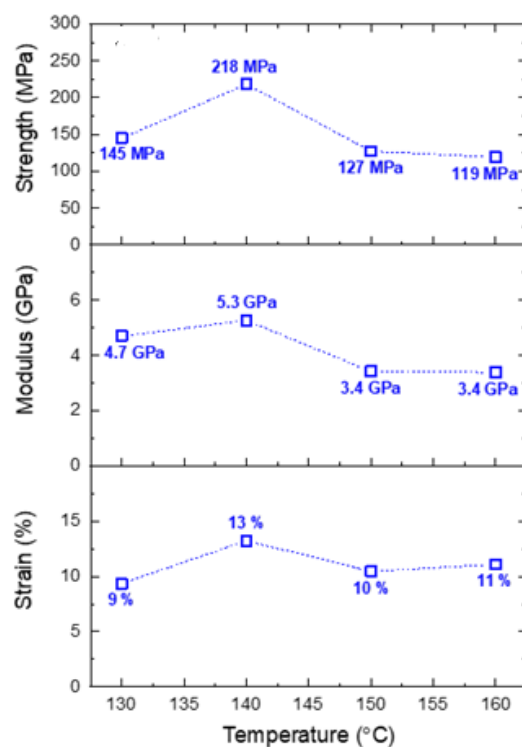


Figure II.3.1.10.16. The mechanical properties of PP fiber-reinforced PP composites fabricated at various compaction temperatures of 130 °C, 140 °C, 150 °C, and 160 °C. Source: ORNL.

The third milestone (e.g., PM3) was set to evaluate the recyclability of the polymer-polymer composite. The material system developed for the polymer-polymer composite was recycled and molded into 4 in. × 4 in. plaques, and the mechanical properties were evaluated using tensile testing. Figure II.3.1.10.17 shows the recycling process for the polymer-polymer composite, which involved remelting and subsequent hot compaction using a press. Figure II.3.1.10.17(a) shows the material system developed for polymer-polymer composite, as presented in earlier sections. The polymer fibers were cut into short lengths, as shown in Figure II.3.1.10.17(b), and fed into a micro-compounder, as presented in Figure II.3.1.10.17(c). The short fibers were melted homogeneously for 10 minutes and then extruded, as shown in Figure II.3.1.10.17(d). The resulting filament was cut into small pieces, as shown in Figure II.3.1.10.17(e), and hot-pressed within a ~1mm metal frame, resulting in a 4 in. × 4 in. plaque, as shown in Figure II.3.1.10.17(f). To assess the mechanical properties of the recycled material, we cut the plaque into multiple tensile bars using a waterjet cutter, as shown in Figure II.3.1.10.17(g). The final tensile bar is presented in Figure II.3.1.10.17(h).

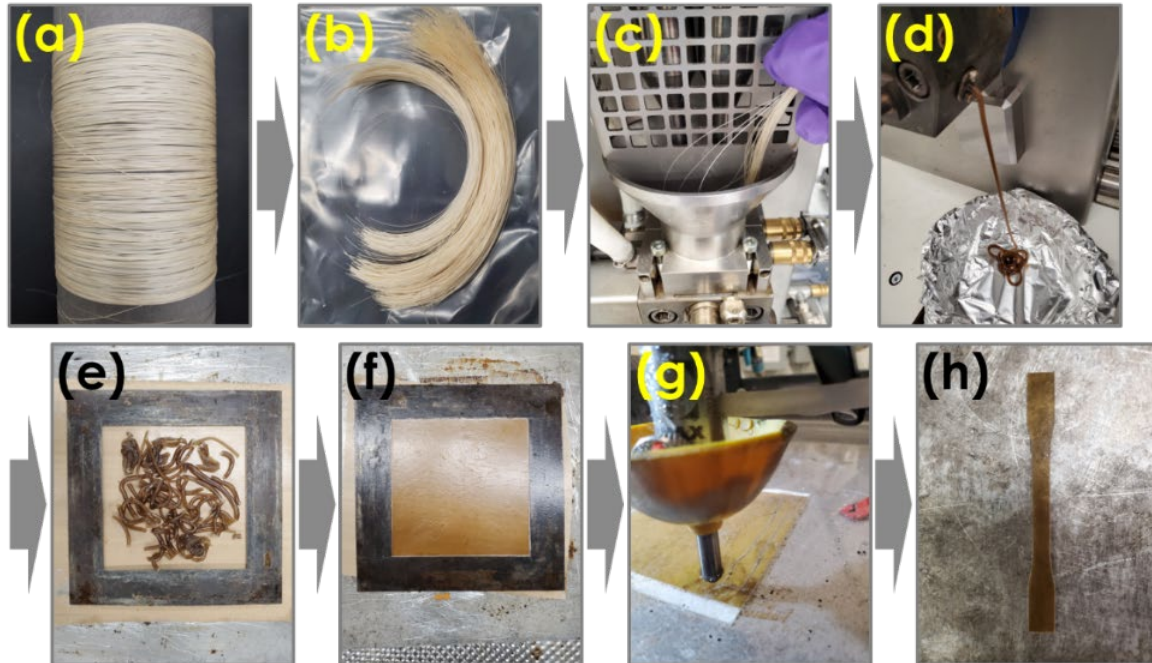


Figure II.3.1.10.17. Recycling process for the polymer-polymer composite. (a) Melt-spun polymer-fiber. (b) Shortened polymer-fiber lengths after cutting. (c) Feeding the cut fiber into a micro-compounder. (d) Re-melted polymer material. (e) Shredded materials in a metal frame. (f) Hot compaction resulting in a plaque. (g) Waterjet-cutting of the plaque. (h) Final tensile bar. Source: ORNL.

Figure II.3.1.10.18 shows the strain-stress curves obtained from six samples. We obtained an average tensile strength, Young's modulus, and failure strains of 28.1 MPa, 0.6 GPa, and 7%, respectively. Since the thermal history of the reinforcing polymer-fiber, such as chain orientation and stretching, was removed beyond the equilibrium melting temperature of the reinforcing PP, the mechanical properties of the recycled material were nearly identical to the neat PP before fiber drawing, which has a tensile strength of ~31 MPa and a Young's modulus of ~1 GPa.

Since PP fibers made in-house from commodity PP grades could only deliver 800–900 MPa tensile strength, the same approach was applied with a different materials system (aligned polyethylene fibers in an ethylene copolymer matrix) to achieve PM4 that aimed for a 500 MPa tensile strength composite for elongations up to 5%. The goal was to demonstrate how the approach involving PP systems is translational for polyethylene systems. The difficulty in achieving high-strength, self-reinforced composites lies in the overlap of fusion heat in the matrix and reinforcing phases. The reinforcing fiber phase relies on significant orientation development to induce a high-degree of crystallinity and chain alignment along the axial direction of the fibers. When laying up composites with overlapping heat of fusion, the thermomechanical processing required for the matrix infiltration enables chain relaxation and crystallite melting to the detriment of the overall composite strength. The incorporation of comonomer in the matrix phase reliably suppresses heat of fusion to provide a processing window such that infiltration of the matrix material can occur without relaxing the reinforcing phase. To assess the melting temperature of the polyethylene fiber and the ethylene copolymer matrix phases, DSC was performed. Figure II.3.1.10.19 shows the thermographs of the separate phases having undergone a 5°C/min. heating cycle. Results indicate the onset of ethylene copolymer melting occurs at about 90°C, while the highly oriented polyethylene fibers showed the onset of melting at about 145°C. Given this, pressing temperatures were selected at 100°C, which is on the lower end of the processing window to ensure minimal relaxation.

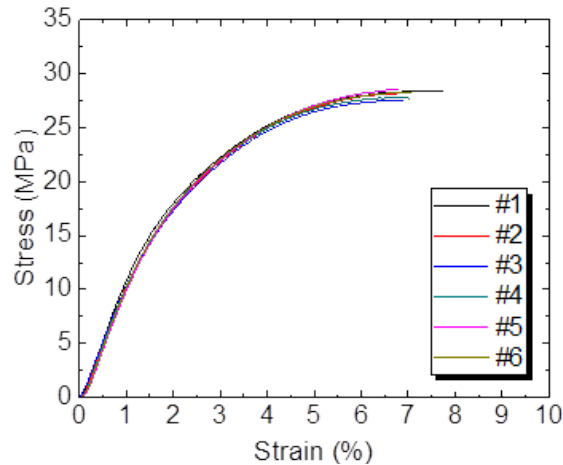


Figure II.3.1.10.18. Stress-strain curves of recycled polymer-polymer composite. Source: ORNL.

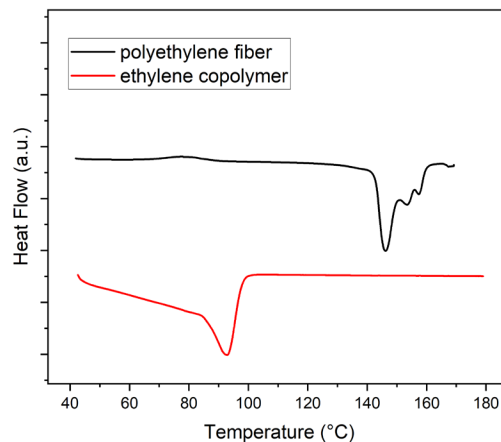


Figure II.3.1.10.19. DSC thermogram showing melting behavior of highly oriented polyethylene fiber (black) and ethylene copolymer (red). Onset of melting occurred at approximately 140°C and 90°C for the polyethylene and ethylene copolymer, respectively. Source: ORNL.

To fabricate the composite prior to filament winding, non-stick sheets were secured to each side of a 6-in. plate, and sheets of polyethylene copolymer were secured atop each non-stick sheet. Pre-pressed composites were then constructed by winding highly oriented polyethylene fiber around the plate using a lab-scale winder, as observed in Figure II.3.1.10.20(a–b), a 90-degree winding direction relative to the rotational axis of the plate, and a wrap offset of 1/16 in. A total of three passes were made, and ethylene copolymer sheets were placed between each layer. A schematic of the final construction of the wound plate is shown for clarity in Figure II.3.1.10.20(c). After layup construction, Teflon non-stick sheets were placed on each side of the composite construction, and the samples were pressed between two steel plates at 100°C with 20,000 lbs. of force for 20 minutes. After pressing, samples were cooled to RT before removing them to prevent warping. After cooling, pressed composite samples were removed from the winding plate and placed in a frame before cutting the samples using a laser cutter for tensile testing as shown in Figure II.3.1.10.20(d). Resulting specimens had rectangular geometries with dimensions of 85 × 7.0 × 0.5 mm, as indicated in Figure II.3.1.10.20(e). After composite samples were constructed, as can be seen in Figure II.3.1.10.20(f), tensile testing was performed to assess the mechanical properties of the composite samples. Figure II.3.1.10.21 shows the results after performing tensile testing using a crosshead speed of 10 mm/min. Samples displayed an average UTS of 87 MPa, and tensile strengths of > 500 MPa at 5% elongation, meeting the final milestone (e.g., PM4). Using a linear best fit in the linear regime of the stress-strain curve, the average modulus was 19.7±2.6 GPa.

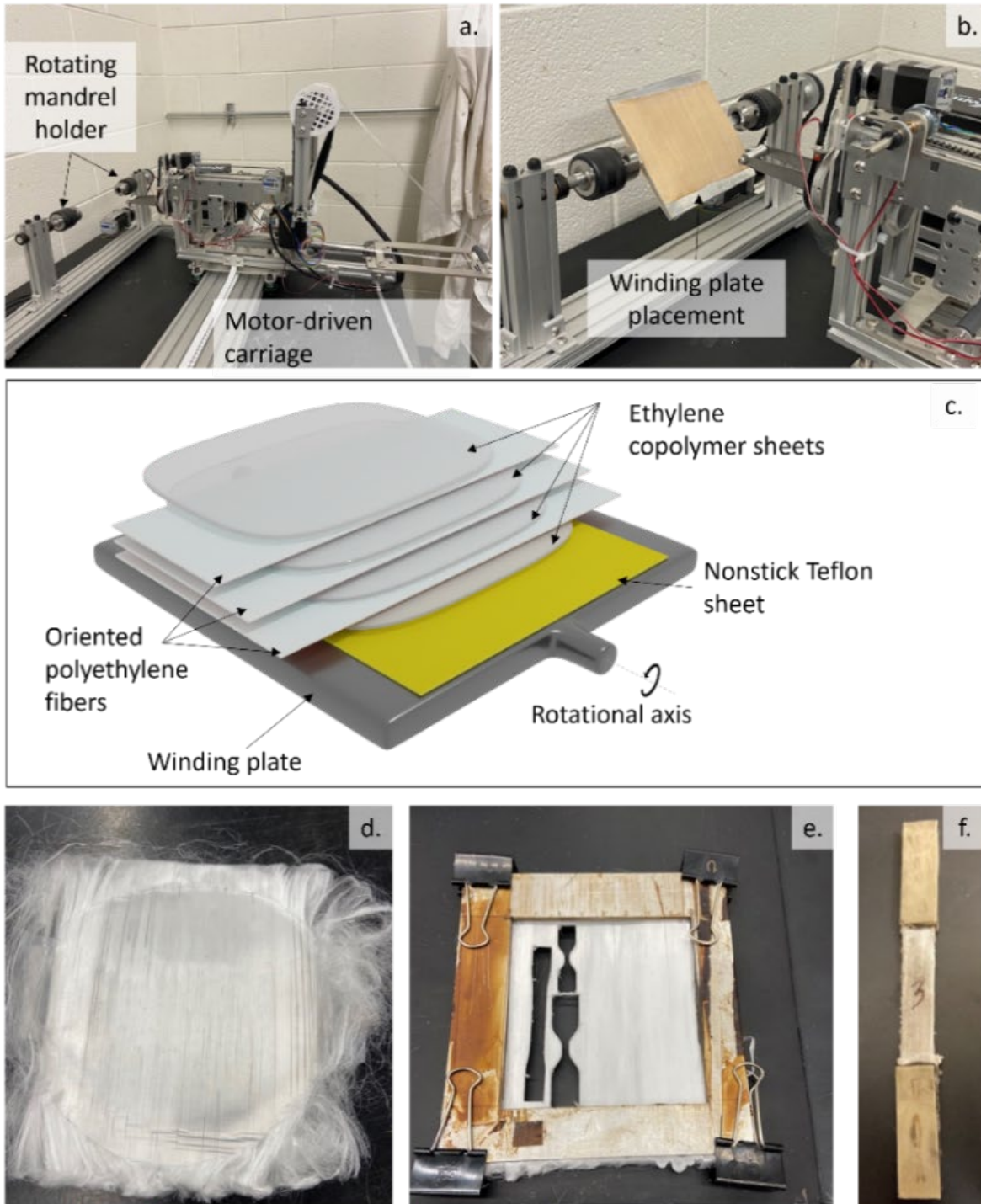


Figure II.3.1.10.20. (a) The laboratory-scale winder setup used to produce uniaxial composites features a motor-driven carriage for fiber-tow placement and a rotating mandrel holder in which (b) a winding plate is secured. (c) This shows a schematic representation of the multilayer composites as constructed within this work. Alternating ethylene copolymer sheets and wound fiber layers are laid up prior to pressing. (d) Photograph displaying pressed composite material prior to the (e) laser cutting of tensile specimens. (f) subsequent attachment of GFRP thermoset tabs to the specimen grip regions prior to tensile testing.

Source: ORNL.

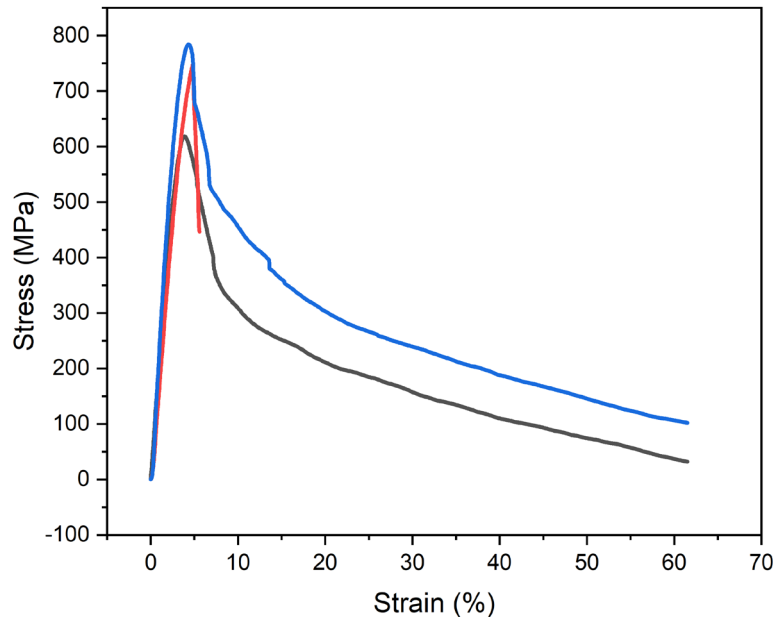


Figure II.3.1.10.21. Results from the tensile tests of the composite samples. The samples displayed a UTS of 717 ± 87 MPa, a 19.7 ± 2.6 GPa modulus, and a > 500 MPa UTS at 5% elongation. Source: ORNL.

Conclusions

Both PNNL and ORNL teams achieved all FY 2023 milestones pertaining to ultra-lightweight polymer-polymer composite using various commercial-scale and lab-scale manufactured polymeric fibers as reinforcing agents for an equivalent polymeric matrix with relatively lower melting temperature. In summary, this project achieved (1) quantification of fiber length variation in PFRPs after injection and compression molding; (2) demonstration of the mechanical recycling of PFRPs using extrusion, injection-molding, and fiber-spinning; (3) investigation of various processing parameters in the filament winding and compression molding processes for manufacturing PFRPs; and (4) optimization of mechanical behaviors and detailed failure morphologies of different PFRPs under quasi-static and impact loads.

Key Publications

1. Ko, S., Y. Qiao, T. J. Rosendaal, A. C. Denny, J. L. Ramos, W. Kuang, K. W. Shahwan, and K. L. Simmons, 2023, "Low-velocity repeated impact behaviors of PFRPs," American Society for Composites (ASC) 38th Annual Technical Conference, Boston, MA, USA.
2. Ko, S., Y. Qiao, T. J. Rosendaal, A. C. Denny, J. L. Ramos, W. Kuang, K. W. Shahwan, and K. L. Simmons, 2023, "Low-velocity impact performances of healed polymer fiber-reinforced plastics," SAMPE Conference (North America Society for the Advancement of Material and Process Engineering).
3. Ko, S., Y. Qiao, T. J. Rosendaal, A. C. Denny, J. L. Ramos, K. W. Shahwan, and K. L. Simmons, "Low-velocity impact resistance and failure characteristics of all thermoplastic woven polymer-fiber-reinforced plastic composites," *J. Compos. Mater.*, under review.
4. Qiao, Y., L. D. Fring, M. R. Pallaka, and K. L. Simmons, 2023, "A review of the fabrication methods and mechanical behavior of thermoplastic polymer-fiber—thermoplastic polymer matrix composites," *Polym. Compos.* 44(2), 694–733. <https://doi.org/10.1002/pc.27139>.
5. Qiao, Y., M. R. Pallaka, E. K. Nickerson, L. D. Fring, and K. L. Simmons, 2022, "Understanding the elastic, plastic, and damage features in fracturing of self-reinforced thermoplastic composites via nondestructive digital imaging correlation," *Proc. SPIE 12047, Nondestructive Characterization and*

Monitoring of Advanced Materials, Aerospace, Civil Infrastructure, and Transportation XVI, 1204707 (18 April 2022).

6. Qiao, Y., S. Ko, J. L. Ramos, E. K. Nickerson, A. C. Denny, K. W. Shahwan, and K.L. Simmons, 2023, "Processing temperature effect on failure behavior of unidirectional thermoplastic PFRPs," American Society for Composites (ASC) 38th Annual Technical Conference, Boston, MA, USA.
7. Qiao, Y., Y. Shin, M. R. Pallaka, E. K. Nickerson, L. D. Fring, S. Ko, J. L. Ramos, H. F. Wu, and K. L. Simmons, 2023, "PFRPs with enhanced interfacial bonding between polypropylene fiber and polyethylene matrix," *J. Reinf. Plast. Comp.*, in revision.
8. Qiao, Y., S. Ko, J. L. Ramos, E. K. Nickerson, A. C. Denny, G. M. Schuler, N. L. Brown, A. Guzman, C. E. Moriel, M. R. Pallaka, Ni Y., K. W. Shahwan, and K. L. Simmons, 2024, "Fully-recyclable unidirectional thermoplastic PFPRs: Investigating the effects of processing temperature, pressure, and fiber volume fractions," *Compos. C: Open Access*, under review.
9. Seo, J., L.T. Kearney, S. Datta, M. D. Toomey, J. K. Keum, and A. K. Naskar, 2022, "Tailoring compatibilization potential of maleic anhydride grafted polypropylene by sequential rheo-chemical processing of polypropylene and polyamide 66 blends," *Polym. Eng. Sci.*, 62(8), 2419–2434. <https://doi.org/10.1002/pen.26016>.
10. Seo, J., L. T. Kearney, M. D. Toomey, J. K. Keum, and A. K. Naskar, 2023. "Polyester-based epoxy vitrimer integrating spent coffee ground as a natural filler," *Compos. B Eng.*, 260, 110756. <https://doi.org/10.1016/j.compositesb.2023.110756>.

Acknowledgements

The PIs would like to acknowledge Y. Qiao, S. Ko, J. Ramos, M. R. Pallaka, L Fring, Y. Shin, E. Nickerson, D. Adam, and K. Shahwan of PNNL; and J. Seo, L. Kearney, N. Kanbargi, M. Toomey, F. Xiong, and J. Keum of ORNL.

II.3.1.11 Efficient Synthesis of Kevlar and Other Fibers from Polyethylene Terephthalate (PET) Waste (Pacific Northwest National Laboratory)

Daniel R. Merkel, Principal Investigator

Pacific Northwest National Laboratory
Energy Processes and Materials Division
908 Battelle Blvd.
Richland, WA 99354
E-mail: daniel.merkel@pnnl.gov

Rich Davies, Composites Core Program Manager

Oak Ridge National Laboratory
Materials Science and Technology Division
1 Bethel Valley Rd.
Oak Ridge, TN 37830
E-mail: daviesrw@ornl.gov

H. Felix Wu, DOE Technology Development Manager

U.S. Department of Energy
E-mail: Felix.Wu@ee.doe.gov

Start Date: July 1, 2020

End Date: September 30, 2023

Project Funding: \$300,000

DOE share: \$300,000

Non-DOE share: \$0

Project Introduction

Lightweighting of automotive components has become of paramount importance, not only to reduce the carbon footprint of final automotive products, but also to conserve valuable and depleting resources. The existing approaches of substitution and structure redesign with traditional materials have reached their limits. An urgent need exists to explore non-metallic—but equally functional—sets of materials to achieve more aggressive fuel savings targets. Lightweight fiber-reinforced plastics have become the material of choice due to their flexibility, functionality, and formability into intricate hybrid and multipart designs. CF is the reinforcement of choice for many applications in the aerospace industry, as CFCs have the most weight-reduction potential. However, CFCs generally have lower impact performance, so designs using CFCs for such applications need to incorporate additional considerations and materials to optimize impact performance. Aramid fiber, such as Kevlar, is one of the fiber systems that can fill this niche, providing enhanced impact performance while preserving the high-strength-to-weight ratio.

Carbon and aramid fiber composites are high-performance fibers, which have been explored in the automotive industry, but their application has been severely limited because of the excessive costs associated with their manufacturing, as well as the manufacturing of composites utilizing them. Presently, Kevlar fiber costs \$12/lb., which is comparable to the cost of CF. In the context of automotive parts, aramid fibers may improve the safety, performance, and durability of automotive components for a wide variety of vehicles, from passenger cars to LD trucks. Components of specific interest include those that demand excellent fatigue and impact performance. For example, belts, tires, and hoses that are subjected to continuous stress cycling require good fatigue properties, fore posts, hoods, and underbody components that are subject to rock impact require excellent impact properties. The replacement of metal components or glass fibers offers additional lightweighting opportunities, owing to the low-density of aramid polymers (e.g., 1.4 g/cm³ for aramid versus at least 2.5 g/cm³ for glass).

This project aims to fabricate Kevlar-like materials from waste PET. This methodology not only contributes to enabling an inexpensive starting material for fiber production, but also provides a means of addressing our plastic waste problem and a novel, exciting pathway to PET chemical upcycling. Various aramid polymers

have been synthesized from waste-PET and will be spun into high-strength fibers, and then demonstrated in composite materials.

Objectives

The objective of this project is to demonstrate waste-PET as an alternative source feedstock for poly(paraphenylene terephthalamide) (PPTA) or Kevlar, in addition to other aramid polymers and produce high-strength fiber at reduced cost as compared to virgin feedstock fiber. The project used waste-PET sourced from used beverage bottles as a primary feedstock for aramid polymers, which were later spun into fiber targeting properties comparable to commercial Kevlar 29. Fiber composite materials were manufactured to demonstrate feasibility in high-performance fiber composites.

Approach

The general chemical scheme requires the preparation of aramid polymers directly from PET waste or via PET-derived building blocks, such as terephthalic acid or terephthaloyl chloride. The direct approach to synthesize aramid from PET waste involved the concerted depolymerization/repolymerization reaction illustrated in Figure II.3.1.11.1, via C-O bond cleavage and C-N bond formation. This methodology was projected to provide a considerable advantage in the cost of aramid polymers, as the starting material is inexpensive PET waste, and the direct reaction eliminates several intermediate processing and purification steps. However, waste-PET, in particular beverage bottle PET, is typically highly crystalline and therefore insoluble in all non-reactive and inexpensive organic solvents, including N,N-dimethylformamide, dimethylsulfoxide, hexamethylphosphoramide, N-methylpyrrolidone, and dichlorobenzene, making solution chemistry difficult. Furthermore, reactions were found to be unlikely to go to completion, and the separation of insoluble starting materials (e.g., unreacted PET) from products (e.g., aramid) proved challenging.

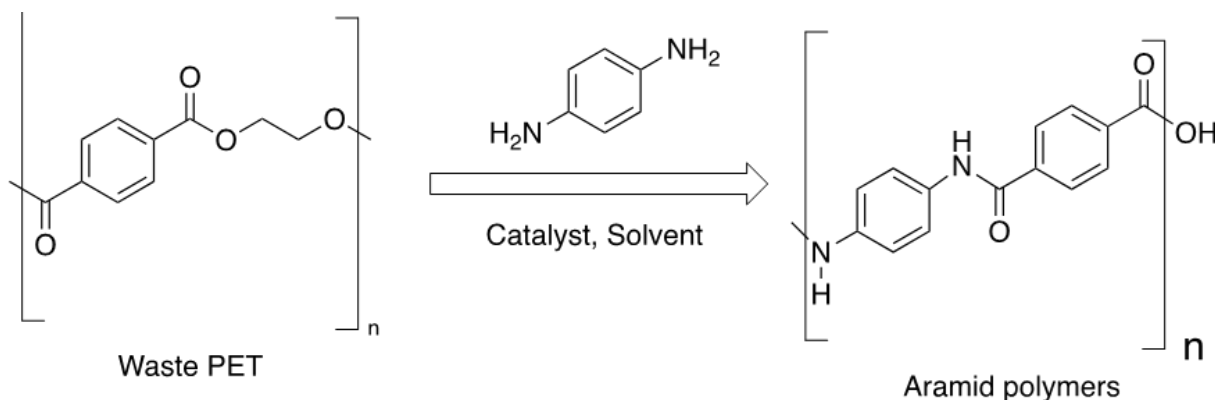


Figure II.3.1.11.1. Direct depolymerization of PET waste and concerted repolymerization. Source: PNNL.

Given these considerations, an alternative methodology was developed to deconstruct waste-PET to a chemically functional intermediate and remove impurities yielding a suitable feedstock for aramid synthesis. A variety of polymerization procedures with different monomer building blocks were developed and optimized to create a several aramid polymers with high-molecular weights suitable for high-strength fibers synthesis. Polymer fibers were spun via dry jet and wet spinning methods to fabricate fibers suitable for composites applications. Finally, the foundations for polymer matrix composites were developed and evaluated for fiber-matrix adhesion to demonstrate the utility of PET-derived fibers for automotive composites.

Results

PPTA fibers derived from waste-PET bottles and fibers derived from commercial feedstock were characterized for mechanical properties in bundles of ~ 75 fibers. A PPTA polymer was synthesized from either PET-derived terephthaloyl chloride (TCl) or TCl purchased from Sigma-Aldrich, which served as the baseline. Polymers were dissolved in 96.8% sulfuric acid at 6 w/v% polymer concentration. The resulting dope was ejected from a syringe tip using a syringe pump into a saturated sodium bicarbonate coagulation bath forming a continuous polymer-fiber. The fiber was wound onto a rotating bobbin, as indicated in Figure II.3.1.11.2(a), at a controlled speed. Fiber was stretched during the spinning process by controlling the draw ratio, which is defined as the ratio of winding speed relative to the speed of ejection from the syringe tip. Draw ratios were varied from 1 to 3 to control fiber diameter and improve uniformity along the fiber length as shown in Figure II.3.1.11.2(b).

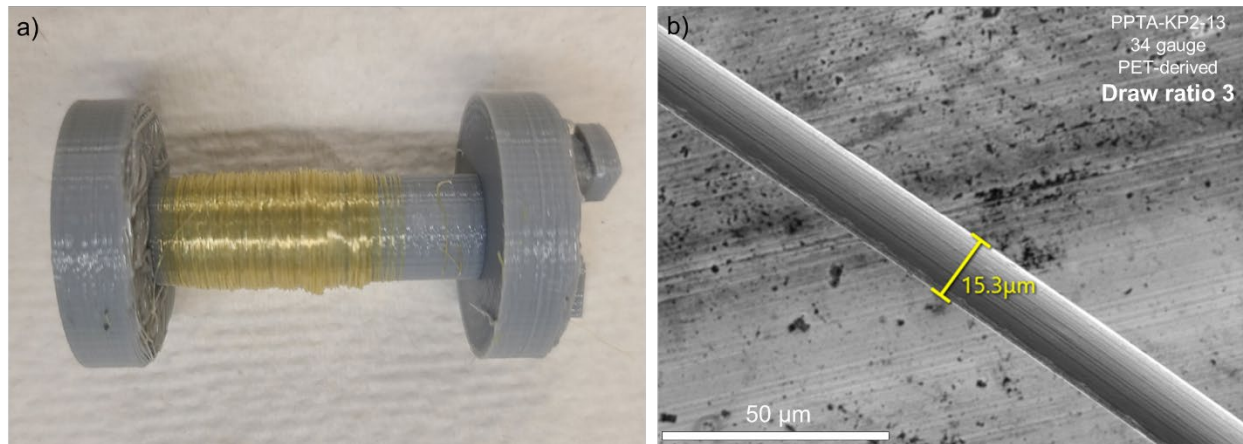


Figure II.3.1.11.2. (a) PET-derived PPTA fiber wound on a bobbin. (b) SEM of PET-derived fiber. Source: PNNL.

Uniform fiber diameter along the length was achieved for both commercially-derived and PET-derived fiber when the draw ratio was greater than 1. Fiber surfaces of both fiber types were relatively defect-free, as shown in Figure II.3.1.11.2(b); some grooves aligned with the fiber length likely resulted from imperfections of the syringe tip orifice. Increasing the draw ratio resulted in decreasing fiber diameter due to stretching of the fiber, as shown in Figure II.3.1.11.3(a), which is also expected to increase the molecular alignment and mechanical strength. The highest draw ratio of 3 that was inspected resulted in a fiber diameter of $15.7 \pm 2.0 \mu\text{m}$ for PET-derived fibers. The diameter for any spinning run may be influenced by many factors, including polymer molecular weight and associated disparities in dope characteristics.

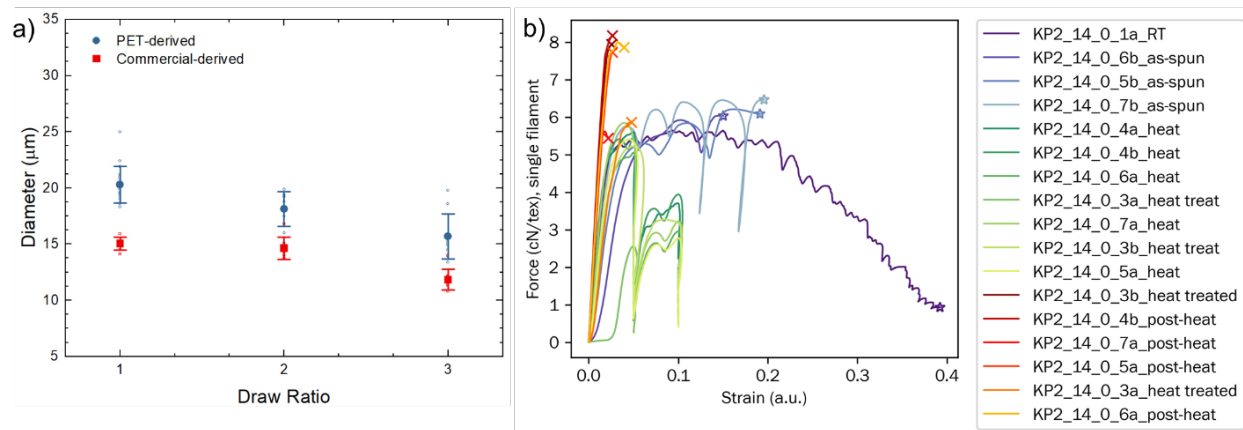


Figure II.3.1.11.3. (a) Fiber diameter decreased as draw ratio increased. (b) Mechanical test results for as-spun and heat-treated fibers. Source: PNNL.

Fibers spun with a draw ratio of 1 were subjected to heat-treatment studies and mechanical testing, as shown in Figure II.3.1.11.3(b). In general, fiber strength depends strongly on spinning conditions including polymer molecular weight, dope concentration, and draw ratio, among others and results in molecular alignment to the fiber direction. Modulus, on the other hand, depends more strongly on heat-treatment of the fiber after spinning and results from the intermolecular bond formation between polymer chains. Table II.3.1.11.1 shows the results for two fibers including the properties of one fiber after heat-treatment, as well as literature data for the similar fibers [1]. Sample KP2_14 was spun from 6 w/v% dope at 25°C with draw ratio of 1. The as-spun properties were relatively poor with tenacity of about 6 cN/tex and modulus of 240 cN/tex. The fiber was heat-treated at either 150°C for 15 minutes or 200°C for 5 minutes, which improved the modulus to 490 cN/tex and 420 cN/tex, respectively. KP2_6 was spun from 6 w/v% dope at 80°C with a draw ratio of 2 and showed significantly improved properties compared to KP2_14. The combination of higher temperature and draw ratio produced fiber with a tenacity of 17 cN/tex and a modulus of 750 cN/tex. While the modulus compares favorably to literature, the tenacity can be improved by refining the spinning conditions, specifically temperature and draw ratio.

Table II.3.1.11.1. Mechanical Testing Results for Various Spinning Conditions

Sample Number and Spinning Conditions	Breaking Tenacity (cN/tex)	EAB (%)	Modulus (cN/tex)	Reference
KP2_6, 6 w/v%, 80°C, as-spun, 2× draw	17.40	11.6	750.88	PNNL
KP2_14, 6 w/v%, 25°C, as-spun, 1× draw	6.19	17.9	244.15	PNNL
KP2_14, 6 w/v%, 25°C, 1× draw, 150°C, 15 min	8.06	2.6	488.92	PNNL
KP2_14, 6 w/v%, 25°C, 1× draw, 200°C, 5 min	7.80	3.3	422.17	PNNL
12 wt.%, as-spun	20.56	19.6	263.01	[1]

The pathway techno-economic analyses (TEAs) and LCAs from waste-PET to PPTA and its intermediate, terephthalic acid (TPA), were conducted to determine economic and environmental viability compared to commercial pathways from petroleum feedstocks. As shown in Figure II.3.1.11.4, commercial technologies are available to produce Kevlar 29 from TCI and p-phenylenediamine (p-PDA), where TCI is produced from TPA and chlorine. In the commercial process, TPA is produced from p-xylene via oxidation.

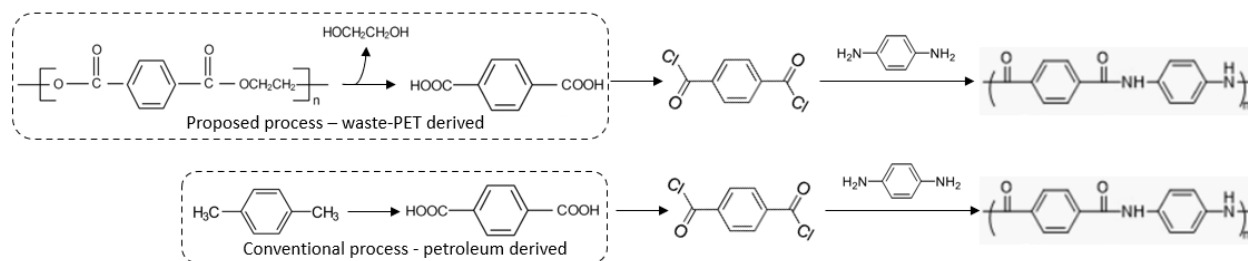


Figure II.3.1.11.4. PNNL's and commercial (Kevlar 29) synthesis approach to PPTA. Source: PNNL.

The block flow diagram of PNNL's waste-PET to TPA and aramid fiber process is shown in Figure II.3.1.11.5. Here, waste-PET is chopped and then sent to the hydrolysis reactor with sodium hydroxide (NaOH) and ethylene glycol (EG)/water solvent to form TPA salt, as observed in Figure II.3.1.11.6 Scheme 1a. The impurities and unreacted PET are removed via filtration. The filtrate from the first filter, which contained dissolved TPA salt, solvent, and excess NaOH, is sent to the acidification reactor to form crude TPA solid, as indicated in Scheme 1b as shown in Figure II.3.1.11.6. The product is sent to the second filter. The filtrate contains mainly EG, water, and sodium chloride (NaCl), which are separated via salt crystallization and distillation. The solid product, crude TPA, is washed by water and dried in an oven before being sent to the downstream TCI and fiber synthesis blocks using commercial technologies.

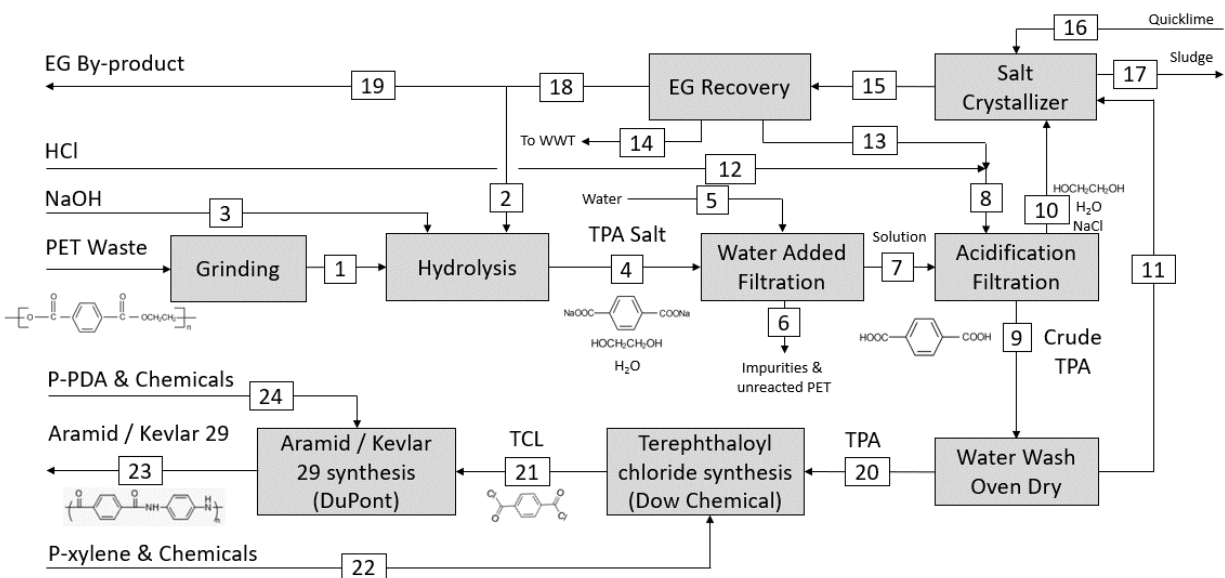
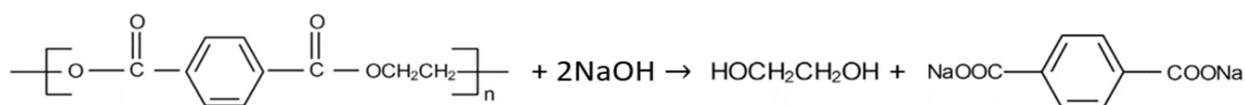
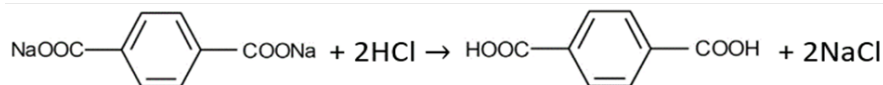


Figure II.3.1.11.5. Block flow diagram of the proposed Kevlar fiber synthesis from waste-PET via hydrolysis. Source: PNNL.



(Scheme 1a)



(Scheme 1b)

Figure II.3.1.11.6. Chemical pathways used to generate PPTA precursors (Scheme 1a) terephthalate salt and (Scheme 1b) TPA from waste-PET. Source: PNNL.

The TEA results were compared to an enzymatic approach reported by Singh et al. [2] are shown in Figure II.3.1.11.7(a). An additional sensitivity study was conducted to evaluate the impact of waste-PET price and potential plastic tax credits [3] on PNNL's approach. The results were compared with the market price of petroleum-derived TPA, as shown in Figure II.3.1.11.7(b). The technology developed by PNNL has a slightly lower minimum TPA selling price (\$1.7/kg) than the enzymatic approach (\$1.93/kg) under the same economic assumptions. This is due to the higher TPA yield, lower utility consumption, and capital investment associated with the PNNL approach. However, Figure II.3.1.11.7(b) indicates the estimated TPA of PNNL's technology is higher than the market price of petroleum-derived TPA [4] due to (1) a conservative waste-PET price, and (2) the much larger scale of a petrochemical plant compared to a PET recycling and utilization plant. However, PNNL's technology would be cost-competitive under the conditions of low waste-PET price and/or a plastic tax credit.

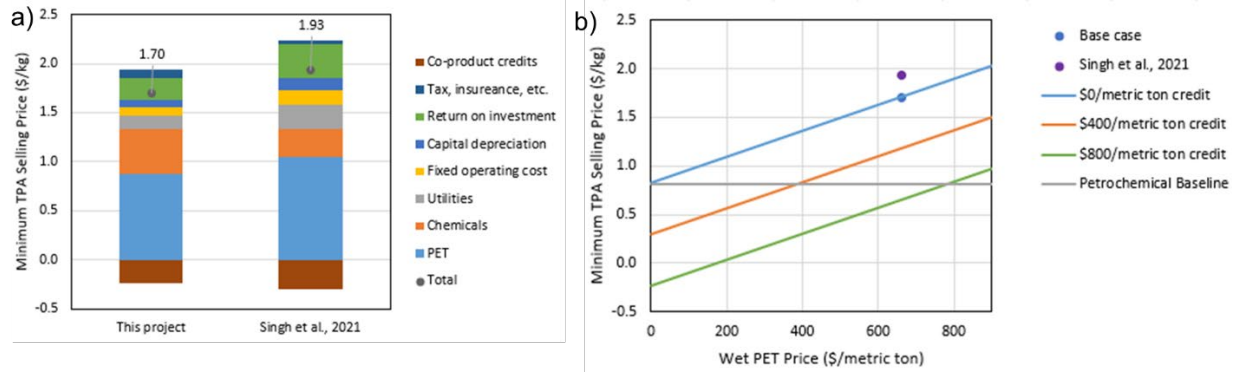


Figure II.3.1.11.7. (a) Minimum selling price of TPA produced from waste-PET compared to an enzymatic approach [2]. (b) Comparison with petroleum-derived TPA. Source: PNNL.

The TEA results for the waste-PET-to-aramid fiber process, which is a Kevlar 29 equivalent, are provided in Figure II.3.1.11.8 with sensitivity studies regarding waste-PET price and plant scale. The result suggests that with a comparable plant scale of a commercial aramid fiber plant, PNNL’s PET-derived aramid fiber has a comparable minimum fiber selling price to the commercial Kevlar 29 fiber (\$24/kg). According to the Process Economics Program Yearbook [5], the main cost drivers of a commercial aramid fiber synthesis plant are the cost of p-PDA feedstock for fiber synthesis and capital investment of downstream fiber synthesis block. However, in this work, the main difference between PNNL’s waste-PET-to-aramid fiber process and commercial process is the upstream TPA production section instead of the downstream fiber synthesis section. With a comparable plant scale, a 10% cost-reduction can be achieved via integrating all synthesis steps in one centralized plant. Note that the typical scale of a large PET recycling plant is larger than that of an aramid synthesis plant. Up to 30% cost-reduction can be achieved by scaling-up the integrated fiber synthesis plant to a typical plant scale of large PET recycling plants.

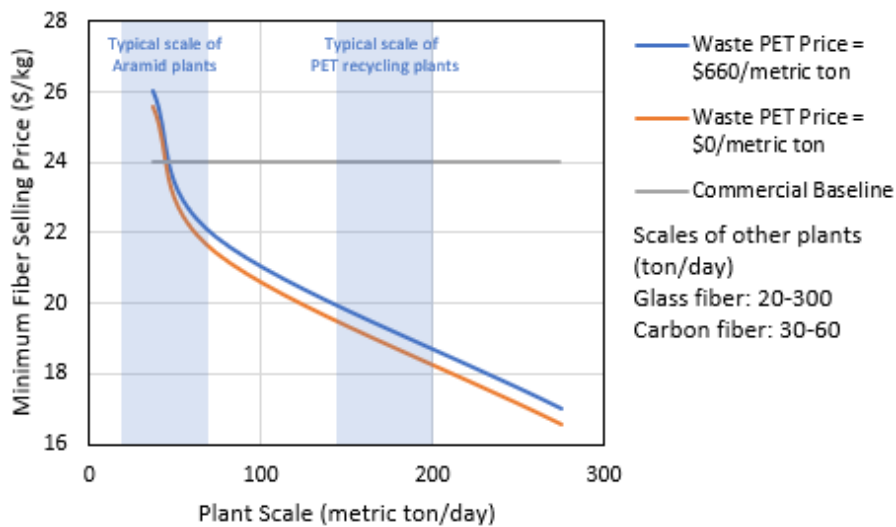


Figure II.3.1.11.8. Minimum selling price of waste-PET derived aramid fiber. Source: PNNL.

The life cycle greenhouse gas (GHG) emission of PNNL’s technology is lower than a comparable enzymatic approach [2] because of the higher TPA yield and lower utility consumption during manufacturing. As shown in Figure II.3.1.11.9(a), the life cycle GHG emission of waste-PET-to-aramid fiber is similar to that of Kevlar 29 because the top two contributors to the life cycle GHG emission is the consumption of p-PDA and utility cost of downstream fiber synthesis; the two routes share the same downstream fiber synthesis technology. The carbon footprints of other fibers are included in Figure II.3.1.11.9(b) for comparison.

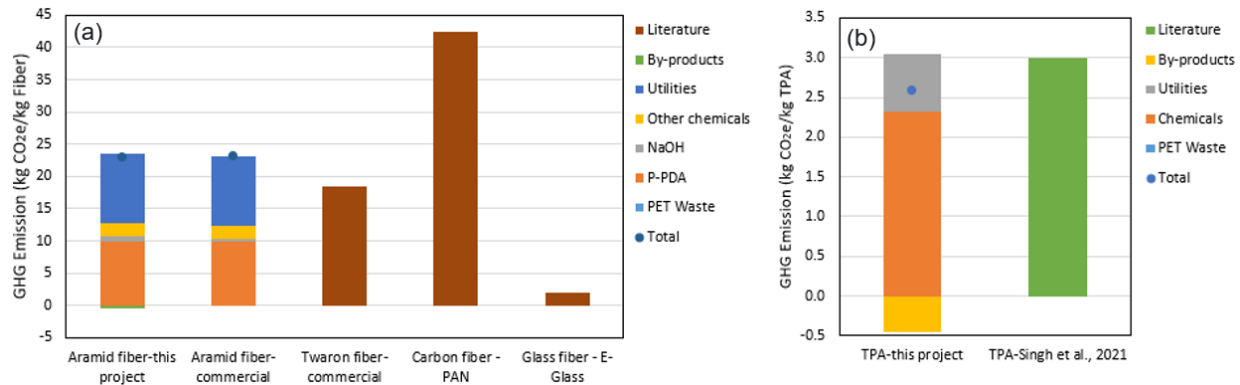


Figure II.3.1.11.9. LCA Results of waste-PET derived TPA and aramid fiber. Source: PNNL.

The contribution from TPA to the total cost and emission of the entire supply-chain of aramid fiber synthesis is relatively small, while the downstream fiber synthesis from TCI is the major contributor. Therefore, replacing petroleum-derived TPA with waste-PET-derived TPA will not significantly impact the total cost and life cycle GHG emissions of aramid fiber synthesis. Further cost and emission reduction can be achieved by an alternative fiber synthesis method such as the proposed direct synthesis method, as indicated previously in Figure II.3.1.11.1. One promising approach is the direct polycondensation of carboxylic acids with amine, which is a much simpler synthesis route requiring less energy and less equipment. This direct polycondensation concept was first developed by Ishihara et al. [6] to synthesis polyamide. However, the expensive catalyst and chemicals demonstrated prevented the industrial deployment.

Conclusions

A fiber-spinning method was developed to produce aramid fiber from waste-PET-derived PPTA, which is chemically identical to Kevlar 29. Fiber diameter was controlled by spinning draw ratio, achieving diameters of less than 20 μm using a draw ratio of 3 and a 34-gauge spinning orifice. Tensile modulus of fibers was increased by various heat treatments, achieving as high as 100% increase in modulus depending on the initial fiber properties and heat-treatment parameters. TEA demonstrated the hydrolytic approach to PET-derived TPA was more cost-effective than an enzymatic approach and was comparable to petroleum-derived TPA under the conditions of inexpensive waste-PET and/or tax credits. The proposed method to produce aramid fiber from PET waste could achieve a 30% cost-reduction as compared to Kevlar 29 with a plant size that is comparable to modern PET recycling centers; 10% cost-reduction could be achieved at a plant scale similar to current Kevlar 29 plants. Emissions associated with the production of PET-derived fiber are comparable to that of Kevlar 29 owing to the emissions-intensive fiber-spinning process, which is identical for PET-derived and Kevlar fiber. Synthesis of PAN-based CF produces about twice the GHG emissions. The most promising pathway toward further reduction in cost and emissions for aramid fiber is further development of the synthesis approach to PPTA. TEA and LCA showed that p-PDA is a significant contributor to both cost and emissions, alluding to large potential progress if p-PDA could be recovered from an alternative source. This research was focused on a PET-derived alternative to Kevlar (e.g., PPTA). Yet the general approach can be leveraged to produce other high value fibers (Nomex, Technora, etc.), which yield different TEA and LCA outcomes.

References

1. Hancock, T.A., J. E. Spruiell, and J. L. White, 1977, "Wet spinning of aliphatic and aromatic polyamides," *J. Appl. Polym. Sci.*, 21(5), 1227–1247. <https://doi.org/10.1002/app.1977.070210506>.
2. Singh, A., N. A. Rorrer, S. R. Nicholson, E. Erickson, J. S. DesVeaux, A. F. T. Avelino, P. Lamers, A. Bhatt, Y. Zhang, G. Avery, L. Tao, A. R. Pickford, A. C. Carpenter, J. E. McGeehan, and G. T. Beckham, 2021, "Techno-economic, life cycle, and socioeconomic impact analysis of enzymatic recycling of poly(ethylene terephthalate)," *Joule*, 5(9), 2479–2503. <https://doi.org/10.1016/j.joule.2021.06.015>.

3. Sustainable Brands website, 2022, “What are plastic credits? A 4-minute explainer,” Available at: <https://sustainablebrands.com/read/defining-the-next-economy/what-are-plastic-credits-a-4-minute-explainer> (accessed 2 November 2023).
4. IHS Markit, 2020, “Terephthaloyl Chloride from P-xylene,” Chemical Process Economics Program (PEP) Yearbook. Updated quarterly. <https://cdn.ihs.com/www/pdf/Process-Economics-Program.pdf>
5. IHS Markit, 2020, “Aramid Spun Yarn,” Chemical PEP Yearbook. Updated quarterly. <https://cdn.ihs.com/www/pdf/Process-Economics-Program.pdf>
6. Ishihara, K., S. Ohara, and H. Yamamoto, 2000, “Direct polycondensation of carboxylic acids and amines catalyzed by 3,4,5-trifluorophenylboronic acid,” *Macromol.*, 33(10), 3511–3513. <https://doi.org/10.1021/ma000085o>.

Acknowledgements

This work would not have been possible without the efforts of D. Mayberry, Y. Ni, J. Ramos, K. Suazo, S. Krishnamoorthy, and J. Kothandaraman. Special thanks are also extended to D. Herling, K. Simmons, K. Shahwan, and S. Madbouly for their guidance.

II.3.1.12 Additively Manufactured, Lightweight, Low-Cost Composite Vessels for Compressed Natural Gas Fuel Storage (Lawrence Livermore National Laboratory)

James P. Lewicki, Principal Investigator

Lawrence Livermore National Laboratory
700 East Ave.
Livermore, CA 94550
E-mail: lewicki1@llnl.gov

Rich Davies, Composites Core Program Manager

Oak Ridge National Laboratory
Materials Science and Technology Division
1 Bethel Valley Rd.
Oak Ridge, TN 37830
E-mail: daviesrw@ornl.gov

H. Felix Wu, DOE Technology Development Manager

U.S. Department of Energy
E-mail: felix.wu@ee.doe.gov

Start Date: July 1, 2020

End Date: September 30, 2023

Project Funding: \$460,000

DOE share: \$460,000

Non-DOE share: \$0

Project Introduction

CF/polymer composites are a transformative class of high-performance, lightweight material, where high-aspect ratio CFs reinforce a polymer matrix and exceed the strength of steel alloys at a fraction of the density. Despite the advantages of such a class of material, the broader implementation of CFCs in a range of automotive, aerospace, and energy applications is hindered by limitations of current manufacturing methods. These current techniques (e.g., hand layup, wet filament winding) are costly and impose severe limitations on fiber placement, orientation, and angle, and thus, the ultimate properties of a CFC. Today's CF composites are expensive to manufacture, limited in form factor, and utilize costly and suboptimal continuous filament CF. Advanced AM processes, combined with computational design optimization and new approaches to resin development, offer alternative design and manufacturing paradigms that have the realistic potential to lift these constraints. Such integrated AM approaches could thus help to realize the full potential of CFC materials.

One relevant application of CFC materials where manufacturing constraints limit the cost-benefit ratio is in the manufacture of high-performance composite pressure vessels for onboard CNG storage. Current Types 3–5 CNG storage vessels are made from load-bearing filament-wound CFC and are $\sim 3.5\times$ as expensive as an all-metallic Type-1 vessel. This cost is invariably tied to the complex and labor-intensive nature of conventional filament winding processes and the large volumes of expensive high-tensile-strength CF tow feedstock required in manufacture. Our proposed approach to CNG storage vessel manufacture is based on a combination of AM technologies for CFC printing and design optimization tools that were pioneered at Lawrence Livermore National Laboratory (LLNL) with advances in resin/composite formulation enabled by chemical and nanomaterial modification. Through the successful development of this technology, LLNL seeks to demonstrate the capability for advanced CNG storage vessel manufacture at reduced cost with no reduction in performance versus the most advanced, extant Type-5 CNG vessel designs.

Objectives

The proposed work addresses three objectives that are critical to the AM of next generation CFCs:

- Objective 1: Enhance resin properties via chemical and nanomaterial modifications to yield an improved resin matrix with significantly increased mechanical performance over baseline winding resins. (Enables reductions in CF content without detriment of performance.)
- Objective 2: Realize compositionally graded CFCs. Apply novel AM and design methodologies to combine continuous and short-fiber structures in a graded, computationally optimized tank design, which maximizes performance while minimizing mass and cost. (Hybrid, optimized design enables increased performance at a lower relative volume fraction of expensive continuous CF filament.)
- Objective 3: Additively manufacture and test a contoured hybrid CF vessel having all the major design elements of a Type-5 CNG tank, providing validation of the materials and design concepts within a relevant laboratory-scale environment. (Enables the development of a technology data package including a cost to benefit assessment for the demonstrated technology and will form a starting point for further maturation [post-project] at scale.)

Approach

This project will develop a process to combine AM via DIW technology for CFC printing and use design optimization tools pioneered at LLNL, with advances in resin/composite formulation enabled by chemical and nanomaterial modification to produce lightweight low-cost CNG vessels. Our approach will yield subscale prototype composite pressure tanks equivalent to Type-5 CNG vessel designs that demonstrate a potential cost-benefit advantage. Central to our vision is using agile AM and design based on computationally informed DIW of both short and continuous CF, further coupled with high-performance thermoset polymer matrixes modified by emergent nanomaterials. Our single-stage, multimaterial AM technology, combined with a decreased CF volume fraction and an increased proportion of economically advantaged short-fiber, all together drive the reduction in manufacturing time and overall cost. Importantly, reductions in continuous fiber and overall FVF will be achieved without detriment to the mechanical strength of the composite vessel. This will be achieved by employing a single process, multimaterials grading process involving the following: (1) a thermoset resin “ink” modified with aligned nanoplatelets to leverage the efficient tortuous-path gas barrier effect, and (2) an inner flexible gas barrier printed as the initial stage in our manufacturing process before compositionally grading the AM feedstock in real-time to transition to a rigid, structural CF-filled resin. The proposed hybrid construction is projected to achieve pressure ratings (e.g., 2,900–3,600 psi service range with a 3× burst safety factor) comparable to conventional filament-wound composite tanks with an estimated 30–50% reduction in total manufacturing cost. The cost reductions are based on a reduction in the levels of CF required and process streamlining achieved via a hybrid DIW manufacturing method, as shown in Figure II.3.1.12.1.

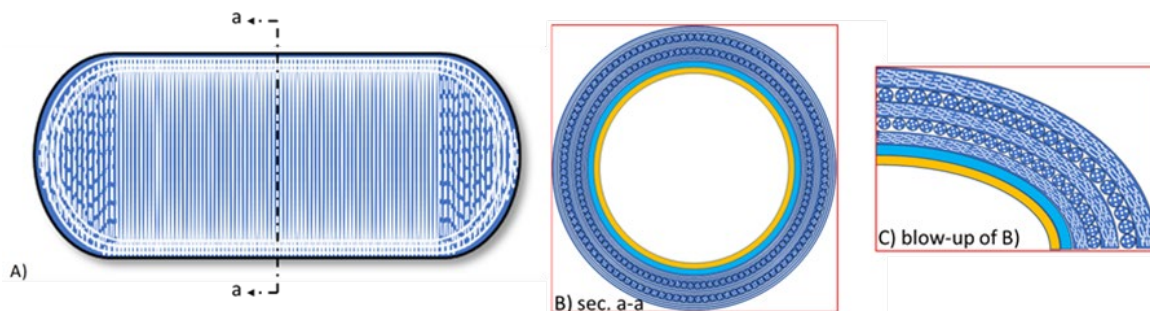


Figure II.3.1.12.1. Schematic of an AM-CNG storage vessel concept. (a) External rigid structural layers of the vessel: load-bearing resin filaments (blue) filled with short and continuous CF (white). (b) Continuous filament material is applied to the midbody yielding maximum hoop strength. (c) Short-fiber extrusion used to fabricate complex end caps. Flexible and cross-linkable polymer compositions reinforced with nanoplatelets shown in (b) and (c) will be printed to serve as the inner layers of a vessel (yellow and blue layers represent the inner gas barrier and transition to structural layers, respectively). Source: LLNL.

A core advantage of our approach over existing technology lies within our high-performance thermosetting resins that are both UV gellable and thermally curable. They are specially formulated to be compatible with the DIW process and to engender enhanced gas barrier and mechanical performance in the final printed material. We will base our gas barrier resin technology on the development of a UV-gel/thermal-post-cure epoxy network that is chemically modified for flexibility and physically modified with two-dimensional graphene nanoplatelets. Our structural resin will be based on a family of LLNL high-performance polymers characterized by hybrids of cyanate ester and aromatic epoxy segments in a contiguous network. To overcome the ubiquitous challenges in CF composites relating to weak polymer matrices and fracturing at CF-matrix interfaces, we will introduce additional hierarchical reinforcement elements based on one-dimensional nanomaterials. Our non-acrylate-based, UV-gel/thermal-cure technology is found in both resin families. This similar chemistry enables a single-stage, multimaterials deposition process wherein one resin can be covalently blended into the next at a range of compositional gradients.

Through hybridizing continuous and short-fiber printing, we will enable the manufacture of novel graded composites. This will realize printing with tunable and enriched concentrations of continuous filament in the center of the vessel body to maximize radial hoop strength while minimizing the overall use of expensive continuous filament fibers. A unified resin deposition process seamlessly blends portions of the build requiring rich continuous filament with short-fiber material to accommodate conformal and open geometries problematic for standard continuous filament techniques (e.g., vessel endcaps). To realize this hybrid composite approach, a new print head is required to be developed, based on LLNL’s patents and extant breadboard demonstrations in the area. The design, manufacture, and testing of a hybrid print head, which enables the laydown of both long-fiber tows and short-fiber ‘ink’ within a single AM structure will be carried out in collaboration with our industrial partner—Materials Sciences LLC, which will design and manufacture a practical hybrid head prototype, based on LLNL breadboard concepts that may be integrated into LLNL’s current AM printing platform, participate in the integration and testing of the system, and execute any improvements/modifications that are necessary after completion of the prototype trials. They will also participate in the design of the hybrid test vessels under Task 3 of this project.

We will maintain optimal mechanical performance of our composite vessel walls using a multi-scaled, hybrid composite structure—realized in a rationally designed manufacturing form derived from DIW. Leveraging our advanced DIW printing technology for short and continuous fiber, we will develop unique capabilities to manufacture the main body of the vessel within one consolidated, cost-efficient process. A series of burst and performance tests of manufactured articles will form the basis of the validation of our design and manufacturing approach. A breakdown of our project schedule at a task level is shown in Figure II.3.1.12.2.

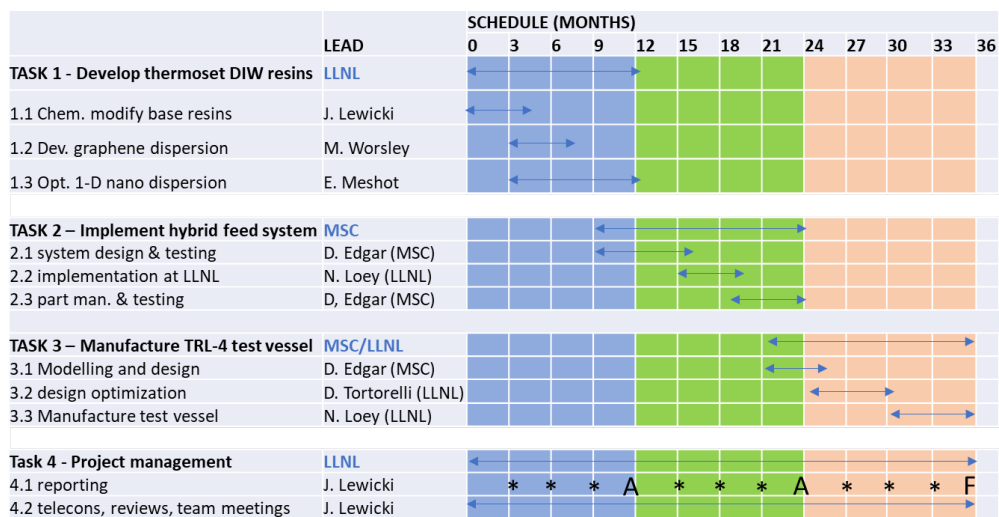


Figure II.3.1.12.2. Project schedule. Source: LLNL.

Results

Our FY 2023 technical focus was the completion of the manufacturable design for a hybrid test vessel, article testing to validate wall strength requirements, and predictions for the complete manufacture of scaled gas bottles that were capable of pressure testing. The design-optimized fiber path solutions that were presented in FY 2022 have been successfully converted into CADWIND machine code instructions all while preserving the “mathematical intent of the optimized solution.” Computational predictions of 20% increases in stiffness per wind layer through non-obvious fiber angle placement. These CADWIND code solutions were tested on a dummy mandrel form incorporating pressure bosses to demonstrate the manufacturability of the wind pattern and the ability of LLNL’s UV capable resin technology to “tack-and-run” long-fiber lengths in a non-tension-dominated regime, as observed in Figure II.3.1.12.3(a). Successful printing of the long-fiber sectional layers demonstrated that design optimization constraints could be met and implemented in a printed form. Following these demonstrations, the mechanical properties of single “zone” layers and hybrid sandwiches of short and long-fiber -as would be found in the final test articles were assessed for mechanical strength and stiffness, as indicated in Figure II.3.1.12.3(b).

A representative hybrid structure was fabricated into a range of coupons forms manufactured into a series of three layers of long-fiber polyacrylonitrile (PAN) fiber composite alternating between three layers of short-fiber composite material, all additively manufactured in a single process, as indicated in Figure II.3.1.12.4.

Coupon-scale fabricated test structures consisted of alternating layers of IM-6 continuous fiber at ~60 volume % and layers of nanomaterial matrix modified IM-10 short-fiber-loaded resin where the short-fiber volume fraction was less than 20 vol.%. Such a structure represented a form expected to both meet the mechanical requirements and have significantly less CF volume-to-volume than a conventional wound vessel wall. Tensile tests to failure of these coupons, indeed demonstrate that the printed hybrid structures, despite their reduced volume fraction of fiber, had average tensile strength and stiffness of **643MPa (peak load at fail) and 50GPa, respectively**, thereby putting the printed low-fiber-content structures in the competitive region for CNG bottle applications.

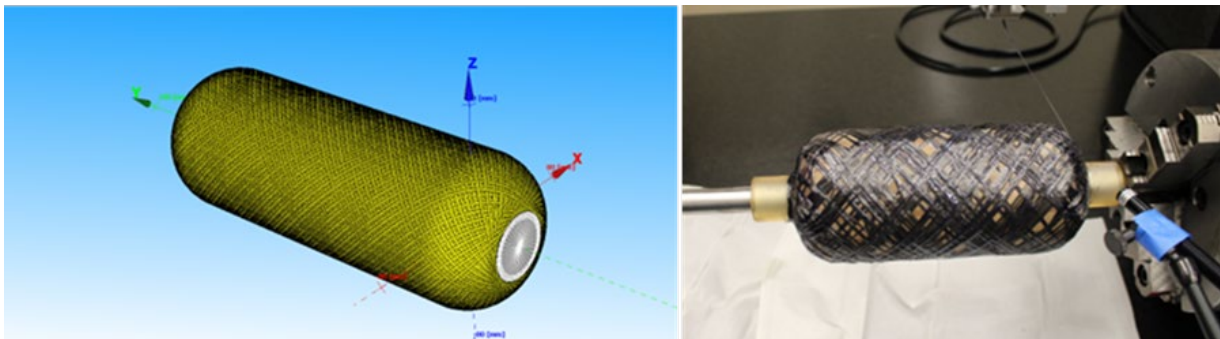


Figure II.3.1.12.3. (a) Optimization informed CADWIND visualization for the midbody sections of the scaled-test vessel, forming toolpath instructions for the midbody print of the hybrid vessel. (b) “Printed” midbody structural section on a dummy mandrel form following the generated code (pre-top-coat addition).

Source: LLNL.

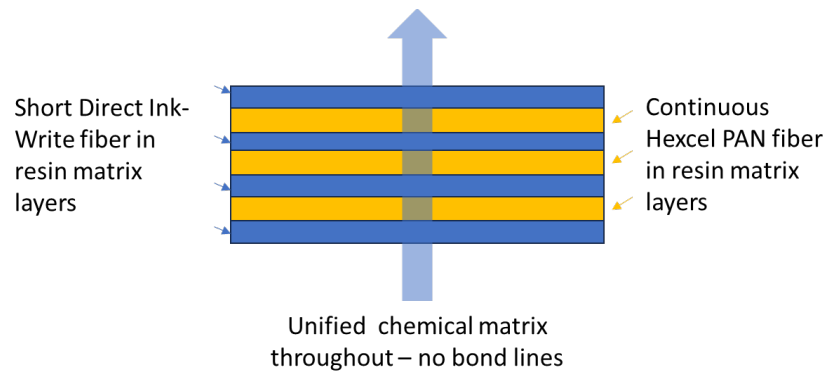


Figure II.3.1.12.4. A representation of the 3D-printed coupon-scale structures fabricated for tensile testing. Source: LLNL.

On the completion of coupon-level testing, complete scaled-test articles per the FY 2022 design definitions were additively manufactured. The goals of the AM demonstration were to (1) demonstrate the ability to fabricate a three-zone bottle geometry serving the roles of liner, structural midbody, and enhanced toughness topcoat layers—all chemically contiguous with each other; (2) demonstrate that the multizone fabrication could be conducted in a single machine operation without resetting of the work; and (3) demonstrate that the conclusion of the printing process would yield a usable finished article without the need for further post-machining or manufacturing operations. To these ends, a manufacturing strategy was designed as follows:

1. Work setup and registration of a sacrificial mandrel on the printing platform.
2. Printing of the liner compound layers with online UV gelation of the liner during printing.
3. Registration of the bosses to the liner ends and overprinting of the bosses with a further liner zone to form a gas-tight seal.
4. Deposition of the structural midbody layers (e.g., PAN continuous fiber in an optimized wind pattern), with real-time gelation of the consolidating resin phase.
5. Printing of the short-fiber topcoat layer with online UV gelation during printing.
6. Removal of the completed green cure work and thermal-cure in a rotary oven.
7. Dissolution of the sacrificial mandrel and removal of the shaft delivering a complete test article.

In FY 2023, steps 1-7 were first simulated in a digital process twin, dry-run using dummy forms, and then exercised twice as an actual process to deliver two identical, complete test articles for testing, as shown in Figure II.3.1.12.5.

Completion of full gas bottle test articles marked a major milestone in FY 2023 with the demonstration that an advanced type-5 bottle configuration, as can be seen in Figure II.3.1.12.6, can be manufactured with reduced CF content, utilizing a small manufacturing footprint additive process. At the time of the writing of this report, nondestructive analysis and pressure testing of the completed articles was ongoing.

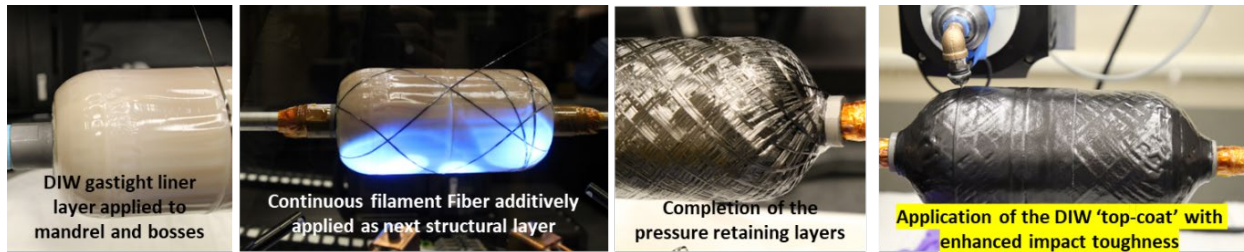


Figure II.3.1.12.5. From left to right: mandrel form showing the complete liner zone, incorporating bosses; beginning of structural midbody print; near completion of midbody long-fiber print showing wrap around boss region; and application of the topcoat layers (incomplete). Source: LLNL.

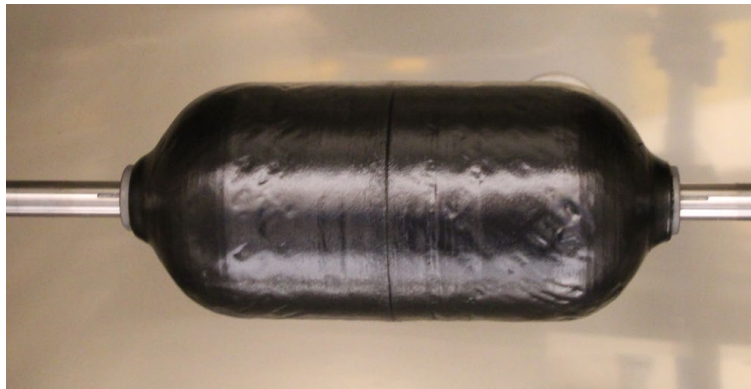


Figure II.3.1.12.6. A complete gas bottle test article shown after thermal-cure and prior to mandrel and shaft removal. Source: LLNL.

Conclusions

In FY 2023, a complete AM process for a Type 5 configuration gas bottle production was demonstrated for the first-time, based on a design-optimized for CNG tank storage applications. Significant innovations included in the design and demonstrated in the manufacturing process were (1) the use of nanomaterial enhanced resin phases to increase mechanical performance of the system, (2) the use of a unique multizone design where differing regions of the structure carry out differing roles yet are unified by a common thermosetting chemistry, (3) the use of computational design optimization to deliver fiber patterns with enhanced load-bearing performance vs. conventional approaches, and (4) the application of UV capable resins to enable wet filament winding without tension-dominated control, and hence, access to wind angles and patterns unavailable to conventional processes. Upon completion of cyclic pressure testing and pressure testing to failure, the economic feasibility of this manufacturing process can be assessed for its potential in CNG tank production processes.

Acknowledgements

The authors gratefully acknowledge Dr. P. Chastain of Areojot-Rocketdyne for his consolation and assistance with gas bottle design and manufacturing methods; Dr. M. A Worsley, Dr. S. Chandrasekaran, Dr. E. Meshot, Mr. M. Tsurumoto, and Ms. M. Davidson of LLNL for their extensive scientific contributions to resin development and testing; Ms. S. Mabery, Mr. T. Bryson, and Ms. K Baron of LLNL for their technical support of material's preparation, printing, testing, and characterization; and Mr. N. Loey, Dr. H. Villanueva, and Mr. J. Kochavi for their extensive contributions on the design, optimization, and mechatronic implementation of the 3D-printing processes in this work. This work was performed under the auspices of DOE by LLNL under contract DE-AC52-07NA27344. LLNL-TR-863944.

II.3.1.13 Biobased, Inherently Recyclable Epoxy Resins to Enable Facile Carbon-Fiber Reinforced Composites Recycling (National Renewable Energy Laboratory)

Nicholas A. Rorrer, Principal Investigator

National Renewable Energy Laboratory
15013 Denver West Parkway
Golden, CO 80401
E-mail: nicholas.orrer@nrel.gov

Gregg T. Beckham, Co-Principal Investigator

National Renewable Energy Laboratory
15013 Denver West Parkway
Golden, CO 80401
E-mail: gregg.beckham@nrel.gov

Rich Davies, Composites Core Program Manager

Oak Ridge National Laboratory
Materials Science and Technology Division
1 Bethel Valley Rd.
Oak Ridge, TN 37830
E-mail: daviesrw@ornl.gov

H. Felix Wu, DOE Technology Development Manager

U.S. Department of Energy
E-mail: Felix.Wu@ee.doe.gov

Start Date: October 1, 2020
Project Funding: \$500,000

End Date: September 30, 2023
DOE share: \$500,000

Non-DOE share: \$0

Project Introduction

The use of carbon-fiber reinforced composites (CFRCs) in vehicles is a promising approach as CFRCs exhibit a superior strength-to-weight ratio and stiffness-to-weight ratio than that of steel at 60–70% of a steel's weight, thus increasing vehicle fuel-efficiency. Despite this promising feature, CFRCs have currently not been widely implemented into the structural components of vehicles because of the high-cost of CF, as well as their brittleness and inability to be repaired when damaged. To this end, we propose to develop biobased, inherently recyclable, high-performance resins for CFRCs using covalent adaptable networks (CANs), otherwise known as vitrimers. These CAN-based CFRCs (CAN-CFRCs) will enable facile CF recycling and improve CFRC mechanical properties and performance.

Objectives

Overall, the proposed project aims to increase the use of reinforced composites in vehicles by enabling the recovery of CF via the use of CAN chemistry. We further aim to demonstrate that:

- The proposed chemistry can reuse CF in multiple material lives without detriment to the performance of the CFRCs as measured by their thermomechanical properties
- The use of bio-derivable building blocks can result in the requisite performance across multiple lives
- The use of bioderived building blocks can result in a cost-competitive resin while simultaneously lower the associated supply-chain energy and greenhouse gas (GHG) emissions [1]
- The reuse of CF across multiple lives can reduce the impacts associated with CF manufacture.

To accomplish these goals, the project work is divided into four tasks including:

- Synthesis of CAN-CFRC

- Sizing of fiber reinforcements for enhanced performance, repairability, and durability
- Validation and scale-up for manufacturing automobile parts
- Techno-economic analysis, life cycle assessment, and supply-chain modeling of the materials relative to incumbent composite materials.

Approach

To accomplish our objectives, the first year of this project was aimed at initially demonstrating our resin could be used alongside CFs to produce CFRCs with thermomechanical properties that are comparable to the industry-standard epoxy-amine chemistries and could be depolymerized without damaging the fiber. Post-depolymerization, the fibers were reused with addition of virgin resin to demonstrate that properties can be obtained across multiple lives and was complimented by a techno-economic analysis and a supply-chain analysis focused on calculating the cost, supply-chain energy, and GHG emissions of the resin and composites. This approach is summarized in Figure II.3.1.13.1.

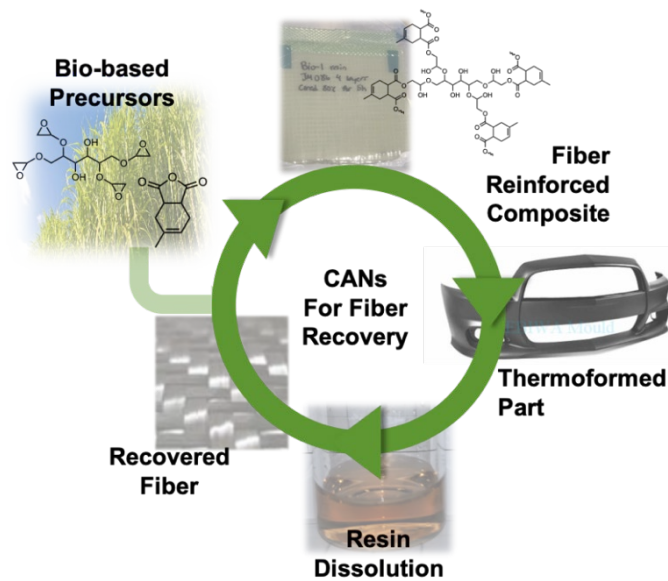
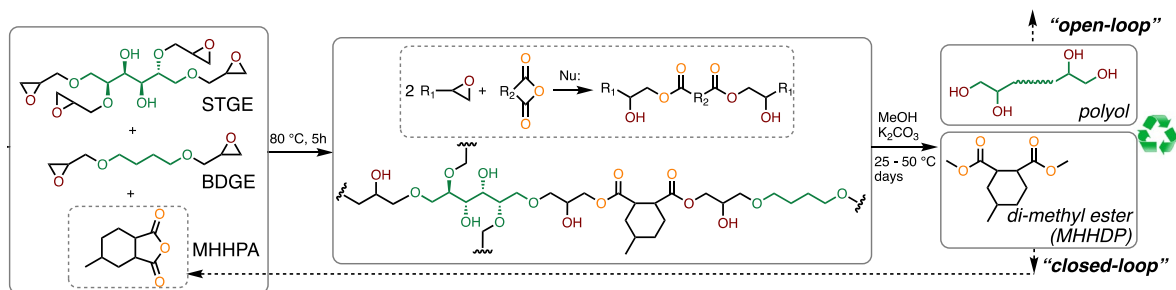


Figure II.3.1.13.1. Project overview. Source: NREL.

To demonstrate the reuse of the CF across multiple lives, it was necessary to develop a recyclable resin, unlike today's standard epoxy-amine resins. To these ends, we implemented a polyester-based covalently adaptable network (PECAN), which consists of both epoxy components and anhydride components. Akin to today's standard resins, PECAN possesses epoxies that enable quick reactivity; however, the PECAN uses an anhydride hardener, instead of an amine hardener, so the resultant chemical bonds are esters instead of carbon-nitrogen. The epoxy and hardener components are biobased. Figure II.3.1.13.2 provides chemical structures of the materials. Designedly, the polymerized esters can be recycled by hydrolysis or alcoholysis.

As outlined below and demonstrated in our project milestones, the second year of this project built upon our previous year results and was overall successful. We demonstrated that (1) the PECAN-CFRCs can enable the reuse of CF over multiple lives, (2) the reuse of the CF can lead to decarbonization benefits, (3) the formulation of the material for ideal properties was possible, and (4) the material could be thermoformed.



Note: SPGE = sorbitol tetraglycidyl ether; BDGE = butanediol diglycidyl ether; MHHPA = methylhexahydrophthalic anhydride; MHHPD = methylhexahydro dimethyl phthalic ester

Figure II.3.1.13.2. PECAN resin chemistry in which bioderived epoxies and anhydrides are combined to a crosslinked network and can be recycled with methanol. Source: NREL.

Results

All results that follow are covered by U.S. Provisional Patent Application No. 63/087,547 [2]. Additionally, this project has experienced minimal delays due to the ongoing COVID-19 pandemic aside from limited laboratory time and space. The results summarized here were reflected in our peer review presentation and quarterly milestones. Some results are still preliminary and will be considered final when published in the peer review literature. Recently, the results were accepted in a peer-reviewed publication with a second publication currently under review. At the time of the writing of this report, the first publication was published in *Matter*. This report provides an overview of our work and the project to date. Not included in this report is our work on fiber-sizing with the PECAN resin. In general, the PECAN resin was found to be compatible with a wide array of fiber-sizing, which is possibly the result of its simple formulation. Relative to the rest of the results presented here, we discovered the effect of sizing was not consequential to the performance or analysis of our CFRCs.

During the first year of this project in FY 2021, we designed a recyclable resin system, as shown in Figure II.3.1.13.2 above and tested its CFRC properties. As those results are important for every aspect of this project, we re-summarize those results here. Relative to two epoxy-amine based CFRCs, the PECAN-CFRCs exhibit comparable strength in both longitudinal and transverse testing. This is indicative that the resin is compatible with the CFs. This is slightly impressive as there are no additives used in the formulation, thus, there is still a huge potential to modify the resin formulation for enhanced performance. Table II.3.1.13.1 provides a list of the PECAN-CFRC properties relative to epoxy-amine CFRCs.

Following the demonstration of first life properties, we subsequently aimed to reuse the CFs across multiple lives. As outlined above, the PECAN resin can be depolymerized using low-energy/temperature-methanolysis. For the depolymerization, potassium carbonate (K_2CO_3) is used as a catalyst alongside methanol (MeOH) and an optional co-solvent (either acetone or dichloromethane), as shown in Figure II.3.1.13.3(a), to break the resins bond and remove it from the CF. Post-depolymerization, the CF is left intact with its orientation substantially maintained, as indicated in Figure II.3.1.13.3(c-d). At the end of FY 2022, we demonstrated the CF could subsequently be reused alongside virgin PECAN resin to exhibit comparable performance across three lives, as demonstrated below, for three CFRCs across multiple generations. When chopped fibers were used, and thus, we did not have to be concerned about orientation, minimal loss in performance was detected across multiple lives, as observed in the graph of Figure II.3.1.13.3(b). For the aligned fibers, across all three generations, the storage moduli, E' , are within the measurement error of 10 ± 2 GPa and the glass transition temperature, T_g , as measured by the maximum of $\tan\delta$, is $139 \pm 1^\circ C$, as shown in Figure II.3.1.13.3(e-g). Supplemental studies were also conducted with virgin fibers and a depolymerization mixture to ensure the depolymerization solution did not affect the properties of the CFRCs, thus demonstrating that PECAN could result in CFRCs with consistent properties ($< 20\%$ variation) across multiple lives. Overall, this makes the PECAN resins an excellent candidate for use and reuse in CFRCs.

Table II.3.1.13.1. PECAN-CFRC Properties Relative to Epoxy-Amine CFRCs

	Longitudinal Tensile Strength (GPa)	Longitudinal Tensile Modulus (GPa)	Transverse Tensile Strength (MPa)	Transverse Tensile Modulus (GPa)
PECAN-39	1.7 ± 0.1	125 ± 4	34 ± 2	7.5 ± 0.4
Epoxy-Amine-RIMR/H135/1366	1.73 ± 0.09	124 ± 3	24 ± 3	7.1 ± 0.9
Zoltek PX35	1.713	129	51	10.1

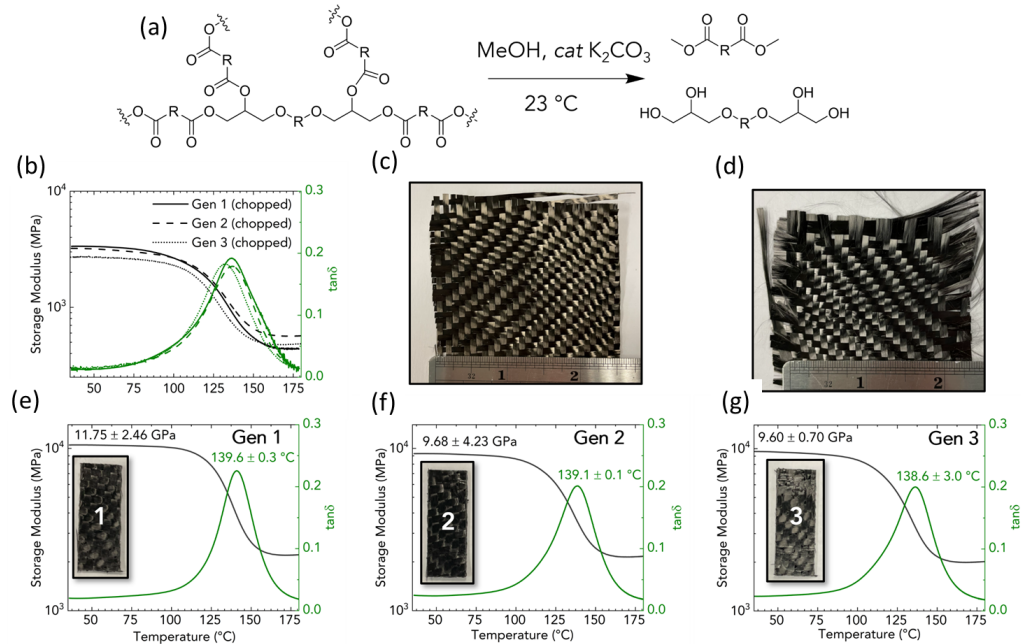


Figure II.3.1.13.3. (a) Methanolysis mechanism for the PECAN-CFRCs. (b) Dynamic mechanical analysis (DMA) temperature sweeps (single-cantilever, 1Hz) of the storage modulus and the tan delta are shown for three generations of chopped CFRP. (c) Virgin and (d) recovered fibers are shown for woven composite depolymerization experiments. DMA temperature sweeps are also shown across (e) the first, (f) the second, and (g) the third-generation for woven PECAN CFRPs. Source: NREL.

During FY 2023, our work primarily focused on demonstrating the weldability, healing, and the thermoforming of the PECAN-CFRCs and resins. This is because the same ester chemistry that makes the resins recyclable also enables for exchange of the chemical bonds to yield rearrangement of the network topology. Due to this, the resins can be repaired with the same resin with no detriment to the materials performance. Figure II.3.1.13.4 (a-f) demonstrates this where a broken resin can be repaired with fresh PECAN resin to yield a complete network in which mechanical failure does not occur at the repair site. This result importantly indicates the PECAN resin and CFRCs made with the PECAN resin can be healed and welded. In addition to being healable, the resin chemistry enables the CFRCs to be thermoformable. Originally, we tested thermoforming by using a multi-faceted mold, as shown in Figure II.3.1.13.4(d), in which the mold has convex, concave, and flat portions of different slopes. The use of this mold to shape the CFRC is indicative that the CFRCs made with the PECAN resin can take multiple shapes. The thermoformed PECAN-CFRC is shown in Figure II.3.1.13.4(e). Finally, we did perform creep analysis on the CFRCs and demonstrated that above 180°C , which is above the PECAN resins glass transitions, the CFRCs can relax and be reshaped, as seen in Figure II.3.1.13.4(f). Importantly, at a temperature of 35°C , which would be a warm day of 95°F , the CFRCs do not exhibit significant ($\sim 0.01\%$) creep.

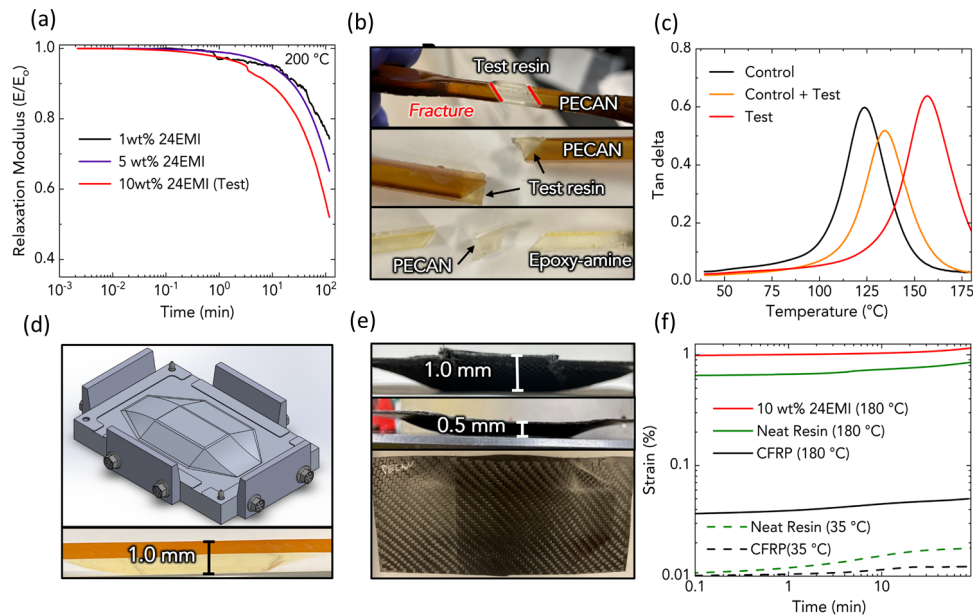


Figure II.3.1.13.4. (a) Stress relaxation experiments were performed with differing loadings of 2-ethyl-4-methyl imidazole (24EMI) catalyst. (b) Repair of the PECAN resin is demonstrated with pictures of repaired PECAN coupon, broken coupon, and epoxy-amine control repair. (c) DMA thermograms of the control and test resins. (d) Thermoforming experiments were performed using a male/female mold and neat resin within a heated hydraulic press. (e) Using the same geometry, a thermoformed panel of PECAN-CFRC is shown with two differing elevations. (f) DMA iso-stress experiments (single-cantilever) at 35 °C (dotted) and 180 °C (solid) are shown for PECAN CFRP (black), neat resin (green), and test resin with 10 wt.% 24EMI. Stresses for each experiment were chosen as 1/1000 of the storage modulus of the material at 35 °C. Source: NREL.

In addition to thermoforming the multifaceted mold, we also thermoformed a demonstrative car hood and car roof. We have demonstrated the thermoformed shapes do not experience material damage, and thus, their properties do not suffer. Additionally, the panels can be thermoformed into a second life application, even changing their shape. We have demonstrated a hood panel can be converted to a flat panel, and subsequently, to a roof panel, once again with no detriment in performance; however, we note we need to develop a better understanding of CF drapping when making these pieces. Of important note, these results indicate that for the PECAN-CFRCs, thermoforming is a viable recycling means for multiple lives.

Finally, this project has been supported by extensive techno-economic, life cycle, and supply-chain analysis throughout the life of the project. Specifically, we have analyzed the production of the PECAN resin relative to an epoxy-amine resin, the recycling and reuse of the CFs by chemical depolymerization, and the reuse of the PECAN-CFRC by thermoforming. Results are summarized in Table II.3.1.13.2. Since the FY 2022 version of this report, we have refined our analysis and updated our datasets; thus, the numbers reported here are not dramatically different, demonstrating the same trends, but are more accurate.

As seen, the second life of the CFRCs, either by chemical recycling or thermoforming, yield dramatic benefits in both cost, supply-chain energy, and supply-chain GHG emissions. Thermoforming exhibits the most benefits, as the infrastructure and heat requirements are minimal and the CFRC remains intact, thus not requiring remanufacture of the entire CFRC.

Table II.3.1.13.2. Techno-economic and Supply-Chain Analyses Results for the PECAN-CFRCs Across Multiple Lives

Resin Components		Supply-Chain Energy, MJ/kg	GHG Emissions, kg CO ₂ -e/kg	Minimum Selling Price, \$/kg
Petroleum-Based Resin	Overall	129	5.7	2.03
Biologically Derivable Resin (PECAN)	Overall	86	4.7	2.17
CF		610 [1]	43.3 [1]	21.50 (Variable) [1]
PECAN-CFRCs (First Life)		367	24.3	11.89
CF Recovery		31.2	1.8	2.36
PECAN-CFRCs (Chemical Recycling, Second Plus Life)		79	4.6	2.24
PECAN-CFRCs (Thermoforming, Second Plus Life)		5.4	0.4	0.90

The results presented in Table II.3.1.13.2 represent the “base case” used in this work. The assumptions in the base case were that (1) the CF could be reused without resizing, as demonstrated above; (2) the entirety of the depolymerized resin was sent to waste; and (3) the CFRCs were reclaimed at a cost near similar to plastics recycling, namely the price that poly(ethylene terephthalate) is reclaimed and sold. Of particular interest are the second and third assumptions. As noted in Figure II.3.1.13.2, the anhydride component of the resin is recyclable. When our modeling is adjusted to recover and reuse the anhydride, the minimal selling price (MSP) of the CF would drop to \$1.56/kg, a 44% reduction from the base case and a 93% reduction relative to the cost of virgin CF, as shown in Figure II.3.1.13.5(a). As evident in Figure II.3.1.13.5(a), the largest contribution to the recycling cost is the “feedstock price,” or the cost to reclaim the CFRC for recycling. As stated in the third assumption, we initially assumed this cost was the cost typically associated with the recycling of poly(ethylene terephthalate). That assumption was made, because currently recyclable CFRC are not a market technology, and thus, that infrastructure does not exist. As presented in Figure II.3.1.13.5(b), the selling price of the reclaimed CF (rCF) is linearly proportional to the feedstock price; thus, the feedstock price, or reclamation cost, represents the largest cost driver for CF. Interestingly, if the CFRCs could be reclaimed for the same cost as vehicles scrap metal, which is a realistic assumption, the rCF cost could be reduced by >50%; thus, representing the potential in this work for a large impact.

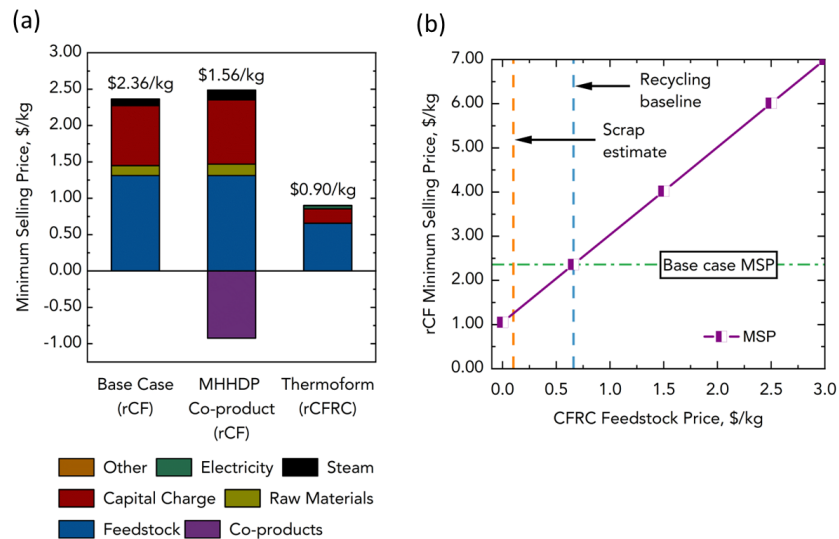


Figure II.3.1.13.5. Techno-economic analysis results for the circularity of the PECAN-CFRCs. (a) The MSP for the different scenarios studied here. (b) The sensitivity of the rCF MSP relative to the feedstock cost noting the base case and a scrap estimate price. Source: NREL.

Conclusions

Overall, this work has demonstrated the potential for using bio-derivable recyclable by designing resins for CFRC and vehicles applications. The use of our PECAN resin enables the reuse of the CF, either via chemical depolymerization and subsequent repolymerization or thermoforming. Importantly, this was validated in this work for both cases across three material lives. When these cases are subject to process analysis, extreme benefits are revealed for the second plus life of the CF. In the case of chemical recycling, when no co-products are recovered, an 89% reduction in the second life CFRC MSP and GHG emissions is achieved. Meanwhile, when the CFRC is reused through thermoforming, a 92% and 98% reduction in the second life CFRC MSP and GHG emissions are achieved relative to virgin CF, respectively. Furthermore, greater reductions are possible if co-products are recovered, or the CF recovery cost is cheaper. Thus, this work demonstrates the viable pathway to reuse CF/CFRCs and decarbonize the manufacture associated with these materials.

Key Publications

1. Rognerud, E. G., J. DeVeaux, G. T. Beckham, and N. A. Rorrer, 2024, “Towards a better steel replacement: Bio-derivable carbon fiber composites across multiple lives,” under review; journal TBD.
2. Wang, C., R. Murray, A. Singh, G. Musgrave, E. G. Rognerud, M. Skala, P. Murdy, S. R. Nicholson, A. Shapiro, J. Miscall, R. Beach, R. D. Allen, N. A. Rorrer, and G. T. Beckham, 2023, “Polyester covalently adaptable networks for composite applications from sugar derived building blocks,” *Matter*, 7, 550–568. <https://doi.org/10.1016/j.matt.2023.10.033>.

References

1. Nicholson, S. R., N. A. Rorrer, A. C. Carpenter, and G. T. Beckham, 2021, “Manufacturing energy and greenhouse gas emissions associated with plastics consumption,” *Joule*, 5(3), 673–686. <https://doi.org/10.1016/j.joule.2020.12.027>.
2. U.S. Patent US20220106442A1, “Bioderived recyclable epoxy-anhydride thermosetting polymers and resins,” April 7, 2022.

Acknowledgements

The project PIs would like to thank the contributors to this work. E. Rognerud is the lead experimentalist. J. DesVeaux and O. Greene were instrumental in the analysis component. R. Murray and her team were instrumental in demonstrating the scalability of the CFRCs using industrially relevant vacuum-assisted resin transfer molding techniques.

II.3.1.14 Soft Smart Tools Using Additive Manufacturing (Savannah River National Laboratory)

Matthew Craps, Principal Investigator

Savannah River National Laboratory
Bldg. 999-2W
Aiken, SC 29808
E-mail: matthew.craps@srnl.doe.gov

Srikanth Pilla, Co-Principal Investigator

Clemson University, International Center for Automotive Research
4 Research Dr.
Greenville, SC 29607
E-mail: spilla@clemson.edu

Richard Czerw, Co-Principal Investigator

Mainland Solutions, LLC
409 W. Maple St.
Yadkinville, NC 27055
E-mail: czerwr@mainlandsolutions.com

Rich Davies, Composites Core Program Manager

Oak Ridge National Laboratory
Materials Science and Technology Division
1 Bethel Valley Rd.
Oak Ridge, TN 37830
E-mail: daviesrw@ornl.gov

H. Felix Wu, DOE Technology Development Manager

U.S. Department of Energy
E-mail: Felix.Wu@ee.doe.gov

Start Date: November 1, 2021

End Date: September 30, 2023

Project Funding: \$220,000

DOE share: \$220,000

Non-DOE share: \$0

Project Introduction

Tooling is an integral part of composites manufacturing. Composite tools, also called “soft” tools, are more easily constructed than ‘hard’ metal tools and, because they are made from materials similar to the manufactured composite part, they can be made in-house and have a good coefficient of thermal expansion match. However, as the ‘soft’ designation suggests, they are more vulnerable to wear and typically find application in relatively low-volume production. AM of thermoplastics has proven to be a lucrative option that can help improve the tooling functionalities, as it offers more design flexibility. Owing to the inherent nature of AM, the possibility of printing sensors within the tool material and at proximity to otherwise inaccessible areas of the tool become a reality. CCF-reinforced 3D printing of engineering thermoplastics has proven to be a viable option to strengthen a part well beyond the ideal moduli of unmodified thermoplastic. Furthermore, adding nanotubes or graphene to the thermoplastic matrix will also improve both the TC and interlaminar shear-strength within the tool. CNTs and CFs are microwave susceptors; exploiting the physics of Joule-heating to increase the energy-efficiency of tool-hardening and cure rates is a core goal of this project. Because of the rapid volumetric heating enabled by the absorption of microwave or radio frequency energy and EM annealing presents an attractive opportunity to significantly reduce manufacturing cycle times while improving part performance.

The introduction of integrated sensors, such as TCs and strain gauges, allow for real-time feedback for the end-user, thus resulting in improved process controls, such as thermal management. Strain gauges provide valuable information about when the tooling becomes warped beyond tolerance and needs to be scrapped. TCs help with reducing wasted processing time because the tooling temperature can be monitored for optimized cure schedules and out-of-tolerance thermal gradients. AM principles allow these integrated smart sensors to be printed simultaneously with production of the soft tool. Incorporation of integrated sensors into composite tools enables process controls that will further improve cycle times and reduce scrap rates.

Objectives

The goal of this Savannah River National Laboratory (SRNL) project is to develop high-toughness, wear-resistant CCF nanocomposite tooling with embedded sensors for vacuum bag molding or autoclaving of automotive parts. Using EM post-annealing of 3D-printed CCF and nanotube composite structures will improve the strength and TC of the tooling as compared to traditionally annealed soft composite tools. AM allows for the integration of printable smart sensors to continuously monitor temperature, strain, and pressure within the tool itself, enabling improved process controls and lower inter-part variability. If successful, this technology will decrease soft-tooling costs by 30%, increase process throughput by 50%, and reduce failures in the molding process.

Approach

To increase process throughput, reduce scrap rates, and lower soft-tooling costs, the project is prototyping soft smart tooling using AM techniques incorporating the following concepts:

- Nanomaterial-filled thermoplastics to improve TC with added tool strength in 3D continuous fiber printing. This allows for thinner tooling with less thermal gradient and thermal lag.
- Post-curing and post-annealing performed by coupling microwave or induction radio frequency energy directly to the susceptor-enhanced nanomaterials, resulting in reinforcement and improved polymer crystallinity for greater mechanical and thermal properties.
- Temperature, heat flux, strain, and pressure sensors printed into the tool to monitor cure kinetics, voids (especially for resin transfer molding), and spring-in.

Our approach seeks to 3D print nanomaterial enhanced CCF soft-tooling with embedded sensors. Incorporating nanomaterials into the soft-tooling adds toughness and improved TC; EM annealing increases polymer crystallinity, further increasing mechanical and thermal properties; and adding sensors allows the user to monitor temperature and pressure during part manufacturing. Process controls implemented using sensor feedback allows the user to identify when a tool needs to be scrapped and replaced.

Figure II.3.1.14.1 provides a detailed schematic of our approach. The CCF tow, prepared with a thermoplastic prepreg containing our nanomaterials, is printed by the layup head. The nanomaterials incorporated within the prepreg, designed to be EM susceptors, are added at a concentration at which TC between z-direction layers increases; this is a major challenge in AM. During printing of the layers using the CCF tow enhanced with nanomaterial-embedded thermoplastic substrate, secondary reservoir heads with conductive inks are used to print TC and/or strain-gauge sensors *in-situ*. Table II.3.1.14.1 provides the milestones and status for FY 2023.

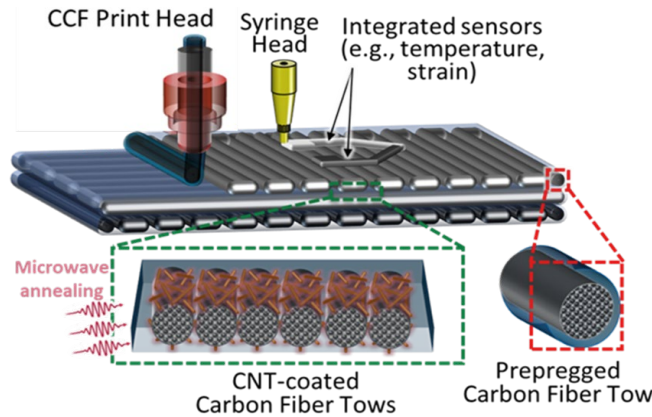


Figure II.3.1.14.1. Diagram of 3D printing equipment for CCF composites: Source: SRNL.

Table II.3.1.14.1. Project Milestones and Status

Milestone Name/Description	Milestone Status
M3.1: Provide final optimization design of the SMART SOFT tool for prototyping.	Complete
M3.2: Demonstrate at least 25% reduction in energy consumption using EM-energy post-heated tools with prototype full integrated SMART sensors.	Complete
Year 3 Milestone: Demonstrate SMART SOFT tool enabling 50% reduction in tool lead time, 40% reduction in energy intensity, and greater than 30% life cycle cost-savings.	Pushed to FY 2024 Q3 due to the relocation of S. Pilla to UD-CCM.

Results

Figure II.3.1.14.2(a–f) illustrates the process and results. TCs are based on the Seebeck effect—as the temperature changes, voltage is generated, which can be correlated to temperature. The 3D-printed TC developed and selected for the final design for prototype tool testing utilizes carbon-based materials resistant to oxidation in air. An all-carbon thermal sensor was produced at the Clemson University International Center for Automotive Research (CU-ICAR) using a multiwall carbon nanotube (MWCNT) and carbon black (CB). This is an improvement on our previous design that had a low-temperature polymer that would degrade. This is now an all-carbon TC capable of measuring the full range of temperatures this tool can see. The CB and MWCNT, along with a small amount of surfactant, were dispersed in water and sonicated. The ink that was subsequently produced was printed on a 3D-printed part, as well as a flexible Kapton piece to test the flexibility of the sensor and followed by drying and rinsing to remove the surfactant. The materials used to produce this sensor are environmentally friendly, and the ink itself is water-based, so no aggressive solvents were used. Since the MWCNT and CB are known to have very high-thermal stability, this TC has the potential to measure a wide range of temperatures. The previous TEA/LCA showed a greater than 25% reduction in energy consumption for the hat structure tool. The results of 3D-scanning and comparing the tool surface with the CAD and initial scan help determine whether the tool is within acceptable tolerance or needs to be resurfaced. After 100, 1000, and 10,000 cycles at RT, the tool was 3D-scanned again and showed no deformation. The next step is to complete the same cycles at 60°C, and then at 90°C, and continue the 3D-scanning while looking for signs of deformation or warpage.

The diameter of the treated CCF filament should be roughly 380 microns to be printed successfully. Glacial acetic acid was chosen as the solvent as it dissolves Nylon 6. Improvements to the CNT coating line for the CCF filaments included a tensioner and lower friction tracking pulleys to ensure the filaments stayed on track without breaking.

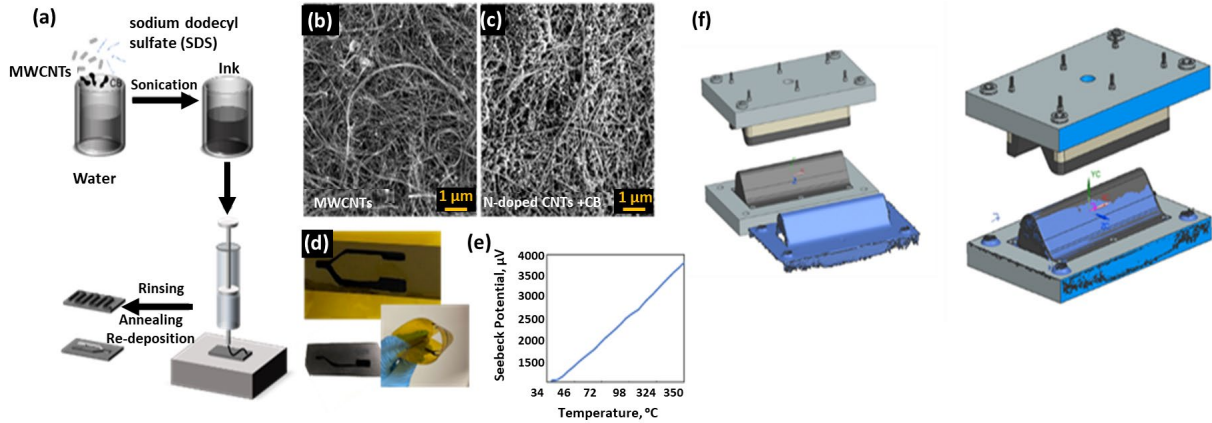


Figure II.3.1.14.2. (a) Schematics of thermocouple printing process. (b–c) SEM images of inks printed using the protocol shown in (a) demonstrate a uniform MWCNT and CB dispersion on the substrate. (d) Thermal sensors printed on the 3D-printed thermoplastic part and Kapton. (e) Typical thermoelectric response of the thermal sensor shown in (d). (f) 3D-scan of the tool before and after 10,000 cycles showing no deformation. Source: SRNL and CU ICAR.

Efforts to develop a methodology to assess the potential energy savings due to the SMART 3D-printed thermoplastic tool for composites manufacturing processes have been described previously. A comparative life cycle energy assessment (LCEA) was proposed to quantify the cumulative energy demand of three unique scenarios, each representing a different material and manufacturing approach to tool-making. The scenarios compare the proposed 3D-printed tool concept with traditional approaches to making tools for medium-to-high-production scale composite manufacturing processes, such as thermoforming and vacuum-infusion on in-autoclave prepreg molding. Since thermoforming is the most demanding in terms of fast cycle times, tool-heating, tool-cooling, and consolidation (compression) pressures, the LCEA considers this process. Thus, the process flows for the three scenarios were compiled with thermoforming in mind. A thermoplastic blank is heated beyond the melt temperature (t_m) and then formed into the shape using a tool that is close to this temperature, thereby resulting in a process representing a hot blank on a heated tool. This ensures gradual cooling and good microstructure properties, translating to good mechanical properties. The results of the assessment show the 3D-printed thermoplastic tool is more energy-efficient than current metal tool, as well as the composite tools as illustrated in Figure II.3.1.14.3.

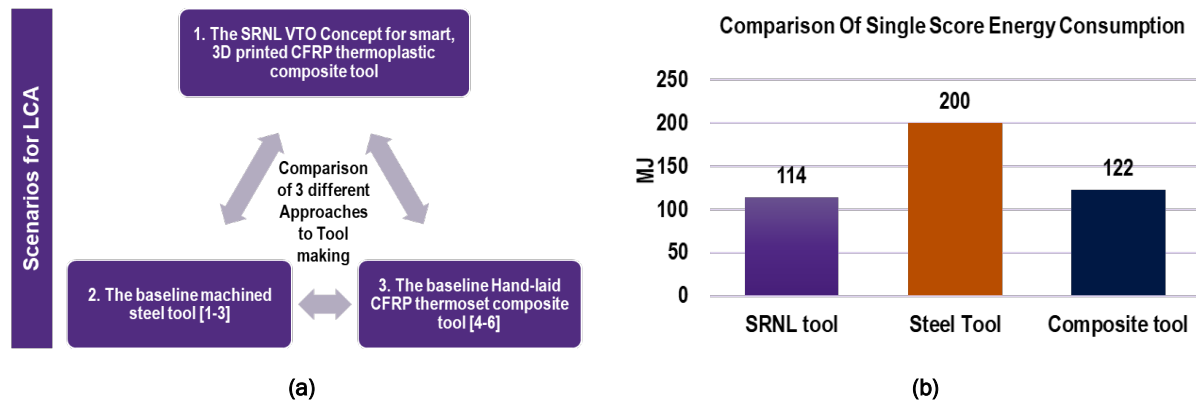


Figure II.3.1.14.3. (a) LCEA scenarios and (b) LCEA results using SimaPro and Ecoinvent 3.0 database. Source: CU ICAR.

However, a major assumption here is that one tool is sufficient to meet the production scale (i.e., the tool wear is equal following a prescribed number of cycles). Lack of data on the wear and tear of tools used for composites manufacturing warrant further study, where a prototype 3D-printed tool is subjected to cyclic compression loading and 3D-scanned after a set number of cycles to determine whether the forming surfaces of the tool are still within tolerance.

Conclusions

In the composites industry, tools are the molds on which layups are applied to create finished parts. Hard tools are tools made of metals that typically have a poor CTE that match with the composite part. Hard tools have to be made by third-party vendors who specialize in such materials because they require precise machining and polishing. Composite tools, sometimes called soft-tooling, are more easily constructed than metal tools and, because they are made from materials similar to those the composite manufacturer will use for the part, they can be made in-house, and have a good CTE match. However, as the “soft” designation suggests, they are more vulnerable to wear, and they typically find application in relatively low-volume production. The tradeoff of lower tooling and setup costs, and low process throughput for composites vs. the higher tooling costs and higher throughput for metals gives rise to a part count threshold in which the advantage lies with the soft-tooling parts. This is why the research conducted here is so valuable to the industry.

Key Publications

Three publications are currently in progress.

Acknowledgements

SRNL would like to acknowledge our sponsor, the DOE VTO, and Dr. H. F. Wu, the DOE VTO Technology Manager. This work was performed at SRNL and managed by Battelle Savannah River Alliance in collaboration with CU-ICAR, the UD-CCM and Mainland Solutions, LLC. Key contributors include J. Gaillard, D. Digby, W. T. Adams III, and N. White of SRNL; D. Huynh of Georgia Tech; and A. Deshpande and U. Lad of CU-ICAR/UD-CCM.

II.3.1.15 Multifunctional Smart Structures for Smart Vehicles (Ford Motor Company)

Patrick Blanchard, Principal Investigator

Ford Motor Company
2101 Village Rd.
Dearborn, MI, 48121
E-mail: pblanch3@ford.com

Rich Davies, Composites Core Program Manager

Oak Ridge National Laboratory
Materials Science and Technology Division
1 Bethel Valley Rd.
Oak Ridge, TN 37830
E-mail: daviesrw@ornl.gov

H. Felix Wu, DOE Technology Development Manager

U.S. Department of Energy
E-mail: Felix.Wu@ee.doe.gov

Start Date: October 1, 2020
Project Funding: \$9,021,422

End Date: December 31, 2023
DOE share: \$5,157,264

Non-DOE share: \$3,864,158

Project Introduction

Adding new content and functionality to a vehicle subsystem can often result in a layering effect, whereby technologies are effectively stacked on top of each other. This design approach can lead to inefficiencies in packaging and an increase in cost and weight. An alternate approach is to integrate new functionality into the base structure to not only provide the structural performance, but other system-level functionality as well. With this in mind, this project aims to develop a new class of multifunctional composite materials and processing technologies that can lead to lightweight fully integrated smart structures and surfaces. These new materials and processing methods promise to have application to a broad range of automotive components, thus magnifying the impact on the ability to achieve long-term fuel economy and/or vehicle range improvements.

Objectives

This project will develop a new class of recyclable multifunctional composite materials to produce lightweight smart structures and surfaces. Functional high-stiffness conductive composites will be processed using novel water-assisted injection-molding, while integrating continuous fiber and additively manufactured hard points for optimized load transfer. Methods for integration of sensing functionality and controls will be developed to reduce system cost while providing a new capability for structural health monitoring. This new class of composites is applicable to a broad range of vehicle interior, exterior, and battery enclosure systems. By way of demonstration, a vehicle instrument panel cross car beam (CCB) will be developed to provide a 40% mass-savings compared to steel while maintaining a cost penalty of less than \$3 per pound saved. These technologies will be validated for implementation by a uniquely qualified project team comprising Ford Motor Company (Ford), Yanfeng Global Automotive Interiors, and with key contributions from ORNL, Purdue University, and Michigan State University (MSU).

Approach

The project covers three budget periods (BPs):

- BP1 focused on concept design and development
- BP2 focused on final design, materials, process scale-up, and optimization
- BP3 is ongoing with an emphasis on manufacturing demonstration, prototype validation, and testing.

In the first year, a conceptual design for a new composite-based CCB was developed using CAD and based on laboratory testing of candidate materials. In the second year, the CCB design was further refined based on

manufacturing feasibility trials and material and process optimization. Unit cell operations for integration of all over-molded structural inserts and sensors were demonstrated. A completed CAD for the CCB was prepared and issued to a supplier for prototype tooling fabrication. In the final year, the team commissioned the aforementioned tooling to manufacture CCB prototypes for testing and validation. Materials and processing optimization has also continued towards a full-scale molding demonstration that is planned in the last quarter. During this exercise, the ability to fixture inserts and continuous fiber into the injection mold and retain them through the injection process will be demonstrated.

To manage all project objectives, 11 different working groups were established in addition to Task 0 that encompasses project management-related tasks, as indicated in Figure II.3.1.15.1. Task 1, “Component Design, Analysis and Prove-out,” is considered the lead work stream with Tasks 2 through 11 as dependents. Therefore, the reporting included in this annual report will highlight the work on tooling fabrication in FY 2023 followed by status on the supporting work streams.

RASIC Chart: Multi-Functional Smart Structures For Smart Vehicles					
R: Responsible: The Institute/Company Responsible for this task					
A: Approve: The company/institute giving the approval					
S: Supporting: The Company/Institute giving support for the completion of the task					
I: Informed: The Company/Institute to inform about this task					
C: Consulted: The company/institute that can act as expert in regard to the task					
Task 0. Program Management				R	
Task 1. Component Design, Analysis & Prove-Out	I	S	S	R, A	S
Task 2. Formulation/Compounding of novel materials	I	I	R	S, A	R
Task 3. Water-Assist Injection Molding (WAIM) Process Development	S	I	S	R	S
Task 4. Tow/Tape Placement of Continuous Fiber	I	R	S	S	S
Task 5. Sensor Integration	I	S	S	R	S
Task 6. Additive Manufactured Hardware Attachment Points	S	S	R	S	S
Task 7. High Volume Manufacturing Concept Feasibility Demonstration (sub-scale)	S	S	S	S	R
Task 8. Process Scale Up & Demonstration	S	S	S	S, A	R
Task 9. Additive Manufacturing of Segmented Tooling	I	S	R	S	I
Task 10. Artificial Intelligence/Machine Learning For Process Optimization		I	R	I	S
Task 11. Closed Loop Recycling		I	R	S	S

Figure II.3.1.15.1. Project task breakdown. Source: Ford.

Results

Task 1. Component Design, Analysis, and Prove-Out

The design activities under Task 1 were broken down into subtasks 1.1 through 1.6, as shown in Figure II.3.1.15.2. With the design freeze in the ninth quarter (Q9) of the project, subtasks 1.1 through 1.3 are now complete. That leaves the milestone referenced in Table II.3.1.15.1. The following sections describe ongoing studies in support of Task 1 and the active work streams.

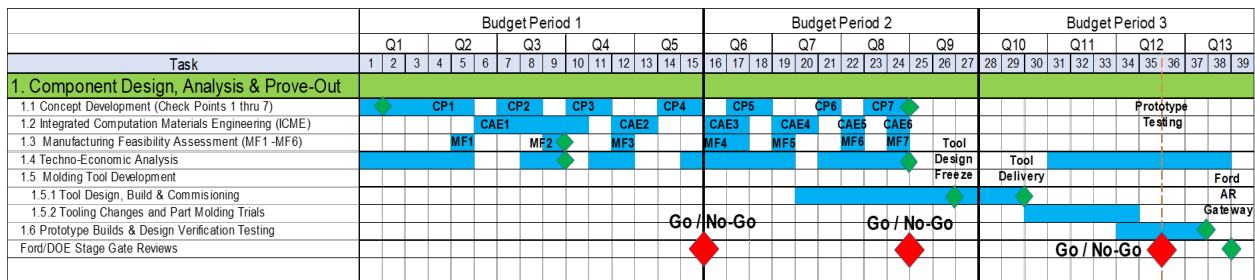


Figure II.3.1.15.2. Task list for component design work stream. Source: Ford.

Table II.3.1.15.1. Milestone for Task 1 Work Stream Activities

Milestone (Project Month)	Lead Organization	Description
---------------------------	-------------------	-------------

3.1.7 Design verification (M37)	Ford	Complete design verification and testing program for CCB assemblies leading to the application readiness gateway.
---------------------------------	------	---

Throughout BP2, the concept for the CCB was finalized into a tool-ready-design that would be ready for prototyping. CAD data was transferred to the tool maker in the fourth quarter of 2022, thus allowing tool design and fabrication to commence. The time required for completion of this work was 26 weeks, leading to a proposed delivery date in June 2023. Hence, during the first and second quarter of this year, the design team worked closely with the tool maker to complete any revisions required to overcome any manufacturing feasibility issues. Figure II.3.1.15.3 shows the finished molding tool that is ready for commissioning.



Figure II.3.1.15.3. Molding tool prior to shipment to MSU. Source: Ford.

Prior to the shipment of the molding tool to MSU, commissioning trials were performed to verify functionality of the molding tool subsystems. Figure II.3.1.15.4 shows an image of the mold mounted into a try-out press contracted through the tool maker. Multiple dry cycles were performed before parts were produced with a glass fiber-filled polypropylene. An example set of these CCB parts are shown in Figure II.3.1.15.5. Based on the success of these trials, the molding tool was shipped for installation at MSU on July 27, 2023. However, after further molding trials at MSU, a problem developed with the ejector plate on the mold. Unfortunately, this required immediate repair thus prompting removal of the tooling from the press at MSU for return to the tool maker. These repairs were completed, however, the absence of a crane at MSU led to further delays in scheduling as rigging services were required to complete the installation. Ultimately operational capability of the tool in the press at MSU was re-established on September 18, 2023. With this task complete, the subsequent months have been focused on the development of the molding process and robot automation. These will support run-at-rate studies that are now planned in November and December 2023. Details of this work are included in Task 3 and Task 8 of this report.

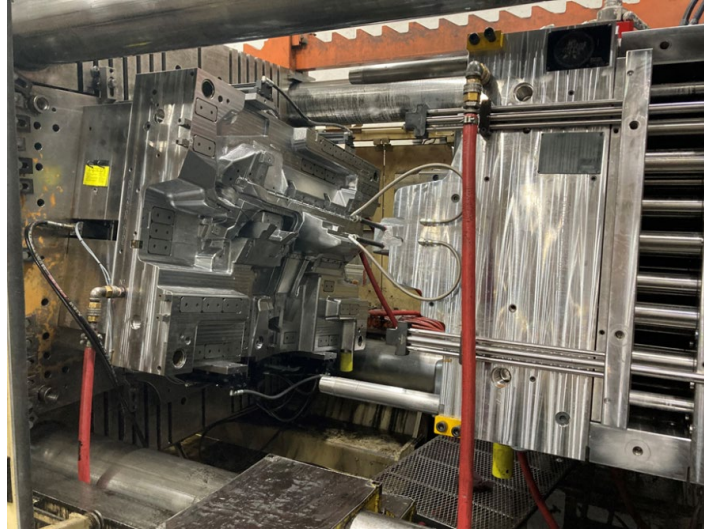


Figure II.3.1.15.4. CCB molding tool prior to shipment to MSU. Source: Ford.



Figure II.3.1.15.5. CCB sample parts from tool commissioning trials in June 2023. Source: Ford.

Task 2. Formulation/Compounding of Novel Materials

During BP3, the materials sub-team has been supporting scale-up of material production in addition to the characterization and verification of mechanical properties. This work has been critical as the material system proposed for the CCB is a new formulation that is not commercially available. Therefore, properties of sample batches from 2022 were compared to larger scale batches produced on a commercial-scale industrial compounding line. The data that follow include a typical fiber content analysis completed for material batches received throughout 2023.

Analysis was carried out by using both thermogravimetric analysis (TGA) and a burn-off method to confirm the target fiber mass fraction was achieved. First, TGA was used to obtain the wt.% vs. temperature profiles. An approximately 10–20 mg sample was heated to an initial temperature of 450°C before increasing the hold temperature to 650°C. The TGA result of polyamide 66 (PA66) with a target 40% fiber loading in Figure II.3.1.15.6 shows that 39.7% weight fraction was calculated for the sample after 450°C, and 9.9% weight residue was left after 650°C. The latter was expected to be given the 30% CF by mass in the compounded materials.

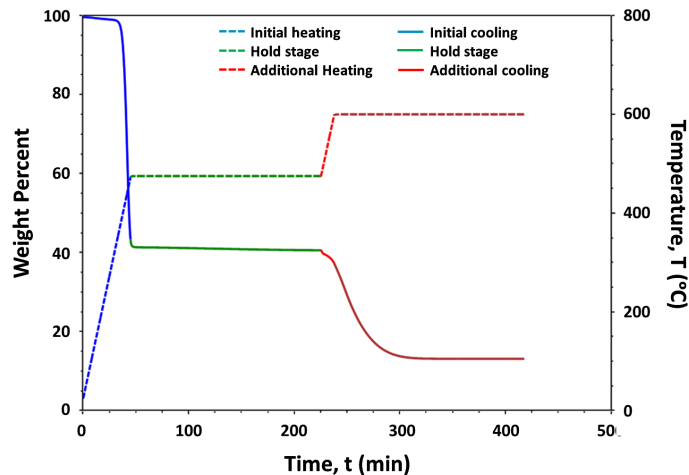


Figure II.3.1.15.6. TGA graph of 40% reinforced PA66. Source: Ford.

Fiber burn-off was used for larger sample sizes to ensure the TGA results were representative of the overall component. As before, samples were heated up to a temperature of 450°C to burn-off the PA66, and then to 650°C to burn-off the CF. To prevent oxidation of CF in air, nitrogen was used as cover gas during the first heating step. Because the nitrogen gas was used, a carbonization-in-nitrogen method was applied for more accurate determination of the fiber content in the matrix. Reference neat resin samples were added during the experiments along with the composite samples. The amount of resin converted to carbon was calculated, and this conversion rate was used as a compensation factor. Figure II.3.1.15.7 shows the progression of the polymer composite samples through the burn-off test. Although there was about ± 2 wt.% variations, both the developmental and production batches of compounded material showed each fiber content close to the target.

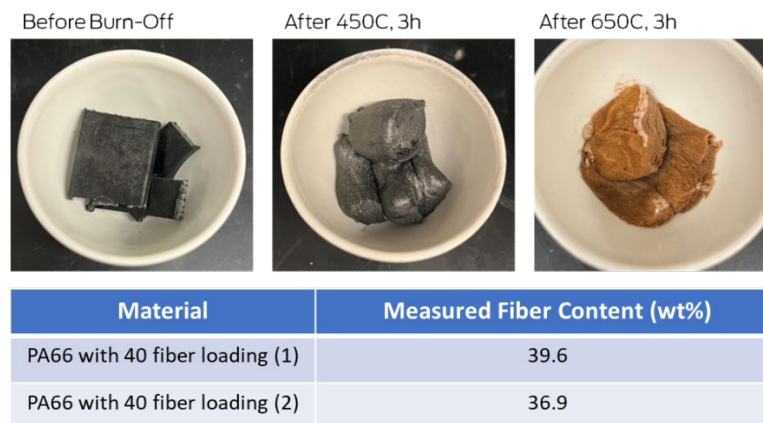


Figure II.3.1.15.7. Polymer composite specimens before and after the burn-off test (top), and weight fractions of each reinforcement fiber obtained after the analysis (bottom). (1) refers to early developmental batches that were used during the past studies, and (2) refers to the batch produced on production intent equipment. Source: Ford.

Task 3. Water Assist Injection-Molding (WAIM) Process Development

To enhance structural design of the CCB, WAIM technology is being investigated to create continuous closed sections within the finished component. BP3 has focused on further process development studies. These trials included development of a valve gate sequence and initial WAIM process parameters, as shown in Figure II.3.1.15.8. Part characterization was performed by sectioning parts, as well as the evaluation of parts utilizing a nondestructive evaluation method for thickness measurements. These techniques helped identify areas of concern with the water channel in the full-scale cross car bumper.



Figure II.3.1.15.8. Parts produced during valve gate sequencing studies. Source: Ford.

The water channel was compared at four intervals along the path, as can be seen in Figure II.3.1.15.9. The channel thickness and consistency were then compared for a 5-second, 10-second, and 15-second pack time. The upper left position is at the water injector transition, the upper right position is the vertical channel, the lower left position is shortly after a ninety-degree turn in the channel, and the lower right position is at the hot runner transition. The channel coring is more prominent with shorter pack times yielding a thinner wall stock on the parts. Processing studies will continue throughout the remainder of the fourth quarter of 2023 to finalize the molding process ahead of prototype part production.

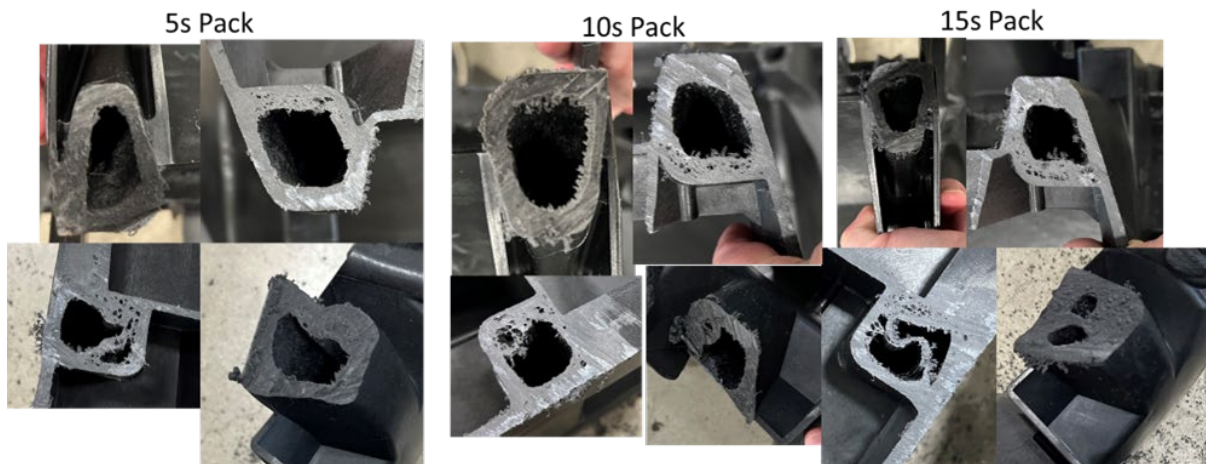


Figure II.3.1.15.9. A comparison of water channel wall thickness with pack time. Source: Ford.

Task 4. Tow/Tape Placement of Continuous Fiber

To support the manufacturing scale-up activities under Task 7, the team at Purdue University has been working to supply multi-tow (M-Tow) preforms for CCB over-molding trials. To produce these preforms, a new automation cell and robot end-of-arm tooling was designed, built, and commissioned. An image of the end-of-arm tooling mounted to the robot is shown in Figure II.3.1.15.10.

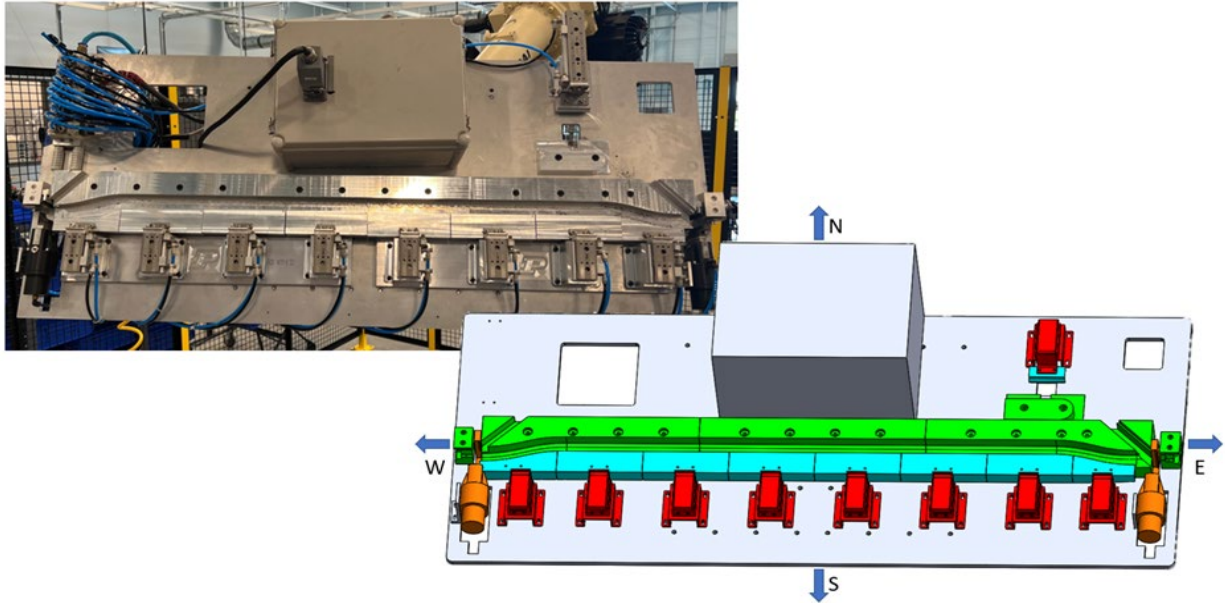


Figure II.3.1.15.10. A comparison of water channel wall thickness with pack time. Source: Ford.

Multiple batches of M-Tow preforms were produced throughout 2023 with a sample set shown in Figure II.3.1.15.11. Initially, there were significant fitment issues of the preforms in the molding tool that prompted development of a checking fixture to provide feedback into the forming process. The fixture shown in Figure II.3.1.15.12 replicates the tool surface and is being used to verify that the hardpoint attachments locate without interference and that the tow follows the prescribed pathway. With the aid of this checking fixture, the M-Tow preforms are now achieving a near 100% acceptance rate. The team's goal is now to produce 100–150 preforms that can be used in scale-up trials and testing. So far, approximately 85 preforms have been delivered to the MSU Scale-up Research Facility for molding.



Figure II.3.1.15.11. M-Tow preforms produced in support of CCB molding studies. Source: Ford.



Figure II.3.1.15.12. M-Tow checking fixtures developed to improve dimensional accuracy of preforms. Source: Ford.

Task 5. Sensor Integration

At the commencement of the project, several sensing and integrated electrical system technologies were investigated. Dead front, capacitive switching, and swappable modular interfaces were identified as having potential for integration into the CCB structure. During BP3, the team focused on finalizing substrate material and printing technologies to ensure the sensor modules could withstand the higher processing temperature of polyamide 66-based composite. Fully populated electronics modules were molded and tested both pre- and post-molding, as shown in Figure II.3.1.15.13, using a test module designed and fabricated by Yanfeng. All components exhibited full functionality both before and after molding. These components are now scheduled for additional testing, including environmental exposure.



Figure II.3.1.15.13. Fully functional over-molded electronics module. Source: Ford.

Dimensional checks using three-dimensional (3D) scanning were also performed on five fully functional electronics modules and were found to be within ± 0.5 mm relative to the original CAD model. A representative 3D scan image with dimensional deviations is shown in Figure II.3.1.15.14. Several components were also test fit in the molding and deemed acceptable at this time. However, robotic pick and place has not yet been performed to ensure fit and function in a fully automated process.

To support the cross car bumper molding development, 200 non-functional over-molded film components were fabricated in addition to fully functional parts, as shown in Figure II.3.1.15.15. The non-functional components will be used for process development activities in lieu of using fully functional components. To date, a total of 25 fully functional parts have been fabricated to date to support various validation testing activities both on a component-level and when incorporated into the CCB.

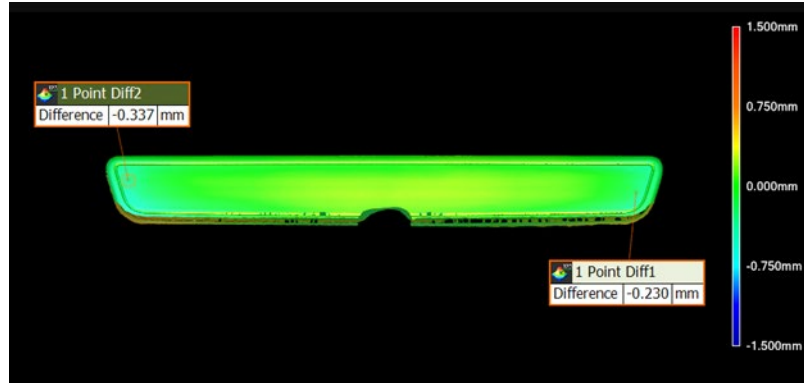


Figure II.3.1.15.14. Dimensional check using 3D scanning of a fully populated electronics module.
Source: Ford.



Figure II.3.1.15.15. (Top) Over-molded films and (bottom) over-molded fully populated films for development activities. Source: Ford.

Task 6. Additive Manufactured Hardware Attachment Points

Due to budgeting constraints at the start of BP3, the AM element of Task 6 was discontinued. Based upon cost analysis performed in BP2, any projected benefits from weight-savings using AM were offset by a substantial cost penalty. As a consequence, a revised design for the attachment hardware was developed using conventional metal forming methods. Figure II.3.1.15.12 above shows an image of the hardware attachment with the M-Tow wrap as a preformed assembly. These parts were supplied to the molding team at MSU Scale-up Research Facility to allow production of full-scale CCB parts with integration of all over-molded inserts. With this work complete, this concludes all work under this subtask.

Task 7. High-Volume Manufacturing Concept Feasibility Demonstration

Activities under Task 7 were concluded at the end of BP2. Remaining work related to manufacturing scale-up and demonstration is reported under Task 8 below.

Task 8. Full Process, Automation, Scale-Up and Demonstration

As indicated in Figure II.3.1.15.2 above, 2023 has focused on scale-up of laboratory-based development from 2022. In practice, this has required preparation and modification of the 3000-ton Milacron injection-molding cell located at the MSU Scale-up Research Facility in Detroit, MI. Initial attention was placed on extending the capability of the mold and barrel heaters to facilitate processing of higher melt temperature engineering thermoplastics. Once these upgrades were complete, automation hardware and software were developed to allow fully automated sequencing of the multifunctional CCB structure. A key component of this work is the end-of-arm tooling that was designed to both remove molded parts and insert all items that were to be over-molded in the subsequent cycle. A CAD rendering of the end-of-arm tooling between the two mold halves is shown in Figure II.3.1.15.16, while Figure II.3.1.15.17 shows the finished article. Final programming of the robot is now under way in support of run-at-rate molding studies planned in November and December 2023. These parts will be set aside for validation testing to ensure the CCB system performs as expected.

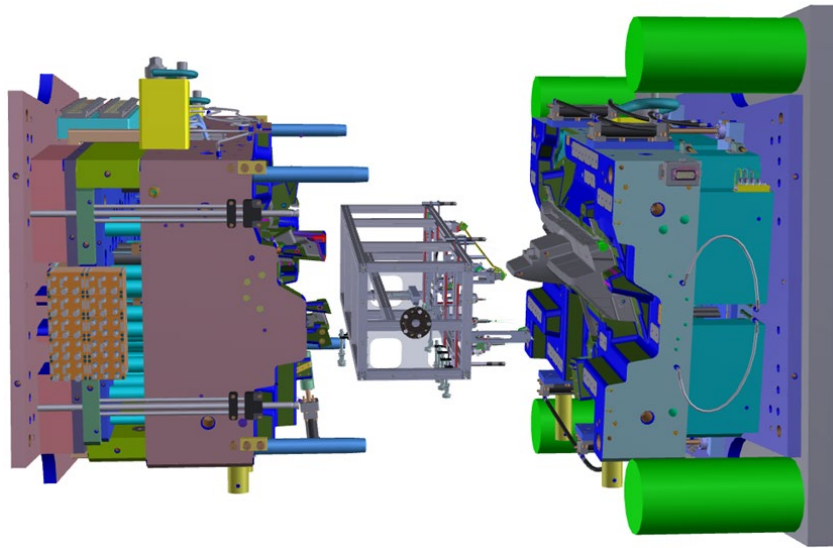


Figure II.3.1.15.16. End-of-arm tooling for insertion of items to be over-molded plus removal of molded parts.
Source: Ford.



Figure II.3.1.15.17. CCB injection-molding tool with end-of-arm. Source: Ford.

Task 9. AM of Segmented Tooling

Due to budgeting constraints at the start of BP3, the AM element of Task 9 was discontinued. Instead, the tooling inserts originally specified for the molding tool were produced using conventional machining methods. Figure II.3.1.15.18 highlights one of the two corners of the molding tool that features an exchangeable insert. This was intended to allow the molding cycle to operate with and without the need for an M-Tow preform to be in position. With this work complete, this concludes all work under this subtask.

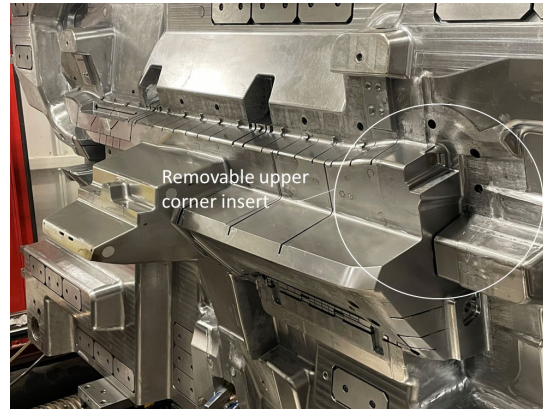


Figure II.3.1.15.18. Location of removable inserts for running with or without M-Tow preforms. Source: Ford.

Task 10. AI/ML for Process Optimization

Due to budgeting constraints at the start of BP3, the AI/ML subtask was discontinued. This decision was made to free up the available budget for the higher priority work within the project. To compensate, process optimization studies have continued albeit using a more conventional design for six sigma approach. This optimization will continue as the molding cycle transitions to a fully automated production demonstration scheduled at the end of this project.

Task 11. Closed-Loop Recycling

In BP3, parts were molded using a surrogate CCB tool for recycling by the ORNL team. These parts, as shown in Figure II.3.1.15.19, have since been delivered, shredded, and granulated, as observed in Figure II.3.1.15.20. Unlike previous parts, these surrogate CCBs were manufactured utilizing the program intent water-assisted injection-molding process in addition to the candidate material system. They were also shredded and granulated using an industrial scale shredder-granulator at ORNL. This contrasts with previous studies whereby the shredding process was carried out using desktop-scale equipment. Thermal, rheological, and particle size characterization of the granulates are in progress; it is intended to mold new parts from these materials by the end of the fourth quarter of 2023.



Figure II.3.1.15.19. Sample CCB parts produced in support of recycling studies. Source: Ford.



Figure II.3.1.15.20. Shredded materials produced from CCB components. Source: Ford.

Conclusions

During BP3, the project team was able to work collaboratively across the work streams to successfully establish full-scale manufacturing capability at the MSU Scale-up Research Facility in Detroit, MI. An initial surrogate tool was modified to allow the team to develop processing parameters ahead of receipt of the new multifunctional CCB tool in June 2023. From that point forward, the sub-teams worked towards producing prototypes for validation testing in addition to establishing an automated process for assessment of manufacturing feasibility. While there have been some delays to the original program timing, most milestones and deliverables for the project were completed. Physical testing of CCB components has also commenced, although a no-cost extension has been requested to accommodate completion of all remaining tasks. The project is now set to conclude with a full-scale manufacturing demonstration in January 2024.

Key Publications

1. Blanchard, P., 2023, “Multifunctional smart structures for smart vehicles,” DOE, 2023 VTO Annual Merit Review, 13 June 2023, Washington, D.C., USA.
2. Lavorata, J., and J.-A. E. Mansson, 2023, “Conductive overbraid of continuous fiber thermoplastic composite tows,” *Compos. B Eng.*, 258, 110678. <https://doi.org/10.1016/j.compositesb.2023.110678>.
3. Rencheck, M., J. Malmstead, H. Tekinalp, B. Knouff, S. Ozcan, V. Kunc, S. Skop, and P. Blanchard, “Large-scale carbon fiber hybrid composite automotive parts from recycled material,” *CAMX 2023*, 30 October–2 November 2023, Atlanta, GA, USA.

Acknowledgements

The project team would like to recognize Dr. H. Felix Wu from the VTO, John Winkel from the Advanced Materials and Manufacturing Technology Office and Aaron Yocum from NETL for their continued support and guidance throughout BP3.

II.3.1.16 Development of Tailored-Fiber Placement, Multifunctional, High-Performance Composite Material Systems for High-Volume Manufacture of Structural Battery Enclosure (General Motors)

Venkateshwar Aitharaju, Principal Investigator

General Motors Global R&D
 General Motors, LLC
 30470 Harley Earl Blvd.
 Warren, MI 48092
 E-mail: venkat.aitharaju@gm.com

Rich Davies, Composites Core Program Manager

Oak Ridge National Laboratory
 Materials Science and Technology Division
 1 Bethel Valley Rd.
 Oak Ridge, TN 37830
 E-mail: daviesrw@ornl.gov

H. Felix Wu, DOE Technology Development Manager

U.S. Department of Energy
 E-mail: Felix.Wu@ee.doe.gov

Start Date: April 1, 2021
 Project Funding: \$2,391,887

End Date: December 31, 2024
 DOE share: \$1,736,510 Non-DOE share: \$\$655,377

Project Introduction

The automotive industry is currently in a major transition from internal combustion engines to a new era of EVs. Challenges, such as increasing the driving range of EVs, minimizing battery system costs, and optimizing vehicle architecture to meet performance and safety criteria, have emerged during this transformative period. To address these challenges, lightweighting through the utilization of high-performance materials, such as advanced composite materials, has become essential. Nevertheless, composites encounter significant obstacles in achieving large-scale implementation in automobile production, including (1) fully realizing multifunctionality to differentiate from metals and making a compelling business case, (2) the absence of predictive tools to eliminate trial-and-error evaluations, (3) the lack of technology for optimizing design parameters in both manufacturing processes and design, and (4) the high costs associated with volume manufacturing. This project aims to tackle these challenges, developing groundbreaking multifunctional capabilities for composites to establish a robust business case for their widespread adoption in the automotive industry. To demonstrate the developed technologies, we will design, engineer, and construct a composite battery enclosure, comparing its performance against a baseline steel design.

Objectives

The objective of the project is to develop advanced composite materials systems with transformative technologies, such as hybrid fiber systems at the lamina or tow level (commingle), strategic tailored-fiber placement (TFP), self-health monitoring (SHM), enhanced thermal and shielding capabilities, and high-volume manufacturing-friendly production methods tailored for the automotive industry. These material systems will be chosen in accordance with structural requirements, aiming to meet or exceed performance criteria set by DOE, such as fiber strength (> 25 ksi), fiber modulus (> 250 msi), and strain-to-failure (> 1%), to achieve the necessary weight-reduction and cost targets. High-pressure resin transfer molding (HP-RTM) will be selected as the high-volume manufacturing process for components, using fast-curing resins to achieve cycle times under three minutes. Computational tools, following an ICME approach, will be developed and validated for the selected material systems. Leveraging these ICME tools, the project team will design, engineer, and construct a structural composite battery enclosure to serve as a baseline for GM's Cadillac Lyriq model

vehicle. This composite battery enclosure will undergo testing to assess its performance compared to the baseline metallic assembly. The project will evaluate and compare weight-savings, material costs, component costs, and cycle times for a production volume of \$85,000/year against DOE metrics.

Approach

Several key technology developments are proposed in this project under the following categories.

Materials

The newly developed TFP technology will be advanced to the next level in this project by creating hybrid fiber reinforcements (e.g., carbon, glass, other fibers) and incorporating them either into a single preform or by commingling them in the tow to significantly enhance material properties. The material systems developed in the project will substantially reduce both material and manufacturing costs, meeting the DOE metric of a maximum increase of \$5/pound saved compared with steel. Additionally, innovative sensor technologies will be embedded within the composite preforms for SHM and environmental conditions (e.g., temperature, humidity) in a self-sustained mode through energy harvesting.

Process/Design

Computational models were developed to optimize the microstructure of composite preforms (e.g., tow size, tow spacing, stitch density) to maximize drapability and permeability. The TFP technology explored in the project offers greater flexibility to vary the microstructure's geometry spatially, opening up opportunities for advanced optimization. HP-RTM is the selected process for this project due to advantages in volume manufacturing—notably its fast cycle time, as demonstrated in our previous DOE-funded project under contract number DE-EE0006826. For the HP-RTM process design, we developed enhanced simulation models to engineer the processing conditions (e.g., molding temperature, injection location, vent placement, injection pressure, flow rate profile) for a fast-curing resin, targeting a cycle time of three minutes, as previously demonstrated. The major sources of defects and scrap in this process stem from variability in preform material properties, preform placement, and process molding conditions. To address these issues, we developed models based on artificial intelligence and ML to correlate data from sensors embedded in the mold (e.g., resin arrival time, pressure, temperature) with the likelihood of dry spot occurrence in the manufactured parts.

Structure/Performance

Predictive tools for the structural performance of hybrid carbon and glass composites will be enhanced by through the extension of the ICME multiscale models previously developed in our project, which were funded under DOE contract number DE-EE0006826. These models will be calibrated using coupon-level tests and validated through component-level tests. Furthermore, a method will be developed to optimize the layup of fiber directions and lamina thickness to minimize fiber mass and cost. Using these ICME models, we will be able to precisely predict the optimal fiber composition, fiber architecture, fiber volume fraction, resin type, manufacturing process, and processing conditions required to manufacture components that meet the necessary structural performance criteria for the composite battery tray components.

Results

The project progress during FY 2023 is provided in the following sections.

Task 1.2 Materials, Process Models, and Technology Development for Future Composite Assembly

Under this task, the development of materials, process simulation models, and structural design tools were carried out for use in the design of future composite battery enclosures. Accomplishments under each of the development subtasks are provided in the sections that follow.

Task 1.2.1 Evaluate and Develop an Optimized Hybrid Material System—Spatially Varying Fiber Reinforcements

We explored spatially varying preforms made using TFP technology to optimize composites further. Open-hole tensile specimens, including baseline and curved fiber path types, were prepared and tested. Baseline specimens contained straight fibers, typical in traditional composites, which became discontinuous when the hole was cut. In contrast, curved path specimens had intact fibers curving around the hole perimeter. Tensile testing with DIC analysis was conducted on both designs. As shown in Figure II.3.1.16.1, the baseline design

exhibited expected axial strain concentrations (highlighted by the red areas) at the hole's sides, leading to crack-initiation and propagation in the test direction. In contrast, the curved path specimens showed lower axial strain on the hole's sides (e.g., 1.6% vs. 4–5% for the baseline), and failure occurred away from the hole.

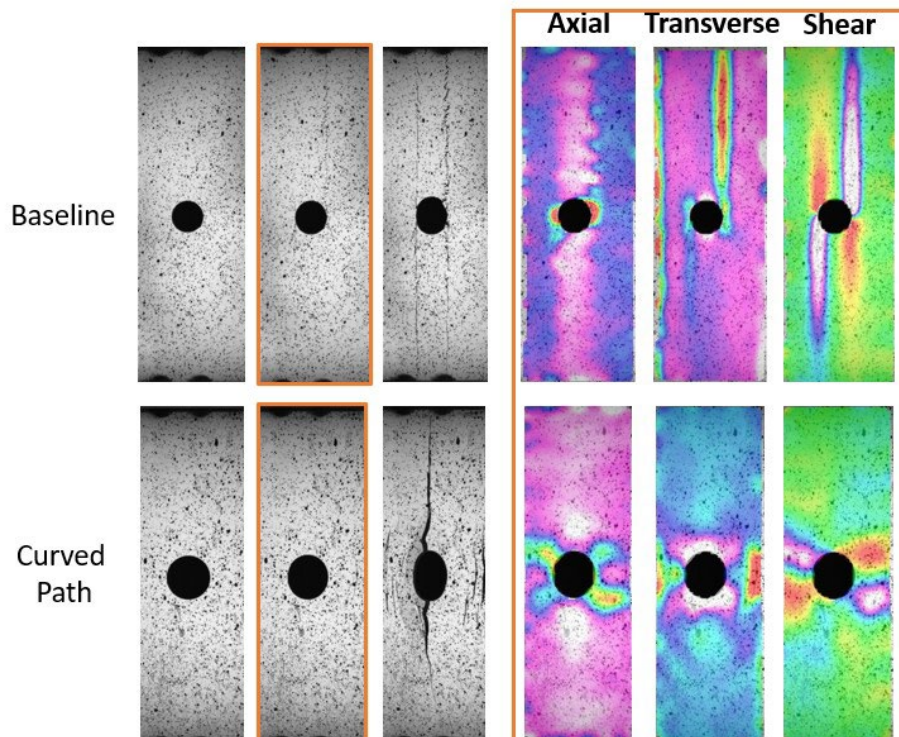


Figure II.3.1.16.1. DIC results showing axial, transverse, and shear strain for the baseline and curved path specimens. Red indicates highest strain and pink indicates lowest strain. Source: Teijin.

However, the curved path specimens exhibited a lower peak load compared to the baseline. We attribute this to the higher shear-stress observed in the curved path specimens, leading to premature matrix failures away from the hole. Subsequently, GM conducted simulations to investigate this unexpected phenomenon, revealing that open-hole tensile specimens should have an elongated hole for optimal performance. Coats Group PLC produced preforms without stitching in the central region, allowing for manual hole creation. Initial molding tests confirmed the feasibility of this manufacturing approach, which will be further explored in the final project year.

Task 1.2.3 Evaluate and Develop the Required Structural Model

The team at the University of Southern California (USC) has harnessed GM's microscale development of hybrid composites for multiscale analysis, resulting in the successful creation of a neural network (NN)-based surrogate to replace microscale calculations. This NN development has been seamlessly integrated into a user subroutine within the LS-DYNA computer program. We believe that this innovation, which substitutes microscale computations with NN-based solutions, is computationally efficient and, to the best of the team's knowledge, has not been previously achieved. Following a similar approach as with hybrid carbon and glass composites, the process begins by assigning samples from Beta distributions to the mechanical properties of each representative volume element, including Young's moduli of tows and resins and Poisson's ratio of tows, strengths, and maximum strain of tows. Representative volume element simulations are conducted to generate a comprehensive training set for deep learning, incorporating intermediate results, such as the energy history of tows and resins, from the simulations for efficient training of the NN development. Figure II.3.1.16.2 displays the NN-based results compared with the experimental results.

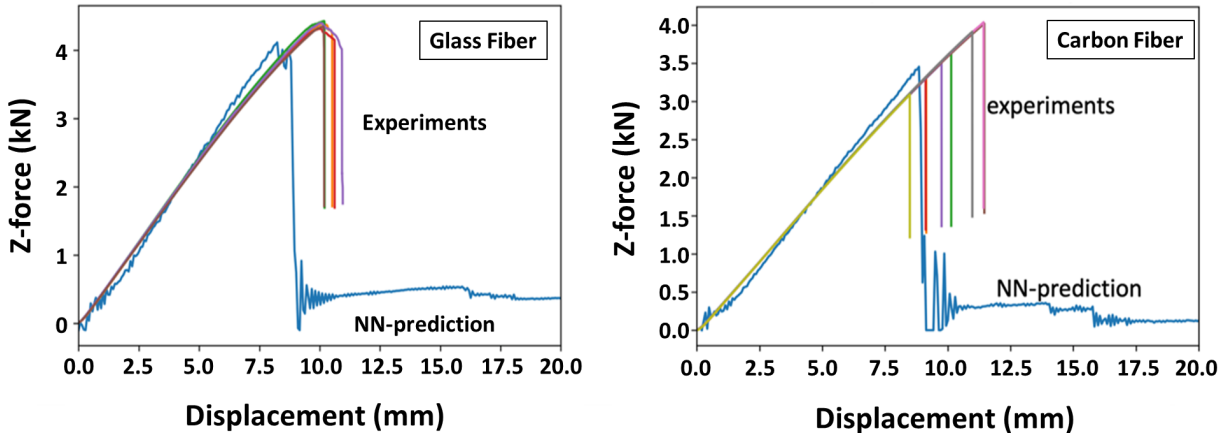


Figure II.3.1.16.2. NN predictions for GF composites and CF composites. Source: USC.

Design Allowables

In the industry, design allowables encompass pre-determined material properties and performance limits that engineers must adhere to when designing products. These allowances cover factors, such as material strength, stiffness, and durability, which play a critical role in ensuring component safety and reliability. Currently, the automotive industry lacks established design allowables for composite materials, and the available methods for determining these allowables (e.g., A-basis, B-basis) in the aerospace sector are primarily experimental and cost-prohibitive for automotive applications. In this project, we have innovatively developed these allowables by combining predictive simulations with a limited number of experiments.

Two developments have been implemented in our design allowables framework. The first generates simulation data used to construct polynomial chaos expansions (PCE) for the quantity of interest (QoI), while the second development describes how the PCE of the QoI is built, updated with experiments, and used to generate A-basis and B-basis allowables. Notably, improvements have been made to expedite the updating process of probabilistic models with experimental data. This allows us to update the joint prior distributions—rather than just the marginals—of the random variables, resulting in improved accuracy of the updated model and, consequently, better propagation of updates to the QoI final distribution. Figure II.3.1.16.3 provides an illustrative example of the results, where prior, posterior, and true A-basis values are compared. As shown, updating our model with 30 observations yields a strong match between the posterior A-basis and true value. The second is the implementation of a framework using NN. In this approach, random models are constructed differently. In the PCE-based implementation, we build PCEs of Beta-distributed material properties for the first set of random variables and introduce a second layer of uncertainty by randomizing the coefficients of the PCEs for the second set of random variables, which then are used to construct a PCE of the QoI. In the NN-based implementation, the first set of random variables randomizes the mean and scale of the Beta distributions, effectively randomizing the minimum and maximum supports of the material properties distributions. Once sampled, a second set of random variables was used to sample the Beta distributions of the material properties. These samples are employed in a FEM to create a NN surrogate of the FEM model. This implementation provides a cost-effective probabilistic mapping from the mean/scale random variables to the QoI. Given the experimental observations, we can easily update the distributions of the mean/scale random variables. Figure II.3.1.16.4 demonstrates how the prior probability density function (PDF) of one of the mean/scale random variables is updated with 10 and 30 experiments.

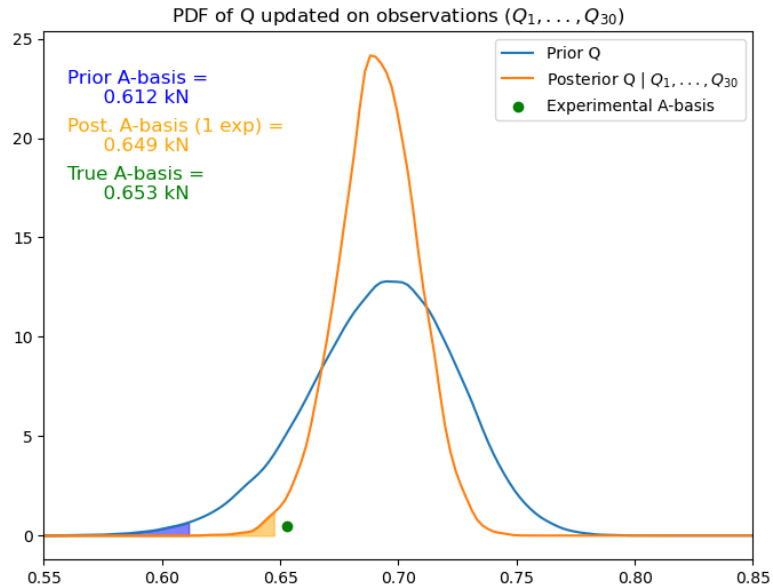


Figure II.3.1.16.3. Prior and updated PDF of the QoI. Source: USC.

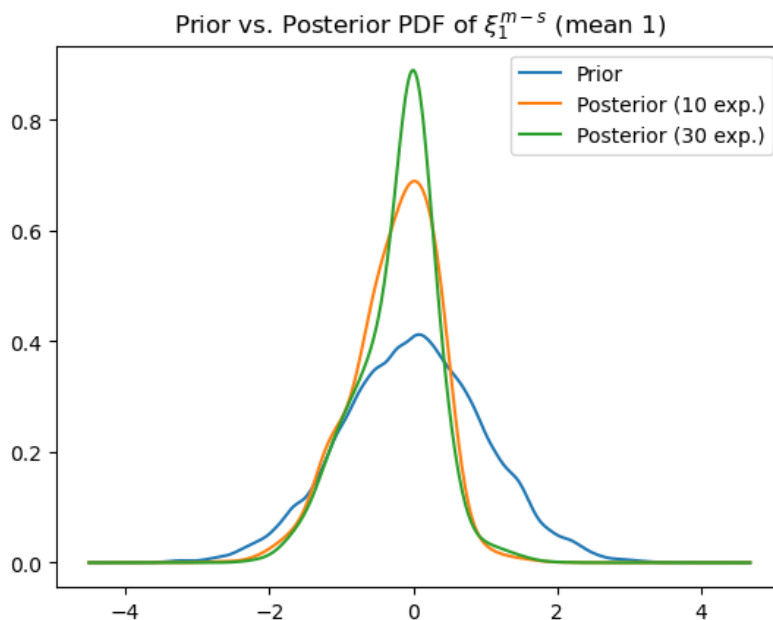


Figure II.3.1.16.4. Prior and updated PDF of the first mean/scale random variables. Source: USC.

Task 1.2.4 Evaluate and Develop SHM Technologies

Under this task, we will develop SHM technology by embedding electronic circuitry in the composites to detect and locate the damage. Further, a temperature/humidity sensor system will be developed to monitor the temperature of battery cells in the battery enclosure. For brevity, the accomplishments in the SHM sensor area are described below.

Teams at Columbia University and GM have developed a patent-pending damage localization framework using CF sensor tow damage detection technology [1]. This method relies on an innovative multi-branch sensor tow design aimed at minimizing the number of sensor terminals and measurement circuits. The resistance of each sensor tow branch is controlled by adjusting the tow length or incorporating a resistor.

For the initial study, Columbia University designed and fabricated two sample types. The first type achieved the desired branch resistance values by adjusting the sensor tow length, while the second type accomplished this by adding resistors to the sensor tows. Both types of samples had the resistance of the overall circuit measured at two locations using copper rivets as electrical terminals. The fabricated samples were subjected to impact loading, and the results showed that both methods of adjusting branch resistance were successful, with experimental results closely aligning with the predicted values of less than 3% error.

In the second stage of the damage localization study, Columbia University tested impact specimens using the setup shown in Figure II.3.1.16.5(a) that were manufactured by Coats Group PLC and MSU to validate the damage localization technology for the most current hybrid composite material design. The damage localization system consisted of two orthogonal 3-branch sensors, as depicted in Figure II.3.1.16.5(b). These sensors were integrated between the third and fourth layers of a four-layer glass composite for impact testing.

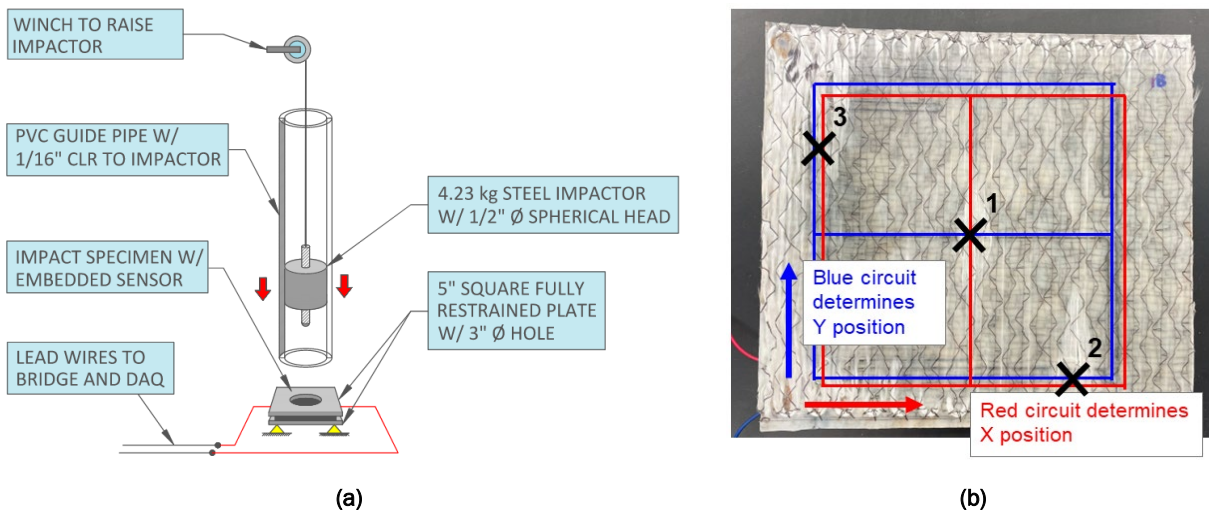


Figure II.3.1.16.5. (a) Impact test setup. (b) Impact sequence of the damage localization specimens consisting of two orthogonal 3-branch sensors. Source: Columbia University.

Three impacts were carried out, successively damaging one sensor branch at a time. For example, the first impact broke Branch 2 of both the blue color and red color circuits. The second impact broke Branch 1 of the blue circuit and Branch 3 of the red color circuit shown in Figure II.3.1.16.5(b) above. Empirical results remained consistent with previous impact tests, with experimental values staying within 3% of the predicted values. Table II.3.1.16.1 shows the correlation of resistance (R) values before and after the impact test results.

Table II.3.1.16.1. Correlation Between Measured and Predicted Resistance Values

	Red Circuit				Blue Circuit				
	Start	Impact 1	Impact 2	Impact 3	Start	Impact 1	Impact 2	Impact 3	
	R mean	R mean	R mean	R mean	R mean	R mean	R mean	R mean	
Measured	13.92	19.54	93.74	Infinite	Measured	13.66	18.78	23.52	Infinite
Predicted	14.01	19.47	98.03	Infinite	Predicted	14.01	19.47	24.29	Infinite
Error	0.7%	0.4%	4.6%	0%	Error	2.6%	03.7%	3.3%	0%

Fatigue Study

Preparations have been made to investigate the potential use of self-SHM sensors for monitoring fatigue life of the composite structure. This application is highly innovative. We believe it will advance SHM technology to the next level. Fatigue specimens were designed and a testing regimen established, including a minimum of three tests at four stress levels. The design of the fatigue samples has been reviewed and coordinated with Coats Group PLC, MSU, and GM. Preforms are currently in the fabrication process at Coats Group PLC.

Six plaques were molded using liquid compression molding at MSU and subsequently received at Columbia University. Each plaque contains six fatigue specimens. Three plaques were made using a unidirectional layup, while the other three were formed in a cross-ply layup. Improvements were made between the successive iterations of plaque moldings. Specimens meeting quality standards were initially rough-cut using a tile saw and tabbed following the ASTM D3039 standard.

Subsequently, select specimens were cut into a dog-bone shape using a waterjet process with a new and refined geometry based on insights gained from an extensive sensor tow damage detection tensile testing program. Six specimens have been prepared for ultimate strength testing to determine the material's maximum stress level, which will serve as an upper bound for the scheduled fatigue tests. The fatigue testing and demonstration will be completed in the next FY.

Implementation in Mini-Battery Enclosures

SHM technology was successfully designed and implemented in the multifunctional demonstration panel, in collaboration with GM, Tenjin, and MSU. The panel serves as a small-scale demonstration on the full battery enclosure. A customized layout for the self-sensing, self-SHM technology was put in place to detect damage for the side-pole impact test. The layout was coordinated with input from each of the team members. GM, Coats Group PLC, MSU, and Tenjin provided design requirements that guided the layout. The sensor was designed with a single-circuit, four-branch layout. The branches were situated using simulation stress/strain field results from GM. The results from the mini-demonstration panel will be used to further refine and design the full-scale battery enclosure. Additionally, the test will include the novel low-cost electrode terminals designed by both the Coats Group PLC and Columbia University teams.

Temperature Sensor

In this section of the work, we investigated the development of temperature sensors in composites using experiments and numerical simulations to gain a deeper understanding for engineering the development and applications. From a numerical perspective, a three-dimensional unit cell geometry thermal analysis model was developed to simulate the thermal response at the surface and internal layers of the hybrid composite, similar to what occurs in a battery enclosure. We incorporated several environmental chamber test results, including both surface-mounted and embedded temperature sensors, to refine the model.

A full-scale thermal model with the same dimensions as the experimental test sample was constructed using the layup of the novel hybrid composite. The geometry consists of four layers of 81% to 19% glass-to-carbon material in a 0/90/90/0 orientation. The initial results are physical, demonstrating the heat flux through the material's thickness as convective heat-transfer is applied to the top surface. The thermal properties of the constituent materials were made anisotropic based on literature values and fine-tuned using the initial experimental data. The thermal simulation results roughly align with the experimental results, and the model was made more realistic by adjusting the convective heat-transfer coefficient and thermal boundary conditions. The numerical FEM is shown in Figure II.3.1.16.6.

In our experiments, it was observed that temperature sensors embedded within the composite exhibit a temperature rise delay as compared to the surface-bonded sensors. Our objective in these experiments was to develop an embedded thermal sensor that occupies less space than a surface-bonded sensor. To achieve this objective, the team plans to develop a Temperature Inference Model to utilize the measurements from the embedded sensor. This Temperature Inference Model (TIM) offers a cost-effective solution for accurately monitoring battery cell temperatures, ensuring the safe operation of EV batteries.

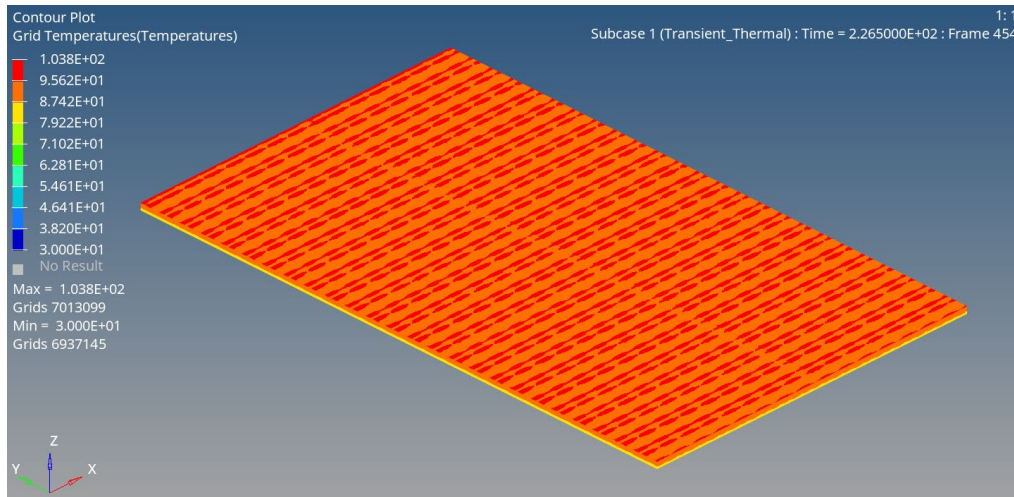


Figure II.3.1.16.6. Full-scale thermal model of hybrid composite test sample with convective heat-transfer applied to the top surface. Source: Columbia University.

We successfully molded a composite test sample measuring 300 mm × 180 mm, consisting of four layers of 81% to 19% glass-to-carbon material arranged in a 0/90/90/0 orientation. This sample contains two embedded temperature sensors positioned beneath carbon tows, which are situated beneath the first and second composite layers. This design was informed by previous environmental chamber test results, which indicated that sensors embedded under glass fiber (GF) exhibit a slightly longer thermal response time delay compared to those embedded under CF. Additionally, the sample includes two surface-mounted temperature sensors, one on the top and one on the bottom. This test sample was created to investigate various thermal conditions, while the sensor placements were strategically designed to support the development of a more robust thermal simulation and TIM. The sample, as shown in Figure II.3.1.16.7, is currently undergoing testing.

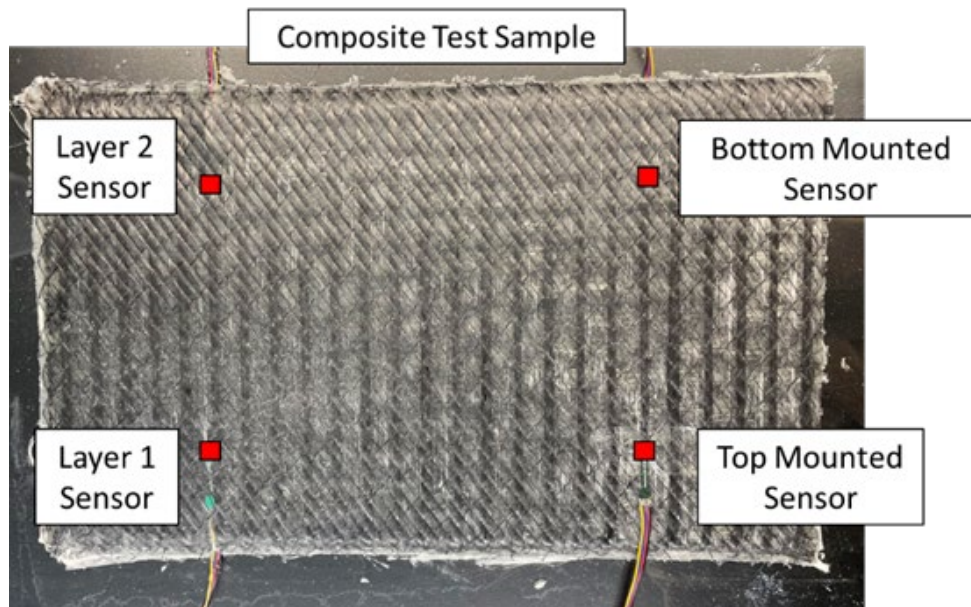


Figure II.3.1.16.7. Hybrid composite test sample with embedded temperature sensors used for environmental chamber experiment to demonstrate thermal response at different composite layers. Source: Columbia University.

This sample was initially tested in an environmental chamber set to 120°C, which represents an extreme case of thermal runaway before combustion. Layers of fiberglass insulation were placed underneath the sample to help simulate a unidirectional heat-transfer condition. In the event of a thermal runaway, there would likely be close to unidirectional heat-transfer, given the significantly higher temperatures emanating from the damaged battery either from beneath the cover or above the tray, compared to the ambient temperature of the vehicle. A similar test was conducted using a heat lamp, which also was maintained at around 120°C. This setup was designed to encourage unidirectional heat-transfer, as the energy input was generated directly above the sample, rather than in the surrounding air. The experimental setups and preliminary results are illustrated in Figure II.3.1.16.8.

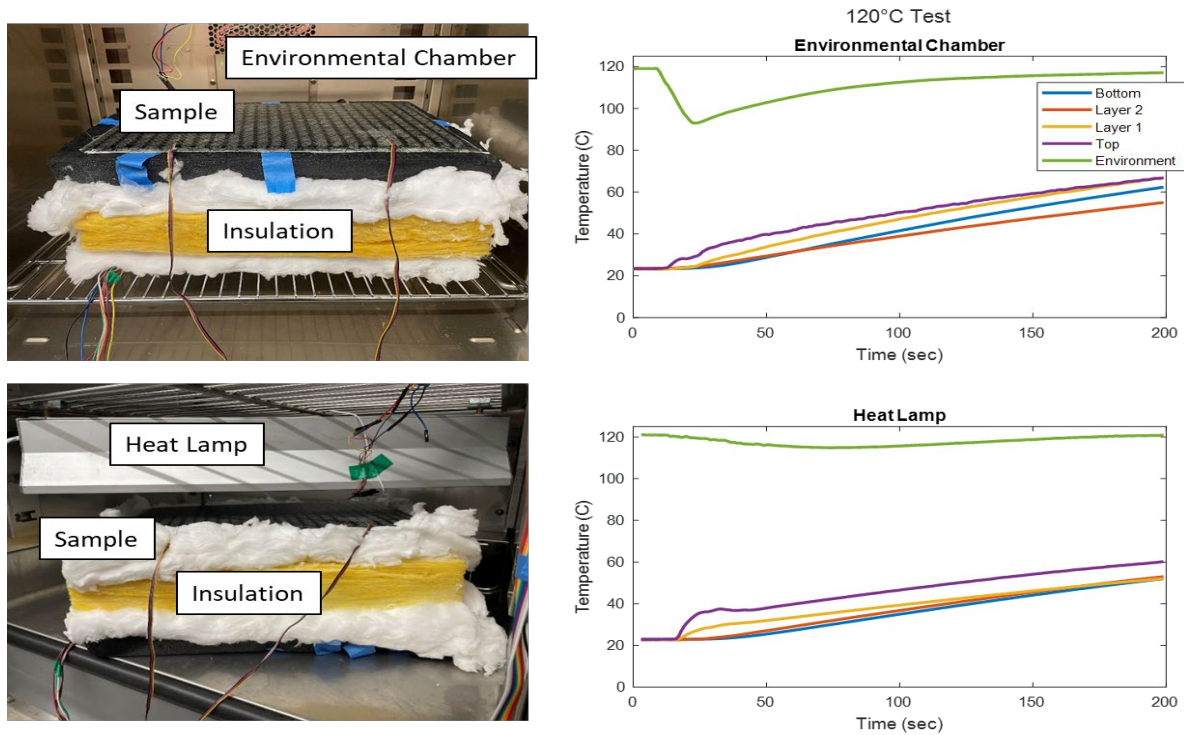


Figure II.3.1.16.8. Experimental setups and results for the environmental chamber and heat lamp temperature response tests. Source: Columbia University.

These results indicate that even with insulation layers, the environmental chamber test does not fully achieve unidirectional heat-transfer, as evidenced by the bottom-mounted sensor registering higher temperatures than the embedded Layer 2 sensor. In contrast, the heat lamp test creates conditions closer to unidirectional heat-transfer, and the larger rate of change observed in the top-mounted and embedded Layer 1 sensors likely resembles the response to a real thermal runaway event more closely. These tests will be repeated or adjusted, and different temperatures will be imposed to fully characterize the thermal simulation and aid in the development of a TIM.

Task 2.1 Finalize the Structural Design of the Composite Battery Enclosure

After detailed discussions with project team members specializing in composite manufacturing, we selected the optimal materials and processes for each component of the composite battery enclosure that will be built in this project, as indicated in Figure II.3.1.16.9.

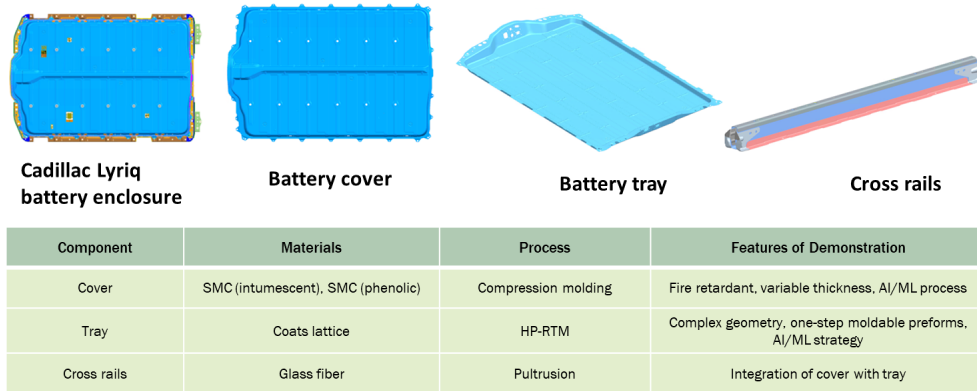


Figure II.3.1.16.9. Finalized materials and process for the components of the composite battery enclosure. Source: GM.

After several iterations of computer simulations involving various material options, the final design of the composite battery enclosure consists of:

- The cover component, made from sheet molding compound (SMC) with fire-retardant materials, incorporates local reinforcements from the baseline metallic assembly by adjusting the thickness of the SMC material. To enhance thermal performance and electromagnetic interference resistance, an aluminum metallic foil will be bonded to the cover.
- The tray component, comprising a variable-thickness CF and GF composite, provides a robust backing for the energy absorber, enabling efficient energy absorption and crushing. The tray is designed to withstand bottom- and side-pole impacts in specific load cases.
- The cross rails are produced through a pultrusion process using GF materials.
- The energy absorber is constructed from low-cost SMC corrugated designs to absorb energy and minimize intrusion in the enclosure.

Figure II.3.1.16.10 displays the part consolidation of the proposed design compared to the baseline metallic assembly.

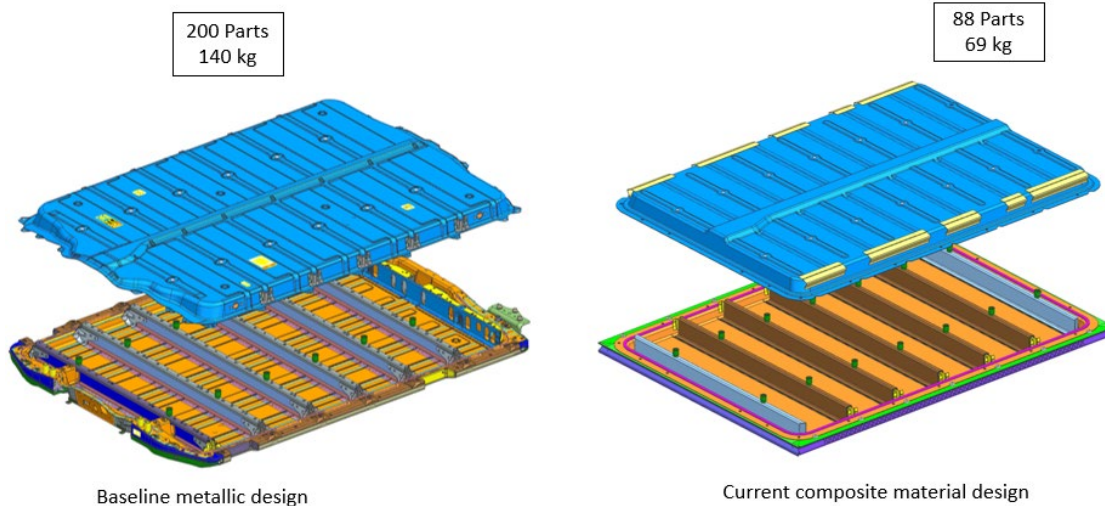


Figure II.3.1.16.10. Parts consolidation advantages of composite material design compared to baseline metallic design. Source: GM.

The all-CF design of the tray achieved a 50% weight-reduction compared to the steel design. However, to optimize the cost of the entire design, some of the CF was replaced with GF. The final material design resulted in a 30% weight-savings over the steel design.

Subtask 2.1.1

Challenge

To the knowledge of the project team, a complete composite material design for the battery enclosure does not yet exist in the industry. This represents a high-risk, high-reward endeavor. To mitigate this risk, the project team has developed a plan to rapidly construct a mini-battery enclosure for design verification before proceeding with the manufacturing tool construction.

Mini-Battery Enclosure

Figure II.3.1.16.11 displays the design of the mini-battery enclosure, which shares similarities with the primary composite battery enclosure. Given the highly localized nature of the side-pole impact load, studying the mini-battery enclosure performance can offer valuable insights into the final composite battery enclosure performance.

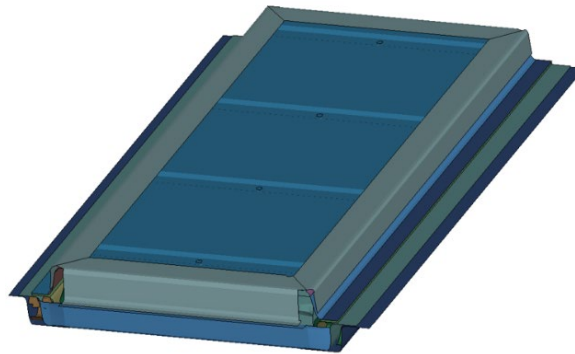


Figure II.3.1.16.11. Design of composite mini-battery enclosure. Source: GM.

Figure II.3.1.16.12 shows the instance of the peak intrusion of the battery enclosure. The intrusion amount obtained from the simulation is 9.5 mm compared to 22 mm of the baseline metallic assembly.

Figure II.3.1.16.13 shows the manufactured cover and tray components of the assembly.

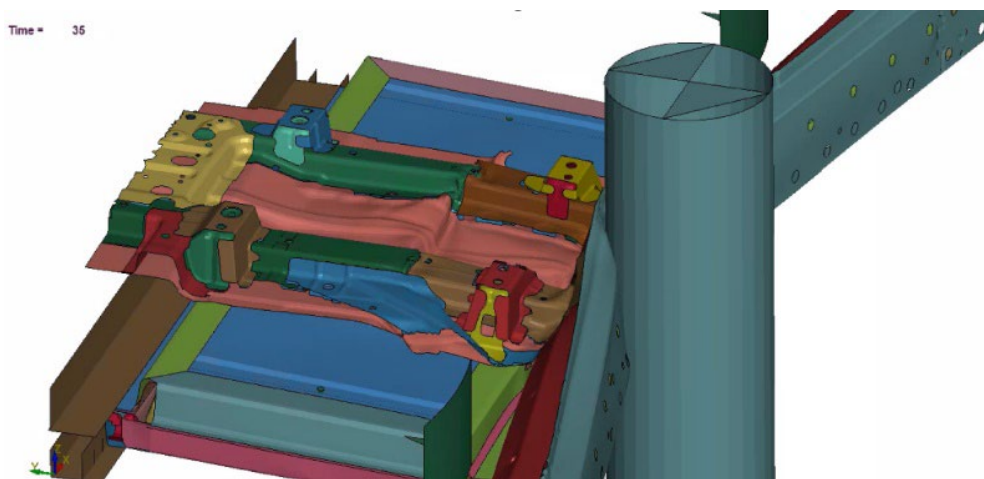
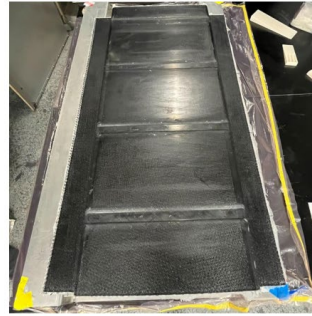


Figure II.3.1.16.12. Virtual simulation of composite mini-battery enclosure (9.5 mm of intrusion). Source: GM.

Mini-battery Enclosure Components



Molded glass fiber cover



Molded carbon fiber tray

Figure II.3.1.16.13. Manufactured cover and tray components for the mini-battery enclosure. Source: GM.

The design of the test fixture is depicted in Figure II.3.1.16.14. It is important to note that the test fixture was designed to ensure that the intrusion and test results obtained from the mini-battery enclosure align with those obtained from the battery enclosure at the vehicle level.

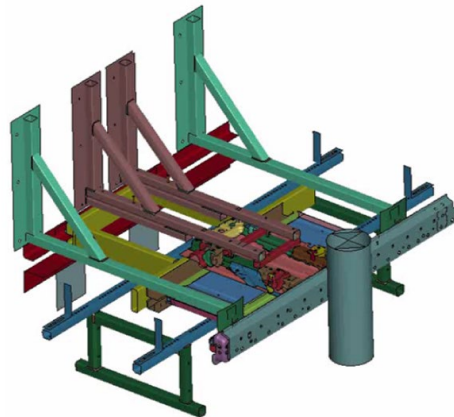


Figure II.3.1.16.14. Test fixture engineered for the battery enclosure. Source: GM.

Both the mini-battery enclosure and the baseline steel were subjected to a 48 kJ impact energy test. Figure II.3.1.16.15 illustrates the setup and results for the sled test with the steel enclosure and composite mini enclosure.

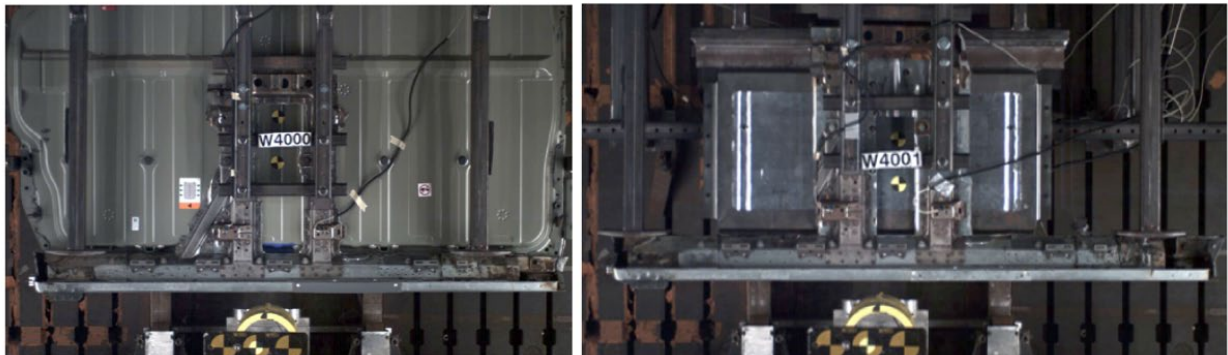


Figure II.3.1.16.15. Steel enclosure and composite mini enclosure under sled test. Source: GM.

Figure II.3.1.16.16 displays a comparison of the deformed shapes of the steel and mini-battery enclosures at the moment of maximum intrusion during the pole impact.

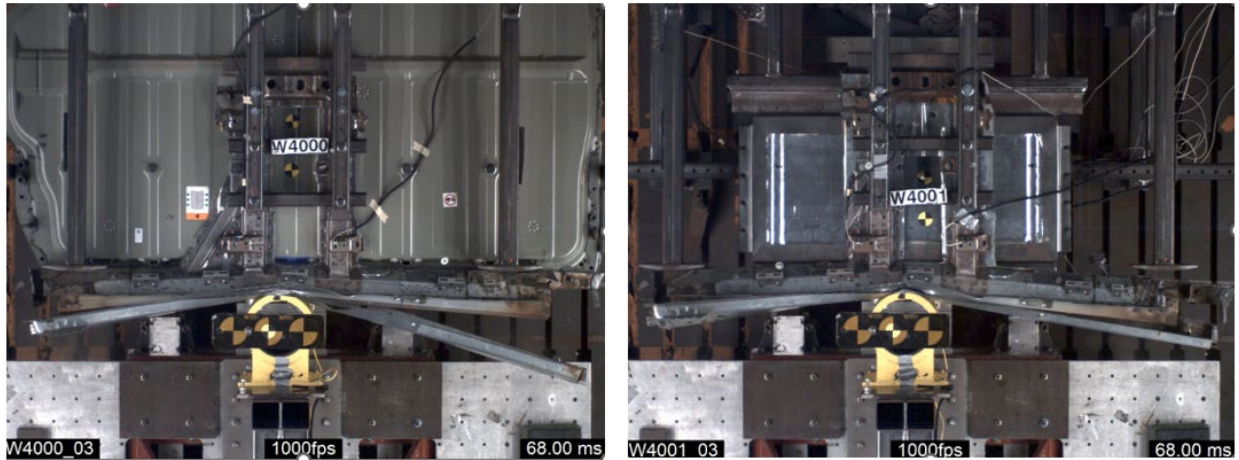


Figure II.3.1.16.16. Deformed shape of the steel and composite mini enclosure at the instant of maximum intrusion. Source: GM.

Figure II.3.1.16.17 provides a comparison of experimental and numerical results, including pole load versus time and pole kinematics of the steel cover with respect to time. The maximum difference between predicted and measured loads is below 5%. These results support the claim that the numerical models for the steel enclosure are highly accurate.

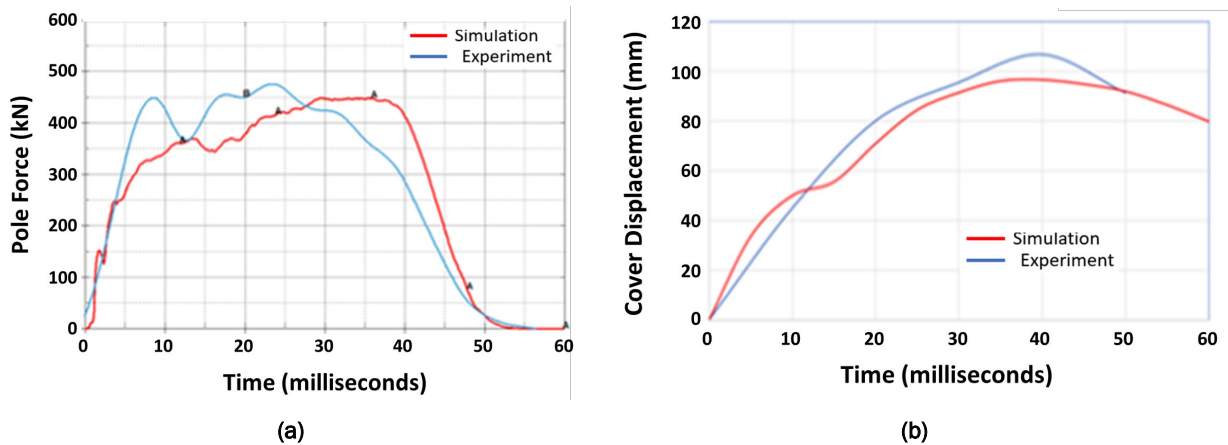


Figure II.3.1.16.17. Comparison of results between the crash experiments and simulations (steel enclosure) for (a) the pole force and (b) the cover displacement. Source: GM.

Figure II.3.1.16.18 presents a comparison of experimental and predicted results for pole force and the kinematic results of the composite cover. An excellent match was observed, providing greater confidence in the composite model's use for crashworthiness.

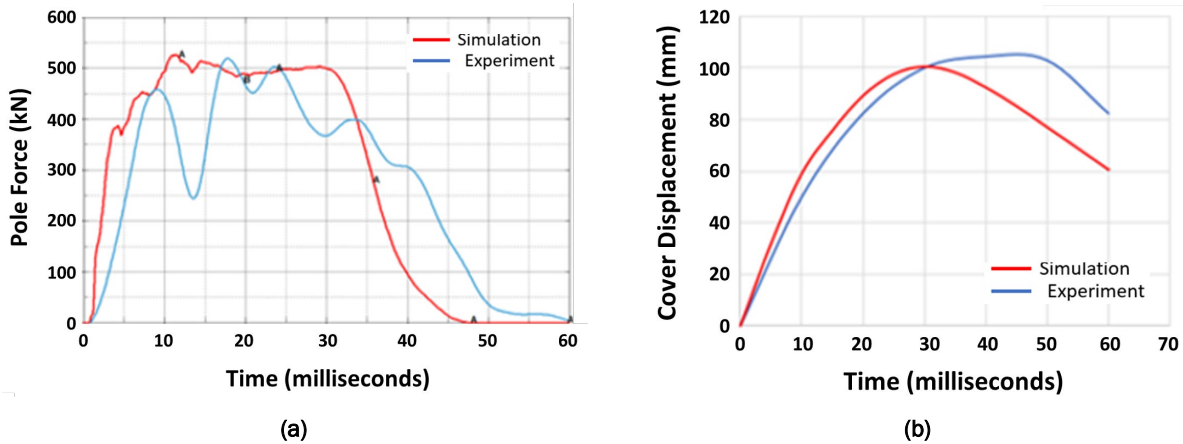


Figure II.3.1.16.18. Comparison of experimental and numerical results (mini-battery enclosure) for (a) the pole force and (b) the cover displacement. Source: GM.

Figure II.3.1.16.19 presents a comparison of intrusion values obtained for the steel enclosure compared with the mini-battery enclosure. The maximum pole displacement observed in the simulation for the steel enclosure is 119.9 mm, whereas the displacement is 103.6 mm for the composite assembly. These results demonstrate that the composite battery enclosure performed exceptionally well compared to the steel assembly.

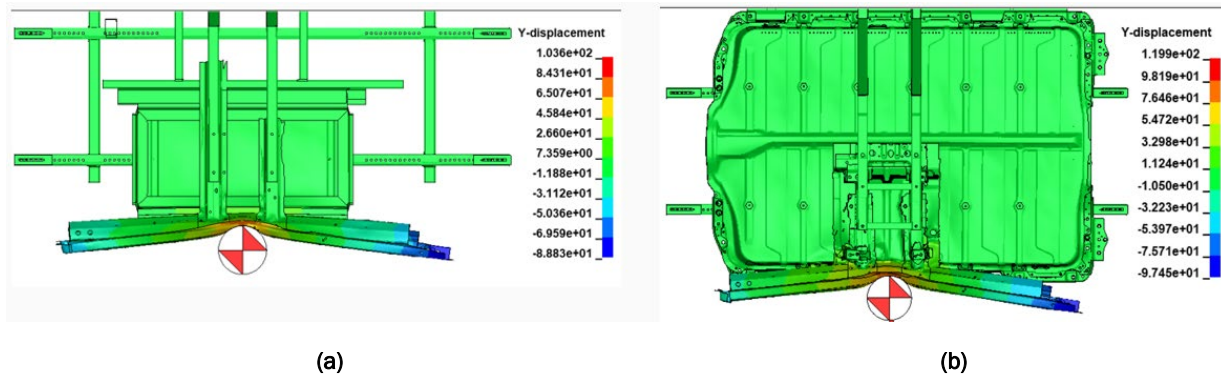


Figure II.3.1.16.19. Comparison of pole intrusion between (a) the composite mini enclosure and (b) the steel enclosure. Source: GM.

Task 2.2 Finalize Manufacturing Process Design of the Composite Assembly

A HP-RTM process was designed for the battery tray using a center injection method. Process simulations were conducted, varying parameters such as injection location, flow rate, mold, and resin temperatures. Figure II.3.1.16.20 illustrates the sequence of resin filling the mold over time. Although a cycle time of less than three minutes was achieved, there was a risk of a dry spot forming on the tray component’s flanges. Subsequent iterations involved adjusting the resin runner length to relocate the dry spot outside the part perimeter and minimize its size.

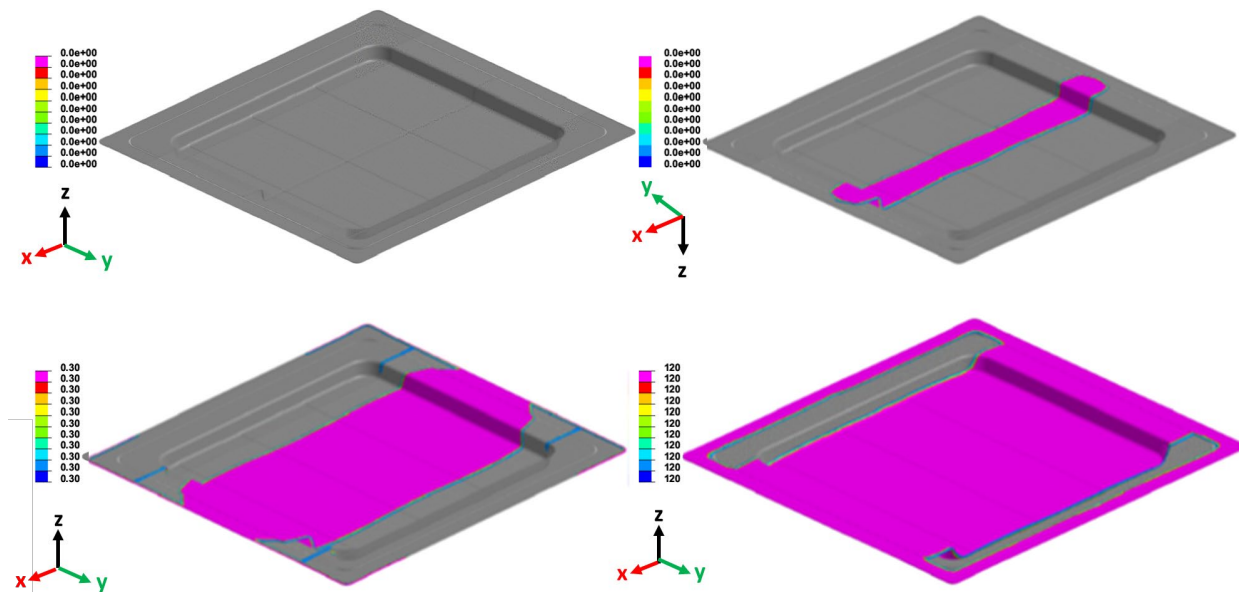


Figure II.3.1.16.20. Resin filling of the mold at various injection times. Source: ESI Group.

For this task, the sensor locations for pressure and temperature were strategically planned to enable prognostics and control of the dry spot, which is currently under development.

Task 2.3 Finalize SHM Technology for Composites Assembly

After conducting multiple studies, SHM circuitry zones were designed in both orthogonal directions to detect and locate damage. Figure II.3.1.16.21 displays the SHM design for the tray component, which is highly innovative. A parallel task was undertaken to evaluate the design at the coupon-level; this subtask has been completed.

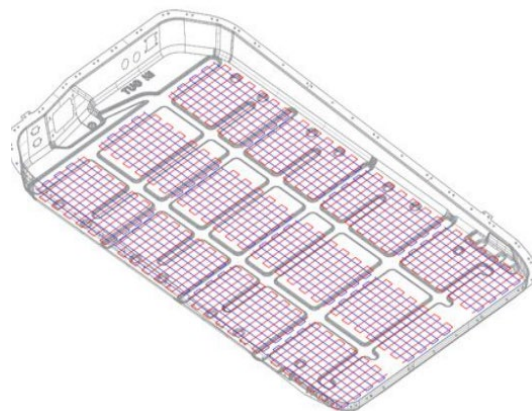


Figure II.3.1.16.21. SHM circuitry for the tray component. Source: Columbia University.

Conclusions

During FY 2023, the project team achieved significant milestones. These milestones included the successful design and manufacture of a mini-battery enclosure, using novel hybrid CF and GF preforms developed in this project. Prior to this accomplishment, the team virtually designed the final battery enclosure, leveraging these advanced composite materials to replace the baseline steel battery enclosure used in GM's Cadillac Lyriq vehicle. The final battery enclosure design not only achieved a weight-reduction of more than 30% but also met the cycle time metric of three minutes. To mitigate the risk associated with using first-in-kind materials, processes, and structural design, a mini-battery enclosure was designed, built, and tested based on the final

composite design. The mini-battery enclosure performed exceptionally well in experimental comparisons with the baseline steel assembly, instilling confidence in sending the computer-assisted drawing designs to the tooling shops for tool manufacturing. Additionally, several multifunctional technologies were developed and validated at the coupon and component levels, including hybridizing GFs and CFs within a single preform, implementing SHM using CF sensors, eliminating the preforming process, enhancing permeability strategically, and improving thermal performance with a hybrid composite and metallic cover. Furthermore, an artificial intelligence and ML strategy was developed to work in conjunction with the HP-RTM process, enabling on-the-fly adjustments in flow rate to mitigate defects and changes in manufacturing process conditions. A novel NN model was also incorporated into a multiscale, ICME-based structural model, significantly improving computational efficiency. These developments are expected to advance the industry.

Key Publications

1. Aitharaju, V., 2023, “Systems and method for resin flow front detection during high-pressure resin transfer molding of composite parts,” Patent Application No. 18/495,227.
2. Aitharaju, V., 2023, “Composite components and multizone fiber preforms for composite components,” Patent Application No. 18/322,178.
3. Aitharaju, V., 2023, “Preform with variable fiber density, forming and molding tool and method of forming of composite materials,” Patent Application No. 17/977,083.
4. Demo, L. B., E. M. Tronci, and M. Q. Feng, 2023, “Multifunctional fiber-reinforced polymer composites for damage detection and memory,” *J. Compos. Sci.*, 7(9), 383. <https://doi.org/10.3390/jcs7090383>.
5. Hawi, P., V. Aitharaju, J. Mahishi, R. Ghanem, “A framework for design allowables accounting for paucity of data and errors in complex models,” *Proceedings of the American Society for Composites 2023 Conference*, 17–20 September 2023, Boston, MA, USA.
6. Yao, Z., P. Hawi, V. Aitharaju, J. Mahishi, R. Ghanem, 2023, “Cross scale simulation of fiber-reinforced composites with uncertainty in ML,” *Proceedings of the American Society for Composites 2023 Conference*, 17–20 September 2023, Boston, MA, USA.

References

1. Demo, L. B., E. M. Tronci, and M. Q. Feng, 2023, “Multifunctional fiber-reinforced polymer composites for damage detection and memory,” *J. Compos. Sci.*, 7(9), 383. <https://doi.org/10.3390/jcs7090383>.

Acknowledgements

The project team is extremely grateful for the valuable technical and administrative support from our DOE Program Managers, H. Felix Wu, A. A. Yokum, and J. Winkel.

II.3.2 Small Business Innovation Research (SBIR)

II.3.2.1 Sustainable Lightweight Intelligent Composites (SLIC) for Next Generation Vehicles (Newport Sensors, Inc.)

Masato Mizuta, Principal Investigator

Newport Sensors, Inc.
P.O. Box 174
Newport Beach, CA 92625
E-mail: info@newportsensors.com

Brandy Greenawalt, SBIR Central Programs Operations Manager

U.S. Department of Energy SC-29
Small Business Innovation Research
19901 Germantown Rd.
Germantown, MD 20874
E-mail: brandy.greenawalt@science.doe.gov

H. Felix Wu, DOE Technology Development Manager

U.S. Department of Energy
E-mail: Felix.Wu@ee.doe.gov

Start Date: August 23, 2021
Project Funding: \$1,100,000

End Date: August 22, 2023
DOE share: \$1,100,000

Non-DOE share: \$0

Project Introduction

Driven by zero-emission goals, the automotive industry is moving toward lightweight vehicles to improve fuel-efficiency or battery mileage and reduce greenhouse gas emissions. A 10% reduction in vehicle weight can improve fuel economy by 6–8% [1]. Every 100-kg decrease in the weight of a vehicle is expected to cut emissions by 3–5% [2]. With half the weight and four times the strength, CFRP composites are an attractive alternative to the traditional steel used for vehicles. In addition to weight-reduction, CFRP composites in general offer several manufacturing advantages, such as design flexibility, lower tooling costs, and opportunities for part consolidation. However, the wide deployment of CFRP composites is hindered by a number of obstacles. A McKinsey study [3] identified the two most significant. The first obstacle is the high-cost of CFs, which is three times higher than the cost of steel. The high-production demand, coupled with the rising cost of petroleum feedstock, has encouraged automakers to exploit plant-based natural fibers to maintain a competitive edge. However, the relatively low mechanical properties and moisture durability of natural fibers present a challenge. The second obstacle is structural reliability concerns coupled with difficult damage inspection. Although CFRP composites have been widely studied for aerospace applications, their crashworthiness, which is uniquely critical for the safety of automotive vehicles, remains to be thoroughly investigated. Due to the brittle nature of the material, CFRP composites are susceptible to impact loads caused by debris and collisions, resulting in damage including matrix cracks, fiber-matrix debonding, fiber breakages, and interlayer delamination. Such damage often cannot be seen by the naked eye but can propagate suddenly and drastically reduce structural strength and stiffness. In addition, the long-term aging effects of CFRP composites when used as automotive structural materials are unknown. Therefore, frequent inspection is required by trained technicians using expensive nondestructive testing and subsurface imaging equipment such as ultrasonic, infrared, and x-ray imaging. All these inspection technologies impose potential equipment and personnel investment costs on dealerships and workshops. Due to these obstacles, the use of CFRP composites has been mostly limited to high-end low-volume racing cars.

Objectives

The major project objective is to develop the proposed SLIC technology, which is a carbon- and natural-fiber-hybridized polymer composite embedded with five distinctive functionalities: (1) Spatially distributed

piezoelectric sensors continuously monitor the structural health and detect and locate, in real-time, any impact load and initiation/propagation of structural damage. (2) Spatially distributed piezoresistive trace sensors on the structural surface continuously monitor strain and detect and locate, in real-time, an unusual change of strain. (3) Piezoelectric energy harvesters integrated in the composite structure harvest sufficient energy from vehicle vibration to power the above dual-sensing SHM system, eliminating the requirement for an external source of power. (4) The hybrid design enhances impact energy absorption while reducing the weight and cost. (5) The economic competitiveness resulting from the sustainable supply of low-cost environmentally friendly natural fibers.

Approach

Our project involves two primary approaches to achieve the desired functionality: the design of a multifunctional composite and the development of a sensing system.

Design Multifunctional Composite

The multifunctional SLIC composite is a key component of our project, integrating both static and dynamic sensing capabilities. We have strategically embedded two types of sensors within the composite structure:

- **Static Sensing:** For monitoring strain, a conductive trace sensor is incorporated into the composite structure.
- **Dynamic Sensing:** To monitor impact loads and detect potential damage, we utilize a polyvinylidene fluoride (PVDF) piezoelectric film.

The SLIC composite, as shown in Figure II.3.2.1.1(a), is designed with three distinct sensing areas. Its cross-section shows a structure where a natural fiber core is sandwiched between CF layers, as illustrated in Figure II.3.2.1.1(b). The PVDF film is bonded to the external CF layer, serving as the piezoelectric material for dynamic sensing. The conductive trace sensor is printed on the PVDF film, and both the trace sensor and CF layer act as electrodes for the PVDF sensor. This design minimizes the wiring requirements, allowing for versatile application across a wide range of structural components.

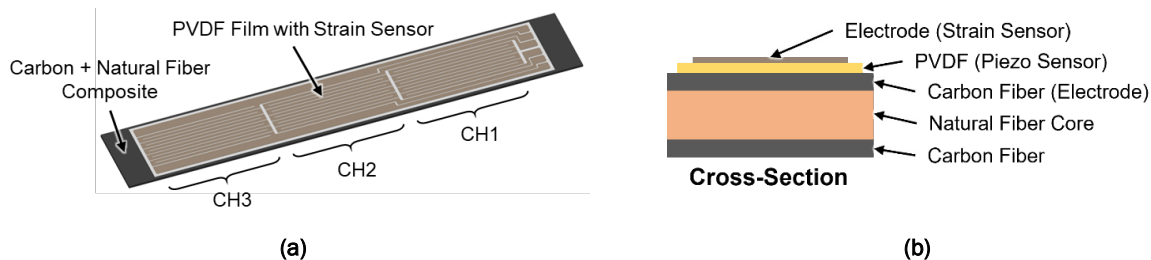


Figure II.3.2.1.1. (a) SLIC composite design and (b) cross-sectional view showing sandwich structure.

Source: Newport Sensors, Inc.

We fabricated three types of SLIC material test coupon specimens for testing mechanical properties via tensile, bending, and impact tests, as well as structural health monitoring functionalities. Each specimen is designed with a sandwich structure in which the natural fiber mat is sandwiched between two CF fabric layers. A piezoelectric PVDF film is bonded to one of the CF layers. On the other side of the PVDF file, two or three copper traces in specially designed patterns are etched to serve as multiple strain sensors for structural damage detection and location identification. These SLIC test specimens were successfully fabricated in collaboration with the UNT Bioproducts Manufacturing Laboratory. A fabricated SLIC specimen is shown in Figure II.3.2.1.2.

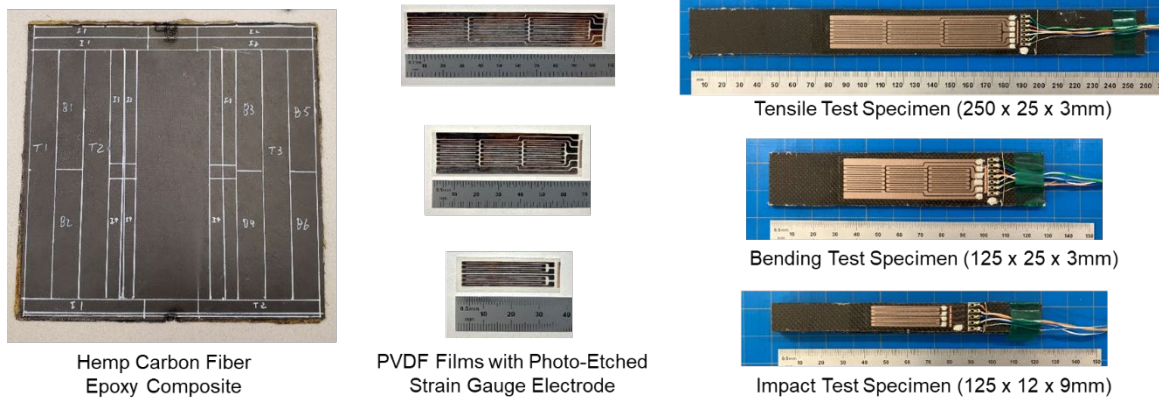


Figure II.3.2.1.2. SLIC specimens for tensile, bending, and impact tests. Source: Newport Sensors, Inc.

Develop Dual-Sensing System Integrated with Structural Material

To effectively interface with the sensors embedded in the composite, we developed a specialized electrical system. The block diagram is shown in Figure II.3.2.1.3. This system seamlessly integrates a strain sensor amplifier and a piezoelectric sensor amplifier into a unified unit. By combining these amplifiers, we streamlined the electrical system, leading to material and integration cost-savings. This integrated approach ensures efficient signal processing and facilitates the implementation of the SHM functionality across various structural elements.

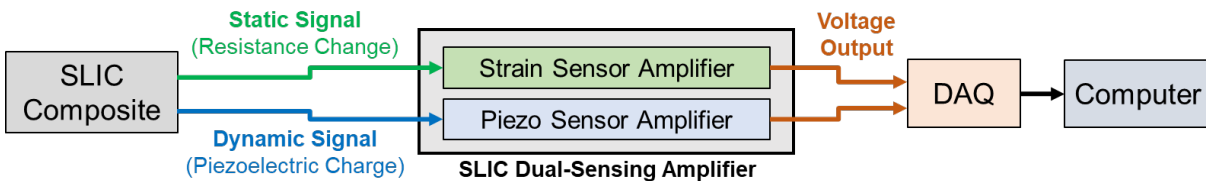


Figure II.3.2.1.3. Block diagram of SLIC dual-sensing system. Source: Newport Sensors, Inc.

The sensing system can simultaneously measure the strain signal and dynamic piezoelectric signal. The strain signal is converted by a strain sensor amplifier, while the piezoelectric signal is converted by a charge amplifier. Figure II.3.2.1.4 shows a single sensing element on the SLIC composite and block diagram of the amplifier circuits. To combine these two amplifiers, the outputs from both amplifiers are electrically isolated using high-impedance buffers, and a power supply of the amplifiers is also electrically isolated using an isolated type of a power supply derived from the main power supply. This circuit design ensures that the electrical current generated by the PVDF can only flow-through the charge amplifier; therefore, the piezoelectric charge is accurately converted to voltage without being affected by the strain amplifier or the data acquisition (DAQ) device.

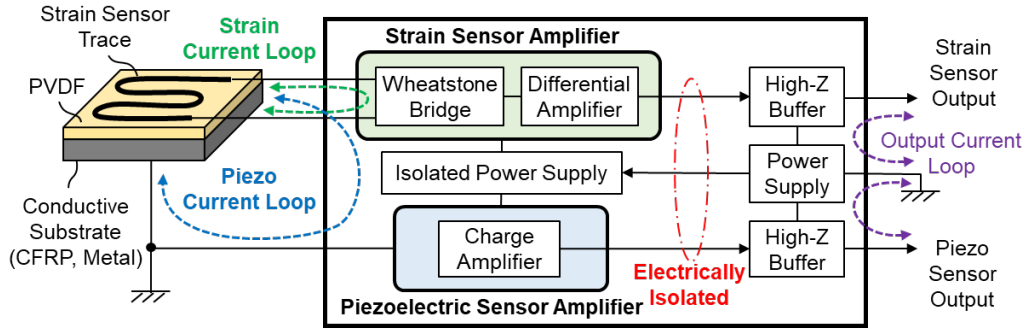


Figure II.3.2.1.4. Block diagram of dual-sensing amplifier for single sensing area. Source: Newport Sensors, Inc.

Extending this circuit design, it can also be combined for multiple sensing areas, as shown in Figure II.3.2.1.5, without encountering mutual interference due to the circuit isolation technique. This flexibility is achieved by implementing the same circuit configuration across various sensing zones. This innovative approach not only optimizes signal accuracy but also facilitates scalability and adaptability across diverse structural components.

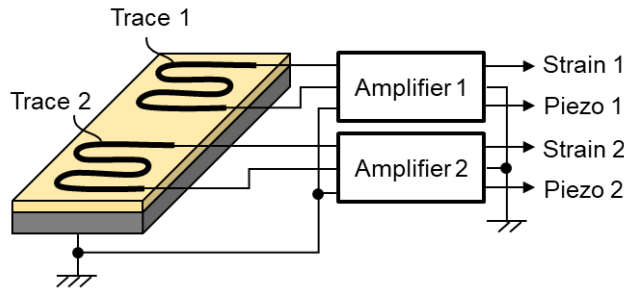


Figure II.3.2.1.5. Block diagram of dual-sensing amplifier for multiple sensing areas. Source: Newport Sensors, Inc.

Figure II.3.2.1.6 shows the amplifier unit fabricated for three sensing areas. It was used during the evaluation testing of SLIC specimens.

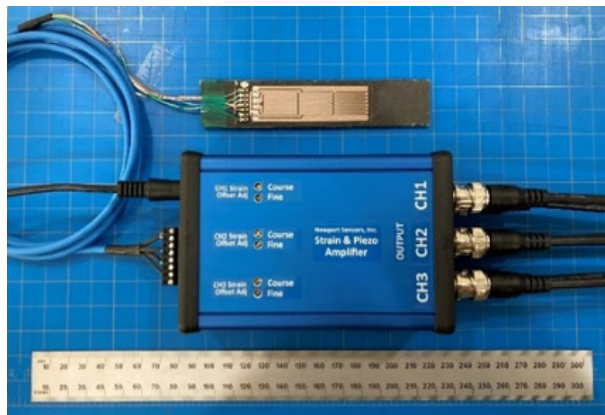


Figure II.3.2.1.6. Developed dual-sensing amplifier for three sensing areas. Source: Newport Sensors, Inc.

As a showcase of SLIC technology, we fabricated a small-scale bumper beam. Figure II.3.2.1.7 shows the bumper beam design and the fabrication process.

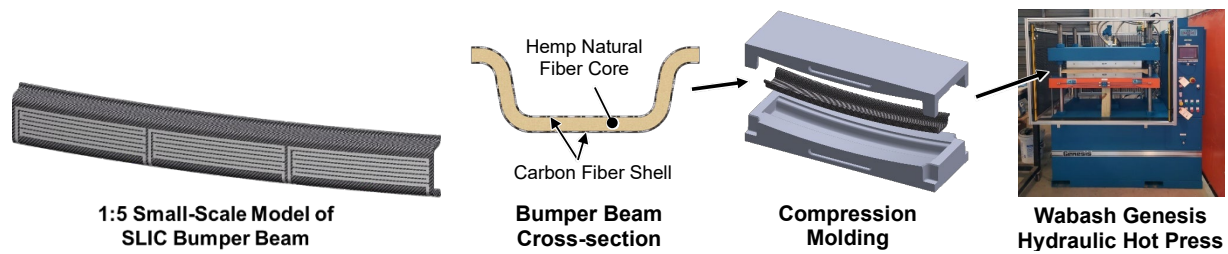


Figure II.3.2.1.7. Small-scale model of SLIC bumper beam design. Source: Newport Sensors, Inc.

Results

We carried out tensile, bending, and impact tests to evaluate the sensor performance and the material's energy absorption. Figure II.3.2.1.8 shows the test setup for tensile, bending and ball drop impact testing.

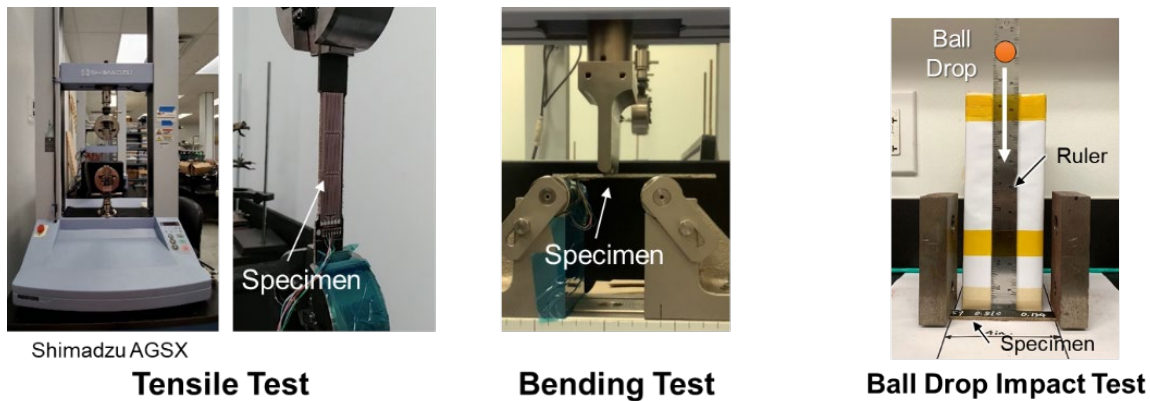


Figure II.3.2.1.8. SLIC specimen test setup. Source: Newport Sensors, Inc.

Tensile Test Result

Figure II.3.2.1.9 shows a tensile test result, including plots of signal time histories simultaneously measured by the three piezoresistive strain sensors and the three piezoelectric sensors embedded in the SLIC specimen. As the tension force increases, the strain sensors successfully measured the increase in electrical resistance. The red area of the specimen where the ultimate failure occurred produced the highest strain signal, enabling the identification of the damage location. On the other hand, the piezoelectric sensors also successfully detected the failure. Furthermore, the sensor located at the failure area (e.g., the red area) generated a pulse signal approximately 50 seconds before the failure. This signal was most likely caused by micro-cracks. This not only validated the high-sensitivity of the piezoelectric sensors built with the novel electrodes, but also demonstrated a significant potential of using the pulse as an early warning signal.

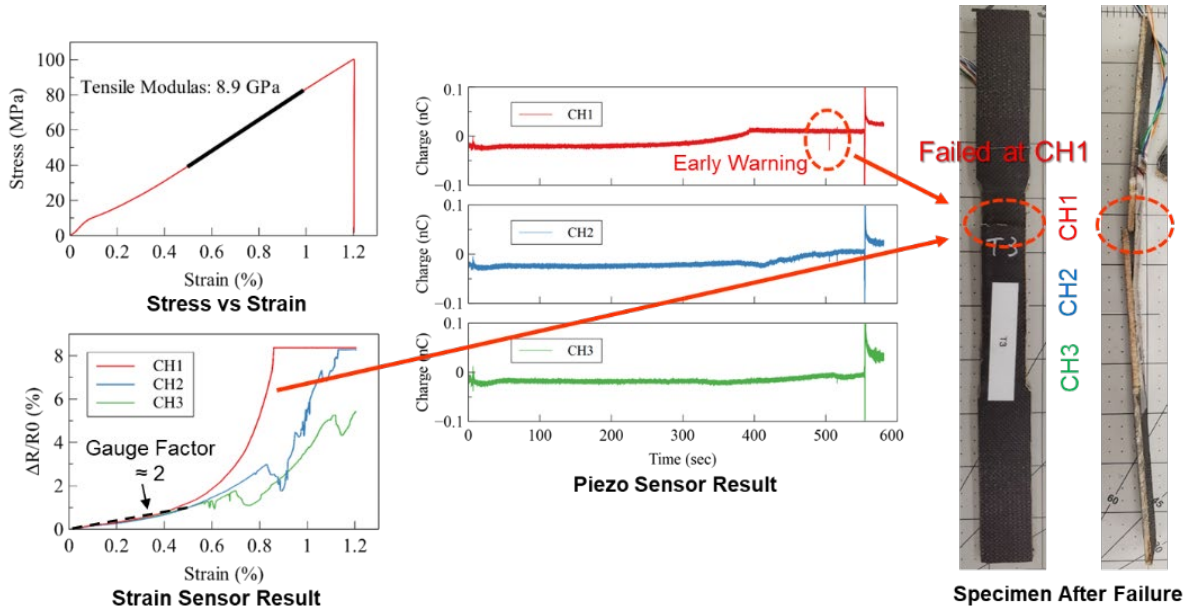


Figure II.3.2.1.9. Tensile test result. Source: Newport Sensors, Inc.

Bending Test Result

Figure II.3.2.1.10 presents a bending test result. The strain sensor at the failure location measured the highest strain. We also observed that the piezo sensors started to generate micro-crack signals after the specimen reached the yield point.

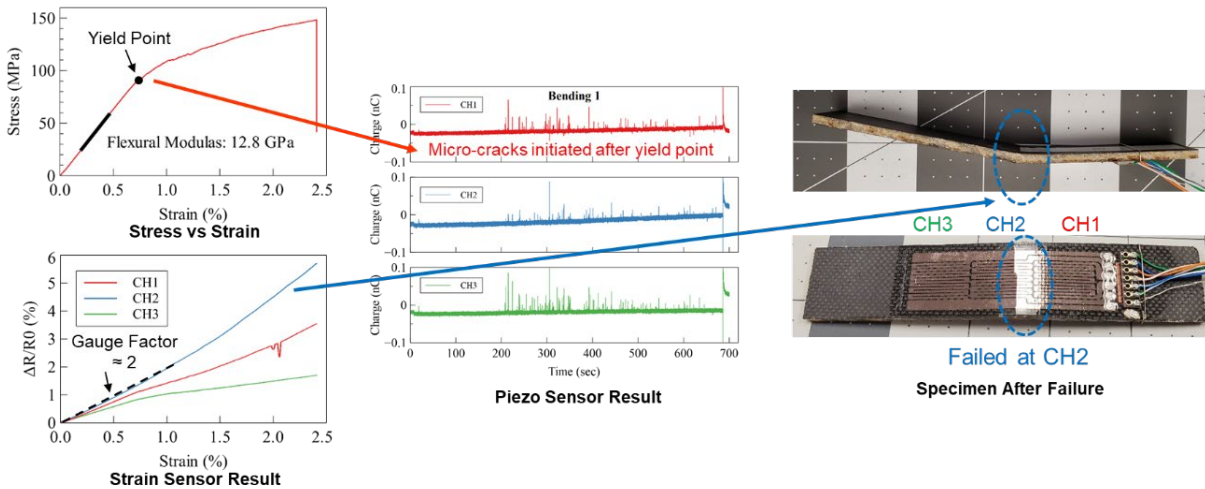


Figure II.3.2.1.10. Bending test result. Source: Newport Sensors, Inc.

Ball Drop Test Result

A ball-dropping test was conducted to compare the difference in impact energy absorption between SLIC and CFRP (control) composites. The result, as shown in Figure II.3.2.1.11, indicated that SLIC absorbed 40% more impact energy compared to the CFRP composite specimen of the same thickness.

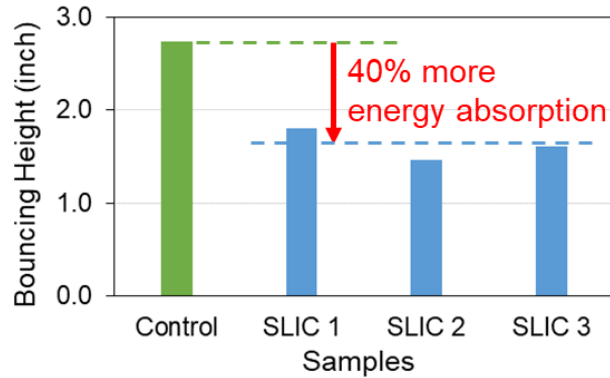


Figure II.3.2.1.11. Ball drop impact test result. Source: Newport Sensors, Inc.

SLIC Bumper Beam Fabrication

To fabricate the bumper beam, we machined the aluminum compression mold tooling in-house as shown in Figure II.3.2.1.12. We sent it to the UNT team, and they fabricated the bumper beam samples as shown in Figure II.3.2.1.13.

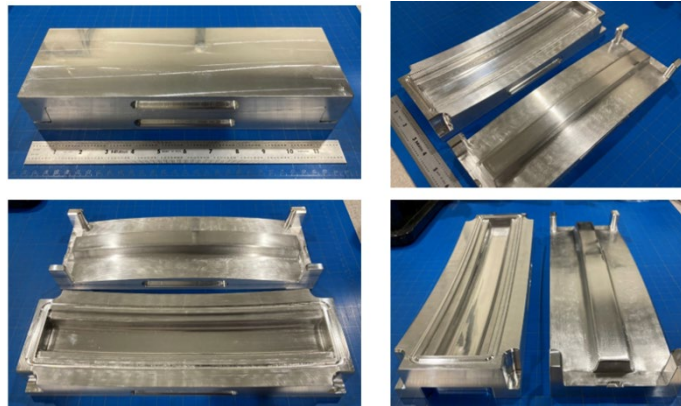


Figure II.3.2.1.12. Fabricated bumper beam compression mold. Source: Newport Sensors, Inc.



Figure II.3.2.1.13. Fabricated small-scale bumper beam. Source: Newport Sensors, Inc.

Conclusions

The SLIC project offers a compelling solution for achieving zero-emission goals in the automotive industry. Through the integration of carbon and natural fibers, SLIC enhances fuel-efficiency, reduces emissions, and ensures structural safety.

SLIC's multifunctional composite design, incorporating piezoelectric and piezoresistive sensors, proves successful in real-time structural health monitoring, and improved impact absorption. Tensile and bending tests demonstrate the capability to provide early warnings for potential failure in CFRP composites. In impact tests, SLIC demonstrates a 40% increase in impact energy absorption compared to traditional CFRP composites.

The fabrication of a SLIC bumper beam showcases the technology's practical application, achieved through in-house tooling and collaboration with UNT. In conclusion, SLIC represents a significant advancement in lightweight and sustainable automotive materials, with potential benefits for safety, efficiency, and environmental impact.

Key Publications

1. Mizuta, M., 2022, "SLIC for Next Generation Vehicles," 2022 DOE VTO Annual Merit Review, June 21, 2022.
2. Mizuta, M., 2022, "An Integrated Strain and Piezoelectric Sensor System," U.S. Patent Application No. 17/984,006, filed November 09, 2022.
3. Mizuta, M., 2023, "SLIC for Next Generation Vehicles," 2023 DOE VTO Annual Merit Review, June 14, 2023.

References

1. VTO, 2014, "Lightweight Materials for Cars and Trucks," Office of Energy-Efficiency & Renewable Energy, Washington, D.C., USA. Available at: <https://www.energy.gov/eere/vehicles/lightweight-materials-cars-and-trucks> (accessed 22 December 2023).
2. Brooke, L., R. Gehm, and B. Visnic, 2016, "Lightweighting: What's next?," *Automotive Engineering*, August 2016, 16–25. Available at: http://www.sae.org.cn/uploads/pubs/magazines/2017/AEI/sae_16AUTP08.pdf (accessed 24 May 2024).
3. Heuss, R., N. Müller, W. van Sintern, A. Starke, and A. Tschiesner, 2012, "Lightweight, heavy impact," *Advanced Industries: Lightweight, Heavy Impact*, McKinsey & Company, New York, NY, USA.

Acknowledgements

The author is grateful for the support provided by F. Wu from the DOE SBIR program under Award No. DE-SC0020707, and S. Shi from UNT for the support of the natural fiber composite source and the material testing equipment.

II.3.2.2 Integrated Self-Sufficient, Structurally Integrated Multifunctional Sensors for Autonomous Vehicles (Acellent Technologies, Inc.)

Amrita Kumar, Principal Investigator

Acellent Technologies Inc.
835 Stewart Dr.
Sunnyvale, CA 94085
E-mail: akumar@acellent.com

Brandy Greenawalt, SBIR Central Programs Operations Manager

U.S. Department of Energy SC-29
Small Business Innovation Research
19901 Germantown Rd.
Germantown, MD 20874
E-mail: brandy.greenawalt@science.doe.gov

H. Felix Wu, DOE Technology Development Manager

U.S. Department of Energy
E-mail: Felix.Wu@ee.doe.gov

Start Date: August 23, 2021
Project Funding: \$1,348,120

End Date: August 22, 2023
DOE share: \$1,348,120

Non-DOE share: \$0

Project Introduction

The DOE VTO Materials Technology subprogram office has identified a need for novel multifunctional composite materials and structures for the automotive industry that have the capability to reduce weight and volume as well as costs of “conventional” structural components. Multifunctional sensors in vehicle structures can revolutionize the usage of structures, render them intelligent, and make them truly “smart.” This can be achieved by developing and linking different sensor technologies into one integrated system for condition-monitoring to enable rapid detection of dangerous situations, optimal use of production facilities, and improved safety control. The proposed program focus is on the development of multifunctionalities in autonomous vehicles that can impact their design and usage resulting in weight-savings, increased safety, and cost efficiencies. In this SBIR project, Acellent Technologies, Inc. (Acellent), is developing an integrated AUTO-SMART sensor system for vehicles providing multifunctional capabilities and making the vehicles self-sufficient. The primary focus is to provide “weight-savings” and “safety” through the integration of structures with sensors to minimize parts counts, create new designs, establish new manufacturing processes, and enable cost-savings.

Objectives

Acellent Technologies Inc. proposes to develop an integrated AUTO-SMART sensor system for the automotive industry that can provide multifunctional capabilities and make the vehicles self-sufficient. The primary focus is on how multifunctionalities in composites can impact the design of automotive vehicles to provide increased pedestrian safety, weight-savings, and structural efficiencies. The proposed development will focus on two multifunctionalities: (1) a PPS, and (2) a battery monitoring system (BMS).

Approach

For the integrated system shown in Figure II.3.2.2.1, the following developments were targeted in this program with Phase II focused on developing a complete design for the AUTO-SMART sensor system:

1. In collaboration with Ford Motor Company (Ford), Acellent is developing the design for a pedestrian crash-sensing system with the capability to detect any impact event occurring on the front bumper of an automobile within a very short duration and generate the proper response signal to a built-in protection system. A primary challenge in this effort was to design and develop an impact event detection technique that can work efficiently even for complex structures with local property variation. Conventional impact detection systems have long response times due to the slow response of traditional sensors. The proposed system utilized lead zirconate titanate (PZT) sensors to generate the impact signal immediately after the impact event happens. By doing this, the passive safety systems, such as air bags and pyrotechnic restraints, can be activated in time to save lives.
2. In collaboration with Stanford University, Acellent is developing the design of a multifunctional energy-storage composite (MESC) structure and a system for monitoring the state of health (SOH) and state of charge (SOC) of typical battery packs for use in automobiles. Key items, such as sensor locations, are developed for the battery.

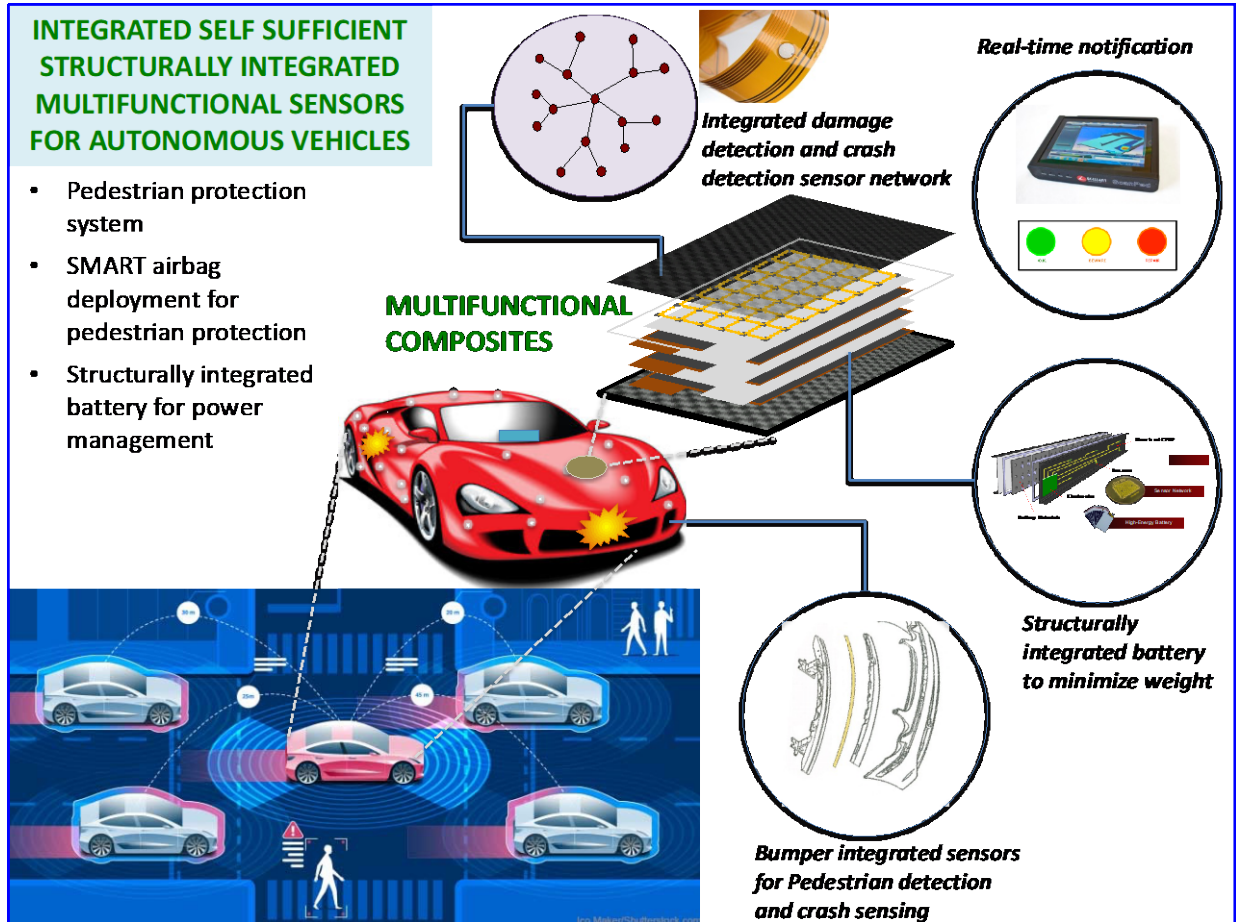


Figure II.3.2.2.1. Proposed AUTO-SMART system. Source: Acellent Technologies, Inc.

Results

Pedestrian Protection System (PPS)

An automotive PPS is generally used for protecting pedestrians from harm caused by frontal collisions. In Phase II, the system is being developed on a stationary bumper. Methods for the design and installation of the sensors on the bumper were developed. This work was conducted closely with Ford, who provided guidance and a test bumper to aid the development.

Sensor Network Design for Pedestrian Crash-Sensing

In Phase II, Acellent used its established SMART Layer[®] sensors for the bumper. The SMART Layer[®] sensor is well established in the field and is currently known for its unique ability to provide a large structural coverage for gathering data with its network of sensors/actuators embedded on a layer, thus eliminating the need for each sensor to be installed individually, as shown in Figure II.3.2.2.2 [1], [2], [3], [4]. The layer consists of a network of embedded, distributed PZT discs acting as both sensors and actuators for monitoring structural condition in real-time. The SMART Layer[®] manufacturing process utilizes the printed circuit technique to connect a number of sensors and actuators embedded in the layer. The SMART Layer[®] is treated as an extra ply that can be embedded between the composite plies during the composite layup process or surface-mounted on both metallic structures and the composite structure using a secondary adhesive such as epoxy.

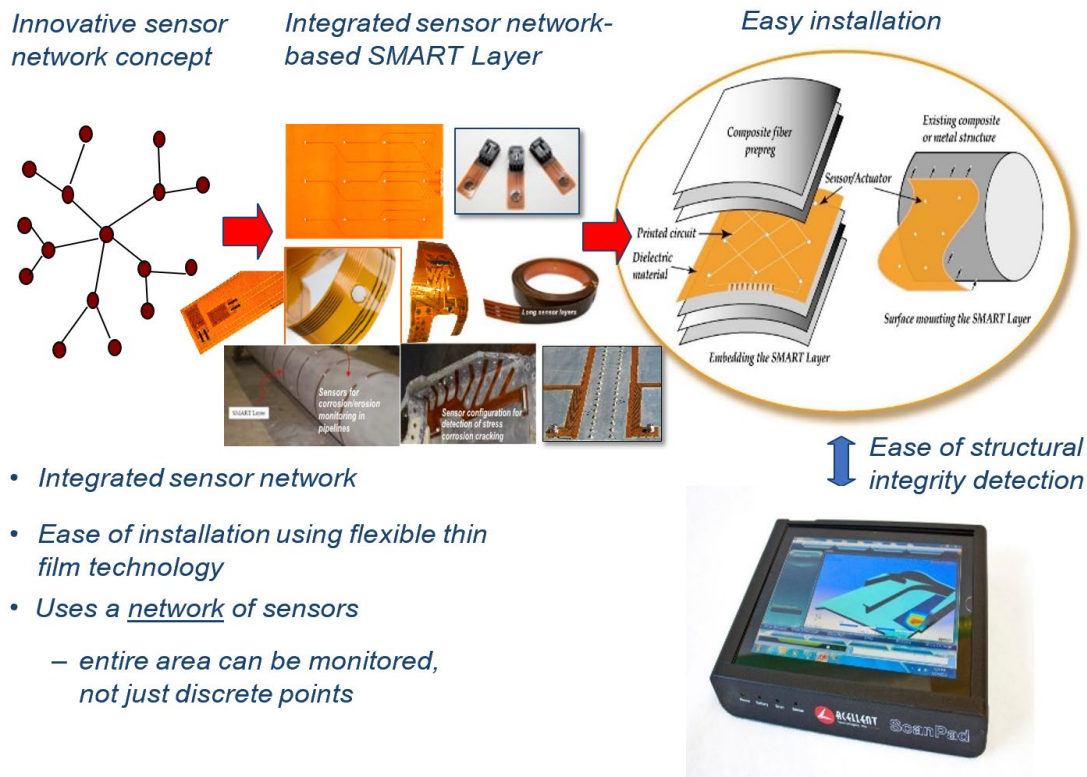


Figure II.3.2.2.2. SMART Layer[®] sensors. Source: Acellent Technologies, Inc.

For this application, Acellent chose small size disc-shaped PZTs. The PZT sensors, capacitors, and wiring can all be embedded in a thin dielectric film, as shown in Figure II.3.2.2.2. Additional shielding layers and wiring were also added to the sensor layer to minimize external electromagnetic interference and crosstalk between sensors. All SMART Layer[®] strips are shielded on one-side of the circuit by a copper layer. The small size of the PZTs is important so that they do not protrude from the bumper and are able to be embedded in the bumper during manufacturing.

To find the optimal sensor density and spacing for our sensor network, our team looked at several factors. Speed and accuracy requirements provided by Ford played a critical role in making this determination. Ideally, the team would like to have sensors instrumented along the entire length of the bumper with minimal spacing between each sensor to account for impacts at every location as discussed in the requirements above. However, cost and practicality issues require us to set a minimum sensor density [5], [6].

Many impact tests were performed on the bumper to determine the locations of the sensors. A total of 12 PZTs were installed on the bumper based on bumper size and test result desired. The SMART Layer[®] sensor locations were designed for the bumper based on this approach.

A prototype PPS was tested by Acellent on a test car bumper provided by Ford from one of their EVs using the test setup shown in Figure II.3.2.2.3. The bumper with sensors installed was fastened securely to two concrete poles. The sensors were connected to the impact data collection hardware through cables. Data then was sent to a laptop via an Ethernet cable for analysis. Figure II.3.2.2.4 shows the logic diagram for the system architecture and a data flow diagram.

To identify the impact signals due to different types of object impacts, impact tests were performed using various objects. For simulating the pedestrian impact on the bumper, a Hybrid II adult test dummy leg was used. This dummy leg represents the 50th percentile adult male, while size and weight represent the “average” adult male population. To study the non-pedestrian impacts and the corresponding signals at the bumper, impacts were performed on the bumper using polyvinyl chloride (PVC) pipe, a wooden dowel rod, a wooden board chunk, a golf club, a stone, etc. The test results of the impact testing are presented in the following sections.

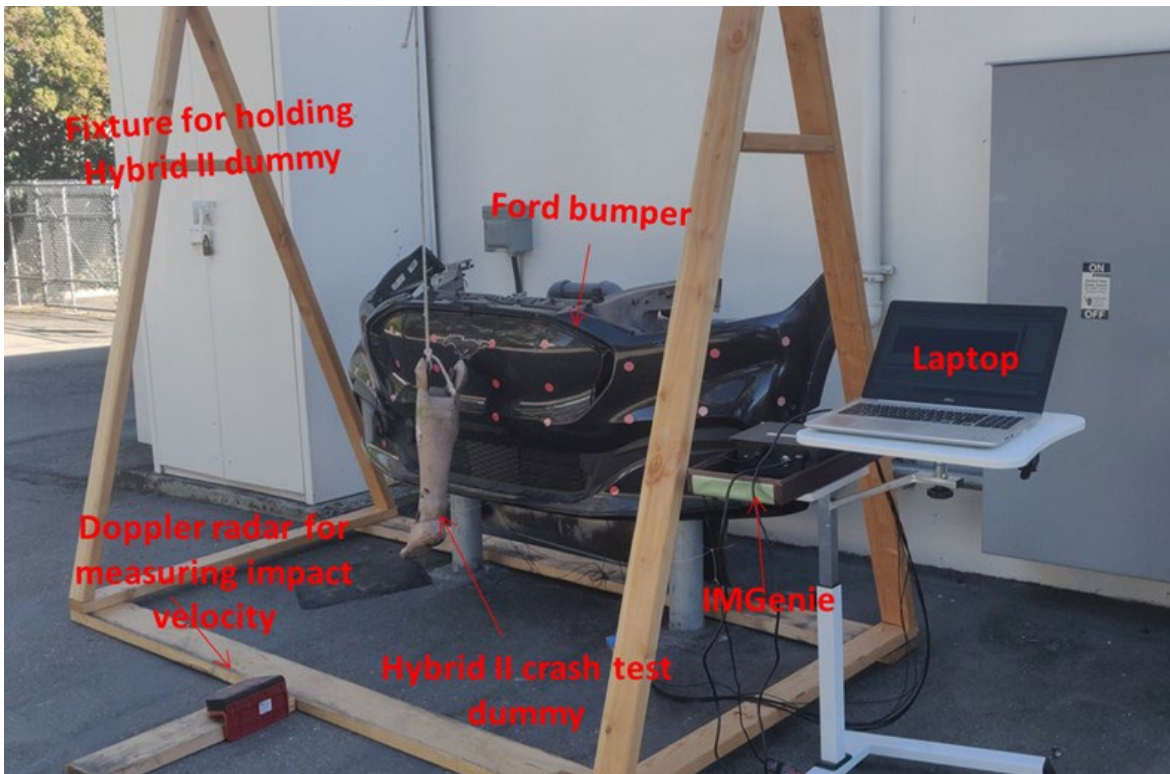


Figure II.3.2.2.3. System test setup. Source: Acellent Technologies, Inc.

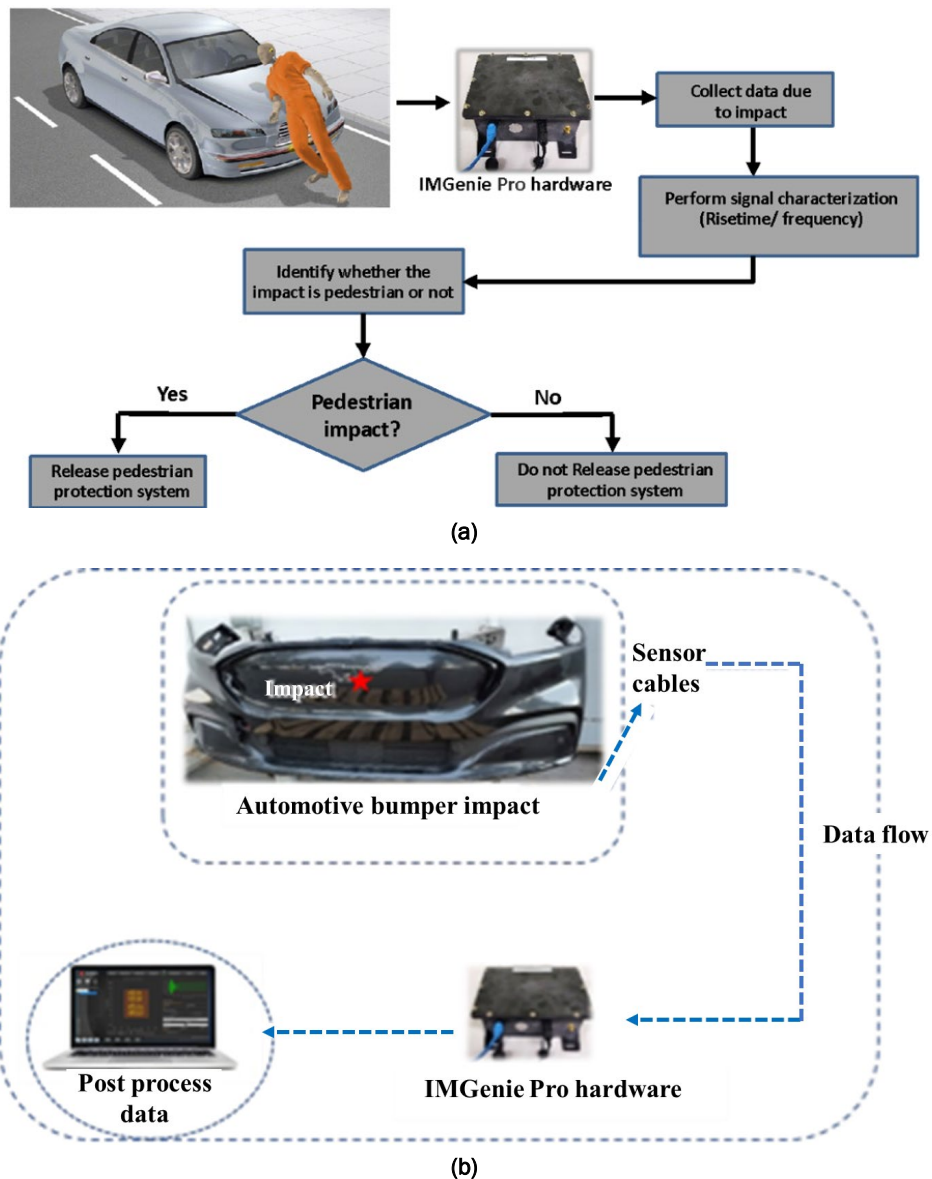


Figure II.3.2.2.4. System usage of PPS. (a) System architecture and (b) system algorithm development. Source: Acellent Technologies, Inc.

Impact with a Golf Club

The car was hit by a golf club at the front of the bumper, as observed in Figure II.3.2.2.5. The impact triggered the system to collect data from the sensors. The image on the right shows the signal received from the sensors and the frequency spectrum of the signal. As shown in Figure II.3.2.2.5, the simple harmonic motion (SHM) system successfully captured the impact. Repeated impact tests were performed to test the repeatability of the signal. The frequency spectrum of the signals was calculated and studied. The peak frequency of the signals was obtained from the tests and observed to be between 269–395 Hz. The golf club impact test results were found repeatable. Impact signals from using the PVC pipe, wooden board, wooden dowel rod, and stone are also recorded and presented as shown in Figure II.3.2.2.6 and Figure II.3.2.2.7, respectively. From several trials, the peak frequency due to the PVC pipe impact was observed to be between 285–363 Hz. The peak frequency due to the wooden dowel rod was identified to be between 269–363 Hz. For the wooden board chunk, the peak frequency was observed to be between 174–316 Hz. For the impact tests performed using a stone object, the peak frequency of the signals was identified to be between 269–442 Hz.

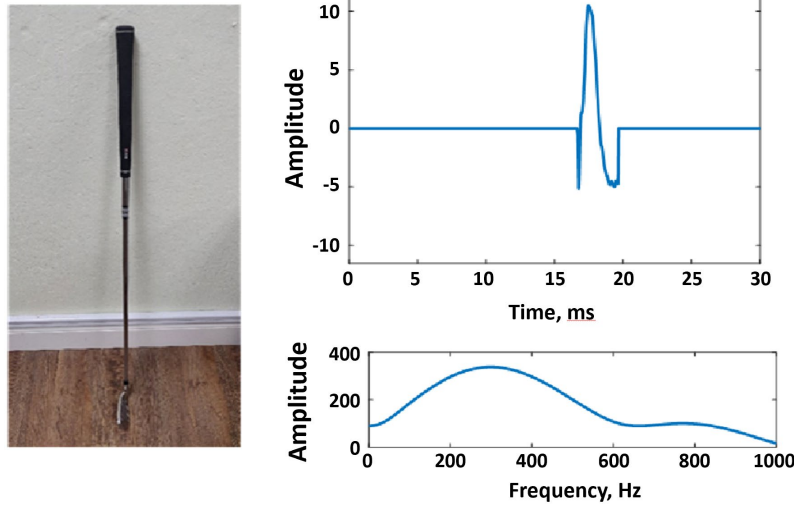
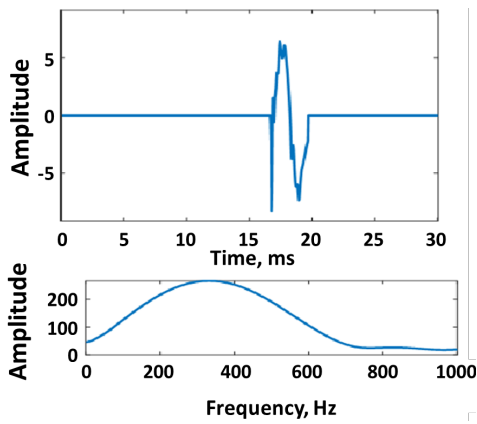
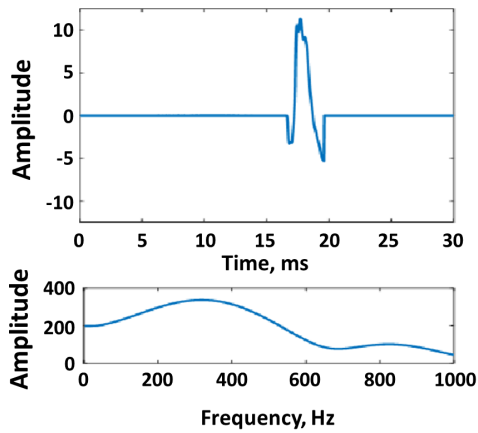


Figure II.3.2.2.5. Voltage impulse received upon an impact with a golf club.
Source: Acellent Technologies, Inc.



PVC Pipe
3.5cm (Outer Dia.) X 60 cm (H)

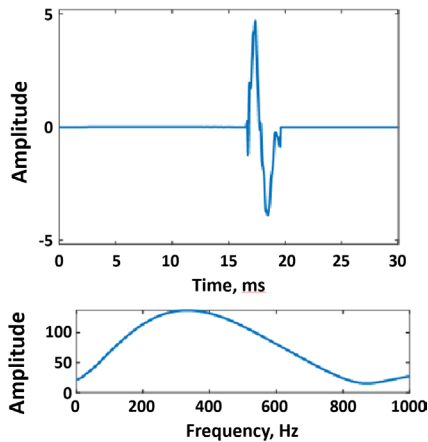
(a)



Wooden board
8.5cm (L) X 3.8cm (B) X 35cm (H)

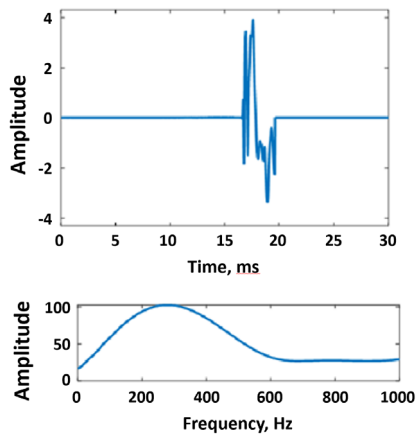
(b)

Figure II.3.2.2.6. Impact signals from (a) a PVC pipe and (b) a wooden board.
Source: Acellent Technologies, Inc.



Stone used for impact

(a)

Wooden dowel rod
2.2 cm (Dia.) X 91 cm (H)

(b)

Figure II.3.2.2.7. Impact signals from (a) a stone and (b) a wooden dowel rod.
Source: Acellent Technologies, Inc.

Impact with a Hybrid II Dummy Leg

The car bumper was hit by a Hybrid II dummy leg, as indicated in Figure II.3.2.2.8, to simulate hitting a pedestrian. The impact triggered the system to collect data from the sensors. The signal received from the sensor and its frequency spectrum is presented in Figure II.3.2.2.8. The SHM system can be seen to successfully capture the impact. The initial three milliseconds of the signal was studied to identify the signal characteristics due to a pedestrian impact. The frequency analysis was performed, and the peak frequency of the signal was identified as less than 100 Hz. Repeated impact tests were performed on the bumper and the Hybrid II impact signals were repeatable.

During Phase II, Acellent utilized data obtained from the tests to identify the frequency responses due to the impact of various objects on the bumper. The peak frequency due to diverse impact objects was studied from several repeated tests. A summary of the peak frequency study is presented in Table II.3.2.2.1. As can be seen from the data obtained, the impact signals obtained from non-pedestrian objects vs. pedestrian objects are significantly different. Based on this, software was developed to meet the requirements for detection of pedestrians. Extensive testing of the software will be performed in the next stage.

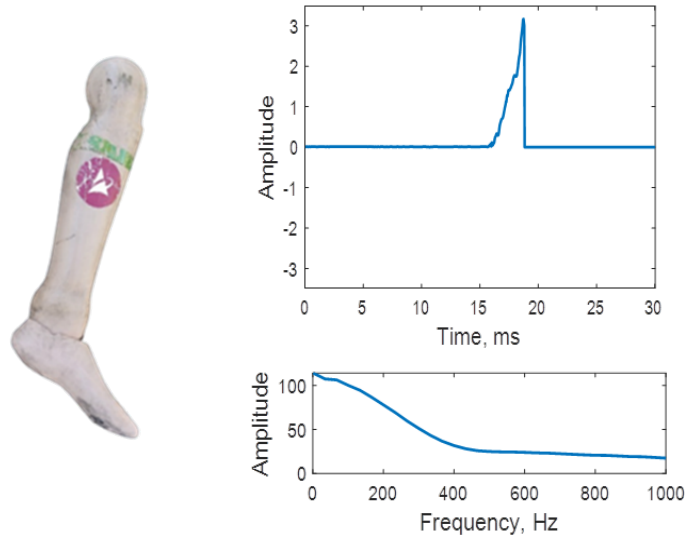


Figure II.3.2.2.8. Voltage impulse received upon an impact with a prosthetic leg.
 Source: Acellent Technologies, Inc.

Table II.3.2.2.1. Peak Frequency due to Various Object Impacts

Object	Peak Frequency Range (Hz)	Avg. Peak Frequency (Hz)
Hybrid II Leg	< 100	35.90
PVC Pipe	285–363	321.35
Wooden Dowel Rod	269–363	320.13
Wooden Board Chunk	174–316	264.54
Golf Club	269–395	314.35
Stone	269–442	358.70

To classify the pedestrian object from the small animal object, a novel signal energy method was developed. In the signal energy method, an additional parameter of the energy of the different signals was considered to further distinguish between a pedestrian object and a small animal object. The energy of the object impact was calculated from the mass (m) and velocity (V) of the impact of the object ($E=1/2mV^2$). The energy of the signals was calculated from the voltage recorded by the sensors (V) and the admittance (Y) of the measuring system ($E=\int YV^2dv$). The impact energy and signal energy were plotted with respect to the velocity of impact. Then, the impact energy of the objects is plotted to fit the impact signal energy. Assumed loss factors for objects were used for fitting the impact energy with the signal energy data points. The fitted curve is extrapolated up to 50 mph. The representative energy plot for the pedestrian object and the small animal object at this velocity range showed a higher range of energy values for the pedestrian object and a lower range of energy values for the small animal object. Thus, the object classification using the impact signals was performed to enhance the ability for distinguishing objects using these three parameters: (1) frequency, the velocity of the vehicle, and signal energy.

A prototype of a pedestrian impact detection system that has the capability to detect and classify any impact events on a bumper of an automobile within a reasonable duration was developed and tested. Initial testing on the bumper was performed to identify the location and the number of sensors for the detection. A test setup was developed to demonstrate the impact-sensing system. The test setup consisted of the bumper, the IMGenie Pro Hardware, a laptop installed with AiM software for data recording, cables, a fixture for holding the test object, and impact objects (Hybrid II dummy leg, small animal model impact object, PVC pipe, wooden board, golf club, wooden dowel rod, etc.). The signals sensed due to various object impacts were recorded by the PZT

sensors. The signal frequency characteristics due to different object impacts were identified from the signals that were recorded. The peak frequency of signals due to the various objects, such as PVC pipe, wooden board, golf club, etc., was observed to be different from the Hybrid II dummy leg impact signals. Similar signal peak frequency characteristics were observed for pedestrian dummy leg and small animal model object impacts. Additional classification of small animal object was achieved by using the developed energy method.

Battery Monitoring System (BMS)

A BMS is used to monitor and control power storage systems, assure the health of battery cells and deliver power to vehicle systems. Lithium-ion (Li-ion) battery technology has performed magnificently and improved significantly over the last decade; however, the chemistry inside the battery is susceptible to certain risks—such as overheating, over-voltage, deep discharge, over-current, and pressure or mechanical stress. To prevent battery failure and mitigate potential hazardous situations, there is a need for a BMS that ensures these batteries function properly in their final applications. The BMS can provide SOC, SOH, and end-of-life status of the battery. This work, which is done in collaboration with Stanford University, introduces MESC structures as an alternate strategy towards the fabrication of structural load-bearing batteries—an intermediate, multidisciplinary strategy. MESCOs represent a novel form of multifunctional structural battery enclosures that can carry mechanical loads while simultaneously providing energy-storage capabilities. MESCOs provide a disruptive integration technique that allows high-energy Li-ion battery electrode materials to be embedded in high-strength CFRP composites. The novelty of MESCOs lies in their incorporation of through-thickness interlocking polymer ‘rivets’ that extend through carefully designed perforations in the battery stack to interlock the electrode layers and securely anchor these layers onto the structural CFRP face sheets. Standard industry electrodes can be adapted to function directly within this design without any requirement for battery chemistry modifications, which may be crucial for industry adoption.

Like sandwich structures, the comparatively stiff CFRP face sheets are placed on either side of the electrode stack, separated by the electrode core thickness, to carry the majority of the bending moment. This sandwich-style construction effectively increases the area moment of the laminate, giving it higher flexural rigidity. Without the interlayer shear resistance of the battery core, the thin CFRP face sheets will tend to bend around their own individual neutral axis, and the structural contributions of the face sheets will be minimized. The interlocking rivets therefore act to inhibit interlaminar slippage between electrode layers, thus allowing effective transfer of the shear-stress through the battery stack to the CFRP face sheets. This is analogous to the use of stud shear connectors in civil construction to enhance the shear interaction and the load transfer between concrete and steel sections. The shear transfer allows the battery laminate to bend around a common neutral axis, thus using the intrinsic mechanical properties of the electrode layers efficiently and making them a suitable sandwich structure core material.

Fabrication of MESC Skateboard

As a demonstration for the MESC applications, we made an MESC skateboard that is representative of an EV. The skateboard consists of 10 MESC cells between two CFRP boards. Figure II.3.2.2.9 shows the dimensions of board, battery cells, wiring, and sensor layers. The MESC cells are connected in series to generate 37 V—the required voltage needed for a BMS to be able to run a typical skateboard’s motor and wheels.

Figure II.3.2.2.10 shows the concept. SMART Layer[®] piezoelectric sensors from Acellent are mounted on the surface of the battery pack. One of the piezoelectric discs can be chosen as an actuator to generate acousto-ultrasonic guided waves. The other piezoelectric disc then serves as a receiver to record the transmitted guided wave signals. The guided wave signals from the piezoelectric sensors can then be co-related with battery SOC/SOH through both experiments and analysis. After fabrication of the 10 MESC cells, all the cells were put into a battery cyler to perform cycling, as well as a Hybrid Pulse Power Characterization (HPPC) test as shown in Figure II.3.2.2.11.

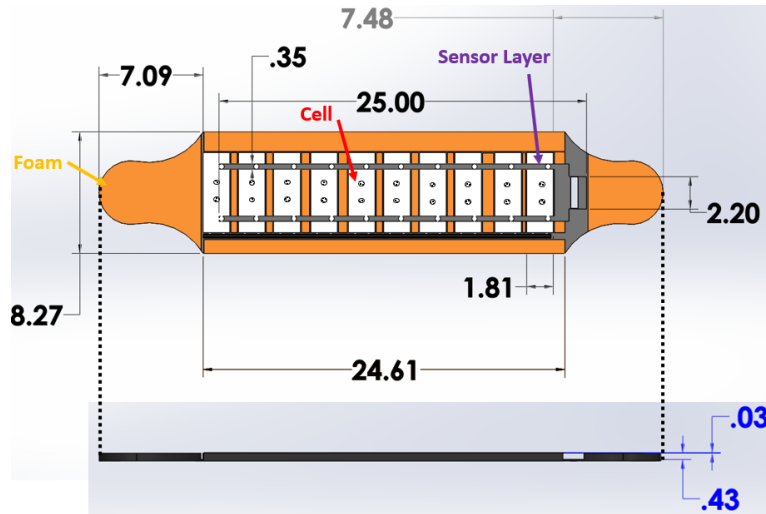


Figure II.3.2.2.9. The dimensions (in inches) and design of the MESC skateboard.
Source: Acellent Technologies, Inc.

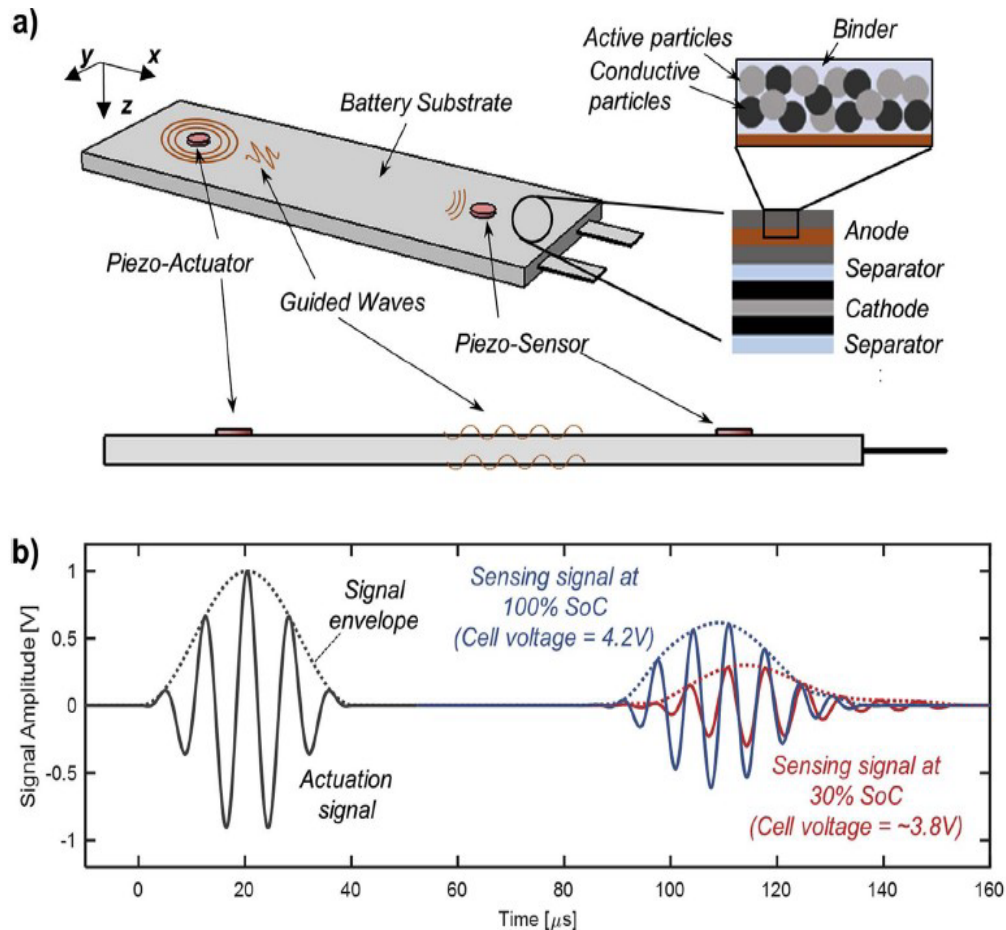


Figure II.3.2.2.10. (a) Schematics of the guided wave inspection setup on an indicative Li-ion battery, showing piezoelectric transducers used for pitch-catch guided wave propagation, as well as different internal layers of the battery and constituent materials. (b) Representative signals at two SoC, illustrating changes in the receiving signal amplitude and time of flight, as a result of changing SoC during charge.
Source: Acellent Technologies, Inc.



Figure II.3.2.2.11. Cycling and HPPC test of the fabricated MESC cells in the battery cycler
Source: Acellent Technologies, Inc.

All cells are required to pass these cycling and HPPC tests in order for the skateboard to be constructed. Figure II.3.2.2.12, Figure II.3.2.2.13, and Figure II.3.2.2.14 show the cycling test results of the individual MESC pouch cells. These cells are meant to be cycled to 200 cycles. Figure II.3.2.2.15 shows the HPPC test results of the MESC pouch cells for the current pulse and corresponding voltage response. After fabrication and usage of the skateboard, it is important to monitor the health status of the MESC battery. To perform this task, SMART PZT layers were embedded into the MESC battery to collect the ultrasonic signals from the embedded battery.

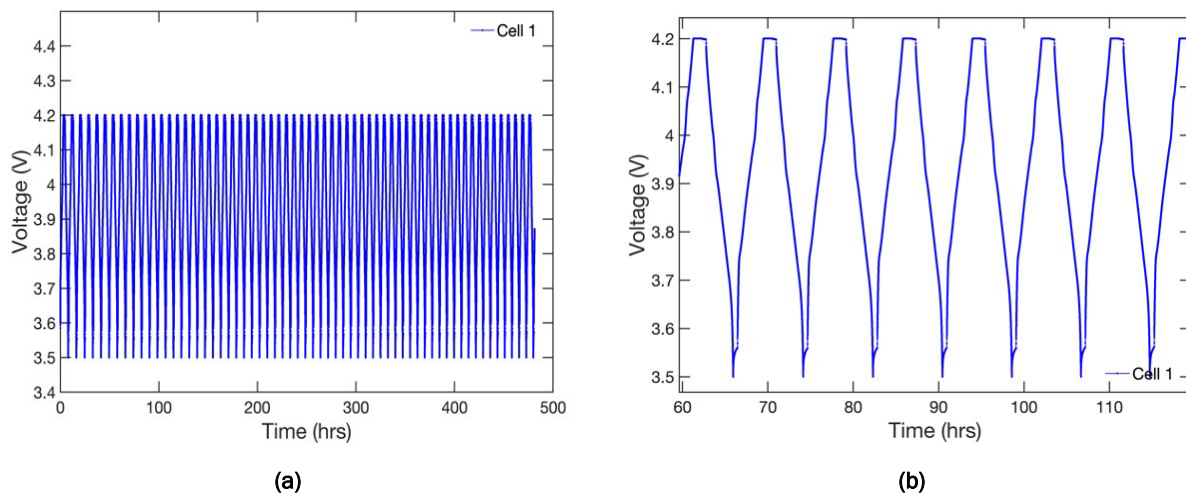


Figure II.3.2.2.12. (a) Voltage obtained from the cyclic test of the MESC pouch cells up to 200 cycles.
(b) A zoomed in view of a part of the voltage cycling. It takes about 500 hr. to perform 63 cycles.
Source: Acellent Technologies, Inc.

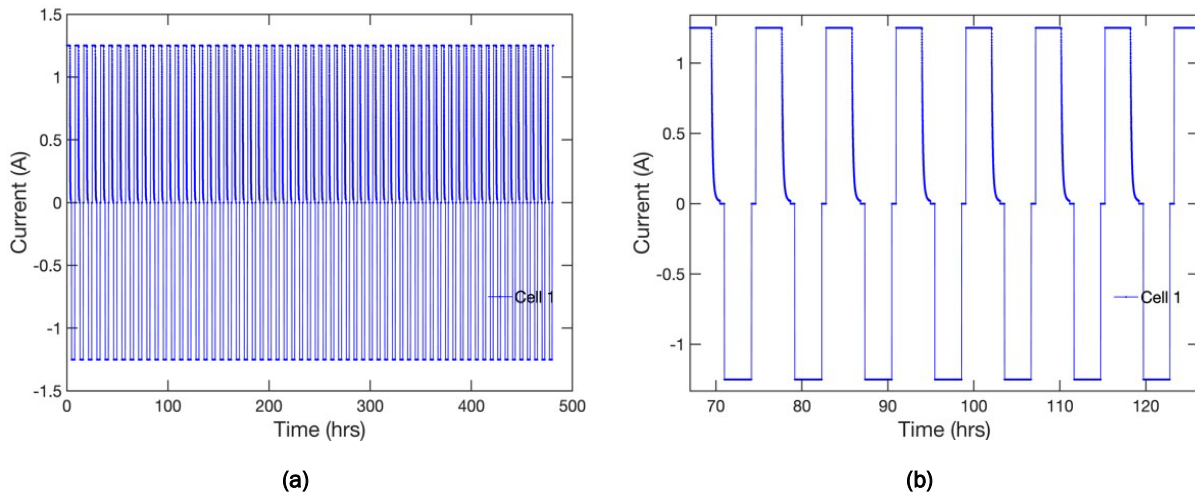


Figure II.3.2.2.13. (a) Current obtained from the cyclic test of the MESC pouch cells up to 200 cycles. (b) A zoomed in view of a part of the current cycling. It takes about 500 hr. to perform 63 cycles. Source: Acellent Technologies, Inc.

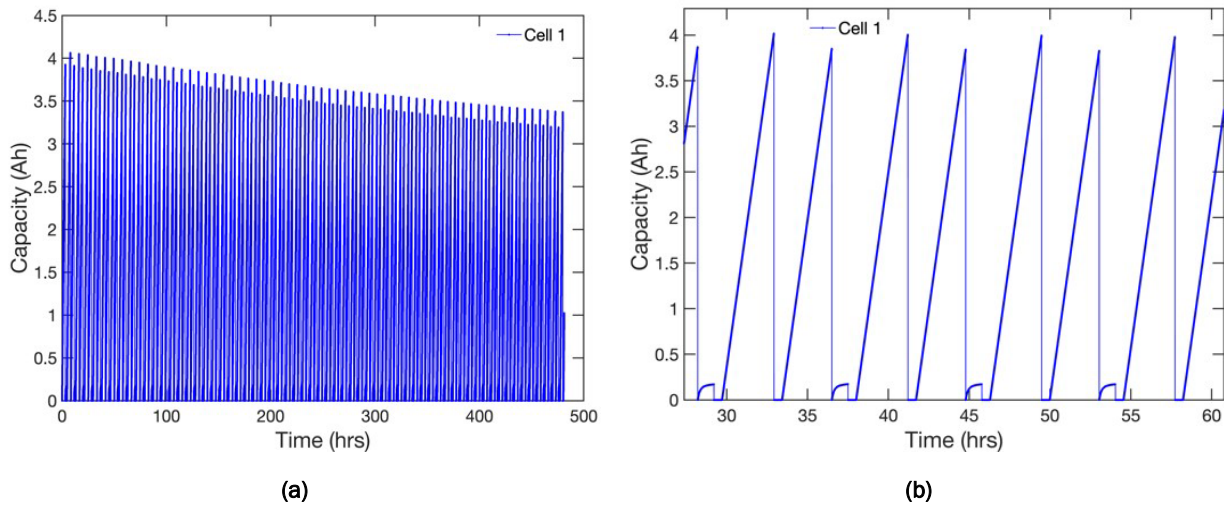


Figure II.3.2.2.14. (a) Capacity obtained from the cyclic test of the MESC pouch cells up to 200 cycles. (b) A zoomed in view of a part of the capacity cycling. It takes about 500 hr. to perform 63 cycles. Notice how capacity decreases with the increasing number of cycles. Source: Acellent Technologies, Inc.

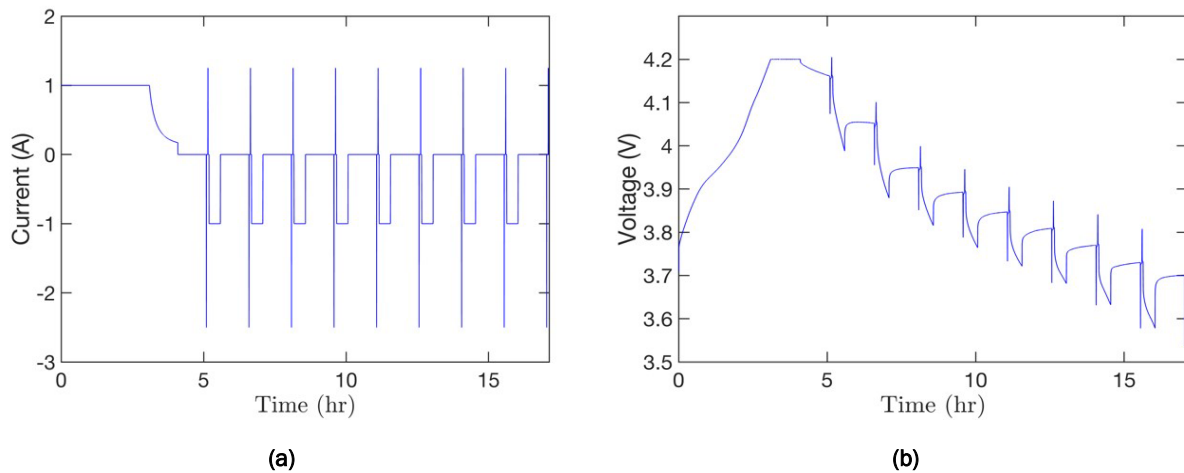


Figure II.3.2.2.15. (a) The current pulse and (b) corresponding voltage response obtained from the HPPC test. It takes about 20 hours to complete one HPPC test. Source: Acellent Technologies, Inc.

Figure II.3.2.2.16 shows the ultrasonic data collection setup using the SMART PZT layer. Once the ultrasonic signals are collected from the skateboard, signals are analyzed to extract meaningful information from them. Figure II.3.2.2.17(a) shows the analysis of the ultrasonic signals for changes when the batteries are charging or discharging and Figure II.3.2.2.17(b) shows the same signals after performing an Autoregressive analysis where α_1 and α_2 are smoothing factors. The baseline, charging, and discharging phase is clearly separated.



Figure II.3.2.2.16. Ultrasonic data collection from the skateboard using the SMART PZT layer while the skateboard was undergoing charging and discharging activities. Source: Acellent Technologies, Inc.

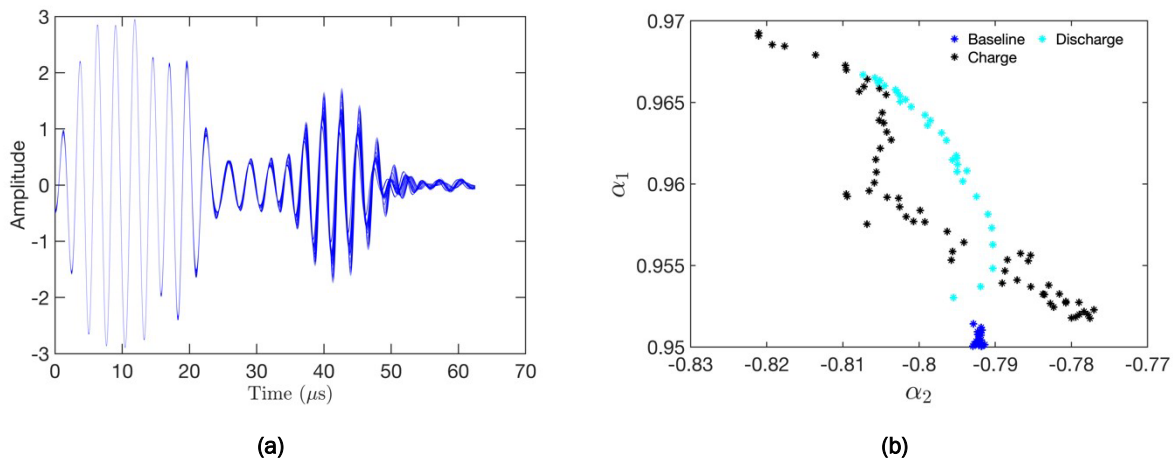


Figure II.3.2.2.17. (a) The collected ultrasonic signals are shown when the skateboard was charging and discharging for a different path; however, no specific trend is found. (b) After performing an autoregressive analysis on the same signals, the baseline, charging, and discharging phase is clearly separated.

Source: Acellent Technologies, Inc.

Conclusions

During the last year, Acellent has developed two multifunctional applications for vehicles—a PPS and a BMS. The PPS was developed and tested. Algorithms required for pedestrian vs. non-pedestrian detection have been developed and tested. For the BMS, a skateboard was manufactured using the MESC technology that includes composites, batteries, and sensors. This skateboard is representative of an EV. Testing has been performed on the skateboard and the signals were able to separate charging, discharging, and baseline phases.

References

1. Acellent website, 2023. Available at: www.acellent.com (accessed 8 January 2024).
2. Chang, F.-K., 2009, *Structural Health Monitoring 2009: Proceedings of the Seventh International Workshop on Structural Health Monitoring*, Stanford University, Stanford, CA, USA.
3. Qing, X. P., S. J. Beard, A. Kumar, A., I. Li, M. Lin, and F.-K. Chang, 2009, “Stanford Multiactuator–Receiver Transduction (SMART) Layer technology and its applications,” *Encyclopedia of Structural Health Monitoring*. <https://doi.org/10.1002/9780470061626.shm098>.
4. Qing, X. P., S. J. Beard, R. Ikegami, F.-K. Chang, and C. Boller, 2009, “Aerospace applications of SMART Layer technology,” *Encyclopedia of Structural Health Monitoring*. <https://doi.org/10.1002/9780470061626.shm152>.
5. Kim, A. C., and F.-K. Chang, 2005, “Rapid detection and identification of pedestrian impacts using a distributed sensor network,” *Proc. SPIE*, 5764, 80–91. <https://doi.org/10.1117/12.600433>.
6. Kim, A. C., 2006, “A rapid method for identifying and characterizing structural impacts using distributed sensors: An application for automotive pedestrian protection,” Thesis (Ph. D.)--Stanford University, 2006, *Diss. Abstr. Int.*, 66-11, B, 6097.

Acknowledgements

The authors would like to acknowledge the guidance of Dr. H. Felix Wu, our DOE Technology Manager, during the program. The authors also express appreciation and gratitude for support from Ford Motor Company in providing the test bumper and guidance for the PPS. This work was conducted under DOE SBIR Phase II, under award number DE-SC0020714.

II.3.2.3 Conductive Lightweight Hybrid Polymer Composites from Recycled Carbon Fibers (RockyTech Ltd.)

Yinghua Jin, Principal Investigator

RockyTech Ltd.
1111 Engineering Dr.
Boulder, CO 80305
E-mail: jin@rockytechs.com

Brandy Greenawalt, SBIR Central Programs Operations Manager

U.S. Department of Energy SC-29
Small Business Innovation Research
19901 Germantown Rd.
Germantown, MD 20874
E-mail: brandy.greenawalt@science.doe.gov

H. Felix Wu, DOE Technology Development Manager

U.S. Department of Energy
E-mail: Felix.Wu@ee.doe.gov

Start Date: June 28, 2021
Project Funding: \$1,299,218

End Date: August 21, 2024
DOE share: \$1,299,218

Non-DOE share: \$0

Project Introduction

By replacing steel with CFRPs, the weight of an automobile body system can be reduced by over 20%, equivalent to a 12–16% increase in fuel economy, per DOE guidelines. However, the production of virgin CF is energy-intensive and costly, and current CFRPs are generally not recyclable. Recycled discontinuous CFs represent valuable fillers in composite materials, offering a means to utilize their inherent conductivity and mechanical strength, which has the potential to substantially enhance CFRP cost-effectiveness and environmental sustainability. Furthermore, substituting the traditionally used, difficult-to-recycle epoxy thermoset matrices with innovative, recyclable, and reprocessable covalent adaptive network polymers—commonly known as vitrimers or malleable thermosets—enables a closed-loop recycling process for end-of-life CFRPs. This advancement further increases their sustainability and reduces overall cost, thereby making lightweight strategies affordable for mainstream vehicles.

Objectives

The overall objective of the project is to develop multifunctional, recyclable, nano- and micro-filler reinforced vitrimer composites made from recycled milled CFs (NMVC-R²), which have combined lightweight, conductive, and electromagnetic shielding properties in addition to robust mechanical performance.

Approach

Lightweight polymer NMVC-R² composites having high-strength, conductivity, and by design recyclability and reprocessability are developed from low-value milled recycled CF (rCF) micro-fillers and carbon-based nanofillers. A vitrimer matrix with excellent mechanical properties is used to provide recyclability, repairability, and reprocessability of the materials. Our approach provides the following key features:

1. Enhanced interfacial adhesion between the fillers and the polymer matrix is achieved via covalent surface modification of rCF micro-fillers with carbon-based nanofillers.
2. A synergistic reinforcement effect arises from the incorporation of both nano- and micro-fillers within the vitrimer matrix, leading to efficient load distribution, minimized stress concentrations, and overall improved mechanical properties.

3. The EC of the NMVC-R2 is significantly increased by creating an interconnected network of conductive hybrid nano- and micro-fillers.
4. The vitrimer matrix enables the NMVC-R2 to be fully reprocessable and 100% recyclable, aligning with sustainability goals.
5. The production of malleable, yet fully cured NMVC-R2 prepregs is possible, offering infinite shelf lives without compromising their quality.

Results

Surface Modification of rCF

It is critical to control the interfacial properties of CFRPs to ensure efficient load transfer from the polymer matrix to the fillers. Poor adhesion between the fiber and the matrix creates an inherent weak zone that easily causes delamination and failure under stress. We developed a synthetic method to functionalize the surface of rCFs having an average length 100 μm with reactive groups to covalently link the vitrimer matrix and improve the interfacial interactions. We also covalently attached conductive carbon-based nanofillers onto the rCF surface to increase the surface contact area of fillers with the polymer matrix and improve the conductivity of CFRPs. Such nano-, micro-combined fillers (NMCFs) show excellent stability over multistep chemical and physical processing (e.g., composite formation through polymerization and subsequent recycling through depolymerization). The recycled NMCFs show a similar grafting density of nanofillers on the surface to that of the as-prepared NMCFs, indicating the stability of the covalently attached nano-micro hybrid fillers, as shown via the SEM images in Figure II.3.2.3.1.



Figure II.3.2.3.1. (a) Covalent surface functionalization of rCF with carbon nanofiller to form highly stable NMCF. SEM images of (b) freshly prepared NMCF and (c) recycled NMCF from NMVC-R². Due to the strong covalent bonding between CF micro-fillers and carbon-based nanofillers, NMCFs are stable even after a series of solution and solid-state processing under heat. Source: RockyTech Ltd.

Development of Vitrimers

Vitrimers are crosslinked polymers that contain thermally activated dynamic covalent bonds. Unlike conventional thermosets, vitrimers can rearrange the network structure through cleavage and reformation of dynamic crosslinks in response to temperature, offering the structural stability of thermosets and the reprocessability of thermoplastics [1], [2]. Under heat and pressure, polymer chains in vitrimers rearrange without losing their crosslink density, allowing internal stresses to be released while maintaining structural integrity. This adaptability enables vitrimers to self-heal, fuse, and be reprocessed multiple times, making them ideal for quick manufacturing of CFRPs via thermal compression molding. The dynamic bonds in vitrimers also allow for closed-loop recycling by breaking down into oligomers and monomers. Additionally, vitrimer composites can act as indefinitely stable prepregs at RT, overcoming the limited shelf-life and irreversible curing issues of traditional half-cured epoxy-based CFRP prepregs. By carefully selecting specific monomers (e.g., rigid aromatic monomers and flexible aliphatic ones) and integrating a combination of dynamic covalent linkages with secondary weak interactions, we have successfully developed an extensive portfolio of over 40 vitrimers, as observed in Figure II.3.2.3.2, with a diverse array of physical properties.

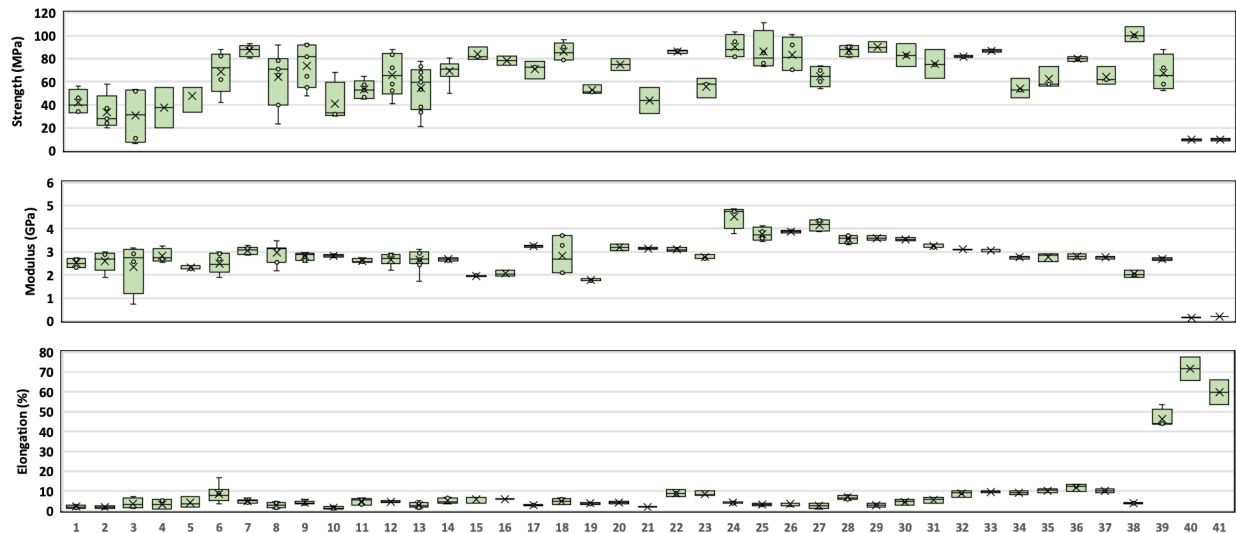


Figure II.3.2.3.2. Tensile properties of various vitrimers. Source: RockyTech Ltd.

Elastomeric Vitrimers

We have developed elastomeric vitrimers with a tensile strength between 9–11 MPa, a modulus between 139–159 MPa, and an elongation at break between 66–78%. These flexible vitrimers with conformability, stretchability, and rehealability could have excellent applications in soft electronics, sensors, and robotics.

Rigid and Strong Vitrimers

We have developed rigid and strong vitrimers with a typical tensile strength between 70–100 MPa, a modulus between 3–5 GPa, and an elongation at break <10%. When combined with CFs, the CFRPs exhibit excellent tensile strength of up to 700 MPa and a modulus of 106 GPa, as can be seen in Figure II.3.2.3.3, which can be used as a structural material.

Development of NMVC-R²

A series of NMVC-R² consisting of various vitrimers and surface-modified rCFs were prepared through a solution-phase gel-impregnation method or a solid-phase powder compression method. We screened various vitrimer compositions, reaction conditions, rCF and nanofiller loadings, and processing conditions, as observed in Figure II.3.2.3.3. We found that the surface modification of rCF with a micro-filler has a profound effect on the mechanical properties and EC of CFRPs, as indicated in Figure II.3.2.3.3(a, b). For unmodified rCF, the modulus of the composite reaches its maximum at 41 wt.% rCF loading, and further increase in loading diminishes mechanical properties. For example, V1-rCF-66% has a modulus similar to that of the vitrimer V1 (e.g., 2 GPa vs. 1.3 GPa), indicating a failure of load transfer from the matrix to the fibers. Surface modification of rCF allows for increased rCF loading up to 60 wt.%. The use of NMCF in composites at 50% loading (e.g., V1-NMCF-50%) results in a high-modulus of 9.06 GPa, which is almost two-fold that of the similar composite (e.g., V1-rCF-50%) consisting of unmodified rCF (e.g., 4.90 GPa). NMCFs can improve not only the mechanical properties, but also the conductivity of the composites when compared to the unmodified rCF. When NMCFs were used as a filler, we observed over a 50-fold increase (e.g., 40 S/m for V1-rCF-41% vs. 2304 S/m for V5-NMCF-50%) in conductivity for the NMVC-R² as compared to the otherwise similar CFRP composite with unmodified rCF. Another remarkable advantage of NMCFs is the effective suppression of nanofiller self-aggregation during processing, achieving efficient dispersion with maximal surface area within the composite. Through the gel-impregnation method, NMVC-R² with tensile moduli up to 15 GPa and EC >2500 S/m could be obtained.

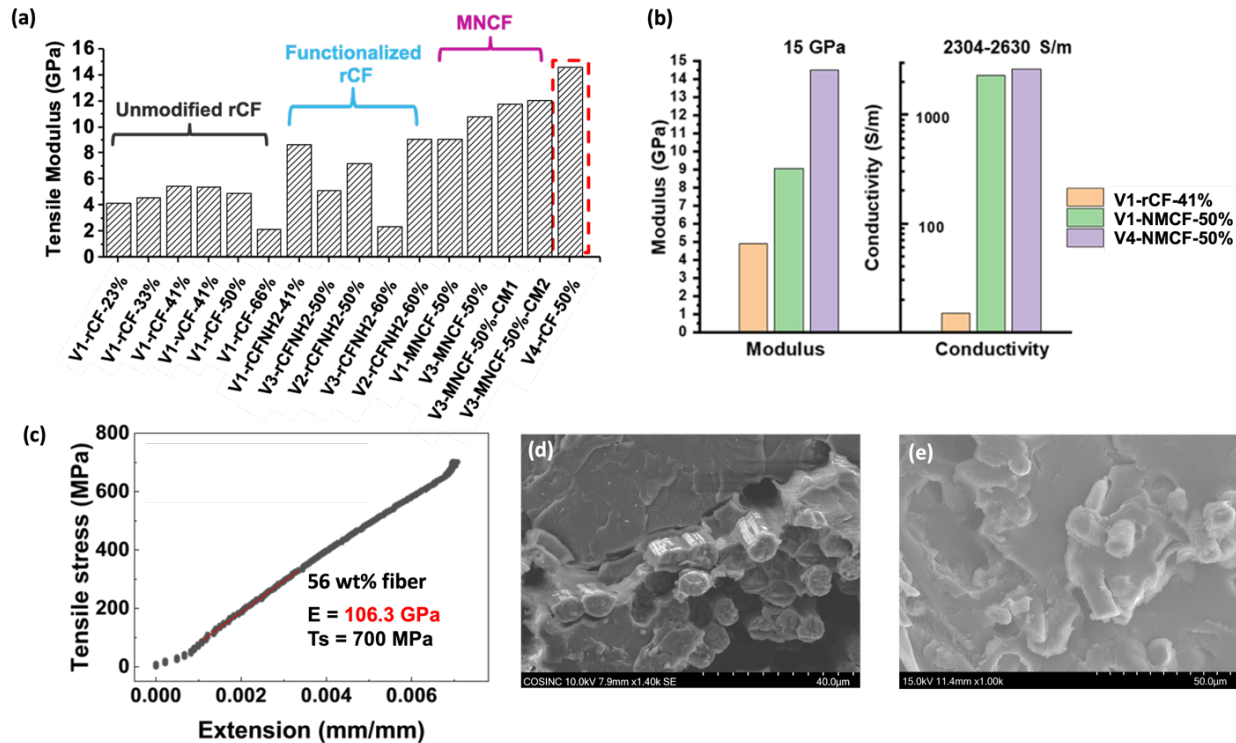


Figure II.3.2.3.3. (a) Comparison graph of tensile properties of various composites consisting of rCF. (b) Comparison graph tensile modulus and conductivity of composites made of rCF and NMCF. (c) Tensile stress-strain curve of CFRP consisting of V4 and unidirectional CFs. (d) SEM image of the CFRP consisting of V4 and woven CFs. (e) SEM image of NMVC-R². Source: RockyTech Ltd.

The unique advantage of a vitrimer matrix is the ability of particle deformation and interfacial healing, enabled by dynamic bond exchange reactions between polymer chains [3], [4]. Such dynamic bonding-enabled malleability offers the opportunity for multiple reprocessing, lamination, and rapid fabrication of vitrimer-based CFRPs. As an alternative approach, we explored the solid-phase compression molding of a mixture of fine vitrimer particles and NMCFs to form NMVC-R². We obtained composites with a tensile modulus up to 12 GPa and a conductivity of 1490 S/m, which are comparable to the properties of those prepared through the gel-impregnation method. These results clearly support the assumption that our powder-to-film design is a suitable manufacturing method for preparing NMVC-R².

Remaining Challenges

All the vitrimers in our portfolio were synthesized through solution polymerization. This process, however, presented several challenges, particularly in achieving batch-to-batch consistency. These challenges stem from factors like varying heat removal capacities, differences in solvent evaporation rates, and reaction times. Moreover, the degree of homogeneity during the bulk polymerization process also contributed to these inconsistencies. Another critical issue we faced was the complete wetting of fibers and removal of voids. Proper wetting is essential for the vitrimer to adhere effectively to the fibers, ensuring optimal mechanical properties in the resulting composites. Inadequate wetting leads to the formation of voids or air pockets within the material. These voids can significantly weaken the structural integrity of the composites. The SEM images shown in Figure II.3.2.3.3(d, e) of the cross-sections of these composites have revealed the presence of these voids within the matrix. Addressing these challenges is crucial for ensuring the consistency, reliability, and overall effectiveness of these advanced composite materials in their intended applications. The investigation and control of void formation are being actively pursued through an integration of empirical and computational modeling methodologies.

Repairability of NMVC-R² Composite

A significant drawback of traditional thermoset-based CFRPs is their inability to be repaired or reprocessed after curing, leading to substantial materials waste. However, vitrimer-based CFRPs can be modified post-curing due to their ability to undergo interface healing through dynamic bond exchange reactions between polymer chains. By simply applying heat and pressure, minor damages can be repaired. For instance, a damaged surface can be restored by applying a small amount of composite powder, and then heat-pressing the material at 150°C under pressure, as indicated in Figure II.3.2.3.4(a). The repaired sample retains a tensile modulus comparable to that of the original, although there is a noticeable decrease in tensile strength and elongation at break as seen in Figure II.3.2.3.4(b), which suggests that the defect was not fully healed and that the repair efficiency requires further improvement—a topic that is currently being explored to enhance the repair process. The thermally activated malleability of vitrimers also allows NMVC-R² composites to be reprocessed into various shapes repeatedly. As demonstrated in Figure II.3.2.3.4(c), these composites can be reshaped multiple times at high-temperatures with the application of a small force. This flexibility in reshaping shows the potential for the material to be reused and reformed, offering a sustainable alternative to traditional thermoset-based composites.

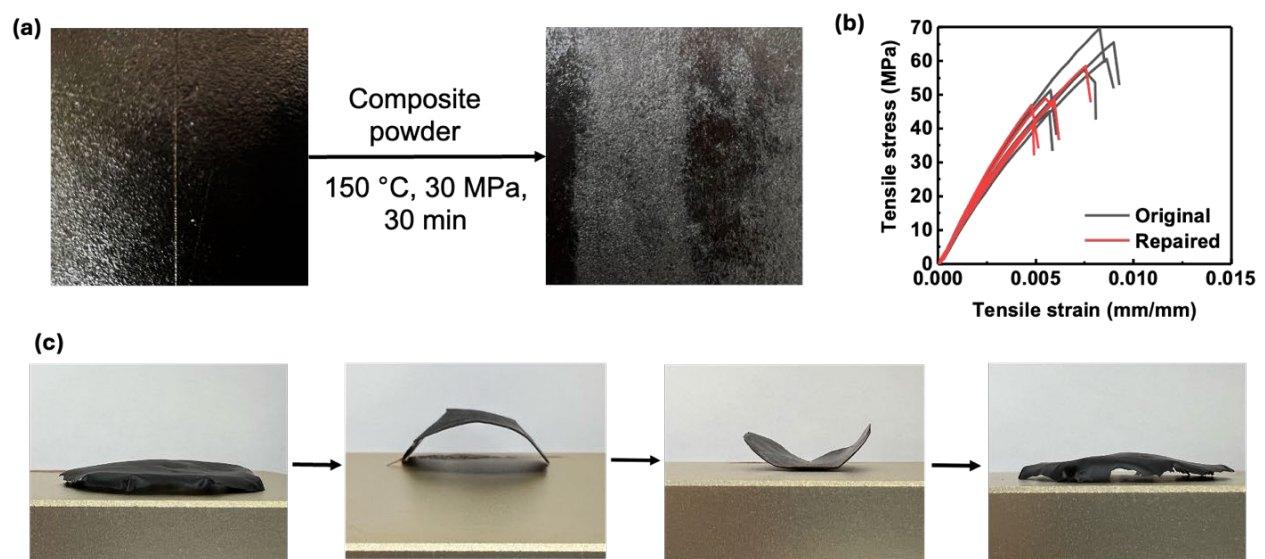


Figure II.3.2.3.4. (a) Repairing of NMVC-R² composite under heat and pressure. (b) Tensile stress-strain curves of repaired NMVC-R² composite in comparison with the original sample. (c) Reshapability of NMVC-R² composite. Source: RockyTech Ltd.

Recyclability of NMVC-R² Composite

The reversibility of dynamic bonds also imparts vitrimers with full degradability and recyclability through depolymerization. When vitrimers are used as a matrix, closed-loop recycling of the composites, including all fillers and chemicals, is possible by converting the vitrimer matrix into soluble oligomers and monomers. Closed-loop recycling of NMVC-R² was achieved through depolymerization of the vitrimer matrix into short soluble oligomers by shifting the equilibrium toward network decomposition. The degradation and solubilization of the vitrimer matrix release NMCFs in their original form, which can directly re-enter the next production cycle after simple drying, as observed in Figure II.3.2.3.5(a). We demonstrated that the first generation recycled NMCFs show a similar grafting density of nanofillers on the surface to that of the original fillers, and by removing all the volatiles from the recycled mixture, we formed second-generation NMVC-R². The first and second generations of the recycled composites exhibit nearly 100% recovery of tensile modulus and strength as indicated by the stress-strain curves in Figure II.3.2.3.5(b). When the NMVC-R² were recycled for the third time, there was a slight decrease in both the tensile strength and the modulus.

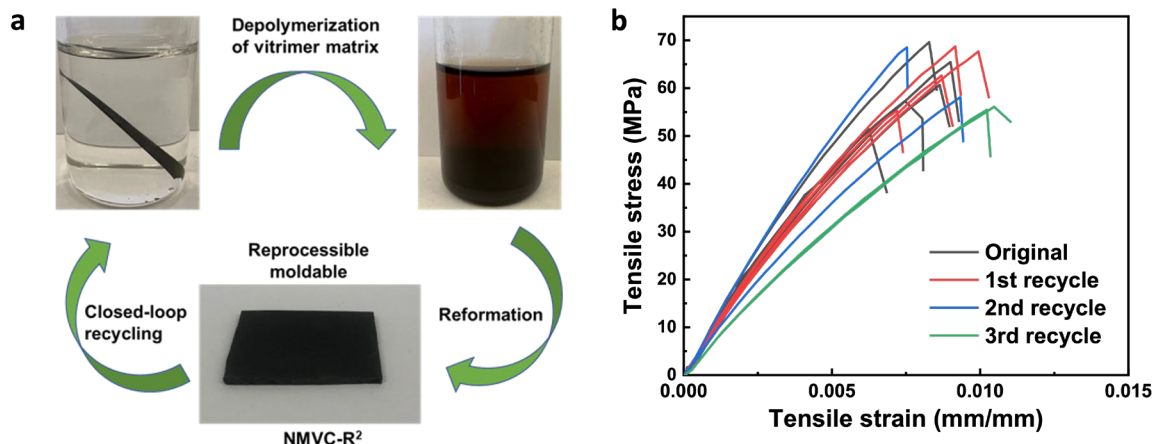


Figure II.3.2.3.5. (a) Closed-loop recycling of NMVC-R² through solution-phase depolymerization and repolymerization. (b) Tensile stress-strain curves of recycled NMVC-R² in comparison with the original sample. Source: RockyTech Ltd.

Conclusions

We have developed a portfolio of vitrimer materials with a wide range of physical properties, including elastomeric, rigid and strong, and flame retardant. By integrating these vitrimers with nanofiller-sized recycled CFs, we have created NMVC-R² composite materials that deliver excellent mechanical properties, EC, and effective electromagnetic interference shielding (e.g., 30 dB, 0.4 mm thickness). Furthermore, these innovative composites are not only capable of being repaired and reshaped, but also feature the capacity for complete recyclability. The use of recycled feedstock, coupled with conscientious end-of-life management practices, markedly enhances both the sustainability and economic viability of these materials.

Key Publications

- Chen, H., Y. Hu, C. Luo, Z. Lei, S. Huang, J. Wu, Y. Jin, K. Yu, and W. Zhang, 2023, "Spiroborate-linked ionic CANs with rapid reprocessability and closed-loop recyclability," *J. Am. Chem. Soc.*, 145(16), 9112–9117. <https://doi.org/10.1021/jacs.3c00774>.
- Jin, Y., Y. Hu, and H. Yu, 2022, "Polyhydroxyurethanes and method of their use," Related provisional application no. 63/322,758; Related nonprovisional application no. 18/100,477.

References

- Jin, Y., Z. Lei, P. Taynton, Huang, S. and Zhang, W. 2019, "Malleable and recyclable thermosets: The next generation of plastics," *Matter*, 1(6), 1456–1493. <https://doi.org/10.1016/j.matt.2019.09.004>.
- Kloxin, C. J., and C. N. Bowman, 2013, "CANs: Smart, reconfigurable, and responsive network systems," *Chem. Soc. Rev.*, 42(6), 7161–7173. <https://doi.org/10.1039/C3CS60046G>.
- Yu, L., Z. Lei, X. Sun, P. Ding, A. Wesche, Y. Jin, W. Zhang, and R. Long, 2021, "Rapid fabrication of fiber-reinforced polyimine composites with reprocessability, repairability, and recyclability," *ACS Appl. Polym. Mater.*, 3(11), 5808–5817. <https://doi.org/10.1021/acsapm.1c01027>.
- Taynton, P., H. Ni, C. Zhu, K. Yu, S. Loob, Y. Jin, H. J. Qi, and W. Zhang, 2016, "Repairable woven carbon fiber composites with full recyclability enabled by malleable polyimine networks," *Adv. Mater.*, 28(15), 2904–2909. <https://doi.org/10.1002/adma.201505245>.

Acknowledgements

The authors would like to thank their collaborators, R. Long and W. Zhang, and their research teams at the University of Colorado–Boulder for their assistance and support throughout the project, as well as the Department of Mechanical Engineering at University of Colorado–Boulder for their general support.

II.3.2.4 Changing the Design Rules of Rubber to Create Lighter Weight, More Fuel-Efficient Tires (Molecular Rebar Design, LLC)

Kurt Swogger, P.E., Principal Investigator

Molecular Rebar Design, LLC
13477 Fitzhugh Rd.
Austin, TX, 78736
E-mail: kswogger@molecularrebar.com

Brandy Greenawalt, , SBIR Central Programs Operations Manager

U.S. Department of Energy SC-29
Small Business Innovation Research
19901 Germantown Rd.
Germantown, MD 20874
E-mail: brandy.greenawalt@science.doe.gov

H. Felix Wu, DOE Technology Development Manager

U.S. Department of Energy
E-mail: Felix.Wu@ee.doe.gov

Start Date: June 28, 2021
Project Funding: \$197,359

End Date: March 27, 2022
DOE share: \$197,359

Non-DOE share: \$0

Project Introduction

EV tire treads are wearing at a rate much faster (30%+) than their ICE counterparts [1]. This is primarily due to the heavier weight of the vehicle, near-instant torque, and urban-oriented driving. Producing a lighter weight, longer-lasting, and more energy-efficient tire will greatly assist in overcoming some of the more adoption-related hurdles for EVs. Longer-lasting tires reduce ownership costs of EVs, while lighter weight tires with more energy-efficient components such as the tread improve miles/kWh or reduce range anxiety. Typically, passenger car tires are produced with tread compounds utilizing a solution styrene-butadiene rubber (SSBR) and butadiene rubber (BR) polymer blend with silica bound by silane. In Phase I (FY 2022) of this work under DOE contract number DE-SC0021823, Molecular Rebar Design, LLC (MRD), demonstrated that SSBR-BR tire tread compounds reinforced with a discrete, silane-coupled multiwall carbon nanotube, called Molecular Rebar® (MR), have drastically improved abrasion resistance and rolling resistance characteristics. The silane-coupled MR was shown to be between 3–10× as reinforcing as the incumbent reinforcing filler of choice, precipitated silica. Optimized tire tread formulations produced in Phase I with the silane-MR demonstrated up to 30% improved abrasion resistance, correlating to about 30% improved tire lifetime, and up to 20% improved rolling resistance, correlating to about 7% improved energy-efficiency, simultaneously.

In Phase II (FY 2023) of this work, MRD developed a commercially viable product form of the functionalized MR material, utilizing a robust carrier agent (e.g., oil, polymer, etc.), focusing on ease of integration for tire manufacturers and consistency of material property improvements—especially the precursor steps of dispersion and bonding capability. The guiding principles of functional MR use in tire tread compounds are established, focusing on understanding the composite property effects as they pertain to the concentration of MR. Then, these “guiding principles” are used to formulate, develop, and test prototype tires that are produced with the silane-coupled MR material. The tire formulation, development, build, and test of prototype tires using the MR-enhanced tires has been subcontracted to The Goodyear Tire and Rubber Company (Goodyear). The testing of these experimental tire prototypes will correlate the laboratory results from Phase I to tire and vehicle effects in Phase II.

Objectives

The Phase II project is divided into four objectives that will culminate in the production of an improved polymer tread composite that improves both the lifetime and energy-efficiency of tires for EVs: at least 25% increased tire lifetime, ~3% lighter weight tires, and ~10% improved tire rolling resistance, giving the test electric vehicle ~7% better energy-efficiency—all of which improve EV sustainability:

- Objective #1: Develop a commercially viable prototype product form: Use a robust carrier agent, minimize barriers to use through intelligent product design, and maintain consistency of material property improvements.
- Objective #2: Develop “guiding principles” of use: Determine optimum concentrations of functional MR, determine corresponding decreases of existing filler content, and determine that relationship (e.g., linear, parabolic, asymptotic). This will further reduce barriers to entry in the marketplace by ‘teaching’ future customers how to utilize the product, including the subcontracted tire company in Phase II.
- Objective #3: Jointly formulate, develop, and test prototype tires with Goodyear, a subcontractor for this project. Correlate laboratory-scale material properties effects to tire effects, and then to EV effects.
- Objective #4: Produce appropriate documentation of the above goals for dissemination to the public and future customers. Accurately report all results in typical scientific discourse—publication, presentation, etc., including to the DOE SBIR program. Technical materials will be produced for the “guiding principles” of use, while marketing material will be produced for the outcome of the tire trial for use with future customers or downstream users of improved EV tires.

Objectives #1 and #2 were accomplished during this FY 2023 reporting period, with Objective #3 in progress at the time of this report.

Approach

The MRD team uses its expertise in business development, polymer science, chemical and mechanical engineering, and previous experience in scaling-up dispersions of carbon nanotubes (CNTs) in various media to design experiments, produce prototype materials in increasing quantities, and limit risks involved with subcontracted work during this Phase II project. In Objectives #1 and #2, the primary focus is on product design and use-case definitions, heavily utilizing polymer science and chemistry expertise. A portion of these initial objectives is devoted to scaling-up the silane-MR product to deliver tens of kgs scale material to Goodyear to complete Objectives #3 and #4, utilizing MRD’s engineering experience. Throughout this work, MRD seeks to insure that commercialization hurdles are reduced by involving potential future customers and industry partners in long-term scale-up plans, integrating silane-MR into the polymer-tire supply-chain, and evaluating the experimental material on a pathway to commercialization in tires. Examples of these commercial partners include Arlanxeo, Goodyear, Swan Chemical, and Bridgestone—all of whom had also originally expressed interest in this project through letters of support during the Phase II application process.

Results

During work on Objective #1, MRD project staff have determined that the optimal carrier agent for delivering functionalized CNTs into the EV tire tread compound is the synthetic polymer itself, with the resultant “masterbatch” being roughly 20 wt.% CNTs. The process utilizes a solvent-borne CNT product that incorporates into the existing polymer production process. This was determined after testing multiple different carrier agent compositions, including oil, silane itself, and different production methods, polymer types, and CNT loadings within the polymer carrier agent, resulting in 25+ different material compositions/formulations. Tests were conducted in the wet laboratory setting, before the resultant materials were tested using typical small-scale rubber compounding techniques in the Haake Rheomix, followed by typical polymer composite testing- tensile properties, hysteric properties, TEM imaging, etc. The superb dispersion of this MR-silane from synthetic polymer masterbatch was verified by TEM imaging is shown in Figure II.3.2.4.1.

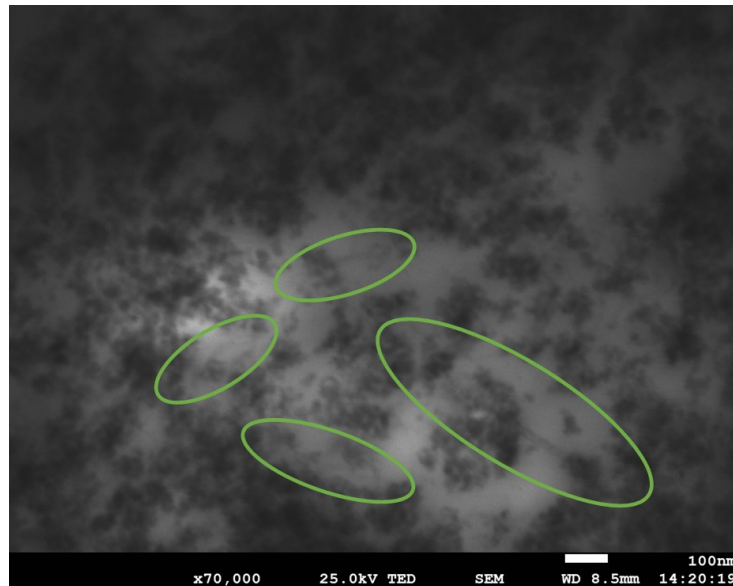


Figure II.3.2.4.1. TEM image demonstrating a good dispersion of silane-functionalized multiwall CNTs in a SSBR-BR-silica-silane EV tread compound. CNTs circled in green. Source: MRD.

The polymer masterbatch product form from the above activity was then scaled-up to the hundreds-of-grams scale in MRD's laboratory, resulting in enough material to test using the 1.6L Banbury mixer, a much more representative polymer composite compounding technique for tire tread manufacture. The efficacy of the functional CNTs delivered via this product form was demonstrated to be very good, with results exceeding the original results demonstrated in Phase I. Results with the polymer masterbatch functional CNT show improvements of 22–43% in rolling resistance (e.g., fuel-efficiency/energy-efficiency) and 13–25% in lifetime Deutsches Institut für Normung (DIN) abrasion standard—better than the rolling resistance results of Phase I, which ranged from 0–20%, but slightly worse than the Phase I results on lifetime, which ranged from a 25–37% improvement. MRD's laboratory experimentation confirmed that the polymer masterbatch product form described above can be produced at the commercial-scale. The manufacturing process can be broken down into the following four unit operations, described below and shown in more detail in Figure II.3.2.4.2:

1. Physically and thermally dewatering the functionalized MR—performed now and in the future at MRD.
2. Incorporating MR into hexane or another solvent so that dispersion quality is sufficient—performed now at MRD, but potentially performed at scale in the future at the polymer manufacturer's site.
3. Mixing the MR-solvent fluid with a typical midstream polymer-solvent mixture—performed now at MRD and in the future at the polymer manufacturer's site.
4. Dewatering the MR-polymer-solvent mixture, which is typically steam-stripped to remove the solvent and then put through a heated-extrusion process. This is simulated at MRD via a hot water bath and internal compounding. This will be performed at the polymer manufacturer's site during scale-up.

In Objective #2, six iterations of compounds utilizing the silane-MR compound were produced and tested for their materials properties. Resultant conclusions and guidelines for their use are described below:

1. Using silane-MR at a replacement ratio of 0.28:1 silane:MR to silica at low silica loadings (e.g., high-silane-MR loadings), on a sliding scale down to 0.17:1 silane:MR to silica at higher silica loadings results in a matched Shore A hardness compound, which is a primary parameter for tire tread compounds.
2. To maintain modulus, with a lower Shore A hardness, a replacement ratio of 1:3 silane-MR to silica should be used at low silica reductions, ramping to a replacement ratio of 1:10 silane-MR:silica at higher

reductions of silica removal, with MRD testing up to a ratio of 3MR:30Si, which resulted in a matched 200% modulus, another primary parameter for tire tread compounds.

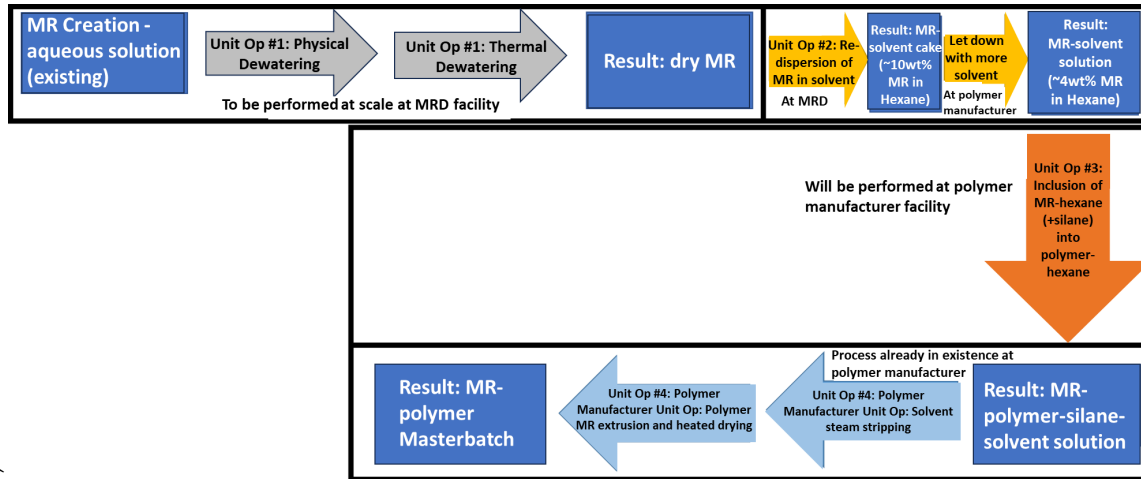


Figure II.3.2.4.2. A simplified block flow diagram showing the primary four unit operations to create a polymer “masterbatch” of silane-functionalized MR, with sub-operations also identified. Source: MRD.

Both of the above guidelines relate to a similar phenomenon, in that with higher loadings of silane-MR, the silane-MR results in an increasing level of stiffness per loading: the +3MR sample is more than three times as stiffening as the +1MR sample. This phenomenon is not currently well understood, but it is hypothesized that the silane-MR is ‘networking’ at higher loadings, exponentially increasing stiffness with increasing loadings. The use of silane-MR does not affect the onset of cure, which is a primary processing and tire building parameter. However, the use of silane-MR does slightly lengthen cure time per loading when silica is not removed. Interestingly, when silica is removed and silane-MR is added, the cure time is substantially shortened. These property shifts are important to communicate to tire manufacturers, which allows for cure package adjustments to meet tire build and molding timeline requirements.

Through the experimentation in Objective #2, material property benefits of silane-MR from a BR masterbatch in optimized tire tread composite formulas created using the guidelines above, are shown in Figure II.3.2.4.3. One optimized formula is the same as was created in Phase I, allowing comparison between a bench top non-scalable product form in Phase I and the prototype masterbatch product form going to tire trial in Phase II.

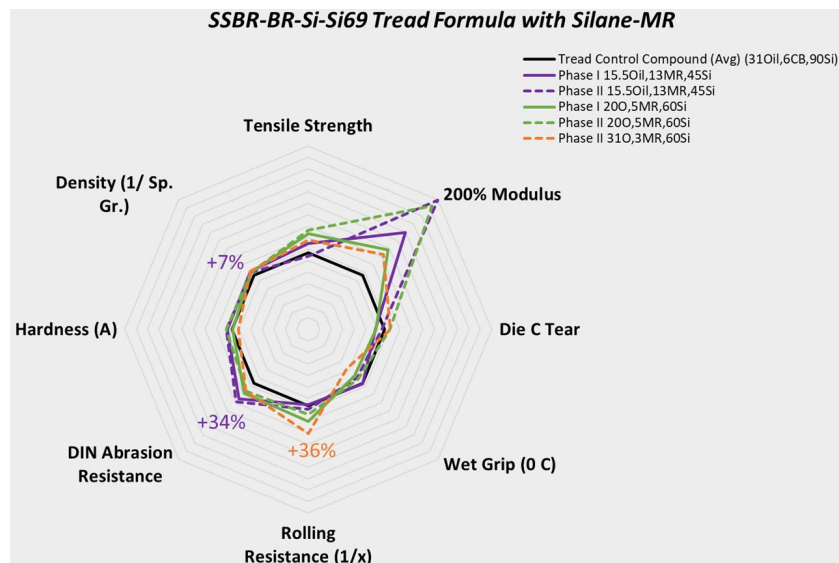


Figure II.3.2.4.3. Spider graph demonstrating materials property changes to an EV tire tread compound with silane-MR from the masterbatch product form. Source: MRD.

The Phase II results using the prototype masterbatch product closely align with the Phase I results excepting the modulus increase, maintaining all expected improvements in lifetime, rolling resistance, and density (e.g., lightweighting). Modulus is typically an indicator of reinforcement, so having a significantly higher modulus as compared to the Phase I results is beneficial and may be an indicator of a strong networking effect. The three formulas shown above using the EV tread model compound demonstrate three strategies for tread improvement: 15.5Oil,13MR,45Si solely improves abrasion resistance (lifetime) by 34%, while 200,5MR,60Si simultaneously improves both abrasion resistance by 15% and rolling resistance (e.g., energy-efficiency) by 11%, and 310,3MR,60Si drastically improves rolling resistance by 36% with an improvement in abrasion resistance of 15%, but a more detrimental effect on wet grip of -28%. These three strategies for improvement give future tire manufacturing customers a variety of ways to optimize a tire tread compound that is lighter weight and demonstrates the versatility of the silane-coupled MR masterbatch product.

In Objective #3, the production scale of the prototype silane-MR masterbatch was again increased up to tens of kilograms per batch. This represents a 1,000-fold increase over the original benchtop production scale of tens of grams at the beginning of Phase II. To produce barrel-scale quantities of the silane-MR masterbatch for experimentation and test tire build with Goodyear, a polymer precipitation unit was built by the engineering team at the MRD facilities in Austin, TX. Figure II.3.2.4.4 shows the design of the polymer precipitation system in use, which has produced over 100 kg of 20 wt.% silane-MR masterbatch to date.

Sub-contractual work with Goodyear is progressing as expected. Two of the expected three laboratory experiments modifying an in use EV tire tread compound have been completed, with the third scheduled prior to the end of calendar year 2023. MRD has produced the silane-MR masterbatch being utilized in experimentation using midstream proprietary Goodyear Chemical BR and Si266, a bis (triethoxysilylpropyl) disulfide organosilane from Evonik. The experimental compounds utilize a 1:3 replacement ratio of MR:silica, which is in line with MRD's findings in Objective #2. Both studies completed thus far have demonstrated the compound property benefits that are in line with the benefits MRD has demonstrated in this report. Further compound modifications at Goodyear also have demonstrated that wet grip could be maintained, while still improving sought-after tread compound properties. The iterative nature of this experimentation is intended to result in a compound that is optimized for use in EV tire treads, which will then be used to produce prototype tires for testing in the first quarter of 2024. Formulations and results from this portion of the work are generalized so as to protect intellectual property. The resultant experimental tire will be compared to an in use EV tire that is currently available for sale. By using an in use tire as a comparative test specimen, and by

producing a commercially viable tire tread compound with the silane-MR in this Phase II work, MRD is reducing barriers to commercialization and adoption of this silane-MR masterbatch product into the EV tire market.

In addition to reducing barriers to commercialization, MRD has identified another driving force for MR adoption in discussions with commercial partners. Particles given off during the wear process of tires are increasingly gaining attention as sources of micro-plastic pollution and potential environmental bad actors [2]. Improving tire tread lifetime, as will be demonstrated in Phase II, reduces the absolute quantity of micro-plastic generated per mile driven. MRD also has found that particle size distribution of tire wear particles is increased with MR-reinforcing effects—dramatically reducing exposure to ultra-fine particles generated during tire wear. This phenomenon needs further study. MRD hopes to measure MR impacts on tire wear particles during the prototype tire test. The combination of improved lifetime, reduced tire wear particles, better energy-efficiency, and lighter weight tires is a unique value proposition that the tire industry is keen to evaluate.

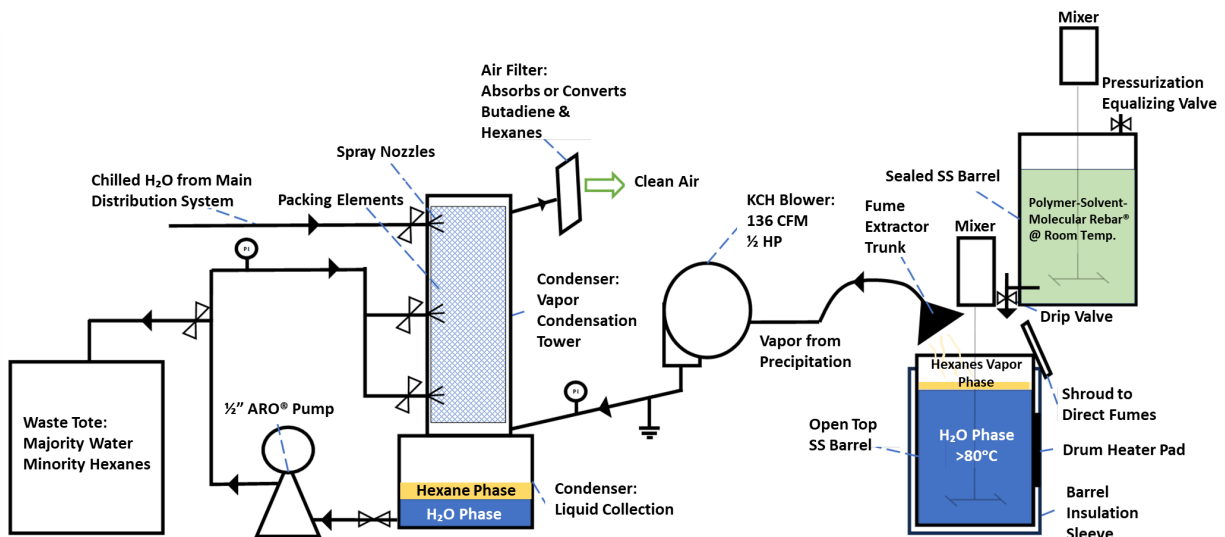


Figure II.3.2.4.4. A simplified piping and instrumentation diagram of the barrel-scale production system in use at MRD to produce silane-MR masterbatch for Objective #3 activities. Source: MRD.

Conclusions

MRD has developed a prototype product form of the silane-coupled MR nanotubes that can be manufactured at scale and used to change the paradigm of wear, grip, and rolling resistance for EV and other tire compounds. The development of guidelines for use in this work enables production of optimized tread compounds, which showcase the versatility of the benefits of silane-MR—lighter weight, longer-lasting, and more fuel-efficient tire treads, tires, and EVs. Goodyear has validated MRD’s results, and further adjusted and optimized the EV tread formulations to meet the prototype test tire design goals. Continuing work with Goodyear in Phase II will result in the development, build, and test of prototype tires on EVs, correlating the laboratory results with the field results.

Key Publications

1. Krupp, A., 2023, “Molecular Rebar[®]: Carbon nanotubes for more sustainable tires,” *Traction Summit 2023 (Tire Industry Conference)*, 23–24 May 2023, San Antonio, TX, USA.
2. Swogger, K., 2023, “Creating new tire tread compounds that can pay for the tires over the life of an EV,” *The Advanced Materials Show USA (Nanotechnology Industry Conference)*, 2–3 October 2023, Columbus, OH, USA.

References

1. Lambert, F., 2018, “Goodyear unveils new tire for electric cars to reduce wear from powerful instant torque.” *Electrek*, 8 March 2018. Available at: <https://electrek.co/2018/03/08/goodyear-tire-electric-cars-reduce-wear-instant-torque/> (last accessed 2 January 2024).
2. Gao, Z., J. V. Cizdziel, K. Wontor, C. Clisham, K. Focia, J. Rausch, and D. Jaramillo-Vogel, 2022, “On airborne tire wear particles along roads with different traffic characteristics using passive sampling and optical microscopy, single-particle SEM/EDX, and μ -ATR-FTIR analyses,” *Front. Environ. Sci.*, 10, 25 October 2022. <https://doi.org/10.3389/fenvs.2022.1022697>.

Acknowledgements

The authors acknowledge the contributions of A. Krupp (akrupp@molecularrebar.com), the Director of Rubber Development for MRD.

II.3.2.5 Green Composites for Future Vehicles, Vitrimer Matrix + Natural and Recycled Fiber Composite Materials for High Performance, Repairable, Recyclable, and Bio-Sourced Automotive Components (Mallinda, Inc.)

Philip Taynton, Principal Investigator

Mallinda, Inc.
720 Gilpin Way, Ste. #180
Denver, CO 80229
E-mail: philip@mallinda.com

Steve Nutt, Co-Principal Investigator

University of Southern California
3651 Watt Way, VHE-604
Los Angeles, CA 90089
E-mail: nutt@usc.edu

Brandy Greenawalt, , SBIR Central Programs Operations Manager

U.S. Department of Energy SC-29
Small Business Innovation Research
19901 Germantown Rd.
Germantown, MD 20874
E-mail: brandy.greenawalt@science.doe.gov

H. Felix Wu, DOE Technology Development Manager

U.S. Department of Energy
E-mail: Felix.Wu@ee.doe.gov

Start Date: August 22, 2022

End Date: April 14, 2023

Project Funding: \$194,000

DOE share: \$194,000

Non-DOE share: \$0

Project Introduction

The primary goal of this project was to demonstrate the compatibility, sustainability, and economic benefits of introducing high-performance natural fiber composites that use a vitrimer matrix. The Small Business Innovation Research Phase I work entailed recyclable resin, recycled fiber, and high-performance natural fiber composites to illustrate the immense potential for high-throughput manufacturability, and thus, has the ability to disrupt current barriers to adoption for advanced composite materials in automotive. The purpose was not only to evaluate a novel combination of recyclable materials, but also to do so in the context of industrially relevant processes, revealing pragmatic insights.

Objectives

The primary objectives of this study were to develop vitrimer matrix natural fiber composite bulk materials by two methods: prepreg and resin infusion. The analysis entailed evaluating mechanical behavior, such as the specific strength and stiffness of the bulk composite material (compared with currently-used materials), and the recyclability and re-use of the composite parts made. The impact of vitrimer chemical recycling would result in recyclable composites, while the natural fiber/vitrimer composites would reduce manufacturing energy. Combining these two benefits would allow an energy- and cost-effective alternative to composites that is also sustainable and closed-loop. The teams involved were quite confident in the strength of flax and vitrimers due to an external study that compared the interfacial shear strength of traditional epoxy with flax and vitrimer with flax. As shown in Figure II.3.2.5.1, imine-linked vitrimer resins exhibit a natural affinity and superior adhesion to commercially available flax fibers. In terms of recycling, the Mallinda team developed a custom process for the dissolution of resin while maintaining the geometry of recovered fibers with minimal disturbance to the fiber orientation in order to remanufacture panels of similar dimensions. Moreover, the scanning electron microscope images in Figure II.3.2.5.2 shows the exceptional quality of recycled parts using Mallinda's

recycling process. Recycled fibers recovered from Mallinda's proprietary vitrimer depolymerization process exhibit pristine surfaces with no resin residue. These two findings led to the study of the compatibility of recycled Vitrimax/flax composites.

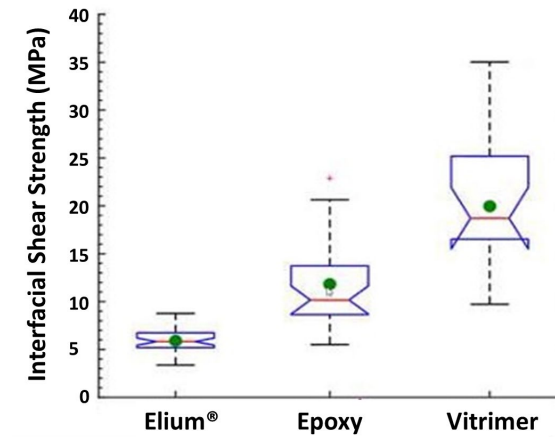


Figure II.3.2.5.1. Interfacial shear strength of various resins with flax fiber. A statistically significant number of replicates ($N > 30$) were used for this analysis. Source: [1].

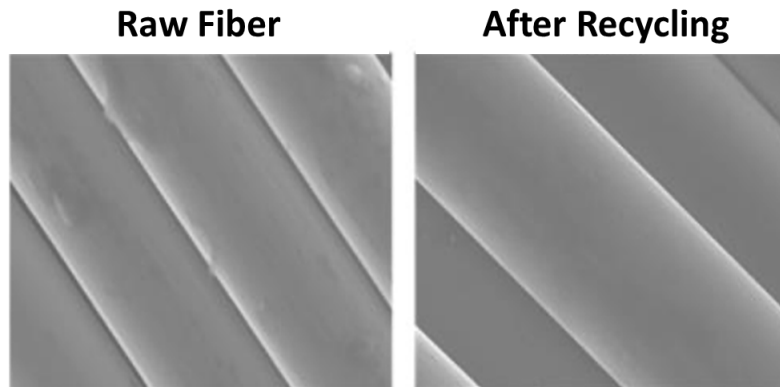


Figure II.3.2.5.2. Scanning electron microscope image of virgin and recovered CF from Mallinda's vitrimer solvolysis recycling process. EDS analysis confirmed no molecular resin residue on the fiber surface. Source: Mallinda, Inc.

Approach

Two approaches were implemented to achieve recyclable green composite materials, as well as to reduce manufacturing energy. These approaches entailed prepregging and infusion processes, and the recycling and reusing of materials. They also involved vitrimer-based recyclable materials, as well as the use of natural fiber (flax) with vitrimers. Implementing flax with Vitrimax illustrates a straightforward path for closing the loop with green recyclable materials within composites. The ability to not only re-use the fiber after going through a recycling process, but also reprocessing the resin itself and finally infusing it back into the original fiber, indicates a closed-loop circular and sustainable manufacturing process.

The Mallinda team took responsibility for the prepreg manufacturing and analysis while the University of Southern California (USC) team evaluated the infusion approach. For the prepreg, a roll of T130 Vitrimax resin film was made, which was then infused with individual layers of unidirectional flax, sourced from Bcomp, with the suggested resin content. The plies were oven-cured at 150°C for 1 hour and 180°C for 1 hour and finally compressed into a panel at 200 psi for 5 min at 160°C. The panel had a thickness of ~3 mm to fit the American Society for Testing and Materials (ASTM) standards for testing. The mechanical tests that were

carried out included ASTM D790 and D2344, flexural strength and short beam shear, which also allowed for modulus calculations. These manufacturing steps and mechanical analysis were repeated to create two more panels that were then recycled with Mallinda's recycling solution. One of these panels was re-infused with fresh resin, while the other was re-infused with its original resin that was balanced and reprocessed. For the reinfusion of fresh fiber into flax, a fresh resin film was made. The reinfusion of recycled resin into recycled flax was completed through a solvent dip approach to allow for balancing and reprocessing the resin. For direct mechanical comparison, the same analysis that was carried out on the first panel was completed on the recycled materials.

For the infusion aspect of this study, Mallinda formulated a lower viscosity resin that would be more suitable for USC's mini resin transfer mold (RTM) process setup, as shown in Figure II.3.2.5.3. Tests for resin characterization included thermogravimetric analysis, differential scanning calorimetry (DSC) (cure kinetics), and rheology. Two different fabrics were used, a natural flax fabric and a synthetic glass fabric, with both fabrics consisting of a 2 x 2 twill weave having an areal weight of 200 g/m². Similarly, two different resins were used, Mallinda's RTM T130 Vitrimax and Hexcell's RTM-6, which is an industry standard RTM epoxy resin. Preforms were produced from dry fabric by spraying a temporary adhesive on the material, and then pressing plies together under a press until a thickness of approximately 3.125 mm was achieved, which was an average of 12 plies of flax and 23 plies of glass fabric. Resin infusion was completed under 50 psi, following the temperature cycle recommended by the manufacturers. The infusion was done in a custom-built test cell developed by the M.C. Gill composite center. Once demolded, laminates were cut and then tested under ASTM standards D3039 and D2344, for tensile and short beam shear, respectively. Figure II.3.2.5.4(a) shows the RTM cell and Figure II.3.2.5.4(b) gives the analytics during infusion and cure.

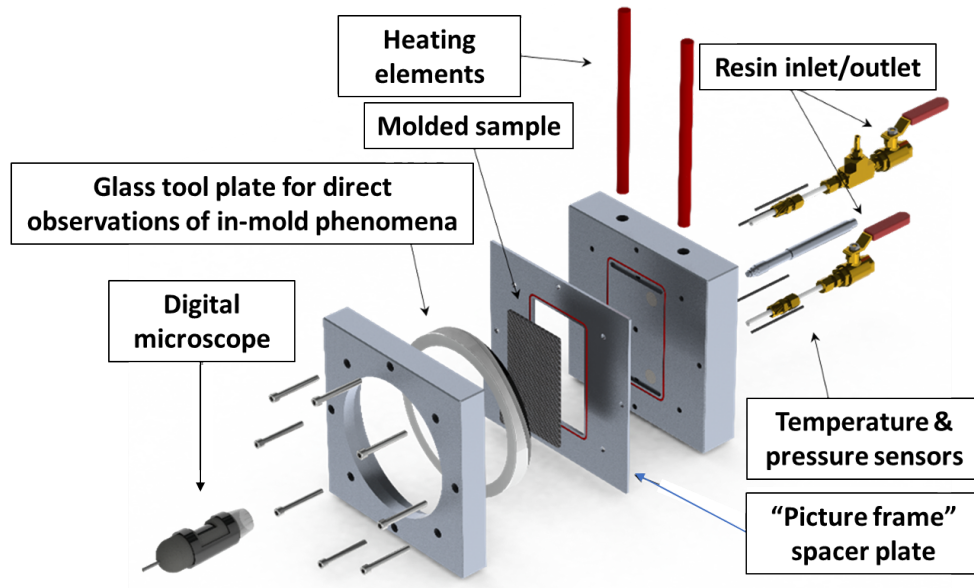
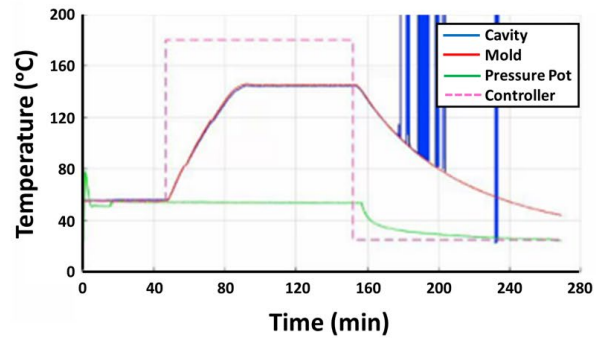
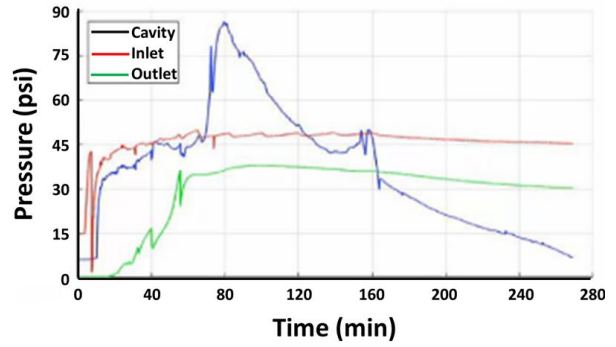


Figure II.3.2.5.3. Mini-RTM set-up at USC. Source: USC

Fabric: Glass 2X2 twill
Number of plies: 23
Inlet opened at 3 min
Outlet closed at 31 min
Resin mixing started 17 min before start of test



(a)



(b)

Figure II.3.2.5.4. RTM cell and analytics during infusion and cure process. Source: USC.

Characterization is required to understand how the lower viscosity Vitrimax behaves at its glass transition temperature, how its viscosity changes over time, and how temperature affects viscosity to accurately predict how the resin will flow when infusing and curing Vitrimax in USC’s RTM system. Figure II.3.2.5.5 provides the DSC results.

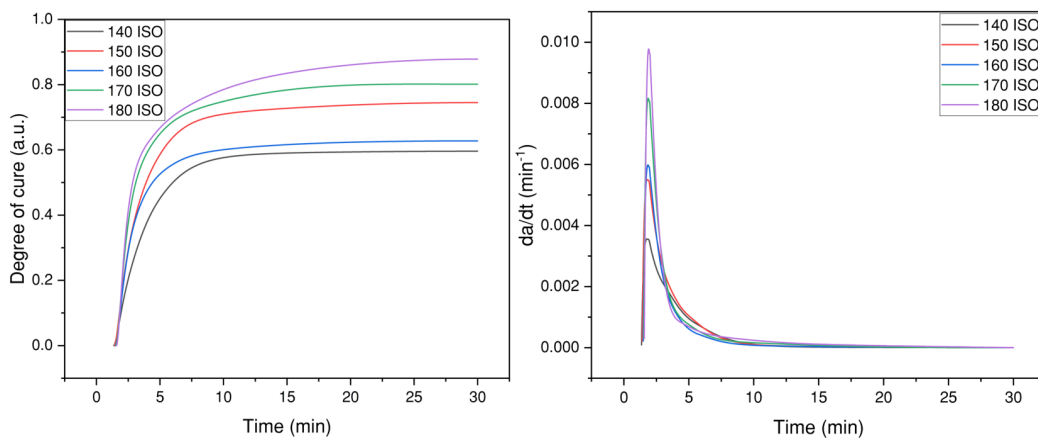


Figure II.3.2.5.5. DSC results with lower viscosity Vitrimax to characterize the resin. Source: USC.

Results

The observations and mechanical results from analyzing the prepreg composites were quite promising. As shown in Table II.3.2.5.1, the flax and glass prepreg made with Vitrimax T130 had very similar results in flexural strength and short beam shear, while the flax outperformed the glass in the flexural modulus. In addition, the recycled flax with Vitrimax T130 had the highest strength across the board. Aside from the recycling of the fiber, the main difference here is that the resin content was around 37%, while the original panels were at 50%. The higher resin content was used under the advice of the flax manufacturer, but with Vitrimax, a lower resin content provided a significant increase in flexural strength. Figure II.3.2.5.6 shows several images of the Vitrimax/flax recycling process.

Table II.3.2.5.1. Mechanical Analysis of Vitrimax/Flax Fiber and Vitrimax/Glass Fiber Composites

Material	Flexural Strength (MPa)	Flexural Modulus (GPa)	Short Beam Shear Strength (MPa)	Resin Weight (%)
Vitrimax/Flax Fiber Prepreg	296 +/- 4	15.2 +/- 0.6	42 +/- 2	50%
Vitrimax/Glass Fiber Prepreg	292 +/- 55	11.7 +/- 0.7	47 +/- 4	50%
Vitrimax/Recycled Flax Fiber Prepreg	356 +/- 7	18.5 +/- 0.2	44 +/- 1.3	37%
Recycled Vitrimax/Recycled Flax Fiber Prepreg	264 +/- 21	16.2 +/- 0.54	20 +/- 2	31%

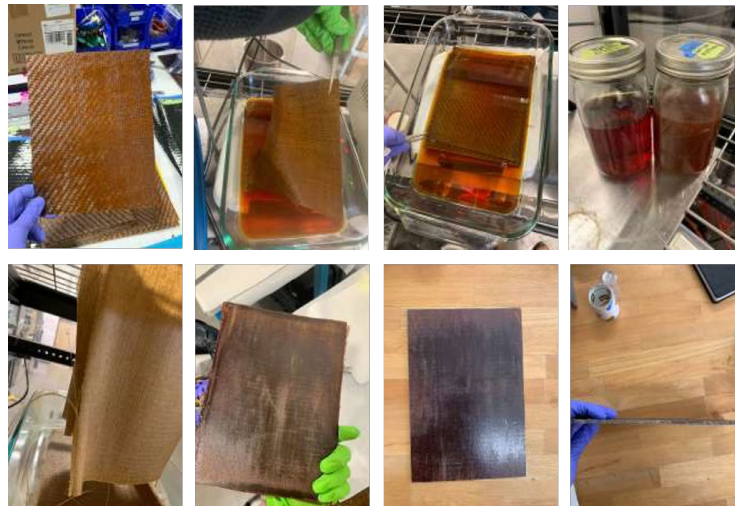


Figure II.3.2.5.6. Images of Vitrimax/flax recycling process. Source: Mallinda, Inc.

Comparing the Vitrimax resin to the standard epoxy, mechanical properties were close, with the RTM-6 laminate exhibiting ~25% higher strength, but ~15% lower modulus in tension, and a flex strength that was approximately 30% lower, as observed in Table II.3.2.5.2. However, comparing the flax to the glass fabric showed the glass-vitrimex laminate exhibited a tensile strength that was at least three times that of the flax-vitrimex laminate, with a tensile modulus that was nearly twice as high; with the flex moduli being similar. The glass laminate had a density that was approximately 35% higher, resulting in the tensile modulus-to-weight ratio being approximately equal for laminates with both fabrics, even if the glass-vitrimex laminate still had a strength-to-weight ratio that was approximately twice that of the flax. Finally, a part was produced using flax fabric recovered from a recycled part. Comparing the recycled flax-vitrimex laminate to the one made with fresh flax, the tensile strength was approximately equal, while the tensile modulus was roughly 14% lower.

Figure II.3.2.5.7 shows the rheology analysis of RTM-6, while Figure II.3.2.5.8 shows the rheology analysis of Vitrimax T130 RTM. Figure II.3.2.5.9 provides a bar chart showing the tensile strength and flex strength of various Vitrimax/RTM-6/flax/recycled flax/glass combinations. Table II.3.2.5.3 shows the short-beam-shear and three-point-bend mechanical data of the Vitrimax T130 RTM compared with the RTM-6. Figure II.3.2.5.10 shows 500 μm and 1000 μm image scans of the Vitrimax/flax prepared with an RTM infusion.

Table II.3.2.5.2. Comparison of the Mechanical Properties of the Vitrimax Resin to the Standard Epoxy

ID	Process	Fabric	Resin	Number of Plies	Thickness (mm)	V_f (%)	Elastic Modulus (GPa)	Tensile Strength (MPa)
FVC	Compression	Flax	Vitrimax	11	4.32±0.10	37±3	11.5±0.3	104.5±2.3
FV	RTM	Flax	Vitrimax	13	3.35±0.05	59±4	16.3±0.5	102.7±3.4
GV	RTM	Grass	Vitrimax	23	3.58±0.04	46±2	22.3	331.0
FE	RTM	Flax	RTM-6	12	3.18±0.04	52±3	13.9±0.5	130.5±8.2
RFV	RTM	Recycled Flax	Vitrimax	12	3.19±0.04	49±2	14.1±0.5	105.4±12.3

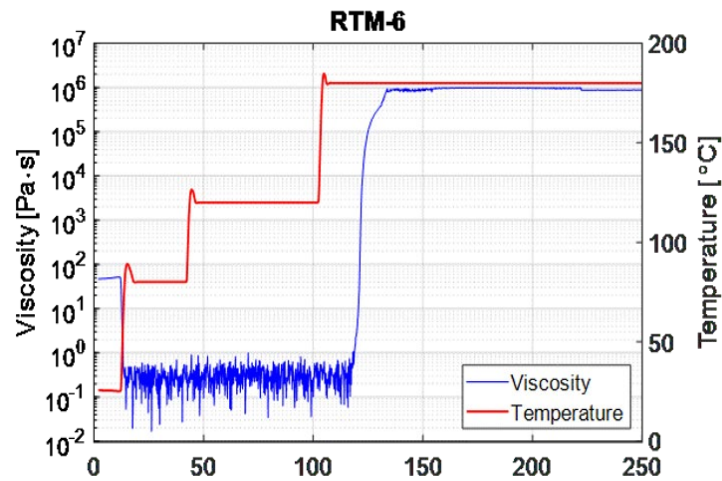


Figure II.3.2.5.7. Rheology analysis of RTM-6. Source: USC.

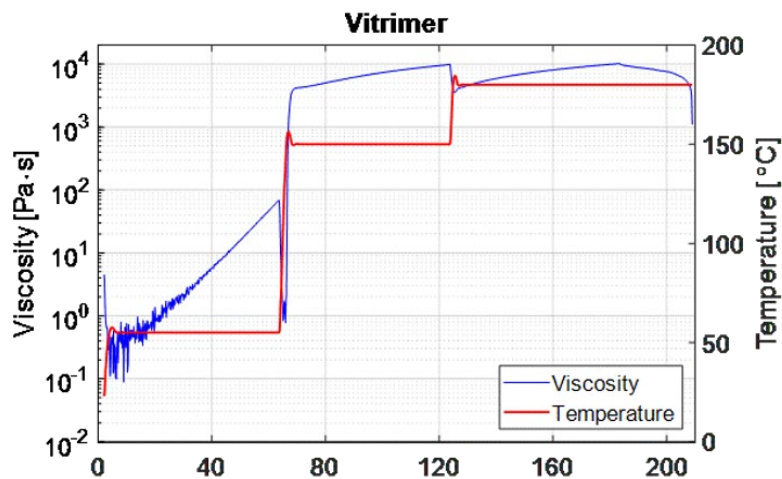


Figure II.3.2.5.8. Rheology analysis of Vitrimax T130 RTM. Source: USC.

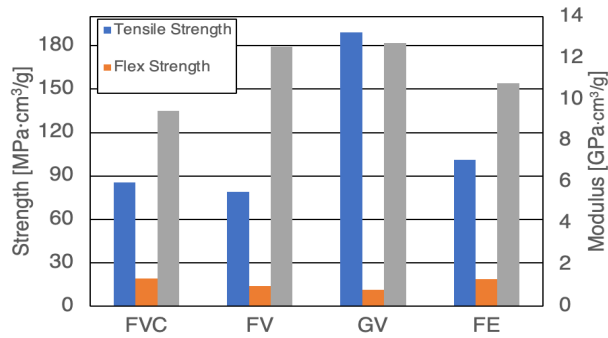


Figure II.3.2.5.9. Graphical representation of tensile strength and flex strength of various combinations of Vitrimax/RTM-6/flax/recycled flax/glass with corresponding data table. Source: USC.

Table II.3.2.5.3. Short Beam Shear and Three Point Bend Mechanical Data Comparing T130 Vitrimax RTM and RTM-6

Sample	Fabric	Resin	Short-Beam Shear (MPa)	Three-Point Bend Flexural Strength (MPa)
F0	Flax	Vitrimax	23.2 ± 2.2	186 ± 18
F1	Flax	Vitrimax	18.5 ± 1.8	148 ± 14
G1	Glass	Vitrimax	19.7 ± 0.8	157 ± 7
F2	Flax	RTM-6	24.1 ± 1.3	193 ± 96

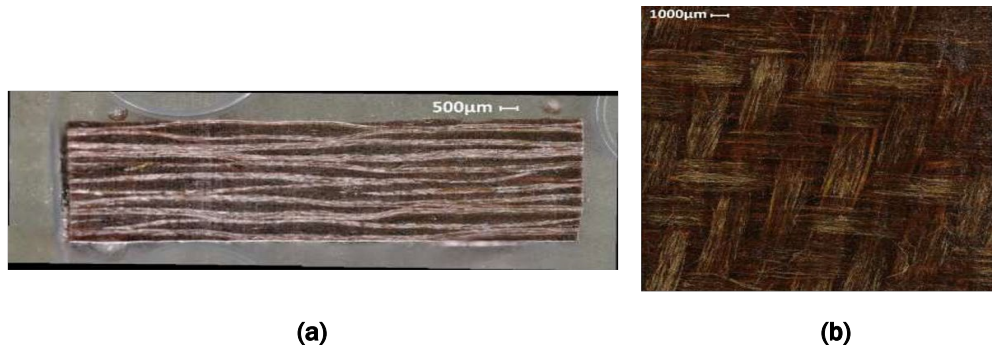


Figure II.3.2.5.10. (a) 500 μm and (b) 1000 μm image scans of Vitrimax/flax prepared with RTM infusion. Source: USC.

Using the adapted Vitrimax resin and the infusion approach developed by the project team, bulk materials were successfully produced in both flax and glass fiber. The resulting materials were characterized mechanically by three-point bending, tensile, and short-beam shear measurements, with the results shown in Table II.3.2.5.4.

Table II.3.2.5.4. Comparison of the Mechanical Properties of the Vitrimax/Flax to Other Materials

Material	Young's Modulus (GPa)	Flexural Modulus (GPa)	Density	Specific Tensile Stiffness	Specific Flexural Stiffness
Steel	215	79.3	7.8	27	10
Aluminum	68	26	2.7	25	9.6
Epoxy/Glass	16	15	1.8	8.9	8.3
Epoxy/Carbon	70	125	1.6	44	78
Vitrimax/Flax	16.3	18.5	1.19	13.7	18.5

Conclusions

Through this study, Mallinda and USC have demonstrated bulk vitrimer matrix natural fiber composite materials with competitive specific strength and stiffness compared with current materials used in automotive structural applications. In addition, practical, low-energy-footprint recycling of these composite materials has been demonstrated with excellent retention of mechanical properties. Prepregging this material with Mallinda's traditional Vitrimax formulation proved to be successful and equal to or surpassing glass in mechanical properties. It also was shown that the RTM process can be used together with vitrimer resins to achieve parts with mechanical properties of leading aerospace-grade epoxies. While, in this instance, glass fabric proved stronger than flax, in weight-focused applications, where the laminate is not intended to be load-bearing, flax-vitrimer composites could provide a sustainable, recyclable material. The vitrimer recycling process leads to minimal damage to the fabric, as shown from the similar mechanical properties between fresh and recycled flax fabric. The next steps in this study would be to further optimize the resin formulation for room temperature infusion so the bulk composites are on par with material prepared by prepreg processing and to analyze the fiber-to-matrix interactions more closely. In addition, more analysis could be done on the integrity of the fiber that is being exposed to high-curing temperatures in case there is some degradation occurring that is affecting mechanical properties.

References

1. Kandemir, A., M. L. Longana, I. Hamerton, and S. J. Eichhorn, 2022, "Developing aligned discontinuous flax fibre composites: Sustainable matrix selection and repair performance of vitrimers," *Compos. B Eng.*, 243, 110139. <https://doi.org/10.1016/j.compositesb.2022.110139>.

II.4 Joining of Dissimilar Materials

II.4.1 Joining Core Program (JCP)

II.4.1.1 Machine Learning for Joint Quality Control (Pacific Northwest National Laboratory and Oak Ridge National Laboratory)

Zhill Feng, Co-Principal Investigator

Oak Ridge National Laboratory
Materials Science and Technology Division
1 Bethel Valley Rd.
Oak Ridge, TN 37830
E-mail: fengz@ornl.gov

Keerti S. Kappagantula, Co-Principal Investigator

Pacific Northwest National Laboratory
Energy Processes and Materials Division
908 Battelle Blvd.
Richland, WA 99352
E-mail: keertisahithi.kappagantula@pnnl.gov

Blair Carlson, Co-Principal Investigator

General Motors, LLC
30500 Mound Rd.
Warren, MI 48090
E-mail: blair.carlson@gm.com

Christopher Schooler, DOE Technology Development Manager

U.S. Department of Energy
E-mail: Christopher.Schooler@ee.doe.gov

Start Date: October 1, 2021
Project Funding: \$1,167,000

End Date: September 30, 2024
DOE share: \$1,167,000

Non-DOE share: \$0

Project Introduction

The use of lightweight material combinations is in high demand in manufacturing automotive structures. However, making robust dissimilar material joints with such materials is challenging. A significant barrier to achieving high-quality and repeatable joint performance is a deficient understanding of the relationship between the welding process, joint attributes, and joint performance. In this context, welding factors refer to material, equipment, environment, and process parameters, while joint features comprise specific attributes such as nugget size, HAZ topology, intermetallic layer thickness, and sheet thickness reduction. Joint performance is quantified in terms of strength (e.g., tensile shear, coach peel, cross-tension), weld size, and hardness, among other factors. While there have been many attempts to establish this process-structure-property relationship by developing a model derived from the associated physics and first-principles, the complexity of the joining processes compounded by the complex interactions with different materials in an automotive assembly line environment, has hindered the usefulness of such attempts. The complexity is further exacerbated using different stacking materials, especially comprising dissimilar material combinations. In practice, the common approach has been the laborious process of creating welds, characterizing them, and then physically testing them through experimentation. But with the emergence of AI methods, an alternative pathway to eliciting the desired process-structure-property relationship at an accelerated pace is to use a data-driven approach using ML techniques.

This approach benefits from the availability of large streams of data, generated through years of research and testing by OEMs, in the form of material, process, environmental, equipment, microstructural, and bulk-scale

performance information from multimodal, multiscale sensors making measurements from laboratory-scale to production-scale processes.

During Phase I efforts, which ended in FY 2021, the ORNL/PNNL team demonstrated the effectiveness of different ML/AI frameworks in modeling complex relationships between RSW process parameters, weld attributes, and joint properties using a subset of data from GM.

In FY 2022, the project team further refined and expanded their respective ML models to analyze additional welds with new weld stack-ups and materials to enhance the ML model predictive capability. ORNL extended its unified DNN ML training and prediction framework with new data streams of process parameters, while PNNL extended its model describing the process parameters of RSW associations with their weld attributes.

In FY 2023, the project team completed the development of the AI/ML architecture for analyzing Al/steel joints manufactured by GM via RSW and transitioned into the inline welding quality monitoring task for steel/steel RSW joints provided by GM.

Objectives

FY 2023 objectives were to develop and apply a ML/AI-based model framework to analyze inline and post-processed joint data from existing and novel sensor streams to achieve automated weld quality monitoring and control. Specific goals include the following:

1. The identification of data streams with the greatest impact on joint performance by developing a data-driven understanding of process/structure/property associations.
2. The translation of ML/AI tools from a test case to parallel configurations/materials/processes using generalized learning methodologies.
3. The application of control programs to maintain process parameters within optimal limits for manufacturing joints with desired performance.

Approach

Project objectives were achieved by demonstrating the application of a suite of ML and AI tools to analyze inline and post-processed joint data for manufacturing assemblies with optimal performance. Al alloy sheet joints manufactured by RSW to different types of steels were evaluated for applications in automotive manufacturing. Data and performance targets assessed were provided by GM, the industry partner of the project.

The large GM dataset covered a wide range of welding data associated with Al- and steel-resistant spot-welded joints comprised of material specifications; welding process parameters, such as voltage, current, pressure, and duration; microstructural features, such as hardness, interface topology, and intermetallic compound; and bulk performance in terms of peak load, elongation, and energy under different loading/mechanical testing conditions (e.g., coach peel, lap-shear, cross-tension tests). Two different ML approaches were explored to establish associations among process parameters, weld attributes, and weld performance. PNNL focused on using explainable, ML-based methods in Approach-I, while ORNL focused on flexible, expandable deep learning methods in Approach-II. This will eventually lead to the construction of a cohesive model from the two different sets of findings from the two national laboratories collated with literature and physics-based model predictions.

Finally, the team predicted the process conditions for making optimized RSW samples per GM's performance metrics using the cohesive set of findings. Both laboratories are transitioning into inline weld quality monitoring tool development by expanding the established ML frameworks with additional data streams of inline signals from GM's new dataset for steel-steel RSWs.

Results

Interpretable ML Models for Process-Structure-Performance Relationships (PNNL)

Local Material Hardness Identification from Weld Structure Data (PNNL)

One of the activities in FY 2023 was to identify the process parameters to optimize the weld quality. Spot weld quality can be measured through several properties such as mechanical strength testing, weld nugget measurements, or microstructural properties (e.g., microhardness). To measure the microstructural properties, welds are placed under a destructive process to obtain the cross-section of a weld. Microhardness was measured using Vickers hardness test in which indentation measurements are made across the weld's cross-section from the steel material to the Al side by GM. Hardness values highly depend on where the indentation was made on the weld. For example, the center region of steel will be harder compared to the outer edges, while Al measurements will be softer than the measurements made on steel. Knowing the coordinate information of the microhardness measurements becomes necessary to study how hardness changes across the weld. Image processing was done on cross-sectional images to automatically locate microhardness measurements and return a data frame with x and y coordinates. Further processing was done once microhardness was detected to classify measurements into either Al or steel material. Coordinates were identified by thresholding cross-sectional images into a black and white scale. A "blob detection algorithm" was applied to detect the hardness measurements. The final output resulted in a data frame with x-y pixel coordinates. The algorithm was applied to 96 cross-sectional images with a total of 5708 microhardness measurements. We achieved a 95% (5425/5708) accuracy and an 87% (5425/6270) precision. Image quality was highly variable, which resulted in detecting false positive measurements.

To classify microhardness measurements into Al/steel material, visual keys were used. The Al material was seen as light gray, while steel was observed as dark gray. A bounding box was created around the center of each microhardness measurement to calculate the median pixel value. The distance was measured from the median value to the distribution of light grays and dark grays. The minimum distance was used to classify each measurement into either Al or steel material. Figure II.4.1.1.1 shows example results from an image: the image at Figure II.4.1.1.1(a) is the identification of hardness sample locations, and the image in Figure II.4.1.1.1(b) is the "classification of hardness" results as either steel or Al. Across the 96 cross-sectional images with 5708 measurements, we achieved a 99% (5675/5708) accuracy. These results are used in several subsequent tasks.

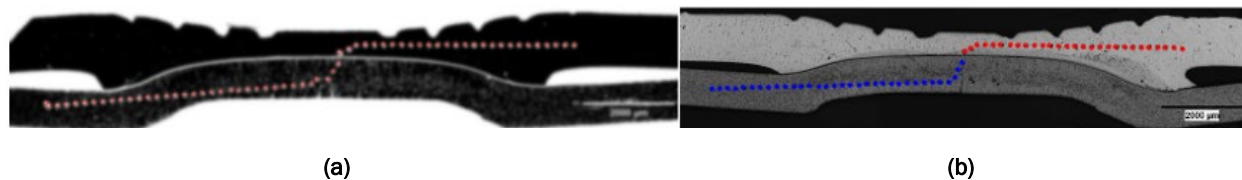


Figure II.4.1.1.1. (a) Microhardness identification and (b) material classification results using the weld structure image and numerical data provided for Al-steel RSW joints. Source: PNNL.

ML with New Derived Variables (PNNL)

The team built upon our FY 2022 analysis by evaluating weld strength, as measured by the five coach peel measures for Al-steel welds, using either AA6022 or X626 Al and low-carbon steel (LCS). The ML model built from FY 2022 was expanded to include previous stack-up and weld process variables, as well as several derived variables that were calculated. ML model predictive performance for each Al type were compared to observe similar patterns. The final result is the group of the most influential process variables, and their combinations, for predicting weld strength for both types of Al-steel joints. We used principal component analysis (PCA) to condense the five welding performance measures into a single response variable, or first-principle component (PC1), using the correlations between them. Subsequently, a random-forest approach was used to model the PC1 as a function of the 75 observed and derived variables. The 10 key variables for quality welds are shown in Figure II.4.1.1.2. Baking condition and clamp load are crucial for welds, but their importance varies (e.g., 48% and 36% for AA6022-LCS vs. 20% and 26% for X626-LCS). Other notable variables for each type differ, with welding machine and adhesive type being paramount for X626-LCS welds.

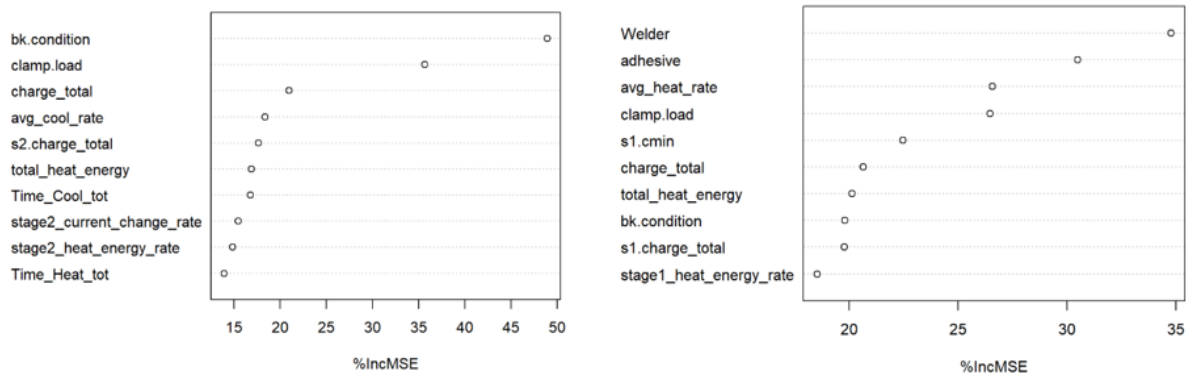


Figure II.4.1.1.2. Important process variables for producing quality AA6022-LCS and X626-LCS welds. Source: PNNL.

Modeling Relationship between HAZ and RSW Weld Schedules (PNNL)

In this activity, we modeled the relationship between the PCA components with HAZ properties using generalized additive models (GAMs) with thin-plate regression splines to identify the relationship between weld performance and HAZ properties, such as hardness and HAZ area, which are obtained by identifying the HAZ from the weld cross-sectional images. To account for the uncertainty in the HAZ property measurements, we included the HAZ measurement “within experiment variability” as predictors in the model.

Figure II.4.1.1.3 shows the partial effects plots obtained by fitting the GAM for PC1 and the second principal component (PC2). Partial effects plots from GAMs fitted for PC1 show a trend that decreases up to mean hardness of 105 HV before increasing. Partial effects plots from GAMs fitted for PC2 yield narrower 95% confidence intervals for both mean hardness and mean HAZ area. Fitted curves for mean hardness decrease up to 105 HV before stabilizing. Fitted curves for mean HAZ area reveal an increasing trend.

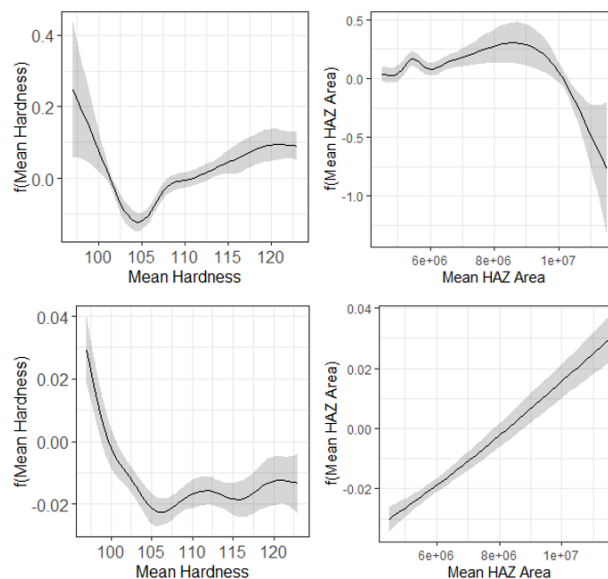


Figure II.4.1.1.3. Partial effects plots with 95% confidence intervals from the GAM fitted for PC1 (top) and PC2 (bottom). Source: PNNL.

Functional PCA to Relate Properties of Weld Regions with Weld Schedule (PNNL)

The goal of this study was to develop a model to describe weld structural attributes, such as hardness curves as a function of space/time, to identify important features and then determine if feature characteristics can be

explained in relation to weld performance and RSW weld schedules. Our approach demonstrates a hybrid functional-ML model for generating proposed process condition ranges associated with optimal welds. Functional principal components were computed for a set of hardness curves from two stack-ups (X626 Al: 82 experiments, 246 curves; 6022 Al: 32 experiments, 96 curves) and rotated with a Varimax rotation to obtain rotated functional principal components (rFPCs). Five rFPCs are used for each stack-up to achieve over 90% cumulative variation explained. Each rFPC corresponds to the variability at a different region of the weld (rFPC1: steel; rFPC2: steel HAZ; rFPC3: nugget; rFPC4: Al HAZ; and rFPC5: Al). The rFPCs are displayed in Figure II.4.1.1.4. Ten random-forest models fit the rFPC observation/curve-specific weight scores according to the process standards as defined as those parameters that result in 10% or higher mean squared error increase when left out of the random-forest model.

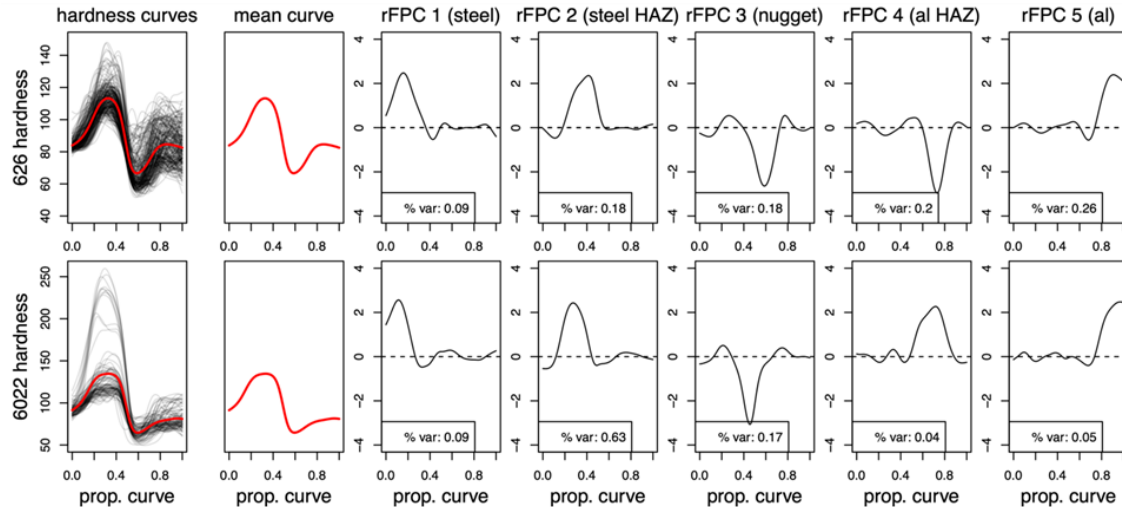


Figure II.4.1.1.4. Hardness curves, mean curves, and five rFPCs for each stack-up. Source: PNNL.

For each rFPC, the 10% highest density region of the scores corresponding to optimal experiments is calculated, and the previously identified important process parameters values that correspond to the observations within the 10% highest density region are collected. The overall mean curve column combines the five rFPC parameter ranges by reducing the suggested values to range from the largest minimum to the smallest maximum, providing a single overall suggested process parameter range. This case study demonstrates a hybrid functional-ML model for generating proposed process condition ranges. These ranges are associated with optimal welds and are presented across the five hardness curve regions.

Ensemble Approach for Process-Structure-Property Relationships (PNNL)

In FY 2023, we developed a framework for joint performance prediction using weld process parameters and engineered features derived from physics. This framework leverages the AutoML capabilities from the Python's PyCaret package and employs a combinatorial feature analysis methodology. The feature significance analysis of trained models demonstrates that engineered features increase prediction performance, and combinatorial feature analysis further improves model performance. We developed a unified framework that uses the capabilities of AutoML (using PyCaret), model fine-tuning, combinatorial feature selection, and ensemble for a performance and weld quality prediction model for the Al/steel RSW stack-ups in this effort. The final ensemble models were used to predict performance metrics of RSW such as mean peak load and mean material indentation, and predict quality metrics like weld size and HAZ size. Figure II.4.1.1.5 shows the information flow for the ensemble model. In some instances, such as describing weld size, we noted that the random-forest model outperformed the ensemble model slightly by demonstrating lower mean absolute percentage error of ~7%, and therefore, an accuracy yielding an of 93%.

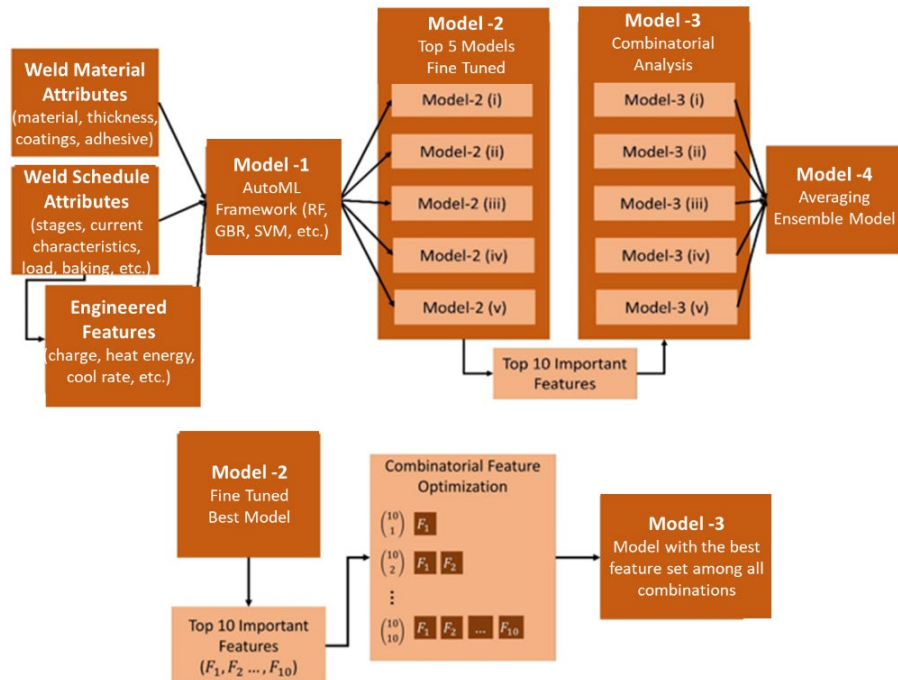


Figure II.4.1.1.5. Information flow for developing the ensemble model. Source: PNNL.

Curating New Dissimilar Steel/Steel RSW Joint Data (PNNL)

As noted earlier, midway through FY 2023, the research focus shifted from examining Al/steel spot welds to steel/steel spot welds of an EV battery enclosure. This shift introduced a new set of data from GM who shared example data to know what to expect for the data transfers, which included .csv, .jpg, and .stl files. Files were first shared through peer-to-peer file sharing, but the team quickly saw the limitation in this method as the number of files and file sizes grew. Data transfer was changed to sharing a PowerBI database so the PNNL team can manage queries and extract the necessary data. To prepare for analysis, the PNNL team studied the various data included in the database, understanding how to interpret each field, communicating questions to GM, and creating a pipeline to go from data ingestion to analysis. Data objects within the lab data set included analysis data: weld-level process parameters and weld performance, graph data (i.e., weld-level time series containing current, force, displacement, heat, energy, and resistance over time), parameter summary used in welding (vspot-id level weld schedule data), material composition data, data dictionary defining variables, and image data (e.g., optical/height [.csv]).

A data pipeline was created to go from data ingestion to analysis. The pipeline can be split into four main components of data storage, data extraction, post-processing, and analysis. Data storage is composed of single PowerBI files (pbix) that hold the various raw data tables sent from GM. These tables hold information such as nugget properties, material information, process parameters, and time series data. Part of the data transfer process included being aware of what data was included in the database and what fields would be relevant to meet our research objectives. GM supported this effort by sharing a data dictionary covering definitions for the fields in the database. The second component of data extraction is handled through Data Analysis Expressions (DAX) Studio. Once we identified the tables and fields pertinent to our needs, we used DAX to create queries and extract the data. The data is transferred to the third step for post-processing with R language. In this step, various transformations are made on the data to prepare for analysis. Through this process, we have identified inconsistencies within the PowerBI database and communicated the findings with GM. This resulted in GM reviewing their database to make updates and increase the quality of their data. Once their updates were implemented, we ingested the new PowerBI file into our data pipeline. The final step in the pipeline is an analysis data set that can be used for modeling through tools such as R and Python.

GM image data is a combination of .csv files, .jpg images, and .stl images. A synthesis of the .csv, .jpg, and .stl image files resulted in a data file called “DOE_analysis_draft4.csv” that summarizes the image data that can be analyzed further. The .csv files contain optical/height data consisting of pixel and depth data. The .jpg files contain images of the welds from a top-view and a metallurgic cross-section view. The .stl files contain 3D images. Out of the 5516 welds in the analysis data set, 1201 were found to have corresponding image data (e.g., 1201/5516 is approximately 22%). The images for the 1201 welds were summarized based on seven identifiers: “DOE_Num,” “vspotid,” “Stackup,” “SampleNum,” “WeldNum,” “MET,” and “NumMaterials,” in the DOE_analysis_draft4.csv file. Optical and weld height images were generated using python scripts on optical/height (.csv) files. A total of 900 images were generated for optical (450) and weld height (450). Figure II.4.1.1.6 provides example images in the dissimilar steel/steel data set optical.csv files.

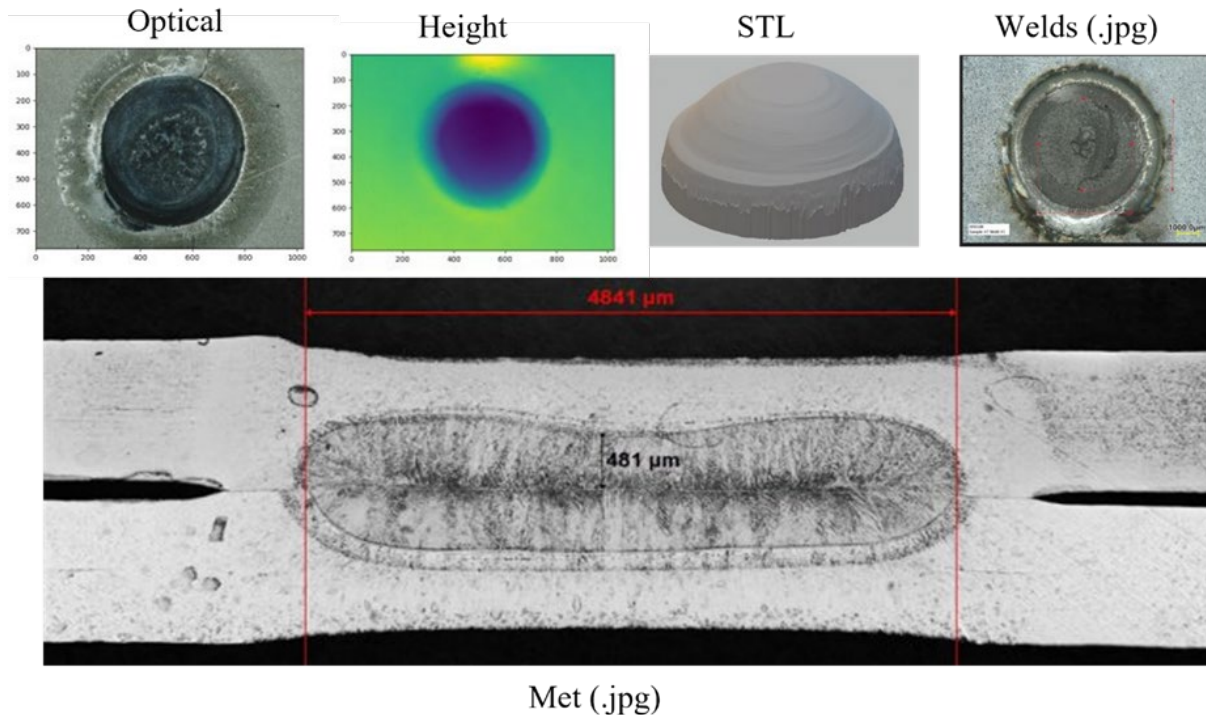


Figure II.4.1.1.6. Example images in the dissimilar steel/steel data set. Optical .csv files contain the top-view weld images. Height .csv files contain the depth-of-weld images. Met .jpg files contain the metallurgic cross-sectional weld images. Weld .jpg files contain the top-view welds with measurements. The *.stl files contain the 3D-rendering of welds. Source: PNNL.

Expandable ML with Unified Architecture of DNNs for Weld Performance Prediction (ORNL)

In FY 2023, ORNL accomplished two major milestones. First, we completed the development of the expandable ML framework for both welding process-performance and weld attribute-performance relationships for the dissimilar Al-steel RSW data sets. The model was applied to derive the process windows required for achieving high-performance and repeatable RSWs. In the second half of FY 2023, we are transitioning into the inline weld quality monitoring task on high-strength steel RSWs for battery trays. In this task, we have built a utility program to standardize and automate the data preparation for ML through physics-based and knowledge-guided quality assurance and control. This procedure covers data acquisition, data cleaning, data transformation, and data infusion of the large volume data set from different lab and plant collections. ORNL’s expandable ML framework has been expanded to include the inline weld process data. An initial version was developed and trained using a subset of lab-fabricated welds with inline welding process signals. Details about the model prediction performance and its applications in guiding the process development are provided below.

Extend the Input Data Stream of Process Conditions into the Unified ML for Process – Performance Relationship with Joint Quality Consistence Quantification (ORNL)

Based on the expansible ML framework developed in a previous FY of the project, the process conditions were added to the ML modeling architecture to add the function to establish the associations between welding process conditions/parameters and joint performance properties. One of the major challenges was to design the model to handle the joint quality variation situation. It is well-known in the automotive industry that the weld quality and strength could vary (or scattered) when multiple repeats are produced under the same welding conditions. The degree of weld quality scattering is also a function of welding process conditions, for example, the applied electrode force and/or the welding current used. In FY 2023, we developed a customized ML approach that enables us to not only predict the statistic average/mean but also quantify the extent of variation or scattering of joint performance properties as the function of the RSW process conditions.

Figure II.4.1.1.7 shows the overall expandable ML architecture. The process conditions were added to the ML framework as input data stream, which included electrode cap shape, welding order, polarity, adhesive, squeeze time, clamp load, and welding current schedule. These process conditions, together with material specifications and other conditions (e.g., post-weld baking, aging), were combined as RSW input conditions to predict the output targets of weld performance properties and their scatterings. The welding current can vary in magnitude and duration through the entire welding cycle for dissimilar RSW of Al alloy and steels. Therefore, it is necessary to incorporate the temporal history of the welding current into ML analysis. Finally, we note the model prediction targets included in both statistical average and scattering quantification of peak load, extension at break, total energy and fracture mode.

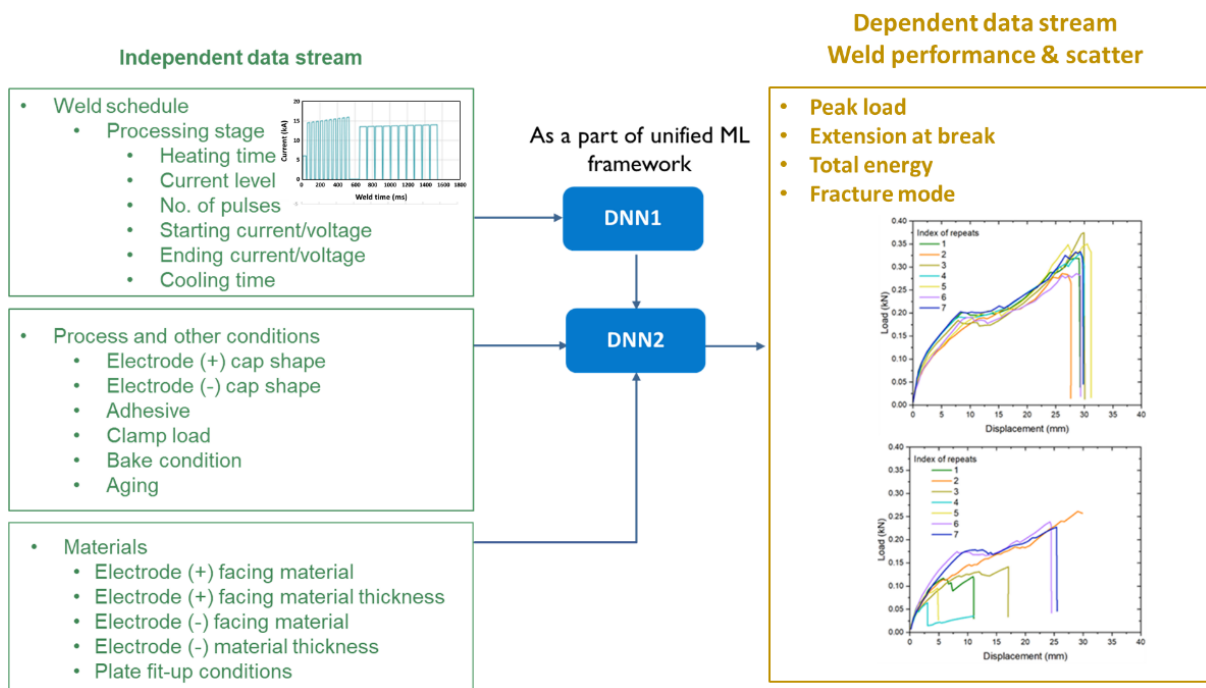


Figure II.4.1.1.7. Extend the input data stream of process conditions into the unified ML for process - performance relationship. Source: ORNL.

The model was trained by a comprehensive data set comprised of 40 stack-ups from more than 20 Al and steel alloy combinations. Figure II.4.1.1.8 summarizes the model's prediction performance through a regression analysis between model predictions and experimental measurements. The model provided the quantitative predictions of the statistical average and the variation range (minimum, maximum) of the joint peak load. This approach demonstrated the overall predictive capability of the expandable ML framework developed in this project over the entire data set, which comprised welds fabricated under around 650 process conditions.

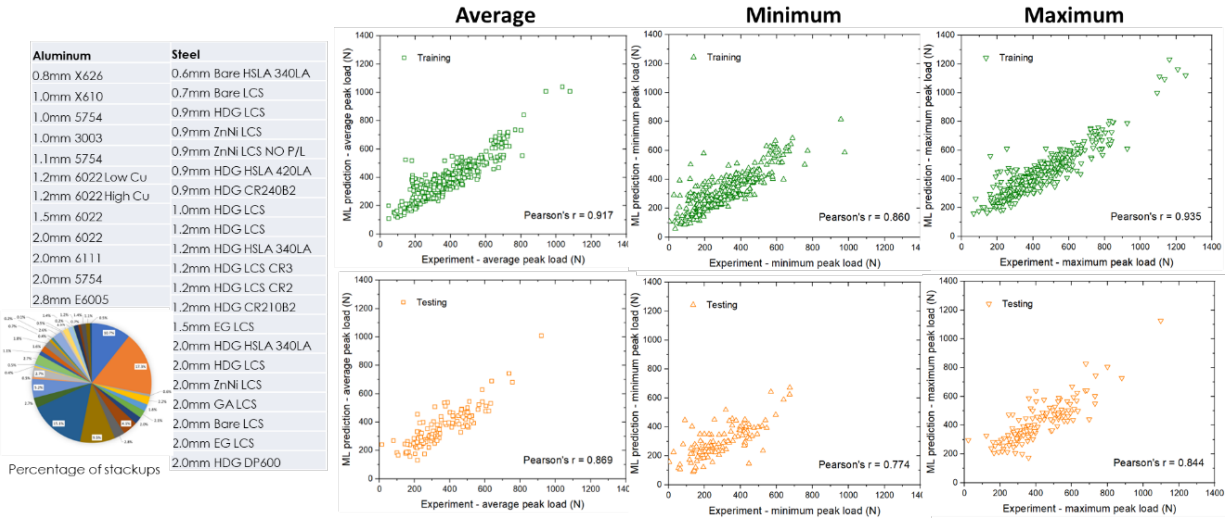
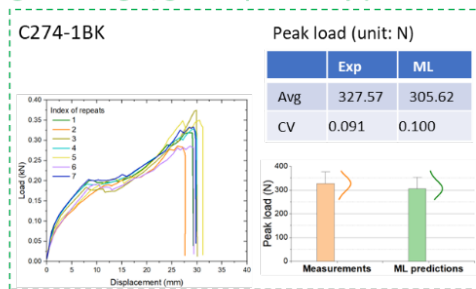


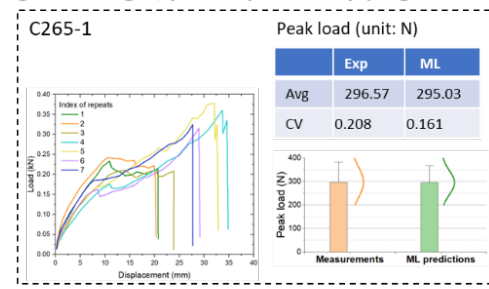
Figure II.4.1.1.8. ML model provided quantitative prediction for joint peak load average and its range (minimum, maximum) for a variety of material combinations. Source: ORNL.

Figure II.4.1.1.9 presented some example cases showing how the model predicted the joint performance while quantifying the repeatability (or consistency) of welds under different situations. The model can predict weld performance in a wide range, for instance, welds with an average high-performance and good consistency, welds with an average high-performance but poor consistency, and those with an average poor performance with different degrees of consistency. For each individual case, the model provided the predictions of the statistical average peak load and a probability distribution describing the probability that the peak load of each weld replication would be distributed around the statistical average value. The narrower probability distribution means that the welds keep consistent quality under certain welding process conditions for a material stack-up, and vice versa.

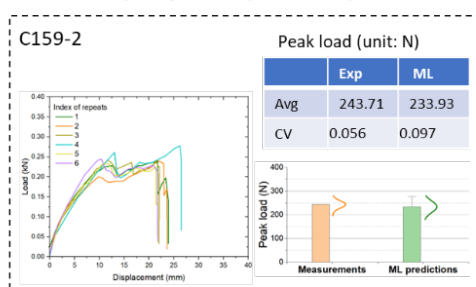
Higher strength, good repeatability (small variation)



Higher strength, poor repeatability (large variation)



Lower strength, good repeatability



Lower strength, poor repeatability

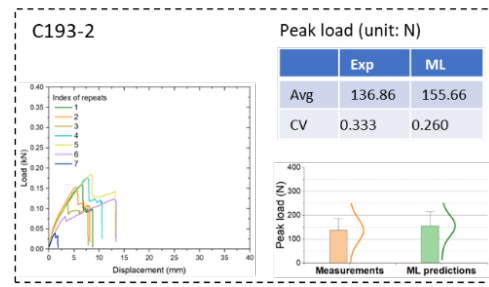


Figure II.4.1.1.9. ML model-predicted weld performance under a variety of materials and welding conditions. Source: ORNL.

Impact of Weld Process Parameters Revealed by ML Model (ORNL)

It is important to understand the causal factors of welding process conditions for the weld quality and consistence under various scenarios. To this end, we applied our DNN-based ML model to quantitatively examine the impact of welding process conditions on joint quality and repeatability. Figure II.4.1.1.10(a) presents the influence of the welding current on the joint peak load as identified by our ML model for a particular material stack-up (0.8 mm X626 Al with 0.9 mm hot-dip galvanized [HDG] LCS). The ML revealed that, at first, the statistical average peak load generally increases with the increase in the welding current at the same time the degree of variation decreases (i.e., the weld's consistency improves). However, as the welding current exceeds a threshold value of 15 kA, the joint strength scattering begins to increase rapidly, that is, the repeatability of the weld steel becomes less controllable. Although the statistical average joint peak load increases steadily, the lower bound value exhibits a declining trend. Indeed, the experimentally determined optimal welding condition, as depicted by the single green dot in Figure II.4.1.1.10(a), supported our ML model prediction of the welding process condition for relatively high-strength with consistent weld quality. In addition to the joint performance properties, the model can predict the welds' fracture modes. As shown in the figure, the model successfully predicted that welds made with a welding current below 9 kA would fail by an interfacial failure mode, which was again confirmed with the experimental testing results.

Furthermore, our expandable ML framework with united DNN architecture could predict the range of weld current and weld time to produce a different weld button size, as presented in Figure II.4.1.1.10(b). The model correctly predicted a welding process window (more commonly known as the weld lobe in RSW) that consists of three categorical regimes: (1) the low regime (red color region) with low current and short welding time conditions, which can result in small weld button sizes and interfacial failure only, (2) the middle regime (green and light blue color region) with mixed interfacial failure and button pullout failure, and (3) the acceptable regime (blue color region) which is consistently the preferred weld button pullout failure mode when multiple welds were repeatedly fabricated. The acceptable process regime should be the regime to further optimize welding process conditions. The previously discussed ML predictions were validated by a number of experimental measurements in the data set received from GM.

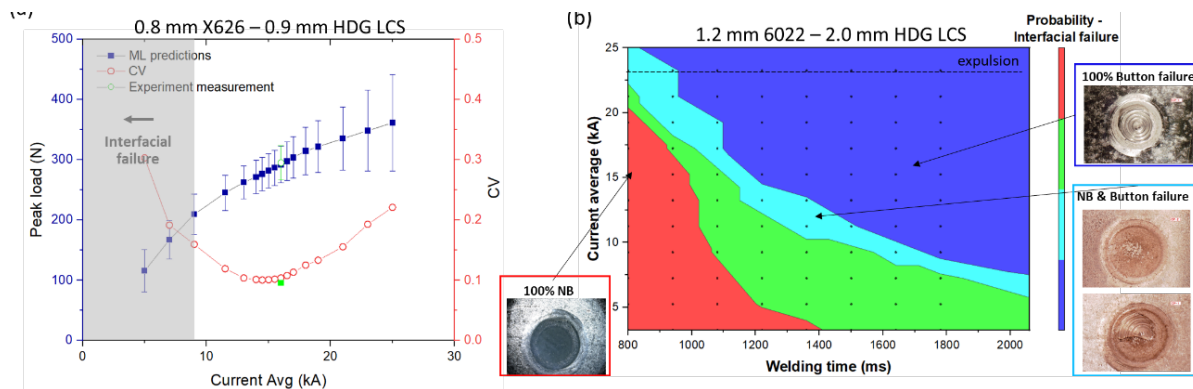


Figure II.4.1.1.10. (a) Influence of welding current on joint peak load identified by DNN model. (b) DNN model predicted the process map for button vs. interfacial failure welds. Source: ORNL.

Determination of Weld Conditions to Achieve Performance Target through Unified ML Model (ORNL)

We connected the fully trained, expandable ML framework with united DNN architecture with an optimization scheme, which made it possible to determine the weld process window within which one would produce welds to meet a specific target performance for a given materials stack-up. In our approach, the welding process parameters were searched within ranges of GM's data sets and optimized in a way to minimize the difference between the ML predictions and targeted joint performances. We adopted the optimization algorithm of stochastic gradient descent with adaptive moments for its convergence capability, computational cost, and memory requirement in searching the high-dimensional weld variable spaces. Figure II.4.1.1.11 schematically shows our approach for weld schedule optimization.

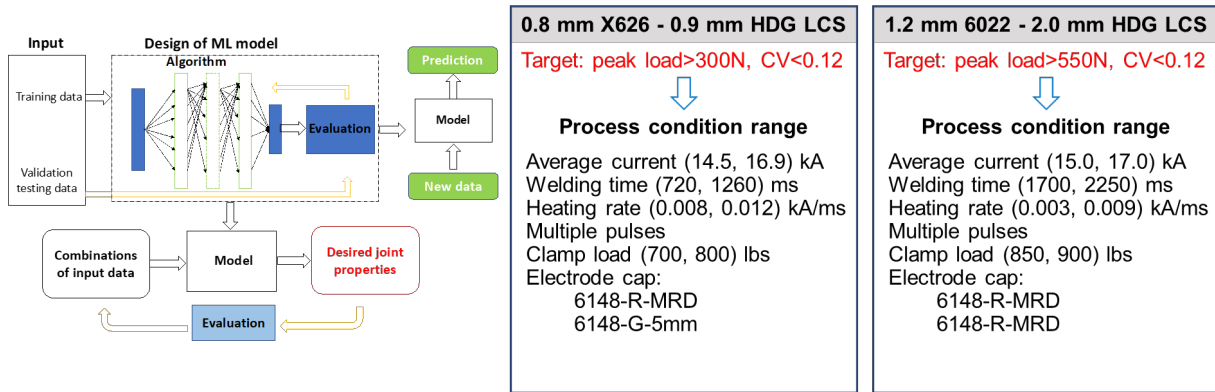


Figure II.4.1.1.11. The fully trained DNN model applied for weld design to identify welding process conditions for meeting joint target performance for two example weld stack-ups of 0.8 mm X626 – 0.9 mm HDG LCS and 1.2 mm 6022 – 2.0 mm HDG LCS. Source: ORNL.

Figure II.4.1.1.11 presented the identified ranges of welding process conditions, which are necessary to meet target high-performance and good repeatability for two-weld stack-ups: 0.8 mm X626 – 0.9 mm HDG LCS (target performance: peak load > 300 N, coefficient of variation [CV] < 12%), and 1.2 mm AA6022 - 2.0 mm HDG LCS (target performance: peak load > 550 N, CV < 12%). Note these above predictions are for welds with no special fit-up issues, for example, no electrode angle and sheet gap. This example demonstrated the ability to apply our unified ML framework to guide RSW development for dissimilar Al and steel alloy combinations. More independent testing is desirable for validating the effectiveness of the unified ML model.

Transitioning into ML for Inline Weld Quality Monitoring of RSW of High-Strength Sheet Steel for EV Battery Enclosures (ORNL)

Upon successful development of our expandable ML framework with united DNN architecture in the second half of FY 2023, we started transitioning into the inline weld quality monitoring task on RSW quality determination of high-strength steels for EV battery enclosures, which is a critical challenge in the automotive industry transition to EV platforms. Working together with PNNL and GM, we completed data transfer from GM. We then developed a utility program to standardize and automate the data preparation for ML through knowledge-guided quality assurance and control. An initial model has been developed based on the expandable ML framework to correlate the inline signals together with other process conditions to the weld quality metrics. The following covers the data transfer, data preprocessing, initial model development, and preliminary results.

Initial Model and Preliminary Results for Inline Weld Quality Monitoring

An initial model was built by infusing the inline signals into the expandable ML framework, which is schematically shown in Figure II.4.1.1.12. The requirement for inline weld quality monitoring was different from the previous Al-steel RSW. The new target is to predict the following quality metrics with decreasing rank of importance: (1) cold weld detection, (2) determination of whether a weld meets the minimum nugget size, (3) nugget size prediction, (4) quantitative expulsion prediction, (5) edge weld detection, (6) welds with extreme sheet gap detection, and (7) press hardened steel (PHS) coating variability detection. Supervised learning was used with DNNs to explore the associations between inline signals, process parameters, stacking materials, and the targeted weld variables. This was realized by developing a special DNN module, which is capable of learning the internal representation of the time series signals. The initial model was trained based on a subset of single-pulse welds (a total number of 708) with the objective of predicting the nugget size.

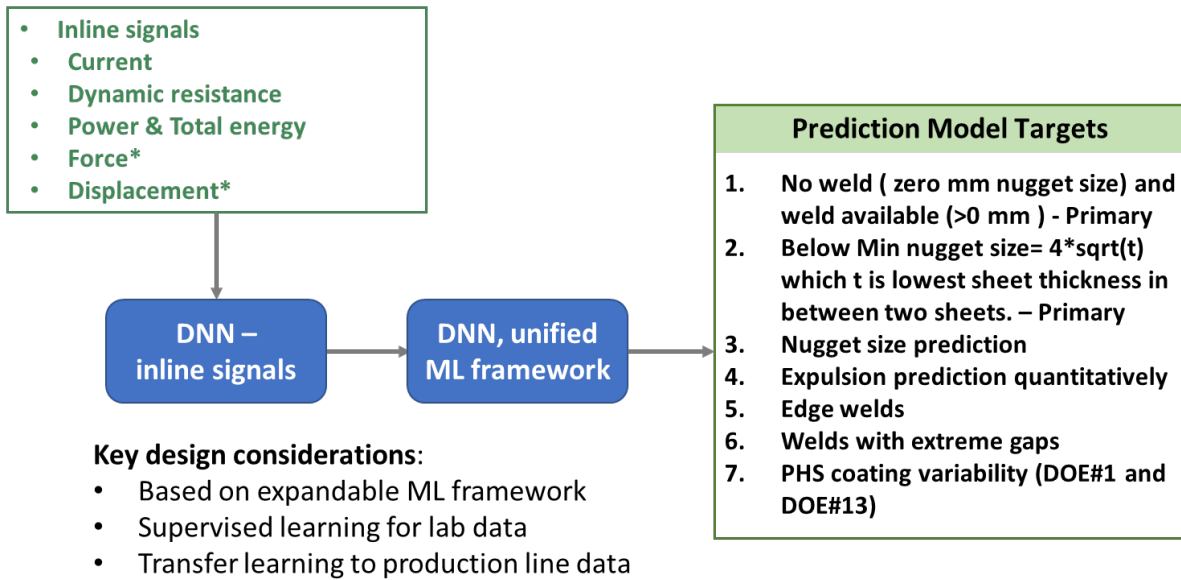


Figure II.4.1.1.12. Integrate the inline signals into ORNL's expandable ML framework for inline weld quality monitoring. Source: ORNL.

The model delivered an accuracy of 91% towards the nugget size prediction, as presented in Figure II.4.1.1.13. The initial model accuracy is encouraging, which also proves the ML framework is highly expandable to inline signals. We plan to further develop and build an inline weld quality monitoring capability by using deep learning techniques with the expandable ML framework.

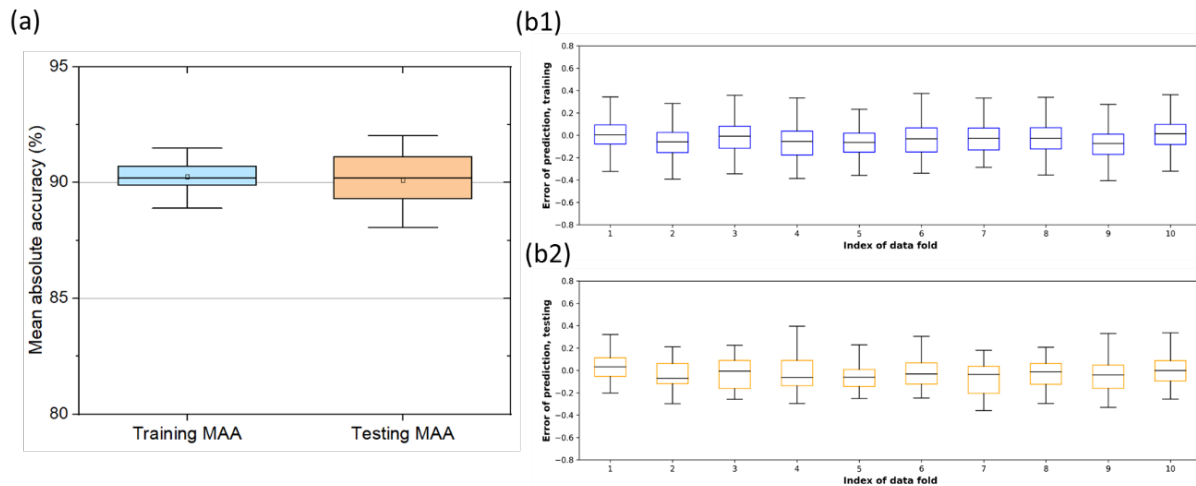


Figure II.4.1.1.13. Initial model prediction of weld nugget size based on inline signals: (a) an average of more than 90% prediction accuracy and (b) error of prediction for 10-fold cross validation. Source: ORNL.

Conclusions

Two classes of ML modeling approach have been built and used to investigate the relationships between the process parameter, weld attributes, and joint performances. ORNL focused on the development of expandable ML with unified DNN architecture for weld performance prediction. PNNL focused on the development of interpretable ML models for process-structure-performance relationships. The key findings and conclusions were as follows:

1. PNNL:
 - a. Ensemble ML approaches are desirable in examining the efficacy of multiple ML models to fit the data and smooth the error over multiple developmental stages.
 - b. Physically derived process parameters provide insight into the RSW process. Using them instead of only the raw process data improves the accuracy of the ML models describing the process-structure-property relationships.
 - c. Detailed structural image analysis provided a method of determining weld attribute dimensions. These were subsequently key to achieving granular relationships between RSW process conditions and individual nugget, HAZ, and other weld regions via functional principal component analyses.
2. ORNL:
 - a. Expandable ML with purposely designed DNN-model-predicted not only the statistic average/mean of a joint performance but also the weld consistency with high confidence.
 - b. DNN model enhanced the physical understanding of RSW by identifying the causal factors of welding process parameters responsible for weld quality and consistency under a variety of scenarios.
 - c. It was possible to predict a set of optimal process parameter ranges necessary to achieve the high-performance, repeatable RSWs for Al-steel RSWs using the developed ML framework.
 - d. Extending the inline signals into ML framework resulted in 91% prediction accuracy toward the joint nugget size—an initial model for inline weld quality monitoring.

Key Publications

1. Durell J. L., M. Y. Obiri, A. Ojeda, H. Ghassemi-Armaki, B. Carlson, D. K. Fagan, and K. S. Kappagantula, 2023, “Hybrid functional ML for modeling the effect of process parameters on microhardness quality,” October 17, 2023, *IMAT 2023*, Detroit, MI, USA.
2. Obiri M. Y., D. K. Fagan, A. Ojeda, K. S. Kappagantula, W. Choi, H. Ghassemi-Armaki, and B. Carlson, 2023, “ML to optimize RSW weld schedule parameters,” *J. Intell. Manuf.*, in review.
3. Ojeda A., M. Y. Obiri, D. K. Fagan, and K. S. Kappagantula, 2022, “ML for joint quality: weld schedule, performance and microstructure,” October 10, 2022, *MS&T 2022*, Pittsburgh, PA, USA.
4. Ojeda A., M. Y. Obiri, D. K. Fagan, W. Choi, and K.S. Kappagantula, 2023, “ML for joint quality performance-A comparison study of the relationship between process parameters and weld microstructure of Al/steel resistance spot welds,” March 19, 2023, *TMS 2023*, San Diego, CA, USA.
5. Zhang, W., D. Wang, J. Chen, H. Ghassemi-Armaki, B. Carlson, and Z. Feng, 2022, “A new perspective of post-weld baking effect on Al-steel resistance spot weld properties through ML and finite element modeling,” *J. Manuf. Mater. Process.*, 7(1), 6. <https://doi.org/10.3390/jmmp7010006>.

6. Zhang, W., Z. Feng, D. Wang, J. Chen, H. Ghassemi-Armaki, and B. Carlson, 2022, “Methods for determining weld quality and properties in RSW process,” Invention Reference Number 202205121, Licensing Agreement Number 47327601. <https://www.ornl.gov/technology/202205121>.
7. Zhang, W., D. Wang, J. Chen, Z. Feng, H. Ghassemi-Armaki, B. Carlson, 2023, “ML for predicting weld quality and properties in RSW process,” *FABTECH 2023*, Chicago, IL, USA.
8. Zhang, W., D. Wang, J. Chen, H. Ghassemi-Armaki, B. Carlson, Z. Feng, 2022, “ML modeling for relationship between joint attributes and weld performance in RSW,” June 17, 2022, *Advances in Welding & AM Research Conference*, Miami, FL, USA.

Acknowledgements

The PIs acknowledge the following key researchers for their contribution to the progress of this program: from ORNL: W. Zhang, D. Wang, and J. Chen; from PNNL: D. Fagan, M. Obiri, A. Ojeda, L. Durell, P. Meher, W. Choi, L. Truong, M. Taufique, and T. G. Nakkina; from GM: H. Ghassemi-Armaki. Finally, we wish to acknowledge the assistance from our DOE VTO Program Manager, C. Schooler.

II.4.1.2 Extending High-Rate Riveting to New Material Pairs (Pacific Northwest National Laboratory)

Kevin L. Simmons, Co-Principal Investigator

Pacific Northwest National Laboratory
Energy Processes and Materials Division
900 Battelle Blvd.
Richland, WA 99352
E-mail: kl.simmons@pnnl.gov

Amit Naskar, Co-Principal Investigator

Oak Ridge National Laboratory
Materials Science and Technology Division
1 Bethel Valley Rd.
Oak Ridge, TN 37830
E-mail: naskarak@ornl.gov

Christopher Schooler, DOE Technology Development Manager

U.S. Department of Energy
E-mail: Christopher.Schooler@ee.doe.gov

Start Date: August 16, 2020
Project Funding: \$683,000

End Date: September 30, 2023
DOE share: \$683,000

Non-DOE share: \$0

Project Introduction

PNNL, ORNL, and ANL are teaming together to develop a combination of adhesive-based bonding and high-velocity mechanical joining methods for multimaterial systems to reduce vehicle component mass.

Objectives

This project aims to develop a hybrid adhesive-mechanical joining method to efficiently join two- and three-ply thickness multimaterial configurations that will exceed lap-shear strength (LSS) by 50% and cross-tension strength by 30% beyond what is possible with adhesive bonding alone. The project also aims to demonstrate its effectiveness as a robust approach that has improved joint integrity. By combining state-of-the-art riveting techniques with adhesive bonding, the project will focus on adhesive curing, thermal stability, and wettability issues both by experimental and modeling methods to enhance the performance of hybrid and non-hybrid joints. We will develop and demonstrate an adhesively bonded multimaterial joint that has high-velocity-formed rivets and high-friction rivets that will increase the performance and reliability of the joined dissimilar material sets.

Approach

The approach will investigate adhesively bonded and non-bonded joints with two-piece (2T) and three-piece (3T) material sets of high-strength steel dual-phase (DP)590, Al alloys (AA5052 and AA6061), and Al castings (< 12 mm) with polyphthalamide (PPA) and polyamide 66 (PA66) CF composites from sheets up to 3 mm in material thickness. These systems represent different combinations that could be used in different vehicle joints. The project will evaluate cured and uncured adhesively bonded joints to determine the effect of the riveting process on the adhesive. Modeling simulations will be performed to optimize rivet design and process parameters. The joints will be mechanically tested and characterized to develop both a physical and chemical understanding of bond strengths and external effects.

Results

Plasma Surface Treatment of Adhesives and Substrates (PNNL)

Building upon our previous studies that explored enhanced bonding behavior in composite-related joints through plasma treatment of composite substrates only, we conducted further investigations to examine how

plasma surface treatment of substrates and adhesive tape (e.g., XP5005F) can improve the LSS of an adhesive joint. For example, AA6061 and short carbon-fiber-reinforced polyphthalamide (CFRPPA) joints were investigated for demonstration. Adherend surfaces were treated with a 500W blown-ion plasma system with compressed air using previously optimized parameters. The top and bottom surfaces of the adhesive were plasma-treated using a low-power (45W) expanded-plasma cleaner using a gas mixture of 14% oxygen and 86% argon, which produced an optimized surface energy condition. As shown in Figure II.4.1.2.1(a–b), the LSS for as-received joints (< 5 MPa) can be improved by 200% (to \approx 12 MPa) after the plasma treatment of substrates and can be further improved by 315% (to \approx 16 MPa) when the adhesive tape and substrate surfaces are treated with plasma. The main enhancement mechanism was due to the formation of a dense network of covalent bonds at the interface, as indicated in Figure II.4.1.2.1(c). A minor enhancement mechanism was due to approximately 20% reduction of voids at CFRPPA-adhesive interface, as shown in Figure II.4.1.2.1(d–e), resulting from improved wettability of the plasma-treated surfaces.

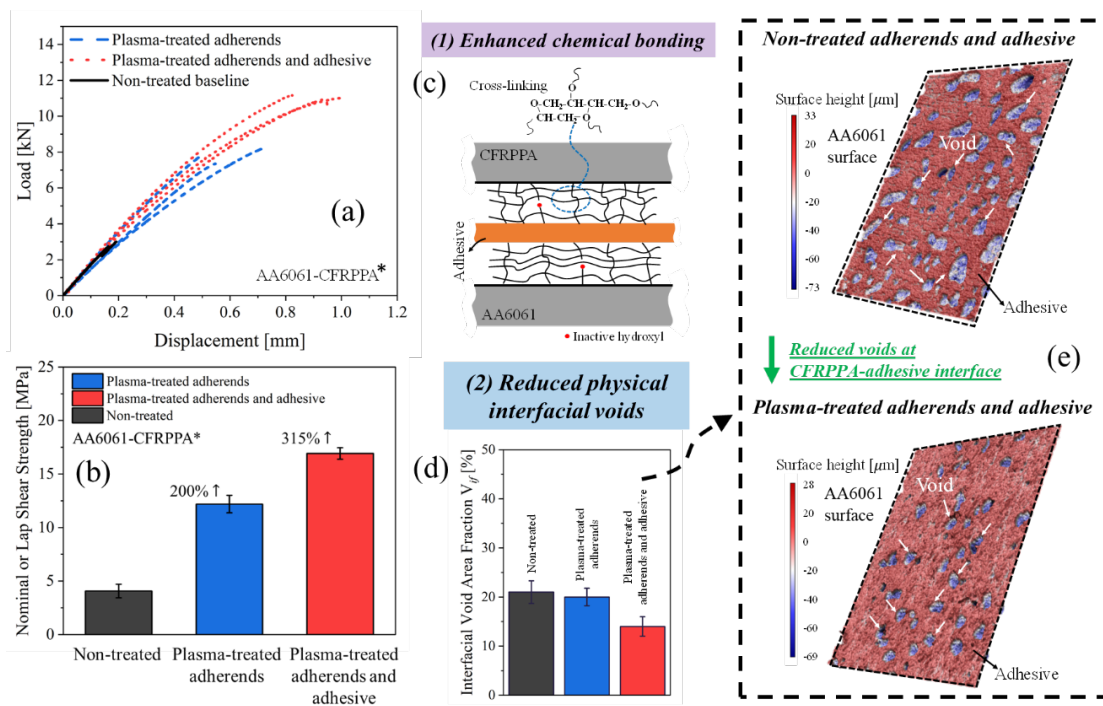


Figure II.4.1.2.1. (a) Load-displacement curves and (b) LSS of AA6061-CFRPPA joints. (c) Enhanced chemical bonding at the substrate-adhesive interface. (d) Percentage of void defects at the CFRPPA-adhesive interface. (e) Surface morphology of AA6061 substrates. Source: PNNL.

We used this treatment strategy during our collaboration with ORNL to investigate the adhesively bonded AA6061 to short carbon-fiber-reinforced nylon polyamide 66 (CFRPA66) joints using the thermoplastic nitrile butadiene rubber (NBR)-lignin adhesive film developed by ORNL. Plasma treatment of the adhesive and substrates, as can be seen via Case #4 in Figure II.4.1.2.2, achieved the highest LSS \approx 13 MPa, as compared to joints without plasma treatment (e.g., Case #1) or treatment of either substrates only (e.g., Case #2) or adhesive only (e.g., Case #3). The results represent a 40% increase in LSS compared to the lowest LSS found in this study (e.g., Case #3). The improvement mechanism was due to the increased density of linear ester bonds formed by pressure-driven thermal dehydration, which occurred during bonding under normal pressure and elevated-temperature.

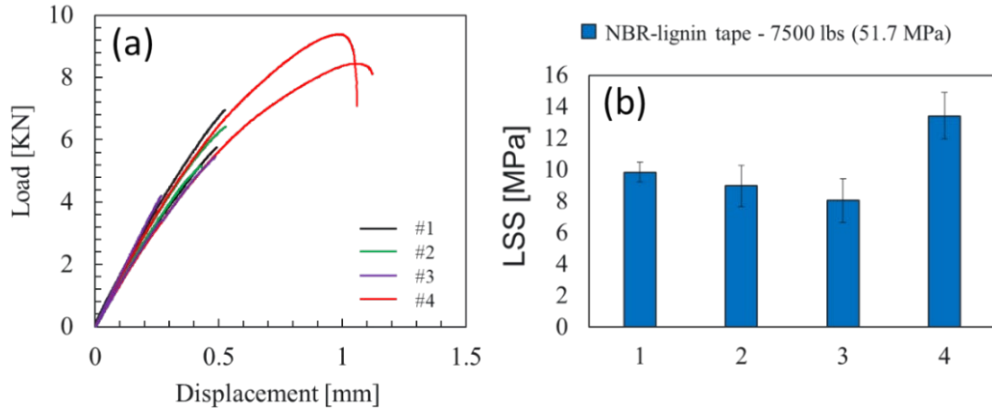


Figure II.4.1.2.2. (a) Load-displacement curves. (b) LSS of AA6061-CFRPA66 joints. Cases #1–4 represent: #1 non-treated adhesive and substrates; #2 non-treated adhesive and plasma-treated substrates; #3 plasma-treated adhesive and non-treated substrates; and #4 plasma-treated adhesive and substrates, respectively. Source: PNNL.

Laser-Surface Modification of Metals, Composites, and Their Joints (PNNL)

A laser-based surface modification approach was used to enhance the interfacial bonding in AA6061-AA6061 adhesive joints. The bonding area of both AA6061 specimens were treated with a nanosecond pulse laser. Each laser pulse produced a crater on the substrate by ablation, as shown in Figure II.4.1.2.3(a); the crater size was controlled by laser pulse energy, as indicated in Figure II.4.1.2.3(b). The treatment resulted in physicochemical changes to the substrate, such as enhanced roughness, removal of surface contaminants, and newly formed Al oxides and hydroxides. Controlled spacing of the laser pulse spots produced individual craters (0% overlap to 50% gap between spots) or uniformly textured surfaces (30–80% spot overlap), as observed in Figure II.4.1.2.3(c). LSS of bonded joints increased by 80% compared to the as-received condition when a 70% overlap ratio was used at 1000 mJ pulse energy, as can be seen in Figure II.4.1.2.3(d). The fracture mode for the as-received specimens involved interfacial adhesive failure, while cohesive failure was achieved for joints subjected to laser-surface treatment, as designated in Figure II.4.1.2.3(e). Moreover, the coverage of the adhesive layer on the fracture surface improved as the laser-pattern overlap ratio increased, indicating improved interfacial bonding due to laser treatment.

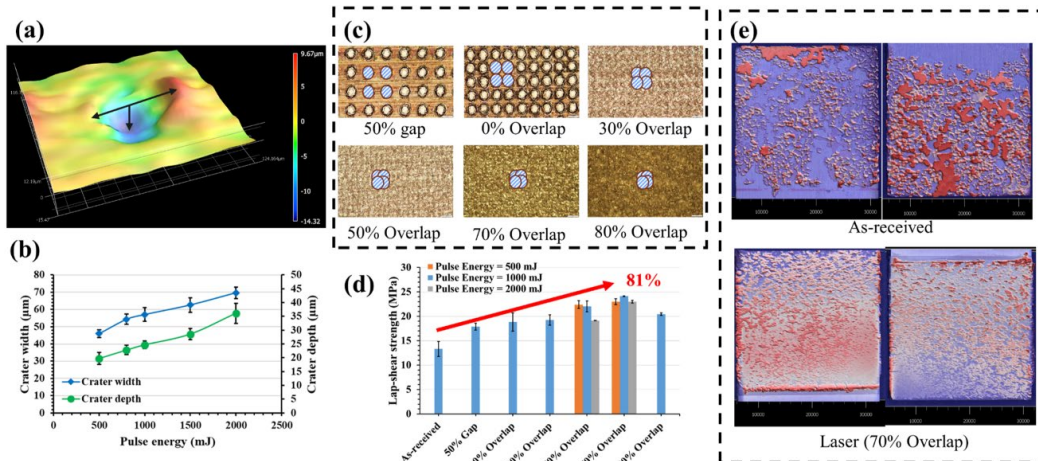


Figure II.4.1.2.3. (a) 3D profile of laser crater. (b) Variation of laser crater size with laser pulse energy. (c) Morphology of AA6061 surface at different overlap ratio. (d) Variation of LSS of AA6061-AA6061 joints at different overlap ratio and laser pulse energy. (e) Comparison of fracture surface morphology of as-received and laser-treated AA6061 substrates, demonstrating transformation from interfacial failure to more cohesive failure after laser treatment. Source: PNNL.

We also investigated the effects of the laser-surface modifications on dissimilar materials in AA6061-CFRPA66 where only the CFRPA66 surface was modified with the nanosecond laser. We investigated over 20 different patterns and found two unique ones that provided enhanced LSS. These patterns, shown in Figure II.4.1.2.4(a), enhanced both the LSS and failure strain of the lap-shear joints. The LSS improved by 14% using Pattern 1 and 20% using Pattern 2. Cross-section views of the dissimilar materials with laser modification, which are shown in Figure II.4.1.2.4(b), reveal a significant number of voids in the adhesive that can deteriorate LSS by reducing the total bonded area. To reduce the void content, we improved the curing process by introducing a vacuum stage to remove voids. The results are shown in Figure II.4.1.2.4(c), where the laser-treated joints, which were bonded using the improved vacuum method, contain significantly reduced voids after the adhesive curing. As a result, the LSS was further improved by 35% for Pattern 1 and 36% for Pattern 2 compared to the base as-received LSS. In Figure II.4.1.2.4(d), the failure images of the CFRPA66 surfaces after lap-shear testing from the base and Pattern 1 with our vacuum-assisted manufacturing process show larger areas of the pink adhesive on the Pattern 1 due to enhanced interfacial bonding, resulting in more widespread cohesive failure induced by laser treatment.

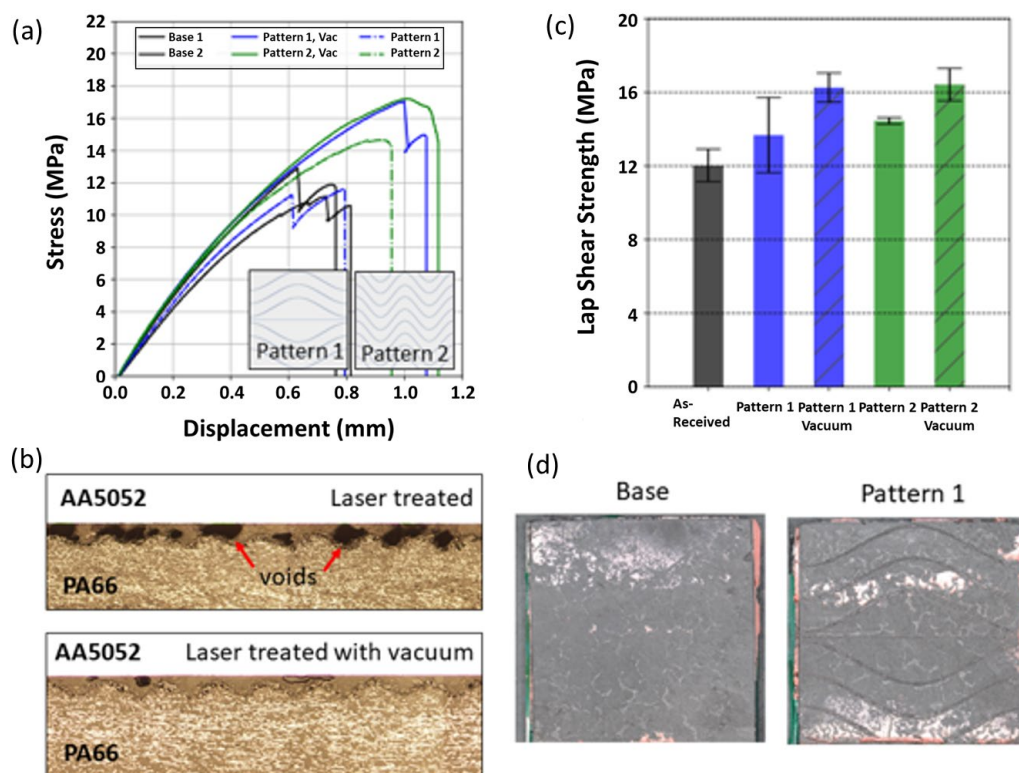


Figure II.4.1.2.4. (a) Lap-shear behaviors of dissimilar materials (AA6061-CFRPA66) with laser-surface modifications. (b) The cross-sectional images of lap-shear joint with and without vacuum-assisted manufacturing process shows void reduction. (c) The LSS comparison between the as-received and laser-pattern samples. (d) Failure morphologies of the lap-shear joints. Source: PNNL.

Microscale Modeling for Interfacial and Internal Voids (PNNL)

In previous studies, we experimentally observed the generation of void defects both inside the adhesive and at the interface of the adhesive and the substrate. Therefore, we conducted microscale numerical modeling to understand the effects of voids on the bonding behavior of adhesively bonded joints, which are summarized in Figure II.4.1.2.5. Three different void volume fractions ($V_{vf} = 0\%$, 1% , 6%) were investigated in this study with voids both inside the adhesive and at the adherend-adhesive interface, defined by the interfacial void area fraction (A_{ivf}). Moreover, two different ratios of interfacial normal strength (σ_{ins}) to adhesive uniaxial tensile strength (σ_{aus}) were investigated, representing different chemical bonding scenarios. For $\sigma_{ins}/\sigma_{aus} = 0.5$, as

plotted in Figure II.4.1.2.5, to represent a weak substrate-adhesive interface, nominal shear-strength was significantly reduced as A_{ivf} increased and was not influenced by V_{vf} , as designated in Figure II.4.1.2.5(a). These results imply that interfacial void defects play a dominant role, rather than internal voids, in the shear failure behavior of an adhesive joint with weaker interfaces due to high-strain localization near interfacial voids and associated damage coalescence, as observed in Figure II.4.1.2.5(c) compared to Figure II.4.1.2.5(d). For $\sigma_{ins}/\sigma_{aus} = 1.5$, as plotted in Figure II.4.1.2.5(b) to represent a strong substrate-adhesive interface, interfacial voids were less influential since the nominal shear-strength showed a mild reduction as A_{ivf} increased, but internal voids were more impactful.

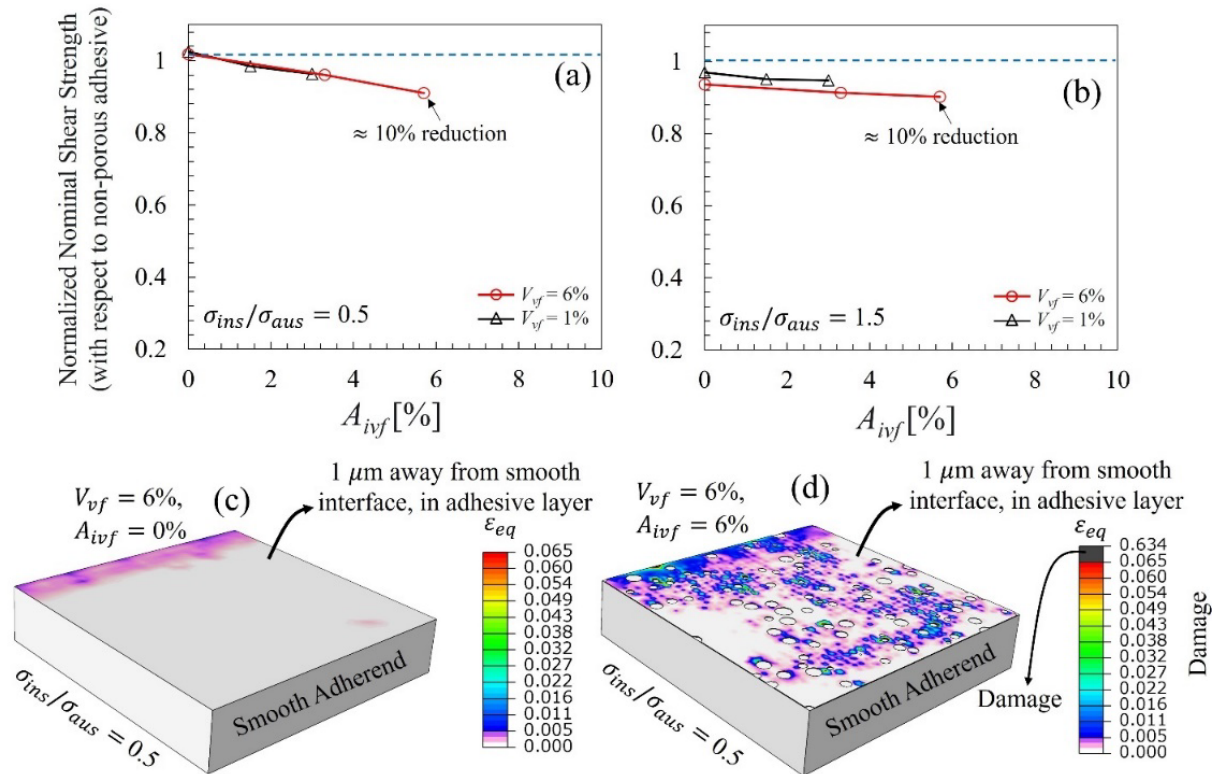


Figure II.4.1.2.5. (a–b) Normalized nominal shear-strength as a function of the interfacial void area fraction for two different ratios of $\sigma_{ins}/\sigma_{aus}$, representing different interfacial bonding behavior. Equivalent plastic strain at $1 \mu\text{m}$ away from substrate surface at the peak loads of two joints: (c) $A_{ivf} = 0\%$ and (d) $A_{ivf} = 6\%$.

Source: PNNL.

Novel Adhesive Development (ORNL)

Conventional thermoset adhesives used in automotive bonding typically require a one-time cure and cannot be disassembled for maintenance and repair of the components. So, developing a thermoplastic adhesive, which provides similar or better adhesion strength compared to thermoset, is a promising route to enable re-assembly or recycling of bonded components. With the growing environmental and health concerns, improving the sustainability of adhesives and production processes have inspired efforts to incorporate renewables into petroleum-based products. A thermoplastic sustainable acrylonitrile-butadiene-lignin (ABL)-based multiphase polymer adhesive was developed at ORNL. A nanoparticle-based thickening agent (TA) was added into the ABL matrix during the melt-blending process to improve the dispersion and separation of lignin particles. As reflected in Figure II.4.1.2.6(a), when using the Al as the substrate, the LSS was enhanced by 100% with optimized nanoparticle loading compared to the ABL control sample. The functionalized reinforcing filler was incorporated into the ABL-TA matrix to modify the mechanical properties and surface chemistry of composite-adhesive. The LSS results were summarized in Figure II.4.1.2.6(b). The best sample yielded an LSS

result of 21 MPa, which was 90% of the performance of a commercial epoxy-based adhesive (YL 230, L&L Products).

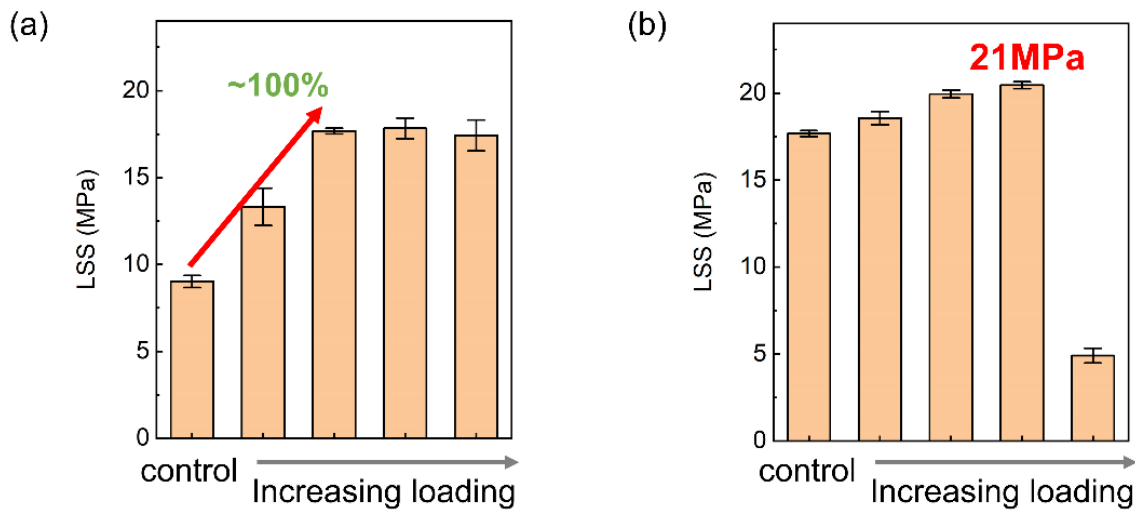


Figure II.4.1.2.6. The LSS results for an ABL-based adhesive using aluminum as the adherent (a) with different loading of TA and (b) with different loading of reinforcing fillers. The control sample in (a) is ABL, and the control sample in (b) is the best ABL-TA sample from (a). Source: ORNL.

The morphology of selected ABL adhesives were shown in Figure II.4.1.2.6. With the addition of TA during the melt-blending process, the modified rheological properties led to higher shear force, resulting in better dispersion and separation conditions of lignin particles. Compared to the control ABL sample, the size of the lignin particle was largely reduced, and a more uniform dispersion status was obtained in the ABL-TA sample. The spherical geometry of the reinforcing fillers provided the ball-milling effect during the shear mixing process. Few lignin chunks can be observed in Figure II.4.1.2.7.

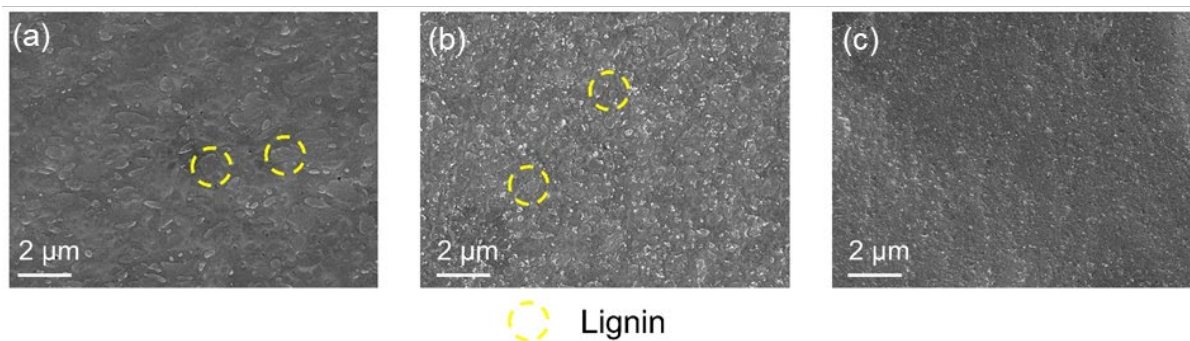


Figure II.4.1.2.7. SEM images for cryogenically fractured surfaces of selected adhesives: (a) ABL, (b) ABL-TA, and (c) ABL-TA-reinforcing filler. Source: ORNL.

To investigate the underlying mechanisms responsible for the reinforcement provided by the fillers and to use this knowledge to inform the development of ABL-based adhesives, a computational framework was developed for these composites. The representative volume element (RVE) offers a means of addressing heterogeneous materials with homogeneous macroscopic structures at a continuum length-scale. In our scenario, ABL-based composites could be simplified as a series of regular microstructures that make up the RVE. Simulation of a typical ABL composite joint debonding process revealed the buildup of plastic deformation inside the RVEs. A continuous band of plastic strain was observed to form in the ABL composites, indicating a global failure of the RVE. However, the stiff reinforcing fillers within the ABL

offered a more torturous pathway towards a continuous failure surface formation. Upon further inspection, we found the deflection of the failure plane from the location of the filler particles, which proved that the fillers could resist the crack propagation, leading to the improved adhesion performance.

High-Velocity Riveting (PNNL)

Thorough modeling efforts were completed on high-velocity (HiVe) riveting joints of various mixed and single Al alloy systems. Figure II.4.1.2.8(a) highlights molecular dynamics simulations for Al-Al type HiVe joints, which exhibited metallurgical bonding at the interface. The temperature and bonding characteristics were studied as a function of interfacial velocities with respect to the top and bottom plates in a AA6061-AA6061 stacking. Upon reaching a certain velocity threshold (~40m/s for both normal and transverse velocities), the adiabatic nature of these processes resulted in melting and mixing the two plate interfaces. After cooling, a fully recrystallized microstructure was predicted with grain sizes in the submicron regime, which was supported via transmission electron micrographs, as shown in Figure II.4.1.2.8(b), which yielded an understanding of the interfacial dynamics of the HiVe process with the Al-Al system for similar and dissimilar alloys. Previous work in this area has shown the ability to bond dissimilar Al-Al stacks, and now a nano- to micron-scale understanding of the thermomechanical behavior of these interfaces is beginning to be elucidated.

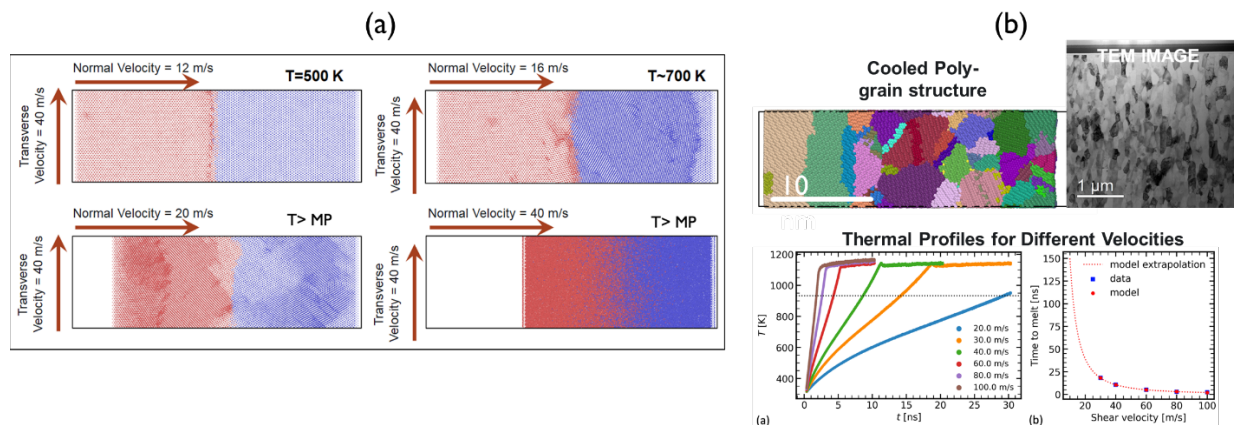


Figure II.4.1.2.8. (a) Molecular dynamics simulations of Al-Al interfaces interacting at various normal and transverse velocities. Varying degrees of mixing can be seen along with the predicted temperature profiles. (b) Predicted cooled molecular dynamic microstructure exhibiting submicron grains and the observed microstructure through TEM. Source: PNNL.

Additional beamline characterization was completed on the APS with collaborators at ANL to study the residual stresses and strains present at the mating interfaces of HiVe clinch joints. Figure II.4.1.2.9 exhibits both Al-Al and Al-DP980 joint stackings, with each case showing lattice strain distributions in both the top and bottom plates. Al-Al joints with metallurgical bonding show a highly compressive state of stress at the bonding interface, which will contribute to limiting crack propagation and fatigue performance. Peak width distributions are indicative of dislocation densities and crystallite sizes present in the materials. For dissimilar metal systems, metallurgical bonding can be difficult and is the focus of extensive modeling efforts to optimize the deformation characteristics to promote a metallurgical bonding on top of the mechanical bonding present after the HiVe process.

The latest mechanical testing came in the form of long-term fatigue testing of Al-Al HiVe clinch joints and 3T dissimilar metal stackings. Figure II.4.1.2.10(a) exhibits increased fatigue performance of Al-Al joints compared to similar material stack-ups and thickness regimes for industrially available clinch and self-piercing rivet (SPR) systems. At higher partial loadings (i.e., 3kN-7kN), the HiVe clinch joints showed the ability to withstand higher operating loads with equivalent cycles to failure compared to clinch/SPR. The performance increase is attributed to the inherent, compressive state of stress at the bonding interface of the HiVe clinch joint that acts to arrest crack propagation at the bonding interface, which is a common point of failure for this

type of joints. The fatigue limit for Al-Al joints is estimated to be around a loading of ~ 2 kN, where there is a marginal concern for joint failure.

From the literature values presented in Figure II.4.1.2.10, there is approximately a 100% increase in fatigue performance. In Figure II.4.1.2.10(b), 3T material stackings were joined via the HiVe rivet configuration, where the maximum lap-shear performance of this DP980-AA6061-DP980 stacking was ~ 12 – 14 kN. Currently, there are not any comparable material stacks in literature to a flow-drill screw (FDS) type joint. We present the first specific use-case for a 3T stacking of alternating DP steel-Al joints.

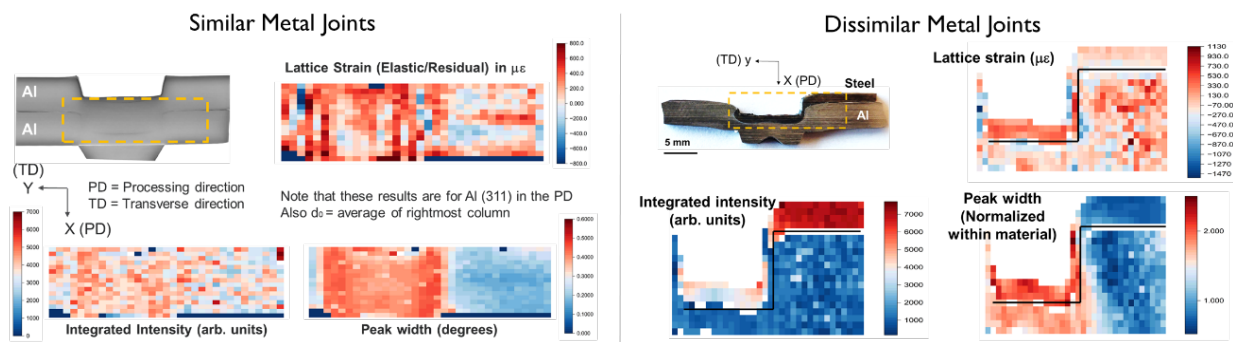


Figure II.4.1.2.9. Interfacial properties generated from the APS at ANL. Both similar and dissimilar metal stacks are shown along with the internal lattice strains, material texture (integrated intensity), and crystallite size (peak width) mappings. Source: ANL.

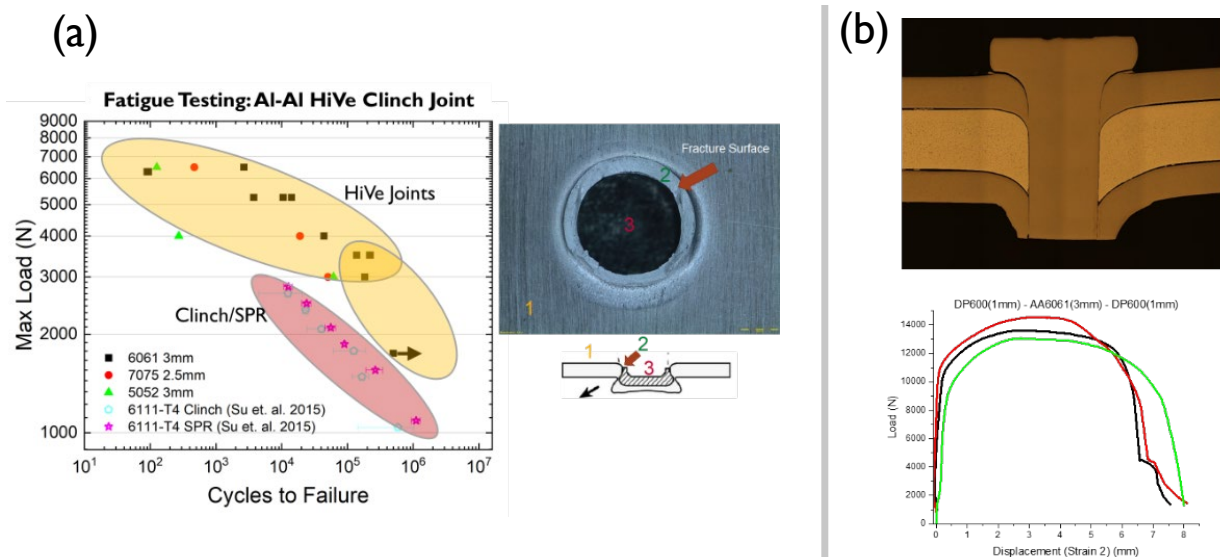


Figure II.4.1.2.10. (a) Long-term fatigue testing of Al-Al HiVe joints showing increased performance at higher loadings than commercially available clinch/SPR. Typical fracture surfaces of Al-Al joints indicating common neck failure mode. (b) 3T DP980-AA6061-DP980 stack cross-section with embedded rivet. Subsequent lap-shear performance of 3T HiVe rivet stacks. Source: PNNL.

Further focus on the lightweight and innovative HiVe process applies this method to steel-steel joints, particularly third-generation advanced high-strength steels used currently in automotive parts. Initial trials for joining steel-steel joints showed difficulty in controlling the amount of deformation while using the backing dies specifically designed for aluminum joints. Finite element modeling of steel-steel deformation mechanics were completed to study the influence of die geometry on the material damage, pressures, and temperatures present at the mating interface of these joints, as shown in Figure II.4.1.2.11.

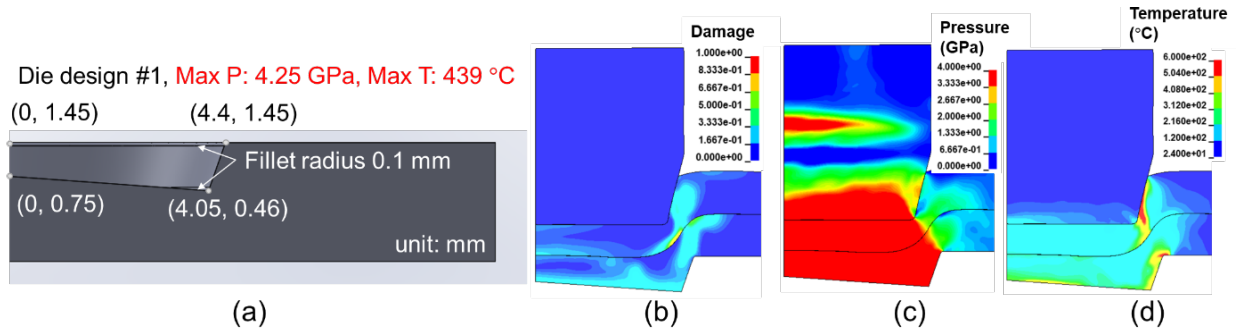


Figure II.4.1.2.11. Finite element simulations of new backing die configurations. (a) Half axisymmetric model of die with 2T DP1180 1.15 mm plates and corresponding (b) damage, (c) pressure, and (d) temperature profiles. Source: PNNL.

High-Rate Friction-Riveting (PNNL)

In FY 2023, efforts with high-rate friction-riveting (HFR) continued to focus on joining dissimilar material combinations, encompassing Al-steel configurations with 2T and 3T stacking. For 2T stacking, the HFR process was employed for joining AA6061 (3-mm) and DP590 (1 mm), with and without surface modification. Previously, it was reported that joints formed via HFR generally exhibit superior performance compared to those formed using the FDS method. Notably, the surface-modified HFR joint—F, as depicted in Figure II.4.1.2.12(a), demonstrated a peak load that exceeded the FDS method, as also indicated in Figure II.4.1.2.12(a), in H samples by 25% and I samples by 55% [1], [2]. In FY 2023, fatigue tests on these joint configurations were conducted under tension-tension loading with a stress ratio of 0.1, graphically represented in Figure II.4.1.2.12(b). At high-load amplitudes, joints with and without surface modification exhibited fatigue life cycles of 60 and 600, respectively. At low-load amplitudes, the fatigue life cycles for joints with and without surface modification were 455,000 and 71,500, respectively. Notably, joints with surface modification displayed a fatigue life 6–10 times longer than those without surface modification, indicating that surface modification effectively extends the fatigue life in both cycle regimes.

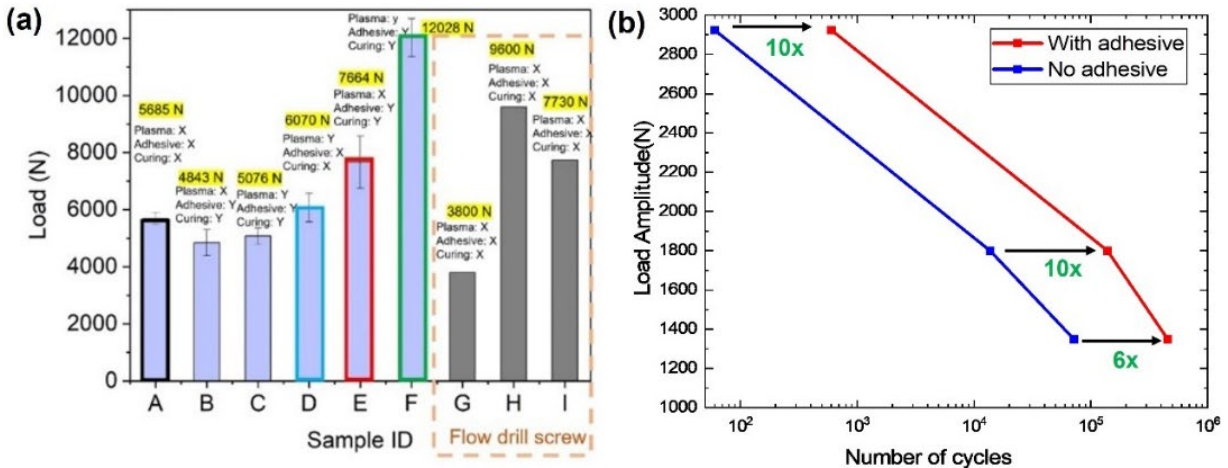


Figure II.4.1.2.12. (a) Maximum LSS obtained in HFR Al-steel joints after various surface modifications and comparisons made with FDS Al-steel joints from the literature. (b) Comparison of fatigue test results of the joint AA6061-DP590 with and without surface modification. Source: PNNL.

For 3T stacking, the HFR process was used to join 3-mm-thick AA6061-T6 sheets with specifically, DP590-1mm and DP780-0.7mm, in two distinct 3T configurations—(1) DP590-AA6061-DP590 and (2) AA6061-DP780-AA6061—employing advanced alloy steel M42 rivets. In Figure II.4.1.2.13(a), the lap-shear tensile test load-displacement curves for the DP590-AA6061-DP590 stacks are depicted. Notably, the highest load-

carrying capacity reached 10,244N in lap-shear testing, representing a 13% improvement over previously reported results. Figure II.4.1.2.13(b) illustrates the cross-section of the AA6061-DP780-AA6061 joint as well as the lap-shear tensile test results. In this configuration, the thin middle layer experienced softening due to frictional heat, subsequently bonding with the rivet tip as the rivet advanced further. This interaction with the bottom sheet led to the formation of a mixed layer between the bottom sheet and the rivet interface. The rivet also exhibited anchoring behavior. Consequently, the joint consistently performed well, with a load-carrying capacity of 7,899N in lap-shear testing.

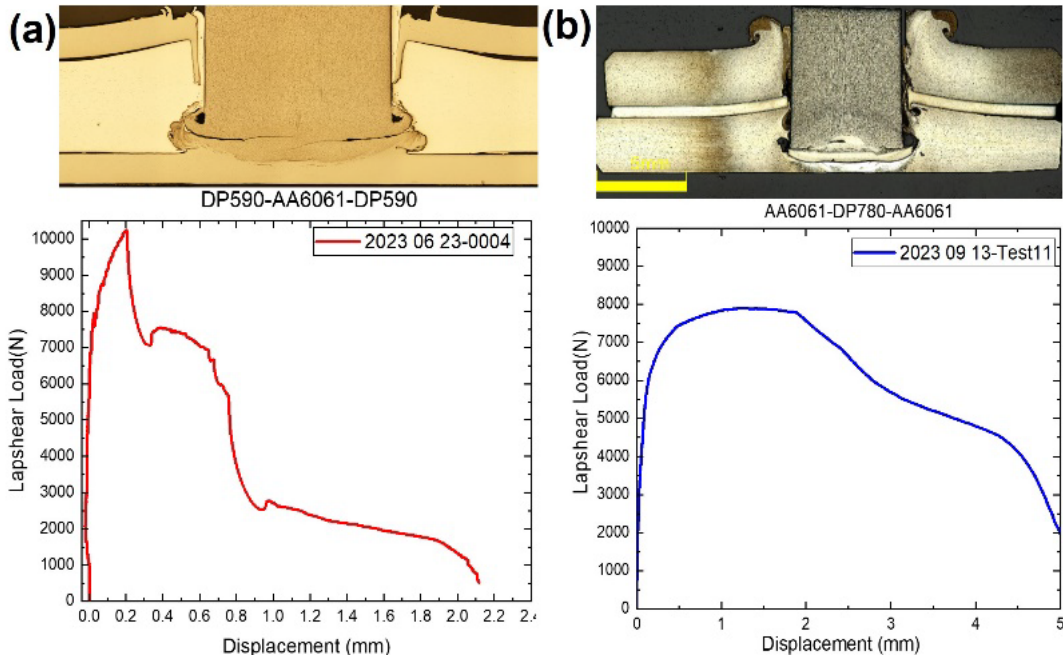


Figure II.4.1.2.13. Joint cross-section and corresponding load vs. displacement curves of 3T configurations: (a) DP590-AA6061-DP590 and (b) AA6061-DP780-AA6061. Source: PNNL.

HFR Process Modeling using SPH

The SPH method was used to simulate the friction-riveting process with the model setup shown in Figure II.4.1.2.14(a). According to post-process observation, the steel rivet was assumed rigid during the process because it is much stronger than Al and had negligible deformation. Thermal boundary conditions were applied on the outer surface of the rigid parts to mimic the real heat conduction condition. The process control parameters used in the model are shown in Figure II.4.1.2.14(b).

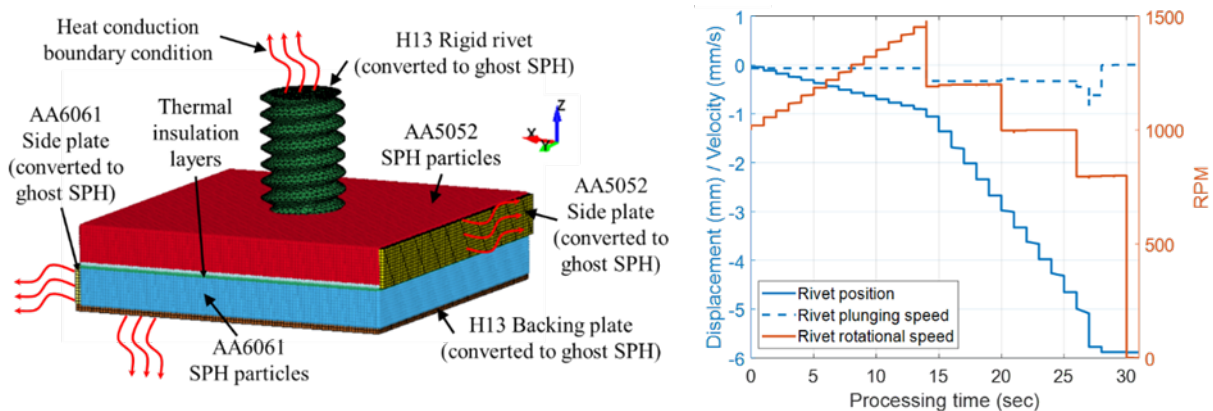


Figure II.4.1.2.14. (a) SPH model setup for friction-riveting and (b) processing parameter. Source: PNNL.

Figure II.4.1.2.15(a) shows the experimental central cross-sectional material morphology, in which an upwards-curved interface between two sheets is observed. This is because the right-handed rivet threads were rotating counterclockwise, which helped stir and move the sheet material upwards. This curved interface was accurately predicted by the SPH model, as shown in Figure II.4.1.2.15(b). A small gap was observed to exist along the sheet interface away from the rivet, demonstrating the validity of assuming thermal insulation layers in the SPH model. However, this small gap transitioned into a diffusion-bonded layer between the top and bottom Al sheets in the vicinity of the rivet due to material stirring and mixing. The vanishing of insulation layers can be observed in the simulation result in Figure II.4.1.2.15(b). Moreover, as illustrated in Figure II.4.1.2.15(a), the steel rivet remained undeformed after the friction-riveting process, indicating the validity of assuming a rigid rivet in the modeling. Based on this comparison, it can be concluded that the model was validated in terms of the material morphology.

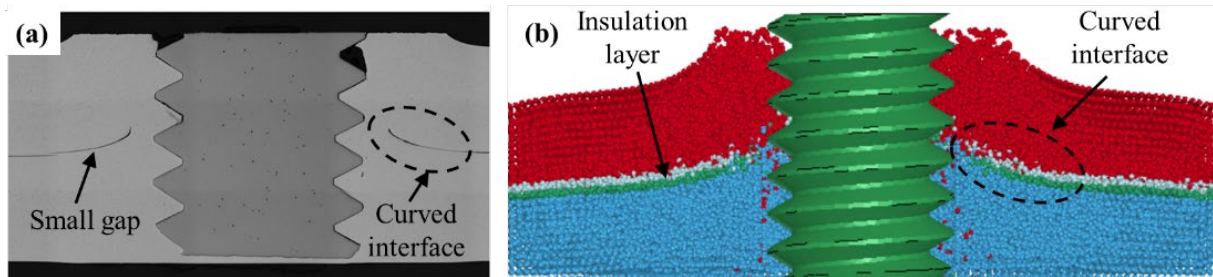


Figure II.4.1.2.15. Central cross-sectional images of friction-riveted joint from (a) experiment and (b) process modeling. Source: PNNL.

Model-predicted temperature distributions at different friction-riveting processing times are given in Figure II.4.1.2.16. In the initial stage (~10 seconds), shown in Figure II.4.1.2.16(a and d), the temperature was mainly developed in the top sheet because of the existence of the insulation layers. After the rivet penetrated the insulation layers (~20 seconds), shown in Figure II.4.1.2.16(b and 3), the temperature started to elevate and propagate in the bottom sheet. In the final stage (~30 seconds) shown in Figure II.4.1.2.16(c and f), the temperature in the bottom sheet was higher than the temperature in the top sheet because the majority of the heat was generated from the bottom sheet. A maximum temperature of around 452°C was reached in the bottom plate, which is 77% of the AA6061 melting point. The temperature distribution is asymmetric around the rivet, and the temperature is lower on the side plate because of the extra heat conduction therein.

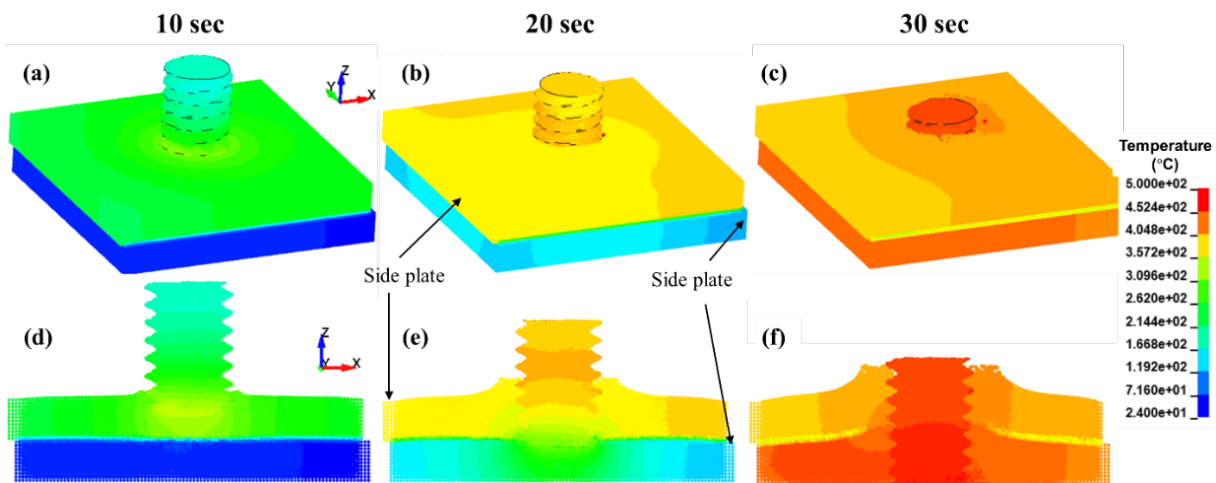


Figure II.4.1.2.16. SPH modeling predicted temperature distributions for isometric view (top row) and central cross-sectional view (bottom row) after 10 seconds (a and d), 20 seconds (b and e), and 30 seconds (c and f) processing time. Source: PNNL.

Figure II.4.1.2.17(a–b) shows the plunge force and temperature comparisons between experimental measurements and model predictions, respectively. The simulation results generally agree with the experimental data. Some discrepancies can be observed from a rivet plunging depth 0 mm to 2 mm, which may be caused by specific material strain-hardening parameters used in the model. However, when strain continued to develop in the Al sheets and the strain-hardening effect was saturating, these discrepancies became less prominent. In Figure II.4.1.2.17(b), the bottom plate temperatures developed slower than the temperature in the top sheet, which demonstrated the existence of the small gap between Al sheets during friction-riveting and the validity of assuming the insulation layers in the SPH model.

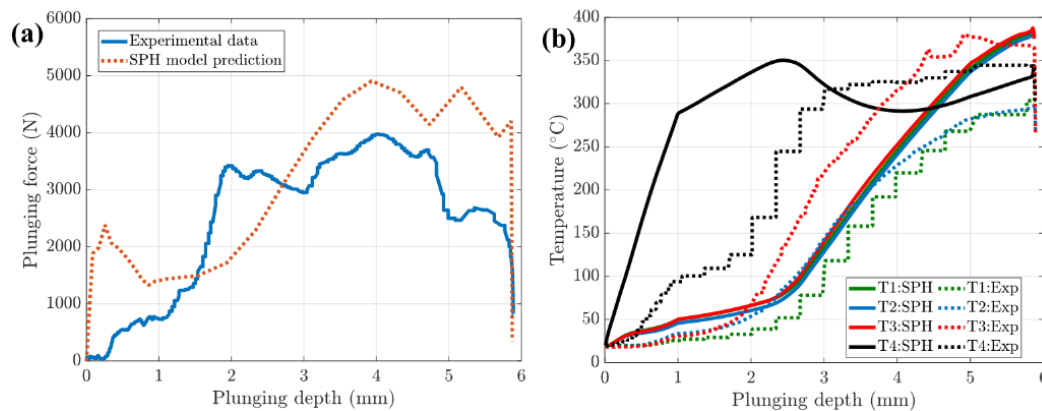


Figure II.4.1.2.17. Validation of SPH model using experimental data: (a) plunge force and (b) multi-point temperature. Source: PNNL.

After validating the SPH model, the model-predicted equivalent plastic strain distributions on the joint central cross-section are shown in Figure II.4.1.2.18. Severe plastic deformation (strain $>1000\%$) occurred along the sheet-rivet interface due to the rivet rotation and plunging. The large deformation region shown in red in Figure II.4.1.2.18(b), together with the HT in Figure II.4.1.2.16(c), could lead to material mixing and grain refinement due to dynamic recrystallization. This also explains why the small gap between Al sheets vanished in the vicinity of the rivet.

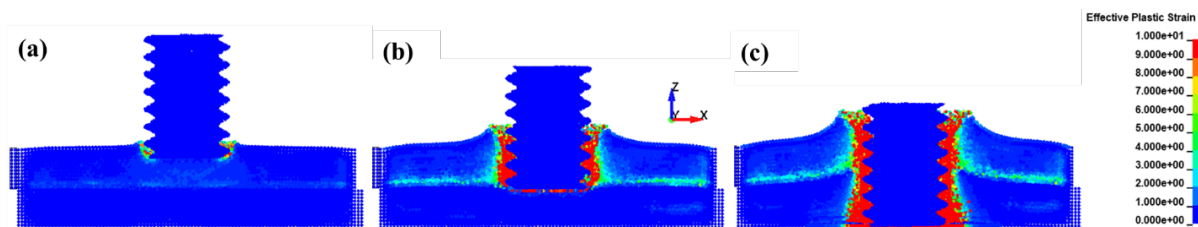


Figure II.4.1.2.18. Central cross-sectional distribution of equivalent plastic strain at (a) 10 seconds, (b) 20 seconds, and (c) 30 seconds of processing time. Source: PNNL.

Conclusions

The conclusions from surface treatments can be summarized as follows: (a) The LSS of AA6061-CFRPPA joints can be improved by 315% through plasma treatment of both the thermoset adhesive tape and substrate surfaces. (b) Plasma treatment of both the NBR51-lignin60 adhesive film and substrates can also result in a 40% improvement in the LSS of AA6061-CFRPA66 joints. (c) Laser-surface treatment with optimized parameters increased the LSS of AA5052-CFRPA66 joints by 37% and that of AA6061-AA6061 joints by 81%, respectively, when compared to the as-received joints. (d) Microscale numerical modeling demonstrated that interfacial voids play a critical role in joints with weak interfaces due to high-strain localization near voids and the resultant damage coalescence.

Novel adhesive development led to greater than a 100% increase in LSS by the inclusion of nanoparticles and reinforcing fillers, which improved lignin distribution throughout the adhesive. ABL adhesive with optimized nanoparticle and filler loading reached 90% LSS performance compared to an epoxy-based commercial automotive adhesive. A computational framework was developed to further elucidate the mechanisms responsible for LSS improvement using the optimized ABL adhesive. It was found that the reinforcing fillers could deflect a propagating debond crack, thereby creating a barrier to failure and corresponding improvement in joint performance.

The HiVe riveting process has been readily applied to Al-Al and dissimilar Al-steel systems. A thorough characterization study of the bonding interfaces was completed with assistance from the APS at ANL and molecular dynamics simulations at PNNL. With an understanding of the bonding behavior, finite element modeling was used to design new backing dies for specific use with HiVe clinching of third-generation AHSS stackings. Parallel to the modeling effort, long-term fatigue studies were completed using Al-Al systems, which showed remarkable improvement of similar material stackings with commercially available joining systems, namely clinch and SPR. Multimaterial stackings of DP steel and Al sheets were joined using the HiVe rivet configuration and exhibited lap-shear performances in the 12–14kN maximum loading range.

The conclusions from HFR can be summarized as follows: (a) The fatigue life of surface-treated (plasma + tape adhesive) HFR joint was significantly improved compared to HFR without adhesive. The number of fatigue cycles was 6–10 times higher for low-to-high-stress levels. (b) The HFR process was successfully transferred from a Manufacturing Technology, Inc. FSW machine to a Haas Automation, Inc. Computer Numerical Control machine for exploring the process parameter with a rotational speed up to 10000 revolutions per minute. (c) The highest load-carrying capacity of the HFR 3T joint configuration of steel-Al-steel (DP590-AA6061-DP590) was 10.3kN (joint performed in Haas Automation, Inc. Computer Numerical Control machine) compared to previously reported 9.1kN (performed in Manufacturing Technology, Inc. FSW machine), indicating the parameter effect of joint performance improvement. (d) The SPH model successfully predicted the material flow and process temperature during the HFR process.

Key Publications

1. Das, H., K. S. Kappagantula, A. Srivastava, P. Upadhyay, J. F. dos Santos, and Md. Reza-E-Rabby, 2023, "Embedded anchoring of multimaterial assemblies by friction-riveting process," in Hovanski, Y., Y. Sato, P. Upadhyay, A. A. Naumov, and N. Kumar (Eds.), *TMS 2023: FSW and Processing XII*. The Minerals, Metals, & Materials Series, Springer, Cham. pp. 149–156. https://doi.org/10.1007/978-3-031-22661-8_14.
2. Kamath, R., J. Thomas, S. Niverty, B. Schuessler, A. Chih-Pin Chuang, V. Joshi, and D. Singh, 2024, "Ex-situ synchrotron x-ray diffraction mapping of Al-Al and Al-steel joints formed using the novel HiVe process," *2024 TMS Annual Meeting & Exhibition*, 3–7 March 2024, Orlando, FL, USA (accepted).
3. Kanbargi, N., D. Hoskins, S. Gupta, Z. Yu, Y. Shin, Y. Qiao, D. R. Merkel, C. C. Bowland, N. Labbe, K. L. Simmons, and A. K. Naskar, 2023, "A renewable lignin-based thermoplastic adhesive for steel joining," *Eur. Polym. J.*, 189, 111981. <https://doi.org/10.1016/j.eurpolymj.2023.111981>.
4. Qiao, Y., E. K. Nickerson, T. J. Roosendaal, J. L. Ramos, and K. L. Simmons, 2023, "Effects of plasma treatment with gradient speeds inspired by spiderweb on mode I fracture of adhesively bonded metal-CFRTP joints," *2023 SAMPE Conference*, 17–20 April 2023, Seattle, WA, USA.
5. Qiao, Y., S. Ko, A. Samanta, Y. Shin, D. R. Merkel, A. Guzman, J. L. Ramos, and K. L. Simmons, 2023, "A microscale numerical investigation of internal and interfacial void defects in adhesive on failure behavior of adhesively bonded materials with rough surfaces," *ASME Aerospace Structures, Structural Dynamics, and Materials (SSDM) 2023 Conference*, 19–21 June 2023, San Diego, CA, USA.

6. Qiao, Y., Y. Shin, J. L. Ramos, M. H. Engelhard, R. J. Seffens, D. R. Merkel, and K. L. Simmons, 2024, "Plasma treatment on both adhesive tape and adherends for significantly enhanced CFRTP-related adhesive joints," *Appl. Surf. Sci.*, 649, 159092. <https://doi.org/10.1016/j.apsusc.2023.159092>.
7. Qiao, Y., R. J. Seffens, E. K. Nickerson, T. J. Roosendaal, D. R. Merkel, Y. Shin, J. L. Ramos, S. Ko, A. Samanta, M. R. Pallaka, A. Ortiz, and K. L. Simmons, 2023, "A study of adhesive bonding in metal-metal, metal- CFRP, and CFRP-CFRP material combinations under shear deformation: Fracture morphologies and damage mechanisms," *Int. J. Adhes. Adhes.*, 127, 103511. <https://doi.org/10.1016/j.ijadhadh.2023.103511>.
8. Qiao, Y., Y. Shin, M. R. Pallaka, E. K. Nickerson, D. R. Merkel, R. J. Seffens, A. Ortiz, L. J. Ramos, and K. L. Simmons, 2023, "Plasma surface modification coupled with thermal and step-over distance effects on significant fracture improvement of adhesively bonded metal-CFRTP dissimilar materials," *Compos. Sci. Technol.*, 232, 109833. <https://doi.org/10.1016/j.compscitech.2022.109833>.
9. Schuessler, B., D. Ramirez-Tamayo, L. Li, A. Soulami, S. Niverty, X. Ma, D. Herling, V. Joshi, 2023, "Enabling multimaterial joining in lightweight automotive structures using novel high-velocity riveting process," *2023 TMS Annual Meeting & Exhibition*, 19–23 March 2023, San Diego, CA, USA.
10. Schuessler, B., L. Li, K. Chaitanya-Pitike, S. Niverty, A. Soulami, D. Herling, V. Joshi, 2024, "Characterization of multimaterial joints formed via high-velocity riveting," *2024 TMS Annual Meeting & Exhibition*, 3–7 March 2024, Orlando, FL, USA (accepted).
11. Schuessler, B., D. Ramirez-Tamayo, S. Niverty, L. Li, A. Soulami, V. Joshi, "Joining of AA6061-T6 sheets via a high-velocity riveting (HiVe) process," *Nat. Comm.*, drafted for future submission.
12. Shin, Y., Y. Qiao, N. Yelin, J. L. Ramos, E. K. Nickerson, D. R. Merkel, and K. L. Simmons, 2023, "Interfacial bond characterization of epoxy adhesives to aluminum alloy and carbon fiber-reinforced polyamide by vibrational spectroscopy," *Surf. Interfaces*, 42(A), 103346. <https://doi.org/10.1016/j.surfin.2023.103346>.
13. Soulami, A., L. Li, K. Chaitanya-Pitike, B. Schuessler, K. Balusu, S. Niverty, and V. Joshi, 2024, "Multiscale modeling to investigate the deformation and bonding mechanism during joining of multimaterials by high-velocity riveting," *2024 TMS Annual Meeting & Exhibition*, 3–7 March 2024, Orlando, FL, USA (accepted).
14. Srivastava, A., H. Das, D. Ramirez-Tamayo, L. Li, M. Pole, B. Gwalani, A. Soulami, J. F. dos Santos, K. S. Kappagantula, and Md. Reza-E-Rabby, 2023, "Extent of interlocking and metallurgical bonding in friction-riveting of aluminum alloy to steel," *Int. J. Adv. Manuf. Technol.*, 128(7), 2899–2911. <https://doi.org/10.1007/s00170-023-12111-8>.
15. Yu, Z., N. Kanbargi, S. Gupta, Y. Shin, Y. Qiao, C. C. Bowland, D. R. Merkel, K. L. Simmons, and A. Naskar, 2023, "ABL thermoplastic Rubber Adhesive for Enhanced Metal-to-Metal Joining," *Polym. Compos.*, Early View published March 6, 2024. <https://doi.org/10.1002/pc.28258>.

References

1. Miles, M., S.-T. Hong, C. Woodward, and Y.-H. Jeong, 2013, "Spot-welding of aluminum and cast-iron by friction bit joining," *Int. J. Precis. Eng. Manuf.*, 14(6), 1003–1006. <https://doi.org/10.1007/s12541-013-0133-8>.
2. Kim J., H. Lee, H. Choi, B. Lee, and D. Kim. "Prediction of load-displacement curves of FDS and RIVTAC joints between dissimilar materials using artificial neural networks," *J. Manuf. Process.*, 57, 400–408. <https://doi.org/10.1016/j.jmapro.2020.06.039>.

Acknowledgements

The authors from PNNL recognize Y. Qiao, Y. Shin, A. Ortiz, J. Ramos, E. Nickerson, S. Ko, A. Samanta, and D. Merkel for the surface treatment work; Z. Yu and N. Kanbargi for the novel adhesive work; B. Schuessler, M. Rhodes, R. Seffens, S. Niverty, A. Guzman, and V. Joshi for the HVR/HiVe work; Md. Reza-E-Rabby, A. Srivastava, H. Das, M. Pole, and K. Kappagantula for the HFR work; and A. Soulami, L. Li, and D. Ramirez-Tomayo for the computational simulations.

The co-PI at ANL would like to acknowledge J. Thomas, R. Kamath, and A. Chuang for their assistance in conducting the APS experiments and data analysis. This research used APS resources, a U.S. Department of Energy-Office of Science (DOE-SC) User Facility, which is operated by ANL under Contract No. DE-AC02-06CH11357.

II.4.1.3 Solid-State Joining of Multimaterial Autobody Parts Toward Industry Readiness (Pacific Northwest National Laboratory and Oak Ridge National Laboratory)

Piyush Upadhyay, Co-Principal Investigator

Pacific Northwest National Laboratory
Energy Processes and Materials Division
900 Battelle Blvd.
Richland, WA 99352
E-mail: piyush.upadhyay@pnnl.gov

Yong Chae Lim, Co-Principal Investigator

Oak Ridge National Laboratory
Materials Science and Technology Division
One Bethel Valley Rd.
Oak Ridge, TN 37830
E-mail: limy@ornl.gov

Christopher Schooler, DOE Technology Development Manager

U.S. Department of Energy
E-mail: Christopher.Schooler@ee.doe.gov

Start Date: October 1, 2020
Project Funding: \$116,600

End Date: September 30, 2024
DOE share: \$116,600

Non-DOE share: \$0

Project Introduction

PNNL, ORNL, and ANL are teaming to further advance and mature friction-based solid-state joining technologies toward industry readiness for the high-volume production of multimaterial autobody structures. Two solid-state joining technologies—friction-self-piercing rivet (F-SPR) and friction-stir-linear welding (FSLW)—have been under development at PNNL, ORNL, and ANL and have been proven to apply to a wide range of material stack-ups at the laboratory coupon-level. We intend to overcome identified technical barriers related to robustness, joint function to process correlation, and equipment scale-up to sufficiently advance joining technologies for industry adoption with support from a partnering OEM, Honda R&D Americas, and a material supplier, Arconic Inc.

The ability to join dissimilar materials with specific properties is critical for lightweight multimaterial design. An approach to achieving this goal in a BIW construction is replacing the steel passenger cage with an appropriately designed stamped Al assembly and using CFRCs to stiffen advanced-high-strength steel in front-end and rear-end sections. This approach comes with two joining challenges: (1) the ability to effectively assemble dissimilar stamped Al subassemblies, and (2) the ability to join the Al subassembly to the advanced-high-strength steel and CFRC subassembly.

This need requires the development of technologies that can join different material sets in a cost-effective, robust manner, in addition to minor modifications to assembly lines that can meet high-volume demands. Friction-stir derived linear and spot-joining technologies provide solutions.

Objectives

The goal of this multi-laboratory, multi-year project is to mature two friction-based joining technologies and to demonstrate the joining of dissimilar Al components and Al-to-steel/CFRC subassemblies. The outcomes of this effort will include process parameters, machine control strategies, and a clamping and fixturing design, which are all necessary to advance the FSLW and F-SPR joining methods from the laboratory-scale plaque and coupon levels to component-level demonstrations geared toward high-volume production.

Approach

PNNL and ORNL are leveraging two friction-stir-based joining processes—FSLW and F-SPR—to develop and demonstrate multimaterial joining so that they can be used for a relevant automotive component assembly. The material stacks to be joined and characterized in this project for both processes in the third year of this project are shown in Figure II.4.1.3.1. The materials, their temper, thicknesses, and configurations have evolved from last year’s report based on the feedback provided by participating OEM.

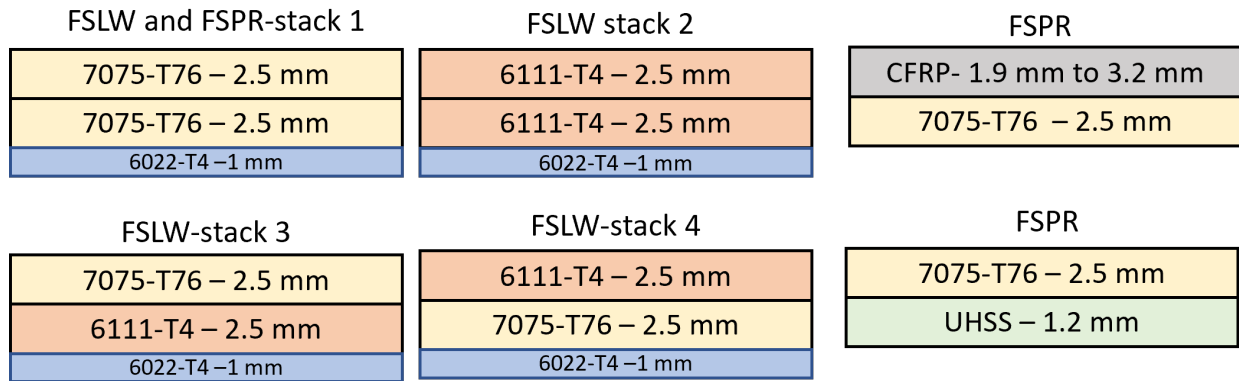


Figure II.4.1.3.1. Material arrangements for the four material stacks to be joined and characterized. Source: PNNL.

The overall tasks to be performed each year and their interactions, as illustrated in Figure II.4.1.3.2, are:

- Linear (short stitches and long continuous welds): FSW of dissimilar Al alloys
- Spot-welding: spot/tack welding for Al structures before FSLW
- F-SPR: spot-welding of Al-CFRC and Al to ultra-high-strength steel (UHSS).

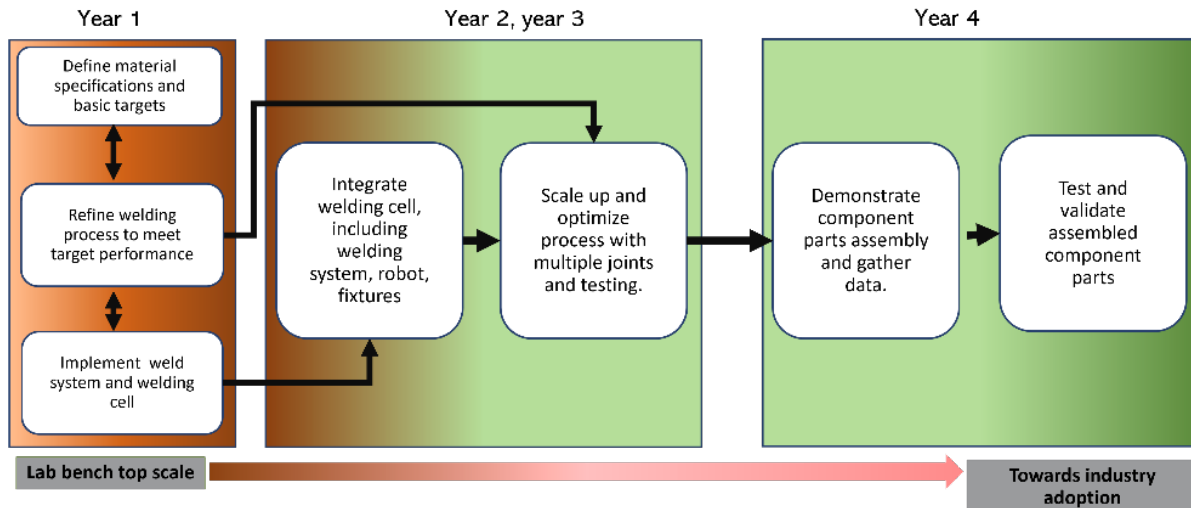


Figure II.4.1.3.2. Overview of project approach. Source: ORNL.

The R&D activities during FY 2023 included further maturation of welding processes and implementation toward the ability to make complex welded joints in various additional configurations, including integration of welding cell and robotic systems.

Results

Friction-Stir Lap Welding Experimental (PNNL)

Since FY 2022, the focus of experimental tasks at PNNL has been to: (1) improve the FSLW joining process for better and more consistent mechanical properties, (2) assess tool life, and (3) prepare for industrial adoption readiness, including stamping demonstration and quality assurance assessments. Figure II.4.1.3.3 provides a summary of a data set obtained from lap-shear testing performed on four different FSLW on 3T stack-ups, as shown in Figure II.4.1.3.1. One-inch-wide lap-shear samples were extracted from 11-in.-long linear FSLW specimens performed on PNNL's robotic platform. Figure II.4.1.3.3(a) shows the load per unit weld width (length of the weld contained in the cut sample) vs. crosshead displacement for one test case for each of the four stack-ups. For all stack-ups, the joint strength far exceeded the minimum target of 375 N/mm at a welding speed of 1 m/min. To further improve the weld macrostructure, four variations of FSW tooling were also explored in FY 2023. The tool's geometric variations include pin thread and shoulder features. While complete characterization of the effects of tool geometric variations is underway, one of the tools with a coarser thread design seems to perform on par with our current baseline design. This may result in a lower extent of tool wear, but this is yet to be evaluated. Figure II.4.1.3.3(b) provides a column chart showing the LSS values.

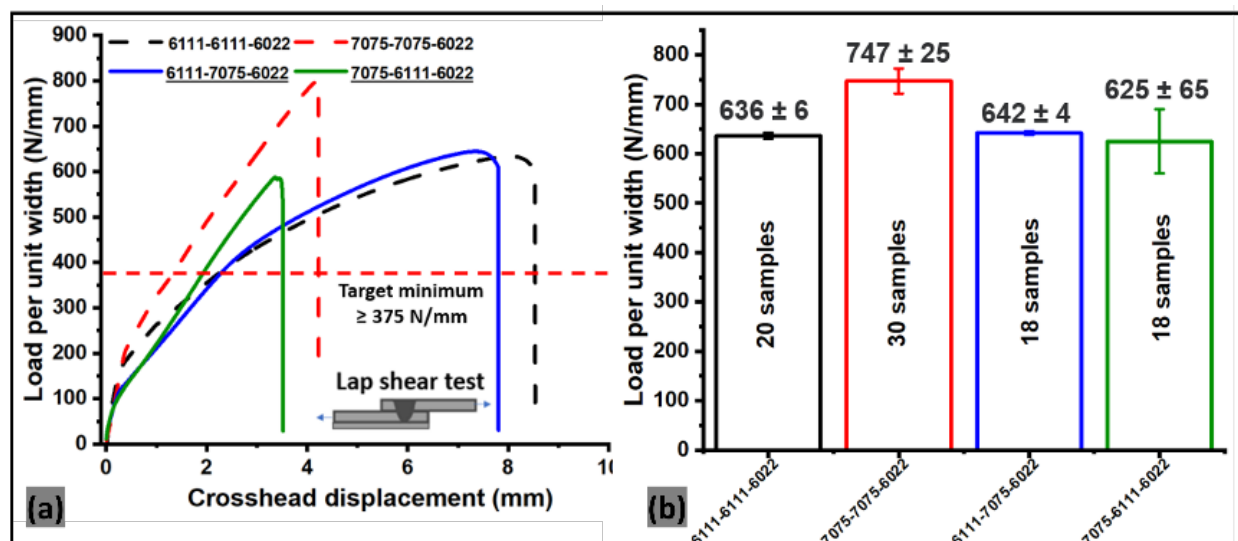


Figure II.4.1.3.3. (a) Load per unit width vs. crosshead displacement for all four stack-ups (e.g., the FSLW stack shown in Figure II.4.1.3.1) upon lap-shear testing. Dashed lines are indicative of top two sheets being dissimilar Al. (b) Column chart showing a summary of repeatability of LSS values for the four stack-ups along with error bars showing standard deviations. Source: PNNL.

A lap-shear performance comparison for the two tooling designs (e.g., baseline tool [51-1] vs. coarser thread [51-8]) is shown in Figure II.4.1.3.4(a-b). Efforts are also underway to hone-in on a parameter window that yields superior T-peel strength. Figure II.4.1.3.4(c) shows the initial data set collected after T-peel testing of 50-mm-long FSLW stitch using the two tool designs. A total of 40 samples were tested using the 51-1 tool, while three other samples have been tested with the 51-8 tool so far.

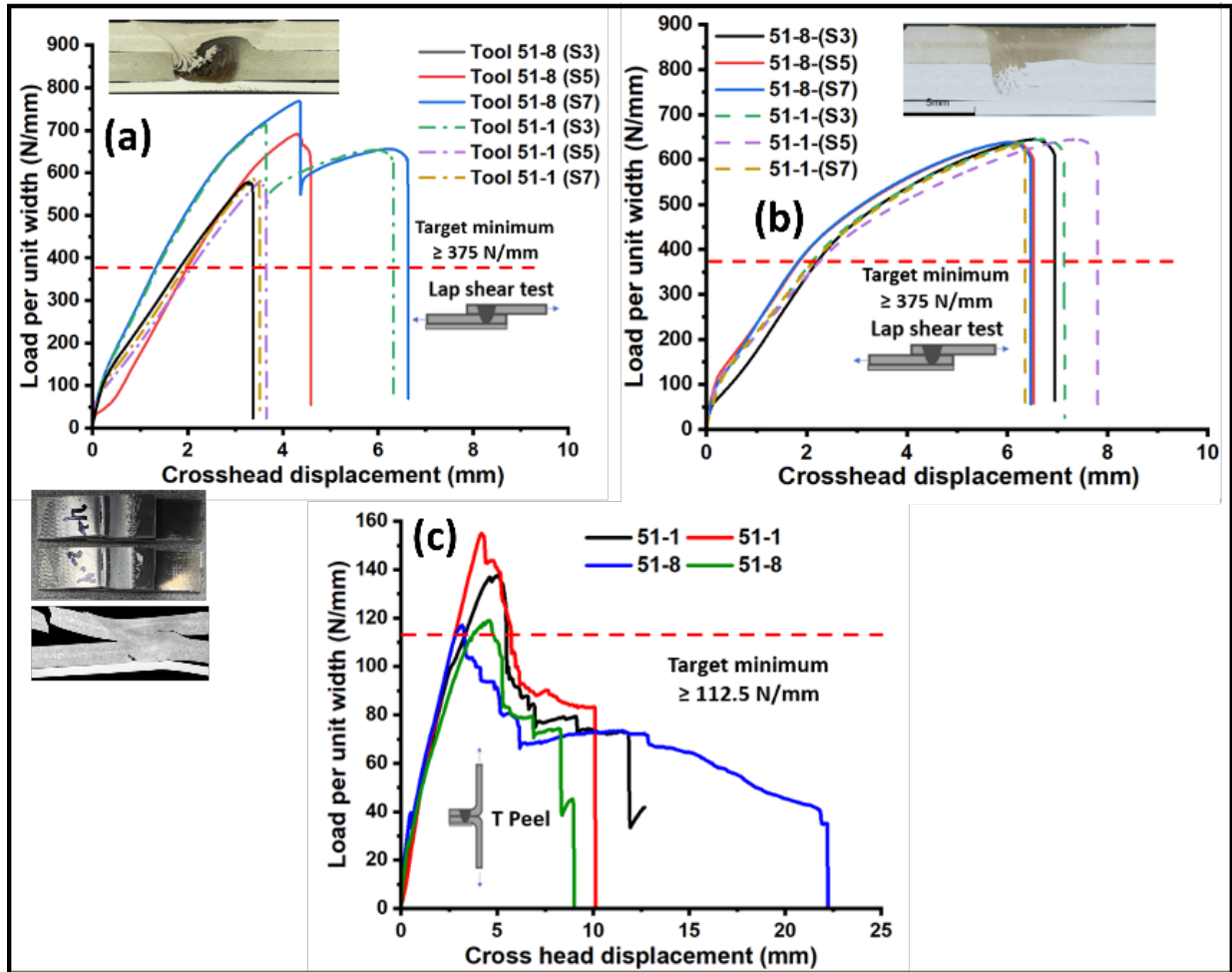


Figure II.4.1.3.4. (a) Load per unit weld width vs. crosshead displacement plotted for three samples each made with baseline tool (51-1) and coarser thread tool (51-8) in the Stack 3. (b) Load per unit weld width vs. crosshead displacement plotted for three samples each made with baseline tool (51-1) and coarser thread tool (51-8) in the Stack 4. Representative transverse cross-section is also shown for each case. Fractured sample for Stack 3 that broke out in the base metal is also shown. (c) Load vs. crosshead displacement for T-peel joints for Stack 1 using two tool designs are shown. Source: PNNL.

Building on the success in developing robotic welding parameters that exceeded lap-shear and T-peel strength for Stacks 1 and 2, we began to evaluate joints containing the top two sheets of dissimilar Al in FY 2023. Mixed long linear and stitch joints will be needed in the transition area between the front and back of an envisioned Al-intensive sedan. As seen in Figure II.4.1.3.1, the stack-up can either be with high-strength AA7075 as the top sheet (Stack 3) or be the reverse (i.e., high-ductility AA6111 as the top sheet—Stack 4).

After some process development, parameters that resulted in well-consolidated weld crowns were developed for dissimilar stacks. Using plunge parameters (e.g., revolutions per minute [rpm], Z velocity, commanded depth, tilt angle) from Stacks 1 and 2 as initial starting points, 12 unique runs were evaluated to obtain a first order understanding of dissimilar Al 3T joining. After development, a good workable window to produce well-consolidated welds was determined. Plunge-in parameters were primarily governed by the top sheet material, while plunge depth and rpm were only slightly different from similar systems (Stacks 1 and 2). The fracture modes for Stacks 3 and 4 are also primarily governed by the top sheet. For example, in Stack 3 (when AA7075 is the top sheet), the fracture occurs typically from the second sheet at the edge of the weld nugget, while in Stack 4 (with AA6111 as the top sheet), the fracture occurred in the base metal. In addition, the variability in

joint strength is also similarly governed by the top sheet material. For instance, while the standard deviation of Stacks 2 and 4 is within 2–5%, and the standard deviation for Stacks 1 and 3 are 5–10%, respectively. Additionally, similar welds (Stacks 1 and 2) exhibit a greater extent of elastic elongation upon lap-shear testing compared to the dissimilar stacks. The top sheet also governs the stiffness values of the plastic regime (when AA7075 is on top, the stiffness of the joint is much higher than when AA6111 is on top).

Significant progress was made in FY 2023 in understanding the FSLW tool life. To have a viable pathway toward commercialization, the length of the weld up to which the tool can perform at its optimum capacity for a given welding condition needs to be well understood. While some estimates can be obtained from open literature, there has been no prior work that has generated data on the 3T stack-up containing a total of 5-mm-thick stack-up in a hardened 7xxx sheet stack at a high welding speed. Additionally, it is expected that the commercial use of FSLW employs a much stiffer robot and appropriate thermal management. To mimic these conditions, the tool life study was conducted in PNNL's Gantry system, which contains a tool holder cooling system that is significantly stiffer than the available robot and is fully instrumented.

A total of four base FSLW tools (three tools made of H13 tool steel and one tool made of MP159) were used for the tool life study this FY. Each tool was imaged in as-received condition using a Keyence microscope capable of measuring three-dimensional tool geometrical features at a micron-scale. A fixed welding-parameter of 1 m/min. at 800 rpm and a 2 degree tilt angle was then used to perform an 800-mm-long linear 3T FSLW for Stack 1. An example of the linear welding runs made is shown in Figure II.4.1.3.5. Thus far, a total of 45-m-long linear welds have been made toward the tool life work. Progressive raw images and color maps showing the tool's top-view indicating the Z height of the tool features at various weld lengths are also shown in the figure. Fiducial markings were applied to the tool to ensure that regions were matched after successive welding runs. Several dimensions of tool pin features were tracked over the length of the weld, including pin tip, pin edge, and inner and outer scrolls, as observed in Figure II.4.1.3.6.

A few patterns have begun to emerge. H13 tools failed with pin shearing after a weld length of approximately nine meters. MP159 tooling did not fail up to 15m of linear weld. The Keyence 3D tool measurements thus far indicate that approximately 40% of the scroll height (as opposed to 2.5% in MP159 at the same weld length) from the shoulder gets worn out after nine minutes of welding. There is minimal wear in the total pin. The H13 tool life with the current design appears to be limited by pin shearing caused by HT cycling loading at the shoulder-pin interface. Modeling efforts discussed following this section are attempting to estimate the extent of tool life improvement with an optimized tool geometry that reduced the stress concentration. Limited data collected on MP159 shows significantly less amount of wear. Additionally, tool shearing did not occur even after 15 minutes of linear welding. Nevertheless, some wear in the tool features was noticed, specifically after 15 minutes of welding. MP159 tool lost 0.5% of pin length and 10% of shoulder scroll height after 15 minutes of 3T FSLW. These results have been discussed with our industry partner, and we will continue to understand the tool life in various conditions that can be anticipated in industrial-manufacturing settings, including robotic platforms, and understand the effect of worn tools on mechanical joint performance. Strategies, including tool change out frequency and dressing (akin to spot-welding), can also be explored.

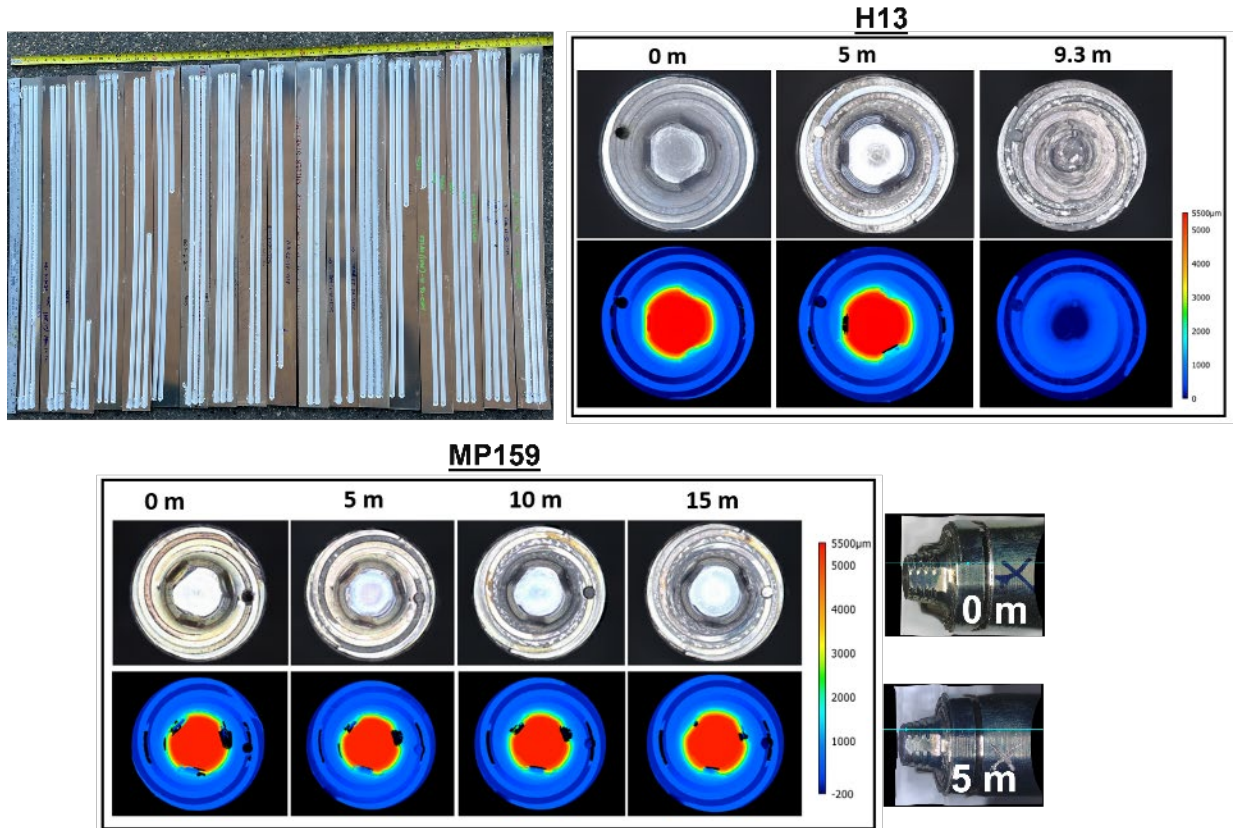


Figure II.4.1.3.5. Multiple lines of FSLW in 3T configurations that were run for the tool like study in Stack 1 (top left). Top-view of FSLW tool at various weld length of 3T FSLW for H13 and MP19 tooling. The color map on the bottom three pictures represent the Z height from the lower feature providing a snapshot of wear over the weld length. Note that at 9.3 mm, the pin was sheared off for H13. Example images of side view of the tooling is also shown. Source: PNNL.

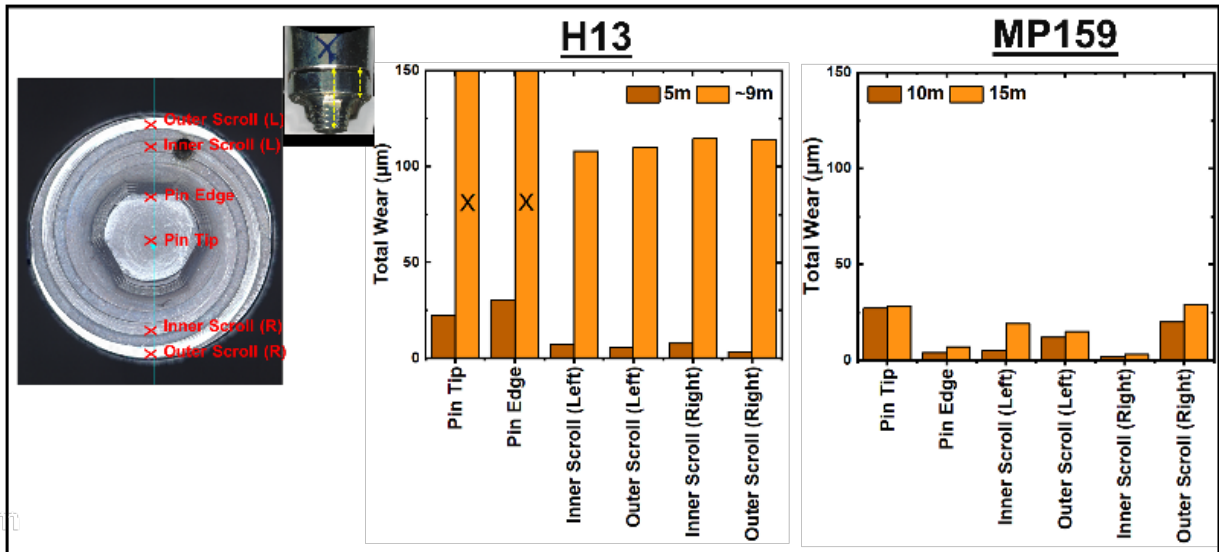


Figure II.4.1.3.6. Several geometric features tracked during the tool life study are shown on the left. The bar chart for H13 and MP19 tool provides a snapshot of total wear measured in this study. Source: PNNL.

The ability to ensure weld quality in a production environment is another important aspect for an emerging joining technology. To this end, we evaluated a method that can correlate the volume of weld defects to the process forces generated during robotic welding. Figure II.4.1.3.7(a) and Figure II.4.1.3.7(b) show images extracted from an X-ray tomography (XRT) video output of Stack 2 joints that were made at two values for the rpm with (a) a significant wormhole defect, and (b) a minimal defect. A large amount of time series data set containing X, Y, and Z forces experienced by the tool during 3T FSLW was collected using a high-speed data acquisition system that was developed and reported previously. Frequency domain analysis of this data set revealed that welds containing large defects exhibit peak amplitude at a frequency that corresponds to half of the tool's rpm, while those with minimal to no defects show a peak coincident with the tool's rpm. These results indicate that with further work in analyzing the vast amount of data collected during this project. Additionally, there is potential to develop an inline a process forces-based nondestructive examination tool capable of predicting weld quality.

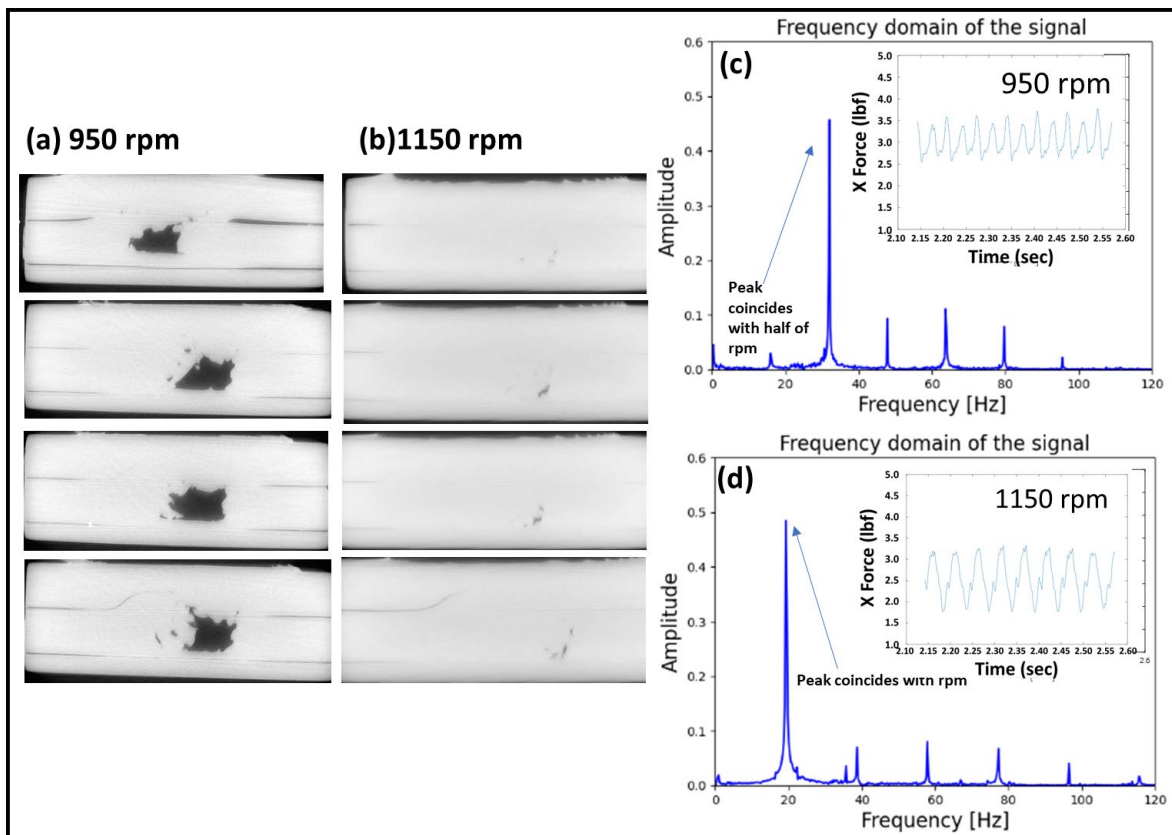


Figure II.4.1.3.7. Screen shots from XRT videos revealing the joint cross-section of Stack 2 at 1m/min. made at two different rpm containing (a) a large AS defect, and (b) a small defect. (c–d) Frequency domain plots of Z-force time series data showing peaks at two distinct frequencies. Source: PNNL.

Friction-Stir Welded Joint Strength Modeling (PNNL)

The mechanical performance, including strength and energy absorption of components assembled by FSLW, relies not only on various features of the joint structure, as previously reported, but also on the configuration of the weld seam. Configurations in context refers to the choice of using short stitches with fixed gaps between welds, longer linear or curvilinear joints, and the position of the start and stop of the joints and sides of the weld. This subsection presents results demonstrating the simulation model's proficiency in predicting strength for different weld configurations. Furthermore, this report also contains results from modeling efforts aimed at predicting tool life.

Data from strength testing a U-Peel/KSII welded joint in a 3-sheet stack-up (AA7055-AA7055-AA6022) was used to confirm the accuracy of the component-scale strength prediction model. Figure II.4.1.3.8 shows the two-weld configurations and their respective strength results. In the first case, as depicted in the insert image of Figure II.4.1.3.8(a), there are four weld stitches—two in the length/longitudinal direction and two in the transverse direction. The second case, shown by the inserted image in Figure II.4.1.3.8(b), has four longitudinal stitches. Both experimental and simulation results indicate that the strength per unit weld length of Seam #2 is higher by 30 N/mm, emphasizing the effectiveness of shorter stitches in strengthening the joint. However, it is noteworthy that the displacement-to-failure of Seam #1 is greater, indicating that joints with longer stitches are more ductile. Simulated strength in both cases deviates from the average of the test results by less than 15%. Predictions of the displacement-to-failure differ from test results by around 0.5 mm to 1 mm. These findings validate the strength predictions of the developed model at the component-scale. Additionally, the model's ability to assist in optimizing weld seam configurations has been successfully demonstrated.

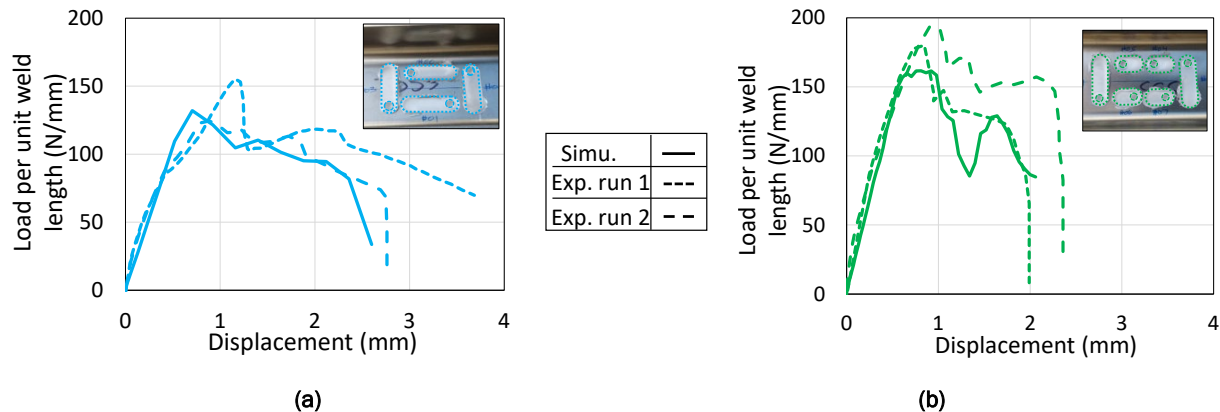


Figure II.4.1.3.8. Simulated load-displacement plots compared with experimental results from strength testing of U-Peel/KSII samples with FSW Seam Configuration (a) #1 and (b) #2. Inset figures show the weld configurations. Source: PNNL.

Predicting tool life requires a model to simulate stress concentrations in the tool during the process. A straightforward approach is employed to achieve this, and basic results are presented in this section. In this approach, the tool's geometry is precisely modeled using the finite element approach, though the force distributions on the tool are approximations. Based on previous studies, force distributions are estimated and calibrated to the net forces and torque on the tool measured in the gantry [3]. Figure II.4.1.3.9 shows the simulated stresses on the tool surface for a specific set of process parameters. Stresses in Figure II.4.1.3.9(a) were obtained when only traction forces (i.e., those contributing to the net torque) were applied to the tool. In this case, the highest stresses are observed at the corner of the thread on the pin closest to the shoulder. Stresses in Figure II.4.1.3.9(b) were obtained when applying only pressure (i.e., forces normal to the surface of the tool). In this scenario, the highest stresses occur at the base of the pin, where the pin is connected to the shoulder. This location aligns with the point directly in front of the tool in the transverse direction. As a result, this specific location changes with tool-rotation. Consequently, a particular material point undergoes cyclic loading, representing a fatigue loading. Consistent with the model's predictions, experimental results also confirm that the tool fails either at the thread closest to the shoulder or at the base of the pin. This developed model enables the exploration of different tool geometries to minimize stress concentrations and enhance tool life. Furthermore, these cyclic stress concentrations can be used to predict tool life when incorporated into fatigue life models based on stress to number of cycle curves.

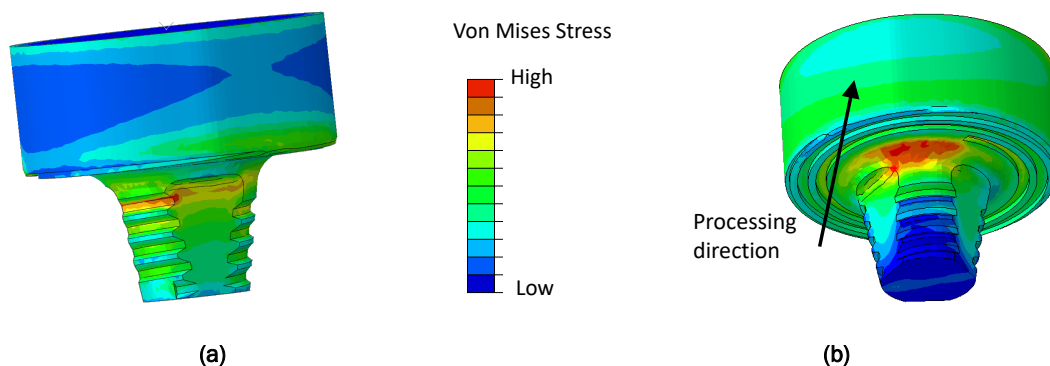


Figure II.4.1.3.9. Simulated stresses on the surface of the tool pin are obtained by applying (a) just the surface tractions and (b) just the pressure distributions normal to the surface. Source: PNNL.

F-SPR Process Development and Characterizations for Various Material Combinations (ANL, ORNL)

As a collaboration effort with PNNL for FSLW in an Al-Al tack spot joint, ORNL-developed and refined the F-SPR joining process for 7xxx Al–7xxx Al to develop a crack-free joint while maximizing the mechanical joint performances. From lap-shear tensile testing, the failure location was located at the bottom Al alloy of the joint, as reported in FY 2022. For this reason, we further investigated the microstructures and microhardness in collaboration with ANL.

HV tests conducted at ORNL showed an expected lowering in hardness as we move closer to the rivet in the HAZ compared to the AA7075 BM values. However, an unexpected increase in hardness in the thermomechanically affected zone (TMAZ-I) region of the joint cross-section was observed. It is also suspected that this is one of the contributors to the increased joint strength. The joint cross-section and hardness variation along it are shown in Figure II.4.1.3.10(a) and Figure II.4.1.3.10(b), respectively. A key determinant of the hardness/strength of the Al alloy system in question is the nature of the precipitates/dispersoids present [1], which are dependent on the thermal cycle experienced at a given location in the processed material. Therefore, with an aim of obtaining the precipitate/dispersoid characteristics in a sufficiently large voxel for multiple locations, SAXS experiments in transmission mode were conducted at beamline 20-ID-B, APS [2]. An X-ray beam with the size of $0.5 \text{ mm} \times 1 \text{ mm}$ and an energy of 21 keV was used to perform a line of measurements (~30) starting next to the rivet shank by the BM for the top and bottom plates with two different die designs. The experimental setup at the beamline is shown in Figure II.4.1.3.10(c). For each measurement location, sequential acquisition of USAXS, SAXS, and WAXS was performed using three separate detectors to cover at least four decades in q (reciprocal space vector), translating to a feature size range of angstrom to μm in real space. The data was pre-processed and stitched (USAXS+SAXS) to obtain a single $I(q)$ vs. q for a given sample using the Nika and Indra software packages in an Igor Pro environment. WAXS analysis was performed using the Irena software package in an Igor Pro environment. The WAXS patterns were used to identify the phases present in measurement locations circled in Figure II.4.1.3.11 (i.e., right next to rivet shank, TMAZ-I, HAZ, and BM). The major phases present were the Al (matrix) and MgZn_2 (precipitate) with a minor fraction of unidentified peaks, which are suspected to arise from other intermetallics (e.g., composed of AlCuFe), commonly seen in the AA7075 and will be probed into in detail following microscopy studies at ORNL to be conducted in FY 2024.

The USAXS spectra for the measurement locations are shown in Figure II.4.1.3.11(b). On the $I(q)$ vs. q plots, the larger mean feature sizes of the precipitates/dispersoids (e.g., thickness and length of MgZn_2) are seen as “knees” (marked using arrows) in the lower q region. The marked knees point to at least two precipitate populations, differing in composition and/or mean feature size, in all the locations. Further, the USAXS curves for BM and mid-HAZ locations are seen to have an additional “knee” marked using a red arrow; this observation provides a qualitative justification for the observation of higher hardness values in these regions.

An initial input of approximate particle size and shape is required for the quantitative SAXS analysis to obtain the precipitate size distributions for each population and will be investigated in detail following microscopy studies at ORNL to be conducted in FY 2024.

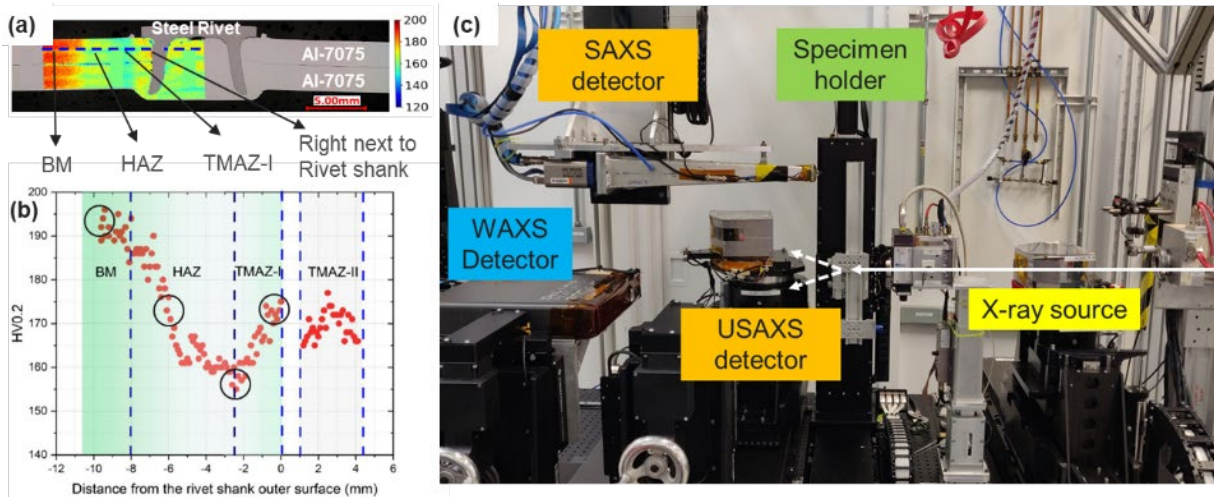


Figure II.4.1.3.10. (a) A macrograph of the FS-PR joint cross-section with the overlaid microhardness map. The key regions are also indicated on the joint cross-section (i.e., BM, HAZ, and TMAZ). (b) Microhardness profile corresponding to the locations marked by the blue dashed line in (a) and the representative locations, in which the USAXS and WAXS were analyzed and are marked in black circles. (c) USAXS+SAXS+WAXS setup in transmission mode at beamline 20-ID-B. The X-ray beam path is marked in white with a solid line showing the incident beam and dashed line showing a couple of scattered beams. Source: ORNL and ANL.

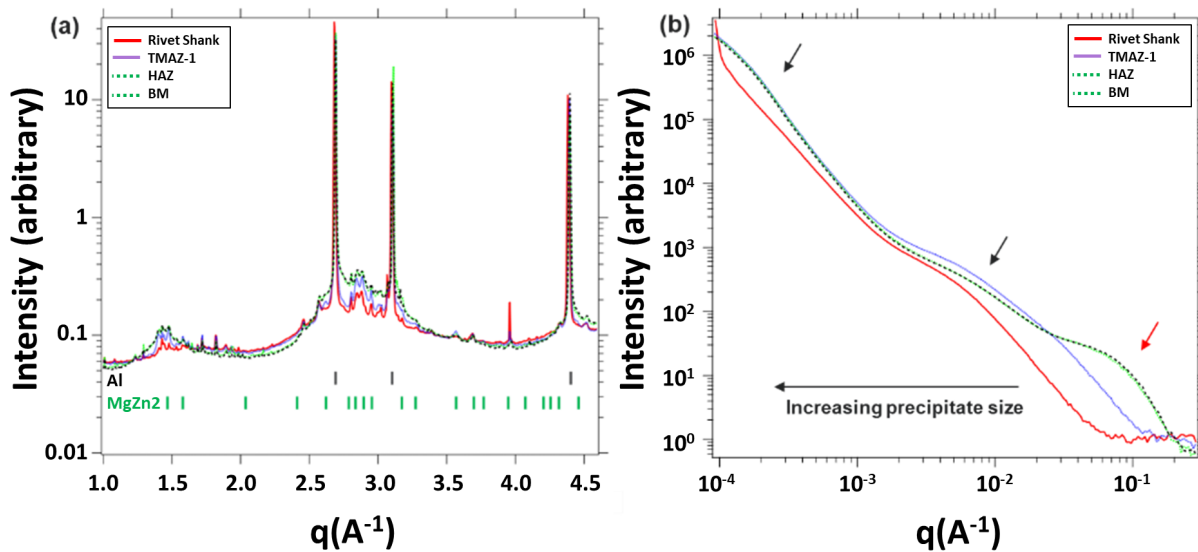


Figure II.4.1.3.11. (a) WAXS patterns from measurement locations marked, with the peak positions of the major phases (Al, MgZn₂) marked below the patterns. (b) $I(q)$ vs. q plots from the USAXS analysis for measurement locations with “knees” in spectra, which correspond to a precipitate/dispersoid population indicated using arrows. Note that a precipitate population “knee” in the lower q value corresponds to a higher value of mean precipitate size. Source: ANL.

ORNL further refined the F-SPR process for spot-joining of high-strength AA7055 to AA7055 from 2T to 3T configuration with different stacking orders. AA6022 was used as guided by industry partner. For the F-SPR

joints, the mechanical interlocking distance between the flared rivet and bottom sheet is critical for mechanical joint strengths. For the 3T joint, rivet leg length and die cavity dimensions were redesigned to ensure the die volume can accommodate the increased rivet volume (i.e., longer rivet for 3T). In general, it is recommended that rivet volume is equal to the die cavity volume to achieve high-quality of joint for F-SPR.

Figure II.4.1.3.12 summarizes the mechanical joint performances (i.e., lap-shear and cross-tension strength) of 2T and 3T configurations with different stacking orders. Overall, lap-shear joint strength of 3T configuration is 6–16% higher than the 2T condition because the effective cross-sectional joint area is increased for 3T compared to the 2T. Also, cross-tension strength for all 3T joints is 16–40% higher than the 2T case. Additionally, the average cross-tension strength for all 2T and 3T cases exceeds 30% of the averaged LSS suggested by our industry partner.

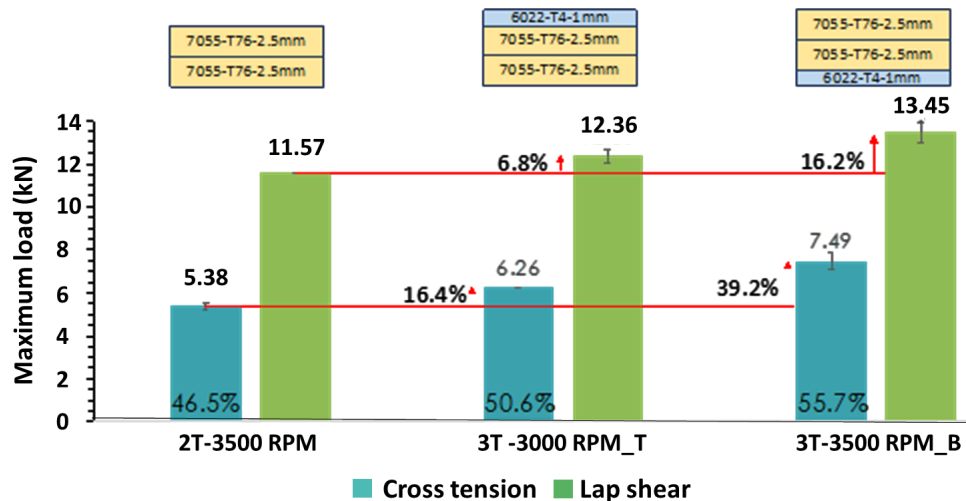


Figure II.4.1.3.12. Summary of averaged lap-shear and cross-tension joint strength of F-SPR AA7055 in 2T and 3T with different stacking orders. Source: ORNL.

After successful lab-scale F-SPR process development using the bench top machine at ORNL, we moved forward to scaling-up the joining process and joining component-level parts. A C-frame type welding head system, featuring an automated rivet feeding and clamping system and vacuum system, was developed and fabricated by the equipment manufacturer. This new system is more suited for a high-volume production environment and is more relevant to the industrial readiness of multimaterial joining in automotive applications. Initially, the team planned to setup and integrate the system at the Eagle Bend Manufacturing (EBM) facility, our Tier 1 supplier, because EBM has extensive technical knowledge and skills for robotic arms, system integration, and fixture designs that are needed for the assembly of automotive components. However, EBM has been experiencing a shortage of human resource and available robotic systems that are still ongoing due to the COVID pandemic, so EBM withdrew their participation for this project. As an alternative solution, the team installed and integrated a new welding system, multi-axis motion stages, and fixtures at ORNL, as shown in Figure II.4.1.3.13.

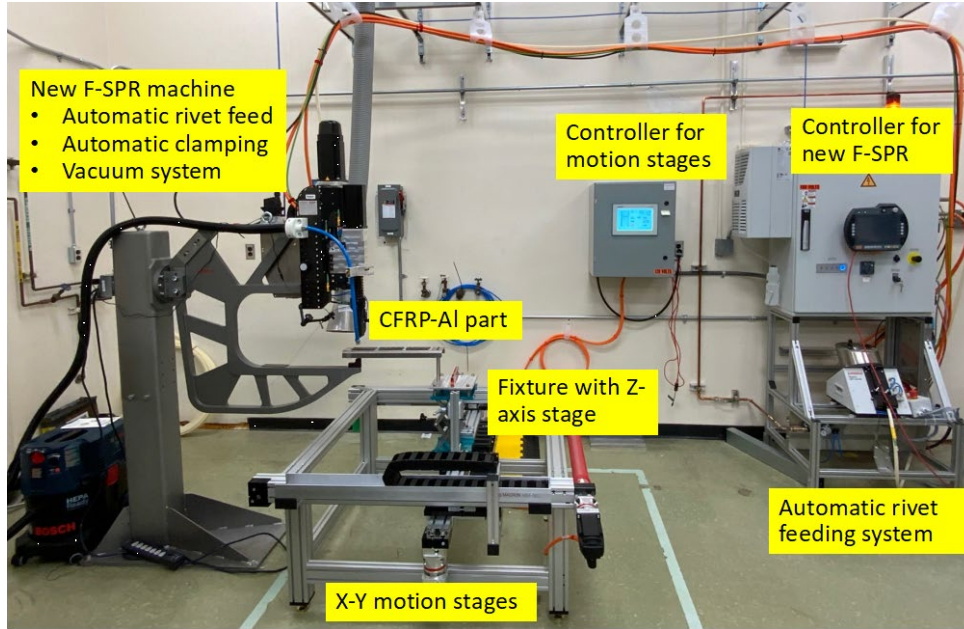


Figure II.4.1.3.13. A new integrated welding system includes C-frame welding head, multi-axis motion stages, and fixture for scale-up part-level joining with multiple joints. Source: ORNL.

After completing the new welding system integration, we evaluated the functionality and weldability of the new system using our selected multimaterials. Visual inspection was used to quickly assess the joint defect, especially cracking of low ductility materials. All joints showed the crack-free joint on 7xxx Al alloy due to the beneficial effect of frictional heat during joining process. Table II.4.1.3.1 summarizes the mechanical joint strengths of dissimilar material joints produced by the new system. Overall, comparable joint strengths were achieved for CFRC-AA7075 and AA7055-DP980. However, lower LSS for AA7055-AA7055 was found because of the rivet size and strength difference between the vendor’s rivet (diameter = 4.5 mm, length = 5.7 mm) and ORNL’s rivet (diameter = 7.2 mm, length = 6.0 mm).

Table II.4.1.3.1. Summary of Mechanical Joint Strengths of Multi-Materials to Validate Weldability of New System

Material combinations	CFRC – AA7075	AIA7055 - DP980	AA7055 - AA7055 (2T)
Averaged lap-shear failure load (kN)	5.13 ± 0.29	11.95 ± 0.3	6.96 ± 0.27
Averaged cross-tension failure load (kN)	–	4.79 ± 0.16	5..84 ± 0.26

Figure II.4.1.3.14 shows an overview of scale-up part-level joining by using the newly integrated welding system. Each weld position was programmed in the motion controller software. After the current weld is completed, the next weld position will be moved by the motion system. Figure II.4.1.3.14(a–b) present two examples of the 7xxx Al part (U-shape) level joining (i.e., 7xxx Al – 7xxx Al and CFRC – 7xxx Al). A full-scale stamped Al part was not available at the time of this project step due to delayed Al material acquisition in the stamping company. For this reason, we employed the U-shape Al part that was used for the previous project. In short summary, this demonstration simulates the multiple spot joints on the component part to aim for a high-volume production environment for automotive applications.

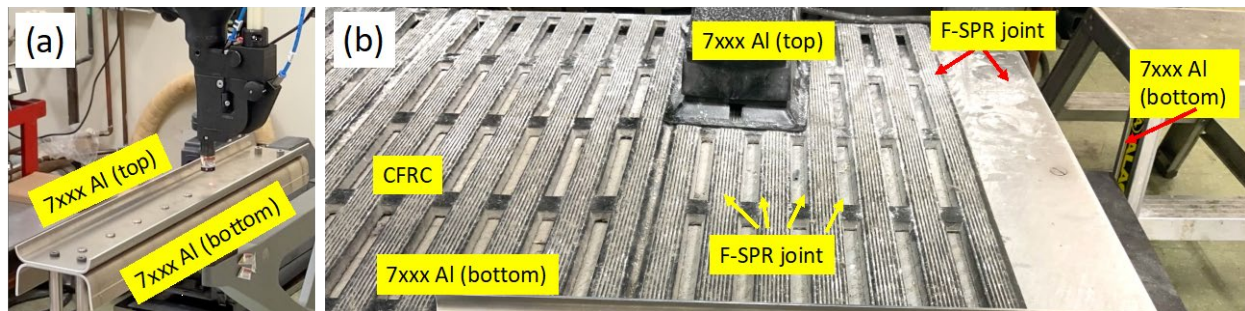


Figure II.4.1.3.14. (a) Overview of scale-up 7xxx Al – 7xxx Al part joining using the newly integrated welding system, (b) demonstration of Al-Al and CFRC-Al part joining with multiple joints. Source: ORNL.

To further demonstrate industrial viability of solid-state joining processes being developed in this project beyond coupon-level samples, we will use high-strength aluminum stampings as a demonstration platform for both aluminum-steel joining using F-SPR and 3T FSLW linear joints. Consequently, our laboratory team is collaborating with a stamping facility and a participating OEM to procure several stamped parts. This part features a three-dimensional region presenting various challenges for joining. Such challenges include the ability to effectively clamp the parts and demonstrate joining on sheets that may exhibit some degree of waviness and thickness variation introduced during the stamping process. Figure II.4.1.3.15 shows an extreme example of waviness. An initial FSLW trial on an early example of stamped AA7055 sheet showed the potential and the challenges of executing a FSLW, as observed in Figure II.4.1.3.15. A new batch of stamped parts is expected to arrive at the PNNL and ORNL in the coming months, and we anticipate beginning the development of processes for demonstrating FSLW and F-SPR joints within these stamped components.

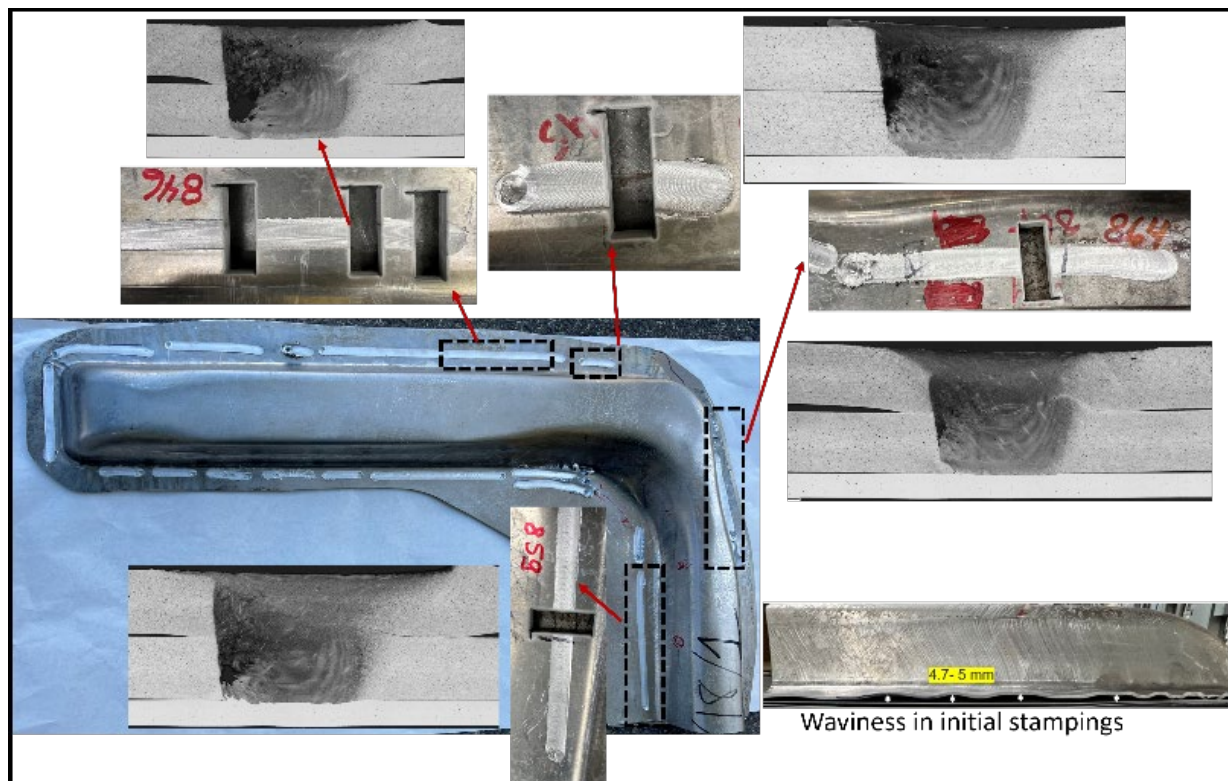


Figure II.4.1.3.15. Practice FSLW runs on an experimental stamping of AA7055 sheet. Several lines of short and long linear welds are shown along with corresponding joint cross-sections with varying degrees of weld defects. Source: ORNL.

Conclusions

This multi-laboratory project is aimed at maturing two solid-phase joining techniques to overcome several identified technological barriers toward enabling missed Al assembly, Al/CFRC, and Al/steel joining in high-volume applications. In FY 2023, the project team at PNNL (developing FSLW for 3T Al joints) and ORNL (developing F-SPR for 2T/3T material stacks) focused on further refining the joining technology, assessing tool life, ensuring quality assurance for high-volume manufacturing, and developing welding strategies for eventual demonstration in stamping.

In collaboration with ANL, AA7075 joints (2T) produced using F-SPR were assessed by USAXS-SAXS-WAXS. The results showed that the MgZn₂ was the major precipitate population in all the locations. The USAXS results qualitatively explained the higher hardness values of the BM and mid-HAZ regions. The F-SPR process was further refined for spot-joining of 7xxx Al – 7xxx Al from 2T to 3T configuration with different material stacking sequences. A crack-free 3T joint was achieved, which improved the mechanical joint strengths compared to the 2T case. The new welding system was setup and integrated with motion stages and fixtures for joining of scale-up component. Functionality and weldability of the new system were validated. Multiple F-SPR spot-joining on Al-Al and CFRC-Al parts were successfully demonstrated toward industry adoption.

Key Publications

1. Huang, H., Y. C. Lim, Y. W. Wang, Y. Li, and Z. Feng, 2023, “Crack-free joining of high-strength AA7055 sheets by friction-based self-piercing riveting with the aid of numerical design,” *J. Manuf. Mater. Process.*, 7(6), 216. <https://doi.org/10.3390/jmmp7060216>.
2. Li, Y., Y. C. Lim, and Z. Feng, 2024, “Effect of die design on joint formation and strength in friction self-piercing riveted AA7055-T76-AA7055-T76.” *J. Manuf. Process.*, under review.
3. Li, Y., Y. C. Lim, J. Chen, and Z. Feng, 2023, “The role of rotational speed on the joint strength of frictional self-piercing riveting AA7055-T76/AA7055-T76,” *Advances in Welding and Addictive Manufacturing* (Proceeding paper).
4. Lim, Y. C., H. Huang, Y. Wang, Y. Li, and Z. Feng, 2023, “Joining of high-strength low ductility AA7055 by F-SPR,” In Hovanski, Y., Y. Sato, P. Upadhyay, A. A. Naumov, and N. Kumar (eds.), *FSW and Processing XII. TMS 2023*. The Minerals, Metals, & Materials Series. Springer, Cham. https://doi.org/10.1007/978-3-031-22661-8_11.
5. Upadhyay, P., Y. C. Lim, et al., 2023, “Solid-state joining of multimaterial autobody parts toward industry readiness,” DOE Vehicle Technology Offices Annual Merit Review, 12–15 June 2023, Virtual.

References

1. Marlaud, T., A. Deschamps, F. Bley, W. Lefebvre, and B. Baroux, 2010, “Evolution of precipitate microstructures during the retrogression and re-ageing heat-treatment of an AlZnMgCu alloy,” *Acta Mater.*, 58(14), 4814–4826. <https://doi.org/10.1016/j.actamat.2010.05.017>.
2. Ilavsky, J., F. Zhang, R. N. Andrews, I. Kuzmenko, P. R. Jemian, L. E. Levine, and A. J. Allen, 2018, “Development of combined microstructure and structure characterization facility for *in-situ* and *operando* studies at the APS,” *J. Appl. Crystallogr.*, 51(3), 867–882. <https://doi.org/10.1107/S160057671800643X>.
3. Sorensen, C. D., and A. L. Stahl, 2007, “Experimental measurements of load distributions on friction-stir weld pin tools,” *Metall. Mater. Trans. B Process Metall. Mater. Process. Sci.*, 38(3), 451–459. <https://doi.org/10.1007/s11663-007-9041-6>.

Acknowledgements

The PNNL PIs would like to acknowledge H. Das and S. Shukla, who were responsible for performing the welding operations and subsequent data analysis. M. Blocher is acknowledged for handling the mechanical design and drafting of the tooling and fixtures. The modeling work was carried out by K. Balusu. C. Smith offered his expertise in robotic welding, providing essential guidance and support. W. Choi dedicated his efforts to analyzing the process force data in the frequency domain, establishing a correlation with the weld's cross-sectional properties. S. Niverty and N. Canfield contributed greatly through their meticulous XRT work. T. Roosendaal, R. Seffens, and E. Nickerson took charge of the mechanical testing. In parallel, A. Ortiz, A. Guzman, and M. Blazon were instrumental in conducting the metallography and hardness testing, ensuring the integrity and consistency of the materials involved.

The ORNL PIs would like to acknowledge R. Davies, Z. Feng, and A. Hayes for their leadership and technical guidance. H. Huang is acknowledged for the modeling work. J. Slade worked on concept development of integrated welding system. Y. Li engaged in process development. P. Agrawal and Y. Wang helped with characterization.

Contributions by D. Singh, R. R. Kamath, and J. Ilavsky at ANL are also acknowledged in conducting the APS experiments and data analysis.

This research used resources of the APS, a U.S. Department of Energy-Office of Science user facility operated for the DOE's Office of Science by ANL under Contract No. DE-AC02-06CH11357. Technical guidance and material support from E. Boettcher at Honda R&D America and S. Prasad at Arconic are also acknowledged.

II.4.1.4 Surface Modifications for Improved Joining and Corrosion Resistance (Pacific Northwest National Laboratory, Oak Ridge National Laboratory, and Argonne National Laboratory)

Yong Chae Lim, Co-Principal Investigator

Oak Ridge National Laboratory
Materials Science and Technology Division
One Bethel Valley Rd.
Oak Ridge, TN 37830
E-mail: limy@ornl.gov

Vineet V. Joshi, Co-Principal Investigator

Pacific Northwest National Laboratory
Energy Processes and Materials Division
900 Battelle Blvd.
Richland, WA 99352
E-mail: vineet.joshi@pnnl.gov

Dileep Singh, Co-Principal Investigator

Argonne National Laboratory
9700 S. Cass Ave.
Lemont, IL 60439
E-mail: dsingh@anl.gov

Christopher Schooler, DOE Technology Development Manager

U.S. Department of Energy
E-mail: Christopher.Schooler@ee.doe.gov

Start Date: October 1, 2020
Project Funding: \$1,000,000

End Date: September 30, 2023
DOE share: \$1,000,000

Non-DOE share: \$0

Project Introduction

PNNL, ORNL, and ANL are teaming up to develop hybrid joining methods (i.e., combining adhesive-based bonding and solid-state spot-joining to achieve higher mechanical performance and corrosion protection) for multimaterial systems to reduce vehicle weight. Specifically, this project will demonstrate the potential of laser or AP surface treatments to achieve high-quality Al alloy-galvanized steel and Al-carbon-fiber composite joints that also offer improved bulk substrate and galvanic corrosion resistance. The team will use several joining techniques, including ultrasonic spot-welding, friction-based fastener joints, and adhesive bonding, which were developed during the first phase of the JCP for this effort. We will also collaborate with other projects in Phase 2 of the project to leverage the understanding of the surfaces and improve joint performance.

Corrosion mitigation (e.g., general and galvanic corrosion) in the joints of dissimilar materials is a key technical challenge that must be overcome to successfully integrate candidate lightweight autobody structures from materials such as Al alloys, CFRP composites, Mg-alloys, and steels [1], [2], [3]. Galvanic couples forming at the joint interface of two different materials can greatly accelerate the corrosion of the more anodic material (i.e., Al alloys can suffer from accelerated corrosion when coupled with steels and stainless steels) [4]. If a mechanical fastener is used in the joining process, additional galvanic coupling interfaces can be formed [5]. Surface modification strategies could be used to enhance the general corrosion resistance of the bulk substrate [6] and to form the electrical isolation between the joint materials to minimize the galvanic effects [7]. However, surface modifications change the surface chemistry and surface morphology of the substrates. These chemical and morphological changes on the surface change the surface energy affecting adhesive wetting and bonding performance. The key challenge is to define the extent to which corrosion protection and

galvanic isolation can be achieved simultaneously using surface modification processes without compromising joint quality and that are also amenable to high-volume vehicle production.

Laser and AP surface treatments are being investigated as an effective way to clean local surfaces for improved joining characteristics as compared with conventional chemical cleaning. Additionally, these methodologies can be scaled-up for high-volume automotive production through integrating automatic translation states or a robotic system. These treatments are also capable of controllably growing oxide and related ceramic phases on substrate alloys that can offer enhanced corrosion protection. Three key aspects will be addressed: (1) how the chemistry, morphology, and thickness of these surface-modified layers evolved on selected Al alloys (or galvanized steel) and CFRP composite surfaces; (2) how the layers impact joining processing and adhesive strength; and (3) whether bulk corrosion resistance can be increased significantly and the coupling effects between the Al and the galvanized steel can be mitigated galvanically by electrically insulating the interface(s).

Objectives

In this project, we will specifically focus on optimizing different faying surfaces to improve the corrosion resistance and adhesion. The surface optimization techniques used in this task are laser and AP surface treatments. These techniques are becoming established as effective methods to clean local surfaces for improved joining characteristics as compared with conventional chemical cleaning and offer enhanced corrosion protection as aforementioned. The project will also evaluate the effect of the riveting process on cured and uncured adhesively bonded joints.

Approach

The surface optimization techniques used are laser and AP surface treatments. Corrosion properties of metal surfaces are being evaluated in post-laser- and AP-treated Al alloys and steel using both macroscopic and microscopic electrochemical measurement techniques. SEM with EDS is used to characterize the sample morphology and chemical element distribution before and after surface modification. Tafel and EIS measurements were performed in the bulk and locally modified regions. Advanced characterization techniques, including optical profilometry, X-ray photoelectron spectroscopy, FTIR, STEM, microbeam synchrotron XRD, and contact angle measurement, are used to study pre- and post-surface-modified samples. Experimental data will be compared to corrosion modeling and joint strength simulations to improve the model prediction to allow for optimum conditions to reach the fullest potential of the joint strength.

In FY 2024, the team investigated industrial standards and methods to perform corrosion tests on plates of materials and joints—including salt fog chamber corrosion—running ASTM B117, simple immersion corrosion, electrochemical characterization, and time-lapse sample imaging. Finally, SECM was employed to probe the microscopic corrosion response of pre-treated and post-treated surfaces. A μm -sized theta probe with a $\sim 10\ \mu\text{m}$ diameter and a 0.01 M NaCl solution was used for a localized electrochemical measurement. Multiple point analyses were completed on the top of the flat sample surface at multiple locations. Also, measurements were performed successfully immediately after plasma treatment. Tafel and EIS measurements were conducted at each location and long-term corrosion tests were conducted on rivet samples with combinations of plasma treatment and adhesives. To understand the role of rivet geometry on corrosion performance, COMSOL multiphysics modeling was performed and combined with a sensitivity analysis for the pre- and post-plasma-treated samples.

Results

Surface Modifications to Improve Surface Energy, Adhesive Bonding Strength, and Corrosion Resistance (ORNL)

Open-air plasma surface treatment was applied on various lightweight materials such as 7xxx Al alloy, DP 980 steel, casting Al-Aurora 5, and thermoset CFRC. Notably, our attention is focused on casting Al due to many benefits (e.g., reduced number of parts and joining required, cost and time effective for manufacturing) for automotive industries. For this reason, casting Al provided by original equipment manufacturers was also used. Then, surface energy of the pre- and post-plasma-treated samples was measured by contact angle measurement and was calculated by Fowke’s law. Higher surface energy, particularly for the polar component, is required for better adhesive bonding strength. Figure II.4.1.4.1 summarizes the measured surface energy, including for polar and disperse components, and the total for the different materials with and without plasma surface treatment. Overall, the measured total surface energy for the open-air plasma-treated materials is significantly increased compared to the control case (i.e., without plasma surface treatment). In particular, surface energy of the polar component for all plasma-treated materials is significantly increased, affecting the adhesive bonding performance because it will produce strong hydrogen bonds with the adhesive.

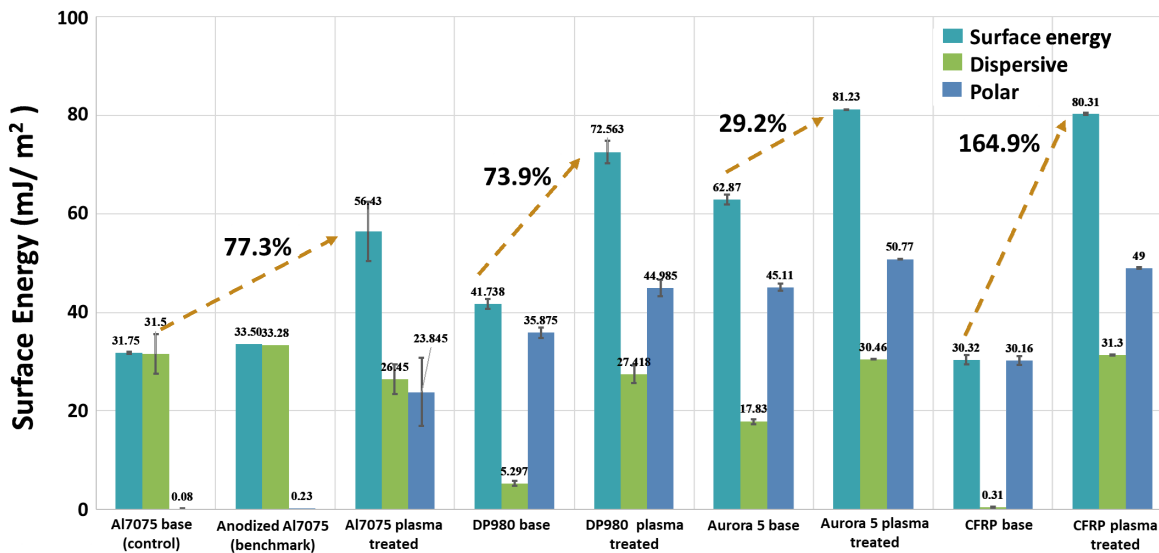


Figure II.4.1.4.1. Summary of measured surface energy for various lightweight materials after open-air plasma treatment. Source: ORNL.

Using epoxy-based adhesive from our collaborator (L&L Products), adhesive-bonded samples were produced for two different material combinations (i.e., Al7075, thermoset CFRC, and Al7075, Zn-coated DP980) before and after plasma treatment to assess surface treatment effect. Figure II.4.1.4.2 compares the measured averaged lap-shear tensile strength for three different surface conditions (i.e., control, 3-µm-anodized, and open-air plasma-treated) on Al alloy adhesive bonded with CFRC and Zn-coated DP 980 steel. It is well-known that anodized Al has higher corrosion resistance. For this reason, we would like to evaluate the adhesive bonding performance as compared with the open-air plasma-treated condition. Open-air plasma treatment improves the adhesive bonding strength by more than 10% for both material combinations compared to the control and anodized Al surface condition. As stated earlier, this is because open-air plasma treatment produced an oxygen-enriched surface to increase polar component interfacial surface energy, leading to strong chemical bonding with adhesive. ORNL-developed sustainable lignin-based thermoplastic adhesives and successfully demonstrated the feasibility of metal bonding. With optimized TA content and loading of reinforcing fillers, the ABL lignin-nitrile rubber adhesive offered an LSS of 21 MPa, which provided 90% performance of a commercial epoxy-based adhesive (YL 230 from L&L Products).

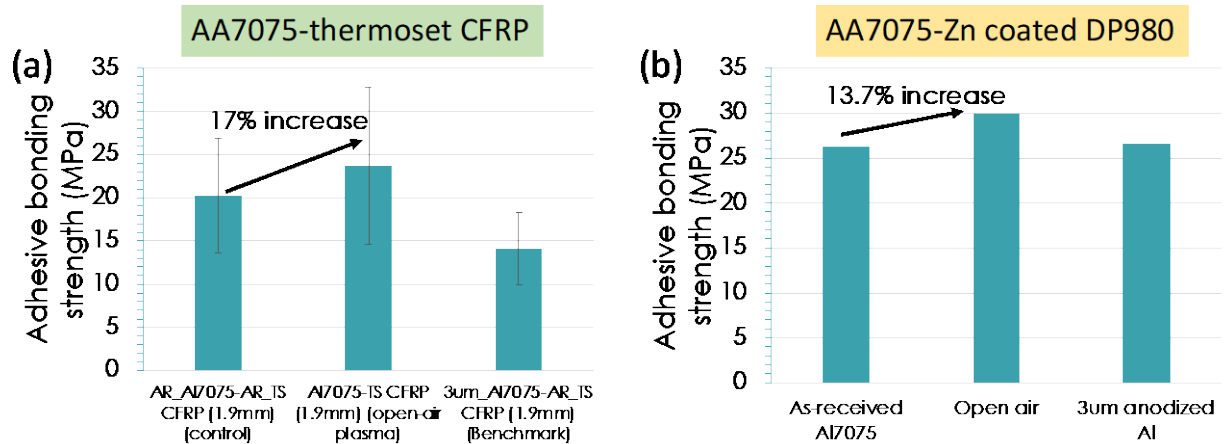


Figure II.4.1.4.2. Summary of lap-shear tensile strength of different material combinations with different surface conditions. (a) Al7075-thermoset (TS) CFRP and (b) Al7075-Zn-coated DP980. Source: ORNL.

Similarly, open-air plasma treatment was applied on the same materials to improve the adhesion between thermoplastic adhesive and substrates. Figure II.4.1.4.3 summarizes the LSS for the adhesive-bonded joints before and after open-air plasma treatment and its fractography. The averaged LSS was elevated by 10–24% after open-air plasma treatment. Also, the failure mode changed from pure adhesive failure (failure at interface) to mixed adhesive/cohesive failures.

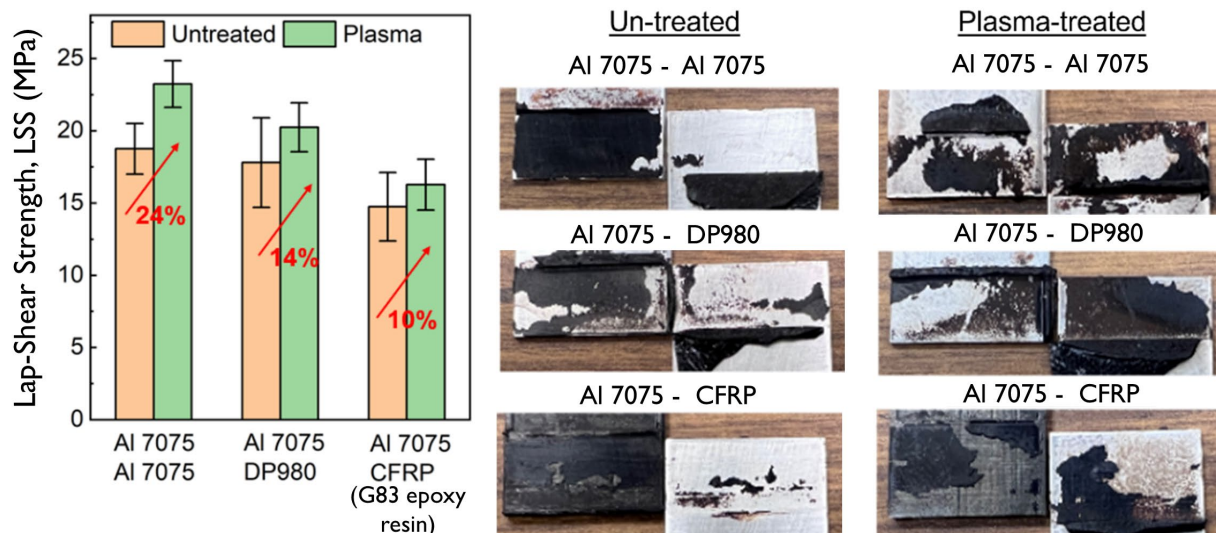


Figure II.4.1.4.3. Summary of LSS for the thermoplastic lignin-nitrile rubber (ABL) adhesive joints with various material combinations and fractography before and after open-air plasma treatment. Source: ORNL.

ASTM B117 salt fog testing was used to assess corrosion resistance of Al7075-Zn-coated DP980 with three different surface conditions. Lap-shear joint configuration was used to evaluate the pre- and post-corrosion exposed samples. Figure II.4.1.4.4 compares the LSS of adhesive-bonded Al7075-galvanized DP980 steel before and after 500 hours of corrosion testing. For the control case, more than 90% of LSS was decreased after 500 h of salty fog exposure. However, the 3- μ m anodized and open-air plasma-treated condition retained more LSS than the control case. In particular, open-air plasma-treated samples retained more than five times higher bonding strength than the control case, demonstrating effectiveness of open-air plasma treatment to improve corrosion resistance of dissimilar material joint.

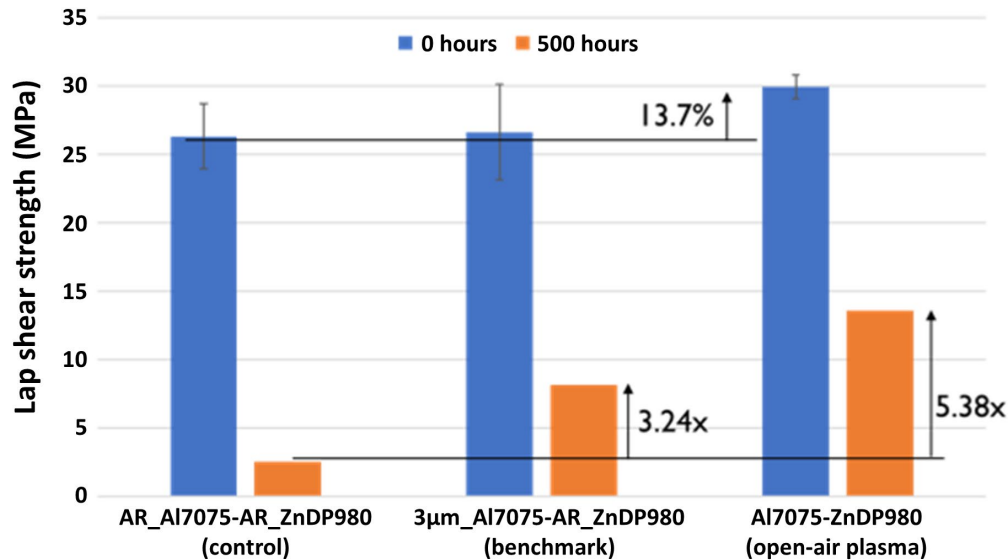


Figure II.4.1.4.4. Summary of lap-shear tensile testing for before and after 500 hours corrosion exposed Al7075 and Zn-coated DP980 with different surface conditions. Source: ORNL.

Novel Galvanic Corrosion Mitigation Approach for CFRP-Metal Mechanical Fastener Joint Using Self-insulation Form AFA Rivet (ORNL)

We investigated the galvanic corrosion of CFRC-metal joint by collaborating with JCP Phase 2 Thrust B at ORNL. Figure II.4.1.4.5(a) illustrates galvanic corrosion circuits possible in the lap-joint configuration. There are three possible corrosion modes in the lap-joint configuration. The first one is general corrosion of individual materials, such as the rivet and metal (e.g., Mg and Al alloys), in corrosive electrolytes. The second mechanism can be crevice corrosion, which can occur in the confined gaps of the joint. The last one is galvanic corrosion driven by the electrical connection of two different materials. Two potential galvanic current (I) paths can form when the friction self-piercing riveting process is used for the CFRC-metal joint. As shown in Figure II.4.1.4.5(a), the steel rivet is contacting both CFRC and bottom metal and serving as a conductor for electrical currents, leading to accelerated galvanic corrosion of more active metal substrate [7], [8]. In order to minimize the galvanic currents through galvanic circuits (i.e., steel rivet-bottom metal substrate and CFRC-steel rivet-bottom metal substrate), an electrical insulation (e.g., polymer or Al_2O_3 ceramic coating) on the steel rivet is needed at the joint interface, as described in Figure II.4.1.4.5(b). Although a polymeric coating can serve as a physical barrier and electrical insulation layer, our preliminary study found that local or partial delamination of the polymer-coating layer on the rivet fastener during F-SPR joining process due to interaction (friction) between the joining material and tool holder. Another issue for polymeric coating can be relatively low melting temperature compared to the temperature generated during the joining process. A ceramic coating on fasteners can be an alternative solution to address the above issues due to the following reasons: good corrosion resistance, low wear rate, and HT endurance. Plasma spray coating is the most well-known technique for ceramic coating of relatively large and simple shape parts. Also, another technique, such as CVD, can be applied, but high vacuum and clean environments are required. However, none of the above techniques can be easily applied to complex and small fasteners. Also, mass volume production is a critical issue. For this reason, ORNL has been extensively investigating an alternative solution to sufficiently grow electrically insulating oxide layer (e.g., Al_2O_3) on the rivet surface by a proper pre-oxidation process. After extensive effort, we identified an alumina-forming alloy (AFA) designed by ORNL for another DOE VTO projects. For proof-of-concept, we evaluated the corrosion resistance of the AFA by electrochemical measurements and characterized the pre-oxidized surface using an advanced electron microscopy technique.

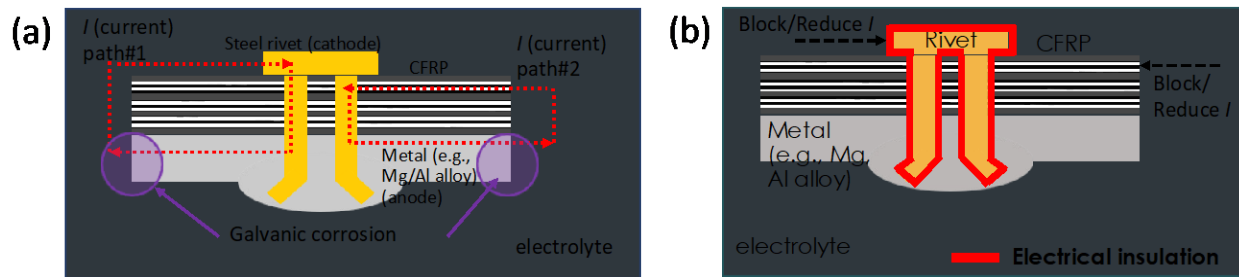


Figure II.4.1.4.5. (a) Schematic of galvanic corrosion mechanism due to galvanic current paths for CFRP-metal joint. (b) An illustration of galvanic corrosion mitigation approach to minimize galvanic current paths using an electrical insulated rivet. Source: ORNL.

Cathodic reactivity of rivet materials, which supports galvanic corrosion of more active metals in lightweight dissimilar joints, was evaluated by EIS and polarization measurements. For EIS data fitting, two equivalent circuit models were used to determine the resistance values against cathodic reaction on the rivet materials. Two rivet materials, carbon steel and AFA stainless-steel, were evaluated, and AFA materials were used with untreated and pre-oxidized conditions. Pre-oxidation of AFA to form Al-rich oxide insulation barrier was performed for 24 h at 800°C, 850°C, 900°C, or 950°C in laboratory air. Figure II.4.1.4.6 presents representative cathodic polarization curves and impedance-spectra of steel, bare AFA, and AFA pre-oxidized at 850°C (850°C AFA). In the polarization curves, as observed in Figure II.4.1.4.6(a), the cathodic currents at 1.5 V_{SCE} (i.e., the potential expected when coupled with Mg-alloys) were notably lower in 850°C AFA than in steel and bare AFA, indicating that the Al-oxide insulation layer on AFA effectively reduced the cathodic reaction, which should also decrease galvanic corrosion of more active metals in dissimilar materials joint configurations. In impedance-spectra of steel and 850°C AFA, as indicated in Figure II.4.1.4.6(b) and (c), the impedance scale, estimated by the right end values on x-axis, was greater in 850°C AFA than in steel, implying that the resistance against cathodic reaction would be greater in the pre-oxidized AFA. As presented later, most of impedance-data were fitted using a single resistance constant phase element ($R//CPE$) model, which was used in the case of one electrochemical interface, bare metallic alloy, or oxide film in contact with 0.1 M NaCl that controlled the cathodic reaction rate. In contrast, a double $R//CPE$ model was used for the case that two electrochemical interfaces, where both oxide film and metallic substrate interacted with 0.1M NaCl, were supposedly dominant. For each case, R_2 or $R_f + R_2$ values were used for comparison of resistance against cathodic reaction. Figure II.4.1.4.7 presents the individual data and average values from R_2 , $R_f + R_2$, and cathodic currents at $-1.5V_{SCE}$ for steel, bare AFA and pre-oxidized AFA samples. For lower galvanic corrosion risk, the rivet material needs to exhibit higher resistance values and lower cathodic currents. In this regard, 800°C, 850°C, and 900°C AFA are considered to be highly effective to mitigate galvanic corrosion in dissimilar materials joint configurations. Interestingly, the effectiveness of pre-oxidation on cathodic reaction mitigation (to reduce galvanic corrosion) was lower in 950°C AFA, indicating the oxide layer formed at 950°C was not as insulating as others grown at 800°C, 850°C, and 900°C. Further investigation and surface characterization are required to study this variation.

STEM equipped with EDS was employed to characterize the chemical element distribution after pre-oxidation process on AFA. Figure II.4.1.4.8 presents STEM with EDS element maps for pre-oxidized AFA at 800°C. Approximately 100–150 nm thickness of continuous and dense Al-oxide was observed. It is well-known that Al-oxide has good mechanical and chemical material properties, such as good corrosion resistance, low wear rate, and HT endurance. Therefore, it is suitable for F-SPR or other joining processes that experience high frictional heat generation and high-shear stress during joining process. In addition, it will provide corrosion resistance of rivet and dissimilar material joint.

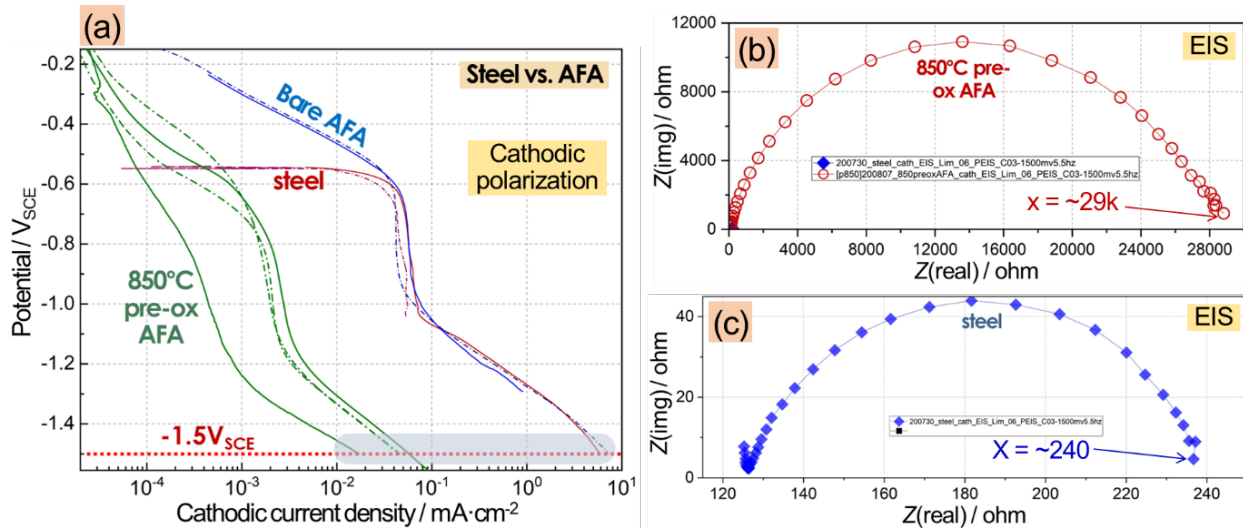


Figure II.4.1.4.6. Examples of (a) representative cathodic polarization curves from steel, untreated, bare AFA and 850 °C pre-oxidized AFA, and (b, c) impedance-spectra of 850 °C pre-oxidized AFA and steel. The cathodic polarization curves in (a) were initiated at natural corrosion potentials of rivet materials in 0.1M NaCl and scanned down to -1.5 V_{SCE} with the rate of 0.5 mV/s. Impedance-spectra was collected at -1.5 V_{SCE} with the amplitude of ±10 mV and the frequency range of 200 kHz to 7 mHz. Source: ORNL.

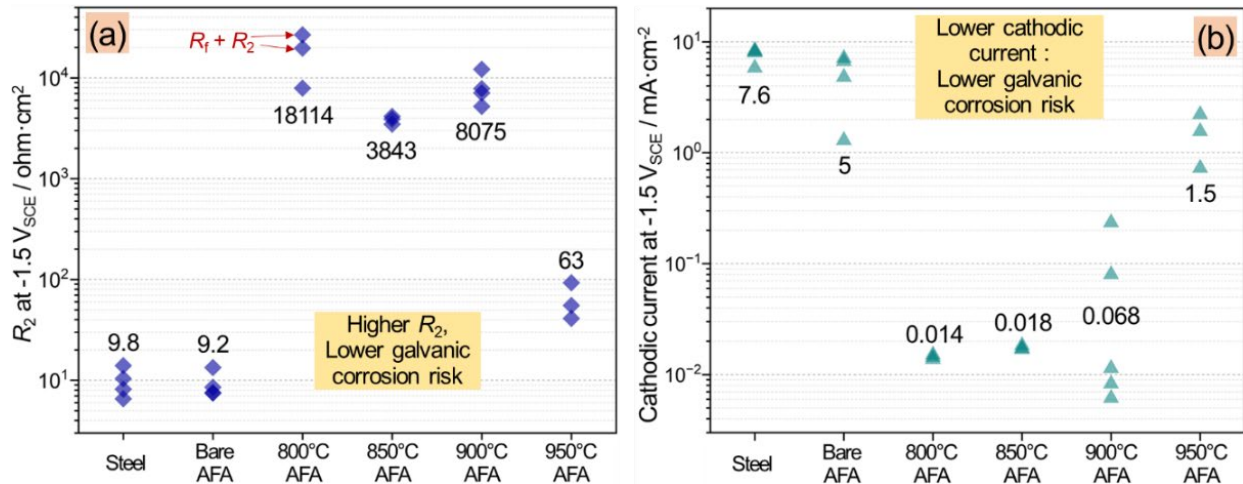


Figure II.4.1.4.7. Individual (symbols) and average (numbers) values of (a) resistance against cathodic reaction, and (b) cathodic current at -1.5 V_{SCE} from steel and AFA with and without pre-oxidation. Source: ORNL.

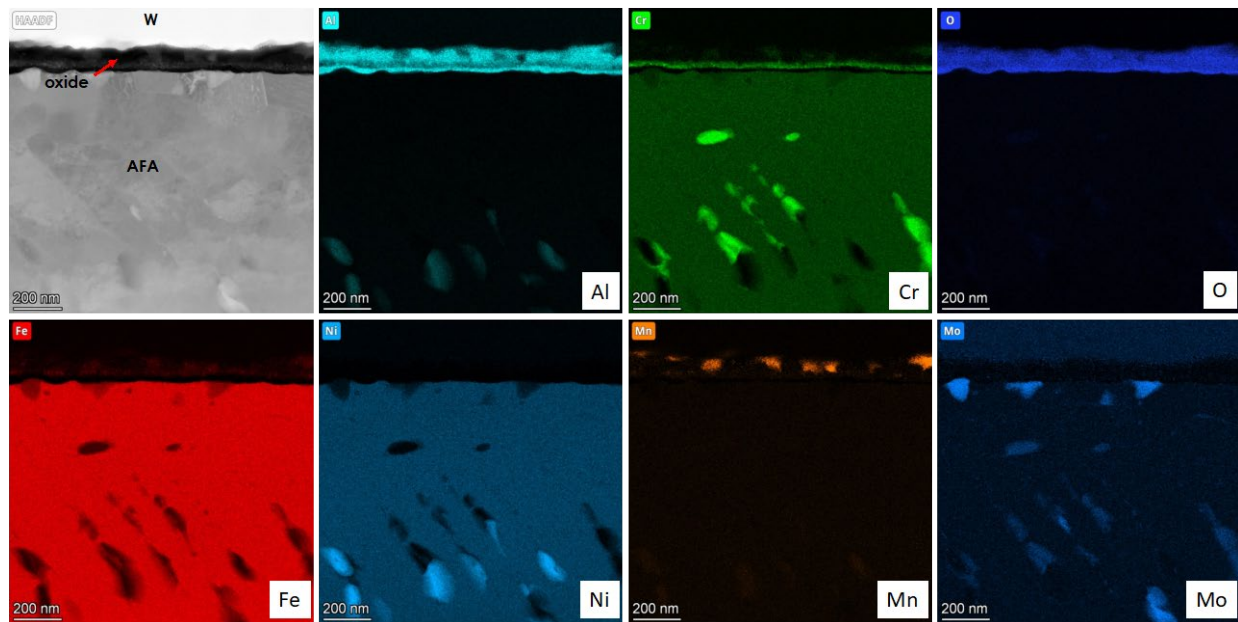


Figure II.4.1.4.8. STEM-EDS element maps for thermal processed AFA at 800°C, showing formation of dense Al-oxide layer. Source: ORNL.

To validate the self-electrical insulation layer formed AFA rivet effect on galvanic corrosion mitigation, we collaborated JCP Phase 2 Thrust B task team for F-SPR joint of CFRP-AZ31B. In particular, Mg alloy, AZ31B, was selected for a proof-of-concept because it has much lower corrosion potential than the steel rivet and CFRP [1]. Therefore, Mg alloy becomes an anode, while more noble material (e.g., steel rivet or CFRP) acts as a cathode, leading to an accelerated corrosion of Mg alloy. We used our recently developed, unique corrosion testing protocol, called “selective corrosion exposure technique,” on our samples to quantitatively study the galvanic corrosion effect of dissimilar materials joints [8]. Figure II.4.1.4.9 compares the calculated galvanic current based on the measured corrosion volumes of AZ31B at the joints for the bare steel rivet (control) and pre-oxidized AFA rivet cases. Approximately 60% reduction of galvanic current was confirmed for pre-oxidized AFA compared to the control case, demonstrating the effective galvanic corrosion mitigation in dissimilar material joints. For future work, more testing should be conducted for statistical study and applied for other material combinations. This novel approach is patented by U.S. Patent office as of November 2023, which was during this reporting period [9].

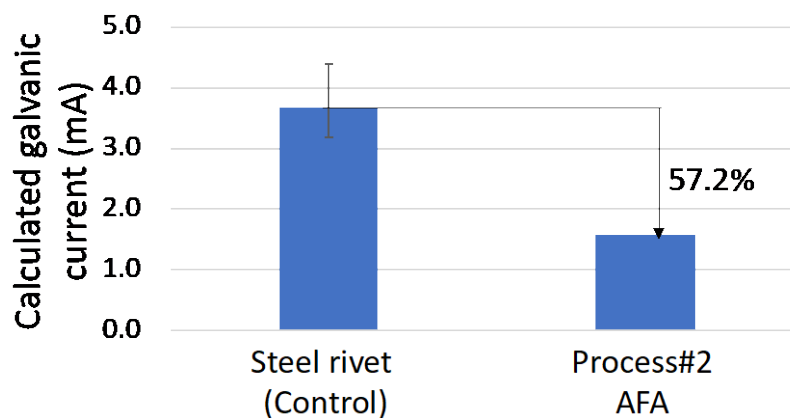


Figure II.4.1.4.9. 0.1M NaCl solution immersion tested CFRP-Mg joints by F-SPR using steel rivet (control), thermal process AFA. Galvanic current for both cases was calculated based on measured corrosion volume of Mg. Source: ORNL.

Microbeam XRD Characterization of Surface-treated Al-7075 (ANL)

Al 7075 alloy plates were subjected to two different surface treatments (open-air plasma and laser) to develop an oxide layer on the surface in a controlled fashion (ranged from nanometer to micro level). It was observed that the surface-treated samples possessed an improved corrosion resistance by electrochemical measurement techniques. Preliminary microscopy (STEM-EDS) studies at ORNL showed the possibility of existence of multiple oxide species (e.g., Al₂O₃, CuO, MgO, MgAl₂O₄ spinel) and morphologies as a function of distance from the top oxide surface. To further probe the oxide species, present as a function of distance from the top surface for multiple process parameters, microbeam XRD measurements were conducted in a reflection geometry at beamline 34-ID-E, APS. An X-ray beam of size 300 nm × 300 nm, with an energy of 20 keV and an exposure time of 60 seconds, was used to collect two-dimensional diffraction patterns at intervals of 1mm along the oxide layer for each sample. Figure II.4.1.4.10(a–b) show the XRD patterns obtained as a function of distance from the top surface of the oxide layer for open-air plasma-treated and laser (75 W) treated + corroded samples. In addition to the Al substrate peaks, the major oxide phase present is the α-Al₂O₃. Among the other expected oxide species, a few peaks from ZnO and CuO are seen in the open-air plasma sample, but they are not found in the laser-treated sample. The unidentified peaks are suspected to be due to the presence of complex oxides, such as the MgAl₂O₄ spinel, and will be investigated in more detail in Year 4.

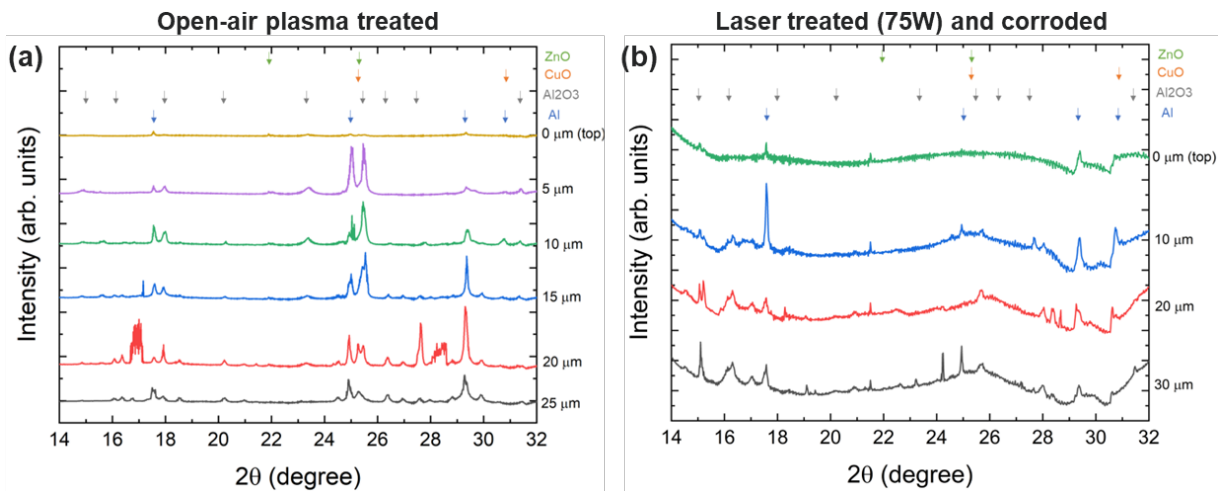


Figure II.4.1.4.10. Microbeam XRD patterns as a function of depth from the top surface of the oxide with the peak positions of the expected oxide phases above the patterns for (a) open-air plasma-treated, (b) laser-treated (75 W) and corroded samples. Source: ANL.

Moisture Effects on Adhesives, Substrates, and Joints (PNNL)

The main goal of this part is to (1) measure the diffusion coefficient of water molecules onto adhesives, metals, and CFRPs; (2) examine how the surfaces chemically change when exposed to absorbed water; and (3) gain an understanding of how these changes affect the interfacial bonds of metal-adhesive and CFRP-adhesive as well as the fracture properties of their adhesively bonded joints. Initially, we tested materials at 35°C and 98% relative humidity (RH) conditions in an environmental chamber. The test materials include adhesives (XP0012: paste type, XP5005F: tape type, provided from L&L Products, Romeo, MI), metals (Al6061, Al5052, and DP590), and CFRPs (CFRP- polyamide 66 [PA66] and CFRP- polyphthalamide [PPA]). Both XP0012 and XP5005F adhesives were square-shaped in a mold and their thickness controlled about 1.6–1.8 mm before they were cured at 150°C for one hour. Weight gains of all the samples were periodically measured until maximum water was reached. The diffusion coefficients of the materials were estimated using a simplified Fick's diffusion equation, $W_t/W_\infty = 4\beta\sqrt{Dt}/(z\sqrt{\pi})$ ($W_t/W_\infty \leq 0.6$), where D is the diffusion coefficient, z is the adhesive sheet thickness (mm), and β is the edge effect (1.05 for a sheet). D can be calculated from the slope of W_t/W_∞ versus \sqrt{t}/z for each sample. XP0012 and XP5005F adhesives showed about 2.60 and 2.25% of the initial maximum water absorption, as observed via the dotted lines in

Figure II.4.1.4.11(a), and non-Fickian moisture absorption. Diffusion coefficients of XP0012 and XP5005F adhesives in Step One were $4.710 \times 10^{-9} \text{ cm}^2/\text{sec}$ and $4.392 \times 10^{-9} \text{ cm}^2/\text{sec}$, respectively, as indicated in Figure II.4.1.4.11(a). The diffusion in Step Two was not calculated due to the absence of maximum water absorption. The other model to better describe non-Fickian diffusion will be used later to evaluate diffusion coefficients in two steps. Both adhesives are epoxy-based adhesives, but they have different sensitivity to moisture because they contain different fillers and co-polymers (vendor's proprietary information). After about 3680 h (e.g., 5 months) exposure to moisture, both adhesives were measured by attenuated total reflectance-Fourier-transform infrared (ATR-FTIR) spectroscopy. It showed an increased oxidation (increased carbonyl intensity at 1736 cm^{-1}) and a decreased oxidation in amide peak (1690 cm^{-1}) for XP0012 adhesive, as observed in Figure II.4.1.4.11(b), whereas XP5005F additionally showed a decrease in the epoxy peak (913 cm^{-1}), as can be seen in Figure II.4.1.4.11(c). This indicates that both adhesives are oxidized and hydrolyzed in the presence of water molecules, and the oxidized and hydrolyzed surfaces contribute to non-Fickian absorption behavior, as observed as Step II in Figure II.4.1.4.11(a).

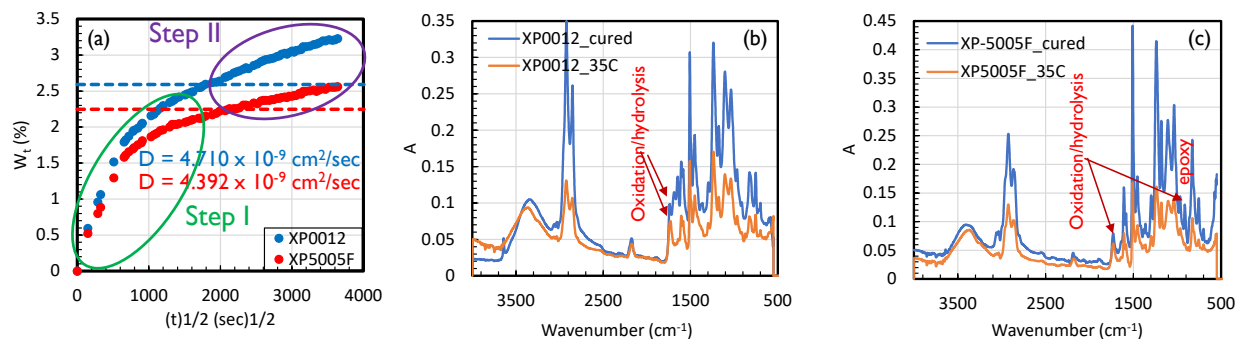


Figure II.4.1.4.11. (a) Moisture absorption plot, (b) and (c) ATR-FTIR spectra of XP0012 and XP5005 adhesives before and after moisture absorption test. Source: PNNL.

As-received and plasma-treated metals (Al6061, Al5052, and DP590) and CFRPs (CFRP-PA66, CFRP-PPA) were also tested at the same condition to evaluate D and surface property change. Plasma treatment condition for metals and CFRPs was reported previously at the maximum surface energy without physical change of surfaces. Figure II.4.1.4.12 shows moisture absorption change in as-received and plasma-treated Al6061, Al5052, and DP590 as a function of the square root of moisture exposure time. After 2100 h (e.g., 3 months) of exposure to moisture, Al6061 and Al5052 absorbed $< 0.01 \text{ wt.}\%$ of moisture, and DP590 absorbed $< 0.025 \text{ wt.}\%$ of moisture. Interestingly, plasma-treated metal surfaces initially absorbed more moisture due to their hydrophilic characteristics, but eventually the as-received surfaces reached the same maximum moisture absorption as plasma-treated surfaces. ATR-FTIR spectra showed significant oxidation (Al_2O_3 and MgO), and hydration by moisture uptake, Al_2O_3 and H_2O , as observed in Figure II.4.1.4.13(a–b). The DP590 surface contained ZnO and $\text{Zn}(\text{OH})_2$ initially (e.g., as-received and plasma-treated) and the zinc-oxide layers turned into hydrozincite ($\text{Zn}_5[\text{OH}]_6[\text{CO}_3]_2$) after moisture uptake, as shown in Figure II.4.1.4.13(c). For hydrozincite, two representative bands were observed at about 1500 cm^{-1} and 1390 cm^{-1} , which bands would be assigned to CO_3^{2-} antisymmetric stretching mode.

Two types of CFRPs (CFRP-PA66 and CFRP-PPA) have been exposed to the same condition. We observed that CFRP-PA66 showed Fickian-type absorption behavior, as can be seen in Figure II.4.1.4.14(a), but CFRP-PPA showed very slow and low moisture absorption and had not been finished after six months exposure ($0.9 \text{ wt}\%$ uptake, did not reach maximum moisture uptake, not shown here). The overall structure of CFRP-PA66 was maintained, but the carbonyl group was significantly hydrated after moisture uptake. The intensity ratio of hydrated carbonyl (at 1726 cm^{-1}) to free carbonyl (at 1741 cm^{-1}) of as-received CFRP-PA66 was 0.6 and that of plasma-treated CFRP-PA66 was 1.5. However, after the moisture uptake test, those of both as-received and plasma-treated CFRP-PA66 had reached up to 3.0, as shown in Figure II.4.1.4.14(c).

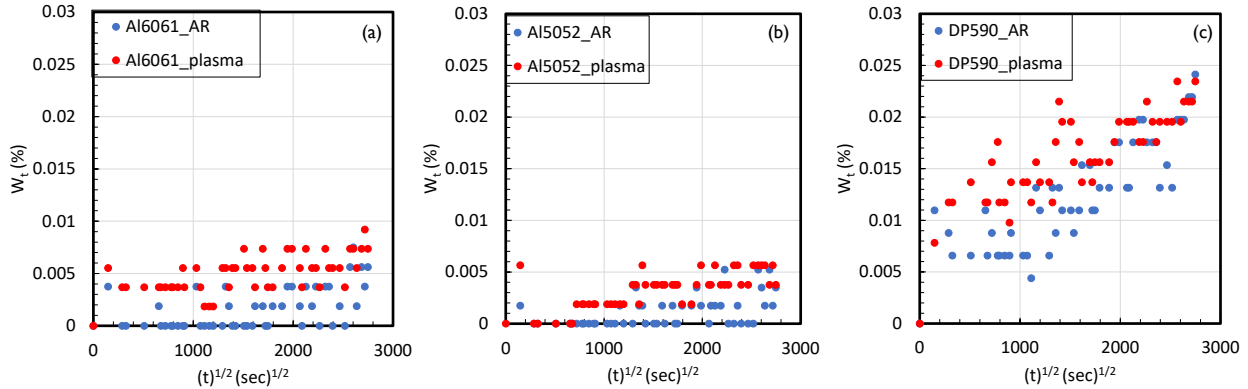


Figure II.4.1.4.12. Moisture absorption plot of as-received and plasma-treated (a) Al6061, (b) Al5052, and (c) DP590 vs. the square root of exposure time to moisture. Source: PNNL.

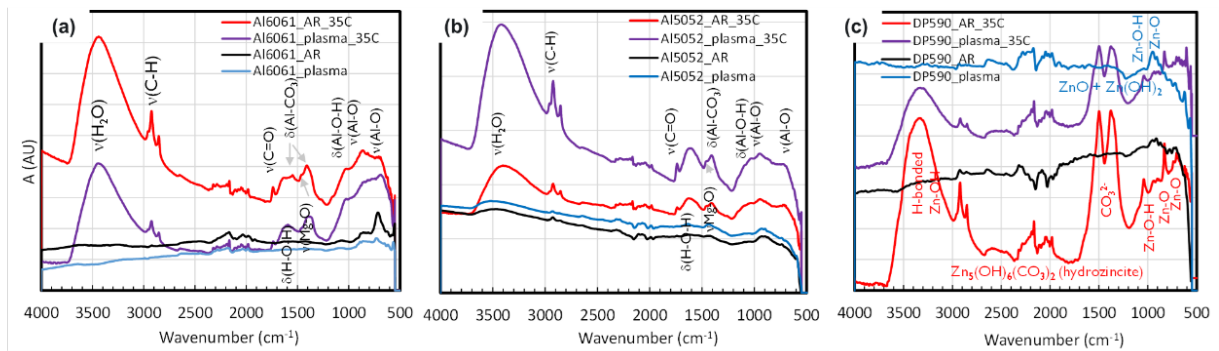


Figure II.4.1.4.13. ATR-FTIR spectra for as-received and plasma-treated (a) Al6061, (b) Al5052, and (c) DP590 before and after exposure to moisture at 35 °C and 98% RH for 3 months. Source: PNNL.

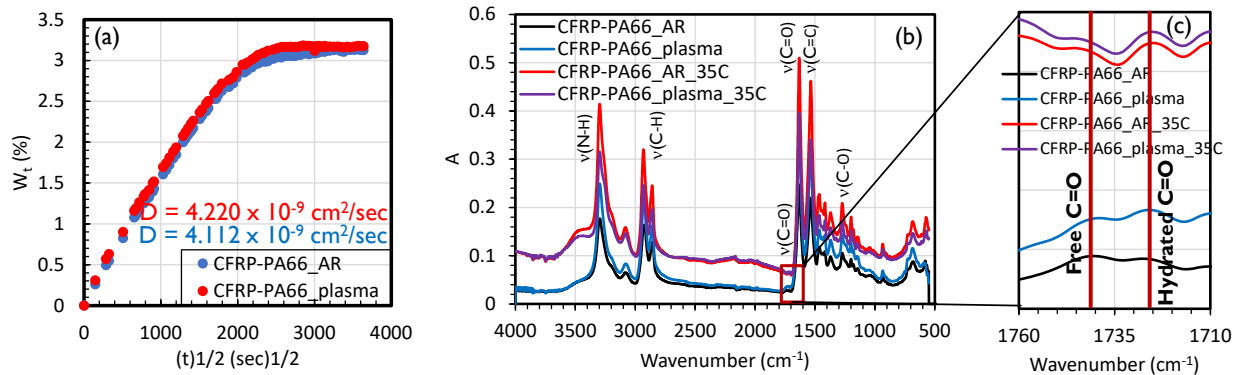


Figure II.4.1.4.14. (a) Moisture absorption plot and (b-c) ATR-FTIR spectra of the as-received and plasma-treated CFRP-PA66 before and after exposure to 98% RH and 35 °C. Source: PNNL.

The effects of moisture on the Mode I fracture resistance of adhesively bonded joints (Al6061/Al6061, Al6061/DP590, and Al5052/CFRP-PA66) was further investigated using double cantilever beam (DCB) tests. The metal surface was cleaned using acetone and a Scotch-Brite pad, while the composite surface was left in its as-received state without any additional abrasion. Two substrate surfaces were bonded together using a thermoset adhesive (XP0012-YL230 from L&L Products). A glass tape was used in front of the bond line to guarantee the uniform front of adhesive after curing. The in-plane dimensions of all the DCB specimens are 25.4 mm × 101.6 mm. The DP590 substrate has a thickness of 1 mm, while the other substrates have a

thickness of 3 mm. The adhesive bond length is 38.1 mm, and the bond thickness is about 100 μm . For Al5052/CFRP-PA66 combination, additional Al5052 substrate was bonded on the back side of CFRP-PA66 to avoid the bending fracture of CFRP-PA66 and the adhesion failure between CFRP-PA66 and metal hinge. Before conducting DCB tests, the samples were placed in an environmental chamber with the condition of 35°C and 98 RH. To prevent the degradation of adhesion between the substrate and metal hinge, green maskant from Maskcoat was used to coat the DCB sample, leaving only the bond area uncovered. In another scenario, we applied the green maskant up to the midpoint between the metal hinge and the bond line; this investigation is ongoing. The samples were exposed to 1400 hours in the chamber, left to dry for approximately 15 days after removal, and then subjected to DCB fracture tests. Load-displacement curves obtained from the DCB fracture tests on the specimens after 1400 hours of moisture exposure were plotted in Figure II.4.1.4.15(a–c). The results indicate that moisture absorption had an effect on the fracture behavior of the investigated joints, although not significantly in the investigated scenario. Moreover, the Mode I fracture energy of the joint was calculated using a work-of-fracture method for Al6061/Al6061 and Al6061/DP590 joints, but a modified beam theory was used for Al5052/CFRP-PA66 joints due to the rapid crack propagation. As shown in Figure II.4.1.4.15(d–f), the range of the average Mode I fracture energy shows a reduction from 3–10% for two metal-metal joints, whereas the average fracture energy of Al5052/CFRP-PA66 joint shows an improvement by approximately 30%. The reduction could be explained due to the formation of weak hydrated/oxidated Al and Zn layers on the metal surfaces, as previously discussed and shown in Figure II.4.1.4.13 above, whereas the improvement could be due to the enhanced adhesive ductility induced by oxidation/hydrolysis, as observed in the images of Figure II.4.1.4.16. The investigation of moisture effects on the mechanical behavior of CFRPs and adhesive is ongoing, and their effects on the metal-composite joints will be comprehensively investigated in FY 2024.

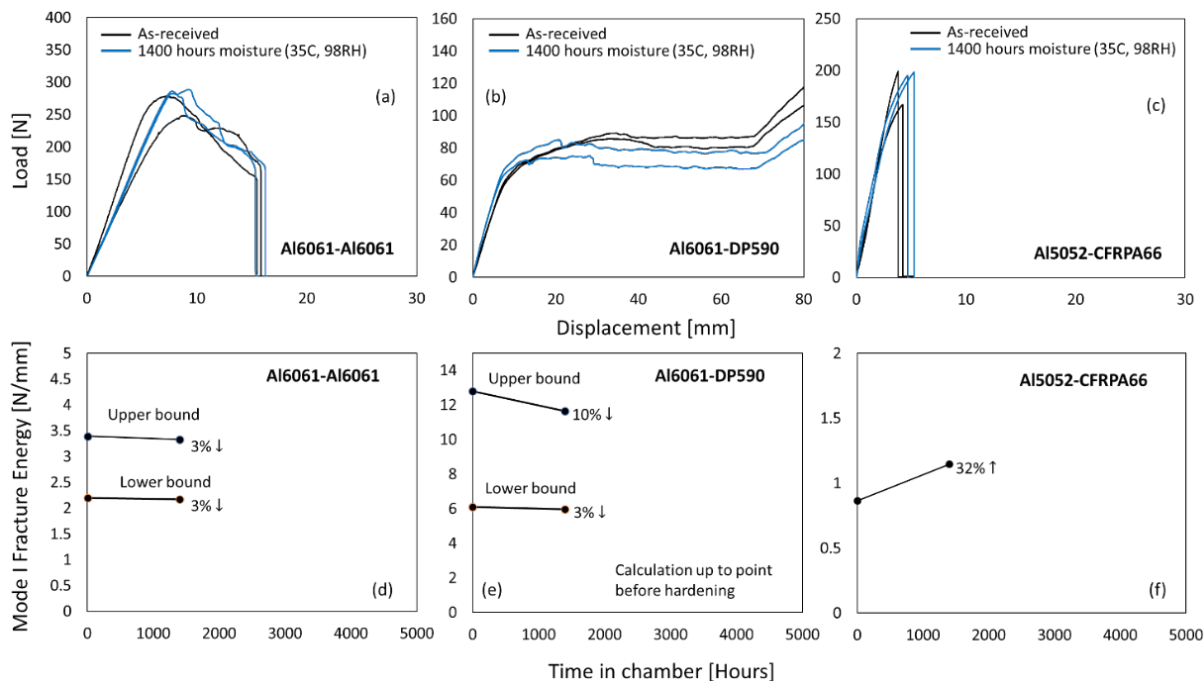


Figure II.4.1.4.15. (a–c) Load-displacement curves and (d–f) the average Mode I fracture energies of adhesively bonded Al6061/Al6061, Al6061/DP590, and Al5052/CFRP-PA66 joints after exposure of 1400 hours in a condition of 98% RH and 35 °C. Source: PNNL.

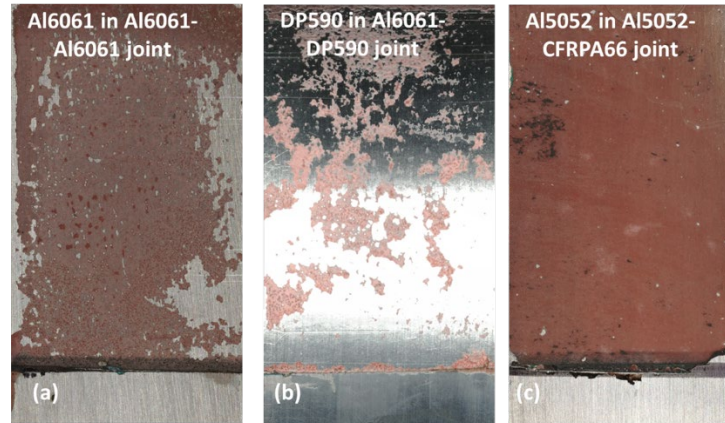


Figure II.4.1.4.16. Surface morphologies of (a) Al6061 in Al6061/Al6061 joint, (b) DP590 in Al6061/DP590 joint, and (c) Al5052 in Al5052/CFRP-PA66 joint after DCB failure. Sample were tested after 1400 hours of exposure in a condition of 98% RH and 35 °C. Source: PNNL.

The surface morphologies of substrates after DCB failure were visualized using a three-dimensional Keyence profilometer, as illustrated in Figure II.4.1.4.16. In the case of Al6061-Al6061, moisture exposure led to partial Al6061-adhesive interfacial debonding, as indicated in Figure II.4.1.4.16(a), even though most failures occurred within the adhesive. Conversely, in the case of Al6061-DP590, failure was primarily due to interfacial debonding between DP590 and the adhesive, as shown in Figure II.4.1.4.16(b). These observations are consistent with the mechanical testing results and suggest the energy required to fracture the oxidized layer on the metal surface due to the moisture being lower than the adhesive's fracture energy. A more detailed comparison of the fracture energy of the oxidized layer between DP590 and Al6061 surfaces will be analyzed in FY 2024 by quantifying the interfacial bonding area and conducting an additional moisture condition with a longer duration. For Al5052/CFRP-PA66 joints, DCB failure occurred entirely at the composite-adhesive interface, as observed in Figure II.4.1.4.16(c), which is similar to the failure mode of as-received Al5052/CFRP-PA66 joints, confirming the catastrophic failure of the Al5052/CFRP-PA66 DCB joint after reaching the peak load, as shown in Figure II.4.1.4.15(c).

Salt Fog Effects on Adhesives, Substrates, and Joints (PNNL)

The environmental conditions for the corrosion tests, using an additional 5.0% NaCl solution salt fog, were 98% RH and 35°C, which were the same as the previous moisture absorption condition. Through the current analysis from the previous moisture absorption tests on different materials, the order of moisture absorption diffusion coefficient is as follows: XP0012 > XP5005 > CFRP-PA66 >> DP590 > Al6061 ≥ Al5052. It is expected that the salt fog testing with the additional 5.0% NaCl solution would have a diffusion rate order similar to that observed in the moisture absorption tests. DCB tests were conducted on adhesively bonded joints with three material combinations (e.g., Al6061/Al6061, Al6061/DP590, Al5052/CFRP-PA66) to further investigate the salt fog effects on the fracture of these joints and compare them with the previous moisture effects. Like the DCB samples exposed to moisture only, we applied a green maskant, leaving only the bond area uncovered to prevent separation between the substrate and metal hinge due to corrosion before testing. In another scenario, we applied the green maskant up to the midpoint between the metal hinge and the bond line. This investigation is ongoing.

The samples were exposed to 800 and 1400 h of salt fog spray in the chamber, left to dry for approximately 15 days after removal, and then subjected to DCB fracture tests. Load-displacement curves obtained from the DCB fracture tests on the specimens after 800 and 1400 h of salt fog exposure were plotted in Figure II.4.1.4.17(a-c). Corrosion had an impact on the failure of metal-metal joints, particularly for Al6061/DP590 dissimilar joints. As shown in Figure II.4.1.4.17(a-b), while the failure displacement of the Al6061/Al6061 joint slightly decreases as salt fog exposure time increases, the significant reduction on the peak load and the final failure displacement was observed from Al6061/DP590 joints. To have a further

quantification, the Mode I fracture energy as a function of exposure time was established, as plotted in Figure II.4.1.4.17(d–f), using the same methods for the previous moisture condition. The range of the average Mode I fracture energy shows about 20% reduction for Al6061/Al6061 joints and up to 70% reduction for the Al6061/DP590 joints. For the Al5052/CFRP-PA66 joints, the average Mode I fracture energy was increased by 22% after 1400 h of salt fog exposure. The foregoing phenomena can be explained using similar reasons as the moisture scenario. The investigation of salt fog effects on the mechanical behavior of CFRPs and adhesive is ongoing, and their effects on the metal-composite joints will be comprehensively investigated in FY 2024.

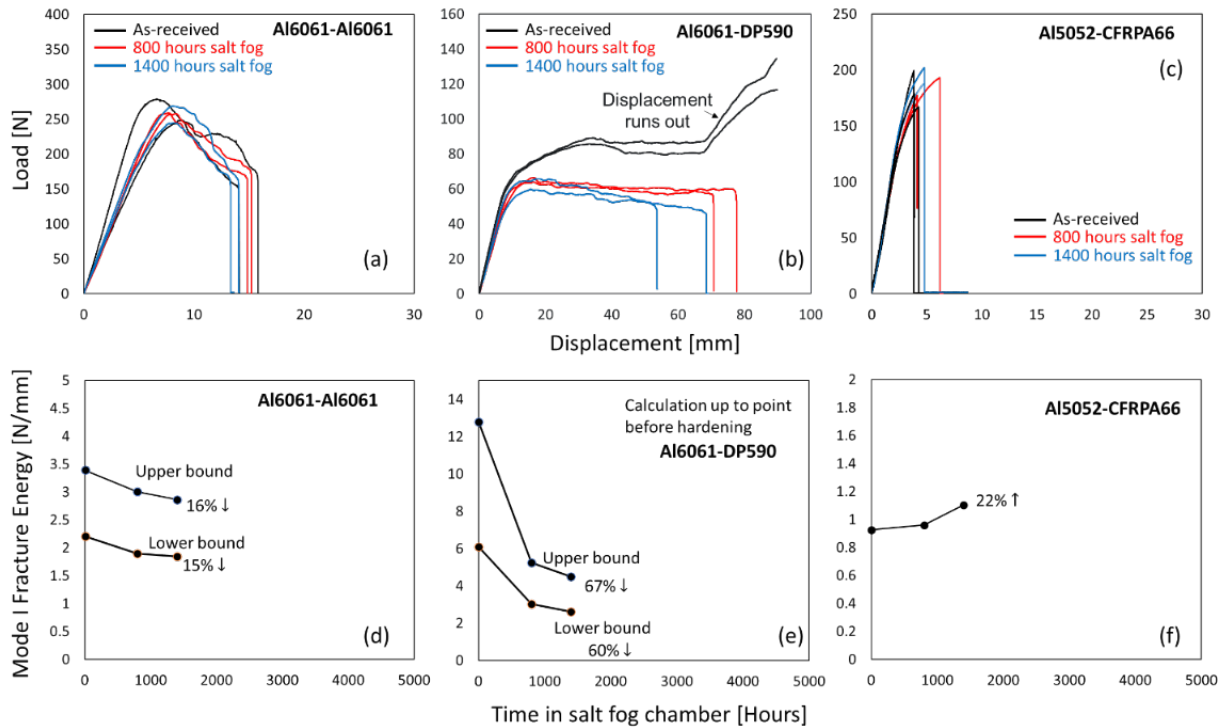


Figure II.4.1.4.17. (a–c) Load-displacement curves and (d–f) average Mode I fracture energies of adhesively bonded Al6061/Al6061, Al6061/DP590, and Al5052/CFRP-PA66 joints after exposure of 800 and 1400 h at 5% salt fog condition of 98% RH and 35 °C. Source: PNNL.

Role of Adhesives and Plasma Treatment on Salt Fog Corrosion of Lap Joints (PNNL)

Long-term corrosion tests were performed on two different rivet configurations, which were made using the high-velocity (HiVe) riveting process: (i) Al6061-Al6061 with a steel rivet; and (ii) Al6061-Al6061 with a clinch joint. A long-term accelerated salt fog corrosion test was performed on rivet samples with optimized surface processing conditions, namely adhesive coating only, optimized plasma treatment only, and combined adhesive and optimized plasma treatment of surfaces. On the other hand, the plates comprising the clinch joint were subjected to optimized plasma treatment and compared to the sample without any plasma treatment. Corrosion tests were performed for up to 1400 h in a singleton salt fog instrument running in accordance with ASTM B117. Absolute weight changes due to corrosion were measured intermediately at 200 h, 800 h, and 1400 h, and only a 1 in. × 1 in. surface area of the sample was exposed—including the head of the rivet in the HiVe rivet sample. At least three replicates of each sample type were corroded for 800 h and 1400 h. The rest of each sample was coated using a protective lacquer of peel seal green. Figure II.4.1.4.18 shows a comparison of the surface of the exposed face of the samples with and without the rivet. Figure II.4.1.4.18 shows the absolute percent weight change (%) results for post-corrosion samples. The HiVe rivet sample without any surface treatment showed the greatest weight change. The use of adhesive and optimized plasma treatments reduced the recorded weight changes by 79% and 75%, respectively, after 1400 h of salt fog corrosion.

Furthermore, the combined use of adhesive and plasma treatment showed a 68% lower weight change compared to samples without any surface treatment. This can be attributed to the possibility of oxidation and hydrolysis that is seen in the adhesives described earlier in this report.

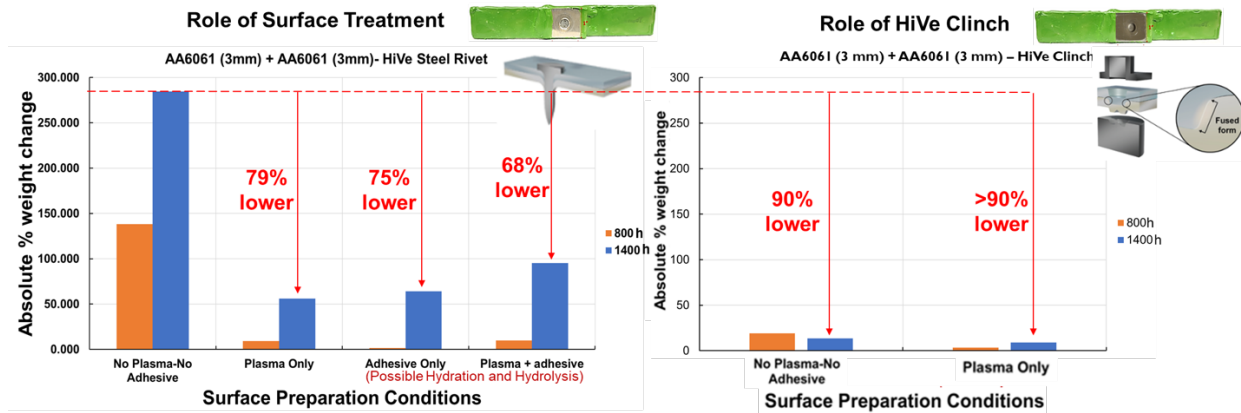
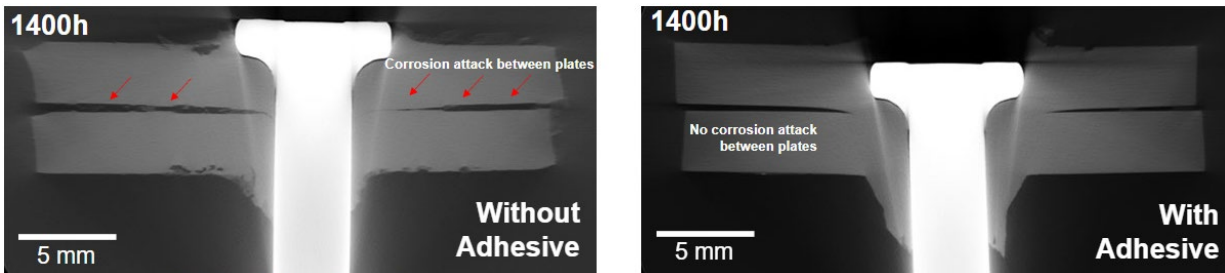


Figure II.4.1.4.18. Plots of corrosion-induced absolute % weight change vs. surface processing conditions in HiVe rivet and HiVe clinch samples of Al6061 joined to an Al6061 plate. Source: PNNL.

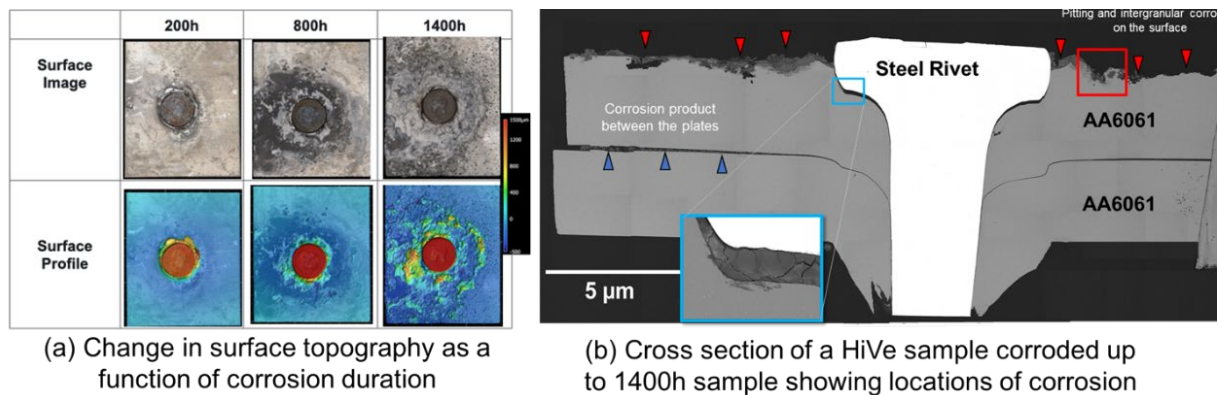
In the case of the HiVe clinched samples, the recorded weights are relatively insignificant, which implies that long-term corrosion progress was almost negligible. Corrosion progress attributed by weight changes was ~90% lower in HiVe joints without any surface processing (no plasma and no adhesive) as compared to its counterpart in which a galvanized steel rivet was used without surface plasma treatment or adhesive addition. Furthermore, the use of a plasma treatment in HiVe clinch joints reduces corrosion progress even further by exhibiting absolute % weight changes greater than 90% lower than the non-plasma-treated HiVe rivet samples without adhesive. The benefit of using adhesives between the plates can be seen in the virtual cross-section images, as shown in Figure II.4.1.4.19. In the case of samples without adhesive exposed on all surfaces of the joint to the corrosive environment, the x-ray computed tomography data shows a corrosion attack between the plates. However, no corrosion attack was observed in the HiVe rivet sample with adhesive between the Al6061 plates even after 1400 h of exposure to salt fog environment. Corrosion tests conducted on the HiVe rivet joints comprising two Al6061 plates (e.g., 3 mm) for 200 h, 800 h, and 1400 h also enabled the visualization of corrosion progress in the samples. Figure II.4.1.4.20 shows a top-view (optical micrograph and corresponding surface profile map) of a sample corroded over 1400 h. Corrosion up to 200 h is restricted to the surface of the head of the rivet where the galvanized Zn layer was corroded first and then removed. Once the steel surface was exposed, the galvanic and crevice corrosion of Al6061 plate in contact with the rivet started to corrode. Signs of this are observed after 800 h of corrosion wherein pits and corrosion products are seen in the Al6061 plate immediately around the head of the rivet. With further increase in time, the surface corrosion around the rivet continues with deeper pits and greater corrosion product deposition. Cross-section SEM characterization shows the corrosive fluid seeps into the gap between the plate and rivet and forms a corrosion product, which prevents further solution ingress. Due to this, the bulk of the corrosion progress is restricted to the exposed surface and does not affect the mechanical performance of the joints.



(a) Al6061-Al6061 HiVe Rivet (without adhesive)

(b) Al6061-Al6061 HiVe Rivet (with adhesive)

Figure II.4.1.4.19. X-ray computed tomography of the virtual cross-sections show corrosion progress after 1400 hours accelerated salt fog corrosion test: (a) Al6061-Al6061 HiVe rivet without adhesive and (b) Al6061-Al6061 HiVe rivet with adhesive. Source: PNNL.



(a) Change in surface topography as a function of corrosion duration

(b) Cross section of a HiVe sample corroded up to 1400h sample showing locations of corrosion

Figure II.4.1.4.20. (a) Sequence of corrosion progress in the HiVe joints over 1400 h of corrosion. (b) Cross-section of a HiVe rivet joint showing the locations of corrosion progress after 1400 h of corrosion. Corrosion is restricted to the exposed face in the form of pits. The gap between the top-plate and rivet head shows corrosion products that prevent further solution ingress. Source: PNNL.

High-Fidelity Simulations to Minimize the Number of Experiments (PNNL)

Figure II.4.1.4.21 shows the corresponding surface depth measurements (highlighting material loss) measured using surface profilometry after salt fog corrosion tests, in the green and red boxes signifying after 800 h and 1400 h, respectively. Included in the figure are simulated material loss plots at 800 h (green line) and 1400 h (red line) obtained by COMSOL multiphysics modeling. The experimental data are well aligned with the COMSOL-predicted values. Less than 10% difference is observed in COMSOL modeling at a distance from plate edge to rivet head of 0.01 m for 800 h and 1400 h tests. This indicates that COMSOL modeling results are able to predict corrosion volume loss in HiVe rivet Al6061/Al6061 joints accurately. These high-fidelity simulations will be used to model corrosion observed using industrial corrosion standards, thereby reducing the total number of experiments and time for comparing samples and accurately model the performance of these joints under harsh automotive environments.

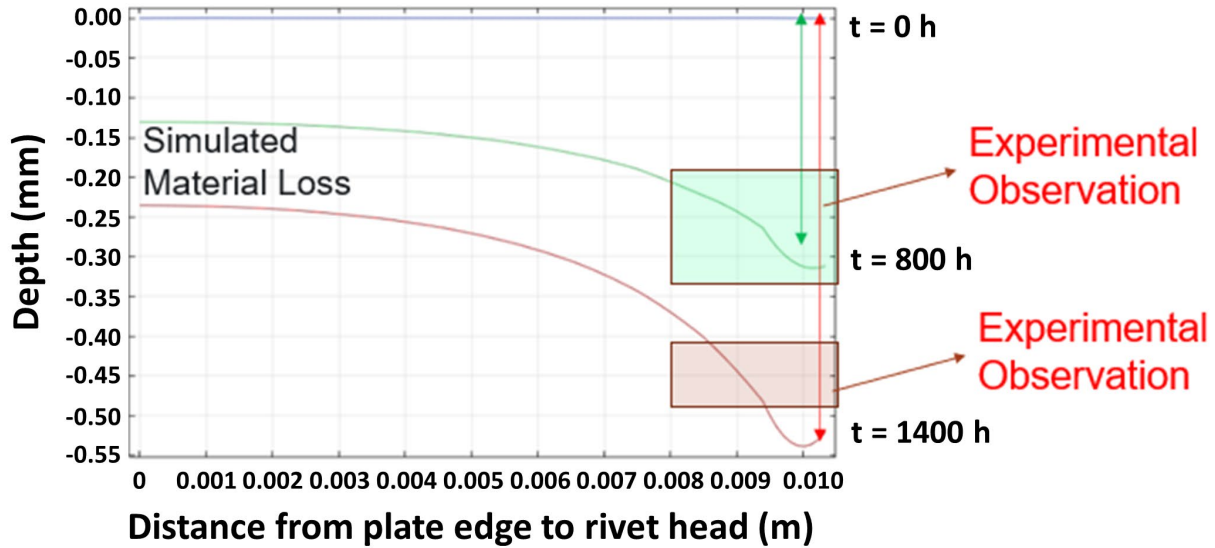


Figure II.4.1.4.21. Absolute weight change (%) results of the salt fog tests and COMSOL multiphysics modeling results for Al6061-Al6061 sample with steel rivet. Source: PNNL.

Conclusions

The following conclusions can be drawn from this work:

- Open-air plasma treatment was applied on various lightweight material combinations, which increased surface energy. More than 10% of adhesive bonding strength was improved using ORNL-developed sustainable thermoplastic and epoxy-based adhesive for CFRP-Al and Al-steel dissimilar material joints. Retain joint strength for open-air plasma-treated Al-steel is more than five times higher than the control case (i.e., no surface treatment).
- Novel self-electrical insulation formed AFA rivet joint methodology was developed by ORNL to mitigate a galvanic corrosion of F-SPR-jointed CFRP-metal. EIS and cathodic polarization measurements confirmed a greatly reduced cathodic reaction—associated with galvanic corrosion mitigation—for AFA after a pre-oxidation process. A thick and dense Al-oxide layer formed on the pre-oxidized AFA surface. Approximately 60% of galvanic corrosion current was reduced for pre-oxidized AFA riveted CFRP-AZ31B compared to the bare steel rivet case, demonstrating effective corrosion mitigation of dissimilar material joints.
- Al-7075 subject to two different surface treatments was probed using microbeam synchrotron XRD. The major oxide phase present at most locations for both surface treatments is α -Al₂O₃. ZnO and CuO are observed in certain locations in the open-air plasma-treated samples. The unidentified peaks are expected to be from complex oxide phases and will be probed in detail during Year 4.
- Epoxy adhesives degrade by oxidation and hydrolysis in long-term exposure to high humidity (no salt) and salt fog environments. This contributes to increased Mode I joint performance for CFRP and aluminum joints, which are stable in both environments.
- DP590-Zn-coating forms an oxide in high humidity that degrades the adhesive bond, leading to reduced Mode I performance. This effect is exaggerated in a salt fog environment, which aggressively oxidizes the ZN-coating.

- High-resolution 3D XRT and surface profilometry were used to map the sequence of corrosion initiation and propagation as a function of corrosion duration in lap Al6061 + Al6061 joints joined with a steel rivet. First, Zn dissolution occurs from the surface of the galvanized rivet. Following this, galvanic coupling is established between the head of the steel rivet and the plate. This leads to Al6061 top-plate corrosion around the rivet. This progresses with an increase in corrosion duration. Minimal corrosion progress is observed in the crevice between the plate and the rivet. The crevice volume is filled with a corrosion product that prevents further solution ingress.
- Adhesives lead to a significant decrease of at least 20% in corrosion between the plates irrespective of the area ratio.
- Simulations show excellent agreement with experiments. Simulations will be used to reduce the number of experiments and to run industrial corrosion protocols in FY 2024.

Key Publications

1. Jun, J., V. V. Joshi, A. Crawford, V. Viswanathan, D. N. Leonard, J. Chen, P. Updadyay, Y. C. Lim, and Z. Feng, 2023, “Galvanic corrosion of AZ31B joined to DP steel with and without Zn layer by ultrasonic and FSW,” *J. Magnes. Alloy.*, 11(2), 462–479. <https://doi.org/10.1016/j.jma.2023.01.016>.
2. Lim, Y.C., J. H. Jun, M. Brady, and Z. Feng, “Fastener joint and associated method for avoiding corrosion of dissimilar material faster joints,” U.S. Patent 11,808,297 B2.
3. Lim, Y. C., J. Jun, D. N. Leonard, Y. Li, J. Chen, M. P. Brady, and Z. Feng, 2022, “Study of galvanic corrosion and mechanical joint properties of AZ31B and carbon-fiber reinforced polymer joined by friction self-piercing riveting,” *J. Magnes. Alloy.*, 10(2), 400–410. <https://doi.org/10.1016/j.jma.2021.05.003>.
4. Lim, Y. C., V. V. Joshi, D. Singh, K. Simmons, R. Kalsar, V. Viswanathan, V. Prabhakaran, A. Crawford, D. N. Leonard, A. Naskar, J. Jun, M. P. Brady, D. Hoskins, and N. Kanbargi, 2023, “Surface modification for improved joining and corrosion resistance,” *DOE VTO Annual Merit Review*, 12–15 June 2023, Virtual.
5. Lim, Y. C., J. Jun, D. N. Leonard, H. Meyer III, J. K. Keum, M. Brady, and Z. Feng, 2022, “AP surface processing of a 7xxx Al alloy surface to improve corrosion resistance,” *TMS 2022 Annual Meeting & Exhibition*, 23–27 February 2022, Anaheim, CA, USA.
6. Lim, Y.C., J. Jun, Y. F. Su, H. M. Meyer III, J. K. Keum, B. Lokitz, A. Sy, R. Robinson, D. Pappas, and Z. Feng, 2023, “Open-air plasma surface processing of Al alloy 7075 surface to form oxide-based corrosion barrier layer,” *TMS 2023 Annual Meeting & Exhibition*, 19–23 March 2023, San Diego, CA, USA (**Invited**).
7. Lim, Y. C., N. Kanbargi, Z. Yu, B. Lokitz, J. Jun, Y. F. Su, A. Naskar, and Z. Feng, 2023, “Adhesive bonding of lightweight multimaterials with surface modifications,” *TMS 2023 Annual Meeting & Exhibition*, 19–23 March 2023, San Diego, CA, USA.
8. Qiao, Y., Y. Shin, M. R. Pallaka, E. K. Nickerson, D. R. Merkel, R. J. Seffens, A. Ortiz, L. J. Ramos, and K. L. Simmons, 2023, “Plasma surface modification coupled with thermal and step-over distance effects on significant fracture improvement of adhesively bonded metal-CFRTP dissimilar materials,” *Compos. Sci. Technol.*, 232, 109833. <https://doi.org/10.1016/j.compscitech.2022.109833>.
9. Qiao, Y., Y. Shin, E. Nickerson, D. Merkel, A. Ortiz, and K. Simmons, 2022, “Adhesively bonded metal-CFRTP bi-materials: Enhanced crack growth resistance via plasma and quantified fracture via size effect method,” *American Society for Composites (ASC) 37th Annual Technical Conference*, Tucson, AZ, USA.

10. Qiao, Y., Y. Shin, J. L. Ramos, H. M. Engelhard, R. J. Seffens, D. R. Merkel, and K. L. Simmons, 2024, "Plasma treatment on both adhesive tape and adherends for significantly enhanced CFRTP-related adhesive joints," *Appl. Surf. Sci.*, 649, 159092. <https://doi.org/10.1016/j.apsusc.2023.159092>.
11. Shin, Y., Y. Qiao, N. Yelin, J. L. Ramos, D. R. Merkel, and K. L. Simmons, 2023, "Interfacial bond characterization of epoxy adhesives to aluminum alloy and carbon-fiber-reinforced polyamide by vibrational spectroscopy," *Surf. Interfaces*, 42(Part A),103346.
12. Shin, Y., Y. Qiao, N. Canfield, Z. Yu, H. M. Meyer, D. R. Merkel, E. K. Nickerson, N. S. Kanbargi, A. Ortiz, A. K. Naskar, and K. L. Simmons, 2022, "Significant slowdown of plasma-optimized surface energy deactivation by vacuum sealing for efficient adhesive bonding," *Compos. B Eng.*, 240, 110001. <https://doi.org/10.1016/j.compositesb.2022.110001>.
13. Su, Y. F., Y. C. Lim, K. M. Faraone, D. A. Frederick, J. Jun, H. Meyer, J. K. Keum, and Z. Feng, 2022, "Laser-surface processing on 7075 Al alloys to improve corrosion resistance," *International Materials Applications & Technologies Conference and Exposition (IMAT) 2022*, 12–15 September 2022, New Orleans, LA, USA.

References

1. Lim, Y. C., J. Chen, J. Jun, D. N. Leonard, M. P. Brady, C. D. Warren, and Z. Feng, 2021, "Mechanical and corrosion assessment of F-SPR joint of carbon fiber-reinforced polymer and magnesium alloy AZ31B," *J. Manuf. Sci. Eng.*, 143(3), 031106. <https://doi.org/10.1115/1.4048378>.
2. Lim, Y. C., H. Park, J. Jang, J. W. McMurray, B. S. Lokitz, J. K. Keum, Z. Wu, and Z. Feng, 2018, "Dissimilar materials joining of carbon fiber-polymer to DP 980 by friction bit joining, adhesive bonding, and weld-bonding," *Metals*, 8(11), 865. <https://doi.org/10.3390/met8110865>.
3. Lim, Y. C., L. Squires, T.-Y. Pan, M. Miles, G.-L. Song, Y. Wang, and Z. Feng, 2015, "Study of mechanical joint strength of aluminum alloy 7075-T6 and DP steel 980 welded by friction bit joining and weld-bonding under corrosion medium," *Mater. Des.*, 69, 37–43. <https://doi.org/10.1016/j.matdes.2014.12.043>.
4. Mansfeld, F., and J. V. Kenkel, 1976, "Laboratory studies of galvanic corrosion of aluminum alloys," In: Baboian, R., W. France, L. Rowe, and J. Rynewicz (eds.), *Galvanic and Pitting Corrosion—Field and Laboratory Studies*, ASTM International, West Conshohocken, PA, USA. <https://doi.org/10.1520/STP41395S>.
5. Mandel, M., and L. Kruger, 2013, "Determination of pitting sensitivity of the aluminum alloy EN AW-6060-T6 in a carbon-fiber-reinforced plastic/aluminum rivet joint by finite element simulation of the galvanic corrosion process," *Corros. Sci.*, 73, 172–180. <https://doi.org/10.1016/j.corsci.2013.03.033>
6. Liu, Z., Y. Dong, Z. Chu, Y. Yang, Y. Li, and D. Yan, 2013, "Corrosion behavior of plasma sprayed ceramic and metallic coatings on carbon steel in simulated seawater," *Mater. Des.*, 52, 630–637. <https://doi.org/10.1016/j.matdes.2013.06.002>.
7. Lim, Y. C., J. Jun, M. P. Brady, and Z. Feng, 2021, "Methodology to avoid accelerated corrosion of dissimilar material fastener joints using alloys forming surface oxides," ORNL invention disclosure No. 202004631, Oak Ridge National Laboratory, Oak Ridge, TN, USA.
8. Lim, Y. C., J. Jun, D. N. Leonard, Y. Li, J. Chen, M. P. Brady, Z. Feng, 2022, "Study of galvanic corrosion and mechanical joint properties of AZ31B and carbon-fiber-reinforced-polymer joined by

friction self-piercing riveting *J. Magnes. Alloy.*, 10(2), 400–410.
<https://doi.org/10.1016/j.jma.2021.05.003>.

9. Lim, Y. C., J. H. Jun, M. Brady, and Z. Feng, “Fastener joint and associated method for avoiding corrosion of dissimilar material faster joints,” US Patent 11,808,297 B2.

Acknowledgements

The co-PI at PNNL would like to acknowledge Y. Shin, D. Merkel, K. Simmons, Y. Qiao, S. Niverty, B. Schuessler, R. Kalsar, A. Guzman, M. Rhodes, V. Prabhakaran, V. Viswanathan, and A. Crawford for the surface processing, characterization, and modeling activities for this project. The co-PIs at ORNL would like to acknowledge R. Davies, Z. Feng, and A. Hayes for their leadership and technical guidance. In addition, the co-PIs recognize the great efforts of the project team members at ORNL, including J. Jun, A. Frederick, H. Meyer III, J. K. Keum, M. Brady, N. Kanbargi, Z. Yu, and A. Naskar. Finally, the co-PIs at ORNL express their appreciation for L&L Products for their providing adhesives for this project. The contributions by R. R. Kamath and W. Liu at ANL in conducting the APS experiments and data analysis are acknowledged. This research used resources of the APS, a DOE Office of Science user facility operated for the DOE’s Office of Science by ANL under Contract No. DE-AC02-06CH11357. Our DOE VTO Program Manager, Chris Schooler, is also acknowledged.

II.4.1.5 Extending Ultrasonic Welding Techniques to New Material Pairs (Oak Ridge National Laboratory)

Jian Chen, Principal Investigator

Oak Ridge National Laboratory
Materials Science and Technology Division
1 Bethel Valley Rd.
Oak Ridge, TN 37830
E-mail: chenj2@ornl.gov

Zhilli Feng, Co-Principal Investigator

Oak Ridge National Laboratory
Materials Science and Technology Division
1 Bethel Valley Rd.
Oak Ridge, TN 37830
E-mail: fengz@ornl.gov

Christopher Schooler, DOE Technology Development Manager

U.S. Department of Energy
E-mail: Christopher.Schooler@ee.doe.gov

Start Date: October 1, 2020
Project Funding: \$584,000

End Date: September 30, 2023
DOE share: \$584,000

Non-DOE share: \$0

Project Introduction

Modern multimaterial vehicles require joining of various lightweight materials, such as Al- and Mg-alloys and CFRP, with advanced high-strength steels together to form a high-performance and lightweight body structure. A variety of joining methodologies (e.g., RSW, adhesive bonding, linear fusion welding, hemming, clinching, bolting, riveting) have been attempted by the automotive industry to join different materials. Often, these joining techniques are limited to only certain material combinations. For capital and operational cost, automobile OEMs need to limit the number of joining technologies implemented on an assembly line.

In Phase I of the JCP, we investigated the versatility of ultrasonic-based spot-joining (UJ) processes to join different material combinations [1], [2]. Ultrasonic spot-welding (USW) is one of the major UJ processes which is a solid-state joining method that produces weld joints by localized high-frequency tangential vibration under moderate clamping pressure. The temperate rise during a USW process is generally not sufficient to melt the material. Instead, the HT and pressure at the interface induce rapid diffusion between the substrates to form the joint. We also successfully demonstrated the ability of joint DP590 steel and AZ31B Mg-alloys with a reasonably high-strength, including bare steel to Mg that were considered to be unweldable as they are metallurgically immiscible, through USW process innovations assisted by extensive physics-based process modeling.

However, a number of technical challenges still remain that hinder the application of USW for automotive body structures. They include challenges to produce consistent joint quality when multiple welds are made on large metal body structures. This is particularly challenging due to the complex ultrasonic wave propagation and interaction with other spot welds in a large structural assembly. In addition, research is required to extend the USW to other material combinations in multimaterial autobody structures. In FY 2021 and FY 2022, ORNL has successfully developed and demonstrated that USW is capable of joining a variety of dissimilar metal combinations (e.g., Mg-steel, Al-steel, Mg-Al). An innovative closed-loop control (CLC) approach was developed to achieve the consistent joint quality through the entire panels (material combinations: Mg-steel, Al-steel, Mg-Al) and the average joint strength exceeded 80% of the small single-joint coupons [3].

In FY 2023, ORNL further demonstrated the feasibility to join metal-polymer (i.e., Al and Al-CFRP), by a recently patented ultrasonic rivet joining (URJ) process [4]. The CLC approach was also used to ensure the consistent joint quality for joining of large samples.

Objectives

The primary objective of this project is to further explore, understand, and extend the unique characteristics of UJ to join various lightweight material combinations in an assembly of a lightweight multimaterial vehicle. The targeted outcomes will be a versatile, ultrasonic-based solid-state spot-joining technology to join representative component-level coupons in which multiple joints are required. The outcome will include extending the joining technology to join a variety of lightweight dissimilar material stack-ups including Al, CFRP, Mg, and steel.

Approach

The project consists of following three major tasks to progressively advance the technology:

FY 2021: Research and develop the process toward multi-spot USW joints in large steel-Mg coupons with the goal to achieve an average joint strength of at least 80% strength of a single spot USW on single-joint coupons.

FY 2022: Extend the USW process to join large Al-steel and Al-Mg coupons consisting of multi-spot joints to achieve an average joint strength of at least 80% strength of a single spot USW on single-joint coupons.

FY 2023: Research and develop a new ultrasonic-based joining process—the URJ process—to address a specific need to join metal to non-metal material combinations. The goal is to achieve an average multi-joint strength of at least 80% of the strength of the single-joint URJ coupons between CFRP and Al7075 structural stack-ups.

The following subtasks were planned to meet FY 2023 milestones:

Subtask 1: Feasibility study of using URJ to join Al-CFRP in single-joint lap-shear coupons.

Subtask 2: Refine process conditions and obtain an optimized joint strength as a reference.

Subtask 3: Extend URJ to join large CFRP-Al components that consist of multiple joints.

Results

The welding trials were performed on based unidirectional CFRP (3-mm-thick) and Al AA7075-T6 (2.3-mm-thick) sheets, as shown in Figure II.4.1.5.1. During welding, the top sonotrode drives a cylindrical Al AA7075-T6 rivet to vibrate laterally at 20kHz. The welding process can be divided into three stages, as shown in Figure II.4.1.5.2. In Stage I, the sonotrode keeps driving the rivet to penetrate through the CFRP until Stage II when the Al rivet reaches the bottom Al sheet. The sonotrode and rivet stops moving and frictional heat keeps accumulating between the rivet and the bottom Al sheet in Stage II. In Stage III, the increased temperature softens the materials to further deform the rivet and a solid-state bond between the rivet and the Al sheet is formed.

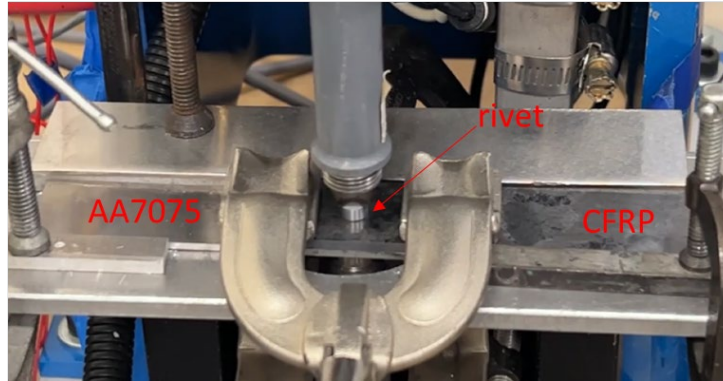


Figure II.4.1.5.1. Schematics and apparatus of URJ. Source: ORNL.

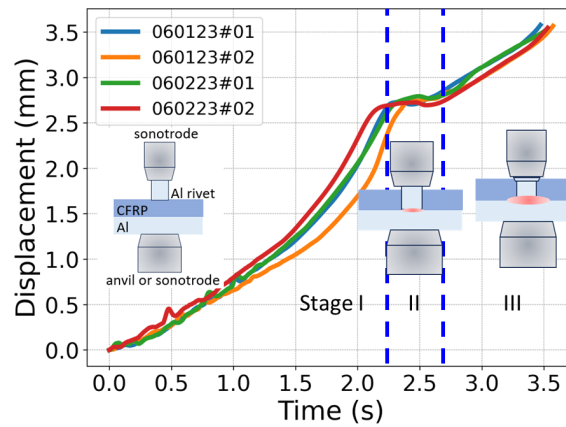


Figure II.4.1.5.2. Sonotrode displacement curve showing three stages of the URJ process. Source: ORNL.

A wide range of welding process conditions including welding power, energy, and sonotrode tip dimensions to determine the process window. Figure II.4.1.5.3(a) shows a single-joint URJ sample welded with the optimized welding parameters, while Figure II.4.1.5.3(b) summarizes the lap-shear loading-displacement curves for all samples welded in the same conditions. The average lap-shear peak load obtained was 3.1 ± 0.4 kN. In most cases, the fracture after lap-shear testing occurred at the rivet-Al joint interface. However, in some cases with a relatively low-peak lap-shear load, the fracture occurred through CFRP. This is likely a result of excessive CFRP damage during the welding process. As shown in Figure II.4.1.5.4, voids were formed in the CFRP adjacent to the rivet due to thermal and mechanical damage.

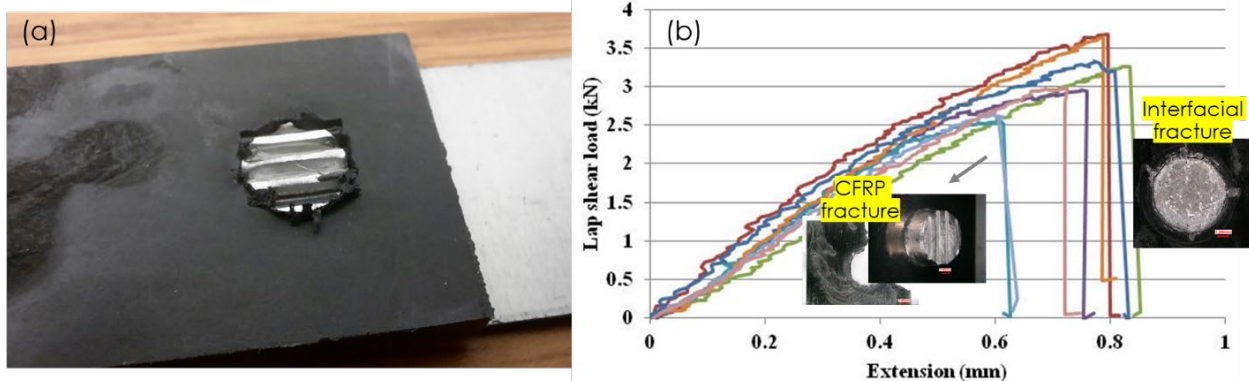


Figure II.4.1.5.3. (a) Single-joint lap-shear sample welded by URJ and (b) lap-shear tensile results. Source: ORNL.

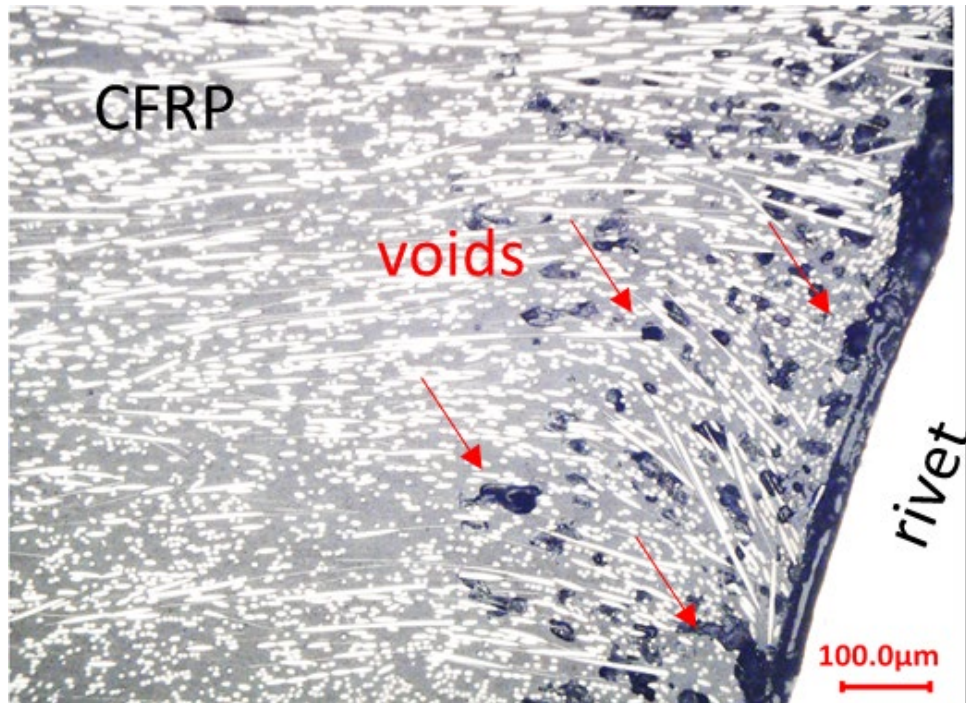


Figure II.4.1.5.4. Cross-section of the joint interface showing the formation of voids in the CFRP adjacent to the rivet. Source: ORNL.

Figure II.4.1.5.5(a) shows an overall cross-section of the joint interface. The dotted line indicates the location of the joint line. No defect was observed at this resolution. Further electron backscatter diffraction analysis in Figure II.4.1.5.5(b–d) reveals that a layer of the refined grains was formed through the entire joint interface.

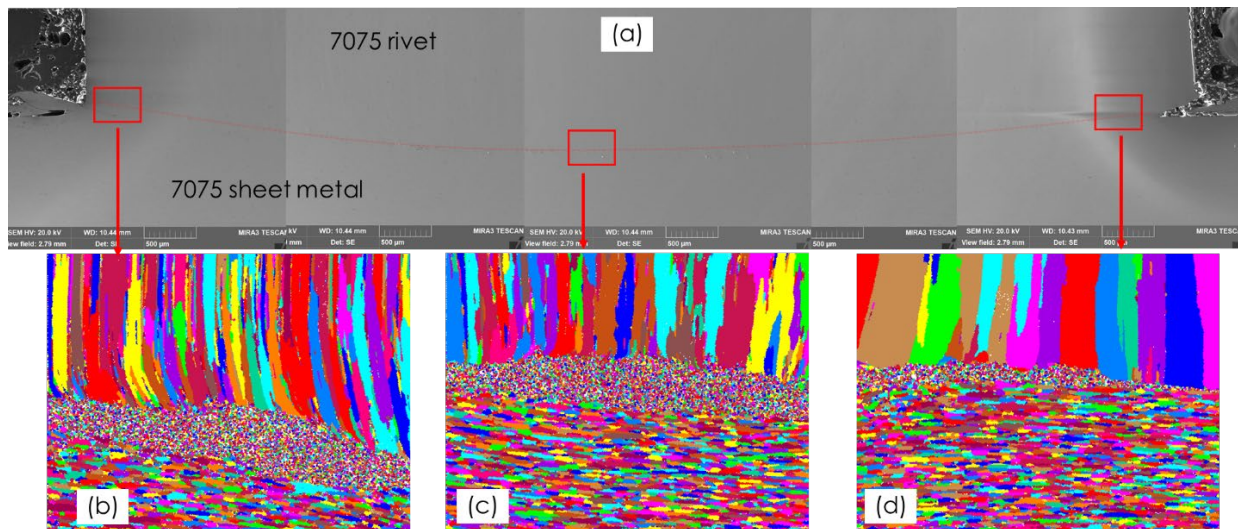


Figure II.4.1.5.5. (a) Cross-section of the URJ joint interface. (b–d) Electron backscatter diffraction maps showing a grain refinement zone through the joint interface. Source: ORNL.

The CLC approach [3] was then applied to join large CFRP-Al coupons consisting of five URJ spots, as shown in Figure II.4.1.5.6(a). Each joint (from “A” to “E”) was cut out and tested individually using a lap-shear tensile setup. The peak load at each location is plotted in Figure II.4.1.5.6(b) showing an average at 2.0 ± 0.6 kN, roughly 87% of the LSS obtained on single-joint coupons.

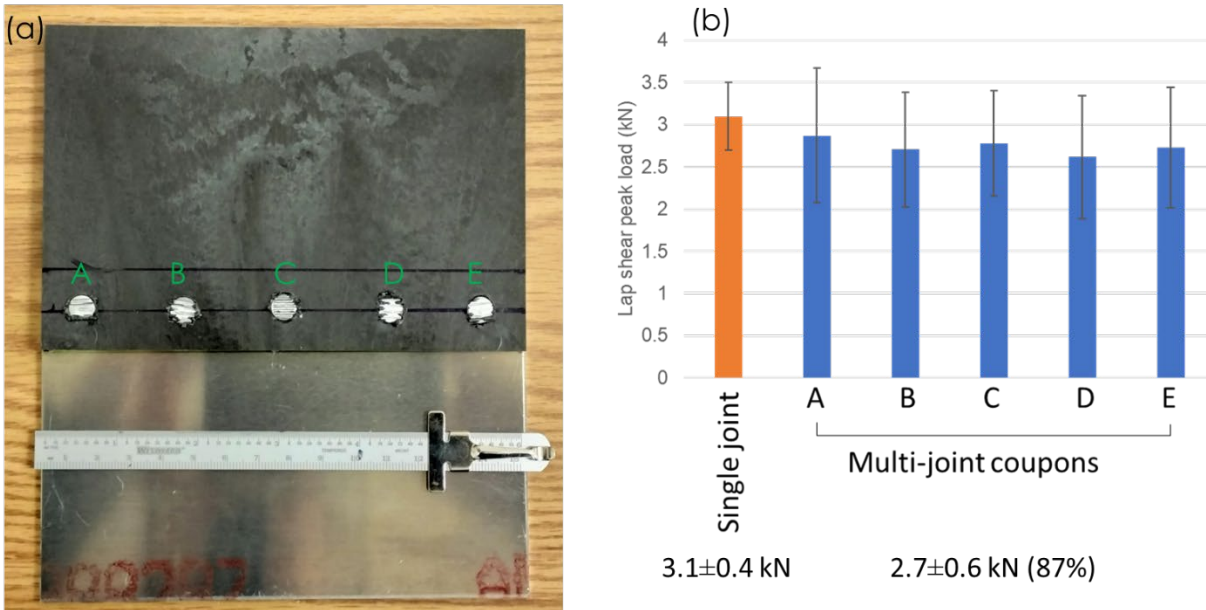


Figure II.4.1.5.6. (a) Large CFRP-Al coupons consisting of five URJ joints. (b) Peak lap-shear load of each individual URJ joint and the comparison with single-joint coupon. Source: ORNL.

Conclusions

The R&D in FY 2023 led to the following major achievements and findings:

- URJ process was successfully applied to join Al-CFRP pairs with an Al rivet. No pilot holes are needed.
- A solid-state metallurgical bond with a layer of refined grains was formed between an Al sheet and an Al rivet without defects.
- With the innovative CLC approach applied, URJ also was to be used to join large Al-CFRP coupons consisting of multiple joints. Consistent joint quality was achieved and the average joint strength was 87% of the reference strength obtained on single-joint Al-CFRP URJ coupons.

Key Publications

1. Chen, J., Y.-C. Lim, H. Huang, Z. Feng, and X. Sun, 2019, "Ultrasonic welding of AZ31B magnesium alloy," *MRS Bull.*, Vol. 44, No. 8, pp. 630–636. <https://doi.org/10.1557/mrs.2019.182>.
2. Chen, J., Y.-C. Lim, H. Huang, and Z. Feng, 2019, "Ultrasonic welding of AZ31B magnesium and DP590 steel," *American Welding Society Annual Conference*, 11–14 November 2019, Chicago, IL, USA.
3. Chen, J., Y. C. Lim, D. N. Leonard, H. Huang, Z. Feng, and X. Sun, 2020, "In-situ and post-mortem characterizations of ultrasonic spot-welded AZ31B and coated DP 590 steel joints," *Metals*, 10(7), 899. <https://doi.org/10.3390/met10070899>.
4. Chen, J., R. W. Davies, Z. Feng, X. Hu, H. Huang, and X. Sun, 2020, "Ultrasonically assisted self-piercing riveting," U.S. Patent Application No. 16/585,754, filed 2 April 2020, UT-Battelle, LLC.
5. Chen, J., Y. Li, H. Huang, J. Cheng, Y.-C. Lim, X. Hu, and Z. Feng, 2022, "USW of immiscible mg/steel: Bonding mechanisms and approach to weld multi-joint components," *Advances In Welding and Additive Manufacturing Research (AWAMR) Conference*, 13–16 June 2022, Virtual (Invited).
6. Chen, J., et al., "Ultrasonic welding of dissimilar body structures," *IMAT Advanced Materials and Manufacturing Technologies*, 16–19 October 2023, Detroit, MI, USA.

7. Huang, H., J. Chen, Y.-C. Lim, X. Hu, J. Cheng, Z. Feng, and X. Sun, 2019, “Heat generation and deformation in ultrasonic welding of magnesium alloy AZ31,” *J. Mater. Process. Technol.*, 272, 125–136. <https://doi.org/10.1016/j.jmatprotec.2019.05.016>.
8. Huang, H., J. Chen, Y.-C. Lim, Z. Feng, and X. Sun, 2019, “Enhance heat generation and joint strength in dissimilar metal ultrasonic welds by surface engineering,” *American Welding Society Annual Conference*, 11–14 November 2019, Chicago, IL, USA.
9. Huang, H., J. Chen, Z. Feng, and X. Sun, 2023, “Modal analysis of USW for lightweight metals joining,” *Metals* 13(10) 1735. <https://doi.org/10.3390/met13101735>.
10. Jun, J., J. Chen, Y.-C. Lim, M. Brady, D. N. Leonard, and Z. Feng, 2020, “Corrosion behavior of ultrasonic-welded AZ31B and DP steel with and without galvanize layer,” *TMS Coatings and Surface Engineering for Environmental Protection II Conference*, 23–27 February 2020, San Diego, CA, USA (Invited).
11. Li, Y., Y. Wang, J. Chen, Y. C. Lim, and Z. Feng, 2024, “Surface grain refinement of casting A380 aluminum alloy by ultrasonic-assisted surface mechanical grinding treatment,” *Mater. Lett.*, 354, 135387. <https://doi.org/10.1016/j.matlet.2023.135387>.
12. Xiong, L., A. Chuang, D. Singh, J. Chen, Y.-C. Lim, and Z. Feng, 2020, “Synchrotron x-ray diffraction and computed tomography studies of ultrasonic welding dissimilar Mg-Fe metals,” *TMS Coatings and Surface Engineering for Environmental Protection II Conference*, 23–27 February 2020, San Diego, CA, USA.

References

1. Upadhyay, P., H. Das, J. Chen, Z. Feng, H. Huang, Y. C. Lim, Y. Li, D. N. Leonard, X. Sun, L. Xiong, C. A. Chuang, and D. Singh, 2021, Solid-State Joining of Magnesium Sheet to High-Strength Steel, ORNL/SPR-2021/1836, Oak Ridge National Laboratory, Oak Ridge, TN, USA. <https://doi.org/10.2172/1772623>.
2. Chen, J., R. W. Davies, Z. Feng, X. Hu, H. Huang, and X. Sun, 2020, “Ultrasonically assisted self-piercing riveting,” U.S. Patent Application No. 16/585,754, filed 2 April 2020, UT-Battelle, LLC.
3. Chen, J., H. Huang, Y. C. Lim, and Z. Feng, 2023, “A method to consistently produce high-quality ultrasonically welded spot joints in large metal structures,” U.S. Patent Application No. 63/525,379.
4. Lim, Y. C., Z. Feng, J. Chen, X. Sun, R. W. Davies, 2021, “URJ of dissimilar materials,” U.S. Patent 11,253,908B2.

Acknowledgements

The authors acknowledge the contributions from the following ORNL team members: Y. Li, H. Huang, Y. C. Lim, Y. Wang, J. Cheng, and A. Frederick. The authors also acknowledge their DOE VTO program manager, C. Schooler.

II.4.2 Multi-Materials Joining

II.4.2.1 Manufacturing Demonstration of a Large-scale, Multimaterial Passenger Vehicle Subsystem (Clemson University)

Srikanth Pilla, Principal Investigator

Department of Automotive Engineering
 Division of Material Science and Engineering
 Clemson University
 4 Research Dr., Ste. #340
 Greenville, SC 29607
 E-mail: spilla@clemson.edu

Christopher Schooler, DOE Technology Development Manager

U.S. Department of Energy
 E-mail: Christopher.Schooler@ee.doe.gov

Start Date: October 1, 2021

End Date: September 30, 2025

Project Funding: \$3,748,617

DOE share: \$1,992,178

Non-DOE share: \$1,756,439

Project Introduction

Transportation accounts for 26.9% of all energy consumption in the U.S. [1] and results in nearly one-third of all CO₂ emissions [2]. Furthermore, recent global energy markets and supply-chain disruptions have given impetus towards developing cost-effective lightweighting utilizing materials, such as Al, Mg, and FRP composites as they have the potential to reduce the weight of a vehicle's BIW by up to 50% [3]. It is estimated that for every kilogram of weight-reduction, approximately 20 kg CO₂ emissions reduction is achievable [4]. However, lightweighting approaches that leverage a single material system do not present a cost-effective solution. Conceptual redesigning and optimization to suit the lightweight material system often result in tradeoffs in cost, increased manufacturing complexity, and higher cycle times. Thus, a multimaterial lightweighting approach, capitalizing on the progress made in multiple domains, is necessary. Despite an increasing trend in the sales of SUVs and trucks, no previous studies specifically address their lightweighting through a systemic multimaterial redesign of the vehicle structure using FRP composites.

However, the joining of FRP composites with metals has its challenges. It is difficult to achieve a metallurgical bond between the FRP composites and metals with conventional welding processes, while mechanical fastening increases assembly complexity, leads to high-stress concentration regions, and reduces the structure's strength, stiffness, and toughness. Adhesives are a promising option; however, the need to have a sufficient contact area for the adhesive to be effective, meticulous preparation of bonding surfaces, the brittle nature of adhesives, and the added adhesive and flange weight are inhibiting factors. This project aims to implement a fiber-metal mechanical interlocking transition joint where the mechanical interlocking between the metal and the composite is molded into the component during the liquid composite molding process without leading to stress concentration.

Objectives

The goal of this project is to employ a systems approach to redesign, manufacture, and validate the BIW glider system of a 2019 mid-size Honda Pilot SUV to achieve cost-effective and sustainable lightweighting of 160 lbs. This will be achieved by aligning with the U.S. DRIVE roadmap to leverage component consolidation, state-of-the-art design optimization tools, and multimaterial transition and joining technologies. By using industry-standard manufacturing processes and proprietary recycling technologies, the final design will meet or exceed benchmark structural requirements, crash performance, and noise, vibration, and harshness (NVH) requirements while preserving the existing factory assembly process of the OEMs. To meet the objectives, the team proposes to evaluate new multimaterial designs via a clean-sheet redesign approach to use novel, lightweight, and low-cost composite materials, multimaterial design optimization, patented CFRP-metal

transitions, and state-of-the-art composites manufacturing technologies. The project partner organizations, as indicated in Table II.4.2.1.1, have significant expertise in the above core methodologies and the ability to provide expert opinions and guidance to ensure success in achieving the project goals.

Table II.4.2.1.1. Project Partner Organizations

Universities	Automotive OEM Partners	Computer-Aided Engineering Partners	Materials and Sustainability Partners
CU	Honda	Moldex3D	Zoltek
UD-CCM		Altair Engineering	WestLake Epoxy
		Siemens	
OSU		Hexagon (Digimat®)	Carbon Conversions, Inc.

Approach

DOE's project objectives clearly define the scope for lightweighting and structural performance requirements, established through benchmarking of the baseline BIW by performing structural analyses for several load cases. The overall technical approach follows the automotive industry's standard practice of product development based on the V-diagram. Because manufacturing processes play a very significant role in the end properties achieved, multiple simulation-validation loops have been incorporated into the approach at the coupon-level, subcomponent-level, and assembly level as illustrated in Figure II.4.2.1.1. The subsequent sections elaborate on efforts made on the design and simulation fronts to develop feasible multimaterial lightweighting concepts for the baseline steel-intensive BIW of the 2019 Honda Pilot. The overall technical approach to the project is divided into four distinct phases addressing various aspects of design development and validation. Phase 1 involves identifying the right structural design targets and methodology to evaluate the final multimaterial BIW design. FEA was performed on the baseline steel BIW for static and crash load cases followed by conceptualization and downselection of conceptual designs. Phase 2 involves the development of a suitable topology based on the downselected conceptual designs, with iterative design refinement based on the results from the cost assessment, FEA, and life cycle assessment. Phase 3 involves utilizing design optimization schedules for the overall topology, optimization of composite material selection at the component-level, ply-level, ply-shape, stacking sequence, and angles. The design features are also proposed to be optimized based on design-for-manufacturability studies utilizing draping simulations, RTM simulations and an analysis of manufacturing-induced effects, such as voids, dry spots, and residual stresses. The simulation inputs will be validated by manufacturing and testing of multimaterial subcomponents. This will ensure the methodology is robust and can be adopted for full-scale multimaterial BIW part designs from the manufacturability point-of-view. Finally, a functional multimaterial BIW will be fabricated, assembled, and crash-tested for specific crash loads identified during Phase 1 of the project.

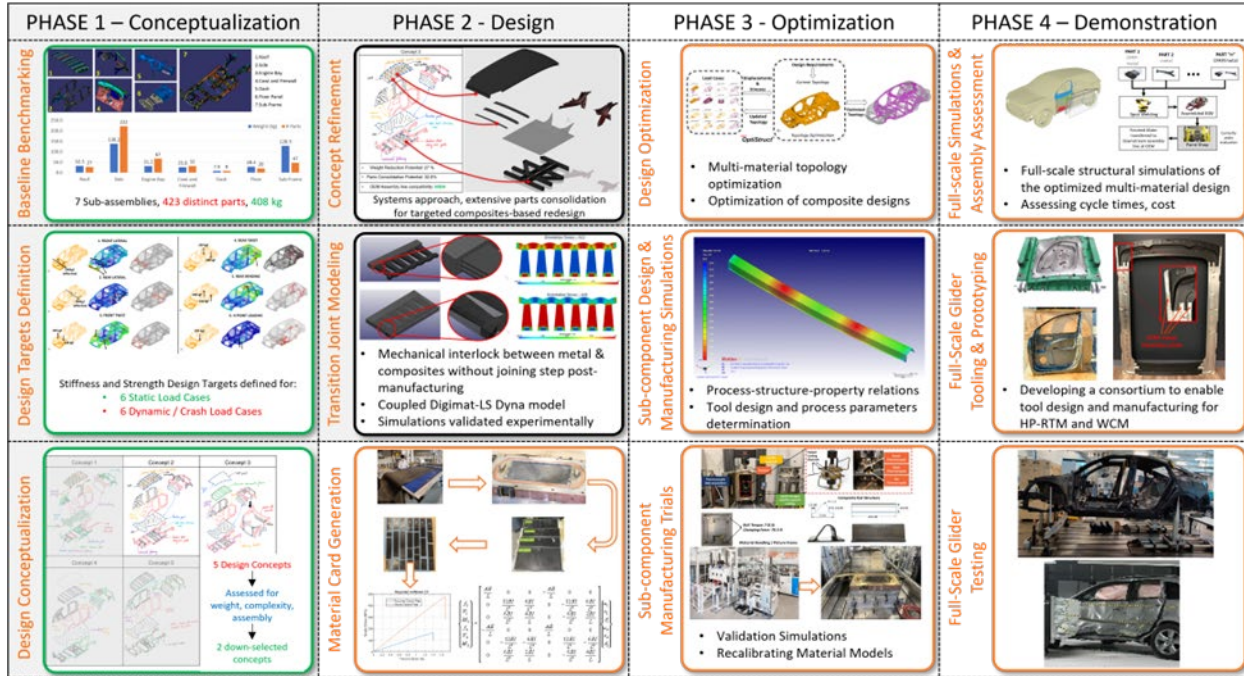


Figure II.4.2.1.1. Systems approach with multiple simulation-validation loops at various component scales. (Figure for illustrative purposes only and not intended to show details.) Source: Clemson University.

Results

CAD Concepts Development

Designs leveraging various lightweight materials like glass fiber-reinforced plastic (GFRP) and CFRP composites, Al, high-strength steel, and AHSS were proposed for various assemblies comprising the BIW, resulting in multiple designs for each of the regions of the BIW. These assembly designs were combined into five unique BIW conceptual designs, which were assessed for lightweighting, and parts consolidation potential using simple parametric models. OEM feedback was used to grade each BIW conceptual design. These three metrics helped down-select the two most promising BIW conceptual designs for further FEA and optimization studies [5], as illustrated in Figure II.4.2.1.2. CFRP and GFRP composites were used at locations requiring high-stiffness and moderate-to-high-strength. However, regions that require high-ductility and high-strength, implying high-toughness, have been retained to be made from baseline steel.

Based on the two downselected conceptual designs, two distinct CAD concepts were developed. The first concept focused on the roof, floor, and subframe assemblies, while the second concept focused on both of the side assemblies. Part consolidation and design simplification were heavily leveraged to ensure cost parity with the baseline steel designs being replaced. This also significantly reduces the costs associated with multiple sheet metal stamping tools and cycle time-savings due to reduced joining and assembly steps while ensuring significant lightweighting.

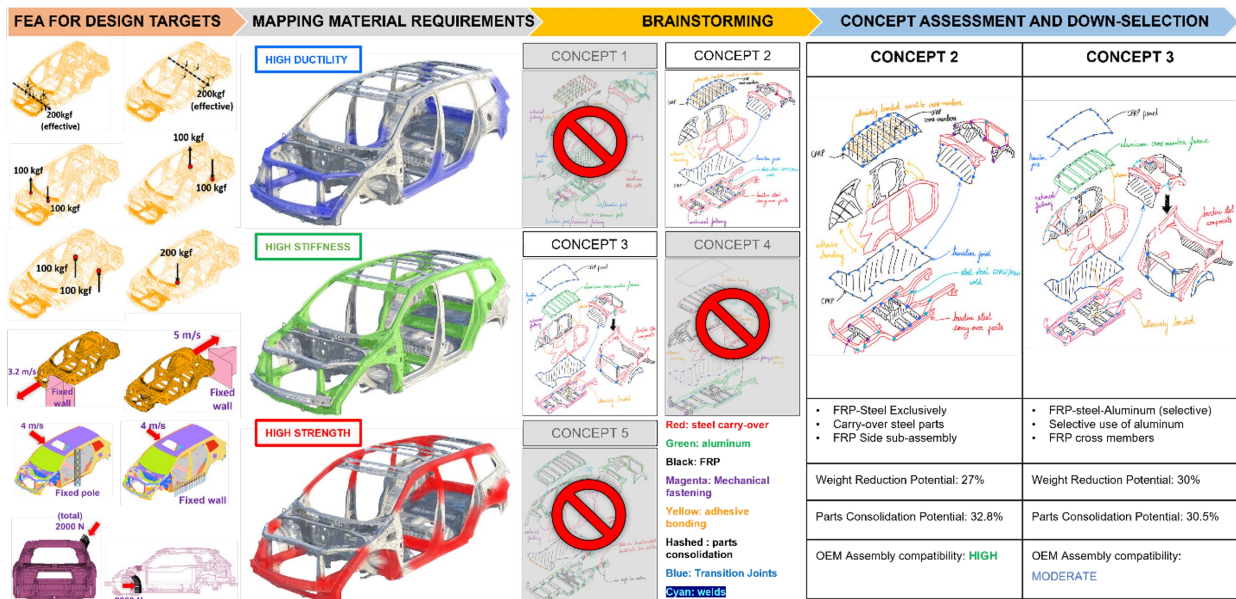


Figure II.4.2.1.2. Structural requirements benchmarking and design conceptualization. (Figure for illustrative purposes only and not intended to show details.) Source: Clemson University.

CAD Concepts Assessment – Structural Performance

Both design concepts were analyzed for their global stiffness response for the same load cases as the ones the baseline model was subjected to when establishing the design requirements, as illustrated in Figure II.4.2.1.3. The composite parts were assumed to be 4-mm-thick with four plies in a [0,45,-45,90] orientation. Each ply is a 1-mm-thick unidirectional continuous CF with Westlake Epikote snap-cure epoxy reinforcement matrix.

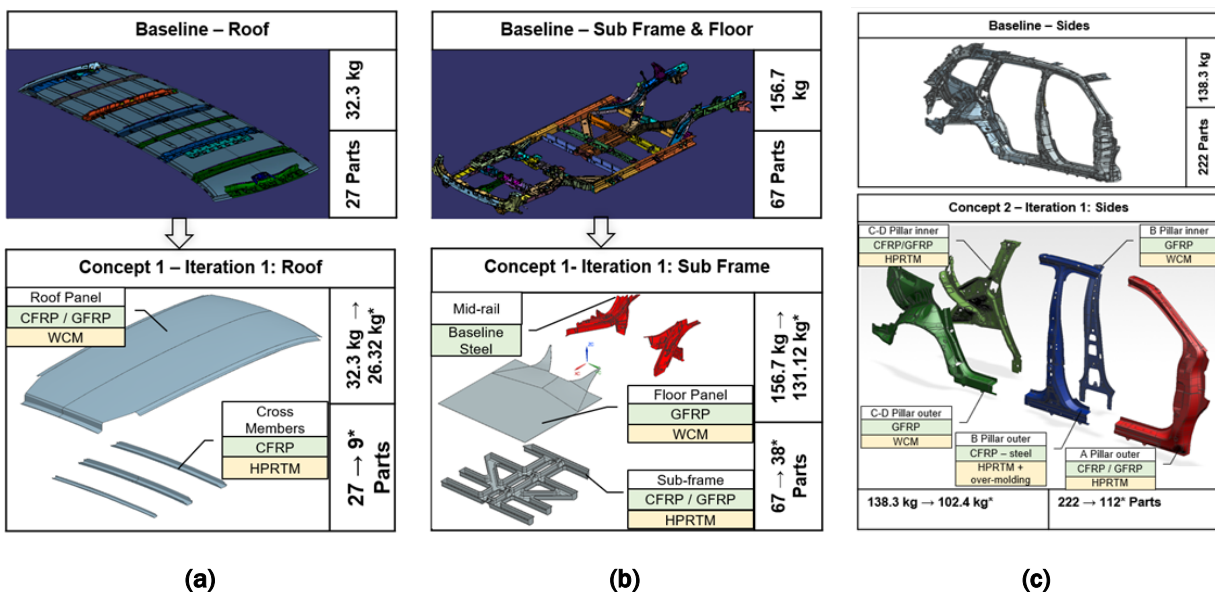


Figure II.4.2.1.3. (a-b) CAD Concept 1 focused on the roof and subframe. (c) CAD Concept 2 focused on the side assemblies [6]. Source: Clemson University.

The composite material system was defined as a MAT8 material card on Altair Optistruct for static load cases while the MAT58 material card on LS-DYNA was used for linear dynamic analyses with large deformation explicit dynamic formulation. Since the intent of the analyses was to establish the viability in comparison to the baseline, the linear material response was considered. As the designs are refined and optimized further, a more detailed viscoelastic non-linear analysis for both the baseline and CAD concepts will be performed. The results for both CAD concepts have been illustrated in Figure II.4.2.1.4 and Figure II.4.2.1.5.

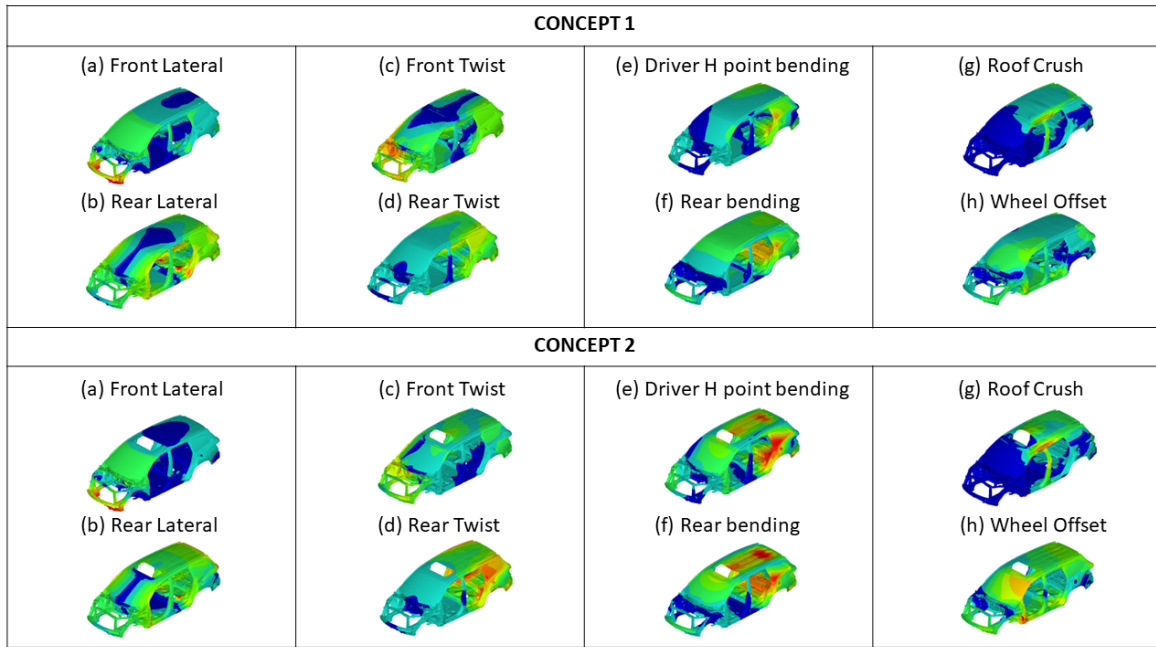


Figure II.4.2.1.4. Displacement plots showing the static structural analysis of Iteration 1 of the two design concepts. Source: Clemson University.

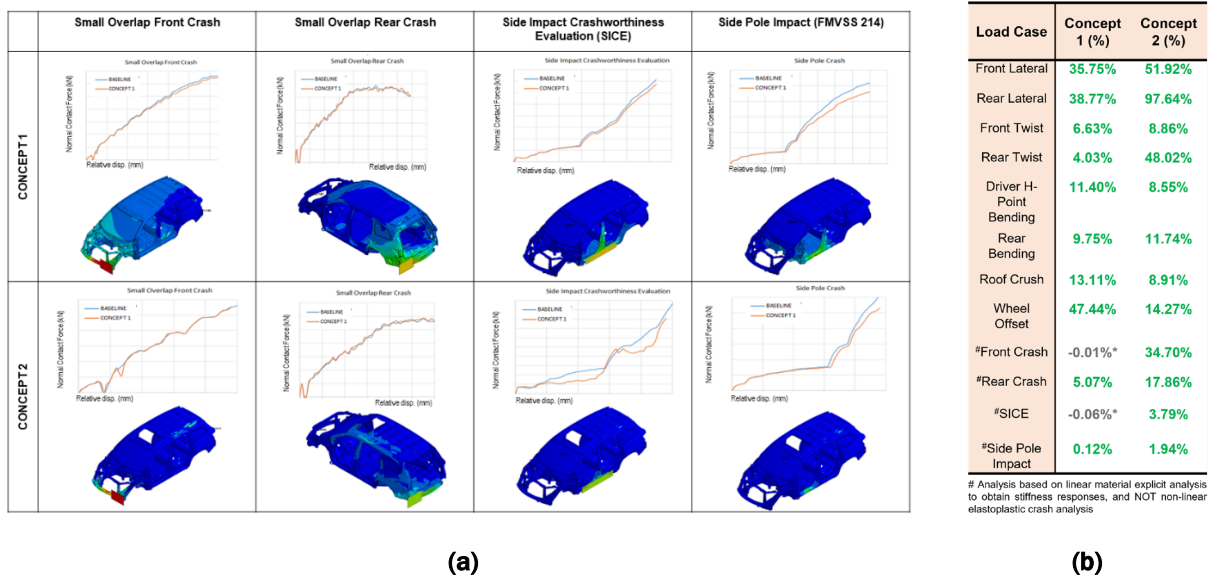


Figure II.4.2.1.5. (a) Dynamic (linear) structural analysis showing the force vs. displacement and displacement contour plots. (b) Stiffness of the design concepts compared to the baseline. Source: Clemson University.

Design Concepts Assessment – Parametric Cost Modeling

Once the proposed design concepts were verified to meet structural performance requirements within acceptable limits, the cost was assessed using a parametric cost model. The model factored in material, manufacturing, machining, tooling, and overhead costs with reasonable assumptions, as illustrated in Figure II.4.2.1.6. The CF-metal transition joint fabrication cost is calculated considering the cost of woven CF and the cost of AA6061. The mass ratio of the parts replaced with composite designs to the total baseline mass was determined to calculate the cost of baseline sheet metal components replaced. This approach allows the efficient estimation of cost vs. lightweighting feasibility without delving into the manufacturing costs of the baseline steel components. The tooling cost required to manufacture the composite components using HP-RTM or WCM was determined by estimating the tool volume (V_t) using the proposed composite design geometry. The cost of computer numerical control machining was determined using an hourly rate calculation to be \$68.39/hr., based on basic asset value and operating overheads. Furthermore, it is assumed the costs of assembly of the composite parts are the same as those of assembling the steel parts. This will be updated once the concepts are refined and a plant layout is developed to meet the yearly production objective.

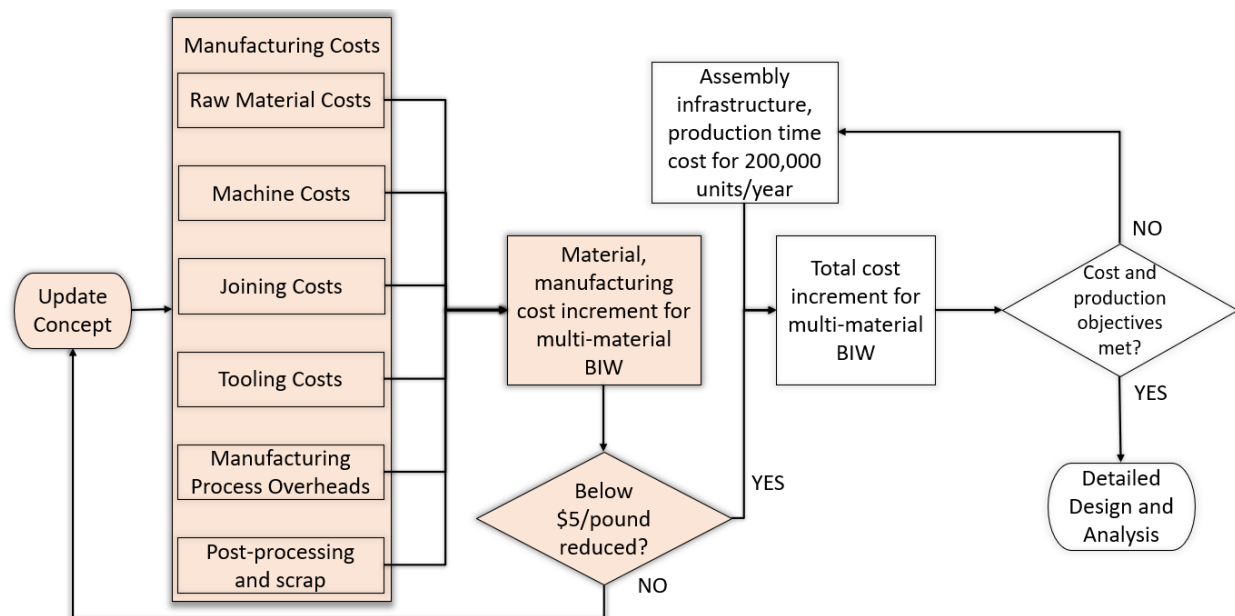


Figure II.4.2.1.6. Factors considered in the development of the parametric cost model [6].

Source: Clemson University.

Although assembly costs have not yet been included, both concepts exceed the project cost targets of \$5/lb. weight-reduction. Concept 1, which focused on the roof and subframe assembly redesign, significantly exceeds the cost margin, necessitating re-evaluation of the design and material choices. It was concluded from the cost analysis that replacing the material system used for large components, such as the roof and floor panel, with expensive composite materials, without associated parts consolidation is ineffective. Thus, further design refinement of this concept is necessary. Concept 2, which focused on the side assemblies, is significantly closer to the cost target and underscores the need for lightweighting and parts consolidation in tandem. The cost distribution by factors also highlights the dominance of material costs for large-scale production of structural composite parts. Additional reduction in cost is achievable as the design progresses and structural optimization of the use of expensive CF is performed. Figure II.4.2.1.7 provides the initial cost analysis for Iteration 1 of CAD Concepts 1 and 2.

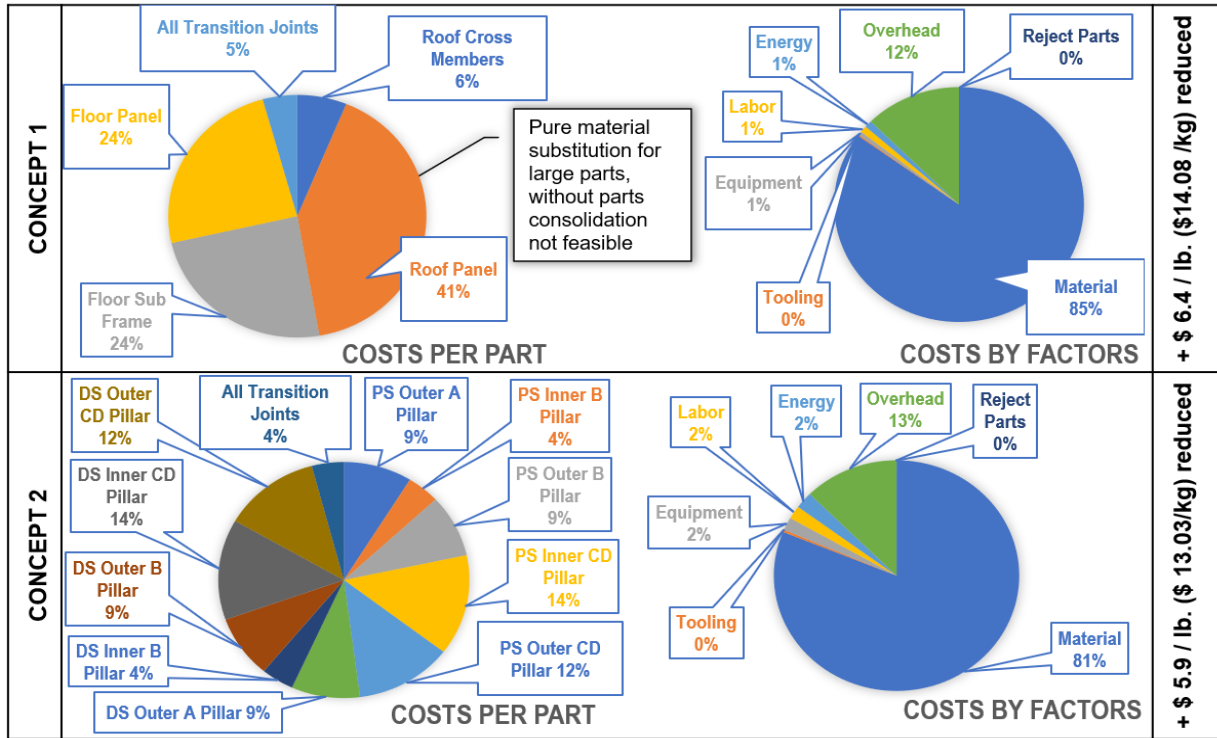
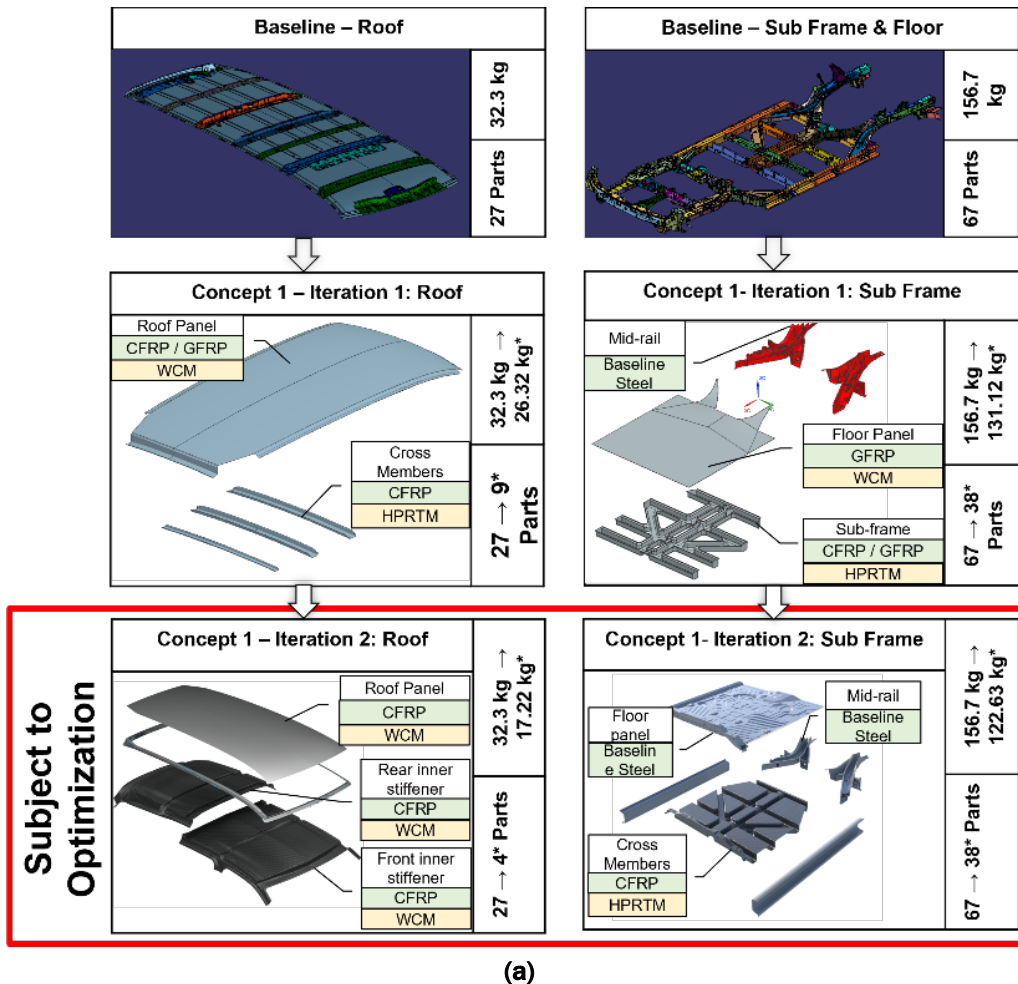


Figure II.4.2.1.7. Initial cost analysis for Iteration 1 of CAD Concepts 1 and 2 [6]. Source: Clemson University.

Design Concepts Refinement and Optimization

Cost analysis corroborated the fact that simple material substitution for some of the larger components, such as the roof and floor panels, despite the geometries being less complex and easily manufacturable with WCM, would not help meet the cost objectives. The material cost was more dominant in such cases, making the designs infeasible. Thus, CAD Concept Iteration 2, as observed in Figure II.4.2.1.8, followed a different approach with major stiffening members consolidated into a single composite component. The baseline designs and materials of the roof and floor panels were retained. Furthermore, instead of assuming a uniform thickness composite component, optimization was used to further lightweight and reduce the use of relatively expensive composite materials without compromising the stiffness requirements. The optimization is performed in two steps; initially, the ply thicknesses are kept free and optimized within the component, resulting in a composite with varying thicknesses at different locations, like topology optimization. However, unlike topology optimization, it is not discrete. Based on these results, zones of common thicknesses are defined in the composite part to reduce manufacturing complexity.

It can be observed in Figure II.4.2.1.9(a-c) that the roof parts have a high-thickness near the side rails of the frame. For their plies, it can be observed that high-thickness zones of the 45-degree plies originate where the frame is attached to the B-pillar of the BIW. The subframe thicknesses are more dispersed than the roof thicknesses. Based on these results, a zone can be established for the next optimization procedure. The total mass of the composite parts is reduced significantly, and the optimized concept meets all design requirements, as shown in Figure II.4.2.1.9(d-e). However, because the baseline roof panel material was retained to be steel in this concept, the weight-reduction achieved was comparably less, despite the design meeting the cost-objective. Hence, the roof panel was again incorporated to be made from composites and subjected to optimization. From the results, it can be inferred that a low-cost alternative fiber composite, such as GFRP, can help achieve the right tradeoffs between the achieved weight-reduction and cost.



The optimization problem is formulated as:

$$\text{Min } m$$

$$\text{S.T. } K_i^c \geq K_i^b + sf \quad i \in 0,1, \dots, n$$

Where,

m is the total mass of the BiW

K_i^c is the stiffness of load case i , at the current iteration.

K_i^b is the stiffness of load case i for the baseline BiW.

sf is a safety factor, currently 5%

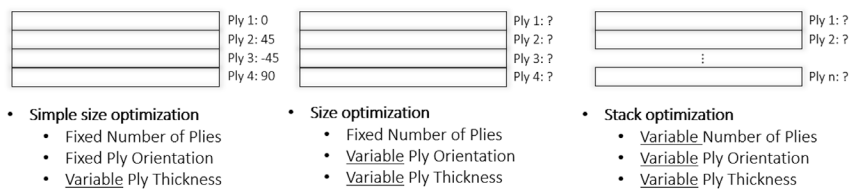


Figure II.4.2.1.8. (a) CAD Concept Iteration 2 based on FEA and cost assessment finding. (b) Composite optimization approach and problem formulation [6]. Source: Clemson University.

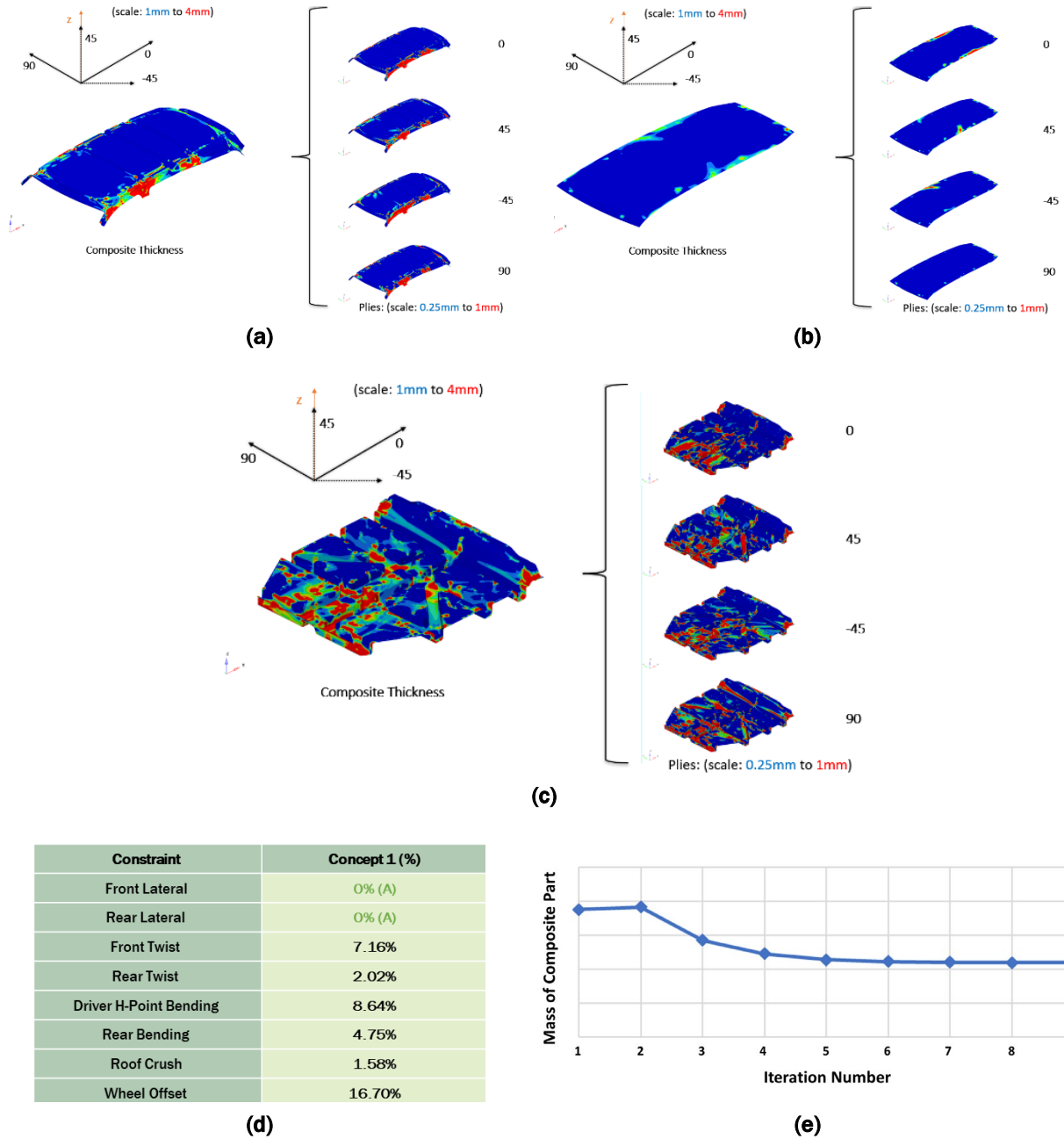


Figure II.4.2.1.9. (a-c) Optimization results for composite components. (d) Optimized concept performance. (e) Weight-reduction through iterative optimization (units for mass are proprietary) [6].

Source: Clemson University.

Simulation, Design, and Optimization for Crash

As the design moves from the conceptualization phase to the refinement phase, a more thorough understanding of the behavior of the baseline BIW under crash loads is needed. This new information will be leveraged to ensure the addition of overly stiff composite components does not diminish the impact attenuation and deformation behavior of the BIW. From the force vs. displacement curves and an inspection of the sequence of deformation initiation in various load members in the load path, it is possible to determine the expected behavior of that member under crash load and its contribution to the overall BIW response. Four key crash

load cases have been simulated with a non-linear material response factored into the simulation setup. This allows a more detailed comparison to be made between the multimaterial BIW and the baseline in terms of occupant space penetration, the transfer of impact forces to the occupants and identification of members that need to demonstrate good deformation (elongation) behavior. Two critical side impact load cases were simulated: (1) the Federal Motor Vehicle Safety Standards (FMVSS) 214 side-pole impact to determine the peak crush force and average crush forces over a range of pole penetration into the vehicle structure, and (2) the side impact crashworthiness evaluation, which represents a vehicle-to-vehicle side impact at 50 kilometers per hour. Both cases and the simulation results are illustrated in Figure II.4.2.1.10 and Figure II.4.2.1.11, respectively.

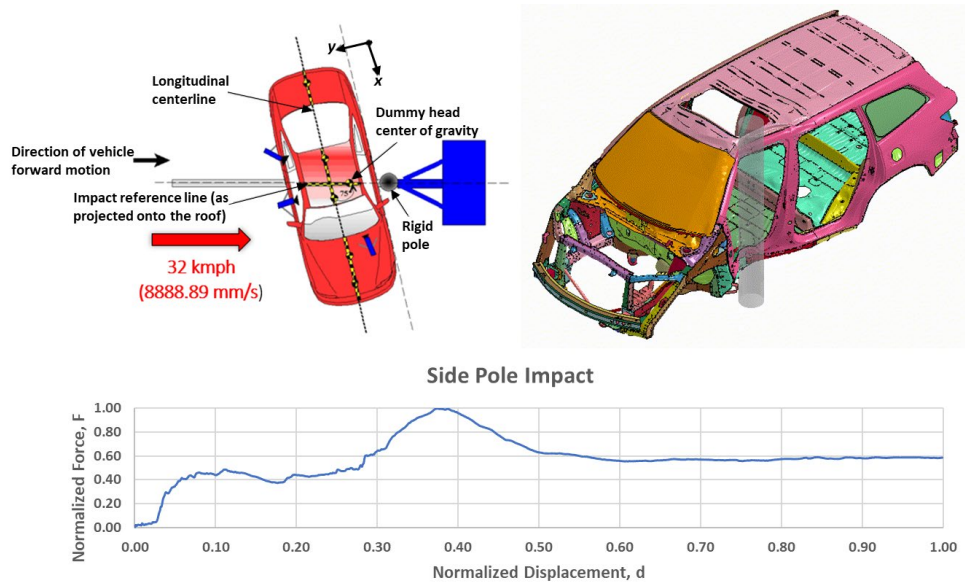


Figure II.4.2.1.10. FMVSS 214 quasi-static side-pole impact simulation with non-linear material response to understand deformation behavior. Source: Clemson University.

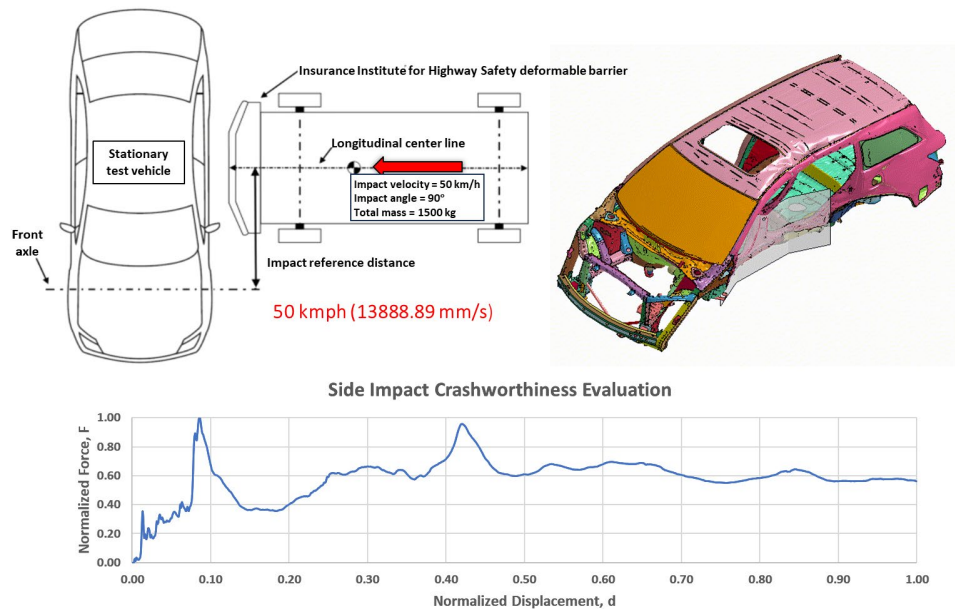


Figure II.4.2.1.11. Side impact crashworthiness evaluation simulation with non-linear material response to understand deformation behavior. Source: Clemson University.

An evaluation of the above simulations for side crash load cases indicate that the rocker beam, B-pillar, and lateral cross-beams in the subframe assembly play a key role in impact attenuation, as well as preventing excess intrusion into the occupant space. Thus, if the Concept 2 side assembly composite designs are to be implemented, additional impact attenuation features may be needed to absorb the impact forces before the stiff thermoset composite parts act to prevent excess intrusion within the occupant space. These inferences will be used to identify suitable design features that may need to be incorporated into the multimaterial designs, such as foam cores, ribs, and honeycomb reinforcements. The baseline BIW response to the front and rear impacts was also simulated, as illustrated in Figure II.4.2.1.12 and Figure II.4.2.1.13. It can be observed that impact forces are attenuated by the front bulkhead assembly and no significant structures proposed to be made from the composites are being required to exhibit high-elongation to absorb the impact forces. This indicates that the proposed composite components need to only exhibit high-strength and stiffness so as not to be the points of failure before the preceding structure has deformed in the process of absorbing impact forces.

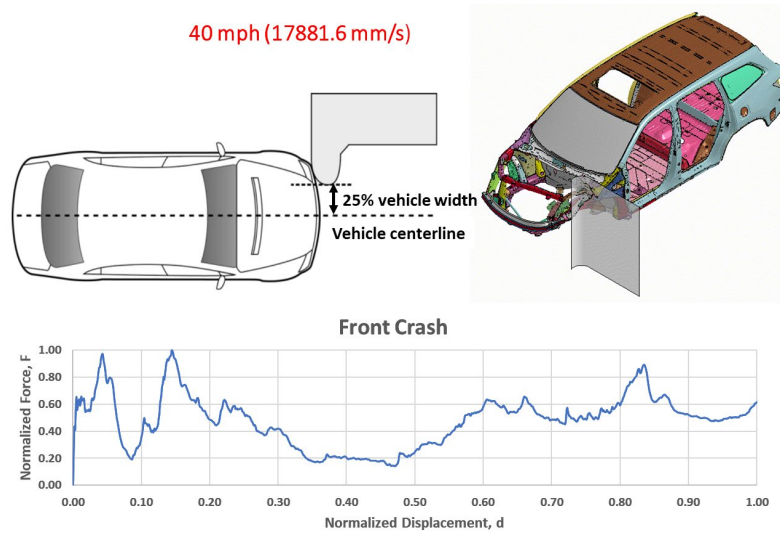


Figure II.4.2.1.12. Front-quarter-overlap impact simulation with non-linear material response to understand deformation behavior. Source: Clemson University.

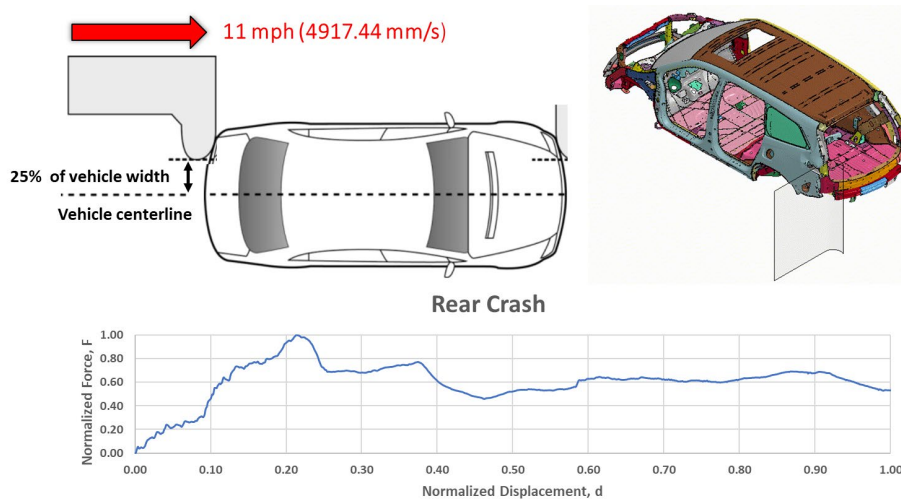


Figure II.4.2.1.13. Rear-quarter-overlap impact simulation with non-linear material response to understand deformation behavior. Source: Clemson University.

Machine Modifications for Metal-Composite Transition Joints Manufacturing

Three modifications have been made to target three primary bottlenecks in the ultrasonic additive manufacturing (UAM) process to reduce the cycle time of metal-composite transition joint fabrication in alignment with achieving cycle times consistent with those seen in automotive manufacturing. The improvements will be captured as a reduction in manufacturing cost of transition joints per unit length due to reduced cycle times. The first modification is the addition of a speed increaser to the computer numerical control system for UAM machines. A speed increaser has been procured that allows for faster machining of the metal-matrix channels within which the fiber material is embedded. The second modification is the development of a fiber alignment device for placement of the fibers in the metal-matrix channels. Three fiber alignment device prototypes have been developed that have identified the primary issue of fiber sticking to the device upon removal from the sample. The third modification involves the addition of a runway welding surface to the table for the UAM machine. The runway increases the maximum possible transition joint length from 14-in. to 52-in. The runway is also targeted to reach a baseplate preheat temperature of 500–600°F, more than 100°F higher than the current welding surface. A higher temperature allows for easier welding of stiff materials like steel. An extensive thermal and structural FEM has been conducted to determine a design capable of reaching the temperature target. The proposed machine modifications are as illustrated in Figure II.4.2.1.14.

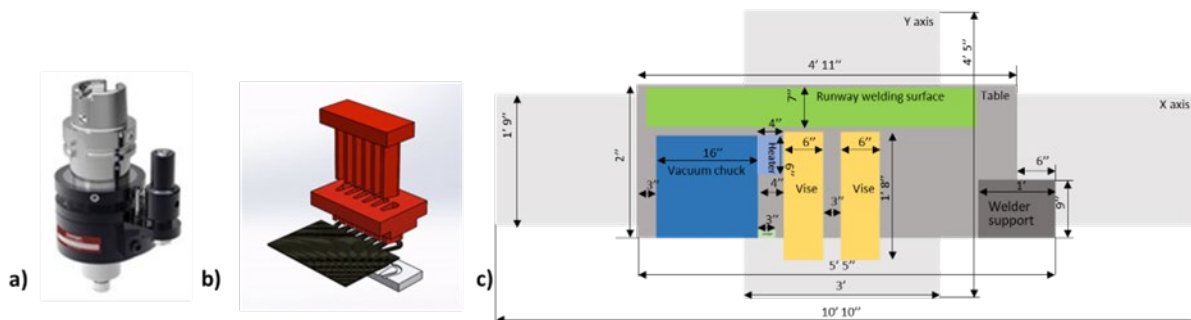


Figure II.4.2.1.14. UAM process modifications: (a) the spindle-speed increaser, (b) the fiber alignment device, and (c) the runway welding surface. Source: The Ohio State University.

The modifications were implemented, and a time study was performed to quantify the benefits. As a result of the modifications the following enhancements were observed:

- Maximum transition joint length increased from 14-in. to 52-in. with heating capabilities up to 500°F.
- Spindle-speed increased from 8,000–36,000 revolutions per minute. This corresponds to a 10× decrease in channel machining time.
- Estimated transition joint throughput increases from 1.33-in./hr. to 5.20-in./hr.

The machine modifications implemented on the UAM setup are shown pictorially in Figure II.4.2.1.15.

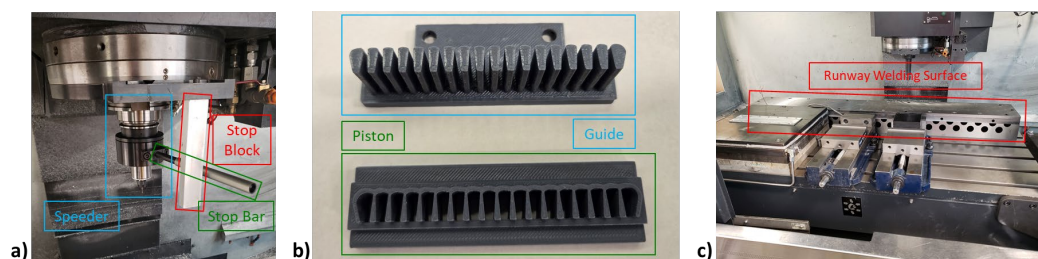


Figure II.4.2.1.15. UAM implemented modifications: (a) the spindle-speed increaser, (b) the fiber alignment device, and (c) the runway welding surface. Source: The Ohio State University.

Metal-Composite Transition Joint Modeling

A highly accurate, yet computationally friendly, model of the joint was developed by segmenting the joint into fiber-only, metal-only, and hybrid regions. The fiber- and metal-only regions were defined using material cards from the literature, while the hybrid region was defined according to stress-strain analyses. This “generalized” transition joint model was validated against a series of experimental tests, as seen in Figure II.4.2.1.16. These results show the generalized model provides a sufficiently accurate representation of the transition joint and can be passed directly into the multimaterial simulations to represent the transition joint.

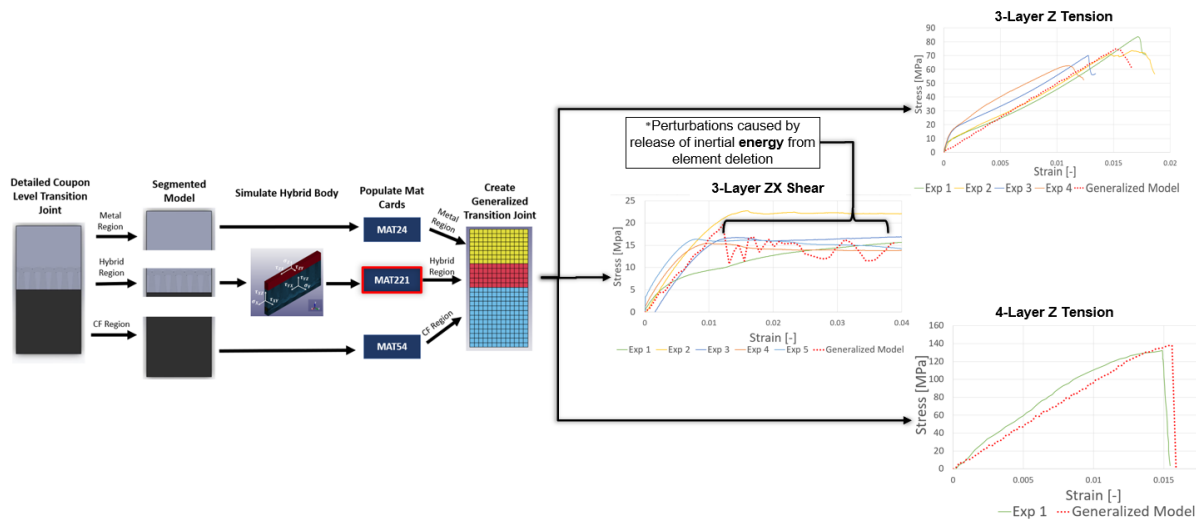


Figure II.4.2.1.16. Methodology for coupon-level simulations to develop, calibrate, and validate the MAT 221 material card using experimental results for the CFRP-Al transition joint [6]. Source: Clemson University.

Metal-Composite Transition Structure Development

To validate the generalized model of the transition joint can be incorporated into the full-body simulations, a series of simulations on complex geometries that incorporate the transition joint will be run. These simulations will ensure the generalized model is sufficiently accurate and computationally inexpensive when tested in practical scenarios like the glider. Following the successful development and validation of the MAT 221 material card for the transition joint, use of this card is being validated at various component length scales. Thus, a subcomponent-level study is being undertaken where the material card will be used for a composite C-section welded to an Al skin via transition joints along its flanges. Both structures incorporate metal-only and CF-only regions, as well as a transition joint. Additionally, certain metal components of the structures are joined using RSW. The C-section will be used for compressive loading and four-point bending validation, while the double-hat structure will be used for twisting validation, as observed in Figure II.4.2.1.17.

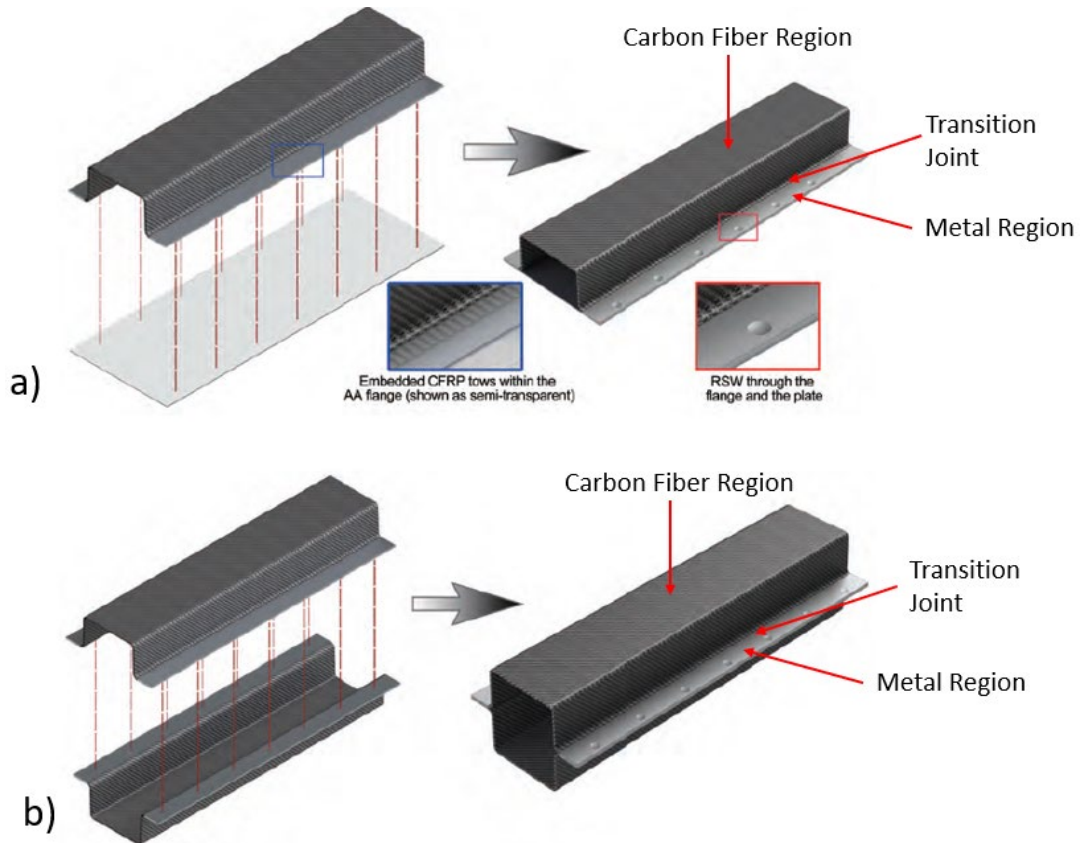


Figure II.4.2.1.17. Complex geometries to be used for transition joint validation. (a) Top-hat section. (b) Double-hat structure. Source: Clemson University.

The simulated load case mimics the experimental setup for the C-section subjected to four-point bending loads. The force vs. displacement curve generated from the simulation are compared with the experimental curve. Currently, the simulated model exhibits similar behavior up until a flexural displacement of 10 mm, after which the simulation exhibits a deviation from experimental results, as seen in Figure II.4.2.1.18. This deviation is currently under investigation and the simulation setup and FEM are being modified to achieve better correlation with the experimental results.

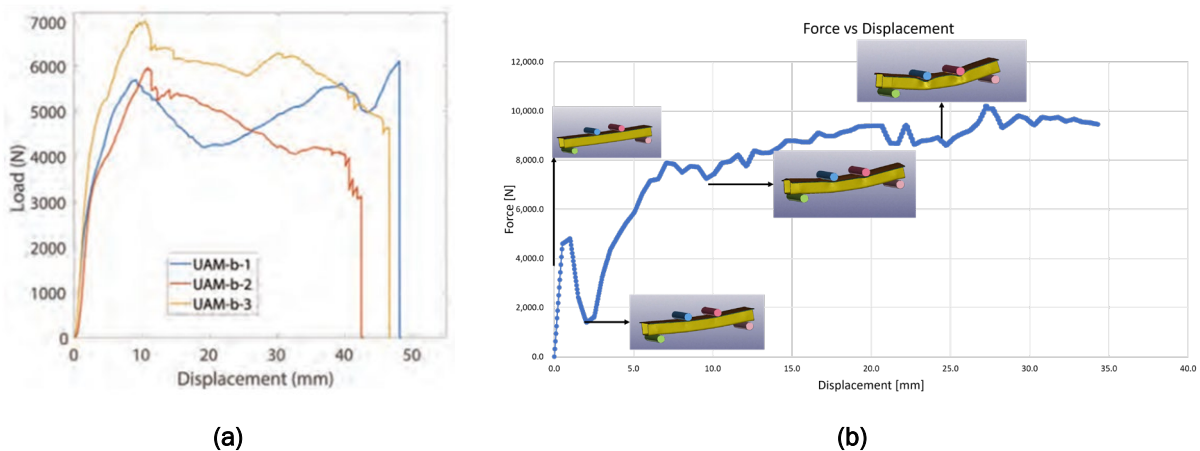


Figure II.4.2.1.18. (a) Experimental force vs. displacement for four-point bending [7]. (b) Simulated experimental force vs. displacement for four-point bending. Source: Clemson University.

Metal-Composite Transitions Fabrication

In addition to development of CFRP-metal transition joints, use of other fiber types such as Kevlar as an intermediate layer between the CF and Al, has been demonstrated to meet the joining requirements. The primary motivation for this investigation was the mitigation of galvanic corrosion between the CF and Al. Currently, glass fiber (GF) is being investigated as a potential option to not only mitigate corrosion but ensure material continuity for the plies proposed to be made from GFRP. Consequently, it is possible to utilize cost-effective GF layers within the component ply stack-up in combination with CF. Figure II.4.2.1.19 illustrates the layout of the cross-section of a woven electrical glass GF-Al transition and its fabrication. Mechanical testing of coupons is currently underway.

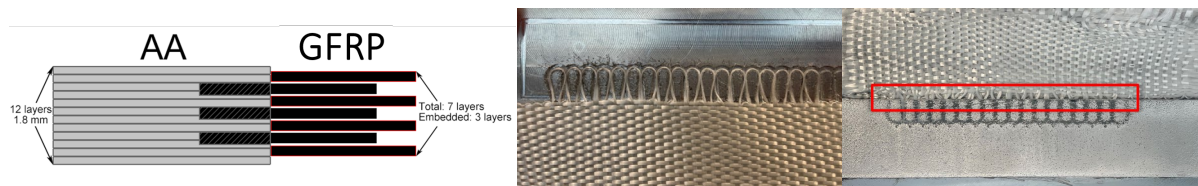


Figure II.4.2.1.19. Fabrication of GF-Al transitions. Source: Source: The Ohio State University.

Conclusions

In conclusion, the overall efforts have been focused on three specific domains:

- The development, assessment, and refinement of CAD concepts with optimization methodologies being employed to ensure alignment of the designs with project objectives.
- The development of a material card and its validation at various length scales—coupon, subcomponent, and assembly level—with the subcomponent-level study currently underway.
- The evaluation of other fiber types for use in the transition joints, leveraging analytical models [8] to down-select feasible options followed by experimental testing of fabricated coupons.

Subsequent efforts will be focused on testing these fabricated GF-metal transitions and employing a similar material card development methodology as the one successfully conceived and demonstrated for CF-Al transitions. Furthermore, design-for-manufacturability studies leveraging the use of draping and RTM simulations will be utilized to predict and design for manufacturing-induced defects. This microstructure will be mapped onto the existing FEM and a coupled structural analysis will be performed, thus capturing the process-structure-property relations at a subcomponent-level.

Key Publications

1. Deshpande, A. M., R. Sadiwala, N. Brown, S. A. Pradeep, L. M. Headings, N. Zhao, B. Losey, R. Hahnen, M. J. Dapino, G. Li, and S. Pilla, 2022, “Design and development of a multimaterial, cost-competitive, lightweight mid-size sports utility vehicle’s BIW,” *CAMX 2022*, 17–20 October 2022, Anaheim, CA, USA. <https://doi.org/10.33599/nasampe/c.22.0148>.
2. Deshpande, A. M., R. Sadiwala, N. Brown, P.-Y. Lavertu, S. A. Pradeep, L. M. Headings, N. Zhao, B. Losey, R. Hahnen, M. J. Dapino, G. Li, and S. Pilla, 2023, “Design optimization of a multimaterial, fiber-reinforced composite-intensive BIW of a mid-size SUV,” *CAMX 2023*, 30 October–2 November 2023, Atlanta, GA, USA. <https://doi.org/10.33599/nasampe/c.23.0169> (**Selected as Outstanding Technical Paper at CAMX 2023**).

References

1. Lawrence Livermore National Laboratory, 2021, “Flowcharts,” Available at: <https://flowcharts.llnl.gov/> (last accessed 23 May 2023).

2. Lawrence Livermore National Laboratory, 2021, “Carbon flow charts | Flowcharts,” Available at: <https://flowcharts.llnl.gov/commodities/carbon> (last accessed 23 May 2023).
3. DOE, 2014, “Lightweight materials for cars and trucks,” Available at: <https://www.energy.gov/eere/vehicles/lightweight-materials-cars-and-trucks> (last accessed 23 May 2023).
4. Bhardwaj, B. P., 2014, *The Complete Book on Production of Automobile Components & Allied Products*. NIIR Project Consultancy Services, Delhi, India.
5. Deshpande, A. M., R. Sadiwala, N. Brown, S. A. Pradeep, L. M. Headings, N. Zhao, B. Losey, R. Hahnen, M. J. Dapino, G. Li, and S. Pilla, 2022, “Design and development of a multimaterial, cost-competitive, lightweight mid-size sports utility vehicle’s BIW,” *CAMX 2022*, 17–20 October 2022, Anaheim, CA, USA. <https://doi.org/10.33599/nasampe/c.22.0148>.
6. Deshpande, A. M., R. Sadiwala, N. Brown, P.-Y. Lavertu, S. A. Pradeep, L. M. Headings, N. Zhao, B. Losey, R. Hahnen, M. J. Dapino, G. Li, and S. Pilla, 2023, “Design optimization of a multimaterial, fiber-reinforced composite-intensive BIW of a mid-size SUV,” *CAMX 2023*, 30 October–2 November 2023, Atlanta, GA, USA. <https://doi.org/10.33599/nasampe/c.23.0169>.
7. H. Guo, M. B. Gingerich, L. M. Headings, R. Hahnen, and M. J. Dapino, 2019, “Seamless joining of carbon fiber and aluminum using UAM,” *Compos. Struct.*, 208, 180–188. <https://doi.org/10.1016/j.compstruct.2018.10.004>.
8. Zhao, N., H. Guo, L. M. Headings, and M. J. Dapino, 2023, “Analytical and computational modeling of FRP-metal joints made by UAM,” *ASME Int. Mech. Eng. Congress Expo, Vol. 2A: Adv. Manuf.*, IMECE2022-96827. <https://doi.org/10.1115/IMECE2022-96827>.

III Crosscutting Activities

III.1 Lightweight Materials Crosscutting

III.1.1 Updated Analysis of the Relationship Between Light-Duty Vehicle Mass, Footprint, and Societal Fatality Risk per Vehicle Mile of Travel (Lawrence Berkeley National Laboratory)

Tom Wenzel, Principal Investigator

Lawrence Berkeley National Laboratory
Environmental Technologies Area
90R2002
1 Cyclotron Rd
Berkeley, CA 94720
E-mail: tpwenzel@lbl.gov

Jerry Gibbs, DOE Technology Development Manager

U.S. Department of Energy
E-mail: Jerry.Gibbs@ee.doe.gov

Start Date: October 1, 2022

End Date: September 30, 2023

Project Funding: \$107,226

DOE share: \$107,226

Non-DOE share: \$0

Project Introduction

One approach to reduce fuel consumption in LD vehicles is to reduce their mass while maintaining their footprint (i.e., track width times wheelbase). However, there is concern that lightweighting vehicles will reduce their ability to protect their occupants in a crash and may lead to an increase in fatalities. This project will explore whether the relationship between vehicle weight/size and societal fatality risk in LD vehicles has changed since the previous analysis completed in 2018 [1]. This information will be critical to the National Highway Transportation Safety Administration (NHTSA) and the EPA when they consider whether to change the current fuel economy/greenhouse gas emission standards for model year (MY) 2027 and later LD vehicles.

Objectives

The objective of the study is to use recent historical data to better understand the relationship between vehicle weight and size (i.e., footprint, or track width times wheelbase) and societal fatality risk (i.e., risk to occupants of the subject vehicle and other crash partners) per mile driven, after accounting for other vehicle attributes, (i.e., four-wheel drive, antilock braking and electronic stability control systems, number and type of airbags, etc.), driver characteristics (i.e., gender and age), and crash circumstances (i.e., in rural counties, high-speed roads, high-fatality states) that can influence crash frequency and severity.

Approach

The Lawrence Berkeley National Laboratory (LBNL) 2018 Phase 1 study [1] was used to estimate the percentage of mass reduction that can be considered without compromising occupant safety in the 2018 Final Determination/Rule. The results of the updated analysis can be applied in the NHTSA Volpe Model and the EPA Optimization Model for Reducing Emissions of Greenhouse Gases from Automobiles (OMEGA) Model to estimate the percentage of mass reduction that can be considered without compromising occupant safety as part of future rulemakings. The 2018 Phase 1 study included model year 2004 to 2011 vehicles between calendar years 2006 and 2012; the current project will update the analysis to include 2010 to 2017 vehicles between calendar years 2012 and 2018.

The methodology used to conduct the analysis is complicated and makes use of data from several sources. LBNL will seek to collaborate with staff at the EPA and NHTSA to update the data used for the revised

analysis, as several components require data from NHTSA. However, if collaboration is not possible, LBNL will undertake additional steps to create the two databases required for the update.

Results

In FY 2021, LBNL downloaded and analyzed the annual national Fatality Analysis Reporting System (FARS) databases compiled by NHTSA for all fatal crashes in the U.S. between 2012 and 2018, which will be used to identify case vehicles from model years 2010 to 2017 that were involved in fatal crashes. Figure III.1.1.1 indicates that the data used in the previous analysis (shown in green) is more heavily weighted towards older vehicles ages six to eight years old, whereas the data for the current analysis (shown in blue) is more evenly distributed across all vehicle ages.

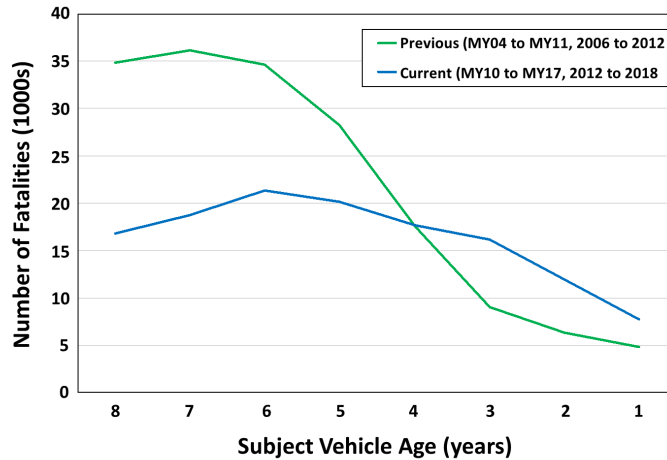


Figure III.1.1.1. Distribution of case vehicles by age from previous and current analysis. Source: NHTSA FARS.

Figure III.1.1.2 compares the distribution of all one- to six-year-old case vehicles involved in fatal crashes by case vehicle type from the previous analysis and the current analysis. There are nearly twice as many case crossover utility vehicles (CUVs) involved in fatal crashes in the current analysis (16%) than in the previous analysis (8%), while the fraction of case vehicles that are light trucks has declined since the previous analysis (from 16% to 11% for small pickups, and from 10% to 5% for truck-based SUVs).

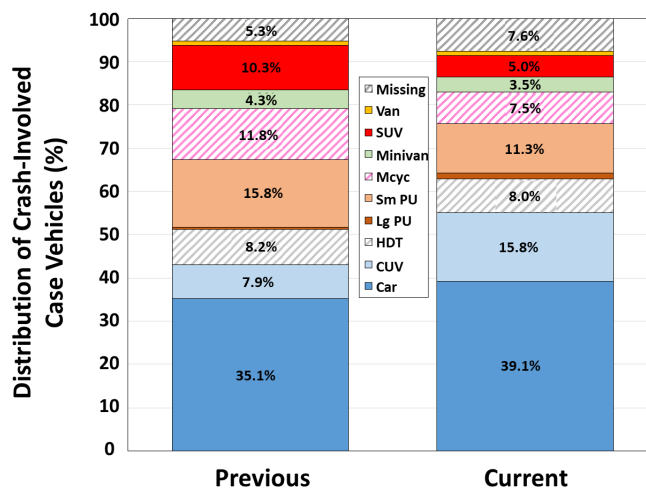


Figure III.1.1.2. Distribution of case vehicles by type from previous and current analysis. Source: NHTSA FARS.

LBNL finished obtaining data on all police-reported crashes from several states, which will be used to develop the induced exposure dataset of non-culpable vehicles and their drivers and used to estimate the number of miles driven by vehicle/driver combinations. LBNL obtained and processed the data for ten states—Florida, Kansas, Maryland, Michigan, Missouri, New Jersey, Pennsylvania, Washington, Wisconsin, and Wyoming—that were used in the previous analyses; two states from the previous analyses (Alabama and Kentucky) no longer provide crash data, including vehicle identification number (VIN). LBNL obtained data on police-reported crashes from two new states (Georgia and Texas) that now provide crash data, including VIN. In FY 2023, LBNL received data from the last state used in the previous analysis (Nebraska).

LBNL obtained additional annual odometer readings from the Texas Department of Public Safety and Texas Council of Environmental Quality, through mid-2023, and analyzed annual vehicle miles of travel by vehicle type, model year, and model. These data will be used to develop the vehicle miles traveled schedules by vehicle type (e.g., passenger cars and LD trucks) and age, as well as the relative weights for specific vehicle models for the current project.

In late FY 2023, LBNL received certification data from the EPA on vehicle attributes, including curb weight, wheelbase, track width, drivetrain, engine characteristics, and safety features for model years 2012 through 2017. These data will be merged with the registration, crash, and vehicle miles traveled data to assign vehicle characteristics by VIN to individual vehicles in each of those datasets. Table III.1.1.1 indicates that the average curb weight between model years 2012 and 2017 increased about 11% for all vehicle types, and that the average footprint increased 4% for 2-door cars, 3% for minivans, and 2% for 4-door cars, and was essentially unchanged for other vehicle types.

Table III.1.1.1. Average Curb Weight and Footprint for Model Year 2012 and 2017 Vehicles by Vehicle Type. Source: EPA

Vehicle Type	Average Curb Weight			Average Footprint		
	MY2012	MY2017	Difference	MY2012	MY2017	Difference
2-door car	3,241	3,616	12%	43.1	44.7	3.8%
4-door car	3,292	3,635	10%	45.5	46.4	2.0%
Pickup	5,051	5,485	9%	64.3	64.7	0.5%
SUV	5,032	5,581	11%	51.1	51.0	0.0%
CUV	4,094	4,559	11%	48.4	48.2	-0.4%
Minivan	4,534	5,097	12%	54.8	56.4	3.0%
2D Car	3,241	3,616	12%	43.1	44.7	3.8%

Finally, LBNL continued discussions with Experian to obtain vehicle registrations by calendar year, vehicle year, and model for the 13 states to be used in the analyses. These data will be used to assign national vehicle registration weights to each induced exposure vehicle in the police-reported crash data in the 13 states. LBNL negotiated an amendment to an existing interagency agreement with the EPA to purchase national vehicle registration data at the county level from Experian for 2012 through 2021. The purchase of these data has been delayed a year while LBNL negotiates a purchase agreement with Experian. We anticipate that the agreement will be approved and the data purchased in the first quarter of FY 2024.

Conclusions

Data are still being gathered to update the analysis of the relationship between vehicle weight/footprint and societal fatality risk. Substantial changes in the composition of the on-road fleet by vehicle type, and the number of fatalities by crash type, suggest that the relationship between vehicle weight/footprint and safety may have changed since the previous analysis.

References

1. Wenzel, T. P., 2018, Assessment of NHTSA's Report "Relationships Between Fatality Risk, Mass, and Footprint in Model Year 2004-2011 Passenger Cars and LTVs" (LBNL Phase 1). LBNL-2001137, Lawrence Berkeley National Laboratory, Berkeley, CA, USA.

Acknowledgements

LBNL is grateful for the assistance provided by various agencies in several states in obtaining the data necessary to update the previous analysis of the relationship between vehicle weight/size and safety, including: the agencies responsible for police-reported crash reporting in Florida, Georgia, Kansas, Maryland, Michigan, Missouri, Nebraska, New Jersey, Pennsylvania, Texas, Washington, Wisconsin, and Wyoming; the Texas agencies responsible for annual safety and emission inspections, Texas Department of Public Safety and Texas Council of Environmental Quality and their contractor Gordon-Darby, Inc.; and staff at EPA who provided who provided datasets of attributes for model year 2012 through 2017 vehicles.

(This page intentionally left blank)

U.S. DEPARTMENT OF
ENERGY

Office of
**ENERGY EFFICIENCY &
RENEWABLE ENERGY**

For more information, visit:
energy.gov/vehicles

DOE/EE-2880 August 2024